DOCTOR OF SCIENCES

Constraints on the formation and the timing of supergene manganese deposits
New insights from geodynamics in Europe and North Africa

Dekoninck, Augustin

Award date:
2019

Awarding institution:
University of Namur

Constraints on the formation and the timing of supergene manganese deposits

New insights from geodynamics in Europe and North Africa

Augustin DEKONINCK

Thesis submitted in fulfillment of the requirements for the degree of Doctor of Sciences

Faculty of Sciences – Department of Geology
University of Namur, Namur, Belgium

August 2019

Collaborators

Cover design : © Presses universitaires de Namur
Cover picture : « Galerie 63 », Bou Arfa mine, Morocco by Gaëtan Rochez (2014)

Printed in Belgium
ISBN: 978-2-39029-064-3
Legal deposit: D/2019/1881/19

“Natural resources are not like a finite number of gifts under the Christmas tree. Nature is given, but resources are created”

Alex Tabarrok – Economist

Author

Augustin DEKONINCK
Department of geology
University of Namur
Namur
Belgium

Thesis Committee

Prof. Dr Johan YANS – supervisor
Department of Geology
University of Namur – Belgium

Prof. Dr Vincent HALLET – president
Department of Geology
University of Namur – Belgium

Prof. Dr Alain BERNARD
Department of geosciences,
environment and society
University of Brussels – Belgium

Prof. Dr Jocelyn BARBARAND
Department of Earth sciences
University of Paris South – France

Prof. Dr Mohammed BOUABDELLAH
Faculty of sciences
University Mohammed I – Morocco

Dr Simon PHILIPPO
National Museum of Natural History – Luxembourg

Prof. Dr Paulo VASCONCELOS
School of Earth and Environmental Sciences
University of Queensland - Australia

Parts of this thesis are based on the following published, accepted and submitted papers:

Dekoninck, A., Bernard, A., Barbarand, J., Saint-Bézar, B., Missenard, Y., Leprêtre, R., Saddiqi, O., Yans, J., 2016a. Detailed mineralogy and petrology of manganese oxyhydroxide deposits of the Imini district (Morocco). Mineralium Deposita 51, 13–23. https://doi.org/10.1007/s00126-015-0590-3

Dekoninck, A., Leprêtre, R., Saddiqi, O., Barbarand, J., Yans, J., 2016b. The High-Grade Imini Manganese District—Karst-Hosted Deposits of Mn Oxides and Oxyhydroxides, in: Bouabdellah, M., Slack, J.F. (Eds.), Mineral Deposits of North Africa. Springer International Publishing, Cham, pp. 575–594.

Dekoninck, A., Moussi, B., Vennemann, T., Jamoussi, F., Mattielli, N., Decrée, S., Chaftar, H.-R., Hatira, N., Yans, J., 2018. Mixed hydrothermal and meteoric fluids evidenced by unusual H- and O-isotope compositions of kaolinite-halloysite in the Fe(-Mn) Tamra deposit (Nefza district, NW Tunisia). Applied Clay Science 163, 33–45. https://doi.org/10.1016/j.clay.2018.07.007

Dekoninck, **A**., Monié, P., Blockmans, S., Hatert, F., Rochez, G., Yans, J., accepted with revisions. Genesis and $^{40}Ar/^{39}Ar$ dating of K-Mn oxides from the Stavelot Massif (Ardenne, Belgium): insights on Oligocene to Pliocene weathering periods. Ore Geology Reviews.

Dekoninck, A., Ruffet, G., Missenard, Y., Parizot, O., Magoua, M., Rochez, G., Yans, J. submitted. Multistage genesis of the late Cretaceous Mn(-Pb) Tasdremt deposits evidenced by petrographic analysis and $^{40}Ar/^{39}Ar$ dating of K-Mn oxides (Souss Basin, Morocco): a lateral equivalent of the Imini ores. Mineralium deposita.

Demoulin, A., Barbier, F., **Dekoninck, A.**, Verhaert, M., Ruffet, G., Dupuis, C., Yans, J., 2018. Erosion Surfaces in the Ardenne–Oesling and Their Associated Kaolinic Weathering Mantle, in: Demoulin, A. (Ed.), Landscapes and Landforms of Belgium and Luxembourg. Springer International Publishing, Cham, pp. 63–84. https://doi.org/10.1007/978-3-319-58239-9_5

Leprêtre, R., Missenard, Y., Saint-Bézar, B., Barbarand, J., Delpech, G., Yans, J., **Dekoninck, A.**, Saddiqi, O., 2015. The three main steps of the Marrakech High Atlas building in Morocco: Structural evidences from the southern foreland, Imini area. Journal of African Earth Sciences 109, 177–194. https://doi.org/10.1016/j.jafrearsci.2015.05.013

Abstract

The interactions between the meteoric agents and the lithosphere transform “fresh” rocks (“protores”) into weathered rocks (“alterites”). Among many factors influencing the weathering of rocks, climate carries the water (fluids) input and determines the kinetics of the chemical reactions, whereas geodynamics allows rocks to be exposed to meteoric agents. The development of weathering profiles in the supergene zone of manganiferous protores produces Mn oxides and increases the grade of several metals within the ore. The detailed mineralogical, geochemical and petrological characterization of these supergene ores is therefore of paramount importance to evaluate their economic potential. The occurrence of K-bearing Mn oxides, belonging to the hollandite supergroup, within this oxidation zone, enables the dating of the supergene processes by using the K-Ar and $^{40}Ar/^{39}Ar$ radiometric methods. Nowadays, the interpretation of these ages is often attributed to favorable climatic periods, probably diminishing the contribution of an essential geodynamics component. Therefore, this thesis has three main objectives: (1) determining the genesis and metallogenesis of the supergene Mn ores in these complex systems; (2) identifying the ore-forming parameters in order to understand the origin of these deposits; and (3) positioning the K-Mn oxides within the crystallization sequences in order to date them. Four sampling areas have been selected to address these issues: (1) the weathering zone of Mn veins in the Vosges (France); (2) the weathering crust of Mn-rich Ordovician slates in the Stavelot massif (Ardenne, Belgium); (3) the karst-hosted deposits in the Imini-Tasdremt district (High Atlas, Morocco); and (4) the mixed hydrothermal-supergene Fe-Mn deposit of Tamra (Tunisia). Vein type deposits produce limited K-Mn oxides, which is probably due to the presence of barite in the protore that favors the formation of hollandite *sensu stricto*. The K-rich phyllosilicates in the weathering crust of sedimentary protores easily recombine with the released Mn to precipitate cryptomelane. The precipitation of Mn in karst-hosted deposits in the Imini-Tasdremt area involves a joint increase of the pH and the Eh, favoring the formation of coronadite, hollandite and cryptomelane, which are probably formed beyond meteoric temperatures. Given the K-Ar and $^{40}Ar/^{39}Ar$ dating of these K-Mn oxides, karst-hosted deposits in the Imini area (Morocco), which are relatively isolated from the climatic influence, favor the expression of the geodynamics component. Such correlation is particularly well illustrated between the ages and the first two steps of the Atlas deformation. These phases, Late Eocene on the one hand and Early Miocene on the other hand, are accompanied by massive pyrolusite mineralization, providing to the Imini ore a high grade. The other weathering products make the geodynamic interpretation on the age record difficult, given the pervasive influence of the climatic component. However, such correlation is suggested in the Stavelot Massif, where the oldest ages obtained in the saprolite correspond to the late Oligocene doming in the Ardenne. The erosion and the weak vertical extension of the weathering zone in the Vosges deposits make this connection unclear. In addition, the hydrothermal contribution on the formation of the Fe-Mn Tamra deposit makes any supergene contribution difficult to recognize. Consequently, karst-hosted Mn mineralization and/or Mn accumulations located in slightly uplifted zones (doming, foreland basins) seem to be the most suitable sites to investigate the geodynamic effect on supergene processes.

Résumé

Les interactions entre les agents météoriques et la lithosphère transforment des roches-mères (« protolithes ») en roches altérées (« altérites »). Parmi de multiples facteurs influençant l'altération météorique des roches, le climat assure l'apport de fluides et détermine la cinétique des réactions chimiques, alors que la géodynamique permet aux roches d'être exposées aux agents météoriques. À partir de protolithes manganésifères, le développement de profils d'altération dans la zone supergène génère de nombreux oxydes de Mn et augmente la concentration en plusieurs métaux. La caractérisation détaillée de ces minerais supergènes, au niveau minéralogique, géochimique et pétrographique, est dès lors indispensable afin d'évaluer leur potentiel économique. Au sein de cette zone oxydée, la présence d'oxydes de Mn riches en K, appartenant au groupe de la hollandite, permet la datation de ces processus par les méthodes radiométriques K-Ar et $^{40}Ar/^{39}Ar$. L'interprétation de ces âges est, aujourd'hui, souvent attribuée à des périodes climatiques favorables, réduisant probablement la contribution d'une composante géodynamique pourtant essentielle. Dès lors, cette thèse poursuit trois principaux objectifs : (1) déterminer la genèse des minerais supergènes de manganèse et leur métallogénie dans ces systèmes complexes ; (2) identifier les paramètres de formation de ces dépôts pour comprendre leur origine ; et (3) positionner les oxydes de Mn potassiques dans les séquences de cristallisation afin de dater les processus d'altération. Quatre régions sont étudiées pour examiner ces questions : (1) la zone d'altération de veines manganésifères dans les Vosges (France) ; (2) la croûte d'altération de schistes ordoviciens riches en Mn dans le massif de Stavelot (Ardenne, Belgique) ; (3) les gisements d'origine karstique du district d'Imini-Tasdremt (Haut Atlas, Maroc), et (4) le gisement de Fe-Mn d'origine mixte de Tamra (Tunisie). Les veines minéralisées semblent produire de faibles quantités d'oxydes de Mn potassiques, ce qui est probablement lié à la présence de baryte au sein de la gangue primaire, favorisant la formation de hollandite *sensu stricto*. En revanche, l'occurrence de phyllosilicates riches en K dans la croûte d'altération de protolithes sédimentaires facilite la précipitation du cryptomélane. L'augmentation conjointe du pH et du potentiel Eh est à l'origine de l'accumulation de Mn dans les dépôts de type karstique de la région d'Imini-Tasdremt, permettant la précipitation de coronadite, hollandite et cryptomélane à des températures probablement supérieures à celles de fluides météoriques. À la lumière des datations K-Ar et $^{40}Ar/^{39}Ar$ des oxydes de Mn potassiques, les gisements d'origine karstique de la région d'Imini (Maroc), relativement isolés de l'influence climatique, favorisent l'expression de la composante géodynamique. Ceci se traduit par une corrélation entre ces âges et les deux premières phases de surrection de l'Atlas. Ces phases, Éocène supérieur d'une part et Miocène inférieur d'autre part, sont accompagnées de minéralisations massives de pyrolusite donnant au district d'Imini un minerai très riche en Mn. Les autres types d'altérations rendent difficile la perception de la géodynamique dans l'enregistrement des âges, en raison des interactions avec la composante climatique. Néanmoins, cette connexion avec la géodynamique est suggérée dans le massif de Stavelot, où les âges les plus anciens de la saprolite correspondent au début du soulèvement de l'Ardenne (Oligocène supérieur). Ce lien est plus ténu dans les Vosges du fait de l'érosion et de la faible extension verticale de la zone d'altération météorique. Par ailleurs, l'altération hydrothermale rend délicate toute interprétation relative à la contribution supergène dans le gisement de Fe-Mn de Tamra. En conséquence, les minéralisations de type karstique et/ou les accumulations situées dans des zones faiblement soulevées (dôme, bassin d'avant pays) semblent constituer des sites privilégiés pour percevoir l'effet de la géodynamique sur les processus supergènes.

Remerciements

Ce travail est avant tout le fruit de nombreuses collaborations internationales engageant différents partenaires du domaine privé et d'organisations publiques, sans qui l'accès aux sites d'échantillonnages et au matériel analytique eu été impossible. Que soient remerciées toutes les personnes qui ont contribué de près ou de loin à l'élaboration de cette thèse.

J'adresse d'abord mes plus vifs remerciements à Johan Yans, promoteur de cette thèse, dont nous avons joui, tous deux, d'une confiance totale l'un envers l'autre, lui qui a toujours facilité ce parcours et montré l'exemple tant d'un point de vue scientifique que d'un point de vue humain, lui qui, sans se ternir d'une touche Belgo-Italienne, a continué une formation transversale durant plus de 6 années. Merci infiniment pour ces moments agréables et ces nombreuses discussions. À présent, tout est dit.

Je remercie chaleureusement les membres du Jury d'avoir donné de leur temps et manifesté un intérêt pour ces recherches qui, je l'espère, les ont autant passionnées que moi. Many thanks to Paulo Vasconcelos from the University of Queensland in Australia, for his constructive comments about this thesis and for sharing his knowledge in this fascinating field. Merci à Mohammed Bouabdellah, depuis Oujda au Maroc, d'avoir apporté un regard neuf et intéressé sur ces recherches dans ce magnifique pays qu'est le Maroc. C'est une rencontre que je n'oublierai pas. Merci à Jocelyn Barbarand pour ses remises en question permanentes qui ont grandement mené à la finalisation de ce manuscrit. Merci à Alain Bernard, dont j'ai pu bénéficier de l'expérience depuis 8 ans. Merci à Simon Philippo du Musée du Luxembourg pour la lecture du manuscrit. Finalement, je remercie Vincent Hallet d'avoir gouverné ce jury et centré les discussions sur les débats essentiels.

Dans la liste des personnes sans qui ce travail n'aurait été possible, se place en haut de la liste, Gaëtan Rochez, qui, bien plus qu'un technicien, a énormément contribué à la concrétisation de ce travail notamment dans l'acquisition des données de terrain au Maroc (surtout les logs), en Tunisie, en France, en Belgique et en laboratoire… C'est un réel bonheur de travailler, au quotidien, avec une personne aussi compétente et agréable (المائدة مفارش بائع).

À Gilles Ruffet de l'Université de Rennes qui, sans relâche, et toujours avec dévotion et persévérance, a montré l'entièreté de ses talents afin de collecter et décortiquer l'ensemble des spectres $^{40}Ar/^{39}Ar$ du district d'Imini-Tasdremt. Les discussions constructives, pleines de rebondissements et munies d'une certaine excitation ont toujours été très agréables. Elles ont

permis de construire un modèle métallogénique robuste et cohérent. Merci, Gilles, pour ces belles proses, inimitables.

J'adresse également mes plus sincères remerciements à Patrick Monié des Géosciences de l'Université de Montpellier pour m'avoir accueilli au sein de son laboratoire afin d'effectuer les datations des cryptomélane du massif de Stavelot et de m'avoir introduit dans les hautes sphères des argonautes. Merci également à Michaël et Delphine pour leur aide technique lors de la mise en marche du spectromètre. J'ai eu le plaisir de rencontrer de nombreuses personnes lors de mon passage et particulièrement mon voisin de bureau Tancredi Rumbolo, avec qui nous avons partagé d'agréables discussions.

Une thèse de doctorat au Maroc sans l'œil précis et aguerri d'une équipe de structuralistes est tout à fait impensable. C'est grâce à cette collaboration fructueuse avec l'Université Paris Sud Orsay dans un domaine si vaste et complexe que la chaîne de l'Atlas que cette thèse s'inscrit. Merci à Jocelyn Barbarand et Yves Missenard qui ont été au cœur des discussions sur le lien entre l'âge du manganèse d'Imini et Tasdremt et celui des déformations de l'Atlas. Rémi Leprêtre, Bertrand Saint-Bézar, Guillaume Delpêche, Benjamin Brigaud, Oriane Parizot, Ludovic Lafforgue, c'est un honneur d'avoir discuté avec vous sur le terrain et lors de nos réunions à Paris. Vous avez toute ma gratitude.

Je voudrais remercier mes collègues et amis marocains qui ont toujours su présenter leur Maroc comme une terre d'accueil et de découverte. Un pays incroyable avec des gens magnifiques. Merci à Omar Saddiqi de l'Université Hassan II (Casablanca) pour l'organisation des missions dans le Sud marocain. Merci chaleureusement (et le mot est faible) à Mohamed Magoua de l'Office National des Mines et des Hydrocarbures (ONHYM) pour son aide précieuse dans l'échantillonnage du gîte de Tasdremt et à Abdellah Mouttaqi pour son soutien logistique et scientifique en tant que secrétaire général de l'ONHYM. Merci à la SACEM et particulièrement à la direction de la mine d'Imini en messieurs A. Maali, A. Ait Bendra et K. Ait Ikken pour leur accueil et leur aide précieuse sur le terrain. Shukraan Bisef aux nombreux chauffeurs qui nous ont accompagné et aidé dans notre démarche, pour notre vocabulaire, limité, de l'arabe et du berbère, notamment via la société BAKABOU (Ahmed, Youssef, Abdallah, Brahim…). Merci également à Lhou Maacha et les collègues de MANAGEM pour d'autres escapades dans le sud marocain.

À l'autre bout du Maghreb, merci à mes collègues, tout aussi charmants et accueillants, de la Tunisie septentrionale. Merci à Fakher Jamoussi et Béchir Moussi du CERTE (Centre de Recherches et des Technologies des Eaux) d'avoir partagé leur connaissance de la Tunisie et d'avoir mis tout en œuvre pour faciliter nos collaborations. Merci pour ces repas quelque peu épicés. Mes plus sincères

remerciements vont à Ridha Chaftar et Nouri Hatira de l'Office National des Mines (ONM) pour leur soutien technique et scientifique dans la région de Nefza et plus particulièrement dans différents indices métalliques. Merci aux autres collaborateurs que j'ai eu le plaisir de côtoyer lors d'échanges en Belgique et en Tunisie (Oumaima Grine, Hajer Chargui, Walid Hajjajji, Emna Fakhfakh, Badrane Smida, et bien d'autres…).

Dans le volet sur les isotopes stables de l'oxygène et de l'hydrogène, je voudrais remercier Torsten Vennemann de l'Université de Lausanne en Suisse de m'avoir accueilli et initié aux analyses des isotopes stables au sein de son laboratoire. Merci également à Albert Gilg de l'Université de Munich pour cette discussion improbable au « Chapitre » de Namur sur l'interprétation des données isotopiques dans la région de Tamra. Merci à Sophie Decrée du Musée Royal des Sciences Naturelles de Belgique pour sa contribution et son prêt intemporel des échantillons de la région de Nefza.

Je remercie chaleureusement Nadine Mattielli de l'Université Libre de Bruxelles pour ces très chouettes moments passés au Maroc et tout le suivi des analyses isotopiques au sein de son laboratoire. Merci tout particulièrement à Zoé Pirson, Wendy Debouge et Jeroen de Jong d'avoir effectué ces analyses, souvent accompagnées de nombreux rebondissements. Merci à Alain Bernard qui avait initié nos travaux au Maroc à travers un mémoire, et d'avoir fait partie du comité d'accompagnement tout au long de ces 6 années. Je voudrais également remercier tous les autres collègues et étudiants de l'ULB avec qui j'ai pu partager de brefs instants.

Merci aux organismes publics pour leur soutien dans certains projets liés à cette thèse. Ces fonds sont indispensables afin d'effectuer une recherche scientifique de qualité. Merci au Service Public de Wallonie pour le soutien logistique et financier dans l'acquisition des données dans le massif de Stavelot. Merci au WBI (Wallonie-Bruxelles International) et leurs intervenants pour leur soutien au projet « Valorisation des argiles tunisiennes ». Certains fonds de mobilités ont également été obtenus grâce au soutien du Fonds National de la Recherche Scientifique (FNRS), notamment pour la valorisation de nos travaux lors de congrès internationaux, de déplacements au sein d'instituts scientifiques extérieurs et de missions à l'étranger. Merci à Politique Scientifique Fédérale Belge (Belspo ; projet BR/121/A3/PALEURAFRICA) pour le financement de missions au Maroc.

Merci à des personnes de tous horizons avec qui j'ai pu échanger des moments agréables tant personnels que scientifiques. Merci à Flavien pour son esprit d'analyse sur nos travaux en Belgique (et pas que sur les joueurs de football). Merci à Pierre Fluck pour son aide et son expérience dans les travaux menés dans les

Vosges. Merci aux collègues du BRGM (Julien, Robert, Jean-Yves) et de L'Université de Rennes 2 (Jessica, Yves) pour les projets futurs.

Petit, mais vaste pays qui regorge de scientifiques de renom. Merci à Maurice Célis et à André Lessuise d'Ardenne Coticule de nous avoir ouvert l'accès à la carrière du Thier del Preu et Regné dans le massif de Stavelot. Merci à Frédérique Hatert de l'Université de Liège de m'avoir permis de travailler sur certains échantillons de cryptomélane. Merci à mon collègue (et ami) François Fontaine (ULg) pour ses conseils dans le domaine de la diffraction aux rayons X. Je ne remercie pas Thierry Mortier (UMons) pour nos discussions sur les péridotites du Col de Haycot, mais bien pour ses malins conseils à déterminer les cépages alsaciens. Merci à Pieter L'Hoëst (KUL) pour l'acquisition des données de microsonde. Je remercie également Christian Dupuis pour les clichés de la mine de Tamra. Je suis aussi reconnaissant à bon nombre de collègues croisés lors de différents évènements.

En interne à l'UNamur, je remercie chaleureusement Corry et Caroline du service de microscopie électronique pour leur aide, leur amabilité et leur patience inestimable dans l'acquisition des données MEB-EDX. Merci à Johan Wouters, Nikolay Tumanov et Bernadette Norberg de l'Unité de chimie physique, théorique et structurale et de la Plateforme de Caractérisation Physico Chimique (PC2) de nous ouvrir l'accès à leur matériel de diffraction. Merci à Zineb Mekhalif, Sébastien et comparses de l'unité de chimie et d'électrochimie des surfaces, ainsi que Sarah de la cellule didactique de chimie pour l'accès au matériel de polissage. Merci aux membres de l'institut ILEE pour les moments de rencontres et de partages scientifiques. Merci à tous les collègues et amis que j'ai eu le plaisir de côtoyer lors de différentes formations, certificats, évènements, galas, soirées… Ce fut inoubliable.

Car force est de constater que c'est dans un cadre détendu que peut naître le meilleur de chacun de nous… Merci spécialement à Amaël (Couz) pour les moments d'égarements et de débats souvent teintés d'un brin de folie. Merci à Lorraine pour sa bonne humeur et le levé des logs dans la région de Tasdremt. Merci à Vincent Hallet pour son aura bienveillante qu'il a sur le département de géologie. Merci à Michèle pour « le retour de la goethite », j'ai hâte de connaître le dénouement… Merci à Sabine Blockmans pour ses conseils dans la région de Stavelot et la danse de la tique (définitivement très utile pour se débarrasser de ces sales bêtes). Merci à l'équipe de la « serre », Alan, Romain, Flore, Samantha, Louise, d'avoir partagé de nombreux moments fantastiques. Merci à Djan pour ses conseils musicaux et footballistiques… Merci aux amis géographes footeux et non-footeux pour les nombreux moments récréatifs à toute heure du jour (et de la nuit) : Nicolas, Sabine, Catherine, Jérémie, Élisabeth, Sébastien, Florence,

Delphine, Fabrice, Clotilde, Andy, Isabelle, Assane... Du haut de notre cabine de pilotage, nous avons survécu aux vents et marées. La tempête est maintenant passée. Place au beau temps et aux sifflements. Merci Corentin. Merci à tous mes compatriotes, Eden, Kévin, etc. de m'avoir donné la force de continuer.

Finalement, merci aux étudiants de géologie que j'ai eu le bonheur d'encadrer durant 6 années. Sans en oublier, merci à la cuvée 2014 (Alan, Helena, Sébastien, Benjamin et Caroline), 2015 (Alice, Diego, Melvin, Tom, Cécile, Robin, Anouk et Guillaume), 2016 (Théo, Camille, Benjamin, Quentin, Sophie, Romain, Alexis, Arnaud, Mathieu et Martin), 2017 (Basile, Julien, François, Timothy, Pierre-Yves, Émilie, Lancelot, Ghéreint), 2018 (Ismaël, Cyril, Alexandre²), 2019 (Xavier, Camille, Simon, Lucas, Gaëlle, Léonard, Coralie, Aurore, Romain et Martin) et futures (Guillaume, Gaëlle, Jean et Maxime).

Merci à mes parents, Jacques et Géraldine, mes frères, ma grand-mère, ma belle-famille, mes amis, pour leur soutien indirect et permanent.

À ma chère et tendre Marie, pour son soutien inconditionnel et d'accepter ce fabuleux métier d'aventurier. Merci pour la relecture très attentive de l'anglais ☺. *W.L.*

Table of contents

Chapter 1

Introduction

Chapter 1

Introduction

Throughout history, the major part of the economy of the world's nations has been driven directly or indirectly by the access to and the use of natural resources (i.e., Rossi and Deutsch, 2014; Sverdrup and Ragnarsdóttir, 2014; Yans and Dekoninck, this thesis, appendix I; 2016; Bustillo Revuelta, 2018). One of our society's biggest challenges over the next century is to provide adequate resources for civilization. Today, the world is heading towards a restricted access to the key resources used by humanity and these restrictions will have a profound impact on the world economies and the lifestyles of future generations. Therefore, the study of metal resources is essential during this transition period from fossil to renewable energies that we are facing today, given that societies will need to find more metals (Arrobas *et al.*, 2017) in a sustainable way. In this context, **metallogeny** plays a central role, from the processes that accumulate elements and commodities into orebodies to the developing exploration techniques that are used to find them. Establishing the composition of these natural occurrences (mineralogy and geochemistry) is important for the processes that transform the resources and redistribute them with the accompanying risks of environmental contamination, threats to human health and social issues.

Nowadays, the main produced metals can be grouped into the so-called "big six": iron (Fe), aluminum (Al), copper (Cu), **manganese (Mn)**, chromium (Cr) and zinc (Zn; ►Fig. 1.1; Sverdrup and Ragnarsdóttir, 2014). Precious (gold, silver and platinum group metals) and other metals are also important for steel (Nb, V, Ni, Mo), technologies (Ta, Zr, In, Ga, Ge, Au, Ag), new technological developments in the renewable energy industry (Eu, Tb, Nd, Li), and the chemical industry (PGM[1], Co, REEs[2]; Sverdrup and Ragnarsdóttir, 2014).

Many people would be aware that steel is made of iron, but far fewer know that it is always partly made of **manganese**. Although the amount of manganese used to make a ton of steel is small, it is as essential as iron to produce this fundamental building block of modern societies. The major interest of manganese in the steel industry is given by its key role in various **steelmaking processes** (e.g., elimination of O and S). That is why 90% of the manganese production goes into steel industries as an alloying element (International Manganese Institute, 2014). Its role in the world market is also important notably for the production of portable batteries, agricultural fungicides, electronic circuit boards or aluminum cans among others.

[1]Platine group metals
[2]Rare earth elements

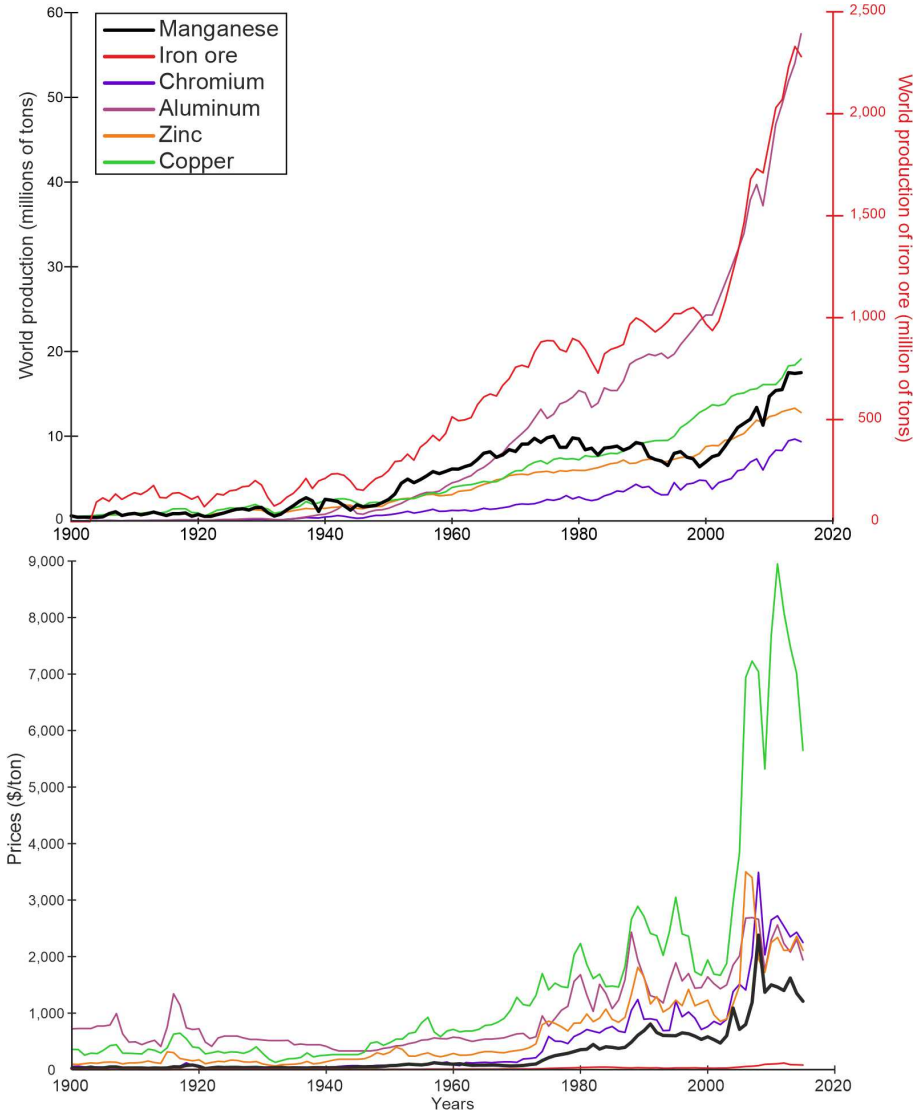

►**Fig. 1.1** Historical world production and prices of the main metals ("big six") from 1900 to 2015. Manganese is shown in black (U.S. Geological Survey, 2014). Note that the production of iron is by far higher (~100) than other metals and not at scale with other commodities.

1.1 Challenges in metallogeny

Since the famous book, *De Re Metallica* (*"on the nature of metals"*) written by Georgius Agricola in 1556 (Agricola, 1556), who has made a state of the art of prospection and mining at that time, the study of metals naturally occurring in rocks and minerals has evolved to currently reach a high degree of excellence. These studies

are compiled in many scientific journals around the world (e.g., Economic Geology, Mineralium Deposita, Ore Geology Reviews, etc.).

Formerly, **metallogeny** (*sensu* de Launay, 1913) dealt with the distribution of metallic deposits in geological time and space. The contemporaneous metallogeny is essentially an extension of regional geochemistry applied to anomalous metal accumulations in various geological settings. It appeared that these resources were not evenly distributed or isolated in the Earth crust, but belonged to "**metallogenic provinces**" forming, for a given (association of) element(s), deposits with comparable features. This has led de Launay (1913) to define each province as to be part of restricted structural zones and to suggest that the composition of these provinces are predictable in given tectonic settings. This concept has evolved through the 20th century (►Fig. 1.2; e.g., Lindgren, 1933; Blondel, 1937; Petrascheck, 1965) concluding the accumulation of metals to be time-dependent. Strictly speaking, *"a metallogenic province is the entity of mineral deposits that formed during a tectonic-metallogenic epoch within a major tectonic unit and which are characterized by related mineral composition, form of the deposits and intensity of mineralization"* (Petrascheck, 1965). The term "metallogenesis" is used when considering the mechanisms and conditions of ore-grade metal accumulation, and "metallogeny" when dealing with the regional pattern of ore distribution, and when referring to a branch of science. Economic and mining geology, as well as ore petrology, are branches of geology limited to current or potentially profitable metal accumulations (Laznicka, 1992).

Modern metallogeny considers that similar metallogenic provinces, with deposits of variable size, group some elements together because they behave similarly in geological processes (i.e., Pb-Zn; Fe-Mn; Ba-F-U-Pb-Zn; Pb-Zn-Fe). Therefore, they are a consequence of the geochemical differentiation of the Earth crust. Gathering the concepts of geodynamic and the geochemical distribution of elements enables geologists to understand and predict their formation (►Fig. 1.2; i.e., Edwards and Atkinson, 1986; Meyer, 1988; Barley and Groves, 1992; Laznicka, 1992, 2014; Roy, 1997, 2006; Groves and Bierlein, 2007; Dill *et al.*, 2008; Dill, 2010; Maynard, 2010; Kuleshov, 2016; Bustillo Revuelta, 2018; Roonwal, 2018). The common pathway to investigate each type of deposit in metallogenic studies relies on (1) the identification of the source, (2) the modality of metal transport, (3) the trap and accumulation of metals in ore-forming minerals (mineralization), and finally (4) their preservation and/or enrichment. These models are essential tools helping miners and mining companies to explore and to evaluate unrecovered resources and their potential interest.

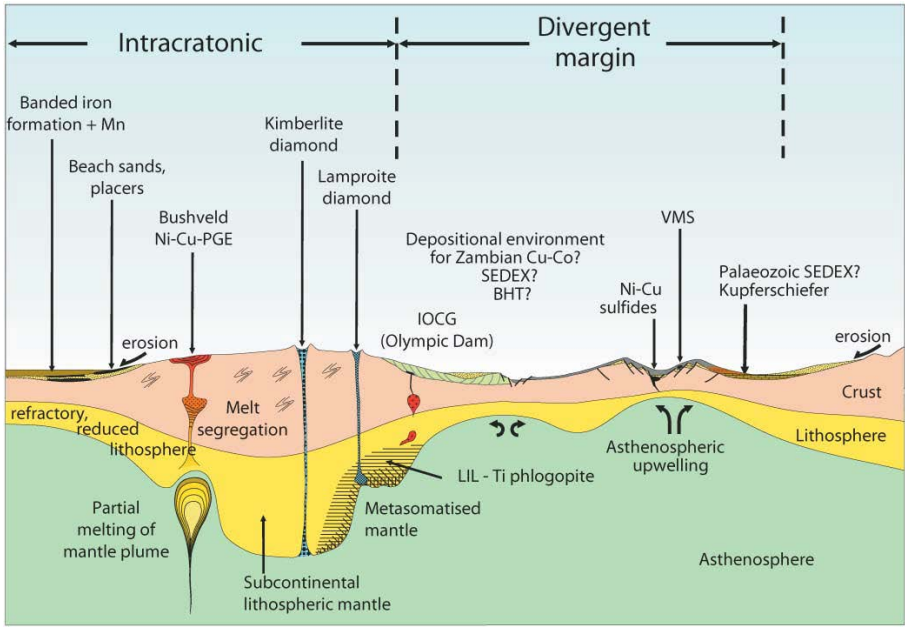

►**Fig. 1.2** Schematic diagram showing major mineral deposit types formed in the continental crust and those formed in passive continental margins and oceanic spreading ridges in divergent margin tectonic settings (Groves and Bierlein, 2007). Not at scale.

1.2 Supergene Mn deposits and their interest in geology

The remarkable property of manganese, in contrast to many other types of mineral resources, is that accumulation of this metal in rocks is distributed in the wide geochronological interval from the Archean to the present time. Various processes are able to accumulate manganese in rocks and minerals. Among them, sedimentary-derived ores are the main valuable resources throughout the world instead of the hydrothermal or metamorphic types, as they offer large extension, constant grades and compositions (Roy, 1997, 2006; Maynard, 2010, 2014; Kuleshov, 2016). However, processes occurring in the **supergene zone**[3] of these deposits (i.e., **weathering processes**) significantly increase their Mn concentration to meet economic grades, where a clear added value is created by the massive presence of secondary **Mn oxides**, hydroxides and oxyhydroxides (here referred to as Mn oxides) forming **supergene deposits** (weathering crusts and karsts; Varentsov, 1996; Vasconcelos, 1999a, 1999b; Beukes *et al.*, 2016). In general terms, the analysis of the world production and consumption of manganese ores by industrial countries convincingly indicates that the highest commercial value belongs to the ores associated with the supergene zone

[3]The supergene zone is defined as the formation of ores in superficial environment, unlike hypogene ores.

(National Materials Advisory Board, 1981; Laznicka, 1992; Varentsov, 1996; Kuleshov, 2016).

The main interest of **supergene deposits** resides in their position at the interface between the lithosphere and the biosphere, the atmosphere and the hydrosphere. These deposits are commonly attributed to physical and chemical transformations resulting from the interaction of the meteoric waters with primary rocks or metal-bearing hypogene deposits (protores) under superficial conditions (atmospheric pressure and surface temperatures). Strictly, it should be considered that **supergene ores** result from the **downward migration** of weathering waters, whereas hypogene ores imply the upward progression of (hot) mineralizing hydrothermal solutions (Bustillo Revuelta, 2018). Interestingly, the world industry development has required, in recent years, an increase of the supergene ores production in different regions of the world. These deposits generally offer an easier access and **higher grades** together with some other commodities which are poorly enriched within the primary ore (see chapter 2; Reich and Vasconcelos, 2015). They are also known as prospecting tools for deeper and hidden resources as a relation exists between the oxidation zone (i.e., gossan[4]) at the surface and the hypogene zone of a deposits (Butt and Zeegers, 1992; Nahon and Tardy, 1992; Marjoribanks, 1997, 2010; Haldar, 2013; Reich and Vasconcelos, 2015; Roonwal, 2018). Determining the mineral and chemical composition, the thickness and the extension of such accumulation are important features to evaluate their economic potential together with the conditions under which they can form valuable deposits.

Within the supergene zone, the manganese accumulations and features of their mineral and chemical compositions are relatively sensitive indicators, reflecting the geometric and geodynamic conditions of their formation. These properties enable the investigation of the Earth's evolution processes. Interestingly, the process from which protores are exposed to meteoric agents implies geodynamic to be one important parameter controlling the development of weathering with climate, the latter being considered as the main driver (Butt *et al.*, 2000; Ruddiman, 2008; Widdowson, 2008). Some K-bearing Mn oxides belonging to the **hollandite supergroup** [$(K,Ba,Pb,Na,Sr)Mn_8O_{16}$] (Biagioni *et al.*, 2013) occur in the supergene zone of Mn (and other) deposits (weathering crusts and karsts) and can accurately be dated by the K-Ar system (Vasconcelos *et al.*, 1992). Therefore, such material offers an incomparable way to unravel the timing of vertical movements of a given area, for example, when rocks have interacted with the atmosphere. However, this convincing picture that aims to assess the timing of geodynamic events in a given area has strong limitations due to the rapid erosion of the weathering blanket into which the whole

[4]A gossan is an intensely oxidized, weathered or decomposed rock occurring in the upper and exposed part of a sulphide ore deposit most often attributed to an iron cap (Taylor, 2011).

age record often completely disappeared, as ages evolve reversely with depth, resulting in the preservation of only young ages in the lowermost part of the weathering zone. Additionally, uncertainties remain about the events dated by K-Mn oxides given that they are considered to record favorable climatic periods (mostly tropical climates). However, the geodynamic effect is probably hidden and not considered to be registered.

1.3 Contribution of this work

Manganese accumulations are found in numerous locations of Western Europe (Lougnon, 1981; Dunning and Evans, 1986; Hautmann and Lippolt, 2000; Dill et al., 2008; Demoulin, 2018). Mainly of small extension, these orebodies have no economic potential today, but most of them were mined in the past and have contributed to the reputation of Europe (i.e., Agricola, 1556). Conversely, North Africa still contains economic Mn deposits currently mined (Beukes *et al.*, 2016; Bouabdellah and Slack, 2016; Lafforgue, 2016). Regardless of their primary mode of formation, most of these deposits display evidence of weathering in the upper part. These secondary processes on primary mineral parageneses, structures and textures is often assumed to have occurred late in the geological history, mostly during in the Tertiary epoch (Segev *et al.*, 1991; Hautmann and Lippolt, 2000; Bruyère *et al.*, 2003; Yans, 2003; Thiry *et al.*, 2006; Barbier *et al.*, 2010; Dill and Wemmer, 2012). As these areas could provide suitable materials to investigate the timing of weathering in well-defined geological settings, the first point of this manuscript refines the conditions from which Mn oxides have precipitated. Because these minerals often display a complex mineralogy and petrography, their mineralogical, petrographical and geochemical characterization will help to determine their **metallogenesis** from the primary accumulation of Mn to their subsequent transformation into oxides composing the supergene ores. The behavior of the K-bearing Mn oxides[5] within the supergene zone of different protores and their position in the weathering mineral sequence, are also specific questions that will help to constrain their relation with other minerals and the significance of their age retrieved from the K-Ar and $^{40}Ar/^{39}Ar$ dating methods. Furthermore, a special focus is also made on supergene deposits, which have undergone slightly higher temperatures after or during the formation of Mn oxides in order to understand their ability to modify the primary supergene assemblage. Additionally, such thermal imprint questions the reliability of some ages recovered from the hollandite group minerals.

[5]Here the K-Mn oxides mostly refer to the hollandite group minerals [$(K,Ba,Pb,Na,Sr)Mn_8O_{16}$], which accommodate substantial amount of structural K (cryptomelane end-member). It could also refer to romanechite in which little K is sometimes incorporated. Both minerals could be dated by the K-Ar system.

The second part of this thesis examine the meaning of the K-Mn oxide ages recovered in different supergene Mn deposits. Are K-Ar and $^{40}Ar/^{39}Ar$ ages only reflecting periods of favorable climatic conditions and/or is there a geodynamic component hidden in the age record of some sampling sites? If so, there might be specific conditions in the geological background of defined sampling sites that can record geodynamic event components rather than the conventional climatic interpretation. This manuscript therefore suggests some specific geodynamic, metallogenic and geological conditions that support a geodynamic interpretation of the K-Ar and $^{40}Ar/^{39}Ar$ ages. Finally, such interpretation is also tested in order to improve metallogenic models aiming to discover new Mn concentrations and associated commodities.

1.4 Structure of the manuscript

Chapters 2 and 3 gather and define all concepts needed for the understanding of the manuscript. Chapter 2 first describes weathering processes and how they operate to modify the chemical and mineralogical composition of various protores. A special focus is made on the economic interest of these deposits. Chapter 3 summarizes the mineral and chemical composition of manganese accumulations and the processes from which they can form Mn ore deposits through different geological and geodynamic settings. Chapter 4 then draws a complete list and describes the methods used in the study of Mn-rich and associated metals, especially focusing on the supergene Mn oxides.

The core section of this manuscript provides an in-depth description of four sampling sites/areas, which have been investigated to build up and harmonize the study of weathering processes in Western Europe and North Africa. These areas include the supergene zone of Mn-rich protores in the Vosges massif (France; chapter 5), the Stavelot massif (Ardenne, Belgium; chapter 6), the Imini-Tasdremt district (Morocco; chapter 7), and the Nefza district (Tunisia; chapter 8). These manganese accumulations are of four types (►Table 1.1): (1) those modified by alteration/weathering of pre-existing hypogene veins comprising di- and trivalent oxides or silicates of manganese (hausmannite, braunite), which form weathering crusts (Vosges, France; chapter 5); (2) those forming a weathering profile upon Mn-rich sedimentary rocks hosting Mn carbonates (rhodochrosite, kutnohorite) and silicates (spessartine, Mn chlorite, Mn chloritoid, …) in the Stavelot massif (Ardenne, Belgium; chapter 6); (3) those formed in open karst systems in the Imini-Tasdremt district (Morocco; chapter 7), including pyrolusite and hollandite group minerals; and (4) those resulting from mixing hydrothermal/weathering processes forming Mn oxides (romanechite, chalcophanite and cryptomelane), Fe oxides (goethite, hematite) and white clays (kaolinite-halloysite). All these deposits occur in different

geodynamic zones related to the European geodynamic. The majority of data is extracted from papers which have been published (Leprêtre *et al.*, 2015; Dekoninck *et al.*, 2016b, 2016a, 2018; Demoulin *et al.*, 2018), accepted, submitted or which are in preparation (►Table 1.1). The content of each published paper is preserved, but the format is adapted to the size of this manuscript. Each chapter provides additional input and insight to further feed the general discussion and draw the conclusion (chapter 9). Each step of the research is introduced by a short paragraph and formulates preliminary conclusions (see gray shade areas).

►**Table 1.1** Papers used in this manuscript.

Sampling site	Location	Chapter	Paper title
Haut-Poirot, Saphoz	Vosges, France	5	/
Chevron, Salmchâteau	Stavelot massif, Ardenne, Belgium	6	Demoulin *et al.* (2018). *Erosion Surfaces in the Ardenne—Oesling and Their Associated Kaolinic Weathering Mantle.* Book Chapter. Dekoninck *et al.* (accepted with revision, in revision). *Genesis and $^{40}Ar/^{39}Ar$ dating of K-Mn oxides from the Stavelot Massif (Ardenne, Belgium): insights on Oligocene to Pliocene weathering periods.* Ore Geology Reviews.
Imini-Tasdremt	High Atlas, Morocco	7	Leprêtre *et al.* (2015). *The three main steps of the Marrakech High Atlas building in Morocco: Structural evidences from the southern foreland, Imini area.* Journal of African Earth Sciences. Dekoninck *et al.* (2016a) *Detailed mineralogy and petrology of manganese oxyhydroxide deposits of the Imini district (Morocco).* Mineralium Deposita. Dekoninck *et al.* (2016b). *The high-grade Imini manganese district—karst-hosted deposits of Mn oxides and oxyhydroxides.* Book Chapter. Dekoninck *et al.* (submitted). *Multistage genesis of the late Cretaceous Mn(-Pb) Tasdremt deposits evidenced by petrographic analysis and $^{40}Ar/^{39}Ar$ dating of K-Mn oxides (Souss Basin, Morocco): a lateral equivalent of the Imini ores.* Mineralium Deposita
Tamra	Nefza district	8	Dekoninck *et al.* (2018). *Mixed hydrothermal and meteoric fluids evidenced by unusual H- and O-isotope compositions of kaolinite-halloysite in the Fe(-Mn) Tamra deposit (Nefza district, NW Tunisia).* Applied Clay Science.

1.5 References

Agricola, G., 1556. De Re Metallica. Basel.

Arrobas, D.L.P., Hund, K.L., Mccormick, M.S., Ningthoujam, J., Drexhage, J.R., 2017. The growing role of minerals and metals for a low carbon future (No. 117581). The World Bank.

Barbier, F., Prognon, C., Quesnel, F., Dupuis, C., Yans, J., 2010. Dating and weathering characterization of the Morialmé quarry (Entre-Sambre-et-Meuse, Belgium), in: 4th French Congress on Stratigraphy. Presented at the Abstract book, Paris, p. 18.

Barley, M.E., Groves, D.I., 1992. Supercontinent cycles and the distribution of metal deposits through time. Geology 20, 291–294. https://doi.org/10.1130/0091-7613(1992)020<0291:SCATDO>2.3.CO;2

Beukes, N.J., Swindell, E.P.W., Wabo, H., 2016. Manganese deposits of Africa. Episodes 39, 285. https://doi.org/10.18814/epiiugs/2016/v39i2/95779

Biagioni, C., Capalbo, C., Pasero, M., 2013. Nomenclature tunings in the hollandite supergroup. Eur. J. Mineral. 25, 85–90. https://doi.org/10.1127/0935-1221/2013/0025-2255

Blondel, F., 1937. La géologie et les mines des vieilles plateformes. Bull. Minéralogie 60, 147–148.

Bouabdellah, M., Slack, J.F. (Eds.), 2016. Mineral deposits of North Africa, Mineral Resource Reviews. Springer International Publishing, Cham. https://doi.org/10.1007/978-3-319-31733-5

Bruyère, D., De Putter, T., Perruchot, A., Dupuis, C., 2003. Neogenesis of halloysite in cryptokarstic environments (Beez, Belgium): chemical modeling., in: Abstract Book. Presented at the Conference of the European clay groups association, Modena, p. 48.

Bustillo Revuelta, M., 2018. Mineral Resources, Springer Textbooks in Earth Sciences, Geography and Environment. Springer International Publishing, Cham. https://doi.org/10.1007/978-3-319-58760-8

Butt, C.R.M., Lintern, M.J., Anand, R.R., 2000. Evolution of regoliths and landscapes in deeply weathered terrain — implications for geochemical exploration. Ore Geol. Rev. 16, 167–183. https://doi.org/10.1016/S0169-1368(99)00029-3

Butt, C.R.M., Zeegers, H. (Eds.), 1992. Regolith exploration geochemistry in tropical and subtropical terrains, Handbook of exploration geochemistry. Elsevier, Amsterdam ; New York.

de Launay, L., 1913. Traité de métallogénie : gîtes minéraux et métallifères : gisements, recherche, production et commerce des minéraux utiles et minerais, description des principales mines., Librairie polytechnique Ch. Béranger. ed. Paris-Liège.

Dekoninck, A., Bernard, A., Barbarand, J., Saint-Bezar, B., Missenard, Y., Lepretre, R., Saddiqi, O., Yans, J., 2016a. Detailed mineralogy and petrology of manganese oxyhydroxide deposits of the Imini district (Morocco). Miner. Deposita 51, 13–23. https://doi.org/10.1007/s00126-015-0590-3

Dekoninck, A., Leprêtre, R., Saddiqi, O., Barbarand, J., Yans, J., 2016b. The high-grade Imini manganese district—karst-hosted deposits of mn oxides and oxyhydroxides, in: Bouabdellah, M., Slack, J.F. (Eds.), Mineral deposits of North Africa. Springer International Publishing, Cham, pp. 575–594.

Dekoninck, A., Moussi, B., Vennemann, T., Jamoussi, F., Mattielli, N., Decrée, S., Chaftar, H.-R., Hatira, N., Yans, J., 2018. Mixed hydrothermal and meteoric fluids evidenced by unusual H- and O-isotope compositions of kaolinite-halloysite in the Fe(-Mn) Tamra deposit (Nefza district, NW Tunisia). Appl. Clay Sci. 163, 33–45. https://doi.org/10.1016/j.clay.2018.07.007

Demoulin, A. (Ed.), 2018. Landscapes and landforms of Belgium and Luxembourg, World Geomorphological Landscapes. Springer International Publishing, Cham. https://doi.org/10.1007/978-3-319-58239-9

Demoulin, A., Barbier, F., Dekoninck, A., Verhaert, M., Ruffet, G., Dupuis, C., Yans, J., 2018. Erosion surfaces in the Ardenne–Oesling and their associated kaolinic weathering mantle, in: Demoulin, A. (Ed.), Landscapes and landforms of Belgium and Luxembourg. Springer International Publishing, Cham, pp. 63–84. https://doi.org/10.1007/978-3-319-58239-9_5

Dill, H.G., 2010. The "chessboard" classification scheme of mineral deposits: Mineralogy and geology from aluminum to zirconium. Earth-Sci. Rev. 100, 1–420. https://doi.org/10.1016/j.earscirev.2009.10.011

Dill, H.G., Sachsenhofer, R.F., Grecula, P., Sasvari, T., Palinkas, L.A., Borojevic-Sostaric, S., Strmic-Palinkas, S., Prochaska, W., Garuti, G., Zaccarini, F., Arbouille, D., Schulz, H.-M., 2008. Fossil fuels, ore and industrial minerals., in: McCann, T. (Ed.), The Geology of Central Europe Volume 2: Mesozoic and Cenozoic. The Geological Society of London, pp. 1341–1449. https://doi.org/10.1144/CEV2P.9

Dill, H.G., Wemmer, K., 2012. Origin and K/Ar age of cryptomelane-bearing Sn placers on silcretes, SE Germany. Sediment. Geol. 275–276, 70–78. https://doi.org/10.1016/j.sedgeo.2012.07.016

Dunning, F.W., Evans, A.M. (Eds.), 1986. Mineral deposits of Europe. Vol.3, Central Europe. Institution of Mining and Metallurgy, London.

Edwards, R., Atkinson, K., 1986. Ore deposit geology and its influence on mineral exploration. Springer Netherlands, Dordrecht. https://doi.org/10.1007/978-94-011-8056-6

Groves, D.I., Bierlein, F.P., 2007. Geodynamic settings of mineral deposit systems. J. Geol. Soc. 164, 19–30. https://doi.org/10.1144/0016-76492006-065

Haldar, S.K. (Ed.), 2013. Mineral explorations: principles and applications. Elsevier, Waltham, MA, USA.

Hautmann, S., Lippolt, H.J., 2000. $^{40}Ar/^{39}Ar$ dating of central European K–Mn oxides — a chronological framework of supergene alteration processes during the Neogene. Chem. Geol. 170, 37–80. https://doi.org/10.1016/S0009-2541(99)00241-7

International Manganese Institute, 2014. About manganese [WWW Document]. Int. Manganese Inst. URL http://www.manganese.org/about-mn

Kuleshov, V., 2016. Isotope geochemistry: the origin and formation of manganese rocks and ores. Elsevier, Amsterdam Boston Heidelberg London New York Oxford Paris San Diego San Francisco Singapore Sydney Tokyo.

Lafforgue, L., 2016. Place de la minéralisation de manganèse de Bouarfa dans l'évolution méso-cénozoique de l'oriental marocain (PhD). Université Paris Sud, Paris.

Laznicka, P., 2014. Giant metallic deposits—A century of progress. Ore Geol. Rev. 62, 259–314. https://doi.org/10.1016/j.oregeorev.2014.03.002

Laznicka, P., 1992. Manganese deposits in the global lithogenetic system: Quantitative approach. Ore Geol. Rev. 7, 279–356. https://doi.org/10.1016/0169-1368(92)90013-B

Leprêtre, R., Missenard, Y., Saint-Bezar, B., Barbarand, J., Delpech, G., Yans, J., Dekoninck, A., Saddiqi, O., 2015. The three main steps of the Marrakech High Atlas building in Morocco: Structural evidences from the southern foreland, Imini area. J. Afr. Earth Sci. 109, 177–194. https://doi.org/10.1016/j.jafrearsci.2015.05.013

Lindgren, W., 1933. Mineral Deposits, 4th ed. McGraw-Hill Book Company, Incorporated, York.

Lougnon, J., 1981. Ressources minières françaises : les gisements de manganèse (Bureau de Recherches Géologiques et Minières No. Tome 10). BRGM.

Marjoribanks, R., 2010. Geological mapping in exploration, in: Geological Methods in Mineral Exploration and Mining. Springer Berlin Heidelberg, Berlin, Heidelberg, pp. 13–49. https://doi.org/10.1007/978-3-540-74375-0_2

Marjoribanks, R.W., 1997. Geological methods in mineral exploration and mining. Springer Netherlands, Dordrecht. https://doi.org/10.1007/978-94-011-5822-0

Maynard, J.B., 2014. Manganiferous sediments, rocks, and ores, in: Treatise on Geochemistry. Elsevier, pp. 327–349.

Maynard, J.B., 2010. The chemistry of manganese ores through time: a signal of increasing diversity of earth-surface environments. Econ. Geol. 105, 535–552. https://doi.org/10.2113/gsecongeo.105.3.535

Meyer, C., 1988. Ore Deposits as Guides to Geologic History of the Earth. Annu. Rev. Earth Planet. Sci. 16, 147–171. https://doi.org/10.1146/annurev.ea.16.050188.001051

Nahon, D.B., Tardy, Y., 1992. The ferruginous laterites, in: Butt, C.R.M., Zeegers, H. (Eds.), The ferruginous laterites, Handbook of Exploration Geochemistry. Elsevier, Amsterdam ; New York; London; Tokyo, pp. 41–55.

National Materials Advisory Board, 1981. Manganese reserves and resources of the world and their industrial implications (Final No. NMAB-374). National Academy of Sciences, Washigton DC.

Petrascheck, W.E., 1965. Typical features of metallogenic provinces. Econ. Geol. 60, 1620–1634. https://doi.org/10.2113/gsecongeo.60.8.1620

Reich, M., Vasconcelos, P.M., 2015. Geological and Economic Significance of Supergene Metal Deposits. Elements 11, 305–310. https://doi.org/10.2113/gselements.11.5.305

Roonwal, G.S., 2018. Mineral Exploration: Practical Application, Springer Geology. Springer Singapore, Singapore. https://doi.org/10.1007/978-981-10-5604-8

Rossi, M.E., Deutsch, C.V., 2014. Mineral Resource Estimation. Springer Netherlands, Dordrecht. https://doi.org/10.1007/978-1-4020-5717-5

Roy, S., 2006. Sedimentary manganese metallogenesis in response to the evolution of the Earth system. Earth-Sci. Rev. 77, 273–305. https://doi.org/10.1016/j.earscirev.2006.03.004

Roy, S., 1997. Genetic diversity of manganese deposition in the terrestrial geological record, in: Geological Society, London, Special Publications. pp. 5–27.

Ruddiman, W.F., 2008. Earth's climate: past and future, 2nd ed. W.H. Freeman, New York.

Segev, A., Lang, B., Halicz, L., 1991. K-Ar dating of manganese minerals from the Eisenbach region, Black Forest, southwest Germany. Schweiz. Mineral. Petrogr. Mitteilungen 71, 101–114. https://doi.org/10.5169/seals-54349

Sverdrup, H., Ragnarsdóttir, K.V., 2014. Natural resources in a planetary perspective. Geochem. Perspect. 129–341. https://doi.org/10.7185/geochempersp.3.2

Taylor, R., 2011. Gossans and leached cappings: field assessment. Springer-Verlag, Berlin Heidelberg.

Thiry, M., Quesnel, F., Yans, J., Wyns, R., Vergari, A., Theveniaut, H., Simon-Coiçon, R., Ricordel, C., Moreau, M.-G., Giot, D., Dupuis, C., Bruxelles, L., Barbarand, J., Baele, J.-M., 2006. Continental France and Belgium during the early Cretaceous: paleoweatherings and paleolandforms. Bull. Société Géologique Fr. 177, 155–175. https://doi.org/10.2113/gssgfbull.177.3.155

U.S. Geological Survey, 2014. Historical statistics for mineral and material commodities in the United States [WWW Document]. US Geol. Surv. Data Ser. URL http://minerals.usgs.gov/minerals/pubs/historical-statistics/. (accessed 9.5.19).

Varentsov, I.M., 1996. Manganese ores of supergene zone: Geochemistry of formation, Solid Earth Sciences Library. Springer Netherlands, Dordrecht.

Vasconcelos, P.M., 1999a. $^{40}Ar/^{39}Ar$ Geochronology of supergene processes in ore deposits, in: Lambert, D.D., Ruiz, J. (Eds.), Application of Radiogenic Isotopes to Ore Deposit Research and Exploration, Reviews in Economic Geologists. Society of Economic Geologists, pp. 73–112.

Vasconcelos, P.M., 1999b. K-Ar and $^{40}Ar/^{39}Ar$ geochronology of weathering processes. Annu. Rev. Earth Planet. Sci. 27, 183–229. https://doi.org/10.1146/annurev.earth.27.1.183

Vasconcelos, P.M., Becker, T.A., Renne, P.R., Brimhall, G.H., 1992. Age and duration of weathering by 40K-40Ar and $^{40}Ar/^{39}Ar$ analysis of potassium-manganese oxides. Science 258, 451–455. https://doi.org/10.1126/science.258.5081.451

Widdowson, M., 2008. Laterite and ferricrete, in: Nash, D.J., McLaren, S.J. (Eds.), Geochemical sediments and landscapes. Blackwell Publishing Ltd, Oxford, UK, pp. 45–94. https://doi.org/10.1002/9780470712917.ch3

Yans, J., 2003. Chronologie des sédiments kaoliniques à faciès wealdien (Barrémien moyen à Albien supérieur ; Bassin de Mons) et de la saprolite polyphasée (Crétacé inférieur et Miocène inférieur) de la Haute-Lesse (Belgique) : implications géodynamiques et paléoclimatiques (Unpublished Ph.D. thesis). Faculté Polytechnique de Mons, Université de Paris XI Orsay, Mons.

Yans, J., Dekoninck, A., 2016. Ressources du sous-sol wallon : historique, état des lieux et perspectives. Mines Carr. Hors Série 18, 5–12.

Chapter 2

Weathering processes

Chapter 2

Weathering processes

The main processes studied in this PhD thesis are located in the upper part of the Earth's crust, onto which weathering agents can easily operate. The aim of this chapter is not to produce an exhaustive overview of these processes but to raise fundamental questions that will help the reader to understand accurately all issues dealt in this manuscript. Solving controversial definitions dealing with "weathering" (i.e., "saprolite", "laterite"…) are therefore not the purpose of this section. However, a better understanding of these fascinating geological objects is necessary to thoroughly study how weathered rocks were formed through geological times. Where do weathering fluids operate? Following which processes? In which conditions? After elucidating these crucial questions, a special focus is made on weathering (or supergene) processes that produce economic deposits.

In a broad sense, **weathering** is the breakdown and the alteration of rocks by physical and chemical processes, resulting in the development of structured **weathering mantles**, also referred to as **weathering profile** or **laterite profile** (laterite *s.l.*; ►Fig. 2.1). Such weathering processes are also known as "supergene", and occur at or near the topographic surface under the influence of atmospheric agents, but are not always restricted to the uppermost few meters of the lithosphere. Actually, the effects of weathering can be observed at much greater depths. Mineralogical and textural changes driven by interactions with meteoric waters are commonly traced until a few tens of meters down (►Fig. 2.1), whereas weathered rocks with thicknesses exceeding 100 meters are common in ancient and recent landmasses over the Earth (Tardy and Roquin, 1992, 2000; Migoń and Lidmar-Bergström, 2001; Taylor and Eggleton, 2001; Migoń, 2013). The demolition of sedimentary, magmatic and metamorphic rocks occurs in response to changes in environmental conditions, when they meet the hydrosphere (i.e., meteoric water), the atmosphere (i.e., oxygen) and the biosphere (i.e., organic activity) after their formation. The products of weathering are materials much more in equilibrium with their environment than those from which they are derived. For example, igneous minerals, which are formed at high temperatures (>500°C), are unstable in the cooler and wetter conditions of the Earth's surface (0–30°C). The minerals of these igneous rocks are altered into low-temperature water-bearing phases or dissolved and removed by erosion. Weathering reactions ultimately correspond to mass transfer of elements from the continental lithosphere to the oceans. Weathering products are therefore temporary accumulations at the geological time scale, as long as the weathering cover resists to the chemical and physical erosion (Laznicka, 1992; Vasconcelos, 1999). The formation and preservation of weathering profiles reflect the balance between chemical and mechanical weathering promoting the formation of a regolith blanket and erosion which wants to transport these products.

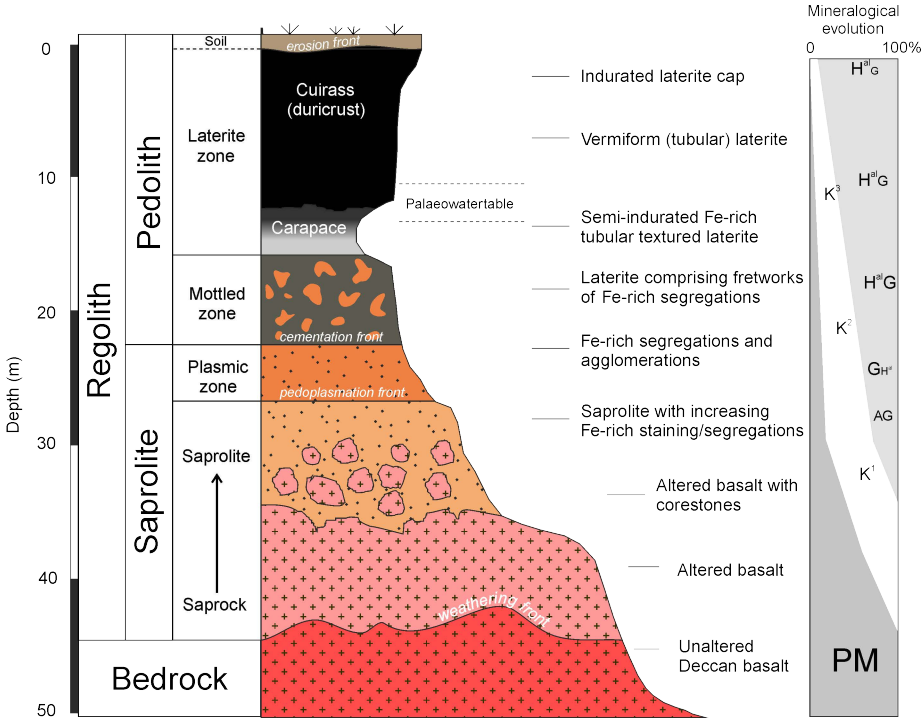

►**Fig. 2.1** Terminology used to describe weathering mantle through the idealized vertical section of Bidar laterite *s.l.* (India), illustrating the compositional and textural progression from the unaltered basalt fresh rock (bedrock) to the indurated laterite *s.s.* (modified after Aleva, 1994; Thomas, 1994; Widdowson, 2008). According to researchers, saprolite means different parts of the weathering mantle. PM: parent rock; K^1 to K^3: well crystallized to poorly crystallized kaolinite; AG: amorphous goethite; G: goethite; $H^{al}G$: Al-rich hematite and goethite. Hematite content increases upward.

The downward progression of weathering or supergene solutions (*per descensum* process) through times allows **different zones** to be systematically identified. The upper part of the profile, in which most features of the parental rocks are obliterated, records a higher level of alteration, whereas the lower part displays remnants structures of the "fresh" parent rock (►Fig. 2.1 and 2.2). Physical weathering disaggregates the rock by creating large surface areas and greater access to meteoric fluids (i.e., fractures, joints, faults, lineaments…). Following this process, chemical weathering could significantly be enhanced and generally acts in two stages: (1) alkaline conditions favor the oxidation of Fe^{2+} into Fe^{3+}, then (2) the acidity increases in the presence of organic acid (i.e., humic and fulvic) and the CO_2 content of the weathering fluid (e.g., Widdowson, 2008). The behavior of the different elements within the silicate minerals is differentially affected by changes in pH. During the alkaline stage, K^+, Na^+, Ca^{2+} may be removed as opposed to stable residual components such as Fe^{3+}, Al^{3+}, Ti^{4+} and $Mn^{3+/4+}$. Along the release of alkaline elements, Fe^{2+} and Mn^{2+} are oxidized into the most stable Fe^{3+}, Mn^{3+} and Mn^{4+}, mainly

as oxides and hydroxides. When conditions become acid due to the release of humic and carbonic (and potentially other) acids, Al-bearing minerals (kaolinite and gibbsite), iron oxides (goethite and hematite) and Mn oxides can migrate to a limited extent, respectively forming Fe laterite *s.s.*, manganese crusts and bauxites (►Fig. 2.3; Edwards and Atkinson, 1986). The acidity (pH) and the oxidation level (Eh) are therefore the main parameters controlling product reactions that often lead to heavy enrichments in some (strategic) metals, such as Au (gold laterite), Al (bauxite), Fe (ferricrete), Mn (manganiferous crust), Ni-Co, Cu, etc. (Nahon *et al.*, 1992; Reich and Vasconcelos, 2015).

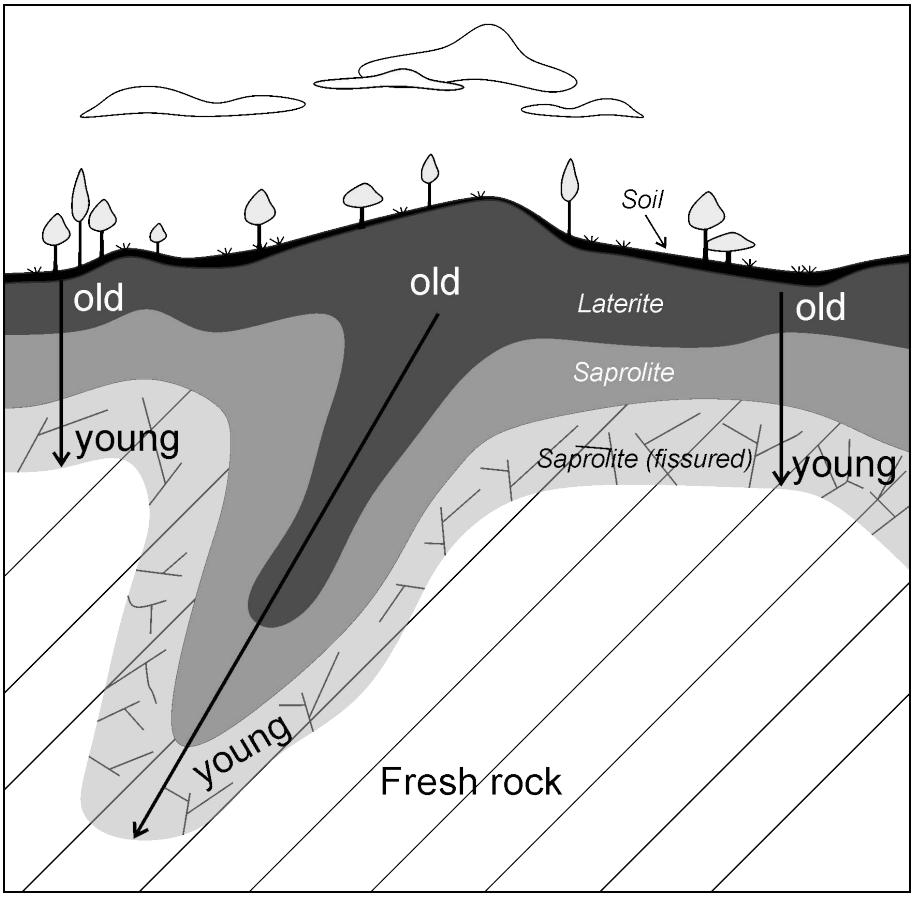

►**Fig. 2.2** Downward percolation (*per descensum*) of O_2-rich and acidic meteoric (weathering or supergene) fluids in a weathering profile. The weathering front propagation is facilitated in zones that are permeable giving younger ages at the base (saprolite) and older ones in the upper part (laterite *s.s.*) of the profile (adapted from Vasconcelos, 1999).

►**Fig. 2.3** Tamra laterite *s.l.* (north Tunisia) showing reddish-yellowish (Fe oxides) and dark zones (Mn oxides). Whitish levels are composed of kaolinite and halloysite clays (see this thesis, chapter 8).

Therefore, weathering mantles are particularly interesting in order to study such alteration and transformation. Their study is however not straightforward and needs to take into account:

- These processes are (bio-)chemical alterations, which have operated for several years to dozens of millions years since the dawn of an atmosphere was created on Earth.
- One third of the emerged land is affected by lateralization, and considering their thickness, more than 85% of the soil cover results from these processes.
- They are mainly composed of kaolinite, Fe and Al oxides and hydroxides, as neoformed mineral phases, which preserve textures, structures and volumes of the parent minerals from which they originate.
- They formed under several (ancient) episodes that can record past geochemical composition, which is, for example, interesting to study paleoclimates.
- They can accumulate significant quantities of metals, forming secondary weathering deposits.

2.1 Preliminary definitions

The development of thick **weathering profiles** with chemical and mineralogical stratified horizons is guided when the balance between weathering and erosion is reached. Two related notions have been introduced to account for the great vertical extent and to differentiate surface breakdown. First, **deep weathering** emphasizes the great *per descensum* evolution of meteoric alteration, usually expected at depth above

2–3 meters (►Fig. 2.2 Migoń, 2013). Accordingly, such profiles consist of an upward progression from unaltered protolith at the base up to an indurated, iron-rich duricrust, at the top (►Fig. 2.1). Secondly, **weathering mantle** denotes the presence of material which has experienced *in situ* mineral and chemical alteration by meteoric fluids. "Saprolite" is sometimes used as an equivalent of "weathering mantle" but a more conspicuous definition restricts saprolite *s.s.* to the lower part of a weathering mantle, in which signs of alteration are pervasive and clearly identified (►Fig. 2.1). Regolith is a term used to describe all materials resting above the non-weathered rock (Merrill, 1897). The **weathering front** (or roll-front) is the boundary surface that separates the weathered and fresh rock.

The term **supergene** is a synonym of weathering, but is rather applied to ore deposits (Jackson *et al.*, 1997; Bustillo Revuelta, 2018). Consequently, supergene ores should strictly originate from the downward migration of meteoric waters, whereas hypogene ores imply the upward progression of (hot) hydrothermal mineralizing solutions. The definition of hydrothermal processes is often confusing because they can develop in almost all geological environments from temperatures ranging between 70-200°C in sedimentary realm or during diagenesis-metamorphism, up to 400°C under endogenous conditions. In a broad sense, hydrothermalism is applied to mineralization fluids evolving along temperature or pressure gradients, from hot to cool areas, or from high pressure to low pressure. They migrate until they reach a suitable site for metal precipitation, forming the so-called hypogene ores (Bustillo Revuelta, 2018).

Etching is used in geomorphology to describe rock decomposition that occurs at the weathering front (Thomas, 1994; Migoń and Lidmar-Bergström, 2001; Migoń, 2013). This emphasizes the different resistance of rocks to chemical decay and consequently the thickness of a weathering mantle over short distances. The removal of products of deep weathering (stripping) exposes the bedrock surface, the topography of which is the direct result of differential etching, which is called an **etched surface** or **etchplain** (►Fig. 2.4). An **erosion surface** is a surface that is formed by erosion. Erosion surfaces in the stratigraphic records are often unconformities. Long-term (10–100 Ma) continental-scale landscape evolution models (e.g., Davis, 1899; Penck, 1924, 1953; King, 1953) have postulated that coeval regional land surfaces (erosion surfaces), often sharing a common elevation, would be generated by widespread incision that would follow a period of uplift (►Fig. 2.5; Vasconcelos and Carmo, 2018). Therefore, weathering is the most crucial and fundamental phenomenon in landscape evolution and topographic development which cannot be overlooked by geomorphologists. The in-place breakdown of geologic material by physical, chemical, and biological processes is a necessary precursor to most forms of erosion, sediment transport and denudation (Turkington *et al.*, 2005).

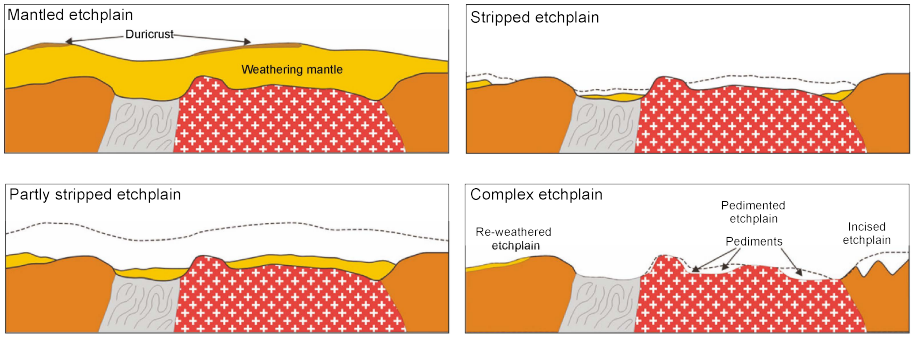

►**Fig. 2.4** Etchplain typology and evolution (Migoń, 2013).

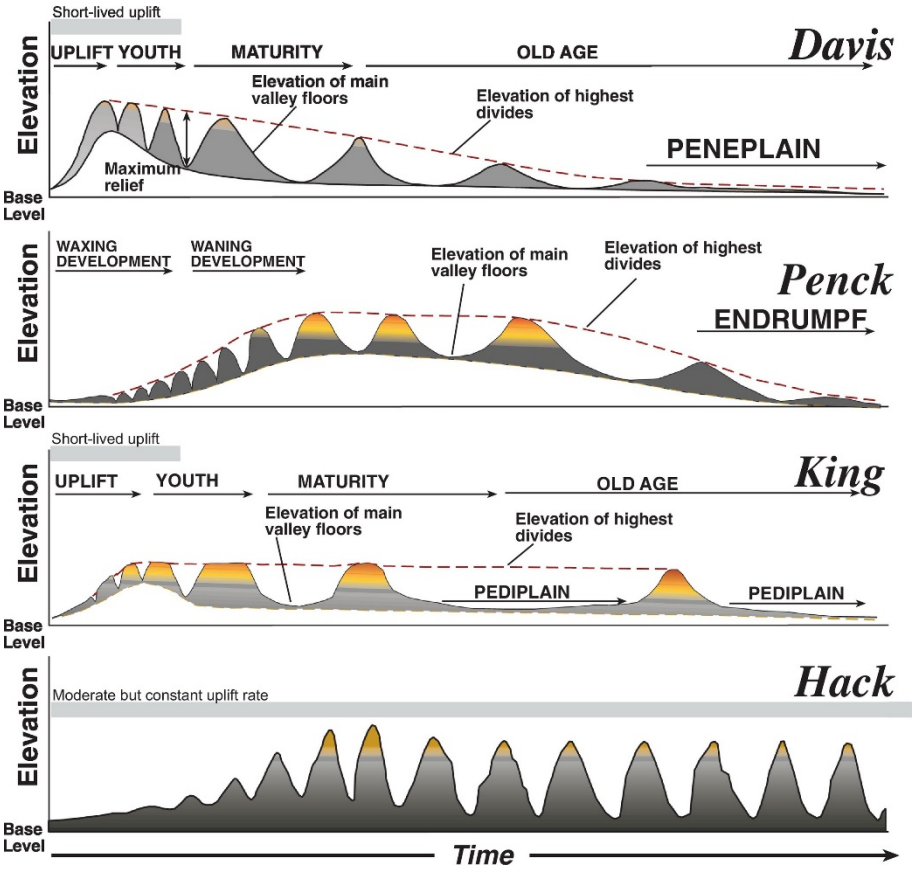

►**Fig. 2.5** Long-term (10–100 Ma) continental scale chronology models interpret landscape evolution as the result of episodic surface uplift and erosion processes, resulting in erosion surfaces of different ages (King, 1953; Grotzinger and Jordan, 2014; Vasconcelos and Carmo, 2018).

"**Laterite**" is an ambiguous term that has various meanings in the literature, mostly attributed to heavily enriched ferruginous crust in the uppermost horizon of

weathering profile (►Fig. 2.1; Tardy, 1992). This has led Taylor and Eggleton (2001) and Bourman and Ollier (2002) to recommend the use of "ferricrete" to describe indurated, hard, Fe-rich upper zones of weathering profiles, instead of laterite *s.s.*. More recently, Widdowson (2008) has distinguished laterite as having an autochthonous origin, whereas ferricretes have an allochthon source, which is somehow a more convincing definition. These autochthon and allochthon origins could be related to the definition of additive (bauxite, kaolin) and subtractive (silcrete, calcrete) weathering evidenced by Wyns (2002). In practice, it is however difficult to determine whether minerals are allochthon or autochthon because many laterite profiles (or laterite *s.l.*) are subsequently modified by the introduction of allochthonous material, or conversely, ferricretes can be subject to *in situ* weathering processes and evolve toward more lateritic-type profiles. Consequently, we should define laterite weathering mantle (or laterite *s.l.*) as mature profile in which all horizons are present, from the upper ferruginous crust (or laterite *s.s.*) to successively mottled, pallid (or plasmic), saprolite zones and finally unaltered bedrock (►Fig. 2.1; McFarlane, 1976; Nahon, 1986; Tardy, 1992, 1997; Anand, 2005; Widdowson, 2008; Migoń, 2013). Some of these horizons may be absent, depending on the host rock composition, the erosion rate of the upper part, as well as on the maturity and evolution of these profiles, as they often develop over long or several periods.

Silcrete is a term used to describe the products of near-surface processes by which silica accumulates in and/or replaces soil, sediment, rock or weathered material to form an indurated mass (Lamplugh, 1902; Nash, 2011). Their formation could originate either from pedogenic or non-pedogenic processes (i.e., ground waters, drainage lines, pan/lacustrine; Thiry, 2009). They crop out in inverted relief as caprock, and may be extensive in paleosurfaces. The silica enrichment is derived from soils, sediments or rock profiles, or transported from distant sites. High pH found in arid and semi-arid environments is the main parameter controlling silica solubility (Chadwick *et al.*, 1989). Enhanced silica concentrations in soils also occur at a very low pH, primarily due to the breakdown of clay minerals under increasingly acidic conditions in soils or sediments sustaining high organic productivity or because of sulfide oxidation (Summerfield, 1979). They are not part of a weathering profile, but are often associated with lateritic environments (Stephens, 1971).

Calcrete (or caliche) is a general term given to the near-surface, terrestrial accumulation of predominantly calcium carbonate crust that results from the cementation, as well as from the displacive and replacive introduction of calcium carbonate into soil profiles, sediments and bedrock in areas where vadose and shallow phreatic ground waters are saturated with respect to calcium carbonate (Wright, 2008). The sources of carbonates are varied (Goudie, 1973; Goudie and Pye, 1983) and include, besides any local lithogenic source, rainfall, sea spray, surface runoff, dust, calcareous fauna and even vegetation (e.g., Garvie, 2003; Cailleau *et al.*, 2004).

Precipitation of carbonate is triggered by a number of processes (Wright *et al.*, 1991), including evaporation, evapotranspiration and degassing, but biological processes also play a crucial role. Profile development can be seen as a simple progressive (linear) process or as a more dynamic one where carbonate accumulation can be interrupted by depositional and erosional events (Wright, 2008).

2.2 Global distribution of weathering products

It is difficult to determine the global distribution of laterite profiles and ferricretes is difficult to determine because few maps make the distinction distinguish between laterite *s.l.* and ferricretes as suggested by Widdowson (2008). However, iron-rich duricrusts have been documented on every continent except Antarctica (Goudie, 1973). Laterites *s.l.* are widespread in India, Asia, Australia, Africa, South America and are uncommon in North America and Europe (►Fig. 2.6; see Widdowson, 2008 for references). These laterites *s.l.* are made up of kaolinite and aluminum, iron oxides and hydroxides, which result from parent minerals. Laterites *s.l.* consist of more than 85% of the current soil cover over the world (Nahon, 2003). They have played an important role in landscape evolution of tropical and subtropical areas. Furthermore, most part of current lateritic covers might be older, as suggested by many $^{40}Ar/^{39}Ar$ dating studies (e.g., Vasconcelos, 1999; Hautmann and Lippolt, 2000; this thesis).

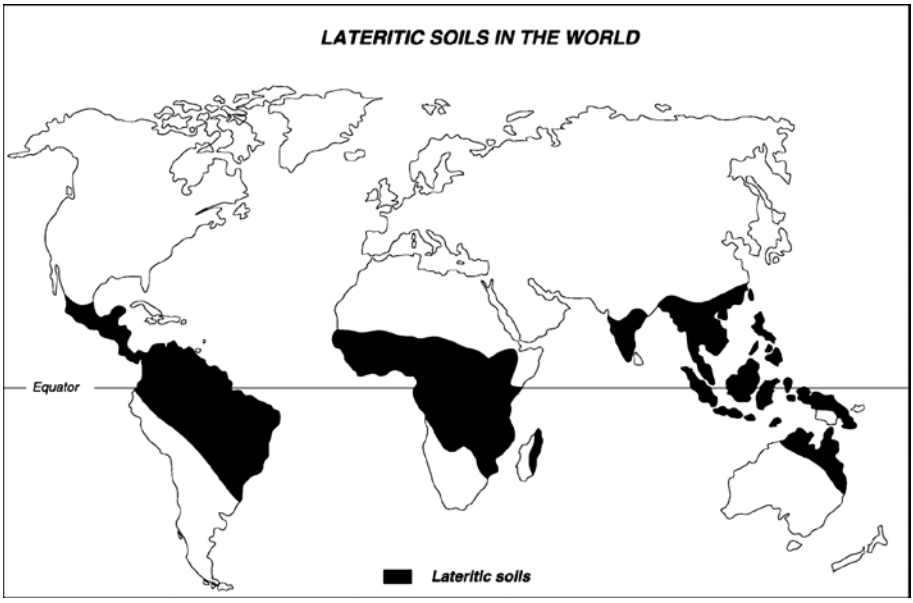

►**Fig. 2.6** Today's distribution of ongoing laterite *s.l.* cover on Earth (Nahon, 2003).

The amount and nature of clay minerals as weathering products are generally good indicators on how advanced weathering is. Most of our knowledge about

weathering mantles is derived from the interaction of meteoric waters with granitoid and gneiss (Migoń and Thomas, 2002; Migoń, 2006) and such a model can also be applied to other rock types (Nahon, 1986, 1991; Niśkiewicz, 2000; Widdowson, 2008; Migoń, 2013). A very different approach uses geochemistry of weathered rock, allowing to infer processes contributing to the origin of the saprolite (Tardy, 1971). Three processes dealt with by all geologists and Earth scientists have been identified in relation to climatic zones of the Earth (►Fig. 2.7; Migoń, 2013):

- Allitization, in which all basic cations and most of the silica is removed. Hence, the weathering products are enriched in Fe and Al hydroxides, such as gibbsite (bauxite) and goethite (Fe laterite *s.l.*). SiO_2:Al_2O_3 ratio is below 2.
- Monosiallitization, in which silica is partially removed and only Al-Si minerals are formed, such as 1:1 clays, mostly kaolinite.
- Bisiallitization occurring when most of the silica is preserved in the weathering product, which results in 2:1 clay minerals containing other remaining cations. The SiO_2:Al_2O_3 ratio is above 2.

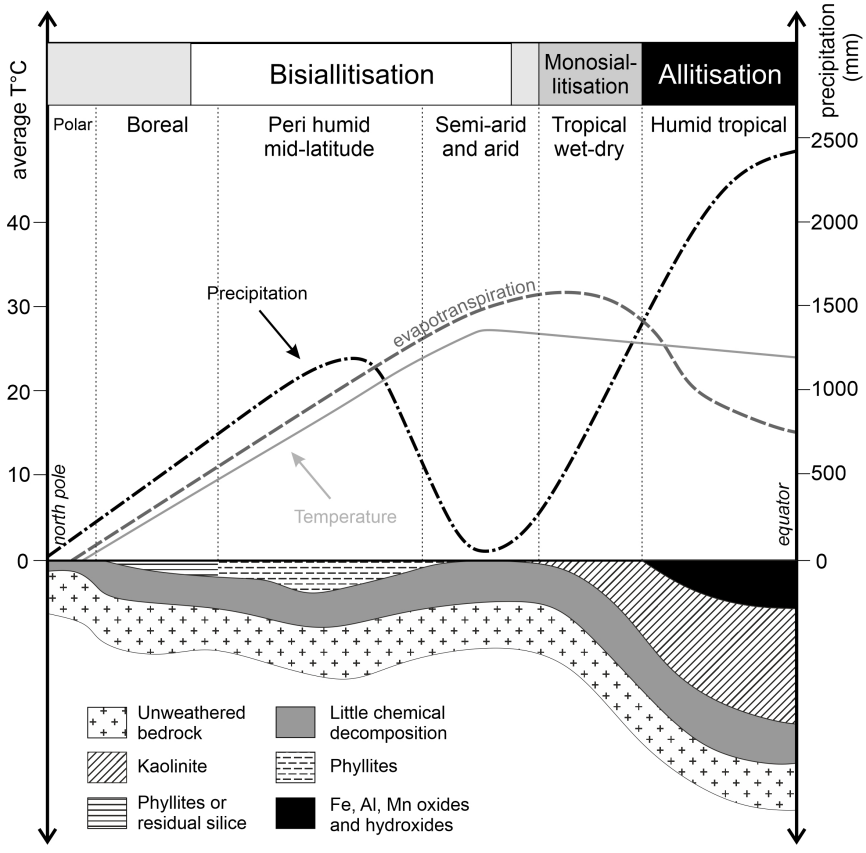

►**Fig. 2.7** Main mineralogy and relative thickness of weathering mantles depending on latitude (climatic and vegetation zones) based upon Strakhov (1967) and Bonnet (2015).

2.3 Key factors controlling weathering processes

Mantles of deeply weathered rocks vary enormously in terms of thickness, mineralogy, and physical properties. These differences result from a multitude of factors which include, among others, (1) rock properties (mineralogy, chemistry, discontinuities and fabric), (2) the climate (►Fig. 2.7), (3) geodynamics (creation of relief, geomorphology, tectonic), and (4) the time, assuming that each factor may influence the extent and the rate of weathering. The formation of lateritic materials has probably occurred since the oxygenation of the atmosphere in the early Proterozoic. The earliest examples of laterite *s.l.* are Proterozoic in age (e.g., South Africa; Gutzmer and Beukes, 1998). These are important since the ferric iron that they contain confirms an early oxygenation of the atmosphere. However, as laterite *s.l.* development depends on the joint climatic and geodynamic factors, it is difficult to predict periods when accelerated laterization has occurred by examining any of these factors independently. Rock properties and local/regional geomorphology and geodynamics determine the susceptibility of a material to undergo weathering at a given location, whereas the climate and the time are external factors controlling the rates and the nature of the product, respectively. These three spatial factors (rock properties, climate and geodynamics) account for the rates at which a weathering front descent into the rock, trigger mineralogical changes and determine the preservation of a weathering profile. Such equilibrium, during which a weathering mantle can persist depends on the ratio of mechanical erosion of the saprolite, and on the rate to form a weathering mantle (Nahon *et al.*, 1992; Migoń, 2013). Time acts independently from the other parameters because rocks in different environments may weather to the same end product with a variable time, mainly depending on the surface stability allowing longer development over geological times (►Fig. 2.5; Taylor and Eggleton, 2001).

Climate has often been invoked as the main driver for weathering processes because it ensures relatively high rates of chemical weathering depending on water availability and thus on rainfall regimes (seasonality, intensity, periodicity). Such approach is reasonable given that weathering mantles commonly reach thickness of 20–40 meters in tropical belts. For example, weathering profiles in the Katanga copper belt are at least 150 meters deep (Thomas, 1994). Such considerable depth of weathering also occurs outside the tropics, reaching 100 meters, for example in the Rhenish shield slates and over the Bohemian Massif granites and arkoses (Migoń and Lidmar-Bergström, 2001), indicating that paleoclimate does not acts alone but together with the other parameters. In Belgium, weathering may reach >65 meters in thickness in some areas (see chapter 6). However, higher depth could also be observed but is rather related to superimposed weathering over older ones (Migoń, 2013). Deep

weathering is not necessarily uniform in space and the weathering front is rarely flat and planar, even at the outcrop scale. The thickness of a weathering mantle could vary from a few to more than 50 meters over distances of a few hundred meters. These variations are even more pronounced when elevation of the relief is higher (►Fig. 2.8; Thomas, 1966; Shaw, 1997; Niśkiewicz, 2000; Wyns *et al.*, 2004; Migoń, 2013).

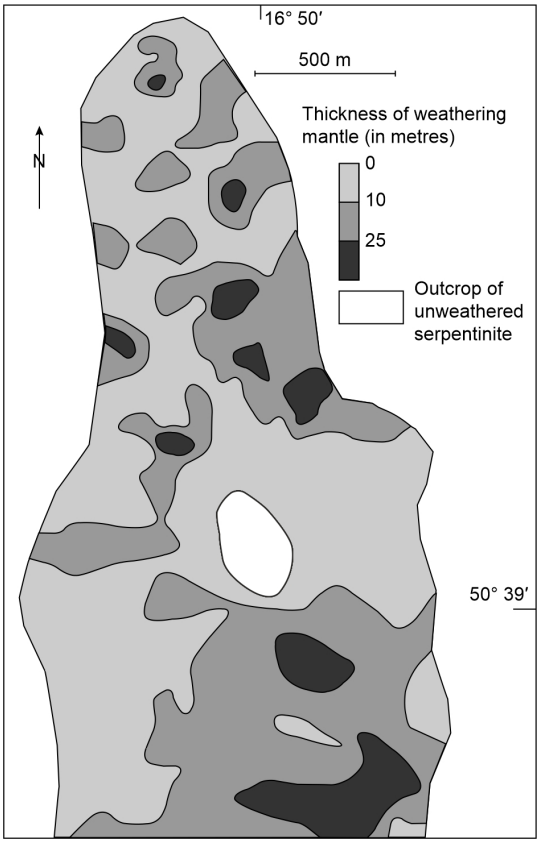

►**Fig. 2.8** Variable thickness of deeply weathered serpentinites at Szklary in southwest Poland (modified after Niśkiewicz, 2000; Migoń, 2013).

2.3.1 Rock properties

Mineral composition and discontinuities can be seen as the most important internal features among many others. Mineralogical alteration depends upon mineral reactions with meteoric fluids, which is enhanced with easily weathered minerals such as olivine, chain silicates or carbonates, instead of quartz-rich rocks that allow a thinner weathering cover. This positive trend is therefore enhanced in rocks containing less amount of silica but more Fe, Ca, Na and Mg. For example, K-feldspar rich rocks are more difficult to break down than Na- and Ca-feldspars, as a reverse result of the

Bowen sequence during crystallization of magma. Discontinuities (faults, fractures, S0-S1 bedding…) usually allows meteoric waters to circulate efficiently in the weathering mantle and, most importantly, into the underlying fresh or non-weathered parental rocks (►Figs. 2.2 and 2.9). Fracture density and irregular network facilitate water movements, whereas dense rocks limit water transfer. Furthermore, wide-open (and continuous) drains favor quick movement of waters and limit water-rock interactions (►Fig. 2.9). Discontinuities could have various scales, from irregular intragranular cracks, bedding planes in sedimentary rocks to major faults commonly associated with mechanical crushing of rocks. Not every rock type can support thick weathering, mostly depending on the cohesion of the material. Granite usually offers thick durable saprolite as neoformed clays can bind poorly weathered remnants of the granite together. Some other rock types that break down into sand and silt (i.e., sandstone) are easily removed by overland flows and produce relatively thin weathering mantles, even under very humid conditions. In easily dissolved rocks, such as limestone and evaporite, only a thin soil is usually present, as most of the rock-forming minerals are washed away. This results in poorly developed weathering mantles and in karst systems, in which water can easily circulate (see chapter 7). Therefore, most deep weathering profiles are known from basement areas, particularly from granite, gneiss, schists and serpentinite. Other rock lithology could have chances to develop thick weathering mantles if a protective duricrust cap protects the underlying horizons from further erosion (Migoń, 2013).

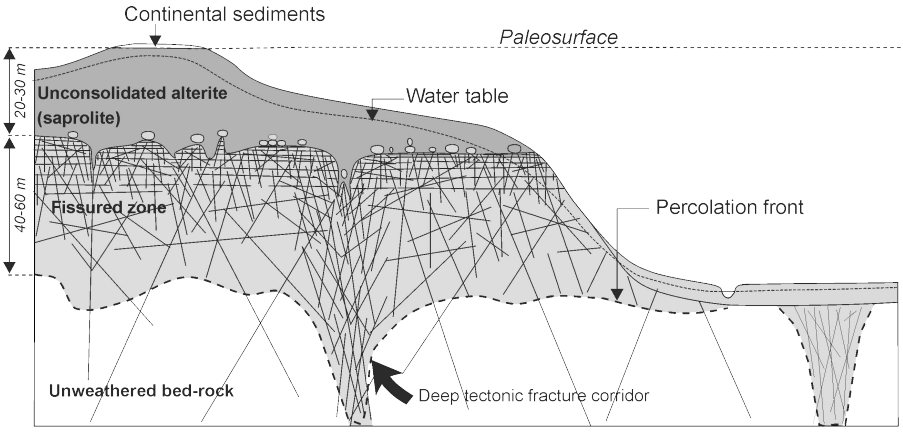

►**Fig. 2.9** Conceptual model of hydrogeological properties in weathered basement rocks (Wyns *et al.*, 2004). Fracture system enhances circulation of meteoric waters and progression of the weathering front.

2.3.2 Climate and environment

Chemical weathering is influenced by three environmental factors which directly or indirectly relate to climate: **temperature, precipitation, and vegetation**. These factors all act in a mutually reinforcing way to intensify chemical weathering (Ruddiman, 2008). Temperature and precipitation are closely linked within the Earth's climate system and make their own contributions to chemical weathering, which are difficult to measure. In the geological record, it is generally accepted that a warmer Earth is likely to be wet, and both factors tend to act together to intensify chemical weathering. The interpretation of the tropical origins of landforms and laterites *s.l.* is not universally accepted as they are overrepresented in middle to high latitudes in the geological record, and slowdown or break of weathering products are difficult to fit with climatic changes (Wyns, 2002; Wyns *et al.*, 2003; this thesis, see chapter 9). However, it is indisputable that high precipitations bring more meteoric water to the weathering system and high temperatures enhance the rate of chemical reactions, making climate as essential as the other factors. Since the effect of temperature is largely kinetic, higher temperatures merely enable reactions to occur more rapidly. Hence, laboratory experiments have demonstrated that silicate weathering rates double for each 10°C increase in temperature, further indicating that an 8 factor exists between cold polar regions (~0) and hot equatorial latitudes (~30°C; Ruddiman, 2008). Deep weathering may occur in cooler climates, but over longer periods of time (Taylor *et al.*, 1992) or in favorable geodynamic conditions. As a whole, humid tropical to (possibly) temperate, and probably seasonal savanna or Mediterranean climates, favor thick weathering mantle development (Butt *et al.*, 2000).

Greenhouse effect is favored during times of elevated CO_2, which have led greater areas of the Earth's surface to be available for tropical-type deep weathering processes (Berner, 1994). Such favorable global periods are Late Cretaceous and Late Paleocene to Eocene, when the CO_2 level was at least twice higher than the current values worldwide (Bardossy, 1981; Valeton, 1983). Climate alterning humid tropical or continental with arid climate is also an essential point, given that the formation of duricrusts, formed by the exposure and the irreversible hardening of the ferruginous residuum or the later precipitation of Fe oxides, silica and carbonates, has an armoring effect that could protect the regolith from erosion (Anand, 2005). Since the formation of laterite profiles depends upon prevailing climate, the distribution of laterites *s.l.*, and to a lesser extent ferricretes (►Fig. 2.5), of different ages has become increasingly used as proxies for paleoclimate reconstruction. However, uncertainties over the precise climatic conditions needed for laterization has led to various climatic interpretations (Bárdossy and Aleva, 1990; Tardy *et al.*, 1991; Taylor *et al.*, 1992; Widdowson, 2008) which require, in a broad sense, warm temperatures and/or high

amounts of seasonal precipitation (Bardossy, 1981; Thomas, 1994; Tardy and Roquin, 1998; Widdowson, 2008).

The vegetation cover also enhances chemical weathering, as plants extract CO_2 from the atmosphere through the process of photosynthesis and deliver it to soils, where it combines with ground water to form carbonic acid (H_2CO_3). Although H_2CO_3 has a low activity, it increases the rate of chemical breakdown of minerals. The presence of a vegetation blanket on landmasses can increase the rate of chemical weathering by a factor of 2 to 10 over the rates typically calculated over land lacking vegetation (Ruddiman, 2008). Vegetation is, in turn, closely linked to temperature and climate, as dense forests are found in regions where constant rainfall (tropical, temperate or savanna zones; ►Fig. 2.6) occur with short dry seasons (Butt *et al.*, 2000).

2.3.3 Geodynamics: geomorphology, relief and tectonics

The formation and preservation of deeply weathered profiles is only possible if the specific point of the land surface does not erode significantly after the formation of the weathering profile. **Long periods of tectonic stability** (i.e., thermal doming or doming uplift), such as those observed in cratonic area (e.g., Guillocheau *et al.*, 2018; Vasconcelos and Carmo, 2018), usually preserve most of the weathering profile. Net weathering rates of 10–20 m/Ma suggest that thick, lateritic regoliths require several million years to develop (Weybeck, 1979, 1987; Nahon and Tardy, 1992; Wyns, 2002) and that the characteristic low relief landscapes of deeply weathered regions form over periods of 10^7 years (Büdel, 1982; Thiry, 2000). Local and regional effect of relief provides higher water availability in mid- and foot slopes, whereas regional and long-term evolution of landscapes strongly limits erosion and denudation, resulting in deeper weathering mantles (►Fig. 2.8). For a deep weathering mantle formation, the rate of chemical weathering and downward progression of the weathering front must exceed the rate of erosion. The relief must be sufficient to have an adequate drainage to further allow leaching of the products of chemical weathering (Butt *et al.*, 2000; Wyns, 2002; Wyns *et al.*, 2003). Therefore, the only process able to create simultaneously (1) sufficient relief to promote the downward progression of a weathering front, and (2) a weak slope to limit runoff and erosion, is a long-wavelength lithosphere deformation (~500-1000 km) such as continental buckling, rift shoulder, hot spots, (Wyns, 2002), thermal doming (Underhill and Partington, 1993), etc. These elements are discussed in chapter 9.

Hence, periods of **tectonic uplift** such as orogenesis are likely to make widespread laterite *s.l.* formation disappear, since the associated deformation and uplift would promote mechanical erosion instead of chemical weathering. Orogenesis

is also often associated with the increasing continental surface and the aridification of continental interiors, thereby limiting the effectiveness of laterization processes (Butt *et al.*, 2000; Widdowson, 2008). The poor preservation of lateritic materials, due to the weaker nature of lower levels of the weathering profile, is also likely to have resulted in underrepresentation in the geological record, when these mantles face erosion. The result is either the *in situ* preservation of the lower part of the profile only, or the occurrence of eroded duricrust remnants (subtractive weathering) in contemporary additive basins (Borger and Widdowson, 2001; Wyns, 2002; Wyns *et al.*, 2003).

Another important point is the availability of fresh rock and mineral surfaces for weathering attack. Ruddiman and Prell (1997), Ruddiman *et al.* (1997) and Ruddiman (2008) suggested that this exposure effect can override the combined effects of the climate-related factors both locally and globally. This uplift-weathering hypothesis evidences that exposure of fragmented and unweathered rock is an important factor in the intensity of chemical weathering, and that exposure of freshly fragmented rock is enhanced in regions of slow tectonic uplift. Faster weathering draws more CO_2 out of the atmosphere and cools global climate by diminishing greenhouse gases. Conversely, during times when slow uplift is less prevalent, chemical weathering is slower, and CO_2 stays in the atmosphere and warms the climate, producing greenhouse conditions. Such retroactive effect indicates that weathering is a major driver for climate change in controlling CO_2 concentration in the atmosphere.

As a whole, laterite profiles develop better in landscapes characterized by near-horizontal elevated surfaces, such as those formed by long-term exogenic (erosional) or endogenic processes (Widdowson, 2008), limiting the denudation of weathered rocks (►Figs. 2.4 and 2.5). These environments are characterized by limited runoff and erosion, and the long-term input of rainfall and/or the establishment of a water table may serve to promote the evacuation of more mobile constituents. Such conditions are typically encountered in tectonically stable areas.

2.3.4 Eustasy and isostasy

Eustasy reflects changes in the ocean volume, which are directly related to the tectonic regime, and more specifically to the activity of the mid-ocean ridge, but also to glaciation episodes (glacio-eustasy) that can trap or release significant amount of water to the sea. Such factor is of a global range relying on eustasy curve calculation (Haq *et al.*, 1987; Hardenbol *et al.*, 1998), rather than truly local variations of the sea level. The creation of a weathering gradient in relation to eustasy includes modifications of infiltrating water fluxes, permeability of the rocks and the net

thickness of rocks in which water can circulate to reach the zero base level (sea water level). Actually, this basic interpretation is essential given that thick weathering mantle need to be more elevated than seawater, and absolute variations of this level could inhibit or favor weathering processes, inducing high or low drainage. The isostasy expresses that condition of the terrestrial surface results from the flotation of the crust upon the upper mantle (Dutton, 1882), also seen as long wave-length vibrations. Modifications of the mantle activity and of the thickness (and thus weight) of the crust resting upon a liquid (mantle) would affect the vertical movements. The relative sea-level change has recently been refined with respect to orbital forcing of climate change involving cycles of 10^1–10^6 years, and changes attributable to tectonic forcing better constrained over a longer time scale.

It is difficult to determine whether land or sea-level is responsible for the relative elevation of a given area compared to the absolute sea-level (Dott, 1992), but both processes result in creating water gradient from which weathering could be enhanced more or less efficiently. The main point is that both eustasy and isostasy are tightly related to the vertical movement of the lithosphere, and therefore to the creation of relief.

2.4 Structure of a weathering profile

There are (too?) many classification schemes that aim to divide the weathering profile in different zones (McFarlane, 1976; Pain *et al.*, 1991; Tardy, 1997; Wyns, 2002; Wyns *et al.*, 2004; Widdowson, 2008), probably arising from confusion terms (see section 2.1), but also the variety of rock types over which weathering mantles can form. However, most of our knowledge about weathering derives from plutonic, volcanic and metamorphic rocks, as they represent widespread material easily reacting with meteoric fluids, and producing thick weathering mantles. Different horizons can be identified in these rocks (►Fig. 2.1), whereas sedimentary rocks give poorly mature profiles, in which these levels are not always present. These zones are commonly discernible in outcrops from observable changes in color, mineralogy and texture. It is generally recognized that the transformation from unaltered rock to saprolite is essentially isovoluminous (e.g., in the preservation of the rock fabric and mineral structures), whereas significant volume reductions (~70%) can occur in the upper zones of the profile (laterite *s.s.*), mainly due to the chemical and mechanical loss liberated by the breakdown of primary minerals (Widdowson, 2008). From the base to the top, an idealized profile of basaltic rocks shows 5 zonations displaying distinct features (►Fig. 2.1).

2.4.1 Unweathered bedrock and fissured zone

Bedrock does not actually belong to the weathering profile itself, but it is worth being mentioned because it provides materials (minerals and textures) and structures from which weathering mantles can form (see subsection 2.3.1 section). Besides their own magmatic, volcanic, metamorphic or sedimentary features, the upper part of the bedrock and the lower part of the saprolite zone display a transition zone delimited by a fissured horizon (►Fig. 2.9), resulting from tectonic faulting and/or early dismantling of the bedrock (Wyns *et al.*, 2004). Such horizon plays a key role for fluid percolation and migration, those being facilitated in heavily fractured zones. The size and intensity of fractures diminish downward the inner bedrock, but could also vary laterally, resulting in variations of the percolation front depth along the profile, and thus, the weathering front (►Figs. 2.1 and 2.9).

2.4.2 Saprolite zone

The **saprolite zone** displays common relicts of parent rock fabrics, in which 1:1 clays (kaolinite) and relict/etched quartz are observed. Saprock contains less than 20% of primary minerals, whereas saprolite, in the upper part of the zone, displays more than 20% of primary weathered minerals (►Figs. 2.1 and 2.2). The weathering front at the base of the profile is the junction between the unaltered bedrock and the overlying chemically weathered materials (i.e., the base of the saprock zone). This transition occurs over a narrow vertical interval (i.e. <1 m), even if it is rather a progressive evolution than truly a sharp boundary (Widdowson, 2008). A zone containing a mixture of a weathered material with unweathered “core stones” typically occurs immediately above the weathering front (►Fig. 2.1), in which structures and pseudomorphs from the protolith may still be recognized. Since porosity and permeability are often higher in the most weathered parts of the profile, water movements and the breakdown of primary minerals might be significantly slower in the lowest levels comprising the saprock and saprolite (►Fig. 2.1).

2.4.3 Plasmic zone

The **plasmic zone** is a homogeneous component of the weathering profile developed on quartz-poor rocks. It is dominated by clay or silty clay, which have neither the primary fabrics of saprolite nor the significant development of secondary segregation such as nodules and pisoliths found in the upper horizons. There are no peculiar features, but rather a stronger and more intense transformation of primary minerals than in the saprolite zone, especially large amounts of clays (more than 90% of the minerals are weathered and contain kaolinic clay with relict/etched quartz). Arenose

is a term used for sand-rich horizon (Butt *et al.*, 2000). Both are transitional zones between the saprolite and the mottled zone, which are characterized by the loss of fabric without significant chemical and mineralogical changes. The **plasmic and arenose zones** are separated from the saprolite zone by a pedoplasmation front which also separates the saprolite from the pedolith (►Fig. 2.1; Butt *et al.*, 2000; Anand, 2005; Widdowson, 2008).

2.4.4 Mottled zone

The **mottled zone** allows the development of microaggregated secondary structures and fabrics, which consist of kaolinite particles forming a matrix, along with crystals of iron oxide and hydroxide (goethite and hematite) increasing in size and frequency upward in the sequence (►Figs. 2.1 and 2.10). Such horizon displays macroscopic segregation of subdominant colors different from that of the surrounding matrix. Such a texture promotes vertical drainage and further accelerates the alteration process. Mottling is not restricted to the mottled zone but may occur in plasmic, arenose and saprolite horizons. It results from either the accumulation of Fe (brown mottles) or the loss of Fe (white mottles; Anand and Paine, 2002). Mottling in saprolite occurs without the loss of the primary fabric, and makes the distinction between the saprolite and the pedolith. Under alternating dry and wet conditions (i.e., in the water table fluctuation zone), this zone becomes characterized by a strong enrichment in iron oxides (►Fig. 2.1). The altered and Fe-rich zones begin with reddening due to the replacement of primary minerals by iron-rich secondary minerals leading to their segregation that progressively evolves to coalesce the Fe oxides in the upper laterite zone (or laterite *s.s.*). It is separated from the lower plasmic zone by a cementation front.

►**Fig. 2.10** Mottled clays showing reddish halos of Fe oxides in a weathered clay sequence (Hautrage, Belgium).

2.4.5 Laterite zone

The **laterite zone** (or laterite *s.s.***)** displays an increasing amalgamation of ferruginous materials forming a crust (►Fig. 2.3), eventually coalescing to form an interconnected three-dimensional boxwork structure (vermiform or tubular) of mechanically resistant hematite- and goethite-bearing masses in the uppermost levels (cuirass/duricrust). Any remaining voids are filled with soft/friable Al-rich goethite or kaolinite/gibbsite material (e.g., Decrée *et al.*, 2008; Dekoninck *et al.*, 2018, see chapter 8). Pisolith (or pisoid) textures are more common in lower duricrust levels (►Fig. 2.1) and seem to form at or near the water table, possibly because of fluctuations in the ground water level or chemistry. Their occurrence may thus be indicative of pronounced seasonality. Laterite *sensu stricto* are defined primarily as residual materials formed by *in situ* rock breakdown. They should not contain any significant allochthonous components, owing their composition to the relative enrichment of iron (and often aluminum) and other less mobile elements (i.e., Mn). Ferricretes do not achieve their high iron content through residual enrichment, but rather through the net input and absolute accumulation of allochthonous iron into a host rock or existing weathering profile. Elements such as Fe, Al and some trace metals can be redistributed or introduced into the evolving profile by ground water, either in solution or as metallic ions attached to organic compounds. These can then be redeposited at specific levels within the alteration profile by reactions associated with variations in ground water chemistry, Eh and pH, and/or water table fluctuations (►Fig. 2.1; Widdowson, 2008). Commonly, lateritic residuum is most developed over mafic and ultramafic rocks, but could never form over felsic rocks (Anand, 2005).

2.5 Mechanism of formation

The formation of weathering profiles implies the dissolution and the removal of mobile cations in the meteoric waters, and the concentration of relatively immobile elements undergoing weathering conditions. Those lithologies containing quantities of Fe-, Mn- or Al-bearing minerals (among many other elements) will most readily produce Fe-(Mn) laterite *s.s.* or bauxite, under proper conditions of weathering (Varentsov, 1996; Widdowson, 2008). The general trend leads mafic rocks and immature[6] sediments which contain relatively high Fe, to laterization, whereas granite and arkoses, in which feldspar is particularly enriched, are more suitable to form bauxite. Reactions leading to transform primary minerals into secondary ones require a source of metal, the latter being mobilized, transported and then oxidized to insoluble Fe(-Mn)-oxides and Al-bearing minerals (oxides or silicates). The most

[6]A sediment is mature when grains become well-sorted and well-rounded due to weathering or abrasion during transport.

common rock-forming minerals are silicates (e.g., feldspar, olivine, pyroxenes, amphiboles), from which cations can be extracted, most of the time by reaction with rain or ground water containing dissolved CO_2 and organic acids. Sulfuric (from oxidation of sulfides) and phosphorous acids (from dissolution of phosphates) may enhance the acidity of meteoric fluids when they occur in parent rock. The basic reactions leading to the liberation of elements from the protolith minerals and the subsequent loss or accumulation of elements in a weathering profile can thus be expressed as a series of reactions involving water, CO_2, carbonic and organic acid (Widdowson, 2008). However, the development of a weathering profile cannot be regarded as a static system, given that the water table usually fluctuates with seasons and time. All horizons are transformed and reformed as both the ground surface and weathering front are lowered (Bremer *et al.*, 1981).

2.5.1 Hydrolysis of Al-bearing silicates

Hydrolysis[7] is responsible for the breakdown of plagioclase (albite-anorthite; $[Na,Ca_x]Al_{1+x}Si_{3-x}O_8$), by releasing the highly mobile Na^+ and less mobile Ca^{2+} cations in the weathering solution, and thus, leading to the concentration of cation-free silica, such as kaolinite (►Equ. 1 and 2). Biotite hydrolysis might follow the same process (►Equ. 3). Any silica not recombining to form kaolinite goes into solution such as silicic acid (►Equ. 4), and may then be lost in the system with the other mobile cations, even though silica filling pores and voids in the weathering profile is more common.

$2NaAlSi_3O_8$ (albite) + $3H_2O$ + CO_2 → $Al_2Si_2O_5(OH)_4$ (kaolinite)+ $4SiO_2$ (silica) + $2Na^+$ + $2HCO_3^-$ (►Equ. 1)

$CaAl_2Si_2O_8$ (anorthite) + $3H_2O$ + CO_2 → $Al_2Si_2O_5(OH)_4$ (kaolinite) + $4SiO_2$ (silica) + Ca^+ + $2HCO_3^-$ (►Equ. 2)

$K_2Mg_6Si_6Al_2O_2O(OH)_4$ (Mg-biotite) + $14H^+$ + $14HCO_3^-$ + H_2O → $Al_2Si_2O_5(OH)_4$ (kaolinite) + $4H_4SiO_4^\circ$ + $2K^+$ + $6Mg_2$ + $14HCO_3^-$ (►Equ. 3)

SiO_2 (silica) + H_2O → 4 $H_4SiO_4^\circ$ (►Equ. 4)

[7]Hydrolysis is a double decomposition reaction with water as one of the reactants that can recombine with other cations.

The formation of gibbsite is possible under weakly acid conditions with sufficient water and free drainage, along which more silica may be removed from the neoformed kaolinite (►Equ. 5), or less commonly from plagioclase (►Equ. 6).

$$Al_2Si_2O_5(OH)_4 + 5H_2O \rightarrow 2Al(OH)_3 + 2H_4SiO_4^\circ \quad (\blacktriangleright \text{Equ. 5})$$

$$NaAlSi_3O_8 + 8H_2O + CO_2 \rightarrow Al(OH)_3 + 3H_4SiO_4^\circ + Na^+ + HCO_3^- \quad (\blacktriangleright \text{Equ. 6})$$

Following these important reactions occurring in a weathering mantle of granitic rocks, we can infer that kaolinite is an important constituent of many laterite profiles and a common product of hydrolysis. Silica is progressively separated from aluminum in aqueous solutions, the latter being able to precipitate Al silicates or oxides, such as kaolinite or gibbsite, especially when drainage is good. Although conditions at the weathering front may initially favor the formation of micaceous clays (e.g., chlorite, vermiculite) and smectite, small quantities of gibbsite may still be formed, while kaolinite could dominate if free-drainage conditions are met. Gibbsite is usually regarded as the end-point of hydrolysis, in which all silica has been washed away (Tardy and Nahon, 1985; Nahon *et al.*, 1992; Tardy and Roquin, 1992).

2.5.2 Oxidation and hydration of Fe-bearing silicates

The presence of iron as an essential component of laterite profiles is also related to the breakdown of Fe-Mg silicates, the most common being Fe-rich olivine (fayalite), pyroxene and amphibole, which are the main constituent of mafic and ultramafic rocks. Fe^{3+} can be released directly from oxidation and hydration reactions of these Fe-bearing silicates (►Equ. 7; Curtis, 1976). However, the presence of acid would generally produce soluble Fe^{2+} in the weathering system by hydrolysis (Krauskopf, 1957; Krauskopf and Bird, 2003), the latter reaction being more common (►Equ. 8; Widdowson, 2008). The soluble Fe^{2+} (and other) cations are first liberated in solutions, and then, in the presence of oxygen, are immediately precipitated with insoluble Fe^{3+} (►Equ. 9).

$$Fe_2SiO_4 \text{ (fayalite)} + \tfrac{1}{2}O_2 + 2H_2O \rightarrow Fe_2O_3 \text{ (hematite)} + H_4SiO_4^\circ \quad (\blacktriangleright \text{Equ. 7})$$

$$Fe_2SiO_4 \text{ (fayalite)} + 4H_2CO_3 \text{ (carbonic acid)} \rightarrow 2Fe^{2+} + 4HCO_3^- + H_4SiO_4^\circ \quad (\blacktriangleright \text{Equ.8})$$

$$4Fe^{2+} + O_2 + 8HCO_3^- \text{ (bicarbonate)} + 4H_2O \rightarrow 2Fe_2O_3 \text{ (hematite)} + 8H_2CO_3 \quad (\blacktriangleright \text{Equ.9})$$

The behavior of iron in weathering systems is often more complicated, as it is the case for kaolinite and gibbsite, because reduction and oxidation as well as, fluctuations in pH conditions are common. Fe is initially liberated during the breakdown of silicate minerals as soluble Fe^{2+}. However, excess oxygen at the surface of and within the weathering profile allows much of the iron to be rapidly oxidized to Fe^{3+} and to form hematite or goethite. Whether or not the reaction is completed to generate ferric iron within the profile, depends upon CO_2 and O_2 availability, and the availability and/or rate of supply of Fe, as it controls the input of these essential reactants (Widdowson, 2008). Other acids released by bacterial activity, vegetation, phosphates or sulfides would additionally affect pH at different levels, either in surficial water, or in ground waters (Crerar *et al.*, 1972; Stone and Morgan, 1984a, 1984b; Stone, 1987; Varentsov, 1996), which makes the understanding of such system even more complex. Thus, the balance between (carbonic) acid and oxygen in pore water and ground water is of paramount importance in determining the pattern of iron distribution in lateritic profiles. For instance, it may be more difficult for oxygen to diffuse into deeper parts of a weathering mantle and, with increasing depth, conditions may become reduced, resulting in the removal of this ferrous iron in the deepest parts. The water table and nearby areas are usually proper places where oxygen supply is limited and/or microbial activity is enhanced, which can lead to liberate dissolved Fe^{2+} at specific levels in the weathering profile. Such transportation may operate over laterally variable distances, and precipitate iron where ground water meets O_2-rich conditions. This could explain why Fe accumulates within the vadose zone or in ferricretes (Widdowson, 2008).

2.6 Mineralogy and chemistry

More than 200 minerals have been described in laterite *s.l.*, bauxites and ferricretes, arising from the various protoliths and from the reactions operating in these complex systems (Bardossy, 1979; Aleva, 1994). Nevertheless, most rock-forming minerals in laterites *s.l.* and ferricretes consist of a combination of less than a dozen secondary minerals (McFarlane, 1983), containing Fe and Al, as both elements are relatively immobile residues and abundant in the primary parent rock (►Table 2.1).

2.6.1 Mineralogy of laterite weathering profile

The mineralogy of laterite profiles obviously depends on the protolith composition and the stability of the primary minerals from which secondary ones can be formed (►Fig. 2.11). Mafic rocks (e.g., gabbro, basalt) provide primary minerals with high Fe content (e.g., olivine, pyroxene and magnetite), which are particularly suitable for the development of laterites *s.l.*. Basalt has commonly high proportions of feldspar

that could release sufficiently high quantities of Al in the weathering system to further precipitate kaolinite and gibbsite (►Figs. 2.1 and 2.12). Other igneous rock types, such as granite, have a high content of feldspar and associated minerals, although they contain significantly less iron. Quartz is a dominant mineral in these rocks, and may be dissolved during the development of laterite, becoming sparse higher in the weathering profile without changing its mineralogy (Borger, 1993; Delvigne, 1998). Immature sediments (e.g., greywackes and arkoses) can also provide suitable parent rock for laterite *s.l.* formation, if a substantial proportion of unstable Fe-bearing minerals are present, including pyroxenes, micas and feldspar. Mature sediments containing large amounts of quartz (e.g., sandstone) or carbonates (e.g., limestone) commonly contain low Fe mineral content and are therefore not suitable to develop into Fe-rich laterite profiles (Widdowson, 2008). These rocks can rather host allochthon iron forming ferricretes, especially when carbonate dissolution operates.

►**Table 2.1** Common weathering minerals found in laterite *s.l.* and bauxite (McFarlane, 1983)

Type	Mineral	Formula
Neoformation	Hematite	Fe_2O_3
	Goethite	FeOOH
	Kaolinite	$Al_2SiO_5(OH)_4$
	Gibbsite	$Al(OH)_3$
	Boehmite	AlOOH
	Diaspore	AlOOH
	Corundum	Al_2O_3
	Anatase	TiO_2
Residue	Rutile	TiO_2
	Quartz	SiO_2

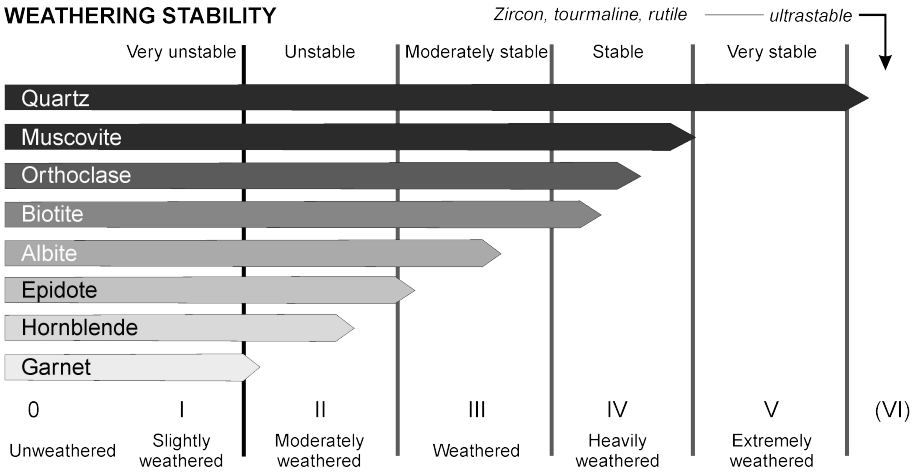

►**Fig. 2.11** Stability field of some primary minerals during increasing weathering conditions (Borger, 2000).

Most of the primary minerals cannot resist longer during weathering, especially under the saprolitization stage, after which few of them can still preserve their shape (►Fig. 2.11). Quartz is usually the only dominant mineral able to support mineralogical transformation by only showing disaggregation. The most durable accessory minerals are zircon, tourmaline and rutile, but magnetite and ilmenite could still be important constituents in some mafic rocks (3–8%; ►Figs. 2.11 and 2.12; Widdowson, 2008). The most widespread minerals formed under weathering conditions are iron and aluminum oxides (►Table 2.1). These minerals may form directly from alteration of primary ones, or via more complex pathways involving the formation of intermediate clays (e.g., chlorite, illite, smectite, vermiculite and halloysite; ►Fig. 2.12), which are themselves converted into more stable Al and Fe oxides (►Table 2.1) in the uppermost part of the profile by losing their mobile cations (Na, K, Ca, Mg; ►Fig. 2.12). This explains why the goethite, hematite, kaolinite and gibbsite content increases progressively upon the upper zone of the profile and are the main constituents of the laterite zone (►Figs. 2.1 and 2.12).

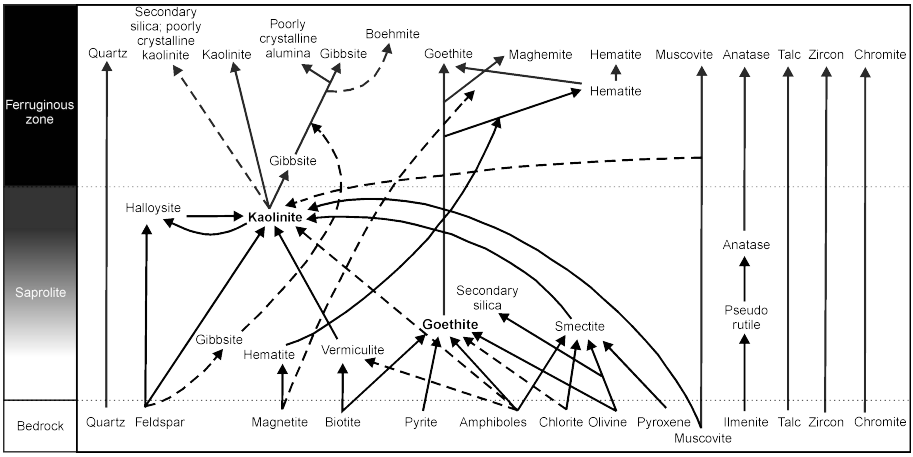

►**Fig. 2.12** Mineralogical chart of secondary minerals in laterite *s.l.* and bauxite profiles in Australia (Anand, 1984, 2005; Anand and Gilkes, 1984a, 1984b, 1984c; Singh and Gilkes, 1991; Robertson and Butt, 1997; Anand and Paine, 2002)**.**

2.6.2 Mineralogy of ferricretes

Instead of the relatively clear succession of minerals and zones forming in saprolite profiles (►Fig. 2.12), ferricretes are often more complex because they derived from unknown sources. The mineral progression in ferricrete profiles is somewhat different than in laterite *s.l.*, probably because ferricrete could lie upon unweathered bedrocks (Bowden, 1987, 1997), or because they are formed by cementation processes that involve remobilization of iron and aluminum as neoformed oxides. Al and Fe oxides inherited from other rocks usually form microcrystalline aggregates. Afterwards, they

coalesce under the supply of external fluids replacing existing silica or carbonates. Bedding planes and joints are suitable places in which these secondary minerals can accumulate. The presence of iron can increase the silica solubility, leading to *in situ* alteration of host-rock silicates that can result, in extreme cases, in the dissolution of quartz grains (Borger, 1993) and their replacement by Fe oxides. Additionally, ferricrete accumulation implies small volume changes (Widdowson, 2008).

2.6.3 Chemical behavior of major and trace elements within a weathering profile

When considering the distribution of chemical elements within a weathering profile, it is important to understand that no mineral remains entirely unaffected by this process, and that no element is entirely immobile or leached from any of the profile horizons. The main driver for chemical variations along a weathering profile is related to the downward progression of the weathering front, and to processes occurring at the water table that can modify pre-existing features (►Fig. 2.1; ►Table 2.2; Butt *et al.*, 2000; Anand, 2005). This general trend is a gross simplification of chemical behavior but is worth being mentioned for the purpose of this section.

►**Table 2.2** Element mobility during deep weathering under humid conditions (Butt *et al.*, 2000).

Host minerals	Leached elements	Partly retained in secondary minerals
Released at the weathering front		
Sulfides	As, Cd, Co, Cu, Mo, Ni, Zn, S	As, Cu, Ni, Pb, Sb, Zn (Fe oxides)
Carbonates	Ca, Mg, Mn, Sr	
Released in lower saprolite		
Al silicates	Ca, Cs, K, Na, Rb	Si, Al (kaolinite); Ba (barite)
Fe-Mg silicates (pyroxenes, olivine, amphiboles, chlorite, biotite)	Ca, Mg	Fe, Ni, Co, Cr, Ga, Mn, Ti, V (Fe and Mn oxides)
Released in upper saprolite		
Al silicates (muscovite)	Cs, K, Rb	Si, Al (kaolinite)
Fe-Mg silicates (chlorite, talc, amphibole)	Mg, Li	Fe, Ni, Co, Cr, Ga, Mn, Ni, Ti, V (Fe oxides)
Smectites	Ca, Mg, Na	Si, Al (kaolinite)
Released in mottled and ferruginous zones		
Al silicates (muscovite, kaolinite)	K, Rb, Cs	Si, Al (kaolinite)
Fe oxides	Trace elements	Si, Al (kaolinite)
Retained in stable minerals	B, Cr, Fe, Hf, K, Nb, Rb, REE, Th, Ti, V, W, Zr	

The distribution of chemical elements within ferricrete alteration profiles is less predictable than the downward progression of weathering in laterite profiles. Their composition directly depends upon the chemical composition of the source, which is usually difficult to identify with absolute certainty (see chapter 7). Analyzing

separate fragments, their geochemical imprint and their mineralogical composition, would in some cases, help to determine their provenance.

2.6.3.a Saprock zone

Sulfides are some of the most unstable minerals in O_2-rich humid environments and can resist in the weathering profile only if they are hosted within resistant quartz veins (Anand, 2005). Many elements hosted in sulfides (e.g., Cd, Co, Cu, Mo, Ni, Zn and S) are commonly leached deeply to the saprock zone (►Fig. 2.1; ►Table 2.2), although some of them can be accommodated in Fe oxides in the near surface environment. Carbonates also have a high sensitivity to weathering agents in the deepest part of a profile, releasing Ca, Mg, Mn and Sr.

2.6.3.b Saprolite zone

The breakdown of feldspar and Fe-Mg minerals in the saprolite zone causes the mobile Na, Ca, K, Mg and Sr to be leached and evacuated from the system. In contrast, Si and Al are partially hosted in kaolinite and halloysite. At least, K can be retained in neoformed clays (illite and smectite) of the early stage of weathering, down in the weathering profile (►Fig. 2.12). In addition, K, Rb and Cs liberation depends upon their primary host, for example, K can survive longer in muscovite than in orthoclase or biotite. Barium, which is commonly hosted by feldspar, is released early during weathering, but is reprecipitated as barite, which remains stable throughout the regolith and is only partly leached in the ferruginous duricrust (►Fig. 2.1). Less stable Fe-Mg minerals produce Fe oxides following the progressive loss of Mg and Si, except if intermediate smectite (Mg, Si), kaolinite (Si) or quartz (Si; ►Fig. 2.12) can partially accommodate these elements and trace elements such as Ni, Co, Cu, Mn and Ni (Nahon *et al.*, 1982; Paquet *et al.*, 1987; Widdowson, 2008). A sharp decline in Mg (and increase in Fe and Si) concentration marks the top of the Mg-saprolite in ultramafic rocks and is characterized by the loss of Mg-bearing phases (carbonates and silicates; Anand, 2005). The more resistant primary minerals and less stable secondary clays (e.g., smectite) may resist until they reach the mid- to upper saprolite zone (►Figs. 2.1 and 2.11). Serpentine, magnetite, ilmenite and chlorite are progressively weathered, leaching from the upper part of the saprolite important strategic metals, such as Ni, Co, Cu and Zn, which precipitate with or within secondary Fe-Mn oxides in the mid to lower saprolite. Under arid conditions, sulfate may also precipitate in saprolite as alunite and halite is commonly a trace constituent throughout the regolith.

2.6.3.c Mottled and laterite zones

Most remaining primary minerals, with the exception of quartz, are destroyed in the mottled and Fe-rich duricrust horizons (►Figs. 2.1 and 2.12). These zones, in particular, demonstrate one of the principal features of deeply weathered regolith

profiles: they are dominated by Si, Al and Fe, which are accommodated in kaolinite, quartz, Fe oxides (goethite, hematite, maghemite) and, in places, gibbsite. Trace elements substitution or precipitation accompanies the formation of kaolinite (e.g., Cr), quartz, Fe oxides (e.g., Cr, As, Ga, Sc and V among others) and gibbsite. The distribution of the relatively immobile Cr, K, Hf, Th, Nb, Ta, W, Sn, some Rare Earth Elements, Ti and V tends to increase upward through the weathering profile, with significant accumulation in the upper laterite zone (Widdowson, 2008). U, V, Ag and Au could be potentially enriched within a weathering profile if there is significant ground water activity (Mann, 1984; Nahon *et al.*, 1992). Enrichment of Ca, Mg, S and Sr in soils and upper horizons, commonly in the top 2 m, relates to the precipitation of secondary sulfates and carbonates (i.e., gypsum, calcite and dolomite) under more arid conditions. Such conditions favor the formation of silica induration protecting the lower parts of the profile of removal.

2.7 Timing of weathering processes

One of the persistent challenge in studying weathering mantles relies on determination of their age. The stratigraphy of weathering profiles shows that some of them in continental landscapes record a complex history, with several periods of weathering, truncation, partial burial, and reweathering (e.g., Finkl, 1984; Tardy and Roquin, 1992; Thiry *et al.*, 2006; Migoń, 2013; Demoulin *et al.*, 2018, this thesis). Stratigraphy also suggests that these superimposed conditions may have operated for an estimated period ranging from tens to hundreds of millions of years, and the resulting profiles may record processes developed under extremely variable climatic and tectonic conditions (Tardy and Roquin, 1992; Demoulin, 2018). Methods of dating laterites *s.l.* can be broadly divided into two major groups. The first is based on geological and/or geomorphological context. Until the early nineties, stratigraphic techniques have provided the most accurate method (Widdowson, 2008). The second method is based upon the saprolite properties themselves, such as clay mineral assemblages or stable isotope ratios, which are correlated with independently established paleoclimatic curves or sediment ages (Bird and Chivas, 1989; Girard *et al.*, 2000). Absolute timing is mainly inferred from K-Ar dating of Mn oxides (detailed in chapter 3) and alunite/jarosite (Vasconcelos *et al.*, 1992; Vasconcelos, 1999), as well as (U-Th)/He dating of Fe oxides for ancient periods (Lippolt *et al.*, 1993) and calculations of abundance of cosmogenic isotopes in recent times (Lal, 1991).

2.7.1 Stratigraphic dating

This method relies on the classic stratigraphic principle of superposition according to which the age of overlying sediments or volcanic rocks provide the minimum age of

weathering. Equally, the age of rocks subjected to weathering provides the maximum age, which in the case of extrusive rocks is almost equal to the actual onset of weathering. As this method provides a relative timing of the weathering profile, relying on a protolith of known age and, in some cases, buried under other rocks of known ages, their precise age often remains unclear (Yans *et al.*, 2003; Thiry *et al.*, 2006; Demoulin, 2018). Establishing the point at which the weathering processes start or cease remains an intricate question. A number of recent studies have however provided some insights to this issue (Théveniaut and Freyssinet, 1999; Vasconcelos, 1999; Migoń and Lidmar-Bergström, 2001; Widdowson, 2008). The stratigraphic method works most effectively in areas subjected to protract volcanic activity, where consecutive lava flows may be preserved in weathering horizons of different ages (Migoń and Lidmar-Bergström, 2001). The method is quite reliable, but is not applicable in most cases, especially where the saprolite occurs at the surface. Even if the saprolite is rapidly covered by sediments, water may still have access beneath permeable and thin cover (Migoń and Lidmar-Bergström, 2001).

2.7.2 Morphostratigraphic dating

The result of continuous removal of material in the upper part of the profile is the lowering of the surface and downward migration of the water table (►Figs. 2.4 and 2.5). This leads weathering profiles to evolve continuously, resulting in migration of the weathering zones until stabilization of the landscape. This situation will end when incision proceeds beyond the rate at which the weathering front progress with the falling water table. This “descending column” model usefully couples laterite *s.l.* development with the long-term evolution of the landscape (Migoń and Lidmar-Bergström, 2002; Demoulin *et al.*, 2018, this thesis, see chapter 6). The methodology of morphostratigraphic dating relies on the accuracy of dating geomorphic surfaces. Unfortunately, their ages are usually poorly constrained.

2.7.3 Secondary mineral interpretation

Much of our present knowledge about the variation in the intensity and rates of weathering processes in the geological past is derived from variations in ocean water composition and from the sedimentary record preserved in the oceanic environment (Robert and Chamley, 1987). The transfer of elements and sediments from continents to oceans identifies increasing erosion (chemical and mechanical), which may or may not be simultaneous with intervals of enhanced mechanical and chemical weathering. The amount of weathering rock clasts in regolith or in transported sediments is often estimated, in addition to other geomorphological and pedological parameters, in order to determine relative ages of geomorphological surfaces. Clast weathering may

therefore be viewed as a "chronofunction" (White *et al.*, 1998), but the parameter that can be used is to some extent site-specific. The paleoclimatic analysis of secondary minerals formed during weathering is the most common method to estimate the age of saprolite. This method is based upon a sequence of assumptions, among which the critical one implies that some secondary minerals (mostly clay minerals), or their associations, are related to specific types of climates. Identification of periods within the geological record, during which climatic conditions have been established, is used to select the most likely weathering periods in local and regional geological settings (Migoń and Lidmar-Bergström, 2001). As this method has proved its usefulness, the role of other factors, such as parent rocks composition, site factors (local geodynamics and hydrology), stage of weathering, and duration of weathering, are difficult to control. It is unlikely that clast roughness, hardness, size, or roundness (Sumner *et al.*, 2002) would yield applicable relative ages of sediments in all cases, the most commonly used indicator of weathering being the depth of weathering (Sak *et al.*, 2004). However, uncertainties remain regarding the exact relationship between weathering and time, which is most likely to be nonlinear and complex.

2.7.4 Environment tracers

Advances in isotope geoscience have also provided a number of environmental tracers (e.g., Savin and Epstein, 1970; Savin and Lee, 1988; Lawrence and Meaux, 1993; Swart *et al.*, 1993). Bird and Chivas (1989) were among the first to recognize the potential of oxygen isotopes in weathering studies, not only as a technique for establishing paleoenvironmental conditions during the formation of weathering profiles, but also as a chronometer for dating residual kaolinite. They noted that pedogenic kaolinite from different stages of the Mesozoic and Tertiary displayed different $\delta^{18}O$ values, and they were able to calibrate this isotopic change over time. Other isotope systems that have been applied to the study of laterite *s.l.* include those of strontium (i.e., $^{87}Sr/^{86}Sr$ ratio), neodymium ($^{143}Nd/^{144}Nd$ ratio reported as ε_{Nd}), and lithium (i.e., $^{7}Li/^{6}Li$ ratio; reported as $\delta^{7}Li$; Widdowson, 2008). A shift in the excursion of such isotopic ratio is commonly attributed to changes in material provenance that could be correlated to global or regional events in some specific periods. Some first-order results of the rhenium-osmium isotope system have shown that rhenium is preferentially mobilized and leached under oxidizing conditions, whereas osmium is retained in upper horizons, mostly by being incorporated in Fe-Al-Mn oxides. Once the upper part of the profile is stripped, low $^{187}Os/^{188}Os$ ratio could be released in the ocean, resulting in high level of non-radiogenic Os in the isotopic record (Peucker-Ehrenbrink and Ravizza, 2000; Wimpenny *et al.*, 2007). The interpretation of such data remains, however, at a preliminary stage.

The assumption that D/H and $^{18}O/^{16}O$ ratios in secondary minerals formed during weathering, namely kaolinite, primarily reflects the isotopic composition of ground water from which they originated and the temperature of formation (e.g., Savin and Epstein, 1970; Savin and Lee, 1988; Lawrence and Meaux, 1993; Gilg and Sheppard, 1996; Sheppard and Gilg, 1996). The stable isotope ratios in ground water in turn reflect the average isotope ratio of rainfall, itself dependent on the mean annual temperature (Bird and Chivas, 1989). Hence, through the analysis of stable isotope geochemistry of weathering products, one can establish the likely temperature ranges of weathering environments and correlate them with the climatic history of a given area (Migoń and Lidmar-Bergström, 2001; Dekoninck *et al.*, 2018, see chapter 8). Such isotopic system could also be applied to other minerals such as goethite, formed in the upper part of the weathering profile (e.g., Savin and Epstein, 1970; Savin and Lee, 1988; Yapp, 1990, 2000; Lawrence and Meaux, 1993; Girard *et al.*, 1997, 2000; Dekoninck *et al.*, 2018), this thesis, chapter 8).

2.7.4 Paleomagnetism

The presence of abundant Fe-bearing minerals in the weathering crust has provided successful material to use paleomagnetic dating techniques, which aim to measure the chemical remnant magnetism (CRM) preserved in Fe minerals (Théveniaut and Freyssinet, 1999). This approach effectively records the cessation of the mineralogical transformations that caused iron accumulation within the profile.

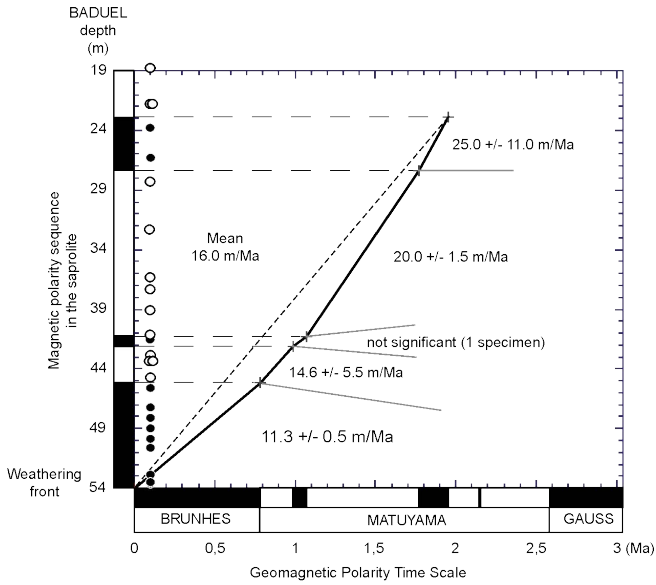

►**Fig. 2.13** Comparisons between magnetic polarity sequence observed through the saprolite of the Mont Baduel profile in French Guiana (Théveniaut and Freyssinet, 1999).

The derived CRM paleomagnetic poles are used to determine weathering ages by comparing them with trajectories of paleomagnetic poles of known age (►Fig. 2.13). The method is particularly useful for sites that have moved their latitudinal position as a result of plate tectonic motion such as Australia, etc. (Schmidt and Embleton, 1976; Schmidt *et al.*, 1983; Kumar, 1986; Acton and Kettles, 1996; Pillans, 1997; Théveniaut and Freyssinet, 1999; Prognon *et al.*, 2011). This method needs to be calibrated by other dating methods.

2.7.5 Geochronological approach

Direct dating of some specific minerals of the weathering mantle has become the focus of earth scientists for studying weathering processes through geological times as it provides a direct age correlation. However, some issues still render such technique tricky, especially when considering partial sampling which does not represent the whole weathering profile, either because erosion has removed some parts (see chapter 6), or outcrop access is not easy (see chapter 5). Regardless of these issues, direct dating still provides material able to restrict the time window over which weathering proceeds, or at least a time interval. The distribution of ages across downward migration of the weathering front creates inverted age profiles (Vasconcelos, 1999). Ideally, older weathering assemblages occur at the top, whereas more recent supergene minerals are present at the bottom of the profile (►Fig. 2.2; Vasconcelos, 1999). This quite simplified model is however more complex than it seems: preferential migration of oxygenated surface waters along permeable horizons or fracture planes may cause the formation of early precipitated, older weathering minerals at lower levels in the profile. This statement suggests a great complexity in the preserved time record because zones that are representative of different weathering stages may occur at the same horizon (►Fig. 2.2; Vasconcelos, 1999). In addition, superimposed weathering events complicate the age distribution owing to recurrent dissolution and reprecipitation of supergene minerals (e.g., Nahon, 1991; Nahon *et al.*, 1992). Finally, weathering profiles are open systems. The continuous flow of mass and energy through the profiles may suggest that these systems are in a continuous state of flux, constantly re-equilibrating with newly imposed environmental conditions (see chapter 7). To provide information about paleoenvironments, weathering profiles must contain minerals precipitated under conditions different from those existing currently. Field and petrographic observations and thermodynamic kinetic models indicate that weathering profiles may exist for extended periods under metastable equilibrium (Vasconcelos, 1999; Migoń and Lidmar-Bergström, 2002; Thiry *et al.*, 2006; Demoulin, 2018; this thesis). Absolute dating of the products of chemical reactions preserved in these weathering profiles can, in this case, provide information about past geochemical and environmental conditions (Vasconcelos *et al.*, 1992, 1994; Vasconcelos, 1999).

Geochronology of weathering processes permits the evaluation of deeply weathered profiles in distinct geomorphological provinces as potential hosts to supergene mineralization (e.g., Vasconcelos *et al.*, 1994; Hénocque *et al.*, 1998; Vasconcelos, 1999; Sillitoe, 2005, 2019; Decrée *et al.*, 2010b; De Putter *et al.*, 2015). Geochronology of weathering profiles provides the database necessary for the correlation between events of global significance (volcanism, tectonic, sea-level changes, chemical changes in oceanic water composition, extinction events, and changes in physical oceanographic patterns) and the weathering record preserved on continents. This database is necessary if cause-and-effect relationships need to be established between global events and continental weathering processes (Vasconcelos 1999).

2.7.5.a K-Ar and $^{40}Ar/^{39}Ar$ dating of sulfates and Mn oxides

Isotopic dating methods such as K-Ar and $^{40}Ar/^{39}Ar$ have been applied to laterites *s.l.* and weathering profiles (see review of Vasconcelos, 1999 and papers later; see chapter 4.4 for details). Target minerals for such investigation are K-bearing minerals that were formed under weathering conditions within a weathering profile. A common problem is that, because protolith-derived micas can survive to considerable alteration (i.e., schists in chapter 6), many weathering profiles contain inherited muscovite, which can generate anomalously old ages. Hence, avoiding this issue is of primary importance and once K-bearing minerals of the parent rocks have been eliminated, the isotopic study can be properly performed. Two main types of K-bearing weathering minerals can be dated. The alunite $[KFe_3(SO_4)_2(OH)_6]$ and jarosite $[KAl_3(SO_4)_2(OH)_6]$ sulfates precipitate through weathering reactions in sulfur-rich systems but also occur in the hydrothermal alteration zones of some ore deposits (Chukhrov *et al.*, 1966; Shanin, 1968; Webb and McDougall, 1968; Vasconcelos *et al.*, 1994; Verhaert *et al.*, 2017, 2018, this thesis, see appendices II and III). K-bearing Mn oxides (cryptomelane, KMn_8O_{16}) of the hollandite group are widespread minerals forming within weathering mantles (Chukhrov *et al.*, 1966; Segev *et al.*, 1991; Vasconcelos *et al.*, 1992, 1995), especially developed upon Mn-rich rocks, but not only. Unlike the dating of igneous or metamorphic rocks, the relationship between these minerals within a laterite profile is often unclear, as these weathering mantles are formed in several stages (see chapter 6). Dating weathering profiles remains challenging as the multistage character of such a system provides potential multiple reactivation and precipitation by meteoric waters and therefore variable ages within a single profile (this thesis; Monteiro *et al.*, 2014, 2018b, 2018a).

2.7.5.b (U-Th)/He dating on Fe oxides

Lateritic weathering profiles host a plethora of supergene iron minerals distributed from the surface (in pisoliths and Fe duricrusts), through the mottled zone, and down into the saprolite and the weathering-bedrock interface. Because weathering products

usually precipitate at near surface temperatures (see chapter 8), and because such conditions are favorable for slow helium diffusion, radiogenic helium is quantitatively retained in supergene goethite. Due to its rapid radiogenic evolution, the (U-Th)/He system offers potential to date a variety of supergene minerals containing even trace amounts of U and/or Th over a range of timescales (~0.5 Ma to ~100 Ma; Shuster *et al.*, 2005). Several studies have used the (U-Th)/He method to obtain dates from pure hydrothermal hematite that were reproducible and consistent with other geological settings (Strutt, 1908; Lippolt *et al.*, 1993, 1995; Wernicke and Lippolt, 1993, 1994a, 1994b, 1997a, 1997b; Farley *et al.*, 1999). However, few of them have investigated the timing of hematite in the weathering environment (Lippolt *et al.*, 1998; Pidgeon *et al.*, 2004; Shuster *et al.*, 2005). More recently, several authors have attempted to apply the (U-Th)/He geochronology to goethite (Lippolt *et al.*, 1998; Shuster *et al.*, 2005; Heim *et al.*, 2006; Yapp and Shuster, 2011; Danišík *et al.*, 2013; Vasconcelos *et al.*, 2013; Monteiro *et al.*, 2014, 2018b, 2018a) and Mn oxides (Lippolt and Hautmann, 1995; Evenson *et al.*, 2014; Reiners *et al.*, 2014). The latter (e.g., cryptomelane) can also be dated by K-Ar and $^{40}Ar/^{39}Ar$ methods and therefore determines the accuracy of both isotopic systems. In young weathering profiles (<1Ma), weathering geochronology by the U-Th dating of pedogenic carbonates and silica minerals provides reliable information on mineral precipitation (Sharp *et al.*, 2003).

2.7.5.c U-Pb dating on carbonates

The most recent improvement in dating methodology arises from the well-known U-Pb system that could have major interest in the study and timing of weathering by meteoric carbonates (Moorbath *et al.*, 1987; Jahn and Cuvellier, 1994; Rasbury *et al.*, 1997; Rasbury and Cole, 2009). Carbonates form in various environments from soils at the surface of the Earth to deep burial associated with hydrothermal fluids. In favorable situations, these carbonates may also be directly dated to constrain the timing of conditions responsible for their precipitation. Because of the long half-lives of ^{238}U and ^{235}U, there is no reason that a limit to date older parts of the rock record exists. For instance, the U-Pb radiometric dating finds mostly applications in diagenetic carbonates (e.g., Jahn and Cuvellier, 1994; Rasbury and Cole, 2009). These studies could be extended, in some points, to meteoric systems (Rasbury *et al.*, 1997), such as speleothems, tuffs, calcretes, and even lacustrine carbonates (Rasbury and Cole, 2009; Columbu *et al.*, 2019). In contrast to many marine settings in which aragonite or Mg calcite dominates, meteoric carbonates tend to be composed of the more stable low Mg calcite. When meteoric carbonates are detritus-free and dense, they often have favorable U-Pb and isotopic systematics and give therefore precise ages. Direct dating of carbonates not only provides the time of sedimentation, but can help to constrain the age of vertebrate in caves, paleoclimatic events recorded in speleothems and paleosoils or unconformities (Hoff *et al.*, 1995; Winter and Johnson, 1995; Rasbury *et al.*, 1997, 1998; Wang *et al.*, 1998; Walker *et al.*, 2006).

2.7.6 Cosmogenic nuclides

The method based on cosmogenic nuclides is another technique for dating exposed lateritic surfaces for a time limited to several thousands of years. The measurement of the accumulated ^{10}Be, ^{36}Cl, ^{26}Al and ^{23}Ne content of surficial materials provides an estimate of the period of surface exposure, and the results have proved valuable in producing denudation chronologies (Lal, 1991). The technique has also been applied to constrain the mechanisms of weathering profile development (Braucher *et al.*, 1998a, 1998b, 2000; Monteiro *et al.*, 2014, 2018b, 2018a) and has revealed information about the erosion and burial of weathering products and lateritic profiles (Brown *et al.*, 1994; Heimsath *et al.*, 2000).

2.7.7 Fission track method on apatite

Apatite fission track (AFT) studies are not directly able to date weathering mantles, but could bring broad information about the thermal history of basement rocks, for example, when they have cooled to reach shallow levels of the Earth crust and likely the Earth surface (►Fig. 2.14; e.g., Barbarand *et al.*, 2001, 2013, 2018; Blaise *et al.*, 2014; Leprêtre *et al.*, 2015, 2017, 2018). They do not provide precise ages but rather long time events of uplifted areas, as this method needs to be calibrated with known periods of exposure or depth in the sedimentary record (Barbarand *et al.*, 2018). This method has not been directly performed in this thesis but results from Belgium (see chapter 6; Barbarand *et al.*, 2018) and Morocco (see chapter 7; Leprêtre *et al.*, 2015b) are used to discuss our data.

The principle of the fission track dating method is based on the spontaneous decay of an unstable mother isotope to a stable daughter at a fixed rate. In this case, a ^{238}U-nuclide decays to fission fragments at a fixed (and known) rate and subsequently, fission track will accumulate spontaneously through time. Temperature and time appear to be the two major geological controlling factors influencing fission track length. Consequently, fission track ages, mean lengths and length distribution (of confined tracks) provide a unique insight into the thermal history of a sample, even allowing for a time-temperature path reconstruction (►Fig. 2.14; Fleischer and Price, 1964; Fleischer *et al.*, 1975; Wagner and Haute, 1992; Gallagher, 2012). The use of apatite [$Ca_5(PO_4)_3(OH,F,Cl)$] is mainly due to its sensitivity to low temperatures and its presence in basement rocks, which allows to calculate the minimal temperature of the total annealing, the total retention temperature and the closure temperature of apatite fission track (Wagner and Reimer, 1972).

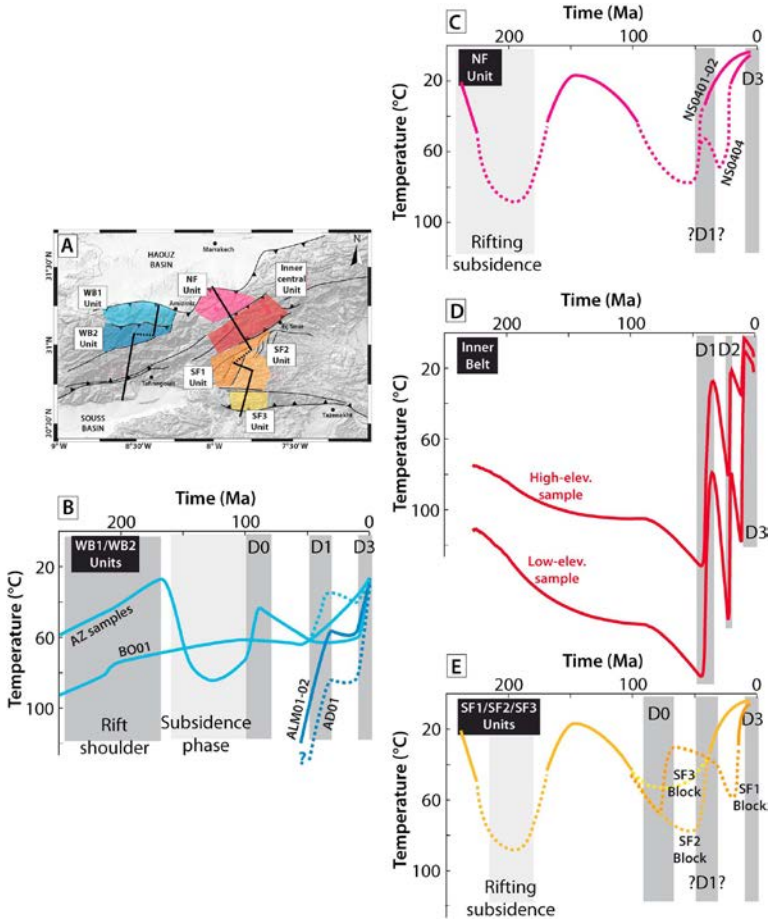

►**Fig. 2.14** Results of the thermal modeling for the western and eastern Moroccan High Atlas based on apatite fission track method showing results of the inverse modeling for different structural domains: Dark and light gray boxes behind the thermal paths correspond respectively to the cooling/erosion phases and to the (re)heating/subsiding phases (Leprêtre *et al.*, 2018).

2.8 Supergene ore deposits

Supergene metal deposits form when rocks or deeply buried primary orebodies (protores) are exposed at or near the Earth's surface and undergo oxidation, dissolution and reconcentration of some metals (e.g., Reich and Vasconcelos, 2015). The interaction of weathering agents with primary rocks or metal-bearing minerals lead some "immobile" elements to be concentrated forming massive supergene deposits. These processes may result in a two- to ten-fold increase in metal grades for such commodities as Cu, Al, Fe, Ni, Mn, U, Au and Zn (Sillitoe, 2005, 2012; Reich and Vasconcelos, 2015). These deposits are usually accessible during the early stages of surface mining and significantly contribute to the overall viability of a mine. This

has been the case since the dawn of civilization, when humans exploited the easily accessible supergene ores in the manufacture of jewels, weapons, alloys, etc. (Dill, 2015). However, the complex mineralogy of most supergene ores implies serious challenges to extractive metallurgy (and mineral processing), and many supergene enrichment zones remain unmined or unprocessed until viable metallurgical processes can be developed (Reich and Vasconcelos, 2015). These deposits also offer an important knowledge about the isotopic fractionation of the metals from their source to more distant secondary sinks, as they are natural analogs of environmental pollution paths (i.e., mine drainage of sulfide deposits; nuclear fuel waste) or corrosion processes (i.e., copper statues, nuclear fuel rods, wastes; Reich and Vasconcelos, 2015). This section provides some of the main weathering deposits in a non-exhaustive way.

2.8.1 Metallogeny of weathering

Weathering processes are complex and operate in different timescales (decades to millions of years) to produce commercial deposits or districts. Such enrichment in metals and raw materials (e.g., kaolin, clays) involves dissolution processes, which are necessarily accompanied by the release of some soluble elements extracted from the parental rock into the weathering fluids, and finally their precipitation forming secondary supergene metal-bearing minerals. Such as any weathering products, these deposits depend on the geodynamics (this thesis), climatic conditions and biological activity. Two processes may lead to concentrate elements: (1) the valuable element is enriched in the residue (weathering crust, *in situ* deposits; see chapters 5, 6 and 8), while much of the rock mass is dissolved and carried away; (2) the valuable element is dissolved from the parental rock and concentrated in other places (karst-hosted and crusts, allochthon deposits; see chapter 7). In most cases, the allochthon material is transported over a short distance (meters or dozen meters), but transport could be efficient over long distances in surface and ground water (Nahon *et al.*, 1992; Reich and Vasconcelos, 2015). Consequently, primary ores that do not have commercial value with low-grade material (called “protores”) can be significantly enriched by supergene processes (►Fig. 2.15).

Supergene enrichment refers to the secondary, *in situ*, accumulation of metals (e.g., Cu, Zn, Ag, Au, Ni, or U) as a result of three processes: (1) the electrochemical oxidation of primary sulfides, oxides or native metals (e.g., native copper Cu^0 to Cu^{2+}); (2) the transport of the released metals as soluble metal species (e.g., $CuSO_4^0$, $AuCl_4^-$); and (3) the reprecipitation of the metals by reduction (e.g., Cu^{2+} to Cu^0), supersaturation (e.g., Mg^{2+} in magnesite deposits), or cation-exchange (e.g., Ni^{2+} exchange for Mg^{2+} in smectite- or serpentine-group minerals; Reich and Vasconcelos, 2015). The generation of metallic concentration occurs during the differentiation of

one or several horizons (►Fig. 2.15). The host minerals that concentrate these metals are secondary carbonates, silicates or oxides that precipitated from solutions. They can also be accumulated as detrital residual particles during the geochemical lowering of the weathering profile. Several examples can illustrate these different situations, such as lateritic concentrations of gold, bauxite, manganese, nickel and copper, among many others.

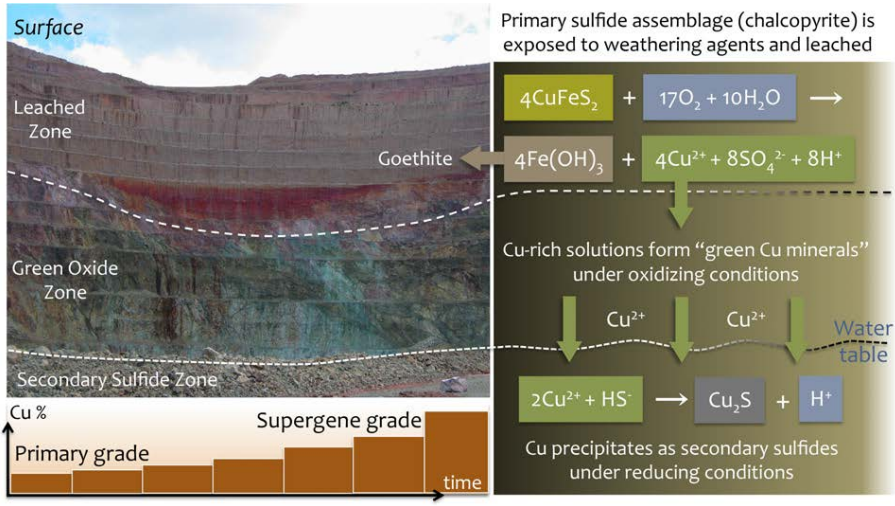

►**Fig. 2.15** Schematic representation of supergene oxidation and enrichment processes for Cu in the south pit of Chino (Santa Rita) porphyry copper mine (New Mexico, USA). Most of the secondary Cu-bearing minerals are cemented in the "green oxide" zone (Reich and Vasconcelos, 2015).

2.8.1.a Gold concentration

Gold-bearing laterites *s.l.* usually overlie or occur immediately adjacent to primary (hypogene) lodes. These secondary supergene deposits contain free particles of high-purity Au (>99 wt.% Au), making them amenable to low-cost open-pit mining (Reith *et al.*, 2012; Reich and Vasconcelos, 2015). Gold-bearing laterites *s.l.* are identified in several places (Gabon, Brazil, United States of America, Australia, New Guinea, India and tropical Africa; references are included in Nahon *et al.*, 1992). They originate from the alteration of primary Au-bearing sulfides, carbonates or quartz. Redistribution of gold within the weathering profile can be controlled by geochemical, biogeochemical or simple mechanical processes. In Gabon, the dissolution of primary gold hosted in quartz veins is recognizable only from the upper part of the saprolite and continues up to the surface (►Fig. 2.16).

Two simultaneous evolutionary trends of gold concentration are observed: a vertical and a lateral one forming a halo around the protores (Colin *et al.*, 1989). The size and roundness forming the typical "nuggets" of gold particles diminishes laterally

and upward of the weathering sequence. Despite tonnages are lower in the surrounding halo, gold particles are purer and richer in Au compared to Ag (Nahon *et al.*, 1992). Gold can concentrate in different ways: (1) at the base of the oxidized zone at the water table level, (2) in fissures, cracks and cavities, and/or (3) at the surface of lateritic nodules within manganese oxides, in clays, or interstratified in Fe oxides. Dissolution of Au proceeds only in advanced weathering conditions within the upper zones and under the presence of chlorite, in order to form Ag and Au chloride complexes.

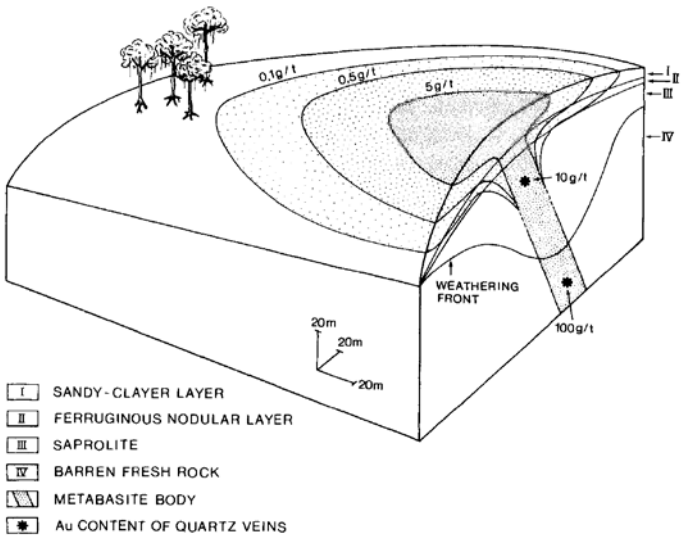

►**Fig. 2.16** Sketch of gold laterite in Gabon showing the dispersion of the gold content (Nahon *et al.*, 1992).

2.9.2.b Bauxite

Concentration of alumina in the humid tropical zone generates lateritic bauxite, which represents the main Al deposits in the world. Parent rocks need to be primarily rich in Al, those being mainly composed of feldspars, such as granite, syenite, nephelinite, etc. Al enrichment follows two processes: direct and indirect bauxitization. The first process, direct bauxitization, is the direct weathering of the parent rock into Al hydroxides under leached and well-drained environments, which preserves the initial texture of the parent rock. This process may be accompanied by transitory minerals (meta-halloysite, halloysite or eve, kaolinite) originating from the parent silica. Although plagioclase and orthoclase are more rapidly weathered than microcline all feldspar are replaced by amorphous alumino-silicate products during the first stage of weathering. Biotite-vermiculite and then goethite with kaolinite replace the primary biotite in the parent rock (►Fig. 2.17). Muscovite is only transformed into gibbsite in the laterite zone after dissolution of quartz, as it can resist under strong weathering conditions (►Figs. 2.11 and 2.12). The porosity resulting from the parent minerals

pseudomorphosis allows gibbsite and Al-rich goethite to precipitate in the upper horizon, finally leading to induration of a massive bauxite crust (Nahon *et al.*, 1992). The second process, indirect bauxitization, produces an important kaolinite weathering product, which subsequently evolves toward aluminum hydroxides. In such environment, mineralogical modifications obliterate primary textures of the parent rocks, which was not the case during direct bauxitization.

Mechanism of bauxite formation are guided by Eh and pH conditions and the prominent role of kaolinite and gibbsite, as they are the main ore-forming minerals in relation with other oxides and hydroxides hosting Al (diaspore, corundum, boehmite, amorphous hydroxides, Al hematite, Al goethite). The formation of whether kaolinite or bauxite depends on the Al/Si ratio but also on the H_2O fugacity of the weathering fluid (Tardy and Novikoff, 1988). The presence of silica strongly influences Al substitutions in Fe oxides, which is low when quartz still occurs in the profile, as well as Fe activity, which can lead to further Fe substitutions in kaolinite, if iron content is high (Tardy and Nahon, 1985).

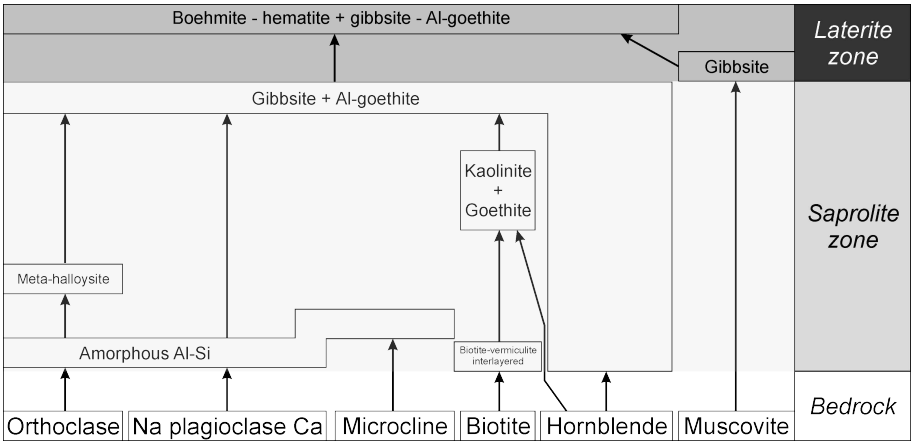

►**Fig. 2.17** Mineral sequence of weathering during direct bauxitization (Lakota, Ivory Coast; Nahon *et al.*, 1992).

2.8.1.c Nickeliferous concentrations

The current decline in magmatic Ni-bearing sulfide lode deposits (Ashok *et al.*, 2004) has led geologists to find an alternative source of Ni, particularly with improved metallurgy processes, making the Ni-Co laterites an important exploration target for future demand of Ni (Mudd, 2010; Butt and Cluzel, 2013). Weathering profiles developed upon ultramafic rocks commonly show commercial grade enrichments in nickel (and cobalt). These profiles contain at the base greenish silicate horizons overlain by a thick oxidized zone (►Fig. 2.18), in which goethite remains the main mineral. Nickel concentration occurs both in the silicate (2-5% NiO) and oxidized zones (1-3% NiO). These Ni-rich laterites are currently reported in several locations

around the world: New Caledonia, Indonesia, Western North America, Brazil, Cuba, Philippines, Venezuela, Australia and South Africa (Nahon *et al.*, 1992; Trescases, 1997; Butt and Cluzel, 2013).

In silicate and oxide deposits, nickel is associated with minerals of the greenish garnierite[8] type (Brindley and Hang, 1973) and with goethite in the upper part of the profile (►Fig. 2.18; Nahon *et al.*, 1992; Dublet *et al.*, 2012). Nickel-bearing parent minerals are essentially olivine (forsterite) and serpentine (mainly lizardite), the latter appearing most often as the hydrothermal alteration product of olivine. Pyroxenes can contain substantial quantities of Ni as well (Nahon *et al.*, 1992). Ni is concentrated by the substitution of Mg or Fe in serpentine or goethite respectively, and by precipitation in Ni-bearing talc. Olivine is weathered faster than orthopyroxene, which is, in turn, faster than clinopyroxene. Serpentine weathers at the slowest rate, and is therefore found higher in the weathering profile. Depending on drainage properties, weathering of primary minerals can generate different products. Olivine can be transformed successively into iddingsite, Ni smectites or Ni carbonates, whereas pyroxenes weather into iddingsite, Ni smectites and Ni talc (pimelite) with quartz. Serpentine is progressively enriched in nickel through the upper part of the weathering profile, forming the Ni end-member nepouite (Brindley and Hang, 1973). In the most oxidized portion of the profiles, all the weathering minerals further weather into goethite, whose nickel content depends upon the mineral from which it originates (Nahon *et al.*, 1992). Other elements, such as cobalt, chromium and manganese can be recovered in such laterite profiles (Decrée *et al.*, 2010a; Marsh and Anderson, 2011).

2.8.2.d Copper concentration

Copper concentration in supergene environments has been widely studied for many decades, mainly because porphyry copper deposits are widespread around the world and offer easy access to investigate weathering processes (►Fig. 2.15; e.g., Alpers and Brimhall, 1988; Sillitoe, 2005, 2012; Ayuso *et al.*, 2010; Taylor, 2011), but also because Cu is an essential element for building our societies (Sverdrup and Ragnarsdóttir, 2014; Arrobas *et al.*, 2017). However, the variable nature of the parent rocks makes a typical profile difficult to assess, given that protores could be massive or disseminated within different host rocks. Furthermore, copper is a very mobile element that is rapidly enriched in secondary minerals in the weathering zones of Cu-rich rocks. Consequently, horizons of Cu concentration do not occur necessarily above parent rocks, such as in bauxite and laterite *s.l.*, but in beds developed laterally or

[8]The term garnierite is a widely used field term referring to the group of green, fine-grained, poorly crystallized, often intimately mixed Ni-bearing magnesium phyllosilicates, mainly composed of nepouite $[(Ni,Mg)_3(Si_2O_5)(OH)_4]$, pimelite $[Ni_3Si_4O_{10}(OH)_2 \cdot 4H_2O]$ and wilemseite $[Ni_3Si_4O_{10}(OH)_2]$.

downslope (►Fig. 2.15), particularly with respect to concentrations of copper carbonates and silicates that can buffer mineralizing fluids (e.g., De Putter *et al.*, 2010, 2018; Decree *et al.*, 2013; Verhaert *et al.*, 2017, 2018, this thesis, see appendices II and III).

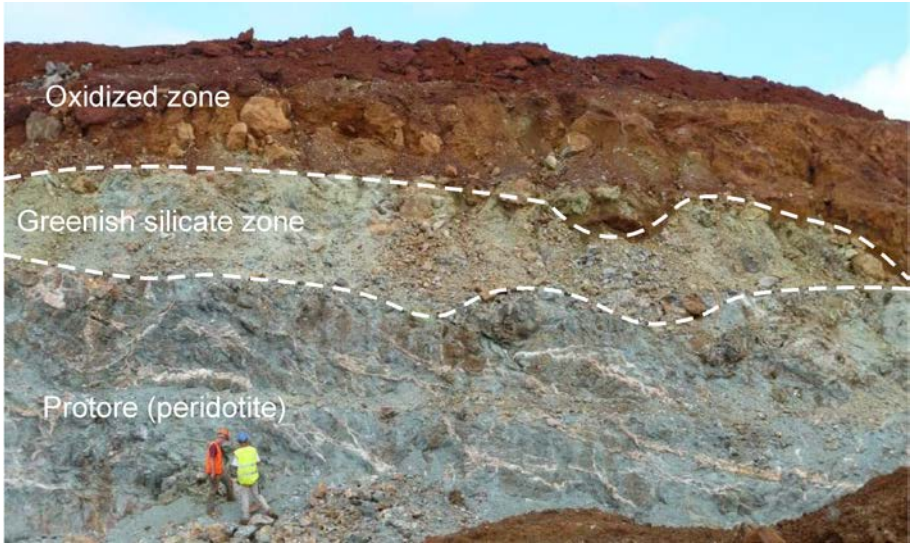

►**Fig. 2.18** Ni-rich laterite profile over ultramafic protores in Tiébaghi (New Caledonia) showing the oxidized and greenish silicate zones.

In most porphyry orebodies, the stepwise hydrolysis and oxidation of primary pyrite-bearing assemblages lead to a decrease in the pH of descending ground waters and to the release of oxidized sulfur as SO_4^{2-} anions. Chalcopyrite ($CuFeS_2$) breaks down, which results in the production of soluble Cu^{2+} ions that are transported downward, encountering progressively greater reducing conditions deep into the profile (►Fig. 2.15). The removal of mobile copper and sulfur from the upper part of the profile leads irrevocably to the formation of Fe oxides and hydroxides forming a crust. Copper is then concentrated below the leached zone, within the oxide zone, which forms laterally extensive deposits composed of assemblages called “green oxides” or “copper oxides” in the vadose zone (►Fig. 2.15). The mineral assemblage is largely controlled by pH and the enclosing rock composition, including oxides (i.e., cuprite, tenorite), sulfates (i.e., brochantite, chalcanthite, antlerite), hydroxyl-chlorides (i.e., atacamite), carbonates (i.e., malachite, azurite), phosphates (i.e., turquoise), silicates (i.e., chrysocolla) and native copper neoformation (Reich and Vasconcelos, 2015). Copper is concentrated to more than 1.0 wt.% in weathering profile of porphyry copper deposits (Sillitoe, 2005; Reich and Vasconcelos, 2015). Under more reducing conditions, the remaining Cu in the descending metal- and sulfate-rich solutions form secondary sulfides in the saturated zone (►Fig. 2.15), below the water table where free oxygen is almost absent. The most common

hypogene minerals (pyrite, chalcopyrite and bornite) are replaced by chalcocite on the top and covelite at the bottom, showing Cu concentration between the 0.4-1.7 wt.% interval, which is 3 to 4 times higher than the primary hypogene concentration (Sillitoe, 2005, 2012; Ayuso *et al.*, 2010).

2.8.2 Supergene metals in a sustainable world

Mineral resources have been extracted and used by mankind since the Stone Age (paleo-meso-neolithic), the Iron Age (siderolithic), the Copper Age (chalcolithic), and the Bronze Age (e.g., Reich and Vasconcelos, 2015; even in Belgium Yans and Dekoninck, 2016, see this thesis appendix I) and are vital blocks to build modern civilization. Therefore, understanding their distribution, the consequences of their use, and the effects of potential mineral supply changes are important themes that societies and public bodies need to deal with (e.g., European Commission, 2015, 2017a; United States Geological Survey, 2017). The demand of common and strategic metals has significantly increased during the past decades and would be maintained by future generations (Rosenau-Tornow *et al.*, 2009; Price, 2013; Graedel *et al.*, 2015; Lusty and Gunn, 2015; Arrobas *et al.*, 2017). The main cause is the transition period from fossil (i.e., oil, gas, and nuclear power plants) to renewable energies (i.e., solar panels, electric cars, wind turbine), and the increasing need of such metals for various manufactures and high technologies (high-tech). This has led communities to define critical metals because of their essential role to modern societies and the risk of supply restriction (►Fig. 2.19; National and Research Council of the National Academies, 2005; European Commission, 2015, 2017b). Ores containing strategic elements such as the rare earth elements (REEs), the platinum group elements (PGEs), as well as cobalt, beryllium, lithium, iodine, tellurium, gallium and rhenium, among others, have become the focus of mining exploration programs and of companies and governments. Significant attention is now paid to alternative sources of these critical raw materials and metals for supplying new types of technologies, including Te, Ga, In, and Ge for solar cells, and the REEs (Nd, Dy, Pr, Sm, Tb, Eu, and La) for high-performance magnets used in wind turbines and electric cars (Reich and Vasconcelos, 2015).

As already mentioned, supergene metal deposits are valuable materials due to their proximity to the surface and their increased metal grades, but also because they allow to diagnose deeper primary mineral assemblages possibly hosting strategic metals. Apart from their major metal components, supergene deposits can contain economic or near-economic concentrations of trace elements, which can limit the risk of shortage (►Fig. 2.19). Base metals (Cu, Zn, Pb, Ni and Co) and associated elements (Al, Fe, Ni, V) significantly contribute to the world supply, such as for example in the supergene zone of the giant porphyry Cu deposits (Sillitoe, 2005). Renew economic interest in supergene Zn deposits ("calamine"-type ore) has also increased during the

past decades, because Zn concentrations are of a higher grade (>30 wt.% Zn) than in hypogene sulfide ores and they can be easily extracted by open-pit methods (Hitzman *et al.*, 2003; Choulet *et al.*, 2014). Economically interesting supergene channel iron deposits are present in Australia (Ramanaidou *et al.*, 2003; Heim *et al.*, 2006; Morris and Ramanaidou, 2007; Danišík *et al.*, 2013). Laterite profiles also constitute another important source of supergene metals, such as Fe, Al (bauxites), Mn, Au, Ni and Co, which are linked to the deep weathering of basement rocks in tropical and tectonically stable areas. Some trace metals can be recovered in association with bauxite deposits, e.g., vanadium and gallium (Reich and Vasconcelos, 2015). Many precious metals (Au, Ag, PGEs[9]) deposits are concentrated in lateritic profiles or supergene enrichment zones within deeply weathered bedrocks. Some precious metals and metalloids are produced entirely as by-products of the major metals, for example Te is produced by Cu refining, Re from Mo, In and Ge from Zn, Ga from Al and Co from Ni ores. Although most critical metals and metalloids rarely form the main commodity in primary ores, supergene enrichment can efficiently concentrate them to economic grades, which in some cases can outweigh the main commodity. Bauxite and laterite *s.l.* deposits represent an important source of Ga and REEs that can reach economic grades and decrease the cost of mining low (Cocker, 2012).

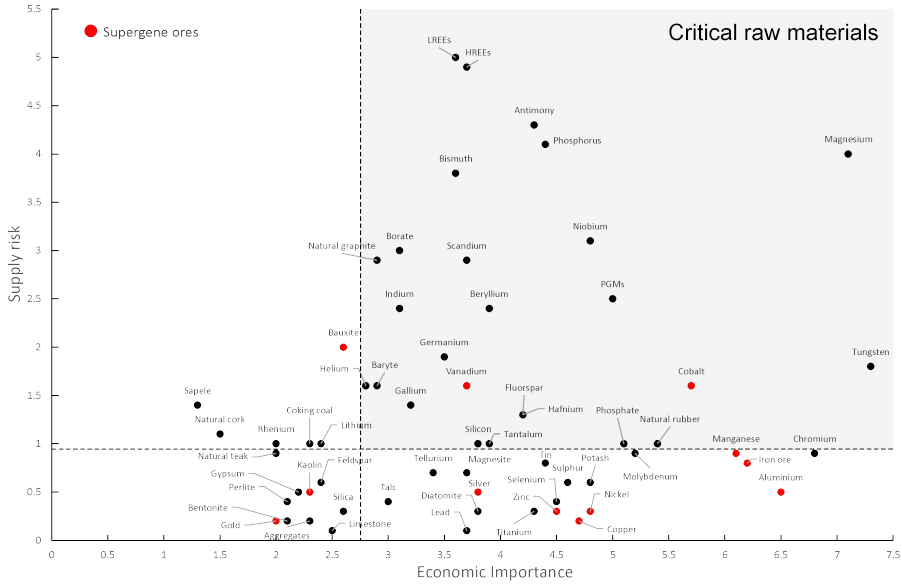

►**Fig. 2.19** Criticality of raw materials for European countries in 2017 and metals mainly or partly mined in supergene ores (European Commission, 2017b).

[9]Platinoid group elements (PGEs) or platinoid group metals (PGMs) include Ru, Rh, Pd, Os, Ir and Pt elements.

2.9 References

Acton, G.D., Kettles, W.A., 1996. Geologic and palaeomagnetic constraints on the formation of weathered profiles near Inverell, Eastern Australia. Palaeogeogr. Palaeoclimatol. Palaeoecol. 126, 211–225. https://doi.org/10.1016/S0031-0182(96)00034-X

Aleva, G.J.J., 1994. Classification of laterites and their textures, in: Banerdji, P.K. (Ed.), Laterisation Processes. Memoirs of the Geological Survey of India, pp. 8–28.

Alpers, C.N., Brimhall, G.H., 1988. Middle Miocene climatic change in the Atacama Desert, northern Chile: Evidence from supergene mineralization at La Escondida. GSA Bull. 100, 1640–1656. https://doi.org/10.1130/0016-7606(1988)100<1640:MMCCIT>2.3.CO;2

Anand, R.R., 2005. Weathering history, landscape evolution and implications for exploration, in: Anand, R.R., de Broekert, P. (Eds.), Regolith Landscape Evolution across Australia. Cooperative Research Centre for Landscape Environments and Mineral Exploration, Bentley, pp. 2–40.

Anand, R.R., 1984. Weathering of Ilmenite in a Lateritic Pallid Zone. Clays Clay Miner. 32, 363–374. https://doi.org/10.1346/CCMN.1984.0320504

Anand, R.R., Gilkes, R.J., 1984a. Weathering of hornblende, plagioclase and chlorite in meta-dolerite, Australia. Geoderma 34, 261–280. https://doi.org/10.1016/0016-7061(84)90043-0

Anand, R.R., Gilkes, R.J., 1984b. Mineralogical and chemical properties of weathered magnetite grains from lateritic saprolite. J. Soil Sci. 35, 559–567. https://doi.org/10.1111/j.1365-2389.1984.tb00613.x

Anand, R.R., Gilkes, R.J., 1984c. Weathering of Ilmenite in a lateritic pallid zone. Clays Clay Miner. 32, 363–374. https://doi.org/10.1346/CCMN.1984.0320504

Anand, R.R., Paine, M., 2002. Regolith geology of the Yilgarn Craton, Western Australia: implications for exploration. Aust. J. Earth Sci. 49, 3–162. https://doi.org/10.1046/j.1440-0952.2002.00912.x

Arrobas, D.L.P., Hund, K.L., Mccormick, M.S., Ningthoujam, J., Drexhage, J.R., 2017. The growing role of minerals and metals for a low carbon future (No. 117581). The World Bank.

Ashok, D., Dalvi, D., Gordon, D.W., Mr, B., Osborne, R.C., 2004. The Past and the Future of Nickel Laterites, in: PDAC 2004 International Convention, Trade Show & Investors Exchange.

Ayuso, R.A., Barton, M.D., Blakely, R.J., Bodnar, R.J., Dilles, J.H., Gray, F., Graybeal, F.T., Mars, J.L., McPhee, D.K., Seal II, R.R., Taylor, R.D., Vikre, P.G., 2010. Porphyry copper deposit model: Chapter B in Mineral deposit models for resource assessment (USGS Numbered Series No. 2010-5070- B), Scientific Investigations Report. U.S. Geological Survey, Reston, VA.

Barbarand, J., Bour, I., Pagel, M., Quesnel, F., Delcambre, B., Dupuis, C., Yans, J., 2018. Post-Paleozoic evolution of the northern Ardenne Massif constrained by apatite fission-track thermochronology and geological data. BSGF - Earth Sci. Bull. 189, 16. https://doi.org/10.1051/bsgf/2018015

Barbarand, J., Lucazeau, F., Pagel, M., Séranne, M., 2001. Burial and exhumation history of the south-eastern Massif Central (France) constrained by apatite fission-track thermochronology. Tectonophysics 335, 275–290. https://doi.org/10.1016/S0040-1951(01)00069-5

Barbarand, J., Quesnel, F., Pagel, M., 2013. Lower Paleogene denudation of Upper Cretaceous cover of the Morvan Massif and southeastern Paris Basin (France) revealed by AFT thermochronology and constrained by stratigraphy and paleosurfaces. Tectonophysics 608, 1310–1327. https://doi.org/10.1016/j.tecto.2013.06.011

Bardossy, G., 1981. Paleoenvironments of laterites and lateritic bauxites – effect of global tectonism on bauxite formation. Presented at the International Seminar on Lateritisation Processes, Balkema, Trivandrum, India, pp. 284–297.

Bardossy, G., 1979. Growing significance of bauxites. Episodes 2, 22–25.

Bárdossy, G., Aleva, G.J.J., 1990. Lateritic bauxites, Developments in economic geology. Elsevier ; Distribution for the U.S.A. and Canada, Elsevier Science Pub. Co, Amsterdam ; New York : New York, N.Y., U.S.A.

Berner, R.A., 1994. GEOCARB II; a revised model of atmospheric CO_2 over Phanerozoic time. Am. J. Sci. 294, 56–91. https://doi.org/10.2475/ajs.294.1.56

Bird, M.I., Chivas, A.R., 1989. Stable-isotope geochronology of the Australian regolith. Geochim. Cosmochim. Acta 53, 3239–3256. https://doi.org/10.1016/0016-7037(89)90104-X

Blaise, T., Barbarand, J., Kars, M., Ploquin, F., Aubourg, C., Brigaud, B., Cathelineau, M., El Albani, A., Gautheron, C., Izart, A., Janots, D., Michels, R., Pagel, M., Pozzi, J.-P., Boiron, M.-C., Landrein, P., 2014. Reconstruction of low temperature (<100 °C) burial in sedimentary basins: A comparison of geothermometer in the intracontinental Paris Basin. Mar. Pet. Geol. 53, 71–87. https://doi.org/10.1016/j.marpetgeo.2013.08.019

Bonnet, N.J., 2015. Dynamique long-terme d'une marge continentale divergente (Les Ghâts Occidentaux de l'Inde péninsulaire) : Contraintes géochronologiques ^{40}Ar-^{39}Ar des paléosurfaces latéritiques (Unpublished Ph.D. thesis). Université d'Aix-Marseille, Marseille.

Borger, H., 2000. Mikromorphologie und Paläoenvironment: die Mineralverwitterung als Zeugnis der cretazisch-tertiären Umwelt in Süddeutschland, Relief, Boden, Paläoklima. Borntraeger, Berlin.

Borger, H., 1993. Penetration of solutions into quartz grains – a scale for weathering intensity, in: Ford, D., McCann, B., Vajoczki, S. (Eds.), Volume of Abstracts. Presented at the Third International Geomorphology Conference, Hamilton.

Borger, H., Widdowson, M., 2001. Indian laterites, and lateritous residues of southern Germany: a petrographic, mineralogical, and geochemical comparison. Z. Für Geomorphol. NF 45, 177–200.

Bourman, R.P., Ollier, C.D., 2002. A critique of the Schellmann definition and classification of 'laterite.' CATENA 47, 117–131. https://doi.org/10.1016/S0341-8162(01)00178-3

Bowden, D.J., 1997. The geochemistry and development of lateritized footslope benches: The Kasewe Hills, Sierra Leone. Geol. Soc. Lond. Spec. Publ. 120, 295–305. https://doi.org/10.1144/GSL.SP.1997.120.01.19

Bowden, D.J., 1987. On the composition and fabric of the footslope laterites (duricrust) of Sierra Leone, West Africa, and their geomorphological significance. Z. Für Geomorphol. NF 64, 39–53.

Braucher, R., Bourlès, D.L., Brown, E.T., Colin, F., Muller, J.-P., Braun, J.-J., Delaune, M., Edou Minko, A., Lescouet, C., Raisbeck, G.M., Yiou, F., 2000. Application of in situ-produced cosmogenic 10Be and 26Al to the study of lateritic soil development in tropical forest: theory and examples from Cameroon and Gabon. Chem. Geol. 170, 95–111. https://doi.org/10.1016/S0009-2541(99)00243-0

Braucher, R., Bourlès, D.L., Colin, F., Brown, E.T., Boulangé, B., 1998a. Brazilian laterite dynamics using in situ-produced 10Be. Earth Planet. Sci. Lett. 163, 197–205. https://doi.org/10.1016/S0012-821X(98)00187-3

Braucher, R., Colin, F., Brown, E.T., Bourlès, D.L., Bamba, O., Raisbeck, G.M., Yiou, F., Koud, J.M., 1998b. African laterite dynamics using in situ-produced ^{10}Be. Geochim. Cosmochim. Acta 62, 1501–1507. https://doi.org/10.1016/S0016-7037(98)00085-4

Bremer, H., Schnütgen, A., Späth, H., 1981. Zur Morphogenese in den feuchten Tropen: Verwitterung und Reliefbildung am Beispiel von Sri Lanka, Relief, Boden, Paläoklima. Borntraeger, Berlin.

Brindley, G.W., Hang, P.T., 1973. The nature of garnierites: I. Structures, chemical compositions and colour characteristics. Clays Clay Min. 21, 27–40.

Brown, E.T., Bourlès, D.L., Colin, F., Sanfo, Z., Raisbeck, G.M., Yiou, F., 1994. The development of iron crust lateritic systems in Burkina Faso, West Africa examined with in-situ-produced cosmogenic nuclides. Earth Planet. Sci. Lett. 124, 19–33. https://doi.org/10.1016/0012-821X(94)00087-5

Büdel, J., 1982. Climatic geomorphology. Princeton University Press, Princeton, N.J.

Bustillo Revuelta, M., 2018. Mineral Resources, Springer Textbooks in Earth Sciences, Geography and Environment. Springer International Publishing, Cham. https://doi.org/10.1007/978-3-319-58760-8

Butt, C.R.M., Cluzel, D., 2013. Nickel laterite ore deposits: weathered serpentinites. Elements 9, 123–128. https://doi.org/10.2113/gselements.9.2.123

Butt, C.R.M., Lintern, M.J., Anand, R.R., 2000. Evolution of regoliths and landscapes in deeply weathered terrain — implications for geochemical exploration. Ore Geol. Rev. 16, 167–183. https://doi.org/10.1016/S0169-1368(99)00029-3

Cailleau, G., Braissant, O., Verrecchia, E.P., 2004. Biomineralization in plants as a long-term carbon sink. Naturwissenschaften 91, 191–194. https://doi.org/10.1007/s00114-004-0512-1

Chadwick, O.A., Hendricks, D.M., Nettleton, W.D., 1989. Silicification of holocene soils in northern Monitor Valley, Nevada. Soil Sci. Soc. Am. J. 53, 158–164.

Choulet, F., Charles, N., Barbanson, L., Branquet, Y., Sizaret, S., Ennaciri, A., Badra, L., Chen, Y., 2014. Non-sulfide zinc deposits of the Moroccan High Atlas: Multi-scale characterization and origin. Ore Geol. Rev. 56, 115–140. https://doi.org/10.1016/j.oregeorev.2013.08.015

Chukhrov, F.V., Shanin, L.L., Yermilov, L.P., 1966. Feasibility of absolute-age determination for potassium-carrying manganese minerals. Int. Geol. Rev. 8, 278–280. https://doi.org/10.1080/00206816609474282

Cocker, M.D., 2012. Lateritic, supergene rare earth element (REE) deposits, in: Conway, F.M. (Ed.), Proceedings of the 48th Annual Forum on the Geology of Industrial Minerals, Arizona Geological Survey Special Paper. Phoenix, Arizona, pp. 1–18.

Colin, F., Minko, E., Nahon, D., 1989. L'or particulaire résiduel dans les profils latéritiques : altération géochimique et dispersion superficielle en conditions équatoriales. Comptes Rendus Académie Sci. - Sér. II 309, 553–560.

Columbu, A., Drysdale, R., Hellstrom, J., Woodhead, J., Cheng, H., Hua, Q., Zhao, J., Montagna, P., Pons-Branchu, E., Edwards, R.L., 2019. U-Th and radiocarbon dating of calcite speleothems from gypsum caves (Emilia Romagna, North Italy). Quat. Geochronol. 52, 51–62. https://doi.org/10.1016/j.quageo.2019.04.002

Crerar, D.A., Cormick, R.K., Barnes, H.L., 1972. Organic controls on the sedimentary geochemistry of manganese. Acta Mineral.-Petrogr. Szeged 20, 217–226.

Curtis, C.D., 1976. Stability of minerals in surface weathering reactions: A general thermochemical approach. Earth Surf. Process. 1, 63–70. https://doi.org/10.1002/esp.3290010107

Danišík, M., Evans, N.J., Ramanaidou, E.R., McDonald, B.J., Mayers, C., McInnes, B.I.A., 2013. (U–Th)/He chronology of the Robe River channel iron deposits, Hamersley Province, Western Australia. Chem. Geol. 354, 150–162. https://doi.org/10.1016/j.chemgeo.2013.06.012

De Putter, T., Liégeois, J.-P., Dewaele, S., Cailteux, J., Boyce, A., Mees, F., 2018. Paleoproterozoic manganese and base metals deposits at Kisenge-Kamata (Katanga, D.R. Congo). Ore Geol. Rev. 96, 181–200. https://doi.org/10.1016/j.oregeorev.2018.04.015

De Putter, T., Mees, F., Decrée, S., Dewaele, S., 2010. Malachite, an indicator of major Pliocene Cu remobilization in a karstic environment (Katanga, Democratic Republic of Congo). Ore Geol. Rev. 38, 90–100. https://doi.org/10.1016/j.oregeorev.2010.07.001

De Putter, T., Ruffet, G., Yans, J., Mees, F., 2015. The age of supergene manganese deposits in Katanga and its implications for the Neogene evolution of the African Great Lakes Region. Ore Geol. Rev. 71, 350–362. https://doi.org/10.1016/j.oregeorev.2015.06.015

Decrée, S., De Putter, T., Yans, J., Moussi, B., Recourt, P., Jamoussi, F., Bruyère, D., Dupuis, C., 2008. Iron mineralisation in Mio-Pliocene sediments of the Tamra iron mine (Nefza mining district, Tunisia): Mixed influence of pedogenesis and hydrothermal alteration. Ore Geol. Rev. 33, 397–410. https://doi.org/10.1016/j.oregeorev.2007.02.001

Decrée, S., Deloule, É., Ruffet, G., Dewaele, S., Mees, F., Marignac, C., Yans, J., De Putter, T., 2010a. Geodynamic and climate controls in the formation of Mio–Pliocene world-class oxidized cobalt and manganese ores in the Katanga province, DR Congo. Miner. Deposita 45, 621–629. https://doi.org/10.1007/s00126-010-0305-8

Decrée, S., Marignac, C., De Putter, T., Yans, J., Clauer, N., Dermech, M., Aloui, K., Baele, J.-M., 2013. The Oued Belif hematite-rich breccia: a Miocene iron oxide Cu-Au-(U-REE) deposit in the Nefza mining district, Tunisia. Econ. Geol. 108, 1425–1457. https://doi.org/10.2113/econgeo.108.6.1425

Decrée, S., Ruffet, G., Putter, T.D., Baele, J.-M., Recourt, P., Jamoussi, F., Yans, J., 2010b. Mn oxides as efficient traps for metal pollutants in a polyphase low-temperature Pliocene environment: A case study in the Tamra iron mine, Nefza mining district, Tunisia. J. Afr. Earth Sci. 57, 249–261. https://doi.org/10.1016/j.jafrearsci.2009.08.005

Dekoninck, A., Moussi, B., Vennemann, T., Jamoussi, F., Mattielli, N., Decrée, S., Chaftar, H.-R., Hatira, N., Yans, J., 2018. Mixed hydrothermal and meteoric fluids evidenced by unusual H- and O-isotope compositions of kaolinite-halloysite in the Fe(-Mn) Tamra deposit (Nefza district, NW Tunisia). Appl. Clay Sci. 163, 33–45. https://doi.org/10.1016/j.clay.2018.07.007

Delvigne, J.E., 1998. Atlas of micromorphology of mineral alteration and weathering, The Canadian mineralogist. Mineralogical Association of Canada ; ORSTOM, Ottawa : Paris.

Demoulin, A. (Ed.), 2018. Landscapes and landforms of Belgium and Luxembourg, World Geomorphological Landscapes. Springer International Publishing, Cham. https://doi.org/10.1007/978-3-319-58239-9

Demoulin, A., Barbier, F., Dekoninck, A., Verhaert, M., Ruffet, G., Dupuis, C., Yans, J., 2018. Erosion surfaces in the Ardenne–Oesling and their associated kaolinic weathering mantle, in: Demoulin, A. (Ed.), Landscapes and landforms of Belgium and Luxembourg. Springer International Publishing, Cham, pp. 63–84. https://doi.org/10.1007/978-3-319-58239-9_5

Dill, H.G., 2015. Supergene Alteration of Ore Deposits: From Nature to Humans. Elements 11, 311–316. https://doi.org/10.2113/gselements.11.5.311

Dott, R.H., 1992. Eustasy: the historical ups and downs of a major geological concept, Geological Society of America Memoirs. Geological Society of America. https://doi.org/10.1130/MEM180

Dublet, G., Juillot, F., Morin, G., Fritsch, E., Fandeur, D., Ona-Nguema, G., Brown, G.E., 2012. Ni speciation in a New Caledonian lateritic regolith: A quantitative X-ray absorption spectroscopy investigation. Geochim. Cosmochim. Acta 95, 119–133. https://doi.org/10.1016/j.gca.2012.07.030

Dutton, C.E., 1882. Physics of the Earth's crust; discussion. Am. J. Sci. Series 3 Vol. 23, 283–290. https://doi.org/10.2475/ajs.s3-23.136.283

Edwards, R., Atkinson, K., 1986. Ore deposit geology and its influence on mineral exploration. Springer Netherlands, Dordrecht. https://doi.org/10.1007/978-94-011-8056-6

European Commission, 2017a. Communication from the commission to the European parliament, the council, the European economic and social committee and the committee of the regions (No. COM(2017) 490). European Commission, Bruxelles.

European Commission, 2017b. Study on the review of the list of Critical Raw Materials, Report of the Ad hoc Working Group on defining critical raw materials. European Commission, Bruxelles.

European Commission, 2015. Report on critical raw materials for the EU (No. Ares(2015)1819503), Report of the Ad hoc Working Group on defining critical raw materials. European Commission, Bruxelles.

Evenson, N.S., Reiners, P.W., Spencer, J.E., Shuster, D.L., 2014. Hematite and Mn oxide (U-Th)/He dates from the Buckskin-Rawhide detachment system, western Arizona: Gaining insights into hematite (U-Th)/He systematics. Am. J. Sci. 314, 1373–1435. https://doi.org/10.2475/10.2014.01

Farley, K.A., Reiners, P.W., Nenow, V., 1999. An apparatus for high-precision helium diffusion measurements from minerals. Anal. Chem. 71, 2059–2061. https://doi.org/10.1021/ac9813078

Finkl, C.W., 1984. Chronology of weathered materials and soil age determination in pedostratigraphic sequences. Chem. Geol. 44, 311–335. https://doi.org/10.1016/0009-2541(84)90079-2

Fleischer, R.L., Price, P.B., 1964. Techniques for geological dating of minerals by chemical etching of fission fragment tracks. Geochim. Cosmochim. Acta 28, 1705–1714. https://doi.org/10.1016/0016-7037(64)90017-1

Fleischer, R.L., Price, P.B., Walker, Robert M., Walker, Robert Mowbray, 1975. Nuclear tracks in solids: principles and applications. University of California Press.

Gallagher, K., 2012. Transdimensional inverse thermal history modeling for quantitative thermochronology. J. Geophys. Res. Solid Earth 117. https://doi.org/10.1029/2011JB008825

Garvie, L., 2003. Decay-induced biomineralization of the saguaro cactus (Carnegiea gigantea). Am. Mineral. 88, 1879–1888.

Gilg, H.A., Sheppard, S.M.F., 1996. Hydrogen isotope fractionation between kaolinite and water revisited. Geochim. Cosmochim. Acta 60, 529–533. https://doi.org/10.1016/0016-7037(95)00417-3

Girard, J.-P., Freyssinet, P., Chazot, G., 2000. Unraveling climatic changes from intraprofile variation in oxygen and hydrogen isotopic composition of goethite and kaolinite in laterites: an integrated study from Yaou, French Guiana. Geochim. Cosmochim. Acta 64, 409–426. https://doi.org/10.1016/S0016-7037(99)00299-9

Girard, J.-P., Razanadranorosoa, D., Freyssinet, P., 1997. Laser oxygen isotope analysis of weathering goethite from the lateritic profile of Yaou, French Guiana: paleoweathering and paleoclimatic implications. Appl. Geochem. 12, 163–174. https://doi.org/10.1016/S0883-2927(96)00062-5

Goudie, A., Pye, K. (Eds.), 1983. Chemical sediments and geomorphology: precipitates and residua in the near-surface environment. Academic Press, London ; New York.

Goudie, A.S., 1973. Duricrust in tropical and subtropical landscapes. Clarendon Press, Oxford.

Graedel, T.E., Harper, E.M., Nassar, N.T., Nuss, P., Reck, B.K., 2015. Criticality of metals and metalloids. Proc. Natl. Acad. Sci. 112, 4257–4262. https://doi.org/10.1073/pnas.1500415112

Grotzinger, J.P., Jordan, T.H., 2014. Understanding Earth, 7th ed. W.H. Freeman and Company, a Macmillan Higher Education Company, New York.

Guillocheau, F., Simon, B., Baby, G., Bessin, P., Robin, C., Dauteuil, O., 2018. Planation surfaces as a record of mantle dynamics: The case example of Africa. Gondwana Res., Rifting to Passive Margins 53, 82–98. https://doi.org/10.1016/j.gr.2017.05.015

Gutzmer, J., Beukes, N.J., 1998. Earliest laterites and possible evidence for terrestrial vegetation in the Early Proterozoic. Geology 26, 263–266. https://doi.org/10.1130/0091-7613(1998)026<0263:ELAPEF>2.3.CO;2

Haq, B.U., Hardenbol, J., Vail, P.R., 1987. Chronology of Fluctuating Sea Levels Since the Triassic. Science 235, 1156–1167. https://doi.org/10.1126/science.235.4793.1156

Hardenbol, J., Thierry, J., Farley, M.B., Jacquin, T., de Graciansky, P.-C., Vail, P.R., 1998. Mesozoic and Cenozoic sequence chronostratigraphic chart, in: Mesozoic and Cenozoic Sequence Stratigraphy of European Basins, SEPM Special Publication. Society for Sedimentary Geology.

Hautmann, S., Lippolt, H.J., 2000. $^{40}Ar/^{39}Ar$ dating of central European K–Mn oxides — a chronological framework of supergene alteration processes during the Neogene. Chem. Geol. 170, 37–80. https://doi.org/10.1016/S0009-2541(99)00241-7

Heim, J.A., Vasconcelos, P.M., Shuster, D.L., Farley, K.A., Broadbent, G., 2006. Dating paleochannel iron ore by (U-Th)/He analysis of supergene goethite, Hamersley province, Australia. Geology 34, 173–176. https://doi.org/10.1130/G22003.1

Heimsath, A.M., Chappell, J., Dietrich, W.E., Nishiizumi, K., Finkel, R.C., 2000. Soil production on a retreating escarpment in southeastern Australia. Geology 28, 787–790. https://doi.org/10.1130/0091-7613(2000)28<787:SPOARE>2.0.CO;2

Hénocque, O., Ruffet, G., Colin, F., Féraud, G., 1998. $^{40}Ar/^{39}Ar$ dating of West African lateritic cryptomelanes. Geochim. Cosmochim. Acta 62, 2739–2756. https://doi.org/10.1016/S0016-7037(98)00185-9

Hitzman, M.W., Reynolds, N.A., Sangster, D.F., Allen, C.R., Carman, C.E., 2003. Classification, genesis, and exploration guides for nonsulfide zinc deposits. Econ. Geol. 98, 685–714. https://doi.org/10.2113/gsecongeo.98.4.685

Hoff, J.A., Jameson, J., Hanson, G.N., 1995. Application of Pb isotopes to the absolute timing of regional exposure events in carbonate rocks; an example from U-rich dolostones from the Wahoo Formation (Pennsylvanian), Prudhoe Bay, Alaska. J. Sediment. Res. 65, 225–233. https://doi.org/10.1306/D426807C-2B26-11D7-8648000102C1865D

Jackson, J.A., Bates, R.L., American Geological Institute (Eds.), 1997. Glossary of geology, 4th ed. American Geological Institute, Alexandria, Va.

Jahn, B., Cuvellier, H., 1994. Pb-Pb and U-Pb geochronology of carbonate rocks: an assessment. Chem. Geol. 115, 125–151. https://doi.org/10.1016/0009-2541(94)90149-X

King, L.C., 1953. Canons of landscape evolution. GSA Bull. 64, 721–752. https://doi.org/10.1130/0016-7606(1953)64[721:COLE]2.0.CO;2

Krauskopf, K.B., 1957. Separation of manganese from iron in sedimentary processes. Geochim. Cosmochim. Acta 12, 61–84. https://doi.org/10.1016/0016-7037(57)90018-2

Krauskopf, K.B., Bird, D.K., 2003. Introduction to geochemistry. McGraw. Hill, New York.

Kumar, A., 1986. Palaeolatitudes and the age of Indian laterites. Palaeogeogr. Palaeoclimatol. Palaeoecol. 53, 231–237. https://doi.org/10.1016/0031-0182(86)90059-3

Lal, D., 1991. Cosmic ray labeling of erosion surfaces: in situ nuclide production rates and erosion models. Earth Planet. Sci. Lett. 104, 424–439. https://doi.org/10.1016/0012-821X(91)90220-C

Lamplugh, G.W., 1902. Calcrete. Geol. Mag. 9, 575–575. https://doi.org/10.1017/S0016756800181646

Lawrence, J.R., Meaux, J.R., 1993. The stable isotopic composition of ancient kaolinites of North America, in: Swart, P.K., Lohmann, K.C., Mckenzie, J., Savin, S. (Eds.), Geophysical Monograph Series. American Geophysical Union, Washington, D. C., pp. 249–261. https://doi.org/10.1029/GM078p0249

Laznicka, P., 1992. Manganese deposits in the global lithogenetic system: Quantitative approach. Ore Geol. Rev. 7, 279–356. https://doi.org/10.1016/0169-1368(92)90013-B

Leprêtre, R., Barbarand, J., Missenard, Y., Gautheron, C., Pinna-Jamme, R., Saddiqi, O., 2017. Mesozoic evolution of NW Africa: implications for the Central Atlantic Ocean dynamics. J. Geol. Soc. 174, 817–835. https://doi.org/10.1144/jgs2016-100

Leprêtre, R., Missenard, Y., Barbarand, J., Gautheron, C., Jouvie, I., Saddiqi, O., 2018. Polyphased inversions of an intracontinental rift: case study of the Marrakech High Atlas, Morocco. Tectonics 37, 818–841. https://doi.org/10.1002/2017TC004693

Leprêtre, R., Missenard, Y., Barbarand, J., Gautheron, C., Saddiqi, O., Pinna-Jamme, R., 2015a. Postrift history of the eastern central Atlantic passive margin: Insights from the Saharan region of South Morocco: Postrift Evolution Moroccan Margin. J. Geophys. Res. Solid Earth 120, 4645–4666. https://doi.org/10.1002/2014JB011549

Leprêtre, R., Missenard, Y., Saint-Bezar, B., Barbarand, J., Delpech, G., Yans, J., Dekoninck, A., Saddiqi, O., 2015b. The three main steps of the Marrakech High Atlas building in Morocco: Structural evidences from the southern foreland, Imini area. J. Afr. Earth Sci. 109, 177–194. https://doi.org/10.1016/j.jafrearsci.2015.05.013

Lippolt, H.J., Brander, T., Mankopf, N.R., 1998. An attempt to determine formation ages of goethites and limonites by (U + Th)-4He dating. Neues Jahrb. Für Mineral. Monatshefte 11, 505–528.

Lippolt, H.J., Hautmann, S., 1995. $^{40}Ar/^{39}Ar$ ages of Precambrian manganese ore minerals from Sweden, India and Morocco. Miner. Deposita 30, 246–256. https://doi.org/10.1007/BF00196360

Lippolt, H.J., Wernicke, R.S., Bähr, R., 1995. Paragenetic specularite and adularia (Elba, Italy): Concordant (U + Th)-He and K-Ar ages. Earth Planet. Sci. Lett. 132, 43–51. https://doi.org/10.1016/0012-821X(95)00046-F

Lippolt, H.J., Wernicke, R.S., Boschmann, W., 1993. ^{4}He diffusion in specular hematite. Phys. Chem. Miner. 20, 415–418. https://doi.org/10.1007/BF00203111

Lusty, P.A.J., Gunn, A.G., 2015. Challenges to global mineral resource security and options for future supply. Geol. Soc. Lond. Spec. Publ. 393, 265–276. https://doi.org/10.1144/SP393.13

Mann, A.W., 1984. Mobility of gold and silver in lateritic weathering profiles; some observations from Western Australia. Econ. Geol. 79, 38–49. https://doi.org/10.2113/gsecongeo.79.1.38

Marsh, E., Anderson, E., 2011. Ni-Co laterites ─ a deposit model (No. 2011–1259). United States Geological Survey, Virginia.

McFarlane, M.J., 1983. Laterites, in: Goudie, A.S., Pye, K. (Eds.), Chemical sediments and geomorphology. Academic Press, London, pp. 7–58.

McFarlane, M.J., 1976. Laterite and landscape. Academic Press, London ; New York.

Merrill, G.P., 1897. A treatise on rocks, rock-weathering and soils. Nature 56, 97–98. https://doi.org/10.1038/056097a0

Migoń, P., 2013. Weathering Mantles and Long-Term Landform Evolution, in: Treatise on Geomorphology. Elsevier, pp. 127–144. https://doi.org/10.1016/B978-0-12-374739-6.00071-3

Migoń, P., 2006. Granite landscapes of the world, geomorphological landscapes of the world. Oxford University Press, Oxford ; New York.

Migoń, P., Lidmar-Bergström, K., 2002. Deep weathering through time in central and northwestern Europe: problems of dating and interpretation of geological record. CATENA 49, 25–40. https://doi.org/10.1016/S0341-8162(02)00015-2

Migoń, P., Lidmar-Bergström, K., 2001. Weathering mantles and their significance for geomorphological evolution of central and northern Europe since the Mesozoic. Earth-Sci. Rev. 56, 285–324. https://doi.org/10.1016/S0012-8252(01)00068-X

Migoń, P., Thomas, M.F., 2002. Grus weathering mantles—problems of interpretation. CATENA 49, 5–24. https://doi.org/10.1016/S0341-8162(02)00014-0

Monteiro, H.S., Vasconcelos, P.M., Farley, K.A., Spier, C.A., Mello, C.L., 2014. (U–Th)/He geochronology of goethite and the origin and evolution of cangas. Geochim. Cosmochim. Acta 131, 267–289. https://doi.org/10.1016/j.gca.2014.01.036

Monteiro, H.S., Vasconcelos, P.M.P., Farley, K.A., 2018a. A Combined (U-Th)/He and Cosmogenic 3He Record of Landscape Armoring by Biogeochemical Iron Cycling. J. Geophys. Res. Earth Surf. 123, 298–323. https://doi.org/10.1002/2017JF004282

Monteiro, H.S., Vasconcelos, P.M.P., Farley, K.A., Lopes, C.A.M., 2018b. Age and evolution of diachronous erosion surfaces in the Amazon: Combining (U-Th)/He and cosmogenic 3He records. Geochim. Cosmochim. Acta 229, 162–183. https://doi.org/10.1016/j.gca.2018.02.045

Moorbath, S., Taylor, P.N., Orpen, J.L., Treloar, P., Wilson, J.F., 1987. First direct radiometric dating of Archaean stromatolitic limestone. Nature 326, 865. https://doi.org/10.1038/326865a0

Morris, R.C., Ramanaidou, E.R., 2007. Genesis of the channel iron deposits (CID) of the Pilbara region, Western Australia. Aust. J. Earth Sci. 54, 733–756. https://doi.org/10.1080/08120090701305251

Mudd, G.M., 2010. Global trends and environmental issues in nickel mining: Sulfides versus laterites. Ore Geol. Rev. 38, 9–26. https://doi.org/10.1016/j.oregeorev.2010.05.003

Nahon, D., 2003. Altérations dans la zone tropicale. Signification à travers les mécanismes anciens et/ou encore actuels. Comptes Rendus Geosci. 335, 1109–1119. https://doi.org/10.1016/j.crte.2003.10.008

Nahon, D., Colin, F., Tardy, Y., 1982. Formation and distribution of Mg,Fe,Mn-smectites in the first stages of the lateritic weathering of forsterite and tephroite. Clay Miner. 17, 339–348.

Nahon, D.B., 1991. Self-organization in chemical lateritic weathering. Geoderma 51, 5–13. https://doi.org/10.1016/0016-7061(91)90063-Y

Nahon, D.B., 1986. Evolution of iron crusts in tropical landscapes, in: Rate of Chemical Weathering of Rocks and Minerals. Dethier, New York, NY, pp. 69–91.

Nahon, D.B., Boulangé, B., Colin, F., 1992. Metallogeny of weathering: an introduction, in: Developments in Earth Surface Processes. Elsevier, pp. 445–471. https://doi.org/10.1016/B978-0-444-89198-3.50022-2

Nahon, D.B., Tardy, Y., 1992. The ferruginous laterites, in: Butt, C.R.M., Zeegers, H. (Eds.), The Ferruginous Laterites, Handbook of Exploration Geochemistry. Elsevier, Amsterdam ; New York; London; Tokyo, pp. 41–55.

Nash, D.J., 2011. Desert Crusts and Rock Coatings, in: Thomas, D.S.G. (Ed.), Arid Zone Geomorphology. John Wiley & Sons, Ltd, Chichester, UK, pp. 131–180. https://doi.org/10.1002/9780470710777.ch8

National, Research Council of the National Academies, 2005. Minerals, Critical Minerals, and the U.S. Economy. https://doi.org/10.17226/12034

Niśkiewicz, J., 2000. Pokrywa zwietrzelinowa masywu Szklar i jej niklonośność. Geol. Sudet. 33, 107–130.

Pain, C.F., Chan, R.A., Craig, M.A., Gibson, D.L., Kilgour, P., Wilford, J.R., 1991. RTMAP regolith database field book and users guide, Bureau of Mineral Resources, Geology and Geophysics. Australia.

Paquet, H., Colin, F., Duplay, J., Nahon, D., Millot, G., 1987. Ni, Mn, Zn, Cr - smectites, early and effective traps for transition elements in supergene ore deposits, in: Rodriguez-Clemente, R., Tardy, Y. (Eds.), Geochemistry and Mineral Formation in the Earth Surface. CSIC, Madrid, pp. 221–229.

Peucker-Ehrenbrink, B., Ravizza, G., 2000. The marine osmium isotope record. Terra Nova 12, 205–219. https://doi.org/10.1046/j.1365-3121.2000.00295.x

Pidgeon, R.T., Brander, T., Lippolt, H.J., 2004. Late Miocene (U+Th)–^{4}He ages of ferruginous nodules from lateritic duricrust, Darling Range, Western Australia. Aust. J. Earth Sci. 51, 901–909. https://doi.org/10.1111/j.1400-0952.2004.01094.x

Pillans, B., 1997. Soil development at snail's pace: evidence from a 6 Ma soil chronosequence on basalt in north Queensland, Australia. Geoderma 80, 117–128. https://doi.org/10.1016/S0016-7061(97)00068-2

Price, J.G., 2013. The challenges of mineral resources for society, in: Geological Society of America Special Papers. Geological Society of America, pp. 1–19. https://doi.org/10.1130/2013.2501(01)

Prognon, F., Lacquement, F., Ricordel-Prognon, C., Quesnel, F., Nehlig, P., Courbouleix, S., Quinquis, J.-P., Martin, P., Rambourg, D., Lebret, P., 2011. Regolith map of France. Quaternaire 357–362. https://doi.org/10.4000/quaternaire.6060

Ramanaidou, E.R., Morris, R.C., Horwitz, R.C., 2003. Channel iron deposits of the Hamersley Province, Western Australia. Aust. J. Earth Sci. 50, 669–690. https://doi.org/10.1111/j.1440-0952.2003.01019.x

Rasbury, E.T., Cole, J.M., 2009. Directly dating geologic events: U-Pb dating of carbonates. Rev. Geophys. 47. https://doi.org/10.1029/2007RG000246

Rasbury, E.T., Hanson, G.N., Meyers, W.J., Holt, W.E., Goldstein, R.H., Saller, A.H., 1998. U-Pb dates of paleosols: Constraints on late Paleozoic cycle durations and boundary ages. Geology 26, 403–406. https://doi.org/10.1130/0091-7613(1998)026<0403:UPDOPC>2.3.CO;2

Rasbury, E.T., Hanson, G.N., Meyers, W.J., Saller, A.H., 1997. Dating of the time of sedimentation using U□Pb ages for paleosol calcite. Geochim. Cosmochim. Acta 61, 1525–1529. https://doi.org/10.1016/S0016-7037(97)00043-4

Reich, M., Vasconcelos, P.M., 2015. Geological and economic significance of supergene metal deposits. elements 11, 305–310. https://doi.org/10.2113/gselements.11.5.305

Reiners, P.W., Chan, M.A., Evenson, N.S., 2014. (U-Th)/He geochronology and chemical compositions of diagenetic cement, concretions, and fracture-filling oxide minerals in Mesozoic sandstones of the Colorado Plateau. GSA Bull. 126, 1363–1383. https://doi.org/10.1130/B30983.1

Reith, F., Stewart, L., Wakelin, S.A., 2012. Supergene gold transformation: Secondary and nano-particulate gold from southern New Zealand. Chem. Geol. 320–321, 32–45. https://doi.org/10.1016/j.chemgeo.2012.05.021

Robert, C., Chamley, H., 1987. Cenozoic evolution of continental humidity and paleoenvironment, deduced from the kaolinite content of oceanic sediments. Palaeogeogr. Palaeoclimatol. Palaeoecol. 60, 171–187. https://doi.org/10.1016/0031-0182(87)90031-9

Robertson, I.D.M., Butt, C.R.M., 1997. Atlas of weathered rocks. Cooperative Research Centre for Landscape Evolution and Mineral Exploration, Wembley, W.A.

Rosenau-Tornow, D., Buchholz, P., Riemann, A., Wagner, M., 2009. Assessing the long-term supply risks for mineral raw materials—a combined evaluation of past and future trends. Resour. Policy 34, 161–175. https://doi.org/10.1016/j.resourpol.2009.07.001

Ruddiman, W.F., 2008. Earth's climate: past and future, 2nd ed. W.H. Freeman, New York.

Ruddiman, W.F., Prell, W.L., 1997. Introduction to the Uplift-Climate Connection, in: Ruddiman, W.F. (Ed.), Tectonic Uplift and Climate Change. Springer US, Boston, MA, pp. 3–15.

Ruddiman, W.F., Raymo, M.E., Prell, W.L., Kutzbach, J.E., 1997. The uplift-climate connection: a synthesis, in: Ruddiman, W.F. (Ed.), Tectonic Uplift and Climate Change. Springer US, Boston, MA, pp. 471–515.

Sak, P.B., Fisher, D.M., Gardner, T.W., Murphy, K., Brantley, S.L., 2004. Rates of weathering rind formation on Costa Rican basalt. Geochim. Cosmochim. Acta 68, 1453–1472. https://doi.org/10.1016/j.gca.2003.09.007

Savin, S.M., Epstein, S., 1970. The oxygen and hydrogen isotope geochemistry of clay minerals. Geochim. Cosmochim. Acta 34, 25–42. https://doi.org/10.1016/0016-7037(70)90149-3

Savin, S.M., Lee, M., 1988. Isotopic studies of phyllosilicates, in: Hydrous Phyllosilicates (Exclusive of Micas), Reviews in Mineralogy. Mineralogical Society of America, pp. 189–223.

Schmidt, P.W., Embleton, B.J.J., 1976. Palaeomagnetic results from sediments of the Perth Basin, Western Australia, and their bearing on the timing of regional lateritisation. Palaeogeogr. Palaeoclimatol. Palaeoecol. 19, 257–273. https://doi.org/10.1016/0031-0182(76)90029-8

Schmidt, P.W., Prasad, V., Ramam, P.K., 1983. Magnetic ages of some Indian laterites. Palaeogeogr. Palaeoclimatol. Palaeoecol. 44, 185–202. https://doi.org/10.1016/0031-0182(83)90102-5

Segev, A., Lang, B., Halicz, L., 1991. K-Ar dating of manganese minerals from the Eisenbach region, Black Forest, southwest Germany. Schweiz. Mineral. Petrogr. Mitteilungen 71, 101–114. https://doi.org/10.5169/seals-54349

Shanin, L.L., 1968. The possible use of alunite in K-Ar geochronometry. Geokhimiya 1, 109–111.

Sharp, W.D., Ludwig, K.R., Chadwick, O.A., Amundson, R., Glaser, L.L., 2003. Dating fluvial terraces by 230Th/U on pedogenic carbonate, Wind River Basin, Wyoming. Quat. Res. 59, 139–150. https://doi.org/10.1016/S0033-5894(03)00003-6

Shaw, R., 1997. Variations in sub-tropical deep weathering profiles over the Kowloon Granite, Hong Kong. J. Geol. Soc. 154, 1077–1085. https://doi.org/10.1144/gsjgs.154.6.1077

Sheppard, S.M.F., Gilg, H.A., 1996. Stable isotope geochemistry of clay minerals. Clay Miner. 31, 1–24. https://doi.org/10.1180/claymin.1996.031.1.01

Shuster, D.L., Vasconcelos, P.M., Heim, J.A., Farley, K.A., 2005. Weathering geochronology by (U-Th)/He dating of goethite. Geochim. Cosmochim. Acta 69, 659–673. https://doi.org/10.1016/j.gca.2004.07.028

Sillitoe, R.H., 2019. Supergene oxidation of epithermal gold-silver mineralization in the Deseado massif, Patagonia, Argentina: response to subduction of the Chile Ridge. Miner. Deposita 54, 381–394. https://doi.org/10.1007/s00126-018-0814-4

Sillitoe, R.H., 2012. Copper provinces, in: Hedenquist, J.W., Harris, M., Camus, F. (Eds.), Geology and Genesis of Major Copper Deposits and Districts of the World: A Tribute to Richard H. Sillitoe. Society of Economic Geologists, pp. 1–18.

Sillitoe, R.H., 2005. Supergene oxidized and enriched porphyry copper and related deposits, in: Hedenquist, J.W., Thompson, J.F.H., Goldfarb, R.J., Richards, J.P. (Eds.), One Hundredth Anniversary Volume. Society of Economic Geologists, pp. 723–768.

Singh, B., Gilkes, R.J., 1991. Weathering of a chromian muscovite to kaolinite. Clays Clay Miner. 39, 571–579. https://doi.org/10.1346/CCMN.1991.0390602

Stephens, C.G., 1971. Laterite and silcrete in Australia: A study of the genetic relationships of laterite and silcrete and their companion materials, and their collective significance in the formation of the weathered mantle, soils, relief and drainage of the australian continent. Geoderma 5, 5–52. https://doi.org/10.1016/0016-7061(71)90023-1

Stone, A.T., 1987. Reductive dissolution of manganese(III/IV) oxides by substituted phenols. Environ. Sci. Technol. 21, 979–988. https://doi.org/10.1021/es50001a011

Stone, A.T., Morgan, J.J., 1984a. Reduction and dissolution of manganese(III) and manganese(IV) oxides by organics: 2. Survey of the reactivity of organics. Environ. Sci. Technol. 18, 617–624. https://doi.org/10.1021/es00126a010

Stone, A.T., Morgan, J.J., 1984b. Reduction and dissolution of manganese(III) and manganese(IV) oxides by organics. 1. Reaction with hydroquinone. Environ. Sci. Technol. 18, 450–456. https://doi.org/10.1021/es00124a011

Strakhov, N.M., 1967. Principles of Lithogenesis. Springer US, Boston, MA. https://doi.org/10.1007/978-1-4684-8923-1

Strutt, R.J., 1908. On the accumulation of helium in geological time. Proc. R. Soc. Lond. Ser. Contain. Pap. Math. Phys. Character 81, 272–277. https://doi.org/10.1098/rspa.1908.0079

Summerfield, M.A., 1979. Origin and palaeoenvironmental interpretation of sarsens. Nature 281, 137. https://doi.org/10.1038/281137a0

Sumner, P., Nel, W., Holness, S., Boelhouwers, J., 2002. Rock weathering characteristics as relative-age indicators for glacial and post-glacial landforms on Marion Island. South Afr. Geogr. J. 84, 153–157. https://doi.org/10.1080/03736245.2002.9713766

Sverdrup, H., Ragnarsdóttir, K.V., 2014. Natural resources in a planetary perspective. Geochem. Perspect. 129–341. https://doi.org/10.7185/geochempersp.3.2

Swart, P.K., Lohmann, K.C., Mckenzie, J., Savin, S. (Eds.), 1993. climate change in continental isotopic records: swart/climate change in continental isotopic records, Geophysical Monograph Series. American Geophysical Union, Washington, D. C. https://doi.org/10.1029/GM078

Tardy, Y., 1997. Petrology of laterites and tropical soils. Balkema, Rotterdam.

Tardy, Y., 1992. Diversity and terminology of lateritic profiles, in: Developments in Earth Surface Processes. Elsevier, pp. 379–405. https://doi.org/10.1016/B978-0-444-89198-3.50020-9

Tardy, Y., 1971. Characterization of the principal weathering types by the geochemistry of waters from some European and African crystalline massifs. Chem. Geol. 7, 253–271. https://doi.org/10.1016/0009-2541(71)90011-8

Tardy, Y., Kobilsek, B., Paquet, H., 1991. Mineralogical composition and geographical distribution of African and Brazilian periatlantic laterites. The influence of continental drift and tropical paleoclimates during the past 150 million years and implications for India and Australia. J. Afr. Earth Sci. Middle East, Sedimentary and Diagenetic Dynamics of Continental Phanerozoic Sediments in Africa 12, 283–295. https://doi.org/10.1016/0899-5362(91)90077-C

Tardy, Y., Nahon, D., 1985. Geochemistry of laterites, stability of Al-goethite, Al-hematite, and Fe (super 3+) -kaolinite in bauxites and ferricretes; an approach to the mechanism of concretion formation. Am. J. Sci. 285, 865–903. https://doi.org/10.2475/ajs.285.10.865

Tardy, Y., Novikoff, A., 1988. Activité de l'eau et déplacement des équilibres gibbsite-kaolinite dans les profils latéritiques. Comptes Rendus Académie Sci. 2 Mécanique 306, 39–44.

Tardy, Y., Roquin, C., 2000. Dérive des continents : paléoclimats et distribution des couvertures pédologiques tropicales (Continental drift : paleoclimates and distribution of the pedological tropical covers). Bull. Assoc. Géographes Fr. 77, 373–383. https://doi.org/10.3406/bagf.2000.2185

Tardy, Y., Roquin, C., 1998. Dérive des continents paléoclimats et altérations tropicales. Ed. BRGM, Orléans.

Tardy, Y., Roquin, C., 1992. Geochemistry and evolution of lateritic landscapes, in: Developments in Earth Surface Processes. Elsevier, pp. 407–443. https://doi.org/10.1016/B978-0-444-89198-3.50021-0

Taylor, G., Eggleton, R.A., 2001. Regolith geology and geomorphology. J. Wiley, Chichester ; New York.

Taylor, G., Eggleton, R.A., Holzhauer, C.C., Maconachie, L.A., Gordon, M., Brown, M.C., McQueen, K.G., 1992. Cool climate lateritic and bauxitic weathering. J. Geol. 100, 669–677. https://doi.org/10.1086/629620

Taylor, R., 2011. Gossans and leached cappings: field assessment. Springer-Verlag, Berlin Heidelberg.

Théveniaut, H., Freyssinet, Ph., 1999. Paleomagnetism applied to lateritic profiles to assess saprolite and duricrust formation processes: the example of Mont Baduel profile (French Guiana). Palaeogeogr. Palaeoclimatol. Palaeoecol. 148, 209–231. https://doi.org/10.1016/S0031-0182(98)00183-7

Thiry, M., 2009. Diversity of continental silicification features: examples from the Cenozoic deposits in the Paris Basin and neighbouring basement, in: Palaeoweathering, Palaeosurfaces and Related Continental Deposits. John Wiley & Sons, Ltd, pp. 85–127. https://doi.org/10.1002/9781444304190.ch4

Thiry, M., 2000. Palaeoclimatic interpretation of clay minerals in marine deposits: an outlook from the continental origin. Earth-Sci. Rev. 49, 201–221. https://doi.org/10.1016/S0012-8252(99)00054-9

Thiry, M., Quesnel, F., Yans, J., Wyns, R., Vergari, A., Theveniaut, H., Simon-Coiçon, R., Ricordel, C., Moreau, M.-G., Giot, D., Dupuis, C., Bruxelles, L., Barbarand, J., Baele, J.-M., 2006. Continental France and Belgium during the early Cretaceous: paleoweatherings and paleolandforms. Bull. Société Géologique Fr. 177, 155–175. https://doi.org/10.2113/gssgfbull.177.3.155

Thomas, M.F., 1994. Geomorphology in the tropics: a study of weathering and denudation in low latitudes. Wiley, Chichester [England] ; New York.

Thomas, M.F., 1966. Some geomorphological implications of deep weathering patterns in crystalline rocks in Nigeria. Inst. Br. Geogr. Trans. 40, 173–193.

Trescases, J.-J., 1997. The lateritic nickel-ore deposits, in: Paquet, H., Clauer, N. (Eds.), Soils and Sediments: Mineralogy and Geochemistry. Springer Berlin Heidelberg, Berlin, Heidelberg, pp. 125–138. https://doi.org/10.1007/978-3-642-60525-3_6

Turkington, A.V., Phillips, J.D., Campbell, S.W., 2005. Weathering and landscape evolution. Geomorphology 67, 1–6. https://doi.org/10.1016/j.geomorph.2004.08.013

Underhill, J.R., Partington, M.A., 1993. Jurassic thermal doming and deflation in the North Sea: implications of the sequence stratigraphic evidence. Geol. Soc. Lond. Pet. Geol. Conf. Ser. 4, 337–345. https://doi.org/10.1144/0040337

United States Geological Survey, 2017. Critical mineral resources of the United States—Economic and environmental geology and prospects for future supply (USGS Numbered Series No. 1802), Professional Paper. U.S. Geological Survey, Reston, VA.

Valeton, I., 1983. Palaeoenvironment of lateritic bauxites with vertical and lateral differentiation. Geol. Soc. Lond. Spec. Publ. 11, 77–90. https://doi.org/10.1144/GSL.SP.1983.011.01.10

Varentsov, I.M., 1996. Manganese ores of supergene zone: Geochemistry of formation, Solid Earth Sciences Library. Springer Netherlands, Dordrecht.

Vasconcelos, P.M., 1999. K-Ar and $^{40}Ar/^{39}Ar$ geochronology of weathering processes. Annu. Rev. Earth Planet. Sci. 27, 183–229. https://doi.org/10.1146/annurev.earth.27.1.183

Vasconcelos, P.M., Becker, T.A., Renne, P.R., Brimhall, G.H., 1992. Age and duration of weathering by ^{40}K-^{40}Ar and $^{40}Ar/^{39}Ar$ analysis of potassium-manganese oxides. Science 258, 451–455. https://doi.org/10.1126/science.258.5081.451

Vasconcelos, P.M., Brimhall, G.H., Becker, T.A., Renne, P.R., 1994. ^{40}Ar-^{39}Ar analysis of supergene jarosite and alunite: Implications to the paleoweathering history of the western USA and West Africa. Geochim. Cosmochim. Acta 58, 401–420. https://doi.org/10.1016/0016-7037(94)90473-1

Vasconcelos, P.M., Carmo, I. de O., 2018. Calibrating denudation chronology through $^{40}Ar/^{39}Ar$ weathering geochronology. Earth-Sci. Rev. 179, 411–435. https://doi.org/10.1016/j.earscirev.2018.01.003

Vasconcelos, P.M., Heim, J.A., Farley, K.A., Monteiro, H., Waltenberg, K., 2013. $^{40}Ar/^{39}Ar$ and (U–Th)/He – $^{4}He/^{3}He$ geochronology of landscape evolution and channel iron deposit genesis at Lynn Peak, Western Australia. Geochim. Cosmochim. Acta 117, 283–312. https://doi.org/10.1016/j.gca.2013.03.037

Vasconcelos, P.M., Renne, P.R., Becker, T.A., Wenk, H.-R., 1995. Mechanisms and kinetics of atmospheric, radiogenic, and nucleogenic argon release from cryptomelane during analysis. Geochim. Cosmochim. Acta 59, 2057–2070. https://doi.org/10.1016/0016-7037(95)00126-3

Verhaert, M., Bernard, A., Dekoninck, A., Lafforgue, L., Saddiqi, O., Yans, J., 2017. Mineralogical and geochemical characterization of supergene Cu–Pb–Zn–V ores in the Oriental High Atlas, Morocco. Miner. Deposita. https://doi.org/10.1007/s00126-017-0753-5

Verhaert, M., Bernard, A., Saddiqi, O., Dekoninck, A., Essalhi, M., Yans, J., 2018. Mineralogy and Genesis of the Polymetallic and Polyphased Low Grade Fe-Mn-Cu Ore of Jbel Rhals Deposit (Eastern High Atlas, Morocco). Minerals 8, 39. https://doi.org/10.3390/min8020039

Wagner, G., Haute, P. van den, 1992. Fission-Track Dating, Solid Earth Sciences Library. Springer Netherlands.

Wagner, G.A., Reimer, G.M., 1972. Fission track tectonics: The tectonic interpretation of fission track apatite ages. Earth Planet. Sci. Lett. 14, 263–268. https://doi.org/10.1016/0012-821X(72)90018-0

Walker, J., Cliff, R.A., Latham, A.G., 2006. U-Pb Isotopic Age of the StW 573 Hominid from Sterkfontein, South Africa. Science 314, 1592–1594. https://doi.org/10.1126/science.1132916

Wang, Z.S., Rasbury, E.T., Hanson, G.N., Meyers, W.J., 1998. Using the U-Pb system of calcretes to date the time of sedimentation of clastic sedimentary rocks. Geochim. Cosmochim. Acta 62, 2823–2835. https://doi.org/10.1016/S0016-7037(98)00201-4

Webb, A.W., McDougall, I., 1968. The geochronology of the igneous rocks of Eastern Queensland. J. Geol. Soc. Aust. 15, 313–346. https://doi.org/10.1080/00167616808728701

Wernicke, R.S., Lippolt, H.J., 1997a. (U+Th)–He evidence of Jurassic continuous hydrothermal activity in the Schwarzwald basement, Germany. Chem. Geol. 138, 273–285. https://doi.org/10.1016/S0009-2541(97)00020-X

Wernicke, R.S., Lippolt, H.J., 1997b. Evidence of Mesozoic multiple hydrothermal activity in the basement at Nonnenmattweiher (southern Schwarzwald), Germany. Miner. Deposita 32, 197–200. https://doi.org/10.1007/s001260050085

Wernicke, R.S., Lippolt, H.J., 1994a. Dating of vein Specularite using internal (U+Th)/4He isochrons. Geophys. Res. Lett. 21, 345–347. https://doi.org/10.1029/94GL00014

Wernicke, R.S., Lippolt, H.J., 1994b. 4He age discordance and release behavior of a double shell botryoidal hematite from the Schwarzwald, Germany. Geochim. Cosmochim. Acta 58, 421–429. https://doi.org/10.1016/0016-7037(94)90474-X

Wernicke, R.S., Lippolt, H.J., 1993. Botryoidal hematite from the Schwarzwald (Germany): heterogeneous uranium distributions and their bearing on the helium dating method. Earth Planet. Sci. Lett. 114, 287–300. https://doi.org/10.1016/0012-821X(93)90031-4

Weybeck, M., 1987. Global chemical weathering of surficial rocks estimated from river dissolved loads. Am. J. Sci. 287, 401–428.

Weybeck, M., 1979. Concentration des eaux fluviales en éléments majeurs et apports en solution aux océans. Rev. Géologie Dyn. Géographie Phys. 21, 215–246.

White, K., Bryant, R., Drake, N., 1998. Techniques for measuring rock weathering: application to a dated fan segment sequence in southern Tunisia. Earth Surf. Process. Landf. 23, 1031–1043. https://doi.org/10.1002/(SICI)1096-9837(1998110)23:11<1031::AID-ESP919>3.0.CO;2-G

Widdowson, M., 2008. Laterite and Ferricrete, in: Nash, D.J., McLaren, S.J. (Eds.), Geochemical Sediments and Landscapes. Blackwell Publishing Ltd, Oxford, UK, pp. 45–94. https://doi.org/10.1002/9780470712917.ch3

Wimpenny, J., Gannoun, A., Burton, K.W., Widdowson, M., James, R.H., Gíslason, S.R., 2007. Rhenium and osmium isotope and elemental behaviour accompanying laterite formation in the Deccan region of India. Earth Planet. Sci. Lett. 261, 239–258. https://doi.org/10.1016/j.epsl.2007.06.028

Winter, B.L., Johnson, C.M., 1995. U-Pb dating of a carbonate subaerial exposure event. Earth Planet. Sci. Lett. 131, 177–187. https://doi.org/10.1016/0012-821X(95)00026-9

Wright, V. P, Wright, V. Paul, Tucker, M.E., service), W.I., 1991. Calcretes. Oxford [England] ; Boston : Blackwell Scientific Publications.

Wright, V.P., 2008. Calcrete, in: Geochemical Sediments and Landscapes. John Wiley & Sons, Ltd, pp. 10–45. https://doi.org/10.1002/9780470712917.ch2

Wyns, R., 2002. Climat, eustatisme, tectonique: quels contrôles pour l'altération continentale? Exemple des séquences d'altération cénozoïques en France. Bull. Inf. Géologues Bassin Paris 39, 5–16.

Wyns, R., Baltassat, J.-M., Lachassagne, P., Legchenko, A., Vairon, J., Mathieu, F., 2004. Application of proton magnetic resonance soundings to groundwater reserve mapping in weathered basement rocks (Brittany, France). Bull. Soc. Geol. Fr. 175, 21–34. https://doi.org/10.2113/175.1.21

Wyns, R., Quesnel, F., Simon-Coinçon, R., Guillocheau, F., Lacquement, F., 2003. Major weathering in France related to lithospheric deformation. Géologie Fr. 79–87.

Yans, J., Chauvin, A., Clauer, N., Dejax, J., De Putter, T., Dupuis, C., Feraud, G., Guillocheau, F., Masure, E., Leost, I., Perruchot, A., Pons, D., Spagna, P., Wyns, R., 2003. An overview of the saprolites of Belgium and their potential kaolinitic supplies to Mesozoic and Cenozoic sediments. Géologie Fr. 1, 33–37.

Yans, J., Dekoninck, A., 2016. Ressources du sous-sol wallon : historique, état des lieux et perspectives. Mines Carr. Hors Série 18, 5–12.

Yapp, C.J., 2000. Climatic implications of surface domains in arrays of dD and $d^{18}O$ from hydroxyl minerals: Goethite as an example. Geochim. Cosmochim. Acta 64, 2009–2025.

Yapp, C.J., 1990. Oxygen isotopes in iron (III) oxides: 1. Mineral-water fractionation factors. Chem. Geol. 85, 329–335. https://doi.org/10.1016/0009-2541(90)90010-5

Yapp, C.J., Shuster, D.L., 2011. Environmental memory and a possible seasonal bias in the stable isotope composition of (U–Th)/He-dated goethite from the Canadian Arctic. Geochim. Cosmochim. Acta 75, 4194–4215. https://doi.org/10.1016/j.gca.2011.04.029

Chapter 3

Manganese metallogenesis

Chapter 3

Manganese metallogenesis

This third chapter draws the big picture of manganese accumulation in the geological record. The chemical element "Mn" for "Manganese" is a little-known element used by metallurgists and chemists, occurring in the form of silicate, carbonate or oxide in natural environment. It is the 10th most abundant element in the Earth crust (Li, 2000) and the 4th most produced in the world (U.S. Geological Survey, 2018; ►Fig. 1.1). It is similar to iron in its chemical properties and often substitutes for iron in its divalent and trivalent form, but it also differs from Fe as tetravalent Mn^{4+} can give rise to Mn oxide minerals that do not have Fe counterparts. The formation of manganese rocks and ores has occurred over practically the entire geological history of the formation of the Earth's upper crust (Kuleshov, 2016). However, economic Mn deposits occur in specific metallogenetic epochs, which are unevenly distributed over geological times and cluster in three groups: Paleoproterozoic, Neoproterozoic, and Cenozoic (►Fig. 3.1; Maynard, 2010). Paleoproterozoic deposits are by far the largest and correspond to the major episode of banded iron ore formation, when the Earth's atmosphere oxygenated after 2.3 Ga. Neoproterozoic Mn deposits are also contemporary to iron ore formation, whereas the Cenozoic (Oligocene—34 to 23 million years ago) deposits are not associated with Fe mineralization (Roy, 2006; Maynard, 2010; Kuleshov, 2011; Beukes *et al.*, 2016). The greatest Paleoproterozoic Mn deposits are situated in the Kalahari Desert of South Africa. The largest Neoproterozoic Mn deposit is located in Brazil and many smaller in China (Maynard, 2010). Oligocene deposits are centered around the Black Sea (Kuleshov, 2011; ►Fig. 3.2). Even though, giant Mn deposits have a sedimentary origin, supergene ores have a significant importance (this thesis), given that they are generally higher grade (Laznicka, 1992; Varentsov, 1996; Kuleshov, 2016). Unexploited manganese resources are found on the oceanic floor as manganese nodules precipitate from seawater (Glasby, 2006; Wang and Müller, 2009).

Within the next sections, I draw the readers' attention on mineralogical considerations and features needed to understand accurately the formation of massive manganese deposits through sedimentary (see chapter 6), metamorphic (e.g., Ardenne, this thesis, chapter 6; Demoulin *et al.*, 2018, Dekoninck *et al.* in revision, in revision), hydrothermal (e.g., Vosges and Nefza districts, see chapters 5 and 8; Dekoninck *et al.*, 2018), and supergene processes (e.g., Imini-Tasdremt district, this thesis, chapter 7; Leprêtre *et al.*, 2015; Dekoninck *et al.*, 2016b, 2016a).

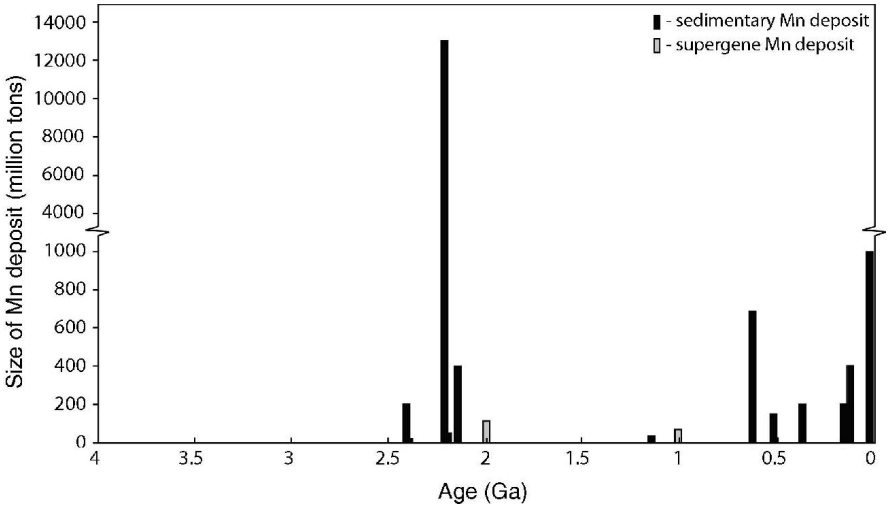

►**Fig. 3.1** Mass-age distribution of sedimentary (black) and supergene (gray) manganese ore deposits through time (Johnson *et al.*, 2016 and references therein). Note that other compilations have included small Archean manganese deposits (Roy, 2006; Maynard, 2010), but because these appear to be derived from later weathering of Archean carbonate strata, they are not included in this figure, as the timing of weathering is poorly constrained.

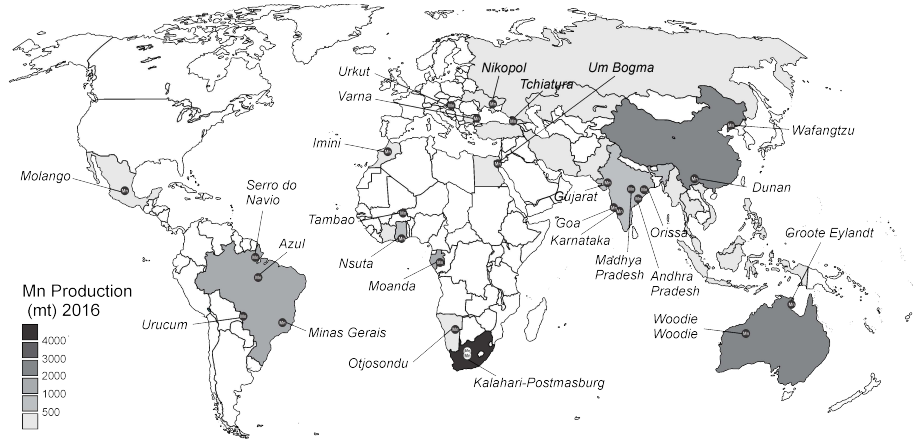

►**Fig. 3.2** World map of manganese producing countries in 2016 (based on International Manganese Institute, 2016; U.S. Geological Survey, 2018 database) showing the main Mn-deposits.

3.1 Distribution and behavior of manganese in the Earth system

Manganese is the 10th most abundant element in the Earth's crust (600-1300 ppm; ►Table 3.1). It is similar to iron in its chemical properties. Both Mn and Fe are commonly found in +2 and +3 valences with high spin states for the 3d electrons and with similar ionic radii (Li, 2000). Geochemically, Mn behaves like Mg, Fe, Ni, and Co and tends to partition into minerals that form in the early stages of magmatic crystallization. Significant quantities of Mn however persist in melts and can be plentiful in late-stage deposits such as pegmatites (see chapter 5). Manganese also has a higher valence state (Mn^{4+}), giving rise to a plethora of complex manganese oxides, which do not have Fe counterparts. By contrast, Mn sulfides are quite rare compared to Fe sulfides (Maynard, 2014; Kuleshov, 2016). Mn is readily extracted from igneous, sedimentary and metamorphic rocks by interactions with surface and ground waters, and is highly mobile in its divalent form (Mn^{2+}; Varentsov, 1996) in acidic aqueous systems. Near the Earth's surface, Mn is easily oxidized, giving rise to Mn oxide/hydroxide minerals (this thesis, chapters 5, 6, 7 and 8). Beside these chemical fundamentals, manganese oxides is significant in two ways. First, Mn oxides are highly effective adsorbent for various metals (especially Cu, Pb, Zn, Ba, etc.; (Burns and Burns, 1979; Crerar *et al.*, 1980; Decrée *et al.*, 2010) and they record the composition of fluids from which they have precipitated. Second, their various redox states provide a useful window into the history of oxidation levels at the Earth's surface (e.g., Roy, 2006; Maynard, 2010; Kuleshov, 2016).

►**Table 3.1** Distribution of Mn and Fe among rock reservoirs, rock types and natural waters (Li, 2000).

Reservoir	**Mn (ppm)**	**Fe (ppm)**	**Mn/Fe**
Carbonaceous chondrite	1,990	190,400	0.010
Upper mantle	1,000	64,000	0.016
Upper continental crust	600	35,000	0.017
Archean upper crust	1,400	62,000	0.023
Oceanic crust	1,300	81,000	0.016
Rocks			
Average basalt	1,550	83,000	0.019
Average granite	390	21,100	0.018
Mudstone	728	41,800	0.017
Sandstone	852	34,500	0.025
Limestone	418	9,500	0.044
Average sediment	852	35,800	0.024
Seawater			
Oceanic sediments	2,700	36,000	0.075
River water	0.0082	0.040	0.21
Seawater	0.72×10^{-6}	250×10^{-6}	0.35

The distribution of manganese and iron among the various reservoirs of the Earth reveals how these elements behave in the geochemical cycle. As mentioned above, the geochemistry of Mn and Fe is quite similar: their Mn/Fe ratio remains relatively unchanged in the main rock reservoirs, showing a narrow range of values between 0.016 and 0.019 (►Table 3.1). Carbonaceous chondrites have a higher content of Fe than Mn, and this Fe/Mn ratio is higher than in the Earth crust and the mantle. This difference reflects the partition of iron, but not manganese, into the Earth's core, leaving the crust and the mantle depleted in its iron component. The Archean crust (0.023) displays a higher Mn/Fe ratio, which indicates that crustal processes differed from those of the younger Earth because the global oxygen level of the Archean ocean was low (►Table 3.1; Maynard, 2010, 2014). This has resulted in an elevated level of Mn in Archean carbonates (up to 1% Mn) compared to Phanerozoic ones (10-50 ppm; Veizer, 1978; Brand and Veizer, 1980; Beukes, 1987; Fischer and Knoll, 2006; Komiya *et al.*, 2008). The Mn/Fe ratio of basalt, granite and shale is close to the composition of the Earth crust (►Table 3.1). However, other sedimentary lithologies show a pronounced enrichment and a depletion of manganese in comparison to iron, indicating that the Earth's exogenic cycle could distribute manganese unevenly, and therefore bring manganese to be concentrated and form massive Mn deposits. Such Mn enrichment relative to Fe is observed in limestone (0.044), whereas depletion is found in black shale (0.005). The cause of both variations is the great stability field of iron sulfide (i.e., pyrite) compared to high solubility of manganese in anoxic conditions. The consequence of this contrasted solubility is that iron is concentrated in deep-water shales under low-oxygen levels, whereas manganese precipitates in the more oxygenated shallow waters, where limestone is deposited (Maynard, 2014). Another mode of manganese enrichment is suggested by the high Mn/Fe ratio in deep-sea pelagic sediments and by the very high ratio in seawater (►Table 3.1).

3.2 Mineralogy

The mineralogy of manganese is complex and analytically difficult to determine, not only because a large number of phases are documented, but also because Mn-bearing minerals are difficult to characterize due to their poor crystallinity, fine-grained size, intimate intergrowth, etc. Such issues are mainly related to three oxidation states of manganese cation in natural environment (Mn^{2+}, Mn^{3+}, Mn^{4+}). Among all mineralogical categories, Mn oxides are the most common ore forming minerals, followed by carbonates and silicates (braunite; ►Table. 3.2). The general tendency shows Mn carbonates (rhodochrosite) in sedimentary environments, braunite in volcanic deposits, and other Mn oxides in karstic and supergene environments (Maynard, 2010). Other minerals, such as sulfides (alabandite), tungstates (scheelite,

wolframite, hübnerite), etc., can contain substantial amounts of Mn in their structure but cannot form Mn ores. Interestingly, minerals containing Mn^{2+}, such as rhodochrosite, tend to be light colored, whereas Mn^{4+} minerals tend to be darker, often black (Maynard, 2014). The following subsections make an in-depth description of the main ore-forming minerals.

3.2.1 Mn oxides, hydroxides and oxyhydroxides

Any scientist who deals with Mn oxides knows that this is generally a messy black material leaving hands very dirty. Accordingly, most Mn oxide minerals are brown-black and typically occur as intimately intermixed, fine-grained, poorly crystalline masses or coatings. This is the reason why most geologists report simply "Mn oxide" instead of a particular mineral phase. Geologists also avoid this problem by simply referring to "wad" all soft, brown-black, fine-grained specimens that blacken fingers. Similarly, "psilomelane" is a hard, gray-black, botroyoidal, massive specimen that (nearly) does not blacken your fingers (see chapter 4). Although this definition is helpful in field investigations, it lacks some crucial points, as wad and psilomelane are not labeled as specific Mn oxides and often have the same mineral composition (this thesis, Dekoninck *et al.*, 2016a). Another way to distinguish these Mn oxides is to separate Mn oxides *sensu lato* into Mn oxides *sensu stricto*, Mn hydroxides and oxyhydroxides, depending on which anion Mn (and other metals) is bonded to. The presence of oxygen (O), hydroxyl group (OH), or oxygen hydroxyl (OH, O) group determines the Mn species, respectively. As this definition is cumbersome to be systematically incorporated in the text, the use of "Mn oxides" or specific mineral phases is preferred. All these features account for most issues encountered when mineralogists try to identify the Mn oxide minerals. Even today, it is not straightforward to identify these minerals in many Mn oxide samples. In general, powder X-ray diffraction enables the identification of well-crystallized monophasic samples. Another difficulty lies in the crystal structures, and consequently the powder diffraction patterns, which are similar between many of the Mn oxide minerals. In many cases, it is necessary to supplement powder X-ray diffraction studies with other techniques, such as light reflexion microscopy (LM), transmission electron microscopy (TEM; Post and Veblen, 1990), IR spectroscopy (Ling *et al.*, 2017), scanning electron microscopy (SEM), electron microprobe analysis (EPMA; see chapter 4; Post, 1999).

Even though Mn oxides have been extensively studied, the details of some of their atomic structures are poorly understood, and there are several phases for which the basic crystal structures are not known. Although the average Mn content is easy to measure, the proportions between Mn^{2+}, Mn^{3+} and Mn^{4+} are difficult to establish.

Structure refinement models (Post *et al.*, 1982; Post and Bish, 1989; Post and Veblen, 1990; Post and Appleman, 1994) can set such approaches, as well as X-ray spectroscopy (McKeown and Post, 2001; Ilton *et al.*, 2016). Each crystal structure of Mn oxide minerals is composed of a basic MnO_6^{8+} octahedron that can be assembled by sharing edges and/or corners into a large variety of different structural arrangements. The chain or tunnel (►Fig. 3.3) and the layer structures (►Fig. 3.4) account for most of the structural arrangement of Mn oxide minerals (Post, 1999). The main Mn oxide minerals are summarized in ►Table. 3.2.

►**Table 3.2** Main Mn-bearing minerals found in natural environments and their abundance. Abundance is the percentage of all deposits in which the mineral listed dominates (Maynard, 2010, 2014).

Mineral	**Chemical formula**	**Abundance (%)**
Tunnel Mn oxide		
Pyrolusite	MnO_2	5
Ramsdellite	MnO_2	<1
Nsutite	$Mn(O,OH)_2$	1
Hollandite	$Ba_x(Mn^{4+},Mn^{3+})_8O_{16}$	<1
Cryptomelane	$K_x(Mn^{4+},Mn^{3+})_8O_{16}$	9
Manjiroite	$Na_x(Mn^{4+},Mn^{3+})_8O_{16}$	<1
Coronadite	$Pb_x(Mn^{4+},Mn^{3+})_8O_{16}$	<1
Romanechite	$Ba_{0.66}(Mn^{4+},Mn^{3+})_5O_{10}.1.34H_2O$	4
Todorokite	$(Ca,Na,K)_x(Mn^{4+},Mn^{3+})_6O_{12}.3.5H_2O$	2
Layer Mn oxides		
Lithiophorite	$LiAl_2(Mn_2{}^{4+}Mn^{3+})O_6(OH)_6$	1
Chalcophanite	$ZnMn_3O_7.3H_2O$	<1
Birnessite	$(Na,Ca)Mn_7O_{14}.2.8H_2O$	<1
Vernadite	$MnO_2.nH2O$	<1
Hydroxides		
Manganite	MnOOH	8
Groutite	MnOOH	<1
Feitknechtite	MnOOH	<1
Pyrochroite	$Mn(OH)_2$	1
Spinel Mn oxide		
Hausmannite	$Mn^{2+}Mn_2{}^{3+}O_4$	5
Trivalent oxide		
Bixbyite	Mn_2O_3	1
Divalent oxide		
Manganosite	MnO	<1
Amorphous oxides		2
Carbonates		
Kutnahorite	$(Ca,Mn)CO_3$	2
Rhodochrosite	$MnCO_3$	32
Mn-calcite		2
Silicates		
Braunite	Mn_7SiO_{12}	24
Rhodonite	$MnSiO_3$	-

3.2.1.a The tunnel-like structure

The tunnel Mn oxides are built of single, double or triple chains of edge-sharing MnO_6 octahedra. These chains share corners with each other to produce frameworks that have tunnels with square or rectangular cross sections, like those in zeolites (►Fig. 3.3). The large tunnels are partially filled with water molecules and/or cations (Turner and Buseck, 1979; Post, 1999). The most important Mn oxides, having tunnel-like structure, are described below. All minerals of this subsection are listed in ►Table. 3.2.

- *Pyrolusite-ramsdellite-nsutite - MnO_2*

There are three known polymorphs of MnO_2: pyrolusite is the most stable and abundant (e.g., chapters 5, 6 and 7; Dekoninck *et al.*, 2016b, 2016b), while ramsdellite and nsutite are generally primary minerals from which pyrolusite is transformed (e.g., chapter 6). Typical prismatic crystals express the morphology of pyrolusite (β-MnO_2) with a metallic brightness, easily identified in hand specimens. The single chains of edge-sharing $Mn^{4+}O_6$ octahedra share corners with neighboring chains to form a framework structure containing tunnels that are 1X1 on a side (Baur, 1976; ►Fig. 3.3). The cavities left by the tunnel-like structure are too small to accommodate other chemical elements or molecules, which results in a homogeneous chemical composition with only slight deviations from the empirical formula (Post, 1999). Pyrolusite occurs in low temperature hydrothermal deposits (see chapter 5) or as replacement of ramsdellite and manganite in supergene zones (see chapters 6 and 7).

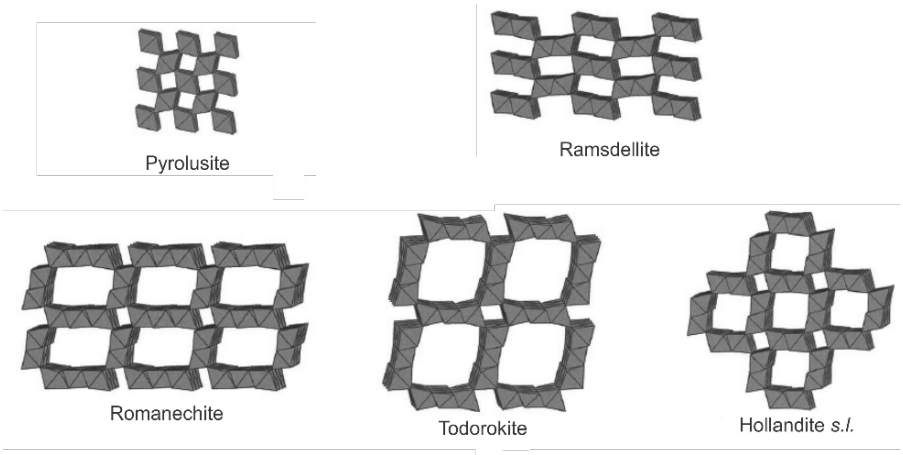

► **Fig. 3.3** Crystal structure representation of the main tunnel-like Mn-oxides (modified after Post, 1999). The octahedra are shown in grey.

In most cases, ramsdellite (α-MnO_2) is relatively rare, usually occurring in low-temperature hydrothermal deposits and transform into pyrolusite in supergene deposits (Post, 1999;see chapter 6). However, ramsdellite can be locally abundant in oxidized zones of Mn-rich deposits (Ostwald, 1984a). In the ramsdellite structure, $Mn^{4+}O_6$ octahedra are linked into double chains, each of which consists of two adjacent single chains that share octahedral edges (Byström *et al.*, 1949); ►Fig. 3.4). The framework resulting from this structure is a rectangular shaped cross-section showing 1X2 octahedra on a side. The tunnel is generally empty but chemical analyses commonly reveal minor amounts of H_2O, Na and Ca (Post, 1999).

Nsutite (γ-MnO_2) occurs as opaque, dark gray to black, porous to dense aggregates and is an important mineral given that it represents the natural analog of electrolytic Mn dioxide (EMD), which is used as a cathode in dry-cell batteries (Paik *et al.*, 2001). Nsutite is actually not a single mineral phase but rather an intergrowth between pyrolusite and ramsdellite (Post, 1999; see chapter 6). To be more specific, the so-called nsutite is a combination of a disordered ramsdellite-like phase and ordered intergrowth of ramsdellite and pyrolusite (Zwicker *et al.*, 1962; Turner and Buseck, 1983). The tunnel size can also be variable, showing 1X3 and 3X3 cross-section as well as numerous defects (Turner and Buseck, 1983). The chemical composition of nsutite typically shows minor amounts of Na, Ca, Mg, K, Zn, Ni, Fe, Al, and Si, and about 2–4 weight percent H_2O, which can be accommodated in the larger tunnels or along grain boundaries. Nsutite is a secondary replacement mineral that commonly forms from oxidation of rhodochrosite (Zwicker *et al.*, 1962).

- *Hollandite group minerals — $(Ba^{2+}, K^{+}, Pb^{2+}, Na^{+}, Sr^{2+})\ (Mn^{4+}{}_7Mn^{4+})\ O_{16}$*

The octahedral double chains of edge-sharing $Mn^{4+}O_6$ to build up a square 2X2 tunnel structure (►Fig. 3.3; Post, 1999) structurally characterizes minerals of the hollandite supergroup. They are typically acicular crystals, usually forming botryoidal masses, often considered as the main component of psilomelane (Post, 1999; Dekoninck *et al.*, 2016b, 2016a; see chapters 4, 5, 6, 7 and 8). The larger size of the tunnel compared to MnO_2 polymorphs is ideal to accommodate univalent and bivalent cations or water molecules, the latter being controversial (Biagioni *et al.*, 2013). The charges on the tunnel cations are balanced by the substitution of trivalent cations (i.e., Al^{3+}, Fe^{3+}, Mn^{3+}) for some Mn^{4+}. The ideal crystal chemical formula of the hollandite supergroup depends on the valence state of both the tunnel and charge-compensating cations, and should be written as follows: $A^{2+}\ [M^{4+}{}_6M^{3+}{}_2]O_{16}$ and $A^{+}[M^{4+}{}_7M^{3+}]O_{16}$, according to the tunnel cation valence. A^{2+} = Pb, Ba, Sr; A^{+} = K, Na; M^{4+} = Mn, Ti; M^{3+} = Mn, Fe, Cr, V (Biagioni *et al.*, 2013). The name of the different minerals composing the hollandite group is defined on the basis of the dominant cation: coronadite (Pb; Lindgren and Hillebrand, 1904), hollandite *s.s.* (Ba; Fermor, 1906), cryptomelane (K;

Richmond and Fleischer, 1942), manjiroite (Na; rare; Nambu and Tanida, 1967), strontiomelane (Sr; rare; Meisser *et al.*, 1999). However, natural end-member composition specimens are uncommon and are rather a wide range of tunnel cation compositions (Post, 1999). They are commonly intermixed and evolve from one to another in a single crystal (see chapter 7; Dekoninck *et al.*, 2016a; b). Biagioni *et al.* (2013) have recently proposed new insights into the hollandite supergroup nomenclature by subdividing them into two groups, based on the dominant tetravalent cation (M^{4+}): (1) the coronadite group refers to hollandite group minerals in which Mn^{4+} is the dominant cation located in the octahedral, and (2) the priderite group has Ti^{4+} as a dominant cation. The most common and naturally occurring minerals belong to the coronadite group (coronadite, hollandite *s.s.*, manjiroite, cryptomelane and strontiomelane).

Hollandite group minerals can be major phases in the oxidized zone of Mn deposits and are considered as important metallurgical ores (Post, 1999; Vasconcelos, 1999; this thesis). They can also form in hydrothermal conditions (hollandite s.s. mainly; Lippolt and Hautmann, 1995). One of the major geological interest of the tunnel-like structure is that volatile elements could be trapped in the cavities, and not released into the atmosphere (Vasconcelos *et al.*, 1992). The presence of K in the tunnel allows the hollandite group minerals to be suitable material for geochronological investigations, as ^{40}K naturally turns into ^{39}Ar by radioactive decay. Such feature is useful when geologists try to study the timing, the rhythm and the development of a weathering profile, or the setting up of hydrothermal veins in which hollandite group minerals have precipitated (this thesis, see chapter 4; e.g., Vasconcelos, 1999). Considerable interest in the hollandite group minerals and hollandite tunnel-like structures has been drawn, both for potential applications as solid ionic conductors (Beyeler, 1976) and for immobilizing radioactive cations (Reid and Ringwood, 1969; Leinekugel-le-Cocq-Errien *et al.*, 2007). These oxides are also natural trap for pollutant metals (Decrée *et al.*, 2010).

- *Romanechite — $Ba_{0.66}Mn^{4+}_{3.68}Mn^{3+}_{1.32}O_{10}.1.34H_2O$*

The romanechite ($Ba_{0.66}Mn^{4+}_{3.68}Mn^{3+}_{1.32}O_{10}.1.34H_2O$) structure is composed of double and triple chains of edge-sharing MnO_6 octahedra, forming large rectangular 2X3 cross-sections (►Fig. 3.3). The size of the tunnel allows water molecules to be easily incorporated with Ba^{2+} cation in a 1:2 ratio (Ba/H_2O). Mn^{3+}, substituted for some of the Mn^{4+}, balances the charges of the tunnel. Romanechite is typically found in supergene zones of Mn deposits (e.g., see chapter 8; Decrée *et al.*, 2010; Dekoninck *et al.*, 2018), but is often microcrystalline and in association with hollandite *s.s.* However, romanechite is not stable at temperatures higher than 550 °C, as water is released through the heating of the sample and transforms into hollandite *s.s.* (Fleischer and Richmond, 1943). Romanechite chemical composition can show slight

amounts of Na, K, Ca and Sr as replacement cations of Ba (Post, 1999). This mineral is also suitable for K-Ar geochronology as it can hosts structural K (Vasconcelos, 1999; Hautmann and Lippolt, 2000; Decrée *et al.*, 2010).

- *Todorokite — $(Ca, Na, K)_{0.3\text{-}0.5}$ $(Mn^{4+}, Mn^{3+}, Mg)_6O_{12}.3—4.5H_2O$*

Among the Mn oxides with a tunnel-like structure, todorokite [$(Ca, Na, K)_{0.3\text{-}0.5}(Mn^{4+},Mn^{3+},Mg)_6O_{12}.3—4.5H_2O$] displays the largest cross-section of edge-sharing MnO_6 octahedra (3X3; ►Fig. 3.3). In other cases, todorokite cross-section could be 3X4, 3X5 and up to 3X9 (Turner and Buseck, 1981). This similarity with the zeolite-like structure has drawn the attention of scientists to use todorokite as a catalyst or molecular sieves (Shen *et al.*, 1993). Todorokite is one of the major Mn minerals identified in ocean nodules as 10Å-manganate and the host phase for strategic metals such as Ni, Co, Cu, etc. (Burns *et al.*, 1977; Manceau *et al.*, 2014). Lower valence cations (Mn^{3+}, Ni^{2+}, Mg^{2+}) can substitute for Mn^{4+} in the site at the edge of the triple chains in order to offset charges on the tunnel cations, as it is the case in romanechite (Post and Bish, 1988). This feature accounts for the large variations in the tunnel-cation composition (Ostwald, 1986). Todorokite often results from the replacement of primary minerals (i.e., braunite, birnessite, vernadite; Manceau *et al.*, 2014). It is also an important phase of the supergene zone of Mn deposits (i.e., Varentsov, 1996; Post, 1999). Todorokite has been tested for the $^{40}Ar/^{39}Ar$ geochronology but the reproducibility of the results was not consistent (Vasconcelos, 1999).

- *Manganite-feitknechtite-groutite — MnOOH*

MnOOH has three polymorphs. Manganite is the most stable and abundant, the other two are feitknechtite and groutite. The manganite (γ-MnOOH) structure is the same as pyrolusite (►Fig. 3.3), but Mn cation is trivalent and one oxygen is replaced by a hydroxyl anion. Such slight difference in the mineral composition leads to a distortion of the Mn^{3+} octahedra. Manganite typically occurs in hydrothermal vein deposits as acicular or prismatic crystals (see chapter 5), or as a weathering product of Mn-bearing minerals (see chapter 6). Manganite transforms into pyrolusite at 300°C, and which is why most of pyrolusite crystals are manganite pseudomorphs (Post, 1999).

Groutite (α-MnOOH) is isostructural with ramsdellite but Mn cation is trivalent and one oxygen is replaced by a hydroxyl anion. Groutite is uncommon, but is sometimes intimately mixed with pyrolusite (Post, 1999).

Feitknechtite (β-MnOOH) has long been considered as a hydrohausmannite (Feitknecht and Marti, 1945), but is rather an intermixed of hausmannite (Mn_3O_4) and

β-MnOOH, the latter being named feitknechtite by Feitknecht *et al.* (1962). Feitknechtite is only found as poorly crystalline and very fine-grained mixtures.

3.1.1.b Layered Mn oxides

The layered Mn oxides, sometimes referred to as "phyllomanganates", consist of stacks of sheets (or layers) of edge-sharing MnO_6 octahedra (►Fig. 3.4, ►Table 3.2). The interlayer regions can host water molecules and a wide range of cations which can easily be exchanged with the environment. Bargar *et al.* (2005) showed that bacterially precipitated manganese appears to always be in the sheet form and concentrate heavy metals or organic molecules due to high-capacity absorption.

- *Lithiophorite — $LiAl_2Mn^{4+}{}_2Mn^{3+}O_6(OH)_6$*

Lithiophorite structure consists of MnO_6 octahedra layers alternating with sheets of $Al(OH)_6$ octahedra in which one third of the octahedral site is empty (►Fig. 3.4). Li^{3+} fills the vacant site in the $Al(OH)_6$ layers, while the balance charge is maintained with the replacement of Mn^{4+} by Mn^{3+}. The global structure of lithiophorite is conserved thanks to H bonds between the hydroxyl anions of Li and Al sheets, and the oxygen of the MnO_6 octahedra (Post, 1999). Lithiophorite is commonly found in the weathering zone of Mn-deposits (see chapters 6 and 7; i.e., Varentsov, 1996; Dekoninck *et al.*, 2016b, 2016a), but is also reported in low-temperature hydrothermal veins (de Villiers 1983). The Li content of lithiophorite ranges between 0.2-3 wt.% and often contains substantial amount of Co, Ni and Cu (Ostwald, 1984b; see chapters 6 and 7). Ni and Cu are accommodated in the $Al(OH)_6$ octahedra and Co in the Mn layers (Manceau *et al.*, 1987). It is assumed that asbolane ($[Ni,Co]_{2-x}Mn^{4+}[O,OH]_4.nH_2O$) has a similar structure than lithiophorite, but with Al replaced by transition metals (Manceau *et al.*, 1992).

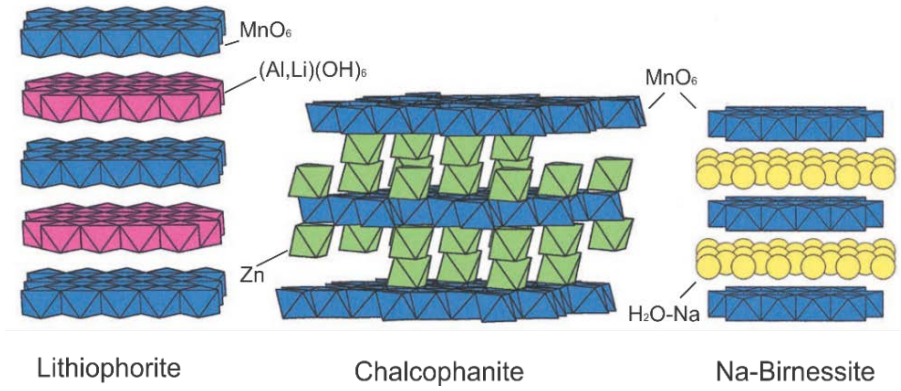

►**Fig. 3.4** Crystal structure representation of the main layered Mn oxides showing alternately layers of $MnO_6{}^{8+}$ radicals (blue) and sheets of different cations (modified after Post 1999).

- *Birnessite group — $(Na,Ca,K,Mn^{2+})Mn_7O_{14}.2.8H_2O$*

Most of birnessite samples are fine-grained and relatively poorly crystalline, which makes the study of its structure very complex (Post, 1999). However, natural and synthetic birnessite showed that birnessite and "buserite[10]" have a layer structure similar to that of chalcophanite. The birnessite-type structure consists of sheets of MnO_6 octahedra separated by ~7 or ~10Å ("buserite") interlayers filled with cations (Na, K, Ca, Mg, etc.) and water (►Fig. 3.4; e.g., Johnson *et al.*, 2016). Birnessite and birnessite-like minerals occur in a wide variety of geological settings. It is a major phase in soils, in desert varnishes and it is commonly found as an alteration product in Mn-rich ore deposits (Post, 1999). Birnessite is an important scavenger of trace metals in soils and aqueous environments because it readily participates in oxidation-reduction and cation exchange reactions (Johnson and Post, 2006). Birnessite is also a primary phase in polymetallic nodules, hosting strategic metals (Co, Ni, Pb among others), before it transforms into other Mn oxides, the most common being todorokite (Glasby, 2006; Manceau *et al.*, 2014). Therefore, birnessite plays an important role in the capture and release of nutrients and toxic elements into the environment because of the high cation-exchange capacity. Birnessite-like layer structures are also used as cathode material in rechargeable Li batteries and are developed as ion-exchange materials for industrial use (Cai *et al.*, 2002).

- *Chalcophanite — $ZnMn_3O_7.3H_2O$*

Chalcophanite is very common in the weathering zone of base metal deposits containing manganese metal and zinc (see chapter 8; e.g., Decrée *et al.*, 2010). The MnO_6 sheets alternate with Zn cations and water molecules (►Fig. 3.4), while one of the seven Zn layers and water molecules is vacant (Post, 1999).

- *Vernadite — $MnO_2.nH_2O$*

The fine-grained and poorly crystalline vernadite is found in the oxidized zone of Mn deposits and might be a major phase in ocean nodules and other crusts and coating (Post, 1999; Manceau *et al.*, 2014). Vernadite is similar to δ-MnO_2 with minor

[10]A natural phase typically found in hydrous environments that is similar to birnessite except for its ~10Å interlayer spacing. The name "buserite" is an unapproved name as the structure is unstable. Cations such as Ni, Mg, Ca, and Co tend to stabilize the buserite structure (Paterson *et al.*, 1986).

amounts of K, Mg, Ca, Ba and Fe, and contains 15–25 wt.% of water. The crystal structure of vernadite is not known, but it has been suggested that vernadite is a variety of birnessite that is disordered in the layer-stacking direction (Giovanoli, 1980; Post, 1999; Manceau *et al.*, 2014).

3.2.1.c Other structures

Other important oxide minerals that could have economic significance are hausmannite ($Mn^{2+}Mn^{3+}{}_2O_4$), with a spinel-like structure, and bixbyite ($[Mn,Fe]_2O_3$; ►Fig. 3.5). Both minerals are typically found in hydrothermal (see chapter 5) and metamorphic deposits, and can contain a substantial amount of Fe in substitution of Mn (Frenzel, 1980). Bixbyite is an important geothermometer because the Fe content incorporated in the bixbyite lattice is temperature dependent (Mason, 1944).

Pyrochroite ($Mn[OH]_2$) consists of stacked sheets of $Mn^{2+}(OH)_6$ octahedra. Manganosite (MnO) is isostructural with halite (NaCl). Both minerals are relatively rare, and occur in low-temperature hydrothermal veins in Mn-rich deposits (Post, 1999). Many other Mn oxides have also been described but are relatively rare and represent only a minor amount in Mn-rich rocks: janggunite $[Mn^{4+}{}_{5-x}(Mn^{2+},Fe^{3+})_{1+x}O_8(OH)_6]$, jacobsite ($Mn^{2+}Fe^{3+}{}_2O_4$), rancieite $[(Ca,Mn^{2+})_{0.2}(Mn^{4+},Mn^{3+})O_2{\cdot}0.6H_2O]$, crednerite ($CuMnO_2$), quenselite $[PbMnO_2(OH)]$, etc. (Kuleshov, 2016).

3.2.2 Mn carbonates

Many deposits contain manganese carbonates and it is assumed that most other land-based deposits have originally a large proportion of Mn carbonates (Maynard, 2014). Compared with the numerous Mn oxides described in the previous section, Mn carbonates are limited to minerals of the isomorphic series: rhodochrosite—Ca-rhodochrosite—Mn-calcite $[MnCO_3\text{-}(Mn_x,Ca_{1-x})CO_3]$, and oligonite-Mn-siderite-kutnahorite $[(Mn_x,Fe_y,Mg_z)CO_3]$. Rhodochrosite ($MnCO_3$) and kutnohorite account for most of the economic Mn deposits and are often associated with minor amounts of Mn calcite ($[Ca,Mn]CO_3$; ►Table 3.2; see chapters 5 and 6). The formation of these minerals depends on the availability of Ca and Mn in the mineralizing fluids, giving different solid solutions (Mucci, 2004). Most carbonate reactions are fast as opposed to silicates and oxides at temperatures below 100 °C, and even though rhodochrosite precipitation is slower than calcite, a near equilibrium can be reached (Sternbeck and Sohlenius, 1997; Maynard, 2014). These minerals could precipitate from seawater under suboxic/anoxic conditions, depending on the Ca:Mn ratio of the pore water and the abundance of calcite surfaces (Mucci, 2004), and they extensively

occur in hydrothermal (see chapter 5) and metamorphic veins (see chapter 6) related to Mn-rich rocks in the form of coarse crystals.

3.2.3 Mn silicates

Braunite (►Table 3.2) is actually the most important Mn-bearing silicate that has an economic significance in Mn deposits (see chapter 5). The most common variety is braunite with an ideal formula $Mn^{2+}Mn^{3+}{}_6SiO_{12}$ containing 8–10 wt. % SiO_2 (de Villiers, 1975; Moore and Araki, 1976), whilst braunite II ($Ca_{0.5}Mn^{3+}{}_7SiO_{12}$) shows only 4–5 wt. % SiO_2 (de Villiers and Herbstein, 1967; de Villiers, 1980; ►Fig. 3.5). Neltnerite is $CaMn^{3+}{}_6SiO_{12}$ (Baudracco-Gritti *et al.*, 1982; Baudracco-Gritti, 1985). The crystal structure of braunite is close to bixbyite and is a fluorite-derived structure (Moore and Araki, 1976). It consists of a stacking sequence of three non-equivalent edge and corner-linked polyhedral sheets, one being octahedral bixbyite whereas the others contain Ca in cubic coordination and Si in tetrahedral coordination (de Villiers, 1980). Braunite is very common in sedimentary-hosted manganese deposits where it occurs as a diagenetic mineral (e.g., Johnson *et al.*, 2016) and is the main ore forming mineral of the giant Postmasburg and Kalahari deposits with kutnahorite (Gutzmer and Beukes, 1997; Chetty, 2008), and the Neoproterozoic Urucum deposit (Piacentini *et al.*, 2013). Braunite also occurs extensively in magmatogenic hydrothermal veins (see chapter 5; e.g., Choubert and Faure-Muret, 1973).

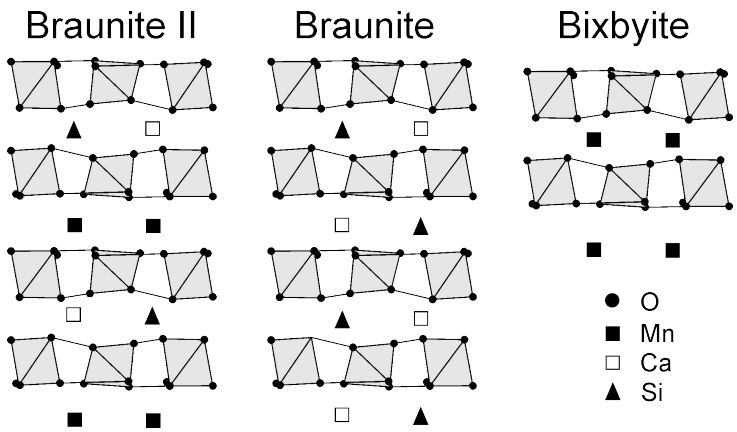

►**Fig. 3.5** Cross-section through the structure of braunite II ($Ca_{0.5}Mn^{3+}{}_7SiO_{12}$), braunite ($Mn^{2+}Mn^{3+}{}_6SiO_{12}$) and bixbyite ($[Mn,Fe]_2O_3$; adapted from de Villiers and Buseck, 1989).

Rhodonite ($MnSiO_3$), spessartine ($Mn_3Al_2[SiO_4]_3$) and tephroite (Mn_2SiO_4) are also important minerals of unweathered protores of weathering crust Mn deposits (Nahon *et al.*, 1983; Nahon and Parc, 1990; Ruffet *et al.*, 1996), although many other silicates have been described and compose Mn-bearing metamorphic

rocks (i.e., kanonaite [Mn_3AlSiO_5], Ottrelite [[Mn,Fe,Mg]$Al_2[SiO_4]O[OH]_2$], Pennantite [$Mn_5Al[AlSi_3O_{10}][OH]_8$], etc.).

3.3 Genetic types of manganese deposits

Several authors have attempted to find a proper classification of Mn deposits based on the genetic types (Roy, 1968, 1976, 1997, 2006; Laznicka, 1992; Kuleshov, 2011, 2016) or on the geochemical footprint (Nicholson, 1992). The current Mn classifications need to take into account complex deposits (i.e., multistage formation), but a global classification is needed to serve the practical purpose and classify the large number of recorded Mn deposits into manageable groups. Most of the conventional hierarchical classifications subdivide Mn deposits into: (1) sedimentary-diagenetic (non-volcanic, volcanic-sedimentary; see chapter 6), (2) metamorphic deposits (see chapter 6), (3) hydrothermal (magmatogenic and contact-metasomatic; see chapters 5 and 8), and (4) supergene deposits (weathering crust, karst-hosted, etc.; see chapter 6 and 7; ►Fig. 3.6; Kuleshov, 2011). All these categories have been investigated in this thesis. A careful review of their composition and formation is therefore interesting to further investigate weathering processes and how these have affected the primary deposits.

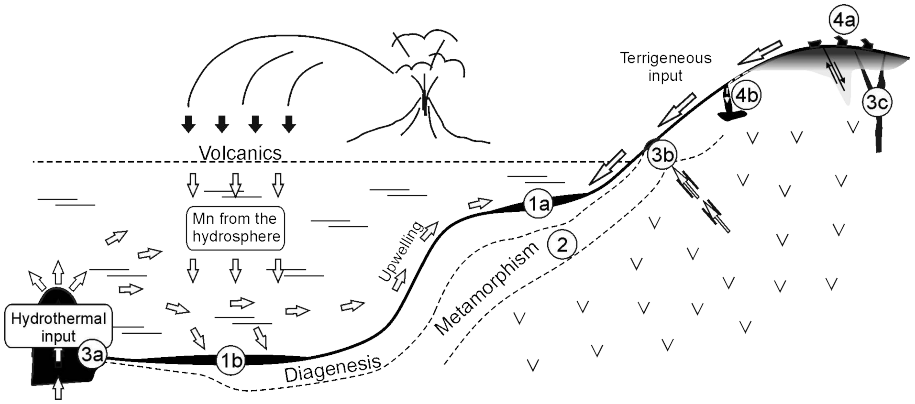

►**Fig. 3.6** Revisited model of the main manganese ore forming processes and genetic types (adapted from Kuleshov, 2011). (1) sedimentary-diagenetic non-volcanic (hydrogenous, 1a), volcanic-sedimentary (hydrothermal; 1b); (2) metamorphism; hydrothermal (SEDEX type; 3a), terrestrial (hot springs, 3b), and hypogene veins (3c); (4) supergene deposits of the weathering crust and oxidation of primary deposits (laterite; 4a) and karst-hosted (4b).

The economic significance of these deposits is unevenly distributed between the different genetic types. Manganese deposits ensuring high longevity, large volumes, and relatively high average concentrations belong to sedimentary deposits (►Table 3.3). The Mn concentration is derived from hydrothermal vents of the mid-

ocean ridge associated with intermediate volcanic rocks, or alternatively from terrestrial input, as it is attested by modern and ancient deep-sea polymetallic nodules (Maynard, 2014). The accumulation of Mn particles in the aqueous environment allows the Mn concentration to increase through sedimentation, and to be preserved once the ore enrichment ceased by the cover of other sediment types. Such positive metallogenesis is rather difficult to obtain in manganese deposits of other types. Igneous and hydrothermal deposits can have a Mn content similar to sedimentary deposits, but with more restricted volumes and concentrations (see chapters 5 and 8). Weathering deposits often offer large volumes of rocks in the first meters of a weathering mantle and strong enrichment factors (see chapters 5, 6, 7 and 8). However, as this process is often associated with erosion, the Mn enrichment occurs only in a narrow window during the geological history of a deposit (Laznicka, 1992).

►**Table 3.3** Average reported compositions of selected major and trace elements from Mn-deposits of various types (Maynard, 2010).

Label	Sediment-hosted	Karst-hosted	Volcanic-hosted	Weathering crust
Average size (million zonnes)	51	3	27	6
MnO (%)	31	48	42	39
$Fe_2O_{3tot\ (\%)}$	6.2	14.9	10.5	6.2
$SiO_{2\ (\%)}$	18.4	5.6	21.3	27.7
$Al_2O_{3\ (\%)}$	3.6	8	4.4	3.5
$TiO_{2\ (\%)}$	0.16	0.14	0.17	0.19
$P_2O_{5\ (\%)}$	0.61	0.41	0.19	0.2
LOI (%)	22.8	12.3	9.3	11.8
Ba (ppm)	4,812	11,305	3,313	6,900
Co (ppm)	232	3,215	289	116
Cr (ppm)	237	122	56	39
Cu (ppm)	55	788	209	1,582
Mo (ppm)	13	6	12	383
Ni (ppm)	217	2,629	256	123
Pb (ppm)	132	263	43	2,138
V (ppm)	98	310	119	215
Zn (ppm)	89	387	143	600
Nb (ppm)	49	7	5	7
Th (ppm)	290	5	3	5
Y (ppm)	-	22	85	36
Zr (ppm)	52	33	53	29

Mn ore grades are classified into high grade (>44–48% Mn), medium grade (35–44% Mn) and low grade (25–35% Mn). Except for supergene deposits, the bulk of the primary Mn deposits (sedimentary and hydrothermal) has a uniform grade throughout an orebody or a band. Therefore, a good classification of Mn deposits allows geologists/economists to visualize the grade when the deposit type is known. Supergene enrichment or erosion modifies this situation and has led geologists to separate the primary zone (protore) from the secondary enrichment zone where weathering processes operate (this thesis). Indeed, weathering usually increases the Mn concentration by a 1–5 factor (see chapters 5 and 6), or exceptionally in karst-

hosted deposits by a 10–20 orders of magnitude (►Table 3.3; see chapter 7). Considering that 93.6% of the Mn deposits worldwide are slightly or completely affected by weathering processes, special care has been taken to this type of Mn accumulation/remobilization (Laznicka, 1992).

3.3.1 Sedimentary-diagenetic Mn deposits

Significant accumulations of manganese (containing >20% Mn) are widely distributed, both in time and space. The formation of manganese deposits is explained by the sedimentary (precipitation of carbonates and manganese oxides from the water column into sediments) and diagenetic (redistribution of elements in the diagenetic zone) processes (e.g., see chapter 6). Depending on the composition of the sediments and the source of manganese, sedimentary deposits can be subdivided into strictly sedimentary and hydrothermal-sedimentary deposits. A substantial amount of Mn is concentrated in banded iron formations (BIF) that often represent a by-product of iron deposits in South Africa (e.g., Beukes *et al.*, 2016).

3.3.1.a Composition of Mn accumulation

The most obvious differences in the composition of manganiferous sediments lie between modern deposits of the ocean floor that have not undergone hydrothermal influences, the so-called “hydrogenous” deposits (non-volcanic), and all of the other occurrences, where a hydrothermal component is overprinted (►Figs. 3.6 and 3.7). The latter are quite similar in many aspects to the ancient ore deposits and represent most of the sedimentary Mn deposits, which indicates a large hydrothermal component in the source of manganese through geological times (Maynard, 2014). The most prominent geochemical difference, and which has been exploited in the classification of sedimentary manganese deposits (e.g., Nicholson, 1992), is the concentration of heavy metals such as Co, Ni and Cu in the hydrogenous deposits. The concentration of Pb, Th and REE[11] is also significantly higher in hydrogenous deposits (Maynard, 2014). Such enrichment is usually attributed to the very slow accumulation rate from oxidizing seawater (0.5-15mm Ma^{-1}; Hein *et al.*, 1997) compared to the rapid deposition of manganese and iron from suddenly cooled hydrothermal fluids (20–100 mm Ma^{-1}). The ancient deposits and the modern hydrothermal deposits are similar in terms of most chemical elements. However,

[11]Rare Earth Elements

ancient deposits show some enrichment in S, As and Se, whereas the modern hydrothermal deposits are relatively enriched in Ni, Cu and Mo. This suggests that the ancient deposits were formed under lower-oxygen conditions, either in the bottom water of the basin or within the sediment (Maynard, 2014). The relative contribution of hydrothermal fluids and seawater in a given deposit can be evaluated in the distribution of REE geochemical patterns. Total REE of Mn deposits influenced by terrestrial and/or seawater input (hydrogenous) have a relatively higher REE content and a pronounced positive Ce anomaly (►Fig. 3.8). The Ce anomaly results from the oxidation of Ce^{3+} into Ce^{4+} under oxidizing conditions, as Ce^{4+} is preferentially removed from seawater compared to other REE, leaving a negative Ce anomaly to sea water (Fleet, 1983). On the opposite, low REE content and negative Ce anomaly is diagnostic of hydrothermal deposits. Mixing this hydrothermal source with, at least, 15% of hydrogenous components, produces a positive Ce anomaly, as the REE content of hydrogenous deposits is much higher, and has, therefore, a strong impact on the REE geochemistry (►Fig. 3.8; Fleet, 1983).

The positive Eu anomalies, which in iron formations are linked to vent-sourced metals, are not seen in most Mn deposits, although they are found in Mn-rich iron formations. By contrast, Fe deposits interbedded with major Mn ores lack the usual Eu signal. Therefore, mechanisms of transport between hydrothermal vents and the sites of deposition differed for Fe and Mn deposits in the Precambrian. The increasing range of values of both Ce and Eu anomalies from Archean to present demonstrates the Earth's exogenic system has evolved from a simple global pattern of manganese cycling to a complex pattern with strong local control of manganese intake (Maynard, 2010).

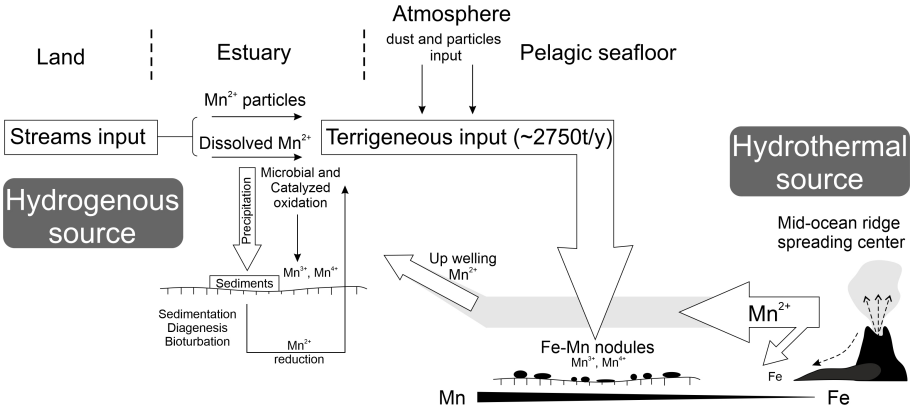

►**Fig. 3.7** Schematic view of the geochemical cycle of Mn (modified after Bender *et al.*, 1977; Sundby *et al.*, 1981). Mn^{2+} is released in seawater by hydrothermal vents of the mid-ocean ridge, the terrigeneous input (aerial, rivers), and reduction during diagenesis.

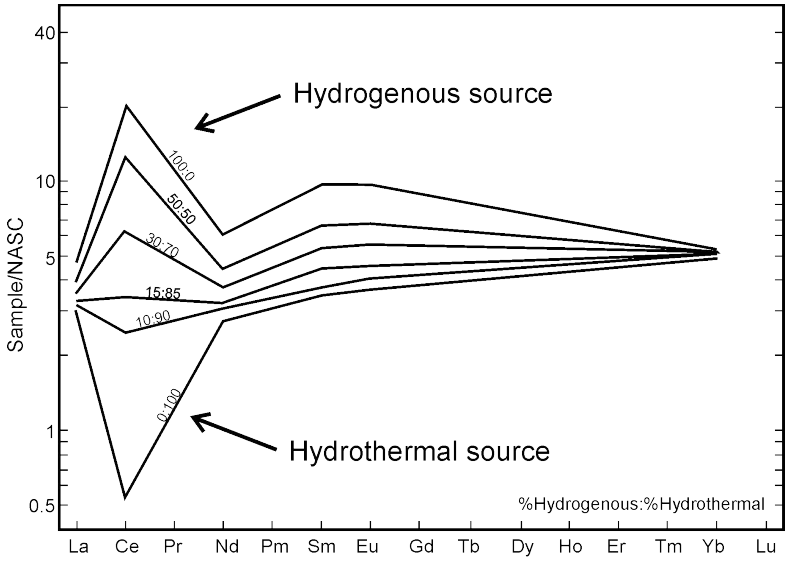

►**Fig. 3.8** Calculated REE abundances in hypothetical mixtures of average nodules from east Pacific Rise hydrothermal metalliferous sediments (Fleet, 1983). North American Shales Composite (NASC) values are from Haskin *et al.* (1968). Note that beyond 10% of hydrogenous derived source, negative Ce anomaly is not even observed.

3.3.1.b Geochemistry of manganese in seawater

Dissolved manganese (Mn^{2+}) has a relatively large field of stability (►Fig. 3.9). At pH values commonly found in surface waters, ~5–7 for freshwater and 8 for seawater, manganese is relatively soluble under mildly to strongly reducing conditions. The addition of aqueous carbonate species to the system creates a large region in which solid manganese, in the form of rhodochrosite, is stable under reducing conditions. Adding sulfur to the system does not significantly change this picture (►Fig. 3.9). Unlike iron, which has insoluble sulfides because of pyrite (FeS_2) formation, manganese has a soluble sulfide, alabandite (MnS). Consequently, manganese solubility under reducing conditions is controlled by carbonate minerals, in contrast to iron, which is rather controlled by sulfides. The result is that, in sedimentary systems with a large redox gradient, iron tends to partition into the most reducing parts of the system (as sulfides), whereas manganese will move toward areas of higher oxidation potential and tends to precipitate when it encounters mildly oxidizing conditions to form oxides. In freshwater, the pH and alkalinity are normally too low for rhodochrosite precipitation, but in seawater, a slight increase in the amount of HCO_3^{2-} should lead to rhodochrosite formation if there is a supply of Mn^{2+} (►Fig. 3.9; Maynard, 2014). Such effect is found few centimeters below the sediment-water interface, as conditions become slightly reducing and result in the mobilization of Mn^{2+} into the pore water, while iron remains fixed as an oxide or hydroxide, or as

sulfide if sulfur content is high. Mn^{2+} can then diffuse at the water-sediment interface and react with oxygen of the bottom waters to form Mn oxides (Calvert and Pedersen, 1996; Maynard, 2014).

The oxidation rate to form Mn oxides is strongly dependent on the speciation of Fe and Mn. Geochemical kinetics of manganese could be conducted in different oxidation and reduction reactions, namely by (1) homogeneous abiotic reaction, (2) ; surface-catalyzed abiotic reaction and (3) bacterial mediation (e.g., Decrée *et al.*, 2010; Maynard, 2014). The homogeneous abiotic oxidation reaction (1) of manganese is relatively slow (half-life of 400 days) compared to Fe at pH values of the ocean and many fresh surface waters (e.g., Morgan, 2005). A faster rate (30 days) of oxidation is enhanced by a surface-catalyzed abiotic reaction (2), which is meaningful in seawater, and explains why most deep-sea nodules appear to have grown at the span of a nuclei (organic and inorganic debris), and alternate layers of Mn oxides and Fe oxides (Maynard, 2014). The slow abiotic oxidation rates (3) for manganese could initiate bacterial mediation that leads to much faster oxidation rate (~10 hours; Morgan, 2005). Various bacterial groups are involved in the precipitation of Mn oxides, which could take place at: (a) the sediment-water interface in oxic bottom waters, where the upward diffusive flux of manganese from the sediments meets oxygen in the bottom water (Jørgensen, 2006); (b) the redoxcline in euxinic basins, where eddy diffusion brings sulfidic bottom waters rich in Mn^{2+} in contact with O_2-bearing surface water (Clement *et al.*, 2009); (c) the submarine hydrothermal vent systems, where hot water circulating through basalt leaches large amounts of Fe^{2+} and Mn^{2+} that are then released to seawater (►Fig. 3.7; Mandernack and Tebo, 1993; Dick *et al.*, 2009).

Bacteria could also catalyze the reduction of Mn^{4+} to Mn^{2+} (if nitrate is absent), resulting in the separation of Fe from Mn, as Fe reduction does not operate until all available MnO_2 has been exhausted (e.g., Maynard, 2014). Unlike the oxides, the reduction process involving the assimilation of Mn^{4+} into the Mn^{2+} carbonates is close enough to equilibrium to be favored by abiotic processes. Most carbonate reactions are fast compared to silicates and oxides at temperatures below 100 °C, and even though rhodochrosite precipitation is considerably slower than calcite (Sternbeck and Sohlenius, 1997), a near-equilibrium state is often reached during diagenesis (Kulik *et al.*, 2000; Mucci, 2004; Johnson *et al.*, 2016). The sorption of Mn^{2+} on calcium carbonate surface is important and may explain the scarcity of manganese nodules in calcareous sediments. Actually, the results of the closed-system equilibration experiments with calcite indicate that, if enough calcite surfaces are available, adsorption or co-precipitation (i.e., formation of a manganoan calcite) onto the calcite surface can lower the Mn^{2+} concentration of the water below the rhodochrosite saturation. In calcite-poor sediments, where the Mn:Ca ratio increases,

Ca-rhodochrosites may precipitate and determine the Mn^{2+} solubility (Mucci, 2004 and references therein). The ratios required for Ca-rhodochrosite precipitation could be reached when Mn-oxide coatings undergo a reductive dissolution following a burial below the oxygen penetration zone (Calvert and Pedersen, 1996), or under conditions where Mn^{2+} concentration is high (Lepland and Stevens, 1998; Kulik *et al.*, 2000).

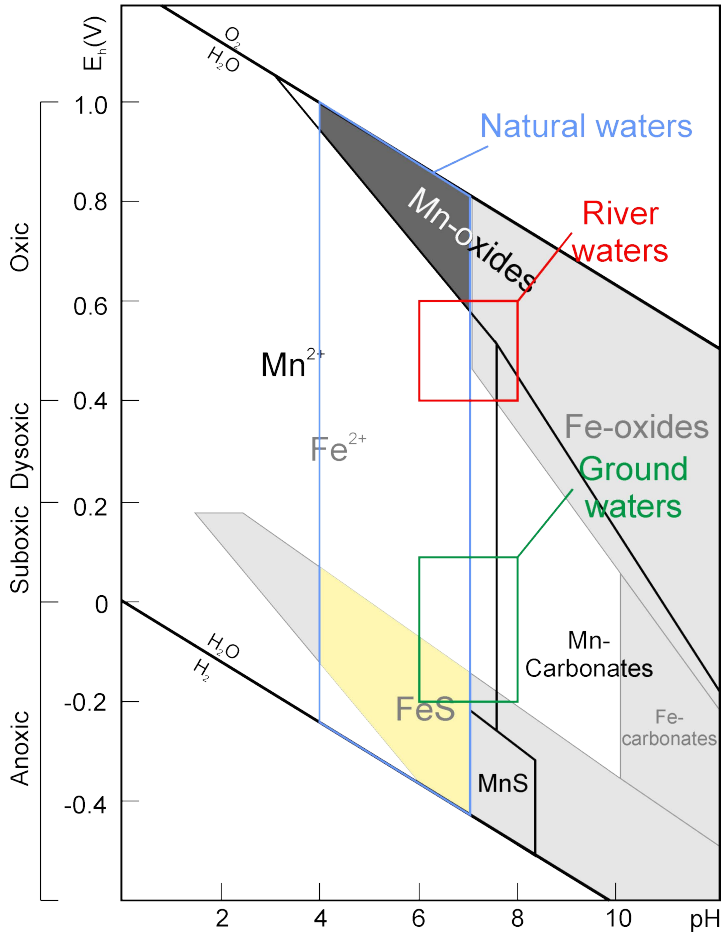

►**Fig. 3.9** Synthetic Eh-pH diagram of Mn and Fe (gray shades) at 25 °C and 1 atm with dissolved CO_2 (2,000 mg/l) and sulfate (2,000 mg/SO_4^{2-}) showing the main domain where Fe sulfides (yellow field) and Mn oxides (black field) precipitate in natural waters (based on data from Hem, 1963; Glasby, 2006; Roy, 2006; Maynard, 2014). Note that these fields could move slightly toward lower and higher pH values, depending on the Mn^{2+}, HCO_3^- and SO_4^{2-} activities (Hem, 1963).

3.3.1.c Mechanism of Mn concentration in sediments

Two groups of modern manganese enrichment in sediments can be examined to better understand the concentration of manganese in ancient deposits: (1) Mn oxides, which form the deep-sea nodules and crusts (►Fig. 3.7), and (2) carbonates, which are not as extensively developed in the present, but are of interest because of the abundance of carbonate or carbonate-derived ores in the past (Maynard, 2010, 2014; Johnson *et al.*, 2016).

(1) Pelagic ferromanganese nodules cover the ocean floor over large areas, particularly in the central Pacific and many volcanic edifices are coated by Fe-Mn crusts built on the rock surfaces (Glasby, 2006). Such accumulation is dominated by a hydrogenous end-member, but is rather a continuous distribution of Fe-Mn between hydrothermal and hydrogenous sources (Hein *et al.*, 1997, 2000). Nodules are of two types: one supplied by the overlying seawater, the other receiving a diagenetic contribution of metals from the underlying sediments. Both processes are often involved together with variable intensities (Maynard, 2014). The mineralogical composition of crusts is dominated by amorphous FeOOH and crystallized γ-MnO_2 (nsutite), whereas diagenetic nodules contain todorokite and birnessite (Glasby, 2006; Maynard, 2014). Trace elements composition of the nodules strongly depends on the amount of Fe (P, Y, REE) and Mn (Ba, Cu, Mo, V, Zn, NI, Co), and the biologic productivity of the overlying surface waters. The latter is determined by the amount of organic carbon in the sediments, which can lead in turn to increase the mobility of Mn, Ni and Cu under suboxic diagenesis, while iron remains insoluble in sulfides (Maynard, 2014).

(2) The abundance of Mn carbonates in modern manganese accumulation is far lower than manganese in nodules and crusts, a feature that is quite different in ancient deposits, where Mn-rich carbonates are often the main ore forming minerals. Most of the Mn carbonates found in sediments result from diagenetic processes, either from precipitation in pore-waters, or by replacement of Mn oxide nodules. Mn carbonates formation involves high dissolved HCO_3^- in pore water (kutnahorite) and/or an organic matter contribution (rhodochrosite; Maynard, 2014 and reference therein). Such differences in the modern and ancient deposits composition is the first clue that diagenesis has a strong impact on the presence of Mn carbonates, given that ancient deposits have a large number of manganiferous carbonates (Maynard, 2014). The presence of organic carbon is another feature needed for the concentration of

manganese and is related to catagenesis[12] of the C-rich sediments (Kuleshov, 2011, 2016). Investigating manganese concentration mechanism is facilitated by geochemical proxies, especially C-isotopes, that can bring insight into the processes from which Mn carbonates were formed (Kuleshov, 2016). Within sedimentary deposits, Maynard (2010) suggested that rhodochrosite is a primary or early diagenetic (secondary) Mn-bearing mineral and that other Mn silicates (braunite) and oxides arose during late diagenesis, metamorphism or supergene alteration. Johnson *et al.* (2016) recently proposed a paragenetic model for the diagenetic stabilization of Mn deposits (►Fig. 3.10). The first precipitates to enter and concentrate Mn in sediments are Mn oxides (e.g., deep sea nodules; e.g., Tebo *et al.*, 2004). The precipitation of Mn-bearing carbonates during burial is first initiated during the reduction of Mn^{4+} of the Mn oxides into Mn^{3+}/Mn^{2+} by organic matter (►Equ. 1; Okita *et al.*, 1988; Polgári *et al.*, 1991; Tsikos *et al.*, 2003). Such reaction results in the increase of the Mn^{2+} concentration of the pore-water cavities of the sediment and not the seawater directly, as concentration of Mn in seawater to form Mn carbonates is insufficient (Calvert and Pedersen, 1996). Either kutnahorite or rhodochrosite can precipitate depending on the Ca:Mn ratio of the pore water from which carbonates have precipitated (Mucci, 2004). The Ca:Mn ratio is relatively high in pore-water, resulting in the formation of kutnahorite first, leaving the pore water Ca-depleted. Rhodochrosite can then precipitate given that the pore fluid evolves to higher Mn^{2+} concentration (Johnson *et al.*, 2016). Braunite also occurs as an early diagenetic mineral from the diagenetic silicification of H_4SiO_4 with primary or secondary Mn oxides (probably bixbyite; ►Equ. 2; Robie *et al.*, 1995; Johnson *et al.*, 2016). The presence of braunite is important to accommodate Mn^{3+} as trivalent Mn cannot be present in reduced Mn carbonates, but in “intermediate ligand” initiated by bacterial reduction (►Equ. 3; ►Fig. 3.10; Johnson *et al.*, 2016).

$$2MnO_2 + CH_2O + 4H^+ + 2CO^{2-}_3 \rightarrow 2Mn^{2+} + CO_2 + 3H_2O + 2CO^{2-}_3 \rightarrow 2MnCO_3 \text{ (rhodochrosite)} + 3H_2O + CO_2 \quad (\blacktriangleright\text{Equ. 1})$$

$$14Mn_2O_3 \text{ (bixbyite) } 4SiO_2 \rightarrow 4Mn^{3+}_6Mn^{2+}SiO_{12} \text{ (braunite)} + O_2 \quad (\blacktriangleright\text{Equ. 2})$$

$$2MnO_2 + Mn^{2+} + 2H_2O \rightarrow 2MnOOH + 2H^+ \quad (\blacktriangleright\text{Equ. 3})$$

[12]Term used in the petroleum industry to describe the process by which organic carbon is converted into hydrocarbons by thermal alteration from 50–200°C.

Later metamorphic processes result in the formation of various Mn-bearing minerals, mainly silicates (rhodonite, spessartine, etc.; see chapter 6). The main outcome of these processes is the transformation of nearly all primary Mn oxides into Mn-bearing carbonates and silicates during increasing burial conditions of Mn-rich sediments, if organic carbon or other reductants are not limited (Johnson *et al.*, 2016).

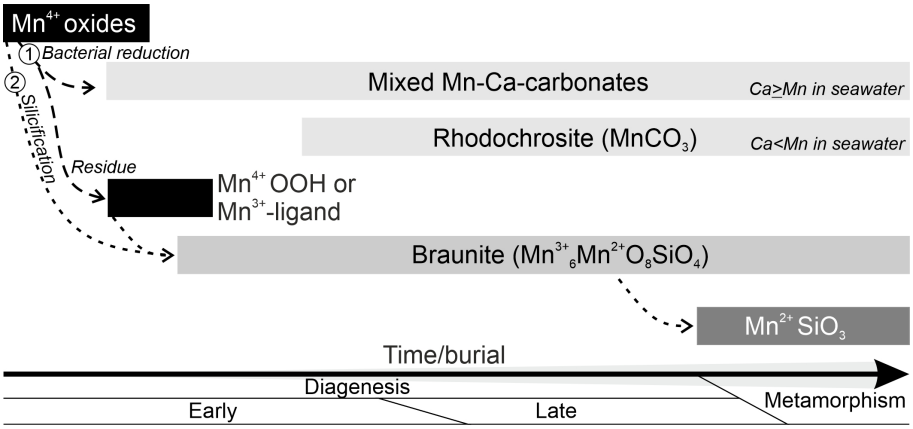

►**Fig. 3.10** Paragenetic model for the diagenetic stabilization of sedimentary Mn deposits. Mn-oxides are bacterially reduced during diagenesis either to Mn^{3+} phases (oxides or braunite) or to Mn^{2+} (Mn-carbonates), depending on the Ca:Mn ratio of pore waters and the Si availability (silicification), respectively. Increasing burial and subsequent metamorphism increase the mineral diversity (adapted from Johnson *et al.*, 2016).

3.3.1.d Models of sedimentary manganese deposits

Two models have been invoked to explain the concentration of manganese in sedimentary rocks (Cannon and Force, 1983; Force and Cannon, 1988; Force and Maynard, 1991; Maynard, 2014). Both models suggest that manganese is solubilized in deep-water sediments under anoxic conditions and precipitates where the redox interface is in contact with the seafloor (Cannon and Force, 1983; Force and Cannon, 1988; Force and Maynard, 1991).

(1) In the *euxinic basin model*, anoxia is caused by restricted circulation in a basin (e.g., Black Sea) that is isolated from open marine conditions and has free H_2S in the bottom water (►Fig. 3.11a). Such model was applied to giant deposits, such as Molango (Mexico; i.e., Okita and Shanks, 1992), Nsuta (Ghana; i.e., Nyame and Beukes, 2006), Minle (China; Tang and Liu, 1999), and Kalahari-Postmasburg (South Africa; Tsikos *et al.*, 2003).

(2) However, improvement of this first version has led Calvert and Pedersen (1996) to suggest the *oxygen minimum zone model*, in which anoxia is the result of a

high primary productivity of organic carbon (►Fig. 3.11b). Such massive carbon production is typically found beneath areas of upwelling of deep nutrient-rich water. Such examples are evidenced for deposits of the Cenomanian-Turonian boundary (Pratt *et al.*, 1991; Dickens and Owen, 1993).

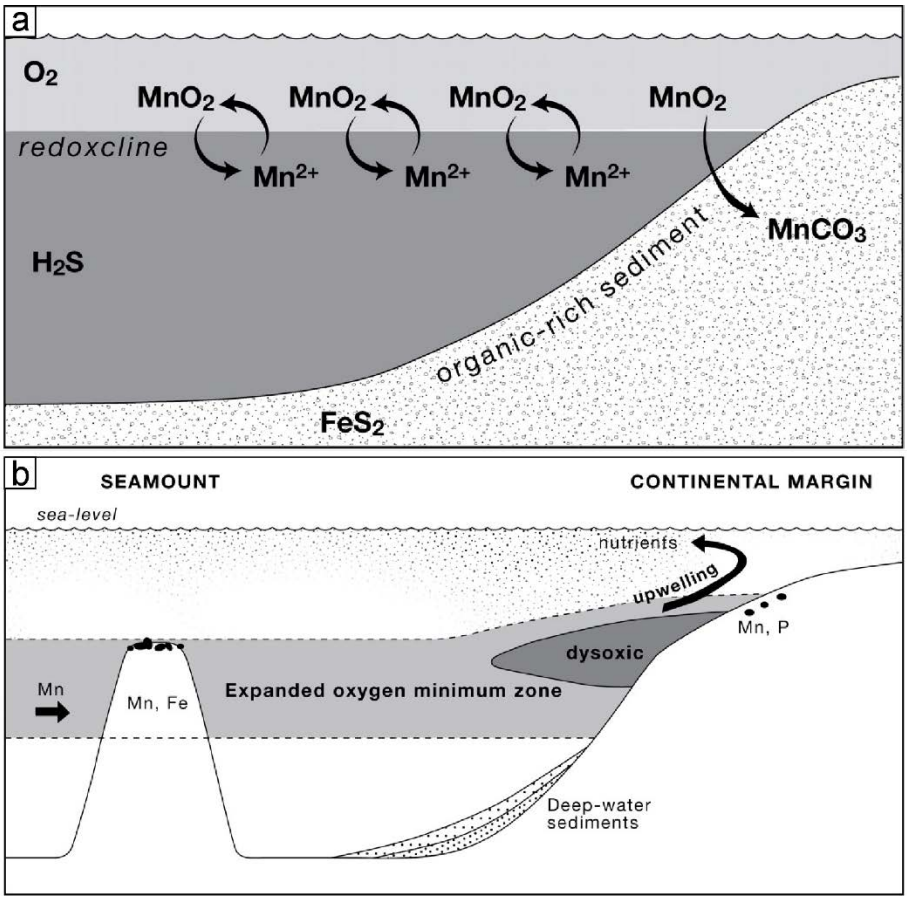

►**Fig. 3.11 a.** Oxygen minimum zone model. This model requires free H_2S below the redoxcline (Liu and Xue, 1999; Maynard, 2010, 2014). **b.** Euxinic basin model. High oxygen content of deep seawater inhibits the formation of H_2S and therefore the precipitation of Fe sulfides. The manganiferous sediments are particularly enriched in phosphorous, given that P follows the upwelling high nutrient zone (Trappe, 1998; Maynard, 2010, 2014).

As both deposits result from oxygen-free bottom waters, their chemical composition is similar in some points. Euxinic deposits are enriched in Ba in the Mn-oxides, because sulfate (barite) is removed from the water column beneath the redoxcline (►Fig. 3.11a), whereas P is enriched in the upwelling zone of the *oxygen minimum zone model* (►Fig. 3.11b; Maynard, 2010). Mn oxides precipitate at the interface between oxidizing and reducing conditions in the water column, most of the

time in the halocline.[13] Most of these oxides are not deposited in deep sediments because they are dissolved again once they deepen in the water column, unless the seafloor is shallow enough to intercept the redox boundary. Sediments at shallow depth have a small amount of manganese, as most of these oxides have precipitated, leaving oxygenated seawater depleted in dissolved manganese. Therefore, sediments can be significantly enriched in Mn oxides only in a narrow window in the water column, at depth of the halocline. Iron is not involved in this process as Fe remains fixed in sulfide minerals at deeper water-sediments interface (Maynard, 2010, 2014). The production of $MnCO_3$ requires the consumption of large amounts of organic matter and must occur after the deposition of Mn oxides, during early diagenesis. Consequently, organic matter can recombine with Mn oxides to produce a large amount of manganese carbonates (►Equ. 1; e.g., Maynard, 2014; Johnson *et al.*, 2016). The oxidation of the organic matter can also attack, at the same time, Fe sulfides in the sediments, and therefore provides Fe oxides accompanying the Mn-carbonates (►Equ. 4; Aller and Rude, 1988; Schippers and Jørgensen, 2001; Maynard, 2014).

$$FeS + 4.5MnO_2 + 4H_2O \rightarrow FeOOH + 4.5Mn^{2+} + SO_4^{2-} + 7OH^- \text{ (►Equ. 4)}$$

Large tonnage deposits seem to form by the Euxinic mechanism (►Fig. 3.11a). Manganese ores, like those of Fe, show a strong concentration of sedimentary deposits in relation with Banded Iron Formation (BIF) of the Paleoproterozoic (~2300-1800 Ma) and a weaker occurrence in the Neoproterozoic (~800-600 Ma), but, unlike Fe, there is an additional strong peak in the Oligocene (28 Ma; ►Fig. 3.1). Therefore, Mn is not entirely controlled by the level of oxygen in the Earth's atmosphere. At each peak of Mn deposition, the associated ore deposits are concentrated in a few districts, suggesting a more local than global control on manganese metallogenesis, unlike iron deposits that respond to more global parameters (Maynard, 2010).

3.3.2 Metamorphic transformations

In nature, Mn-bearing rocks of metamorphic genesis are also widely distributed, resulting from metamorphism of initial manganese sediments and Mn-bearing rocks (e.g., see chapter 6). Trace Mn contents of the common metamorphic rocks have the

[13]Halocline is a zone of maximum concentration of dissolved salts providing high density to the seawater.

same order of magnitude as their unmetamorphosed progenitors, indicating that major transfer of Mn during metamorphism is not efficient to produce Mn enrichment. A major Mn transfer can take only place by the action of (metamorphic) hydrothermal fluids along shears and faults that provided the necessary permeability (Laznicka, 1992). These deposits are not considered to be primary, mostly because Mn is accommodated in various Mn-bearing minerals from which manganese could difficultly be processed. However, metamorphic protores are a good source rock for manganese deposits subjected to weathering agent, as it is the case in most of Chinese, Indian and Brazilian deposits (Varentsov, 1996; Fan and Yang, 1999; Kuleshov, 2011; Beukes *et al.*, 2016) or in Belgium (see chapter 6). Manganese is hosted in metamorphic minerals, mainly silicates (rhodonite, spessartine, tephroite, braunite, ottrélite, kanonaite, amphiboles, pyroxenes, etc.) and carbonates, which vary in terms of composition and degree of metamorphism (Kuleshov, 2016).

3.3.3 Hydrothermal and magmatic-related deposits

Igneous processes do not produce manganese enrichment because they do not partition manganese from iron in minerals, given that strongly oxidizing conditions are often missing. Such oxidation gradient can be found where magmas reach the surface via volcanic activity. High heat flows around volcanic vents can therefore induce hydrothermal circulation of water (seawater or ground water) in the surrounding rocks (e.g., chapter 8, Dekoninck *et al.*, 2018), as it is the case for porphyry cupper deposits (Maynard, 2014). Unlike the sedimentary-diagenetic ores, hydrothermal Mn-Fe oxide deposits are usually small or medium and therefore considered as non-commercial, characterized by an association of Mn with Fe (Fe-Mn deposits). However, in some cases, hydrothermal processes significantly enrich the primary ore as it has been observed in the world-class Postmasburg and Kalahari deposits of South Africa (►Fig. 3.2; Tsikos *et al.*, 2003; Chetty, 2008). Hydrothermal deposits are widespread, occurring in various geological settings and different depositional environments. These deposits are often stratabound, but may also occur as irregular bodies and epithermal veins in a large variety of host rocks (see chapter 5; Roy, 1997).

Nicholson (1992) has attempted to define a classification of hydrothermal deposits in three subtypes: (1) sedimentary-exhalative, (2) terrestrial, and (3) hypogene. Sedimentary-exhalative hydrothermal deposits (SEDEX) are bedded manganiferous sediments formed at the contact between hydrothermal springs and seawater (i.e., hydrothermal systems related to mid-ocean ridge vents). Terrestrial hydrothermal deposits are a variety of the SEDEX type, except that the contact of the hydrothermal fluids is much more oxygenated, given that they face directly

atmospheric conditions. These deposits result directly from geothermal waters around hot springs and pools. Hypogene veins are related to the setting up of volcanic and plutonic bodies (►Fig. 3.2; see chapter 5; Roy, 1968; Nicholson, 1992; Kuleshov, 2011). Nicholson (1992) proposed that the element association As, Ba, Cu, Li, Mo, Pb, Sb, Sr, V and Zn is typical for Mn oxide deposits of hydrothermal origin, and W and Tl were identified as being enriched in hypogene Mn-Fe vein deposits (Roy, 1981; Leal *et al.*, 2008).

3.3.3.a Sedimentary exhalative hydrothermal deposits

In systems that are closely associated with volcanic rocks, the boiling of fluids at greater depths has been invoked to explain sulfide precipitation, while the Mn-Fe mineralization is observed at shallower levels by the residual liquid phase (i.e., Saphoz deposit, chapter 5; Fusswinkel *et al.*, 2013). Earlier studies have shown that consistent similarities in trace element enrichment (As, W, Pb, Zn, Cu) exist between sedimentary–exhalative and terrestrial deposits. These have been essentially related to interactions with felsic (and often volcanic) source rocks (Hewett, 1964; Roy, 1981; Nicholson, 1992; Glasby *et al.*, 2005). The driving force for fluid convection and migration in most hydrothermal Mn-Fe deposits is considered to be an anomalously high heat flow due to volcanic activity (e.g., chapter 8; Roy, 1981; Dekoninck *et al.*, 2018). The oxygen gradient needed for ore minerals precipitation in Mn-Fe deposits is found where metal-bearing hydrothermal fluids encounter stagnant ground waters or seawater (Hewett, 1964; Roy, 1981; Maynard, 2014). Such combination of favorable conditions is commonly observed in mid-ocean ridge hydrothermal systems, as the alteration of the basaltic crust, continually supplies hydrothermal fluids in metals and associated elements (e.g., Rona *et al.*, 1983; Murton *et al.*, 1999). These key exchanges involve the release of H_2SO_4, Ca^{2+}, Fe^{2+}, Mn^{2+} and Ba^{2+} from basalt into the seawater, and the reduction of SO_4^{2-} to H_2S. However, only high-temperature vents (300–400°C) release manganese (Murton *et al.*, 1999; Fontaine *et al.*, 2007), together with a high water/rock ratio (>10 at 300°C; e.g., Seyfried and Ding, 2013). The insolubility of iron and manganese oxides and of barium sulfate in seawater leads to their precipitation and consequent enrichment of surrounding sediment. Because Fe^{2+} oxidizes more rapidly than Mn^{2+}, iron first precipitates close or within the mid-ocean ridge vent system, and manganese is dispersed farther from the vents, giving a Fe to Mn sequence from the center to the edge (►Fig. 3.7; Maynard, 2014).

3.3.3.b Terrestrial hydrothermal deposits

In terrestrial Mn-rich hydrothermal systems, a clear zonation of Mn minerals with increasing depth has been documented (Roy, 1981). The deepest parts of the vein

systems contain Mn^{2+}-bearing minerals (rhodochrosite, rhodonite, tephroite; Hewett, 1964; Roy, 1981). These reduced associations then evolve into shallower zones dominated by mixed valence oxides (bixbyite, braunite), and finally into tetravalent Mn oxides in the uppermost zones. This systematic mineral zoning reflects increasing oxidation via fluid mixing with shallow oxygenated ground waters at decreasing deposition temperatures (see chapter 8). Low-temperature veins consist of pyrolusite, cryptomelane, psilomelane, hollandite and todorokite, whereas veins formed from relatively higher temperature solutions exhibit braunite, bixbyite, hausmannite, huebnerite and/or Mn silicates (rhodonite, bustamite, tephroite), Mn carbonate and Mn-sulfide (alabandite). Barite, fluorite, calcite and quartz are characteristic accessory minerals. In many cases, the Mn-rich veins show spatial and temporal relations with hydrothermal base metal sulfides and gold-silver mineralization (Roy, 1981).

3.3.3.c Hypogene veins

Igneous-related manganese ore veins are widespread in nature and characterized by variable formation environments and sources. These deposits represent mineralization spots, ore occurrences, and rarely, small deposits, which have limited reserves and lack economic significance (Laznicka, 1992; Kuleshov, 2011). Consequently, manganese is embedded within its own minerals (oxides, carbonates, silicates, or more rarely sulfides), as it occurs as a component of hydrothermal minerals. Actually, these occurrences are genetically related to magmatic bodies, and crystallize at the end of the fractional crystallization of magmatic rocks in which manganese is enriched in residual fluids, together with quartz and feldspar. Late Fe-rich minerals (i.e., micas, amphiboles) are generally enriched in Mn, and if Mn concentration in the magmatic fluid is too high to be accommodated in these minerals (threshold value of 0.16 wt.% MnO), Mn veins with relatively pure Mn-bearing minerals (such as in pegmatite) can crystallize (Guérin, 1979). There is therefore a straightforward relation between the Mn content of the parental rock and the presence of magmatogenic Mn deposits. Mn oxides in the hydrothermal veins of deep genesis are associated with other elements (Pb, Ba, Zn, Ag, etc.). Spatially and genetically hypogenous Mn-bearing minerals are commonly connected with other types of deposit (barite, fluorite, calcite, sulfides of nonferrous metals, and Au-Ag mineralization; i.e., Vosges, Morocco), forming polymetallic ore belts (Choubert and Faure-Muret, 1973; Fluck and Weil, 1976; Kuleshov, 2016).

3.3.4 Supergene deposits

Manganese ores in the supergene environment represent the highest grade of manganese (consequently, the economically most valuable; i.e., Imini-Tasdremt district; see chapter 7), in particular in laterite weathering crusts (►Fig. 3.6). The formation of manganese ores in weathering zones is based on processes of interaction of natural meteoric waters with primary rocks, which are triggered by climate (temperature, precipitation and seasonality), and exposed by geodynamics (creation of a weathering gradient), among other factors (lithology, etc.; see chapter 2; Varentsov, 1996; Ruddiman *et al.*, 1997). These Mn accumulations are formed by replacing different primary manganiferous rocks (gondites[14], ampelites, Mn carbonates, metamorphic rocks, etc.; this thesis) subjected to weathering agents. The result is a strong enrichment of manganese and associated metals, from 1 to 5 times the protore or, more rarely, 10 to 20 times in karst deposits (Laznicka, 1992; Dekoninck *et al.*, 2016b, 2016a, see chapter 7). For example, the Lower Proterozoic Franceville Formation (Moanda, Gabon) is an economically important supergene deposit in which the relatively poor primary ore (13.5% Mn metal) has been upgraded after Mn carbonates and shales have undergone weathering, and transformed into Mn oxides (e.g., Varentsov, 1996). Another remarkable example is Archean carbonates that naturally contain a higher Mn content compared to Phanerozoic carbonates (►Table 3.1). Mn-bearing Archean carbonates can lead to further supergene concentration of Mn as the carbonate is dissolved and Mn^{2+} is oxidized and released in the environment. This process can produce small but economic Mn ores after weathering, as exemplified in the Postmasburg and Woodie Woodie Mn deposits (►Fig. 3.1; ►Table 3.1; Gutzmer and Beukes, 1996; Maynard, 2014). The chemical and mineral composition of manganese ores is determined, to a considerable degree, by the relatively high Mn content of primary rocks (e.g., West Africa; Nahon *et al.*, 1983; Parc *et al.*, 1989; Nahon and Parc, 1990; South America; Ruffet *et al.*, 1996; Chisonga *et al.*, 2012; Piacentini *et al.*, 2013), contrary to bauxite deposits for example, in which protores could have an Al content lower than clark values (Bárdossy and Aleva, 1990; Nahon *et al.*, 1992; Varentsov, 1996). Weathering deposits are temporary accumulations at geological time scale, as long as the weathering cover resists to chemical alteration and physical erosion (Laznicka, 1992, 2014; Vasconcelos, 1999). This is why these higher-grade ores are considered to have

[14]Metamorphic Mn-bearing rock containing a quartz-spessartine assemblage in West Africa.

relatively poor reserves compared to the giant sedimentary deposits (►Table 3.1; Laznicka, 1992, 2014).

The manganese ores can be accumulated in different ways, and have been distinguished in two subtypes of supergene manganese deposits (►Fig.3.6; (Varentsov, 1996): weathering crust and karst deposits. Mn deposits of the **weathering crust** are *in situ* deposition of Mn ores mostly developed in hot and humid tropical zones. They are laterite *s.l.* (see chapter 2) deposits occurring in the oxidation zone of primary Mn-rich sedimentary or metamorphic accumulations (see chapter 6), and account for most of the supergene deposits (►Fig.3.6). Groote Eylandt (North Australia), Moanda (Gabon), Nsuta (Ghana), and Tambao (Burkina Faso) are the most important Mn deposits of this type among many others.The weathering crust could also form over hypogene ores (e.g., Verhaert *et al.*, 2018, this thesis, see appendix III), in which Mn carbonates and silicates are common gangue of Fe, Zn, Cu and Pb veins (see chapter 5). **Karst-hosted deposits** are associated with the leaching, the infiltration and the redeposition of Mn ores in an open karst system, in which Mn has an allochthon origin. The best examples of these deposits are the Urkut (Hungary), the Postmasburg (South Africa) and the Imini-Tasdremt (Morocco; Dekoninck *et al.*, 2016b, 2016a, see chapter 7) deposits (Varentsov, 1996 and references therein; ►Table 3.3).

Deposits of the laterite *s.l.* (see chapter 2) crusts are typically formed under a humid tropical climate (i.e., equatorial latitudes), and are considered as the largest deposits, whereas the karst-hosted deposits and oxidation zone deposits could be formed under temperate, or less commonly, semi-arid conditions (e.g., Varentsov, 1996). The tropical climate is not the single driver for further weathering. Indeed, the most considerable deposits of manganese (and other metals) are also associated with large uplifted, geomorphologically differentiated, and tectonically stable areas (see chapter 2 and discussion in chapter 9; Parc *et al.*, 1989; Ostwald, 1992; Ruffet *et al.*, 1996; Hénocque *et al.*, 1998; Vasconcelos, 1999; Colin *et al.*, 2005; Beauvais *et al.*, 2008, 2016; Vasconcelos *et al.*, 2008, 2013; Dill *et al.*, 2010; Bonnet *et al.*, 2014, 2016; De Putter *et al.*, 2015, 2018; Riffel *et al.*, 2015; Vasconcelos and Carmo, 2018). The combination of a humid tropical environment with an optimum structural-geomorphological (here called “geodynamics”) setting determines a high drainage and the washing up of rocks (water exchange intensity), which significantly increase the rate of weathering profile formation (Varentsov, 1996). The formation of Mn oxides is generally accompanied by other weathering minerals (Fe oxides, kaolinite, gibbsite, illite, smectite, etc.; e.g., see chapter 2, Dekoninck *et al.*, 2018), due to the release of other cations such as Al, Fe and Si, among others (see chapter 2).

3.3.4. a Geochemical behavior of Mn in surficial waters

The solubility of manganese in natural waters is strongly influenced by the chemical equilibria involving Mn^{2+}, Mn^{3+} and Mn^{4+}, redox potential, pH and dissolved bicarbonate and sulfate (►Fig. 3.9). Mn^{2+} is soluble in ground and surface waters in the range of 0.10 and 1.0 ppm Mn, but concentrations are often lower because most waters cannot maintain saturation of Mn species (►Table 3.2). Additionally, Mn^{2+} is more soluble than Fe^{2+} in the Eh-pH window commonly found in surface waters, but both become quite similar when near neutral pH prevail in ground waters (Hem, 1963). At pH > 10.5, the complex $MnOH^{+}$ is favored, and in solutions with high concentrations of HCO_3^{-} or SO_4^{2-} the complexes $MnHCO_3^{+}$ and $MnSO_{4\ (aq)}$ may be important (Hem, 1989). The surficial environments could also contain dissolved organic matter, in particular humic and fulvic acids, those increasing the manganese solubility with respect to pH (Crerar *et al.*, 1972; Stone and Morgan, 1984a, 1984b; Stone, 1987; Varentsov, 1996). The chemical oxidation of Mn^{2+} and Mn^{3+} and the disproportionation[15] of Mn^{3+} in aerated surface waters lead to the formation of Mn^{4+} oxides, which stimulate other Mn oxides to precipitate by the autocatalyst effect. Mn oxides are therefore deposited on the previous formed Mn-oxides, forming the typical growth bands observed in supergene ores. Such colloform aggregates also favor the precipitation of other cations from solutions (Ba, K, Pb, Na, Co, Cu, Ni, etc.), leading to the formation of complex supergene phases. Hollandite, coronadite, cryptomelane, romanechite, todorokite and vernadite are commonly found in soils and weathering profiles (this thesis; Burns and Burns, 1979; Post, 1999; Vasconcelos, 1999).

Due to these profoundly different properties of oxidation states, the geochemical behavior of manganese is particularly sensitive to environmental changes (Bricker, 1965; Varentsov and Grasselly, 1980; Dixon *et al.*, 1989; Parc *et al.*, 1989; Nahon and Parc, 1990). There are various pathways to which Mn oxides may be formed, mostly depending on the primary mineral hosting the Mn cations that aim to be released and then oxidized. The di- and tri-valent oxides are readily altered through oxidation (►Equ. 5) or disproportionation and subsequent oxidation (►Equ. 6).

$$Mn_3O_{4\ (hausmannite)} + 4H^{+} \rightarrow 2Mn^{2+} + Mn^{4+}O_{2\ (pyrolusite)} + 2H_2O \qquad \text{►Equ. 5}$$

$$Mn^{2+} + H_2O + 0.5O_2 \rightarrow Mn^{4+}O_{2\ (pyrolusite)} + 2H^{+} \qquad \text{►Equ. 6}$$

[15]Redox reaction in which a compound of intermediate oxidation state is converted to two different compounds, one of higher and one of lower oxidation states.

The release of Mn during the weathering of silicates involves protolysis and oxidation, two processes that may be combined in various ways. Braunite, for example, may break down by this reaction in the presence of protons (►Equ. 7). The liberated Mn may then be transformed into tetravalent oxides immediately after its release when O_2 is available. When this is not the case, it may migrate until reaching an oxygenated milieu. Oxidation may also take place within the braunite structure itself and facilitate its breakdown.

$$Mn_7SiO_{12\ (braunite)} + 12H^+ \rightarrow 6Mn^{3+} + Mn^{2+} + H_4SiO_4 + 8OH^- \qquad \text{►Equ. 7}$$

Carbonates are the most readily leached rock types under humid conditions. Water charged with CO rapidly dissolves rhodochrosite or any other Mn-bearing carbonates (►Equ. 8), that finally form the tetravalent oxides (►Equ. 9).

$$MnCO_{3\ (rhodochrosite)} \rightarrow Mn^{2+} + CO_3^{2-} \qquad \text{►Equ. 8}$$

$$CaCO_{3\ (calcite)} + MnCO_{3\ (rhodochrosite)} + H_2O + 0.5O_2 \rightarrow Ca(HCO_3)_2 + MnO_{2\ (pyrolusite)} \qquad \text{►Equ. 9}$$

In the presence of potassium or barium, respectively originating from K-feldspars and/or micas and barite, cryptomelane, hollandite or romanechite may form instead of or together with pure MnO (pyrolusite; see chapters 6 and 7). The formation of cryptomelane (KMn_8O_{16}) could be determined by the direct precipitation from the weathering solution (►Equ. 10), by pyrolusite destabilization (►Equ. 11), by the oxidative dissolution of rhodochrosite (►Equ. 12), or by the oxidative dissolution of Mn silicates (tephroite, rhodonite, braunite, spessartine, etc.; ►Equ. 13; Vasconcelos, 1999). It is worth noting that in these reactions, dissolved K^+ is released from other K-bearing minerals in the weathering solution (i.e., muscovite, illite, feldspars, etc., Parc *et al.*, 1989; see chapter 6).

$$K^+ + 8Mn^{2+} + 8H_2O + 4O_2 + OH^- \rightarrow KMn_8O_{16} + 16H^+ \qquad \text{►Equ. 10}$$

$$8MnO_{2\ (pyrolusite)} + K^+ \rightarrow KMn_8O_{16} \qquad \text{►Equ. 11}$$

$$8MnCO_{3\ (rhodochrosite)} + K^+ + 4O_2 + 8H_2O \rightarrow KMn_8O_{16} + 8H_2CO_3 \qquad \text{►Equ. 12}$$

$$8MnSiO_{3\ (rhodonite)} + K^+ + 4O_2 + 16H_2O \rightarrow KMn_8O_{16} + 8H_4SiO_4 \qquad \text{►Equ. 13}$$

In some cases, the precipitation of Mn oxides could be followed by their partial dissolution and then their reprecipitation in suitable zones, mostly because the influx and the composition of the weathering conditions could change through time. Therefore, reduction processes necessarily operate as Mn^{2+} is the only soluble Mn-

bearing cation in meteoric waters. Such reductive conditions can be driven by the increasing acidity (i.e., organic acids; ►Equ. 14) and the complexation with organic ligands (►Equ. 15), or the dissolution with soluble Fe^{2+} (►Equ. 16). The released Mn^{2+} reprecipitates nearby within the weathering profile following reactions in ►Equ. 10 to 13 (Vasconcelos, 1999).

$$KMn_8O_{16} + 17H^+ \rightarrow K^+ + 8Mn^{2+} + 9H_2O + 4O_2 \qquad \text{►Equ. 14}$$

$$KMn_8O_{16} + 8CHO_2^- + 25H^+ \rightarrow K^+ + 8Mn^{2+} + 8CO_2 + 17H_2O \qquad \text{►Equ. 15}$$

$$KMn_8O_{16} + 16Fe2+ + 16H_2O \rightarrow 16FeOOH_{(goethite)} + K^+ + 8Mn^{2+} + 16H^+ \qquad \text{►Equ. 16}$$

The kinetics of Mn^{2+} oxidation in aqueous solutions is generally slow in neutral to slightly acidic oxygenated weathering waters (Crerar *et al.*, 1972). However, oxidation can be accelerated by alkaline conditions (pH > 8; Hem, 1989), as well as by bacterial catalysis (Mandernack *et al.*, 1995a, 1995b; Tebo *et al.*, 2004, 2005) and by surface minerals (Davies and Morgan, 1989).

3.3.4.b Transformation in weathering crusts

Mn deposits of the weathering crust are usually characterized by a zonal structure, which is determined by specific mineral parageneses. The evolution of mineral assemblages is driven by changes in Eh and pH regimes and the content of dissolved organic matter and CO_2. The general picture encloses the dissolution of primary minerals and their *in situ* precipitation or slight migration to accumulate in the main ore bodies. Parc *et al.* (1989), Nahon *et al.* (1992) and Varentsov (1996) tentatively proposed several mineral sequences during the weathering of different protores, showing that manganese is more and more oxidized from Mn^{2+} hosted in the primary minerals (Mn-silicates and carbonates) to Mn^{4+}-oxides (►Fig. 3.12). Actually, oxidation processes and phase relations are more complex in a weathering profile, which gives various sequences depending on the host rock composition, the weathering fluid and the rate of alteration. It seems that different parent minerals are able to generate the same oxidized weathering products and that different minerals may produce in the same horizon different weathering minerals. ►Fig. 3.12 is gross simplification, which is probably partially incorrect, but remains interesting to evidence that various mineral transformations occur in the weathering crust.

Laznicka (1992) divided weathering deposits in three fundamental zones (from top to bottom): (1) laterite s.s., (2) saprolite and (3) protore. The zone of residual metalliferous soil (**laterite *s.s.***; see chapter 2) is characterized by the authigenic precipitation of Mn oxide concretions, pisoliths, crusts, colloform aggregates, etc. The

zone of complete or partial *in situ* supergene replacement (**saprolite**; see chapter 2) mainly consists in chemical and mineralogical changes related to the breakdown of primary minerals (silicates and carbonates of Mn). These changes are accompanied by structural modifications (load, collapse). The saprolite is mainly transitory between the upper laterite *s.s.*, and the third zone, the unweathered, fresh primary rock or **protore**. Sometimes, the latter is crisscrossed by fractures filled by Mn oxides precipitated from descending meteoric waters (►Fig. 2.2). As a general rule, mineral formation follows the oxidation potential of manganese, providing Mn^{4+}-dominated oxides in the upper part of the weathering profile, and Mn^{2+} in the lower part (►Fig. 3.12). Intermediate oxidation states allow several Mn-bearing oxides to precipitate in the middle part of a weathering profile (►Figs. 3.13a and b). The geochemical trend of the development of a laterite weathering crust profile evolves from a slightly oxidized neutral environment to an acid environment with normal Eh (Varentsov, 1996).

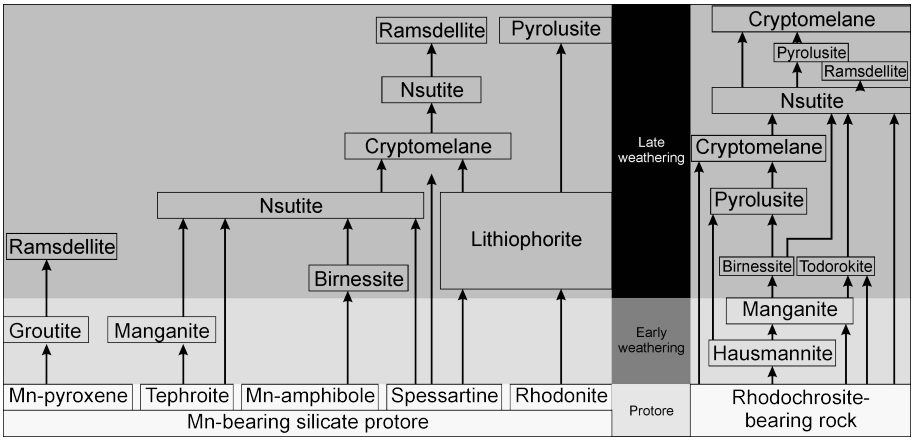

►**Fig. 3.12** Tentative chart of weathering parageneses depending on the protore composition (Mn carbonates or Mn silicates; based upon works of Bouladon *et al.*, 1965; Grandin and Perseil, 1977, 1983; Perseil and Grandin, 1978, 1985; Weber *et al.*, 1979; Leclerc and Weber, 1980; Nahon *et al.*, 1982, 1983, 1992; Parc *et al.*, 1989; Varentsov, 1996).

During the *early stages* of the weathering profile (saprolite) development, neutral to slightly alkaline conditions prevail, due to neutralizing reactions and the release of alkaline and alkaline-earth cations. Manganite (γ-MnOOH) is the early product formed under these conditions, and not nsutite (γ-MnO_2) which occurs with lower pH and a dissolved Mn^{2+} concentration (►Figs. 3.12, 3.13a and b; Varentsov, 1996). The initial mineral-forming solutions (slightly alkaline with a soft oxidizing regime) are also enriched in Si, Ca, Mg and a number of transition metals, in addition to Mn, that are accommodated by the forming solid phase (e.g., todorokite, birnessite, chalcophanite, etc.).

During long and intensive circulation of acid ground waters in the higher horizons of the weathering crusts (laterite), an accumulation of some Mn^{4+} minerals may occur (lithiophorite, birnessite, cryptomelane, nsutite, pyrolusite, etc.). The weathering mineralogy of Mn oxides formed during such *major stages* of oxidation depends on the protore composition (Varentsov, 1996). Lithiophorite precipitation generally occurs in silicate protores, given that a relatively high amount of Al is needed, either from the parent rock or from the destruction of kaolinite in the upper part of the profile (►Figs. 3.12 and 3.13b). Under acid conditions (3–5 pH units) and an oxidizing regime of ground waters, Al is poorly mobile in comparison with manganese. Similar Al:Mn ratio (~1) in spessartine and lithiophorite indicates that lithiophorite is a residual product of the Mn-garnet dissolution (see chapter 6). In order to increase the mobility of Al (and Mn) in the weathering fluids, more acid solutions are needed to precipitate lithiophorite in other places of the weathering profiles. This enrichment in aluminum at the top of lateritic weathering profiles can generate concentrations of gibbsite by the dissolution of lithiophorite (Nahon *et al.*, 1992). Cryptomelane occurs during the supergene alteration of silicates, carbonates and Mn-bearing protores (►Figs. 3.13a and b). Cryptomelane follows lithiophorite (silicate protore) or pyrolusite (carbonate protore; ►Figs. 3.12) in the mineralizing sequence. Cryptomelane is found as an essential ore-forming mineral in the mature or final stage of a weathering crust (i.e., cap). The only limiting parameter is the presence of K^+ in the system, or at least elements that can be hosted in other species of the hollandite group (i.e., Ba, Pb, Na, Sr; Varentsov, 1996). A low pH (1–3) is generally needed, depending on an increasing K^+ concentration of the weathering solutions to precipitate cryptomelane (Hypolito *et al.*, 1984), but other settings (Eh, pH, pressure, temperature and O_2) could also stabilize hollandite group minerals (Varentsov, 1996). The release of potassium by the late weathering of micaceous minerals (i.e., muscovite) allows the retromorphosis of nsutite and even pyrolusite into cryptomelane (Nahon *et al.*, 1992). Under an acid pH and oxidizing conditions and in the absence of alkaline and alkaline-earth elements, nsutite precipitates directly. Later on, nsutite is completely converted into pyrolusite (►Figs. 3.12). In this environment, the sorption of chemical elements (Co, Ni, Ba, K, etc.) by autocatalytic interactions of Mn-bearing oxides plays an important role (i.e., asbolane and clays; Varentsov, 1996; Vasconcelos, 1999). The weathering of basic and ultrabasic rocks can produce a substantial enrichment in Ni and Co (~1%), especially in limonite zones of regolith above the lateritic Mn crust (►Table 3.3; Elias *et al.*, 1981; Manceau *et al.*, 1987).

- *Weathering of carbonate protore*

The process by which carbonate primary ores are weathered by interacting with ground waters is determined by the composition of the protores, the presence of organic matter and the drainage intensity (e.g., Varentsov, 1996). Depending on the

rate of weathering and the oxidation level, mineral parasequences could differ. A slow gradation in the oxidation level in the upper part of the weathering profile allows rhodochrosite to transform into manganite (even if an intermediate groutite is not excluded), pyrolusite, cryptomelane and nsutite/ramsdellite (►Fig. 3.13a).

- *Weathering of silicate protore*

Mn protores in some West Africa deposits are composed of tephroite ($MnSiO_4$), spessartine ($Mn_3Al_2[SiO_4]_3$), maganoan calcite ($[Ca,Mn]CO_3$), Mn-chlorite and sulfides. It has been shown that tephroite, Mn-calcite and Mn-chlorite are easily dissolved in the early stages of weathering to form Mn-oxides, unlike spessartine that can resist until the upper part of the weathering profile (see chapter 6) where early generation of Mn oxides are substituted by later ones. The early stages of weathering are not able to fully oxidize Mn^{2+}, instead tephroite transforms into Mn^{2+}-smectite (saponite; ►Fig. 3.13b). Manganite formation is observed in the upper levels of the weathering profile, as replacement of Mn-smectite or tephroite (Nahon *et al.*, 1982, 1983; Parc *et al.*, 1989). Manganite is the initial product of the *in situ* oxidation process, but does not account for the transportation of manganese. The main stage of weathering is attested by the alteration of spessartine into successive lithiophorite, cryptomelane, ramsdellite and nsutite (►Fig. 3.13b).

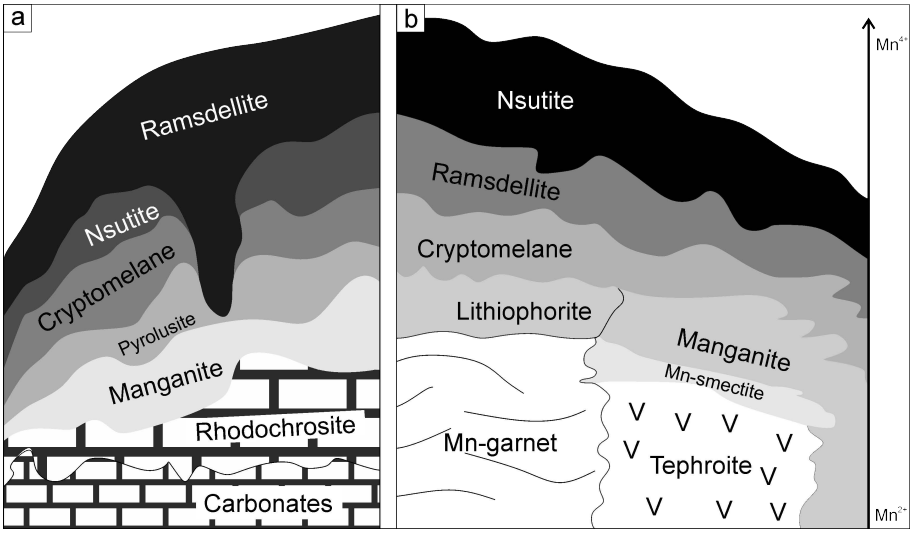

►**Fig. 3.13** Successive formation of Mn-bearing minerals in the weathering crust of some West Africa deposits (Varentsov 1996). **a.** Carbonate parent rock (Bouladon *et al.*, 1965; Grandin and Perseil, 1977, 1983; Perseil and Grandin, 1978, 1985; Weber *et al.*, 1979; Boeglin *et al.*, 1980; Leclerc and Weber, 1980; Nahon *et al.*, 1982, 1983). **b.** Silicate parent rock (Grandin and Perseil, 1977, 1983; Perseil and Grandin, 1978, 1985; Nahon *et al.*, 1982, 1983).

3.3.4.c Weathering transformation in karst-hosted deposits

Mn oxides mineralized in karst are a variety of manganiferous weathering profiles, empirically and genetically close to bauxites. These karst-hosted deposits are structurally and texturally equivalent to the saprolite level hosted in dolostone or limestone (Laznicka, 1992). Manganese ores in paleokarst are characterized by (1) supergene associations showing the typical accumulation associated with events of leaching and the redeposition of ore components by surface meteoric waters, and (2) deep epigenetic features due to the high dissolution and the migration of solutions. This dualistic feature is determined by different hydrogeological settings in the supergene, diagenetic and epigenetic zones where ground waters can circulate (Varentsov, 1996). Such processes can occur at a depth reaching 4–6 kilometers, where temperatures of 100–200°C are similar to hydrothermal systems (Postmasburg manganese field; von Plehwe-Leisen and Klemm, 1995; Gutzmer and Beukes, 1996, 1997). Under the near-surface conditions and with the general development of karst, supergene processes of manganese ore accumulation are similar to what happen in the weathering crust of Mn-bearing carbonate rocks (Varentsov, 1996; Maynard, 2014). Multiple breccia formations and polychronous accumulations of the manganese ore may be the result of dissolution events.

3.3.d Dating weathering processes by Mn oxides

K-bearing Mn oxides of the hollandite group minerals are among the few ore minerals potentially suitable to isotopic dating (►Fig. 3.3; ►Table 3.2). Due to their wide occurrence and their association with geological features of interest, minerals such as cryptomelane ($KMnO_8O_{16}$) and romanechite ($Ba_{0.66}Mn^{4+}_{3.68}Mn^{3+}_{1.32}O_{10}.1.34H_2O$) have become the focus of geochronological studies in the past decades (e.g., Segev *et al.*, 1991; Vasconcelos *et al.*, 1992). The suitability of Mn oxides to geochronological investigations by the K-Ar and $^{40}Ar/^{39}Ar$ methods arises from the fact that most of the hollandite group minerals (and to a lesser extent romanechite) can host K in relatively high quantities (up to 5.32% K in pure cryptomelane) in well-defined crystallographic sites (see chapter 4 for more details about the methods). These sites are relatively retentive of K and radiogenic ^{40}Ar, because of their tunnel-like structure (►Fig. 3.3). However, not all tunnel-like Mn oxides are suitable for accurate geochronological studies. For example, todorokite has a relatively high exchange capacity due to its large 3X3 (or more) cross-section, and cannot retain quantitatively argon (Ostwald, 1986; Post, 1999; Vasconcelos, 1999). The pyrolusite-ramsdellite-nsutite system virtually contains no K because of its small 1X1 (or 1X2 in ramsdellite) tunnel diameters (►Fig. 2.3; Ostwald, 1984a; Post, 1999), and has therefore not been studied, considering that 0.2-0.4 wt.% K is needed for reliable analyses (Vasconcelos, 1999). The suitability of Mn oxides as a chronometer of weathering and the methodology in isotopic systems are detailed in chapter 4.

K-Mn oxides dating may provide reliable and reproducible geochronological informations about chemical processes occurring in the weathering environment (i.e., the longevity and the evolution of laterite profile). If K-Mn oxides have simultaneously precipitated, such approach could estimate the timing of the ore formation of various metals (Fe, Mn, Pb, Zn, etc.) and raw materials (kaolin, clays) of primary accumulation subjected to weathering agent, and the processes by which they were concentrated. One of the main challenge in determining the age is that weathering profiles are often the result of combined long-lasting superimposed weathering processes active during long periods (Vasconcelos, 1999). The erosion could also plays a role in this issue, as it considerably modifies the structure of a weathering mantle, implying the disappearance of the upper part, and, therefore, the loss of some geochronological information. Consequently, the oldest periods are removed, given that the weathering front migrate downward, and only the youngest ages are preserved in the lower part of the profile (►Fig. 2.2). In this scenario, weathering geochronology can only provide a minimum age for the profile. In the ferruginous crusts associated with lateritic profiles, Mn oxides may be absent due to the reduction of Mn^{4+} to Mn^{2+} released in meteoric waters (Vasconcelos, 1999). This reduction process occurs in soils, indicating that Mn oxides are concentrated in the saprolite, and are thus relatively protected from erosion and may actually reflect the initial age of the formation of the profile (Ruffet *et al.*, 1996; Dammer *et al.*, 1999; Vasconcelos, 1999; Li *et al.*, 2007; Vasconcelos and Carmo, 2018).

Weathering geochronology provides constraints on the maximum rates of denudation if the profile is entirely preserved and the thickness well constrained. Therefore, issues about the continuous or episodic development of a weathering profile arise from the geochronology of Mn oxides (Vasconcelos, 1999). It has been suggested by Vasconcelos (1999) that the evolution of weathering profiles should reflect the variations in temperatures and the composition of the weathering solutions percolating through the profile. Chemical weathering is strongly limited in cold systems or in the absence of high water-rock interactions. This implies that an increase in the availability of water in the system should drive these reactions forward and should promote the formation of supergene minerals. Therefore, weathering rates could strongly vary with time depending on the quantity of rainfall waters, the surface temperature and the abundance of vegetation. The timing of exhumation (geodynamics) also delimits the periods during which the rocks can weather. Wet conditions and a slow uplift volumetrically favor important supergene minerals and limit erosion (see discussion in chapter 9).

3.4 Manganese uses

Few people know that Mn is as essential as iron to the production of steel. Manganese is the 4th produced element in terms of tonnage with more than 18 million metric tons (mt) in 2017 (U.S. Geological Survey, 2018; ►Fig. 1.1). Its role in the world market is important because it is widely used as an alloy in steel, in other sectors as well: in the production of portable batteries, in agricultural fungicide, in electronic circuit boards or in aluminum beverage cans. Manganese is also an important nutrient in soils and can be a limiting factor in plant nutrition. In this section, the role of manganese the industrial sector and in the world market is reviewed.

3.4.1 A page of history

Manganese was isolated by the Swedish chemist Johan Gottlied Gahn in 1774 by heating the naturally occurring mineral pyrolusite (MnO_2) in the presence of charcoal. However, his co-worker Carl Wilhelm Scheele was the first to consider manganese as a single element in 1771 (Scheele, 1777). The first evidence of manganese utilization come from the Stone Age where it was already used as a pigment for painting in caves in the upper Paleolithic (17,000 years ago). Spartans from the Ancient Greece period exploited iron deposits when manganese was associated. The presence of manganese naturally gave to Spartans alloyed steel weapons a strong advantage, i.e., their stronger resistance. Since the Egyptian and Roman empires, manganese has been used in glassmaking thanks to its coloring feature. The 19th century marked the beginning of manganese in steelmaking in France and United Kingdom, but it was in 1816 that a German researcher pointed out the strengthening effect of manganese in steel manufacturing. After 1840, Pourcel began the industrial-scale production of spiegeleisen (=iron mirror), a pig iron composed of 65% Mn content. In 1856, Mushet suggested adding pig iron to the Henry Bessemer steelmaking process with the objective to remove excess of oxygen. In 1866, William Siemens introduced the use of ferromanganese to control phosphorous and sulfur contents in steelmaking. In 1868, dry cell batteries were finally developed by Leclanché. The 20th century brought improvements of previous processes and chemical/metallurgical applications, such as agricultural fungicides, beverage cans and electronic circuits (Eramet, 2019).

3.4.2 Manganese in the metallurgical industry

The steel industry accounts for as much as 90 percent of the manganese consumption. Steel is a metal alloy consisting of an iron phase and an iron carbide. The increase in carbon content (between 0.02 to 2 wt. %) provides a harder and stronger steel,

preventing dislocation in the iron atom crystal lattice. A higher silicon content gives steel an additional deoxidizer property. Crude steel produced from iron contains an undesirable amount of oxygen and sulfur. Manganese plays a key role during the refinement of steel, as it removes oxygen and sulfur when crude iron ore is converted into metallic iron. When there is insufficient manganese, the sulfur combines with iron to form a low melting point sulfide, which melts at hot rolling temperatures, causing a surface cracking phenomenon. About 30% of Mn is used during this refinement step of iron ore, and the remaining 70% is added as an alloy along the steelmaking process. As an alloy, it decreases the brittleness of steel and adds strength. The amount of manganese used per ton of steel is rather small, ranging from 6 to 9 kilograms (0.6-0.9 wt. %). In almost every instance manganese is added to the steel as a ferroalloy, which is produced in a submerged-arc furnace by reduction of manganese ore (Van Deventer, 1987; Eramet, 2019).

Other alloys could be involved during steelmaking, which are known as cast iron and ferroalloys but are not considered as steel. The ferroalloys refer to various alloys of iron with a high proportion of one or more other metals such as Mn, Al, C, Si, B, Ce, Cr, Mo, Nb, Ni, P, Mg, Ti, U, V and W. Alloys are secondary materials providing distinctive qualities to steel and cast iron. They are therefore, closely associated with the iron and steel industries (►Table 3.4; Fichte, 2000).

The second use of manganese as alloy (far behind steel), is in aluminum production. In small quantities, it plays an important role in enhancing corrosion resistance. Aluminum-manganese alloys and aluminum-manganese-magnesium alloys contain up to 9% Mn, and have found applications in diversified areas such as kitchenware, roofing, car radiators and transportation. However, the most important use of AlMn alloy is for beverage cans. AlMn alloys find a potential interest in the aerospace industry as well, as this type of alloy has very fast cooling rates, which allow a good strength, a smooth surface to steel and needs no machining to meet product specifications (Eramet, 2019).

Manganese is probably the most versatile element, as it can also be added to copper alloys. Small additions of Mn (0.1-0.3%) are used to deoxidise the alloy and improve its castability and mechanical strength. Cu alloys could contain 1–2% Mn to improve its strength and its hot workability, and therefore replace Ni and NiAg alloys to reduce production costs. Some other alloys have a higher Mn content (>50% Mn) in specific applications: for bimetallic strips in temperature control devices fitted to cars and other vehicles, or for the watchmaking industry.

Manganese is also used in titanium-base alloys (8% Mn content) in the aerospace industry, or with zinc and magnesium alloys (0.1-0.2% Mn content).

►**Table 3.4** Different ferroalloys and their uses in the steel industry.

Name	Full name	Uses	Composition
FeMn	Ferromanganese	Steelmaking process	7% ≥ Si, 8 % ≥ C, 74-90 % Mn
FeSi	Ferrosilicon	Stainless steel, Steelmaking process	15-90 % Si
FeAl	Ferroaluminium	Stainless steel, Scrap moulding	35-40 % Al, 1 % ≥ Cu, 1% ≥ Si, 0.5 % ≥ Mn, 0.1 % ≥ C
FeB	Ferroboron	Strong and durable steel, Nd-Fe-B magnets	12-2 % B, 3 % ≥Si, 2% ≥Al, 1%≥C
FeCe	Ferrocerium	Clockwork toys, gas striker welding, "flint-and-steel",	8% Ce, 22% La, 4% Nd, 4% Pr, 4% Mg
FeCr	Ferrochromium	Stainless steel	10-18 % Cr
FeMo	Ferromolybdenum	Corrosion resistant, weldable and strong steel, munitions, …	60 % ≤ Mo, 1% ≥ Si, 1% ≥ Cu
FeNb	Ferroniobium	HSLA steel, land based and aircraft turbines blades	63-70 % Nb
FeNi	Ferronickel	Corrosion resistant, Stainless steel,	8.5-25 % Ni,
FeP	Ferrophosphorous		
FeSiMg	Ferrosilicon magnesium/nodulizer	Flexible steel	4-25 % Mg
FeTi	Ferrotitanium	Sheeted and stainless steel	10-75 % Ti, 5-6.5 % ≥ Al, 1-4 % ≥ Si
FeU	Ferrouranium		
FeV	Ferrovanadium	Corrosion resistant and strong steel, automobile	
FeW	Ferrotungsten	High-speed steel, super alloy, turbine blade, munitions, aicrafts, …	
SiMn	Silicomanganese		

3.4.3 Manganese for non-metallurgical uses

Non-metallurgical Mn is mostly used as a depolarizer in dry-cell batteries in the form of manganese dioxide. The function of manganese dioxide is to oxidize hydrogen and form water. The rate at which this occurs depends on the reactivity of dioxide. The alkaline MnO_2 zinc cell has a very low resistance and impedance, giving under certain conditions greater service life than the standard cell. Naturally occurring manganese dioxides (NMD) can be used in standard cells. Improved manganese dioxide grades required in high performance cells are obtained synthetically. The major producing countries of natural MnO_2 are Gabon, Ghana, Brazil, China, Mexico, and India (►Fig. 3.2; Eramet, 2019).

Potassium permanganate is one of the best-known manganese products in the chemical industry. It is a powerful oxidizing agent, which enables it to be used in purifying drinking water and treating waste water. It is also used for odor control, including deodorization of discharges from paint factories, fish-processing plants, etc. Permanganate has a variety of other applications as an oxidant (International Manganese Institute, 2014).

An important application for manganese is “Maneb” (manganese-ethylene bisdithiocarbamate), a yellow organo-chemical compound. It is known as an agricultural fungicide and is widely used for controlling crop and cereal diseases, downy mildew in vines, scab in fruit trees, banana and peanut diseases among others. An organic manganese compound known as MMT (methylcyclo-pentadienyl manganese tricarbonyl) is used on a small scale as an octane booster or anti-knock agent in gasoline. MMT can drastically improve oil combustion, reducing boiler clogging and soot levels. This application is interesting from an environmental point of view as it allows lead to be replaced, but it has not been fully developed yet (Eramet, 2019).

Another material is manganese ferrite, a soft ferrite widely used in electronics. Large amounts are consumed in the manufacture of television circuit boards.

3.4.4 Manganese in the world market

The world market mainly comprises the production, the demand and the export of manganese. Because of its high demand in steel industries (more than 90% of the Mn production), manganese is processed into suitable metallic alloys with the exception of Japan where manganese ore is directly used. Three main alloys are produced depending on the use and the steelmaking process (►Table 3.5):

- **Silicomanganese alloys** (SiMn) provide a low-carbon grade (2%) with an additional content in Si (14-16%). Silicon and manganese improve the mechanical properties of steel thank to their strong deoxidizer capacity. SiMn alloy offers a cleaner steel with a silvery luster because it is more easily separated when melted (Eramet, 2019). The low carbon content is responsible for more ductile steel. Silicomanganese was the first manganese alloy used and it is responsible for the major part of the production.
- **The ferromanganese alloys** (FeMn) are subdivided in two main alloys: high carbon ferromanganese (HC FeMn) and medium/low carbon ferromanganese alloys (MC/LC FeMn or Ref FeMn). They only represent half of the production of silicomanganese. The combination of Fe and Mn

provides a lower melting point than pure manganese, good antioxidant proprieties, and an excellent chemical composition, and it decreases the energetic consumption (International Manganese Institute, 2014; Eramet, 2019).

- HC FeMn alloys are lumpy materials covered by a dark layer of oxides. HC FeMn alloys improve the hardenability of steels thanks to their high manganese and carbon contents (>76%). They provide different effects on the properties and the structure of steel depending on the manganese content. Manganese also reacts with sulfur remains and prevents hot shortness. They are mainly used as steel tools, alloy steel, heat-resistant steel and abrasion resistant steel.
- Refined FeMn alloys (MC/LC FeMn or Ref FeMn) are lumpy silvery luster materials. The properties are quite similar to those of HC FeMn alloys but the increased Mn content (up to 83%) decreases the carbon demand, giving a higher manganese yield compared to electrolytic manganese (EMM). The uses of Ref FeMn alloys comprise the steel industry, metallurgy, thermic process industry and chemical industry.

- **Electrolytic manganese metal** (EMM) is a derived product of high silicon SiMn, which gives a pure powder of manganese (up to 98% Mn) with very low carbon content. However the production cost is higher. EMM is mainly used for stainless steel, aluminum and Li-batteries. The production is dominated by China (>95%).

Among some 300 minerals containing manganese, only a dozen are of mining significance (►Table 3.2): various Mn oxides representing 39.8% of Mn deposits; carbonates, which are dominated by rhodochrosite (and a small amount of kutnohorite and Mn-calcite), representing 35.8%; and braunite, which is the only Mn-silicate from which Mn could be processed, and representing 24.3% of Mn production. The world production of manganese ore reached close to 15,700,000 mt in 2016, and was estimated to be 18,600,000 mt in 2017 (U.S. Geological Survey, 2018). South Africa accounted for 34% of the world production in 2016 due to the intense extracting activities of the Neoproterozoic Mn deposits in the Postmasburg and the Kalahari deposits (►Figs. 3.2 and 3.14). China has slowed down its domestic production during the past years. China was the uncontested leader until 2011 (International Manganese Institute, 2016), representing 15% in 2016 (compared to 22% in 2011). Manganese ore deposits are widely distributed in China, but there are no high-grade ores left, nor important reserves, and mines are generally located far from industries. As a result, China imports high-grade ores to blend with domestic production. However, alloy production in China is by far the largest in the world market,

accounting for almost 58% of global output. Other significant and historical deposits are situated in Australia (14% in 2016), Gabon (10% in 2016) and Brazil (7% in 2016). Africa leads the world market with significant deposits located in South Africa, Gabon, and Ghana, accounting for 48% of the world production of Mn ores in 2016 (International Manganese Institute, 2016). The Imini district (Morocco) supplies the world market in high-grade ores due to the presence of massive pyrolusite (see chapter 7, Dekoninck *et al.*, 2016b). It is worth pointing that Europe produces only limited quantities of Mn ores, as only Bulgaria has economic Mn deposits. The same is observed in the United States of America, Japan and South Korea, which are important producers of steel, therefore depending on Mn imports to maintain their industry (International Manganese Institute, 2016). Manganese production has doubled in a decade (8,600,000 mt in 2003 and 18,600,00 mt in 2013), and this trend may intensify in the coming years. It is assumed that manganese, among other metals, will play a potentially prominent role in the energy shift to a carbon-constrained future (Arrobas *et al.*, 2017).

►**Table 3.5** Composition of different manganese products (International Manganese Institute, 2016; Eramet, 2019) and their production in 2016 (International Manganese Institute, 2016).

Mn alloys	Si (%)	C (%)	Mn (%)	P, S, B, Ti, N (%)	Production (2013)
SiMn	14-28	1.5-3	50-74	0.24-0.36	12.0 million mt
HC FeMn	0.3-1.2	6-8	74-82	0.4	4.5 million mt
MC FeMn	0.35-1	1-3	80-85	0.22-0.32	1.8 million mt
LC FeMn	2-7	0.07-0.75	85-90	0.4	
EMM	0.01-1	0.006-0.2	93-99	0.05-0.15	1.4 million mt

Current estimates of world manganese reserves (including low-grade ores) reach several billion tons. But if only high-grade ores (defined as having more than 44% Mn content) are considered, then ore reserves amount to approximate 680 million tonnes, essentially located in the southern hemisphere, with Australia, Brazil, Gabon and South Africa supplying over 90% of the international market (►Fig. 3.2; International Manganese Institute, 2016). There are also large manganese reserves on deep ocean floors in the form of polymetallic nodules (Mn-Ni-Cu-Co). These nodules contain on average 25% of Mn (main constituent), and lie in thin layers at a depth of approximately 5,000 meters. Quantitative estimates vary considerably, as the recovery is difficult and very expensive (i.e., Wang and Müller, 2009).

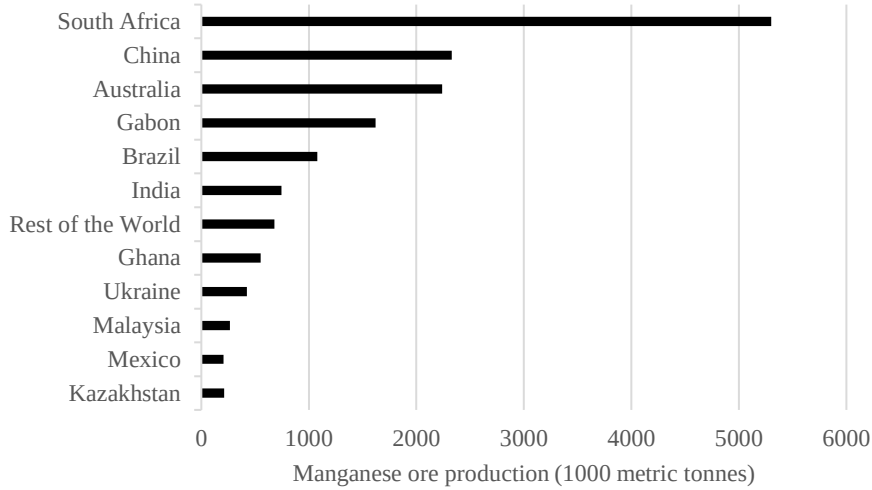

►**Fig. 3.14** Top 10 of Mn producing countries in 2016 based on U.S. Geological Survey (2018) data. World production was 15,658,000 metric tonnes in 2016.

3.5 References

Aller, R.C., Rude, P.D., 1988. Complete oxidation of solid phase sulfides by manganese and bacteria in anoxic marine sediments. Geochim. Cosmochim. Acta 52, 751–765. https://doi.org/10.1016/0016-7037(88)90335-3

Arrobas, D.L.P., Hund, K.L., Mccormick, M.S., Ningthoujam, J., Drexhage, J.R., 2017. The growing role of minerals and metals for a low carbon future (Working paper). World Bank Group, Washigton DC.

Bárdossy, G., Aleva, G.J.J., 1990. Lateritic bauxites, Developments in economic geology. Elsevier ; Distribution for the U.S.A. and Canada, Elsevier Science Pub. Co, Amsterdam ; New York : New York, N.Y., U.S.A.

Bargar, J.R., Webb, S.M., Tebo, B.M., 2005. EXAFS, XANES and In-Situ SRXRD Characterization of biogenic manganese oxides produced in sea water. Phys. Scr. 888. https://doi.org/10.1238/Physica.Topical.115a00888

Baudracco-Gritti, C., 1985. Substitution du manganèse bivalent par du calcium dans les minéraux du groupe: braunite, neltnerite, braunite II. Bull. Minéralogie 108, 437–445.

Baudracco-Gritti, C., Caye, R., Permingeat, F., Protas, J., 1982. La neltnerite $CaMn_6SiO_{12}$, une nouvelle espèce minérale du groupe de la braunite. Bull. Minéralogie 105, 161–165.

Baur, W.H., 1976. Rutile-type compounds. V. Refinement of MnO_2 and MgF_2. Acta Crystallogr. B 32, 2200–2204. https://doi.org/10.1107/S0567740876007371

Beauvais, A., Bonnet, N.J., Chardon, D., Arnaud, N., Jayananda, M., 2016. Very long-term stability of passive margin escarpment constrained by $^{40}Ar/^{39}Ar$ dating of K-Mn oxides. Geology 44, 299–302. https://doi.org/10.1130/G37303.1

Beauvais, A., Ruffet, G., Hénocque, O., Colin, F., 2008. Chemical and physical erosion rhythms of the West African Cenozoic morphogenesis: The ^{39} Ar-^{40}Ar dating of supergene K-Mn oxides. J. Geophys. Res. 113. https://doi.org/10.1029/2008JF000996

Bender, M.L., Klinkhammer, G.P., Spencer, D.W., 1977. Manganese in seawater and the marine manganese balance. Deep Sea Res. 24, 799–812. https://doi.org/10.1016/0146-6291(77)90473-8

Beukes, N.J., 1987. Facies relations, depositional environments and diagenesis in a major early Proterozoic stromatolitic carbonate platform to basinal sequence, Campbellrand Subgroup, Transvaal Supergroup, Southern Africa. Sediment. Geol. 54, 1–46. https://doi.org/10.1016/0037-0738(87)90002-9

Beukes, N.J., Swindell, E.P.W., Wabo, H., 2016. Manganese Deposits of Africa. Episodes 39, 285. https://doi.org/10.18814/epiiugs/2016/v39i2/95779

Beyeler, H.U., 1976. Cationic Short-Range Order in the Hollandite $K_{1.54}Mg_{0.77}Ti_{7.23}O_{16}$: Evidence for the importance of Ion-Ion Interactions in Superionic Conductors. Phys. Rev. Lett. 37, 1557–1560. https://doi.org/10.1103/PhysRevLett.37.1557

Biagioni, C., Capalbo, C., Pasero, M., 2013. Nomenclature tunings in the hollandite supergroup. Eur. J. Mineral. 25, 85–90. https://doi.org/10.1127/0935-1221/2013/0025-2255

Boeglin, J.-L., Melfi, A.J., Nahon, D.B., Tardy, Y., 1980. Solutions solides caractérisant plusieurs générations de rhodochrosites dans les protores des districts de Conselheiro Lafaiete, au Bresil et de Ziemougoula en Côte-d'Ivoire. Comptes Rendus Académie Sci. Paris 291, 13–15.

Bonnet, N.J., Beauvais, A., Arnaud, N., Chardon, D., Jayananda, M., 2016. Cenozoic lateritic weathering and erosion history of Peninsular India from 40Ar/39Ar dating of supergene K–Mn oxides. Chem. Geol. 446, 33–53. https://doi.org/10.1016/j.chemgeo.2016.04.018

Bonnet, N.J., Beauvais, A., Arnaud, N., Chardon, D., Jayananda, M., 2014. First $^{40}Ar/^{39}Ar$ dating of intense Late Palaeogene lateritic weathering in Peninsular India. Earth Planet. Sci. Lett. 386, 126–137. https://doi.org/10.1016/j.epsl.2013.11.002

Bouladon, J., Weber, F., Veysset, C., Favre-Mercuret, R., 1965. Sur la situation geologique et la type métallogénique du gisement de manganèse de Moanda, près de Franceville (Republique Gabonaise). Bull. Serv. Carte Géologique Alsace Lorraine 18, 253–276.

Brand, J., Veizer, J., 1980. Chemical diagenesis of a multicomponent carbonate system: trace elements. SEPM J. Sediment. Res. Vol. 50. https://doi.org/10.1306/212F7BB7-2B24-11D7-8648000102C1865D

Bricker, O., 1965. Some stability relations in the system Mn-O2-H2O at 25° and one atmosphere total pressure. Am. Mineral. 50, 1296–1354.

Burns, R.G., Burns, V.M., 1979. Manganese oxides, in: Marine Minerals. Mineral Society of America, Washigton DC, pp. 1–46.

Burns, R.G., Burns, V.M., Easton, A.J., 1977. The mineralogy and crystal chemistry of deep-sea manganese nodules, a polymetallic resource of the twenty-first century [and discussion]. Philos. Trans. R. Soc. Math. Phys. Eng. Sci. 286, 283–301. https://doi.org/10.1098/rsta.1977.0118

Byström, A.M., Lund, E.W., Lund, L.K., Hakala, M., 1949. The crystal structure of ramsdellite, an orthorhombic modification of MnO_2. Acta Chem. Scand. 3, 163–173. https://doi.org/10.3891/acta.chem.scand.03-0163

Cai, J., Liu, J., Suib, S.L., 2002. Preparative parameters and framework dopant effects in the synthesis of layer-structure birnessite by air oxidation. Chem. Mater. 14, 2071–2077. https://doi.org/10.1021/cm010771h

Calvert, S.E., Pedersen, T.F., 1996. Sedimentary geochemistry of manganese; implications for the environment of formation of manganiferous black shales. Econ. Geol. 91, 36–47. https://doi.org/10.2113/gsecongeo.91.1.36

Cannon, W.F., Force, E.R., 1983. Potential for high-grade shallow-marine manganese deposits in North America, in: Cameron Volume on Unconventional Mineral Deposits. American Institute of Mining, Metallurgical and Petroleum Engineers, New York, NY, pp. 175–189.

Chetty, D., 2008. A geometallurgical evaluation of the ores of the northern Kalahari manganese deposit, South Africa (Unpublished Ph.D. thesis). University of Johannesburg, Johannesburg.

Chisonga, B.C., Gutzmer, J., Beukes, N.J., Huizenga, J.M., 2012. Nature and origin of the protolith succession to the Paleoproterozoic Serra do Navio manganese deposit, Amapa Province, Brazil. Ore Geol. Rev. 47, 59–76. https://doi.org/10.1016/j.oregeorev.2011.06.006

Choubert, G., Faure-Muret, A., 1973. The Precambrian iron and manganese deposits of the Anti-Atlas, in: Genesis of Precambrian Iron and Manganese Deposits. Presented at the Unesco Earth Sciences Symposium, Kiev, pp. 115–124.

Clement, B.G., Luther, G.W., Tebo, B.M., 2009. Rapid, oxygen-dependent microbial Mn(II) oxidation kinetics at sub-micromolar oxygen concentrations in the Black Sea suboxic zone. Geochim. Cosmochim. Acta 73, 1878–1889. https://doi.org/10.1016/j.gca.2008.12.023

Colin, F., Beauvais, A., Ruffet, G., Henocque, O., 2005. First $^{40}Ar/^{39}Ar$ geochronology of lateritic manganiferous pisolites: Implications for the Palaeogene history of a West African landscape. Earth Planet. Sci. Lett. 238, 172–188. https://doi.org/10.1016/j.epsl.2005.06.052

Crerar, D.A., Cormick, R.K., Barnes, H.L., 1980. Geochemistry of manganese: an overview. Geol. Geochem. Manganese 1, 63–77.

Crerar, D.A., Cormick, R.K., Barnes, H.L., 1972. Organic controls on the sedimentary geochemistry of manganese. Acta Mineral.-Petrogr. Szeged 20, 217–226.

Dammer, D., McDougall, I., Chivas, A.R., 1999. Timing of weathering-induced alteration of manganese deposits in Western Australia; evidence from K/Ar and $^{40}Ar/^{39}Ar$ dating. Econ. Geol. 94, 87–108. https://doi.org/10.2113/gsecongeo.94.1.87

Davies, S.H.R., Morgan, J.J., 1989. Manganese(II) oxidation kinetics on metal oxide surfaces. J. Colloid Interface Sci. 129, 63–77. https://doi.org/10.1016/0021-9797(89)90416-5

De Putter, T., Liégeois, J.-P., Dewaele, S., Cailteux, J., Boyce, A., Mees, F., 2018. Paleoproterozoic manganese and base metals deposits at Kisenge-Kamata (Katanga, D.R. Congo). Ore Geol. Rev. 96, 181–200. https://doi.org/10.1016/j.oregeorev.2018.04.015

De Putter, T., Ruffet, G., Yans, J., Mees, F., 2015. The age of supergene manganese deposits in Katanga and its implications for the Neogene evolution of the African Great Lakes Region. Ore Geol. Rev. 71, 350–362. https://doi.org/10.1016/j.oregeorev.2015.06.015

de Villiers, J.P.R., 1980. The crystal structure of braunite II and its relation to bixbyite and braunite. Am. Mineral. 65, 756–765.

de Villiers, J.P.R., 1975. The crystal structure of braunite with reference to its solid-solution behavior. Am. Mineral. 60, 1098–1104.

de Villiers, J.P.R., Buseck, P.R., 1989. Stacking variations and nonstoichiometry in the bixbyite-braunite polysomatic mineral group. Am. Mineral. 74, 1325–1336.

de Villiers, J.P.R., Herbstein, F.H., 1967. Distinction between two members of the braunite group. Am. Mineral. 52, 20–30.

Decrée, S., Ruffet, G., Putter, T.D., Baele, J.-M., Recourt, P., Jamoussi, F., Yans, J., 2010. Mn oxides as efficient traps for metal pollutants in a polyphase low-temperature Pliocene environment: A case study in the Tamra iron mine, Nefza mining district, Tunisia. J. Afr. Earth Sci. 57, 249–261. https://doi.org/10.1016/j.jafrearsci.2009.08.005

Dekoninck, A., Bernard, A., Barbarand, J., Saint-Bezar, B., Missenard, Y., Lepretre, R., Saddiqi, O., Yans, J., 2016a. Detailed mineralogy and petrology of manganese oxyhydroxide deposits of the Imini district (Morocco). Miner. Deposita 51, 13–23. https://doi.org/10.1007/s00126-015-0590-3

Dekoninck, A., Leprêtre, R., Saddiqi, O., Barbarand, J., Yans, J., 2016b. The high-grade Imini manganese district—karst-hosted deposits of mn oxides and oxyhydroxides, in: Bouabdellah, M., Slack, J.F. (Eds.), Mineral Deposits of North Africa. Springer International Publishing, Cham, pp. 575–594.

Dekoninck, A., Moussi, B., Vennemann, T., Jamoussi, F., Mattielli, N., Decrée, S., Chaftar, H.-R., Hatira, N., Yans, J., 2018. Mixed hydrothermal and meteoric fluids evidenced by unusual H- and O-isotope compositions of kaolinite-halloysite in the Fe(-Mn) Tamra deposit (Nefza district, NW Tunisia). Appl. Clay Sci. 163, 33–45. https://doi.org/10.1016/j.clay.2018.07.007

Demoulin, A., Barbier, F., Dekoninck, A., Verhaert, M., Ruffet, G., Dupuis, C., Yans, J., 2018. Erosion Surfaces in the Ardenne–Oesling and Their Associated Kaolinic Weathering Mantle, in: Demoulin, A. (Ed.), Landscapes and Landforms of Belgium and Luxembourg. Springer International Publishing, Cham, pp. 63–84. https://doi.org/10.1007/978-3-319-58239-9_5

Dick, G.J., Clement, B.G., Webb, S.M., Fodrie, F.J., Bargar, J.R., Tebo, B.M., 2009. Enzymatic microbial Mn(II) oxidation and Mn biooxide production in the Guaymas Basin deep-sea hydrothermal plume. Geochim. Cosmochim. Acta 73, 6517–6530. https://doi.org/10.1016/j.gca.2009.07.039

Dickens, G.R., Owen, R.M., 1993. Global change and manganese deposition at the Cenomanian-turonian boundary. Mar. Georesources Geotechnol. 11, 27–43. https://doi.org/10.1080/10641199309379904

Dill, H.G., Hansen, B., Keck, E., Weber, B., 2010. Cryptomelane: A tool to determine the age and the physical–chemical regime of a Plio-Pleistocene weathering zone in a granitic terrain (Hagendorf, SE Germany). Geomorphology 121, 370–377. https://doi.org/10.1016/j.geomorph.2010.05.004

Dixon, J.B., Weed, S.B., Mc Kenzie, R.M., 1989. Manganese oxides and hydroxides, in: Mineral in Soil Environments. Soil Science Society of America.

Elias, M., Donaldson, M.J., Giorgetta, N.E., 1981. Geology, mineralogy, and chemistry of lateritic nickel-cobalt deposits near Kalgoorlie, Western Australia. Econ. Geol. 76, 1775–1783. https://doi.org/10.2113/gsecongeo.76.6.1775

Eramet, 2019. Le manganèse [WWW Document]. Eramet. URL http://www.eramet.com/nos-activites/extraire-valoriser/le-manganese/notre-activite

Fan, D., Yang, P., 1999. Introduction to and classification of manganese deposits of China. Ore Geol. Rev. 15, 1–13. https://doi.org/10.1016/S0169-1368(99)00011-6

Feitknecht, W., Brunner, P., Oswaldw, H.R., 1962. Über den Einfluss der Feuchtigkeit auf die Oxydation von Manganhydroxid durch molekularen Sauerstoff. Z. Für Anorg. Allg. Chem. 316, 154–160. https://doi.org/10.1002/zaac.19623160307

Feitknecht, W., Marti, W., 1945. Über die Oxydation von Mangan(II)-hydroxyd mit molekularem Sauerstoff. Helv. Chim. Acta 28, 129–148. https://doi.org/10.1002/hlca.19450280113

Fermor, L.L., 1906. Manganese in India. Trans. Min. Geol. Metall. Inst. India 1, 76.
Fichte, R., 2000. Ferroalloys, in: Wiley-VCH Verlag GmbH & Co. KGaA (Ed.), Ullmann's Encyclopedia of Industrial Chemistry. Wiley-VCH Verlag GmbH & Co. KGaA, Weinheim, Germany.
Fischer, W.W., Knoll, A.H., 2006. An iron shuttle for deepwater silica in Late Archean and early Paleoproterozoic iron formation. Geol. Soc. Am. Bull. preprint, 1. https://doi.org/10.1130/B26328.1
Fleet, A.J., 1983. Hydrothermal and Hydrogenous Ferro-Manganese Deposits: Do They form a Continuum? The Rare Earth Element Evidence, in: Rona, P.A., Boström, K., Laubier, L., Smith, K.L. (Eds.), Hydrothermal Processes at Seafloor Spreading Centers. Springer US, Boston, MA, pp. 535–555. https://doi.org/10.1007/978-1-4899-0402-7_23
Fleischer, M., Richmond, W.E., 1943. The manganese oxide minerals, a preliminary report. Econ. Geol. 38, 269–286. https://doi.org/10.2113/gsecongeo.38.4.269
Fluck, P., Weil, R., 1976. Géologie des gîtes minéraux des Vosges et des régions limitrophes. Corrélation métallogénique Vosges - Forêt-Noire, Mémoires du B.R.G.M., Gîtes minéraux de la France. BRGM.
Fontaine, F.J., Wilcock, W.S.D., Butterfield, D.A., 2007. Physical controls on the salinity of mid-ocean ridge hydrothermal vent fluids. Earth Planet. Sci. Lett. 257, 132–145. https://doi.org/10.1016/j.epsl.2007.02.027
Force, E.R., Cannon, W.F., 1988. Depositional model for shallow-marine manganese deposits around black shale basins. Econ. Geol. 83, 93–117. https://doi.org/10.2113/gsecongeo.83.1.93
Force, E.R., Maynard, J.B., 1991. Manganese: Syngenetic deposits on the margins of anoxic basins, in: Sedimentary and Diagenetic Mineral Deposits: A Basin Analysis Approach to Exploration. Society of Economic Geologists, Littleton, Colorado, pp. 147–159.
Frenzel, G., 1980. The manganese ore minerals, in: Geology and Geochemistry of Manganese. General Problems. Akademia Kiaod, Budapest, pp. 25–158.
Fusswinkel, T., Wagner, T., Wenzel, T., Wälle, M., Lorenz, J., 2013. Evolution of unconformity-related MnFeAs vein mineralization, Sailauf (Germany): Insight from major and trace elements in oxide and carbonate minerals. Ore Geol. Rev. 50, 28–51. https://doi.org/10.1016/j.oregeorev.2012.08.001
Giovanoli, R., 1980. Vernadite is random-stacked birnessite: A discussion of the paper by F. V. Chukhrov *et al.*: ? Contributions to the mineralogy of authigenic manganese phases from marine manganese deposits? [Mineralium Deposita 14, 249-261 (1979)]. Miner. Deposita 15. https://doi.org/10.1007/BF00206520
Glasby, G.P., 2006. Manganese: Predominant Role of Nodules and Crusts, in: Schulz, H.D., Zabel, M. (Eds.), Marine Geochemistry. Springer-Verlag, Berlin/Heidelberg, pp. 371–427. https://doi.org/10.1007/3-540-32144-6_11
Glasby, G.P., Papavassiliou, C.T., Mitsis, J., Valsami-Jones, E., Liakopoulos, A., Renner, R.M., 2005. The Vani manganese deposit, Milos island, Greece: A fossil stratabound Mn−Ba−Pb−Zn−As−Sb−W-rich hydrothermal deposit, in: Developments in Volcanology. Elsevier, pp. 255–291. https://doi.org/10.1016/S1871-644X(05)80045-2
Grandin, G., Perseil, E.-A., 1983. Les minéralisations manganésifères volcano-sédimentaires du BIafo-Guéto (Côte d'Ivoire). Paragenesis-alteration climatique. Miner. Deposita 18, 99–111.
Grandin, G., Perseil, E.-A., 1977. Le gisement de manganèse de Mokta (Côte d'Ivoire). Transformations minéralogiques des minerais par action météorique. Bull. Société Géologique Fr. 19, 309–317.
Guérin, H., 1979. Distribution du manganèse dans les séries volcaniques: un guide de la genèse des gisements manganésifères volcanogènes. Phys. Chem. Earth 11, 717–725. https://doi.org/10.1016/0079-1946(79)90067-3
Gutzmer, J., Beukes, N.J., 1997. Mineralogy and mineral chemistry of oxide-facies manganese ores of the Postmasburg Manganese Field, South Africa. Mineral. Mag. 61, 213–231. https://doi.org/10.1180/minmag.1997.061.405.05
Gutzmer, J., Beukes, N.J., 1996. Karst-hosted fresh-water Paleoproterozoic manganese deposits, Postmasburg, South Africa. Econ. Geol. 91, 1435–1454. https://doi.org/10.2113/gsecongeo.91.8.1435
Haskin, L.A., Wildeman, T.R., Haskin, M.A., 1968. An accurate procedure for the determination of the rare earths by neutron activation. J. Radioanal. Chem. 1, 337–348. https://doi.org/10.1007/BF02513689
Hautmann, S., Lippolt, H.J., 2000. $^{40}Ar/^{39}Ar$ dating of central European K–Mn oxides — a chronological framework of supergene alteration processes during the Neogene. Chem. Geol. 170, 37–80. https://doi.org/10.1016/S0009-2541(99)00241-7
Hein, J.R., Koschinsky, A., Bau, M., Manheim, F.T., Kang, J.-K., Roberts, L., 2000. Cobalt-rich ferromanganese crusts in the Pacific, in: Handbook of Marine Minerals Deposits. CRC Press LLC, Boca Raton, pp. 239–279.

Hein, J.R., Koschinsky, A., Halbach, P., Manheim, F.T., Bau, M., Kang, J.-K., Lubick, N., 1997. Iron and manganese oxide mineralization in the Pacific. Geol. Soc. Lond. Spec. Publ. 119, 123–138. https://doi.org/10.1144/GSL.SP.1997.119.01.09

Hem, J.D., 1989. Study and interpretation of the chemical characteristics of natural water, Geological Survey Water-Supply Paper. U.S. Geological Survey, Alexandria.

Hem, J.D., 1963. Chemical equilibria and rates of manganese oxidation: chemistry of manganese in natural water. Geol. Surv. Water-Supply Pap. 71.

Hénocque, O., Ruffet, G., Colin, F., Féraud, G., 1998. $^{40}Ar/^{39}Ar$ dating of West African lateritic cryptomelanes. Geochim. Cosmochim. Acta 62, 2739–2756. https://doi.org/10.1016/S0016-7037(98)00185-9

Hewett, D.F., 1964. Veins of hypogene manganese oxide minerals in the southwestern United States. Econ. Geol. 59, 1429–1472. https://doi.org/10.2113/gsecongeo.59.8.1429

Hypolito, R., Valarelli, J.V., Giovanoli, R., Netto, S.M., 1984. Gibbs free energy of formation of synthetic cryptomelane. Chimia 38, 98–99.

Ilton, E.S., Post, J.E., Heaney, P.J., Ling, F.T., Kerisit, S.N., 2016. XPS determination of Mn oxidation states in Mn (hydr)oxides. Appl. Surf. Sci. 366, 475–485. https://doi.org/10.1016/j.apsusc.2015.12.159

International Manganese Institute, 2016. Public Annual Market Research Report.

International Manganese Institute, 2014. About Manganese [WWW Document]. Int. Manganese Inst. URL http://www.manganese.org/

Johnson, E.A., Post, J.E., 2006. Water in the interlayer region of birnessite: Importance in cation exchange and structural stability. Am. Mineral. 91, 609–618. https://doi.org/10.2138/am.2006.2090

Johnson, J.E., Webb, S.M., Ma, C., Fischer, W.W., 2016. Manganese mineralogy and diagenesis in the sedimentary rock record. Geochim. Cosmochim. Acta 173, 210–231. https://doi.org/10.1016/j.gca.2015.10.027

Jørgensen, B.B., 2006. Bacteria and marine biogeochemistry, in: Schulz, H.D., Zabel, M. (Eds.), Marine Geochemistry. Springer-Verlag, Berlin/Heidelberg, pp. 169–206. https://doi.org/10.1007/3-540-32144-6_5

Komiya, T., Hirata, T., Kitajima, K., Yamamoto, S., Shibuya, T., Sawaki, Y., Ishikawa, T., Shu, D., Li, Y., Han, J., 2008. Evolution of the composition of seawater through geologic time, and its influence on the evolution of life. Gondwana Res. 14, 159–174. https://doi.org/10.1016/j.gr.2007.10.006

Kuleshov, V., 2016. Isotope geochemistry: the origin and formation of manganese rocks and ores. Elsevier, Amsterdam Boston Heidelberg London New York Oxford Paris San Diego San Francisco Singapore Sydney Tokyo.

Kuleshov, V.N., 2011. Manganese deposits: Communication 1. Genetic models of manganese ore formation. Lithol. Miner. Resour. 46, 473–493. https://doi.org/10.1134/S0024490211050038

Kulik, D.A., Kersten, M., Heiser, U., Neumann, T., 2000. Application of Gibbs energy minimization to model early-diagenetic solid-solution aqueous-solution equilibria involving authigenic rhodochrosites in anoxic Baltic Sea sediments. Aquat. Geochem. 6, 147–199. https://doi.org/10.1023/A:1009694703207

Laznicka, P., 2014. Giant metallic deposits—A century of progress. Ore Geol. Rev. 62, 259–314. https://doi.org/10.1016/j.oregeorev.2014.03.002

Laznicka, P., 1992. Manganese deposits in the global lithogenetic system: Quantitative approach. Ore Geol. Rev. 7, 279–356. https://doi.org/10.1016/0169-1368(92)90013-B

Leal, P.R., Correa, M.J., Ametrano, S.J., Etcheverry, R.O., de Brodtkorb, M.K., 2008. The manganese deposits of the Pampean Ranges, Argentina. Can. Mineral. 46, 1215–1233. https://doi.org/10.3749/canmin.46.5.1215

Leclerc, J., Weber, F., 1980. Geology and genesis ofthe Moanda manganese deposits, Republic of Gabon, in: Geology and Geochemistry of Manganese. Vol. II. Manganese Deposits on Continents. Publishing House of Hungarian Academy of Sciences, Budapest, pp. 89–109.

Leinekugel-le-Cocq-Errien, A.Y., Deniard, P., Jobic, S., Gautier, E., Evain, M., Aubin, V., Bart, F., 2007. Structural characterization of the hollandite host lattice for the confinement of radioactive cesium: Quantification of the amorphous phase taking into account the incommensurate modulated character of the crystallized part. J. Solid State Chem. 180, 322–330. https://doi.org/10.1016/j.jssc.2006.10.013

Lepland, A., Stevens, R.L., 1998. Manganese authigenesis in the Landsort Deep, Baltic Sea. Mar. Geol. 151, 1–25. https://doi.org/10.1016/S0025-3227(98)00046-2

Leprêtre, R., Missenard, Y., Saint-Bezar, B., Barbarand, J., Delpech, G., Yans, J., Dekoninck, A., Saddiqi, O., 2015. The three main steps of the Marrakech High Atlas building in Morocco: Structural evidences from the southern foreland, Imini area. J. Afr. Earth Sci. 109, 177–194. https://doi.org/10.1016/j.jafrearsci.2015.05.013

Li, J.-W., Vasconcelos, P., Duzgoren-Aydin, N., Yan, D.-R., Zhang, W., Deng, X.-D., Zhao, X.-F., Zeng, Z.-P., Hu, M.-A., 2007. Neogene weathering and supergene manganese enrichment in subtropical South China: An 40Ar/39Ar approach and paleoclimatic significance. Earth Planet. Sci. Lett. 256, 389–402. https://doi.org/10.1016/j.epsl.2007.01.021

Li, Y.-H., 2000. A compendium of geochemistry: from solar nebula to the human brain. Princeton University Press, Princeton, N.J.

Lindgren, W., Hillebrand, W.F., 1904. Minerals from the Clifton-Morenci District, Arizona. Am. J. Sci. s4-18, 448–460. https://doi.org/10.2475/ajs.s4-18.108.448

Ling, F.T., Post, J.E., Heaney, P.J., Kubicki, J.D., Santelli, C.M., 2017. Fourier-transform infrared spectroscopy (FTIR) analysis of triclinic and hexagonal birnessites. Spectrochim. Acta. A. Mol. Biomol. Spectrosc. 178, 32–46. https://doi.org/10.1016/j.saa.2017.01.032

Lippolt, H.J., Hautmann, S., 1995. $^{40}Ar/^{39}Ar$ ages of Precambrian manganese ore minerals from Sweden, India and Morocco. Miner. Deposita 30, 246–256. https://doi.org/10.1007/BF00196360

Liu, H., Xue, Y., 1999. Sedimentology of Triassic Dounan-type manganese deposits, western margin, Yangtze Platform, China. Ore Geol. Rev. 15, 165–176. https://doi.org/10.1016/S0169-1368(99)00020-7

Manceau, A., Gorshkov, A.I., Drits, V.A., 1992. Structural chemistry of Mn, Fe, Co, and Ni in manganese hydrous oxides: Part II. Information from EXAFS spectroscopy and electron and X-ray diffraction. Am. Mineral. 77, 1144–1157.

Manceau, A., Lanson, M., Takahashi, Y., 2014. Mineralogy and crystal chemistry of Mn, Fe, Co, Ni, and Cu in a deep-sea Pacific polymetallic nodule. Am. Mineral. 99, 2068–2083. https://doi.org/10.2138/am-2014-4742

Manceau, A., Llorca, S., Calas, G., 1987. Crystal chemistry of cobalt and nickel in lithiophorite and asbolane from New Caledonia. Geochim. Cosmochim. Acta 51, 105–113. https://doi.org/10.1016/0016-7037(87)90011-1

Mandernack, K.W., Fogel, M.L., Tebo, B.M., Usui, A., 1995a. Oxygen isotope analyses of chemically and microbially produced manganese oxides and manganates. Geochim. Cosmochim. Acta 59, 4409–4425. https://doi.org/10.1016/0016-7037(95)00299-F

Mandernack, K.W., Post, J., Tebo, B.M., 1995b. Manganese mineral formation by bacterial spores of the marine Bacillus, strain SG-1: Evidence for the direct oxidation of Mn(II) to Mn(IV). Geochim. Cosmochim. Acta 59, 4393–4408. https://doi.org/10.1016/0016-7037(95)00298-E

Mandernack, K.W., Tebo, B.M., 1993. Manganese scavenging and oxidation at hydrothermal vents and in vent plumes. Geochim. Cosmochim. Acta 57, 3907–3923. https://doi.org/10.1016/0016-7037(93)90343-U

Mason, B., 1944. Crystal structure refinement of lithiophorite. Am. Mineral. 29, 66–69.

Maynard, J.B., 2014. Manganiferous sediments, rocks, and ores, in: Treatise on Geochemistry. Elsevier, pp. 327–349.

Maynard, J.B., 2010. The chemistry of manganese ores through time: a signal of increasing diversity of earth-surface environments. Econ. Geol. 105, 535–552. https://doi.org/10.2113/gsecongeo.105.3.535

McKeown, D.A., Post, J.E., 2001. Characterization of manganese oxide mineralogy in rock varnish and dendrites using X-ray absorption spectroscopy. Am. Mineral. 86, 701–713. https://doi.org/10.2138/am-2001-5-611

Meisser, N., Perseil, E.-A., Brugger, J., Chiappero, P.-J., 1999. Strontiomelane, $SrMn^{4+}{}_6Mn^{3+}$, a new mineral of the cryptomelane group from St. Marcel-Praborna, Aosta Valley, Italy. Can. Mineral. 37, 673–678.

Moore, P.B., Araki, T., 1976. Braunite: its structure and relationship to bixbyite, and some insights on the genealogy of fluorite derivative structures. Am. Mineral. 61, 1226–1240.

Morgan, J.J., 2005. Kinetics of reaction between O2 and Mn(II) species in aqueous solutions. Geochim. Cosmochim. Acta 69, 35–48. https://doi.org/10.1016/j.gca.2004.06.013

Mucci, A., 2004. The behavior of mixed Ca–Mn carbonates in water and seawater: controls of manganese concentrations in marine porewaters. Aquat. Geochem. 10, 139–169. https://doi.org/10.1023/B:AQUA.0000038958.56221.b4

Murton, B.J., Redbourn, L.J., German, C.R., Baker, E.T., 1999. Sources and fluxes of hydrothermal heat, chemicals and biology within a segment of the Mid-Atlantic Ridge. Earth Planet. Sci. Lett. 171, 301–317. https://doi.org/10.1016/S0012-821X(99)00157-0

Nahon, D., Beauvais, A., Boeglin, J.-L., Ducloux, J., Nziengui-Mapangou, P., 1983. Manganite formation in the first stage of the lateritic manganese ores in Africa. Chem. Geol. 40, 25–42. https://doi.org/10.1016/0009-2541(83)90089-X

Nahon, D., Colin, F., Tardy, Y., 1982. Formation and distribution of Mg,Fe,Mn-smectites in the first stages of the lateritic weathering of forsterite and tephroite. Clay Miner. 17, 339–348.

Nahon, D., Parc, S., 1990. Lateritic concentrations of manganese oxyhydroxides and oxides. Geol. Rundsch. 79, 319–326. https://doi.org/10.1007/BF01830628

Nahon, D.B., Boulangé, B., Colin, F., 1992. Metallogeny of weathering: an introduction, in: Developments in Earth Surface Processes. Elsevier, pp. 445–471. https://doi.org/10.1016/B978-0-444-89198-3.50022-2

Nambu, M., Tanida, K., 1967. Manjiroite, a new manganese dioxide mineral, from Kohare Mine, Iwate Prefecture, Japan. J. Jpn. Assoc. Mineral. Petrol. Econ. Geol. 58, 39–54. https://doi.org/10.2465/ganko1941.58.39

Nicholson, K., 1992. Genetic types of manganese oxide deposits in Scotland; indicators of paleo-ocean-spreading rate and a Devonian geochemical mobility boundary. Econ. Geol. 87, 1301–1309. https://doi.org/10.2113/gsecongeo.87.5.1301

Nyame, F.K., Beukes, N.J., 2006. The genetic significance of carbon and oxygen isotopic variations in Mn-bearing carbonates from the Palaeo-Proterozoic (~2.2GA) Nsuta deposit in the Birimian of Ghana. Carbonates Evaporites 21, 21–32. https://doi.org/10.1007/BF03175465

Okita, P.M., Maynard, J.B., Spiker, E.C., Force, E.R., 1988. Isotopic evidence for organic matter oxidation by manganese reduction in the formation of stratiform manganese carbonate ore. Geochim. Cosmochim. Acta 52, 2679–2685. https://doi.org/10.1016/0016-7037(88)90036-1

Okita, P.M., Shanks, W.C., 1992. Origin of stratiform sediment-hosted manganese carbonate ore deposits: Examples from Molango, Mexico, and TaoJiang, China. Chem. Geol. 99, 139–163. https://doi.org/10.1016/0009-2541(92)90036-5

Ostwald, J., 1992. Genesis and paragenesis of the tetravalent manganese oxides of the Australian continent. Econ. Geol. 87, 1237–1252. https://doi.org/10.2113/gsecongeo.87.5.1237

Ostwald, J., 1986. Some observations on the chemical composition of todorokite. Mineral. Mag. 50, 336–340. https://doi.org/10.1180/minmag.1986.050.356.25

Ostwald, J., 1984a. Some observations on the genesis of nsutite. Neues Jahrb. Für Mineral. - Abh. H9, 385–392.

Ostwald, J., 1984b. Two varieties of lithiophorite in some Australian deposits. Mineral. Mag. 48, 383–388. https://doi.org/10.1180/minmag.1984.048.348.08

Paik, Y., Osegovic, J.P., Wang, F., Bowden, W., Grey, C.P., 2001. ^{2}H MAS NMR Studies of the Manganese Dioxide Tunnel Structures and Hydroxides Used as Cathode Materials in Primary Batteries. J. Am. Chem. Soc. 123, 9367–9377. https://doi.org/10.1021/ja015999k

Parc, S., Nahon, D., Tardy, Y., Vieillard, P., 1989. Estimated solubility products and fields of stability for cryptomelane, nsutite, birnessite, and lithiophorite based on natural lateritic weathering sequences. Am. Mineral. 74, 466–475.

Paterson, E., Clark, D.R., Russell, J.D., Swaffield, R., 1986. Cation exchange in synthetic manganates; II, The structure of an alkylammonium-saturated phyllomanganate. Clay Miner. 21, 957–964.

Perseil, E.-A., Grandin, G., 1985. Altération supergène des protores à grenats manganésifères dans quelques gisements d'Afrique de l'Ouest. Miner. Deposita 20, 211–219.

Perseil, E.-A., Grandin, G., 1978. Evolution minéralogique du manganèse dans trois gisements d'Afrique de l'Ouest: Mokta, Tambao, Nsuta. Miner. Deposita 13, 295–311.

Piacentini, T., Vasconcelos, P.M., Farley, K.A., 2013. ^{40}Ar/^{39}Ar constraints on the age and thermal history of the Urucum Neoproterozoic banded iron-formation, Brazil. Precambrian Res. 228, 48–62. https://doi.org/10.1016/j.precamres.2013.01.002

Polgári, M., Okita, P.M., Hein, J.R., 1991. Stable Isotope evidence for the origin of the Urkut Manganese ore deposit, Hungary. SEPM J. Sediment. Res. 61. https://doi.org/10.1306/D426771C-2B26-11D7-8648000102C1865D

Post, J.E., 1999. Manganese oxide minerals: crystal structures and economic and environmental significance. Proc. Natl. Acad. Sci. 96, 3447–3454. https://doi.org/10.1073/pnas.96.7.3447

Post, J.E., Appleman, D.E., 1994. Crystal structure refinement of lithiophorite. Am. Mineral. 79, 370–374.

Post, J.E., Bish, D.L., 1989. Rietveld refinement of the coronadite structure. Am. Mineral. 74, 913–917.

Post, J.E., Bish, D.L., 1988. Rietveld refinement of the todorokite structure. Am. Mineral. 73, 861–869.

Post, J.E., Veblen, D.R., 1990. Crystal structure determinations of synthetic sodium, magnesium, and potassium birnessite using TEM and the Rietveld method. Am. Mineral. 75, 477–489.

Post, J.E., Von Dreele, R.B., Buseck, P.R., 1982. Symmetry and cation displacements in hollandites: structure refinements of hollandite, cryptomelane and priderite. Acta Crystallogr. B 38, 1056–1065. https://doi.org/10.1107/S0567740882004968

Pratt, L.M., Force, E.R., Pomerol, B., 1991. Coupled manganese and carbon-isotopic events in marine carbonates at the Cenomanian-Turonian boundary. SEPM J. Sediment. Res. Vol. 61. https://doi.org/10.1306/D4267717-2B26-11D7-8648000102C1865D

Reid, A.F., Ringwood, A.E., 1969. Six-coordinate silicon: High pressure strontium and barium aluminosilicates with the hollandite structure. J. Solid State Chem. 1, 6–9. https://doi.org/10.1016/0022-4596(69)90002-4

Richmond, W.E., Fleischer, M., 1942. Cryptomelane, a new name for the commonest of the '"psilomelane"' minerals. Am. Mineral. 27, 607–610.

Riffel, S.B., Vasconcelos, P.M., Carmo, I.O., Farley, K.A., 2015. Combined $^{40}Ar/^{39}Ar$ and (U–Th)/He geochronological constraints on long-term landscape evolution of the Second Paraná Plateau and its ruiniform surface features, Paraná, Brazil. Geomorphology 233, 52–63. https://doi.org/10.1016/j.geomorph.2014.10.041

Robie, R.A., Huebner, J.S., Hemingway, B.S., 1995. Heat capacities and thermodynamic properties of braunite (Mn7SiO12) and rhodonite (MnSiO3). Am. Mineral. 80, 560–575. https://doi.org/10.2138/am-1995-5-615

Rona, P.A., Boström, K., Laubier, L., Smith, K.L. (Eds.), 1983. Hydrothermal Processes at Seafloor Spreading Centers. Springer US, Boston, MA. https://doi.org/10.1007/978-1-4899-0402-7

Roy, S., 2006. Sedimentary manganese metallogenesis in response to the evolution of the Earth system. Earth-Sci. Rev. 77, 273–305. https://doi.org/10.1016/j.earscirev.2006.03.004

Roy, S., 1997. Genetic diversity of manganese deposition in the terrestrial geological record, in: Geological Society, London, Special Publications. pp. 5–27.

Roy, S., 1981. Manganese deposits. Academic Press, London ; New York.

Roy, S., 1976. Ancient manganese deposits, in: Handbook of Stratiform and Strata-Bound Ore Deposits. Elsevier, Amsterdam, pp. 395–476.

Roy, S., 1968. Mineralogy of the different genetic types of manganese deposits. Econ. Geol. 63, 760–786. https://doi.org/10.2113/gsecongeo.63.7.760

Ruddiman, W.F., Raymo, M.E., Prell, W.L., Kutzbach, J.E., 1997. The uplift-climate connection: A synthesis, in: Ruddiman, W.F. (Ed.), Tectonic Uplift and Climate Change. Springer US, Boston, MA, pp. 471–515.

Ruffet, G., Innocent, C., Michard, A., Féraud, G., Beauvais, A., Nahon, D., Hamelin, B., 1996. A geochronological and study of K-Mn oxides from the weathering sequence of Azul, Brazil. Geochim. Cosmochim. Acta 60, 2219–2232. https://doi.org/10.1016/0016-7037(96)00080-4

Scheele, C.W., 1777. Chemische abhandlung von der luft und dem feuer, 1st ed. Salzwasser-Verlag, Liepzig.

Schippers, A., Jørgensen, B.B., 2001. Oxidation of pyrite and iron sulfide by manganese dioxide in marine sediments. Geochim. Cosmochim. Acta 65, 915–922. https://doi.org/10.1016/S0016-7037(00)00589-5

Segev, A., Lang, B., Halicz, L., 1991. K-Ar dating of manganese minerals from the Eisenbach region, Black Forest, southwest Germany. Schweiz. Mineral. Petrogr. Mitteilungen 71, 101–114. https://doi.org/10.5169/seals-54349

Seyfried, W.E., Ding, K., 2013. Phase equilibria in subseafloor hydrothermal systems: a review of the role of redox, temperature, pH and dissolved Cl on the chemistry of hot spring fluids at mid-ocean ridges, in: Humphris, S.E., Zierenberg, R.A., Mullineaux, L.S., Thomson, R.E. (Eds.), Geophysical Monograph Series. American Geophysical Union, Washington, D. C., pp. 248–272. https://doi.org/10.1029/GM091p0248

Shen, Y.F., Zerger, R.P., DeGuzman, R.N., Suib, S.L., McCurdy, L., Potter, D.I., O'Young, C.L., 1993. Manganese Oxide Octahedral Molecular Sieves: Preparation, Characterization, and Applications. Science 260, 511–515. https://doi.org/10.1126/science.260.5107.511

Sternbeck, J., Sohlenius, G., 1997. Authigenic sulfide and carbonate mineral formation in Holocene sediments of the Baltic Sea. Chem. Geol. 135, 55–73. https://doi.org/10.1016/S0009-2541(96)00104-0

Stone, A.T., 1987. Reductive dissolution of manganese(III/IV) oxides by substituted phenols. Environ. Sci. Technol. 21, 979–988. https://doi.org/10.1021/es50001a011

Stone, A.T., Morgan, J.J., 1984a. Reduction and dissolution of manganese(III) and manganese(IV) oxides by organics: 2. Survey of the reactivity of organics. Environ. Sci. Technol. 18, 617–624. https://doi.org/10.1021/es00126a010

Stone, A.T., Morgan, J.J., 1984b. Reduction and dissolution of manganese(III) and manganese(IV) oxides by organics. 1. Reaction with hydroquinone. Environ. Sci. Technol. 18, 450–456. https://doi.org/10.1021/es00124a011

Sundby, B., Silverberg, N., Chesselet, R., 1981. Pathways of manganese in an open estuarine system. Geochim. Cosmochim. Acta 45, 293–307. https://doi.org/10.1016/0016-7037(81)90240-4

Tang, S., Liu, T., 1999. Origin of the early Sinian Minle manganese deposit, Hunan Province, China. Ore Geol. Rev. 15, 71–78. https://doi.org/10.1016/S0169-1368(99)00015-3

Tebo, B.M., Bargar, J.R., Clement, B.G., Dick, G.J., Murray, K.J., Parker, D., Verity, R., Webb, S.M., 2004. Biogenic manganese oxides: properties and mechanisms of formation. Annu. Rev. Earth Planet. Sci. 32, 287–328. https://doi.org/10.1146/annurev.earth.32.101802.120213

Tebo, B.M., Johnson, H.A., McCarthy, J.K., Templeton, A.S., 2005. Geomicrobiology of manganese(II) oxidation. Trends Microbiol. 13, 421–428. https://doi.org/10.1016/j.tim.2005.07.009

Trappe, J. (Ed.), 1998. Phanerozoic Phosphorite Depositional Systems, Lecture Notes in Earth Sciences. Springer-Verlag, Berlin/Heidelberg. https://doi.org/10.1007/BFb0009670

Tsikos, H., Beukes, N.J., Moore, P.B., Harris, C., 2003. Deposition, diagenesis, and secondary enrichment of metals in the paleoproterozoic hotazel iron formation, Kalahari Manganese Field, South Africa. Econ. Geol. 98, 1449–1462. https://doi.org/10.2113/98.7.1449

Turner, S., Buseck, P.R., 1983. Defects in nsutite (γ-MnO_2) and dry-cell battery efficiency. Nature 304, 143–146. https://doi.org/10.1038/304143a0

Turner, S., Buseck, P.R., 1981. Todorokites: A new family of naturally occurring manganese oxides. Science 212, 1024–1027. https://doi.org/10.1126/science.212.4498.1024

Turner, S., Buseck, P.R., 1979. Manganese oxide tunnel structures and their intergrowths. Science 203, 456–458. https://doi.org/10.1126/science.203.4379.456

U.S. Geological Survey, 2018. Mineral Commodity Summaries. US Government. Printing Office, Washigton DC.

Van Deventer, J.S.J., 1987. The effect of gangue components on the reduction of manganosite by graphite: an isothermal kinetic study. Thermochim. Acta 112, 365–377. https://doi.org/10.1016/0040-6031(87)88293-X

Varentsov, I.M., 1996. Manganese ores of supergene zone: Geochemistry of formation, Solid Earth Sciences Library. Springer Netherlands, Dordrecht.

Varentsov, I.M., Grasselly, G.Y. (Eds.), 1980. Geology and geochemistry of manganese: general problems: mineralogy, geochemistry, methods, Geology and geochemistry of manganese. Schweizerbart, Stuttgart.

Vasconcelos, P.M., 1999. K-Ar and $^{40}Ar/^{39}Ar$ geochronology of weathering processes. Annu. Rev. Earth Planet. Sci. 27, 183–229. https://doi.org/10.1146/annurev.earth.27.1.183

Vasconcelos, P.M., Becker, T.A., Renne, P.R., Brimhall, G.H., 1992. Age and duration of weathering by ^{40}K-^{40}Ar and $^{40}Ar/^{39}Ar$ analysis of potassium-manganese oxides. Science 258, 451–455. https://doi.org/10.1126/science.258.5081.451

Vasconcelos, P.M., Carmo, I. de O., 2018. Calibrating denudation chronology through $^{40}Ar/^{39}Ar$ weathering geochronology. Earth-Sci. Rev. 179, 411–435. https://doi.org/10.1016/j.earscirev.2018.01.003

Vasconcelos, P.M., Heim, J.A., Farley, K.A., Monteiro, H., Waltenberg, K., 2013. $^{40}Ar/^{39}Ar$ and (U–Th)/He – $^{4}He/^{3}He$ geochronology of landscape evolution and channel iron deposit genesis at Lynn Peak, Western Australia. Geochim. Cosmochim. Acta 117, 283–312. https://doi.org/10.1016/j.gca.2013.03.037

Vasconcelos, P.M., Knesel, K.M., Cohen, B.E., Heim, J.A., 2008. Geochronology of the Australian Cenozoic: a history of tectonic and igneous activity, weathering, erosion, and sedimentation. Aust. J. Earth Sci. 55, 865–914. https://doi.org/10.1080/08120090802120120

Veizer, J., 1978. Secular variations in the composition of sedimentary carbonate rocks, II. Fe, Mn, Ca, Mg, Si and minor constituents. Precambrian Res. 6, 381–413. https://doi.org/10.1016/0301-9268(78)90024-4

Verhaert, M., Bernard, A., Saddiqi, O., Dekoninck, A., Essalhi, M., Yans, J., 2018. Mineralogy and genesis of the polymetallic and polyphased low grade Fe-Mn-Cu Ore of Jbel Rhals deposit (Eastern High Atlas, Morocco). Minerals 8, 39. https://doi.org/10.3390/min8020039

von Plehwe-Leisen, E., Klemm, D.D., 1995. Geology and ore genesis of the manganese ore deposits of the Postmasburg manganese-field, South Africa. Miner. Deposita 30, 257–267. https://doi.org/10.1007/BF00196361

Wang, X., Müller, W.E.G., 2009. Marine biominerals: perspectives and challenges for polymetallic nodules and crusts. Trends Biotechnol. 27, 375–383. https://doi.org/10.1016/j.tibtech.2009.03.004

Weber, F., Leclerc, J., Millot, G., 1979. Epigénies manganésifères successives dans le gisement de Moanda (Gabon). Bull. Académie Sci. 32, 147–164.

Zwicker, W.K., Groeneveld-Meijer, W.O.J., Jaffe, H.W., 1962. Nsutite - a widespread manganese oxide mineral. Am. Mineral. 47, 618–623.

Chapter 4

Material and methods

Chapter 4

Material and methods

There is not a straightforward path to investigate rocks and minerals formed by supergene processes. Many analytical tools used in other scientific disciplines allow geological material to be fully characterized from their observation on the field to their preparation in laboratories, to their mineralogical determination and chemical composition. Such investigation necessarily implies a deep background knowledge dealing with mineralogy, geochemistry, petrography and geochronology. Therefore, this chapter presents all techniques used in this thesis to characterize the composition and features of Mn-rich weathered rocks and protores. A special care is taken to the identification of Mn oxides and more specifically to the presence of K-bearing Mn oxides and their feasibility to bring geochronological information through the K-Ar and derived $^{40}Ar/^{39}Ar$ dating methods. Other specific tools dealing with stable isotopes are also presented.

4.1 Sampling strategy

Establishing and executing a strategy for collecting samples in suitable and relevant sites, which can both meet the practical and scientific purposes, is of primary importance in Earth science studies. Such an approach is somewhat difficult to fulfill, considering that field bias (i.e., access to outcrops, galleries, mines, etc.) or the uncertain nature of the collected samples, are often unpredictable, forcing geologists to adapt their strategies constantly. Working as a team, especially with local authorities, mining companies and other institutions (Universities, research centers, etc.) is fundamental to the success of a sampling campaign in a multidisciplinary approach. In such that way, I have based the selection of sampling sites upon several features in order to study the formation of secondary (supergene) Mn oxides as well as the processes explaining their formation. Among these factors, the most relevant belong to (1) the genetic origins (i.e., hydrothermal, supergene, sedimentary, metamorphic) of the manganese deposits (see chapter 3), (2) the variable intensity of the weathering processes operating in these deposits (see chapter 2), and (3) their location in different geological settings related to the broad European-African geodynamic. Four manganiferous districts have been investigated so far (►Fig. 4.1):

(1) The Vosges district in eastern France (Mn Haut-Poirot, Mn-Fe Saphoz) is located on the left flank of the Rhine Graben (see chapter 5), and is related to the setting up of volcanic and plutonic bodies forming vein-type ores;
(2) The Stavelot massif (Ardenne) in eastern Belgium (Chevron and Salmchâteau deposits; see chapter 6) displays Ordovician Mn-rich sedimentary rocks, which have undergone low grade metamorphism (green schist facies; Demoulin *et al.*, 2018; Dekoninck *et al.*, accepted with revision, in revision);

(3) The Imini-Tasdremt district south of the High Atlas in Morocco (see chapter 7), where the Mn orebodies are hosted in Cretaceous dolostones forming a karst-hosted supergene deposit (Dekoninck *et al.*, 2016b, 2016a, submitted).
(4) The Nefza district in the Nappe zone of northern Tunisia (Fe-Mn Tamra deposit; see chapter 8) is a mixed hydrothermal-supergene deposit hosted in Pliocene detritic sediments (Dekoninck *et al.*, 2018);

4.2 Sampling methodology

The successful dating of K-Mn oxides depends strongly on a careful selection of samples on field, their good integration in the geological context and their subsequent characterization in the laboratory (Vasconcelos, 1999). Avoiding contamination effects with other K-bearing minerals of the parent rocks (i.e., muscovite) or co-genetic minerals (i.e., illite, smectite or other generations of K-Mn oxides) is of primary importance to further obtain accurate and meaningful $^{40}Ar/^{39}Ar$ ages. Those steps are only possible through detailed microscopic investigations to identify and avoid any obstacles during the $^{40}Ar/^{39}Ar$ protocol.

All Mn oxides are easily distinguished from Fe oxides, the latter being rather brownish showing a brown (goethite) or reddish (hematite) trail, whereas Mn oxides display a deep black mark (►Fig. 4.2a). Key identification criteria are often missing on the field because most of the Mn oxides have similar features (i.e., black, microcrystalline, and botryoidal; ►Fig. 4.2). Only pyrolusite is easily identified with its well-developed shiny crystals forming a palisade (►Fig. 4.2b). It is however difficult to distinguish hollandite group minerals from romanechite or nsutite, these minerals being often associated (►Figs. 4.2a and c). Lithiophorite is however soft and of very low density. Some features are somewhat characteristic of the hollandite group minerals from which $^{40}Ar/^{39}Ar$ can be retrieved. Cryptomelane can be identified by its dark gray to black color, more often showing discrete bluish tints (►Figs. 4.2c and d) and conchoidal fractures (►Fig. 4.2d). It most often exhibits colloform or botryoidal habits, which is typical of the “psilomelane” fabric, forming veins, filling geodes or lying the surfaces of veins and cavities (►Figs. 4.2a, c and d). However, there are some variations within the hollandite group minerals. For example, the luster is brighter in the coronadite-hollandite end-members rather than in cryptomelane showing a dull gray tint. The only key identification criteria that distinguishes hollandite group minerals from other Mn oxides is their needle-shaped habits observed under microscopic views, unless it is poorly crystalline (►Figs. 4.3a), combined with their chemical composition.

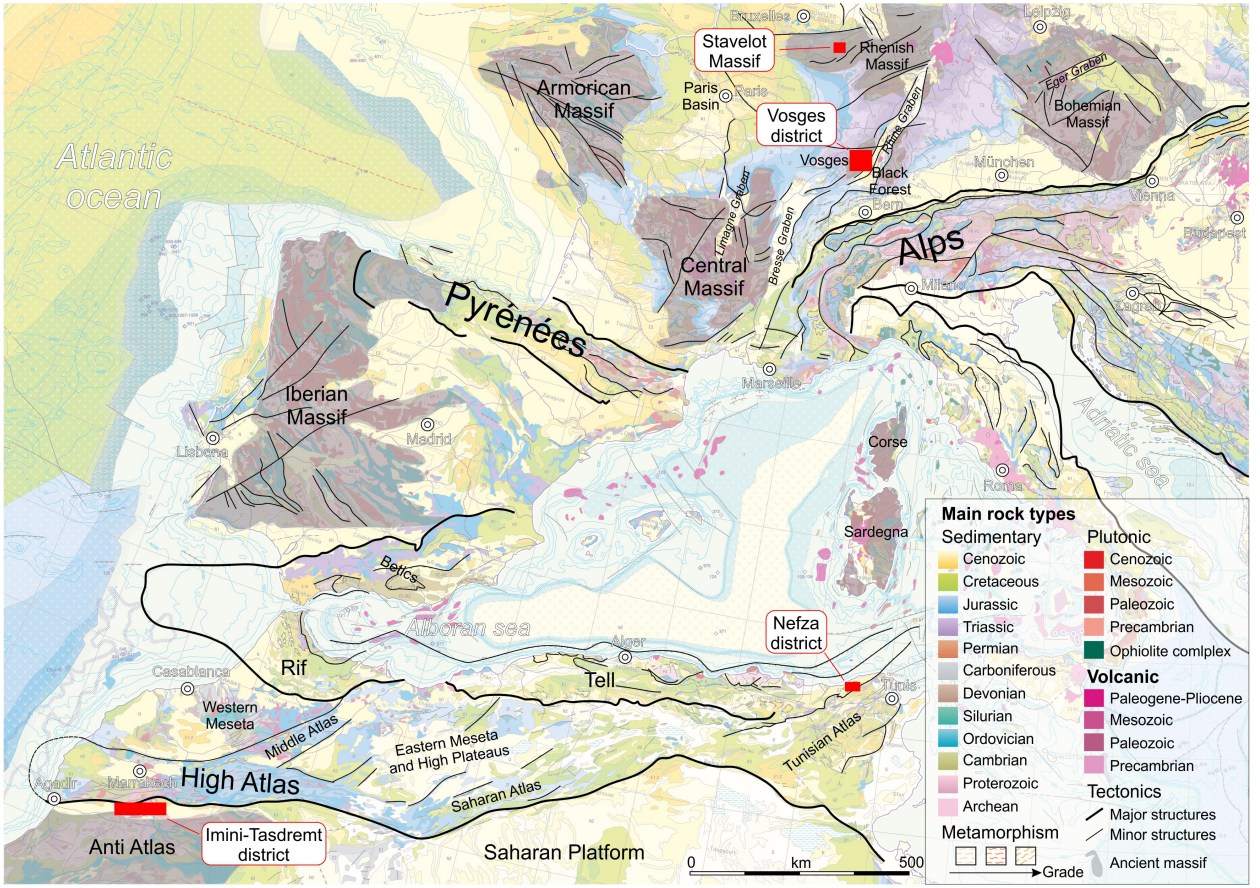

►**Fig. 4.1** Location of the main districts sampled in this thesis onto the geological map of Europe (Asch, 2003). The main tectonic structures and structural domains are highlighted. Old Precambrian-Paleozoic massifs are evidenced in gray shades.

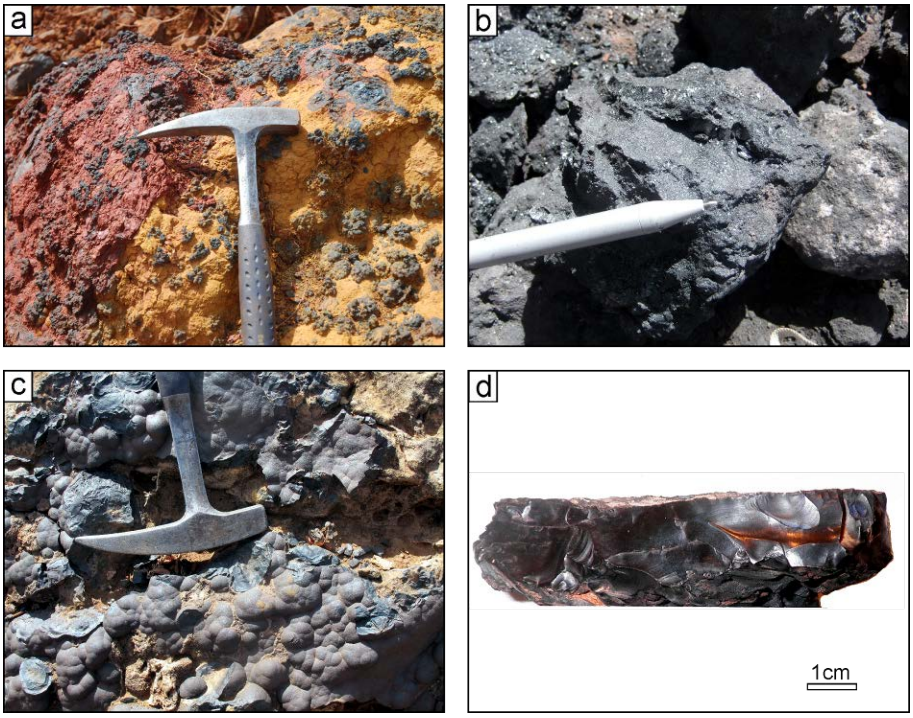

►**Fig. 4.2** Field observations and hand specimens of Mn oxides. **a.** Botryoidal Mn oxides (romanechite, hollandite, chalcophanite) associated with Fe oxides and clays (red and yellow zones) in the Fe-Mn deposit (Tamra, Tunisia; see chapter 8). **b.** Pyrolusite mined in the Imini deposits (Morocco; see chapter 7). **c.** Botryoidal hollandite *s.s.* in the Tasdremt deposit (Morocco; see chapter 7). **d.** The conchoidal fracture of cryptomelane in the Stavelot Massif (Belgium; see chapter 6).

4.3 Petrographic and mineralogical identification

The routinely combined use of microscopic techniques, reflected light or scanning electron microscopy (SEM; ►Figs. 4.3a and b) and X-ray diffraction (XRD) usually makes it possible to discriminate among most of the Mn oxides. X-ray diffraction implies the partial destruction of the hand specimen to form a powder, using a hammer and then a crusher. The powder is also used for geochemical analyses. Microscopical analyses needs the hand sample to be cut by a saw in order to produce 30 µm thick thin or polished sections, both being coated in a resin. As these two methods bring valuable and complementary mineralogical and petrographic information, a major limitation is that they are not performed on the same portion of a sample, but on different aliquots. This could result in (slight) differences between these complementary analyses. However, as they remain the best method to investigate the mineralogy and the textures (microscope only), and since no alternative process has been developed yet, this approach is still relevant. In the following lines, I would like

to draw the attention onto the best methods to determine the mineralogy and petrography of samples.

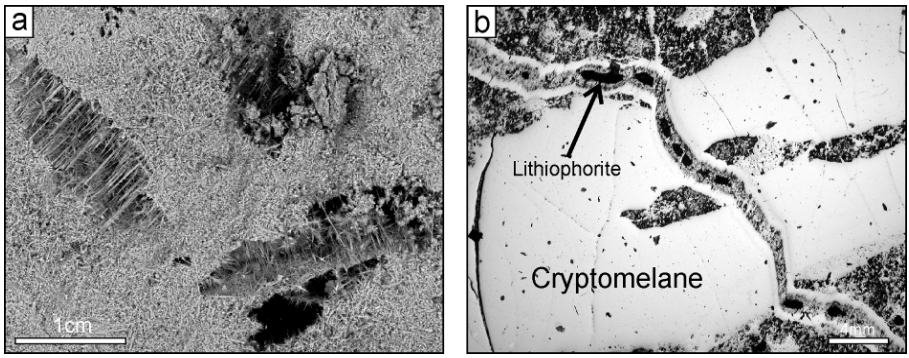

►**Fig. 4.3 a.** Backscattered electron view of hollandite needles forming a matrix in the Tasdremt ores (Morocco; see chapter 7). **b.** Two generations of cryptomelane veinlets occurring with lithiophorite in the Stavelot massif (Belgium; see chapter 6) observed under reflected polarized light microscope.

4.3.1 X-ray diffraction

X-ray diffraction (XRD) is a widely used method to identify unknown minerals or mixing of them (i.e., in rocks) by comparing XRD spectrum of an unknown material to a reference database (PDF-2). X-ray diffraction is the elastic scattering of X-ray photons by atoms in a periodic lattice. The scattered monochromatic X-rays that are in phase give constructive interference. The diffraction of X-rays by crystal planes allows to derive lattice spacing by using Bragg's law (►Equ. 4.1):

$$n\lambda = 2dsin\theta \quad (\blacktriangleright \text{Equ. 4.1})$$

where n is an integer called the order of reflection, λ is the wavelength of X-rays, d is the characteristic spacing between the crystal planes of a given specimen and θ is the angle between the incident beam and the normal to the reflecting lattice plane.

By measuring the angles (θ) under which the constructively interfering X-rays leave the crystal, the interplanar spacing (d) of every single crystallographic phase can be determined (►Fig. 4.4).

Samples for X-ray diffraction were crushed to powder in stainless steel grinding jar, introduced in a RETSCHER PM 100 planetary ball mills and sieved to 125 µm prior their analysis. A PHILIPPS X-ray diffractometer with a PW3710 BASED CuKα detector was used to generate XRD patterns. Major phases were identified using ICDD View software with PDF-2 database (Powder Diffraction

File 2009) in the "Unité de chimie physique, théorique et structurale" of the University of Namur.

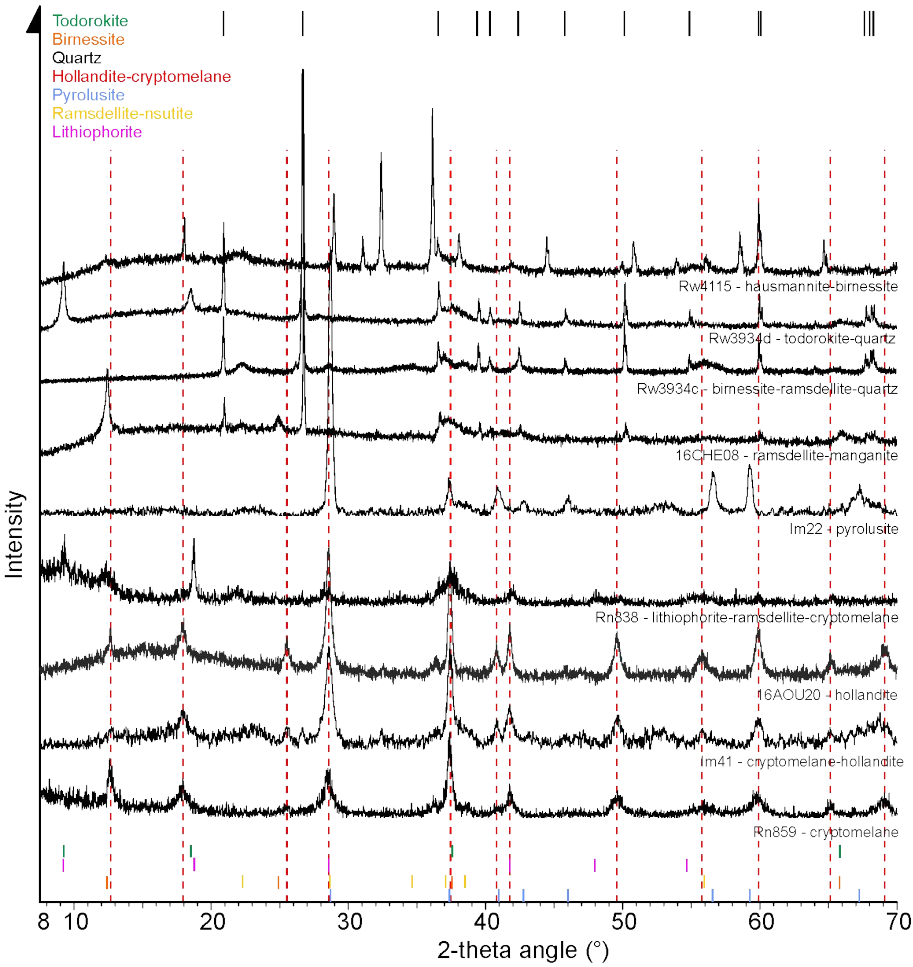

Fig. 4.4 Diffraction patterns of different Mn oxides showing their poor crystallinity and their close crystallographic structure (this work).

4.3.2 Polarized light microscopy

The information retrieved from polarized light microscopy are major and minor mineral identification. Furthermore, the contrast-enhancing technique reveals detailed information about the texture and composition of rocks that are invaluable for mineral identification. For that purpose, a Zeiss Axiophot microscope was used to emphasize the mineralogy and texture and complement the X-ray identification on aliquot samples. Some Mn oxides are easily identified under reflected light, such as pyrolusite

showing a high reflectivity and a strong anisotropism. However, the distinction between minerals belonging to the hollandite group is difficult, especially from nsutite or lithiophorite (►Fig. 4.3b).

Thin sections were made in the Sedimentary Petrology unit of the Geology Department of the University of Liège. Polished sections were made at the University of Brussels in the Applied Mineralogy and Geochemistry Laboratory of the Earth and Environmental Sciences Department and, more recently, in our own laboratories.

4.3.3 Scanning electron microscopy

Many structures and phases are beyond the limit of resolution of light microscopy. High spatial resolution complementary information can be recovered from scanning electron microscopy (SEM) as it allows observations resulting from interactions of an electron beam with the surface of a sample. It permits, for example, a quick diagnostic of unprepared samples, showing the size and shape of the crystals (►Fig. 4.3a). Alternatively, the study of polished surfaces reveal fine textures and supplement mineralogical determinations. The addition of an energy dispersive spectrometer (EDS or EDX) allows for *in situ* semi-quantitative chemical analysis of minerals.

4.3.3.a Electron probe microanalysis

In order to advance in the chemical characterization of hollandite group minerals (i.e., to determine the trace element contents quantitatively), the use of an electron probe microanalyses (EPMA or microprobe) is particularly useful as it is a quantitative and non-destructive method. Because the wavelengths of these X-rays are characteristic of the emitting species, the sample composition can be easily identified by recording WDS spectra (Wavelength Dispersive Spectroscopy). WDS spectrometers operate based on Bragg's law (►Equ. 4.1) and use various moveable shaped monocrystals as monochromators defined by the Holland Circle method. EPMA is a qualitative and quantitative method of non-destructive elemental analysis of micron-sized volumes at the surface of materials, with sensitivity at the level of tens of ppm, depending on the beam acceleration, the probe current and the mineral matrix. This technique is complementary to energy dispersive spectroscopy (EDS) in that WDS spectrometers have significantly higher spectral resolution and enhanced quantitative potential (Goldstein *et al.*, 2003). These analyses were operated in the Katholiek Universiteit Leuven (KUL, Belgium) in the department Materiaalkunde.

4.3.3.b Sample preparation

The sample preparation procedure to be used depends on the material and the objectives of the study. We have separated samples in two categories, one for the

determination of the mineralogy and petrography in polished and thin sections (also used in light microscopy); the second for checking the homogeneity and the chemical purity of K-bearing Mn oxide fragments (cryptomelane) to be used in $^{40}Ar/^{39}Ar$ geochronology (see below). In both cases, the surface of the sample needs to be a good conductor to avoid concentration of electrons at the surface (charging effect) due to the insulating nature of most rocks and minerals. Coating of the sample with carbon or other metal films (i.e., gold, platinum…) is then required and should allow the imaging and the microanalysis to be performed. The preferred coating element for X-ray analysis is carbon because it has a minimal effect on the X-ray spectrum (Goldstein *et al.*, 2003). However, the use of a thin carbon layer is not always necessary for checking the composition of Mn oxide fragments (i.e., during sample preparation of $^{40}Ar/^{39}Ar$ dating), given that they are relatively good conductors, unless other minerals, such as quartz or carbonates occur. The preparation of polished and thin sections remains the same as in light microscopy, but a prior examination in a transmitted-light optical microscope is necessary to locate areas of interest.

4.4 Geochronology of K-Mn oxides by K-Ar and $^{40}Ar/^{39}Ar$

Potassium (K) is the 8th most abundant element in the earth crust (Li, 2000), forming minerals such as K-feldspar and micas, among many others. Three isotopes are naturally found: ^{39}K and ^{41}K are stable and account for 93.2581 $\pm$ 0.0029% and 6.7302 $\pm$ 0.0029% of the natural K, respectively, whereas ^{40}K is radioactive and represents only 0.01167 $\pm$ 0.00004% of the total K (Garner *et al.*, 1975). The abundance of K in rocks makes the K-Ar and its alternative $^{40}Ar/^{39}Ar$ systems widely used to determine the age of unknown K-bearing minerals and extrapolate the age of rocks in various environments. The aim of this section is to accustom the reader to challenges encountered in the determination of K-Mn oxide ages by the K-Ar method and how age determination is not as straightforward as it seems.

K-bearing Mn oxides, belonging to the hollandite group minerals (see chapter 3), are one of the most suitable phases to estimate the age of supergene processes with jarosite-alunite (Shanin, 1968; Chukhrov *et al.*, 1969; Vasconcelos *et al.*, 1994a; Vasconcelos, 1999). The accuracy of Mn oxides as a geochronometer by the K-Ar and $^{40}Ar/^{39}Ar$ systems arises from the fact that most of the hollandite group minerals (and to a lesser extent romanechite) can host structural K in relatively high quantities (up to 5.32% K in pure cryptomelane) within the crystallographic sites. These sites are retentive of K and radiogenic ^{40}Ar loss, because of their tunnel-like structure (►Fig. 3.3). First attempts to assess the K-Ar chronometric suitability of Mn oxides dates back to Chukhrov *et al.* (1966). Subsequent investigations by Yashvili and Gukasyan (1974) in Armenia, Segev *et al.* (1991, 1992) in western Germany, Vasconcelos *et al.* (1992, 1994b, 1995) and Ruffet *et al.* (1996) in Brazil and Lippolt

and Hautmann (1995) in Sweden, India and Morocco, supported substantially the chronometric potential of this mineral. In 1999, P. M. Vasconcelos reviewed and presented the viability of this method in a complete synthesis, from which the following concepts have been borrowed. Using the K-Ar method and its $^{40}Ar/^{39}Ar$ technique, these successive generations of geologists demonstrated that cryptomelane and hollandite may be successfully used to date manganese deposits of different types (hydrothermal, metamorphic, sedimentary and supergene; see chapter 3), as well as weathering profiles, where K-bearing Mn oxides occur. Such innovative approach at that time has more recently led Earth scientists to investigate the timing and duration of weathering (e.g., Vasconcelos *et al.*, 1994b, 1994a; Hénocque *et al.*, 1998; Dammer *et al.*, 1999; Hautmann and Lippolt, 2000; Li *et al.*, 2007b, 2007a, among many others), especially given that these oxides occur massively in the weathering zone of Mn-rich rocks (Vasconcelos, 1999). However, K-bearing Mn oxides still remain a geochronological challenge largely due to their fine-grained nature and complex intergrowth (Post, 1999). Associated problems, such as sample contamination, uptake of extraneous argon, or gas loss and redistribution during irradiation, may therefore severely limit their use as reliable chronometers (Hautmann and Lippolt, 2000).

Mn levels of the Stavelot massif (Belgium; see chapter 6) and the Vosges massif (France; see chapter 5) were analyzed for their $^{40}Ar/^{39}Ar$ composition in the Noble Gas laboratory of Géosciences at the University of Montpellier 2 (France), using a new generation multicollector mass spectrometer (Thermo Scientific Argus VI MS). Samples from the Imini and Tasdremt areas (Morocco; see chapter 7) were analyzed with a $^{40}Ar/^{39}Ar$ laser probe and a Map-215-50 spectrometer following the step-heating experimental procedure (Ruffet *et al.*, 1991, 1995, 1996, 1997) at the University of Rennes (France). Additionally, several samples of the Imini-Tasdrelt district (Morocco) were analyzed by the K-Ar method in the Activation Laboratories (Ontario, Canada).

4.4.1 Sample preparation

Most of the K-Mn oxide samples show the typical botryoidal and banded textures forming successive growth bands during supergene alteration (►Fig. 4.2). Such crystallization of Mn oxides represents the direct precipitation of manganese from weathering fluids into open spaces and are generally devoid of contaminants. The poor crystallinity and low purity of mixed Mn oxides (for example in wad) are therefore not considered during the selection of the samples. All dated materials are hand-picked from crushed rocks, washed in distilled water and then treated in an ultrasonic bath and dried to avoid dust size particles adsorbed on grain surfaces. The resultant grain size is between hundreds of µm to 1–2 mm. The crystallinity, purity and composition of the samples are determined by X-ray diffraction (XRD) on aliquot of

the same sample. Several grains from each sample are investigated with a SEM-EDS. Imperfect samples, containing heterogeneous material are moved aside to avoid elemental contamination and interference of K, Ca and Cl. Such heterogeneous samples were sometimes selected only if they contained the best-preserved minerals for some specific levels that do not have counterparts. One of the advantages of the $^{40}Ar/^{39}Ar$ method is that any contaminant not identified during sample preparation should be further detected during the incremental heating study. The K-Ar method cannot detect the presence of contaminants (Vasconcelos, 1999). Most Mn oxides present in weathering profiles contain rhythmic growth bands, which, if they are dated separately, will provide information on the rate of Mn oxide precipitation (Vasconcelos *et al.*, 1992, 1994b; Hénocque *et al.*, 1998).

4.4.2 K-Ar and $^{40}Ar/^{39}Ar$ methodology

The K-Ar and the $^{40}Ar/^{39}Ar$ methods are well-established geochronological techniques (e.g., Dalrymple and Lanphere, 1969; Faure, 1986; McDougall and Harrison, 1999). They are able to determine the timing of cooling of a rock or a mineral in hypogene processes (magmatism, metamorphism and hydrothermalism), for example in muscovite, biotite or K-feldspar. The age records to closure temperature of a mineral, when K and its radioactive product ^{40}Ar are is quantitatively retained in crystallographic sites. The unstable parent ^{40}K is disintegrated naturally into ^{40}Ca (88.74%) and ^{40}Ar (11.16%) by electronic capture or β^- decay, with a half-life of 1.248 Ga, making this system suitable over long periods, such as those acting in geological systems. However, the interpretation of geochronological results obtained for minerals formed under low-temperature, for example in the weathering zone, is based on the assumption that the age should correspond to the precipitation of a K-rich mineral. Therefore, closure temperature is not a relevant concept because the minerals under investigation precipitate and remain at surface conditions. However, the ease of exchange of K and Ar with the external environment plays a very important role in determining the suitability of a supergene phase to geochronology. Vasconcelos (1999) set down several basic recommendations to consider the application of the K-Ar and $^{40}Ar/^{39}Ar$ methods in the supergene zone:

- The mineral has remained closed to gains or losses of radiogenic $^{40}Ar^*$ soon after its formation.
- The mineral has remained closed to gains or losses of K soon after its formation.
- No excess Ar was incorporated into the mineral.
- Correction can be made for atmospheric ^{40}Ar adsorbed onto or included in the mineral structure at the time of precipitation.

- The isotopic composition of K in the mineral is known and has changed only due to the radioactive decay of ^{40}Ar.
- The decay constants of K are known and have been constant through time.

The incorporation of excess Ar may pose problems in the $^{40}Ar/^{39}Ar$ technique, but the application of isotope correlation diagrams enables this identification and correction for the excess Ar component. Comparatively, the K-Ar and $^{40}Ar/^{39}Ar$ have different advantages and disadvantages (►Table 4.1)

►**Table 4.1.** Comparison between the K-Ar and $^{40}Ar/^{39}Ar$ methods (Vasconcelos, 1999).

Parameter	**K-Ar**	**$^{40}Ar/^{39}Ar$**
Age range	>~1 Ma	> 250,000 ka
Sample size	0.1-1.0 g	0.5 µm to 2 mm (1.0 g)
K determination	Atomic absorption spectrometry or flame photometry on separate aliquot	Mass spectrometry of ^{39}Ar generated by neutron irradiation of ^{39}K
Ar determination	Isotope dilution mass spectrometry	Mass spectrometry
Analytical precision	0.4-5%	0.05-1%
Irradiation	No	Yes (several weeks)
Duration	0.5-1 day/sample	0.5-2 days/sample

4.4.2.a The K-Ar system

The initial population of the parent radioelement (N_0) decays according to the statistic law of radioactivity, giving at a moment (t) the population of the parent element (N_t; ►Equ. 4.2):

$$N_t = N_0.e^{-\lambda t} \qquad (►\text{Equ. 4.2})$$

At each moment and given the decay constant of ^{40}Ar ($5.8.10^{-11}$ year^{-1}) and ^{40}Ca ($4.96.10^{-10}$ year^{-1}) the equation ►Equ. 4.3 can be obtained:

$$[^{40}Ca]_t^* + [^{40}Ar]_t^* = [^{40}K]_0 - [^{40}K]_0 \quad (►\text{Equ. 4.3})$$

where * illustrates the radiogenic origin of the element.

Assuming that λ is the addition of both λ_{Ca} and λ_{Ar}, we obtain the ►Equ. 4.4.

$$\frac{[^{40}Ar]}{[^{40}Ca]} = \frac{\lambda_{Ar}}{\lambda_{Ca}} \qquad (►\text{Equ. 4.4})$$

Therefore, in the K-Ar method, time (t) is given by ►Equ. 4.5.

$$t = \frac{1}{\lambda} ln[\left(\frac{\lambda c}{\lambda_{Ca}}\right).\frac{[^{40}Ar]}{[^{40}K]} + 1] \qquad (►\text{Equ. 4.5})$$

where $\lambda_,$ is the total decay constant for ^{40}K ($5{,}543.10^{-10}$ $year^{-1}$); λ_c is the decay constant of ^{40}K to ^{40}Ar; ^{40}Ar is the number of moles of radiogenic ^{40}Ar calculated from the total amount of ^{40}Ar measured by mass spectrometric techniques and corrected for atmospheric ^{40}Ar; ^{40}K is the number of moles of ^{40}K calculated from the total number of moles of K measured by atomic absorption spectroscopy, flame photometry or ICP-OES.

^{40}K and ^{40}Ar are measured separately in two samples. The date (*t*) obtained is simply a numerical result from the application of a geochronological technique. This straightforward result may represent a meaningful geological age or may be an artefact resulting from contamination, from analytical errors or from the study of an unsuitable sample, thereby limiting further interpretation. Hence, a date may or may not have age significance, but an age, however, is a numerical result from the application of a geochronological technique, which, given the analytical uncertainties, is the best estimate of a geological event, if the analyzed sample is representative of its geological environment (Vasconcelos, 1999).

4.4.2.b The $^{40}Ar/^{39}Ar$ system

As the K-Ar method needs two aliquots of the same sample (one for K, and the other for Ar determination), which may induce errors, and considering the challenges encountered when numerous generations of cryptomelane occur in some samples (see sections 3.2 and 4.2), the age retrieved from the K-Ar methodology method is often uncertain. The $^{40}Ar/^{39}Ar$ is based upon the same radioactive decay system, but with the difference that a unique aliquot is needed to date a sample (Merrihue and Turner, 1966). The principle is that the irradiation of ^{39}K under a rapid neutron flux leads to the formation of ^{39}Ar. ^{39}K is stable and the $[^{39}K]/[^{40}K]$ ratio remains constant in nature (Garner *et al.*, 1975). By measuring the $^{39}Ar_K$ quantity in an irradiated sample, the exact number of atoms of ^{39}K from which the $^{39}Ar_K$ originates can be evaluated (►Equ. 4.6), thereby avoiding the need for two aliquots of the analyzed sample (McDougall and Harrison, 1999).

$$[^{40}Ar]_K = [^{39}K].\Delta T \int \phi(E)\sigma(E)dE \qquad (\blacktriangleright \text{Equ. 4.6})$$

where $[^{39}Ar]_K$ is the produced Ar from the ^{39}K irradiation; $[^{39}K]$ is the initial number of ^{39}K atoms; ΔT is the irradiation time; $\phi(E)$ is the neutron flux and its energy; $\sigma(E)$ is the captured section of the $^{39}K(n,p)^{39}Ar$ reaction from energy (E).

From the equation (►Equ. 4.7), we can define the J, a dimensionless irradiation parameter empirically measured through the analyses of neutron fluency monitors of known ages.

$$J = \frac{(e^{\lambda t}-1)}{[^{40}Ar]^* / [^{39}Ar]_K} \qquad (\blacktriangleright \text{Equ. 4.7})$$

In the $^{40}Ar/^{39}Ar$ technique, time (t) is finally obtained from ►Equ. 4.8.

$$t = \frac{1}{\lambda}\ln[J.\frac{[^{40}Ar]}{[^{39}Ar]} + 1] \qquad (\blacktriangleright \text{Equ. 4.8})$$

where λ, is the total decay constant for ^{40}K ($5{,}543.10^{-10}$ year^{-1}); $^{40}Ar^*$ is the number of moles of radiogenic ^{40}Ar calculated from the total amount of ^{40}Ar measured by mass spectrometric techniques and corrected for atmospheric ^{40}Ar and nucleogenic interferences; ^{39}Ar is the total amount of ^{39}Ar generated by the reaction $^{39}K(n,p)^{39}Ar$, also measured by mass spectrometry and corrected for nucleogenic interferences; and J is a dimensionless irradiation parameter empirically measured through the analyses of neutron fluency monitors of known ages. In this approach the atmospheric $^{40}Ar/^{36}Ar$ value is assumed to be 298.53 $\pm$ 0.5 (McDougall and Harrison, 1999).

An additional requirement in the application of the $^{40}Ar/^{39}Ar$ technique is that the mineral must be stable and not subject to any loss of $^{40}Ar^*$ by heating, or ^{39}Ar loss by recoil[16], during neutron irradiation (Harrison, 1983; McDougall and Harrison, 1999). During neutron irradiation the daughter ^{39}Ar generated from parent ^{39}K may recoil from its original site in a range from 0 to 0.5 ¹m (McDougall and Harrison, 1999), depending on the density of the mineral structure. The effect of recoil over the age spectra of large crystals (>100 µm) is volumetrically insignificant, but it becomes a problem in dating fine-grained minerals (Vasconcelos, 1999). For example, the volume subjected to ^{39}Ar recoiled may be significant in supergene Mn oxides given that crystal domains are often <5 µm (►Fig. 4.3a; Huneke and Smith, 1976), resulting in poorly constrained ages in finely crystalline supergene phases by the $^{40}Ar/^{39}Ar$ method (Vasconcelos, 1999). However, several authors showed that recoil losses are relatively small and do not prevent successful dating of K-Mn oxides (Vasconcelos *et al.*, 1992, 1994b, 1995; Ruffet *et al.*, 1996).

Two distinct analytical procedures are possible with the $^{40}Ar/^{39}Ar$ technique: (1) total fusion or (2) incremental heating (step heating) analyses. In the absence of recoil issues, a total fusion $^{40}Ar/^{39}Ar$ result is equivalent to a K-Ar age (Vasconcelos, 1999). However, the step-heating analysis yields several **apparent ages** for a single sample, each date corresponding to one analyzed step. Step-heating results are generally illustrated in two different ways: through **step-heating spectra** or by $^{39}Ar/^{40}Ar$ versus $^{36}Ar/^{40}Ar$ **isotope correlation diagrams** (►Figs. 4.5a and b; Vasconcelos, 1999). From the $^{40}Ar/^{39}Ar$ technique, three age estimates can be obtained and therefore examine the convergence of the method**: the plateau age, the integrated age, and the isochron age** (Vasconcelos, 1999). In addition, several total fusion analyses for grains from a single sample or the results of step-heating analyses

[16]Recoil effect is the movement ^{39}Ar from its originate sites, therefore affecting the age distribution within a single grain or crystal.

for one grain can be combined in **ideogram plots**, which yield "most probable" age estimates for these results (►Fig 4.9c; Deino and Potts, 1990). These results may or may not represent a true geological age.

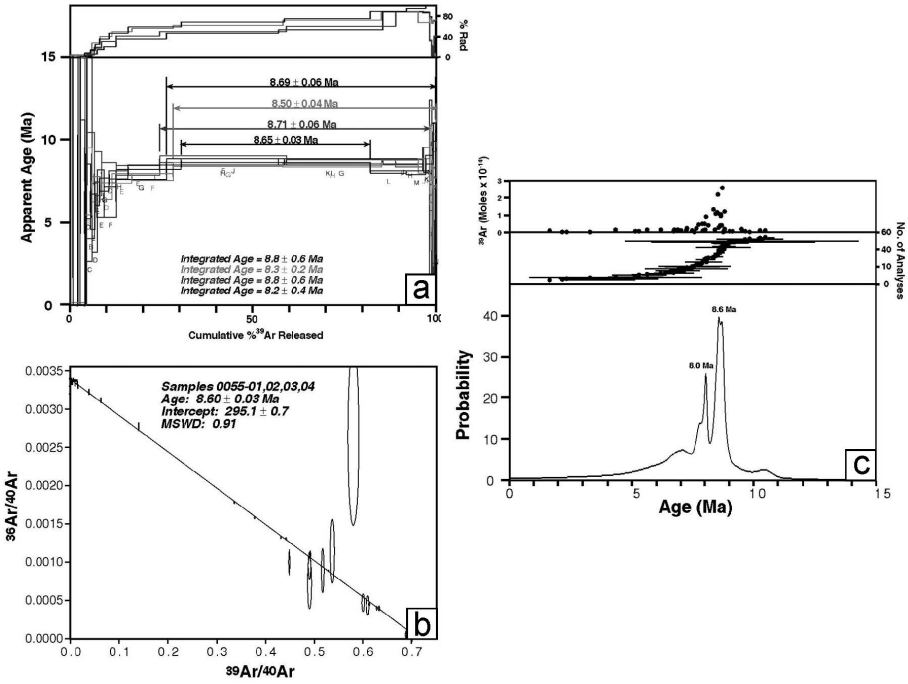

►**Fig. 4.5** Geochronological information retrieved from the $^{40}Ar/^{39}Ar$ heating-step procedure. **a.** Step-heating spectra of four distinct cryptomelane grains, illustrating the reproducibility of the results obtained for each of the grains analyzed. **b.** Isotope correlation diagram obtained for the same four grains yielding a well-defined isochron with atmospheric intercept and a slope that corresponds to the ages calculated by the plateaus in the step-heating spectra. **c.** Ideogram illustrating the well-defined peak for the highly radiogenic steps (age = 8.6 Ma; Vasconcelos, 1999).

4.4.3 Step-heating spectra, plateau ages and integrated ages

The weakness of the K-Ar and total fusion $^{40}Ar/^{39}Ar$ analyses (see above) results from several assumptions in the determination of the age of the sample, including the absence of significant inherited Ar components, absence of Ar or K losses by exchange or recoil, absence of contaminants. As these parameters often influence the age determination, the step-heating analysis of a single grain or crystal remains, by far, the most powerful application of the $^{40}Ar/^{39}Ar$ method. The results of step-heating analyses are generally plotted as the cumulative percent of ^{39}Ar released, which follow the increasing degassing temperatures, against **apparent age** for each step (►Fig. 4.5a). Apparent ages are calculated for each step using ►Equ. 4.3. An

integrated age is the apparent age calculated from the total gas yielded by the sample (►Figs. 4.5a and b). This integrated age should be the same as K-Ar date, if no recoil effect is observed in the low temperature domain. In the absence of recoil, $^{40}Ar^*$ loss or contamination, the integrated age should correspond to the **plateau age** of the sample (Vasconcelos, 1999). Vasconcelos (1999) has identified several step-heating patterns that can help to decipher any Ar or K contamination (►Fig. 4.6). These degassing patterns are commonly end-members, and could be displayed together in a more complex way.

4.4.3.a Ideal spectrum

An ideal spectrum is given in ►Fig. 4.6a, in which the first steps (from a to h) are related to large amounts of atmospheric ^{40}Ar adsorbed onto the grain surface or trapped in intercrystalline sites, providing irrelevant ages and large atmospheric and radiogenetic Ar ratio. Middle temperature steps (from i to m) represent mixtures of atmospheric ^{40}Ar released from intercrystalline sites and $^{40}Ar^*$ from tunnel sites (►Fig. 3.3). Increasing temperatures steps progressively provide more accurate ages. The last steps (n to o) correspond to remaining $^{40}Ar^*$ and ^{39}Ar derived from small amounts of gas still trapped in the collapsed Mn oxide structure (Vasconcelos, 1999). At this stage the sample is undergoing phase transformations from Mn_3O_4 to MnO by increased temperatures, releasing large volumes of oxygen into the vacuum system and thus increasing the measurement uncertainties (Vasconcelos *et al.*, 1995).

►Fig. 4.6b illustrates a well-defined spectrum but showing evidence for the presence of small $^{40}Ar^*$ losses from less retentive, poorly crystalline sites. The amount of atmospheric gases released decreases with temperature, whereas the $^{40}Ar^*$ progressively increases (steps c to g), but is derived from poorly crystallized sites, then resulting in younger ages than true precipitation age for the mineral. The plateau age represented by steps h, i and j, is the best estimate of the true precipitation age for the sample. Steps k, l, and m represent small amounts of gas still trapped in the collapsed Mn_3O_4 or MnO structure at high temperature (►Fig. 4.6b). If the open sites are abundant and the losses of $^{40}Ar^*$ are volumetrically significant, the integrated ages will be significantly younger than the plateau ages (Vasconcelos, 1999).

4.4.3.b Disturbed spectra

►Fig. 4.6c shows the spectrum obtained for a sample that has lost the recoiled ^{39}Ar to the surrounding atmosphere during irradiation or heating procedure. The first two steps (a and b) contain mostly atmospheric ^{40}Ar, and small amounts of radiogenic $^{40}Ar^*$ are derived from sites that have experienced ^{39}Ar loss by recoil. The apparent age obtained is significantly older than the true sample age because the ^{40}K content is underestimated. If there is only limited recoil, progressively higher temperatures will release $^{40}Ar^*$ and ^{39}Ar from retentive tunnel sites, an age plateau is obtained as the

best estimate of the precipitation age. The integrated age is older than the plateau age. An alternative explanation for the younger ages in the low temperature segment could be assigned to an excess ^{40}Ar component adsorbed onto the mineral surface or trapped within intercrystalline lattice. However, such interpretation is less likely as excess Ar necessary to be detected needs to be volumetrically important because excess Ar component remains in the aqueous solution during mineral precipitation (Murray and Riley, 1971).

►Fig. 4.6d illustrates the spectrum of a sample in which the recoiled ^{39}Ar has been implanted or trapped within less retentive sites in the mineral. The initial steps (a through e), although mostly atmospheric Ar, contain radiogenic $^{40}Ar^*$ and ^{39}Ar recoiled easily released from their implantation or trapping sites. An apparent age younger than the true age of the sample is obtained because of the extra amount of ^{39}Ar released at these steps. If, at higher temperatures (h, i), retentive sites not subject to recoil losses and hosting significant amounts of $^{40}Ar^*$ and ^{39}Ar are analyzed, a plateau age representing the true precipitation age for the mineral is obtained.

The presence of a hypogene component intergrown with the supergene phase, releases $^{40}Ar^*$ in the high temperature steps, resulting in much older than the age of the supergene phase itself finally determining a staircase or climbing spectra (►Fig. 4.6e; see chapter 7). When the supergene and the hypogene phases yield their Ar contents at different temperatures, a plateau age can be obtained for the cryptomelane. However, if an old phase of a K-bearing Mn oxide is present, it yields $^{40}Ar^*$ throughout the same heating schedule than the more recent phase, resulting in unreliable precipitation age. The integrated ages obtained for the sample are older than the true precipitation ages.

The loss of Ar and/or K since the formation of K-bearing Mn oxides is represented by a staircase spectra (►Fig. 4.6f), into which apparent ages progressively increase through the degassing of the released ^{39}Ar. The initial steps (a and b) represent the atmospheric component, whereas all subsequent steps represent mixtures of gases derived from sites that have lost Ar, K, or both after mineral precipitation. Sometimes such spectra will reach a plateau; in other cases, a plateau is never reached, and no age can be retrieved. However, the highest temperature steps reveal the minimum age of the Mn oxides. Such spectra clearly point to the limit of the K-Ar and the total fusion $^{40}Ar/^{36}Ar$ method, as these methods would produce irrelevant ages with no way to identify their provenance (Vasconcelos, 1999).

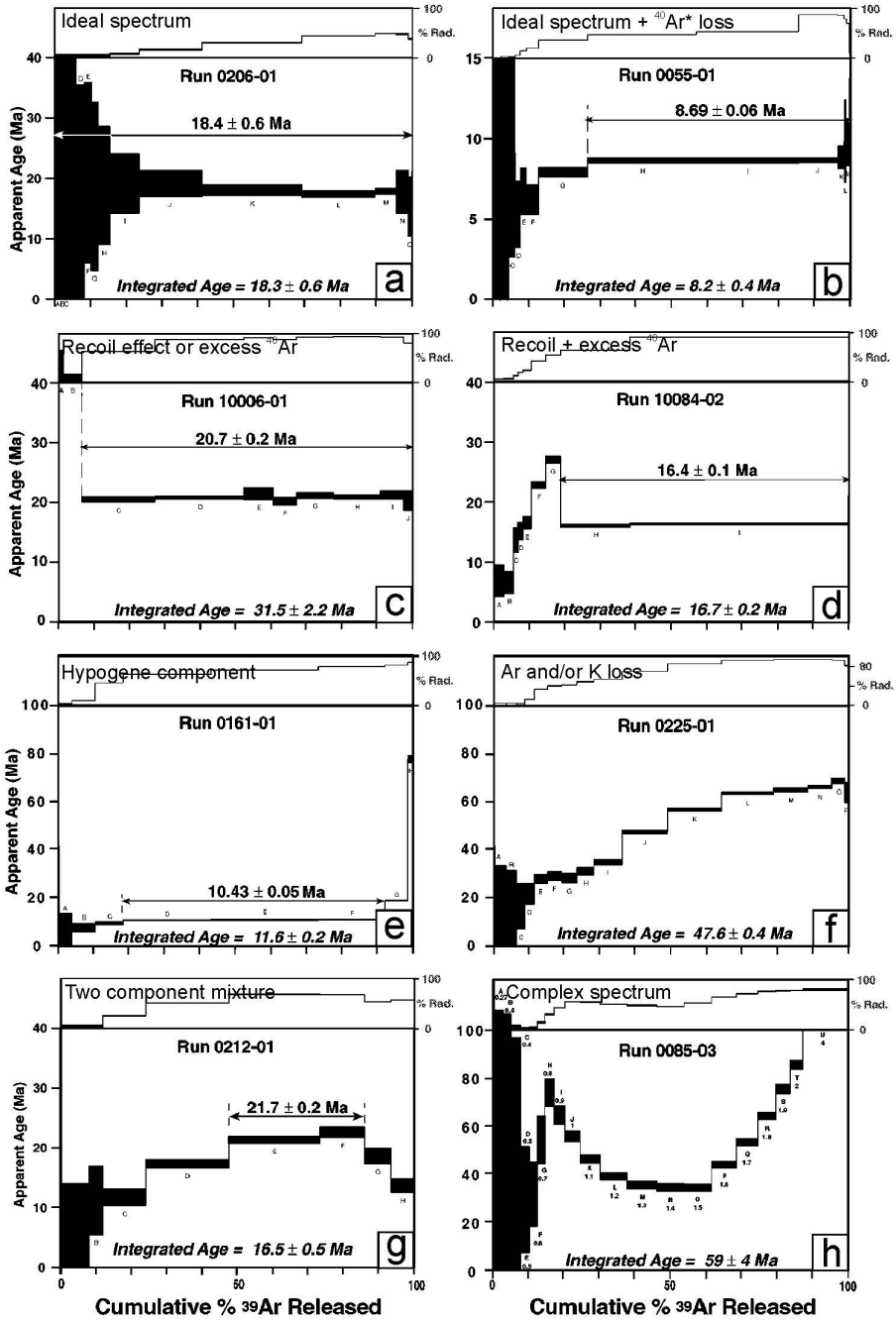

►**Fig. 4.6** End-member $^{40}Ar/^{39}Ar$ spectra evidenced by Vasconcelos (1999) for supergene Mn oxides studied by the incremental heating technique.

The mixture of two or more distinct minerals, which are intimately intergrown, results generally in a spectrum displaying ascending apparent ages at low temperatures (similar to ►Figs. 4.6b and f) and their decline at high temperatures (►Fig. 4.6g). Sometimes, a plateau age is reached in mid-temperatures, providing true precipitation age of one generation of minerals (►Fig. 4.6g). An alternative explanation would imply implantation of recoiled ^{39}Ar into crystallographic sites that are more retentive than the sites from where ^{39}Ar was derived. More complex spectra are a mixing of the previous patterns. For example, ►Fig. 4.6h displays a combined result of open system, recoil and contamination. This type of spectrum cannot provide reliable age and evidence the importance of a careful analysis by the $^{40}Ar/^{39}Ar$.

4.4.4 Isochron and isochron ages

Age calculation can be easily determined following ►Equ. 4.8, assuming that no excess ^{40}Ar and ^{36}Ar have been incorporated within the mineral structure through time, and that the $^{40}Ar/^{36}Ar$ ratio is 295.5. It is also possible to determine an age by plotting $^{39}Ar/^{40}Ar$ versus $^{36}Ar/^{40}Ar$ ratios (Faure, 1986; McDougall and Harrison, 1999). Such isochron age is possible when the analyzed sample hosts argon in different crystallographic sites, with varying ratios of atmospheric, nucleogenic, and radiogenic components. The result is an isotope correlation line in a $^{39}Ar/^{40}Ar$ versus $^{36}Ar/^{40}Ar$ plot (►Equ. 4.9; Vasconcelos, 1999).

$$(^{40}Ar/^{39}Ar)_m = (^{40}Ar/^{36}Ar)_c + (^{40}Ar^*/^{39}Ar)_k \cdot (^{39}Ar/^{36}Ar)_m \qquad (\blacktriangleright \text{Equ. 4.9})$$

where *m* are measured ratios, *c* are ratios of Ar gas contamination (excess ^{40}Ar or ^{36}Ar), and *k* identifies the argon isotopes produced by potassium in the samples (Faure, 1986).

The slope $[(^{40}Ar^*/^{39}Ar)_k]$ can be used in ►Equ. 4.8 to calculate the age of the cryptomelane. The discrepancy between the $^{40}Ar/^{36}Ar$ intercept ("y" in a linear equation) and the atmospheric value (295.5) allows the accuracy of the age to be identified (►Fig. 4.5b). Any increase or decrease of this ratio is interpreted to be a ^{40}Ar or a ^{36}Ar contamination, respectively. The reproducibility of the plateau and isochron ages is needed to certify both ages (►Figs. 4.5a and b; Vasconcelos, 1999).

4.4.5 Ideograms

Ideograms are based on the assumption that errors in a date have a Gaussian distribution. Such age-probability plot is built from the sum of the individual Gaussian curves for each date (►Fig. 4.5a Deino and Potts, 1990). Geochronological information can be retrieved, but they have less interest considering that ideograms do not always take into account the amount of gas released during each step.This can

be set by weighted and resized the data of each step (see chapter 7). The most reliable way to interpret the ideogram peaks is to compare them with plateau ages (►Figs. 4.5a and c).

4.5 Geochemistry

Geology borrows many theoretical concepts from other disciplines, applying the principles and techniques of physicists, chemists, and materials scientists, among others, to geological problems. Geochemistry is a broad subject commonly used in Earth sciences as tools and principles of chemistry, which have been brought to meet the full range of issues in the Earth and environmental sciences. Chemical composition of rocks is conveniently distinguished between major (>1.0 wt.%; e.g., SiO_2, Al_2O_3, FeO, MgO, CaO, Na_2O, and K_2O), minor (0.1-1.0 wt.%; e.g., TiO_2, MnO, P_2O_5) and trace elements (<0.1 wt.%; e.g., As, Au, REE, etc.). Victor Goldschmidt (1888–1947) was the first to systematize the behavior of the chemical elements in Earth sciences into a classification scheme of them according to their preferred host phases on the silicate Earth (lithophile, siderophile, chalcophile and atmophile; ►Fig. 4.7; Turekian and Holland, 2014).

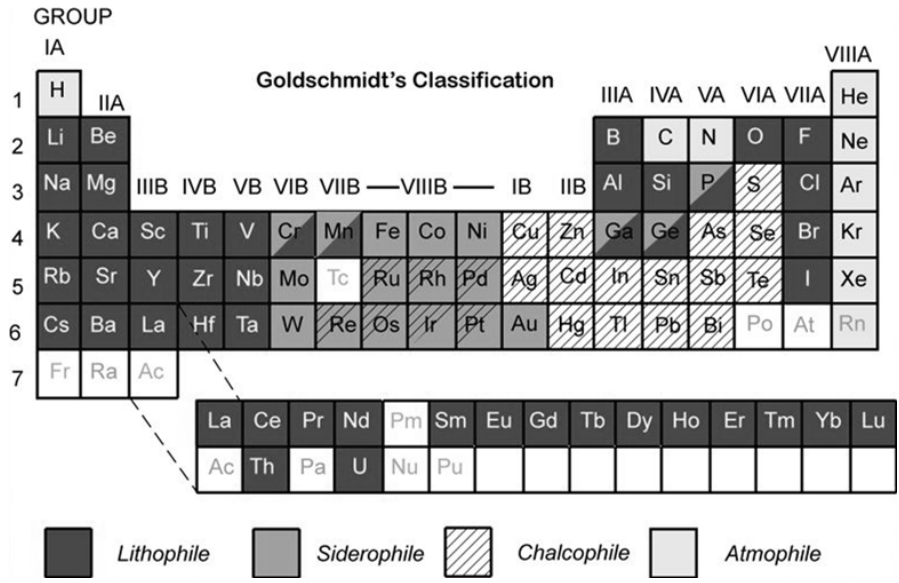

►**Fig. 4.7** Goldschmidt's classification of the elements (Winter, 2001).

These elements can also be represented by their presence in different reservoirs in the Earth, the mantle and crust, in order to evidence (►Fig. 4.8). These groups behave in the same range in geological processes, allowing geologists to

decipher chemical processes that cannot be directly observed within the Earth (Winter, 2014).

There are many sub-field of geochemistry aiming to explain and understand processes related to volcanic and magmatic activity, hydrothermalism, contemporary and past carbon cycle, composition of organic matter, cycle of chemical elements, the origin of planets, the composition of waters (ocean, rivers, sea...), development of soils and weathering profiles, etc. Division criteria include: analytical geochemistry in contrast to theoretical studies, the technique being employed or the types of measurements in a constrained area with (e.g., isotope geochemistry); the type of sample (e.g., igneous geochemistry and organic and petroleum geochemistry); the class of scientific questions being addressed (e.g., cosmochemistry); the pressure-temperature regime that a certain subset of geochemists are engaged with (e.g., low-temperature geochemistry; Winter, 2014). In this section, I would like to present some specific tools that help geologists to understand elemental distribution in the supergene environment (environmental geochemistry). In addition, I will discuss the stable isotope systematics of oxygen and hydrogen which may help to determine the precipitation temperature of some minerals within the weathering crust.

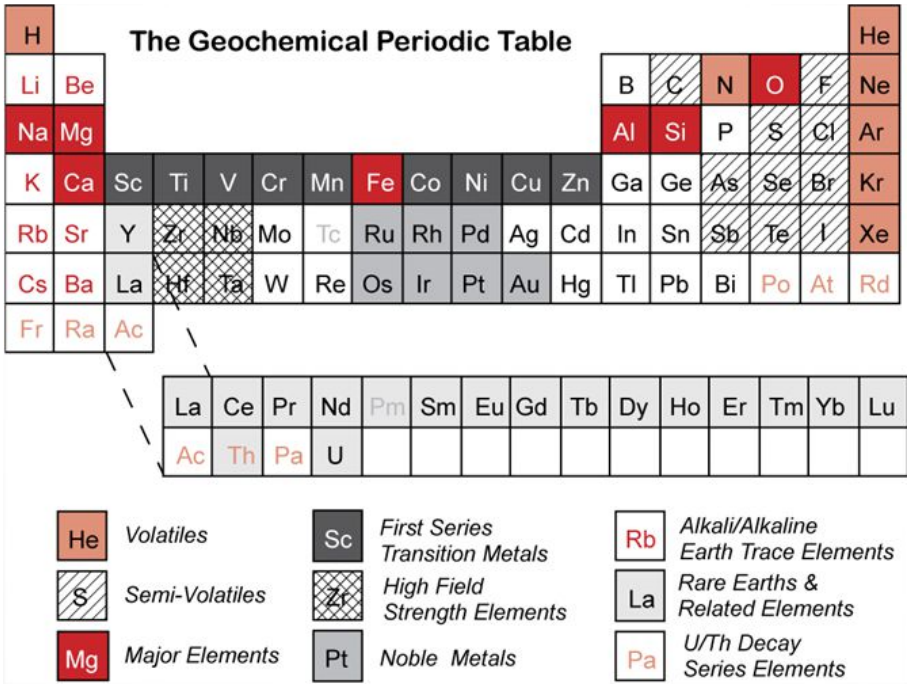

►**Fig. 4.8** The geochemical periodic table, in which elements are grouped according to their geochemical behavior (Winter, 2001).

4.5.1 The geochemical composition of the Earth

In most geochemical systems, there are 10 or fewer major components that together account for 99% or more of the system (Li, 2000), leaving places for more than 80 trace elements (►Fig. 4.12). These major elements account for most of the crustal rock composition, forming directly several minerals. Minor elements easily substitute for major elements in small quantities (i.e., Mn for Fe) or form accessory minerals (i.e., P_2O_5 forms apatite), whereas trace elements are too diluted to form a separate phase, so they substitute for major or minor elements. Winter (2014) has summarized some groups of elements according to their distribution in Earth processes (►Fig. 4.8).

The defining feature of the *volatile elements* (noble gases) is their filled outer electron shell, making them chemically inert as well as volatile (►Fig. 4.8). Hence, they are never chemically bound in rocks and minerals. The shared characteristic of the *semi-volatile elements* is that they partition readily into a fluid or a gas phase (e.g., Cl, Br), or form compounds that are volatile (e.g., SO_2, CO_2).

The high electronegativity and the low ionic potential (ratio of charge to ionic radius) makes *alkali and alkaline earth elements* relatively soluble in aqueous solution (►Fig. 4.8). Because of their solubility, they are quite mobile during metamorphism and weathering (see chapter 2). In magmatic and volcanic settings, these elements tend to be concentrated in the melt phase when melting or crystallization occurs (incompatible elements).

The *rare earth elements* are divided in two rows of elements (►Fig. 4.8): the first row is the lanthanide rare earths and the second is the actinide rare earths. However, the term "rare earths" is often used in geochemistry to refer only to the lanthanide rare earths (Winter, 2001). The lanthanide rare earths are in the +3 valence state over a wide range of oxygen fugacity. At the oxygen fugacity of the Earth's surface Ce can be partly or fully oxidized in the +4 state, whereas Eu can be partly in the +2 state at the low oxygen fugacity of the Earth's interior. Th is always in a +4 valence state, whereas U may be in a +4 or +6 valence state, depending on the oxygen fugacity. These elements are relatively insoluble in aqueous solutions, except U^{6+}, which forms a soluble oxyanion complex, UO_2^{2+} (uranyl), in fully oxidizing conditions, as those reported on the Earth surface. Because of their high charge and large radii, the rare earths are incompatible elements. However, the heavy rare earths (HREE) have a sufficiently small radii, allowing them to be accommodated in many common early minerals, such as substitute for Al^{3+} in garnet, or for Ca^{2+} by Eu^{2+} in plagioclase. In order to illustrate the distribution of these elements in terms of depletion or enrichment, they are plotted by dividing the concentration of each rare earth by its concentration in a set of normalizing values, such as the concentrations of

rare earths in chondritic meteorites, in the Earth crust, in sedimentary rocks, etc. (Gromet *et al.*, 1984; Taylor and McLennan, 1985; Ben Othman *et al.*, 1989; McLennan, 1989, 2001, 2001; Condie, 1993; McDonough and Sun, 1995; Piper and Bau, 2013; Rudnick and Gao, 2014). Because the rare earths are highly insoluble and immobile, rare earth patterns often remain unchanged during metamorphism. Indeed, even during the production of sediments from crystalline rock by weathering and then erosion, the rare earth patterns often remain little changed, and have been used to identify the provenance, i.e., the source of sedimentary rocks (Winter, 2014).

The *high field strength* (HFS) elements are so-called because of their high ionic charge (►Fig. 4.8). Th and U are sometimes included in this group. Their charge is too high and requires one or more coupled substitutions to maintain the charge balance. Hf and Zr are moderately incompatible elements, whereas Nb and Ta are highly incompatible elements. The consequence of their high ionic potential or ionic charge to ionic radius ratio, is that the HFS elements are particularly insoluble and very immobile during weathering and metamorphism (see chapter 2; Winter, 2014).

Transition metals are likely the most complex elements (Sc, Ti, V, Cr, Fe, Mn, Ni, Co, Cu, Zn) due to their two or more valence states and high electronegativity (►Fig. 4.8). The solubility of these elements is quite variable in comparison with the alkali and alkaline earths, and depends upon valence state as well as the availability of the anions with which they can form soluble coordination complexes. *Noble metals*, including the platinum group elements (Rh, Ru, Pd, Os, Ir, Pt), gold and silver are relatively rare chalcophile or siderophile elements. These elements are transition elements and, like the first transition series, can exist in multiple valence states, ranging from 0 to +8, making their chemistry complex.

Other elements do not belong to any of the previous groups but are of particular interest in some processes, for example, in the formation of deposits (i.e., Pb, Mo, Re, Ge, Ga, Sn, Sb, Ag, Bi; Winter, 2001).

4.5.2 Analytical methods for whole rock geochemistry

Chemical techniques were first applied to rocks during the 16th century in Europe in order to understand and exploit ore veins. It was only in the 18th and 19th centuries that the majority of the elements were recognized and organized on the basis of their similar properties (giving rise to the Mendeleev periodic table of the elements in 1869; Winter, 2014). Our analyses were based on whole rock investigations, using the advanced technologies of inductively coupled plasma (ICP) and mass spectrometry (MS). These analyses were subcontracted to Activation Laboratories Ltd (Ontario, Canada).

4.5.2.a Inductively coupled plasma

The use of the inductively coupled plasma (ICP) technique needs samples to be crushed and dissolved before their introduction into the ICP. The most aggressive fusion technique employs a lithium metaborate/tetraborate fusion. Fusion is performed by a robot at Activation Laboratories (Ontario, Canada), which provides a fast fusion of the highest quality in the industry. The resulting molten bead is rapidly digested in a weak nitric acid solution. The fusion ensures that the entire sample is dissolved. It is only with this attack that major (immobile) oxides, including SiO2, refractory minerals (i.e., zircon, sphene, monazite, chromite, etc.), REE and other HFSE, can be liberated into solution. The dissolved sample is mixed with argon gas, and then aspirated into a tiny radio frequency generator, where a plasma[17] is created (►Fig. 4.9). Elements, in the form of atoms, are introduced into the plasma. The plasma is formed by seeding the argon gas passing through a plasma torch with electrons. The electrons are accelerated and collide with argon atoms releasing more electrons and forming argon ions. A proportion of the sample atoms become ionized within the plasma. When an atom or ion is excited within the plasma, they jump from a lower to a higher energy (excited) level. Upon relaxation of these electrons to their initial "ground" state, an energy is emitted in the form of photons, similarly to the EDS analyses (►Fig. 4.7). The emitted photons possess wavelengths that are characteristic of their respective elements. The emission line related to each element is isolated by a diffraction grating and detected by a series of photomultipliers, each on a separate channel tuned for a specific element (►Fig. 4.9). All channels are simultaneously counted and fed to an on-board computer, where the data are reduced and the concentration of each element is calculated.

In addition to this spectroscopic method that relies upon electron interactions, the addition of a mass spectrometer (MS) allows a more reliable determination of trace elements and isotopic ratios. In this method, a sample is heated and ionized, and the ions are introduced into an evacuated chamber with a strong magnetic field. The stream of charged ions follows a curved path in the magnetic field. Due to their greater momentum, heavier ions follow a path with a larger radius of curvature. Ions of each mass are counted because they pass through slits in a charged detector (►Fig. 4.9). This instrument counts the particles of a particular mass (Lindon *et al.*, 2017). It is capable of analyzing almost all elements in the periodic table and can be applied to solutions, solids, and gases.

[17]A plasma is a gas, in this case argon, which contains a significant number of argon ions at very high temperature.

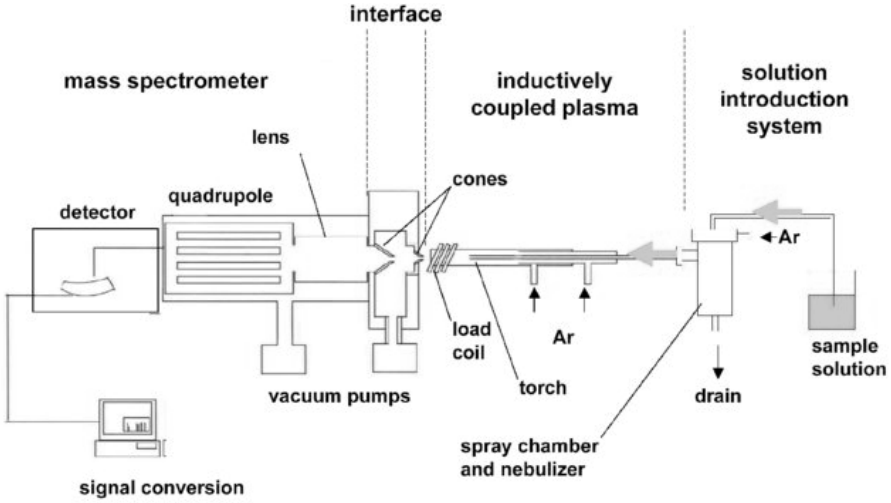

►**Fig. 4.9** Schematic of an inductively coupled plasma mass spectrometer (ICP-MS; Gilstrap, 2009).

The inductively coupled plasma optical emission spectrometry (ICP-OES) is an alternative technique for elemental analysis based on the measurement of the characteristic wavelength of almost all elements. The instrumentation associated with an ICP-OES system is relatively simple. A portion of the photons emitted by the ICP is collected with a lens or a concave mirror. This focusing optic forms an image of the ICP on the entrance aperture of a wavelength selection device, such as a monochromator. The particular wavelength exiting the monochromator is converted into an electrical signal by a photodetector. The signal is amplified and processed by the detector electronics and finally displayed and stored by a personal computer. Compared to other techniques, ICP-OES enjoys a higher atomization temperature, a more inert environment, and the natural ability to provide simultaneous determinations for up to 70 elements. This makes the ICP less susceptible to matrix interferences and able to correct for them when they occur (Hou and Jones, 2000).

4.5.2.b Normalization values

After obtaining analyses for each element, data are standardized to reference values. Choosing the appropriate normalization standard is not straightforward in geochemical analyses and depends on which rock type a geologist studies and which processes are to be investigated. Such normalization is mainly used for REE patterns, but applies to trace and some major elements. According to this method, geologists aim to demonstrate total enrichment of an element (mostly REE and traces) compared to some standard reservoir (i.e., https://earthref.org/GERMRD/datamodel/). Anomalies of some elements or asymmetric patterns of REE distribution that can be interpreted to reflect specific geological processes.

Chondritic meteorites are commonly chosen as standard normalization value because they are relatively unfractionated samples of the solar system and represent the average composition of the undifferentiated Earth (McDonough and Sun, 1995). The chondrite normalized pattern is particularly useful because it eliminates the abundant variations of the "Odd effect" and allows the identification of any fractionation process, a feature that is welcom in petrology (Rollinson, 2014). These patterns are commonly presented in a concentration (ratio between the analyzed sample and the normalization value) vs atomic number diagram, expressed as the base 10 logarithm of the values (►Fig. 4.10). The variation of chondrite composition has led some authors to suggest other reservoirs from which petrological processes can be highlighted (mantle, crust, etc.; e.g., Taylor and McLennan, 1985; Sun and McDonough, 1989; Condie, 1993; McDonough and Sun, 1995).

As chondrite is an appropriate reference to study magmatic processes, they are less interesting in the study of the erosion cycle. It has been observed that the concentration of many elements in fine-grained sedimentary rocks (i.e., shale) of the continental platforms around the world display similar chemical compositions as a consequence of mixing through repeated cycles of erosion (Rollinson, 2014). The sedimentary rocks and the seawater have rare earth patterns similar to each other, and to that of the continental crust. In order to accentuate the difference in REE patterns between different type of sediments, low temperature geochemists often normalize REE and trace elements abundances to the concentrations of the average shale. The North American Shale Composite (NASC; Gromet *et al.*, 1984), the European shale (Haskin and Haskin, 1966) and the Post Archean Australian Shale (PAAS; McLennan, 1989) are currently used, among other sedimentary reservoirs (Elderfield and Greaves, 1982; Ben Othman *et al.*, 1989). The average Upper Continental Crust (UCC; McLennan, 2001) is also used as a reference value for sedimentary rocks, assuming that sedimentary processes homogenize chemical elements previously fractionated during the formation of igneous rocks (Rollinson, 2014). The UCC reference also displays a larger panel of trace elements to be compared with the sample under investigation. The NASC, the European shale, the PAAS and the UCC normalization values have about 10 to 100 times the REE content of chondrite (►Fig. 4.10).

In some specific fields, chemical element concentrations are compared to peculiar samples as a measure of relative changes. For example, in order to identify enrichment or depletion of some elements in the weathering environment, weathered rocks are commonly compared to the unweathered rock from which they originate. A similar approach is used in the weathering zone of metal-bearing ores, showing enrichment or depletion of trace elements having genetic relation to parent mineralization or protores. Such method is also usefully applied to exploration geology, in the way of identifying "primary" or "secondary haloes" formed by natural

dispersion of indicators. Haloes exist around parent orebodies or progress at some distances by physical and chemical process (Haldar, 2013).

The choice of a normalization standard remains a tool that allows geologists to manifest enrichment or depletion of elements, those standards being themselves compared to others (►Fig. 4.10). Thus, choosing the appropriate standard is a case-by-case choice, depending on what geologists want to show, but also from which field of geology the analyzed samples are derived.

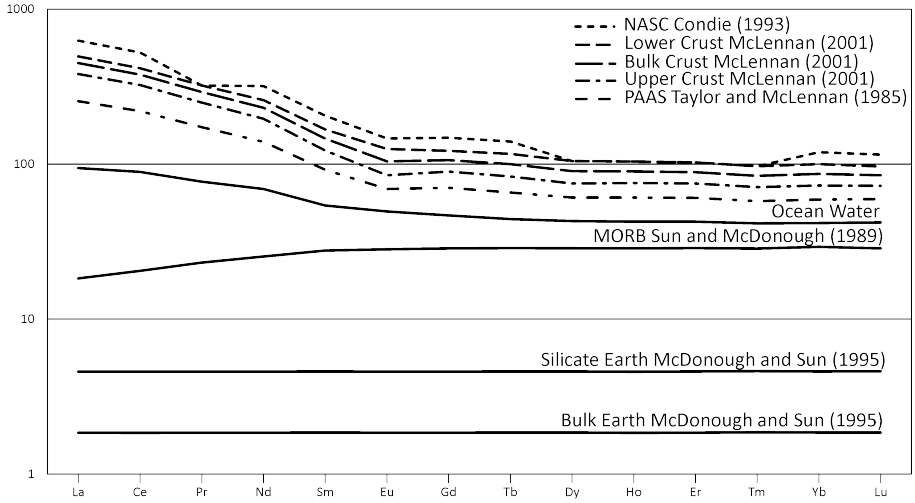

►**Fig. 4.10** Normalization values of different reservoirs compared to the chondrite reference (Taylor and McLennan, 1985; Sun and McDonough, 1989; Condie, 1993; McDonough and Sun, 1995; McLennan, 2001).

4.5.3 Stable isotope geochemistry of oxygen and hydrogen

The study of the oxygen and hydrogen isotopes of naturally occurring clay minerals (kaolinite, illite, smectite,…) and Fe oxides (goethite, hematite) carries information about the conditions under which these minerals were formed. Clay minerals usually form in equilibrium with the environment and then reflect their temperature of formation and the δD and $\delta^{18}O$ of water (Savin and Epstein, 1970a; Yapp, 1990a; Gilg and Sheppard, 1996; Sheppard and Gilg, 1996; Savin and Hsieh, 1998). The minerals investigated here are kaolinite [$Al_2SiO_5(OH)_4$] and goethite (FeOOH), given that they can host significant amounts of both hydrogen and oxygen. Since kaolinite and iron oxides (hematite and goethite) are often associated with co-genetic Mn oxides, they can provide suitable temperature under which they were formed in the supergene zone (see chapter 2).

Oxygen is the most abundant element in the earth crust with three stable isotopes: ^{16}O = 99.762%; ^{17}O = 0.038%; ^{18}O = 0.2%. The most useful aspect of oxygen is its occurrence in most solids, liquids and gases and its thermal stability over a large range of temperatures. Hydrogen contains only two stable isotopes: ^{1}H = 99.985; and ^{2}H = D (deuterium) = 0.015%. The isotope geochemistry of hydrogen is particularly interesting because of: (1) its omnipresence in a wide variety of geological processes, and also (2) its large mass difference (=ratio) in comparison with mass differences of stable isotopes of other elements (Hoefs, 2009).

All goethite and kaolinite δD and $\delta^{18}O$ compositions were obtained at the Institute of Earth Surface Dynamics of the University of Lausanne (Switzerland). Only the Tamra area (Tunisia) has provided separated Fe oxides and kaolinite from which stable hydrogen and oxygen measurements could be obtained. Silicates (quartz, feldspar, clays) and oxides (goethite-hematite) were analyzed for their $\delta^{18}O$ values in various rock types (rhyodacites, claystones, sandstone, marls, skarns). Hydrogen isotope compositions were measured on hydrous silicates (kaolinite-halloysite), and hydroxide (goethite).

4.5.3.a Isotopic ratio

The ratio between the heavy and the light isotope is obtained by $^{18}O/^{16}O$ and D/H (or $^{2}H/^{1}H$). The variation of these ratios is very small and physically difficult to measure in absolute terms. It is easier to compare these ratios in a relative way with other components of known values by measuring the difference (δ) between the sample and a standard value. The Standard Mean Ocean Water (SMOW) reference has been chosen as a standard because of its constant value. The following equations define the isotopic differences between a sample and a standard (►Equ. 4.9).

$$\delta^{18}O = \left[\frac{\frac{^{18}O_{ech}}{^{16}O_{ech}} - \frac{^{18}O_{std}}{^{16}O_{Std}}}{\frac{^{18}O_{std}}{^{16}O_{Std}}}\right].1000\ (‰) \quad \delta D = \left[\frac{\frac{D_{ech}}{H_{ech}} - \frac{D_{std}}{H_{std}}}{\frac{D_{std}}{H_{std}}}\right].1000\ (‰)\ (►\text{Equ. 4.9})$$

4.5.3.b Fractionation process

The isotopic composition of a mineral can provide useful information about the geological processes only if the mineral has retained its isotopic signal acquired during that process (Savin and Lee, 1988). At temperatures between 100–350 °C, the rate of isotopic exchange is always much larger for hydrogen than for oxygen (O'Neil and Kharaka, 1976). However, these data cannot be extrapolated to low temperature (<100 °C) because of the uncertainties in the regression of the kinetic data, and the slow exchange rate (Criss *et al.*, 1987; Sheppard and Gilg, 1996). The isotopic signature of water in the weathering environment is a function of latitude, elevation, continentality and climate. Clay minerals are resistant to isotopic resetting in the near

surface conditions because of the slow isotopic exchange at low temperature (Savin and Hsieh, 1998). The evolution of the weathering environment through time implies changes in the isotopic signal at a supergene mineral after its formation. Most of the time, a non-equilibrium state, for example along a weathering profile (Girard *et al.*, 2000) gives alternative H and O isotope values (Sheppard and Gilg, 1996).

There are three types of fractionations. (1) Equilibrium fractionation depends on the thermodynamic properties of different species. The equilibrium precipitation of minerals in water is an isotopic equilibrium (liquid—solid). (2) Kinetic fractionation indicates an excess (or a lack) of some isotopes in particular phases due to rates of reactions. For example, ^{16}O is readily integrated into the gas phase during the evaporation of water in comparison to the heavier ^{18}O. Dissociation reaction, biologically mediated reactions and diffusion also have kinetic effects on isotopic fractionation (Hoefs, 2009). (3) Biogenic fractionation during mineral formation (particular case of kinetic fractionation) is due to the metabolic activity of organisms.

Therefore, it is essential to determine the fractionation coefficient, which reflects how isotopes are fractioned between two phases. This coefficient is a temperature dependent equilibrium constant (►Equ. 4.10).

$$\alpha_{\text{mineral}-\text{water}} = \frac{(1000+\delta_{mineral}{}^{18}\text{O})}{(1000+\delta_{water}{}^{18}\text{O})} = \frac{{}^{18}\text{O}/{}^{16}\text{O}_{\text{mineral}}}{{}^{18}\text{O}/{}^{16}\text{O}_{\text{water}}} \qquad (\blacktriangleright\text{Equ. 4.10})$$

Because α is temperature dependent, isotopes of hydrogen and oxygen can be used as geothermometers. According to experimental results in minerals, the oxygen values vary as a linear or sub-linear function (►Equ. 4.11). This function explains that fractionation becomes less intense when temperature increases. Nevertheless, the temperature of hydrogen isotopes is more complicated and less understood than that of oxygen (Savin and Lee, 1988).

$$1000\ln\alpha_{\text{mineral}-\text{water}} = \text{a}.10^{6}.\text{T}^{-2} - \text{b} \qquad (\blacktriangleright\text{Equ. 4.11})$$

where a and b are considered as constants of the linear function. T is the temperature.

Water is used to refer to the aqueous-rich fluid phase associated with clay minerals. Its composition can be more or less saline and does not directly influence the H- and O-isotopes, unless salinities are very high and temperatures low (Truesdell, 1974; Graham *et al.*, 1980; Horita *et al.*, 1993).

- *Isotopic fractionation between water and kaolinite*

Studies of stable isotopes in clay minerals started with Savin's thesis (Savin and Epstein, 1970a, 1970b). These authors provided a number of isotopic values of clays coming from continental and oceanic environments. Subsequent studies reviewed in

the paper of Savin and Lee (1988) developed the stable isotope geochemistry of clay minerals in a wide range of disciplines: geothermometry, provenance of clays, detrital or authigenic origin, diagenetic processes, origin and evolution of upper crustal fluids, hypogene or supergene origin, hydrothermal systems, mineral-water interaction and paleoclimates. The precipitation of clay minerals at low temperatures occurs in the presence of water, showing that ^{18}O and ^{1}H are readily integrated in the solid phase (►Fig. 4.11). The isotopic composition of clay minerals directly depends on the isotopic composition of water, the fractionation coefficient between the clay mineral and water, and temperature. Some investigations made by Sheppard and Gilg (1996) explain the temperature dependency of the fractionation of O and H isotopes in the kaolinite-water system as a function of $10^3 \ln\alpha$ and T^{-2} (►Equ. 4.12; 4.13).

Oxygen: $10^3 \ln\alpha_{\text{kaolinite-water}} = -2.76\text{x}10^6\text{x}T^{-2} - 6.75$ (►Equ. 4.12)

Hydrogen: $10^3 \ln\alpha_{\text{kaolinite-water}} = -2.2\text{x}10^6\text{x}T^{-2} - 7.7$ (►Equ. 4.13)

Based on structural arguments and the experimental data of O'Neil and Kharaka (1976) differential isotopic exchange is faster for hydrogen than oxygen in systems where phases are neither destroyed nor created (Sheppard and Gilg, 1996). These authors show that many of the kaolinite samples are not in equilibrium with the present meteoric waters but plot with minor dispersion onto the so-called "kaolinite line" (►Fig. 4.11). This indicates that no subsequent isotopic exchange occurs between the mineral and any later waters, with which it may come into contact. The kaolinite line corresponds to the equilibrium of kaolinite with meteoric water (Savin and Epstein, 1970a), whereas the supergene-hypogene line (S/H) is the equilibrium at 35 °C (Sheppard and Gilg, 1996). These lines express the temperature dependency of kaolinite in equilibrium with water (►Fig. 4.11). Therefore, any shift from the kaolinite line would reflect (1) contamination with other minerals with different stable isotope compositions, (2) a higher formation temperature (3) recrystallization, and/or (4) a post depositional exchange at low temperature (Bird and Chivas, 1989).

- *Isotopic fractionation between water and goethite*

The temperature surface domains can be calculated for any hydroxyl mineral for which both the hydrogen and oxygen isotope mineral—water fractionation factors are known. The concept of a surface domain provides a criterion for assessing the likelihood that a particular sample records information about paleotemperatures. Experimental studies of Yapp (1990a) have demonstrated the suitability of stable isotope studies for goethite and hematite, and that both minerals are isotopically indistinguishable at equilibrium. The hematite (goethite)-water oxygen isotope fractionation over the range from 25° to 120°C is represented by the expression ►Equ. 4.14. Because only goethite can host structural hydrogen within the hydroxyl

group (FeOOH), the $\delta^{18}O$ and δD plots represent only the goethite precipitation conditions.

Oxygen: $10^3 \ln\alpha_{\text{hematite(goethite)}-\text{water}} = 1.63\text{x}10^6\text{x}T^{-2} - 12.3$ (►Equ. 4.14)

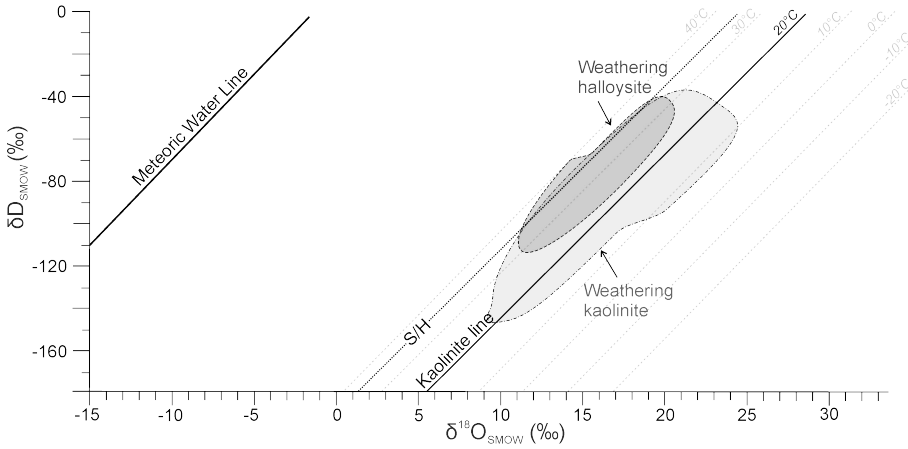

►**Fig. 4.11** Compilation plot of $\delta^{18}O$ and δD for supergene kaolinite and halloysite (modified after Sheppard and Gilg, 1996).

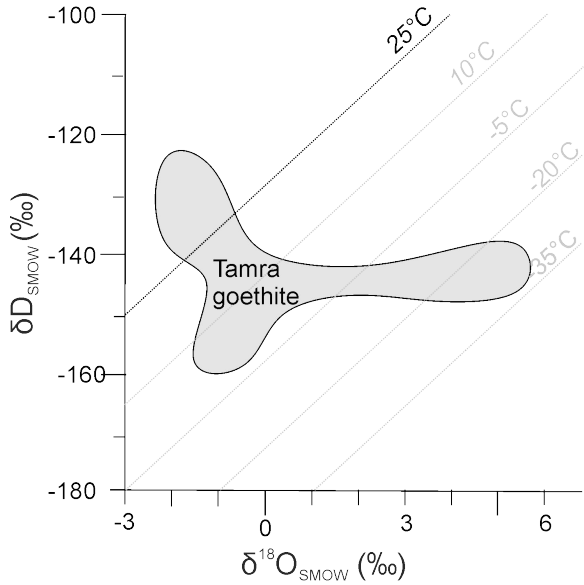

►**Fig. 4.12** Compilation plot of $\delta^{18}O$ and δD for the Tamra Fe oxides (Dekoninck *et al.*, 2018, this thesis, see chapter 8) based on mineral-water fractionation equation (Yapp and Pedley, 1985; Yapp, 1990b, 2000; Girard *et al.*, 2000).

Such isotopic system is more complex and less accurate than in kaolinite due to many substitutions of Mn and Al which could influence the hydrogen isotopic

composition of goethite (Yapp and Pedley, 1985). Several authors (Yapp, 1990b, 2000; Girard *et al.*, 2000) have estimated temperature domains for goethite precipitation rather than true equations, such as those obtained for oxygen isotopes (►Equ. 4.14). From this equation, temperature lines can assess the water conditions under which goethite has precipitated, similarly to the kaolinite system (►Fig. 4.12).

4.6 References

Asch, K., 2003. The 1:5 Million international geological map of Europe and adjacent areas: development and implementation of a GIS-enabled concept ; with 46 tables, Geologisches Jahrbuch Sonderhefte, Reihe A, Allgemeine und regionale Geologie Bundesrepublik Deutschland und Nachbargebiete, Tektonik, Stratigraphie, Paläontologie. Schweizerbart, Stuttgart.

Ben Othman, D., White, W.M., Patchett, J., 1989. The geochemistry of marine sediments, island arc magma genesis, and crust-mantle recycling. Earth Planet. Sci. Lett. 94, 1–21. https://doi.org/10.1016/0012-821X(89)90079-4

Bird, M.I., Chivas, A.R., 1989. Stable-isotope geochronology of the Australian regolith. Geochim. Cosmochim. Acta 53, 3239–3256. https://doi.org/10.1016/0016-7037(89)90104-X

Chukhrov, F.V., Shanin, L.L., Yermilov, L.P., 1966. Feasibility of absolute-age determination for potassium-carrying manganese minerals. Int. Geol. Rev. 8, 278–280. https://doi.org/10.1080/00206816609474282

Chukhrov, F.V., Yermilova, L.P., Shanin, L.L., 1969. Age of alunite from certain deposits. Trans. Dokl. USSR Acad. Sci. Earth Sci. Sect. 185, 49–51.

Condie, K.C., 1993. Chemical composition and evolution of the upper continental crust: Contrasting results from surface samples and shales. Chem. Geol. 104, 1–37. https://doi.org/10.1016/0009-2541(93)90140-E

Criss, R.E., Gregory, R.T., Taylor, H.P., 1987. Kinetic theory of oxygen isotopic exchange between minerals and water. Geochim. Cosmochim. Acta 51, 1099–1108. https://doi.org/10.1016/0016-7037(87)90203-1

Dalrymple, G.B., Lanphere, M.L., 1969. Potassium-argon dating: principles, techniques, and applications to geochronology, 1st ed. Freeman, San Francisco.

Dammer, D., McDougall, I., Chivas, A.R., 1999. Timing of weathering-induced alteration of manganese deposits in Western Australia; evidence from K/Ar and $^{40}Ar/^{39}Ar$ dating. Econ. Geol. 94, 87–108. https://doi.org/10.2113/gsecongeo.94.1.87

Deino, A., Potts, R., 1990. Single-crystal $^{40}Ar/^{39}Ar$ dating of the Olorgesailie Formation, Southern Kenya Rift. J. Geophys. Res. Solid Earth 95, 8453–8470. https://doi.org/10.1029/JB095iB06p08453

Dekoninck, A., Bernard, A., Barbarand, J., Saint-Bezar, B., Missenard, Y., Lepretre, R., Saddiqi, O., Yans, J., 2016a. Detailed mineralogy and petrology of manganese oxyhydroxide deposits of the Imini district (Morocco). Miner. Deposita 51, 13–23. https://doi.org/10.1007/s00126-015-0590-3

Dekoninck, A., Leprêtre, R., Saddiqi, O., Barbarand, J., Yans, J., 2016b. The high-grade Imini manganese district—karst-hosted deposits of mn oxides and oxyhydroxides, in: Bouabdellah, M., Slack, J.F. (Eds.), Mineral Deposits of North Africa. Springer International Publishing, Cham, pp. 575–594.

Dekoninck, A., Moussi, B., Vennemann, T., Jamoussi, F., Mattielli, N., Decrée, S., Chaftar, H.-R., Hatira, N., Yans, J., 2018. Mixed hydrothermal and meteoric fluids evidenced by unusual H- and O-isotope compositions of kaolinite-halloysite in the Fe(-Mn) Tamra deposit (Nefza district, NW Tunisia). Appl. Clay Sci. 163, 33–45. https://doi.org/10.1016/j.clay.2018.07.007

Demoulin, A., Barbier, F., Dekoninck, A., Verhaert, M., Ruffet, G., Dupuis, C., Yans, J., 2018. Erosion surfaces in the Ardenne–Oesling and their associated kaolinic weathering mantle, in: Demoulin, A. (Ed.), Landscapes and landforms of Belgium and Luxembourg. Springer International Publishing, Cham, pp. 63–84. https://doi.org/10.1007/978-3-319-58239-9_5

Elderfield, H., Greaves, M.J., 1982. The rare earth elements in seawater. Nature 296, 214. https://doi.org/10.1038/296214a0

Faure, G., 1986. Principles of isotope geology, 2nd ed. Wiley, New York.

Garner, E.L., Murphy, T.J., Gramlich, J.W., Paulsen, P.J., Barnes, I.L., 1975. Absolute isotopic abundance ratios and the atomic weight of a reference sample of potassium. J. Res. Natl. Bur. Stand. Sect. Phys. Chem. 79A, 713. https://doi.org/10.6028/jres.079A.028

Gilg, H.A., Sheppard, S.M.F., 1996. Hydrogen isotope fractionation between kaolinite and water revisited. Geochim. Cosmochim. Acta 60, 529–533. https://doi.org/10.1016/0016-7037(95)00417-3

Gilstrap, R.A., 2009. A colloidal nanoparticle form of indium tin oxide: system development and characterization.

Girard, J.-P., Freyssinet, P., Chazot, G., 2000. Unraveling climatic changes from intraprofile variation in oxygen and hydrogen isotopic composition of goethite and kaolinite in laterites: an integrated study from Yaou, French Guiana. Geochim. Cosmochim. Acta 64, 409–426. https://doi.org/10.1016/S0016-7037(99)00299-9

Goldstein, J., Newbury, D.E., Joy, D.C., Lyman, C.E., Echlin, P., Lifshin, E., Sawyer, L., Michael, J.R., 2003. Scanning Electron Microscopy and X-Ray Microanalysis, 3rd ed. Springer US.

Graham, C.M., Sheppard, S.M.F., Heaton, T.H.E., 1980. Experimental hydrogen isotope studies—I. Systematics of hydrogen isotope fractionation in the systems epidote-H_2O, zoisite-H_2O and AlO(OH)-H_2O. Geochim. Cosmochim. Acta 44, 353–364. https://doi.org/10.1016/0016-7037(80)90143-X

Gromet, L.P., Haskin, L.A., Korotev, R.L., Dymek, R.F., 1984. The "North American shale composite": Its compilation, major and trace element characteristics. Geochim. Cosmochim. Acta 48, 2469–2482. https://doi.org/10.1016/0016-7037(84)90298-9

Haldar, S.K. (Ed.), 2013. Mineral explorations: principles and applications. Elsevier, Waltham, MA, USA.

Harrison, T.M., 1983. Some observations on the interpretation of $^{40}Ar/^{39}Ar$ age spectra. Chem. Geol. 41, 319–338. https://doi.org/10.1016/S0009-2541(83)80027-8

Haskin, M.A., Haskin, L.A., 1966. Rare earths in european shales: a redetermination. Science 154, 507–509. https://doi.org/10.1126/science.154.3748.507

Hautmann, S., Lippolt, H.J., 2000. $^{40}Ar/^{39}Ar$ dating of central European K–Mn oxides — a chronological framework of supergene alteration processes during the Neogene. Chem. Geol. 170, 37–80. https://doi.org/10.1016/S0009-2541(99)00241-7

Hénocque, O., Ruffet, G., Colin, F., Féraud, G., 1998. $^{40}Ar/^{39}Ar$ dating of West African lateritic cryptomelanes. Geochim. Cosmochim. Acta 62, 2739–2756. https://doi.org/10.1016/S0016-7037(98)00185-9

Hoefs, J., 2009. Stable isotope geochemistry, 6th ed. Springer, Berlin.

Horita, J., Wesolowski, D.J., Cole, D.R., 1993. The activity-composition relationship of oxygen and hydrogen isotopes in aqueous salt solutions: I. Vapor-liquid water equilibration of single salt solutions from 50 to 100°C. Geochim. Cosmochim. Acta 57, 2797–2817. https://doi.org/10.1016/0016-7037(93)90391-9

Hou, X., Jones, B.T., 2000. Inductively Coupled Plasma/Optical Emission Spectrometry, in: Meyers, R.A. (Ed.), Encyclopedia of Analytical Chemistry. John Wiley & Sons, Ltd, Chichester, UK. https://doi.org/10.1002/9780470027318.a5110

Huneke, J.C., Smith, S.P., 1976. The realities of recoil - Ar-39 recoil out of small grains and anomalous age patterns in ^{39}Ar-^{40}Ar dating. Presented at the 7th Lunar Science Conference, Pergamon Press Inc., Houston, pp. 1987–2008.

Li, J.-W., Vasconcelos, P., Duzgoren-Aydin, N., Yan, D.-R., Zhang, W., Deng, X.-D., Zhao, X.-F., Zeng, Z.-P., Hu, M.-A., 2007a. Neogene weathering and supergene manganese enrichment in subtropical South China: An $^{40}Ar/^{39}Ar$ approach and paleoclimatic significance. Earth Planet. Sci. Lett. 256, 389–402. https://doi.org/10.1016/j.epsl.2007.01.021

Li, J.-W., Vasconcelos, P., Zhang, W., Deng, X.-D., Duzgoren-Aydin, N., Yan, D.-R., Zhang, J.-Q., Hu, M.-A., 2007b. Timing and duration of supergene mineralization at the Xinrong manganese deposit, western Guangdong Province, South China: cryptomelane $^{40}Ar/^{39}Ar$ dating. Miner. Deposita 42, 361–383. https://doi.org/10.1007/s00126-006-0118-y

Li, Y.-H., 2000. A compendium of geochemistry: from solar nebula to the human brain. Princeton University Press, Princeton, N.J.

Lindon, J.C., Tranter, G.E., Koppenaal, D.W. (Eds.), 2017. Encyclopedia of spectroscopy and spectrometry, 3rd ed. Elsevier/AP, Academic Press is an imprint of Elsevier, Amsterdam ; Boston.

Lippolt, H.J., Hautmann, S., 1995. $^{40}Ar/^{39}Ar$ ages of Precambrian manganese ore minerals from Sweden, India and Morocco. Miner. Deposita 30, 246–256. https://doi.org/10.1007/BF00196360

McDonough, W.F., Sun, S.-s., 1995. The composition of the Earth. Chem. Geol. 120, 223–253. https://doi.org/10.1016/0009-2541(94)00140-4

McDougall, I., Harrison, M.J., 1999. Geochronology and thermochronology by the $^{40}Ar/^{39}Ar$ method. Oxford University Press, United Kingdom.

McLennan, S.M., 2001. Relationships between the trace element composition of sedimentary rocks and upper continental crust. Geochem. Geophys. Geosystems 2, 24. https://doi.org/10.1029/2000GC000109

McLennan, S.M., 1989. Rare earth elements in sedimentary rocks; influence of provenance and sedimentary processes. Rev. Mineral. Geochem. 21, 169–200.

Merrihue, C., Turner, G., 1966. Potassium-argon dating by activation with fast neutrons. J. Geophys. Res. 71, 2852–2857. https://doi.org/10.1029/JZ071i011p02852

Murray, C.N., Riley, J.P., 1971. The solubility of gases in distilled water and sea water—IV. Carbon dioxide. Deep Sea Res. Oceanogr. Abstr. 18, 533–541. https://doi.org/10.1016/0011-7471(71)90077-5

O'Neil, J.R., Kharaka, Y.K., 1976. Hydrogen and oxygen isotope exchange reactions between clay minerals and water. Geochim. Cosmochim. Acta 40, 241–246. https://doi.org/10.1016/0016-7037(76)90181-2

Piper, D.Z., Bau, M., 2013. Normalized Rare Earth Elements in Water, Sediments, and Wine: Identifying Sources and Environmental Redox Conditions. Am. J. Anal. Chem. 04, 69–83. https://doi.org/10.4236/ajac.2013.410A1009

Post, J.E., 1999. Manganese oxide minerals: crystal structures and economic and environmental significance. Proc. Natl. Acad. Sci. 96, 3447–3454. https://doi.org/10.1073/pnas.96.7.3447

Rollinson, H.R., 2014. Using Geochemical Data: Evaluation, Presentation, Interpretation. Routledge.

Rudnick, R.L., Gao, S., 2014. Composition of the Continental Crust, in: Treatise on Geochemistry. Elsevier, pp. 1–51.

Ruffet, G., Féraud, G., Amouric, M., 1991. Comparison of 40Ar-39Ar conventional and laser dating of biotites from the North Trégor Batholith. Geochim. Cosmochim. Acta 55, 1675–1688. https://doi.org/10.1016/0016-7037(91)90138-U

Ruffet, G., Féraud, G., Balèvre, M., Kiénast, J.-R., 1995. Plateau ages and excess argon in phengites: an $^{40}Ar/^{39}Ar$ laser probe study of Alpine micas (Sesia Zone, Western Alps, northern Italy). Chem. Geol. 121, 327–343. https://doi.org/10.1016/0009-2541(94)00132-R

Ruffet, G., Gruau, G., Ballèvre, M., Féraud, G., Philippot, P., 1997. Rb/Sr and $^{40}Ar/^{39}Ar$ laser probe dating of high-pressure phengites from the Sesia zone (Western Alps): underscoring of excess argon and new age constraints on the high-pressure metamorphism. Chem. Geol. 141, 1–18. https://doi.org/10.1016/S0009-2541(97)00052-1

Ruffet, G., Innocent, C., Michard, A., Féraud, G., Beauvais, A., Nahon, D., Hamelin, B., 1996. A geochronological and study of K-Mn oxides from the weathering sequence of Azul, Brazil. Geochim. Cosmochim. Acta 60, 2219–2232. https://doi.org/10.1016/0016-7037(96)00080-4

Savin, S.M., Epstein, S., 1970a. The oxygen and hydrogen isotope geochemistry of clay minerals. Geochim. Cosmochim. Acta 34, 25–42. https://doi.org/10.1016/0016-7037(70)90149-3

Savin, S.M., Epstein, S., 1970b. The oyxgen and hydrogen isotope geochemistry of ocean sediments and shales. Geochim. Cosmochim. Acta 34, 43–63. https://doi.org/10.1016/0016-7037(70)90150-X

Savin, S.M., Hsieh, J.C.C., 1998. The hydrogen and oxygen isotope geochemistry of pedogenic clay minerals: principles and theoretical background. Geoderma 82, 227–253. https://doi.org/10.1016/S0016-7061(97)00103-1

Savin, S.M., Lee, M., 1988. Isotopic studies of phyllosilicates, in: Hydrous Phyllosilicates (Exclusive of Micas), Reviews in Mineralogy. Mineralogical Society of America, pp. 189–223.

Segev, A., Lang, B., Halicz, L., 1991. K-Ar dating of manganese minerals from the Eisenbach region, Black Forest, southwest Germany. Schweiz. Mineral. Petrogr. Mitteilungen 71, 101–114. https://doi.org/10.5169/seals-54349

Segev, A., Steinitz, G., Wauschkuhn, A., 1992. Dating of K-bearing manganese minerals - preliminary results. Geol. Surv. Isr. Curr. Res. 7, 39–41.

Shanin, L.L., 1968. The possible use of alunite in K-Ar geochronometry. Geokhimiya 1, 109–111.

Sheppard, S.M.F., Gilg, H.A., 1996. Stable isotope geochemistry of clay minerals. Clay Miner. 31, 1–24. https://doi.org/10.1180/claymin.1996.031.1.01

Sun, S. -s., McDonough, W.F., 1989. Chemical and isotopic systematics of oceanic basalts: implications for mantle composition and processes. Geol. Soc. Lond. Spec. Publ. 42, 313–345. https://doi.org/10.1144/GSL.SP.1989.042.01.19

Taylor, S.R., McLennan, S.M., 1985. The continental crust: its composition and evolution: an examination of the geochem. record preserved in sedimentary rocks, Geoscience texts. Blackwell, Oxford.

Truesdell, A.H., 1974. Oxygen isotope activities and concentrations in aqueous salt solutions at elevated temperatures: Consequences for isotope geochemistry. Earth Planet. Sci. Lett. 23, 387–396. https://doi.org/10.1016/0012-821X(74)90128-9

Turekian, K.K., Holland, H.D., 2014. Treatise on geochemistry. Elsevier Science.

Vasconcelos, P.M., 1999. K-Ar and $^{40}Ar/^{39}Ar$ geochronology of weathering processes. Annu. Rev. Earth Planet. Sci. 27, 183–229. https://doi.org/10.1146/annurev.earth.27.1.183

Vasconcelos, P.M., Becker, T.A., Renne, P.R., Brimhall, G.H., 1992. Age and duration of weathering by ^{40}K-^{40}Ar and $^{40}Ar/^{39}Ar$ analysis of potassium-manganese oxides. Science 258, 451–455. https://doi.org/10.1126/science.258.5081.451

Vasconcelos, P.M., Brimhall, G.H., Becker, T.A., Renne, P.R., 1994a. $^{40}Ar/^{39}Ar$ analysis of supergene jarosite and alunite: Implications to the paleoweathering history of the western USA and West Africa. Geochim. Cosmochim. Acta 58, 401–420. https://doi.org/10.1016/0016-7037(94)90473-1

Vasconcelos, P.M., Renne, P.R., Becker, T.A., Wenk, H.-R., 1995. Mechanisms and kinetics of atmospheric, radiogenic, and nucleogenic argon release from cryptomelane during analysis. Geochim. Cosmochim. Acta 59, 2057–2070. https://doi.org/10.1016/0016-7037(95)00126-3

Vasconcelos, P.M., Renne, P.R., Brimhall, G.H., Becker, T.A., 1994b. Direct dating of weathering phenomena by and K-Ar analysis of supergene K-Mn oxides. Geochim. Cosmochim. Acta 58, 1635–1665. https://doi.org/10.1016/0016-7037(94)90565-7

Winter, J.D., 2014. Principles of igneous and metamorphic petrology, 2nd ed. Pearson new international, Harlow.

Winter, J.D., 2001. An introduction to igneous and metamorphic petrology. Prentice Hall, Upper Saddle River, NJ.

Yapp, C.J., 2000. Climatic implications of surface domains in arrays of dD and $d^{18}O$ from hydroxyl minerals: Goethite as an example. Geochim. Cosmochim. Acta 64, 2009–2025.

Yapp, C.J., 1990a. Oxygen isotopes in iron (III) oxides: 2. Possible constraints on the depositional environment of a Precambrian quartz-hematite banded iron formation. Chem. Geol. 85, 337–344. https://doi.org/10.1016/0009-2541(90)90011-U

Yapp, C.J., 1990b. Oxygen isotopes in iron (III) oxides: 1. Mineral-water fractionation factors. Chem. Geol. 85, 329–335. https://doi.org/10.1016/0009-2541(90)90010-5

Yapp, C.J., Pedley, M.D., 1985. Stable hydrogen isotopes in iron oxides—II. DH variations among natural goethites. Geochim. Cosmochim. Acta 49, 487–495. https://doi.org/10.1016/0016-7037(85)90040-7

Yashvili, L., Gukasyan, R., 1974. Use of cryptomelane for potassium–argon dating of manganese ore of the Sevkar–Sarigyukh deposit, Armenia. Dokl. Earth Sci. 212, 49–51.

Chapter 5

Weathering zone of the vein-type Mn deposits in the Vosges massif (France)

Chapter 5

Weathering zone of the vein-type Mn deposits in the Vosges massif (France)

Hypogene manganese deposits occur in several locations in the Vosges (NE France) and Black Forest (or Schwarzwald, SW Germany) massifs both of them being located on the flanks of the Upper Rhine Graben (URG; ►Figs 5.1a and b; Fluck and Weil, 1976). Mn-bearing veins are exclusively structure-related and are formed in close relation with the activation and the reactivation of crustal faults inherited from the Variscan orogenic cycle. These faults are reactivated during the Jurassic hydrothermalism phase and during the Cenozoic rifting (Fluck and Weil, 1976). The Vosges and Black Forest regions have a long and rich mining heritage, particularly for base metals (Ag-Co-Cu-Fe-Mn-Mo-Sb-As-Pb-Zn-Ba-F; ►Fig. 5.1b), which are reported in two main historic periods: (1) the "golden age" of silver through the Middle Ages (10^{th}-15^{th} century); and (2) the recovery of base metal mining during the Renaissance (16^{th}-17^{th} century; Fluck and Weil, 1976; Fluck and Ancel, 1989). Mining activity in the 19^{th} and 20^{th} century focused on Fe and associated elements such as Mn, As, Ag, Cu, Pb, Sb, Ba and F.

These massifs correspond to the same portion of the Variscan orogenic belt (►Fig. 5.1a). The Lalaye-Lubine and Baden-Baden Fault Zone are respectively located to the north of the Vosges and Black Forest, and define the Saxothuringian-Moldanubian boundary (►Figs. 5.1a and b; Wickert and Eisbacher, 1988; Wickert *et al.*, 1990). Lower Paleozoic and Post-Devonian formations are quite similar between the massifs, but Precambrian and some intrusive rocks could be significantly different between them (►Fig. 5.1b). Late granites, and especially two-mica granites, as well as microgranites and lamprophyres, show strong similarities. The nearly perfect geomorphological symmetry of the Vosges and the Black Forest on the shoulders of the Upper Rhine Graben (►Fig. 5.1c) is due to extensive uplift associated with a continental rifting during the Cenozoic (Illies and Fuchs, 1974; Ziegler, 1992; Prodehl *et al.*, 2006) that exposes rocks to weathering agents. The evolution of the Cenozoic URG was controlled by a repeatedly changing stress field and the reactivation of a complex set of crustal discontinuities originating from the Carboniferous-Permian Variscan orogeny (►Fig. 5.1b; Illies, 1978; Schumacher, 2002; Hinsken *et al.*, 2007). These structures are particularly reactivated during the late Eocene and the early Oligocene. Shifting of the Baden-Baden Shear Zone in the Black Forest massif 40 km northward of its western equivalent (the Lalaye-Lubine Shear Zone) is another effect of the NW-SE development of the URG (►Fig. 5.1b; Edel *et al.*, 2007). Mineralizing events are mostly related to these two geodynamic phases. However, the timing is poorly documented but seems to be associated with the activation or the reactivation of major fault systems (►Fig. 5.1b; Fluck and Weil, 1976; Autran *et al.*, 1980; Edel *et al.*, 2007).

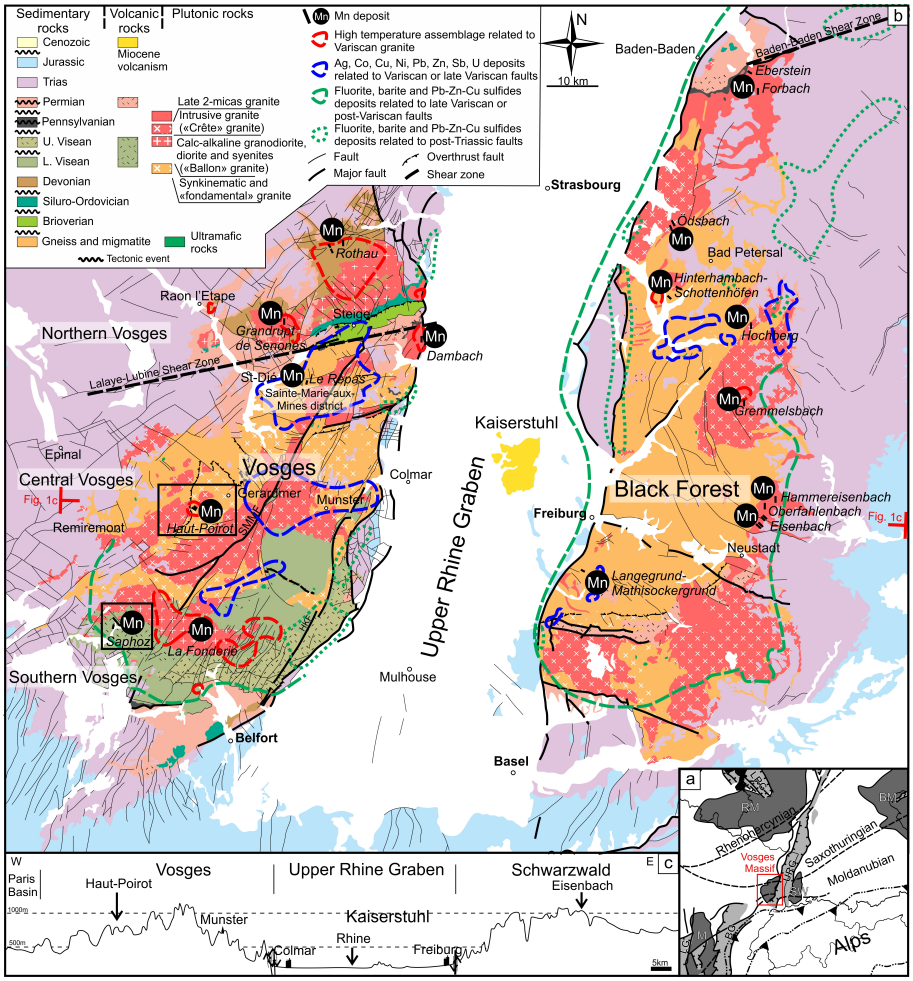

►**Fig. 5.2 a.** Location of Vosges and other Variscan massifs of Western Europe (modified after Dèzes *et al.*, 2004). URG: Upper Rhine Graben; LRG: Lower Rhine Graben; SW: Black Forest; BM: Bohemian Massif, RM: Rhenish Massif; BG: Bresse Graben; MC: Massif Central; LG: Limagne Graben. **b.** Metallogeny map of Vosges and Black Forest massifs, and the location of reported manganese deposits (modified after Fluck and Weil, 1976). SMMF=Sainte-Marie-aux-Mines Fault, HKF=Hunsruck-Kohlschlag Fault. **c.** Simplified cross section of Vosges, Upper Rhine Graben and Black Forest, showing the nearly perfect symmetry between Vosges and Black Forest massifs.

As these geological settings imply great vertical movements of the Vosges and the Black Forest massifs in relation with the dawn of the Rhine Graben rifting during the Cenozoic, it seems relevant to investigate some of these deposits to depict traces of weathering, sometimes forming a gossan onto primary manganiferous carbonate and silicate ores (see chapter 3). Mn deposits in the Black Forest have been investigated by Segev *et al.* (1991, 1992) and Hautmann and Lippolt (2000), who have

provided K-Ar and $^{40}Ar/^{39}Ar$ dating insights to mineralization and weathering processes, respectively. Because similar studies are lacking in the Vosges massif and considering the close evolution of these two massifs, a careful assessment on how weathering processes may have affected some of these deposits seemed necessary. In that order, this chapter focuses on two historical and important Mn deposits located in the Vosges mountain: the Mn(-W) Haut-Poirot and Mn-Fe Saphoz deposits (Lougnon, 1981). Therefore, the following paragraphs will focus on the mineralogy, petrology and geochemistry of these deposits in order to identify the processes responsible for Mn concentration, and especially the potential supergene imprint affecting them. Secondly, I consider the relative timing of these deposits regarding the common geodynamic evolution of the Vosges and Black Forest.

5.1 Geological background

Large granitoid intrusions were emplaced in the Vosges (and Black Forest) during the Variscan orogenic cycle in an interval roughly ranging from 370 to 310 Ma (►Fig. 5.2; e.g., Segev *et al.*, 1991; Tabaud *et al.*, 2015). Two major late Visean NE-SW trending faults are activated, the Sainte-Marie-Aux-Mines (SMMF) and Hunsruck-Kohlschlag faults (HKF, ►Fig. 5.1b; Fluck, 1980; Fluck *et al.*, 1991), along which late granite formed between 330-320 Ma (Hameurt, 1967; Schaltegger *et al.*, 1999; Kratinová *et al.*, 2007; Tabaud, 2012). These faults host numerous Cu-Pb and associated base metal deposits, whereas granite intrusions present high temperature mineral assemblages (►Fig. 5.1b; Fluck and Weil, 1976). During the Variscan orogeny, the Central and Southern Vosges (►Fig. 5.1b) were also characterized by Visean sedimentary and volcano-sedimentary basins. The end of plutonism is marked by acid hypothermal veins of leucogranite (i.e., Kagenfels) containing disseminated Sn and F, in association with W-skarns and Fe veins (von Eller and Sittler, 1974; Fluck and Weil, 1976; Boutin *et al.*, 1995; Hess *et al.*, 1995). The final stage of the Variscan orogeny corresponds to a Late Carboniferous-Permian relaxation and collapse of the whole belt that brings extensional pulses coupled with a high asthenosphere heat flow (Wilson *et al.*, 2004). Thick series of Rhyolite and tuff were formed at ~294–299 Ma (Hess and Lippolt, 1986) to the North and South of the Lalaye-Lubine Shear Zone (►Fig. 5.1b; (von Eller and Sittler, 1974; Tabaud, 2012). This post-Variscan phase could be responsible for numerous mineralization in the Black Forest (►Fig. 5.2; Segev *et al.*, 1991).

The Mesozoic was a period of relative tectonic quiescence characterized by up to 1500 m of Triassic to Jurassic sediments accumulated on the Variscan basement after the Permian-Triassic peneplain (►Fig. 5.2; Geyer *et al.*, 2011). K-Ar dating of diagenetic illites (Bonhomme *et al.*, 1983; Liewig *et al.*, 1987; Liewig, 1993; Clauer *et al.*, 1996) and magnetic overprinting on Triassic sandstones also indicate a

hydrothermal activity by the Early Jurassic (Edel, 1997; Tournier *et al.*, 1999). An important part of intermediate to low temperature base metal and Fe-Mn mineralization (►Fig. 5.2; Fluck and Stein, 1992) occurred along basement faults during the Early Jurassic subsidence, which constitutes an indirect effect of the break-up of Pangea at that time (►Fig. 5.1b, Edel, 1997; Wernicke and Lippolt, 1997; Wetzel *et al.*, 2003). The lack of Cretaceous to Paleocene deposits is due to an emersion period induced by a large-scale domal uplift since the end of the Jurassic (►Fig. 5.2; Illies, 1977; Geyer *et al.*, 2011). Red siderolithic formations and residual clays document lateritic and karstic weathering of Mesozoic platform carbonates under a humid tropical climate by the Eocene (Fluck and Weil, 1976). The first pebbles derived from the Vosges basement are observed in early Rupelian sediments, indicative of uplift of the Southern Vosges at that time (Picot *et al.*, 2005). However, the main Cenozoic exhumation of the Vosges and Black Forest started in the Burdigalian (Laubscher, 1992) and continued progressively until the early Pliocene (e.g., Dèzes *et al.*, 2004; Berger *et al.*, 2005a, 2005b). This uplift is attributed to folding of the entire lithosphere (Dèzes *et al.*, 2004). Post-Variscan metal-bearing faults (Pb, Zn, Cu, Ba, F and Fe) are mainly associated with Cenozoic rifting (Fluck and Weil, 1976; Fluck and Stein, 1992) during which Carboniferous NE-SW faults were reactivated, in and at the edge of the Vosges and Black Forest massifs (►Fig. 5.2; e.g., Edel *et al.*, 2007).

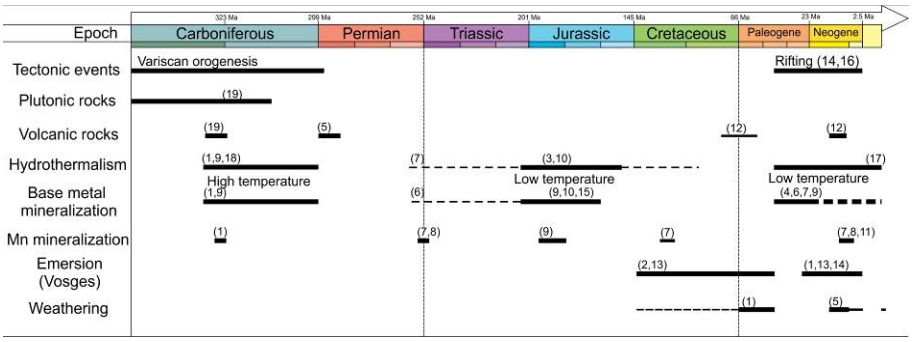

►**Fig. 5.2** Time-event chart for the Vosges area (including data from the Black Forest and Upper Rhine Graben). e.g. (1) (Fluck and Weil, 1976), (2) (Illies, 1977; Geyer *et al.*, 2011), (3) (Bonhomme *et al.*, 1983; Boulay, 1984; Liewig *et al.*, 1987; Clauer *et al.*, 1996; Tournier *et al.*, 1999; Wetzel *et al.*, 2003), (4) (Gutierrez Lanz, 1985), (5) (Hess and Lippolt, 1986), (6) (Rabenandrasana, 1989), (7) (Segev *et al.*, 1991), (8) (Segev *et al.*, 1992), (9) (Fluck and Colas, 1992; Fluck and Stein, 1992), (10) (Edel, 1997), (11) (Hautmann and Lippolt, 2000), (12) (Keller *et al.*, 2002; Prodehl *et al.*, 2006), (13) (Quesnel, 2003), (14) (Dèzes *et al.*, 2004; Berger *et al.*, 2005a), (15) (Edel *et al.*, 2007), (16) (Hinsken *et al.*, 2007), (17) (Baillieux *et al.*, 2013), (18) (Edel *et al.*, 2013), (19) (Tabaud *et al.*, 2014, 2015).

5.2 The Vosges and Black Forest base-metal districts

As previously explained, the common evolution of the Vosges and Black Forest has led to consider their metallogenic features together (Fluck and Weil, 1976; Fluck and Stein, 1992). Sedimentary deposits are missing in the Paleozoic series and occur only in the Mesozoic cover: Triassic uranium and coal deposits (Southern Vosges), Jurassic evaporites (Vosges and Black Forest) and Fe-oolithe (Black Forest), and K-rich basins (Rhine Valley; ►Fig. 5.1b).

Structure and/or magmatic-related are the most common deposits, but their complexity has made a clear classification between the two regions difficult. Based on structural interactions, Fluck and Weil (1976) proposed these deposits to be associated directly to plutonic rocks (red dashed lines in ►Fig. 5.1b) or post-Triassic faults that clearly cross over the Triassic cover or follow the flanks of the Upper Rhine Graben (Ba, Ba-Fe, F and quartz veins; green dotted lines in ►Fig. 5.1b; Boulay, 1984; Gutierrez Lanz, 1985; Rabenandrasana, 1989). Some Cu-Bi vein deposits could be Permo-Triassic (Rabenandrasana, 1989), whereas Pb-Zn-Cu-Ba-F veins are restricted to Lutetian and/or Oligocene (early Rupelian), both originating from surficial mixing brines (►Fig. 5.1b; Gutierrez Lanz, 1985; Rabenandrasana, 1989). However, most of the tectonic-related veins are randomly distributed. Actually, their source could be related to three periods: Variscan (blue dashed lines in ►Fig. 5.1b), post-Variscan (green dashed lines in ►Fig. 5.1b) or post-Triassic (green dotted lines in ►Fig. 5.1b). Although Co-U, Sb, Pb-Ba, Pb-F, Cu-Ba, Ba, F, S and Mn deposits are quite similar between the Vosges and Black Forest, it is not possible to correlate Cu-Ag and Pb-Ag deposits of Sainte-Marie-aux-Mines to other Pb-Ba, Cu-Ba or Pb-F deposits in the Black Forest (Fluck and Colas, 1992).

One can see that the timing of the numerous ore veins has long been unclear, mainly because of the lack of datable materials. However, several hydrothermal events reported in the area may be responsible for mineral deposition in veins (principal references are included in ►Fig. 5.2):

- The Carboniferous is associated with a magmatic-metallogenic period (330-280 Ma) corresponding to a high temperature hydrothermal activity. This phase is recognized in the “Ballons” (SVG Mg-K) and “Brézouard” (CVG) granite (Fluck and Stein, 1992) as well as in other Variscan massifs and is connected to intensive, short-duration endogenic processes. It is responsible for late granitoid rocks and related Sn-W associations (Thomas and Tischendorf, 1987). Sn, W, Mo, Cu, Fe, Mn, Au (red dashed lines in ►Fig. 5.1b) occurring in late two-mica granite are also related to magmatic bodies (Fluck and Weil, 1976).

- Early Jurassic is probably the most prominent mineralizing event recorded along basement faults in the Vosges and Black Forest massifs (Clauer *et al.*, 1996). Four successive pulses characterize this activity around 200 Ma, 180 Ma, 170 Ma and 150 Ma. Hydrothermal activity is synchronous with episodes of enhanced subsidence. As large parts of Europe were affected by an extensional stress regime, it is suggested that hydrothermal activity and subsidence resulted from extension, and pre-existing faults became reactivated (e.g., Wetzel *et al.*, 2003). The granitoid rocks register temperature of mineralizing fluids up to 230 °C (e.g., Clauer *et al.*, 1996 and reference therein).
- The Cenozoic witnesses a higher temperature magmatic-metallogenic activity in relation to rifting and reactivation of crustal faults (Fluck and Weil, 1976; Segev *et al.*, 1991; Fluck and Stein, 1992).
- Recent low temperature hydrothermalism is still present with temperatures of about 140–160°C (e.g., Boulay, 1984; Gutierrez Lanz, 1985; Rabenandrasana, 1989; Clauer *et al.*, 1996) leading to geothermal activity in the Upper Rhine Graben (Baillieux *et al.*, 2013).

The Permian (280-260 Ma) could additionally correspond to the initiation a of long duration low temperature hydrothermal activity, responsible for barite-fluorite mineralization in the Black Forest as mentioned by Segev *et al.* (1991) and reference therein. A shorter hydrothermal episode could also be reported in the Cretaceous (130-110 Ma), characterized by higher temperature fluids (Segev *et al.*, 1991; Wetzel *et al.*, 2003).

Emersion periods from Cretaceous to Paleocene (Illies, 1977; Geyer *et al.*, 2011) suggest weathering processes to be recorded in the Vosges and Black Forest areas. However, the first clear signs of weathering are reported during early Eocene in the Vosges massif (Fluck and Weil, 1976) and Miocene in Black Forest (Segev *et al.*, 1991; Hautmann and Lippolt, 2000), in relation with the Upper Rhine Graben rifting, and subsequent uplift of the two massifs, leading to the formation of Fe or Mn gossans (Fluck and Weil, 1976).

5.3 The Mn(-W) Haut-Poirot deposit

Between 1890 and the end of the Second World War, the Haut-Poirot deposit intermittently provided 60 tons of metallurgic manganese ores with grades of 45–46 wt. % Mn (Lougnon, 1981). Nowadays, the manganese and related tungsten occurrences have no more economic significance, due mainly to their restricted extension and poor accessibility. The veins are located in the Haut-Poirot and Lyris woods in the Central Vosges massif (►Figs. 5.1b), 7 km Westward of Gérardmer

(►Figs. 5.1c). They are hosted in biotite (south) and two-mica granite (north), part of the Central Vosges Granites (CVG; Tabaud *et al.*, 2015).

5.3.1 Distribution and style of mineralization

Mn(-W)-rich quartz-hosted veins are located in the Haut-Poirot and Lyris woods in the Central Vosges Mountain, 7 km westward of Gérardmer (France), along "Le Roulier" stream (►Fig. 5.3). Ore veins outcrop in several underground mines or in waste dump ore, but most of them are currently flooded or filled by various material. The mineralized veins are hosted in two different S-type Central Vosges Granite (CVG, Tabaud *et al.*, 2015): a biotite- and sometimes actinote-rich Fondamental granite on the left side of the stream, and two-mica Remiremont granite on the right side (►Fig. 5.3, Fluck and Weil, 1976). These granites host numerous veins of quartz, red chalcedony and barite nearby of the Straiture-Cellet overthrust zone, 500 meters westward of the ore deposits (►Fig. 5.3). The orebodies form two subparallel veins with direction N110° to N140° (Hameurt *et al.*, 1979) associated with a mylonite zone and a hematite-rich quartz vein (►Fig. 5.3; Lougnon, 1981). Vein 1 is ~600 m long with a thickness ranging from 1 to 0.4 m and a dip angle of 80° N (Hameurt *et al.*, 1979). The thickness of the ore decreases with depth to reach 0.2 m at 20 meters beneath the surface (Lougnon, 1981). The second vein is subdivided in two segments with a thickness of about 0.4 m (Bonhomme, 1958; Lougnon, 1981).

Field observations show that the Haut-Poirot manganese deposit is characterized by a tectonic breccia in contact with the main ore vein (►Figs. 5.4a, b and c). Fragments originate from the granite and are filled by a manganiferous matrix composed of well-developed crystals of pyrolusite associated to braunite (►Figs. 5.4c, d and e). The same association characterizes the main ore vein. Gangue minerals are quartz and large crystals of translucent barite (►Figs. 5.4d and e). Several studies also report tungsten and uranium anomalies. Tungsten forms scheelite crystals or is incorporated in hollandite minerals (~0.7%) in the ore and the granite walls. Secondary minerals of autunite, metachalcocite and francevillite, containing uranium metal, are hosted in hollandite minerals or in granite fractures (Jurain, 1956; Bonhomme, 1958; Weil *et al.*, 1959). Mn calcite and trace amounts of bornite and chalcocite are observed by Lougnon (1981). Weil *et al.* (1959) recognized three stages of ore formation: (1) an iron stage characterized by the formation of small crystals of hematite, (2) a quartz phase linked to a first brecciation episode, according to the occurrence of the hematite-rich quartz vein, and (3) a manganese phase characterized by the successive crystallization of braunite-manganite-pyrolusite, and then barite. The whole ore is brecciated several times.

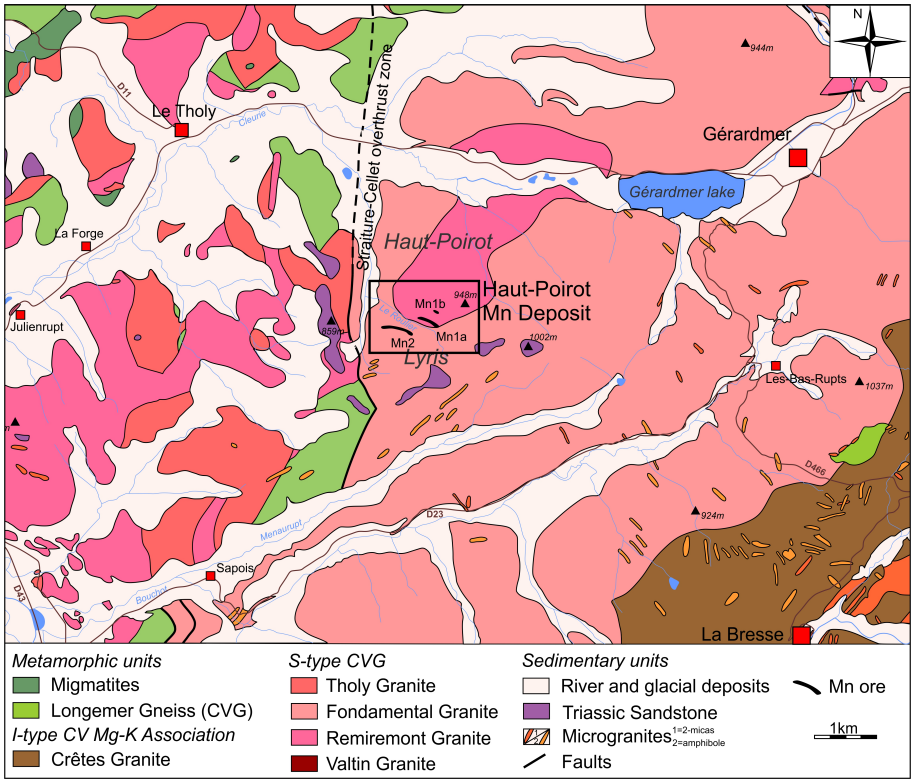

►**Fig. 5.3** Geological map of the studied area and location of the Haut-Poirot deposit (Ménillet and Fluck, 1978; Hameurt *et al.*, 1979).

5.3.2 Material and methods

During the years 2012 and 2014, we investigated the second ore vein (Mn2 in ►Fig. 5.3) in four well-preserved galleries. Galleries in the first vein (Mn1) have probably been filled in during past decades or poorly explored in ancient works. We have collected 64 samples of various materials (granite, veins and breccia), performed 31 X-ray diffraction patterns, 7 scanning electron microscope observations, 9 geochemical analyses (major and trace elements) and prepared 2 thin sections of the host rock.

5.3.3 Results

5.3.3.a Mineralogy and petrography

The refinement of the mineralogy and the petrography of the granite host rock and manganese ores were investigated by light microscopy, electron microscopy and powder XRD.

- *Host rock granite*

The Fondamental and Remiremont granites, redefined as the Central Vosges Granites (Tabaud *et al.*, 2015), are characterized by biotite or muscovite-biotite assemblages. They occupy the major part of the Vosges Mountain (Hameurt *et al.*, 1979) and are separated by the striking Sainte-Marie-aux-Mines Fault (►Fig. 5.3). They correspond to K-rich S-type granite dated between 330 and 320 Ma (e.g., Tabaud *et al.*, 2015), which follow the first magmatic event at 340 Ma registered in the Vosges massif (Schaltegger *et al.*, 1999; Kratinová *et al.*, 2007). The Fondamental granite is gray showing a porphyroid texture subdivided in different subtypes corresponding to two reservoirs: biotite and actinote-biotite granites. The Remiremont granite corresponds to a light-gray muscovite and biotite granite. Petrographic observations corroborate the descriptions made by Hameurt *et al.* (1979), where no signs of contamination by the Mn ores are observed in the Fondamental granite (►Fig. 5.5a). However, in brecciated ore zones, small concentrations of La-arsenate, though to be La-kemmlitzite ($[Sr,Ce]Al_3[AsO_4][SO_4][OH]_6$) and colloform hematite are disseminated in the host granite. Fe oxides and hollandite group minerals replace some of the biotite (►Fig. 5.5b) while pyrolusite appears in veinlets close to the Mn-ore veins. Rutile and ilmenite occur in fresh biotite.

- *Manganiferous veins*

The structure-related veins of the Haut-Poirot deposit records distinct pulses of ore deposition, brecciation and remobilization. The main outcome, regarding the mineralogy of the ore, is the near absence of Fe oxides and the occurrence of W-rich minerals in the main Mn ore vein. The mineral composition of manganiferous ore is relatively homogeneous with the dominance of pyrolusite (►Fig. 5.4d, 5c) and braunite (►Fig. 5.4e, 5d) associated with amounts of hollandite *sensu stricto* (►Fig. 5.5c) and scheelite (►Fig. 5.5d). The ore veins are often brecciated themselves and cemented by quartz, manganoan calcite and likely hausmannite (►Fig. 5.5e). These veins also display spherules composed of braunite and barite containing small crystals of scheelite (►Fig. 5.5f). A thin rim of hausmannite (?) is associated with these minerals (►Fig. 5.5f). Formation of spherules could be related to the boundaries of mineral grains as it is observed on K-feldspar of the wall-granite (►Fig. 5.5g). The following paragraphs summarize the observation made on the main ore-forming minerals.

Braunite is a widespread Mn silicate in manganese ore deposits (Maynard 2010). The most common variety is braunite with ideal formula $Mn^{2+}Mn^{3+}{}_6SiO_{12}$ containing 8–10 wt. % SiO_2 (de Villiers, 1975; Moore and Araki, 1976), whilst braunite II ($Ca_{0.5}Mn^{3+}{}_7SiO_{12}$) shows only 4–5 wt. % SiO_2 (de Villiers and Herbstein, 1967; de Villiers, 1980). Neltnerite is $CaMn^{3+}{}_6SiO_{12}$ (Baudracco-Gritti *et al.*, 1982; Baudracco-Gritti, 1985). The Haut-Poirot deposit contains braunite with little amount of CaO (1–2 wt. %) and Al_2O_3 (~1 wt. %), but high SiO_2 content (7–10 wt. %) in SEM-EDS measurements. This mineral systematically shows Ca-F-arsenate inclusions (►Fig. 5.5h), especially in brecciated samples. The chemical composition corresponds to svabite ($Ca_5[AsO_4]_3F$). It occurs as homogeneous masses (►Fig. 5.5d) with euhedral crystals (►Fig. 5.5d, f, g) or replacement of micas and K-feldspar in the wall-granite (►Fig. 5.5g). Braunite also replaces quartz grains (►Fig. 5.6a). In some cases, braunite is replaced and crisscrossed by pyrolusite and hollandite veins (►Fig. 5.6a) as already observed by Weil *et al.* (1959).

Pyrolusite (MnO_2) is easily identified in the field by its silver brightness and brilliance (►Fig. 5.4d, e). It forms colloform textures (►Fig. 5.6b) showing the typical palisade texture (►Fig. 5.5c) in the core of quartz geodes and veins (►Fig. 5.6c). The latter is characterized by enrichment in tungsten (~1–2 wt. % WO_4). Pyrolusite occurs in thin veinlets in the wall granite, where it often replaces biotite and K-feldspar (►Fig. 5.6d). Pyrolusite probably results from manganite alteration (Weil *et al.*, 1959).

Scheelite ($CaWO_4$) is observed in the center of Mn veins as small euhedral crystals (►Fig. 5.5d). These crystals grow onto the wall-granite and braunite. Scheelite could contain some Mo (Weil *et al.*, 1959). Wolframite is not observed.

Hollandite *sensu stricto* ($BaMn_8O_{16}$) is observed as small impregnations and filaments in braunite (►Fig. 5.6a, b) but mostly in pyrolusite crystals and fractures (►Fig. 5.5c, 6c). It rarely forms large crystals or masses compared to other Mn-bearing minerals. Larger specimens are composed of numerous needles oriented to the center of veinlets (►Fig. 5.6e). Its composition shows mainly barium with small W concentrations. This W-rich hollandite is sometimes called “tungomelane” for its unusual content in tungsten (Picot and Johan, 1982). Small needles of Pb-rich hollandite are also observed in Mn-rich calcite cement. In the brecciated ore zone, W-rich hollandite (►Fig. 5.5b), Pb-rich hollandite and/or coronadite replace biotite crystals and pyrolusite. Some pyrolusite crystals replace Pb-rich hollandite (►Fig. 5.6f): Pb-rich hollandite forms colloform texture enclosed in W-rich pyrolusite; hollandite might be the former mineral because in case of replacement of pyrolusite by hollandite, we could expect hollandite to be formed along cleavages or fractures, not as colloform. W- and K-rich hollandite and then manganoan calcite grow onto the former pyrolusite crystals (►Fig. 5.6g).

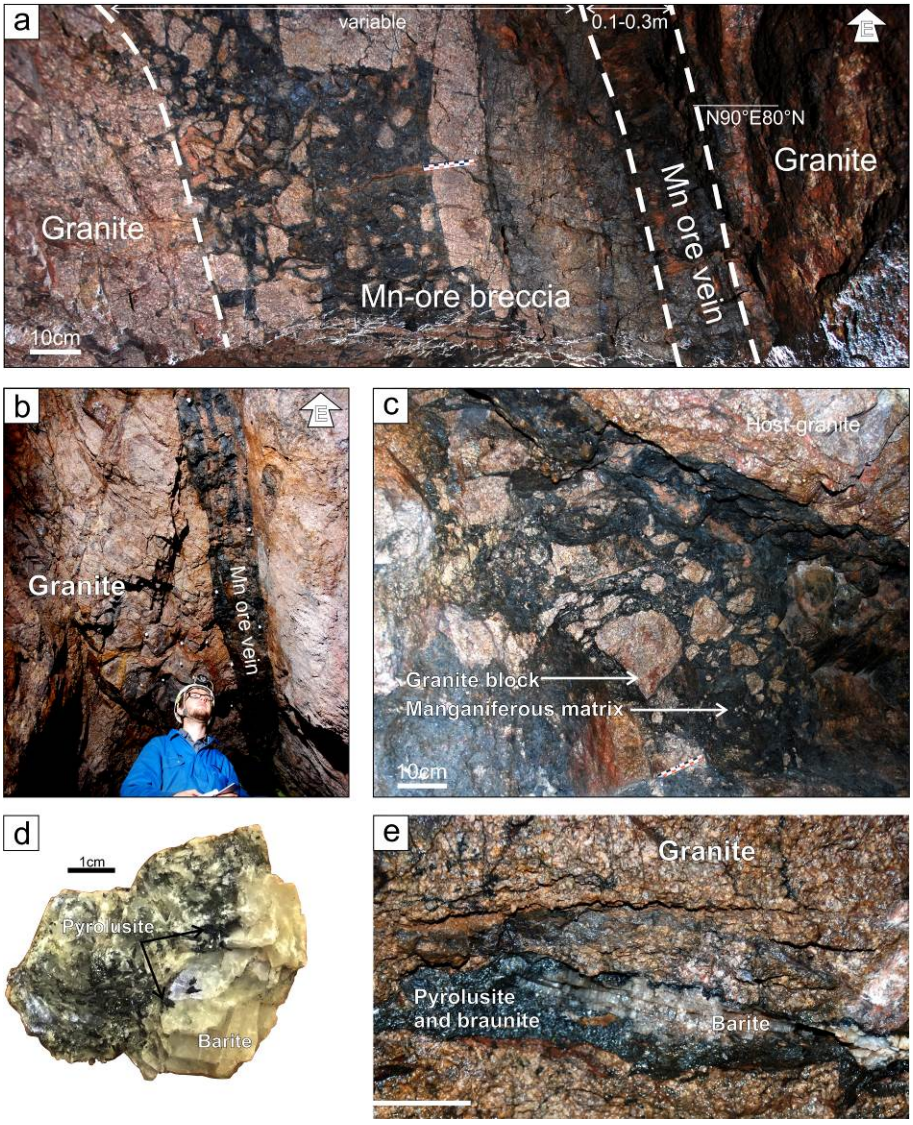

►**Fig. 5.4** Underground exposures and field relationships of Mn veins. **a.** Main ore vein and the associated manganiferous breccia. **b.** Main ore vein in the wall granite. **c.** Granite blocks cemented by a manganiferous matrix in the brecciated zone. **d.** Hand specimen of well-developed crystals of pyrolusite embedded in large crystals of translucent barite. **e.** Pyrolusite and braunite vein cemented by large barite crystals.

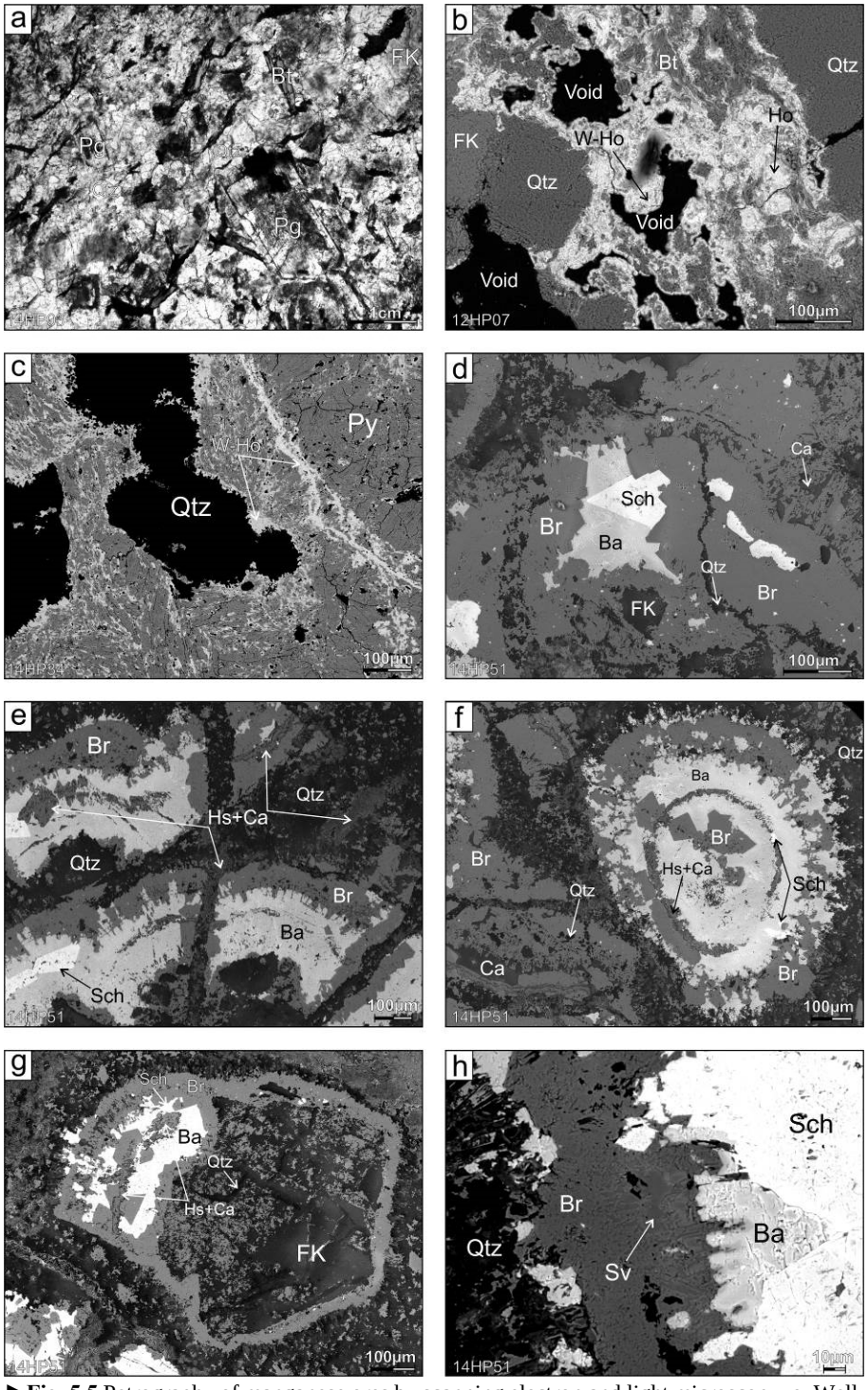

►**Fig. 5.5** Petrography of manganese ores by scanning electron and light microscopy. **a.** Well-

developed crystals of biotite, plagioclase, K-feldspar and quartz in the Fondamental granite. **b.** Biotite crystals replaced by W-hollandite minerals. **c.** Replacement texture of pyrolusite by W-rich hollandite *s.s.* **d.** Replacement texture of K-feldspar by braunite. Successive crystallization of scheelite and barite onto braunite crystals. Brecciation of the braunite crystals cemented by manganoan calcite and quartz. **e.** Secondary brecciation of the former braunite, barite and scheelite by quartz, hausmannite and manganoan calcite. **f.** Spherule of braunite, barite and scheelite partly replaced and brecciated by manganoan calcite and hausmannite. **g.** Partial replacement of K-feldspar by braunite and subsequent brecciation and cementation of braunite by quartz, hausmannite and manganoan calcite. **h.** Replacement texture of braunite by svabite. Bt=biotite; Pg=plagioclase; FK=K-feldspar; Qtz=quartz; Ho=hollandite; Py=pyrolusite; Br=braunite; Sch=scheelite; Ba=barite; Ca=manganoan calcite; Hs=hausmannite; Sv=svabite.

Hausmannite ($Mn^{2+}Mn^{3+}{}_2O_4$) naturally occurs only in hydrothermal manganese deposits (Hewett, 1972). In the Haut-Poirot deposit, hausmannite does not contain any iron, contrary to most of hausmannite of hydrothermal origin (Frenzel, 1980). It forms small veinlets with Mn calcite cement (►Fig. 5.5e, f, g). These veinlets cross over the previous formed minerals (braunite, pyrolusite, barite) leading to a second breccia. Hausmannite also occurs in the center of well-developed manganiferous veins or in spherules (►Fig. 5.5e, f, g).

Gangue minerals are mainly quartz and barite. Quartz forms small euhedral crystals in geodes or on the border of thin veins onto which W-rich pyrolusite and hollandite form (►Fig. 5.6c). Barite fills most of the geodes and encloses pyrolusite and scheelite with large euhedral crystals (►Fig. 5.4e, 5d). Barite also grows onto quartz veins. Chalcedony has been reported by Weil *et al.* (1959) as well as the replacement of barite by quartz.

5.3.3.b Geochemistry

Host granite geochemistry is typical for peraluminous S-type granite with enrichments in Al_2O_3 compared to CaO, Na_2O and K_2O (Aluminum Saturation Index>1, Shand, 1927). The presence of manganese (450 ppm) in this granite is close to the mean value of granitoid rocks (390–700 ppm) referred in Li (2000), as well as the Mn/Fe ratio (►Table 5.1) calculated by Maynard (2014). The latter together with the dominance of FeO (Fe^{2+}) relative to Fe_2O_3 (Fe^{3+}) indicate that manganese may substitute to reduced iron in mafic minerals. Hence, granite collected in the Haut-Poirot wood does not show any strong contamination in manganese. REE pattern of the Fondamental granite is also typical of granitoid rocks characterized by a negative anomaly in Eu (Eu_N/Eu_N*=0:31) and a general enrichment of total REE (∑REE=273.83 ppm). HREE are relatively low compared to LREE (La_N/Lu_N=20.52), showing an asymmetric pattern (►Table 5.2).

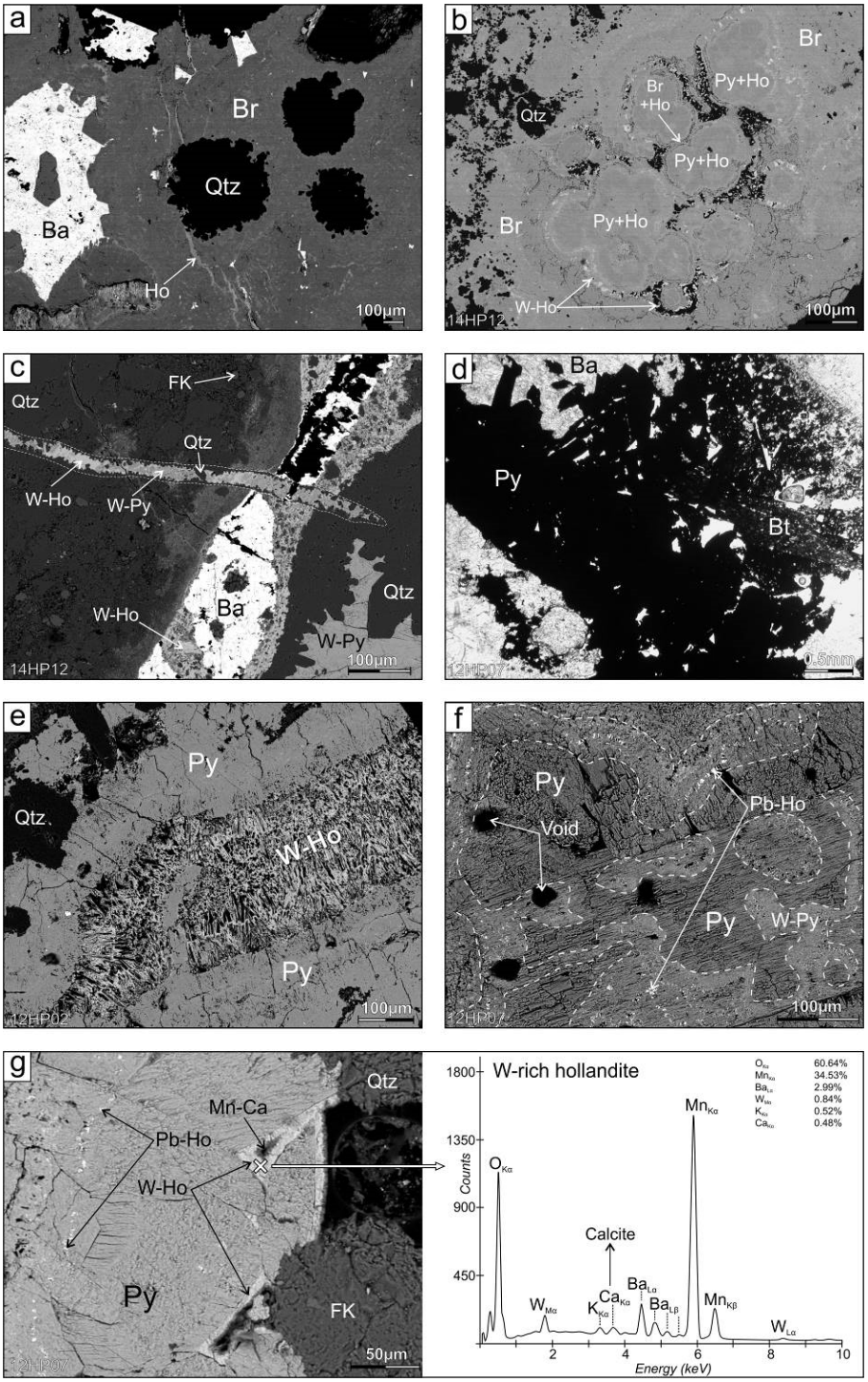

►**Fig. 5.6** Petrography of manganese ores by scanning electron and light microscopy.

a. Replacement of quartz by braunite, and alteration of braunite by hollandite *s.s.* **b.** Colloform pyrolusite and hollandite replacing braunite. **c.** Hollandite and barite vein crossed by a veinlet composed of quartz on the border and W-rich pyrolusite in the center. W-rich hollandite replaces pyrolusite. Note that pyrolusite fills small geodes of quartz. **d.** Replacement of biotite by pyrolusite. Barite occurs as cement between pyrolusite crystals. **e.** Vein composed of pyrolusite on the border and small needles of W-rich hollandite in the center. **f.** Replacement of Pb-rich hollandite by pyrolusite. The former crystals of Pb-hollandite conserve their colloform texture (dashed lines) and are delimited by W-rich pyrolusite. **g.** Replacement of Pb-rich hollandite by pyrolusite, and successive growing of W-rich hollandite (with EDS spectra) and Mn-calcite onto pyrolusite crystals. See caption of ►Fig. 5.5 for abbreviations.

►**Table 5.1** Major element geochemistry (in wt. %) of the granite host rock, main ore vein and brecciated ore vein of the Haut-Poirot deposit. Data for major elements were determined by fusion ICP-MS, FeO by titration and SO_4 by infrared spectrometry (see chapter 4). - = not analyzed.

Sample	**14HP03**	**14HP12a**	**14HP16**	**14HP34**	**14HP37**	**14HP12b**	**14HP51**
Location	Eastern Gallery	Ore vein n°2					
Type	Granite	Main ore vein				Brecciated ore vein	
SO_4	-	-	-	1.9	1.4	-	-
SiO_2	69.96	8.14	3.87	7.26	12.39	78.55	46.63
Al_2O_3	14.90	0.45	0.83	1.15	0.83	4.48	4.30
Fe_2O_3	0.35	0.08	0.14	0.55	0.11	0.74	0.55
FeO	1.70	<0.1	<0.1	<0.1	<0.1	<0.1	<0.1
MnO	0.05	69.57	72.02	69.64	69.72	8.81	29.84
MgO	0.98	0.02	0.03	0.04	0.04	0.12	0.31
CaO	0.96	0.84	0.43	0.24	0.56	0.14	4.36
Na_2O	3.05	< 0.01	0.03	0.02	0.01	0.09	0.06
K_2O	6.33	0.01	0.07	0.16	0.06	2.70	2.38
TiO_2	0.42	0.01	0.01	0.01	0.01	0.08	0.05
P_2O_5	0.39	0.03	0.08	0.04	0.07	0.04	0.07
LOI	0.89	6.53	12.35	12.06	8.99	2.15	5.56
Total	100.20	85.69	89.87	91.18	92.81	97.91	94.12
$Fe_2O_{3(t)}$	2.24	0.09	0.15	0.56	0.12	0.75	0.56
Mn/Fe	0.02	962.91	569.61	140.20	701.81	13.18	60.08

Pure Mn ores of the Haut-Poirot deposit are logically characterized by a high grade in MnO (69.57-72.02 wt. %), SiO_2 (3.87-12.39 wt. %), W (0.48-0.89 wt. %), Cu (0.05-0.25 wt. %), with low P_2O_5 (0.03-0.08 wt. %) and Fe_2O_3 (0.08-0.14 wt. %, Tab. 1, 3). Tungsten enrichment is a peculiar feature of the Haut-Poirot deposit compared to other Mn deposits in the Vosges (Lougnon, 1985). Transition metals such as As and Sb could be significantly enriched to thousands of ppm, and U to hundreds of ppm in (►Table 5.3). One sample shows very high content in REE (up to 0.1 REE wt. %, ►Table 5.2). Tungsten forms scheelite but can also be accommodated in pyrolusite and hollandite (►Fig. 5.6c, e). Arsenic is mainly expressed in svabite (►Fig. 5.5h). Neither Cu nor Sb are identified in any of the ore-forming minerals and are then probably disseminated as substitution elements or form bornite and chalcocite as mentioned by Lougnon (1981). U-bearing minerals, such as autunite, metachalcocite and francevillite (Jurain, 1956; Bonhomme, 1958; Weil *et al.*, 1959) could contain U, but none of these minerals have been observed. U-minerals could be

related rather to the host granite than the ore veins (Lougnon, 1985). The geochemical signature of the ore is typical of hydrothermal deposits: As-Cu-Mo-Pb-V-Zn (►Fig. 5.7a) and W are strongly enriched, whereas Ni and Co are depleted (►Fig. 5.7a, b; Moorby and Cronan, 1983; Nicholson, 1992). Mn/Fe ratios are very high and reduced iron (FeO) is under the detection limit in all analyses (►Table 5.1). REE patterns of Mn ores are characterized by a general enrichment in REE (∑REE=111-1037 ppm, ►Table 5.2) and a strong negative anomaly in Eu (Eu_N/Eu_N*=0:31). From Sm to Lu, MREE and HREE follow the granite trend, although MREE are much more enriched in some ore samples. One can see here the effect of relatively high content in Ba (Cao *et al.*, 2001). The REE pattern in the ore strongly differs from that of the host granite, particularly regarding the LREE content. This is marked by a decrease in LREE starting from Sm until La (►Fig. 5.7c). Note that the 14HP12b sample (►Fig. 5.7c) is clearly controlled by the granite composition: REE pattern follows the general trend of the host granite.

►**Table 5.2** Rare Earth elements (REE) geochemistry (in ppm) of the granite host rock, main ore vein and brecciated ore vein of the Haut-Poirot deposit. Data for REE were determined by FUS-MS. Eu_N and La_N are normalized to chondrite values (McDonough and Sun, 1995).

Sample	**14HP03**	**14HP12a**	**14HP16**	**14HP34**	**14HP37**	**14HP12b**	**14HP51**
Location	Eastern Gallery	Ore vein n°2					
Type	Granite	Main ore vein				Brecciated ore vein	
La	59.9	12	10.6	11.5	12.4	24.3	12.9
Ce	123	44.4	48.7	36.8	237	33.7	29
Pr	13.8	4.32	3.52	6.59	35.6	4.34	4.89
Nd	48.4	23.5	20.6	46.1	385	13.2	29.9
Sm	9.37	12.5	10.6	26.7	182	1.91	10.6
Eu	0.794	1.86	1.3	3.94	12	0.291	1.13
Gd	6.41	12.2	8.39	31.6	115	1	9.97
Tb	0.91	1.13	0.86	3.47	9.43	0.11	1.21
Dy	5.14	4.52	3.45	15	31.7	0.56	6
Ho	0.87	0.77	0.5	2.31	4.02	0.09	1.12
Er	2.46	1.52	1.18	4.92	8.06	0.28	2.67
Tm	0.34	0.234	0.138	0.523	0.727	0.04	0.324
Yb	2.13	1.2	0.83	2.51	3.38	0.24	1.69
Lu	0.303	0.167	0.11	0.268	0.45	0.037	0.254
Eu_N/Eu_N*	0.31	0.46	0.42	0.41	0.25	0.64	0.34
La_N/Lu_N	20.52	7.46	10.00	4.45	2.86	68.17	5.27
∑REE	273.83	120.32	110.78	192.23	1036.77	80.10	111.66

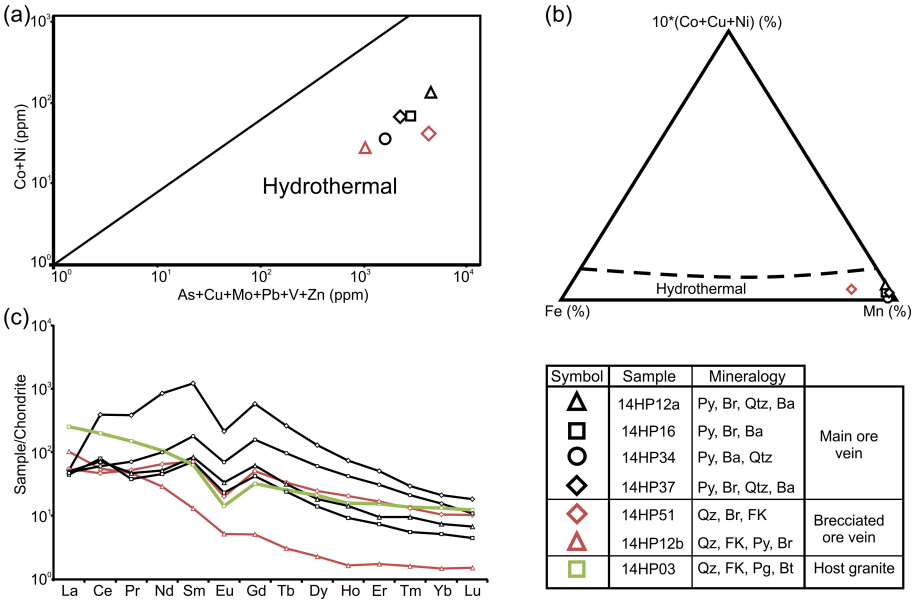

►**Fig. 5.7** Geochemical diagrams. **a.** High content of As-Cu-Mo-Pb-V-Zn compared to Co-Ni in Nicholson (1992) diagram showing the clear hydrothermal character of the ore. **b.** Ternary plot from Moorby and Cronan (1983) showing the hydrothermal character of the ore and the abundance of Mn relative to Fe. **c.** REE profile of the host rock and manganese ores of the Haut-Poirot deposit normalized to chondrite values (McDonough and Sun, 1995). See caption of ►Fig. 5.5 for abbreviations.

5.3.4 Paragenetic sequences

The most striking feature of the manganiferous vein in the Haut-Poirot deposit is the occurrence of, at least, two major distinct mineral assemblages (►Fig. 5.8): (1) the main ore stage (itself divided in two parts; see below) is marked by the formation of a high temperature paragenesis (braunite and scheelite) after the brecciation of the granite (►Fig. 5.4a, b, c), (2) the brecciation of the ore itself, characterizes a second minor mineralizing event marked by carbonates, hausmannite and probably arsenate (svabite). This second phase could only be observed at microscopic scale and does not reset the geochemistry of the ore (►Fig. 5.5e). A pre-ore stage is identified by Weil *et al.* (1959) and corresponds to the formation of the quartz-hematite breccia. Only a poor contribution of weathering processes to the ore enrichment is observed.

5.3.4.a Pre ore stage

Weil *et al.* (1959) indicate that quartz-hematite veins clearly correspond to a distinct phase, not associated directly to the manganese formation. The pre-ore stage consists of the successive formation of lamellar hematite with a poor contribution of quartz,

and then a quartz-hematite vein in close relation with the brecciation of the host rock. Weil *et al.* (1959) also report that the second generation of quartz could have replaced some early barite.

►**Table 5.3** Trace element geochemistry (in ppm) of the granite host rock, main ore vein and brecciated ore vein of the Haut-Poirot deposit. Data for trace elements were determined by FUS-MS, except V and Sr analyzed by fusion ICP-MS (see chapter 4).

Sample	**14HP03**	**14HP12a**	**14HP16**	**14HP34**	**14HP37**	**14HP12b**	**14HP51**
Location	Eastern Gallery	Ore vein n°2					
Type	Granite	Main ore vein				Brecciated ore vein	
Sc	6	5	4	3	4	2	6
Be	3	51	66	114	53	12	127
V	27	228	204	154	139	58	89
Cr	180	80	< 20	< 20	40	250	120
Co	4	88	69	15	66	26	41
Ni	< 20	40	< 20	20	< 20	< 20	< 20
Cu	< 10	2560	1460	460	1300	350	1070
Zn	70	340	110	100	140	0	40
Ga	26	81	47	29	39	33	41
Ge	1.6	42.8	20.5	14.6	23.9	7.5	21.9
As	6	918	747	766	612	378	2820
Rb	396	< 1	2	14	4	180	149
Sr	179	456	299	557	282	267	939
Y	25.9	23.4	18.9	57.1	206	2.7	48.2
Zr	353	5	7	6	11	57	17
Nb	13.1	< 0.2	0.4	0.2	0.3	2.7	1.1
Mo	< 2	107	39	17	36	22	77
Ag	1.4	< 0.5	< 0.5	< 0.5	< 0.5	0.6	< 0.5
In	< 0.1	0.4	< 0.1	0.2	0.7	< 0.1	0.1
Sn	13	< 1	< 1	< 1	< 1	4	4
Sb	1	1490	1080	1000	1130	121	766
Cs	41.7	0.5	0.2	9.3	2.2	56	86
Ba	785	48960	60730	43360	42960	8495	19670
Hf	10.4	< 0.1	0.2	0.2	0.3	1.6	0.4
Ta	1.83	< 0.01	0.02	< 0.01	< 0.01	0.57	0.29
W	< 0.5	5770	7570	4840	7050	1390	8880
Tl	2.36	< 0.05	< 0.05	0.46	< 0.05	2.02	< 0.05
Pb	49	423	388	169	103	242	230
Bi	0.1	11.5	6.8	1.4	21.4	0.9	51.1
Th	35.3	1.07	0.86	1.46	1.76	6.11	2.16
U	8.96	246	254	129	165	39.3	112

5.3.4.b Main ore stage (stages 1 and 2)

The main ore formation could be subdivided in two sub-ore stages in connection with the ore forming conditions. Ore stage 1 corresponds to a relatively high temperature mineral assemblage characterized by braunite and scheelite, while ore stage 2 is rather controlled by the O_2 content of the mineralizing fluid to precipitate pyrolusite and barite.

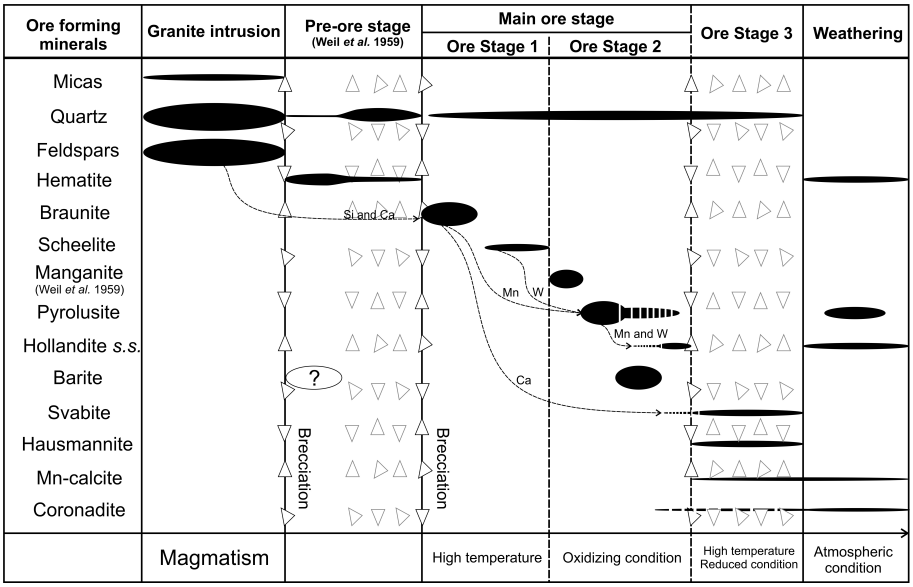

►**Fig. 5.8** Refined paragenetic sequence for the Mn(-W) deposit of the Haut-Poirot. Triangles correspond to the main brecciation events.

The first main mineral assemblage is characterized by the successive crystallization of braunite and euhedral crystals of scheelite (►Fig. 5.5d). Braunite replaces some of the minerals pulled off from the host granite after the brecciation event (►Fig. 5.5g, 6a). Braunite could form in a wide range of P-T conditions where Si and Mn are associated (Nicholson, 1992). On the other hand, scheelite ($CaWO_4$) and wolframite ([Mn, Fe]WO_4) are generally deposited between 200–500°C, but field stability of scheelite expands with increasing temperature, much more than the Fe-rich wolframite known as ferberite ($FeWO_4$, Wood and Samson, 2000). Hence, the first ore forming conditions could be of high temperature, especially considering their close relation to magmatic bodies (Fluck and Weil, 1976). In Mn-rich hydrothermal veins, we could expect W to be associated with Mn to form wolframite rather than scheelite ($CaWO_4$). The lack of wolframite in the Haut-Poirot deposit might indicate that scheelite crystallized separately from Mn-rich fluids.

The process by which pyrolusite forms, by simply replacing braunite (►Fig. 5.6b) or even precipitating in veins and geodes (►Fig. 5.6c), implies an addition in the O_2 content of the mineralizing fluid to oxidize Mn^{2+} or Mn^{3+} into Mn^{4+}. This new redox situation leads to an increase of the ore grade. Manganite could form in these conditions but is subsequently replaced by pyrolusite (Weil *et al.*, 1959). Ba is also highly sensitive to redox conditions and could then precipitate barite that encloses most of the previous formed minerals (►Fig. 5.4d, 5d). Barite is stable over a wide range of P-T and is often found associated with hypogene manganese deposits

(Hewett *et al.*, 1963; Hanor, 2000). The new composition of the Ba-rich fluid could lead to subsequent hydrothermal alteration of previous formed braunite and pyrolusite to form hollandite *s.s.* impregnation (►Fig. 5.5c, 6a), but also free crystals in the center of pyrolusite veins (►Fig. 5.6e). The presence of tungsten in the composition of both hollandite and pyrolusite indicates that the mineralizing fluid still contains W but not at the proper conditions to form scheelite (nor wolframite). Note that it could also be a reworking of the previous formed scheelite. In both cases, we could expect these conditions to be lower in temperature than ore stage 1, considering that scheelite is not stable anymore. One notes that pyrolusite probably occurs in different stages. We actually observe quartz and pyrolusite veins that cross-cut some of the barite and hollandite veins (►Fig. 5.6c). Further investigation should be made regarding the Sr and S isotope composition of barite in order to refine the origin and the processes responsible for its precipitation.

5.3.4.c Minor ore stage (ore stage 3)

The main ore is brecciated during a second mineralizing event that brings some carbonates in the system. Manganoan calcite and hausmannite crystallize in small veinlets (►Fig. 5.5e). Formation of hausmannite and Mn calcite is not only responsible for the brecciation of the ore but also to the replacement of the previous formed minerals: hausmannite and calcite are found inside the main mineralized veins, splitting some of the previous formed crystals (►Fig. 5.5e, f, g). However, these minerals poorly contribute to the Mn enrichment of the ore. The most striking effect is the increase in arsenic (up to 2820 ppm, Tab. 3) contained in svabite that replaces some of the braunite crystals (►Fig. 5.5h). Arsenic is frequent in hypogene deposits (Hewett *et al.*, 1963; Nicholson, 1992; Decrée *et al.*, 2010). The main parameter controlling the formation of carbonates is the CO_2 content of the hydrothermal mineralizing fluid. We could expect the fugacity of oxygen to be low to allow the formation of hausmannite that contains only Mn^{2+} and Mn^{3+} and temperature relatively high (Frenzel, 1980; Varentsov, 1996).

5.3.4.d Weathering processes

Weathering is poorly recorded in the Haut-Poirot deposits in the form of a Mn-rich gossan that could be found in other deposits worldwide (see this thesis, chapters 3, 6, 7 and 8). However, we could expect some of the observed textures and minerals to be attributed to supergene processes. For example, it is complex to assign hollandite *s.s.* to hydrothermal alteration, or weathering processes. According to Hewett and Fleischer (1960), hollandite could form by both processes. However, the Pb-rich end member of the hollandite group, known as coronadite, is very common in Pb-Zn and Mn supergene deposits and less able to precipitate in hydrothermal deposits (Hewett, 1971; Nicholson, 1992). Coronadite and Pb-rich hollandite occur in the Haut-Poirot deposit as replacement material for biotite in the wall-granite (►Fig. 5.5b). Biotite is

sensitive to oxidation at surface conditions, and can then be easily weathered into oxide minerals (►Fig. 5.6d). Lead enrichment in hollandite might be assigned to weathering processes, while pure and tungsten-rich hollandite could be formed by hypogene and supergene processes. Nevertheless, further investigations should be made about the origin of this "tungomelane". Colloform coronadite is replaced by pyrolusite (►Fig. 5.6b, f) highlighting pyrolusite to be formed in several stages (►Fig. 5.8), as already stressed by Dekoninck *et al.* (2016a) in karst-hosted deposits in the Imini district (Morocco, this thesis, see chapter 7).

The paragenetic sequence of the ore-forming minerals based on microtextures shows the evolution of the mineralizing fluid from Mn silicate, Mn oxides to Mn carbonates. Dasgupta *et al.* (1989) indicate that the main controlling parameters of Mn ore deposition are O_2 content and temperature of the mineralizing solution. Low-temperature veins consist generally of pyrolusite, cryptomelane, psilomelane, hollandite and todorokite, whereas other manganese species formed from relatively higher temperature solutions, exhibit braunite, bixbyite, hausmannite, huebnerite and/or Mn silicates (rhodonite, bustamite, tephroite), Mn carbonate and Mn sulfide (alabandite). Barite, fluorite, calcite and quartz are characteristic accessory minerals (Roy, 1981). The evolution of the mineralizing fluids, responsible for the different manganiferous parageneses, is most likely connected to several brecciation episodes occurring in the Vosges Mountain.

5.3.5 Source and origin of manganese

Because most of the magmatic rocks are considered to be reduced with low pH, manganese and iron are associated with their Mn^{2+} and Fe^{2+} valence state in Fe-Mg minerals (Maynard, 2014). Mafic rocks display much more Mn (i.e., average 1550 ppm in basalt) than felsic rocks (i.e. average 390 ppm in granite; Li, 2000). Even if Fe-Mg minerals are less abundant in felsic rocks; they could contain much more Mn in their structure compared to mafic minerals (Guérin, 1979). If Fe-Mg minerals are not present to host Mn, this metal concentrates in residual fluids to form manganese veins. In a general trend, Guérin (1979) shows that when the concentration of Mn in the acid host rock is poor, the manganese deposits it hosts are richer. Ore forming minerals of the Haut-Poirot deposit display a very weak affiliation with Fe. Low Fe/Mn (►Table 5.1) ratios indicate that Mn and Fe are decoupled one from each other during mineralizing processes. This is stressed by field observation of Weil *et al.*, (1959) reporting that hematite-quartz veins formed in a different way (pre-ore stage) than manganese veins (►Fig. 5.8). Small amount of Mn substitutes in Fe minerals, and lead the residual solution to be enriched in Mn, accompanied with other elements, including W and Ba. The origin of the mineralizing fluid could be related to the magmatic host rock, concerning the REE geochemical signature (►Fig. 5.7c); Eu

negative anomalies in Mn ores and granite host rock are similar and suggest the ore to be genetically derived from the granite. Moreover, decreasing LREE values in the Mn ore, whereas the LREE pattern of the host granite increases, strongly supports the hypothesis of a late derivative hydrothermal fluid: HREE and MREE values evolve simultaneously between the Mn ore and the granite until Sm, where the LREE decrease in the ore and increase in the granite (►Fig. 5.7c). This indicates that LREE have already been incorporated in the granitic minerals, before the ore-bearing fluid escaped from the granite.

The ore deposition is linked to a brittle regime (►Fig. 5.4a), somewhat different from ductile mylonitization of the nearby Straiture-Cellet overthrust zone (►Fig. 5.3). Manganese mineralization (and quartz-hematite veins) are associated with a complex set of faults along the deposit (Lougnon, 1981). Mylonite zone could be a precursor for brittle tectonic, providing the space for fluid circulation and subsequent precipitation. Tectonic reactivation leads to different stages of ore formation, characterized by specific mineral assemblages (►Fig. 5.8). These events are probably linked to a larger scale geodynamic of the Vosges massif (and Upper Rhine Graben activity). Given that the Haut-Poirot deposit is located at a significant distance from the main metallogenic districts of the Vosges (►Fig. 5.1b), we should consider this deposit to be a structure-related manganese type derived from plutonic rocks.

5.4 The Mn-Fe Saphoz deposit

The Saphoz deposit belongs to the Haute-Saône Fe district (Southern Vosges), where numerous Fe and Mn carbonate-bearing occurrences have been described in several locations (Hamanxard, Saphoz, Servance, La Fonderie, Envers de la Grève and Salbert; Griveaux *et al.*, 1974; Lougnon, 1985). Fe (ankerite) and Mn carbonate (rhodochrosite) veins outcrop in surface, often forming an oxidation zone, instead of the deeper part where most of the Mn and Fe reserves are preserved in their primary form. In deeper zones, iron could also form massive hematite bodies. Gangue minerals are mainly quartz and barite (Fluck and Weil, 1976).

The Saphoz deposit has been exploited since the 18th century (~1755) as the most important Mn deposit in the Vosges massif (►Fig. 5.1b) with a production estimated between 2,000 and 3,000 tons of Mn ore. It has been sporadically mined until its final closure in 1932, as a result of low tonnage and ore grade with Mn concentration between 32 and 38%, 35-37% SiO_2, 0.12-0.14 P_2O_5 and 0.01-0.67% As (Lougnon, 1981). Mn-Fe veins are hosted in Carboniferous (Late Visean) volcano-sedimentary rocks (►Fig. 5.1b) between Faucogney and Esmoulières (►Fig. 5.9). These rocks have a trachyte and andesite composition related to a third volcanic pulse

of the Culm volcano-sedimentary series (labradorite, conglomerates, volcanic breccia, andesite, trachyte, rhyolite, tuff, shale, greywacke; Griveaux *et al.*, 1974). The presence of an oxidation zone (gossan) in the deposit is particularly interesting to investigate weathering processes in the Southern Vosges, despite its narrow thickness of ~20 meters (Lougnon, 1981, 1985). Therefore, the following lines aim to review the primary and secondary mineralogy, petrography and geochemistry of these Mn-Fe ores. A special care is taken from observation of the oxidation zone, from which one sample, also has been studied by the $^{40}Ar/^{39}Ar$ geochronology method.

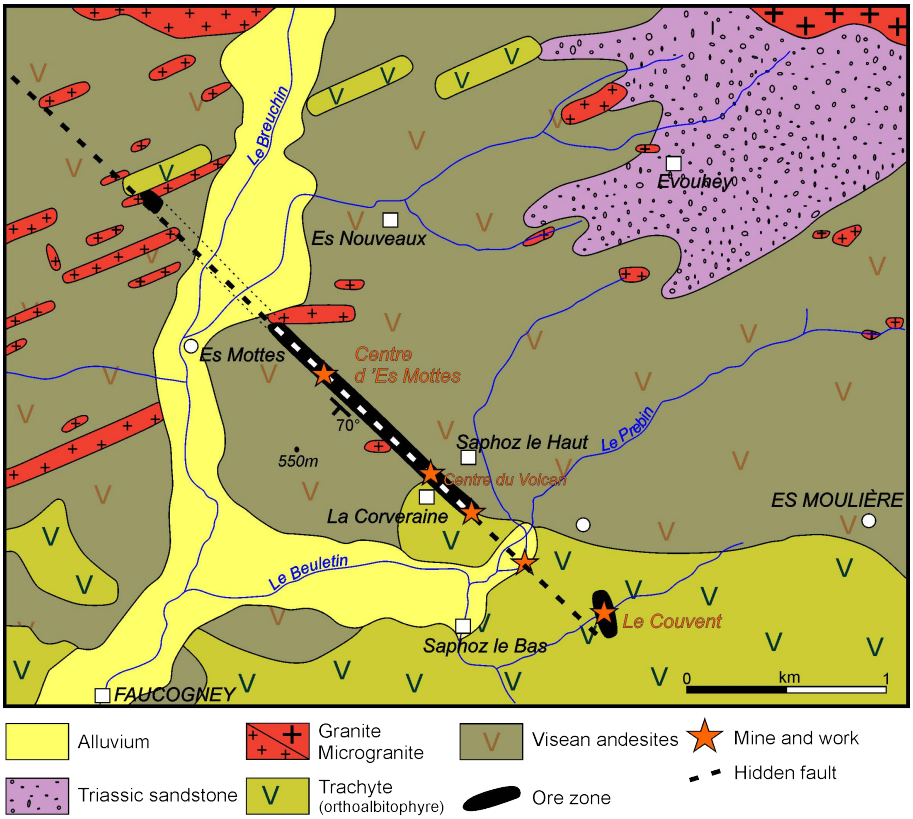

►**Fig. 5.9** Geological map of the studied area and location of the Saphoz deposit (modified after Lougnon (1985).

5.4.1 Distribution and style of mineralization

The Mn vein belongs to a 3 km long fractured zone crossing over trachyte and andesite volcanic rocks with a dip angle of approximately 40-70°SW. The ore is actually composed of several veinlets and lenses connected one to each other along the mineralization band, those reaching up 100m width in the so-called “Volcan” and

"Maison Toinot" locations (►Fig. 5.9). These veins have a maximum thickness of 0.9-1.3m to few centimeters forming a breccia in the "Volcan" mine, but the thickness decreases toward La Corveraine to be 10 to 15cm or alternatively 60 to 70cm in a second vein oriented N25°E (►Fig. 5.9). Le Couvent corresponds to the southern limit of the Saphoz deposit showing two parallel Ba-rich veins of 0.6-1.5m in thickness, in which the Mn content is very low (Lougnon, 1985).

The ore is composed of Mn oxides in the upper 20 meters, delimiting a gossan in upper part of the deposit (Es Mottes; ►Fig. 5.9) onto a carbonate protore (Perseil, 1975; Lougnon, 1981, 1985). The oxidized ore is mainly composed of braunite replaced by psilomelane, romanechite and todorokite, or groutite and ramsdellite in deeper zones (►Fig. 5.10a). Primary hausmannite is partly replaced by birnessite, whereas manganite is oxidized into the more stable pyrolusite forming veinlets or associated with hematite crystals (Perseil, 1975). This oxidation zone provides a higher grade reaching up 60% Mn with 2% Fe, 3% SiO_2 and 2% BaO (Lougnon, 1981). Mn carbonates are mostly kutnohorite with little amount of rhodochrosite, associated with Fe carbonates, dolomite and massive barite. Well-crystallized hematite can compose an important part of the ore, especially in the zone located between the Mn gossan and the protore in the Volcan location (►Fig. 5.10b), in association with calcite, chalcedony, quartz, pinkish-white barite (►Fig. 5.10c) and braunite crystals with small amount of psilomelane (Lougnon, 1981). Additionally, this Fe-rich zone displays an anomalous grades in As, Cu, Pb and Zn, probably related to deeper sulfides, whereas WO_3 concentration can reach 0.38 wt.%, similarly to the Haut-Poirot deposit (Lougnon, 1985). Some of these levels are weathered into clayey assemblages (►Fig. 5.10d).

5.4.2 Material and methods

The Volcan, La Corveraine and Le Couvent sites were investigated in 2014 and 2015 (►Fig. 5.9). We visited the Es Mottes site at the north-western edge of the deposit, but without identifying any old galleries or outcrops of the oxidation zone. Most samples were recovered from galleries and waste dumps as dense vegetation blanket obliterates most surface observations. This is also the reason why most of the ore sampled here are located in the hypogene zone of the deposit, where galleries are still preserved. We collected 63 samples (including Fe ore, Mn ore and parent rocks), performed 53 X-ray diffraction patterns, confected 8 polished sections and 4 thin sections. These samples have been further investigated under light and scanning electron microscopes in order to identify the mineralogy and textures. Additionally, 13 geochemical analyses (major and trace elements) have been performed. REE patterns are standardized to chondrite values (McDonough and Sun, 1995). One

sample has been dated by the $^{40}Ar/^{39}Ar$ method on two aliquots, as it was the only specimen in which hollandite *sensu stricto* and cryptomelane have been identified.

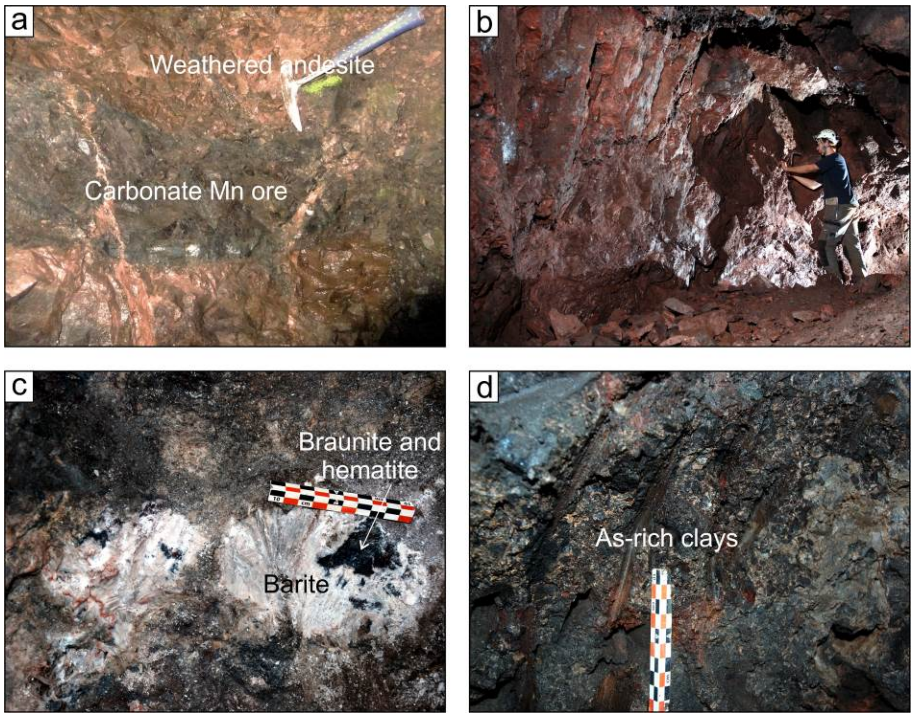

►**Fig. 5.10** Field observations of the different zones in the Saphoz deposit. **a.** Mn carbonate vein occurring within trachytic volcanic rocks in the Le Couvent site (►Fig. 5.9). **b.** The hematite-rich ore zone displaying the typical reddish tint of jasper in the Volcan mine. **c.** Whitish to pinkish barite filling pockets within the volcanic host rock containing black zones of mixed braunite-hematite in the Volcan mine. **d.** As-rich clays belonging to the oxidation zone of the host volcanic rock at the top of the Volcan mine.

5.4.3 Results

The results presented here focus on the carbonate and hematite-rich ores as most of the observations from the oxidized zone are missing. The mineralogy and petrography of the host rocks and Mn ores are presented separately from the geochemical observations. These results include $^{40}Ar/^{39}Ar$ dating of a single hollandite group mineral sample in the last section.

5.4.3.a Mineralogy and petrography

The rock hosting Mn-Fe mineralization are aphanitic or porphyric andesite and trachyte (►Fig. 5.11a) sometimes showing cubic dissolution figures indicating that

some sulfides (likely pyrite) were present and have been dissolved by further weathering. The combined use of light microscopy and X-ray diffraction indicates the presence of quartz, plagioclase and numerous opaque minerals disseminated within the rock, or as veinlets, the latter being related to the nearby Mn mineralization (►Fig. 5.11a), together with carbonate veinlets. K-feldspars are identified in trachytic rocks as a dominant mineral (►Fig. 5.11a). However, most of these minerals are heavily weathered obscuring most of the volcanic textures and the identification of other mafic minerals such as pyroxenes, amphiboles or biotite. All these minerals are commonly found in minor quantities in the Mn and Fe ores as remnants of the brecciated rock hosting these mineralization. Arsenoflorencite [$CeAl_3(AsO_4)_2(OH)_6$] is disseminated in hematite-rich zones of the host rock (►Fig. 5.11b) and account for the As anomaly observed by Lougnon (1981) in the area.

Braunite is the main primary Mn-bearing mineral occurring throughout the Saphoz deposit (►Figs. 5.11c, d, e and f), either in close association with various carbonates (dolomite, calcite, rhodochrosite; ►Figs. 5.11b, d and e) or quartz-hematite jasper (►Fig. 5.10b). Another important Mn source in the Saphoz deposit is the presence of little amount of Mn accommodated in many carbonates (calcite, dolomite), including rhodochrosite and to a lesser extent kutnohorite (►Figs. 5.11d, e, f and g). Hematite is observed throughout the deposit and is the main ore-forming mineral in the Volcan gallery (►Figs. 5.10b and 11b). Traces of hausmannite and Zn-rich hausmannite (hetaerolite?) and hollandite group minerals are identified in the Volcan and Le Couvent deposition sites (►Figs. 5.11c and f).

Most of the samples in the carbonate ores (Le Couvent) display a complex association of carbonates, likely formed in several stages. They are brecciated, displaying fragments of Mn-rich botryoidal hematite (►Fig. 5.11f) with braunite, in association with other carbonates, mainly a pinkish rhodochrosite and other carbonate cements (►Fig. 5.11e). Either calcite and dolomite display systematically a slight enrichment of Mn, sometimes forming kutnohorite (►Figs. 11d and f). Rhodochrosite is only identified in the southern part of the deposit (Le Couvent; ►Fig. 5.11e). There are several generation of carbonates, some of them forming brown fragments (rhodochrosite, chlorite, quartz) with a halo in contact with a carbonate cement (dolomite, calcite, kutnohorite) around the former ones (►Figs. 5.11d and f). Braunite occurs at the contact of these generations of carbonate (►Figs. 5.11d and f). These late carbonates enclose veins successively filled by braunite, hollandite *s.s.*, hausmannite and Mn-rich calcite (►Fig. 5.11g). Braunite could be replaced by dolomite (►Figs. 5.11f). Braunite seems also to accommodate some specific minerals in the core, those including Mn-rich scheelite (►Fig. 5.11d), Pb-rich vanadate, likely pyrobelonite [$PbMn(VO_4)(OH)$] enriched in Zn, Cu and Sr (►Figs. 5.11d and f) and Mn-rich chlorite (►Fig. 5.11d). Zn-Pb Mn oxide (chalcophanite or woodruffite) occur within the carbonate cement, whereas botryoidal Mn-rich hematite occurs inside

the first generation of carbonates (►Fig. 12a). Cation-free Mn oxides are also observed in association with carbonate ores (►Figs. 5.11f and g), but their mineralogy is difficult to determine accurately because they are accessory minerals and display the same chemical composition in EDS spectra. These minerals could be hausmannite or manganite, as these minerals have been described in earlier studies (Lougnon, 1981, 1985). Pyrolusite is unlikely as no palisade texture is identified.

The hematite-rich zone (Volcan and Corveraine; ►Fig. 5.9) is actually a mixing of lamellar hematite with quartz forming red jasper (►Fig. 5.12b) or chalcedony (if hematite is not present). Within this zone, growth bands of calcite alternate with layers of red-brown jasper in various proportions (►Fig. 5.12c). White to pinkish barite pockets, enclosing blocks of mixed braunite and hematite, are identified in the vicinity of the hematite-rich zone (►Fig. 5.10c). The upper part of the hematite-zone is sometimes affected by deep weathering processes transforming the host rock and mineralization in a clayey matrix, probably related to vertical fracture, which facilitate access to weathering fluids (►Fig. 5.10d). Only hematite remains stable in these pockets, as most of the host rock minerals are replaced, although the texture is preserved. The mineralogical composition of these clays exhibit a dominance of illite accompanied by smectite, swelling chlorite, kaolinite and quartz remnants (►Fig. 5.12d).

Outcrops of the oxidized zone are mostly missing along the Mn vein resulting in scattered observation of the secondary mineral assemblage. One sample clearly shows replacement of hausmannite and Zn-rich hausmannite by hollandite *s.s.* (sometimes enriched up to ~1% in K and Zn) and probably romanechite (►Fig. 5.12d). Cryptomelane is associated with these minerals (►Fig. 5.12f). Other Mn oxides of undetermined nature replacing formerly hausmannite could be nsutite, ramsdellite or groutite as already described by Lougnon (1981). In this sequence, hollandite *s.s.* coats some of these Mn oxides or hydroxides and crisscross cryptomelane (►Fig. 5.12f), filling voids with sometimes other Mn oxides. Therefore, some of the hollandite group minerals and Zn-Pb Mn oxides (chalcophanite or woodruffite; ►Fig. 5.11f) could be part of this zone, as well as a very late meteoric calcite. However, as uncertainties remain in the study of this assemblage, there is not a straightforward mineralogical determination from our observations. At least, some pure hollandite, cryptomelane, undetermined cation-free Mn oxides and clays described above are part of this zone.

5.4.3.b Geochemistry

The variability in the major, minor and trace elements content of the samples is directly related to variation in the mineralogy. In that order, the presentation of the geochemical analyses have been separated into: carbonate ore, Fe-rich ore, oxidized ore and host rock (►Tables 5.4, 5.5 and 5.6).

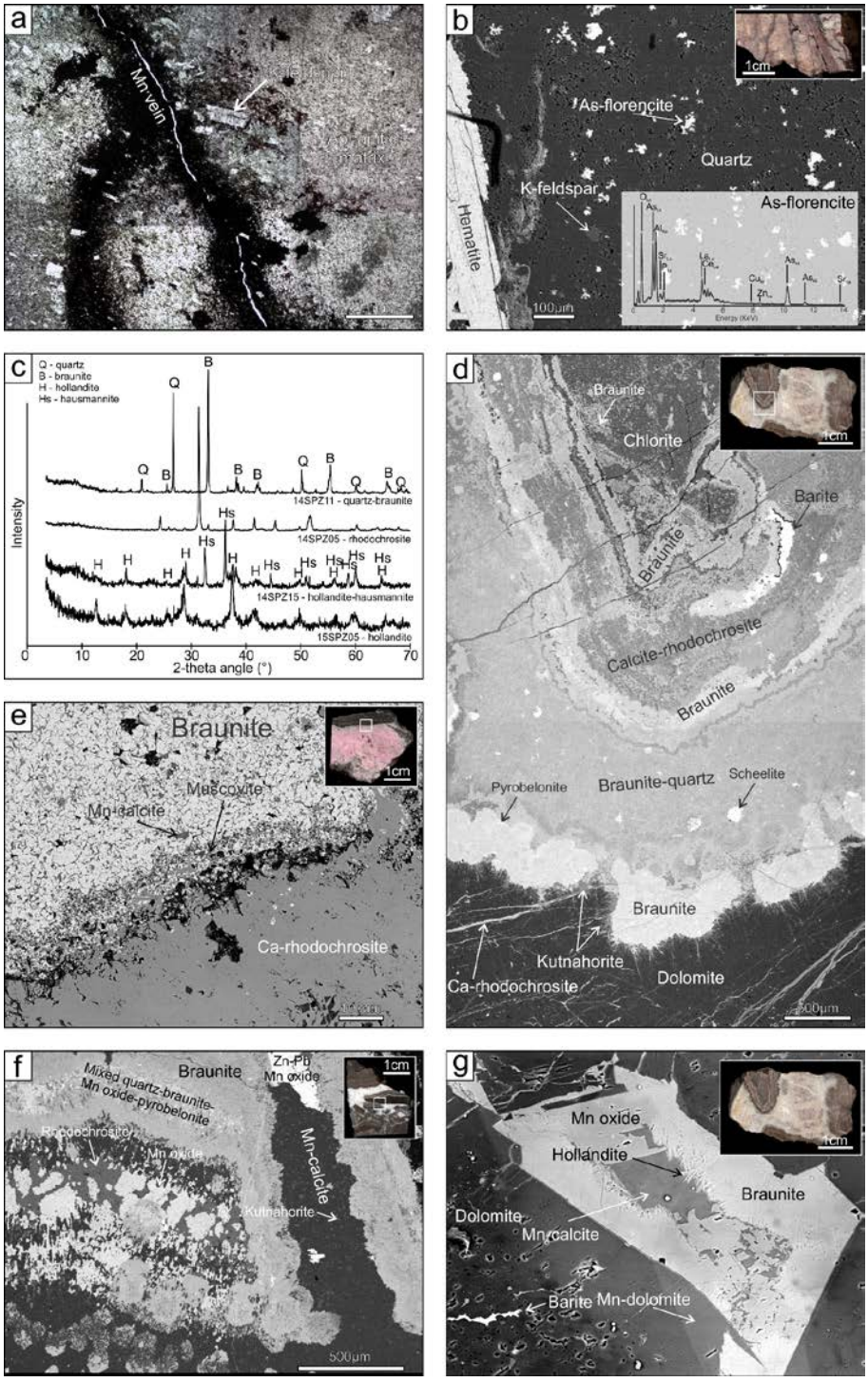

►**Fig. 5.11** Petrographic observations of the host rocks and the ores. **a.** Polarized view of Mn-

rich vein crossing over trachyte in the Le Couvent site (15SPZ01; ►Fig. 5.9). **b.** Backscattered electron view of disseminated arsenoflorencite within trachytic host rock in the hematite-rich zone of La Corveraine trench (14SPZ13). **c.** XRD spectra of different Mn ores. **d.** Backscattered electron view of a primary halo of Mn carbonates with chlorite, braunite, and little amount of scheelite, barite and pyrobelonite, cemented by secondary dolomite crystals. Kutnohorite and rhodochrosite veinlets crisscross dolomite cement (Le Couvent; 14SPZ03). **e.** Backscattered electron view displaying the contact between Ca-rich rhodochrosite and braunite zone in Le Couvent site (14SPZ05). **f.** Backscattered electron view of primary carbonates with braunite, cation-free Mn oxides (hausmannite?) and rhodochrosite, all being cemented by a second generation of Mn-rich calcite and kutnohorite in Le Couvent site (14SPZ06). **g.** Backscattered electron view of a braunite with cation-free Mn oxide and Mn calcite in a dolomite matrix. Mn-rich dolomite occurs at the contact with this vein (14SPZ03).

Andesite (14SPZ54) and trachyte (14SPZ30) have variable composition in SiO_2 depending on the nature of these rocks, but also on the silicification associated to the setting up of Mn-Fe mineralization in a quartz gangue (►Table 5.4). For example, the trachyte of La Corveraine (►Fig. 5.11a and b) contains veinlets of the nearby Fe-Mn mineralization and numerous opaque minerals related to their formation or alternatively to oxidation of Fe-Mg minerals by weathering solutions (►Fig. 5.11a). Therefore TiO_2 (2.5 wt.%) and Fe_2O_3 (12.1 wt.%) content is relatively high (►Table 5.4). Both volcanic rocks contain several ppm of arsenic (32 and 261; ►Table 5.5) due to the presence of arsenoflorencite (►Fig. 5.11b). The presence of manganese in the andesite (3010 ppm) is high, as well as the Mn/Fe ratio (►Table 5.4) calculated by Maynard (2014). Hence, contamination in andesite is high compared to trachyte. REE pattern of trachyte is typical of crustal rocks with a negative anomaly in Eu (Eu_N/Eu_N*=0.47; ►Fig. 5.13) and a general enrichment of total REE (∑REE=260.5 ppm), whereas this value is quite low for andesite (∑REE=260.5 ppm), in which no Eu anomaly is evidenced (Eu_N/Eu_N*=0.95). LREE are strongly enriched in comparison with HREE (La_N/Lu_N=4.7-6.8), ►Table 5.6).

Mn ores of the Saphoz deposit are characterized by a mid to low grade depending on the volume percentage of Mn-bearing minerals. MnO ranges between 13.2 and 55.0 wt.% in carbonate ores, 10.1 in clays and 80.7 in pure Mn oxides, whereas it only reaches 0.1-0.2 wt. % in the Fe-rich zone (►Table 5.4). SiO_2 (0.1-92.2 wt. %) and Ba (86-55070 ppm of Ba) are variable depending on the amount of quartz and barite in the gangue (or hollandite), as well as the total Fe_2O_3 (not detected to 33.4 wt.%) due to the presence (or not) of hematite (►Tables 5.4 and 5.5). Carbonate ores are particularly enriched in MgO (1.01-14.4 wt.%) and CaO (3.5-26.7 wt.%) as both Mg and Ca are distributed between different carbonate end-members (dolomite, calcite, kutnohorite and rhodochrosite; ►Table 5.4). As is generally enriched to hundreds of ppm in the Saphoz deposit and enclosing rocks and is related to the occurrence of As-florencite in the volcanic rocks (Lougnon, 1985). As is concentrated up to 0.5 wt.% in weathering clays and Zn to 1.7 wt.% in Mn most likely due to the presence of Zn-Pb oxides (i.e., chalcophanite) or Zn within the hollandite

and hausmannite lattice (►Table 5.5; ►Fig. 5.11g). The REE content ranges between 5.4 to 671.1 ppm in the hematite-rich zone, specifically due to high content in La and Ce in arsenoflorencite (►Table 5.6; ►Fig. 5.11b) disseminated within the surrounding volcanic rocks. The geochemical signature of the ore is typical of hydrothermal deposits: As-Cu-Mo-Pb-V-Zn are enriched, instead of Ni and Co (►Fig. 5.13b; Moorby and Cronan, 1983; Nicholson, 1992), similarly to the Haut-Poirot deposit. Mn/Fe ratios are high in the oxidized and carbonate ores, whereas it is obviously very low in the Fe-rich zone. Reduced iron (FeO) is low and almost always under the detection limit (►Table 5.4).

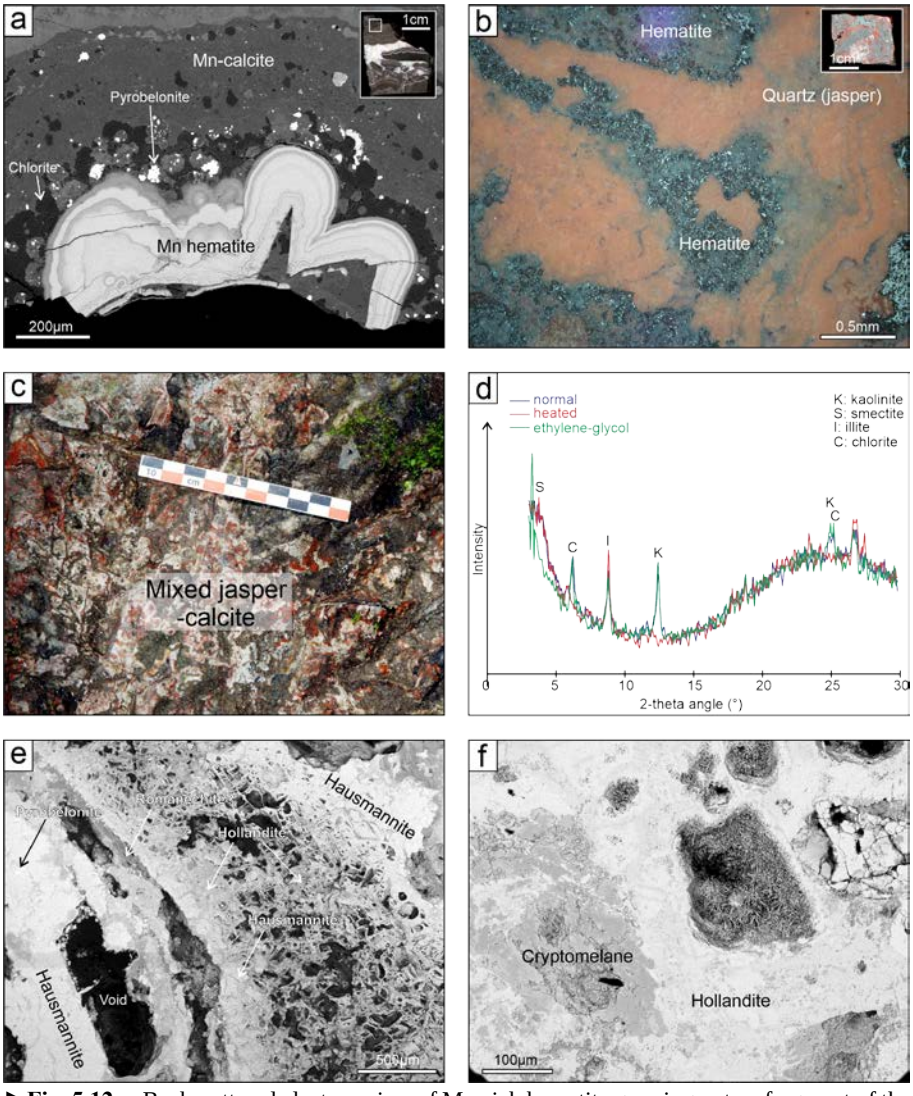

►**Fig. 5.12 a.** Backscattered electron view of Mn-rich hematite growing onto a fragment of the host rock and cemented by a succession of carbonates (14SPZ03; Le Couvent). **b.** Jasper

containing veinlets of lamellar hematite crystals in cross-polarized view (La Corveraine). **c.** Field view of a mixed layers of hematite-rich jasper and calcite in the Volcan mine. **d.** XRD pattern of the <2µm clay fraction of As-rich clays (►Fig. 5.10d). **e.** Backscattered electron view of hollandite *s.s.* and other Mn oxides (romanechite?) replacing hausmannite crystals (14SPZ15; Le Couvent). **f.** Backscattered electron view of hollandite *s.s.* replacing cryptomelane and filling open voids with the typical needle-shape crystals.

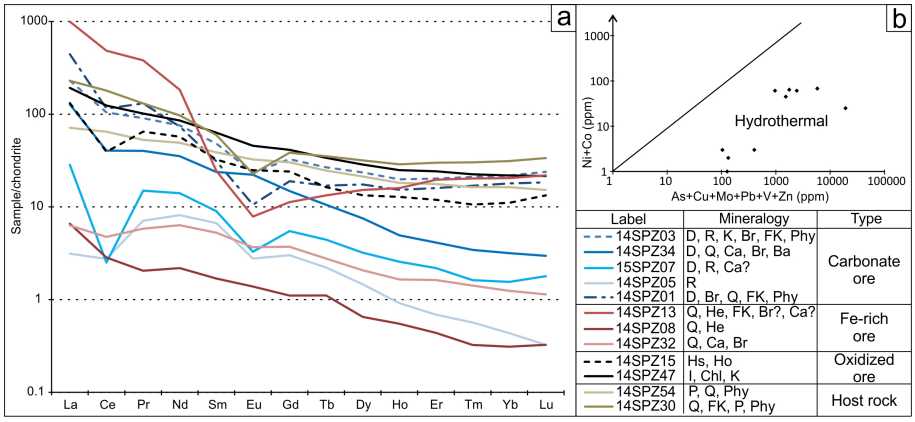

►**Fig. 5.13** Geochemical diagrams. **a.** REE profile of the host rocks and manganese ores of the Saphoz deposit normalized to chondrite values (McDonough and Sun, 1995). **b.** High content of As-Cu-Mo-Pb-V-Zn compared to Co-Ni in Nicholson (1992) diagram showing the clear hydrothermal character of the ore. D: dolomite; R: rhodochrosite; K: kaolinite; Br: braunite; FK: K-feldspar; Phy: 10A-phyllosilicate; Q: quartz; Ca: calcite; Ba: barite; He: hematite; Hs: hausmannite; Ho: hollandite; I: illite; Chl: chlorite; P: plagioclase.

REE patterns of the Mn ores are characterized by a general enrichment in REE and a slight negative anomaly in both in Eu (Eu_N/Eu_N*=0.43- 1.18) and Ce (Ce_N/Ce_N*=0.12-0.89) compared to chondrite values (►Fig. 5.13a). Despite the presence of arsenoflorencite, the REE content is relatively low (∑REE=5 to 671 ppm; ►Table 5.6). The shape of these profiles are in the same order than the host rocks, showing an asymmetric pattern with a strong enrichment of LREE compared to MREE and HREE (La_N/Lu_N=10-45; ►Table 5.6), the latter being lower than chondritic values in some carbonate levels (►Fig. 5.13a). Note that the clayey levels of the oxidation zone have a similar pattern than the host rocks (►Fig. 5.13a), indicating they are genetically related and are more likely the weathering product of these rocks, as it is also supported by pseudomorph features (►Fig. 5.10d).

►**Table 5.4** Major element geochemistry (in wt. %) of the host rocks (andesite and trachyte), main ore veins of the Mn-Fe Saphoz deposit. Data for major elements were determined by fusion ICP-MS, FeO by titration, SO_4, CO_2 and S by infrared spectrometry. - = not analyzed.

Label	**14SPZ01**	**14SPZ03**	**14SPZ05**	**14SPZ34**	**15SPZ07**	**14SPZ08**	**14SPZ13**	**14SPZ32**	**14SPZ47**	**14SPZ15**	**14SPZ30**	**14SPZ54**	**14SPZ35**
Type	Carbonate ore					Fe ore			Clays	Oxidized ore	Andesite	Trachyte	Barite
SiO_2	23.68	31	0.22	17.54	0.07	73.65	52.54	92.21	43.9	0.25	68.46	52.59	4.9
Al_2O_3	5.65	6.14	0.07	0.47	0.02	0.37	8.04	0.13	10.2	0.75	15.3	15.61	0.05
Fe_2O_3	1.77	3.07	< 0.01	1.47	0.02	23.76	33.4	2.24	15.2	0.09	3.03	12.11	0.18
FeO	< 0.1	< 0.1	0.1	< 0.1	< 0.1	0.2	< 0.1	0.2	< 0.1	< 0.1	0.4	0.6	0.2
$Fe_2O_{3(t)}$	1.78	3.08	0.05	1.49	0.04	23.98	33.42	2.46	15.2	0.1	3.48	12.78	0.4
MnO	20.05	22.09	54.96	15.41	13.17	0.081	0.049	0.164	10.1	80.66	0.037	0.301	0.019
MgO	11.58	6.69	1.01	7.58	14.39	0.03	0.16	0.08	2	0.06	0.04	3.3	0.03
CaO	11.51	8.72	3.45	19.52	26.69	0.04	0.03	2.68	1.62	0.17	0.11	1.19	0.06
Na_2O	0.09	0.63	< 0.01	0.03	< 0.01	0.02	1.51	0.02	0.28	0.07	3.96	3.88	< 0.01
K_2O	2.18	2.21	< 0.01	0.18	< 0.01	0.14	3.18	0.03	2.49	0.03	6.63	3.51	0.01
TiO_2	0.132	0.217	0.001	0.049	0.001	0.016	0.243	0.001	0.67	0.005	0.399	2.481	0.004
P_2O_5	0.02	0.02	< 0.01	0.03	< 0.01	< 0.01	0.03	< 0.01	0.2	0.04	0.06	0.57	0.02
LOI	21	17.62	38.61	25.99	44.43	0.58	1.22	2.58	10.4	9.78	0.77	3.54	0.31
Total	97.67	98.41	98.38	88.28	98.81	98.9	100.4	100.3	97.1	91.91	99.25	99.77	5.8
CO_2	17.5	13.3	37.8	24.3	43.8	-	-	-	-	-	-	-	-
Total S	0.11	0.01	0.12	1.25	< 0.01	-	< 0.01	-	-	-	< 0.01	< 0.01	-
SO_4	-	-	-	-	-	-	-	-	-	-	-	-	40.4
Mn/Fe	12.5	7.9	1217.1	11.5	364.6	0.0	0.0	0.1	0.7	893.1	0.0	0.0	0.1

►**Table 5.5** Rare Earth elements (REE) geochemistry (in ppm) of the host rocks (andesite and trachyte) and the main ore veins of the Mn-Fe Saphoz. Data for trace elements were determined by FUS-MS, except V and Sr analyzed by fusion ICP-MS

Label	**14SPZ01**	**14SPZ03**	**14SPZ05**	**14SPZ34**	**15SPZ07**	**14SPZ08**	**14SPZ13**	**14SPZ32**	**14SPZ47**	**14SPZ15**	**14SPZ30**	**14SPZ54**	**14SPZ35**
Type	Carbonate ore					Fe ore			Clays	Oxidized ore	Andesite	Trachyte	Barite
Sc	4	4	< 1	2	1	1	8	< 1	19	2	7	40	< 1
Be	35	19	< 1	9	< 1	8	2	9	30	12	2	10	< 1
V	81	328	8	352	< 5	121	88	33	393	688	9	309	19
Cr	< 20	40	< 20	50	< 20	380	100	280	60	30	190	50	< 20
Co	45	61	1	64	2	3	41	3	38	25	2	99	< 1
Ni	< 20	< 20	< 20	< 20	< 20	< 20	20	< 20	30	< 20	< 20	40	< 20
Cu	280	220	40	400	80	20	20	< 10	210	280	10	100	10
Zn	640	450	< 30	70	< 30	< 30	< 30	< 30	250	17000	< 30	220	< 30
Ga	26	29	37	27	9	31	17	22	27	57	33	28	8
Ge	14.4	12.5	< 0.5	11.7	< 0.5	7	3.1	7.2	9.7	12.7	1.6	3.3	< 0.5
As	458	459	42	626	45	192	805	55	4750	823	32	261	14
Rb	90	114	< 1	15	< 1	11	198	4	175	< 1	244	261	< 1
Sr	131	72	61	1432	25	6	138	11	103	71	42	238	4562
Y	17.4	25	1.4	9.7	5.3	0.7	25.4	3	48.4	27.1	46.1	24.6	1.5
Zr	111	135	2	6	3	< 1	184	4	69	4	355	92	5
Nb	3.7	4.2	< 0.2	< 0.2	< 0.2	< 0.2	6.6	< 0.2	3.2	< 0.2	12.4	3.6	< 0.2
Mo	8	19	37	32	< 2	35	34	4	5	18	3	< 2	< 2
Ag	< 0.5	< 0.5	< 0.5	< 0.5	< 0.5	< 0.5	1	< 0.5	< 0.5	< 0.5	1.6	0.8	< 0.5
In	< 0.1	< 0.1	< 0.1	< 0.1	< 0.1	< 0.1	< 0.1	< 0.1	0.1	0.3	< 0.1	< 0.1	< 0.1
Sn	1	< 1	< 1	< 1	< 1	< 1	1	< 1	2	< 1	4	1	< 1
Sb	106	78.1	3.3	56.8	0.8	19.4	20.9	11.7	161	113	1.9	17.7	1.9
Cs	78	145	< 0.1	8.4	< 0.1	8.2	93.6	6.3	72.3	0.2	8.6	71.4	< 0.1
Ba	5494	1324	5168	55070	352	86	354	207	8276	31650	1405	549	551700
Hf	2.7	3.3	< 0.1	0.1	< 0.1	< 0.1	4.8	< 0.1	1.8	< 0.1	9	2.7	0.7
Ta	0.17	0.27	< 0.01	0.03	< 0.01	< 0.01	0.44	< 0.01	0.26	< 0.01	0.96	0.28	0.57
W	167	176	90	390	3.2	464	158	62	428	313	< 0.5	154	19.1
Tl	< 0.05	< 0.05	< 0.05	< 0.05	< 0.05	1.2	1.69	0.94	0.91	< 0.05	1.37	2.05	< 0.05
Pb	59	953	< 5	283	8	33	16	12	190	331	17	51	< 5
Bi	< 0.1	0.3	< 0.1	3.6	< 0.1	< 0.1	1.1	0.1	2.1	< 0.1	0.2	< 0.1	< 0.1
Th	7.04	8.54	< 0.05	< 0.05	< 0.05	0.1	13.5	< 0.05	6.65	< 0.05	35.9	4.47	< 0.05

U	8.22	16.6	0.3	27	0.21	67.5	9.48	30.1	9.77	19.7	11.9	22.8	0.22

►**Table 5.6** Rare Earth elements (REE) geochemistry (in ppm) of the host rocks (andesite and trachyte) and the main ore veins of the Mn-Fe Saphoz. Data for REE were determined by FUS-MS. Eu_N and La_N are normalized to chondrite values (McDonough and Sun, 1995).

Label	**14SPZ01**	**14SPZ03**	**14SPZ05**	**14SPZ34**	**15SPZ07**	**14SPZ08**	**14SPZ13**	**14SPZ32**	**14SPZ47**	**14SPZ15**	**14SPZ30**	**14SPZ54**	**14SPZ35**
Type	Carbonate ore					Fe ore			Clays	Oxidized ore	Andesite	Trachyte	Barite
La	80.5	41.8	0.74	30.2	6.72	1.56	236	1.49	45.5	31.2	54.3	16.9	5.26
Ce	54.1	49.2	1.69	24.8	1.54	1.74	297	2.91	76	24.1	110	39.6	0.78
Pr	9.3	6.44	0.66	3.73	1.39	0.19	35.4	0.54	9.43	6.01	12.1	4.9	0.07
Nd	25.8	26.5	3.72	16.1	6.43	1	83.8	2.9	39.1	26.1	44.3	22.5	0.5
Sm	3.5	5.48	0.99	3.52	1.33	0.25	3.62	0.78	9.36	4.79	8.82	5.73	1.17
Eu	0.5	1.01	0.156	1.25	0.185	0.078	0.443	0.207	2.57	1.4	1.28	1.83	1.28
Gd	2.9	4.99	0.6	2.95	1.09	0.22	2.24	0.74	8.21	4.79	7.64	6.02	1.17
Tb	0.5	0.74	0.08	0.38	0.16	0.04	0.48	0.1	1.22	0.59	1.27	0.89	0.06
Dy	3.3	4.44	0.36	1.85	0.79	0.16	3.75	0.51	7.03	3.28	7.82	5.23	0.11
Ho	0.6	0.83	0.05	0.27	0.14	0.03	0.87	0.09	1.36	0.7	1.57	0.99	0.02
Er	2.0	2.48	0.11	0.66	0.35	0.07	3.14	0.26	3.87	1.91	4.79	2.82	0.05
Tm	0.3	0.398	0.014	0.085	0.04	0.008	0.501	0.035	0.555	0.262	0.747	0.403	< 0.005
Yb	2.2	2.69	0.07	0.51	0.25	0.05	3.29	0.2	3.51	1.78	5.03	2.63	0.06
Lu	0.3	0.451	0.008	0.073	0.044	0.008	0.539	0.028	0.53	0.327	0.828	0.375	0.008
∑REE	185.8	147.5	9.3	86.4	20.5	5.4	671.1	10.8	208.3	107.2	260.5	110.8	10.5
La_N/Lu_N	24.08	9.62	9.60	42.94	15.85	20.24	45.45	5.52	8.91	9.90	6.81	4.68	68.25
Eu_N/Eu_N*	0.44	0.59	0.62	1.18	0.47	1.01	0.47	0.83	0.89	0.89	0.48	0.95	3.33
Ce_N/Ce_N*	0.48	0.73	0.59	0.57	0.12	0.77	0.79	0.78	0.89	0.43	1.04	1.05	0.31

5.4.3.c K-Mn oxide geochronology

Only one sample contains relatively pure hollandite group minerals (►Fig. 5.14) suitable for $^{40}Ar/^{39}Ar$ geochronology. Geochemical analyses of this sample coupled with EDS spectra (►Fig. 5.12f) on individual grains and polished section have determined the Ba-rich end-member of the hollandite group (hollandite *sensu stricto*) containing few percent of K, sometimes close to the cryptomelane end-member. Hence, $^{40}Ar/^{39}Ar$ dating can be performed despite the moderate potassium contents (up to 1.8 wt.% K). Low K-content commonly results in poorly constrained spectra as radiogenic Ar can be retained quantitatively in the tunnel in hollandite structure but in low quantity. This is demonstrated in ►Fig. 5.14, where uncertainties of the ages are very large for recent ages: 0.54 $\pm$ 1.71, 2.46 $\pm$ 1.68 and 1.95 $\pm$ 1.36 Ma. Both aliquots of sample 15SPZ05 have accumulated large amounts of atmospheric ^{40}Ar adsorbed onto the grain surface or trapped in intercrystalline sites, providing ages with large uncertainties and large atmospheric and radiogenic Ar ratio in the first steps (0 to ~35 of the cumulative ^{39}Ar released; ►Fig. 5.14). Middle to high temperature steps still show large errors. Despite large errors, pseudo-plateau ages can be tentatively obtained from the high temperature degassing steps (►Fig. 5.14). Moreover, isochron ages are in the same range of values and error, supporting the pseudo-plateau ages. There are, at least, two possible explanations of this poorly constrained age distribution. (1) the very low content of K in the structure of the hollandite was not able to produce sufficiently high radiogenic argon or the sample has lost most of this signal by diffusion. (2) Both samples have precipitated recently, in which the Ar released through the heating step procedure has a composition close to that of the modern 295.5 $^{40}Ar/^{36}Ar$ intercept and represent the true age of precipitation. Such interpretation is strengthened by close $^{40}Ar/^{36}Ar$ intercept of 288.1 $\pm$ 1.9 and 303.6 $\pm$ 3.3 ratio, but also by relatively stable K/Ca ratio, at least for the steps considered in the plateau age calculation (►Fig. 5.14). In addition, SEM-EDS observation make the second hypothesis more likely. The only valuable information is that Mn oxides still undergo weathering processes in current times or in an interval lasting from 2.46 $\pm$ 1.68 Ma. Regardless of this interpretation, the formation of the Mn oxides is very recent and has already pointed out in the Black Forest (►Table 7.5; Hautmann and Lippolt, 2000).

5.4.4 Ore-forming processes

The ore could be subdivided in, at least, two main stages: (1) the primary mineral assemblage takes place in the form of Mn carbonates, Mn silicates and Mn oxides in a carbonate-quartz-barite gangue; (2) the more recent weathering stage transforms the primary minerals into secondary Mn oxides (►Fig. 5.15).

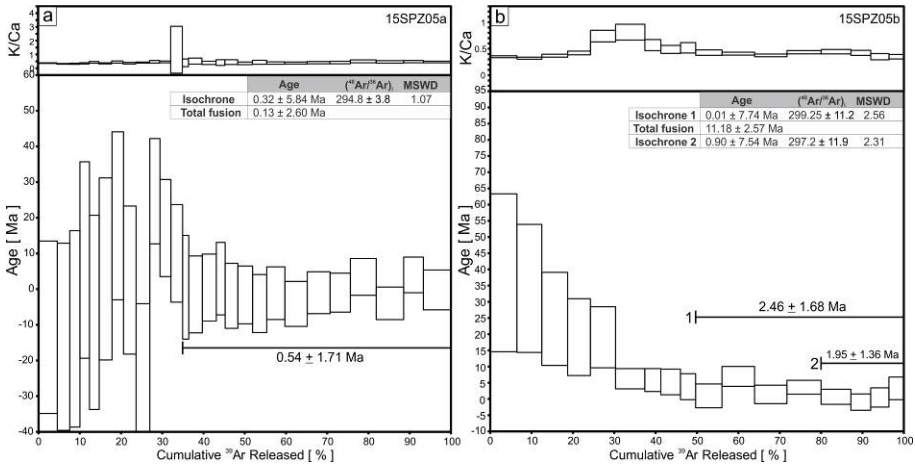

►**Fig. 5.14** $^{40}Ar/^{39}Ar$ degassing pattern of sample 15SPZ05 (►Fig. 5.12f) showing very recent pseudo-plateau ages in agreement with $(^{40}Ar/^{36}Ar)_i$ intercept.

5.4.4.a Protore stage

The carbonate stage could be subdivided in two phases (►Fig. 5.15) encompassing the main ore oxide stage, showing fragments of a first dark to brown carbonate ore cemented later by dolomite (►Fig. 5.11d), Mn-rich calcite (►Fig. 5.11f) or rhodochrosite (►Fig. 5.11e). It is challenging to assign the different carbonates to the first or second generation of protore carbonates, as these associations are complex and represented in both generations. However, it seems obvious that the first stage is accompanied by the precipitation of numerous metals in the form of scheelite, pyrobelonite, chlorite, braunite, botryoidal Mn-rich hematite and cation-free Mn oxides (probably hausmannite or manganite; ►Figs. 5.11d, f and 5.12a), whereas the second generation could host Pb-Zn Mn oxides (►Fig. 5.11f). Very late rhodochrosite and kutnohorite veinlets crisscross both generations of carbonates, indicating that carbonate formation could have persisted after the second carbonate stage (Fig. 5.11d). However, most of the braunite and cation-free Mn oxides crystals are formed at the contact between the two generations of carbonates, and could be therefore be considered as the main Mn input. Note that several recrystallizations of the former carbonates are observed at the contact with the second generation resulting in different zones within or around carbonate fragments (►Fig. 5.11d). This is evidenced by the formation of Ca-rich rhodochrosite (►Fig. 5.11d), Mn calcite and Mn dolomite (►Fig. 5.11g) on the borders of braunite crystals.

These minerals, and their close association within reworked fragments of mixed braunite-hematite in a barite matrix, suggest that the main Mn input is accompanied by the formation of lamellar hematite and red-brown jasper (Figs. 5.12b and c). As-rich florencite is also associated to lamellar hematite formation, but within the wall of the Mn-Fe vein in the host rocks (►Fig. 5.11b). Quartz occurs throughout

the deposition of carbonate minerals as free quartz crystals in geodes or forming red-brown jasper, whereas barite occurs mainly at the end of this process, filling voids within second generation of carbonate and enclosing fragments of the main ore stage (►Figs. 5.10c and 15). Other Mn-bearing minerals which could be formed during this hydrothermal stage are hausmannite, manganite and pyrolusite, despite direct observations of these phases are lacking (►Fig. 5.15).

5.4.4.b Weathering stage

The weathering stage is poorly recorded in the collected sample as most of the gossan is located in a narrow range of elevation of maximum 20 meters from the top surface (Lougnon, 1981, 1985), now mostly obliterated by vegetation. However, numerous Mn oxides have been described in previous studies and could be incorporated in the paragenetic sequence (►Fig. 5.15). These minerals include the transformation of the primary minerals, namely hausmannite into birnessite, hollandite and possibly romanechite (►Fig. 5.12e), manganite into pyrolusite and braunite into respectively cryptomelane, todorokite, romanechite and groutite (Lougnon, 1981, 1985). Mineralogical transformations within the supergene assemblage itself are very common in the oxidized zone of carbonate-silicate protores (Parc *et al.*, 1989; Nahon, 1991; Varentsov, 1996). For example groutite transforms into ramsdellite and pyrolusite is replaced by romanechite (Lougnon, 1981, 1985). It is difficult to assign pure hollandite *s.s.* to supergene or late hydrothermal alteration, as it is the case in the Haut-Poirot deposit, because hollandite *s.s.* could precipitate under both conditions, as replacement of braunite (►Fig. 5.11g) or hausmannite (►Fig. 5.12e). However, hollandite *s.s.* crisscross cryptomelane formed under weathering conditions, given their recent age (2.46 $\pm$ 1.68 Ma) that can be retrieved from $^{40}Ar/^{39}Ar$ spectra (►Fig. 5.14). Therefore, this indicates that hollandite *s.s.* and cryptomelane are very late, suggesting a supergene origin.

The formation of clay assemblages composed of chlorite, kaolinite, illite and smectite, resulting from the deep weathering of the host rocks on the border of the main Mn-Fe vein, clearly indicates that some metals, and especially As, are enriched in this zone and that weathering processes have operated (recently?) in the Saphoz deposit.

5.4.5 Source and origin of the Mn-Fe mineralization

The primary mineral assemblage made up of braunite-hematite in association with complex Mn-bearing carbonates is a typical feature of hydrothermal Mn-Fe deposits, as well as their chemical footprint (►Fig. 5.13b; Hewett, 1964; Lougnon, 1981, 1985; Roy, 1981; Nicholson, 1992; Hein *et al.*, 2000; Glasby *et al.*, 2005; Fusswinkel *et al.*, 2013). Their formation is probably related to magmatism that has enhanced volcanic-

hydrothermal activity, after the setting up of andesite and trachyte rocks in the uppermost Visean. This is also suggested by enrichment in the high LREE content and the similar pattern of these ores with their host rocks (►Fig. 5.13a). Fluid convection and migration in most hydrothermal Mn-Fe deposits is considered to be the result of an anomalously high heat flow due to volcanic activity (Roy, 1981). However, following Griveaux *et al.* (1974), the Mn-Fe Saphoz deposits and other base metal deposits in this area have a post-Triassic origin in relation to the setting up of faults, those having been reactivated during the Oligocene.

Faults and fractures have played an important role for fluid circulation and crystallization of Mn-Fe veins in shallower levels of the crust. The deepest parts of the vein systems usually display Mn^{2+}-bearing minerals, such as Mn-rich carbonates (i.e., rhodochrosite; Hewett, 1964; Roy, 1981). These reduced ore associations then grade into shallower zones dominated by mixed valence Mn-bearing minerals (i.e., hausmannite, braunite) and hematite. This systematic mineral zoning reflects increasing oxidation via fluid mixing with shallow oxygenated ground waters at decreasing deposition temperatures (Hewett, 1964). The brecciated character of the ore is related to an extension phase, which led to the opening of previous formed fractures and finally the setting up of carbonates, quartz, barite, Mn silicate (braunite) and Mn oxides (hausmannite, manganite, pyrolusite) during a hydrothermal activity. The exact timing of formation of the primary ore is difficult to determine as structural relations of the ore vein with the post-Variscan cover are lacking, as well as dating hypogene minerals. However, mineralizing events could be related to hydrothermal activity at the end of the Variscan orogenesis, the Jurassic heating or the Cenozoic rifting (►Fig. 5.2).

5.5 Timing of the mineralization and their relation to other manganese deposits

The absolute timing of Mn mineralization can be difficult to determine considering the absence of datable mineral phases in the Mn(-W) Haut-Poirot and Mn-Fe Saphoz deposits. Although hollandite group minerals are a well-known datable material (see chapters 3 and 4), the size of the mineral grains in the Haut-Poirot deposit is too small to isolate them and further perform K-Ar or $^{40}Ar/^{39}Ar$ determinations. Such material has been dated within a single hollandite-cryptomelane sample (►Figs. 5.12f and 5.14) in the Mn-Fe deposit of Saphoz, which has provided inconsistent ages to match hydrothermal phases reported in the Vosges massif (►Fig. 5.2). Consequently, these recent ages (0.54 ± 1.71, 2.46 ± 1.68 and 1.95 ± 1.36 Ma) might be related to ongoing or recent weathering processes.

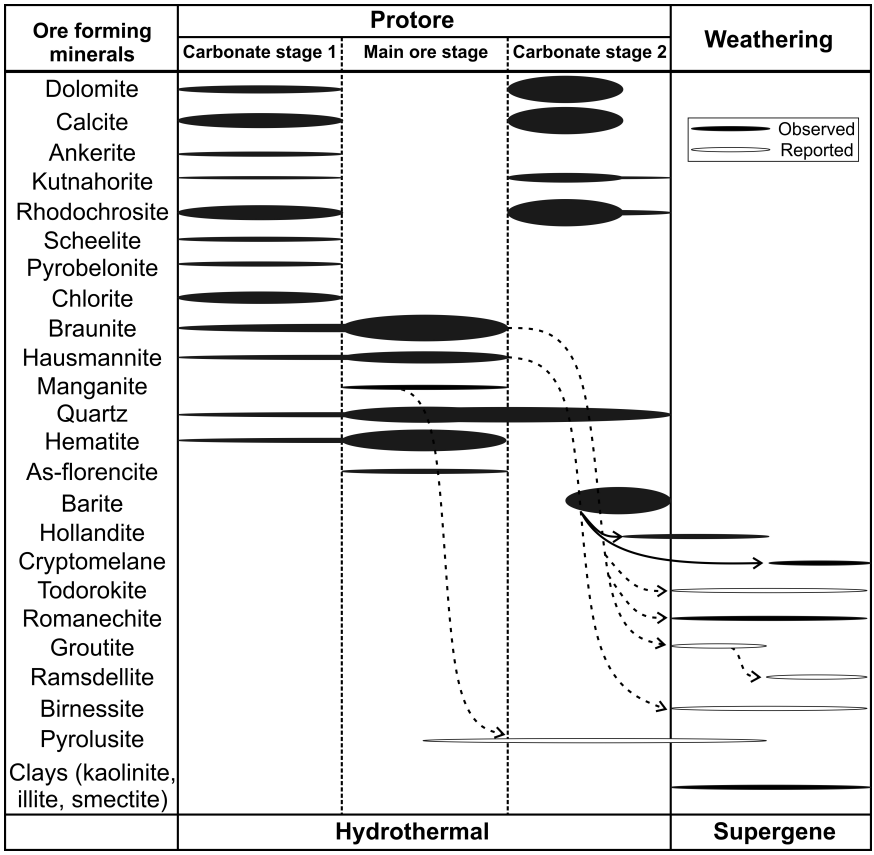

►**Fig. 5.15** Tentative paragenetic sequence of the Mn-Fe Saphoz deposit. Some minerals are reported from Lougnon (1981).

However, considering the close genetic relation between the Vosges and the Black Forest massifs, present investigation of the Mn deposits of the Vosges massif show clear similarities with the Eisenbach deposit (Segev *et al.*, 1991, 1992; Eastern Black Forest; ►Fig. 5.1b, c). Indeed, the Eisenbach and the Mn(-W) Haut-Poirot deposits show that: (1) the host rock granite in both deposits were formed during the same time interval; (2) the mineralogical association is quite similar, except for psilomelane (nearly absent in the Haut-Poirot deposit); and (3) a multistage ore deposition is observed in both deposits. The Mn-Fe Saphoz deposit has no clear equivalent but seems to be associated with other deposits in the Vosges and Black Forest (►Fig. 5.1b) as they are related to magmatism or, alternatively, to subsequent hydrothermal events (►Fig. 5.2; Fluck and Weil, 1976).

Pioneer studies of Segev *et al.* (1991) about K-Ar dating of colloform cryptomelane in the Eisenbach deposit (►Fig. 5.1b) provided three direct ages: 253±5 Ma (Permian), 116±4 Ma (early Cretaceous) and 16±1 Ma (Neogene; ►Fig. 5.2;

►Table 5.7). The Permian age is probably younger than the true precipitation age because several generations of hollandite are mixed in the sample. Early Cretaceous ages could be related to (i) a homogeneous mixture of hollandite from both parts of the sample, whereas each part has a different age, or (ii) the deposition of the whole colloform hollandite in the same time interval (►Fig. 5.16). The youngest Neogene age corresponds to a pure phase and does not reflect any mixing. However, further studies by Segev *et al.* (1992) have only identified Tertiary and Permian ages of the Eisenbach manganese veins to be responsible for the ore formation. The other ages are meaningless ranging between the younger and older ages. Direct ages are considered to be in good agreement with hydrothermal phases and other mineralization products documented in the area. The earliest Mn mineralization probably belongs to the oldest hydrothermal episode expected in the Black Forest area (260–280 Ma, Segev *et al.*, 1991, 1992), whereas the first mineralization stage in the Variscan belt (290–310 Ma) occurred under much higher temperatures (Thomas and Tischendorf, 1987). A post-Variscan mineralization episode is thus responsible for the main manganese ore formation (Segev *et al.*, 1991). The geochemistry of the ore together with the occurrence of a high temperature mineral assemblage indicate the age of the Haut-Poirot mineralization could be related to the late Variscan hydrothermal activity. Post-Variscan vein deposits are considered to be low in temperature (►Fig. 5.2) and do not control the mineralogy of the Haut-Poirot veins (i.e., scheelite formation; ►Fig. 5.8), while the Mn-Fe Saphoz deposit display a second carbonate stage (►Fig. 5.15) which could have a shallower and a lower temperature origin. Following the multistage character of these deposits, reactivation of faults and low temperature hydrothermalism would contribute to the ore reworking and enrichment.

Neogene ages are interpreted as a result of intense tectonic movements, here to the Upper Rhine Graben rifting. Following Segev *et al.* (1991, 1992) these ages may reflect young activity of mineralizing fluids along fracture zones in relation with alkaline volcanism in their close vicinity (i.e., alkaline Kaiserstuhl volcanism; ►Fig. 5.1b). However, a greater precision of $^{40}Ar/^{39}Ar$ determinations has led Hautmann and Lippolt (2000) to suggest a more consistent explanation of the Neogene ages lasting from Langhian (14.6 $\pm$ 0.1 Ma) to Pleistocene (1.0 $\pm$ 0.1 Ma; ►Table 5.7). Actually, these ages are rather related to weathering than volcanogenic processes. Cryptomelane and hollandite *s.l.* ages from the Black Forest and other sub-alpine Variscan massifs should be related to extensive chemical weathering under subtropical to temperate humid climatic conditions (►Fig. 5.16). The main controlling factor is, however, interpreted to be tectonic, owing to widespread and intense Cenozoic faulting and uplift, and subsequent subaerial exposure of fresh rocks and Mn-bearing veins. Manganese concentration in the neighboring Black Forest massif indicates that weathering processes have contributed to the manganese ore enrichment as soon as Langhian times (►Fig. 5.16; ►Table 5.7; Hautmann and Lippolt, 2000), which

correspond to the uplift and erosion in the Vosges and Black Forest (Schumacher, 2002) to reach their current elevation (►Fig. 5.16). Such interpretation could be extended to the Vosges massif regarding their close tectonic evolution and metallogenesis (Fluck and Weil, 1976; Quesnel, 2003). However, the lack of pure cryptomelane in the Haut-Poirot and Saphoz deposits (we rather observe hollandite *s.s.*) suggests weathering processes to be poorly registered, or, at least, recorded more recently as supported by the very recent ages (►Fig. 5.13) also measured in the Black Forest massif (►Fig. 5.16). Older weathering periods could also be extended to the Cretaceous considering that most of the ancient massifs of Western Europe are exposed during that time (e.g., Hautmann and Lippolt, 2000; Migoń and Lidmar-Bergström, 2001, 2002; Wyns, 2002; Quesnel, 2003; Thiry *et al.*, 2006), and explain some of the early Cretaceous ages obtained by Segev *et al.* (1991), the latter still being controversial. Whether or not ancient weathering phases (i.e., Cretaceous and Eocene) have formed Mn gossans, their upper part (and therefore older ages) have probably been eroded and are no longer available for sampling and geochronology.

►**Table 5.7** Synthesis of K-Ar and $^{40}Ar/^{39}Ar$ dating obtained from Mn deposits in the Black Forest massif. Note that K-Ar ages have a large error and are probably mixed with older radiogenic components.

Mineral	Method	Location	Age (Ma)	Error (Ma)	Reference
Hollandite	K-Ar	Eisenbach	255	5	Segev *et al.* (1991)
			275	33	
			156	3	
			66	1.5	
			18	1	
			253	5	Segev *et al.* (1992)
			116	4	
			109	5	
			103	2	
			55	1	
			21	2	
			16	1	
			7	7	
Cryptomelane	$^{40}Ar/^{39}Ar$	Witichen district	1.00	0.1	Hautmann and Lippolt (2000)
		Neuenbürg district	7.41	0.05	
			14.62	0.11	
		Kinzing valey	12.58	0.07	
Hollandite		Rankach valley	13.66	1.84	
			13.52	1.35	
			7.38	0.64	
		Hornisgrinde	6.99	0.23	
		Eisenbach	10.94	0.28	
			9.51	0.06	

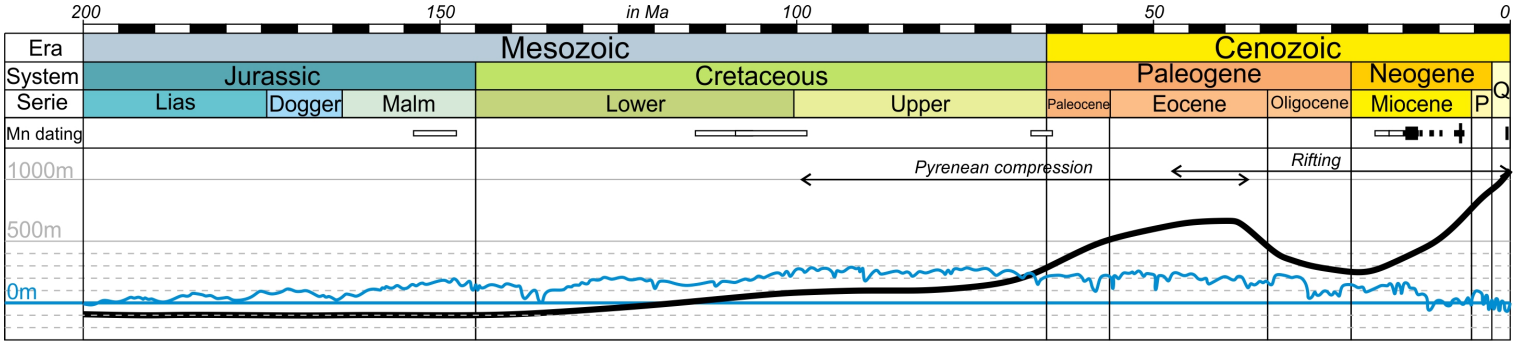

►**Fig. 5.16** Elevation of the southern Vosges massif through time (black line; Quesnel, 2003) and the eustatic curve reference (blue line; Hardenbol *et al.*, 1998). K-Ar (white rectangles; Segev *et al.*, 1991, 1992) and $^{40}Ar/^{39}Ar$ (black rectangles; Hautmann and Lippolt, 2000) dating are given for the Black Forest (see also ►Table 5.7). Not that the uncertainties over K-Ar ages is significant compared to ages obtained by the $^{40}Ar/^{39}Ar$.

🔎 Hydrothermal Mn-vein type deposits in the Vosges massif only register the most recent Pleistocene phase of weathering, which is only identified in the Saphoz deposit. This further questions why such material is lacking within the two main historical Mn deposits in the Vosges massif, whereas older ages scattered since the Langhian stage are evidenced in the laterally equivalent Mn deposits of the Black Forest massif. The latter Miocene ages fit with the recovering of uplift of these massifs. In this context, erosion of the Vosges massif is probably higher, leaving only parts of the Mn gossans to be preserved.

5.6 References

Autran, A., Bouladon, J., Laffite, P., Ziserman, A., 1980. Les ressources minérales et énergétiques. Les gîtes minéraux (substances non énergétique), in: Géologie de la France. Orléans, pp. 295–317.

Baillieux, P., Schill, E., Edel, J.-B., Mauri, G., 2013. Localization of temperature anomalies in the Upper Rhine Graben: insights from geophysics and neotectonic activity. Int. Geol. Rev. 55, 1744–1762. https://doi.org/10.1080/00206814.2013.794914

Baudracco-Gritti, C., 1985. Substitution du manganèse bivalent par du calcium dans les minéraux du groupe: braunite, neltnerite, braunite II. Bull. Minéralogie 108, 437–445.

Baudracco-Gritti, C., Caye, R., Permingeat, F., Protas, J., 1982. La neltnerite $CaMn_6SiO_{12}$, une nouvelle espèce minérale du groupe de la braunite. Bull. Minéralogie 105, 161–165.

Berger, J.-P., Reichenbacher, B., Becker, D., Grimm, M., Grimm, K., Picot, L., Storni, A., Pirkenseer, C., Derer, C., Schaefer, A., 2005a. Paleogeography of the Upper Rhine Graben (URG) and the Swiss Molasse Basin (SMB) from Eocene to Pliocene. Int. J. Earth Sci. 94, 697–710. https://doi.org/10.1007/s00531-005-0475-2

Berger, J.-P., Reichenbacher, B., Becker, D., Grimm, M., Grimm, K., Picot, L., Storni, A., Pirkenseer, C., Schaefer, A., 2005b. Eocene-Pliocene time scale and stratigraphy of the Upper Rhine Graben (URG) and the Swiss Molasse Basin (SMB). Int. J. Earth Sci. 94, 711–731. https://doi.org/10.1007/s00531-005-0479-y

Bonhomme, M., 1958. Contribution à l'étude d'une mine de manganèse dans la région de Gérardmer.

Bonhomme, M.G., Bühmann, D., Besnus, Y., 1983. Reliability of K-Ar dating of clays and silicifications associated with vein mineralizations in Western Europe. Geol. Rundsch. 72, 105–117. https://doi.org/10.1007/BF01765902

Boulay, C., 1984. Étude de filons métallifères (Cu, Pb, Zn, F, Ba) à gangue d'anhydrite silicifiée des régions de Giromagny, Auxelles et Sewen-Urbès (Vosges du sud-est, France) (PhD). Université de Lorraine, Nancy.

Boutin, R., Montigny, R., Thuizat, R., 1995. Chronologie K-Ar et $^{40}Ar/^{39}Ar$ du métamorphisme et du magmatisme des Vosges. Comparaison avec les massifs varisques avoisinants. Géologie Fr. 1, 3–25.

Cao, X., Yin, M., Wang, X., 2001. Elimination of the spectral interference from polyatomic ions with rare earth elements in inductively coupled plasma mass spectrometry by combining algebraic correction with chromatographic separation. Spectrochim. Acta Part B At. Spectrosc. 56, 431–441. https://doi.org/10.1016/S0584-8547(01)00170-7

Clauer, N., Zwingmann, H., Chaudhuri, S., 1996. Isotopic (K-Ar and oxygen) constraints on the extent and importance of the Liassic hydrothermal activity in Western Europe. Clay Miner. 31, 301–318. https://doi.org/10.1180/claymin.1996.031.3.02

Dasgupta, S., Sengupta, P., Bhattacharya, P.K., Mukherjee, M., Fukuoka, M., Banerjee, H., Roy, S., 1989. Mineral reactions in manganese oxide rocks; P-T-X phase relations. Econ. Geol. 84, 434–443. https://doi.org/10.2113/gsecongeo.84.2.434

de Villiers, J.P.R., 1980. The crystal structure of braunite II and its relation to bixbyite and braunite. Am. Mineral. 65, 756–765.

de Villiers, J.P.R., 1975. The crystal structure of braunite with reference to its solid-solution behavior. Am. Mineral. 60, 1098–1104.

de Villiers, J.P.R., Herbstein, F.H., 1967. Distinction between two members of the braunite group. Am. Mineral. 52, 20–30.

Decrée, S., Ruffet, G., Putter, T.D., Baele, J.-M., Recourt, P., Jamoussi, F., Yans, J., 2010. Mn oxides as efficient traps for metal pollutants in a polyphase low-temperature Pliocene environment: A case study in the Tamra iron mine, Nefza mining district, Tunisia. J. Afr. Earth Sci. 57, 249–261. https://doi.org/10.1016/j.jafrearsci.2009.08.005

Dekoninck, A., Bernard, A., Barbarand, J., Saint-Bezar, B., Missenard, Y., Lepretre, R., Saddiqi, O., Yans, J., 2016. Detailed mineralogy and petrology of manganese oxyhydroxide deposits of the Imini district (Morocco). Miner. Deposita 51, 13–23. https://doi.org/10.1007/s00126-015-0590-3

Dèzes, P., Schmid, S.M., Ziegler, P.A., 2004. Evolution of the European Cenozoic Rift System: interaction of the Alpine and Pyrenean orogens with their foreland lithosphere. Tectonophysics 389, 1–33. https://doi.org/10.1016/j.tecto.2004.06.011

Edel, J.-B., 1997. Post-Permian magnetic overprinting in the Devonian-Dinantian basin of the Southern Vosges : an overprinting phase in Liassic times contemporaneous with ore mineralizations. Comptes Rendus Académie Sci. Sér. 2 Sci. Terre Planètes 324, 617–624.

Edel, J.-B., Schulmann, K., Rotstein, Y., 2007. The Variscan tectonic inheritance of the Upper Rhine Graben: evidence of reactivations in the Lias, Late Eocene–Oligocene up to the recent. Int. J. Earth Sci. 96, 305–325. https://doi.org/10.1007/s00531-006-0092-8

Edel, J.B., Schulmann, K., Skrzypek, E., Cocherie, A., 2013. Tectonic evolution of the European Variscan belt constrained by palaeomagnetic, structural and anisotropy of magnetic susceptibility data from the Northern Vosges magmatic arc (Eastern France). J. Geol. Soc. 170, 785–804. https://doi.org/10.1144/jgs2011-138

Fluck, P., 1980. Métamorphisme et magmatisme dans les Vosges moyennes d'Alsace : contribution à l'histoire de la chaîne varisque (PhD). Université Louis Pasteur, Strasbourg.

Fluck, P., Ancel, B., 1989. Le paysage minier des sites métalliques des Vosges et de la Forêt-Noire. Ann. Bretagne Pays Ouest 96, 183–201. https://doi.org/10.3406/abpo.1989.3323

Fluck, P., Colas, R., 1992. Les méga-structures filoniennes à galène et sidérite dans le socle rhénan : âge tertiaire des minéralisations de type Sainte-Marie-aux-Mines ? Pierres Terre 35, 117–120.

Fluck, P., Pique, A., Schneider, J.-L., Whitechurch, H., 1991. The Vosges basement. Sci. Géologiques Bull. 44, 207–235.

Fluck, P., Stein, S., 1992. Espèces minérales des principaux districts miniers du massif vosgien. Pierres Terre 106–115.

Fluck, P., Weil, R., 1976. Géologie des gîtes minéraux des Vosges et des régions limitrophes. Corrélation métallogénique Vosges - Forêt-Noire, Mémoires du B.R.G.M., Gîtes minéraux de la France. BRGM.

Frenzel, G., 1980. The manganese ore minerals, in: Geology and Geochemistry of Manganese. General Problems. Akademia Kiaod, Budapest, pp. 25–158.

Fusswinkel, T., Wagner, T., Wenzel, T., Wälle, M., Lorenz, J., 2013. Evolution of unconformity-related MnFeAs vein mineralization, Sailauf (Germany): Insight from major and trace elements in oxide and carbonate minerals. Ore Geol. Rev. 50, 28–51. https://doi.org/10.1016/j.oregeorev.2012.08.001

Geyer, O.F., Gwinner, M.P., Geyer, M., Nitsch, E., Simon, T., Ellwanger, D., 2011. Geologie von Baden-Württemberg, 5., völlig neu bearb. Aufl. ed. Schweizerbart, Stuttgart.

Glasby, G.P., Papavassiliou, C.T., Mitsis, J., Valsami-Jones, E., Liakopoulos, A., Renner, R.M., 2005. The Vani manganese deposit, Milos island, Greece: A fossil stratabound Mn−Ba−Pb−Zn−As−Sb−W-rich hydrothermal deposit, in: Developments in Volcanology. Elsevier, pp. 255–291. https://doi.org/10.1016/S1871-644X(05)80045-2

Griveaux, B., Zarayan, M.-S., Guérin, H., Fourquin, C., Hudeley, H., Théobald, N., Thiébaut, J., Guintrand, Y., 1974. Carte géologique de la France à 1/50 000, 411, Giromagny.

Guérin, H., 1979. Distribution du manganèse dans les séries volcaniques: un guide de la genèse des gisements manganésifères volcanogènes. Phys. Chem. Earth 11, 717–725. https://doi.org/10.1016/0079-1946(79)90067-3

Gutierrez Lanz, J.R., 1985. Etude des filons à Pb-Zn-Cu comportant une gangue sulfatée silicifiée de la région de Thann-Wattwiller (Vospes du Sud) (PhD I.N.P.L.). Université de Lorraine, Nancy.

Hameurt, J., 1967. Les terrains cristallins et cristallophylliens du versant occidental des Vosges moyennes. Mém. Serv. Carte Géologique Alsace Lorraine 402.

Hameurt, J., Durand, M., Flageollet, J.-C., Vincent, P.-L., 1979. Carte géologique de la France à 1/50 000, 376, Remiremont.

Hanor, J.S., 2000. Barite-celestine geochemistry and environments of formation. Rev. Mineral. Geochem. 40, 193–275. https://doi.org/10.2138/rmg.2000.40.4

Hardenbol, J., Thierry, J., Farley, M.B., Jacquin, T., de Graciansky, P.-C., Vail, P.R., 1998. Mesozoic and Cenozoic sequence chronostratigraphic chart, in: Mesozoic and Cenozoic Sequence Stratigraphy of European Basins, SEPM Special Publication. Society for Sedimentary Geology.

Hautmann, S., Lippolt, H.J., 2000. $^{40}Ar/^{39}Ar$ dating of central European K–Mn oxides — a chronological framework of supergene alteration processes during the Neogene. Chem. Geol. 170, 37–80. https://doi.org/10.1016/S0009-2541(99)00241-7

Hein, J.R., Stamatakis, G., Dowling, J.S., 2000. Trace metal-rich Quaternary hydrothermal manganese oxide and barite deposit, Milos Island, Greece. Appl. Earth Sci. 109, 10. https://doi.org/10.1179/aes.2000.109.2.67

Hess, J.C., Lippolt, H.J., 1986. Kinetics of Ar isotopes during neutron irradiation: ^{39}Ar loss from minerals as a source of error in $^{40}Ar/^{39}Ar$ dating. Chem. Geol. Isot. Geosci. Sect. 59, 223–236. https://doi.org/10.1016/0168-9622(86)90073-4

Hess, J.C., Lippolt, H.J., Kober, B., 1995. The age of the Kagenfels granite (northern Vosges) and its bearing on the intrusion scheme of late Variscan granitoids. Geol. Rundsch. 84, 568–577. https://doi.org/10.1007/BF00284521

Hewett, D.F., 1972. Manganite, hausmannite, braunite: features, modes of origin. Econ. Geol. 67, 83–102. https://doi.org/10.2113/gsecongeo.67.1.83

Hewett, D.F., 1971. Coronadite; modes of occurrence and origin. Econ. Geol. 66, 164–177. https://doi.org/10.2113/gsecongeo.66.1.164

Hewett, D.F., 1964. Veins of hypogene manganese oxide minerals in the southwestern United States. Econ. Geol. 59, 1429–1472. https://doi.org/10.2113/gsecongeo.59.8.1429

Hewett, D.F., Fleischer, M., 1960. Deposits of the manganese oxides. Econ. Geol. 55, 1–55. https://doi.org/10.2113/gsecongeo.55.1.1

Hewett, D.F., Fleischer, M., Conklin, N., 1963. Deposits of the manganese oxides; supplement. Econ. Geol. 58, 1–51. https://doi.org/10.2113/gsecongeo.58.1.1

Hinsken, S., Ustaszewski, K., Wetzel, A., 2007. Graben width controlling syn-rift sedimentation: the Palaeogene southern Upper Rhine Graben as an example. Int. J. Earth Sci. 96, 979–1002. https://doi.org/10.1007/s00531-006-0162-y

Illies, J.H., 1978. Two stages rhinegraben rifting, in: Ramberg, I.B., Neumann, E.-R. (Eds.), Tectonics and Geophysics of Continental Rifts. Springer Netherlands, Dordrecht, pp. 63–71.

Illies, J.H., 1977. Ancient and recent rifting in the Rhinegraben. Geol. En Mijnb. 56, 329–350.

Illies, J.H., Fuchs, K., 1974. Approaches to taphrogenesis, in: Proceedings of an International Rift Symposium. Schweizerbart (Nägele u. Obermiller), Karlsruhe, pp. 13–15.

Jurain, G., 1956. Présence d'uranium dans quelques gîtes de manganèse dans les Vosges méridionales et centrales. Comptes Rendus Académie Sci. 243, 1044–1045.

Keller, J., Kraml, M., Henjes-Kunst, F., 2002. $^{40}Ar/^{39}Ar$ single crystal laser dating of early volcanism in the Upper Rhine Graben and tectonic implications. Schweiz. Mineral. Petrogr. Mitteilungen 121–130. https://doi.org/10.5169/seals-62355

Kratinová, Z., Schulmann, K., Edel, J.-B., Ježek, J., Schaltegger, U., 2007. Model of successive granite sheet emplacement in transtensional setting: Integrated microstructural and anisotropy of magnetic susceptibility study: Granite Emplacement in Transtension. Tectonics 26, 1-26. https://doi.org/10.1029/2006TC002035

Laubscher, H., 1992. Jura kinematics and the Molasse Basin. Eclogae Geol. Helvetiae 83, 653–675. https://doi.org/10.5169/seals-167024

Li, Y.-H., 2000. A compendium of geochemistry: from solar nebula to the human brain. Princeton University Press, Princeton, N.J.

Liewig, N., 1993. Datations isotopiques d'illites diagénétiques de grès réservoir à gaz, huile et eau du nord-ouest de l'Europe. Implications pétrogénétiques et géodynamiques (Unpublished Ph.D. thesis). Université de Strasbourg, Strasbourg.

Liewig, N., Clauer, N., Sommer, F., 1987. Rb-Sr and K-Ar dating of clay diagenesis in Jurassic sandstone oil reservoir, North Sea. Am. Assoc. Pet. Geol. Bull. 71, 1467–1474. https://doi.org/10.1306/703C80EC-1707-11D7-8645000102C1865D

Lougnon, J., 1985. Contribution à la connaissance de la gîtologie de la région Vosges-Alsace-Moselle après 14 années de prospection de la part du B.R.G.M. (No. 85 DAM 038 OP4). BRGM, Orléans.

Lougnon, J., 1981. Ressources minières françaises : les gisements de manganèse (Bureau de Recherches Géologiques et Minières No. Tome 10). BRGM.

Maynard, J.B., 2014. Manganiferous sediments, rocks, and ores, in: Treatise on Geochemistry. Elsevier, pp. 327–349.

McDonough, W.F., Sun, S.-s., 1995. The composition of the Earth. Chem. Geol. 120, 223–253. https://doi.org/10.1016/0009-2541(94)00140-4

Ménillet, F., Fluck, P., 1978. Carte géologique de la France à 1/50 000, 341, Gérardmer.

Migoń, P., Lidmar-Bergström, K., 2002. Deep weathering through time in central and northwestern Europe: problems of dating and interpretation of geological record. Catena 49, 25–40. https://doi.org/10.1016/S0341-8162(02)00015-2

Migoń, P., Lidmar-Bergström, K., 2001. Weathering mantles and their significance for geomorphological evolution of central and northern Europe since the Mesozoic. Earth-Sci. Rev. 56, 285–324. https://doi.org/10.1016/S0012-8252(01)00068-X

Moorby, S.A., Cronan, D.S., 1983. The geochemistry of hydrothermal and pelagic sediments from the Galapagos hydrothermal mounds field, D.S.D.P. Leg 70. Mineral. Mag. 47, 291–300. https://doi.org/10.1180/minmag.1983.047.344.03

Moore, P.B., Araki, T., 1976. Braunite: its structure and relationship to bixbyite, and some insights on the genealogy of fluorite derivative structures. Am. Mineral. 61, 1226–1240.

Nahon, D.B., 1991. Self-organization in chemical lateritic weathering. Geoderma 51, 5–13. https://doi.org/10.1016/0016-7061(91)90063-Y

Nicholson, K., 1992. Genetic types of manganese oxide deposits in Scotland; indicators of paleo-ocean-spreading rate and a Devonian geochemical mobility boundary. Econ. Geol. 87, 1301–1309. https://doi.org/10.2113/gsecongeo.87.5.1301

Parc, S., Nahon, D., Tardy, Y., Vieillard, P., 1989. Estimated solubility products and fields of stability for cryptomelane, nsutite, birnessite, and lithiophorite based on natural lateritic weathering sequences. Am. Mineral. 74, 466–475.

Perseil, E.-A., 1975. Nature et caractères minéralogiques des oxydes et carbonates manganésifères de Faucogney (Haute-Saône). Comptes Rendus Académie Sci. Paris, D 280, 1931–1934.

Picot, L., Becker, D., Lapaire, F., Ustaszewski, K., Hug, W.A., Berger, J.-P., 2005. Sédimentologie, paléontologie et paléoenvironnements côtiers de la région de Porrentruy (Sud-Rhénan, Paléogène, Jura, Suisse): implications géodynamiques. Eclogae Geol. Helvetiae 98, 281–296. https://doi.org/10.1007/s00015-005-1154-9

Picot, P., Johan, Z., 1982. Atlas of ore minerals. BRGM ; Elsevier, Orléans, Cedex, France : Amsterdam, Netherlands.

Prodehl, C., Mueller, St., Haak, V., 2006. The European Cenozoic rift system, in: Continental Rifts: Evolution, Structure, Tectonics, Developments in Geotectonics. Elsevier, pp. 133–212.

Quesnel, F., 2003. Paleoweathering and paleosurfaces from northern and eastern France to Belgium and Luxembourg: geometry, dating and geodynamic implications. Géologie Fr. 1, 95–104.

Rabenandrasana, S., 1989. Minéralisations filoniennes à Cu-Bi-gangue de sidérite-anhydrite silicifiée et "karstiques" à Pb-Zn-gangue de fluorine-barytine, en bordure du fossé rhénan (région de Colmar-Ribeauvillé) (PhD I.N.P.L.). Université de Lorraine, Nancy.

Roy, S., 1981. Manganese deposits. Academic Press, London ; New York.

Schaltegger, U., Fanning, C.M., Günther, D., Maurin, J.C., Schulmann, K., Gebauer, D., 1999. Growth, annealing and recrystallization of zircon and preservation of monazite in high-grade metamorphism: conventional and in-situ U-Pb isotope, cathodoluminescence and microchemical evidence. Contrib. Mineral. Petrol. 134, 186–201. https://doi.org/10.1007/s004100050478

Schumacher, M.E., 2002. Upper Rhine Graben: Role of preexisting structures during rift evolution: Upper Rhine Graben Evolution. Tectonics 21, 1-17. https://doi.org/10.1029/2001TC900022

Segev, A., Lang, B., Halicz, L., 1991. K-Ar dating of manganese minerals from the Eisenbach region, Black Forest, southwest Germany. Schweiz. Mineral. Petrogr. Mitteilungen 71, 101–114. https://doi.org/10.5169/seals-54349

Segev, A., Steinitz, G., Wauschkuhn, A., 1992. Dating of K-bearing manganese minerals - preliminary results. Geol. Surv. Isr. Curr. Res. 7, 39–41.

Shand, J., 1927. Eruptive Rocks. Nature 120, 872–872. https://doi.org/10.1038/120872a0

Tabaud, A.-S., 2012. Le magmatisme des Vosges : conséquence des subductions paléozoïques (PhD). Université de Strasbourg, Strasbourg.

Tabaud, A.-S., Janou ek, V., Skrzypek, E., Schulmann, K., Rossi, P., Whitechurch, H., Guerrot, C., Paquette, J.-L., 2015. Chronology, petrogenesis and heat sources for successive Carboniferous magmatic events in the Southern-Central Variscan Vosges Mts (NE France). J. Geol. Soc. 172, 87–102. https://doi.org/10.1144/jgs2013-123

Tabaud, A.-S., Whitechurch, H., Rossi, P., Schulmann, K., Guerrot, C., Cocherie, A., 2014. Devonian-Permian magmatic pulses in the northern Vosges Mountains (NE France): result of continuous subduction of the Rhenohercynian Ocean and Avalonian passive margin. Geol. Soc. Lond. Spec. Publ. 405, 197–223. https://doi.org/10.1144/SP405.12

Thiry, M., Quesnel, F., Yans, J., Wyns, R., Vergari, A., Theveniaut, H., Simon-Coiçon, R., Ricordel, C., Moreau, M.-G., Giot, D., Dupuis, C., Bruxelles, L., Barbarand, J., Baele, J.-M., 2006. Continental France and Belgium during the early Cretaceous: paleoweatherings and paleolandforms. Bull. Société Géologique Fr. 177, 155–175. https://doi.org/10.2113/gssgfbull.177.3.155

Thomas, R., Tischendorf, G., 1987. Evolution of Variscan magmatic-metallogenetic processes in the Erzgebirge according thermometric investigations. Z. Geol. Wiss. 15, 25–42.

Tournier, B., Liewig, N., Edel, J.-B., Montigny, R., 1999. Concordance d'âges K-Ar sur illite avec des âges de réaimantations: exemple des grès triasiques d'Alsace. Comptes Rendus Académie Sci. - Ser. IIA - Earth Planet. Sci. 329, 7–13. https://doi.org/10.1016/S1251-8050(99)80221-3

Varentsov, I.M., 1996. Manganese ores of supergene zone: Geochemistry of formation, Solid Earth Sciences Library. Springer Netherlands, Dordrecht.

von Eller, J.-P., Sittler, C., 1974. Les Vosges et le Fossé Rhénan, in: Géologie de La France, Vieux Massifs et Grands Bassins Sédimentaires. Doin, Paris, pp. 63–78.

Weil, R., Stat, A., Meister, L., Bonhomme, M., 1959. Les espèces minérales du gisement de manganèse du Haut-Poirot, près de Gérardmer (Vosges). Bull. Serv. Carte Géologique Alsace Lorraine 2, 49–59.

Wernicke, R.S., Lippolt, H.J., 1997. (U+Th)–He evidence of Jurassic continuous hydrothermal activity in the Schwarzwald basement, Germany. Chem. Geol. 138, 273–285. https://doi.org/10.1016/S0009-2541(97)00020-X

Wetzel, A., Allenbach, R., Allia, V., 2003. Reactivated basement structures affecting the sedimentary facies in a tectonically "quiescent" epicontinental basin: an example from NW Switzerland. Sediment. Geol. 157, 153–172. https://doi.org/10.1016/S0037-0738(02)00230-0

Wickert, F., Altherr, R., Deutsch, M., 1990. Polyphase Variscan tectonics and metamorphism along a segment of the Saxothuringian-Moldanubian boundary: The Baden-Baden Zone, northern Schwarzwald (F.R.G.). Geol. Rundsch. 79, 627–647. https://doi.org/10.1007/BF01879206

Wickert, F., Eisbacher, G.H., 1988. Two-sided Variscan thrust tectonics in the Vosges Mountains, northeastern France. Geodin. Acta 2, 101–120. https://doi.org/10.1080/09853111.1988.11105160

Wilson, M., Neumann, E.-R., Davies, G.R., Timmerman, M.J., Heeremans, M., Larsen, B.T., 2004. Permo-Carboniferous magmatism and rifting in Europe: introduction. Geol. Soc. Lond. Spec. Publ. 223, 1–10. https://doi.org/10.1144/GSL.SP.2004.223.01.01

Wood, S.A., Samson, I.M., 2000. The hydrothermal geochemistry of tungsten in granitoid environments: I. relative solubilities of ferberite and scheelite as a function of T, P, pH, and mNaCl. Econ. Geol. 95, 143–182. https://doi.org/10.2113/gsecongeo.95.1.143

Wyns, R., 2002. Climat, eustatisme, tectonique: quels contrôles pour l'altération continentale? Exemple des séquences d'altération cénozoïques en France. Bull. Inf. Géologues Bassin Paris 39, 5–16.

Ziegler, P.A., 1992. European Cenozoic rift system. Tectonophysics 208, 91–111. https://doi.org/10.1016/0040-1951(92)90338-7

Chapter 6

Weathering crust of the Mn-rich Ordovician sediments in the Stavelot massif (Ardenne, Belgium)

Chapter 6

Weathering crust of the Mn-rich Ordovician sediments in the Stavelot massif (Ardenne, Belgium)

The occurrence of Ordovician Fe-Mn-rich sediments (Ottré Formation, Salm Group) in the Stavelot inlier (NE Ardenne, Belgium) has drawn the attention of geoscientists for more than one century, as they contain natural "coticule" whetstones and numerous weathered Mn deposits mined until 1934. Two locations expose the Fe-Mn-bearing rocks. The Chevron area, to the north, is located at an altitude of 230-380 m and the Salmchâteau at 480-570 m. The Mn-bearing sediments underwent a greenschist facies metamorphism during the Caledonian and/or Variscan orogenesis. More recently, weathering processes transformed the primary mineral assemblages (mainly rhodochrosite, spessartine, muscovite, chloritoid, andalusite, hematite) into secondary Mn oxides, —hydroxides and —oxyhydroxides (namely cryptomelane, nsutite, lithiophorite, manganite, pyrolusite), clays (mainly kaolinite) and Fe oxides (goethite). As with other scattered weathering deposits in the Ardenne (mainly kaolin), the presence of K-bearing Mn oxides (i.e., hollandite *s.s.* or cryptomelane) offers the opportunity to date the weathering processes by the $^{40}Ar/^{39}Ar$ method.

The first part of this chapter is based on a published book chapter in "Landscapes and Landforms of Belgium and Luxembourg" (Demoulin, 2018) entitled "*Erosion Surfaces in the Ardenne–Oesling and Their Associated Kaolinic Weathering Mantle*" authored by Demoulin Alain, Barbier François, Dekoninck Augustin, Verhaert Michèle, Ruffet Gilles, Dupuis Christian and Yans Johan (63-84 p.) in 2018. This paper (Demoulin *et al.*, 2018a) presents the long-term geomorphology of the Paleozoic Ardenne–Oesling massif of Southern Belgium and the landforms that attest to the very long persistence and high resistance to erosion of landscape elements created as far back in time as the Lower Cretaceous in a region of predominantly under a continental regime and at constant low to moderate elevation since the Permian times. The results deal with the antiquity of kaolinic weathering mantles preserved in four sites on or close to the plateau surfaces characteristic of the Ardennian landscape, showing that they record several weathering phases. Then, a special care is taken from the Stavelot massif (Hautes Fagnes), which constitutes the highest NE part of the Ardenne. Four erosion surfaces have been recognized during the Cretaceous and the Cenozoic in response to the variable interplay of the marine transgression-regression, climatic, and tectonic controls.

The second paper is accepted with revision in Ore Geology Reviews and entitled "*Genesis and $^{40}Ar/^{39}Ar$ dating of K-Mn oxides from the Stavelot Massif (Ardenne, Belgium): insights on Oligocene to Pliocene weathering periods*". Dekoninck *et al.* (accepted with revision, in revision) investigate weathering processes of Mn-rich rocks by providing (1) refined mineralogical, petrographical and geochemical data, and (2) new $^{40}Ar/^{39}Ar$ geochronology of K-Mn oxides. The data show the multistage character of weathering and a detailed formation of these secondary Mn oxides. Within this sequence, K-Mn oxides yield several stages of weathering during Miocene times.

6.1 Erosion surfaces in the Ardenne–Oesling and their associated kaolinic weathering mantle

It has long been recognized that erosion surfaces are a main component of the landscape in the southern part of Belgium and the northern Grand-Duchy of Luxembourg, where they impose the levelled horizons and extended flat areas characterizing the Paleozoic Ardenne–Oesling Plateau (Oesling, or Éislek in Luxembourgian, is the name given to the part of the Rhenish massif situated in the Grand-Duchy of Luxembourg). Bearing witness to the Mesozoic and Cenozoic geomorphological evolution of the region, they constitute the long-term frame in which incision of the Plio-Quaternary drainage network has not yet been nibbled the pre-Quaternary heritage.

The Ardenne massif is famous for its well-preserved erosion surfaces, the so-called peneplains that W. Davis commented on already in the end of the nineteenth century (Davis, 1895, 1899) after having visited the area with A. de Lapparent during one of his European travels. The age of the surfaces and the uplift history of the massif revealed by their arrangement, were already a subject of discussion. This testing by Davis of his normal cycle of erosion in the Ardennian landscape was possible because, ten years earlier, Gosselet (1888) had provided a very modern overview of the nature and age of the post-Paleozoic sediments sparsely preserved on the surfaces and had discussed the tectonic deformations implied by their distribution.

Many studies dealt with the Ardennian erosion surfaces in the first half of the twentieth-century, building on the Davis' theory or sometimes adapting it, such as Baulig (1926), with his multifaceted Ardennian platform. However, it was a long time before one realized that these surfaces had been formed under climatic conditions totally different from those currently prevailing. Being the product of a long evolution under tropical conditions, they essentially respond to the etchplanation processes proposed by Wayland (1933), possibly flavored with features of the pedimentation model of King (1947), much more than to the normal erosion model of Davis (1899). Gullentops (1954) was probably the first to show real interest in the remnants of the weathering mantle often accompanying the old surfaces and to take advantage of them in his reconstruction of the long-term geomorphic history of the massif. Recently, qualitative observations gave way to quantitative data about the age of the Ardennian kaolinic saprolites, which bring additional support to the chronology of such reconstructions (Yans, 2003; Thiry *et al.*, 2006).

In this section, the geomorphic history of the Ardenne–Oesling massif will be reexplored through the analysis of four archetypal sites of the Ardenne. We first describe the deep weathering profile exposed at Transinne, in the last quarry active in kaolin exploitation in west-central Ardenne, for which we present new

geochronological results. Then, moving to the eastern part of the Ardenne (Plateau des Tailles area, Bihain site), we provide a new Ar–Ar dating of the weathering profiles. The Hautes Fagnes Plateau, a recently uplifted area that has preserved several well-developed erosion surfaces of Cretaceous and Paleogene ages will also be described because it offers a condensed view of various modes of surface evolution. Finally, new dating of supergene minerals from the northern part of the Ardenne (Beez and Morialmé sites, Entre-Sambre-et-Meuse) will be discussed against the background of the Ardenne evolution.

6.1.1 Weathering mantles

6.1.1.a Geographical and geological setting

Located in the southern part of Belgium, the Ardenne region geologically corresponds to the Ardenne allochthon, which is part of the Rheno-hercynian fold-and-thrust belt. Belanger *et al.* (2012) recently distinguished the following structural units, from north to south, across the Paleozoic of Belgium: the Brabant Massif and the base of its Devonian cover unaffected by the Variscan orogeny, the Brabant parautochthon, the Haine-Sambre-Meuse overturned thrust sheets (HSM-OTS) and the Ardenne allochthon where the Transinne and Bihain sites are located (►Fig. 6.1). The third presented site, Morialmé, is situated in the Entre-Sambre-et-Meuse area, which is the northwestern part of the Ardenne allochthon, whereas the fourth one, Beez, is located in the HSM-OTS.

Thick saprolites are widespread in Belgium (e.g., Quesnel *et al.*, 2002; Yans, 2003; Dejonghe and Boni, 2005; Dusar and Lagrou, 2007). Yans (2003) highlighted at least ten areas that experienced period(s) of deep chemical weathering in Belgium. ►Fig. 6.2 provides an overview of those affected by weathering period(s) well constrained in time in and around the Ardenne, but additional areas with unconstrained timing of weathering may also be listed (e.g., Welkenraedt, Hautes Fagnes, Rocroi, northern part of the Mons Basin; (Yans, 2013). The weathering led to the formation of saprolites up to 80- and 65 m-thick in the Brabant Massif and the Haute-Lesse area, respectively.

North of the Ardenne, the long phase of weathering and kaolinization that affected the Paleozoic basement of the Brabant Massif to depths reaching a maximum of 80 m started in the Early Cretaceous and continued up until the Cenomanian along the southern margin of the massif and the Santonian or later along its northern margin, depending on the local time of flooding and onset of subsequent marine sedimentation (Dusar and Lagrou, 2007). The saprolites are widely preserved, with thickness varying strongly even at the local scale (Mees and Stoops, 1999). In the Belgian Lorraine,

south of the Ardenne, the Lower Devonian sediments were similarly weathered before being covered by Permo-Triassic sediments (Boulvain *et al.*, 2000).

West of the Ardenne, in the eastern Mons Basin, weathering of glauconiferous levels of the Grandglise Member (Hannut Formation, Late Thanetian) was likely responsible for the formation of the so-called Landenian quartzites and Sparnacian silcretes (e.g., Dupuis, 1979; Quesnel *et al.*, 2002), possibly in relation with volcanic ashfalls (Baele *et al.*, 2016), before they were buried beneath the Ypresian sediment cover.

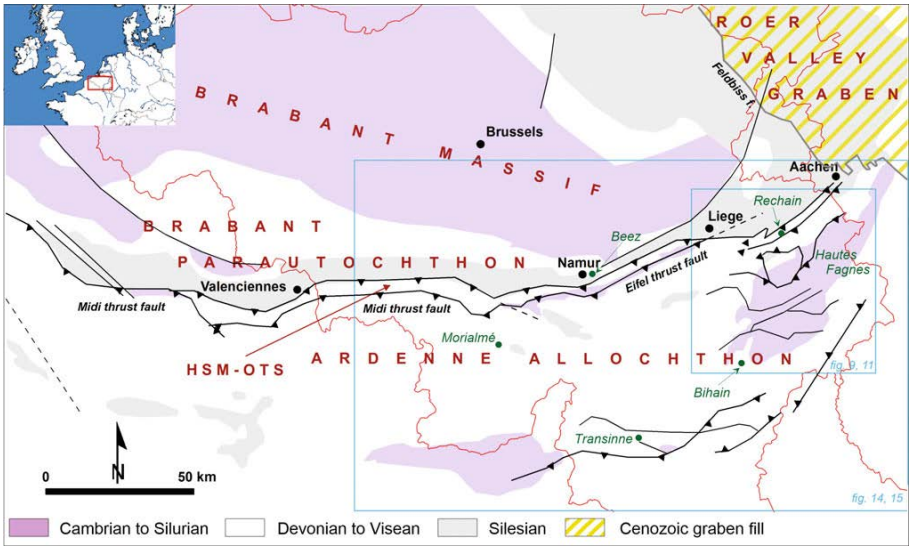

►**Fig. 6.1** Main structural units of the Paleozoic in Belgium and Luxembourg (stripped of their Meso-Cenozoic cover in Middle and Low Belgium). Four units are distinguished within the Paleozoic basement (Brabant Massif, Brabant parautochthon, HSM-OTS: Haine-Sambre-Meuse overthrust sheets, and Ardenne allochthon). The Variscan front is marked by the Midi and Eifel thrust faults, from west to east. In the NE, up to 1.5-km-thick Cenozoic deposits were accumulated in the Roer Valley Graben. Green dots and names locate the sites mentioned in this chapter

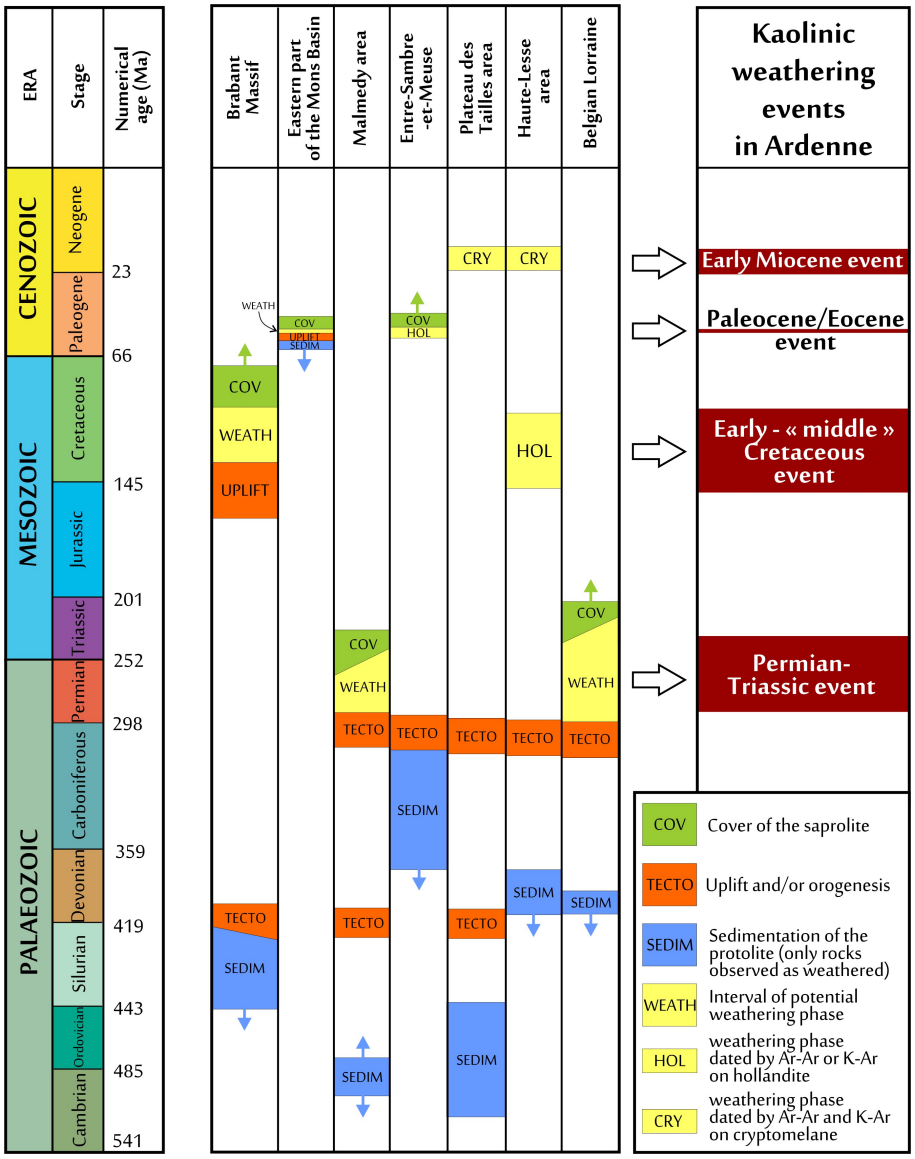

►**Fig. 6.2** Chronology of sedimentation (only rocks affected by deep weathering are represented here), geodynamic activity—essentially uplift, weathering, and burial, defining the history of the saprolites recognized in Belgium (and Luxembourg).

6.1.1.b Characterization and dating of key Ardennian saprolites

Residual saprolites are especially widespread in the little dissected plateau areas of central Ardenne. While occurrences, more limited in extent and depth, are also present outside the Early Devonian core of the massif, it is remarkable that the summit ridges of the Condroz area, at elevations between 250 and 400 m north of central Ardenne,

only contain very local spots of in situ weathering (Gullentops, 1954; Alexandre and Thorez, 1995). Although the Ardennian saprolites were developed by ferrallitic processes under climates warmer than present, the ferruginous upper part of the profiles has mostly been removed by later erosion of the uplifted plateau and is only preserved in scattered places around the massif (e.g., at the Borne-de-Fer, French–Luxembourgian border; Théveniaut *et al.*, 2007), where uninterrupted Mesozoic and Cenozoic tectonic stability strongly limited denudation. Elsewhere, only the saprolite *sensu* Nahon (1991), i.e., the bulk of the deeply weathered bedrock below the lateritic soil, is (partly) preserved. Depending on bedrock lithology, the neoformed minerals are essentially made of kaolinite, often poorly crystallized and mainly derived from the chlorite component of the Ardennian shales (Alexandre and Thorez, 1995), and iron oxides and hydroxides. Quartz is the dominant residual mineral over sandstone and quartzitic bedrock. The saprolite retains the sedimentary and metamorphic structures of the parent rock, as exemplified by the Transinne outcrop, in west-central Ardenne, where stratification is clearly preserved in the weathered material (►Fig. 6.3). The distribution of weathering depths may be highly unequal at the local scale over the Ardennian erosion surfaces because erosion led to the preservation of only the roots of the original weathering mantles and the weathering front is very irregular, mainly in relation with the variable degree of bedrock fracturing and the fracture geometry.

In order to improve the understanding and, especially, the chronology of the long-term geomorphic evolution of the Ardenne–Oesling, its erosion surface landscape and the associated kaolinic weathering mantles, we focused on four saprolite sampling sites in central Ardenne (Transinne in the Haute-Lesse area and Bihain in the Plateau des Tailles), the Entre-Sambre-et-Meuse (Morialmé), and the Haine-Sambre-Meuse overturned thrust sheets (Beez, a karst-controlled site near Namur). The dating of weathering periods is obviously very helpful for reconstructing the chronology of paleosurface development because, by definition, the erosion surface itself leaves few datable traces of its evolution. Moreover, it contributes to highlight the interplay between weathering and erosion processes, including the estimation of denudation rates and sediment budgets in the adjacent basins (e.g., De Putter *et al.*, 2015).

- *Transinne*

The Paleozoic basement of the Ardenne and adjacent areas experienced intense weathering during successive post-Variscan periods. These weathering phases generated kaolinic profiles that reach a depth of 65 m below the levelled plateau surface cut by the Transinne quarry at 445 m asl (►Fig. 6.4). By contrast, outcrops in the nearby valley of the Haute Lesse expose fresh, though densely jointed bedrock at elevations of ~330 m. Discovered by Jérôme (1907), the kaolin has been mined since

1922 in this area and is now used for the cement and the ceramics industries. In Transinne, the mineralogy of the saprolite developed over Late Lochkovian shales and sandstones mainly consists of neoformed kaolinite, iron, and manganese oxides in various proportions, with residual illite and quartz (Dupuis *et al.*, 1996; Yans, 2003).

►**Fig. 6.3** View of the kaolinized Lochkovian shales and sandstones at Transinne (see location in Fig. 5.1) showing the preservation of the rock structures by the saprolite.

Weathered mantles may contain neoformed cryptomelane, a potassium-bearing Mn oxide with tunnel structure, and hollandite, its barium-bearing equivalent that may also include potassium cations. Belonging to the hollandite supergroup (Biagioni *et al.* 2013), both are suitable for radiometric dating using the K–Ar system. The ^{39}Ar–^{40}Ar and ^{40}K–^{40}Ar methods have been widely used on Mn oxides to date weathering periods around the world (e.g., Vasconcelos *et al.*, 1995), including in Western Europe (e.g., Hautmann and Lippolt, 2000; Dill *et al.*, 2010). Dating hollandites and cryptomelanes of the Transinne section by these methods, Yans (2003) showed that the saprolite in Transinne is the result of polyphase weathering. K–Ar ages of hollandites in the upper part of the profile range between 120 and 135 Ma (Early Cretaceous), while Ar–Ar and K–Ar results consistently point to ages around 21 Ma (Early Miocene) for cryptomelanes from the basal part of the profile. Additional K–Ar ages on hollandites provided by Thiry *et al.* (2006) date the intermediate part of the profile to ~88–94 Ma (early Late Cretaceous). Moreover, paleomagnetic dating on iron (hydr)oxides sampled in the upper part of the Transinne

profile yielded ages around 110–120 Ma, fully supporting the K–Ar ages obtained in that part of the profile (Yans, 2003; Thiry *et al.*, 2006). This vertical succession of ages is consistent with the long-term development of the weathering mantle by downward progression of the weathering front whenever the climatic and tectonic conditions were favourable to deep chemical weathering. The very old age of the upper part of the preserved profile underlines that Cenozoic denudation was almost zero in interior parts of the Ardennian erosion surfaces, and the ages obtained close to the weathering front suggest that the Early Miocene was the last period favourable to resumption of kaolinization in the Ardenne. Finally, Pb–Pb dating of secondary U-bearing phosphates emplaced *per descensum* in fractures located just below the weathering front and probably closed since the time of phosphate precipitation might indicate active weathering as early as the Late Permian-Early Triassic, further confirming the antiquity of parts of the Ardennian landscape (Yans and Dupuis, 2005). However, this dating requires further investigation because lead is very mobile during weathering.

►**Fig. 6.4** The Transinne quarry cuts into Lochkovian shales and sandstones outcropping on the Selandian erosion surface of western and central Ardenne, here at 445 m asl, exposing a ~65-m-thick mantle of deeply kaolinized rocks (© Google Earth 2015).

- *Bihain*

Saprolite thicknesses of up to 50 m have also been recorded over phyllites and quartzites of the Cambrian, Revin Group, of the Stavelot massif, for instance in the Plateau des Tailles area (►Fig. 6.5; Cosan, 1969). At Bihain, a hamlet established at 580–600 m asl on a remnant of an Early Paleocene erosion surface (see below), the

saprolite formed on the phyllites of the Ordovician Ottré Formation. Here too, weathering led to the neoformation of kaolinite, iron oxi-hydroxides and iron–manganese oxides (►Fig. 6.6); Fransolet (1979) already identified the presence of cryptomelane in the lower part of the saprolite of this area. Recent ^{40}Ar–^{39}Ar dating of homogeneous cryptomelane and of a mixture of cryptomelane-lithiophorite suggests an Early Miocene age for the lower part of the weathered profile at Bihain (►Fig. 6.7), consistent with findings in Transinne.

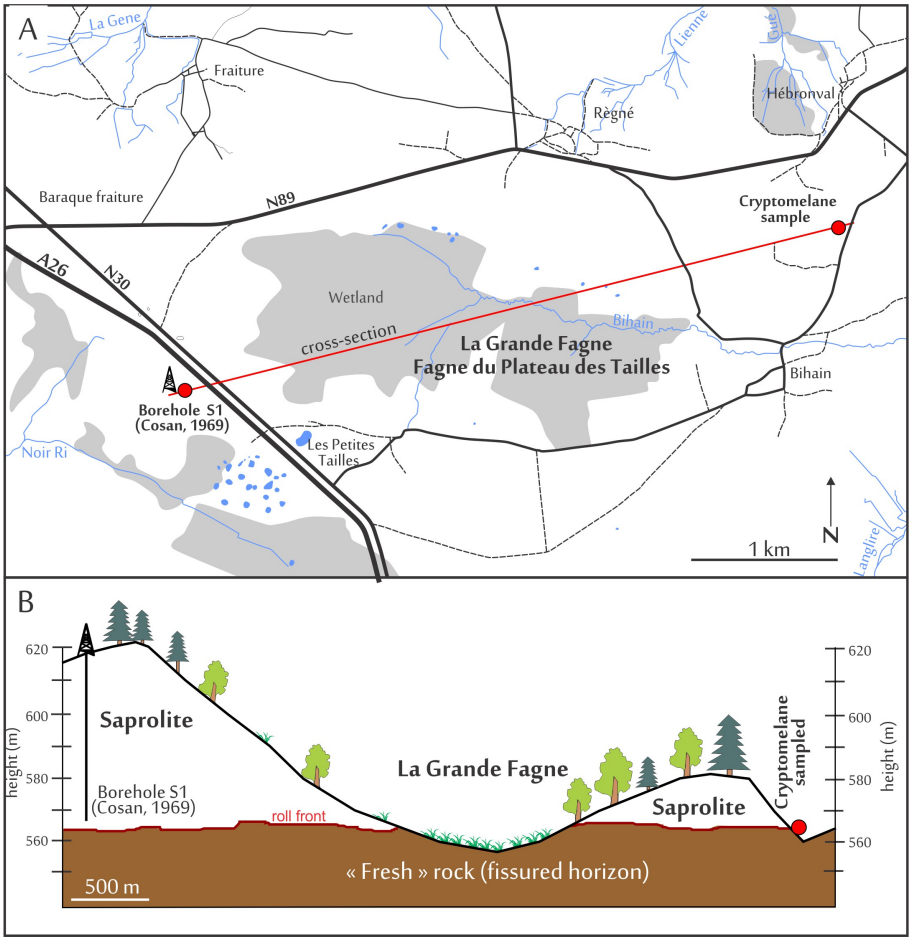

►**Fig. 6.4 a.** Map of the Bihain site in the Plateau des Tailles (see location in ►Fig. 6.1), one of the few areas of central Ardenne-Eifel whose summits still bear witness to the pre-Senonian surface in a region where the Late Cretaceous topography was possibly never covered by marine transgressions. **b**. Weathering profile across the Plateau des Tailles. Note the location of the dated saprolite close to the weathering front (roll front) at 565 m asl, i.e., ~90 m below the summit surface of Cretaceous age.

Of course, such ages obtained close to the weathering front do not preclude older period(s) of weathering for the upper parts of the profile. Interestingly, K–Ar dating of neoformed Mn oxides found in deposits at the base of dissolution pockets within Dinantian limestones at Rechain, just north of NE Ardenne (►Fig. 6.1), yielded ages between 88 and 95 Ma (Cenomanian to Santonian; Demoulin *et al.*, 2010). These Late Cretaceous ages are in good agreement with the topographic position of the samples, situated very close beneath the trace of the pre-Cretaceous erosion surface emerging from below the nearby Cretaceous cover of the Herve Plateau. These deposits thus represent the westernmost extension of the continental sediments making the basal Hergenrath Member of the Late Cretaceous cover in the area, corresponding to a wealden-type lowland sedimentation contemporaneous with the deep weathering that took place farther inland (Demoulin *et al.*, 2010).

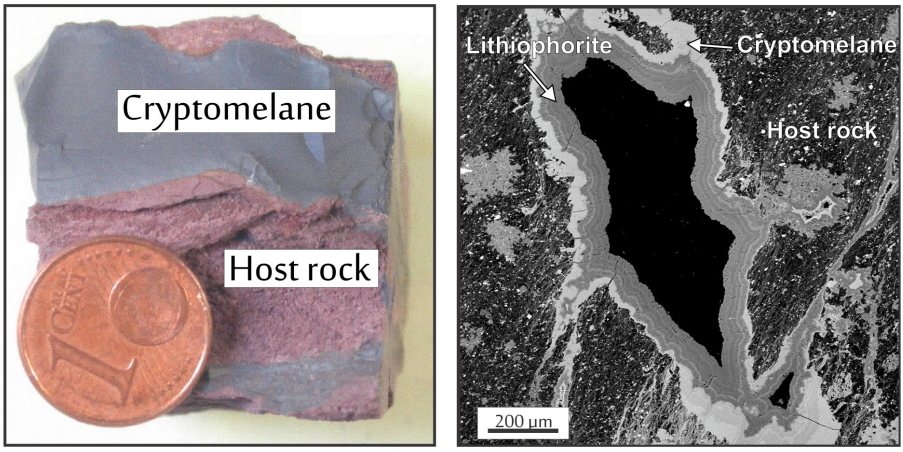

►**Fig. 6.6 a**. Sample of cryptomelane of the Bihain quarry (collection of the Laboratory of Mineralogy, University of Liège, and courtesy A.-M. Fransolet). The host rock is an alternation of Ordovician quartzite and phyllite. **b.** SEM-EDS (Scanning Electron Microscopy with Energy Dispersive X-ray Spectroscopy) view of the mixture cryptomelane-lithiophorite in Bihain.

- *Morialmé*

The Morialmé weathering profile is located in the "Le Faya" quarry, at 260 m asl near Morialmé, in the Entre-Sambre-et-Meuse (ESEM). The quarry cuts the southern flank of an anticline and is mined for the brick industry. The saprolite was developed on micaceous slates of the Famennian Etroeungt and Ciney Formations, weathering processes being mainly kaolinite neoformation in the upper part of the profile and swelling clay formation in its lower part (Barbier *et al.*, 2012). Although the degree of weathering is highly variable inside the quarry (Barbier *et al.*, 2010), the top of the weathering profile still displays the alloterite (Barbier *et al.*, 2012), i.e., the upper part of the profile that has undergone structure collapse and compaction (Wyns *et al.*, 1999), showing that the profile top was quasi unaffected by erosion at the time of its

burial under fluviatile sediments in the Late Paleocene (Schuler *et al.*, 1992) to Early Eocene (►Fig. 6.8; Barbier *et al.*, 2012). Two samples of hollandite from the lower middle part of the profile yielded K–Ar ages of 53.3 ± 2.3 Ma and 58.2 ± 2.4 Ma (►Table 6.1; Barbier *et al.*, 2010), confirming that weathering was still active just prior to this fluvial sedimentation episode at the Paleocene-Eocene transition. This sequence of events is also consistent with the Selandian age assigned by Demoulin (1995) to the erosion surface preserved in the western part of the Ardenne and ESEM, which continued to evolve during the Thanetian where it was not drowned by the Early Thanetian Sea.

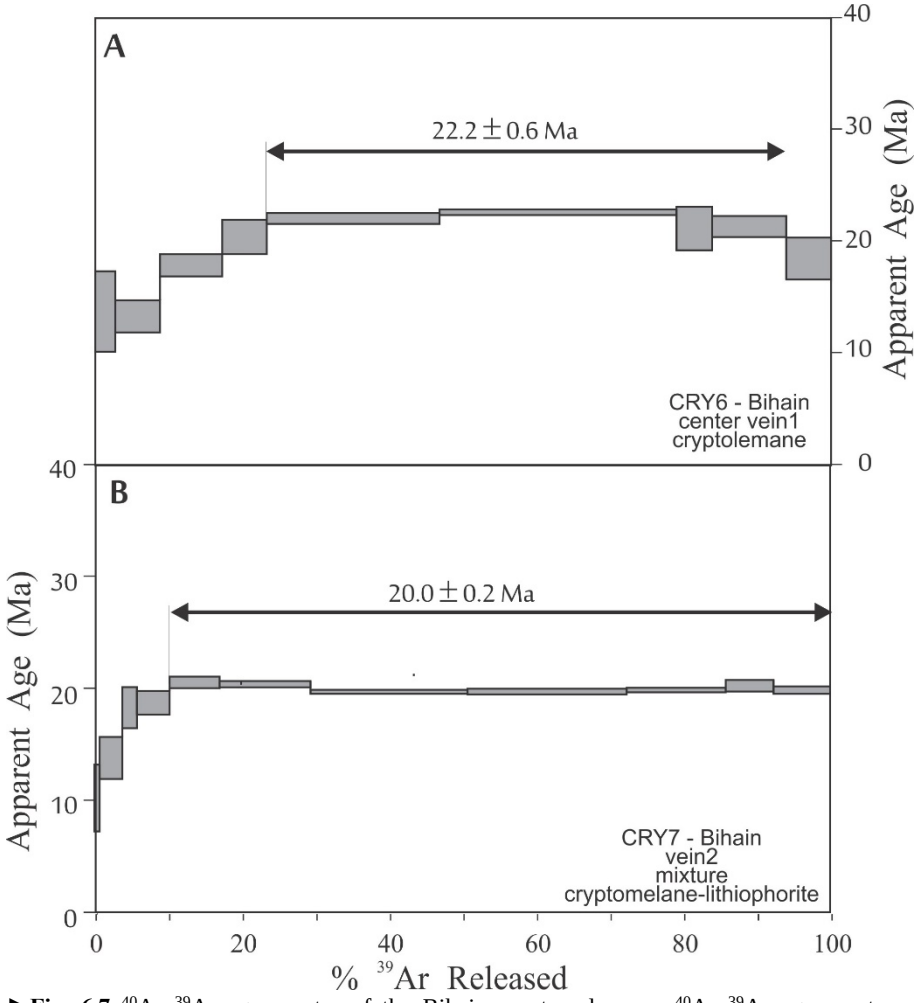

►**Fig. 6.7** ^{40}Ar–^{39}Ar age spectra of the Bihain cryptomelane. **a.** ^{40}Ar–^{39}Ar age spectrum obtained for an homogeneous vein of cryptomelane, yielding a calculated plateau age of 22.2 ± 0.6 Ma (70, 6% of ^{39}Ar released). **b.** ^{39}Ar–^{40}Ar age spectrum of a mixture of cryptomelane and lithiophorite, yielding a calculated plateau age of 20.0 ± 0.2 Ma (89, 8% of ^{39}Ar released).

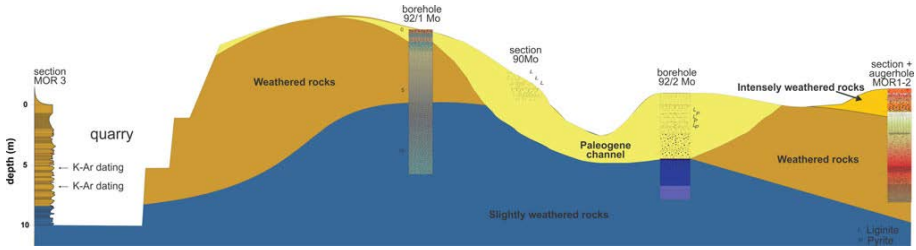

►**Fig. 6.8** The weathering profile at Morialmé (see location in ►Fig. 6.1), with location of the samples for K–Ar dating on hollandite.

- *Beez*

Cut into a bench at ~160 m asl along the northern valley side of the Meuse valley close to Namur, the Beez quarry exposes a cryptokarst developed in Visean limestones. In this karstic setting, possibly in relation with the circulation of acid fluids originating from pyrite leaching and oxidation in the overlying Namurian black shales, the weathering paragenesis includes neoformed halloysite, gibbsite, Fe and Mn (hydr)oxides, gypsum, and jarosite. Based on data from neighbouring cryptokarsts and saprolites, Bruyère *et al.* (2003) pointed to a possible Miocene age of this weathering. New K–Ar analyses performed on jarosite yielded ages of 16.5 ± 0.8 and 16.8 ± 0.5 Ma that confirm the Miocene timing of weathering in Beez (►Table 6.1). One notes that these ages are somewhat younger than those obtained at the base of the Transinne and Bihain profiles. However, the weathering history at Beez might have responded mainly to local geochemical (leaching of iron sulphides) and drainage conditions (karstic vertical transfer, possibly linked to the Meuse valley downcutting) and have a more limited climatic and geodynamic meaning than that assigned to the weathering mantles dated elsewhere in the Ardenne. Moreover, the unknown original depth of the cryptokarst makes it very difficult to relate this weathering episode with any contemporaneous topography.

Summarizing, the available age data for weathering mantles and residues in the Ardenne identify periods favourable to deep weathering that are in excellent agreement with those recognized in neighbouring areas throughout the Mesozoic and the Cenozoic, namely during the Early and early Late Cretaceous, the Late Paleocene, and the Early Miocene plus, to a lesser extent, the Late Permian-Early Triassic. As we will show in the next section, these periods fit also very well with the periods of planation and surface development inferred in the Ardenne from independent data, weathering and planation going hand in hand under conditions of warm humid climate and relative tectonic stability in regions where mean elevation is high enough to create the vadose zone required for effective leaching. It remains of course a possibility that further dating of weathering products may point to other phases of weathering, whose climatic/geodynamic meaning will have to be examined carefully in any case,

avoiding to put too much emphasis on isolated occurrences linked to specific environments (e.g. karstic setting, water table fluctuation zone).

►**Table 6.1** K–Ar dating results on hollandite in Morialmé and jarosite in Beez (see location in ►Fig. 6.1).

Location	Sample	K_2O (%)	Ar (%)	^{40}Ar (10−6 cm^3/g)	Age (Ma ± 2σ)
Morialmé	08mori-oxmn1	0.52	17.38	0.9	53.3 ± 2.3
	08mori-oxmn2	0.66	13	1.25	58.2 ± 2.4
Beez	Jar-Beez-A	3.39	67.5	1.85	16.5 ± 0.8
	Jar-Beez-B	1.92	18.25	1.05	16.8 ± 0.5

6.1.2 Erosion surfaces in the Ardenne and Oesling

6.1.2.a Geographical and geological setting

Beyond being famous for its unique periglacial features (Demoulin *et al.*, 2018b), the Hautes Fagnes Plateau of NE Ardenne (E Belgium) exposes remarkably well-preserved remnants of erosion surfaces of various Mesozoic and Cenozoic ages. Located at the tip of the recently uplifted Paleozoic Ardenne (e.g. Demoulin *et al.*, 2009), this old erosional landscape of stepped surfaces dominates by ~400 m the Pays de Herve, the northern foreland of the massif, to which it connects by a narrow margin of moderately steep slopes drained by the Vesdre River flowing at its foot. While all slopes are covered by dense forests, the top of the plateau above 550 m bears extended moorland that enhances the flat character of the inherited topography, which is still only marginally affected by the Plio-Quaternary incision of rivers. This presence of large peat bogs is a specificity of the Hautes Fagnes Plateau, which is otherwise similar to all plateau areas of the Ardenne (and the nearby Eifel as well).

The Ardenne–Oesling massif belongs mostly to the Rheno-hercynian zone of the Variscan fold-and-thrust belt of middle Europe, the northern limit of the present-day plateau corresponding more or less to the Variscan front (►Fig. 6.9). Structures inherited from the Caledonian orogeny and deformed again in Variscan times crop out along the axis of the uplifted massif, and especially in its northeastern part, resulting in a structurally complex basement wherein longitudinal ENE–WSW folds and thrust faults are cut by numerous NW–SE to NNW–SSE striking normal faults (Demoulin and Ek, 1995). The Hautes Fagnes Plateau pertains almost entirely to the Cambrian-Ordovician Stavelot inlier, one of these inherited Caledonian structures aligned along the axis of the Ardenne anticlinorium and essentially made of variably erodible phyllites and very resistant quartzites. To the south of this anticlinorium, the bulk of the Ardenne Plateau corresponds to the Neufchateau synclinorium, which mainly exposes fairly homogeneous Lower Devonian slates and where marked lithological contrasts arise only locally from intercalations of conglomerate or arkose formations. Such arkoses crop out for instance along the

eastern limit of the Stavelot inlier, in the SE of the Hautes Fagnes area. To the north of the Ardenne anticlinorium, the northern part of the Ardenne allochthon corresponds to the Dinant synclinorium, where the slaty bedrock of the Ardenne *s.s.* gives way to alternating Middle Devonian to Lower Carboniferous sandstones, shales and limestones. These rocks define the particular landscapes of the Famenne, a wide depression carved in Fammenian shales, and of the Condroz plateau, with alternating elongated ridges on sandstones and valleys cut in the limestones (►Fig. 6.9). Scattered over the Condroz ridges and the flat summits of W and NE Ardenne, few remnants of loose sediments, mainly marine sand and clay-with flints, also attest that the massif was partly drowned by marine transgressions coming either from the north or the west during the Cretaceous and the Paleogene (e.g. Demoulin, 2003).

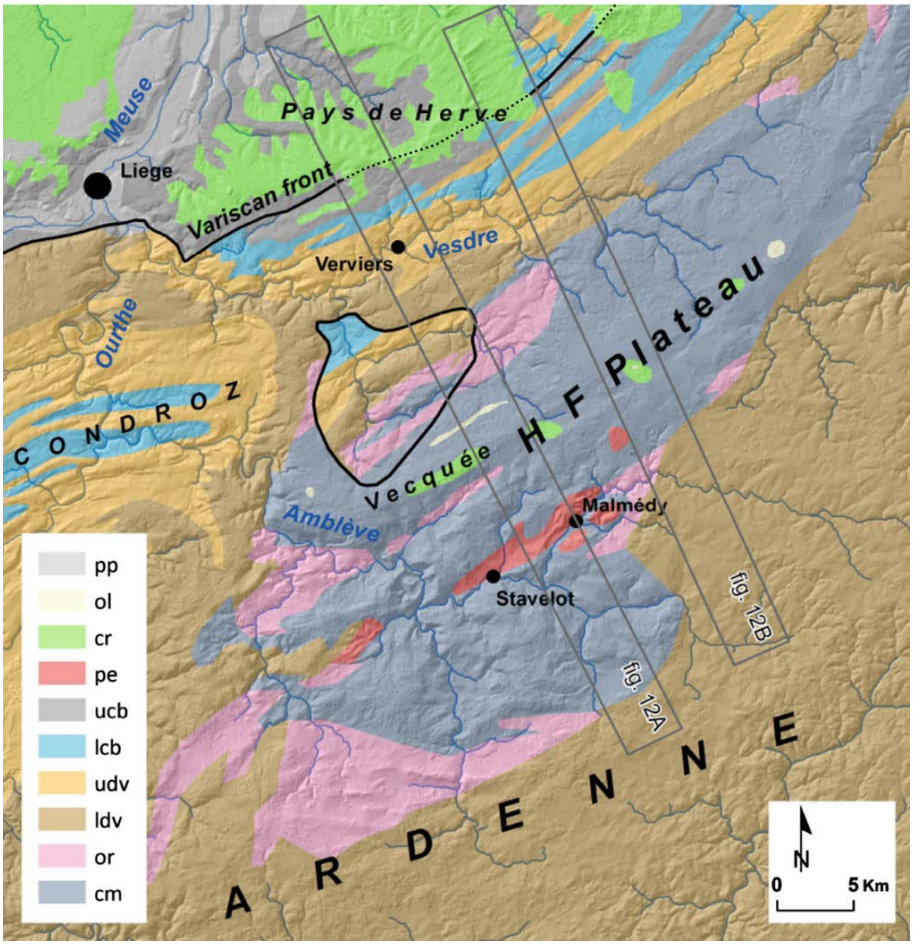

►**Fig. 6.9** Simplified geological map of the Hautes Fagnes Plateau and surrounding areas in NE Ardenne (see location in Fig. 5.1) draped on a hillshade of the SRTM 3″ digital elevation model. cm Cambrian or Ordovician. ldv Lower Devonian. udv Middle and Upper Devonian.

Lcb Lower Carboniferous. ucb Upper Carboniferous. pe Permian. Cr Cretaceous. ol Oligocene. pp Plio-Pleistocene.

Morphologically, the Ardenne represents a western annex to the Rhenish shield in the form of an E–W elongated relief whose flat summits gradually descend from elevations above 600 m in the east to 500–600 m in the central domain and below 400 m west of the Meuse valley. As a consequence, the transition from the massif to its N and S forelands, rather sharp in the east, is progressively less conspicuous westward and, would geology not witness its limit, the Ardenne goes imperceptibly into the Mesozoic cover of the Thiérache to the west. Except its SE confines drained by the Sûre River towards the Mosel and the Rhine, the Ardenne Plateau is drained by rivers of the Meuse basin that have incised 100- to 150-m-deep Plio-Pleistocene valleys through it (Rixhon and Demoulin, 2018). Culminating at ~700 m asl, the Hautes Fagnes Plateau corresponds to the highest part of the massif.

6.1.2.b Shape and characteristic of an erosion surface

Being remote descendants of etchplains formed under warm-humid conditions, the Ardennian erosion surfaces display a variable mix of extremely flat areas and more undulating topographies (►Fig. 6.10). In principle, active etchplains are essentially flat and remarkably horizontal as long as a deep weathering mantle covers them uniformly, leaving only large-scale inselbergs that emerge abruptly from the surrounding surface and dominate it often by 100 or more meters (Thomas, 1994). However, when climatic conditions turn drier or cooler, it is common that the etchplain is stripped of part or all of its weathering mantle and that the weathering front becomes exposed. Being more sensitive to lithological and joint density contrasts, this front usually presents irregularities at all scales that appear then at the surface, forming topographic bumps from m- to dm-sized whalebacks to large subdued hilly reliefs up to a few tens of meters in height. This is the large-scale shape most usually shown by the Ardennian surfaces, in agreement with the patchy preservation of their associated weathering mantles, whose stripping probably mainly resulted from the drastic slowdown of weathering imposed by generally cooler conditions since the Oligocene. Recognising the weak relief currently displayed by the erosion surfaces is important in paleolandscape reconstructions because it prevents one from the temptation of distinguishing supposed surfaces vertically too close to each other.

6.1.2.c Identifying an erosion surface

The most obvious criterion of surface identification is the overall geometry of individual levelled elements and ensembles of elements in the present landscape. However, it relies on the assumption that the envelope of part of the topography may correspond to one particular ancient erosion surface, which is sometimes questionable in regions with a complex history involving many episodes of planation and

intervening deformation and degradation. Nevertheless, the reconstructed surfaces display in general, and especially in the Ardenne, a large-scale plane shape, more or less tilted, sometimes locally or regionally flexured, and displaying a relief amplitude in the order of 20–30 m (Demoulin, 2006). Beyond post-planation deformation, two factors complicate such geometry-based surface reconstructions. The first one relates to the inherent relief of any erosion surface, especially when stripped of their weathering mantle. It implies that the reconstruction allows for a careful balance between topographic variations within a single-stage paleolandscape and close positions of successive surfaces in some areas, especially where differently tilted surfaces are intersecting each other. The second factor refers to the issue of defining the moment when a given surface ceases to evolve as such and begins to degrade, thus giving way to the formation of a new, distinct landscape. This comes to find a clear separation between pure acyclism and clear-cut morphogenetic cyclicity, whereas all transitions actually exist between these end-members in real landscape evolution (Klein, 1990).

►**Fig. 6.10** The pre-Senonian surface as it appears on top of the Hautes Fagnes Plateau, near Baraque Michel, underlain by a widespread peat cover that still locally overlies residual Cretaceous clay-with-flint and sand, and Oligocene marine sands. The faint ~8‰ slope to the north (toward the left of the photograph) was produced by post-Cretaceous tilting of N Ardenne (essentially in the very Early Paleogene, as all Cenozoic erosion surfaces are horizontal across central and northern Ardenne).

Facing such difficulties, geometric reconstructions are advantageously supported by the analysis of the so-called correlative deposits. In particular, when geometry allows the connection of the exhumed part of a paleosurface with its counterpart buried as the base surface of a sedimentary cover in the massif's foreland, the very existence of the latter attests to an episode of aggradation, continental or marine, that clearly ended the previous planation stage and defines its specific topography. In such cases, there is most often a more or less extended transition zone where scattered remnants of the sedimentary cover confirm the position of the exhumed surface within the uplifted massif. In any case, as scarcely as it may be preserved, the sedimentary record is a key element in the analysis of erosional paleolandscapes. In this respect, next to sediments, the weathering mantle associated with the surfaces may also be helpful for distinguishing planation episodes, thanks to specific features such as depth, degree of preservation, secondary products (e.g. duricrusts) and, of course, dating of weathering profiles.

6.1.2.d Erosion surfaces of the Hautes Fagnes plateau

The area whose successive paleolandscapes we describe in some detail corresponds to the Hautes Fagnes region *s.l.*, which is made of the Hautes Fagnes massif *s.s.* (HFM), its western prolongation in the Vecquée ridge (VR), their northern margin, gently sloping toward the Plateau de Herve in the north, and the high plateau area to the SE of the HFM (►Fig. 6.11). Mapping of the intricate erosion surfaces will be aided by the analysis of topographic swath profiles (►Fig. 6.12).

The most conspicuous surface element is represented by the remarkably flat, almost horizontal plateau surface covering the HFM at >600 m asl and currently occupied by peat bogs and extensive heath that confer to the area its wild character and wide horizons (►Fig. 6.10). In the east, this surface is dominated by a few subdued summits rising a few tens of meters above their surroundings. To the NW, it goes rather abruptly in a tilted and dissected surface that makes the margin of NE Ardenne. The forested interfluves materialising the surface remnants slope regularly (by ~4 %) down to ~320 m asl, where they joint the upper edge of the incised Plio-Quaternary valley of the Vesdre. On the opposite side of the HFM, steeper slopes rapidly lead down southeastward to another very regular, hardly dissected surface at 560–580 m asl, covered by pasture and interrupted by small wooden areas only where upper valley reaches of the Roer catchment begin to incise. Though essentially horizontal, this 560–580 m landscape element shows imperceptible slopes going up in a residual relief that culminates in the SE at ~690 m asl at the Weisser Stein (►Fig. 6.12). On its southwest flank, the HFM displays a stepped descent toward the perfectly horizontal ridge of the Vecquée. Extending at 560–570 m asl for ~15 km to the SW and with a width of 0.5–1.5 km, the VR represents a distinct topographic element in the present landscape of the area. On the north, it is bordered by a ~120-m-high escarpment that links it to a lower surface well preserved on the interfluves

between the incised valleys of the Gileppe, the Hoëgne, and the Wayai. This surface, which skirts the western end of the ridge, is observed at elevations around 450 m at its foot, from where it slopes very gently (~0.6 %) toward NW. It includes extended levelled areas at 360–390 m asl between the villages of Theux, Sart-lez-Spa, and Jalhay (►Figs. 6.11 and 6.13). On the south of the VR, a smaller, ~60-m-high escarpment leads down to a local intramontane basin whose levelled bottom appears in the form of wide flat interfluves at uniform elevations of 500–510 m asl. Centred on the area where weak rocks of the Permian graben of Malmédy crop out (►Fig. 6.9), this erosional feature opens towards the massif's exterior in the west, where it is geometrically connected to the 450-m surface.

ggeration x33.

In the northern foreland of the massif, the Meso-Cenozoic sedimentary cover of the Pays de Herve offers an opportunity for reconstructing the profile of two paleosurfaces onto which transgressing seas encroached. The first one is the base surface of the Senonian deposits (the clays and sands of the basal Aachen Formation are dated to the Santonian), which shows a slight but consistent tilt of 1.4% towards NNW. Emerging at the topographic surface in the south of the Pays de Herve, it appears there in the form of large exhumed remnants, similarly tilted and preserving sands and clays of early Late Cretacous age in solution pockets of the underlying Dinantian limestones (Demoulin *et al.*, 2010). Prolonged southward toward the Hautes Fagnes summits, the 1.4% tilt angle connects the VR surface and the tilted surface on the northern flank of the HFM with the Senonian base surface in the Pays de Herve (►Fig. 6.12). The second marker interface in the Meso-Cenozoic cover is the base surface of the sand formation that accumulated during the last marine transgression that covered the northern part of the Ardenne in the Oligocene (Rupelian?). Again, NNW–SSE sections of the cover indicate a minor (0.6%) but uniform NNW tilt of this interface that can easily be followed across the Vesdre valley to the 360–450-m surface in the massif, north of the VR, which shows exactly the same tilt in the same direction.

Finally, remnants of the Cretaceous sands and clay-with-flints and Oligocene marine sands scattered over the northern margin and summits of the Hautes Fagnes region provide additional evidence of the geometric connections established between the massif's erosion surfaces and their buried counterpart in the Pays de Herve. Discontinuous clay-with-flint, often overlying Aachen sand and gravel, are still widespread over the VR and the HFM and are found locally on the sloping surface leading up to the latter, especially southeast of Eupen (►Fig. 6.11). Elsewhere, beyond rare occurrences of isolated reworked flints lying around on the 500-m surface south of the VR, the 360–450-m surface in the north and the 560–580-m surface in the south are completely devoid of Cretaceous sediments. By contrast, sparse deposits of Oligocene sands are mainly encountered all over the 360–450-m surface, while

rarer remnants of this cover also exist next to, and sometimes over, Cretaceous sediments on the HFM summit and northern slope and on the VR.

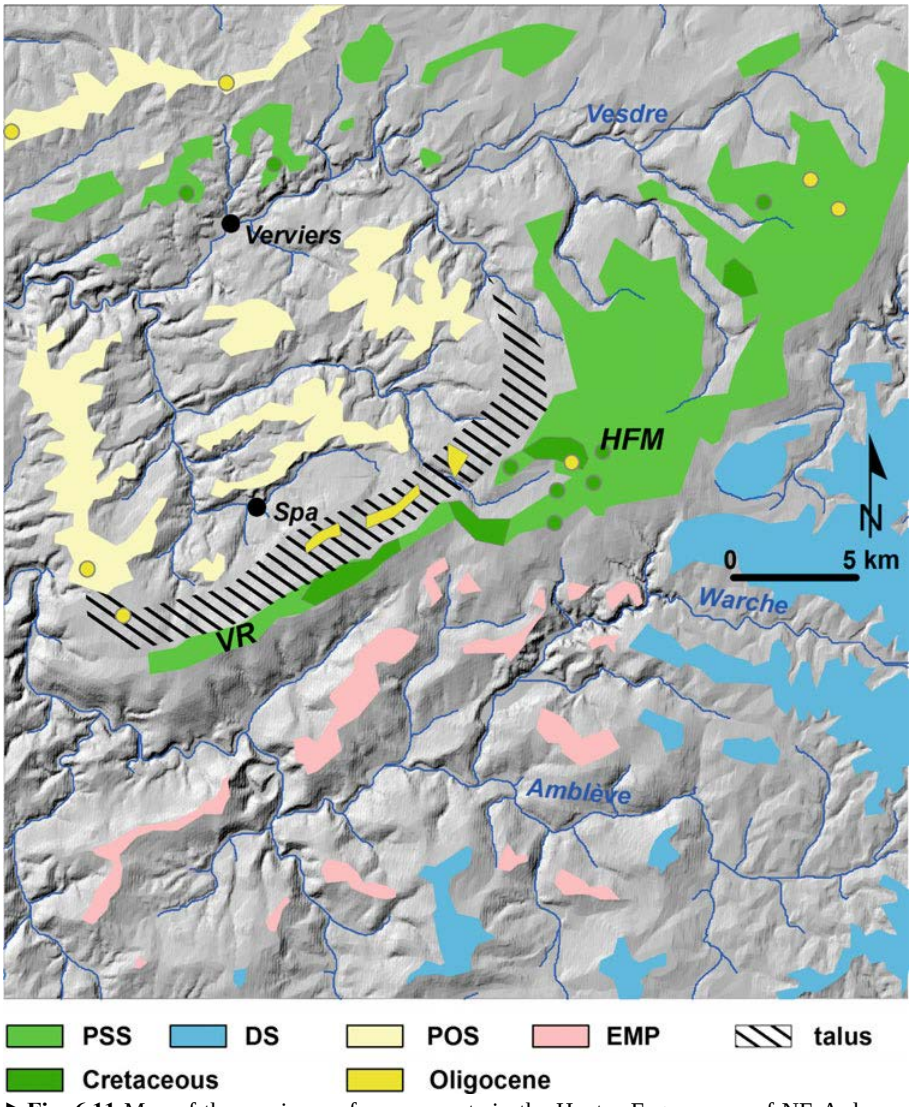

►**Fig. 6.11** Map of the erosion surface remnants in the Hautes Fagnes area of NE Ardenne, draped on a hillshade of the SRTM 3″ digital elevation model. All flat interfluves and broader plateau areas belong to pre-Quaternary topographies of various ages. PSS Pre-Senonian surface. DS Danian surface. POS Pre-Oligocene surface. EMP Early Miocene planation, developed in less resistant Permian conglomerates and Ordovician shales. Talus: ~100-m-high erosional riser between the pre-Senonian/Danian and the pre-Oligocene surfaces as it is preserved since it was carved in the regional topography during the Paleogene.

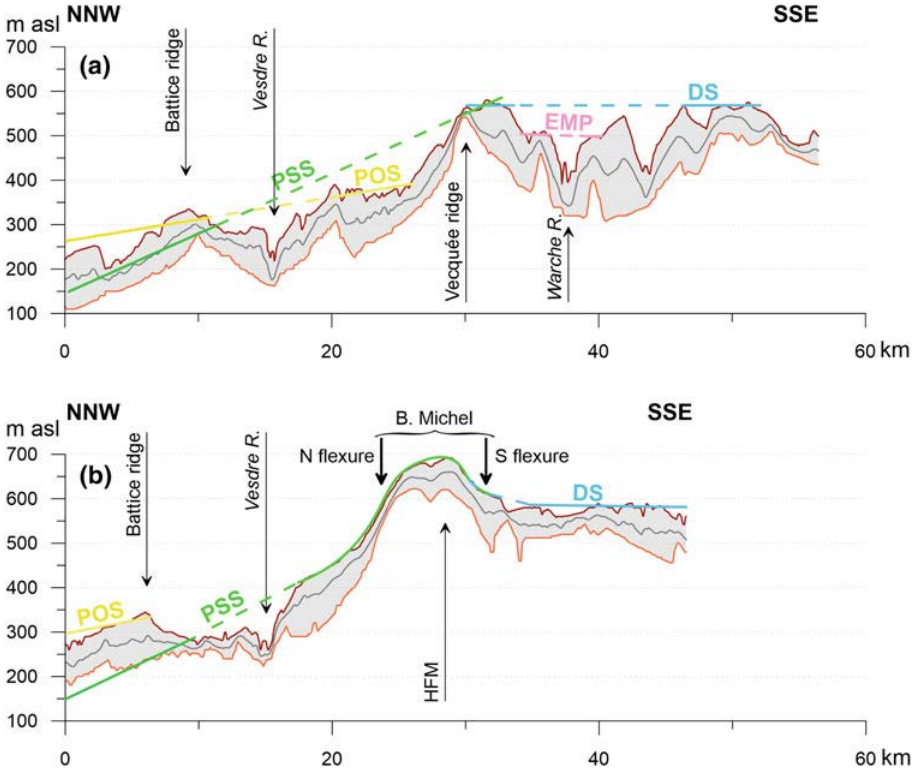

►**Fig. 6.12** NNW-oriented 4-km-wide swath profiles (see location in ►Fig. 6.9; orange, grey, and ruby brown lines are for minimum, mean, and maximum elevations, respectively) showing the geometry of the erosion surfaces across the northern margin of NE Ardenne at the height of the Vecquée ridge (a) and the Hautes Fagnes Plateau (b), where the general tilt to north is complicated by post-Oligocene uplift of the Baraque Michel block inducing the flexure of the surfaces. PSS Pre-Senonian surface. DS Danian surface. POS Pre-Oligocene surface. EMP Early Miocene planation level. The trace of exhumed erosion surfaces obviously follows maximum elevation lines of the swath profiles. By contrast, north of the Vesdre valley, the pre-Senonian surface is still buried under a continuous Upper Cretaceous cover. Height exa

Integrating all these observations, one obtains the following consistent reconstruction of the successive paleosurfaces whose fingerprint is still visible in the present landscape (►Fig. 6.11). The oldest preserved surface in the Hautes Fagnes area is pre-Senonian in age and includes the levelled summits of the region (VR and HFM) and also the tilted surface that makes the northern margin of the HFM and links it to its foreland east of a line joining Verviers to Malmédy (►Fig. 6.12). The unity of this surface made of distinct topographic elements is demonstrated by the Cretaceous deposits that all of them still expose. However, the pre-Senonian surface underwent strong post-planation deformation during the Cenozoic, mainly in the form of a marked differential uplift of the HFM. Its overall geometry shows that the HFM block uplift was limited by flexures on its northern and southern sides (►Fig. 6.12b),

while a series of NNW-striking Variscan faults, reactivated in normal mode, accommodated the ~100 m height difference with the adjacent Vecquée ridge to the west.

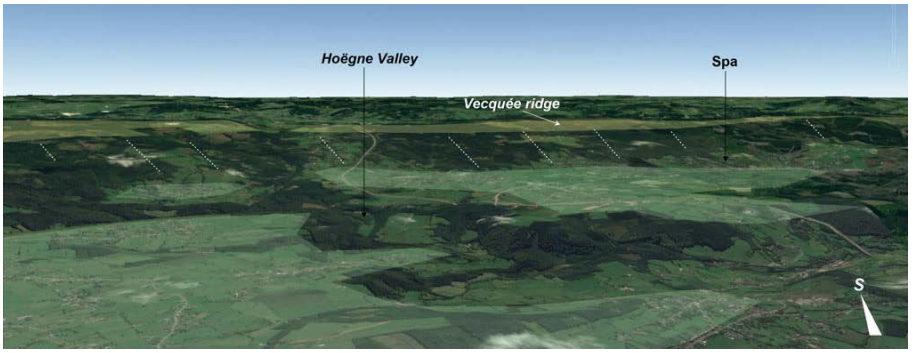

►**Fig. 6.13** S-looking oblique aerial view of the pre-Oligocene surface (in light green transparency) developed at 350–400 m asl north of the Vecquée ridge, which represents the pre-Senonian surface, exhumed and reexposed since the Danian (in light yellow transparency). The erosional scarp between both surfaces (dotted white lines) clearly appears as a regional morphological feature. In the background, beyond the barely visible Early Miocene planation level developed in the Stavelot-Malmédy area, south of the Vecquée, the uniform horizon line shows the well-preserved Danian surface of central Ardenne. Scale the visible length of the Vecquée ridge is ~20 km. Elevation factor 2 (© Google Earth 2015).

Even if they share the VR summit (►Fig. 6.12), the 560– 580-m surface to the SE of the HFM represents a planation episode different than that attested by the pre-Senonian surface. Indeed, with the exception of few residual reliefs such as the Weisser Stein, whose summits are probably hardly degraded isolated remnants of the pre-Senonian surface, the remarkable horizontality of the 560–580-m surface across the whole central Ardenne and nearby Eifel shows that it resulted from low-angle bevelling of the slightly tilted previous (pre-Senonian) topography, the intersection between both surfaces occurring along the VR (►Fig. 6.12a). This interpretation is further supported by the absence of Cretaceous sediments on the 560–580-m surface south of the VR, where their complete removal (their former presence in this area being only proved by isolated clay-with-flints remains on the SE flank of the Weisser Stein) had to precede regradation of their base surface (regradation being the process of tending towards a new grade after a perturbation; Fairbridge, 1968).

Finally, the last envelope surface of the topography locates a third nested paleolandscape that is chiefly associated with the 360–450-m surface developed in the north and west of the Hautes Fagnes region and prolonged inside the massif by the 500-m intramontane basin south of the VR. However, whereas remnants of the Oligocene sand cover scattered over the surface north of the VR attest that it was developed before the Oligocene transgression on the massif, the absence of

corresponding deposits in the intramontane basin despite drowning of the VR by the Oligocene sea strongly suggests that this inward extension of the 360–450-m surface was carved in later times.

Separation between the different surfaces occurs in two ways. While the 560–580-m and, north of the Vesdre valley, the 360–450-m surfaces both cut at low angle the tilted older pre-Senonian surface, a well-developed 60- to 150-m-high erosion scarp, making the northern flank of the VR, separates them from each other (►Fig. 6.12a). The erosional nature of this scarp, as opposed to the tectonic flexures limiting the uplifted HFM, is demonstrated by the fact that N–S sections north of the VR show no equivalent to this flexure in the older, uniformly tilted pre-Senonian surface (►Fig. 6.12). The two types of surface separation suggest distinct erosional mechanisms. Low-angle bevelling is typical of acyclic morphogenesis where surfaces temporally distinguished by their associated sedimentary record gradually regrade their predecessor under etchplanation regime in response to slow, low amplitude deformation. By contrast, erosional scarps signal morphogenic cyclicity, implying a combination of etchplanation and scarp retreat in response to more rapid, larger tectonic deformation with a significant component of en-bloc uplift.

6.1.2.e Dating a surface

It is clear from the Hautes Fagnes example that geometric relationships between paleosurfaces and their links to buried base surfaces within foreland sedimentary covers already provide powerful tools for unravelling the chronology of long-term geomorphology in erosional settings. Taking into account the various types of discontinuity that give rhythm to such a “surface stratigraphy” further allows inferences about the nature of the often tectonic triggers of morphogenesis.

The paleolandscape chronology is also aided by the analysis of correlative deposits preserved on the erosion surfaces. In the Ardenne–Oesling, the oldest sediments of ►Fig. 6.13 interest in this respect correspond to the band of Bunter sandstones (Lower Triassic) cropping out at the southern edge of the Oesling, and continuing eastward inside the massif into the N–S Eifel zone. More to the west, the Mesozoic deposits directly resting on the southern border of the Ardenne are younger, mainly Liassic, and ending with Turonian and Coniacian chalks at the limit between W Ardenne and Thierache (►Fig. 6.14). The equivalent first post-Variscan sediments present on the northern side of the massif are Upper Cretaceous sands and chalks (weathered to clay-with-flint). Their outcrop zone is restricted to the Hautes Fagnes region in the NE (Bless and Felder, 1989), where they nevertheless covered large areas inside the massif as witnessed by the clay-with-flint retrieved at Dalhem, east of the Weisser Stein (►Fig. 6.14). Later, further seas which encroached upon the Ardenne are recorded during the Early Thanetian in the west, where Upper Thanetian continental sands also sparsely cover the western Rocroi Plateau, and during the

Rupelian, when marine sands were deposited not only in the Hautes Fagnes but also over the whole Condroz Plateau and in the ESEM region (►Fig. 6.14).

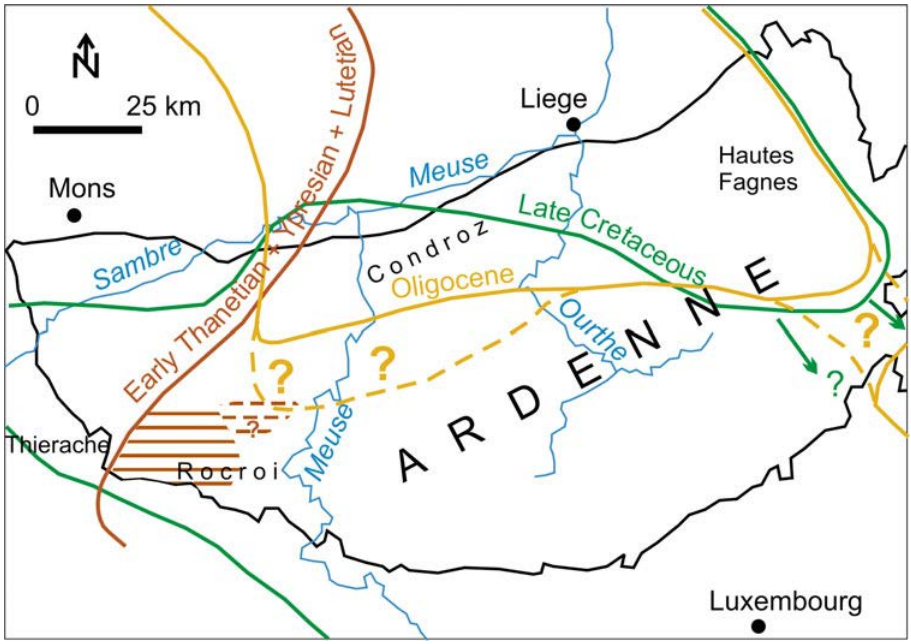

►**Fig. 6.14** Map of the Mesozoic and Cenozoic marine transgressions over the Ardenne massif (modified after Demoulin, 1995). Horizontal brown hatching denotes the area of occurrence of Upper Thanetian continental deposits.

Finally, as indicated in the first part of this chapter, dating techniques applied in the past two decades to minerals precipitated during weathering brought significant improvement in the appraisal of the age of erosional paleolandscapes in uplifted massifs, and especially in the Ardenne, by incorporating in the discussion quantitative information about the age of the associated weathering mantles. The next section brings a brief overview of the current understanding of the long-term geomorphic evolution in the Ardenne–Oesling at the light of this diverse, recently enlarged body of evidence.

6.1.2.f The whole picture: stepped surfaces of the Ardenne-Oesling

During Mesozoic and Cenozoic times, the Ardenne–Oesling underwent many phases of subaerial denudation, only interrupted by limited marine transgressions. The seas that drowned the margins of the massif came from E to SE in Triassic and Liassic times, from W during the Eocene and from N in the Early Oligocene. Only the Late Cretaceous sea probably submerged larger parts of central Ardenne. Seven generations of paleolandscape may be recognized (►Fig. 5.15; Demoulin, 1995,

2003). A pre-Triassic topography, mainly observed in W Eifel, where it displays a fairly animated relief (Junge, 1987), also emerges from below the Triassic cover to form the slopes of the SE margin of the Oesling. It is continued westwards by the diachronic, so-called post-Hercynian peneplain, which constitutes the southern margin of the Ardenne, with interfluves tilted by 1–3% to the south. In NE Ardenne, following a longer phase of post-Variscan denudation, the oldest paleosurface preserved as part of the modern landscape dates back to the Late Cretaceous. As stated above, remnants of this pre-Senonian surface are also preserved as the highest summits, at 650–700 m elevation, in the heart of the massif (Baraque Michel, Baraque Fraiture, Weisser Stein, Schneifel). Then, after the Late Cretaceous regression, acyclic erosion of the Ardenne–Oesling removed its Cretaceous cover almost completely and caused an extensive erosion surface to develop over northern and central Ardenne by regrading the pre-Cretaceous landscape during the Danian. Corresponding to the *"surface supérieure"* of Macar (1938), this Danian surface is now observed at altitudes of 560–580 m, going down slowly in the south to reach ~500 m asl along the southern border of the massif. In contrast with previous surfaces, it developed independently of any marine ingression and its age is primarily inferred from geometrical considerations and the derived *"surface stratigraphy"*. Another information is, however, provided by the Early Cretaceous radiometric ages obtained for the upper part of the weathering profile at Transinne, which roughly locates the weathering front at (modern) 450 m asl at 130 Ma, i.e., ~80 m lower than the trace of the Danian surface in the same location, suggesting that the Danian regradation of the pre-Cretaceous topography was minimal in this area.

The Danian surface represents the end product of the long-lasting acyclic evolution of the Ardenne–Oesling under conditions of prevailing tectonic stability during the Mesozoic. From the Middle Paleocene onwards, rather than regrading the older surfaces more or less uniformly and cutting them at low angle, new paleosurfaces developed at their expense by creating 50–170 m-high scarps that retreated inward, progressively nibbling the higher topography and producing a stepped landscape in response to more perceptible tilt of the massif. This happened so first on the western side of the massif, where the Danian landscape was replaced by a lower erosion surface during the Selandian, until this surface was buried by the Early Thanetian Sea in the west. In the east, it probably remained emerged and continued to evolve and proceed inward for some time, as attested by the 55 Ma radiometric age of the Morialmé weathering profile and the presence of Upper Thanetian continental sands scattered on the Rocroi Plateau (►Fig. 6.15; Voisin, 1981). At its eastern limit, east of the Meuse valley, the Selandian surface abuts the Danian one through a ~70-m-high gently sloping erosional scarp.

Then, another phase of massif uplift caused new surfaces to develop along the northern and southern sides of the Ardenne–Oesling, news scarps separating them

from the inner Selandian and Danian topographies. Such a Late Eocene surface (usually called “pre-Oligocene”) formed in N Ardenne, erasing the former landscape in part of the ESEM, in the Condroz, and along the NW slopes of the Hautes Fagnes before being sealed by the sand cover abandoned by the Rupelian sea. The scarp leading to the Danian surface is up to 170-m-high near Nassogne (►Fig. 6.15). Likewise, south of the massif, active denudation and scarp retreat produced another well-developed surface with elevations around 300–420 m asl in the NE Paris basin and the Gutland area, prolonging eastward in the Moselle trough. While the age of this surface, Upper Eocene to Miocene, is still debated (Baeckeroot, 1942; Quesnel, 2003; Demoulin, 2006), its antiquity is not disputed, identifying the southern margin of the Ardenne –Oesling as a Tertiary erosional feature and disqualifying the assumption that it primarily resulted from the Plio-Quaternary differential uplift of the massif.

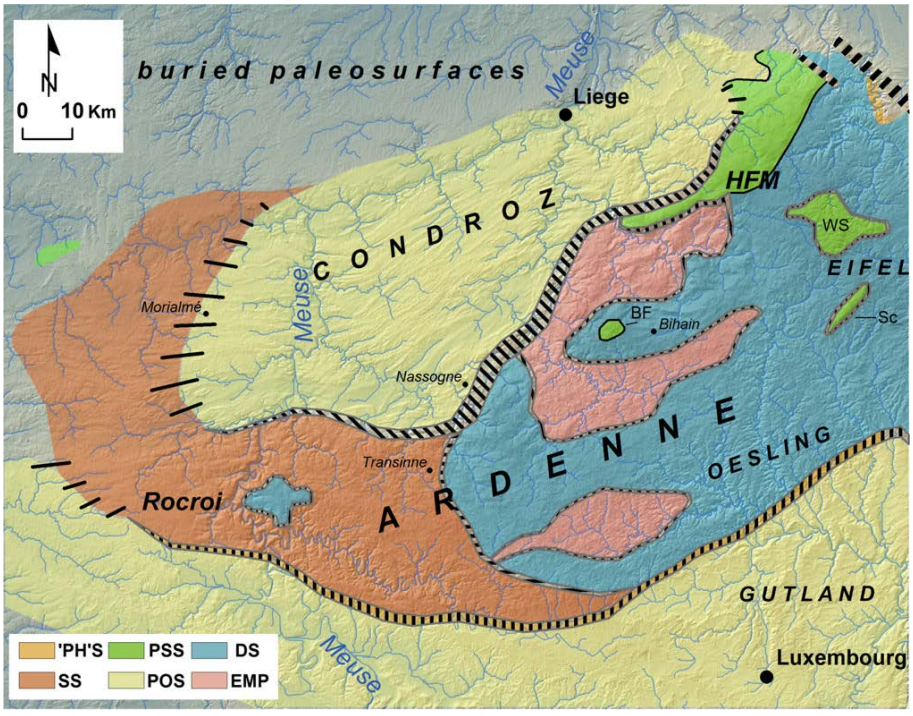

►**Fig. 6.15** Map of the erosion surfaces of the Ardenne and its margins, draped on a hillshade of the SRTM 3″ digital elevation model. “PH”S. Post-Hercynian surface (including its more specific pre-Triassic variant in Luxembourg and north Eifel). PSS. Pre-Senonian surface. DS. Danian surface. SS. Selandian surface. POS. Pre-Oligocene surface. EMP. Early Miocene planation level. Thin hatching denotes erosional scarps between surfaces. In the west, the scarps between the Selandian and pre-Oligocene surfaces are progressively less conspicuous, finally giving way to a regradational type transition between the two surfaces (widely spaced black lines). Bold hatching (in top right corner of the map) is for fault scarps. BF Baraque Faiture. WS Weisser Stein. Sc Schneifel.

Finally, while the Paleogene sand covers were progressively removed from the younger surfaces, the Oligo-Miocene evolution of the massif's interior was restricted to the development of intramontane planation basins of limited extent within the Danian topography, owing to climatic conditions generally less favourable to chemical weathering and etchplanation. These basins formed preferentially on weaker bedrock, in relation with the main drainage axes of the massif, and open all to the west, where their base level corresponded to the top surface of the sand covers of the pre-Oligocene and Selandian surfaces (►Fig. 6.15). Their Early Miocene age is consistently supported by the absence of Paleogene marine deposits and the evidence of a last phase of active bedrock kaolinization around 20 Ma from K–Ar and Ar–Ar dating of cryptomelanes at the base of the weathering mantle at Transinne and on the Plateau des Tailles (Bihain).

6.1.3 Erosion surfaces, tectonic uplift and denudation rates in the Ardenne-Oesling

Although paleosurface reconstruction is now often deemed superseded by developments in the thermochronological and cosmogenic nuclide approaches of long-term landscape evolution, the recent progress in the dating of weathering products allows for sounder such reconstructions, with important implications regarding the underlying tectonic evolution of the Ardennian erosional setting and the associated denudation volumes.

Beyond local tectonics such as the HFM block uplift, broad-scale differential deformation between the originally almost horizontal surfaces of different ages suggests that every particular uplift episode of the massif during the Cenozoic did not exceed a few hundred meters with respect to the forelands. For example, the difference of tilt between the pre-Senonian and Danian surfaces in NE Ardenne indicates a ~400-m-high broad upwarping of central Ardenne in the Early Paleocene, which however never raised the massif's heart to such elevations, as surface regradation more or less kept pace with uplift. The varying tilt angle of the external facets of the acyclic surface developed over Ardenne–Oesling, systematically larger for older facets, attest that this slow doming of the massif was a background trait of its tectonic behaviour during the Mesozoic.

The change for cyclic morphogenesis during the Selandian was probably related to more focused uplift of the massif, highlighted especially in N Ardenne by the contrast between horizontal topography in the massif's interior and abruptly, though weakly, tilted surfaces close to its margins. At least in the north, probably in relation with the dawn of the Lower Rhine rift activity, subdued doming thus gave way to more en-bloc, multiphased uplift. The cumulated heights of the erosional

scarps that were consequently produced between the successive surfaces amount to ~200 m from Selandian to Rupelian times, while the surfaces deformation points to an additional few tens of meters of Neogene marginal tilt and the Plio-Quaternary component of en-bloc uplift may be estimated from river incision in the order of 150 m (Willems and Rodet, 2018).

Paleosurface analysis and the dating of weathering products are also useful tools to assess the plausibility of long-term landscape evolution and denudation rates derived from thermochronology and cosmogenic nuclide data in regions of low to moderate uplift and elevation. In the Ardenne, thermochronological data are so far limited to fission track (FT), mainly on apatite (Glasmacher *et al.*, 1998; Xu *et al.*, 2009; Bour, 2010) and led to a variety of interpretations. From the stand-alone analysis of their FT data, Xu *et al.* (2009) infer that slow exhumation prevailed in the Ardenne from 230 to 45 Ma, as indicated by cooling rates of 0.1–0.3 °C/Ma. Based on the usually used thermal gradient of 30 °C/km, this corresponds to denudation rates of 4–13 m/Ma. Then, from 45 Ma onwards, they model a phase of faster cooling (0.7–1.1 °C/Ma) that translates in denudation rates of 20–30 m/Ma, and suggest that an exhumation of 0.9–1.3 km would have occurred since the Middle Eocene. However, in a thermal history modelling that does not call for a thick Upper Cretaceous cover over the Ardenne, this km-scale amount of Cenozoic exhumation is in contradiction with field data showing the preservation of Lower Cretaceous weathering products and Upper Cretaceous sediments on the Ardennian surfaces. In order to overcome such discrepancies between field data and FT inferences, Bour (2010) introduces in the modelling of his own FT data constraints imposed by the measured ages of the weathering mantle and the timing of marine transgressions upon the massif's margins. Consequently, following a long stay from 230 to 90 Ma in the [10–50 °C] domain not resolved by FT but most probably with insignificant denudation rates, his best-fit thermal histories display a heating episode indicating that the Upper Cretaceous sea would have buried the N Ardenne under a more than 1 km-thick sediment cover, succeeded by rapid cooling during the Cenozoic, which Bour (2010) interprets as the result of tectonic inversion and massif uplift. However, though consistent with Lower Cretaceous kaolinic weathering in central Ardenne and the observed burial under Upper Cretaceous chalks along the massif's northern margin, this thermal history faces another difficulty because the Thanetian marine cover directly resting on the Paleozoic basement of the ESEM's western confines and the 55-Ma age of weathering products at Morialmé imply that this thick Cretaceous cover should have been removed very rapidly in the beginning of the Paleocene, at rates of 100–150 m/Ma. Though not impossible per se, such rates would imply comparatively high Paleogene rock uplift rates in the Ardenne, which no other evidence supports. Independent information about the volume of the Late Cretaceous Ardennian cover is thus required, which might perhaps be derived from estimates of the fraction of reworked Cretaceous material included in the Selandian and Thanetian sediment covers

surrounding the massif. While the apparent inconsistencies between paleosurface and paleoweathering observation on one hand, FT modelling results on the other hand, might refer to the use of inappropriate T°-depth profiles in the latter, they especially stress the importance of the former data type and the need for further efforts towards dating of weathered material, sediments, and exposed surfaces in slow evolving erosional settings, which the Ardenne massif represents.

Likewise, cosmogenic radionuclide (CRN) studies have yielded a lot of denudation estimates in uplifting massifs, and especially in the Ardenne (Schaller *et al.*, 2002, 2004; Sougnez *et al.*, 2011) and the Rhenish shield (Meyer *et al.*, 2010), which, though indicative of shorter term denudation, are often compared to the long-term evolution of the massif. These estimates are obtained from measurements of cosmogenic ^{10}Be concentration in the quartz sand fraction of river bed loads, assumed to carry information on the average denudation rate in the river's catchment upstream of the sampling point. Most CRN estimates from Ardennian rivers fall in the range 20–80 mm/ky at least for the last 50 ky. However, as secularequilibrium is assumed in the calculation of CRN denudation rates and the climatic conditions of the last 50 ky are indeed representative of those of at least the last 1 My, this suggests that a rock slice 50–200 m-thick would have been removed from the massif just during the Quaternary, a figure hardly compatible with the preservation of >30-Ma-old loose sediments and kaolinized rocks over many levelled interfluves. Moreover, Demoulin *et al.* (2009) showed that these rate estimates are much closer to the rates of valley incision since 0.7 Ma in the Ardenne, concluding that the CRN rate estimates in the massif are not representative of average denudation because the river bed load does not sample the extended horizontal remnants of the paleosurfaces where virtually no erosion takes place currently. Here again, the geomorphological reconstructions of paleolandscapes appear thus as a welcome counterweight to sometimes hasty conclusions derived from new techniques.

6.1.4 Conclusion

Praised by writers, celebrated by painters, the Ardenne's scenic landscapes have also been studied for more than a century by geoscientists. While several local names were chosen already in the nineteenth century, and are still often in use, to describe stages, especially of the Devonian System, of the international stratigraphic chart, geomorphologists studied the Ardennian relief as a well-preserved example of the long-term geomorphic features of temperate latitudes' old massifs, highlighting their typical evolution most probably under former warm, often wet, climatic conditions. Within the Ardenne, the Hautes Fagnes area, with its wild beauty, is certainly one of the best places to observe the general character of extended remnants of etchplains and unravel the complex relationships between regional tectonic deformation,

continental weathering and relief development, and episodic marine transgressions leading to the present layout of variously intersecting or stepped paleosurfaces. The sections offered by the Transinne quarry and the Bihain outcrop across the deeply kaolinized bedrock of west- and north-central Ardenne are also key localities for observing the thick profile produced by long-lived chemical weathering, indispensable to etchplanation. In other words, the Ardenne–Oesling is not only a world-class area for its contribution to the history of the understanding of long-term landscape evolution in temperate regions (i.e., the typical setting of the Davisian "normal" geomorphic evolution) but also a remarkable example of how the geomorphic landscape record may be as powerful a tool as the geological rock record for reconstructing the long-term history of regions where continental, tectonically stable or weakly active regimes prevailed over 10^7–10^8 yr timescales. Moreover, the recent results presented in this overview reveal new perspectives for future research and advances, especially in the chronology of the Ardennian evolution and its meaning as a piece in the history of the large-scale foreland domain of the Alpine collision zone in Europe. Meanwhile, every rambler walking through the Ardenne plateau's wild scenery and deep forested valleys cannot keep from having a strong feeling of the grandeur and long time scale of the landscapes in which humans pass so quickly.

6.2 Genesis and $^{40}Ar/^{39}Ar$ dating of K-Mn oxides from the Stavelot Massif (Ardenne, Belgium): insights into Oligocene to Pliocene weathering periods

In the Stavelot massif (Eastern Belgium, ►Figs. 6.1a and b), the Ottré Formation (Salm Group, Lower to Middle Ordovician) is mainly composed of Mn- and Fe-rich red to purple pelitic rocks corresponding to the Les Plattes and Meuville Members (►Fig. 6.16). These levels are known worldwide for their coticule layers, a metasedimentary yellowish rock composed of fine-grained Mn-garnet (spessartine), quartz and white micas (Lamens and Geukens, 1984; Baijot *et al.*, 2011; Herbosch *et al.*, 2016). These strata have undergone strong weathering processes leading to the formation of supergene manganese oxides (Fransolet, 1979; Schreyer *et al.*, 2001; Gustine, 2002; Blondieau, 2005, 2006, 2019). The investigation proposed here focuses on the characterization and timing of weathering in these sediments in order to integrate them into the large scale weathering phases in Belgium and foreign areas.

6.2.1 Regional settings of the Ardenne and Stavelot massif

6.2.1.a Geological features

The Stavelot Massif belongs to the larger Ardenne region, which is part of the Rheno-hercynian fold-and-thrust belt (►Fig. 6.1a and b). Structural units of Paleozoic rocks in Belgium have recently been distinguished and include, from north to south, the Brabant Massif and the base of its Devonian cover unaffected by the Variscan orogeny, the Brabant parautochton, the Haine-Sambre-Meuse overturned thrust sheets (HSM-OTS) and the Ardenne allochthon (Belanger *et al.*, 2012). The Stavelot Massif is the largest and best-exposed lower Paleozoic inlier among the four in Belgium (Serpont, Givonne, Rocroi, Stavelot) and extends into Germany (Venn Massif) to the east (►Figs. 6.1b and 6.16). These locations are often considered together and compose the eastern part of the Ardenne allochthon (Fielitz and Mansy, 1999; Oncken *et al.*, 1999). This inlier is situated in the northwestern part end of the Rhenish Massif and has undergone Variscan folding and Late Carboniferous very low (anchizone) to low-grade (epizone) metamorphism (Theye *et al.*, 1996; Fielitz and Mansy, 1999). Caledonian folding is recorded by an unconformity between the Stavelot inlier and the overlying Lower Devonian series (Adams and Vandenberghe, 1999; Hance *et al.*, 1999).

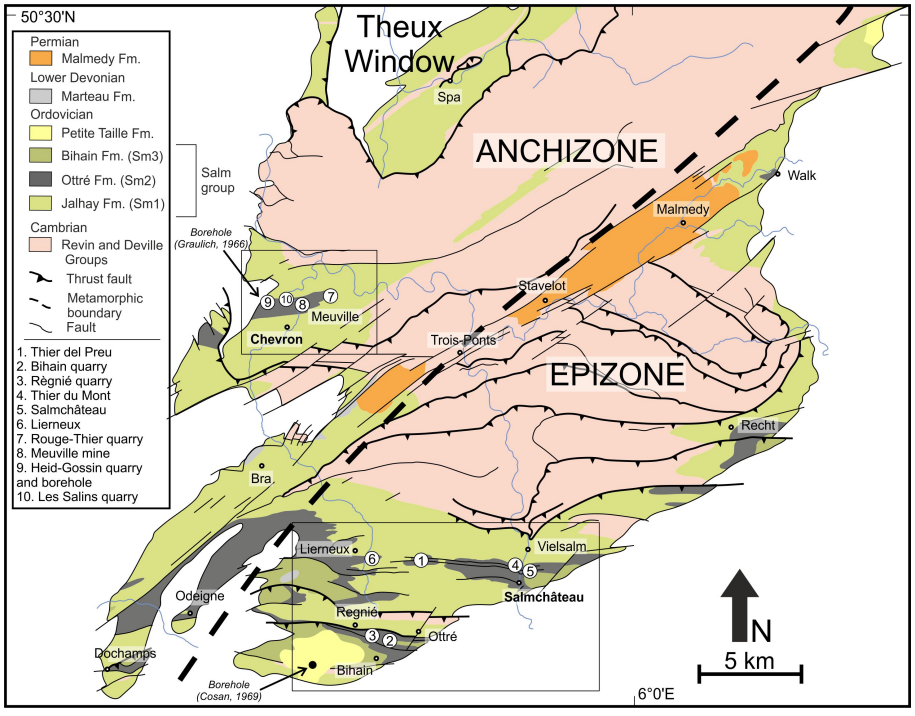

►**Fig. 6.16** Simplified geological map of the Stavelot Massif (after Geukens, 1999, 1986) showing the Ottré Formation containing the Fe-Mn-rich slates and coticule layers. Sampling

sites are located in the main Mn ores and indicated by numbers from 1 to 10. Also shown are two metamorphic zones separated by the Malmedy graben.

The Cambrian-Ordovician succession of the Stavelot Massif is a continuous, mainly terrigenous sedimentary succession (Verniers *et al.*, 2001), with minor volcanic events (Lamens and Geukens, 1984; Kramm and Bühl, 1985). The stratigraphy is subdivided into three groups (Geukens, 1999; Verniers *et al.*, 2001; von Hoegen *et al.*, 1985, ►Fig. 6.16): (1) the Deville Group (400-600m, Lower Cambrian); (2) the Revin Group (1900m, Middle to Upper Cambrian); and (3) the Salm Group (900-1200 m, Lower and Middle Ordovician). Special care has been taken to the Salm Group as it contains Mn-rich sediments mined during the last centuries (Goemaere *et al.*, 2016). This group is a thick series of terrigenous rocks subdivided into three Formations (►Fig. 6.16). The Jalhay Formation (Sm1) corresponds to a turbidite sequence evolving into wavy bedded siltstones and then to greenish slates and siltstones. The Ottré Formation (Sm2) is mainly composed of Fe- and Mn-rich red to purple pelitic rocks, which were deposited in a quiet basin deepening toward the southeast. Three members are distinguished (Geukens, 1999; Lamens, 1986, ►Fig. 6.17a): the Meuville Member (Sm2a, 60–80 m thick), the Les Plattes Member (Sm2b, 0–50 m thick) and the Colanhan Member (Sm2c, 50–100 m thick). Their precise age is unknown as stratigraphic microfossils are lacking due to their relatively high oxidizing depositional environment. However, the occurrence of conodonts at the boundary between the Meuville and Les Plattes members in the Chevron area gives an Early Ordovician, tentatively the latest Tremadocian age, even if a Floian age cannot be excluded (Vanguestaine *et al.*, 2004). The Ottré Formation was probably deposited between 478 and 467 Ma (Herbosch *et al.*, 2016). Turbiditic sedimentation is evidenced in siltstone beds (Lamens, 1985a); volcanic activity also occurred during sedimentation (Lamens and Geukens, 1984). The upper Bihain Formation (Sm3) is composed of black silty slates and greenish sandstones containing pyrite and showing evidence of bioturbation. The Salm Group ends with the Petites Tailles Formation, a quartzite sandstone, which is often brecciated with bedded chloritic slates and conglomerate sandstone with greenish shale pebbles. Lochkovian conglomerate of the Marteau Formation overlies, in an angular unconformity, the Lower Paleozoic units (Vandenven, 1991; Hance et al., 1992; ►Fig. 6.16).

6.2.1.b Structure and tectonic of the Stavelot massif

The Massif is strongly tectonized by both the Caledonian and the Variscan orogenic cycles, although the main features of the Caledonian deformation is still a matter of debate (Piessens and Sintubin, 1997; Ferket *et al.*, 1998; Sintubin *et al.*, 2009). Two main structural domains can be distinguished (Geukens, 1999, 1986; ►Fig. 6.16). A northern domain consists mainly of rocks of the Revin Group showing a succession of closed synclinal structures interpreted to be Variscan (Hance *et al.*, 1999; Mansy *et al.*, 1999). Brittle tectonics overprinted earlier Caledonian east—west oriented

structures. The southern domain is characterized by east—west oriented upright isoclinal folds and flat overthrusts interpreted to be of Caledonian origin (Geukens, 1986; Piessens and Sintubin, 1997). Some early east—west oriented faults were reactivated during the Variscan orogenic cycle. These two structural domains are separated by a N50°E oriented graben filled by Permian conglomerates (Geukens, 1957, 1975), delimiting two metamorphic zones. The southern part of the Massif, where the Ottré Formation outcrops in the Salmchâteau syncline and in the Recht area, records an epizonal low-grade metamorphism, while the northern part of the massif corresponds to an anchizonal metamorphism, both related to the Variscan orogenic cycle (►Fig. 6.16, Ferket *et al.*, 1998). The metamorphic p-T conditions of the epizone are estimated between 400 and 450 °C, and 2 to 3 kbar, based on the presence of Mn-andalusite, Mn-chloritoid, spessartine and muscovite, which corresponds to a greenschist-facies (Ferket *et al.*, 1998; Fielitz and Mansy, 1999; Schreyer *et al.*, 2004). The occurrence of carpholite and sursassite, instead of andalusite in the northern domain (Chevron area), implies p-T conditions of about 300 °C and 1 to 2 kbar (Theye *et al.*, 1996; Fransolet *et al.*, 2007).

The relative tectonic stability during the Mesozoic is inverted in the Upper Cretaceous, resulting in the subsidence of the northern part of the Ardenne Massif and the tilt from south to north (Demoulin, 1995b). The Cenozoic evolution of the Ardenne poorly records the effect of the Alpine orogenic cycle as folding is not observed (e.g., Demoulin, 1995b). However, beyond local tectonics, broad scale differential deformation suggests that every particular uplift episode of the massif during the Cenozoic did not exceed a few hundred meters with respect to the foreland (Demoulin *et al.*, 2018a). The age of the planation surfaces and the remains of Paleocene and Late Cretaceous sediments led Demoulin (1995a) to conclude that Tertiary uplift of the Ardennes started with large scale tilting during Paleocene, after a very long period of tectonic quiescence and even potential Jurassic cover (Barbarand *et al.*, 2018) during the Mesozoic. This is well demonstrated by a tilt between the pre-Senonian and Danian paleosurfaces (Demoulin *et al.*, 2018a) and hiatus in the Danian chalk (Boulvain and Vandenberghe, 2018). This was followed by a doming event during the Eocene, responsible for 200 m heights cumulated between the Selandian and Rupelian (Demoulin *et al.*, 2018a). This tectonic rearrangement is interpreted to be a response to the Pyrenean deformation pulse at the end of the Eocene (Boulvain and Vandenberghe, 2018), but also in relation to the dawn of the Lower Rhine rift activity (Roer Valley Graben) at least in the North (Demoulin *et al.*, 2018a, ►Fig. 6.1a). The major doming of the Ardennes started at the Late Oligocene, after the last deposition of the early Oligocene transgression, continued during Neogene and accelerated at the Pliocene (Demoulin, 1995b). This acceleration uplift is evidenced by river terraces during Middle Pleistocene (e.g., Garcia-Castellanos *et al.*, 2000).

6.2.1.c Weathering of the Ardenne massif

During Mesozoic and Cenozoic times, the Ardenne underwent many phases of exposure, only interrupted by marine transgressions onto the borders (Demoulin, 1995b; Demoulin *et al.*, 2018a, see previous section, this chapter) or above the massif itself (Barbarand *et al.*, 2018). The most significant sedimentation episodes occurred in the Triassic, Jurassic, Eocene and Early Oligocene. Seven generations of paleolandscapes have been identified (Demoulin, 1995a, 2003; Demoulin et al., 2018a). The age of these weathering periods is particularly well documented in kaolinic saprolites developed the Paleozoic sediments (►Fig. 6.2). Four periods record such events in and around the Ardenne Massif, namely during the Permian-Triassic event, in the Early Cretaceous (extending in the "middle" Cretaceous), the late Paleocene/early Eocene and the Early Miocene (e.g., Yans, 2003; Yans *et al.*, 2003; Thiry *et al.*, 2006; Demoulin *et al.*, 2018a).

Although the Ardennian saprolites were developed by ferrallitic processes under climates warmer (and more humid) than present, the ferruginous upper part of the profile (laterite *sensu* Nahon, 1991) was mostly removed by later erosion of the uplifted plateaus and is only preserved in scattered places (Théveniaut *et al.*, 2007), where uninterrupted Mesozoic and Cenozoic tectonic stability strongly limited denudation (Barbarand *et al.*, 2018). The high elevation of the Stavelot Massif between 400 and 700 m (NE of Ardenne) allows weathering mantles to be developed onto the Paleozoic bedrock to a thickness of about 50 m (Plateau des Tailles; Cosan, 1969; ►Figs . 6.4 and 6.16). Paleozoic quartzite and slates are respectively weathered into sands and clays, the latter being dominated by neoformed kaolinite and illite (Alexandre and Thorez, 1995), together with Fe- and Mn oxides, -hydroxides and -oxyhydroxides. The only remaining evidence are the roots of these profiles (Cosan, 1969; Alexandre and Thorez, 1995). The borehole of Brackvenn in the northern part of the Stavelot Massif (►Fig. 6.16) indicates a (pre-)Cretaceous weathering period, as the Paleozoic weathered rocks are covered by Maastrichtian chalk deposits. However, the depth of 22.5 m thick saprolite differs from those observed in the same area with only few meters in thickness (Alexandre and Thorez, 1995).

6.2.2 The Fe-Mn levels

Two locations expose manganiferous sediments, in the Chevron area on the western margin of the Stavelot Massif, and in the Salmchâteau area in the southernmost part (►Fig. 6.16). The main manganese ores of Belgium are located in the southern part of the Stavelot Massif in the red to purple slates of the Meuville Member (Salm Group, Ottré Formation, ►Figs. 6.16 and 6.17). These manganese ores were mined for desulfurization component in the manufacturing of cast iron (Goemaere *et al.*, 2016) periodically between 1886 and 1934 in the Chevron area (Berger, 1965), from which

180,000 tonnes of ore was produced (Libert, 1905; Dejonghe, 1985; Dussart and Dussart, 1991). However, most of the manganese levels were mined for the cm-size coticule whetstones in the Salmchâteau area within the Les Plattes Member (►Fig. 6.17a, Herbosch *et al.*, 2016). Note that coticule layers cannot be considered as a manganese ore, because they are mined for the production of whetstone. No coticule has ever been exploited in the north-western margin, as the composition of the yellow levels differs too much from those of the southern part (►Fig. 6.17a). The underlying Mn ore was mined for Mn ores in many places in the Salmchâteau area (Goemaere *et al.*, 2016 and reference therein), but also as a by-product of coticule mining until 2015 in Thier del Preu quarry, mainly assigned to the manufacture of black ceramic products (Herbosch *et al.*, 2016). Two other places expose the Ottré Formation in the eastern part of the Massif, east of the village of Recht, and near Walk (►Fig. 6.16). In the Odeigne-Doschamps strips, where the Ottré Formation is widely exposed, coticule has never been observed (Lamens, 1985a; Geukens, 1986; Lamens, 1986; Dejonghe, 2008), as well as in the German northeast part (Echle *et al.*, 1985; Meyer and Walter, 1985, ►Fig. 6.16).

6.2.2.a Stratigraphic position of the Mn ores

The Mn-rich sediments are located in the upper part of the Meuville member, while coticule layers are enclosed in the Les Plattes Member (►Fig. 6.17a). The latter consists of red slates interbedded with cm-size coticule beds. The thickness of the Les Plattes Member is variable, which corresponds to important variations in its paleogeographic distribution (Herbosch *et al.*, 2016). The thickness of 40–45 m observed in Salmchâteau decreases rapidly to <10 m in Lierneux, vanishing toward the west of Regné (Lamens, 1985a; Lamens *et al.*, 1986). This member also thins toward the north-northeast from 30–35 m in Recht, to only a few meters in Walk (Herbosch *et al.*, 2016, 2016; ►Fig. 6.16). In the Chevron syncline, the Meuville and Les Plattes Members reach 47–52 m in thickness (Graulich, 1966; Lamens, 1985a; ►Fig. 6.17a).

The manganese ores are quite different between the two locations. In the Chevron area, the ore is mostly a carbonate-bearing assemblage of poorly weathered metamorphic minerals. A mixture of coarse rhodochrosite and spessartine (0.05 to 0.2 mm) is associated with quartz, chlorite and hematite, forming a massive dark purple rock (►Fig. 6.17b). The Salmchâteau Mn ore consists of purple slates replaced by secondary Mn oxides, which originate from strong weathering of the host slates. Some Mn oxides found in the Salmchâteau area could also have a hypogene origin, as demonstrated by hollandite-strontiomelane association in quartz veins with kanonaite and braunite (Schreyer *et al.*, 2001; ►Fig. 6.16). Muscovite, hematite, spessartine, Mn-chloritoïde, quartz and accessory minerals are remaining minerals of the enclosing slates (►Fig. 6.17c).

- *Salmchâteau area*

The red slates are composed of fine-grained micas, quartz and hematite with small amounts of spessartine, andalusite and kaolinite blasts (Lamens *et al.*, 1986). Lamens (1985a, 1985b) described in detail the lithological succession of the Ottré Formation in the Vielsalm and Salmchâteau section. This author subdivided the Ottré Formation in 8 Units distributed into three members (from base to top of the Ottré Formation; ►Fig. 6.17a). The Meuville Member comprises Units 1 to 4 and is composed of red slates rich in hematite and spessartine. The base of Unit 1 is marked by a characteristic chloritoïd-rich quartzite bed (Geukens, 1965). Unit 2 contains red slates with some beds rich in 50–100 µm spessartine porphyroblasts (Herbosch, 1965; Nicaise, 1985). The occurrence of large poikiloblasts (0.5-5 mm) of rhodochrosite in Unit 3 has led the level to be considered as the main Mn ore level of the southern area. Unit 4 also contains hematite-spessartine-bearing violet slates, but with common mm-scale spots of kaolinite and/or andalusite (Theunissen, 1971), which are sometimes replaced by massive purple slates rich in hematite, kanonaite and braunite (Herbosch, 1967; Schreyer *et al.*, 2001, 2004). The Les Plattes Member consists of purple slate interbedded with mm to cm size dominantly yellowish folded coticule. Unit 5 contains most of the minable coticule-bearing strata and differs from Unit 6 by the occurrence of chloritoïd porphyroblasts instead of spessartine. Finally, units 7 and 8 characterize the Colanhan Member with purple and green chloritoïd-rich slates containing "pseudocoticule" layers characterized by large spessartine garnets enclosed in a quartz matrix (Baijot *et al.*, 2011).

Purple slates show very regular millimeter-scale laminations corresponding to small variations in the terrigeneous influx. Some of these beds are light-colored and thus richer in quartz, while other darker laminae are very rich in hematite. Two major forms of hematite are recognized: (1) as a very fine micron-size dust dispersed within the phyllosilicate matrix and (2) as a more concentrated form with 10–50 µm-size crystals in dark laminae (►Fig. 6.18a). The spessartine content is quite variable in the purple slates, ranging from absent to 10–15% in laminae (►Fig. 6.18a), and even more abundant near dark hematite laminae. Hematite content is highly variable but relatively abundant in unit 5 (3.58-20.9 % wt., mean=13.4% wt. Fe_2O_3), while FeO is very low (0.2-0.7% wt., mean=0.32% wt. FeO; Herbosch *et al.*, 2016). Manganese is generally less abundant than iron in the slates (0.46-14.8% wt., Mean=3.86% wt. MnO) due to the presence of disseminated crystals of spessartine. Mn content decreases strongly in the chloritoïd-slates of Unit 6 (0.65-1.4% wt., mean=0.89% wt. MnO) due to the absence of Mn-garnet (Herbosch *et al.*, 2016). The mean mineralogical composition of these slates is 38% phyllosilicates, 26% quartz, 14% hematite, 13% andalusite-kaolinite spots, 4% chlorite and 3% spessartine (Lamens, 1985a) close to that of the coticule layers composition (Kramm, 1976; Krosse and Schreyer, 1993).

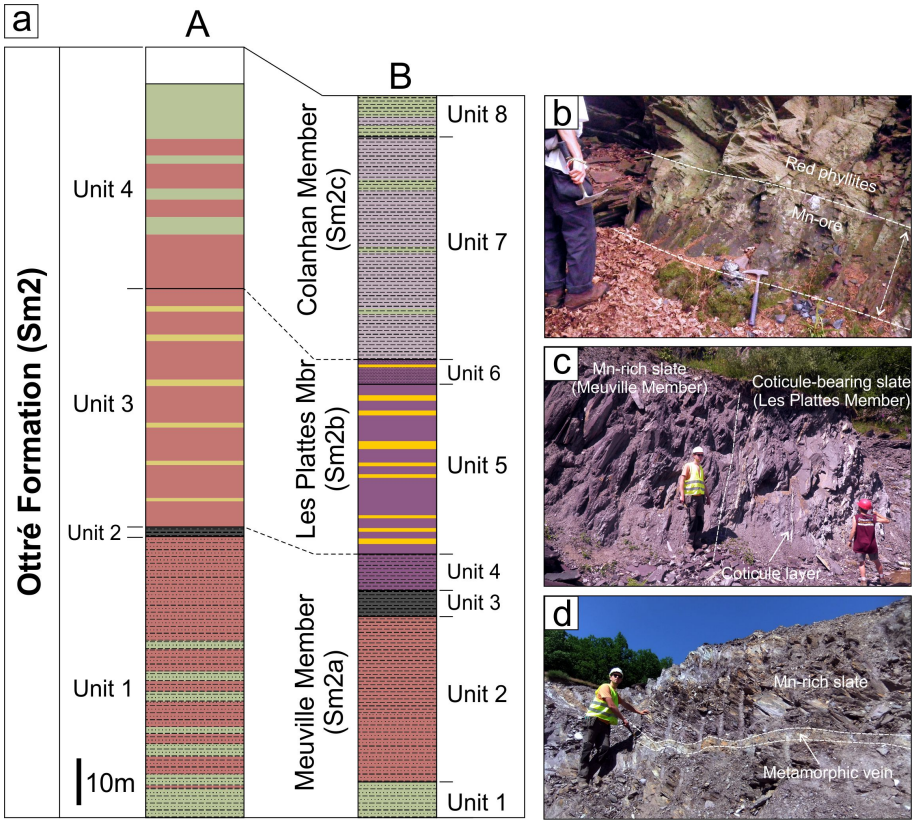

►**Fig. 6.17 a.** Lithostratigraphic log of the Ottré Formation members and their correlation between the Chevron (A) and Salmchâteau (B) areas (Lamens, 1985b; Herbosch *et al.*, 2016). See text and Herbosch *et al.* (2016) for the description of lithology. Mn ores are evidenced in dark gray and coticule layers in yellow. **b.** Mn ore level interbedded in the red phyllites in the Chevron area (Meuville mine, Unit 4). **c.** Limit between the Mn-rich purple slates of the Meuville Member (Unit 4) and coticule-bearing strata of the Les Plattes Member (Unit 5) in the Thier del Preu quarry (see Fig. 2 for location). **d.** Quartz-pyrophyllite-andalusite metamorphic veins crossing the Mn-rich dark slates (Unit 3) in the Thier del Preu quarry (see ►Fig. 6.16 for location).

The contact of purple slates with enclosed coticule is usually sharp in Les Plattes Member. Coticule layer composition is usually 39% of 1 to 5 µm (sometime 25 µm) spessartine, 28% quartz, 24% phyllosilicates, 3% chlorite and 3% of other minerals (hematite, chloritoïd, kaolinite, andalusite, rutile, tourmaline;(Lamens, 1985b). Kramm (1976), Lamens (1985a) and more recently Herbosch *et al.* (2016) subdivided coticule veins in five types, depending on their chemical or mineralogical composition and texture. Sometimes, these coticule are found as mm-size globules in the red slates (Schreyer *et al.*, 1992). Coticule layers are even more folded or micro-folded than the host-slates, most of these structures having been attributed to metamorphism. However, some sedimentary or diagenetic features such as load casts,

ball and pillow, flames or flute mark structures can be found when the purple enclosing slates are very regularly laminated (Lamens *et al.*, 1986), which led Herbosch *et al.* (2016) to interpret coticule layers as distal turbidites. The evolution from quartz-rich, to spessartine-rich coticule from the base to the top of a single layer corroborates the sedimentary deposition (►Fig. 6.18b, Lamens *et al.*, 1986), as well as the lateral extension of coticule-bearing slates, which is estimated to be at least 5 to 6 km (Herbosch *et al.*, 2016). The geochemical contact between the slates and the coticule strata is sharp too, showing a reverse evolution between Fe_2O_3 and MnO content: Fe_2O_3 content decreases progressively from the slates to the outer rim of the coticule layers, whereas MnO increases, and reach a maximum peak inside the coticule that overtakes the Fe_2O_3 content. FeO is low in both coticules and slates (Kramm, 1976). Coticule chemical composition is enriched in MnO (0.8-22.8% wt., mean=9.83% wt. MnO) and poor in Fe_2O_3 (0.3-4.34% wt., mean=0.3% wt. Fe_2O_3), as spessartine is very common and hematite is often depleted. However, pseudocoticule layers in the Colanhan Member (at the top of the Les Plattes Member, unit 6) shows higher manganese (8.6-25.4% wt., mean=16.6% wt. MnO) and iron contents than other coticules (2.7-5.5% wt., mean=3.59% wt. Fe_2O_3), which might be related to the higher amounts of hematite (Baijot *et al.*, 2011).

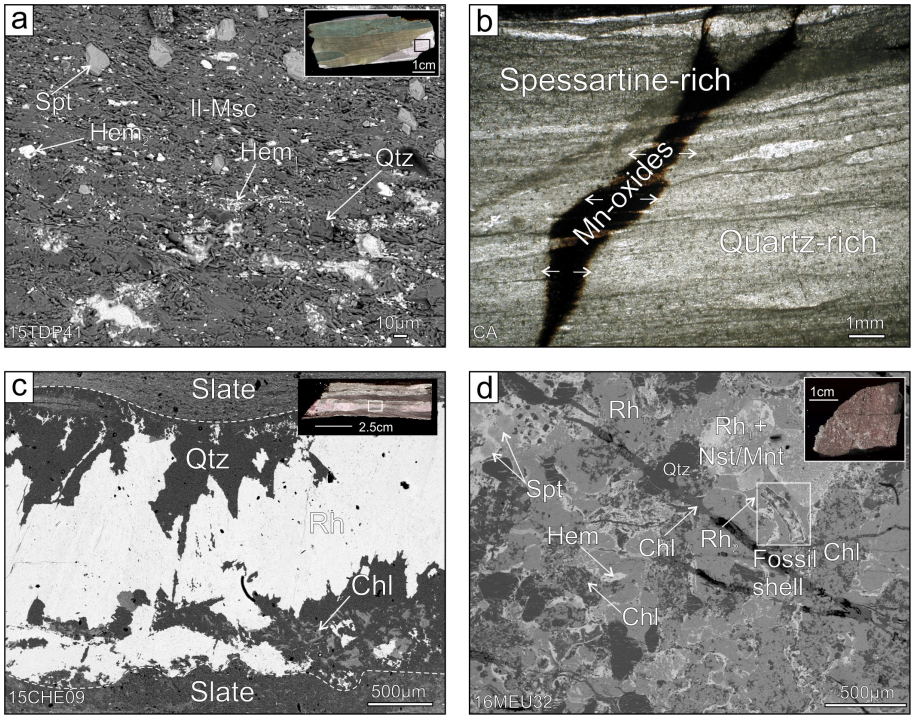

►**Fig. 6.18** Petrographic features of the primary Mn-rich levels and coticule. **a.** Back-scattered electron view of disseminated spessartine and hematite in the micaceous purple slate (Units 3–4) in the Thier del Preu quarry. **b.** Transmitted light view of a coticule level showing the

variation in the spessartine-quartz composition in Thier del Preu quarry. Coticule is crossed by a Mn oxide vein forming a dark halo into the coticule level. **c.** Back-scattered electron view of red phyllites showing rhodochrosite-quartz lenses formed during diagenesis-metamorphism in the Heid-Gossin borehole (Graulich, 1966). **d.** Back-scattered electron view of the Mn ore (Unit 4) in the Meuville mine showing rhodochrosite nodules (Rh_1) cemented by a second generation of rhodochrosite (Rh_2) together with quartz, spessartine, hematite and chlorite. Fossil shell remains into the Mn ore evidence the sedimentary feature of this level. Hem: hematite; Il: illite; Musc: muscovite; Qtz: quartz; spt: spessartine; Rh: rhodochrosite; Chl: chlorite; Nst: nsutite; Mnt: manganite.

- *Chevron area*

Lamens (1985b) recognized four lithological units of the Ottré Formation, corroborated by the borehole drilled on the western side of the Chevron syncline (Graulich, 1966; ►Fig. 6.16). The lower unit C1 is a red laminated siltstone with some intercalation of green siltstones and red hematite-rich phyllites in the upper part. Rhodochrosite clearly occurs in lenticular forms, following stratification of the slate (►Fig. 6.18c). Unit C2 corresponds to the main Fe-Mn ore bodies 1 to 3 m in thickness (►Fig. 6.17b). On the western side of the Chevron area, C2 unit is only 0.7 cm thick (Graulich, 1966; ►Fig. 6.16). The manganese level consists of interbedded red phyllites, siltstone and coarse-grained beds 1–20 cm thick. The coarse beds are composed of 1–5 mm fossils (rhodochrosite echinoderm fragments, oncolites, elongate apatite fossil remnants) and rock fragments (mudstone, quartzite, well-rounded quartz, volcanic material) embedded in hematite, spessartine, chlorite and rhodochrosite-rich matrix (►Fig. 6.18d) associated with scarce siderite and pyrolusite (Berger, 1965). Carbonate is nearly pure rhodochrosite (Berger, 1965) to kutnohorite (Theye *et al.*, 1996). Units C1 and C2 are considered as the lateral equivalent of the Meuville Member (Lamens, 1985a, 1985b). Unit C3 is a 45 m thick succession of red slates (quartz, muscovite, paragonite, hematite and rhodochrosite) alternating with whitish, greenish or pinkish beds (phyllosilicates, quartz, spessartine and scarce hematite) 1–10 cm thick, attributed to the Les Plattes Member coticule-bearing strata (Lamens, 1985b). Rhodochrosite spherules are dispersed or concentrated in nodules or as lenticular beds 0.5-3 cm thick (►Fig. 6.18c). The 45 m thick unit C4 shows red and green silty slates without any rhodochrosite, and is considered as the equivalent of the Colanhan Member (Lamens, 1985b). These metapelites often show intensive veining, which includes deposition of centimeters size quartz, hematite and rhodochrosite, indicating local migration of manganese during metamorphism. Manganese carbonates are partly replaced by spessartine and chlorite (Fig. 4d, Theye *et al.*, 1996).

6.2.2.b Origin, formation and evolution of the Fe-Mn-rich sediments

Several models have been proposed for the origin of the Mn-rich slates and coticule levels, and all consider a protolith deposited in a basin then subjected to diagenesis and later metamorphism. The slates and coticules from the Les Plattes Member were deposited in a small basin of about 40–50 km from north to south (currently 20 km) and 25 km for its east—west extension, currently delimited by Chevron to the northwest, Walk and Recht to the northeast and Bihain-Ottré to the south (►Fig. 6.16, Herbosch *et al.*, 2016). This basin was fed to the north by the emerged Brabant Massif (►Fig. 6.1, Herbosch and Verniers, 2014, 2013; Linnemann *et al.*, 2012) during the drifting of Avalonia from Gondwana and the consequent opening of the Rheic Ocean (Cocks and Torsvik, 2002; Cocks and Fortey, 2009; Torsvik *et al.*, 2012). Kramm (1976) proposed first a volcanoclastic model for the coticule, refined successively by Kramm (1980) and Krosse and Schreyer (1993) involving a hydrothermal origin for manganese and iron given by the geochemical data. However, coticule and adjacent slates represent two different sedimentary processes, as the slates were deposited in a quiet, deep and O_2-rich environment, and coticule in a deep but high-energy environment (Lamens *et al.*, 1986; Herbosch *et al.*, 2016). This has led Lamens *et al.* (1986) to suggest that coticule layers were water-oversaturated limy mud sediments rapidly deposited under high-energy conditions, whereas the purple slates originated from slow sedimentation of suspended clay, silt and Fe-Mn particles. Herbosch *et al.* (2016) recently improved the density current model, in particular the paleogeography of those sediments. The enrichment of Fe and Mn is related to the flocculation of Fe and Mn particles coming from hydrothermal vents in the mid-ocean spreading ridge of the Rheic Ocean. The *in situ* precipitation of dissolved Mn^{2+} and Fe^{2+} from seawater is, however, difficult to entail but probably that primary Mn-oxides or hydroxides are the earliest minerals hosting Mn and associated metals following the model of Johnson *et al.* (2016). The protore of the coticule was deposited in a deep oceanic basin as limy mud turbidites, which is enriched in Mn during early diagenesis by replacement of calcium by manganese through diffusion of divalent manganese from the enclosing Fe-Mn-rich slates to form rhodochrosite (Herbosch *et al.*, 2016). Alternativelly, microbially-mediated rhodochrosite formation is also likely (Maynard, 2014), as well as other diagenetic Mn-bearing silicates (Johnson *et al.*, 2016). Processes of Mn precipitation in sediments are also summarized in Maynard (2014). The Mn-slates, rich in spessartine and hematite, were formed when the terrigenous input was low, and/or when the hydrothermal flux was high. This density current model is responsible for the rapid deposition of the coticule protolith and the dilution of the Fe-Mn compounds, compared with the enclosing slates.

Metamorphic transformations of the former shales of the Ottré Formation has led to the formation of slates and quartz veins containing spessartine, Mn-chloritoïd, andalusite-kanonaite, pyrophyllite, paragonite, kaolinite and chlorite in the southern

area. Spessartine crystallization resulted from the recombination of elements contained in rhodochrosite and clay minerals in both coticule and slates (Lamens *et al.*, 1986). This explains the difference between the spessartine content in the epizone (Salmchâteau), and rhodochrosite in the anchizone (Chevron). However, this metamorphic reaction is nearly complete as both spessartine and rhodochrosite occur together in the Chevron area. Therefore, differences between the Chevron and Salmchâteau areas are mostly attributed to the variation in metamorphic grades higher to the south (epizone, 360-420°C, 2kbar; Kramm, 1982; Kramm *et al.*, 1985) and lower to the north (anchizone, 280-320°C; Theye *et al.*, 1996; ►Fig. 6.16).

6.2.3 Material and methods

We focused our investigations on the Salmchâteau (Thier del Preu quarry, Bihain quarry, Règnié quarry, Thier du Mont and Salmchâteau) and Chevron areas (Rouge-Thier quarry, Meuville mine, borehole 159W1215, Heid-Gossin quarry and "Les Salins" quarry), where Les Plattes and Meuville Members crop out (►Fig. 6.16). More than one-hundred samples were collected on the field or taken from the collections of the Geological Service of Belgium and from the Laboratory of Mineralogy (University of Liège). From these samples, twenty-six geochemical analyses were performed for major and trace elements (►Tables 6.2, 6.3 and 6.4) and thirteen $^{40}Ar/^{39}Ar$ ages were obtained from K-Mn oxides (►Table 6.5). All these samples were analyzed for their mineralogy using XRD patterns. Additionally, twenty-four polished sections and twenty-two thin sections were prepared.

The studied samples for $^{40}Ar/^{39}Ar$ geochronology were collected in Thier del Preu (15TDP25, TDPR-003) and Bihain quarries (15HEB01, 15HEB03, BIHD-009, BH311, BH11b), which are respectively located at 490 m and 570 m of elevation. No elevation was available for samples RA8432, RA8433, RN859, as they were taken from the Belgium Geological Survey Desk (Lierneux location; ►Fig. 6.16). K-Mn oxides are well crystallized and contain between 1 and 2 wt. % of K_2O, without any Ba and Pb, suggesting these minerals are cryptomelane, despite the slight Cu, Co, Ni and Sr enrichment (►Table 6.3).

$^{40}Ar/^{39}Ar$ analyses were conducted in the Noble Gas laboratory of Géosciences at the University of Montpellier 2, France, using a new generation multicollector mass spectrometer (Thermo Scientific Argus VI MS) with a nominal mass resolution of ~ 200 and a sensitivity for argon measurements of 3.55×10^{-17} moles/fA at 200 μA trap current. The mass spectrometer is equipped with a Nier-type source and a fixed array of five Faraday detectors and one Compact Discrete Dynode (CDD) detector. It is linked to a stainless steel gas extraction/purification line and CO_2 laser system for step-heating which produces, after focusing, a 1 mm

diameter beam that is used for step heating. The samples selected for dating were irradiated for 40 hours in the core of the Triga Mark II nuclear reactor of Pavia (Italy) with several aliquots of the Taylor Creek sanidine standard (28.34 ± 0.10 Ma) as flux monitor. Argon isotopic interferences on K and Ca were determined by irradiation of KF and CaF_2 pure salts from which the following correction factors were obtained: $(^{40}Ar/^{39}Ar)_K$ = 0.00969 ± 0.00038, $(^{38}Ar/^{39}Ar)_K$ = 0.01297 ± 0.00045, $(^{39}Ar/^{37}Ar)_{Ca}$ = 0.0007474 ± 0.000021 and $(^{36}Ar/^{37}Ar)_{Ca}$ = 0.000288 ± 0.000016. After loading in the sample chamber, the samples were baked at about 120 °C during 24 hours to remove atmospheric argon from the sample surface. Air aliquots from the automated pipette system were analyzed prior to the sample analyses to monitor mass discrimination and detector bias. Line blanks were analyzed between every 3 sample analyses and were subtracted from succeeding sample data. Step-heating experiments on single grains were conducted with a duration of heating of 45 seconds at each step. A custom-made software was used to control the laser intensity, the timing of extraction/purification and the data acquisition. The ArArCalc software© v2.5.2 (Koppers, 2002) was used for data reduction and plotting. All the data were corrected for system blanks, radioactive decay, isotopic interferences and mass discrimination. Atmospheric ^{40}Ar was estimated using a value of the initial $^{40}Ar/^{36}Ar$ ratio of 298.56 $\pm$ 0.31. Plateau ages are defined as including >50% of the total ^{39}Ar released, distributed over at least 3 contiguous steps, with $^{40}Ar*/^{39}Ar$ ratios within agreement of the means at the 95% confidence level. Calculated ages are reported at the 2σ level and include uncertainties in the J-values, but exclude errors associated with the age of the flux monitor and the decay constants.

6.2.4 Results

The purple and red slates of the Ottré Formation are weathered into a clayey rock containing Mn oxides. Despite this weathering is much more intense in the Salmchâteau area compared to the Chevron area, it seems that the formation of supergene mineral assemblage is associated with the same process in both areas. The results presented here focus on the weathering mineral assemblages, first presenting the general mineralogy and petrography of the weathered manganiferous sediments and then the geochemistry of these weathered rocks. $^{40}Ar/^{39}Ar$ dating is presented separately.

6.2.4.a Mineralogy of the weathered ores

As the Ottré Formation is particularly enriched in Fe and Mn, the secondary mineralogy resulting from weathering processes, is extensively dominated by the formation of Mn oxides, -hydroxides and -oxyhydroxides (here resumed as Mn oxides). Cryptomelane and nsutite are the most abundant minerals in the weathered manganese ores in the Salmchâteau and Chevron areas. Lithiophorite is often

concentrated, and some other pure Mn oxides, such as manganite and pyrolusite could also be observed in some samples (►Fig. 6.19a), together with clays (illite and kaolinite) and goethite.

►**Table 6.2** List of samples and abbreviation. S=spessartine, Q=quartz, M=muscovite, L=lithiophorite, C=cryptomelane, H=hematite, Pl=pyrophyllite, Ch=chlorite, A=andalusite, R=rhodochrosite, N=nsutite, M=manganite, Pr=pyrolusite, Cd=chloritoïd, F=feldspar, G=goethite, K=kaolinite.

Label	Mineralogy	Rock type	Outcrop
15RN01	S, Q, M	Coticule	3
CA	Q, S, M, L, C	Coticule (weathered)	3
15RN04	S, M, Q, H, Pl		3
15RN05	Q, Pl, Ch, A	Metamorphic vein	3
16CHE01	R, Q, Ch		9
16MEU34	R, Q, H, Ch, M		8
16CHE08	N, Q, Mt, Pr	Metamorphic vein (weathered)	9
16MEU32	Q, S, Ch, R	Mn ore	8
16CHE09	Q, H, Ch, R		9
16MEU38	Q, H, R, Ch, S	Mn ore (weathered)	10
RN838	C, L, N	Mn oxide	6
RN859	C		6
RA8432	C, Q		6
15HEB03	Q, M, H S, C, L	Mn slate	2
15TDP07	Q, M, H, S, N		1
16TDM10	Q, M, H, Cd		4
16MEU23	Q, H, M, Ch		8
16MEU33	Q, H, M, Ch, F		8
16MEU03	Q, C, H, M		7
15TDP32	Q, M, H, Ch		1
16MEU01	Q, M, Ch, H		7
15HEB01	Q, M, H, C, L	Weathered Mn slate	2
RA8431	Q, M, H, C		6
15TDP12	M, Q, C, H, L		1
15TDP45	Q, M, K, H, G, L, C, S		1

►**Table 6.3** Major oxides (in wt. %) and minor element (in ppm) geochemical analyses. LOI: Lost on ignition.

Label	SiO_2	Al_2O_3	$Fe_2O_{3(T)}$	MnO	MgO	CaO	Na_2O	K_2O	TiO_2	P_2O_5	LOI	Total
15RN01	48.46	18.99	1.2	26.42	0.62	0.4	0.39	1.37	1.042	0.07	1.43	100.4
CA	52.56	16.98	1.06	24.81	0.36	0.42	0.35	1.07	0.927	0.07	1.56	100.2
15RN04	46.77	19.97	8.43	16.92	0.54	0.26	0.71	2.3	1.084	0.12	3.31	100.4
15RN05	78.25	17.31	0.46	0.04	0.44	0.03	0.12	0.18	0.004	< 0.01	3.1	99.92
16CHE01	48.12	0.71	1.27	29.24	0.38	1.77	< 0.01	0.03	0.006	0.02	17.06	98.62
16MEU34	27.15	6.61	26.72	24.05	1.26	1.88	0.17	0.48	0.3	0.43	9.21	98.26
16CHE08	44.36	0.81	1.53	40.44	0.11	0.08	0.01	0.1	0.009	0.04	7.16	94.63
16MEU32	31.46	8.55	30.07	21.11	0.93	1.81	0.31	0.6	0.486	0.53	4.35	100.2
16CHE09	38.97	7.65	35.69	7.321	0.99	0.73	0.08	1.83	0.297	0.51	4.9	98.98
16MEU38	37.78	5.61	38.24	9.372	0.79	1.09	0.42	0.97	0.259	0.44	5.07	100
RN838	1.45	4.86	1.02	60.93	0.06	0.25	0.28	0.69	0.03	0.5	15.91	86.01
RN859	0.23	1.01	0.5	65.99	0	0.19	0.4	1.14	0.004	0.67	12.92	83.06
RA8432	2.07	1.88	1.02	65.29	0.03	0.23	0.44	2.44	0.042	0.89	12.47	86.81
15HEB03	51.91	18.47	12.78	5.392	0.27	0.08	1.2	3.15	0.82	0.12	4.3	98.47
15TDP07	43.88	17.53	20.89	7.099	1.06	0.42	0.68	2.88	0.76	0.19	4	99.39
16TDM10	49.2	18.84	15.33	3.853	1.16	0.42	2.11	3.81	0.842	0.21	2.76	98.53
16MEU23	38.45	14.87	36.54	0.322	0.76	0.37	0.64	2.63	0.628	0.26	3.09	98.56
16MEU33	63.27	7.7	20.4	1.412	1.18	0.31	0.65	1.64	0.826	0.14	1.82	99.34
16MEU03	61.22	14.52	10.66	2.777	3.25	0.44	0.2	1.28	0.683	0.41	4.36	99.79
15TDP32	51.42	22	12.44	1.228	2.18	0.32	0.97	3.24	1.025	0.21	4.1	99.14
16MEU01	46.97	21.38	14.79	2.494	2.13	1.93	0.5	2.8	0.896	1.37	4.46	99.71
15HEB01	31.57	12.49	9.54	30.19	0.1	0.13	1.17	3.1	0.522	0.37	6.94	96.12
RA8431	18.38	7.27	17.24	39.15	0.09	0.18	0.67	2.25	0.289	0.52	9.45	95.49
15TDP12	36.82	17.49	17.48	15.76	0.19	0.08	0.59	3.11	0.703	0.23	7.69	100.2
15TDP45	27.53	12.65	16.15	29.73	0.16	0.31	0.85	2.21	0.499	0.27	8.3	98.65
15TDP42	39.35	15.56	14.05	17.2	0.24	0.14	0.51	2.86	0.667	0.28	7.67	98.51

►**Table 6.3** Suite

Label	Ag	Sn	Sb	Cs	Ba	Hf	Ta	W	Tl	Pb	Bi	Th	U
15RN01	<0.5	3	2.8	4	434	4	1.33	21.4	0.13	26	<0.1	12.8	3.1
CA	<0.5	3	3.1	3.3	423	3.8	1.22	8	0.16	17	<0.1	10.6	2.49
15RN04	<0.5	4	3	6.3	881	4.3	4.26	20.2	0.37	39	1	15.5	4.11
15RN05	<0.5	2	0.7	0.9	45	0.1	0.06	1.1	<0.05	6	0.1	0.08	0.16
16CHE01	<0.5	<1	<0.2	< 0.1	24	0.1	0.29	28.4	<0.05	< 5	0.1	0.21	0.38
16MEU34	0.6	1	4.2	0.9	182	6.2	0.41	10.6	<0.05	101	1.4	9.8	5.53
16CHE08	<0.5	<1	<0.2	0.3	27	0.1	1.12	15	<0.05	6	0.1	0.36	0.19
16MEU32	<0.5	2	3.3	1	260	6.1	1.11	19.5	0.12	112	1.5	14.1	5.92
16CHE09	<0.5	1	4.3	3.6	578	3.8	0.46	5.7	0.15	77	1.8	10.5	3.56
16MEU38	<0.5	<1	4.8	2.2	537	4.4	0.45	10.4	0.09	143	2.6	10.9	4.66
RN838	<0.5	<1	<0.2	0.9	591	<0.1	<0.01	<0.5	<0.05	<5	<0.1	0.47	2.23
RN859	<0.5	<1	<0.2	<0.1	100	<0.1	<0.01	<0.5	<0.05	<5	<0.1	0.06	3.22
RA8432	<0.5	<1	2.2	0.4	439	0.2	0.19	9.9	<0.05	<5	<0.1	0.82	22.5
15HEB03	<0.5	3	6.4	12.6	973	3.2	1.05	4.5	0.52	59	0.3	12.8	1.84
15TDP07	<0.5	3	3.7	9.3	962	2.7	0.94	4.6	0.44	52	0.5	11.6	1.79
16TDM10	<0.5	3	4	18.9	1357	3.4	1.11	5.7	0.79	44	0.4	13	1.11
16MEU23	<0.5	2	2.6	4.9	1009	2.3	0.81	5.1	0.39	73	1	10.3	2.02
16MEU33	4.3	2	2.9	3.3	545	35.2	1	5.2	0.2	80	0.6	21.3	3.93
16MEU03	<0.5	2	1.8	2.4	497	2.8	0.83	5.1	0.16	24	0.2	9.53	1.7
15TDP32	<0.5	4	4.2	6.5	1374	3.6	1.21	4.6	0.53	45	0.5	13.7	2.17
16MEU01	<0.5	3	2.3	4.9	963	3.8	1.09	3.8	0.48	38	0.4	12.1	2.91
15HEB01	<0.5	2	15.4	11.8	901	2.1	0.87	11.1	0.08	72	0.4	8.88	2.38
RA8431	<0.5	3	1.7	4.7	3697	1.3	0.41	12.4	<0.05	33	0.2	5.23	3.45
15TDP12	<0.5	3	3	8.8	965	3	1.09	8.6	0.38	52	0.4	12	3.78
15TDP45	<0.5	2	3.6	6.8	640	2	0.76	15.4	0.18	62	0.5	8.07	3.84
15TDP42	<0.5	2	3.2	8.5	890	2.8	0.85	6.2	0.5	54	0.3	10.5	4.91

►**Table 6.4** Rare Earth Elements geochemistry (in ppm).

Label	La	Ce	Pr	Nd	Sm	Eu	Gd	Tb	Dy	Ho	Er	Tm	Yb	Lu	∑RE	Ce_N/Ce_N	Eu_N/Eu_N	La_N/Lu_N
15RN01	43.	94.	9.7	38	15.	8.75	15.	1.9	8.9	1.4	3.8	0.57	3.8	0.60	247.0	1.04	2.66	1.03
CA	31.	73	7.2	28	13.	6.86	12.	1.6	7.7	1.3	3.5	0.49	3.2	0.52	191.6	1.10	2.47	0.87
15RN04	56.	147	13.	48.	13.	5.17	16.	2.6	13.	2.4	6.3	0.91	5.7	0.85	333.3	1.23	1.60	0.95
15RN05	0.2	0.5	0.0	0.3	0.2	0.10	0.5	0.0	0.2	0.0	0.1	0.01	0.0	0.01	2.71	1.19	1.27	0.16
16CHE01	2.4	20.	0.9	4.6	1.2	0.28	1.0	0.1	1.0	0.1	0.4	0.06	0.4	0.07	33.72	2.98	1.18	0.36
16MEU3	51.	201	11.	46.	10.	2.23	10	1.6	9.7	1.8	4.8	0.71	4.5	0.67	357.9	1.84	1.03	0.82
16CHE08	2.2	8.8	0.6	2.7	0.7	0.18	0.6	0.1	0.5	0.1	0.2	0.04	0.3	0.04	17.42	1.70	1.22	0.50
16MEU3	55.	224	12.	51.	12.	3	11.	1.9	11.	2.0	5.6	0.82	5.3	0.81	398.6	1.91	1.20	0.98
16CHE09	30.	127	8.6	37.	8.7	2.17	9.2	1.4	8.1	1.5	4.2	0.63	3.9	0.66	244.1	1.78	1.14	0.66
16MEU3	28.	135	7.8	33.	8.2	1.8	8.1	1.3	7.8	1.5	4.2	0.63	4.1	0.65	243.6	2.05	1.03	0.63
RN838	4.6	9.6	0.9	4.3	1.1	0.30	1.6	0.2	1.8	0.5	1.9	0.39	2.8	0.46	31.18	1.02	1.04	0.11
RN859	0.7	2.1	0.1	0.9	0.3	0.12	0.7	0.1	0.8	0.2	0.6	0.08	0.5	0.07	7.66	1.32	1.08	0.10
RA8432	3.6	10.	0.8	3.7	1	0.25	1.2	0.1	0.8	0.1	0.4	0.05	0.4	0.06	23.75	1.38	1.08	0.60
15HEB03	55.	138	12.	47.	8.8	1.85	7.3	1.2	7.5	1.4	4.0	0.58	3.8	0.60	290.8	1.19	1.08	0.98
15TDP07	61.	144	13.	49.	9.4	2.2	8.8	1.2	6.8	1.2	3.3	0.47	2.9	0.44	304.7	1.15	1.13	1.46
16TDM1	63	172	14.	53.	9.9	2.28	8.7	1.3	7.9	1.5	4.2	0.59	3.9	0.61	343.7	1.32	1.15	1.09
16MEU2	47.	127	11.	43.	9.9	2.36	8.4	1.2	6.8	1.2	3.3	0.46	2.9	0.45	266.1	1.26	1.21	1.11
16MEU3	48.	109	12.	49.	10.	1.58	9.3	1.3	7.4	1.3	3.6	0.54	3.8	0.59	259.2	1.01	0.75	0.87
16MEU0	44.	105	10.	40.	8.1	1.98	8.2	1.3	8.3	1.6	4.4	0.64	3.8	0.62	239.1	1.12	1.14	0.76
15TDP32	55.	130	12.	45.	8.7	1.62	7.0	1.2	7.3	1.3	3.7	0.51	3.2	0.49	278.7	1.14	0.97	1.20
16MEU0	76.	185	17.	66.	13.	3.39	13.	2	11.	2.1	6.0	0.86	5.2	0.77	404.3	1.17	1.18	1.05
15HEB01	42.	140	10.	39.	8.4	1.91	7.3	1.1	6.3	1.2	3.5	0.50	3.1	0.48	266.8	1.53	1.14	0.95
RA8431	23.	68	6.3	33.	12.	2.82	11.	1.6	9.0	1.7	4.6	0.66	4.3	0.69	180.7	1.28	1.10	0.36
15TDP12	64.	172	15.	57.	10.	2.41	11.	2.4	16.	3.5	10.	1.63	10.	1.66	381.2	1.25	1.03	0.42
15TDP45	30.	124	8.3	35.	9.8	2.4	9.5	1.5	8.7	1.7	4.8	0.69	4.4	0.70	243.2	1.77	1.17	0.46
15TDP42	52.	136	11.	44.	8.4	1.99	8.7	1.5	9.7	1.9	5.8	0.83	5.2	0.79	289.8	1.25	1.09	0.70

►**Table 6.5** Summary of $^{40}Ar/^{39}Ar$ ages of supergene K-Mn oxides in the Salmchâteau area. [a]: pseudo-plateau age; * range of individual step-heating ages; [+]: integrated age determined by less than 20% of ^{39}Ar released; n.a. : not applicable.

Label	Outcrop	Elevation	Plateau age (Ma)	±2σ	Total fusion age (Ma)	±2σ	Isochron age (Ma)	±2σ	Intercept $^{40}Ar/^{36}Ar$	±2σ	MSWD (steps)	Comments
15TDP25a		486m	11.97[a]	0.31	11.60	0.20	14.33	3.59	-665.1	1480.8	0.27 (16 to 21)	Pseudo-plateau
15TDP25b	Their del Preu quarry (1)	486m	11.07[a]	0.30	11.07	0.30	9.50	3.49	687.2	877.2	5.93 (7 to 9)	Pseudo-plateau
TDPR-003		480m	17.66[a]	0.19	18.46	0.11	19.68	1.09	-247.1	291.5	11.07 (24 to 30)	^{39}Ar recoil, excess argon, saddle shaped spectrum
15HEB01		572m	15.61[a]	0.16	16.83	0.10	15.55	0.76	302.6	102.5	17.89 (10 to 14)	^{39}Ar recoil, excess argon, saddle shaped spectrum
15HEB03	Bihain quarry (2)	573m	20.01[+]	0.34	33.30	0.24	n.a.	n.a.	n.a.	n.a.	n.a.	^{39}Ar recoil, excess argon, saddle shaped spectrum
BH311		570m	11.43	0.08	11.38	0.07	11.23	0.22	335.7	43.0	9.94 (12 to 31)	Plateau
BH311b		570m	11.79	0.10	11.69	0.11	12.14	0.39	152.1	143.4	13.27 (5 to 20)	Plateau
BIHD-009		570m	26.83	0.20	26.33	0.17	25.98	1.74	412.2	238.5	2.10 (8 to 12)	Plateau
RA8432	Lierneux (6)	-	11.38[+]	0.25	14.26	0.08	10.68	1.51	355.6	128.4	0.16 (2 to 8)	Staircase spectrum
RA8433a		-	5.30[a]	0.76	4.92	0.65	5.04	1.67	296.4	5.1	1.41 (2 to11)	Recent ages
RA8433b		-	4.11[a]	0.57	3.02	0.36	2.74	2.03	305.1	13.9	1.15 (1 to 9)	Recent ages
RN859		-	11.74[+]	0.19	14.17	0.09	11.88	0.20	291.8	2.9	1.03 (1 to 8)	Staircase spectrum
Verleu 1399	Verleumont	-	10.12[+]	0.18	11.71	0.07	10.13	0.28	295.1	4.4	3.51 (1 to 12)	Staircase spectrum

Cryptomelane (KMn_8O_{16}), frequently used for $^{40}Ar/^{39}Ar$ dating, occurs as a deep black matrix, which is mixed with the enclosing red phyllites, often showing a homogeneous composition and sometimes the typical botryoidal habit composed of micrometric growth bands (►Fig. 6.19b). The mineral typically displays a needle-like crystal form, with each crystal being less than 15 µm long and 0.5-1 µm in diameter (►Fig. 6.19c). However, most of these crystals are difficult to identify because they are agglomerated in a dense and cryptocrystalline matrix as commonly observed in other places in the world (Decrée *et al.*, 2010; Dekoninck *et al.*, 2016a, this thesis, chapter 7). This K-Mn oxide is identified by XRD (►Fig. 6.19a) and SEM-EDS analyses (►Fig. 6.19d) in almost all locations, but is abundant in Thier del Preu and Bihain quarries (►Fig. 6.16). The composition is nearly pure cryptomelane as Ba, Na and Pb are nearly absent, and K_2O composition ranges between 1.0 and 3.0 wt. % in chemical and EDS analyses (►Fig. 6.19d, ►Table 6.3). Slight enrichment in Al is frequently observed, as well as trace elements such as Co, Cu, Zn, Sr, P and Fe (this issue, Gustine, 2002). Inclusions of halite, hematite and zincite are also observed and could explain the enrichment in other metals.

Lithiophorite [(Al, Li) MnO_2 $(OH)_2$] occurs as small tabular crystals of less than 10 µm long and 2 µm in diameter or as euhedral cubic crystals of 1–5 µm (►Fig. 6.19e). However, lithiophorite is generally poorly crystalline forming a homogeneous matrix similar to that of cryptomelane. Micrometric bands are also observed in veins, and relate to the variation of lithiophorite composition, these containing few percent of Ca, K, P, Si, Co and Cu under EDS analyses, while Li is relatively low (800 ppm, ►Table 6.3). Small quantities of As-sulfate inclusions (undetermined) can be found.

Pure cation-free[18] Mn oxides are also present in the weathered ores. Manganite (MnOOH) and nsutite [Mn^{4+}, Mn^{2+}) $(O,OH)_2$] are clearly identified by XRD in weathered rhodochrosite veins of the Chevron area (Fig. 5a). These minerals are associated with pyrolusite (►Fig. 6.19f, MnO_2). The presence of small quantities of pyrolusite is a common feature of these mineral associations as nsutite is considered as an intergrowth of cryptocrystalline ramsdellite and pyrolusite (Post, 1999). Pyrolusite is easily recognized by its coarse prismatic crystals 5–50 µm long and 1–15 µm wide and well-developed cleavages in Scanning Electron views. Petrographic features, such as high reflectivity, yellow reflection color, well-developed bireflection, and strong anisotropism, makes it easily recognizable under an optical microscope (►Fig. 6.19f). The determination of nsutite is more complicated in light and scanning electron microscopy because of the similar features with other cation-

[18]This determines Mn oxides with composition containing only Mn, O and/or H (i.e., ramsdellite, pyrolusite, manganite, nsutite…) without other metal than Mn.

free Mn oxides (►Fig. 6.19f). Despite they are composed of only Mn and O, manganite is darker than nsutite in back-scattered electron views. This feature is related to the heavier average molecular mass of nsutite than manganite. These three Mn oxides are often associated with Mn ores worldwide and commonly form from oxidation of Mn carbonates (Post, 1999).

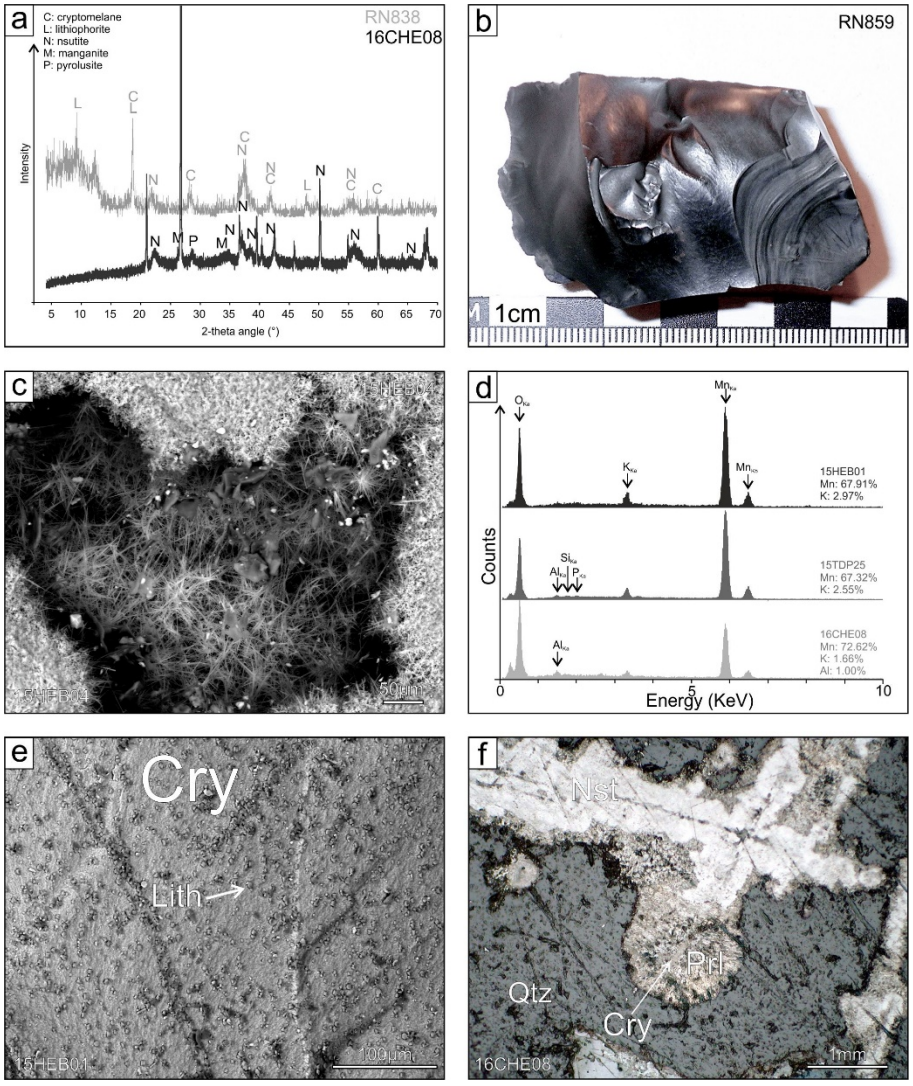

►**Fig. 6.19** Mineralogy of the Mn oxides. **a.** XRD pattern of two samples containing the dominant Mn oxide minerals. **b.** Pure cryptomelane sample showing the typical black color and colloform textures. **c.** Back-scattered electron view of cryptomelane needles in the Bihain quarry. **d.** Energy Dispersive Spectra (EDX) of three cryptomelane samples located in the Bihain quarry (15HEB01), Thier del Preu quarry (15TDP25) and Heid-Gossin quarry (16CHE08). The composition is nearly pure cryptomelane which can contain little amount of

Al, Si and P. **e.** Back-scattered electron view of lithiophorite coating onto pure cryptomelane vein in the Bihain quarry. **f.** Reflected light view of nsutite, cryptomelane and tabular pyrolusite in the Heid-Gossin quarry. Cry: cryptomelane; Lith: lithiophorite; Nst: nsutite; Qtz: quartz; Prl: pyrolusite.

Hematite and goethite are extensively disseminated in the host slates, the latter giving yellow to brown tints to the weathered host slates (►Fig. 6.20a). Hematite (►Fig. 6.18a) follows the stratification. Its presence in the weathered slates is due to the relative stability of hematite under supergene conditions. This could explain why goethite is relatively rare in most of the sampling sites, as Fe remains hosted in the hematite structure, even so botryoidal goethite is observed filling voids in the host slates and where Mn oxides are highly concentrated (►Fig. 6.20b). This goethite is characterized by Mn, P and Al substitutions to Fe^{3+}. Undetermined Fe-Mn oxides are also detected in some samples and could be a mixture of Fe oxides and Mn oxides.

Secondary clay minerals widely occur in the form of illite, as a replacement for the former muscovite present in the manganiferous slates. Kaolinite is also identified as a replacement product of rhodochrosite and weathering product of the slates. Chlorite is present in some levels of the host slates and in quartz veins. However, its formation is most likely related to metamorphic conditions rather than supergene transformation. Their chemical composition allows the distinction of two chlorites, one being Mg-rich and the other Fe-rich. Most of these chlorites contain small amounts of Mn (1–10 %) in their structure.

6.2.4.b Petrographic features of the weathered ores

In order to deal with the petrography of the weathered ore, we consider the Salmchâteau area (south) and the Chevron area (north) separately, because (1) they underwent weathering processes with variable intensity, and (2) the primary Mn-bearing assemblage is slightly different due to metamorphism. It is also necessary to keep in mind that Mn-rich sediments are composed of a succession of purple to red slates, cm-size coticule layers and Mn ore level, which are all crossed by several metamorphic veins in both locations.

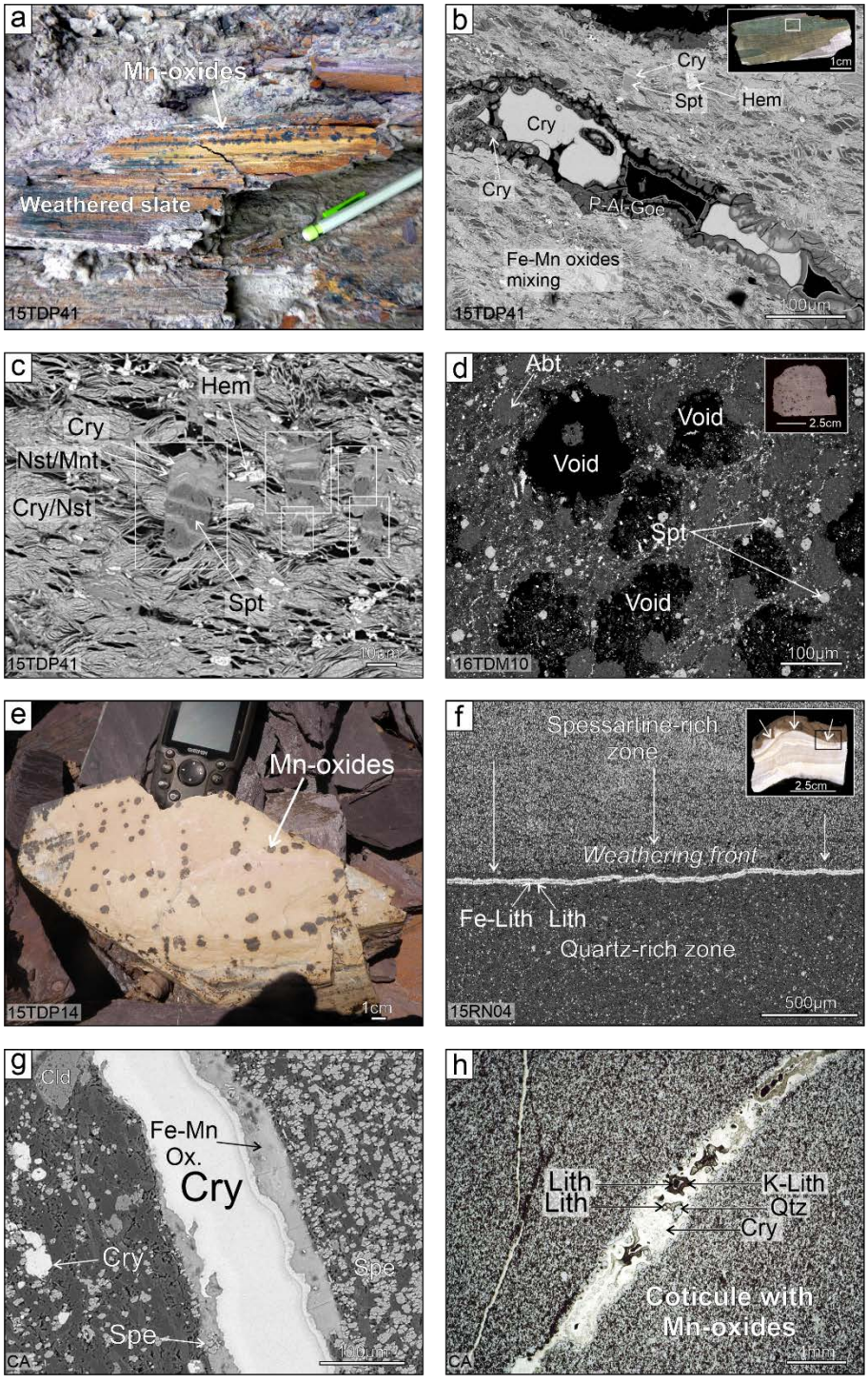

►**Fig. 6.20** Petrographic features of Thier del Preu and Regnié quarries with their coticule

levels. **a.** Weathered Mn-rich purple slate showing Mn oxides (black halos) and secondary Fe-oxides (yellow to brown tints) on the surface. **b.** Back-scattered electron view of heavily weathered lenses containing botryoidal P-Al-rich goethite veins filled by cryptomelane. The micaceous matrix is replaced by nsutite/manganite and cryptomelane, conserving the typical habitus of muscovite-illite. Spessartine is also partially replaced, whereas hematite remains stable. **c.** Back-scattered electron view of spessartine crystals (delimited by white rectangles) partially replaced by cryptomelane and nsutite/manganite, together with the micaceous matrix. **d.** Dissolved pyrite in the red slates (Unit 2) in Thier du Mont Hill (►Fig. 6.16). Spessartine and albite are well preserved. **e.** Weathered coticule level showing dark halos composed of Mn oxides. **f.** Back-scattered electron view of a weathering front in a coticule sample delimited by the formation of lithiophorite and Fe-lithiophorite. The boundary is well marked between the spessartine-rich and quartz-rich layers of the coticule sample. **g.** Back-scattered electron view of a cryptomelane vein crossing the coticule levels as it is shown in ►Fig. 6.18b. Fe-Mn oxides (undetermined) occur on the border of this vein. **h.** Reflected light view of a cryptomelane vein in the coticule sample showing successively the formation of cryptomelane, K-rich lithiophorite and lithiophorite from the border to the center. Cry: cryptomelane; Lith: lithiophorite; Nst: nsutite; Mnt: manganite; Qtz: quartz; Hem: hematite; Spt: spessartine; Goe: goethite; Abt: albite; Cld: Mn chloritoid.

- *Salmchâteau area*

The manganiferous purple slates in Thier del Preu quarry are weathered into a reddish to purple clayey rock, which is impregnated by black Mn oxides (►Fig. 6.20a) intimately mixed with the phyllosilicate matrix. Where Mn is more concentrated by weathering processes, cryptomelane and nsutite/manganite precipitate in the cleavage of these K-phyllosilicates (illite or muscovite), or even preserve their typical habitus when replacement is nearly complete (►Figs. 6.20b and c). Despite the fact that spessartine is generally well preserved in the weathered slates, there are evidence that cryptomelane and nsutite/manganite partially replace some of the garnet crystals (►Fig. 6.20c). Mn veins are enclosed in the host slates and are mostly composed of cryptomelane (►Fig. 6.20b). P-Al-rich goethite is identified on the borders of these veins, which could also contain nsutite/manganite in the center. Further east of Thier del Preu quarry, in Thier du Mont (►Fig. 6.16), the Fe-rich purple to red slates of the Meuville Member contain diagenetic grains of pyrite following the stratification of the sediments. These grains of pyrite are dissolved, leaving only cubic voids, sometimes filled by sulfate (►Fig. 6.20d). Mn oxides are not reported at this location; instead spessartine, hematite and Mn-chlorite are widely preserved.

Coticule layers exhibit black to brown halos (►Figs. 6.18b and 6.20e), which surround black veins or spots composed of lithiophorite, Fe-Mn oxides (thought to be Fe-lithiophorite) and cryptomelane (►Figs. 6.20f, g and h). These veins are also present in the enclosing slates. Their occurrence is only clearly shown when the rock is strongly weathered, as coticule seems to be more resistant to weathering than the host slates. These veins display a mineral sequence of successive Mn-Fe-oxides,

cryptomelane, K-rich lithiophorite and lithiophorite from the edge to the core (►Figs. 6.20f, g and h). K-rich lithiophorite makes the transition between the aforementioned minerals (►Fig. 6.20h); Fe-Mn oxides (Fe-lithiophorite?) are present on the borders (►Fig. 6.20g). These Mn oxides also separate the brownish weathered coticule and the "fresh" coticule, as a sharp boundary (►Fig. 6.20f). The delimitation is not randomly distributed, but occurs mainly between the spessartine-rich layers of the coticule samples. This observation clearly shows the link between primary spessartine and secondary supergene Mn oxides in coticule (►Fig. 6.20f). We also noted that some muscovite could be slightly enriched in Fe and Mn, probably because they were partially replaced by Mn oxides, as already demonstrated in the weathered Mn-slates (►Fig. 6.20c).

The study of Mn oxides in the Bihain quarry brings new insights to the petrography of the Mn-rich slates, as they are higher elevated (572 m) and more weathered than in Thier Del Preu quarry (486 m). Centimeter-size Mn-veins crosscut the red clayey rocks (►Figs. 6.21a and b). These veins are successively filled by cryptomelane, and sometimes lithiophorite in the core (Figs. 6.21b and c) or as a coating onto cryptomelane crystals (►Fig. 6.19e). The latter could be present in small quantities at the contact of these veins and the host slates. Scanning Electron views also show that cryptomelane replaces a former mineral, as cryptomelane contains ~1 wt. % Ca. An analogue observation exhibits rhombohedral nsutite/manganite crystals, which means this mineral could have replaced a former carbonate (Post, 1999; ►Fig. 6.21d). These crystals are embedded in a cryptomelane matrix and located only in the highly mineralized zones. Lithiophorite and a second generation of cryptomelane veinlets also crosscut this first cryptomelane generation (►Fig. 6.21b). Another interesting petrographic feature is the presence of cryptomelane spots disseminated in the host slates (►Fig. 6.21e), which is a common feature with Thier del Preu quarry. Goethite crystals are associated with cryptomelane and lithiophorite.

The slates are crossed by several metamorphic veins, most of them being composed of quartz, andalusite-kanonaite, pyrophyllite, hematite, Mn-chlorite and muscovite. No replacement texture of the metamorphic Mn-silicates by Mn oxides were evidenced in these veins. However, pure cryptomelane veinlets cross such kind of veins and form cement to the brecciated quartz (►Fig. 6.21f).

- *Chevron area*

The slates are rather red than purple in the Chevron area, which is probably due to the combination of lower metamorphic grade and the relative Fe content of the sediments (►Fig. 6.17a). These red slates are interbedded with gray levels of sandstone and show Mn-Fe laminations (►Fig. 6.22a). Weathering processes are less recorded in the Chevron area: most of the red slates show only partial dissolution features and black impregnations. These impregnations and veinlets are mainly composed of

manganite/nsutite sometimes enriched in Ca (►Fig. 6.22b), and subordinate amount of cryptomelane or lithiophorite.

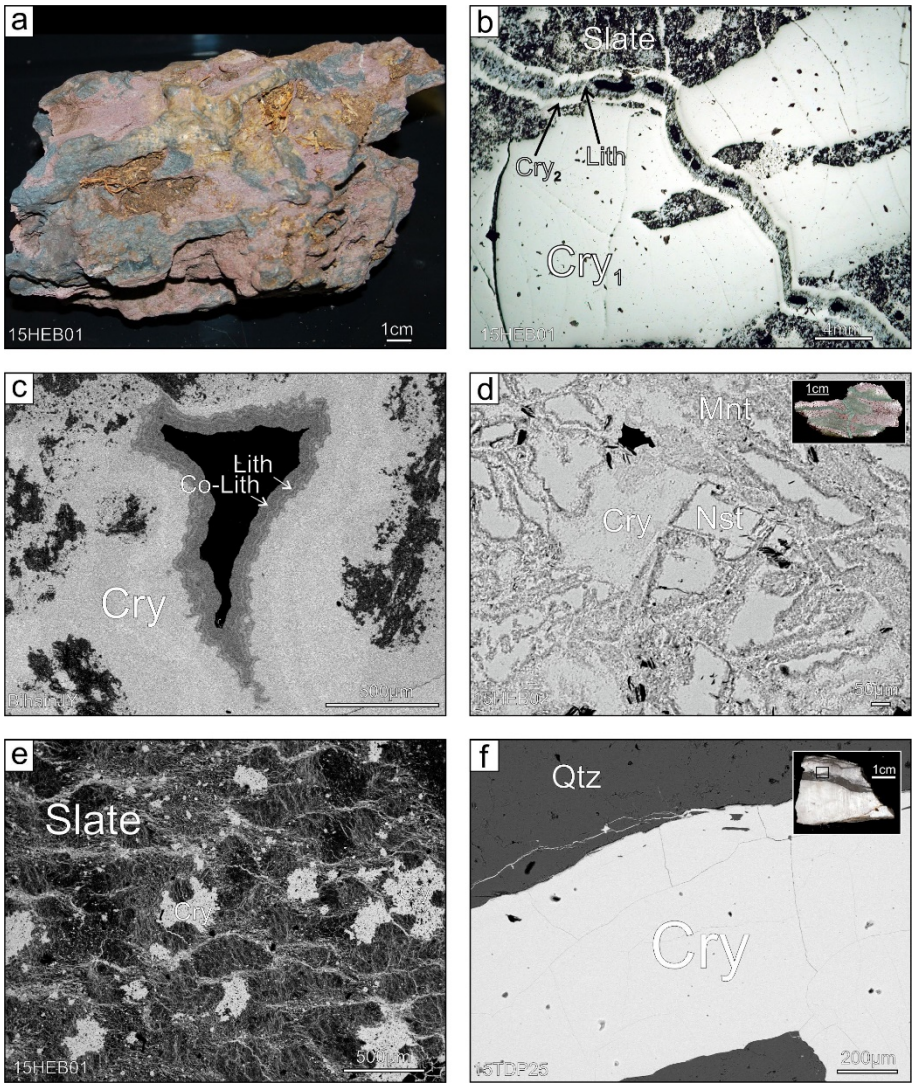

►**Fig. 6.21** Petrographic features of the Bihain quarry and metamorphic veins. **a.** Heavily mineralized slate crossed by several veins of Mn oxides (mainly cryptomelane) in the Bihain quarry. **b.** Reflected light view of a cryptomelane vein (Cry_1) crossed by a second generation of cryptomelane veinlet (Cry_2), subsequently filled by lithiophorite. **c.** Back scattered electrons view of cryptomelane and lithiophorite filling voids, showing the typical colloform texture. **d.** Back scattered electrons view of nsutite replacing rhomboedral crystals and cemented by cryptomelane and manganite/nsutite. **e.** Back scattered electrons view of disseminated spots of cryptomelane in the host slate. **f.** Back scattered electrons view of cryptomelane veinlets crossing a metamorphic quartz vein in Thier del Preu quarry. Cry: cryptomelane; Lith: lithiophorite; Nst: nsutite; Mnt: manganite; Qtz: quartz.

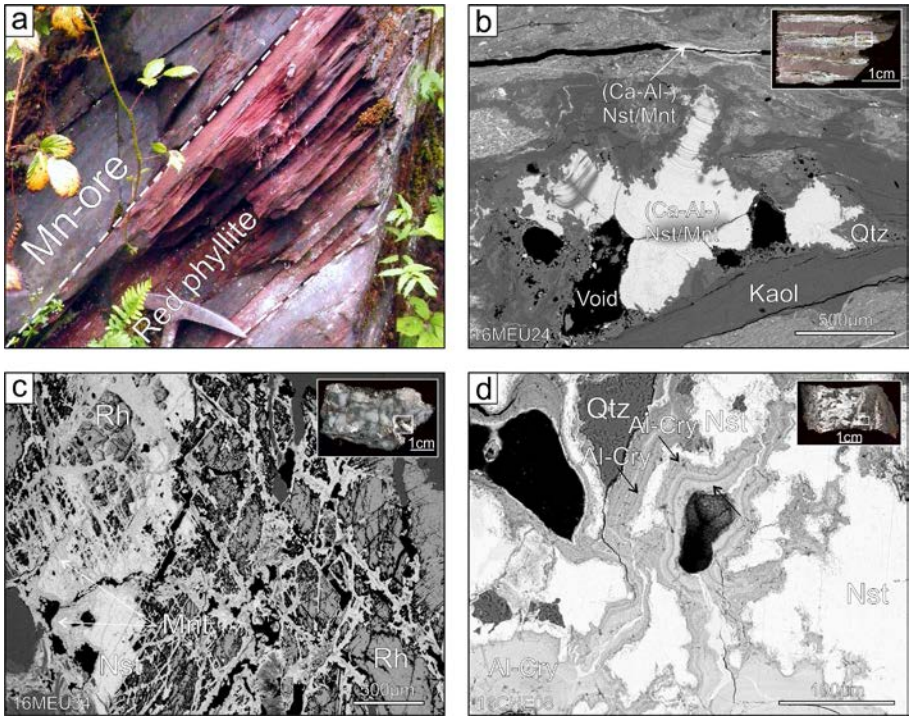

►**Fig. 6.22** Petrographic features of the Chevron area. **a.** Mn ore level interbedded with red phyllites in "Les Salins" quarry (see ►Fig. 6.16 for location). **b.** Back scattered electrons view of rhodochrosite lenses replaced by successive kaolinite and Ca-Al-bearing nsutite/manganite in the Meuville mine. See the similar texture between this weathered sample and the non-weathered sample of ►Fig. 6.18c containing well-preserved rhodochrosite lenses. **c.** Back-scattered electron view of the Mn ore (Unit 4) in the Meuville mine, showing rhodochrosite partially replaced by nsutite and manganite. **d.** Back-scattered electron view of rhodochrosite-quartz veins extensively replaced by nsutite and manganite in the Meuville mine, and filled by several generations of Al-rich cryptomelane. Nst: nsuite; Mnt: manganite; Kaol: kaolinite; Qtz: quartz; Hem: hematite; Rh: rhodochrosite; Spt: spessartine.

The base of the Les Plattes Member consists of a coarse dark red Mn-Fe-ore level composed of rhodochrosite, spessartine, hematite, chlorite, Mn-chlorite, kutnohorite and quartz (►Figs. 6.18d and 6.22a). Two generations of rhodochrosite occur, as nodules and cement in the brecciated ore. Spessartine also replaces rhodochrosite nodules on the border (►Fig. 6.18d). Folded hematite in spessartine crystals indicates that hematite was present before metamorphism, and confirms hematite to be the results of sedimentary or diagenetic processes. The Mn ores are poorly weathered but when this is the case, Mn carbonates are replaced or crossed by manganite/nsutite veinlets, which are enriched in Ca in some sections (►Fig. 6.18d).

Metamorphic rhodochrosite-quartz-chlorite veins usually occur across the Salm Group in the Chevron area, but also as cm-size lenses following the stratification

of the red slates (Chevron borehole; Graulich, 1966; ►Fig. 6.18c). When these veins are weathered, they are characterized by black, red or orange mineral assemblage tints (►Fig. 6.22b). The composition of the weathering product is mainly manganite, nsutite and pyrolusite (►Figs. 6.19f, 6.22b, c and d) together with kaolinite (►Fig. 6.22b). Al-cryptomelane is a subordinate mineral growing onto the cation-free Mn oxide minerals with typical growth bands (►Fig. 6.22d). Red to orange tints are typical features of Fe-oxides (hematite, goethite and limonite).

6.2.4.c Geochemistry of the ores

In order to better understand the geochemical signature of the Mn-rich rocks, we have subdivided the analyzed samples into different categories: (1) Mn-rich slates, (2) weathered Mn-rich slates, (3) pure Mn oxides, (4) carbonate Mn ores, (5) coticule layers and (6) metamorphic veins. Previous geochemical studies (e.g., Herbosch *et al.*, 2016) mainly focused on the sedimentary features of the Ottré Formation, trying to identify the nature of the primary Mn-rich rocks. Thereby, these sediments were enriched in iron and manganese before they underwent subsequent weathering conditions, the first enrichment of Mn being related to the input from hydrothermal vents in the Rheic ocean (Herbosch *et al.*, 2016).

- *Chemical composition*

Major element composition is compared to the average slate of the Les Plattes Member (Herbosch *et al.*, 2016) in order to show variation in the chemical compositions with weathering (►Fig. 6.23a). Manganese enrichment is slightly higher in the weathered Mn-rich slates than in the carbonate Mn ores, showing 4.1-10.1 and 1.9-5.5 times the average Mn-slate composition, respectively. Coticule layers have intermediate MnO composition between 4.4-6.8 the average Mn-slate (►Table 6.3, ►Fig. 6.23a). As coticule and slates result from two different sedimentary processes, their Mn/Fe ratios differ quite well, showing high Mn/Fe ratio (1.6-22.4) and low Mn/Fe, respectively (0.01-0.4; Herbosch *et al.*, 2016). Heavily weathered Mn-rich slates, where Mn oxides widely occur, are significantly enriched in Mn, reaching Mn/Fe ratios higher than 0.90, which correspond to concentration ranging between 15.8 and 39.2 wt. % MnO (►Table 6.3). Carbonate Mn ores of the Chevron area have higher enrichment in CaO and Fe_2O_3 than the average slate and weathered Mn-rich sediments of the Salmchâteau area, a feature related to the carbonate nature of the sediments containing abundant Ca-rhodochrosite (and kutnohorite) and hematite. Na_2O, K_2O and TiO_2 are slightly depleted in the carbonate Mn ores because detrital and/or authigenic clays and Fe-oxides are less abundant (►Fig. 6.23a). Slate patterns are variable as a whole, because some of them could be slightly weathered, or because they do not originate from the same stratigraphic level than the average Mn-slate (►Fig. 6.23a). An interesting style of these majors is the

decrease in the SiO_2, Al_2O_3 and MgO content of the weathered Mn-slates in comparison with the average slate.

- *Rare Earth Elements*

Rare Earth Elements (REEs) in the Mn-rich slates, carbonate Mn ores, metamorphic veins and coticule layers are poorly concentrated. The maximum value is reached in coticule layers (431 ppm) and minima in metamorphic veins (2 ppm). Pure Mn oxides contain little amount of REEs ranging between 8 and 31 ppm, while weathered Mn-slates do not show significantly higher values (239 and 381 ppm) than the poorly weathered Mn-slates (243 to 404 ppm), indicating there is no additional concentration of these elements during weathering processes (►Figs. 6.23b and c; ►Table 6.4).

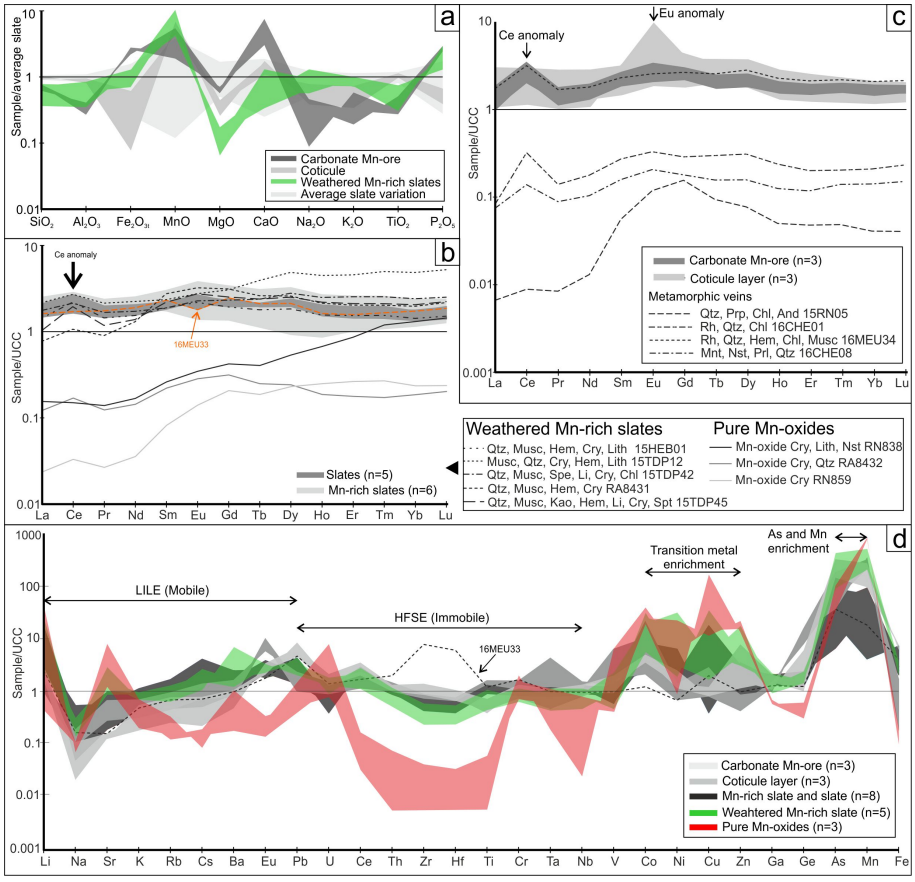

►**Fig. 6.23** Geochemistry of the Mn-rich slates, weathered Mn-rich slates, pure Mn oxides, carbonate Mn ores, coticule layers and metamorphic veins. **a.** Major element patterns compared to the average slate of the Ottré Formation (Herbosch *et al.*, 2016). **b.** Rare Earth Elements patterns of some slates (light gray) and Mn-rich slates (dark gray) together with the patterns of each individual weathered Mn-rich slate (dashed and dotted lines) and pure Mn oxide minerals

(full lines) compared to the Upper Continental Crust (McLennan, 2001). **c.** Rare Earth Elements patterns of the carbonate Mn ore of the Chevron area (dark gray) and coticule layers (light gray) together with metamorphic veins (dashed and dotted lines) compared to the Upper Continental Crust (McLennan, 2001). **d.** Trace element pattern of carbonate-hosted Mn ores of Chevron, coticule layers of Salmchâteau, Mn-rich slates and slates, weathered Mn-rich slates and pure Mn oxides, compared to the Upper Continental Crust (McLennan, 2001).

The Mn-rich slates display a flat pattern, which actually follows the UCC reference with a slight enrichment and possibly some slight Ce positive anomalies (1.01<Ce/Ce*<1.95; McLennan 2001; ►Fig. 6.23b). Note that a positive Eu anomaly could be observed in the Mn-rich slates (1.07<Eu/Eu*<1.21), whereas only sample 16MEU33 displays a negative Eu anomaly (Eu/Eu*=0.75; ►Fig. 6.23b). The Ce (1.27<Ce/Ce*<1.77) anomaly is reinforced in the weathered Mn-slates probably because Mn oxides widely occur in comparison with other analyzed slates (►Fig. 6.23b). The flat pattern is not significant in all of these samples, as MREE or HREE could be favored instead of LREE, showing an asymmetric trend with low La_N/Lu_N ratios ranging from 0.36 to 0.95 (►Table 6.4). The REE content of the carbonate Mn ores and metamorphic veins in the Chevron area exhibit the same pattern in the weathered and non-weathered samples, showing a relatively flat pattern with a clear positive Ce anomaly (1.78<Ce/Ce*<2.05 and 1.19<Ce/Ce*2.98, respectively; ►Fig. 6.23c). While the REE values are close to that of the UCC reference for the carbonate Mn ores, metamorphic veins are largely below the values of McLennan (2001), except sample 16MEU34 which follows the carbonate Mn ore (►Fig. 6.23c). An interesting feature of these geochemical patterns is the absence of a Ce anomaly in metamorphic veins of the Salmchâteau area, together with relative enrichment in MREE compared to LREE and HREE (►Fig. 6.23c). Pure Mn oxides are characterized by an asymmetric pattern, where HREE are clearly favored, providing La_N/Lu_N ratios between 0.10 and 0.63 (►Fig. 6.23b). However, all these profiles are below the UCC reference and slight positive Ce anomalies can be observed in pure cryptomelane samples (1.32<Ce/Ce*<1.38). Coticule layers exhibit a flat pattern, but where a positive Eu (and MREE in general) anomaly is clearly shown, ranging between 1.60 and 2.66 (►Table 6.4; ►Fig. 6.23c).

- *Trace elements*

A particular feature of trace element spider diagrams resides in a relatively strong enrichment in some transition metals (►Fig. 6.23d). Arsenic is the most obvious one, showing enrichment overpassing 10 times the UCC reference of McLennan (2001) in all samples that are linked to the Mn-content of the sediments. Other metals, such as Co, Cu, Zn and Ni (Pb?), are particularly enriched in the weathered Mn-rich slates or in pure Mn oxide minerals up to 10 times the UCC reference (McLennan, 2001). Weathered coticule layers exhibit an enrichment in Co and Cu only, while carbonate Mn ores have relatively high Co and Zn values (►Table 6.3). Note that V could be

high but is rather related to the composition of spessartine or chloritoid in coticule layers than in weathering minerals. Lithium is enriched in all samples when compared to the Upper Continental Crust, and is more concentrated in the weathered Mn-slates (46-477 ppm) and in pure Mn oxides (9-862 ppm), especially those samples containing lithiophorite. Despite the fact that Na is depleted in almost all rock types, mobile and immobile elements do not shift away from the average UCC reference. However, an exception is made for some elements: the substitution of Sr in cryptomelane can lead to a slight enrichment in the weathered Mn-rich slates and pure Mn oxides; Zr and Hf are relatively low in the weathered Mn-rich slates and high in Mn-slate 16MEU33 depending on the detrital input of the former sediments.

6.2.4.d $^{40}Ar/^{39}Ar$ dating

The examination suggests that the K-Mn oxides studied for geochronology consist mainly of cryptomelane, with subordinate amount of lithiophorite, manganite and nsutite (►Fig. 6.19a). Void-filling cryptomelane is generally very pure, cryptocrystalline, and characterized by a homogeneous composition (►Figs. 6.19b and d). All $^{40}Ar/^{39}Ar$ results, corrected for interfering isotopes and mass discrimination, are included in appendix IV and summarized in ►Table 6.5. These results are illustrated in ►Fig. 6.24. The plateau ages are defined by a sequence of three or more continuous steps that contain more than 50% of the total amount of ^{39}Ar released and yield apparent ages that are overlapping at 2σ (95% confidence level). Pseudo-plateau ages are determined as a sequence of three steps containing less than 50% of the total ^{39}Ar released, but the age values reproduce only 90% of the confidence level (2σ; ►Fig. 6.24a). Other ages are generally not considered as they are defined by less than 50% of the total amounts, of ^{39}Ar released and age values of each step are only reproducible by less than 90% confidence level (►Fig. 6.24b, c, and d). Although this third type of age cannot provide absolute ages, they still contain valid geochronological information (Vasconcelos, 1999), which can be helpful to better understand the formation and timing of Mn oxides.

Plateau ages are difficult to be determined in the studied samples as they often reproduce less than 95% of the confidence level (2σ). Three samples yield pretty well-defined plateau ages of 11.29 $\pm$ 0.08 Ma, 11.79 $\pm$ 0.10 Ma and 26.83 $\pm$ 0.20 Ma (►Fig. 6.24a), which are similar to the intercept ages in the inverse correlation plots and correspond to homogeneous K/Ca ratios (►Table 6.5 and appendix IV). These data suggest the lack of recent radiogenic loss and ^{39}Ar recoil effect (e.g., Onstott *et al.*, 1995), of contamination by old minerals or of inherited argon resulting from the decomposition of parent minerals. Therefore, the plateau ages are reliable and interpreted as precipitation age. Note that samples BIHD-009 and BH311 spectra show some minor interaction of the crystals with non-atmospheric or ground water argon resulting in an increase of the ages in the first steps (►Fig. 6.24a). This effect

is not significant because the subsequent plateau ages are well-defined in the middle to high temperature steps.

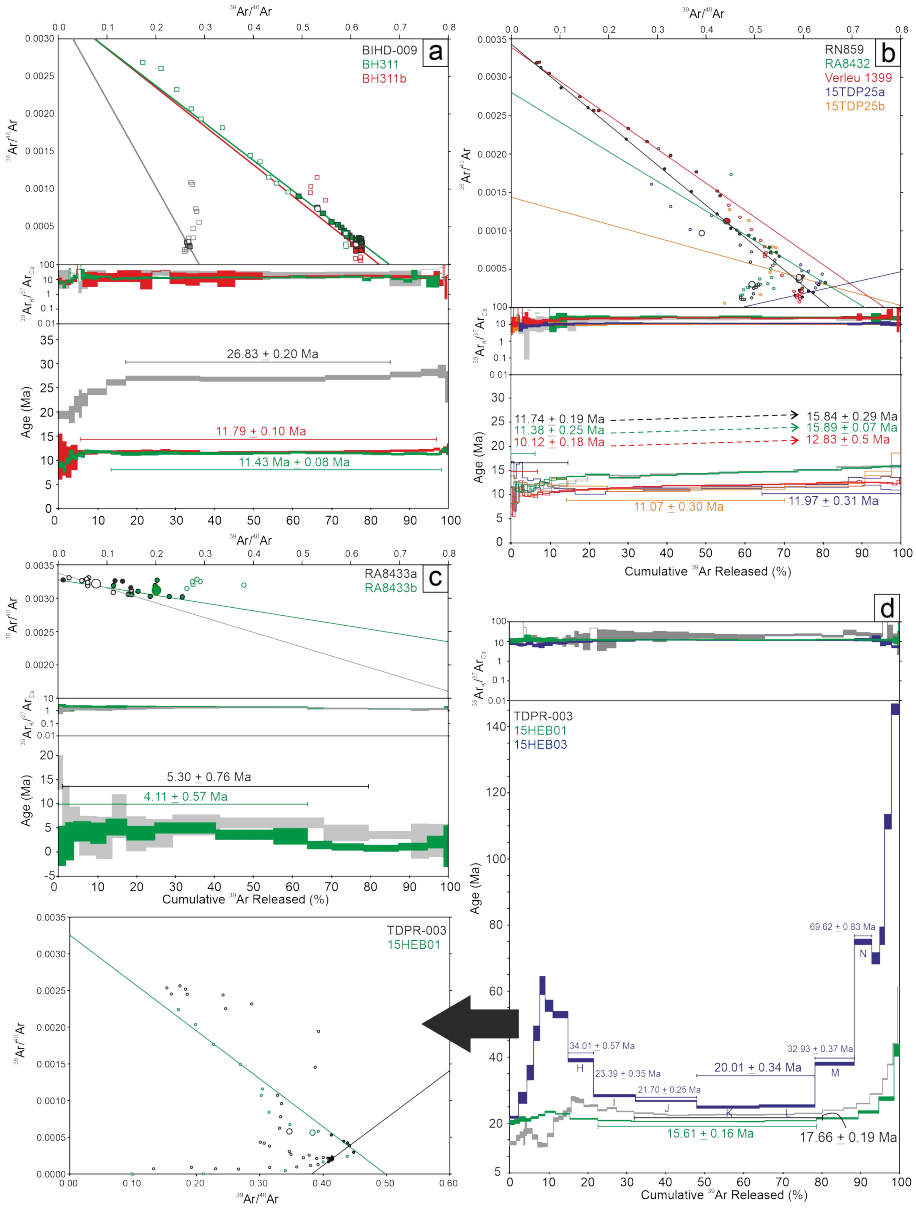

►**Fig. 6.24** $^{40}Ar/^{39}Ar$ geochronological data of the Salmchâteau area. **a.** Plateau ages obtained from three cryptomelane samples. **b.** Staircase spectra with non-plateau ages. **c.** Younger ages yielded from cryptomelane samples. **d.** Pseudo-plateau ages followed by staircase spectra showing increasing ages in the high temperature domain.

Despite the relative chemical homogeneity of the collected samples, and the absence of growth bands, most of the analyzed samples do not show well-constrained plateaus. When the grains contain multiple generations of cryptomelane (►Fig. 6.21b), which possess variable retentivity properties, incremental heating analyses result in staircase spectra (►Fig. 6.24b; e.g., Vasconcelos, 1999). Samples RN859, RA8432 and Verleu 1399 yield pseudo-plateaus in the low-temperature steps with 11.74 ± 0.19, 11.38 ± 0.25 and 10.12 ± 0.18 Ma ages, respectively, represented by less than 20% of the total amount of ^{39}Ar released. The inverse correlation diagrams using these steps provide similar intercept ages and atmospheric initial ^{40}Ar/^{36}Ar ratios. Subsequent mid-to high-temperature steps increase progressively to reach 15.84 ± 0.29, 15.89 ± 0.07 and 12.83 ± 0.50 Ma, respectively, at the end of the incremental degassing, without intermediate plateau ages. For RN859 and Verleu 1399, K/Ca values also show a slight increase during step-heating, while they remain constant for RA8432 (see appendix IV). For samples 15TDP25a and b (►Figs. 6.21f and 24b), two pseudo-plateau ages of 11.97 ± 0.31 and 11.07 ± 0.30 Ma can be calculated, respectively, on the final and intermediate portion of each spectrum (related to 36 and 56% of ^{39}Ar released), which are quite similar to their total fusion ages. For both samples, the K/Ca ratios remain stable but no intercept age can be determined in the inverse correlation plot (►Table 6.5). Ages outside the range 11–12 Ma for these samples are interpreted as a consequence of argon losses (sample 15TDP25a) or excess argon contamination (sample 15TDP25b). Two other plateau ages of 5.30 ± 0.76 and 4.11 ± 0.57 Ma are determined in samples RA8433a and RA8433b (►Fig. 6.24c) and yield the youngest ages for the area. It is noteworthy that the atmospheric contents in these samples is very high (see appendix IV), resulting in large errors on individual step ages and meaningless intercept ages in the isochron plots since the experimental points concentrate near the ordinate axis. Moreover, the age decrease observed for sample RA8433b at the end of degassing can suggest that ^{39}Ar recoil effect modified the original distribution of argon in this sample, or alternatively mixed generations of cryptomelane. Therefore, careful attention has to be taken interpreting these ages that do not necessarily correspond to the timing of this Mn oxide formation, the true precipitation being younger.

^{39}Ar loss by neutron induced recoil is common in ^{40}Ar/^{39}Ar geochronology of Mn oxides (Vasconcelos, 1999), mainly due to the very fine-grained nature of the minerals (<1–10 μm; ►Fig. 6.19c). When significant ^{39}Ar loss occurs, reliable age information on the samples cannot be retrieved. However, if only a minor amount of ^{39}Ar is lost by recoil, a plateau or pseudo-plateau age may still be obtained (Vasconcelos, 1999). ►Fig. 6.24d illustrates age spectra for samples that appear to have experienced ^{39}Ar recoil during neutron irradiation procedures. The spectra are characterized by apparent old ages in the low-temperature steps, which decrease progressively at middle and higher temperatures, and finally reach a pseudo-plateau

defined by the mid-high temperature steps. The pseudo-plateau ages are 17.66 ± 0.19 and 15.61 ± 0.16 Ma for samples TDPR-003 and 15HEB01, respectively (►Fig. 6.24d), being the maximum estimates for the age of these samples. However, these spectra are often more complex because they cumulate recoil effect and contamination of other generations of cryptomelane or minerals, resulting in a saddle-shaped profile. For example, sample 15HEB03 could contain at least two generations of cryptomelane veins as it has been observed in other samples of the same area, or that micas have contaminated the sample (►Fig. 6.19a and b). This is materialized by five mid-temperatures steps accounting for more than 60% of the total ^{39}Ar released. These steps yield descending apparent ages at 34.01 ± 0.57, 23.39 ± 0.35 and 21.70 ± 0.25 Ma (H, I, J), respectively, while the two subsequent steps yield an internally concordant but much younger apparent age of 20.01 ± 0.34 Ma. The following high-temperature steps provide older ages of 32.93 ± 0.37 Ma and 69.62 ± 0.83 Ma and finish with 139.52 ± 1.76 Ma (►Fig. 6.24d). Variation of the ages and the K/Ca ratios (see ►Table 6.5 and appendix IV) for a single grain indicates mixing of radiogenic component domains, for example by recrystallization of older material (cryptomelane or other Mn-bearing minerals). Contamination of K-micas could not influence these ages, as the K/Ca ratio decreases when the age of the sample increases (►Fig. 6.24d). However, mid-temperature steps in samples TDPR-003 and 15HEB01 contain internal pseudo-plateau ages of 17.66 ± 0.19 Ma and 15.61 ± 0.16, respectively. Subsequent high-temperature steps end with 56.45 ± 0.50 and 77.31 ± 1.88 Ma. For these samples, the minimum ages provided by the intermediate portion of the spectra have to be considered as maximum ages for the last recrystallization of cryptomelane. The 20.01 ± 0.34 Ma age of sample 15HEB03 is also a maximum age consistent with the 20.0 ± 0.2 and 22.2 ± 0.6 Ma obtained by Demoulin *et al.* (2018a) in the same area.

6.2.5 Discussion

6.2.5.a Paragenetic sequences

The determination of the relative timing of each mineral that is formed during weathering of the Mn-slates, coticules, carbonated Mn ore and metamorphic veins, is an essential point to (i) decipher the genesis/processes of the weathering and (ii) interpret the ^{40}Ar/^{39}Ar dating of secondary K-Mn oxides. Such paragenetic sequence is summarized in ►Fig. 6.25a. Petrographic observations indicate that the formation of Mn oxides in the Chevron and Salmchâteau area could follow two processes. First, rhodochrosite is weathered into cation-free Mn oxides only, as this mineral is successively replaced by manganite, itself replaced by nsutite (►Fig. 6.22c) and then pyrolusite (►Fig. 6.19f). Such replacement of rhodochrosite has already been proposed by Gustine (2002), this feature being very common in supergene manganese deposits worldwide (Post, 1999). Most of nsutite is genetically derived from early

carbonates (Zwicker *et al.*, 1962) and this mineral with cryptomelane and lithiophorite are known as late alteration or weathering products of carbonates and, possibly, silicate minerals rich in Mn. Cryptomelane occurs after the formation of these cation-free Mn oxides as they fill open voids and form the typical growth band textures growing onto weathered rhodochrosite (►Fig. 6.22d) in the Chevron area. The same observation is made in the Salmchâteau area where nsutite/manganite replace former carbonate crystals and are cemented by a first generation of cryptomelane (►Fig. 6.21d). This generation of cryptomelane forms also cm-size veins crossed by a second generation of K-Mn oxide, indicating that these minerals were formed at different stages along weathering of the host rock (►Figs. 6.21b and f) and corroborate discordant $^{40}Ar/^{39}Ar$ spectra (►Figs. 6.24b and d). Lithiophorite occurs only in the core of cryptomelane veins, and is therefore the last Mn oxide to form during weathering (►Figs. 6.20h, 6.21b and c). Fransolet (1979) and Gustine (2002) also identified replacement of cryptomelane veins by nsutite and cryptomelane by lithiophorite. Other supergene minerals associated with these Mn oxides include goethite and kaolinite. In the Salmchâteau area, small veins of goethite precipitate at the border of cryptomelane veins (►Figs. 6.20b and g). In the Chevron area, kaolinite clearly precipitates before nsutite/manganite, as they fill the border of small geodes, when nsutite/manganite occurs in the core (►Fig. 6.22b). Kaolinite is evenly dispersed in the weathered slates and coticule in the Salmchâteau area. Note that groutite (MnOOH), hausmannite (Mn_3O_4), hollandite-strontiomelane [$(Ba,Sr)Mn_8O_{16}$], hetaerolite ($ZnMn_2O_4$) and todorokite [$(Ca,Na,K)_X(Mn^{4+}, Mn^{3+})_6O_{12}.3.5H_2O$] have also been described in relation to these metasediments of the area, some of them having a hypogene origin (Herbosch, 1967; Fransolet and Mélon, 1975; Mélon *et al.*, 1976; Fransolet, 1979; Schreyer *et al.*, 2001; Gustine, 2002; Hatert *et al.*, 2014; Blondieau *et al.*, 2017; Blondieau, 2019), but are not detected in this study.

The final sequence of supergene minerals (►Figs. 6.25a) indicates that weathering processes differ between the Chevron and Salmchâteau area. Weathering is incomplete in the Chevron area, as cryptomelane and lithiophorite are very scarce, while cation-free Mn oxides prevail. The polyphased formation of cryptomelane in the Salmchâteau area corroborate the high weathering state of the Mn-rich slates.

6.2.5.b Origin of manganese and weathering transformations

One of the most important questions about the formation of weathering manganese deposits is the origin of manganese. Here, manganese seems not to have been transported for long distances, as the weathering manganese phases are restricted to the Mn-rich stratigraphic levels, and not present in the upper Bihain and lower Jalhay Formations. Transport of Mn is local (millimeter to meter) as it is supported by the occurrence of disseminated cryptomelane (►Fig. 6.21e), cryptomelane-lithiophorite veins within the host Mn-bearing slates in the Salmchâteau area (►Figs. 6.21a and

b), and in situ replacement of rhodochrosite by manganite, nsutite and pyrolusite in the Chevron (►Fig. 6.22c) and Salmchâteau areas (►Fig. 6.21d). Major elements show that the enrichment factor of the weathered Mn-slates is, at least, between 4 and 10 times the composition of the average Mn-slates (►Fig. 6.23a). This clearly shows that Mn is favored, instead of iron under weathering conditions in the Ottré Formation Mn-rich slates.

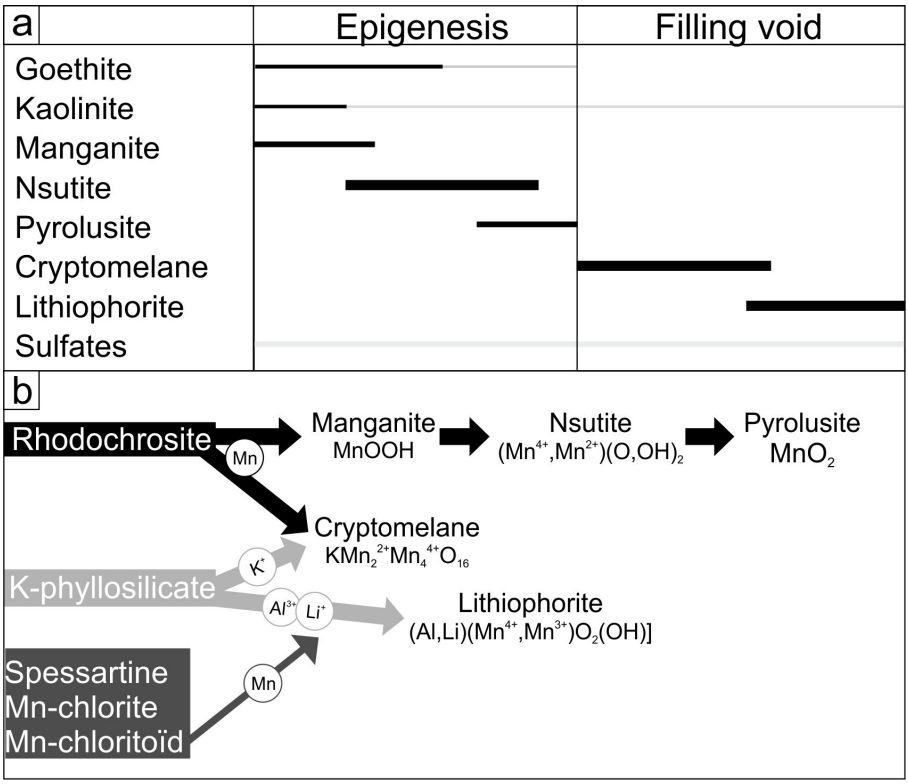

►**Fig. 6.25 a.** Tentative paragenetic sequence of the manganese oxides and other supergene minerals during weathering processes. The first stage corresponds to the epigenesis of the host rock as shown in ►Figs. 6.20c and 6.22, while the second generation fills open cavities or veins (►Figs. 6.20b and 6.21b). **b.** Mineral transformation chart during weathering of the primary Mn-bearing minerals.

Several modes could explain the formation of Mn oxides. It may result from oxidative dissolution and replacement of primary Mn carbonates (rhodochrosite and kutnohorite) and Mn phyllosilicates (Mn-rich chlorite), but also to the replacement of spessartine, a feature which is quite unusual considering that garnet weathering rate is slow in saprolites (Velbel, 1984; Parc et al., 1989; Varentsov, 1996; Price et al., 2005). In metamorphic veins and carbonated Mn ores, rhodochrosite is weathered into cation-free Mn oxides. The Mn^{2+} is released and oxidized through the increasing weathering conditions, leading Mn to be incorporated first, into manganite as Mn^{3+}

($Mn^{3+}OOH$), then into nsutite as a combination of Mn^{2+} and Mn^{4+} [(Mn^{4+}, Mn^{2+})$(O,OH)_2$; Fig. 8c], and finally into Mn^{4+} to form pyrolusite ($Mn^{4+}O_2$; ►Figs. 6.19f and 6.251b). Cryptomelane, lithiophorite and some nsutite/manganite seems to be tightly associated with the phyllosilicate matrix (illite-muscovite; ►Fig. 6.20c). From the dissolution of the primary minerals, cryptomelane ($KMn^{4+}{}_6Mn^{2+}{}_2O_{16}$) and lithiophorite [(Al, Li)(Mn^{4+}, Mn^{3+})O_2(OH)] result from the recombination of K^+, Al^{3+} and Li^+ of the K-phyllosilicate matrix, and Mn^{2+}, Mn^{3+} and Mn^{4+} from primary Mn-bearing minerals into open voids of the weathering solutions (►Fig. 6.25b). Despite the fact that these two minerals are often associated, cryptomelane usually forms prior to lithiophorite, probably because K^+ is a mobile element leached from K-phyllosilicates (muscovite-illite) and act as a limiting cation in the formation of K-bearing Mn oxides, as observed in many deposits (Parc *et al.*, 1989; Varentsov, 1996). The less mobile Al and poorly concentrated Li cations lead to the formation of lithiophorite in the center of cryptomelane veins (►Figs. 6.21b and c). Al-rich cryptomelane or K-rich lithiophorite are probably intermediate products resulting from this reaction (►Figs. 6.20h and 6.25b). However, the Mn content in the phyllosilicate matrix is low and could not provide sufficient manganese to form large number of Mn oxides. Therefore, early Mn-bearing minerals to be considered as the source of manganese could be spessartine, Mn-chloritoid, Mn-chlorite and rhodochrosite, as they are the dominant Mn-minerals in the Salmchâteau and Chevron areas (►Fig. 6.25b).

Scanning electron microscopic views show that spessartine is partly weathered into cryptomelane and nsutite/manganite (►Fig. 6.20c). Spessartine could contain up to 43 wt. % MnO following its empirical formula. The relative abundance of spessartine, and the concentration of manganese oxides in spessartine-rich zones (►Fig. 6.20f) strengthen the interpretation that Mn could be released from partially dissolved garnet. Despite that coticule displays Mn/Fe ratios and Mn concentration higher than the host slates, weathering seems to be relatively poor where spessartine occurs. Their contribution into the weathering fluid could be limited, as they are preserved in most of the weathered rocks (►Figs. 6.20d and g), exception made from samples that are highly affected by weathering processes (►Figs. 6.20b and c). Therefore, other primary Mn-bearing minerals could be responsible for significant quantities of Mn to form Mn oxides. Rhodochrosite is generally a common primary mineral in Mn deposits worldwide, as it could release large amount of Mn during weathering (up to 61.71 wt. % MnO), but also because it is readily dissolved than metamorphic minerals, such as garnet (i.e., Parc *et al.*, 1989; Varentsov, 1996). Mn carbonates are not directly observed in the Salmchâteau area, but rhodochrosite has been described by Herbosch *et al.* (2016) and suggested as the primary Mn-bearing phase to the formation of Mn oxides by Fransolet (1979). Some enrichments of Ca in Mn oxides might indicate that primary Mn carbonates (rhodochrosite, kutnohorite) were present in the Mn-slates, as well as the presence of nsutite/manganite (Post,

1999; ►Fig. 6.21d), which could have therefore provided Mn into the weathering fluid. A better interpretation is supported by the Rare Earth Elements geochemistry. Positive Ce anomalies in carbonate Mn ores and metamorphic veins of the Chevron area could be attributed to the presence of rhodochrosite, which usually traps Mn and also concentrates Ce relative to other LREE (Chisonga *et al.*, 2012; Beukes *et al.*, 2016; De Putter *et al.*, 2018). Therefore, repeated positive Ce anomalies in carbonated Mn ores and metamorphic veins of the Chevron area are attributed to the presence of rhodochrosite, which is later weathered into a mixture of manganite, nsutite and pyrolusite (►Fig. 6.24c). As this anomaly is preserved into the cation-free Mn oxides, this supports that small modifications are encountered through weathering processes, at least regarding the REE pattern (i.e., Varentsov, 1996). Following these observations, the presence of Ce positive anomalies in the weathered Mn-rich slates, as well as in pure Mn oxides in the Salmchâteau could decipher the former presence of rhodochrosite, or at least Mn carbonates, formed through diagenesis and metamorphism (►Fig. 6.23b). However, the same conclusion cannot be achieved in the coticule layers, where a positive Eu (and MREE) anomaly replaces the positive Ce anomaly of Mn carbonate (►Fig. 6.23c). Such changes in the geochemical behavior of the coticule layers, where Eu anomaly prevails instead of the Ce anomaly found in the enclosing slates, might be related to conditions during the deposition of the limy mud turbidites, now metamorphosed into coticule layers (Herbosch *et al.*, 2016; Lamens *et al.*, 1986; ►Fig. 6.23b and c). Other primary Mn-bearing minerals, such as Mn-chlorite and Mn-chloritoid, have probably poorly contributed to the mobilization of Mn in the supergene fluids, as they are not the dominant minerals in these rocks, but also because they are relatively stable under supergene conditions (e.g., chlorite). All these interpretations are summarized in ►Fig. 6.25b: rhodochrosite is the main primary Mn-bearing mineral from which Mn has been released to form pure Mn oxides, while the phyllosilicate matrix (muscovite) has provided K, Al and Li to form cryptomelane and lithiophorite. Other Mn-bearing minerals have a limited impact into Mn and other cations mobilization.

Other trace elements could follow the same process: arsenic enrichment and its association with manganese has already been pointed out in the Chevron area (Fonseca, 1969), but also to a larger extent in Mn deposits where a hydrothermal origin is likely (Nicholson, 1992). Although the geochemistry results from the primary composition (Herbosch *et al.*, 2016), arsenic seems to be accommodated and retained within the Mn oxides during weathering. This observation could be extended to other transition metals, i.e. Co, Ni, Cu and Zn (►Fig. 6.23d), which are incorporated in Mn oxides, especially in late minerals such as lithiophorite and cryptomelane (►Fig. 6.21c). As hematite remains stable from its formation during sedimentary deposition of the slates, the presence of goethite indicates that some Fe is released during weathering. Such limited input of Fe, whereas hematite remains stable under supergene conditions implies that Fe could originate from weathering of diagenetic

pyrites or carbonates, as it is found in Thier du Mont right to the east of Thier del Preu quarry (►Fig. 6.20d). The general decrease in the SiO_2, Al_2O_3 and MgO content of the weathered Mn-slates could also be due to the general increase in the MnO content (SiO_2 and MnO have a negative correlation) and/or to the loss of these elements during weathering as it is sometimes observed in the laterite (Widdowson, 2008 in Nash and McLaren, 2008), which would decrease the dominant major elements (i.e., SiO_2 and Al_2O_3).

6.2.5.c Intensity of weathering

One can see that mineralogical differences between the northern and southern areas of the Stavelot inlier clearly determines the nature of the Mn ore composition of the Salmchâteau and Chevron areas: manganese ores mined in the Salmchâteau area (coticule is not considered as Mn ore) correspond to a weathering Mn-deposit, while in the Chevron area, the carbonate Mn ore has a sedimentary (metamorphic) origin. The Mn-bearing phases are mostly cryptomelane with subordinate amount of nsutite and lithiophorite in the Bihain and Thier del Preu quarries (►Fig. 6.16), while rhodochrosite dominates the Mn ore in the Chevron mines. The Chevron borehole shows that slates are poorly weathered and saprolite is not thick (probably only few meters; (Graulich, 1966), further indicating that Mn orebeds are situated beneath the saprolite, in the fissured horizon. On the other side, weathering deposits in the Salmchâteau area are located in the lower part of the saprolite, at least for the Bihain quarry (►Figs 6.162 and 6.26), and might probably be situated in the upper part of the fissured horizon in the Thier del Preu quarry, close enough to the weathering roll front (Cosan, 1969; Demoulin *et al.*, 2018a) to further precipitate numerous Mn oxides. The topographic difference between these two areas is probably the most important factor explaining these variations, as the Mn ores in the Chevron area are located at relatively low elevation between 230 m and 380 m, compared to the Bihain and Thier del Preu quarries, culminating at 573 m and 486 m, respectively (►Fig. 6.26). The Chevron Mn levels poorly underwent weathering processes compared to the southern area, which has contributed to the preservation of Mn carbonates in the Mn ore. This interpretation might explain the absence of rhodochrosite in the Salmchâteau area and the partial dissolution and replacement of spessartine in the slates and coticule layers. The effect of elevation on the weathering processes could also be demonstrated by old cryptomelane ages in the Bihain quarry and younger ages in Thier del Preu quarry (see discussion below; ►Table 6.5), which corresponds to the *per descensum* evolution of the weathering fluid (De Putter *et al.*, 2015). Such elevation effect on the development of weathering profiles is well documented in Belgium, where low elevation is nearly totally devoid of more than local spots of weathering (Gullentops, 1954; Alexandre and Thorez, 1995; Demoulin *et al.*, 2018a). However, differences in metamorphic grades, and therefore in the primary mineralogical composition between the Chevron and Salmchâteau areas, could be an additional factor explaining this distribution.

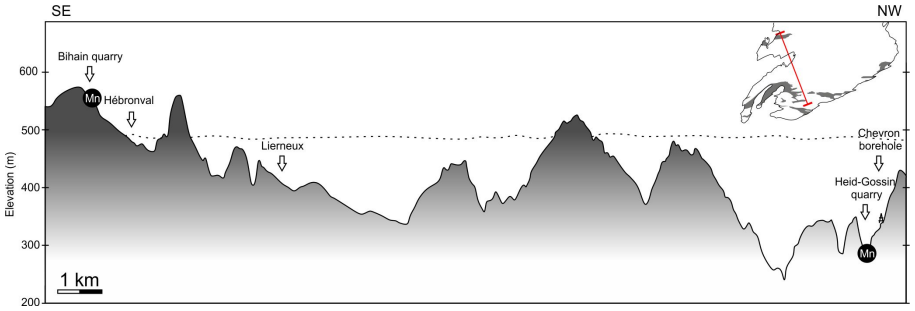

►**Fig. 6.26** NW-SE cross-section and sketch of the weathering intensity and its relation to the elevation of the area. Most of the Mn-rich slates occur below 500 m heights in the Chevron area, while these sediments are exposed to weathering agents beyond 500 m of elevation in the Salmechâteau area.

6.2.5.d Timing of weathering and regional implications

The ages obtained by $^{40}Ar/^{39}Ar$ methodology onto cryptomelane samples have provided four stages for the formation of the Mn oxides, lasting from late Oligocene to Pliocene or younger (►Fig. 6.27): Chattian (26.83 ± 0.20 Ma), Aquitanian (22.2 ± 0.6 and 20.0 ± 0.2 Ma according to Demoulin *et al.* (2018a), Serravalian-Tortonian (11.97 ± 0.31 to 10.12 ± 0.18 Ma) and Pliocene or younger (5.30 ± 0.76 and 4.11 ± 0.57 Ma). These ages reveal that, at least, two young periods (Serravalian-Tortonian and Pliocene or younger) of weathering have affected the Stavelot Massif, and on a larger scale the Ardenne region. There is no evidence that the whole period from late Oligocene to Pliocene has recorded a continuous weathering event, but this period seems to have produced conditions suitable for the formation of weathered rocks. Most of the ages determined by $^{40}Ar/^{39}Ar$ geochronology are concentrated in the middle-late Miocene (10–12 Ma), which can be considered as the main weathering event responsible for a large amount of Mn oxides (►Fig. 6.24e). However, the stability of cryptomelane under supergene conditions through time (Vasconcelos, 1999) allows older ages to be preserved. The 26.8 ± 0.2 Ma age (►Fig. 6.24a) indicates that the Mn sediments were exposed to meteoric agents at least since late Oligocene, a period when the main uplift of the Ardenne was ongoing (Demoulin, 1995c). Moreover, some older periods could be evidenced in staircase spectra, where high temperature steps indicate ages beyond 50 Ma (►Fig. 6.24d). The meaning of these ages is somewhat difficult to interpret but could be attributed to different cryptomelane phases, to inclusions of other minerals containing radiogenic argon or to the presence of excess argon. As no inclusion of K-bearing minerals were found in scanning electron microscopic analyses, and K/Ca ratio exclude the presence of variscan K-bearing phyllosilicates, this indicates that staircase spectrum could originate from older cryptomelane phases by recrystallization processes during weathering, a feature which has been observed in polyphased Mn deposits of RDC (De Putter *et al.*, 2015). This period is unknown but could be early Cretaceous as

weathering periods have already been determined in kaolinic deposits in the adjacent Brabant and Ardenne massifs (Barbier *et al.*, 2010; Mees and Stoops, 1999; Thiry *et al.*, 2006; Yans and Dupuis, 2005; ►Fig. 7.27) and laterite (Théveniaut *et al.*, 2007). Late Paleocene cannot be excluded, as climatic conditions were favorable to the setting up of deep weathering mantles (i.e., Quesnel *et al.*, 2002a; Yans, 2003; Baele *et al.*, 2016; Demoulin *et al.*, 2018a). Erosion of the upper part of the saprolite and laterite could additionally explain the lack of any older cryptomelane ages (Demoulin *et al.*, 2018a).

The formation of K-Mn oxides during the late Oligocene, early Miocene, middle-late Miocene and Pliocene or younger periods are the results of intense chemical weathering of the Mn-rich slates. Conditions suitable for the development of a weathering profile and the formation of supergene Mn oxides are generally a combination of a humid tropical or subtropical climate (Varentsov, 1996; Vasconcelos, 1999; Kuleshov, 2016), and slow large-scale tectonic movements (Ruddiman and Prell, 1997; Ruddiman *et al.*, 1997; Wyns, 2002; Wyns *et al.*, 2003; Ruddiman, 2008). Intertropical temperatures prevailed during almost the whole Eocene and, to a lesser extent, during the Middle Miocene (Buchardt, 1978; Alexandre and Thorez, 1995). Such Miocene weathering event could be supported by the development of thick kaolin deposits in Central Ardenne (Yans, 2003), but also by Fe-crust in the Hautes-Fagnes where a Neogene age is suggested (Alexandre and Thorez, 1995). The tropical to subtropical continental climate of Europe during the Paleocene and early Eocene turned successively into warm temperate to temperate from the Oligocene to the Pliocene (Mosbrugger *et al.*, 2005; ►Fig. 6.27). Most of the variations in temperature are accompanied by a relatively constant high humidity during the whole Cenozoic, whereas seasonality has progressively increased until present days. Middle and late Eocene record the first drop of temperatures in Central Europe: the climate was gradually cooling but a sharper cooling occurred worldwide at the end of the short-lived earliest Oligocene (Zachos *et al.*, 2001; De Man *et al.*, 2004; Boulvain and Vandenberghe, 2018). These temperatures are low until the uppermost Chattian, where a peak of temperature records the Late Oligocene Warming (Mosbrugger *et al.*, 2005). Such climate is slightly warmer in the early Miocene and persist until the middle Miocene, but is more stepwise and show several short-term variations. However, temperatures are below those recorded during the Paleocene and Eocene at a global and local scale (Zachos *et al.*, 2001; Mosbrugger *et al.*, 2005), exception made for the Mid-Miocene Climatic Optimum where temperatures increased significantly in different Cenozoic basins of Central and Western Europe (Mosbrugger *et al.*, 2005). The onset of the Miocene cooling seems to be between 13 and 14 Ma and is intensified until present days with several variations, the best example being the late Tortonian and early Zanclean warming. The Quaternary period marks the end of any weathering products because of the setting up of a periglacial climate (Alexandre and Thorez, 1995). Comparing these

climatic variations with the weathering periods obtained by K-Mn oxides indicates that climate (►Fig. 6.27) is probably not the main factor responsible for the development of deep weathering profiles in the Salmchâteau area, as most of the cryptomelane ages do not match with tropical or subtropical climates in the geological record (►Fig. 6.27). Therefore, the main process from which weathering mantles can develop could be attributed to geodynamics (i.e., Vasconcelos and Carmo, 2018; Wyns *et al.*, 2003). At least high precipitation and increasing seasonality during the Cenozoic can provide water to the weathering fluids (Mosbrugger *et al.*, 2005), when differential uplift movements generate the weathering gradient. The role of warm climate (tropical) in the development of weathering profile cannot be dismissed totally, as some ages obtained by cryptomelane could correspond to warm peaks in the paleoclimatic record (Mosbrugger *et al.*, 2005). For example, the late Oligocene age could correspond to the late Oligocene Warming, some Miocene ages could be linked to the Langhian Mid-Miocene Climatic Optimum or Pliocene (or younger) ages could be attributed to the Tortonian-Zanclean warming (e.g., Zachos *et al.*, 2001; Mosbrugger *et al.*, 2005). However, the most represented cryptomelane ages range between 10 and 12 Ma (►Fig. 6.24e), when cold climatic conditions prevailed in Europe. When these climatic conditions turn drier or cooler, it is common that the weathering mantle becomes stripped and exposes the weathering front in some parts. These features put together account for most of the Ardennian surfaces during the slowdown of weathering that is imposed by cooler conditions since the Oligocene (Demoulin *et al.*, 2018a). Therefore, $^{40}Ar/^{39}Ar$ geochronological results need to consider that erosion processes have probably removed some of the oldest dating material, especially the upper part of the weathering mantle in which older ages could have been preserved.

The Ardenne is quite stable in a tectonic point of view at least until the early Paleocene. Only the borders of the Massif record a slow uplift, in fact, the Ardenne remains as high as the sea level but its borders are subjected to subsidence and then sedimentation (Demoulin, 1995b; ►Fig. 6.27). The Ardenne records its first progressive dome uplift in the middle Paleocene, leading to a slight slope oriented to the west, and then the formation of weathering mantles under a warm and humid subtropical climate (Albers, 1981; Demoulin, 1995b; Mosbrugger *et al.*, 2005; ►Fig. 6.27). A new uplift phase can be deduced from the Lutetian, but is not associated with a huge weathering phase, as the climate is dryer and temperatures lower than the Paleocene (Albers, 1981; Demoulin, 1995a). Post-Paleocene and Eocene phases have led to only 10 Ma for the development of weathering mantles before the acceleration of the tectonic movements in the middle Oligocene (Demoulin, 1995a). Although the Alpine tectonic is poorly recorded in the sedimentary series of Western Europe, the Alpine Cycle could be responsible for the uplift of most of the Variscan massifs across Central Europe (Prodehl *et al.*, 1995; Ziegler and Dèzes, 2007) including the Rhenish Massif (►Fig. 6.1a). The Alpine orogenesis is

particularly active from the Oligocene to the Miocene and has probably affected the Ardenne until present days (Demoulin and Hallot, 2009). Additionally, the Roer Valley rifting activity (also known as the Lower Rhine Graben; Prodehl *et al.*, 2006) could have influenced the elevation of the Stavelot Massif, the latter being situated on the shoulders of this rift system (Van Balen *et al.*, 2000; Demoulin, 2018). The Roer rifting activity developed upon Paleozoic and Mesozoic basins and is characterized by several episodes of inversion and subsidence during Mesozoic and Cenozoic times. However, the rifting activity (subsidence) increased strongly during the late Oligocene, was inverted again during the Early Miocene and continued until the present days (e.g., Michon *et al.*, 2003; Deckers, 2016). Therefore, the acceleration of the Ardenne uplift could trigger the development of weathering, as tectonic movement slightly predates the first weathering period recorded in the Salmchâteau area by the early Chattian (►Fig. 6.27). Moreover, the joint effect of these uplift phases with low stand levels of the sea level, both contribute to the creation of a weathering gradient, from which deep weathering mantles can develop.

Vasconcelos (1999) already noted that most of the cryptomelane ages worldwide provide Miocene weathering period and probably represent an increase in the weathering rates at that time. Such ages are well represented in Variscan massifs of Central Europe, lasting from late Oligocene to Pliocene (Hautmann and Lippolt, 2000). The similarity between global, regional and local ages obtained in the Stavelot Massif might corroborate a global weathering process/period during Miocene times. As climate seems to be an efficient parameter in most of the manganese deposits worldwide (e.g., Hénocque *et al.*, 1998; Li *et al.*, 2007; Riffel *et al.*, 2015; Vasconcelos *et al.*, 2013), other parameters such as slow differential uplift and variations in the sea level (particularly low during the Miocene, ►Fig. 6.27), could be significant parameters to explain such important Miocene ages in the global manganese record.

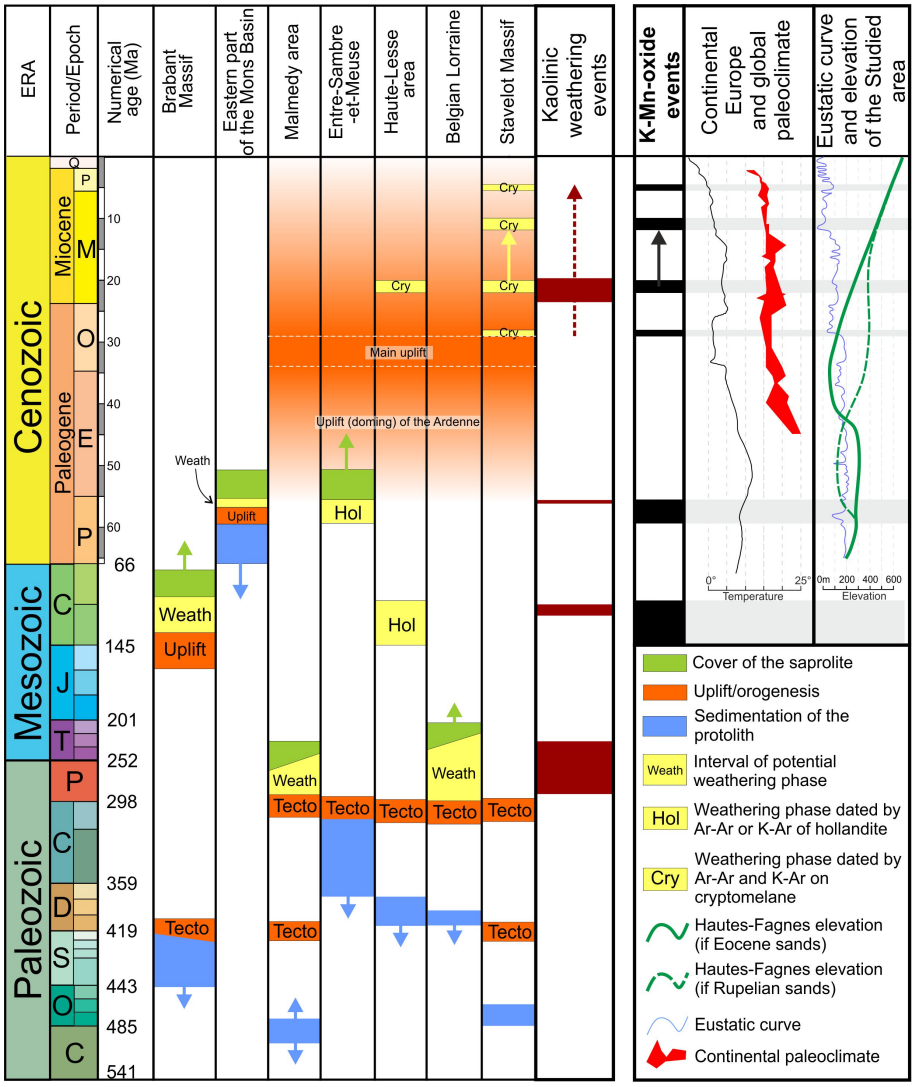

►**Fig. 6.27** Tentative chronology chart of weathering in Belgium including periods determined by $^{40}Ar/^{39}Ar$ datings of cryptomelane in the Stavelot Massif (Salmchâteau). Note that the latter periods are delimited by the late Oligocene and Pliocene. Sedimentation and geodynamic (uplift or deformation) are documented only for the weathered protolite rocks (modified after Demoulin *et al.*, 2018a). Continental European paleoclimate curves are from Mosbrugger *et al.* (2005), while marine climate curve is from Zachos *et al.* (2001). Supposed elevation of the Stavelot Massif (Hautes Fagnes) is adapted from (Quesnel *et al.*, 2002a) and eustatic curve of Europe is from Hardenbol *et al.* (1998). K-Mn oxide events are documented by $^{40}Ar/^{39}Ar$ and K/Ar ages.

6.2.6 Conclusion

New geochronological, petrographic, mineralogical and geochemical data of the Mn-rich slates and coticule of the Ottré Formation in the Stavelot Massif (eastern Ardenne, Belgium) indicate that these deposits record several stages of weathering. The two investigated areas correspond to two types of Mn deposits: the Chevron area (north) is poorly affected by weathering processes and correspond mainly to a carbonate-hosted sedimentary deposit, whereas the Salmchâteau Mn-rich rocks (south) are considered as weathering deposits. The difference in the intensity of weathering between these ores is attributed to the elevation of these two locations, higher elevated in the Salmchâteau area, leading to position the Mn orebeds in the lower part of the saprolite and in the fissured horizon in the Salmchâteau and Chevron areas, respectively. This has led weathered Mn-rich slates to be even more enriched in Mn and associated transition metals (As, Co, Cu, Ni) than poorly weathered ones. The mineralogy of the weathering products is dominated by cryptomelane and nsutite, with subordinate amount of lithiophorite, manganite and pyrolusite, together with goethite and kaolinite. Mn oxides without supplementary cations (nsutite, manganite and pyrolusite) result from the weathering of Mn carbonates (rhodochrosite and/or kutnohorite), whereas subsequent neoformed cryptomelane and lithiophorite fill open voids or replace the phyllosilicate matrix of the slates by the recombination of K, Li and Al with Mn released from the dissolution of phyllosilicate and Mn carbonates, respectively. The input of Mn from spessartine and other Mn-bearing silicates have poorly contributed to the weathering fluid.

$^{40}Ar/^{39}Ar$ dating of cryptomelane from the Salmchâteau Mn deposits yields, at least, four weathering periods lasting from late Oligocene to Pliocene or younger, without excluding older periods, as the upper part of the saprolite (and laterite) have been removed. As the tropical Paleocene-Eocene climate evolves into temperate by the Oligocene, and temperatures decrease progressively until the present, climate seems not to be the major parameter controlling the formation of Mn oxides and the development of weathering profiles in the Salmchâteau area. An additional parameter implies the acceleration of the Ardenne Massif uplift from late Oligocene to present days to trigger the development of weathering mantles. The constant precipitations and increasing seasonality provide water to the weathering fluids, when the dooming of the Massif, maybe associated with Alpine and/or Roer graben activity, account for most of the weathering gradient.

►**Table 6.6** Synthesis of saprolite dating by different methods in the Ardenne massif.

Material	Method	Location	Age (Ma)	Error (Ma)	Reference
Cryptomelane	Ar/Ar	Transinne	21.54	0.45	Yans (2003)
	K-Ar		126	10	
	K-Ar		131	15	
Hollandite *s.l.*	K-Ar		135	8	
	K-Ar		88	-	Thiry *et al.* (2006)
	K-Ar		94	-	
Hematite	Paleomag		110-120	-	Yans (2003)
Hollandite *s.l.*	Ar/Ar	Gembes	378-414	-	
Cryptomelane	Ar/Ar	Bihain	25.06	0.88	Yans (2003); Demoulin *et al.* (2018a)
	Ar/Ar		21.1	0.3	
	Ar/Ar		22.2	0.6	
	Ar/Ar		20	0.2	
	Ar/Ar		15.61	0.16	Dekoninck *et al.* (accepted with revision, in revision)
	Ar/Ar		20.01	0.34	
	Ar/Ar		11.43	0.08	
	Ar/Ar		11.79	0.1	
	Ar/Ar		26.83	0.2	
	Ar/Ar	Lierneux	11.38	0.25	
	Ar/Ar		5.3	0.76	
	Ar/Ar		4.11	0.57	
	Ar/Ar		11.74	0.19	
	Ar/Ar	Verleumont	10.12	0.18	
	Ar/Ar	Thier del Preu	11.97	0.31	
	Ar/Ar		11.07	0.3	
	Ar/Ar		17.66	0.19	
Cryptomelane	K-Ar	Rechain	94.8	4	Demoulin *et al.* (2010)
	K-Ar		88.4	3.8	
Hollandite *s.l.*	K-Ar	Morialmé	53.3	2.3	Barbier *et al.* (2010)
	K-Ar		58.2	2.4	
Jarosite	K-Ar	Beez	16.5	0.8	Bruyère *et al.* (2003)
	K-Ar		16.8	0.5	

6.3 Concluding remarks

🔎Both papers (Demoulin *et al.*, 2018a; Dekoninck *et al.*, accepted with revision, in revision) evidence that weathering periods in the Ardenne last from early Cretaceous times and are recorded by K-Ar and $^{40}Ar/^{39}Ar$ dating on alunite and K-Mn oxides (►Figs. 6.2 and 6.27). The age distribution between the different weathering mantles in the Ardenne region clusters in three distinct periods (►Table 6.6): (1) Early to Late Cretaceous (Transinne, Rechain), (2) late Paleocene – early Eocene (Morialmé) and a more or less continuous period lasting from late Oligocene (Chattian) to the uppermost Miocene (Beez, Bihain, Thier del Preu, Lierneux, Verleumont). Why these ages are not recorded in every saprolite in Ardenne area is directly related to their preservation through times, and denudation of the massif. The inner part of the Ardenne (Transinne) displays a well-preserved weathering profile, in which Miocene ages are obtained in the lower part of the saprolite, whereas Cretaceous ages are preserved in the upper part (Yans, 2003). This age distribution is common in weathering mantles through the downward progression of a weathering front (►Figs. 2.2 and 6.2).

Cretaceous or Paleogene ages are not observed in the weathered Mn-rich slates in the southern part of the Stavelot massif, as only the lower part of the saprolite is preserved in elevated areas. The late Oligocene to Miocene ages (mostly grouped at the Serravalian-Tortonian period) of cryptomelane samples support the absence of the upper part of the saprolite and laterite *s.s.*, the latter being totally absent in the northern area, where elevation is low. As tropical conditions, combining the joint effect of warm and humid climate, have operated during the whole Cretaceous and the early Eocene periods, late Oligocene to Miocene ages do not support the prevailing effect of climate to trigger weathering conditions as temperatures are getting cooler since late Eocene times. One can see here the consistency of the late Oligocene uplift onset with the Chattian ages obtained in these weathered Mn-rich slates, further indicating that doming of the Ardenne might be a determinant factor in the setting up of the third weathering phase reported in the area.

6.4 References

Adams, R., Vandenberghe, N., 1999. The Meuse section across the Condroz–Ardennes (Belgium) based on a predeformational sediment wedge. Tectonophysics 309, 179–195. https://doi.org/10.1016/S0040-1951(99)00138-9

Albers, H.J., 1981. Neue daten zum klima des nordwesteuropälschen Alttertiars. Fortschritte Geol. Von Rheinl. Westfal. 29, 483–504.

Alexandre, J., Thorez, J., 1995. Au secondaire et au tertiaire, l'Ardenne tropicale. L'altération des roches et les climats anciens, in: L'Ardenne. Essai de Géographie Physique. Publication du Département de Géographie physique et Quaternaire de l'Université de Liège, Liège, pp. 53–67.

Baeckeroot, G., 1942. Oesling et Gutland. Morphologie du bassin ardennais et luxembourgeois de la Moselle, Colin. ed. Paris.

Baele, J.-M., Quesnel, F., Dupuis, C., 2016. Silcrete in northern France and Belgium: a terrestrial record of surface environments under the influence of pyroclastic ash-falls, in: Abstract Book. Presented at the 5th International Geologica Belgica Meeting, Mons, p. 40.

Baijot, M., Hatert, F., Fransolet, A.-M., 2011. Mineralogical and geochemical study of pseudocoticule from the Stavelot Massif, Ardennes (Belgium), and redefinition of coticule. Eur. J. Mineral. 23, 633–644. https://doi.org/10.1127/0935-1221/2011/0023-2115

Barbarand, J., Bour, I., Pagel, M., Quesnel, F., Delcambre, B., Dupuis, C., Yans, J., 2018. Post-Paleozoic evolution of the northern Ardenne Massif constrained by apatite fission-track thermochronology and geological data. BSGF - Earth Sci. Bull. 189, 16. https://doi.org/10.1051/bsgf/2018015

Barbier, F., Prognon, C., Quesnel, F., Dupuis, C., Yans, J., 2010. Dating and weathering characterization of the Morialmé quarry (Entre-Sambre-et-Meuse, Belgium), in: 4th French Congress on Stratigraphy. Presented at the Abstract book, Paris, p. 18.

Barbier, F., Quesnel, F., Dupuis, C., Yans, J., 2012. The Late Paleocene - Early Eocene interval as a potential period for weathering in Western Europe: the case of the Morialmé section (Belgium), in: 4th International Geologica Belgica Meeting. Presented at the Abstract book, Bruxelles, p. 59.

Baulig, H., 1926. Le relief de la Haute Belgique. Ann. Société Géographique Belg. 35, 206–235.

Belanger, I., Delaby, S., Delcambre, B., Ghysel, P., Michel, H., Laloux, M., Marion, J.-M., Mottequin, B., Pingot, J.-L., 2012. Redéfinition des unités structurales du front varisque utilisées dans le cadre de la nouvelle Carte géologique de Wallonie (Belgique). Geol. Belg. 15, 169–175.

Berger, P., 1965. Les dépôts sédimentaires de manganèse de la Lienne inférieure. Ann. Société Géologique Belg. 88, 245–267.

Beukes, N.J., Swindell, E.P.W., Wabo, H., 2016. Manganese Deposits of Africa. Episodes 39, 285. https://doi.org/10.18814/epiiugs/2016/v39i2/95779

Bless, M.J., Felder, P.J., 1989. Note on the Cretaceous of Hockai (Hautes Fagnes, NE Belgium). Ann. Société Géologique Belg. 112, 47–56.

Blondieau, M., 2019. Le manganèse en Ardenne, Stâve dès Boûs. ed, Nature, histoire et vien en Ardenne. Trois-Ponts.

Blondieau, M., 2006. Description des espèces minérales présentes dans les gisements salmiens du Massif de Stavelot.

Blondieau, M., 2005. Les gisements minéraux du Salmien dans le massif de Stavelot.

Blondieau, M., Puccio, S., Compere, P., Hatert, F., 2017. Données nouvelles sur quelques espèces minérales de Vielsalm et de Salmchâteau. Bull. Société R. Sci. Liège 86, 1–48.

Boulvain, F., Belanger, I., Ghysel, P., Laloux, M., Roche, M., Delsate, D., Dosquet, D., Thorez, J., Godefroit, P., 2000. New lithostratigraphical, sedimentological, mineralogical and palaeontological data on the Mesozoic of Belgian Lorraine. Geol. Belg. 3, 3–33.

Boulvain, F., Vandenberghe, N., 2018. An introduction to the geology of belgium and luxembourg, in: Demoulin, A. (Ed.), Landscapes and Landforms of Belgium and Luxembourg. Springer International Publishing, Cham, pp. 9–33. https://doi.org/10.1007/978-3-319-58239-9_2

Bour, I., 2010. Histoire thermique des massifs ardennais et bohémien: conséquences sur la géodynamique de l'Europe de l'Ouest au méso-cénozoïque. Université Paris Sud, Orsay.

Bruyère, D., De Putter, T., Perruchot, A., Dupuis, C., 2003. Neogenesis of halloysite in cryptokarstic environments (Beez, Belgium): chemical modeling., in: Abstract Book. Presented at the Conference of the European clay groups association, Modena, p. 48.

Buchardt, B., 1978. Oxygen isotope palaeotemperatures from the Tertiary period in the North Sea area. Nature 275, 121–123. https://doi.org/10.1038/275121a0

Chisonga, B.C., Gutzmer, J., Beukes, N.J., Huizenga, J.M., 2012. Nature and origin of the protolith succession to the Paleoproterozoic Serra do Navio manganese deposit, Amapa Province, Brazil. Ore Geol. Rev. 47, 59–76. https://doi.org/10.1016/j.oregeorev.2011.06.006

Cocks, L.R.M., Fortey, R.A., 2009. Avalonia: a long-lived terrane in the Lower Palaeozoic? Geol. Soc. Lond. Spec. Publ. 325, 141–155. https://doi.org/10.1144/SP325.7

Cocks, L.R.M., Torsvik, T.H., 2002. Earth geography from 500 to 400 million years ago: a faunal and palaeomagnetic review. J. Geol. Soc. 159, 631–644. https://doi.org/10.1144/0016-764901-118

Cosan, Y., 1969. Etude géologique de sondages au Plateau des tailles. Mém. Serv. Géologique Belg. 32.

Davis, W.M., 1899. The Geographical Cycle. Geogr. J. 14, 481–504. https://doi.org/10.2307/1774538

Davis, W.M., 1895. La Seine, la Meuse et la Moselle. Ann. Géographie 4, 25–49. https://doi.org/10.3406/geo.1895.5779

De Man, E., Ivany, L., Vandenberghe, N., 2004. Stable oxygen isotope record of the Eocene-Oligocene transition in the southern North Sea Basin: positioning the Oi-1 event. Neth. J. Geosci. 83, 193–197. https://doi.org/10.1017/S0016774600020266

De Putter, T., Liégeois, J.-P., Dewaele, S., Cailteux, J., Boyce, A., Mees, F., 2018. Paleoproterozoic manganese and base metals deposits at Kisenge-Kamata (Katanga, D.R. Congo). Ore Geol. Rev. 96, 181–200. https://doi.org/10.1016/j.oregeorev.2018.04.015

De Putter, T., Ruffet, G., Yans, J., Mees, F., 2015. The age of supergene manganese deposits in Katanga and its implications for the Neogene evolution of the African Great Lakes Region. Ore Geol. Rev. 71, 350–362. https://doi.org/10.1016/j.oregeorev.2015.06.015

Deckers, J., 2016. The Late Oligocene to Early Miocene early evolution of rifting in the southwestern part of the Roer Valley Graben. Int. J. Earth Sci. 105, 1233–1243. https://doi.org/10.1007/s00531-015-1236-5

Decrée, S., Ruffet, G., Putter, T.D., Baele, J.-M., Recourt, P., Jamoussi, F., Yans, J., 2010. Mn oxides as efficient traps for metal pollutants in a polyphase low-temperature Pliocene environment: A case study in the Tamra iron mine, Nefza mining district, Tunisia. J. Afr. Earth Sci. 57, 249–261. https://doi.org/10.1016/j.jafrearsci.2009.08.005

Dejonghe, L., 2008. Notice de la carte géologique de Wallonie, 55/5-6, Hotton Dochamps.

Dejonghe, L., 1985. Mineral deposits of Belgium. Bull. Société Belge Géologie 94, 283–297.

Dejonghe, L., Boni, M., 2005. The “Calamine-type” zinc lead deposits in Belgium and West Germany: a product of Mesozoic paleoweathering processes. Geol. Belg. 8, 3–14.

Dekoninck, A., Bernard, A., Barbarand, J., Saint-Bezar, B., Missenard, Y., Lepretre, R., Saddiqi, O., Yans, J., 2016. Detailed mineralogy and petrology of manganese oxyhydroxide deposits of the Imini district (Morocco). Miner. Deposita 51, 13–23. https://doi.org/10.1007/s00126-015-0590-3

Demoulin, A. (Ed.), 2018. Landscapes and landforms of Belgium and Luxembourg, World Geomorphological Landscapes. Springer International Publishing, Cham. https://doi.org/10.1007/978-3-319-58239-9

Demoulin, A., 2006. La néotectonique de l’Ardenne-Eifel et des regions avoisinantes, Mémoire de la Classe des Sciences Collection. Académie Royale de Belgique, Bruxelles.

Demoulin, A., 2003. Paleosurfaces and residual deposits in Ardenne-Eifel: historical overview and perspectives. Géologie Fr. 17–21.

Demoulin, A., 1995a. L’Ardenne, essai de géographie physique. Publication du Département de Géographie physique et Quaternaire de l’Université de Liège, Liège.

Demoulin, A., 1995b. L’Ardenne des plateaux, héritage des temps anciens. Surfaces d’érosion en Ardenne, in: L’Ardenne. Essai de Géographie Physique. Publication du Département de Géographie physique et Quaternaire de l’Université de Liège, Liège, pp. 68–93.

Demoulin, A., 1995c. Neotectonique du Massif Ardennais, in: Demoulin, A., L’Ardenne. Essai de Géographie Physique. Publication du Département de Géographie physique et Quaternaire de l’Université de Liège, Liège, pp. 110–135.

Demoulin, A., Barbier, F., Dekoninck, A., Verhaert, M., Ruffet, G., Dupuis, C., Yans, J., 2018a. Erosion surfaces in the Ardenne–Oesling and their associated kaolinic weathering mantle, in: Demoulin, A. (Ed.), Landscapes and Landforms of Belgium and Luxembourg. Springer International Publishing, Cham, pp. 63–84. https://doi.org/10.1007/978-3-319-58239-9_5

Demoulin, A., Ek, C., 1995. La naissance de l’Ardenne. Mise en place du massif Paléozoïque de l’Ardenne, in: L’Ardenne. Essai de Géographie Physique. Publication du Département de Géographie physique et Quaternaire de l’Université de Liège, Liège, pp. 68-9353–67.

Demoulin, A., Hallot, E., 2009. Shape and amount of the Quaternary uplift of the western Rhenish shield and the Ardennes (western Europe). Tectonophysics 474, 696–708. https://doi.org/10.1016/j.tecto.2009.05.015

Demoulin, A., Hallot, E., Rixhon, G., 2009. Amount and controls of the quaternary denudation in the Ardennes massif (western Europe). Earth Surf. Process. Landf. 34, 1487–1496. https://doi.org/10.1002/esp.1834

Demoulin, A., Juvigné, E., Houbrechts, G., 2018b. The Periglacial Ramparted Depressions of the Hautes Fagnes Plateau: Traces of Late Weichselian Lithalsas, in: Demoulin, A. (Ed.), Landscapes and landforms of Belgium and Luxembourg, World Geomorphological Landscapes. Springer International Publishing, Cham, pp. 101–113. https://doi.org/10.1007/978-3-319-58239-9_7

Demoulin, A., Quesnel, F., Dupuis, C., Gerrienne, P., Yans, J., 2010. Cenomanian sands and clays north of the Vesdre valley: The oldest known Cretaceous deposits in Eastern Belgium. Geol. Belg. 11, 241–256.

Dill, H.G., Hansen, B., Keck, E., Weber, B., 2010. Cryptomelane: A tool to determine the age and the physical–chemical regime of a Plio-Pleistocene weathering zone in a granitic terrain (Hagendorf, SE Germany). Geomorphology 121, 370–377. https://doi.org/10.1016/j.geomorph.2010.05.004

Dupuis, C., 1979. Esquisse paléogéographique du Nord et du Nord-Ouest du Bassin de Paris au Paléocéne et à l’Eocène inférieur. Incidences structurales. Comptes Rendus Académie Sci. Paris 288, 1587–1590.

Dupuis, C., Charlet, J.-M., Dejonghe, L., Thorez, J., 1996. Reconnaissance par carottage des paléoaltérations kaolinisées mésozoïques de la Haute Ardenne (Belgique). Ann. Société Géologique Belg. 119, 91–109.

Dusar, M., Lagrou, D., 2007. Cretaceous flooding of the Brabant Massif and the lithostratigraphic characteristics of its chalk cover in northern Belgium. Geol. Belg. 10, 27–38.

Dussart, N., Dussart, J., 1991. Les mines de Chevron et Rahier. Le manganèse de la basse vallée de la Lienne. 1857-1934.

Echle, W., Plüger, W.L., Zielinski, J., Frank, B., Scheps, V., 1985. Petrography, mineralogy and geochemistry of the Salmian rocks from research borehole Konzen, Hohes Venn (West Germany). Neues Jahrb. Für Geol. Paläontol. Abh. 171, 31–50.

Fairbridge, R.W., 1968. Gradation, in: Fairbridge, R.W. (Ed.), Encyclopedia of Earth Science, Geomorphology. Berlin, pp. 485–486.

Ferket, H., Muchez, P., Schroyen, K., Sintubin, M., 1998. Metamorphism in the Stavelot-Venn Massif: a study of quartz veins in the basal Devonian conglomerates (Lochkovian). Aardkd. Meded. 9, 7–16.

Fielitz, W., Mansy, J.-L., 1999. Pre- and synorogenic burial metamorphism in the Ardenne and neighbouring areas (Rhenohercynian zone, central European Variscides). Tectonophysics 309, 227–256. https://doi.org/10.1016/S0040-1951(99)00141-9

Fonseca, E., 1969. Contribution de la géochimie de l'arsenic dans le gisement sédimentaire de manganèse de la Lienne inférieure. Bull. Société Belge Géologie 78, 147–154.

Fransolet, A.-M., 1979. Occurences de lithiophorite, nsutite et cryptomélane dans le massif de Stavelot, Belgique. Ann. Société Géologique Belg. 102, 303–312.

Fransolet, A.-M., Hatert, F., Bernhardt, H.-J., Theye, T., Maresch, W., 2007. Occurrence of sursassite in the Lienne valley, Stavelot Massif, Belgian Ardennes, in: Goldschmidt Conference Abstracts. Presented at the Goldschmit, Cologne, p. A294.

Fransolet, A.-M., Mélon, J., 1975. Données nouvelles sur des minéraux de Belgique. Extr. Bull. Société R. Sci. Liège 157–160.

Garcia-Castellanos, D., Cloetingh, S., Van Balen, R., 2000. Modelling the Middle Pleistocene uplift in the Ardennes–Rhenish Massif: thermo-mechanical weakening under the Eifel? Glob. Planet. Change 27, 39–52. https://doi.org/10.1016/S0921-8181(01)00058-3

Geukens, F., 1999. Notes accompagnant une révision de la carte structurale du Massif de Stavelot. Aardkd. Meded. 9, 183–190.

Geukens, F., 1986. Commentaires à la carte géologique du Massif de Stavelot. Aardkd. Meded. 3, 15–30.

Geukens, F., 1975. La faille de Bra et le graben de Malmedy. Ann. Société Géologique Belg. 98, 331–339.

Geukens, F., 1965. Problèmes stratigraphiques relatifs aux planchettes Odeigne-Bihain. Bull. Société Belge Géologie 73, 214–219.

Geukens, F., 1957. Quelques remarques au sujet de la répartition des Dicyionema flabelliforme dans le Massif Cambrien de Stavelot (Belgique), in: Congrès Géologique International. Alger XV, pp. 45–52.

Glasmacher, U., Zentilli, M., Grist, A.M., 1998. Apatite fission track thermochronology of Paleozoic sandstones and the Hill-intrusion, Northern Linksrheinisches Schiefergebirge, Germany, in: van den Haute, P., de Corte, F. (Eds.), Advances in Fission-Track Geochronology: A Selection of Papers Presented at the International Workshop on Fission-Track Dating, Ghent, Belgium, 1996, Solid Earth Sciences Library. Springer Netherlands, Dordrecht, pp. 151–172. https://doi.org/10.1007/978-94-015-9133-1_10

Goemaere, E., Demarque, S., Dreesen, R., Declercq, P.-Y., 2016. The geological and cultural heritage of the Caledonian Stavelot-Venn Massif, Belgium. Geoheritage 8, 211–233. https://doi.org/10.1007/s12371-015-0155-y

Gosselet, J., 1888. Mémoires pour servir à l'explication de la carte géologique détaillée de la France - L'Ardenne, Baudry et cie. ed. Paris.

Graulich, J.-M., 1966. Le sondage du bois des Hovas-Chevron (Sondage No. 7). Ministère des affaires économiques, administration des mines, Bruxelles.

Gullentops, F., 1954. Contribution à la chronologie du Pleistocene et des formes du relief en Belgique. Mém. Inst. Géologie Univ. Cathol. Louvain 18, 123–252.

Gustine, C., 2002. Les associations d'oxydes et hydroxydes de manganèse dans le Massif de Stavelot (Unpublished Master thesis). Université de Liège, Liège.

Hance, L., Dejonghe, L., Ghysel, P., Laloux, M., Mansy, J.L., 1999. Influence of heterogeneous lithostructural layering on orogenic deformation in the Variscan Front Zone (eastern Belgium). Tectonophysics 309, 161–177. https://doi.org/10.1016/S0040-1951(99)00137-7

Hance, L., Dejonghe, L., Graulich, J.-M., 1992. Lower Devonian stratigraphy in the Vesdre Massif, Belgium. Ann. Société Géologique Belg. 115, 119–134.

Hardenbol, J., Thierry, J., Farley, M.B., Jacquin, T., de Graciansky, P.-C., Vail, P.R., 1998. Mesozoic and Cenozoic sequence chronostratigraphic chart, in: Mesozoic and Cenozoic Sequence Stratigraphy of European Basins, SEPM Special Publication. Society for Sedimentary Geology.

Hatert, F., Blondieau, M., Puccio, S., Baijot, M., Gustine, C., 2014. Le gisement de manganèse de la Vallée de la Lienne (Belgique). Règne Minéral 117, 5–24.

Hautmann, S., Lippolt, H.J., 2000. $^{40}Ar/^{39}Ar$ dating of central European K–Mn oxides — a chronological framework of supergene alteration processes during the Neogene. Chem. Geol. 170, 37–80. https://doi.org/10.1016/S0009-2541(99)00241-7

Hénocque, O., Ruffet, G., Colin, F., Féraud, G., 1998. $^{40}Ar/^{39}Ar$ dating of West African lateritic cryptomelanes. Geochim. Cosmochim. Acta 62, 2739–2756. https://doi.org/10.1016/S0016-7037(98)00185-9

Herbosch, A., 1967. La viridine et la braunite de Salmchâteau. Bull. Société Belge Géologie 80, 183–201.

Herbosch, A., 1965. Contribution à l'étude géochimique de l'arsenic dans le Salmien entre Vielsalm et Salm-Château (Unpublished Master thesis). Université Libre de Bruxelles, Bruxelles.

Herbosch, A., Liégeois, J.-P., Pin, C., 2016. Coticules of the Belgian type area (Stavelot-Venn Massif): Limy turbidites within the nascent Rheic oceanic basin. Earth-Sci. Rev. 159, 186–214. https://doi.org/10.1016/j.earscirev.2016.05.012

Herbosch, A., Verniers, J., 2014. Stratigraphy of the Lower Palaeozoic of the Brabant Massif, Belgium. Part II: The Middle Ordovician to lowest Silurian of the Rebecq Group. Geol. Belg. 17, 115–136.

Herbosch, A., Verniers, J., 2013. Stratigraphy of the Lower Palaeozoic of the Brabant Massif, Belgium. Part I: The Cambro-Ordovician from the Halle and Ottignies groups. Geol. Belg. 16, 49–65.

Jérôme, A., 1907. De la découverte d'un gisement notable de kaolin en Ardenne. Bull. Société Belge Géologie 21, 217–222.

Johnson, J.E., Webb, S.M., Ma, C., Fischer, W.W., 2016. Manganese mineralogy and diagenesis in the sedimentary rock record. Geochim. Cosmochim. Acta 173, 210–231. https://doi.org/10.1016/j.gca.2015.10.027

Junge, H., 1987. Der Einfluss von Tektonik und eustatischen Meeresspielgelschwankungen auf die Ausbildung der Reliefgenerationen im Norden der Eifeler Nord-Süd-Zone. Z. Für Geomorphol. 65, 35–84.

King, L.C., 1947. Landscape study in southern Africa, in: Proceedings of the Geological Society of South Africa. pp. 23–102.

Klein, C., 1990. L'évolution géomorphologique de l'Europe hercynienne occidentale et centrale: aspects régionaux et essai de synthèse, Editions du Centre national de la recherche scientifique. ed. Diffusion, Presses du CNRS, Paris.

Koppers, A.A.P., 2002. ArArCALC—software for $^{40}Ar/^{39}Ar$ age calculations. Comput. Geosci. 28, 605–619. https://doi.org/10.1016/S0098-3004(01)00095-4

Kramm, U., 1982. Die metamorphose des Venn-Stavelot Massivs, nordwestliches Rheinisches Schiefergebirge: grad, alter und ursach. Decheniana 135, 121–178.

Kramm, U., 1980. Muskovit-Paragonit Phasenbeziehungen in niedriggradig metamorphen Schiefern des Venn-Stavelot Massivs, Ardennen. Tschermaks Mineral. Petrogr. Mitteilungen 27, 153–167. https://doi.org/10.1007/BF01082405

Kramm, U., 1976. The coticule rocks (spessartine quartzites) of the Venn-Stavelot Massif, Ardennes, a volcanoclastic Metasediment? Contrib. Mineral. Petrol. 56, 135–155. https://doi.org/10.1007/BF00399600

Kramm, U., Bühl, D., 1985. U-Pb zircon dating of the Hill Tonalite, Venn-Stavelot Massif, Ardennes. Neues Jahrb. Für Geol. Paläontol. Abh. 171, 329–337.

Kramm, U., Spaeth, G., Wolf, M., 1985. Variscan metamorphism in the NE Stavelot—Venn Massif, Ardennes: a new approach to the question of regional dynamothermal or contact metamorphism. Neues Jahrb. Für Geol. Paläontol. Abh. 171, 311–327.

Krosse, S., Schreyer, W., 1993. Comparative geochemistry of coticules (spessartine-quartzites) and their redschist country rocks in the Ordovician of the Ardennes Mountains, Belgium. Chem. Erde - Geochem. 53, 1–20.

Kuleshov, V., 2016. Isotope geochemistry: the origin and formation of manganese rocks and ores. Elsevier, Amsterdam Boston Heidelberg London New York Oxford Paris San Diego San Francisco Singapore Sydney Tokyo.

Lamens, J., 1986. Depositional history of Salmian (Lower Ordovician sediments in Belgium). Aardkd. Meded. 3, 125–138.

Lamens, J., 1985a. Transition from turbidite to shallow-water sedimentation in the Lower Salmian (Tremadocian, Lower Ordovician) of the Stavelot Massif, Belgium. Sediment. Geol. 44, 121–142. https://doi.org/10.1016/0037-0738(85)90036-3

Lamens, J., 1985b. Het Salmiaan (Onder Ordivicium) in het Massief van Stavelot (Unpublished Ph.D. thesis). Katholieke Universiteit Leuven, Leuven.

Lamens, J., Geukens, F., 1984. Volcanic activity in the Lower Ordovician of the Stavelot Massif, Belgium. Meded. Van K. Acad. Voor Wet. Lett. En Schone Kunsten Van Belgïe 46, 1–13.

Lamens, J., Geukens, F., Viaene, W., 1986. Geological setting and genesis of coticules (spessartine metapelites) in the Lower Ordovician of the Stavelot Massif, Belgium. J. Geol. Soc. 143, 253–258. https://doi.org/10.1144/gsjgs.143.2.0253

Li, J.-W., Vasconcelos, P., Duzgoren-Aydin, N., Yan, D.-R., Zhang, W., Deng, X.-D., Zhao, X.-F., Zeng, Z.-P., Hu, M.-A., 2007. Neogene weathering and supergene manganese enrichment in subtropical South China: An $^{40}Ar/^{39}Ar$ approach and paleoclimatic significance. Earth Planet. Sci. Lett. 256, 389–402. https://doi.org/10.1016/j.epsl.2007.01.021

Libert, J., 1905. Les gisements ferro-manganésifères de la Lienne. Ann. Société Géologique Belg. 32, 144–154.

Linnemann, U., Herbosch, A., Liégeois, J.-P., Pin, C., Gärtner, A., Hofmann, M., 2012. The Cambrian to Devonian odyssey of the Brabant Massif within Avalonia: A review with new zircon ages, geochemistry, Sm–Nd isotopes, stratigraphy and palaeogeography. Earth-Sci. Rev. 112, 126–154. https://doi.org/10.1016/j.earscirev.2012.02.007

Mansy, J.L., Everaerts, M., De Vos, W., 1999. Structural analysis of the adjacent Acadian and Variscan fold belts in Belgium and northern France from geophysical and geological evidence. Tectonophysics 309, 99–116. https://doi.org/10.1016/S0040-1951(99)00134-1

Maynard, J.B., 2014. Manganiferous sediments, rocks, and ores, in: Treatise on Geochemistry. Elsevier, pp. 327–349.

McLennan, S.M., 2001. Relationships between the trace element composition of sedimentary rocks and upper continental crust. Geochem. Geophys. Geosystems 2, 24. https://doi.org/10.1029/2000GC000109

Mees, F., Stoops, G., 1999. Palaeoweathering of Lower Palaeozoic rocks of the Brabant Massif, Belgium: a mineralogical and petrographical analysis. Geol. J. 34, 349–367. https://doi.org/10.1002/(SICI)1099-1034(199911/12)34:4<349::AID-GJ830>3.0.CO;2-S

Mélon, J., Bourguignon, P., Fransolet, A.-M., 1976. Les minéraux de Belgique, Lelotte. ed. Dison, Belgique.

Meyer, H., Hetzel, R., Strauss, H., 2010. Erosion rates on different timescales derived from cosmogenic 10Be and river loads: implications for landscape evolution in the Rhenish Massif, Germany. Int. J. Earth Sci. 99, 395–412. https://doi.org/10.1007/s00531-008-0388-y

Meyer, H.J., Walter, R., 1985. Technical performance and geological profile of the research borehole Konzen, Hohes Venn (West Germany). Neues Jahrb. Für Geol. Paläontol. Abh. 171, 17–29.

Michon, L., Van Balen, R.T., Merle, O., Pagnier, H., 2003. The Cenozoic evolution of the Roer Valley Rift System integrated at a European scale. Tectonophysics 367, 101–126. https://doi.org/10.1016/S0040-1951(03)00132-X

Mosbrugger, V., Utescher, T., Dilcher, D.L., 2005. Cenozoic continental climatic evolution of Central Europe. Proc. Natl. Acad. Sci. 102, 14964–14969. https://doi.org/10.1073/pnas.0505267102

Nahon, D.B., 1991. Self-organization in chemical lateritic weathering. Geoderma 51, 5–13. https://doi.org/10.1016/0016-7061(91)90063-Y

Nash, D.J., McLaren, S.J. (Eds.), 2008. Geochemical sediments and landscapes, RGS-IBG book series. Blackwell Pub, Malden, MA.

Nicaise, D., 1985. Etude sédimentologique et géochimique du Salmien (Ordovicien Inférieur) de la coupe de la Salm (Unpublished Master thesis). Université Libre de Bruxelles, Bruxelles.

Nicholson, K., 1992. Genetic types of manganese oxide deposits in Scotland; indicators of paleo-ocean-spreading rate and a Devonian geochemical mobility boundary. Econ. Geol. 87, 1301–1309. https://doi.org/10.2113/gsecongeo.87.5.1301

Oncken, O., von Winterfeld, C., Dittmar, U., 1999. Accretion of a rifted passive margin: The Late Paleozoic Rhenohercynian fold and thrust belt (Middle European Variscides). Tectonics 18, 75–91. https://doi.org/10.1029/98TC02763

Onstott, T.C., Miller, M.L., Ewing, R.C., Arnold, G.W., Walsh, D.S., 1995. Recoil refinements: Implications for the 40Ar/39Ar dating technique. Geochim. Cosmochim. Acta 59, 1821–1834. https://doi.org/10.1016/0016-7037(95)00085-E

Parc, S., Nahon, D., Tardy, Y., Vieillard, P., 1989. Estimated solubility products and fields of stability for cryptomelane, nsutite, birnessite, and lithiophorite based on natural lateritic weathering sequences. Am. Mineral. 74, 466–475.

Piessens, K., Sintubin, M., 1997. Partitioning of Variscan strain in the southern part of the Caledonian Stavelot-Venn inlier in the Ardenne Allochthon (Belgium). Aardkd. Meded. 8, 135–138.

Post, J.E., 1999. Manganese oxide minerals: crystal structures and economic and environmental significance. Proc. Natl. Acad. Sci. 96, 3447–3454. https://doi.org/10.1073/pnas.96.7.3447

Price, J.R., Velbel, M.A., Patino, L.C., 2005. Rates and time scales of clay-mineral formation by weathering in saprolitic regoliths of the southern Appalachians from geochemical mass balance. Geol. Soc. Am. Bull. 117, 783. https://doi.org/10.1130/B25547.1

Prodehl, C., Mueller, S., Glahn, A., Gutscher, M., Haak, V., 1995. Continental rifts: evolution, structure, tectonics, in: Continental Rifts: Evolution, Structure, Tectonics. K.H. Olsen, New York, pp. 133–212.

Prodehl, C., Mueller, St., Haak, V., 2006. The European Cenozoic rift system, in: Continental Rifts: Evolution, Structure, Tectonics, Developments in Geotectonics. Elsevier, pp. 133–212.

Quesnel, F., 2003. Paleoweathering and paleosurfaces from northern and eastern France to Belgium and Luxembourg: geometry, dating and geodynamic implications. Géologie Fr. 1, 95–104.

Quesnel, F., Dupuis, C., Yans, J., Demoulin, A., Wyns, R., Théveniaut, H., Farjanel, G., Voisin, L., Vergari, A., Baele, J.-M., De Putter, T., Colbach, R., Muller, A., Lacquement, F., Vandycke, S., Brulhet, J., 2002a. Les paléoaltérations et paléosurfaces au NE de la France, en Belgique et au Luxembourg : état des connaissances, recherches en cours et implications géodynamiques méso-cénozoïques à l'échelle de la lithosphère nord-ouest européenne. Géologie Fr. 40.

Quesnel, F., Dupuis, C., Yans, J., Wyns, R., Farjanel, G., Théveniaut, H., Voisin, L., Lacquement, F., Vergari, A., Baele, J.-M., De Putter, T., Colbach, R., Muller, A., Vandycke, S., Giot, D., Brulhet, J., 2002b. Paléosurfaces et paléoaltérations dans le Nord de la France et en Belgique. Géologues 133–134, 40–43.

Riffel, S.B., Vasconcelos, P.M., Carmo, I.O., Farley, K.A., 2015. Combined $^{40}Ar/^{39}Ar$ and (U–Th)/He geochronological constraints on long-term landscape evolution of the Second Paraná Plateau and its ruiniform surface features, Paraná, Brazil. Geomorphology 233, 52–63. https://doi.org/10.1016/j.geomorph.2014.10.041

Rixhon, G., Demoulin, A., 2018. The Picturesque Ardennian Valleys: Plio-Quaternary Incision of the Drainage System in the Uplifting Ardenne, in: Demoulin, A. (Ed.), Landscapes and Landforms of Belgium and Luxembourg, World Geomorphological Landscapes. Springer International Publishing, Cham, pp. 159–175. https://doi.org/10.1007/978-3-319-58239-9_10

Ruddiman, W.F., 2008. Earth's climate: past and future, 2nd ed. W.H. Freeman, New York.

Ruddiman, W.F., Prell, W.L., 1997. Introduction to the Uplift-Climate Connection, in: Ruddiman, W.F. (Ed.), Tectonic Uplift and Climate Change. Springer US, Boston, MA, pp. 3–15.

Ruddiman, W.F., Raymo, M.E., Prell, W.L., Kutzbach, J.E., 1997. The uplift-climate connection: a synthesis, in: Ruddiman, W.F. (Ed.), Tectonic Uplift and Climate Change. Springer US, Boston, MA, pp. 471–515.

Schaller, M., Blanckenburg, F. von, Hovius, N., Veldkamp, A., van den Berg, M.W., Kubik, P.W., 2004. Paleoerosion rates from cosmogenic ^{10}Be in a 1.3 ma terrace sequence: response of the river Meuse to changes in climate and rock uplift. J. Geol. 112, 127–144. https://doi.org/10.1086/381654

Schaller, M., Blanckenburg, F. von, Veldkamp, A., Tebbens, L.A., Hovius, N., Kubik, P.W., 2002. A 30 000 yr record of erosion rates from cosmogenic ^{10}Be in Middle European river terraces.

Schreyer, W., Bernhardt, H.-J., Fransolet, A.-M., Armbruster, T., 2004. End-member ferrian kanonaite: an andalusite phase with one Al fully replaced by $(Mn, Fe)^{3+}$ in a quartz vein from the Ardennes mountains, Belgium, and its origin. Contrib. Mineral. Petrol. 147, 276–287. https://doi.org/10.1007/s00410-004-0557-3

Schreyer, W., Bernhardt, H.-J., Medenbach, O., 1992. Petrologic Evidence for a Rhodochrosite Precursor of Spessartine in Coticules of the Venn-Stavelot Massif, Belgium. Mineral. Mag. 56, 527–532. https://doi.org/10.1180/minmag.1992.056.385.08

Schreyer, W., Fransolet, A.-M., Bernhardt, H.-J., 2001. Hollandite–strontiomelane solid solutions coexisting with kanonaite and braunite in late quartz veins of the Stavelot Massif, Ardennes, Belgium. Contrib. Mineral. Petrol. 141, 560–571. https://doi.org/10.1007/s004100100260

Schuler, M., Cavelier, C., Dupuis, C., Steurbaut, E., Vandenberghe, N., 1992. The Paleogene of the Paris and Belgian Basins. Standard-Stages and regional stratotypes. Cah. Micropaléontologie 7, 29–92.

Sintubin, M., Debacker, T.N., Van Baelen, H., 2009. Early Palaeozoic orogenic events north of the Rheic suture (Brabant, Ardenne): A review. Comptes Rendus Geosci. 341, 156–173. https://doi.org/10.1016/j.crte.2008.11.012

Sougnez, N., Vanacker, V., Kubik, P., 2011. Reconstruction of Quaternary landscape evolution based on 10Be denudation rates and tectonic uplift data in a moderate uplifted region (Ardennes Massif, Belgium). Presented at the 18th International Union for Quaternary Research congress, Bern, p. 683.

Theunissen, K., 1971. Verband tussen de tectonische vervorming en de metamorphe rekristallisatie in het doorbraakdal van de Salm te Salmchâteau (Unpublished Ph.D. thesis). Katholieke Universiteit Leuven, Leuven.

Théveniaut, H., Quesnel, F., Wyns, R., Hugues, G., 2007. Palaeomagnetic dating of the "Borne de Fer" ferricrete (NE France): Lower Cretaceous continental weathering. Palaeogeogr. Palaeoclimatol. Palaeoecol. 253, 271–279. https://doi.org/10.1016/j.palaeo.2007.01.010

Theye, T., Schreyer, W., Fransolet, A.-M., 1996. Low-temperature, low-pressure metamorphism of Mn-rich rocks in the Lienne syncline, Venn—Stavelot Massif (Belgian Ardennes), and the role of Carpholite. J. Petrol. 37, 767–783. https://doi.org/10.1093/petrology/37.4.767

Thiry, M., Quesnel, F., Yans, J., Wyns, R., Vergari, A., Theveniaut, H., Simon-Coiçon, R., Ricordel, C., Moreau, M.-G., Giot, D., Dupuis, C., Bruxelles, L., Barbarand, J., Baele, J.-M., 2006. Continental France and Belgium during the early Cretaceous: paleoweatherings and paleolandforms. Bull. Société Géologique Fr. 177, 155–175. https://doi.org/10.2113/gssgfbull.177.3.155

Thomas, M.F., 1994. Geomorphology in the tropics: a study of weathering and denudation in low latitudes. Wiley, Chichester [England] ; New York.

Torsvik, T.H., Van der Voo, R., Preeden, U., Mac Niocaill, C., Steinberger, B., Doubrovine, P.V., van Hinsbergen, D.J.J., Domeier, M., Gaina, C., Tohver, E., Meert, J.G., McCausland, P.J.A., Cocks, L.R.M., 2012. Phanerozoic polar wander, palaeogeography and dynamics. Earth-Sci. Rev. 114, 325–368. https://doi.org/10.1016/j.earscirev.2012.06.007

Van Balen, R.T., Houtgast, R.F., Van der Wateren, F.M., Vandenberghe, J., Bogaart, P.W., 2000. Sediment budget and tectonic evolution of the Meuse catchment in the Ardennes and the Roer Valley Rift System. Glob. Planet. Change 27, 113–129. https://doi.org/10.1016/S0921-8181(01)00062-5

Vandenven, G., 1991. Explications de la carte géologique du synclinorium de l'Eifel. Ann. Société Géologique Belg. 113, 103–113.

Vanguestaine, M., Breuer, P., Lehnert, O., 2004. Discovery of an Early Ordovician conodont fauna in the Salm Group of the Stavelot Inlier, Belgium. Bull. Inst. R. Sci. Nat. Belg. Sci. Terre 74, 39–48.

Varentsov, I.M., 1996. Manganese ores of supergene zone: Geochemistry of formation, Solid Earth Sciences Library. Springer Netherlands, Dordrecht.

Vasconcelos, P.M., 1999. K-Ar and $^{40}Ar/^{39}Ar$ geochronology of weathering processes. Annu. Rev. Earth Planet. Sci. 27, 183–229. https://doi.org/10.1146/annurev.earth.27.1.183

Vasconcelos, P.M., Carmo, I. de O., 2018. Calibrating denudation chronology through $^{40}Ar/^{39}Ar$ weathering geochronology. Earth-Sci. Rev. 179, 411–435. https://doi.org/10.1016/j.earscirev.2018.01.003

Vasconcelos, P.M., Heim, J.A., Farley, K.A., Monteiro, H., Waltenberg, K., 2013. $^{40}Ar/^{39}Ar$ and (U–Th)/He – 4He/3He geochronology of landscape evolution and channel iron deposit genesis at Lynn Peak, Western Australia. Geochim. Cosmochim. Acta 117, 283–312. https://doi.org/10.1016/j.gca.2013.03.037

Vasconcelos, P.M., Renne, P.R., Becker, T.A., Wenk, H.-R., 1995. Mechanisms and kinetics of atmospheric, radiogenic, and nucleogenic argon release from cryptomelane during analysis. Geochim. Cosmochim. Acta 59, 2057–2070. https://doi.org/10.1016/0016-7037(95)00126-3

Velbel, M.A., 1984. Natural weathering mechanisms of almandine garnet. Geology 12, 631. https://doi.org/10.1130/0091-7613(1984)12<631:NWMOAG>2.0.CO;2

Verniers, J., Herbosch, A., Vanguestaine, M., Geukens, F., Delcambre, B., Pingot, J.-L., Belanger, I., Hennebert, M., Debacker, T., Sintubin, M., De Vos, W., 2001. Cambrian-Ordovician-Silurian lithostratigraphic units (Belgium). Geol. Belg. 4, 5–38.

Voisin, L., 1981. Analyse géomorphologique d'une région-type: l'Ardenne occidentale (Unpublished Ph.D. thesis). Université de Lille 2, Lille.

von Hoegen, J., von Lemme, B., Zielinski, J., Walter, R., 1985. Cambrian and Lower Ordovician in the Stavelot-Venn Massif: a model for the depositional history. Geol. Rundsch. 87, 407–435.

Wayland, E.J., 1933. Peneplains and some other erosional platforms. Prot. Uganda Geol. Surv. 1, 77–79.

Widdowson, M., 2008. Laterite and Ferricrete, in: Nash, D.J., McLaren, S.J. (Eds.), Geochemical Sediments and Landscapes. Blackwell Publishing Ltd, Oxford, UK, pp. 45–94. https://doi.org/10.1002/9780470712917.ch3

Willems, L., Rodet, J., 2018. Karst and underground landscapes in the Cretaceous Chalk and calcarenite of the Belgian-Dutch border—the Montagne Saint-Pierre, in: Demoulin, A. (Ed.), Landscapes and Landforms of Belgium and Luxembourg, World Geomorphological Landscapes. Springer International Publishing, Cham, pp. 177–192. https://doi.org/10.1007/978-3-319-58239-9_11

Wyns, R., 2002. Climat, eustatisme, tectonique: quels contrôles pour l'altération continentale? Exemple des séquences d'altération cénozoïques en France. Bull. Inf. Géologues Bassin Paris 39, 5–16.

Wyns, R., Gourry, J.C., Baltassat, J.M., Lebert, F., 1999. Caractérisation multiparamètre des horizons de subsurface (0–100 m) en contexte de socle altéré. Pangea 31, 51–54.

Wyns, R., Quesnel, F., Simon-Coinçon, R., Guillocheau, F., Lacquement, F., 2003. Major weathering in France related to lithospheric deformation. Géologie Fr. 79–87.

Xu, C., Mansy, J.L., Van Den Haute, P., Guillot, F., Zhou, Z., Chen, J., De Grave, J., 2009. Late- and post-Variscan evolution of the Ardennes in France and Belgium: constraints from apatite fission-track data. Geol. Soc. Lond. Spec. Publ. 324, 167–179. https://doi.org/10.1144/SP324.13

Yans, J., 2013. Gestion durable des ressources minérales wallonnes: pistes de réflexions en vue d'une meilleure intégration de la problématique, in: Actes Du 1er Congrès Interdisciplinaire Du Développement Durable. Presented at the Congrès interdisciplinaire du développement durable, Namur, pp. 195–206.

Yans, J., 2003. Chronologie des sédiments kaoliniques à faciès wealdien (Barrémien moyen à Albien supérieur ; Bassin de Mons) et de la saprolite polyphasée (Crétacé inférieur et Miocène inférieur) de la Haute-Lesse (Belgique) : implications géodynamiques et paléoclimatiques (Unpublished Ph.D. thesis). Faculté Polytechnique de Mons, Université de Paris XI Orsay, Mons.

Yans, J., Chauvin, A., Clauer, N., Dejax, J., De Putter, T., Dupuis, C., Feraud, G., Guillocheau, F., Masure, E., Leost, I., Perruchot, A., Pons, D., Spagna, P., Wyns, R., 2003. An overview of the saprolites of Belgium and their potential kaolinitic supplies to Mesozoic and Cenozoic sediments. Géologie Fr. 1, 33–37.

Yans, J., Dupuis, C., 2005. Timing of saprolitisation in the Haute-Lesse area (Belgium), in: Geophysical Research Abstract. Presented at the European union of Geosciences Meeting, Vienna.

Zachos, J., Pagani, M., Sloan, L., Thomas, E., Billups, K., 2001. Trends, rhythms, and aberrations in global climate 65 Ma to Present. Science 292, 686–693. https://doi.org/10.1126/science.1059412

Ziegler, P.A., Dèzes, P., 2007. Cenozoic uplift of Variscan Massifs in the Alpine foreland: Timing and controlling mechanisms. Glob. Planet. Change 58, 237–269. https://doi.org/10.1016/j.gloplacha.2006.12.004

Zwicker, W.K., Groeneveld-Meijer, W.O.J., Jaffe, H.W., 1962. Nsutite - a widespread manganese oxide mineral. Am. Mineral. 47, 618–623.

Chapter 7

The karst-hosted Mn deposits of the Imini-Tasdremt district (High Atlas, Morocco)

Chapter 7

The karst-hosted Mn deposits of the Imini-Tasdremt district (High Atlas, Morocco)

The Atlas belt is an intracontinental belt that roughly follows a SW-NE direction displaying higher elevated surfaces crossing over North Africa from Morocco to Tunisia (►Fig. 7.1). This belt is a fascinating geological target where several phases of uplift have been recorded since late Cretaceous times (Froitzheim, 1984; Frizon de Lamotte *et al.*, 2000b; Leprêtre *et al.*, 2015b, 2018). The Atlas belt has been structured by three geological processes: (1) the Triassic-Jurassic rifting, (2) the Cretaceous-Paleocene plate convergence and finally (3) the Atlas uplift during Cenozoic times. The formation of the belt is related to the evolution of the Mediterranean geodynamic and the opening of the Tethys Ocean. Accordingly, the Atlas is composed of Mesozoic-Cenozoic basins, those having been inverted by the distant effect of the Alpine orogenesis, except for the eastern and western mesetas onto which the Mesozoic-Cenozoic cover is relatively thin (►Fig. 7.1; Frizon de Lamotte *et al.*, 2009). Both the High Atlas and the Anti Atlas further south are more elevated than their lateral equivalent, due to a Neogene (?) thermal uplift (Missenard, 2006) observed through the setting up of alkaline volcanism (i.e., Siroua volcanism). In these areas, and mostly in the Anti Atlas, Precambrian rocks and its Paleozoic cover are exhumed displaying an asymmetric elevation profile from the western part of the Atlas belt to its eastern portion (Frizon de Lamotte *et al.*, 2009).

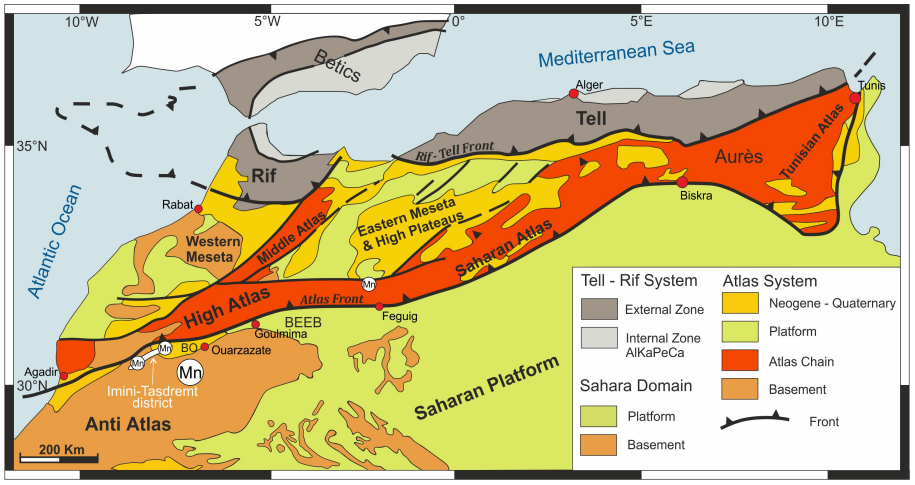

►**Fig. 7.1** Main structural domains of the Atlasic belt of North Africa and the position of the Imini-Tasdremt district (modified after Frizon de Lamotte *et al.*, 2000). BO: Ouarzazate Basin; BEEB: Errachidia-Erfoud-Boudnib basin.

Manganese deposits are widespread in Morocco, especially, in the Moroccan Atlas and Anti Atlas (►Fig. 7.1), the most important being located in the Bou Arfa city area (Pouit, 1980 ; Lafforgue *et al.*, 2015 ; Lafforgue, 2016), Ouarzazate (Bouladon *et al.*, 1955; Jouravsky, 1963; Jouravsky and Pouit, 1963; Choubert and Faure-Muret, 1973; Pouit, 1980; Lippolt and Hautmann, 1995) and Imini districts (►Fig. 7.1; Thein, 1990 ; Lalaoui *et al.*, 1991 ; Gutzmer *et al.*, 2006 ; Dekoninck *et*

al., 2016a, 2016 b). The Paleoproterozoic volcanosedimentary Tiouine ores (Ouarzazate district) and the karst-hosted Imini deposits hosted in Cenomanian-Turonian dolostone are the only Mn deposits currently mined with commercial and valuable Mn products (►Fig. 7.1).

For more than 80 years of mining the economically important Imini district has been the main producer of manganese in Morocco. Three *stratabound* manganiferous orebodies are hosted in a ~10-m-thick Cenomanian-Turonian dolostone that records the effects of laterally extensive dissolution and epigenetic processes. The predominance of pyrolusite, which is accompanied by hollandite group minerals (cryptomelane, hollandite *s.s.*, coronadite), lithiophorite, and romanechite, provide a high grade ore having more than 70 wt.% MnO and low contents in SiO_2, Fe_2O_3, and P_2O_5. The accepted metallogenic model (Gutzmer *et al.*, 2006) suggests that the main mineralization stage is related to a period of terrestrial exposure and weathering, leading to the formation of an extensive karst system, following the host rock deposition and dolomitization. This model envisages Mn mineralization prior to the deposition of Coniacian-Maastrichitan (Senonian) red beds, carbonates and evaporites. In 1951, Bouladon and Meunes investigated Mn occurrences 60–100 kilometers to the south-west of the Imini district, in the Tasdremt and Aoufour areas (Souss Basin; ►Fig. 7.1). The Mn mineralization displays common features with the Imini ores as they are hosted in Cretaceous dolostones, but more interestingly, they show also significant differences, including lower grade, and discontinuous orebodies and an atypical composition, containing up to ~6% of Pb (and Ba; Bouladon and Meune, 1951). Therefore, the Tasdremt manganese deposit should be considered as a lateral equivalent of the high-grade Imini district, and potentially a target for mining companies (Bouladon and Meune, 1951 ; Pouit, 1980 ; Office National des Mines et des Hydrocarbures, 2016).

The presence of these Mn deposits in the southern foreland of the High Atlas Mountain, from Imini to the east to Tasdremt 100 kilometers to the west (►Fig. 7.1), offers an exceptional opportunity to evaluate the timing of these deposits as K-Mn oxide (hollandite *sensu lato*) occur massively within the ore. Consequently, this area is probably the most promising sampling site to assess the effect of uplift and geodynamic in the control of the age recovered from these oxides (see chapter 9). Additionally, the economic interest of the Imini and Tasdremt districts needs a clear and detailed geological framework for further prospection of similar Mn deposits in Morocco and other places in the world. We also propose to consider a single Imini-Tasdremt district.

This chapter refers to five papers dealing with (1) the tectonic history of Cenozoic deformation in the Atlas belt and (2) the mineralogy, the petrography, the geochemistry and the geochronology of the Imini and Tasdremt deposits.

The first paper (Leprêtre *et al.*, 2015b), co-authored by Rémi Leprêtre, Yves Missenard, Bertrand Saint-Bézar, Jocelyn Barbarand, Guillaume Delpech, Johan Yans, **Augustin Dekoninck** and Omar Saddiqi, presents the timing and the tectonic setting of the Imini area and, for the first time, the presence of three steps responsible for the Atlas building during the Cenozoic. (1) A Late Eocene tectonic event set local and minor structures, barely visible nowadays, but important enough to trigger the record of a first detrital pulse; (2) An Early–Middle Miocene doming event is not related to important shortening, setting gravity "sheets" that drove cover deformation and fed a second detrital pulse; (3) A Late Pliocene–Quaternary tectonic event is mainly observed through the activity of basement features such as the South Atlas Front and the Imini Fault. This study is entitled "*The three main steps of the Marrakech High Atlas building in Morocco: Structural evidences from the southern foreland, Imini area*" and published in the Journal of African Earth Sciences n°109 (pages 177-194) in 2015.

The second part of the chapter focuses on different mines of the Imini district, aiming to refine the mineralogy and petrology of Mn-bearing oxides (pyrolusite) and oxyhydroxides (hollandite *s.s.*, cryptomelane, coronadite, lithiophorite and romanechite; Dekoninck *et al.*, 2016) showing that the deposition and concentration of Mn oxyhydroxides follows a two-step scenario after dolomitization of the host rock: (1) replacement of dolomite fabric (dolomite micrite and dolomite rhombs) by hollandite group minerals leading to a textural conservation and then (2) the neoformation of colloform aggregates in an open and brecciated system. "*Detailed mineralogy and petrology of manganese oxyhydroxide deposits of the Imini district (Morocco)*" was published in the volume 51 of the journal Mineralium Deposita (pages 13-23) in 2016 and authored by Augustin Dekoninck, Alain Bernard, Jocelyn Barbarand, Bertrand Saint-Bézar, Yves Missenard, Rémi Leprêtre, Omar Saddiqi and Johan Yans (Dekoninck *et al.*, 2016a). I have complemented this part with a second paper (Dekoninck *et al.*, 2016b) published as a chapter in the book "*Mineral deposits of North Africa*" (Bouabdellah and Slack, 2016) by Springer Verlag. This 22th chapter entitled "*The high-grade Imini manganese district—karst-hosted deposits of Mn oxides and oxyhydroxides*" presents an overview of the Imini district and bring new geochemical data to better constrain the formation of the Imini ores (Dekoninck *et al.*, 2016b). All these data suggest a primary late Cretaceous supergene stage for the ore formation and possibly several remobilization after their precipitation.

Recent investigations made in the Tasdremt area have provided significant improvements to the understanding of Mn ore formation in the area and the genetically related Imini deposits, supplemented by a set of new $^{40}Ar/^{39}Ar$ dating on hollandite group minerals. The authors (Augustin Dekoninck, Gilles Ruffet, Yves Missenard, Oriane Parizot, Mohamed Magoua, Gaëtan Rochez and Johan Yans) identify clearly the first late Cretaceous mineralization phase of hollandite group minerals, following

a similar process than the one evidenced by Dekoninck *et al.* (2016a) at Imini, making these deposits similar in some points, although the absence of pyrolusite in Tasdremt is one of the major difference with the Imini ores. The paper entitled "*Multistage genesis of the late Cretaceous Mn(-Pb) karst-hosted Tasdremt deposits by $^{40}Ar/^{39}Ar$ dating of K-Mn oxide (Souss Basin, Morocco): a lateral equivalent of the high-grade Imini ores*" has been submitted for review and publication in the journal Mineralium Deposita.

The fourth section of this chapter is based on a paper still in preparation. This paper is formerly entitled "*Polyphase Cenozoic Mn remobilizations in the high-grade Imini ores (High Atlas, Morocco) deciphered by K-Mn oxide dating: role of the Atlasic tectonics*", and supplement the primary late Cretaceous ore deposition evidenced in the nearby Tasdremt area, with the identification of more recent remobilization/input of Mn in the Imini deposits thanks to new $^{40}Ar/^{39}Ar$ datings on hollandite group minerals sampled by Dekoninck *et al.* (2016a) throughout the Imini district. A link with the geodynamic of the High Atlas is clearly supported by these data. Such interpretation is a significant point that allows pyrolusite to massively precipitate in the Imini area, as opposed to the Tasdremt deposits, in which no observation of this mineral has been reported.

The last section of this chapter deals with the study of two hollandite concretions collected in the Tasdremt mine, from which several grains have been carefully selected in order to investigate age dispersion along a growth band. These data are supplemented by EPMA analyses and suggest a thermal imprint over the formation of these Mn oxides.

7.1 The three main steps of the Marrakech High Atlas building in Morocco: structural evidences from the southern foreland, Imini area

The present study focuses on the Marrakech High Atlas (►Fig. 7.2). We investigated the Imini district, situated south of the Marrakech High Atlas (►Fig. 7.2b). This region is located at the intersection between the Variscan fold-and-thrust belt of the Anti-Atlas, the uplifted Panafrican basement of the Marrakech High Atlas, the Neogene Siroua (or Siroua) volcano and the Ouarzazate basin (Saddiqi *et al.*, 2011; ►Fig. 7.2b). The area is well known for its economic manganese ore deposits (Pouit, 1964; Gutzmer *et al.*, 2006; Dekoninck *et al.*, 2016a), but it has not been thoroughly investigated from a structural point of view (Moret, 1931; Pouit, 1964; Errarhaoui, 1998; Missenard *et al.*, 2007), maybe due to its low grade deformation that resulted in a monoclinal Cretaceous–Tertiary plateau (Imini plateau ►Fig. 7.3) slightly inclined toward the south and limited to the north by the South

Atlas Front (SAF, ►Fig. 7.2b). The main outcropping feature is the N90° Imini anticline (►Fig. 7.3), which has an Ordovician shale core and which is surrounded by an apparently poorly deformed plateau of Meso-Cenozoic sedimentary rocks (►Fig. 7.3).

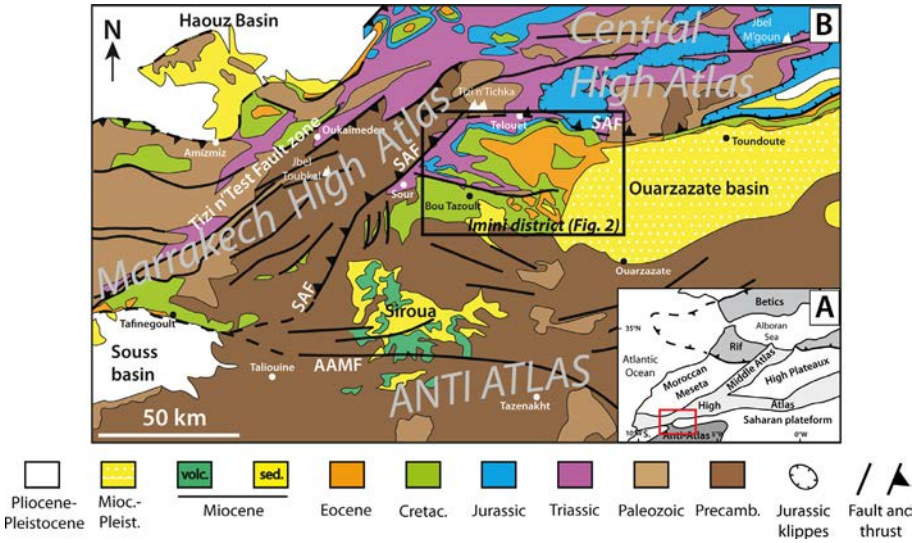

►**Fig. 7.2 a.** Geodynamic situation of the Atlas in the Western Mediterranean frame (modified from Frizon de Lamotte *et al.*, 2000). Location of the studied region presented in (**b**) is indicated with the red window. **b.** Schematic geological map of the studied part of the Atlas orogeny and localization of ►Fig. 7.3. SAF: South Atlas Front; AAMF: Anti-Atlas Major Fault. (For interpretation of the references to color in this figure legend, the reader is referred to the web version of this article.

In this study, we present a structural analysis of the Imini district combining fieldwork and elevation maps of the Cenomanian–Turonian layer (CT layer), which is the most prominent benchmark of the region. This new data reveals that the tectonic history in the Atlas of Morocco is more complex than elsewhere in the Maghreb with the occurrence of three distinct Cenozoic tectonic events, separated by apparent quiescent phases. The peculiar position of the Moroccan Atlas with respect to the rest of the Atlas belt in the Maghreb is then discussed in the light of these results.

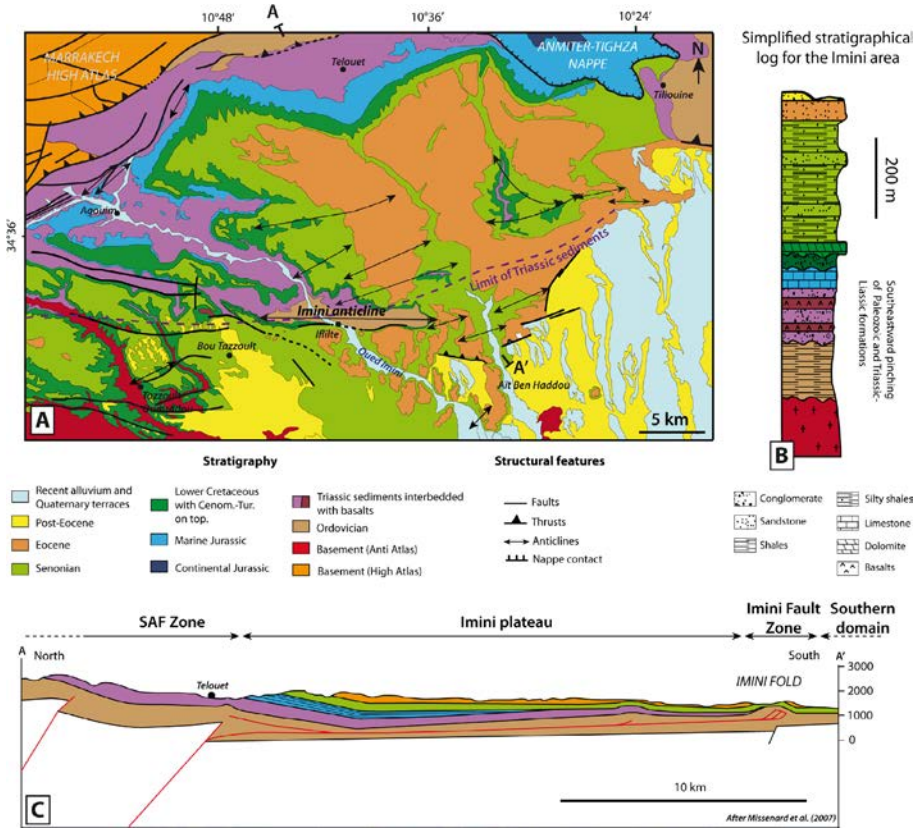

►**Fig. 7.3 a.** Structural map of the Imini area, modified with reference to the Geological map of Morocco, scale 1:200,000, sheet Ouarzazate, and Rhalmi (1992). **b.** Simplified stratigraphical log of the Imini area from the basement to the Cenozoic formations. **c.** Cross-section is modified with reference to Missenard *et al.* (2007) and Zouhri *et al.* (2008).

7.1.1 Geological settings

7.1.1.a High Atlas – South Atlas Front

The Triassic–Liassic rifting events are linked to the opening of the Neo-Tethys and Atlantic oceans (Medina, 1991; Le Roy *et al.*, 1997; El Arabi *et al.*, 2003, 2006; Hafid *et al.*, 2006; El Arabi, 2007). In Morocco, the basins are filled by Triassic red coarse clastic sediments, interbedded with evaporitic levels and basaltic flows. Deposition of massive quantities of carbonates occurred during Early to Middle Jurassic Choubert and Faure-Muret, 1962; Jacobshagen *et al.*, 1988; Jabour *et al.*, 2004; Laville *et al.*, 2004 and references therein for the Atlas rifting). The Bathonian–Barremian interval corresponds to the deposition of continental red beds probably over the whole of Morocco (Faure-Muret and Choubert, 1971; Charrière *et al.*, 1994, 2005; Haddoumi *et al.*, 2008, 2010). In contrast, the Cenomanian–Turonian shows a major

transgression over north-west Africa with the extensive deposition of shallow water carbonates (Zouhri *et al.*, 2008 and references therein). The Coniacian to Paleocene period is dominated by continental influences including evaporitic red bed deposits (Ensslin, 1992; Wurster and Stets, 1992; Charrière, 1996; Charrière *et al.*, 1998; Ettachfini *et al.*, 2005; Haddoumi *et al.*, 2008; Saddiqi *et al.*, 2011). The end of the Cretaceous and Cenozoic periods corresponds to the beginning of the orogenic processes, linked to the Africa–Eurasia convergence. The timing of this inversion is still highly debated between two main models: a single phase or a two-step orogeny.

There is a consensus that the Atlas system in Morocco (►Fig. 7.2b) mainly results from the Cenozoic inversion of the Triassic–Jurassic basins described above (Mattauer *et al.*, 1977; Dewey *et al.*, 1989; Frizon de Lamotte *et al.*, 2000b; Hafid *et al.*, 2006; El Arabi, 2007). The role of a Mesozoic transpressional event was suggested by some authors (Piqué *et al.*, 2002; Laville *et al.*, 2004), but has been discarded on the basis of field and seismic profile evidence (Frizon de Lamotte *et al.*, 2008 and reference therein; Saddiqi *et al.*, 2011). The high elevation of the belt, particularly in its western part, results from the influence of an upper mantle anomaly at the time of the convergence between Africa and Europe (Teixell *et al.*, 2005; Zeyen *et al.*, 2005; Missenard *et al.*, 2006; Fullea *et al.*, 2007).

The orogen is bounded to the south by the South Atlas Front (SAF), a crustal scale fault partly superimposed on older Variscan faults on its western part (the Tizi n'Test fault zone, see (Proust *et al.*, 1977; Ouanaimi and Petit, 1992; Qarbous *et al.*, 2003, 2008; Michard *et al.*, 2008). The SAF was probably the main southern boundary of the Mesozoic rift, likely controlling the Mesozoic sedimentation, as witnessed by the small thickness and extension of the Jurassic and Triassic formations southward. Along the SAF, deformation style strongly varies, as described by Missenard *et al.* (2007): to the west, in the Souss Basin, large anticlines due to décollement levels in Lower Paleozoic and high-angle reverse faults coexist with small folds developed through shallower Coniacian–Maastrichtian ("Senonian") levels. To the east, the SAF separates the Marrakech High Atlas from the Siroua Precambrian high plateau (►Fig. 7.2b) and may represent a relay zone between the SAF and the Anti-Atlas Major Fault (Frizon de Lamotte *et al.*, 2008; ►Fig. 7.2b). The Imini district with Cretaceous–Tertiary, Sub-Saharan type formations (Zouhri *et al.*, 2008) is interpreted as a large triangle zone, controlled by décollements in Lower Paleozoic shales (►Fig. 7.3; Missenard *et al.*, 2007; Zouhri *et al.*, 2008). In this region, the SAF follows a N50–60_ orientation to the west, whereas it becomes N90° northward in the Tizi n'Tichka area (►Fig. 7.2b, and Saddiqi *et al.*, 2011, their cross-section ►Fig. 7.11).

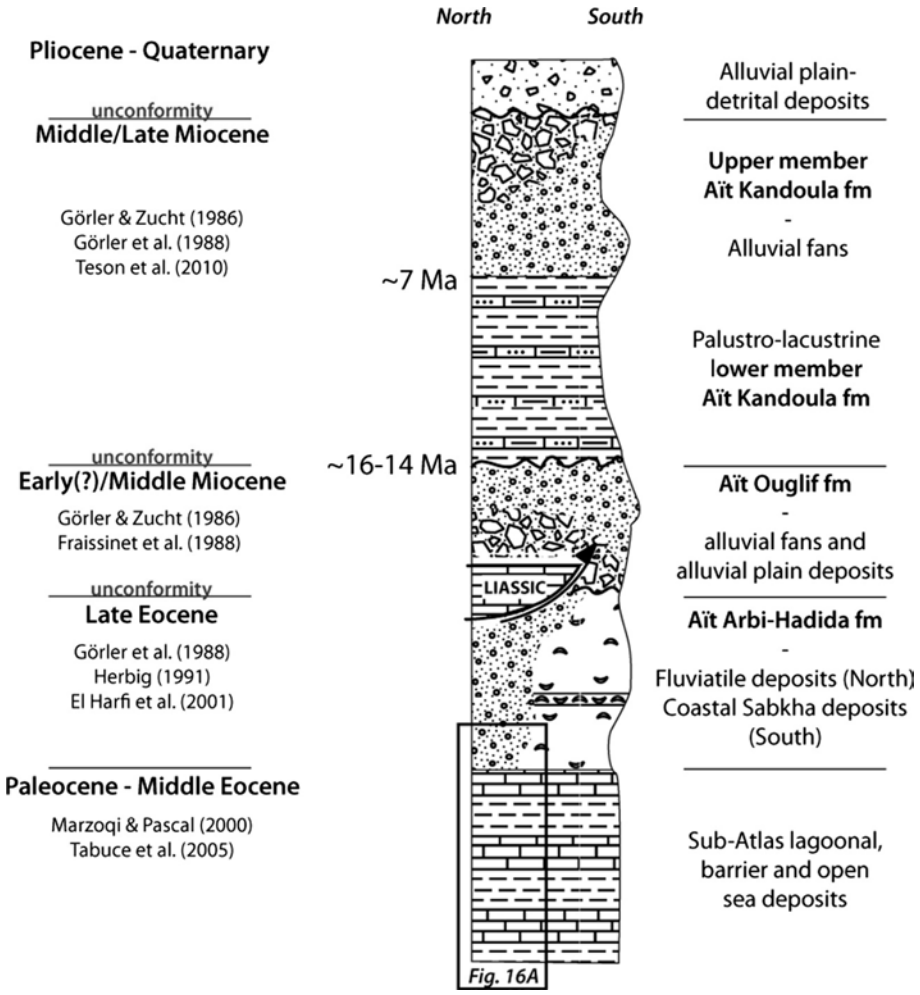

►**Fig. 7.4** Precise stratigraphical log for the Cenozoic formations of the Ouarzazate Basin (with reference to El Harfi *et al.*, 2001). On the left side is indicated the time division we have chosen to adopt in this study with the appropriate references. Absolute dating come from Tesón *et al.* (2010) for the lower member of the Aït Kandoula formation. On the right side, we give the type of paleo-environments for each stratigraphical formation (with corresponding symbols in the log). These formations can reach a few hundred meters where they are well-developed (El Harfi *et al.*, 2001). In the Imini district they are significantly reduced in thickness and except for the palustrine–lacustrine Aït Kandoula formation, they are not continuous.

The SAF then extends along the northern limit of the Ouarzazate Basin (►Fig. 7.2b). The Ouarzazate Basin is filled by Upper Cretaceous and Cenozoic sediments up to 1200 m-thick (El Harfi *et al.*, 2001; Tabuce *et al.*, 2005) and lies today at a high elevation (>1300 m). The Cenozoic stratigraphical record in this basin is fairly well-developed and is worth describing in detail. On top of the Paleocene–Middle Eocene marine formations, numerous continental formations have been

identified. El Harfi *et al.* (2001) proposed a unified classification for all of them (►Fig. 7.4): (1) a first detrital formation (Aït Arbi/Hadida Formations) conformably overlying the last marine Eocene deposits, (2) a coarse conglomeratic member (Aït Ouglif Formation), unconformable on both the previous and Jurassic formations, and (3) palustrine–lacustrine deposits followed by a last detrital pulse (Aït Kandoula Formation). Ages of these formations are however poorly documented. The first member of El Harfi *et al.* (2001) is classically attributed to the Upper Eocene, given its conformable position on the marine deposits. Paleontological data gives a Langhian–Early Serravallian age for the base of the Aït Kandoula member (Helmdach, 1988), whereas magnetostratigraphic data has given a similar age for the base of the Aït Ouglif member (Tesón *et al.*, 2010). Magnetostratigraphy is not conclusive concerning the Aït Ouglif Formation, compared to the better dating for the Aït Kandoula Formation (Görler *et al.*, 1988; Tesón *et al.*, 2010). El Harfi *et al.* (2001) proposed no convincing arguments other than attributing this formation to Oligocene–Early Miocene times, given the ages of the Upper Eocene detrital member and the Aït Kandoula lacustro-palustrine member. We favor the Early–Middle Miocene age for the Aït Ouglif Formation. The top of the Aït Kandoula member has been linked to a younger Messinian age by magnetostratigraphy (Tesón *et al.*, 2010), and an Upper Pliocene age by El Harfi *et al.* (2001), based on paleontological data.

During the Cenozoic inversion, the Ouarzazate Basin underwent deformation on its northern edge with imbricate fans on its western part (Errarhaoui, 1998; Beauchamp *et al.*, 1999; Benammi *et al.*, 2001; Tesón, 2005; Tesón and Teixell, 2008), whereas eastern regions of the southern foreland show tip-line folds (Saint-Bézar *et al.*, 1998). Various décollement levels are activated such as “Senonian” gypsum and Late Triassic–Early Liassic evaporites (Missenard *et al.*, 2007; Frizon de Lamotte *et al.*, 2008).

7.1.1.b Imini district

In the Imini district (►Fig. 7.3), the sedimentary cover begins with a basal sequence of Triassic clastic beds interbedded with basalt flows (El Arabi, 1988, 2007) dated from ca. 200 to 195 Ma ($^{40}Ar/^{39}Ar$; see Marzoli *et al.*, 2004; Nomade *et al.*, 2007; Verati *et al.*, 2007). Triassic beds, as well as overlying Liassic limestones, are pinched out southward, following a roughly N90° limit (►Fig. 7.2), which becomes ENE–WSW eastward. The “Infracenomanian” red beds (Upper Jurassic to probably Lower Cretaceous) consist of a clastic, reddish formation, unconformably overlying Triassic, Liassic or Precambrian formations, and directly capped by the Cenomanian–Turonian (CT) dolostones. The CT formation, that dominates the topography of this area, has been studied by (Rhalmi, 1992; Rhalmi *et al.*, 2000). It consists of a highly dolomitized limestone level, with quite constant thickness (10–15 m). Senonian layers (ca. 400 m thick) show interbedded sandstones, red clays and gypsum beds. Paleocene–Middle Eocene levels lie on the top and form a second benchmark (>100

m-thick), with marine carbonate and siliciclastic-carbonate facies (Choubert, 1970). Lastly, Miocene lacustrine deposits (limestones and clays) and conglomerates (Pouit, 1964) outcrop to the south and to the east of the Imini anticline. Oligocene deposits are not observed in this region of Morocco. Southward, Paleozoic and Precambrian formations outcrop in the Anti-Atlas, due to the erosion of a previous thin Mesozoic–Cenozoic cover (Ruiz *et al.*, 2011; Oukassou *et al.*, 2013).

Two main fault system strikes can be distinguished in the Imini area: a N45–N90° striking group and a N110–N130° striking group in the area (►Figs. 7.2b and 3). The SAF adopts a N45° orientation in the west and changes to a more N90° orientation in the north. Faults parallel to this orientation are well represented by N45° and N90° faults and thrusts (►Fig. 7.3). For example, a N45° to N70° fault system is well-represented east of the Imini anticline (►Fig. 7.3). In the south, the roughly N90° Anti-Atlas Major Fault (AAMF, ►Fig. 7.2b) is a major Variscan tectonic structure of the area (Choubert, 1963; Ennih et al., 2001; Ennih and Liégeois, 2001; Gasquet et al., 2008) and in the Anti-Atlas basement N90° to N130° faults are well represented (►Figs. 2b and 3). These faults could account for a portion of the Cenozoic inversion.

7.1.2 Methodology

In addition to the structural data acquired in the field and processed with the WinTensor program (Delvaux and Sperner, 2003), an elevation map of the CT layer has been performed by using a DEM based on DigitalGlobe data with the Surfer9 software. We have targeted the CT surface of the Imini plateau where deformations have been observed and we have digitized elevations of the CT outcrops. Where the CT was buried under Senonian to Eocene series, reference levels have been digitized, and corrected with their thickness relative to the CT. These corrections assume the hypothesis of isopach layers for Senonian and younger units, which has previously been verified by extensive studies (Rhalmi, 1992; Rhalmi *et al.*, 2000). Various methods of gridding have been tested in order to obtain the best spatial likelihood for the imaged structures. We have tested minimum curvature, triangulation with linear interpolation and kriging gridding methods. The minimum curvature method seeks a “mean surface” and ignores some data. Moreover, it extrapolates over the surface limited by the data points, sometimes emphasizing non-existing trends. Conversely, kriging and triangulation with linear interpolation are exact interpolators. The main difference between these two methods is the ability of the kriging method to extrapolate over the limits of data points, as the minimum curvature method does. Consequently, we have chosen the triangulation with linear interpolation gridding method. Details about this gridding method can be found in Lawson (1977), Lee and Schachter (1980) and Guibas and Stolfi (1985). The resulting elevation maps allow us to observe deformation trends, and compare them to the fieldwork studied structures.

Three areas have been mapped and are presented in the following section, together with the fieldwork observations.

7.1.3 Results

In the following section, we present the fieldwork observations and CT elevation maps. Three main domains have been distinguished, from south to north (►Figs. 7.3 and 7.5): (1) a southern domain, poorly deformed and bounded to the North by the "Imini Fault Zone" which extends from Sour to the Imini anticline and becomes N45° eastward joining the SAF (►Figs. 7.2 and 7.3); (2) the tilted Cretaceous–Tertiary Imini plateau, apparently poorly deformed; and (3) the SAF zone.

7.1.3.a Southern domain

- *Relationships between Miocene–Pliocene formations and older ones – Paleoreliefs*

In the southern domain, the Miocene–Pliocene formations often fill large geomorphological depressions. We observed their contact on older formations close to the Anti-Atlas basement in the South (►Fig. 7.3). On a regional scale (►Fig. 7.3), the Miocene–Pliocene formations rest unconformably on the older ones (basement and Senonian–Eocene). This unconformity corresponds to an erosional surface, as observed in the field (►Figs. 7.6a and b): these outcrops show that Miocene–Pliocene formations fill geomorphological depressions in the Senonian–Eocene units. Furthermore, the Miocene–Pliocene formations overflow the Eocene layer that shapes the reliefs (Figs. 7.6b and c). The real thicknesses and extent reached by the Miocene–Pliocene formations are unknown, since they are capped in many places by erosive quaternary terraces and are extensively eroded.

In the southern domain, tectonic structures are scattered. For example, in the north of the southern domain, a small N90° thrust is observed and involves the Senonian and Eocene formations, thrusting onto the Miocene–Pliocene ones (►Fig. 7.7a). Simple systems of folds and thrusts explain the tectonic structures along this small N90° "front". South of this thrust, a small detachment fold also affects both Miocene–Pliocene formations and older ones (►Fig. 7.6d). When following the fold axis eastward, Miocene–Pliocene formations are indeed folded in the same way as the Senonian–Eocene ones shown westward, implying a post-Miocene–Pliocene deformation. To the northwest, close to Bou Tazzoult, a N45°-fold affects the CT and Senonian layers that crop out, through an inverse fault (►Figs. 7.3 and 7.7b). Here, the sedimentary cover is very thin and the deformation affects the basement, setting a fold with a steeper forelimb compared to the almost flat back limb. This N45° strike is parallel to the orientation of the SAF westward of this location (►Figs. 7.2a and

7.3). Also, isolated small folded structures, with a N20–30° to N45° axis deform the Senonian–Eocene formations and even the Miocene–Pliocene ones (►Fig. 7.6). Shortening on these structures is similarly small across the whole southern area.

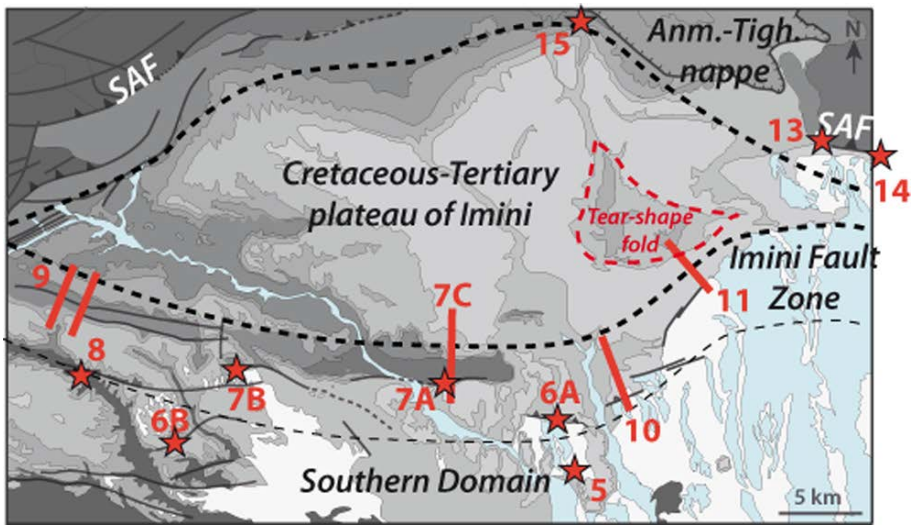

►**Fig. 7.5** Locations of the outcrops and cross-sections of this study. The geological map of ►Fig. 7.3 is grayscale in the background. The Imini area has been divided into three structural domains: (1) A southern domain, with a southernmost poorly deformed part and an approximately E–W faulted zone, the Imini Fault Zone, (2) an intermediate domain, the Cretaceous–Tertiary Imini plateau and (3) the SAF zone and the Jurassic "nappe" of Anmiter-Tighza (Anm.-Tigh. nappe). Red stars and lines indicate outcrops for each figure. A red dotted line locates the tear-shaped anticline (for interpretation of the references to color in this figure legend, the reader is referred to the web version of this article).

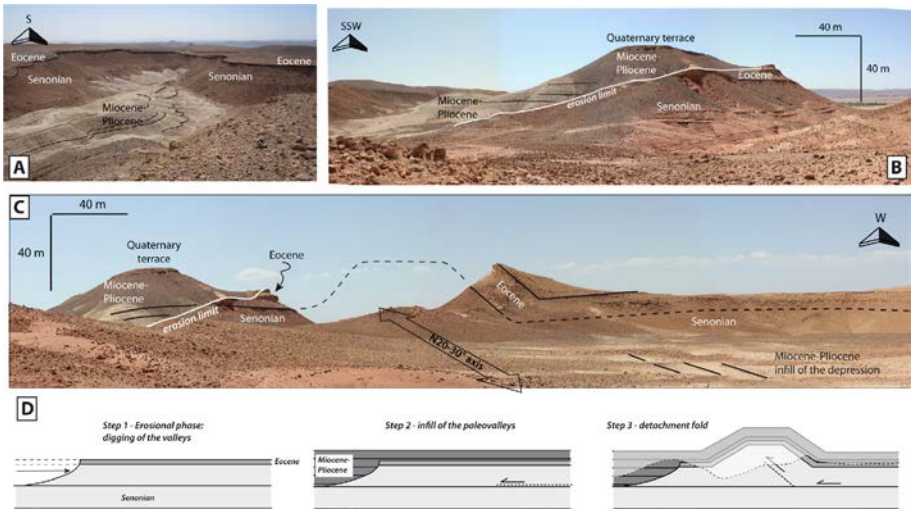

►**Fig. 7.6** Paleovalleys filled by Miocene–Pliocene formations. **a.** The Senonian and Eocene

sedimentary cover is dissected by the Miocene–Pliocene formations that lie geometrically coherent with the underlying older ones. **b.**View of the infill by Miocene–Pliocene formations inside a paleovalley. **c.** Folding of the Senonian to Miocene–Pliocene formations with schematic explanation. A dashed line represents the present erosion profile. Location is indicated in ►Fig. 7.5.

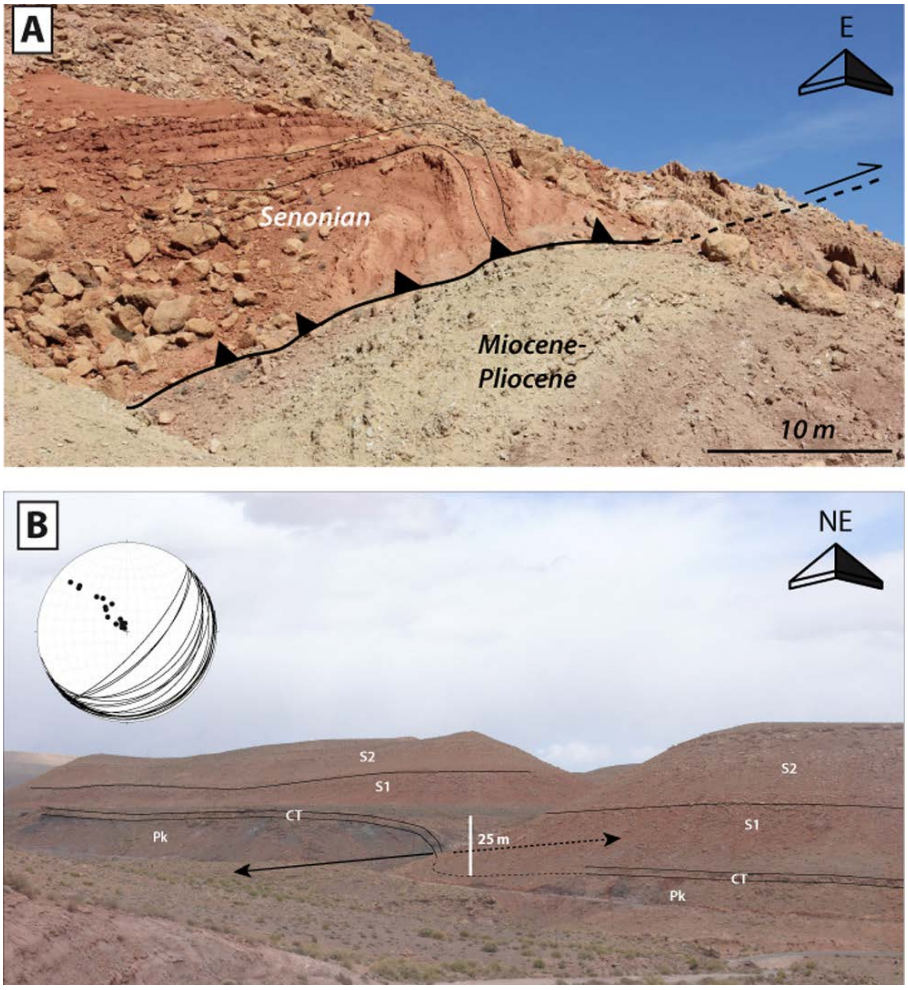

►**Fig. 7.7** Deformations in the southern domain. **a.** Folded Senonian layers over a thrust folding Miocene–Pliocene formations. **b.** Folding of CT and "Senonian" formations, south-west of the Imini anticline, location in ►Fig. 7.3. Stereogram is presented with poles from the various stratigraphic planes. Measurements were made all along the curvature, in "Senonian" and CT formations. Pk. Precambrian, CT. Cenomanian–Turonian, S1. Lower portion of the "Senonian", S2. Upper portion of the "Senonian". Location is indicated in ►Fig. 7.5.

- *The Imini fault zone*

This fault zone concentrates the main deformation of the southern domain, whose best illustration is the Imini anticline (►Fig. 7.3), which extends westward until Sour (►Fig. 7..2b). Along this globally N90° path (►Fig. 7.4), structures show various deformation types.

Inside the Imini anticline, east of Iflilte (►Fig. 7.3), the southern flank exposes Ordovician green shales, thrusting verticalized Senonian beds (►Fig. 7.8a). Roughly parallel to the Senonian beds, thick barite veins striking N90°–100° and dipping N50° mark the presence of the thrust fault. In the westernmost part of the Imini anticline (►Fig. 7.3), the Triassic and "Infracenomanian" formations are brought onto Miocene–Pliocene sub-horizontal deposits due to a north dipping reverse fault (►Fig. 7.7b). This fault, striking N90°, extends eastward and changes to a N110° direction, where it brings Triassic and "Infracenomanian" formations onto Senonian ones (►Fig. 7.3).

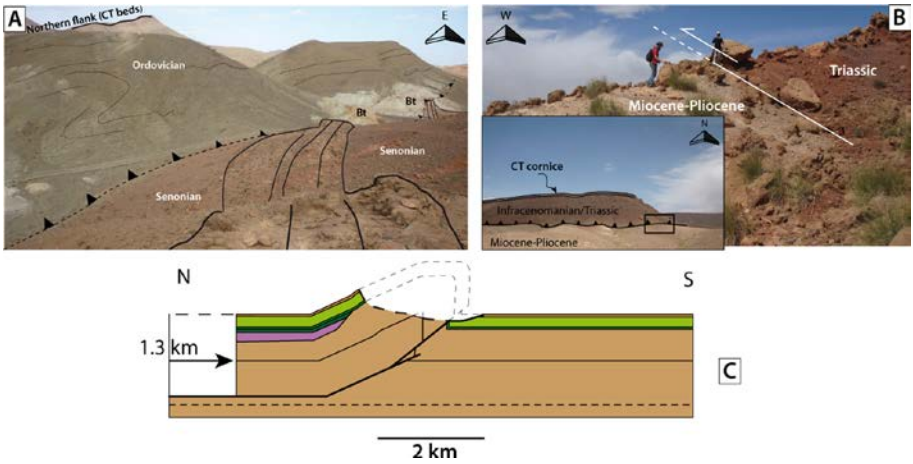

►**Fig. 7.8** Imini anticline. **a.** View of the Imini fault inside the Imini anticline, at its southern border. **b.** Thrust of Infracenomanian/Triassic formations onto Miocene deposits, west of the Imini anticline. Small panorama, view from south. Photographic focus on the thrust, view from east. **c.** N/S balanced cross-section inside the Imini anticline (approximately at the location of the photo (A)). Locations are indicated in ►Fig. 7.5. Bt: Barite.

Westward, the Senonian series and the underlying basement (Precambrian rhyolites) are thrust onto the Senonian beds (►Fig. 7.9). The fault shows an N110° strike, changing to an N90° direction eastward (►Figs. 7.3 and 7.5). Similarly, further north, two N110° striking faults deform the cover (►Fig. 7.3) and are associated with two south verging folds (►Fig. 7.10).

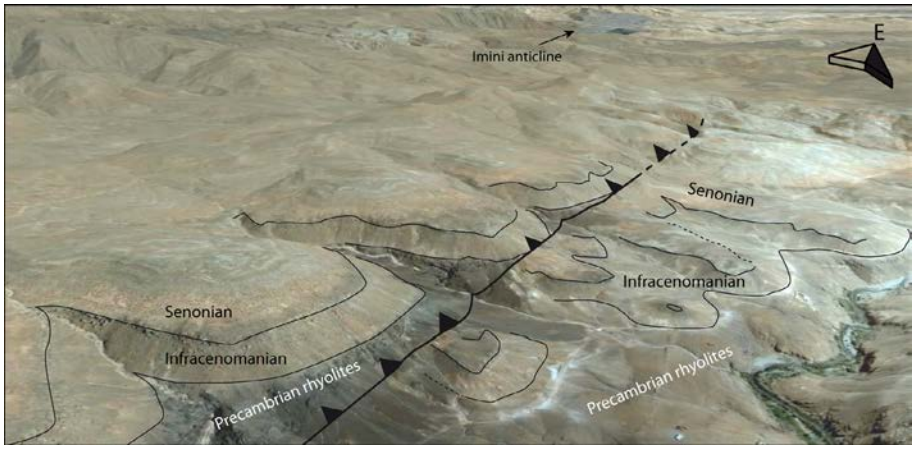

►**Fig. 7.9** Oblique view from west, North of Tazzoult-Oumradou (GoogleEarth website). A fault cuts across the basement and its Cretaceous cover, duplicating the sedimentary succession. Location is indicated in ►Fig. 7.5.

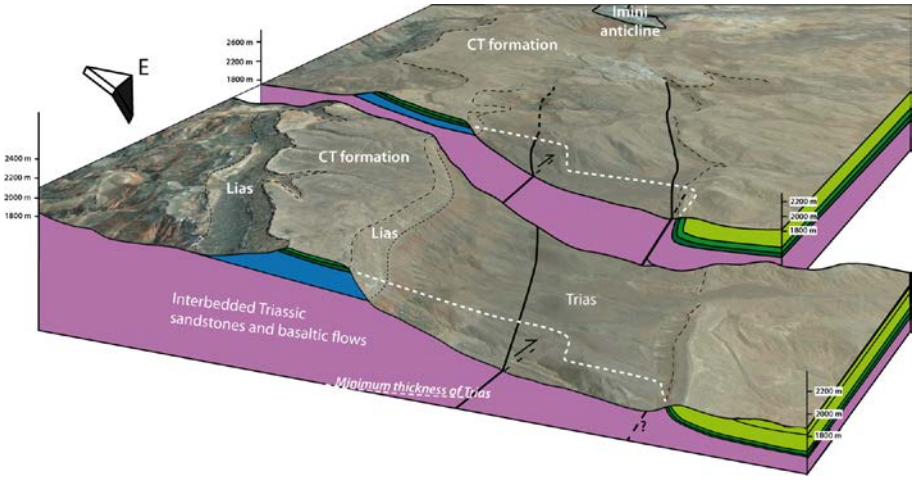

►**Fig. 7.10** Oblique view from SW in the Tazzoult Oumradou valley (►Fig. 7.3). Cross-sections are drawn from two ENE–WSW transects to illustrate the drop in elevation from North to South, due to basement faults, with N110° strikes (see ►Fig. 7.3). Location is indicated in ►Fig. 7.5.

The N90° fault of the Imini anticline (►Fig. 7.8) also extends eastward, where it becomes N70°, then N45° before probably joining the SAF (►Fig. 7.3). We examine two cross-sections in this eastern region, located in ►Fig. 7.4. The first cross-section cuts across the N70° striking fault system (►Figs. 7.5 and 7.11a and b). In this area, the river flowing southward dissects the Imini anticline prolongation striking N70° (►Fig. 7.3). The main anticlinal structure involves the basement that crops out within the core. Locally, the main thrust fault emerges and leads to a weak throw (►Fig. 7.11a). The deformation extends southward through small-scale folds

that likely result from gravity sliding on the weaker Senonian gypsum levels. The southern frontal fold involves the Miocene–Pliocene formations thrust by the Senonian–Eocene ones (►Figs. 7.11a and b).

The second cross-section is located northeast of the previous one (►Figs. 7.5 and 7.12). A schematic geological map of the region is given in ►Fig. 7.12a. The cross-section follows a N135° direction. It shows one principal reverse fault accounting for the main structure, i.e.,the major doming of the topography in the northern part of the cross-section (►Figs. 7.12b and c). As we saw in ►Fig. 7.11, the Senonian layers also underwent folding due to gravity sliding setting small-scale folds. The deformation is not transferred further south which seems to correlate with the underneath thinned Triassic layers. Miocene–Pliocene formations seem to be geometrically conformable on the Eocene ones below and folded in the same way.

7.1.3.b Imini plateau small-scale deformation

North of Iflilte, on the eastern slope of Imini valley (►Fig. 7.3), the CT cliffs show a small-scale fold (►Fig. 7.13a), which extends eastward, also folding Senonian formations. The major fold direction strikes N65° (►Figs. 7.13a and b). Disharmonic small folds in the Senonian beds show a N45° axis (N40°; ►Fig. 7.13a fold 2). Similar results are obtained for another fold located north. The axes of the folds were calculated with WinTensor (Delvaux and Sperner, 2003) using measurements (>10 for each limb) taken in the field. It is also evidenced by the elevation map of this structure (►Fig. 7.13b), the latter confirming the orientations predicted by the elevation maps.

The most striking result based on our elevation maps is seen north of the Imini anticline (►Fig. 7.13c). In ►Fig. 7.13, a succession of large folds is evidenced. They all mainly follow N70° direction, clearly oblique to the N90° Imini anticline. The Imini anticline begins to disturb the contours of the map (►Fig. 7.13c) in the southernmost part, where they become N90° oriented. The mapped folds in ►Fig. 7.13c have longer wavelengths (2–2.5 km) and higher elevations (>100 m) compared to the folds of ►Fig. 7.13b (approximate wavelength < 1 km and elevation amplitude ca. 50 m). They all involve CT, “Senonian” and Eocene formations and display very symmetrical cylindrical shapes, without associated faults.

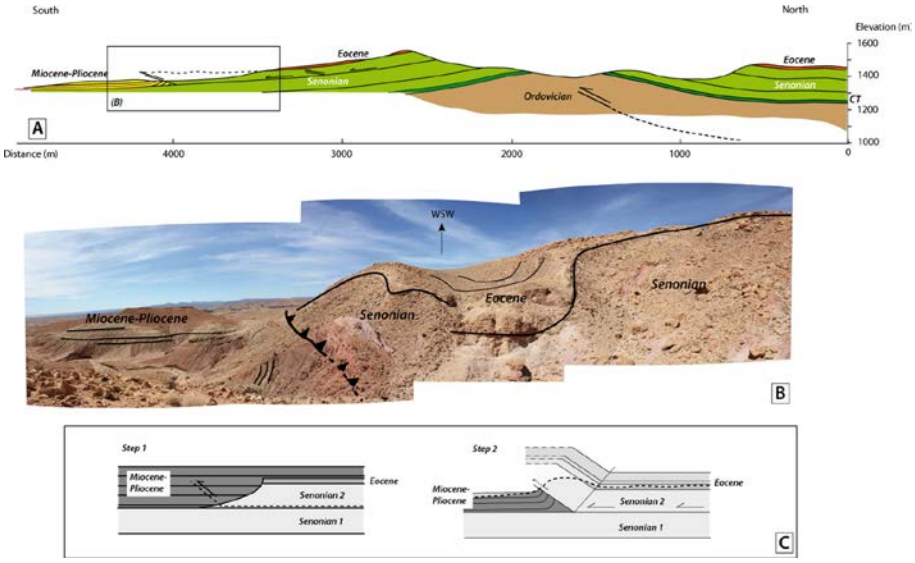

►**Fig. 7.11** Eastward cross-section 1. **a.** Interpretative cross-section. **b.** Photography of a typical outcrop in the region of the emerging outward ramps. **c.** Simple model explaining the geometry between Senonian–Eocene series and Miocene–Pliocene ones. Location is indicated in ►Fig. 7.5.

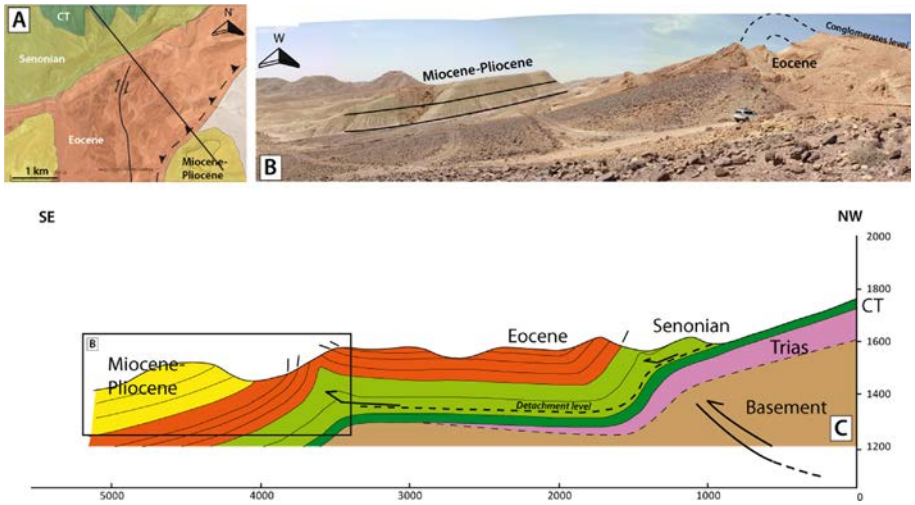

►**Fig. 7.12** Eastward cross-section 2. **a.** Geological map of the area where the cross-section is realized. Topographic bottom is extracted from Google Earth elevation data. **b.** Cross-section interpreting the main outcropping features. Under the CT could lie very thin Triassic (see ►Fig. 7.3) and thin "Infracenomanian" formations, but we have no evidence on the outcrops to confirm that. We therefore propose that it mechanically behaves as if the basement directly underlies the CT level. Locations are indicated in ►Fig. 7.5.

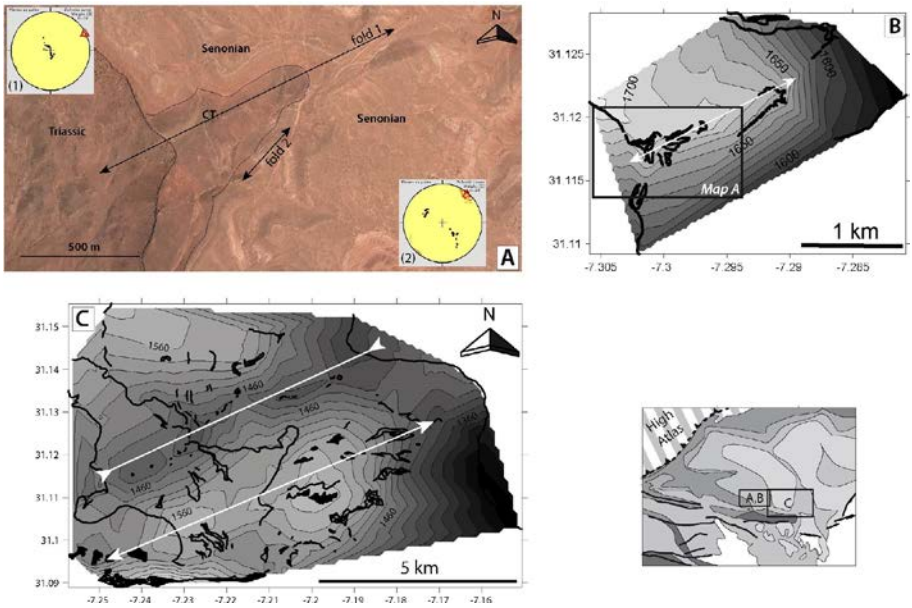

►**Fig. 7.13** «N70°» folds in the sedimentary cover north of the Imini anticline, with comparison to elevation maps. **a.** and **b.** Google Earth and elevation map views of the same fold. For fold (a), N65° (fold 1) and N40° (fold 2) horizontal axes have been calculated, and the major N64° direction compares to the one determined through the building of elevation map (b). **c.** Elevation map of the northern limb of the Imini anticline. It shows the alternation of anticlines and synclines which have wider wavelengths than folds in (a) and (b). The gray simplified map of the Imini area shows the locations of the two elevation maps.

7.1.3.c SAF zone – « nappe de Tighza/Anmiter »

- *Deformation in the district of Tiliouine (►Figs. 7.14 and 7.15)*

The SAF outcrops southeast of Tiliouine (►Fig. 7.3) and extends further east as a steep reverse fault. From the south of Tiliouine, this major fault disappears westward and instead, a large anticline folds the Mesozoic–Cenozoic cover as well as the Ordovician basement (►Figs. 7.14b and e). To the east, the SAF outcrops as a steep inverse fault, bringing the Ordovician greenish shales onto Senonian, Eocene and younger units (►Figs. 14d and c).

At the location of the first cross-section (►Fig. 7.14b), outcrops do not allow us to decipher the subsurface relationships between Eocene beds and younger Miocene–Pliocene formations. Following the SAF eastward, some valleys dissect the verticalized beds on contact with the SAF and give valuable outcrops which allow further investigation of this contact. In ►Fig. 7.15, we show an angular unconformity between detrital beds with clearly oblique contact. These beds are interpreted as overturned Eocene beds covered by overlapping unconformable Miocene–Pliocene

conglomeratic formations with a 15–20° angle. We will discuss this age attribution later.

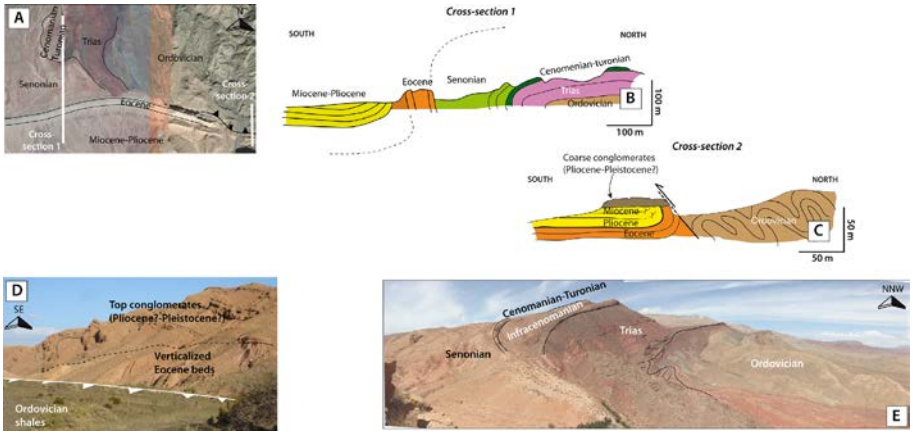

►**Fig. 7.14** SAF features in the Tiliouine area. **a.** Simplified structural map, overprinted on GoogleEarth view around Tiliouine. See more precise location through ►Fig. 7.5. **b.** N–S cross-section 1, in the "folded" western part of the area. **c.** Outcrop showing the contact between Ordovician shales and younger series Eocene and Miocene–Pliocene in age. **d.** N–S interpretative cross-section 2, in the faulted eastern part, at the location of (c). **e.** Panorama toward the NNW, seated on top of the verticalized Eocene beds.

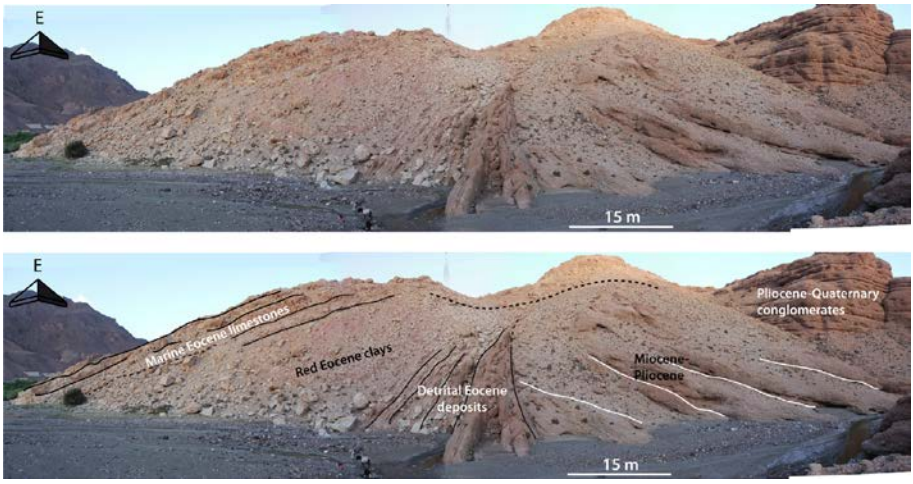

►**Fig. 7.15** Unconformity between Eocene and Miocene–Pliocene formations east of cross-section in ►Fig. 7.14. Eocene formations are overturned by the SAF in the north that brings the Ordovician shales onto younger units. They are progressively verticalized. The Miocene–Pliocene deposits overlie them through a clear angular unconformity in the center of the picture. To the south, Miocene–Pliocene formations are then capped by very coarse conglomerates, probably Pliocene or younger in age, that lie horizontally. Location in ►Fig. 7.5.

- *Anmiter-Tighza nappe (►Figs. 7.16)*

Northeast of the Telouet locality (►Fig. 7.3), a thrust sheet has been identified. It is part of a group of various Jurassic thrust sheets or "nappes" that exist along the SAF, whose best-studied example is the Toundout "nappe" (Laville, 1975; Tesón and Teixell, 2008). Here, a minimum 500 m-thick succession of mainly marine limestones topped with 100–200 m of Jurassic continental red beds has slid southwards (►Figs. 7.3 and 7.16). ►Fig. 7.16a shows the "nappe" contact, looking west. Senonian, CT and "Infracenomanian" are overturned in front of the "nappe" contact (►Fig. 7.16b). The basal contact of the "nappe" is marked by deformed and faulted slices of Liassic–Triassic sediments. Going north, the "nappe" forms a broad anticline, with poorly deformed beds. The fact that the décollement at the base of the thrust sheet is folded indicates a two-step chronology (►Fig. 7.16b). First, the sliding of the "nappe" was triggered by the uplift of the belt, enabled by the Triassic décollement on evaporite layers. This gravity gliding generates the slices of Liassic–Triassic material at the bottom of the "nappe". Second, a folding step shaped the "nappe" into a wide anticline whose hinge has subsequently been eroded.

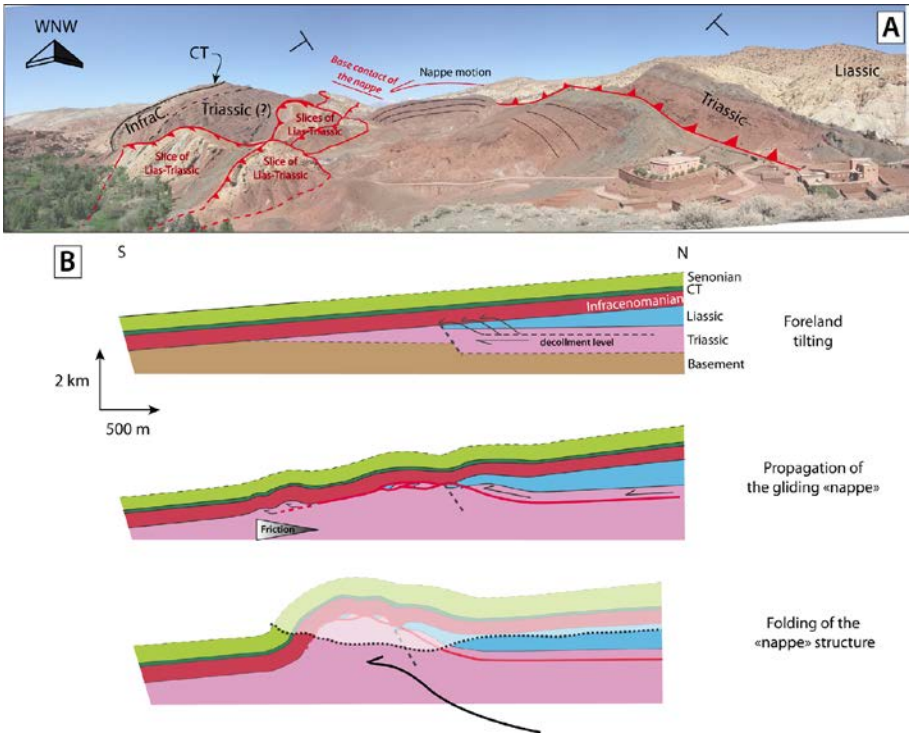

►**Fig. 7.16 a.** Anmiter-Tighza Nappe. Interpreted view from the East. Location in ►Fig. 7.5. **b.** Interpretative cross-section of the Anmiter-Tighza Nappe. Vertical and horizontal scales are approximative.

7.1.3.d The Eocene stratigraphy in the Imini area

From our observations and the available bibliography, the basal Paleogene is marked by a fossil-rich carbonate layer, which constitutes a remarkable benchmark in the topography of the region (15–25 m thick). Above, a white clay package with few carbonate beds and abundant marine fauna conformably overlies it (30–50 m-thick). In the studied area, the marine Eocene sedimentation ends between Lutetian and Bartonian (El Harfi *et al.*, 2001). On top of this sequence lies a more or less horizontal erosion surface with unconformable conglomerates (►Fig. 7.17; observations close to ►Fig. 7.11). The same conglomerates can also be observed directly on top of the basal Paleogene or older series, with an erosion limit between them. These unconformable deposits rest apparently parallel to older formations (south of cross-section in ►Fig. 7.12b). These conglomerates mainly reworked the underlying marine rocks. Based on our observations, few pebbles from the Central High Atlas region can be identified within. When they exist, these pebbles are made of Precambrian rhyolites, scarce Triassic basalts and sandstones, whereas Jurassic carbonates are very rare. These conglomerates are then tilted by later deformation events, and measures of strike-slip fault systems in these conglomerates proved to be compatible with the general stress regime in the Atlas belt (►Fig. 7.17d; Frizon de Lamotte *et al.*, 2000). The whole Eocene formation is rarely fully preserved in this region. It is better known eastward in the Ouarzazate basin (Choubert, 1970, Ouarzazate sheet 1:200,000; and review in El Harfi *et al.*, 2001).

7.1.4 Discussion

Based on the collected data, we discuss the ages and styles of deformation in the Imini area, along the SAF and further into the foreland. Our structural data and stratigraphical constraints are used to support time constraints on the relative chronology of the tectonic events. After proposing a chronology for these various tectonic events and discussing the styles of deformation, we then integrate this data into the larger geodynamic frame of the Atlas orogeny.

7.1.4.a Time constraints for the deformation in the Imini area

- *First detrital deposits – post-marine Eocene*

Given their parallel position on marine Eocene in our region, we believe the first detrital deposits (►Fig. 7.17) to be Upper Eocene in age following El Harfi *et al.* (2001). These deposits do not show a significant southward extension. Moreover, they consist in mostly reworked material from the underlying sediments with Paleogene fossil-rich limestone, and very few elements of basement (►Fig. 7.17). The decimetric size of the pebbles indicates a close source, whereas the scarcity of

basement elements and Jurassic limestones indicates either poor erosion of the Central High Atlas basement and cover, or the dismantling of a potentially thin Senonian–Eocene cover now eroded in the Central High Atlas. However, the building of a relatively significant topography is required to explain these deposits, here in the Imini area, but also along the northern border of the Ouarzazate basin (El Harfi *et al.*, 2001). The unconformity in the Tiliouine area (►Fig. 7.15, this study) and another outcrop described in Pastor *et al.* (2012) may originate from this early event, but the main inferences concerning this event come from the sedimentary record (see review in Frizon de Lamotte *et al.*, 2000; El Harfi *et al.*, 2001).

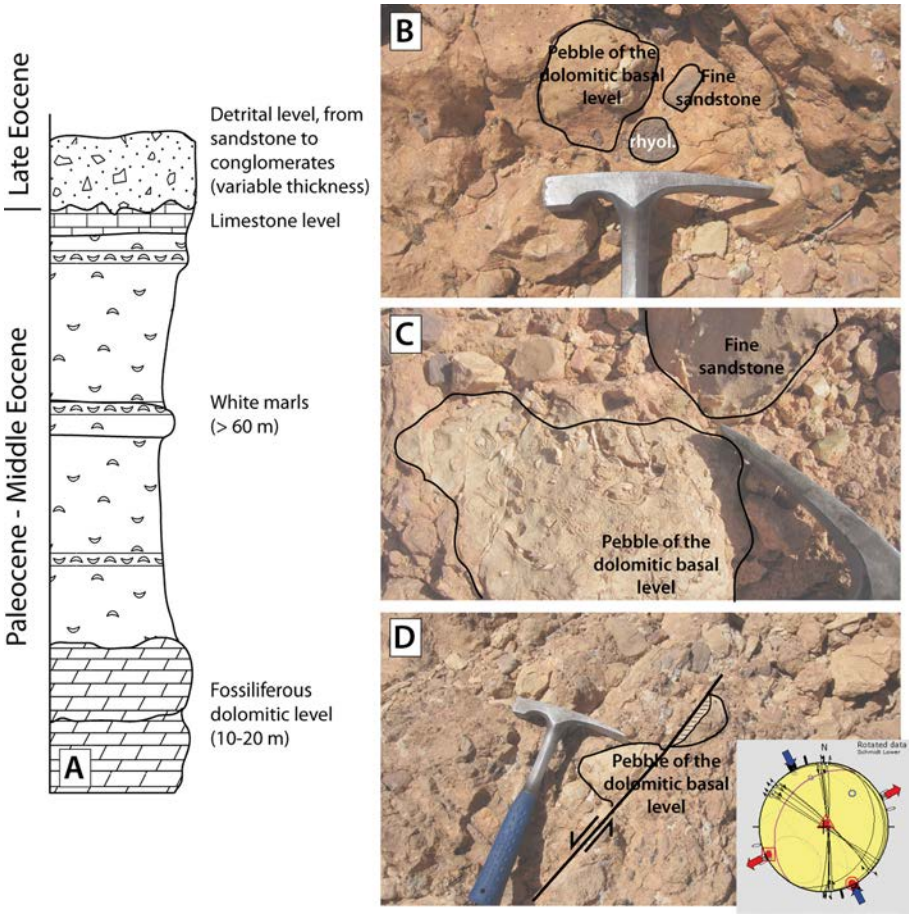

►**Fig. 7.17** Facies of the detrital Upper Eocene formation and schematic log of the Eocene *s.l.* (the dolomitic level could be Paleocene in age). **a.** Paleogene stratigraphic log of the Imini area, with the upper detrital member (Aït Arbi/Hadida Formation) where we took the pictures b, c and d. **b.** and **c.** Conglomerates with pebbles from the lower levels: dolomitic and limestone levels from Paleogene, sandstone from Triassic and Precambrian rhyolite pebbles. **d.** Conglomerate with a dolomitic pebble faulted by one of the strike-slip faults, perpendicular to bedding. Conjugate fault systems allow the calculation of a stress tensor (10 data) that we

present unfolded with σ1 = N153°–03° NW; σ2 = N31°–84°NE; σ3 = N63°–05° SW. This strike-slip regime is compatible with our observations and with the general compressive stress regime of the Atlas region (Frizon de Lamotte *et al.*, 2000b; Bracène and Frizon de Lamotte, 2002).

- *Relationships between Miocene–Pliocene formations and older ones*

Overall, in the Imini district, there is no clear evidence of an angular unconformity between Senonian–Eocene formations and the Miocene–Pliocene ones. In most of the studied sites, the Miocene–Pliocene formations display the same dip as the older ones, either Senonian or Eocene. They can even be involved in deformation in such way that they keep the same dips as the older Senonian—Eocene formations (►Figs. 7.6b and c, 7.7, 7.11, 7.12, 7.14).

The Miocene–Pliocene deposits are mostly visible in the southern domain where they fill and sometimes overflow on the older reliefs (►Figs. 6b and c). At the location of ►Figs. 7.12 and 7.14, detrital Eocene deposits are overlain by unconformable palustrine–lacustrine Miocene–Pliocene formations which show the same dip. For the outcrops described in ►Fig. 7.6, wherever the sedimentary contact is observed, horizontal Miocene–Pliocene formations always fill eroded reliefs made of older horizontal formations. The same can be deduced from the observation of the southern termination of the cross-section in ►Figs. 7.11a and c, the region being the northeast lateral equivalent of ►Fig. 7.6b and c outcrops. All these observations point to a major erosion event before the deposition of the palustrine–lacustrine Miocene–Pliocene units of the studied area.

Following the observations made in ►Fig. 7.5, this erosion phase must have occurred between the end of the deposition of marine Eocene and the base of palustrine–lacustrine Miocene–Pliocene deposits, i.e.,before the Langhian–Early Serravallian (Tesón *et al.*, 2010). On this site (►Fig. 7.6), no conglomerates underline either the base of the Miocene–Pliocene formations or the top of the Senonian–Eocene formations and we can tentatively explain this by the large distance (25–30 km) from the SAF. With a maximum duration from Late Eocene to Early Miocene, an erosion phase thus occurs and can be explained by either (1) the creation of a relief and its dismantling and/or (2) an important drop in base-level. A low-stand sea-level is recorded during the Oligocene, with maximum amplitude of 50 m (Miller *et al.*, 2005) 2005), which is close to the approximate height of the Eocene cliffs (40–50 m) compared to the base of Miocene–Pliocene formations in ►Fig. 7.6. Nevertheless, as underlined by El Harfi *et al.* (2001), sedimentation is considered endorheic in the Ouarzazate realm during most of the Neogene. Thus, given the distance to the sea at that time, it is unlikely that this erosion was triggered by the sea-level drop. We favor the hypothesis of an active mechanism uplifting the surface after the Late Eocene.

We note that the infill of paleovalleys in older formations is also observed southward in the Anti-Atlas (Görler *et al.*, 1988), and probably indicates that a considerable area was subjected to erosion before the sedimentation of the palustrine–lacustrine member of the Aït Kandoula Formation in Middle–Late Miocene. The observations and interpretations made in ►Figs. 7.6 and 7.11 imply that this erosion phase cannot be correlated to tectonic deformation and needs to be linked to other processes.

- *Post-Miocene–Pliocene deformations*

On many sites, the Miocene–Pliocene formations are involved in deformation that occurred clearly after their deposition. In the southernmost location, we favor a Late Miocene or post-Miocene age for the setting of the small detachment fold (►Fig. 7.6a) and for the thrust that lies north of this Miocene–Pliocene depression (►Figs. 7.3 and 7.7). There, and in most places where the Miocene– Pliocene formations present this lacustrine–palustrine facies (►Figs. 7.8b, 7.11, 7.12, 7.14), we must postpone its deformation to the Late Miocene or later. This is also confirmed by the fact that this lacustrine–palustrine member is often unconformably overlaid by Quaternary terraces.

Red and detrital Miocene–Pliocene deposits increase in proportion to the north, close to the front and the coarsest deposits often top the underlying lacustrine facies (►Figs. 7.14d and 7.15). In our interpretation of the geometry of the front in ►Fig. 7.14d, we also note that coarse deposits can sometimes be unconformable with Miocene–Pliocene formations. We suggest that these conglomerates accumulations represent younger formations, linked to the activity of the SAF at that location. They prove the occurrence of a late and probably still active deformation event on the SAF. This ongoing deformation is also identified elsewhere in the Atlas orogeny (Sébrier *et al.*, 2006; Pastor *et al.*, 2012).

- *The "nappe" issue*

North of the Imini district, the contact of the Jurassic Anmiter-Tighza "nappe" has been described in this study. Nonetheless, the allochtonous sediments of this "nappe" are not younger than Upper Jurassic and cannot help to date its setting. At the front of the "nappe", Eocene sediments are however overturned by the frontal contact and help to constrain the motion of the "nappe" to post-Eocene times. Other Jurassic "nappes" are identified in the Central High Atlas, whose origins are considered both gravitational and tectonic (►Fig. 7.2; Laville *et al.*, 1977; Görler *et al.*, 1988; Laville and Piqué, 1992). They were probably set at the same time as the Toundout "nappe". Sediments from the Aït Ouglif Formation (Middle Miocene; ►Fig. 7.4) are transported by the Toundout "nappe" and are unconformable (Görler *et al.*, 1988). Moreover, the Toundout "nappe" also overlies slices of the Aït Ouglif Formation. This

double constraint demonstrates that its motion occurred in Early(?)–Middle Miocene times (based on paleontological evidence in Görler *et al.*, 1988). Moreover, protracted deformation occurred given the progressive aspect of the Aït Ouglif unconformity on the Lias "nappe" of Toundout (Laville *et al.*, 1977; Görler *et al.*, 1988). In this case, "nappes" setting is suggested to occur during the Early(?)–Middle Miocene, and is probably linked to the building of a topography. We suggest a similar timing for the Anmiter-Tighza "nappe" setting, at least for the initial sliding event, given its later re-folding (►Fig. 7.16). The later folding can tentatively be related to the activation of the SAF and occurred during the Late Miocene/post-Miocene period.

7.1.4.b Styles of deformation across the Imini area

We show in the following discussion that the style of deformation in the Imini area can be separated between an early cover phenomenon with detachment folds or gravity sliding and late deformations involving the basement. Cases of interactions between these two types can also occur.

- *Early cover deformations and "nappes" setting*

Cover deformations of varying amplitudes are recorded widely in the area. Deformation affecting the cover is expressed through the setting of folds and thrusts of usually low amplitude observed in the cover from the Cenomanian–Turonian (e.g., ►Fig. 7.13) to the Miocene–Pliocene formations (e.g., ►Figs. 7.6 and 7.7). Moreover, more large-scale deformations occurred through the setting of "nappes".

North of the Imini anticline, the Imini plateau shows the setting of N70° folds of weak amplitude (shortening is less than 1–2%), that deform the cover from Cenomanian–Turonian to Eocene formations (►Fig. 7.13). We could not identify faults related to their formation and interpreted them as detachment folds. Their orientation is quite parallel to the orientation of the Atlas belt and we propose that they result from a limited sliding of the Imini plateau, from the northwest. This possibility of sliding is also attested by highly folded Triassic evaporites layers in the western part of the Imini area. The slide of the plateau southward, favored by the efficient Triassic evaporites décollement levels, would have stopped to the south with the thinning and disappearance of these evaporitic units (cross-section in ►Fig. 7.3). The shortening associated with the diminution of transport to the south would then have been accommodated by detachment folds in the cover (►Figs. 7.11–13) due to the increasing friction. At the northern limb of the Imini anticline, a cross-cutting relationship also exists between the N70° folds of the cover (►Fig. 7.13) and the N90° Imini anticline. This sliding was then followed by the subsequent Late or post-Miocene deformation phase that set the Imini anticline and the Imini Fault Zone. The "nappe" issue also concerns the Anmiter-Tighza "nappe". The sliding was probably favored by a décollement level in the Upper Triassic salts, as witnessed by the Lias-

Triassic chips brought by the basal contact with the "nappe" (►Fig. 7.16). Later deformation events have refolded the structure when the SAF was activated in Late Miocene/post-Miocene.

A peculiar "domal" anticline, with a Triassic sediment core, is located ENE of the Imini anticline (►Figs. 7.3 and 7.5; north of the cross-section in ►Fig. 7.12), with a tear or drop shape. Its southern boundary is involved in the NE–SW structures presented in ►Fig. 7.12, and follows the N90–N70° directions already identified further west (►Figs. 7.5 and 7.13). On the opposite side, its "northern" limb is refolded in a direction parallel to the border of the Anmiter-Tigzha "nappe" in this area (►Fig. 7.3). This structure could result from a two-step evolution: one is related to the sliding of the Anmiter-Tigzha "nappe", whereas the other must be related to the setting of E–W, NE–SW structures and was structured later. For the "nappes" setting, cover deformation might nonetheless have been possible only through the activation of basement faults in the inner belt that triggered the increase of topography or the development of a lithospheric anomaly at that time (Teixell et al., 2005; Missenard et al., 2006, 2008).

Where the Miocene–Pliocene formations exist, i.e.,mainly south of the Imini anticline (►Fig. 7.3), they underwent very weak deformations that also involve the Senonian. They develop small folds (fault-propagation folds, ►Fig. 7.6) and thrusts (►Fig. 7.7). For example, the N90° thrust in ►Fig. 7.7 is representative of these weakly accommodating structures (vertical throw ~60–80 m; horizontal shortening ~40–45 m). It probably connects to a quite shallow décollement level, maybe the gypsum levels of Senonian formations. Orientations of these structures are mainly N90° or N45°, or even N20–30° as observed in ►Fig. 7.6a, and potentially influenced by deeper inherited structures of the Anti-Atlas. The weak Senonian levels play a major role as they act as a major décollement level (►Fig. 7.11; (Missenard *et al.*, 2007).

- *Late thick-skinned deformations*

Across the whole studied area, deformations involving the basement are concentrated on the SAF and the Imini Fault Zone (►Fig. 7.5). The role of the basement is obvious in the Imini anticline and its prolongations (►Fig. 7.8), east and west in the Imini Fault Zone (►Figs. 7.9 and 7.10). This deformation belt accommodates an important shortening. For example, in ►Fig. 7.10, a double inverse fault system dismantles the sedimentary cover with an average vertical throw of 400 m, whereas the horizontal shortening on this structure is estimated at 15–20% (ca. 300–400 m, based on ►Fig. 7.10). This double fault system is likely to be the westward prolongation of the fault bounding the southern edge of the Imini anticline (►Fig. 7.8c). The Imini anticline is the location where the maximum shortening is accommodated in the Imini Fault Zone, with 1.3 km (with a *Integration in the general frame of the Atlas*

geodynamics fault-propagation model, ►Fig. 7.8C, designed with Ramp (Mercier *et al.*, 1997). The interpretation of the folding at the location of the Imini anticline shows a décollement level in the Ordovician green shales (►Figs. 7.8a and c). This décollement level does not exist further west (►Fig. 7.10), and appears as a basement fault. Overall, the deformation in this western part is characterized by the involvement of the Precambrian and Paleozoic basement, which characterized a thick-skinned deformation.

Eastward from the Imini anticline, the fault zone also extends in the Ordovician shales since they outcrop in the core of the anticline (►Fig. 7.11). Here, the Triassic formations are lacking, as these formations end along a N60–70° direction from the Imini anticline eastward (►Fig. 7.3). The shortening decreased compared to the Imini given the poor amplitude of the structure (►Fig. 7.11). A small part of the shortening is also accommodated on secondary structures, following a Senonian décollement level (►Fig. 7.11), which folded the Senonian to Miocene–Pliocene formations. Further east, the post-Senonian cover becomes thicker (►Fig. 7.12), with a thickening of Eocene white clays up to ~50 m, on which detrital conformable deposits exist. Structure strike also changes from a more N90° trend to a N45° one (►Figs. 7.3 and 7.12). Here, the northern fold is controlled by a basement fault that propagates southward in the Senonian cover (►Fig. 7.12).

South of the Imini Fault Zone (►Fig. 7.5), small secondary deformations also involve the basement where the sedimentary cover becomes very thin. In ►Fig. 7.9, a N110° reverse fault with a 40–60 m vertical throw affects the Precambrian rhyolites and overlying sedimentary cover and in ►Fig. 7.7, a basement fault sets a small N45° fold with a 25–30 m amplitude.

The SAF bounds the Imini Cretaceous–Tertiary plateau to the west and to the north (►Figs. 7.2 and 7.3). It has been described by Missenard *et al.* (2007; ►Fig. 7.3, cross-section). It corresponds to a steep thrust fault that disappears eastward of Telouet (►Fig. 7.3), below the Anmiter-Tigzha “nappe”, where it could be responsible for the late refolding of the “nappe”. The SAF remains hidden in the Tiliouine area, giving rise to large folded series (►Figs. 7.14b and e). It emerges to the East as a thrust fault that brings the Ordovician shales onto overturned Mesozoic–Cenozoic formations (►Figs. 7.14c and d). The outcrop of ►Fig. 7.14d and its interpretation demonstrate that the last movements along the SAF must be post-Miocene–Pliocene.

7.1.4.c Integration in the general frame of the Atlas geodynamics

- *Eocene/early post-Eocene events (►Fig. 7.18a)*

This event is not widely documented in Morocco and very little structural evidence exists to attest to its existence. Late Eocene represents one of the main pulses of detrital sedimentation recorded in the Imini area (this study) and the Ouarzazate basin (El Harfi *et al.*, 2001). Detrital deposits lie conformably on marine Eocene in most of the outcrops, and suggest either distal uplift of a proto-orogen compared to the present position of the front, or localized uplifting source areas. These deposits were mostly supplied by Paleogene sedimentary cover, and further east by the uplift of the Skoura massif (El Harfi *et al.*, 2001). Compared to what happened in Algeria (Laffitte, 1939; Ghandriche, 1991; Vially *et al.*, 1994; Mekireche *et al.*, 1998) or Tunisia (Snoke *et al.*, 1988; El Euchi, 1993; Khomsi *et al.*, 2006), where a Late Eocene phase is clearly identified, Morocco is poorly deformed at that time. The Atlas domain in Morocco underwent significant uplift, enough to trigger the infill of foreland basins with detrital deposits. The decreasing deformation gradient from East to West has already been suspected on the basis of calculated shortening rates (Brede *et al.*, 1992; Teixell *et al.*, 2003). Given the anti-clockwise direction of the rotation of Africa at that time (Rosenbaum *et al.*, 2002), linear speed of convergence was clearly higher in the East of the Maghreb, whereas Morocco was closer to the rotation pole. This simple explanation could account for the decrease of deformation leading to more discrete tectonic structures in Morocco during Late Eocene. Also, a lithospheric component has been suggested as being responsible for a portion of the created topography (Missenard and Cadoux, 2012; Kaislaniemi and Hunen, 2014).

- *Early(?)–Middle Miocene to Quaternary deformations events (►Figs. 7.18c and e)*

Langhian(-Early Serravallian?) times (following Tesón *et al.*, 2010; Aït Ouglif Formation age) witnessed the earliest recorded structural deformation and the development of the topography. This is shown by: (1) the setting of the various "nappes" across the High Atlas of Marrakech and the Central High Atlas (Laville *et al.*, 1977; this study), (2) the influx of the unconformable detrital deposits of the Aït Ouglif formation (El Harfi *et al.*, 2001), (3) the resuming of deformation, as suggested by a structural study of Tesón and Teixell (2008) and (4) the record of an important exhumation within the Marrakech High Atlas (Missenard et al., 2008; Balestrieri et al., 2009).

Wherever Miocene–Pliocene palustrine–lacustrine formations were deposited in the Imini area and eastward in the Ouarzazate basin, they are either unconformable with dips similar to those of older formations (this study), or clearly unconformable (in the Ouarzazate Basin; Görler *et al.*, 1988; El Harfi *et al.*, 2001;

►Fig. 7.15). The fact they generally fill an old topography requires a prior general uplift of the southern region of the Imini district. Such uplift is unlikely to be a local feature and probably extended to the whole studied area and even to the Anti Atlas (Görler *et al.*, 1988) and the High Atlas. This uplift took place before the deposition of palustrine–lacustrine sediments of the Aït Kandoula Formation (with a Langhian–Early Serravallian age for its basal part). The palustrine–lacustrine lower member of the Aït Kandoula Formation indicates that this uplifting period must have been followed by an actively subsiding phase to allow the Miocene–Pliocene formations to overflow the paleotopography. We propose that this large uplift recorded in the Imini area was at the origin of the topography initiating the "nappes" setting further north.

Following the studies of Missenard *et al.* (2008) and Balestrieri *et al.* (2009), based on low-temperature thermochronology (LTT), we suggest that this Early(?)–Middle Miocene exhumation is linked to lithospheric thinning at that time (i.e.,before Langhian–Early Serravalian). The timing of this lithospheric thinning deduced from LTT data is nevertheless at odds with the interpretation by Babault *et al.* (2008). Based on stratigraphical evidence of (1) marine Messinian deposits at present day elevation of ca. 1000 m and (2) tilted lacustrine Pliocene deposits (from 500 to more than 1000 m in elevation), these authors proposed a post-Messinian age for the setting of the lithospheric thinning and the associated uplift. Considering that the lithospheric thinning resulted from edge-driven convection (Missenard and Cadoux, 2012), Kaislaniemi and Hunen (2014) have conducted numerical modeling of edge-driven convection. They show, in the case of Morocco, that a 17–27 Ma periodicity could separate two pulses of magmatism. These pulses may be correlated to the surface uplift. Thus, with a first lithospheric thinning during Early(?)– Middle Miocene (23–14 Ma) and a second one proposed by Babault *et al.* (2008) to be post-Messinian (younger than 5 Ma), the minimal periodicity of 17 Ma is likely and might explain why two different deformation phases exist in Morocco after the Late Eocene phase.

In this interpretation, the Early(?)–Middle Miocene uplift created the topographic conditions to initiate the sliding of the "nappes" (Jurassic "nappes", Imini plateau). Nonetheless, a shortening component may have also played a role during this first lithospheric thinning phase (Tesón and Teixell, 2008), even for the sliding of the Jurassic "nappes" (Laville *et al.*, 1977; Görler *et al.*, 1988; Laville and Piqué, 1992). The lithospheric issue is intrinsic to Morocco compared to the rest of the Maghreb and mostly located under the Marrakech and western High Atlas (Missenard and Cadoux, 2012). Moreover, no coeval tectonic phase was recorded elsewhere in the Algerian and Tunisian Atlas before Langhian–Early Serravallian times(Frizon de Lamotte *et al.*, 2000b). Then, a unique tectono-thermal phase occurred in the Marrakech High Atlas at that period.

A remaining question is why the "nappe" setting occurred during the Early(?)–Middle Miocene deformation phase if a first topographic building event took place earlier in the Late Eocene. We propose, based on an analogy with salt tectonics on passive margins (Brun and Fort, 2011) that given a tilt angle, the thickness of the cover is the primary determining factor for the sliding. Here the same reasoning is suggested: (1) the thick cover in the High Atlas began to be dismantled during the Late Eocene event, but remains thick enough to prevent the sliding and (2) the renewal increase in topography during Miocene happened with a sufficiently thin cover to trigger the décollement of the evaporites layers.

Finally, deformation resumes in Late Miocene–Pliocene to give the Moroccan Atlas its present shape. This phase is widely recorded in the Imini area (Imini Fault Zone, SAF in the Tiliouine area) and is the most important phase in the actual shaping of the belt at least in its southern foreland (►Fig. 7.18e; this study; (Saint-Bézar *et al.*, 1998; Frizon de Lamotte *et al.*, 2000b; Missenard *et al.*, 2007; Tesón and Teixell, 2008). Moreover, this last deformation phase is overprinted by the late lithospheric thinning event (Babault *et al.*, 2008) that produces an additional kilometer of topography across the Marrakech High Atlas (Missenard *et al.*, 2006).

- *What about the "quiescent" phases?*

One remaining question concerns the "quiescent" phases. This is the case between (1) Serravallian and Messinian and (2) Oligocene and Early Miocene.

The Serravallian to Messinian quiescent event occurred when the sediments of the lower member of the Aït Kandoula Formation were deposited, in such a way that they even overflowed the old topography (►Fig. 7.6). This formation does not crop out only in the southern foreland but also in many regions: the interior of the Central High Atlas (in "la Cathédrale" and related outcrops, Görler *et al.*, 1988) and in the Anti-Atlas directly south of the Imini district (Choubert, 1945; Gauthier, 1957). These sediments, mainly palustrine–lacustrine in this region, become more detrital in the north (El Harfi *et al.*, 2001, their ►Fig. 7.12a) where they belong to a proximal alluvial deposits complex, probably washing up the remnants of a low topography. Elsewhere far from the Middle Miocene front of the belt, deposition occurred in the calm palustrine–lacustrine environments of the endorheic Ouarzazate Basin. Following the onset of the first lithospheric thinning, this large-scale thermal uplift decreased in intensity, allowing a transiently subsident context that allowed the deposition of the lower member of the Aït Kandoula Formation (►Fig. 7.18d).

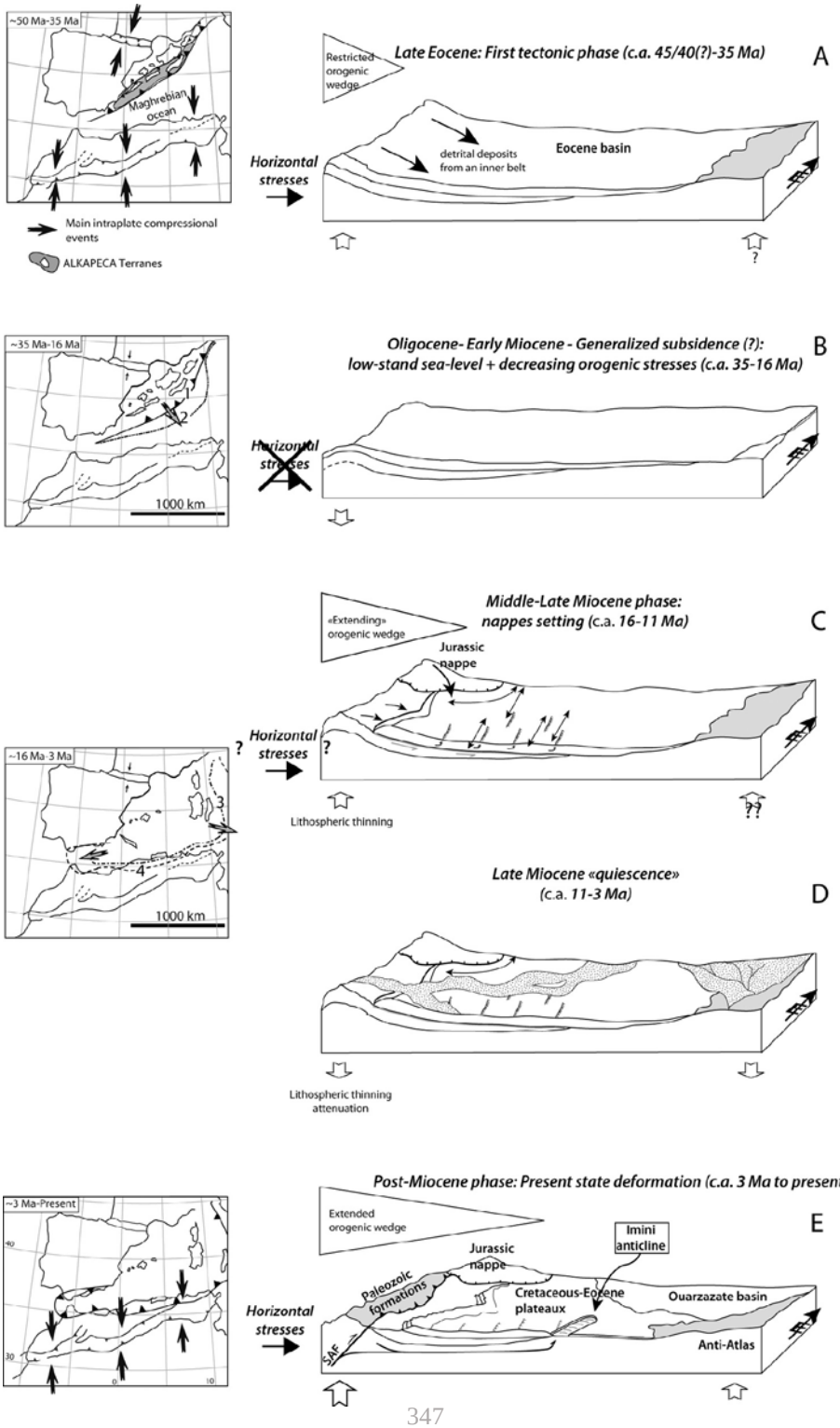
~50 Ma-35 Ma
Maghrebian ocean
Main intraplate compressional events
ALKAPECA Terranes
Restricted orogenic wedge
Late Eocene: First tectonic phase (c.a. 45/40(?)-35 Ma)
A
Horizontal stresses
detrital deposits from an inner belt
Eocene basin
?
~35 Ma-16 Ma
1000 km
Oligocene- Early Miocene - Generalized subsidence (?):
low-stand sea-level + decreasing orogenic stresses (c.a. 35-16 Ma)
B
Horizontal stresses
«Extending» orogenic wedge
Middle-Late Miocene phase:
nappes setting (c.a. 16-11 Ma)
C
Jurassic nappe
Horizontal stresses
?
Lithospheric thinning
??
~16 Ma-3 Ma
1000 km
Late Miocene «quiescence»
(c.a. 11-3 Ma)
D
Lithospheric thinning attenuation
~3 Ma-Present
Post-Miocene phase: Present state deformation (c.a. 3 Ma to present)
Extended orogenic wedge
E
Imini anticline
Jurassic nappe
Paleozoic formations
Cretaceous-Eocene plateaux
Ouarzazate basin
Anti-Atlas
SAF
Horizontal stresses

►**Fig. 7.18** Schematic evolution of the Imini region during the various steps of the Atlas orogeny. A paleogeographic map of the Western Mediterranean is provided for each step, adapted from Missenard (2006). Dislocation of the ALKAPECA terrane (Bouillin, 1986) is shown through the evolution of the trench position of the retreating slab, materialized with the bold dashed lines. **a.** Late Eocene events. **b.** Oligocene–Miocene ‘‘quiescent’’ phase. **c.** Middle Miocene phase, corresponding to the ‘‘nappes’’ setting and the occurrence of the uplift related to the lithospheric thinning. Deposition of the detrital Aït Ouglif Formation. **d.** Late Miocene ‘‘quiescent’’ phase, with large-scale subsidence. Deposition of the alluvial/palustrine–lacustrine Aït Kandoula Formation. **e.** Post-Miocene tectonic phase. Extension of the orogenic wedge through the setting of the Imini Fault Zone and activation of the SAF. For each time step, mean positions of the trench are represented for various intervals i.e., (1) 34–23 Ma, (2) 23–16 Ma, (3) 16–11 Ma and from (4) 11 Ma to present.

The Oligocene–Early(?) Miocene quiescent phase is more puzzling, because we need to explain a time gap from the end of Eocene–Early Oligocene to at least the Early Miocene–Middle Miocene (up to a maximum of 20 Ma). No Oligocene deposit exists in this region of Morocco and the topography was likely decreased to a minimum height. The deformation in the Atlas of Morocco is usually thought to result from the transfer of the Africa/Europe convergence accommodation (Frizon de Lamotte *et al.*, 2000b). The forces exerting during Late Eocene were suddenly released from the beginning of the roll-back of the African slab in the Oligocene, helping the volume’s forces to overcome the horizontal orogenic stresses. This led the topography to crumble at that time and stop the sedimentary supply of the foreland basins (►Fig. 7.18b). Moreover, a decrease of the sea-level occurred during the Oligocene (Miller *et al.*, 2005) preventing important accumulations of sediments within the Ouarzazate basin maybe still connected to the Atlantic Ocean.

7.1.5 Conclusion

We have studied here the southern foreland of the High Atlas of Marrakech-Central High Atlas in the Imini area. This region represents the westernmost tip of the Ouarzazate foreland basin before the Siroua massif uplift dismantles the cover westward between this basin and the Souss basin. The Imini area displays an important portion of the Cenozoic sedimentary record and tectonic structures that allow us to discuss the chronology of deformation events in the setting of the High Atlas in Morocco:

(1) An early event occurred in Late Eocene. The sedimentary record shows a brutal transition from a marine to a conglomeratic continental formation, which is preserved mainly close to the inner belt. The latter is conformable in the Imini area and the Ouarzazate basin and suggests the existence of a narrow Late Eocene belt, whose front was further north.

(2) Oligocene–Early Miocene times witnessed a “quiescent” phase related to the release of orogenic horizontal stresses at the Africa/Europe plate limit and a rapid decrease of topography coupled to the Oligocene low-stand sea-level.

(3) From Early(?)–Middle Miocene times onward (before Langhian), an early topography due to a first phase of lithospheric thinning plus a shortening component triggered the setting of tectono-gravity nappes along the southern front of the High Atlas. This was followed by a large-scale subsiding state related to a decrease in the lithospheric thinning intensity.

(4) Shortening resumed and finally increased during Pliocene–Quaternary with the building of the present orogeny with an additional contribution of a second lithospheric thinning event.

We also underline that the peculiar position of Morocco is responsible for two unique features of the Marrakech High Atlas in Morocco. The first is the low development of the Late Eocene belt, probably due to the close position of Morocco at that time of the Africa anti-clockwise rotation toward Europe. Second, contrary to Algeria and Tunisia, the building of an early topography as soon as Early(?)–Middle Miocene resulted from the thinning of the Moroccan lithosphere.

7.2 The high-grade karst-hosted Imini manganese deposits: detailed mineralogy, petrography and geochemistry

Manganese ore occurs in the Imini district as three *stratabound* layers (not *stratiform* as already mentioned by Gutzmer *et al.* (2006) of Mn oxides and oxyhydroxides along a ~25 km WSW-ENE belt in the approximately ten-meter-thick dolostone that is Cenomanian-Turonian in age (►Figs. 7.19a, b and c). Previous authors proposed three main models to form the manganese ore deposits of Imini: (1) The synsedimentary model assigned a *stratiform* nature to the three orebodies closely parallel to the Cenomanian-Turonian paleoshoreline (Neltner, 1933; Orcel, 1942; Bouladon and Jouravsky, 1952; Pouit, 1964, 1976, 1980; Lesavre, 1975; Lalaoui, 1987; Thein, 1990; Lalaoui *et al.*, 1991; Rhalmi *et al.*, 1997); (2) A second model promoted the relevance of diagenetic processes in a mixing zone between saline ground water and anoxic seawater (Force *et al.*, 1986; Thein, 1990); (3) Karst formation has been assumed to either transform previous Mn carbonates to Mn oxides and oxyhydroxides (Beaudoin *et al.*, 1976) or, alternatively, karst cavities provided a mixing zone between Mn-bearing reduced fluids and oxygenated meteoric waters (Gutzmer *et al.*, 2006).

In this study, we provide detailed mineralogical and petrological data for the host rock Cenomanian-Turonian dolostone in order to highlight the processes contributing to ore formation, and to refine previous metallogenic models.

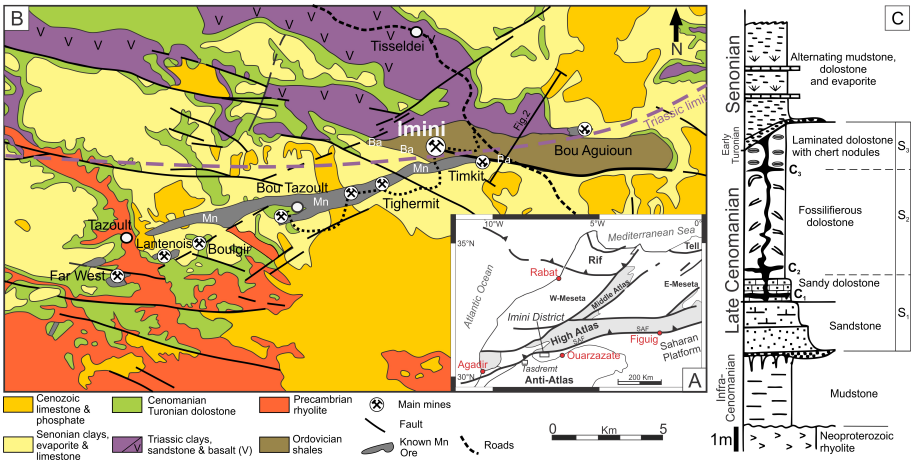

►**Fig. 7.19 a.** Location of the Imini district, south of the South Atlas Front (SAF). **b.** Simplified geological map of the Imini district showing the Mn ore belt trapped in the Cenomanian-Turonian dolostone (modified after Lalaoui *et al.*, 1991). Geographic coordinates of unrepresented outcrops of distal dolostones on the map (UTM latitude and longitude) : (19) - 31°10'0.19"N and 7°30'42.16"W; (20) - 31°9'7.55"N and 7°33'45.91"W; (21) - 31°0'32.27"N and 7°42'42.17"W; (J1) - 30°59'35.54"N and 7°40'43.78"W; (J4) - 30°55'0"N and 7°46'0"W. **c.** Detailed stratigraphic log of Lantenois galleries (west of the district; modified after Gutzmer *et al.*, 2006). The three sedimentary systems (S_1, S_2, S_3) come from Rhalmi *et al.* (2000).

7.2.1 Geological settings

Rhalmi (1992) and Rhalmi *et al.* (1997, 2000) described three main sedimentary systems. The first two (S_1 and S_2) correspond to a sandy dolostone and a fossiliferous dolostone, respectively, of Late Cenomanian age while the third system (S_3), of Early Turonian age, is a fossiliferous dolostone with flints (►Fig. 7.19c). Lenses of sandstone known as “entre-deux gréseux” (Beaudoin *et al.*, 1976) are often found in the first sedimentary system (Rhalmi, 1992). The whole succession is completely dolomitized with two generations of dolomite that erase sedimentary textures; dolomitization decreases with distance from the Imini district and suggests a likely link to Mn oxyhydroxide occurrences (Force *et al.*, 1986). Karstic cavities occur mainly in the lower part of the second sedimentary system (S_2) in contact with the fossiliferous dolostone and C_2 mineralized layer (Pouit, 1964). These cavities, 1 to 10 meters long, are filled by variable successions of unconsolidated sediments (see Gutzmer *et al.*, 2006 for more details).

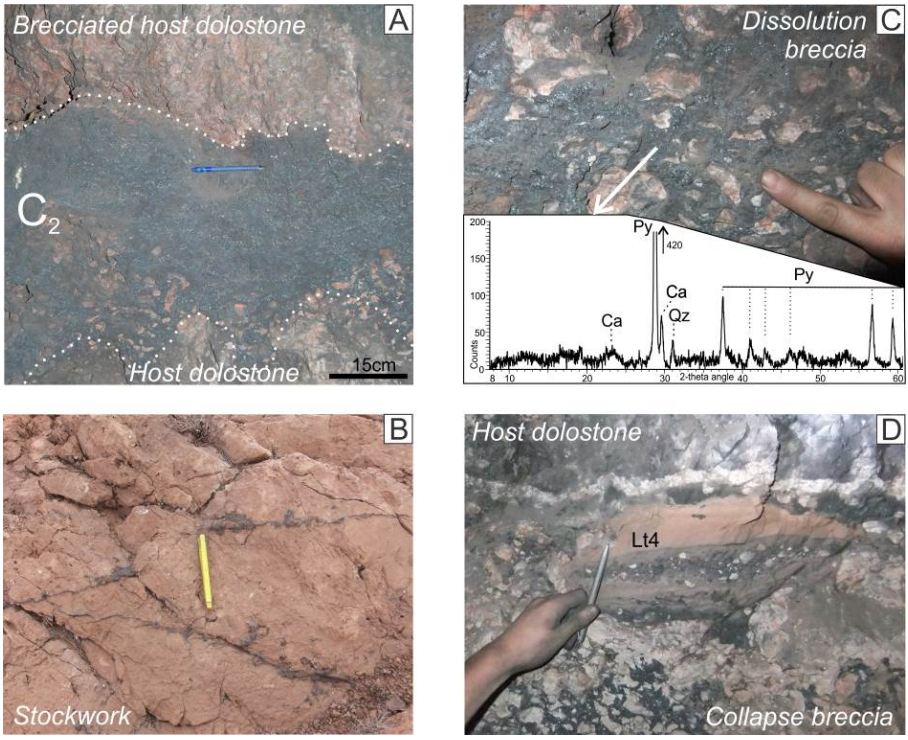

►**Fig. 7.20 a.** Repeated sequence observed in Lantenois galleries comprising, from bottom to top: the brecciated dolostone, the *stratabound* layer C_2 forming a dissolution front and the host rock dolostone. **b.** Stockwork veinlet composed of Mn oxides and oxyhydroxides in the fossiliferous level at Timkit. **c.** Mineralized dissolution breccia (with XRD pattern) above C_2 layer in Lantenois galleries. Qz = quartz, Py = pyrolusite, Ca = calcite. **d.** Internal sediments of lithotype 4 (Lt4 *sensu* Gutzmer *et al.*, 2006) containing reworked Mn oxyhydroxides in the Lantenois galleries (see ►Fig. 7.19 for location).

7.2.2 Distribution and styles of mineralization

While the southern boundary of the ore deposit is quite variable, the northern part is remarkably straight with a Fe-rich front (e.g.,Pouit, 1964; Lesavre, 1975). According to Lalaoui *et al.* (1991), the ore belt shapes anastomosing lenses 2 km long following a WSW-ENE direction (►Fig. 7.19b). The high-grade Mn ore of Imini is found mainly as three *stratabound* layers (►Fig. 7.20a), as stockworks and veinlets (►Fig. 7.20b) and cement in dissolution breccia (►Fig. 7.20c; Gutzmer *et al.*, 2006). Apart from these notable occurrences, disseminated grains of Mn oxyhydroxides are also found throughout the host rock dolostone and internal sediments (►Fig. 7.20d; (Gutzmer *et al.*, 2006).

The three *stratabound* orebodies (from bottom to top), defined as C_1, C_2 and C_3 in previous investigations (►Figs. 7.19c and 7.20a), have variable thickness depending on their location in the Imini district. The layers C_1 and C_2 (1 to 2.5 m thick; Gebert, 1989) contain the bulk of Mn mineralization and are closely spaced, quite continuous at the district scale, and located in the sandy dolostone (S_1; ►Fig. 7.19c). However, their spacing and stratigraphic position are not equal along the ore belt and therefore Gutzmer *et al.* (2006) highlight the *stratabound* character of these layers rather than a *stratiform* one. Close to the top of the fossiliferous dolostone (S_2), the C_3 layer (< 1 to 2.5 m thick) is more fragmented than C_1 and C_2 except to the north where it can be continuous (►Fig. 7.19c). C_1 and C_2 layers are dominated by pyrolusite (MnO_2) and part of the Mn oxyhydroxides form a soft and easy material to extract known as "wad" (Post, 1999). Hollandite group minerals [$(K,Ba,Pb)Mn_8O_{16}$] and associated Ba and Pb impurities in C_3 provide a lesser economic interest for this layer in comparison with C_1 and C_2 (Gutzmer *et al.*, 2006). In the Lantenois galleries (►Fig. 7.19b), the transition between host rock dolostone and C_2 forms a dissolution front (►Fig. 7.20a). Finally, the C_3 layer has been overprinted by superficial karstification, which separates the host rock dolostone and the overlying rhythmic interbedded Senonian clayey sandstone, dolostone, limestone and evaporite (►Fig. 7.19c).

Stockworks and veinlets of Mn oxyhydroxides are extensively developed in the whole Cenomanian-Turonian sequence and especially in the footwall and hanging-wall dolostone of cave zones (Gutzmer *et al.*, 2006; ►Fig. 7.20b). The latter authors point out two breccias mainly located between C_2 and C_3 orebodies: (1) a collapse breccia formed by physical collapse of roof material into the Mn orebody (►Fig. 7.20d) and, (2) a "*pseudobreccia*" formed by chemical wear closely associated to stockwork (►Fig. 7.20c).

Five lithotypes described by Gutzmer *et al.* (2006) contain clay minerals (kaolinite predominance and illite) and dolomite of authigenic origin. Quartz is also present and reworked grains of Mn oxyhydroxides (►Fig. 7.20d) indicate that karstic processes partly postdate the ore formation.

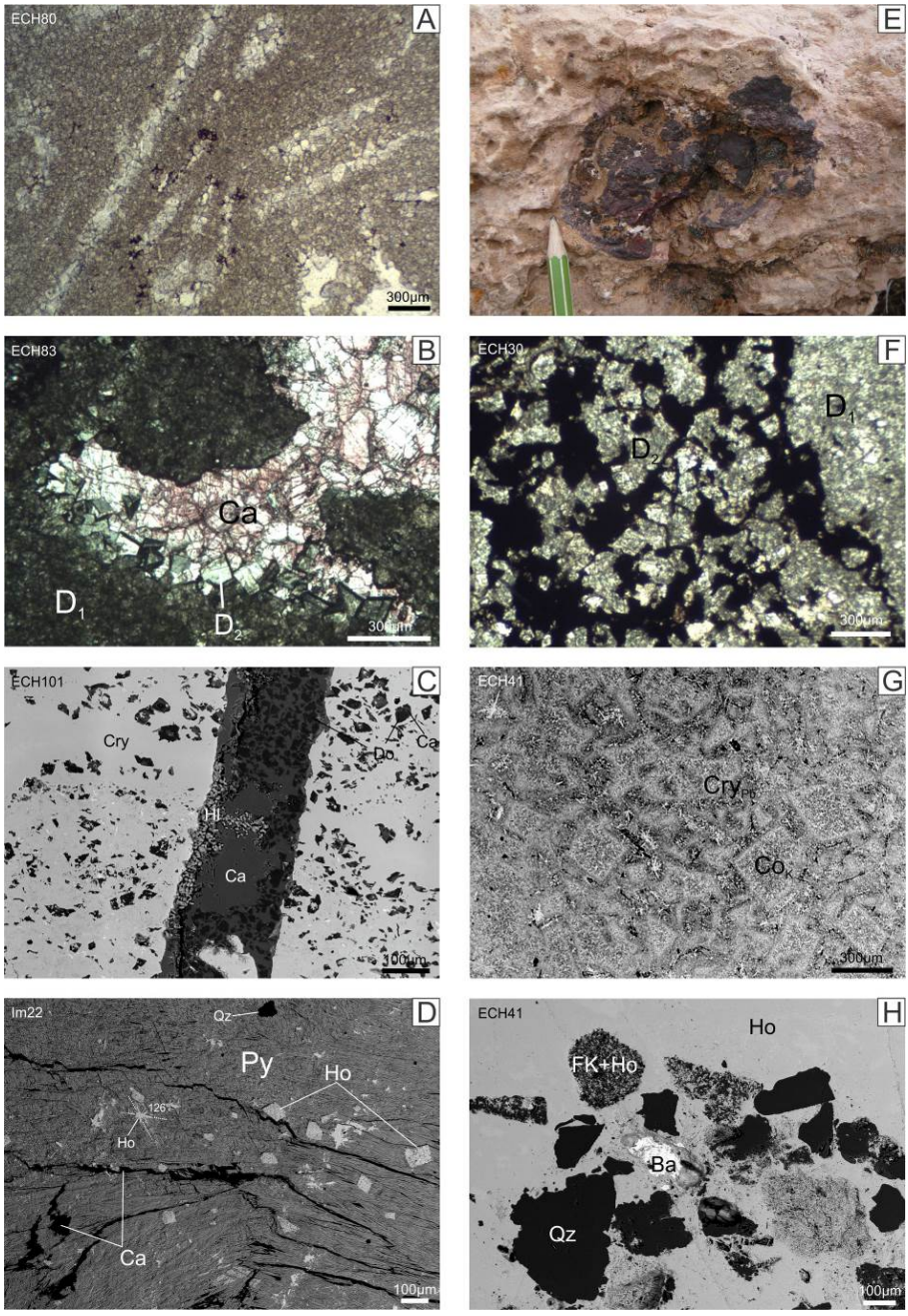

►**Fig. 7.21 a.** Laths of anhydrite ghosts filled by dolomite rhombs in dolomite microspar in site 21 (►Fig. 7.19). **b.** Light microscopy view of dolomite micrite and microspar (D_1) and calcite cement (Ca) surrounded by dolomite rhombs (D_2) in distal dolostone (site 21). **c.** Cryptomelane (Cry) containing dolomite rhombs (Do) partially replaced by calcium carbonate (dedolomitization?). Fractures are filled by dolomite and cryptomelane remains but also by halite (Hl) pods and then calcium carbonate (Ca). **d.** SEM view of pyrolusite matrix

(Py) comprising hollandite *s.s.* (Ho) rhombs and calcium carbonate (Ca; Timkit). Hollandite *s.s.* crystals follow pyrolusite cleavages. **e.** Fe-Mn nodule on the top of distal dolostone sequence (site 21). **f.** Replacement of dolomite micrite and part of microspar (D_1) by Mn-oxides and –oxyhydroxides. Dolomite rhombs (D_2) are not replaced (C_1 ; Timkit). **g.** Replacement of dolomite rhombs by K-rich coronadite (Co_K) in the previously formed Pb-rich cryptomelane (Cry_{Pb}; C_3; Far West mine). **h.** SEM picture showing crystals of quartz (Qz) and K-feldspar (FK) partly or totally replaced by hollandite *s.s.* (Ho) in C_3 orebody. Minor barite (Ba) is also observed. Note that quartz grains are corroded by Mn oxyhydroxides giving anhedral quartz (Far West mine).

7.2.3 Materials and methods

We have focused our investigations on three main sampling sites in the Imini district (from WSW to ENE): Lantenois gallery (sites 14, 15), Timkit (sites 5, 6, 8, 9, 10, 11, 12) and Bou Agguioun (sites 23, 24; ►Fig. 7.19b). A fourth site is located westward of the district close to Larba in a distal Cenomanian-Turonian dolostone (site 21; ►Fig. 7.19b). A BRUKER X Ray Diffractometer (XRD) with a HI STAR GADDS CuK_α detector has been used to generate XRD patterns on powder samples. In addition, Scanning Electron Microscope (SEM) JEOL JXA-8600 coupled with NORAN Energy Dispersive Spectrometer (EDS) provides useful information about mineral composition and paragenesis in polished sections. Note that "distal" and "proximal" dolostones are defined by their distance from the known distribution of *stratabound* orebodies C_1-C_3.

7.2.4 Results

7.2.4.a Host rock dolostone

The sediments formed in the Cenomanian-Turonian marine environment have been completely dolomitized during diagenesis (Force *et al.*, 1986). The only relics correspond to terrigeneous residues such as quartz, feldspars and accessory minerals (apatite, zircon…) as well as brachiopod-shells and organism prints (Rhalmi *et al.*, 1997). Primary calcite has been described by Force *et al.* (1986) with high $\delta^{18}O/\delta^{13}C$ range of isotopic values. Our study highlights new evidence of anhydrite ghosts (►Fig. 7.21a) that are in good agreement with the saline and proximal environment proposed by Force *et al.* (1986) and Thein (1990). According to Force *et al.* (1986), Rhalmi (1992) and Rhalmi *et al.* (1997), widespread dolomitization took place at an early stage of diagenesis by replacement, resulting in the formation of dolomite microspar and micrite (►Fig. 7.21b). This first dolomitization episode strongly erased primary textures (Rhalmi, 1992). A second dolomitization episode took place by replacing dolomite microspar and filling porosity associated to meteoric dissolution (►Fig. 7.21b; Force *et al.*, 1986). Sr concentrations and $\delta^{18}O/\delta^{13}C$ isotopic

values close to zero suggest that dolomitization may correspond to a mixing zone between meteoric and marine waters involving minor organic processes (Rhalmi, 1992). The end of late diagenesis is marked by dedolomitization (Gutzmer *et al.*, 2006). Dolomitization is responsible for the high porosity of the host rock dolostone. Calcite and/or aragonite cement fill the porosity (►Fig. 7.21b), fractures (►Fig. 7.21c) and intercrystalline spaces of dolomite and Mn oxyhydroxides (►Fig. 7.21d). This late calcite/aragonite originates from recent meteoric waters associated to low $\delta^{18}O/\delta^{13}C$ values (Force *et al.*, 1986). This study demonstrated the occurrence of small pods of halite in association with calcite/aragonite in brecciated ore zones (►Fig. 7.21c). Only proximal dolostone contains clay minerals (mainly kaolinite).

Small amounts of finely disseminated Mn oxyhydroxides occur between dolomite rhombs in proximal dolostone. However, both distal and proximal dolostones show large Fe-Mn-nodules (0.1 to 2 cm) at macroscopic scale (►Fig. 7.21e). Aggregates of microcrystalline or needle-shaped Mn oxyhydroxides replace both the early diagenetic dolomite microspar (Gutzmer *et al.*, 2006; ►Fig. 7.21f) and the late diagenetic dolomite rhombs (►Fig. 7.21g). This last process results in the conservation of the dolomite rhomb texture by Mn oxyhydroxides (especially hollandite group minerals), indicating that mineralization postdates dolomitization. In some cases Mn oxyhydroxides replace clay minerals (Gutzmer *et al.*, 2006), detrital quartz and feldspars (►Fig. 7.21h).

7.2.4.b Manganese ores

Mn oxides and oxyhydroxides have only been identified in the mineralized zones by X ray diffraction and SEM-EDS analysis. The mineralized succession shows mainly pyrolusite (MnO_2; ►Figs. 7.20a-c and 7.21d) and hollandite group minerals (►Figs. 7.21c, d, g and h): cryptomelane (KMn_8O_{16}), coronadite ($PbMn_8O_{16}$) and hollandite *sensu stricto* ($BaMn_8O_{16}$). XRD patterns and SEM-EDS analyses highlight small amounts of lithiophorite [$LiAl_2Mn_3O_6(OH)_6$] and romanechite [$(Ba,H_2O)_2Mn_5O_{10}$; ►Fig. 7.22a]. In some samples, barite ($BaSO_4$) is present as small infill of thin veinlets or isolated crystals in romanechite/hollandite *s.s.* masses (►Fig. 7.21h). Ores are often fractured and partly or totally filled by variable clasts composed of the *in situ* brecciated host dolostone and Mn oxyhydroxides minerals (►Fig. 7.21c).

Pyrolusite (MnO_2) occurs as coarse prismatic crystals and forms palisade texture aggregates (►Fig. 7.21d). It surrounds dolostone residues either at macroscopic scale in the dissolution breccia (►Fig. 7.20c) or microscopic scale. Pyrolusite also surrounds dolomite rhombs replaced by hollandite *s.s.* indicating that pyrolusite predates the formation of hollandite *s.s* (►Fig. 7.21d). Macrocrystalline

pyrolusite fills subhorizontal stockworks that crosscut and thus postdate the microcrystalline Mn oxyhydroxides (Gutzmer *et al.*, 2006).

"The different minerals in the hollandite group are defined on the basis of the predominant tunnel cation: hollandite (Ba), cryptomelane (K) and coronadite (Pb). Natural specimens having end-member compositions are unusual, and chemical analyses show a wide range of tunnel cation compositions. Hollandite minerals commonly occur intermixed and, in some cases, grade from one to another along a single crystal" (Post, 1999). In the Imini ores, they occur mainly as (1) replacement of dolomite rhombs (►Figs. 7.21g, 7.22b and c) and as (2) collomorphous aggregates in brecciated zones (►Figs. 7.22c and d). (1) Replacement of dolomite rhombs comprises mainly needles of coronadite oriented to the center (►Figs. 7.21g and 7.22b), as already observed by (Decrée *et al.*, 2010b) in Mn ores of Tunisia. These rhombs are surrounded by needles of hollandite *s.s.* and cryptomelane (►Figs. 7.21g and 7.22b). The previous framework and the growth of successively hollandite *s.s.*, cryptomelane and then coronadite (►Fig. 7.22b) reflect the main crystallizing sequence of the dolostone. (2) Collomorphous aggregates show various tints of grey trading changes in composition. Cryptomelane prevails with variable concentrations in Ba, Pb and K (►Figs. 7.22c and d). Nevertheless, some samples have high Pb content associated to coronadite episodes. Cryptomelane fragments are observed in hollandite *s.s.* layers (►Fig. 7.22e). Collomorphous needles of hollandite *s.s.* occur between dolomite rhombs and pyrolusite but also follow cleavages of pyrolusite (►Fig. 7.21d). We have observed exclusively coronadite crystals growing on the host rock dolostone, forming small geodes with a regular sequence: dolomite, coronadite, calcite/aragonite and finally pore spaces (►Fig. 7.22f). Late coronadite crystalizes following calcite cleavages and grows perpendicular on collomorphous fragments of hollandite group minerals (►Fig. 7.22g).

Romanechite appears as homogeneous masses with only Ba, O and Mn energy peaks and no Pb or K impurities (contrary to hollandite group minerals; ►Fig. 7.22a). Romanechite is an uncommon mineral in the Imini district. Romanechite is often linked to hollandite *s.s.* probably due to its close composition (Turner and Buseck, 1979; ►Fig. 7.22a). This is why Gutzmer *et al.* (2006) refer to the mixing of coronadite, romanechite and cryptomelane as manganomelane.

Lithiophorite always occurs as small square/hexagonal needles (►Figs. 7.22a and g) within Ba-rich masses of hollandite group minerals or romanechite. Lithiophorite shows darker tints of grey in SEM images compared to other Mn oxyhydroxides because of Al and possibly Li low atomic number as well as the absence of Pb or Ba in EDS spectra (►Fig. 7.22a). Intergrowth between lithiophorite and romanechite is observed in well-mineralized sections (►Fig. 7.22a).

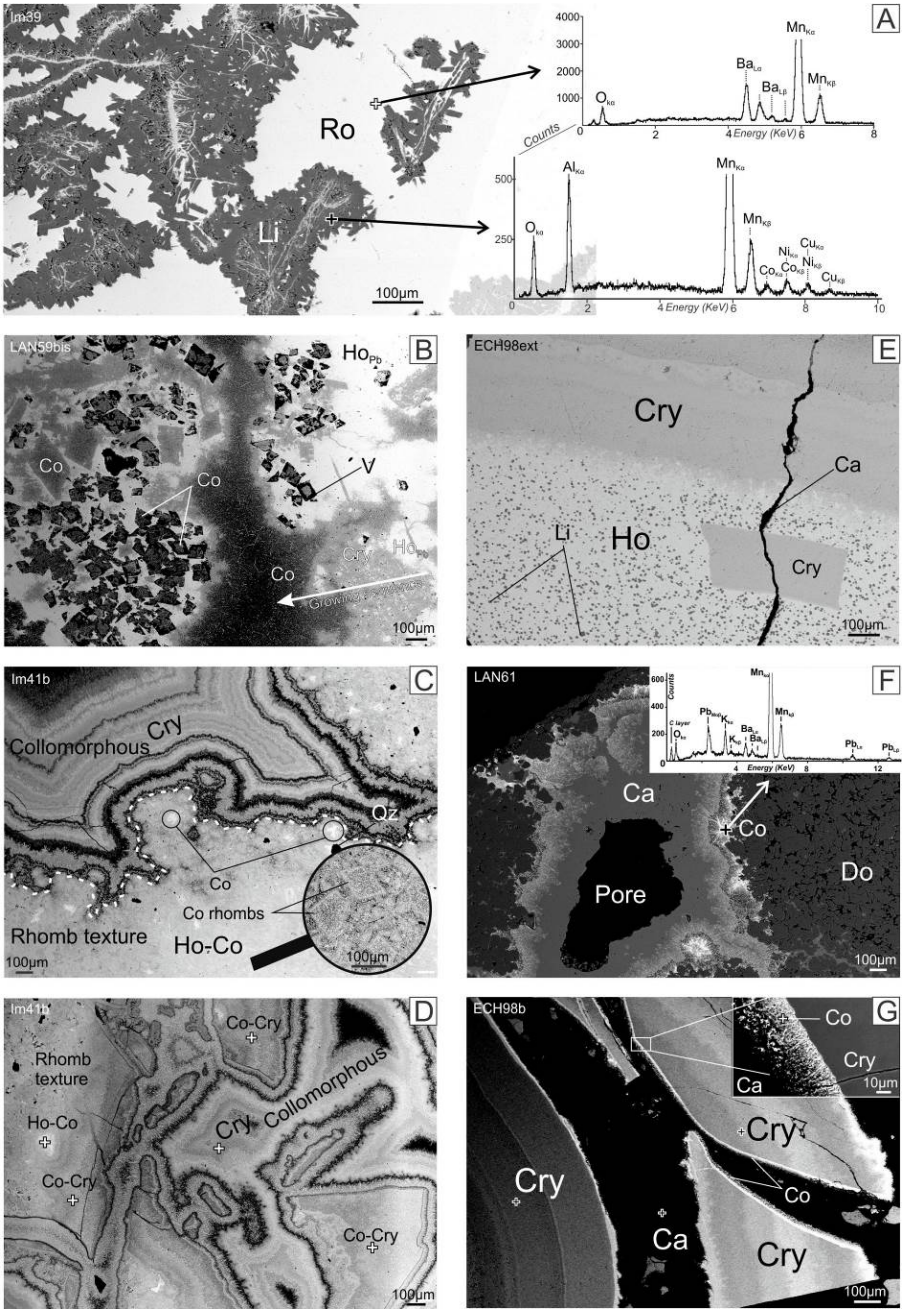

►**Fig. 7.22 a.** SEM picture showing relationship between lithiophorite laths and romanechite, with their respective spectra in a mixing zone between C_1 and C_2 orebodies (Timkit). Note the fibrous filaments. **b.** SEM view of cryptomelane sequence and rhomboidal forms of coronadite with voids (V) in Pb-rich hollandite *s.s.* (Ho_{Pb}; Timkit). **c.** SEM view of collomorphous cryptomelane (Cry) and rhombs of hollandite group minerals, mainly coronadite (Co) and hollandite *s.s.* (Ho), in the C_3 (Far West mine). Quartz remains are also present (Qz). **d.** SEM

view of collomorphous cryptomelane (Cry) surrounding hollandite *s.s.* (Ho) and coronadite (Co) remains with rhomboidal fabric (C_3 ; Far West mine). **e.** SEM view of hollandite *s.s.* (Ho) and cryptomelane (Cry) banded boundary (C_1; Bou Agguioun – Ancienne Mine). Small crystals of lithiophorite (Li) are located close to the boundary between the Ba-rich zone dominated by hollandite *s.s.* and cryptomelane (Cry). Note the cryptomelane fragment in hollandite *s.s.* band. **f.** SEM picture of coronadite (Co) and its energy spectrum growing into cavities and fractures. Calcium carbonate (Ca) occurs as a cement in the fossiliferous host rock dolostone (Do; Lantenois). **g.** SEM view of collomorphous cryptomelane (Cry) fragments enclosed in calcium carbonate (Ca) cement (C_1; Bou Agguioun – Ancienne Mine). Small needles of coronadite (Co) grow onto cryptomelane fragments prior to calcite/aragonite cement.

7.2.5 Geochemistry

7.2.5.a Host dolostone

The dolostone host to the Mn orebodies has a major element composition close to pure dolomite without significant detrital components (Table 1). Both distal and proximal dolostones display typical flat and depleted REE patterns of carbonate rocks (La_N/Yb_N 1.16-2.29, ►Table 7.2) with large negative Ce anomalies (Ce/Ce^* 0.39-0.63, ►Fig. 7.23a; Piper, 1974; Palmer, 1985). The presence of Mn oxyhydroxides has a significant effect on the bulk compositions: (1) Mn concentrations of distal dolostone (0.12–0.2 wt. % MnO) are characteristic of Phanerozoic dolostone (trace to 0.2 wt. % MnO, Hill *et al.*, 1967), whereas proximal dolostone has much higher MnO contents (0.38–0.61 wt. % MnO; ►Table 7.1) due to the occurrence of finely dispersed Mn oxyhydroxides (Gutzmer *et al.*, 2006); (2) higher REE contents in proximal than distal dolostone are controlled by the occurrence of dispersed Mn oxyhydroxides and clay assemblages (►Fig. 7.23a). Iron contents are unusually low because Fe^{2+} is nearly absent compared to Fe^{3+}, and Mn/Fe ratios are systematically higher than 1.0 even in distal dolostone (4.72–13.6, ►Tables 7.1 and 7.3; Hill *et al.*, 1967).

7.2.5.b Internal karst-fill sediments

Whilst internal karst-fill sediments have high SiO_2 concentrations compared to host dolostone, the molar ratios of immobile elements are similar (►Table 7.3). This pattern suggests that most of the clay assemblages of lt1-2 represent the insoluble residue that was preserved during karstification. Dolomite is also an important mineral phase of authigenic origin in the internal sediments. Geochemical data for REE support this interpretation based on the presence of identical patterns in distal and proximal dolostones, as well as in the internal sediments (►Fig. 7.23a; Gutzmer *et al.*, 2006).

7.2.5.c Manganese ore

Ore samples were collected selectively from *stratabound* bodies, breccias, and stockworks. The most distinctive feature of the manganese ores of the Imini district is the high contents of MnO (typically >70 wt. % MnO, ►Table 7.1), which is improved by very low Fe_2O_3 (and SiO_2, Al_2O_3, TiO_2, and P_2O_5; ►Table 7.1) compared to other Mn deposits (<0.6 wt. % Fe_2O_3; ►Table 7.1; e.g., Maynard, 2014). The observed enrichments in Ba, Pb, and K , as well as Cu, Sr, and V, are related to the abundance of hollandite group minerals (►Table 7.1), but not for other metals such as Zn, Ni, Co, As, Cr, Rb, La, and Ce that commonly are much higher than in other Mn deposits (►Table 7.2 and 7.3; Gutzmer *et al.* 2006). Using a discrimination plot proposed by Nicholson (1992), a high concentration of Pb (and Ba, ►Table 7.1) within the hollandite group minerals reflects a Mn-rich gossan in the Imini district (►Fig. 7.23b). The low Mn/Fe ratios and correlation of Fe with detrital elements within the internal karst-fill sediments suggests that iron was geochemically decoupled from manganese and records weathering processes (Gutzmer *et al.*, 2006; ►Table 7.3).

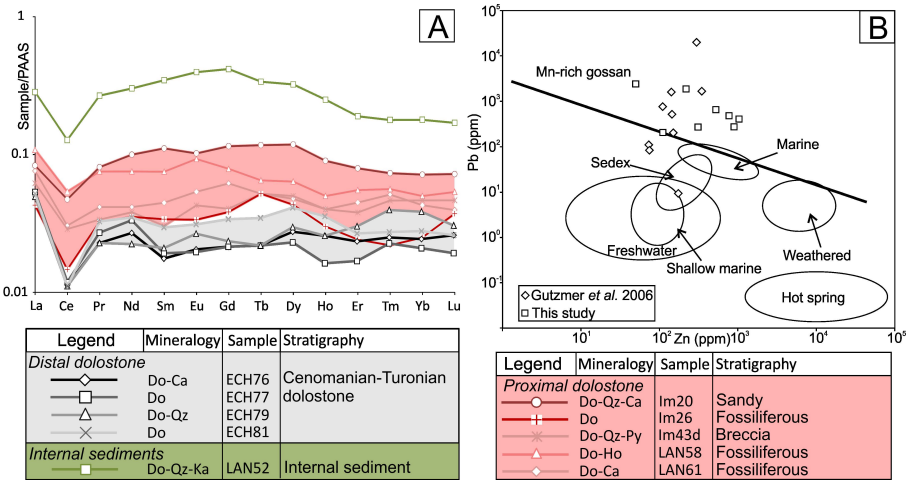

►**Fig. 7.23** Geochemistry of manganese orebodies of Imini district. **a.** Rare earth element (REE) patterns of internal karst-fill sediments (green), and distal (pink) and proximal (grey) dolostones, normalized to average Post-Archean Australian Shale (PAAS) reference (Taylor and McLennan, 1985). REE patterns of Cenomanian-Turonian dolostone are typical of Phanerozoic marine dolostone; conservation of the dolostone REE pattern for the internal sediments indicates that dolomite residues come from authigenic deposition during karstification. Proximal dolostone contains dispersed grains of Mn oxides. **b.** Zinc and Pb concentrations for manganese orebodies from Gutzmer *et al.* (2006) and this study plot mainly in Mn-rich gossan field on discrimination plot of Nicholson (1992). Abbreviations: Do, dolomite; Ca, calcite; Qz, quartz; Ka, kaolinite; Py, pyrolusite; Ho, hollandite *s.s.*

►**Table 7.1** Geochemistry of internal karst-fill sediments, manganese orebodies, distal and proximal host rocks of the Imini district. Samples were analyzed by Activation Laboratories (Ontario, Canada). Data for major elements were determined by fusion ICP-MS. "Distal" and "proximal" dolostones are defined by distance from known *stratabound* orebodies C_1-C_3. Abbreviations: IS Lt (no.), internal sediment lithotype (no.); N.A., not analyzed.

Sample	Locality	Type	SiO_2	TiO_2	Al_2O_3	Fe_2O_3	MnO	MgO	CaO	PbO	BaO	Na_2O	K_2O	P_2O_5	LOI	Total	FeO
IM20	Timkit	Proximal dolostone	5.00	0.03	0.80	0.08	0.54	19.16	27.79	0	0.02	0.03	0.24	0.05	44.25	98.08	<0.1
IM26			0.88	0.02	0.31	0.05	0.61	20.53	29.84	0	0	0.02	0.06	0.03	46.59	99.05	<0.1
IM43d	Lantenois		2.62	0.03	0.56	0.12	0.57	21.33	28.8	0.01	0.03	0	0.03	0.01	45.75	99.94	<0.1
LAN58			8.59	0.03	0.86	0.01	0.38	18.6	27.34	0.01	0.02	0.02	0.26	0.02	42.46	98.67	<0.1
LAN61			0.75	0.02	0.43	0.07	0.55	19.98	30.98	0.02	0.02	0.01	0.05	0.03	46.23	99.22	<0.1
ECH98b	Bou Aguioun	C1	4.62	0.03	1.00	0.16	63.84	0.18	3.08	0.52	2.34	0.18	4.88	0.14	12.43	90.65	<0.1
ECH102b			2.75	0.05	1.33	0.3	59.75	1.13	5.65	0.44	1.71	0.25	4.61	0.15	14.61	90.67	<0.1
IM37	Timkit	C1-C2	3.59	0.03	1.39	0.17	54.42	0.13	5.96	0.7	11.37	0.07	0.43	0.06	13.85	80.22	<0.1
IM22		C2	0.99	0	0.34	0.01	82.72	0.12	1.13	0.22	1.17	0.01	0.16	0.03	13.16	98.79	<0.1
IM29			0.49	0	1.39	<0.01	76.37	0.14	0.13	0.29	3.37	0.01	0.25	0.04	12.25	91.1	<0.1
LAN51	Lantenois		26.74	0.29	5.71	2.4	40.17	0.38	0.46	2.03	4.59	0.11	1.79	0.1	8.54	86.81	<0.1
IM41c	Far West	C3	2.67	0.02	0.78	0.04	67.2	0.03	0.18	2.54	6.07	0.25	1.04	0.09	10.29	82.69	<0.1
ECH101b	Bou Aguioun	Stockwork	7.72	0.1	2.17	0.59	54.69	1.73	5.76	0.29	2.4	0.57	2.22	0.36	15.02	91.03	0.1
IM43m	Lantenois	Breccia	3.16	0.04	0.76	0.58	37.89	7.75	11.33	2.66	4.09	0.1	0.96	0.03	23.69	86.4	<0.1
LAN52		Lt(2)	7.31	0.1	1.98	0.75	1.22	18.64	26.56	0.03	0.09	0.02	0.37	0.05	41.82	98.92	<0.1
ECH76	Larba	Distal dolostone	0.35	0.01	0.17	0.03	0.13	19.75	30.86	0	0	0.02	0.02	0.12	46.97	98.52	<0.1
ECH77			0.35	0.01	0.17	<0.01	0.12	21.28	31	0	0	0.02	0.01	0.16	47	100.2	<0.1
ECH79			0.37	0.01	0.19	<0.01	0.2	20.24	30.31	0	0	0.02	0.02	0.24	46.85	98.53	<0.1
ECH81			0.67	0.01	0.24	<0.01	0.13	20.27	29.8	0	0	0.02	0.02	0.03	46.99	98.27	<0.1
ECH85	Taouerda		0.58	0.01	0.17	0.01	0.17	18.23	33.01	0	0	0.04	0.02	0.11	46.45	98.9	<0.1

►**Table 7.2** Data for rare earth elements (REE) normalized to average Post-Archean Australian Shale (PAAS; Taylor and McLennan 1985). Determinations by fusion ICP-MS at Activation Laboratories (Ontario, Canada).

Sample	Locality	Type	La	Ce	Pr	Nd	Sm	Eu	Gd	Tb	Dy	Ho	Er	Tm	Yb	Lu	Ce/Ce*
IM20	Timkit	Proximal dolostone	3	4	0.72	3.19	0.62	0.11	0.54	0.09	0.52	0.09	0.23	0.03	0.2	0.03	2.72
IM26			2	1	0.29	1.13	0.19	0.04	0.18	0.04	0.19	0.03	0.07	0.01	0.07	0.02	1.31
IM43d			2	2	0.3	1.22	0.17	0.05	0.19	0.04	0.22	0.04	0.11	0.02	0.13	0.02	2.58
LAN58	Lantenois		4	4	0.67	2.41	0.42	0.1	0.37	0.05	0.28	0.05	0.16	0.02	0.14	0.02	2.44
LAN61			3	2	0.37	1.33	0.25	0.06	0.29	0.04	0.21	0.04	0.13	0.02	0.12	0.02	1.9
ECH98b	Bou Aguioun	C1	4	10	0.63	2.18	0.46	0.37	0.59	0.06	0.31	0.06	0.18	0.03	0.21	0.04	6.3
ECH102b			8	14	0.91	3.07	0.62	0.36	0.81	0.1	0.51	0.1	0.28	0.05	0.34	0.07	5.19
IM37	Timkit	C1-C2	6	10	2.21	9.66	1.82	0.34	1.89	0.22	1.13	0.19	0.45	0.05	0.29	0.05	2.75
IM22		C2	7	6	1.53	5.54	1.02	0.28	1.3	0.21	1.23	0.26	0.71	0.09	0.57	0.09	1.83
IM29			4	10	0.5	1.67	0.47	0.61	0.82	0.08	0.44	0.1	0.28	0.04	0.23	0.04	7.07
LAN51	Lantenois		31	42	4.16	14.8	2.49	0.38	2.14	0.31	1.61	0.32	0.92	0.14	0.9	0.16	3.7
IM41c	Far West	C3	20	25	1.89	5.82	1.18	1.15	1.43	0.13	0.58	0.12	0.34	0.05	0.33	0.05	4.07
ECH101b	Bou Aguioun	Stockwork	18	23	2.91	11.5	2.28	0.43	2.17	0.3	1.67	0.3	0.77	0.1	0.64	0.1	3.18
IM43m	Lantenois	Breccia	8	12	0.72	2.07	0.53	0.7	0.78	0.06	0.26	0.04	0.13	0.02	0.16	0.02	5
LAN52		Lt(2)	11	10	2.38	9.66	1.94	0.44	1.96	0.26	1.42	0.25	0.55	0.07	0.5	0.07	1.95
ECH76	Larba	Distal dolostone	2	1	0.24	1	0.12	0.03	0.12	0.02	0.14	0.03	0.08	0.01	0.08	0.01	1.44
ECH77			2	1	0.28	1.21	0.13	0.03	0.12	0.02	0.12	0.02	0.06	0.01	0.07	0.01	1.34
ECH79			2	1	0.24	0.85	0.14	0.03	0.13	0.02	0.15	0.03	0.1	0.02	0.12	0.02	1.44
ECH81			2	1	0.33	1.26	0.19	0.04	0.18	0.03	0.2	0.04	0.09	0.01	0.09	0.01	1.23
ECH85	Taouerda		2	2	0.22	0.96	0.12	0.03	0.15	0.02	0.12	0.02	0.07	0.01	0.07	0.01	3.02

►**Table 7.3** Trace element geochemistry of internal sediments, manganese orebodies, distal and proximal host rocks of Imini district. V and Sr were analyzed by fusion ICP-MS methods and other elements by FUS-MS. Abbreviations: IS Lt (no.), internal sediment lithotype (no.); N.A., not analyzed.

Sample	Locality	Type	Mn/Fe	V	Cu	Zn	Ni	Co	As	Cr	Zr	Rb	Sr	La	Ce
IM20	Timkit	Proximal dolostone	7	14	20	<30	<20	2	<5	<20	13	6	61	3	4
IM26			14	12	< 10	80	<20	1	<5	20	2	2	47	2	1
IM43d	Lantenois		5	9	20	<30	<20	2	<5	30	14	5	64	2	2
LAN58			42	11	20	<30	<20	2	<5	30	16	4	59	4	4
LAN61			9	15	10	<30	<20	4	<5	<20	4	<1	57	3	2
ECH98b	Bou Aguioun	C1	442	1469	1510	770	40	1120	443	20	17	15	2577	4	10
ECH102b			221	874	2170	1030	250	2480	230	40	13	17	3014	8	14
IM37	Timkit	C1-C2	354	1795	830	520	80	540	80	30	12	4	1091	6	10
IM22		C2	9159	392	1430	110	40	68	39	<20	7	<1	423	7	6
IM29			/	832	1930	310	330	429	153	60	8	<1	449	4	10
LAN51	Lantenois		19	522	1120	220	50	190	72	110	208	39	1464	31	42
IM41c	Far West	C3	1860	921	1550	50	30	476	66	20	12	5	1912	20	25
ECH101b	Bou Aguioun	Stockwork	ECH101b	103	1190	1500	890	340	1230	222	30	31	19	2933	18
IM43m	Lantenois	Breccia	IM43m	72	289	690	<30	<20	135	49	30	18	4	1545	8
LAN52		Lt(2)	LAN52	2	53	110	60	<20	9	6	40	34	14	53	11
1ECH76	Larba	Distal dolostone	ECH76	5	23	<10	140	<20	<1	<5	<20	2	<1	47	2
1ECH77			ECH77	/	25	<10	180	<20	<1	<5	<20	1	<1	50	2
1ECH79			ECH79	/	26	<10	260	<20	<1	<5	<20	<1	<1	55	2
1ECH81			ECH81	/	22	<10	260	<20	<1	<5	40	3	<1	45	2
1ECH85	Taouerda		ECH85	19	22	<10	<30	<20	<1	<5	30	1	<1	125	2
				Chaclophile						Immobile		Mobile		REE	

7.2.6 Discussion

The main outcomes of this study are the recognition of two major mineralizing processes and the multistage character of the Mn ores after dolomitization (►Figs. 7.24 and 7.25). These processes are responsible for the high Mn content of the ore.

7.2.6.a Mineralization process

After dolomitization, mineralizing meteoric (?) fluids seep through the host rock dolostone and replace dolomite micrite and microspar. Dolomite rhombs occur as residues in less mineralized samples where dolomicrite is almost absent (►Figs. 7.21f and 7.24). The high porosity of the host dolostone plays a major role for the free movement of mineralizing fluids as suggested in ►Fig. 7.22f. This first step is followed by the dissolution of dolomite rhombs recognized in well-mineralized samples containing empty rhomboidal forms (►Figs. 7.22b and 7.24). Dissolution processes are also observed at macroscopic scale mostly by dissolution breccias (►Fig. 7.20c) and by dissolution fronts on contact with mineralized layers (►Fig. 7.20a). In the third step, needles oriented to the center of rhomboidal forms indicate that hollandite group minerals grow after a dissolution episode (►Figs. 7.21g, 7.22b and 7.24). In earlier stages, crystal needles also grow out of dolomite rhombs. This last observation indicates that dolomite micrite and microspar have been replaced by hollandite group minerals prior to the dolomite rhombs. This epigenesis continues by progressively replacing feldspars and quartz (►Figs. 7.21h and 7.24). This fourth step only takes place in well mineralized samples where dolomite has been already replaced. Mineralizing fluids containing Mn and associated elements (Ba, K, Pb, etc.) are responsible for the epigenetic replacement of the host rock dolostone related to dissolution processes (►Fig. 7.24). Collomorphous aggregates do not conserve the dolomite rhomb fabric. The banded texture in hollandite group minerals may indicate that it (1) took place in an opened system equilibrated to mineralizing fluids, and (2) that it corresponds to direct precipitation of hollandite group minerals without a previous Mn oxyhydroxide stage. Collomorphous aggregates of hollandite group minerals postdate the end of dolomite replacement by Mn oxyhydroxides because they grow onto the rhomboidal matrix as a well-marked limit (►Figs. 7.22c and d).

7.2.6.b Relative sequence of manganese oxides and oxyhydroxides

Although previous authors studied the mineralogy of Mn-oxides and -oxyhydroxides *sensu lato* (Lesavre, 1975; Force *et al.*, 1986; Lalaoui *et al.*, 1991; Gutzmer *et al.*, 2006), we have investigated their relative arrangement to propose a refined paragenetic sequence (►Fig. 7.25). It starts after the two dolomitization events and

probably involves several generations due to many precipitation-dissolution processes.

A first generation of pyrolusite does appear after dolomitization and before hollandite group minerals because hollandite *s.s.* crystals grow onto pyrolusite either in dolomite rhomb ghosts or following its cleavages/fractures (►Fig. 7.21d). However, a late macrocrystalline pyrolusite phase prevails in the Imini district because it fills extensive stockwork that crosscuts hollandite group minerals (Gutzmer *et al.*, 2006), surrounds hollandite group minerals (Lesavre, 1975; Thein, 1990) and corresponds to a higher oxidation level (Beaudoin *et al.*, 1976; Force *et al.*, 1986; Gutzmer *et al.*, 2006).

We separated hollandite group minerals in three epigenetic sequences related to (1) early epigenetic processes (Ho_R, Cry_R, Co_R), (2) intermediate collomorphous aggregates (Ho_C, Cry_C, Co_C) and (3) late (recent) processes (Co_L; ►Fig. 7.25). (1) Replacement processes follow a regular sequence with hollandite *s.s.* (Ho_R), cryptomelane (Cry_R) and then coronadite (Co_R). This is confirmed by the orientation of crystal needles and associations in rhomboidal texture (►Fig. 7.22b). (2) Collomorphous mineralization occur after replacement processes in form of multiple generations corresponding to the supply of Ba, Pb and K by external fluids. Cryptomelane (Cry_C) and, at a lesser extent, hollandite *s.s.*, (Ho_C; ►Figs. 7.22c and d) dominate collomorphous aggregates. Coronadite (Co_C) is abundant in specific and restricted levels. (3) Recent coronadite has been observed in many samples and is associated to late calcite/aragonite (►Fig. 7.22g).

Lithiophorite only occurs inside collomorphous aggregates of hollandite group minerals indicating an early or syngenetic formation (►Fig. 7.22e). However, the reason why lithiophorite is mainly located in Ba-rich minerals is not well established. Romanechite probably forms with or after lithiophorite because of intergrowth prismatic crystals of lithiophorite in romanechite (►Fig. 7.22a). The formation of the lithiophorite/romanechite sequence probably starts before or at the same time with collomorphous aggregates.

The end of the sequence is marked by recent processes including late calcite/aragonite (►Figs. 7.21c, d, 7.22e, f and g) and locally halite (►Fig. 7.21c). Fe oxides are sometimes observed in fractures and in the form of disseminated grains in the core of the orebodies. Barite also appears in hollandite-romanechite rich samples as small patches (►Fig. 7.21h) or in veins, indicating that barite occurs at the end of the sequence.

Brecciation and reworking processes affect the whole district. The main observation of these processes is the occurrence of internal sediments, two breccias and veins containing calcite/aragonite, quartz, feldspars, Mn oxyhydroxides and

dolomite relics. According to Gutzmer *et al.* (2006), brecciation may be associated to karstification periods because of the succession of five lithotypes showing successively the absence, the occurrence and the reworking of Mn oxyhydroxides. Brecciation and reworking probably occur synchronously to the major ore formation.

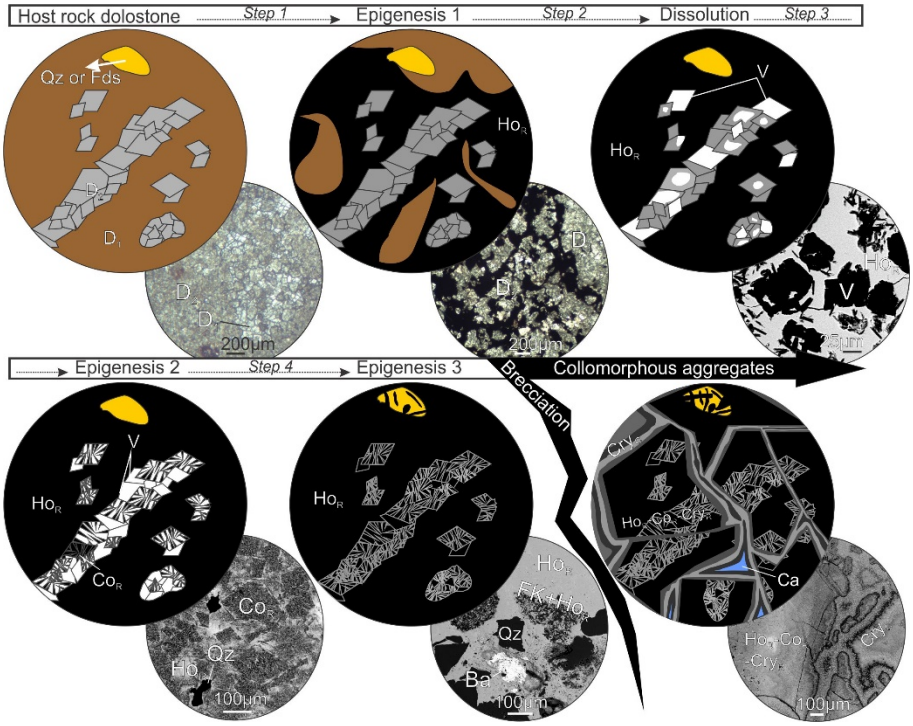

►**Fig. 7.24** Main epigenetic scheme for the ore formation: the host dolostone has been progressively replaced mainly by hollandite group minerals, and then, during brecciation periods providing open spaces where collomorphous aggregates can grow. Epigenesis 1, 2 and 3 correspond respectively to the replacement of dolomite micrite, dolomite rhombs and quartz by Mn minerals. From left to right: IM61 (fossiliferous dolostone); IM30 (fossiliferous dolostone); IM37 (C_1-C_2 layers); LAN59 (fossiliferous dolostone); IM39 (C_1-C_2 layers); IM41b (C_3 layer). D_1 = dolomicrite, D_2 = dolosparite, V = void, Ho_R = replacement of dolomite by hollandite *s.s.*, Cry_R = replacement of dolomite by cryptomelane; Co_R = replacement of dolomite by coronadite, Cry_C = collomorphous cryptomelane, Qz = quartz, V = void, FK = K-feldspar, Fds = feldspar, Ca = calcium carbonate.

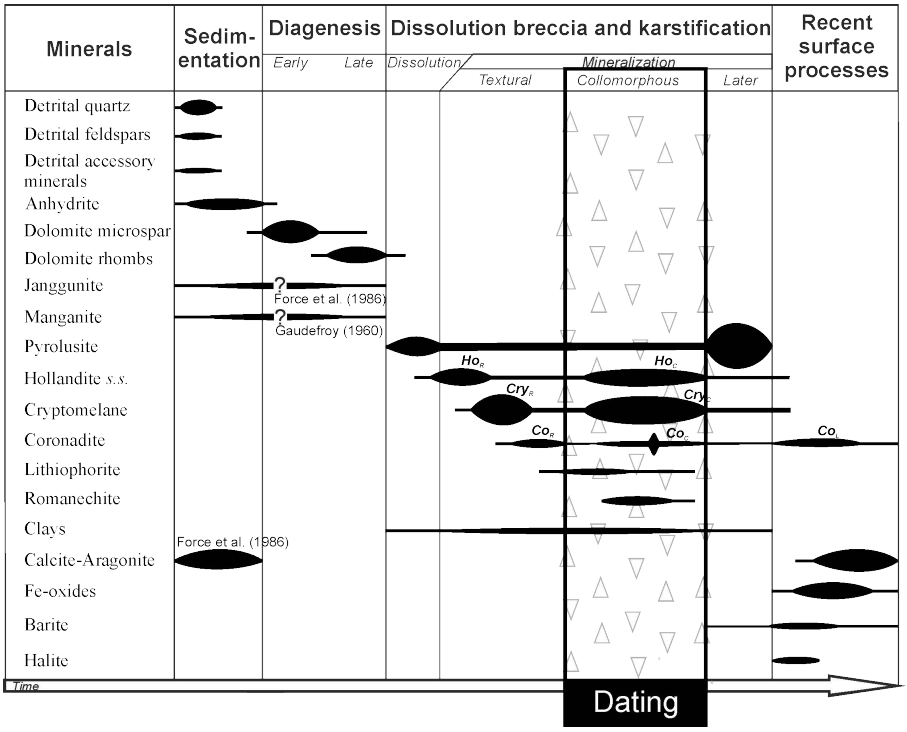

►**Fig. 7.25** Tentative paragenetic sequence for the Mn oxyhydroxide deposits of the Imini district. The dated samples (see section 7.5) are colloformous cryptomelane. Ho_R = replacement of dolomite by hollandite *s.s.*; Cry_R = replacement of dolomite by cryptomelane; Co_R = replacement of dolomite by coronadite; Ho_C = collomorphous hollandite *s.s.*; Cry_C = collomorphous cryptomelane; Co_B = collomorphous coronadite; Co_L = late coronadite, Triangle = main brecciation events. Janggunite and manganite are reported from Gaudefroy (1960).

7.2.7 Metallogenic models and classification

Since 1929, the manganese deposits of the Imini district have been attributed to four different metallogenic models: (1) synsedimentary, (2) diagenetic, (3) hydrothermal, and (4) karst-hosted. We summarize below the main aspects of these models.

(1) Most workers have proposed a synsedimentary origin in order to explain the stratiform character of the orebodies (Neltner, 1933; Orcel, 1942; Bouladon and Jouravsky, 1952; Lesavre, 1975; Pouit, 1980; Force *et al.*, 1986; Thein, 1990; Lalaoui *et al.*, 1991; Rhalmi *et al.*, 1997). The interbedded orebodies seem to occur between transitional facies of the dolomite host rock, and have been linked to transgressional phases of the Cenomanian-Turonian paleoshoreline (Bouladon and Jouravsky, 1952) or to marine paleocurrents (Pouit, 1964; Lesavre, 1975). The presence of Mn-dolomite

below the cherty dolostone in the Aghbalou deposit (30 km SW of Imini) and of psilomelane interbedded in the dolostone (Lesavre, 1975) or chert (Force *et al.*, 1986) supports this synsedimentary model. Large regional halos of minor metals in the surrounding carbonates record a geochemical anomaly that could be related to remobilization of these metals and Mn in an anoxic deep ocean with deposition occurring near the coast where reducing metalliferous seawater mixed with oxidized ground waters (Thein, 1990).

(2) An alternative diagenetic model, proposed by Force *et al.* (1986) and revised by Thein (1990), argues that the host rock became dolomitized in a mixing zone between CO_2-bearing fresh ground water and Mg-bearing saline seawater. In this model, chert, hollandite group minerals, and calcite precipitated concurrently in the uppermost part of the meteoric zone. The first Mn-mineral janggunite subsequently formed hollandite group minerals followed by pyrolusite owing to increased oxidation (►Fig. 7.25; Force *et al.*, 1986). Two variants of the model have been proposed: (i) primary sedimentary manganese was modified by diagenesis, or (ii) Mn oxides precipitated in a ground-water mixing zone. A sedimentary origin for the Mn necessarily implies lower Pb and Ba (►Table 7.1) contents and the existence of primary sedimentary Mn minerals (Force *et al.*, 1986; Lalaoui *et al.*, 1991). On the other hand, precipitation of Mn oxides during diagenesis requires the transport of reduced Mn, and the presence of other Mn oxide deposits at the same stratigraphic level in Cenomanian-Turonian dolostone that formed on the margin of anoxic seas (Force *et al.*, 1986). Both synsedimentary and early diagenetic models need to be revisited because Mn oxides in the district form *stratabound* lenses rather than stratiform beds (Gutzmer *et al.*, 2006), and because the Mn minerals clearly postdate dolomitization (►Fig. 7.25; Dekoninck *et al.*, 2016a).

(3) Close to the Imini area, several epithermal Mn-rich veins that cut both Triassic and Cenomanian rocks have been attributed to a deep hydrothermal origin (Westerveld, 1951; Pouit and Jouravsky, 1960a). However, such veins are small and local, and do not relate to the main mineralogy of the *stratabound* ores. We should rather expect enrichment in As-Cu-Mo-Pb-V-Zn within hydrothermal Mn deposits, which is not observed (►Table 7.3, ►Fig. 7.23b; Nicholson, 1992).

(4) Moret (1931) suggested a lateritic formation for the Imini deposits following the Cenomanian-Turonian transgression. However, Lesavre (1975) and Beaudoin *et al.* (1976) provided the first observations on the role of weathering processes in Mn ore concentration after the Cenomanian and Turonian. These authors noted that the host dolostone has preferentially undergone weathering and dissolution due to its permeable character (►Figs. 7.20a, c and d). Nonetheless, it might be argued that these processes only affected the primary Mn concentrations and conserved original sedimentary morphology. The main issue is the low solubility of

Mn^{4+} in meteoric waters (Lesavre, 1975; Beaudoin *et al.*, 1976). Geochemical data and petrographic observations obtained by Gutzmer *et al.* (2006) and in these studies indicate that a karst-hosted model, involving epigenetic processes of Mn deposition, is the best mechanism to explain Mn ores in the Imini district. The manganese ores are spatially associated with siliciclastic sediments that were washed into the cave system by meteoric waters and then transported and redistributed by ground waters (►Fig. 7.20d). Evidence for this process is recorded by sedimentary textures and reworked grains of Mn oxides within internal karst-fill sediments (►Fig. 7.20d), as well as by the dissolution and collapse breccias (►Figs. 7.20; Gutzmer *et al.*, 2006). Distal dolostone contains only trace amounts of manganese and little insoluble siliciclastic components such as SiO_2 and Al_2O_3 (►Table 7.1). Total dissolution of the host dolostone to form *stratabound* Mn orebodies, 1 to 2 m thick, would only lead to a few centimeters of *in situ* insoluble siliciclastic residue (Gutzmer *et al.* 2006). Recent observations in the district of Fe oxide nodules within distal and proximal host rocks (►Figs. 7.21e; Dekoninck *et al.*, 2016a) suggest an authigenic source for the manganese. However, the thickness and the amount of Fe nodules, which could host Mn, are not sufficient to provide the high Mn/Fe ratios and concentration in manganese present in the Imini orebodies (►Tables 7.1 and 7.3). Therefore, both siliciclastic internal sediments and *stratabound* Mn oxides and oxyhydroxides must have been introduced from one or more external sources during *in situ* chemical and mechanical dissolution of the host dolostone (Gutzmer *et al.*, 2006). The presence of compositionally different layers in the colloform cryptomelane supports this model (►Fig. 7.22c; Dekoninck *et al.*, 2016a). Moreover, the occurrence of hollandite *s.s.* and coronadite provides large enrichments of Ba and Pb, which are very unusual in synsedimentary Mn deposits (►Table 7.1, ►Fig. 7.23b; Nicholson, 1992), as coronadite and lithiophorite are normally found in the weathering zones of hypogene manganese and lead deposits (Hewett, 1971; de Villiers, 1983). The proposed external input of manganese gives to the Imini deposits an unusual feature compared to other well-known karst-hosted Mn deposits, such as those in the Postmasburg manganese field of South Africa (Gutzmer and Beukes, 1997).

7.2.8 Timing of manganese mineralization

The replacement of late diagenetic dolomite rhombs by hollandite group minerals (►Fig. 7.22b) indicates that Mn mineralization occurred after dolomitization and late diagenesis, and therefore after the Turonian stage (Dekoninck *et al.*, 2016a). Dissolution of the host dolostone led to the formation of the *stratabound* manganese orebodies, within karstic pipes that are connected to the paleosurface and were infilled by epigenetic processes (►Figs. 7.20a and b). Gutzmer *et al.* (2006) suggested that karstification occurred prior to, and continued throughout, manganese oxide deposition by the early Senonian. However, attempts to accurately date the internal

karst-fill sediments and their origin should be discussed. Age constraints are mainly based on the change in physicochemical conditions in lithotypes attributed to a climate change between the Upper Turonian and Senonian, as well as on the exposure of the manganese ores to a pre-Senonian erosion surface. Moreover, alignment of the orebodies along a N70°E direction might indicate a structural origin of the karstification. However, no tectonic phase is recorded during the Late Cretaceous, which thus argues for a later mineralization during building of the Atlas Mountains. During the Cenozoic exhumation of the Atlas Mountains (Leprêtre *et al.*, 2015b), mineralizing fluids could have percolated down through weak zones such as faults, permeable strata, or stratigraphic boundaries in the dolostone, and then reactivated mineral deposition or reworked the previously formed manganiferous orebodies as well as the karst features (►Fig. 7.26). Alignment of orebodies in the district also might be controlled by the paleoshoreline of the Triassic red beds, having formed a stratigraphic trap for the Mn ore. The enrichment in Fe minerals to the north and Mn minerals to the south may be explained by the flow of meteoric waters preferentially in this direction. Iron precipitates faster in O_2-rich environments than manganese (e.g., Maynard, 2014), a process that might be responsible for the presence of pyrolusite to the north and psilomelane to the south (Lesavre, 1975).

7.2.9 Fluid composition and potential sources

Manganese is a soluble element with a bivalent state in reduced and acidic environments (e.g., Hem, 1963). Aqueous fluids at low temperature (<100°C) can transport significant quantities of Mn, Ba, and Pb only if acidic, at low to moderate Eh, and sulfur-poor. The presence of appreciable sulfate or sulfide ions in fluids leads to the precipitation of barite and galena and, under alkaline conditions Ba and Pb form witherite and cerussite, respectively. However, these minerals are absent or scarce in the Imini orebodies. Higher temperatures or salt contents would have increased the capacity of the fluids to transport Mn, Ba, and Pb (e.g., Seward and Barnes, 1997). Gutzmer *et al.* (2006) proposed that manganese orebodies in the karstic environment formed during a period of terrestrial exposure, in which the well-developed karst system corresponded to the mixing vadose zone between O_2-rich surficial waters and O_2-poor (and mildly acidic) low-temperature fluids derived from deeper sources (►Fig. 7.26). In this model, the latter fluids ascended through basement rocks and leached metal cations. The laterally extensive cave system tended to form in the zone of a fluctuating ground water table. Fluctuations of this water table could be responsible for occurrence of the three epigenetic *stratabound* orebodies from C_1 to C_3. The presence of modern halite (Dekoninck *et al.*, 2016a) suggests that the Mn-bearing fluids also were saline and originated from surface input. Dissolution of the host dolostone could explain the precipitation and epigenetic replacement of Mn-Ba-Pb-rich oxyhydroxides and quartz by hollandite group minerals (►Fig. 7.21h;

Dekoninck *et al.*, 2016a). In addition, the Mn accumulation also could have been enhanced by bacterial filament formation, as observed in the romanechite-rich samples (►Fig. 7.22a) and also in stromatolites from the upper part of the C_3 orebody (Lesavre, 1975).

Voluminous volcanic rocks of the Anti-Atlas region may be the ultimate source rocks for the unusual metal assemblage in the manganese ores of the Imini district. These rocks constitute the Senonian hinterland to the south of the district, and contain several manganese, barite, and Pb-rich base-metal deposits (Neltner, 1933; Orcel, 1942; Westerveld, 1951; Bouladon and Jouravsky, 1952; Pouit and Jouravsky, 1960a; Pouit, 1964; Lesavre, 1975; Pouit, 1976). Also important is the presence in the volcanic rocks of large amounts of K and Ba in K-feldspar, and base metals in mafic minerals (Gutzmer *et al.*, 2006). An alternative source of the metals could also be the High Atlas Mountain to the north, where Triassic basalts are exposed (Moret, 1931).

7.2.10 Other manganese deposits hosted in Cenomanian-Turonian dolostone

A small manganese deposit is situated at the Upper Souss River, near the village of Tasdremt, 100 km to the west of the Imini area (►Fig. 7.19a). This deposit was mined from 1930 to the 1960s with reported grades of 39 to 56 wt. % MnO, 4.8 to 6.9 wt. % PbO, 5.1 to 7.2 wt. % BaO, 0.5 to 1.1 wt. % Fe_2O_3, and 6.9 to 26.3 wt. % SiO_2, including some similarities to the manganese deposits at Imini (Bouladon and Meune, 1951; Bouladon and Jouravsky, 1952; Lesavre, 1975). The Tasdremt deposit is hosted in Cenomanian-Turonian dolostone and separated from the basement by a few meters of red “infra-Cenomanian”. Manganese oxides and oxyhydroxides are dominated by coronadite and hollandite *s.s.* (Lesavre, 1975), which occur in two irregular layers ~0.2 m and 0.6 m thick that replace some corals and other organisms. Pyrolusite constitutes a minor mineral in contrast to the Imini ores. The deposition of manganese at the Tasdremt deposit is considered to be synsedimentary (Thein, 1990) or linked to dolomitization (Lesavre, 1975). The Aghbalou deposit ca. 30 km southwest of Imini (precise location is not known) shows little enrichment of stratiform Mn and Fe below the cherty dolostone that corresponds to the C_3 orebody. This deposit produced only 5 kt of manganese at an average grade of 30 wt. % MnO. Manganese there occurs as small needles of coronadite within the host dolostone (Lesavre, 1975).

►**Fig. 7.26** Time-event chart and revisited metallogenic model for Imini district illustrating multistage character of ore deposition and likely tectonic control during the Cenozoic. See text for discussion on role of mineralizing fluids and potential metal sources. Abbreviations: Py, pyrolusite; HGM, hollandite group minerals; Co, coronadite.

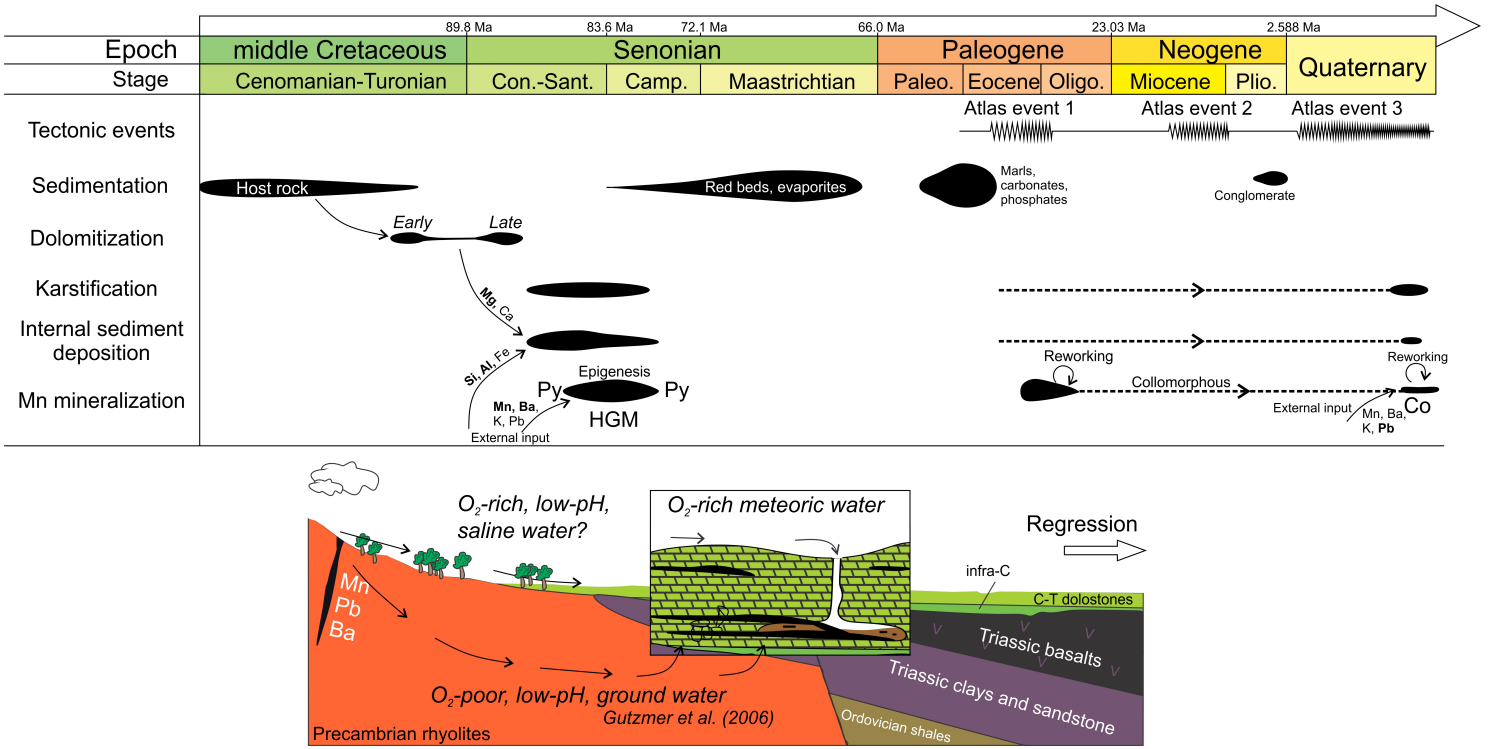

7.2.11 Conclusion

Our mineralogical and petrological observations provide new insights to the multistage formation of Mn oxides and oxyhydroxides after dolomitization with an early pyrolusite, Mn oxyhydroxides (romanechite, lithiophorite and hollandite group minerals: hollandite *s.s.*, cryptomelane and coronadite) and then late pyrolusite. The relative timing of Mn oxyhydroxide precipitation is rather complex and probably involves several phases of dissolution/precipitation and karstification. Microscopic observations point out **two different stages of epigenetic neoformation** of hollandite group minerals: (1) replacement of the dolomite fabric, firstly on dolomite micrite and, secondly on dolomite rhombs, and then (2) collomorphous aggregates formed in an opened system. Recent mineral formation continues with late coronadite associated to calcite/aragonite. The occurrence of Mn oxides and oxyhydroxides indicates a high oxidizing and supergene environment, without local precursors of Mn such as silicates or carbonates. The multiple external influxes of Mn and associated elements (Pb, Ba, K …) are well marked in collomorphous aggregates with various compositional layers deposited in an *in situ* chemical and mechanical dissolution environment. The absence of significant amounts of MnO in distal dolostone and in primary minerals, as well as the close spatial relationship between internal sediments and ore beds, suggests an epigenetic, **karst-filling deposition of manganese** oxides in the Imini area.

Ore deposition in the district occurred after host-rock formation and diagenesis, probably during post-Turonian karstification of the dolostone, followed by reactivation or/and reworking of the Mn minerals during Cenozoic uplift(s) of the Atlas Mountains. Formation of the orebodies implies neutralization of the host dolostone by fluids to provide the high pH and O_2-rich conditions necessary for manganese precipitation. The *stratabound* character of the ore is attributed here to preferential karstification and epigenetic processes, permeability, and lithological heterogeneities within the dolostone sequence in comparison with the surrounding rocks (magmatic bedrock, Ordovician shales, Infra-Cenomanian clayey sandstone and overlying Senonian red beds and evaporites). Fe oxides are almost absent and quartz is partly replaced by Mn oxides in ore zones. These observations probably explain the low content in Fe and Si compared to other Mn deposits. Geological WSW-ENE structures may play a role in manganese concentration in the Imini area by focusing the ore fluids. The main sources for manganese and related metals (Pb, Ba) in the Imini orebodies may be the Anti-Atlas basement or Triassic basalt of the High Atlas Mountains.

7.3 Multistage genesis of the late Cretaceous Mn(-Pb) Tasdremt deposits evidenced by petrographic analysis and $^{40}Ar/^{39}Ar$ dating of K-Mn oxides (Souss Basin, Morocco): a lateral equivalent of the Imini ores.

In 1951, Bouladon and Meunes investigated Mn occurrences 60–100 km to the south-west of the Imini district, in the Tasdremt and Aoufour areas (Souss Basin; ►Figs. 7.27a and b). The Mn mineralization displays common features with the Imini ores as they are hosted in Cretaceous dolostones, but more interestingly, they show also significant differences, including lower grade ores and discontinuous orebodies. Only 22,000 tons of manganese were extracted from the Tasdremt deposits because of their atypical composition containing up to ~6% of Pb (and Ba; Bouladon and Meune, 1951), a feature quite uncommon in manganese deposits (i.e., Varentsov, 1996; Maynard, 2010; Kuleshov, 2016). Only the upper C3 Mn orebody of the Imini ores contained such high Pb concentration due to the presence of coronadite and Pb-rich hollandite group minerals (Gutzmer *et al.*, 2006 ; Dekoninck *et al.*, 2016b, 2016a). Therefore, the Tasdremt manganese deposit could be seen as a potential equivalent of the high-grade Imini district and a target for mining companies (Bouladon and Meune, 1951 ; Pouit, 1980 ; Office National des Mines et des Hydrocarbures, 2016). Other Mn spots also occur between the Imini and Tasdremt deposits (►Fig. 7.27b).

In this paper, we investigate the Tasdremt ores and their genetic relation to the nearby Imini mineralization with a systematic review of their mineralogy, petrology, chemistry and timing.

7.3.1 Geological setting

The Tasdremt district is located in the eastern termination of the Souss Basin, between the Anti Atlas (South), the High Atlas (North) and the Siroua plateau (East), 70 km to the east of Taroudant, and 90 km to the south-west of the Imini manganese mine (►Figs. 7.27a and b). The manganese ores are hosted in Cretaceous rocks along a SW-NE direction in the Tasdremt and Aoufour areas, parallel to Atlasic structures (►Figs. 7.27b and c; Bouladon, 1948). The Anti Atlas has undergone numerous folding during the Panafrican and Variscan orogenic cycle (Gasquet *et al.*, 2005; Youbi *et al.*, 2013; Michard *et al.*, 2017), whereas the Atlas is clearly an intraplate belt structured during a late Eocene and a late Pliocene-Quaternary event, mostly in relation to the distant effect of the Alpine orogenesis (Frizon de Lamotte *et al.*, 2000b, 2008, 2009; Leprêtre *et al.*, 2015b). The anomalously high elevation of the High Atlas, Middle Atlas as well as the Anti Atlas in Morocco and the lack of crustal roots, led several authors to propose that lithospheric thinning supports the current topography

and was superimposed to the tectonic settings in these areas during an Early-Middle Miocene doming (Seber et al., 1996; Teixell et al., 2005; Zeyen et al., 2005; Missenard et al., 2006, 2007, 2008; Fullea et al., 2007, 2010; Jiménez-Munt et al., 2011; Gouiza et al., 2017). Therefore, the Atlas building results from both Cenozoic tectonic inversion and thermal uplift associated to alkaline Neogene volcanism in the Siroua area (►Fig. 7.27b). This uplift is likely to have dismantled Eocene foreland basins over the Siroua plateau (Missenard *et al.*, 2006; Frizon de Lamotte *et al.*, 2009).

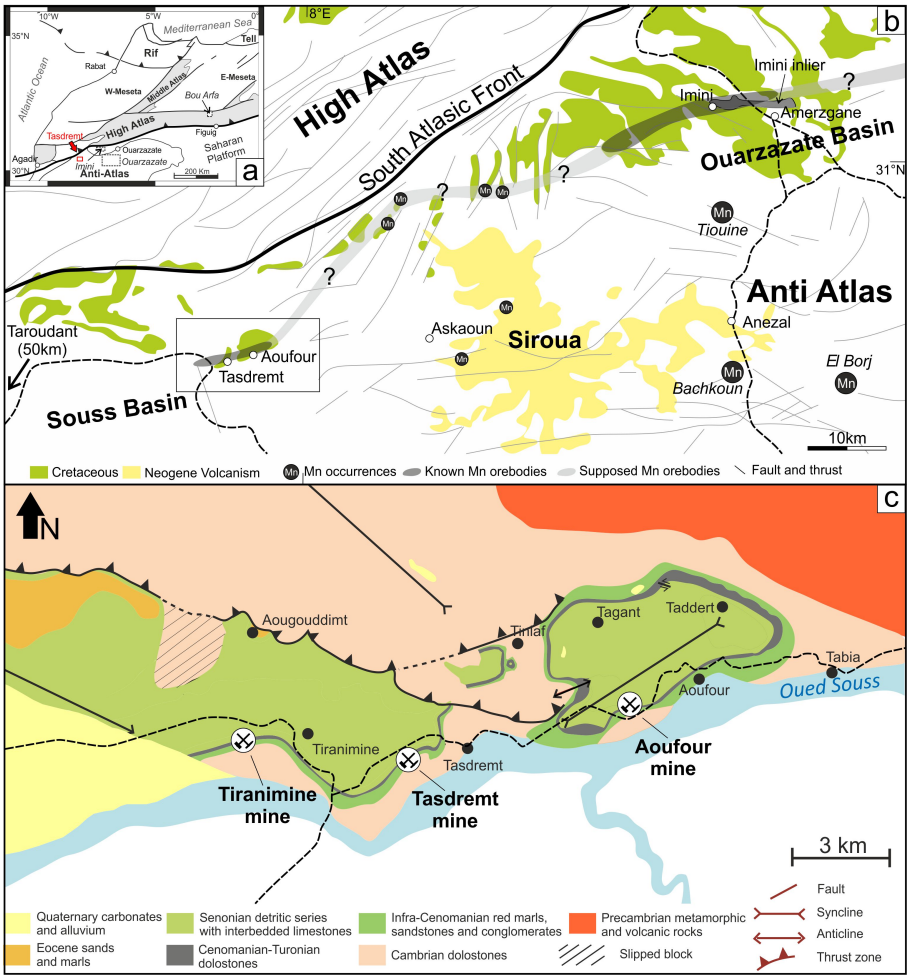

►**Fig. 7.27 a.** Location of the Tasdremt and Imini districts in the structural map of North Africa. SAF=South Atlasic Front. **b.** Geological map of Cretaceous sediments and Neogene volcanism showing known reserves of Imini and Tasdremt ores (drawn from Hollard, 1985). **c.** Simplified geological map of the Tasdremt area, showing the location of the ancient Tiranimine, Tasdremt and Aoufour mining sites (modified after Choubert, 1957; Hollard, 1985).

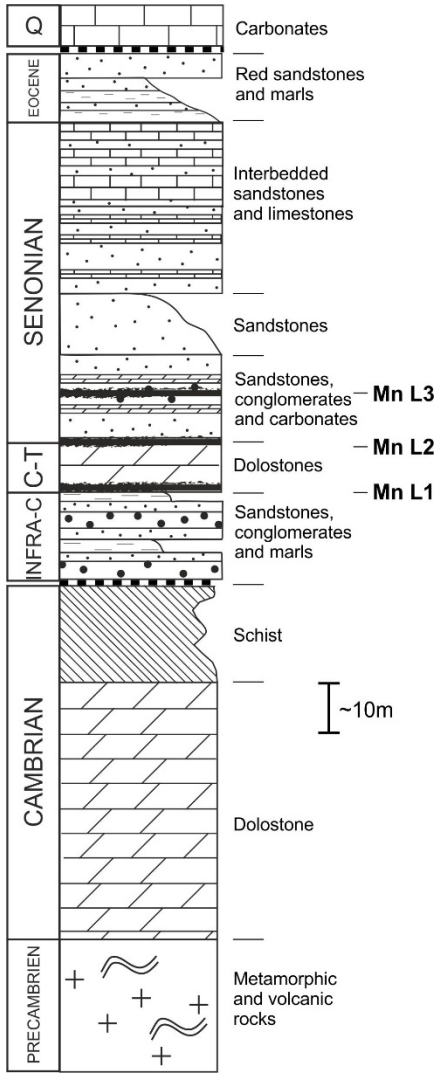

►**Fig. 7.28** Simplified stratigraphic log of the Tasdremt area, showing the three manganiferous levels (modified after Bouladon and Meune, 1951; Ambroggi, 1963).

The Cretaceous succession lies unconformably over the Paleozoic bedrock (►Fig. 7.28). The basement exposes mostly a fine grained massive gray dolostone Early Cambrian in age (early Georgian; ►Figs. 7.27c and 7.29a) in the Tasdremt district, but younger Cambrian-Ordovician (undetermined) colored marls and schists occur progressively to the east in the Aoufour area (Neltner, 1938; Dresch, 1941). These Paleozoic rocks are dissected leading to variable thickness along the district and characterize therefore a pre-Cenomanian paleosurface, as no sediments were deposited since the Cambrian (►Fig. 7.29a). Some of these rocks (south of Tasdremt) contain Mn veins deposits capped by gossans, indicating pre-Cretaceous

mineralization (Bouladon and Meune, 1951), well-known in Neoproterozoic volcanic rocks of the Anti Atlas (Bouladon *et al.*, 1955; Pouit and Jouravsky, 1962; Jouravsky, 1963; Jouravsky and Pouit, 1963; Choubert and Faure-Muret, 1973; Pouit, 1980; Lippolt and Hautmann, 1995). The Cretaceous sedimentation is a transgressive succession of a 0–30 m thick detritic series (infra-Cenomanian; ►Figs. 7.28, 7.29a and b), a 0–20 m thick dolostone Cenomanian-Turonian in age (►Figs 7.28 and 7.29b), and a Senonian continental detritic succession (70–200 m thick; ►Figs. 7.28, 7.29c and d). The infra-Cenomanian sediments correspond to red sandstones and conglomerates reworking some of the Lower Cambrian dolostone, with interbedded red clay levels (►Figs 7.28, 7.29a and b). These levels contain paleosoils evidenced by roots epigenized by Mn oxides. The Cenomanian-Turonian dolostone is subdivided into (i) a yellow/gray dolostone containing ursine fossils at the base (2–14 m thick), which is covered by (ii) a pinkish/white fossiliferous dolostone (1–8 m thick; ►Fig. 7.28 and 7.30), the top being brecciated in contact with the Senonian conglomerates and determine the pre-Senonian erosion surface (►Figs. 7.29e and f). The detrital part of the Cenomanian-Turonian dolostone increases to the top of the sequence. The Senonian succession is mostly detritic but differs from the infra-Cenomanian by the higher content in dolomite. Some sandy dolostone levels are interbedded with the conglomerate and sandstone in the first 20–50 m and leave only red sandstone for the next 50–150 m (►Fig. 7.29d). The upper part could contain red sandstone alternating with white limestone in the Tasdremt area (Bouladon and Meune 1951; ►Figs. 7.28 and 7.29d). Note that Bouladon and Meune (1951) considered the lower part of the upper detritic series as the upper part of the Cretaceous sequence. However, considering the common points between the Cenomanian-Turonian dolostone sequence in the Tasdremt area with the one previously described by several authors along the Moroccan Atlas (Ambroggi, 1963; Rhalmi, 1992; Algouti *et al.*, 1999; Rhalmi *et al.*, 2000), we should consider the dolomitized sandstone, conglomerates and marls as part of the Senonian, and the fossiliferous dolostone as the uppermost part of the Cenomanian-Turonian (►Fig. 7.28). The boundary between these two series is additionally marked by an oxidized erosion surface and reworked blocks of Mn ore (►Figs 7.29c,e and f). The variable thickness of the whole Cretaceous series is attributed to paleotopographic heights of the Cambrian dolostones (►Fig. 7.30). Eocene red sands and marls are only present in the western part of the Tasdremt district (►Fig. 7.27c; Ambroggi, 1963).

Atlasic deformations have been superimposed on the Variscan folding of the Cambrian bedrock. Cretaceous and Cenozoic rocks were deformed during a post-Cretaceous phase, which has resulted in (1) the formation of the NE-SW Aoufour syncline, (2) a NW-SE anticline in the western part of the Tasdremt area and (3) the thrusting of Cambrian bedrock onto Cretaceous sediments (►Fig. 7.27b). Such

deformation is also evidenced by an angular unconformity of quaternary sands onto Cretaceous rocks (Bouladon and Meune, 1951; Parizot, 2017).

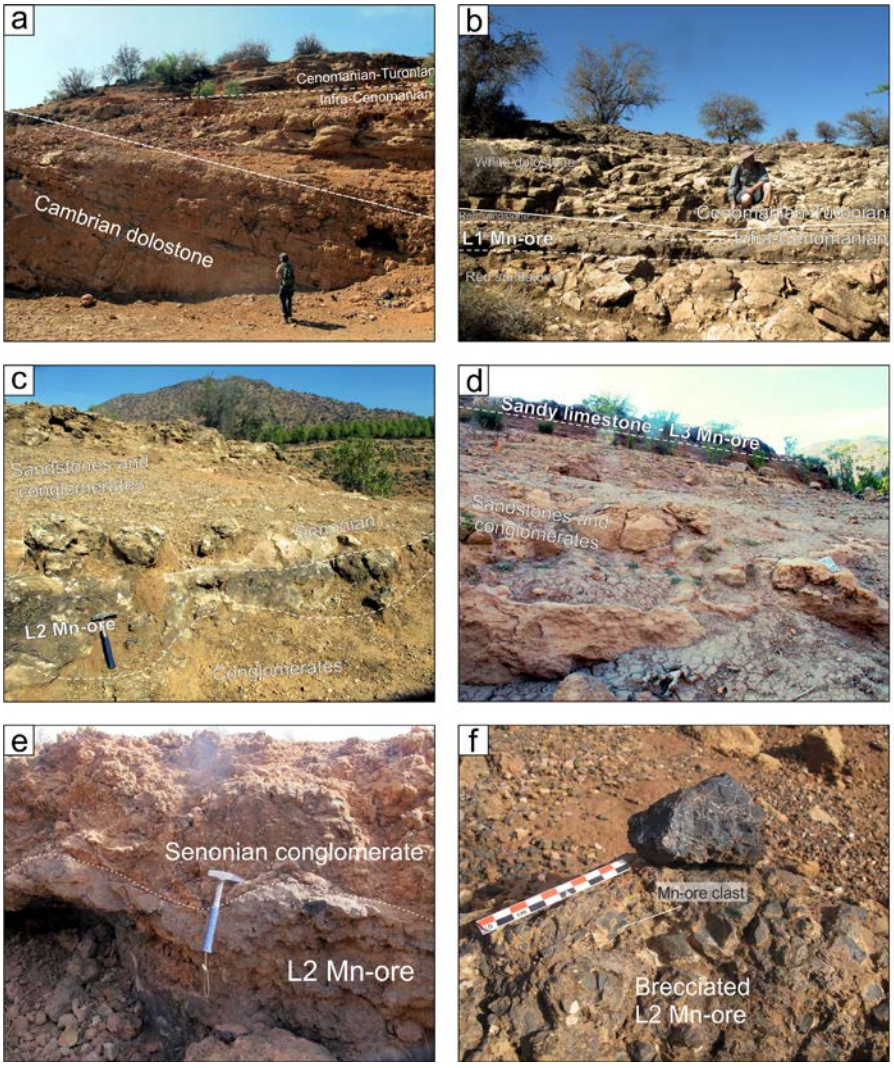

►**Fig. 7.29** Field observations. **a.** Angular unconformity between the Cambrian dolostones and the Cretaceous succession at Tasdremt. **b.** L1 Mn ore levels at the boundary between red sandstone (infra-Cenomanian) and dolostones (Cenomanian) at Tiranimine. **c.** L2 orebody located in the Senonian conglomerates and sandstones at Tasdremt. **d.** Upper L3 orebody situated in a sandy limestone level (Senonian) at Tasdremt. **e.** L2 manganiferous level at the boundary between the lower fossiliferous dolostone and the upper Senonian conglomerates in the Aoufour mine. The ore is a breccia delimited by a paleosurface. **f.** Brecciated L2 Mn ore at the top of the fossiliferous dolostone at Aoufour.

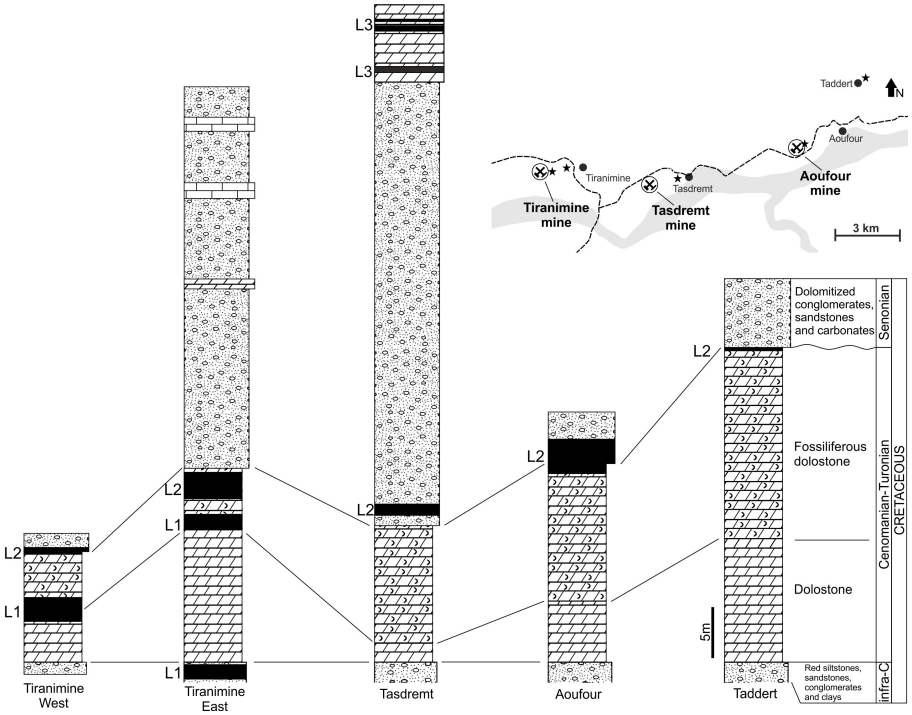

►**Fig. 7.30** Stratigraphic position of the Mn orebodies along a West—East transect showing the *stratabound* character. Stratigraphic logs are located by stars on the map of the upper right corner.

7.3.2 Material and methods

Our investigations focused on three ancient mining sites located at Tiranimine, Tasdremt and Aoufour, where Mn ores crop out (►Fig. 7.27c). Small trenches and galleries of several meters long are the only witness of this mining activity and constitute target areas to investigate the orebodies, as well as dry streams. Note also that the southern part of the Tasdremt mine has been flooded since 1990 by the Aoulouz dam (►Fig. 7.27c). We have also investigated "fresh" distal rocks located at Taddert, several kilometers from the main Mn concentrations (►Fig. 7.27c). From these sampling sites, we have built five stratigraphic logs, and reported them in ►Fig. 7.30 to show up the stratigraphic position and lateral variations of the Mn ore levels. More than one hundred samples were collected from these sites in order to determine the chemical composition, the mineralogy and petrography of these ores and host rocks. From these samples, twenty-three geochemical analyses were performed for major and trace elements (►Tables 7.4, 7.5 and 7.6), twenty-seven polished sections and twenty-two thin sections were prepared for petrographic analyses. All these samples were analyzed for their mineralogy by XRD. Additionally,

fourteen $^{40}Ar/^{39}Ar$ step-heating experiments were performed on carefully selected fragments of K-Mn oxides from the different sampling sites.

7.3.2.a Mineralogy and petrography

XRD analyses of powdered samples were performed using X-ray Panalytical X'Pert Pro diffractometer and a PHILLIPS PW3710 (CuKα radiation) at the PC2 platform (UNamur), operating at 40kV and 30mA. Thin and polished sections were studied by light microscopy and some of them by a JEOL 6010 LV and 7500-F Scanning Electron Microscopes coupled with an ULTRA MINI-CUP Energy Dispersive Spectrometer.

7.3.2.b Geochemistry

Geochemical analyses were carried out at Activation Laboratories Ltd (Actlabs, Ontario, Canada; ►Tables 7.4, 7.5 and 7.6). REE and trace elements were analyzed by Fusion Mass Spectrometry (FUS-MS) and major elements by Fusion Inductively Coupled Plasma Optical Emission Spectrometry (FUS-ICP). FeO was quantified by titration. Trace elements Ba, Sc, Be, Sr, Y, Zr and V were determined with FUS-ICP. Gold was evaluated by the Instrumental Neutron Activation Analysis (INAA): samples were encapsulated and irradiated in a nuclear reactor. After a suitable decay, samples were measured for the emitted gamma ray fingerprint. FUS-ICP, ICP-OES was used to evaluate Pb and Mo concentration, after a 4-acid digestion process (hydrochloric-nitric-perchloric-hydrofluoric acids), when values higher than the detection limits (10,000 ppm and 100 ppm, respectively) were reached. Considering the supergene nature of the Mn ores and the lack of several metals in the Post Archean Australian Shale reference, REE and trace elements are normalized to the Upper Continental Crust (McLennan, 2001).

7.3.2.c K-Mn oxides geochronology

Fourteen grains of hollandite group minerals were selected in the three investigated sampling sites: six samples come from Tasdremt, four from Tiranimine and four from Aoufour. One sample is located in the L1 Mn ore level at Tiranimine, twelve samples in the L2 Mn orebody (in the fossiliferous Cenomanian-Turonian dolostone and/or in the Senonian conglomerates) and one sample in the L3 Mn ore level in the Senonian dolostones at Tasdremt (►Table 7.7). Eight of these samples are pure hollandite group minerals, whereas six others could display quartz, dolomite and calcite inclusions. Such heterogeneous material was deliberately selected because they represent the best-preserved samples for some specific levels (i.e., L3 Mn ore) as other equivalent cannot provide pure K-Mn oxide phases.

$^{40}Ar/^{39}Ar$ step-heating analyses of millimetric Mn oxide fragments, carefully handpicked under a binocular microscope, were performed with a CO_2 laser probe

coupled with a MAP 215 mass spectrometer, using procedure described by Ruffet *et al.* (1991, 1995, 1996, 1997). Irradiation of samples was performed at McMaster Nuclear Reactor (Hamilton, Ontario, Canada) in the 8F facility and lasted 66.667 h with a global efficiency (J/h) of 9.767 x 10^{-5} h^{-1}. The irradiation standard was sanidine TCRs (28.608 ± 0.033 Ma according to Renne *et al.*, 1998, 2010 and 2011). Blanks were performed routinely each first or third/fourth run, and are subtracted from the subsequent sample gas fractions. Apparent age errors are plotted at the 1σ level and do not include the errors on the $^{40}Ar^{*}/^{39}Ar_K$ ratio and age of the monitor and decay constant. Plateau ages were calculated if 50% or more of the $^{39}Ar_K$ was released in at least three or more contiguous steps, the apparent ages of which agreeing to within 1σ of the integrated age of the plateau segment. Pseudo-plateau ages can be defined with less than 50% of the $^{39}Ar_K$ released and possibly less than three contiguous steps. The errors on the $^{40}Ar^{*}/^{39}Ar_K$ ratio and age of the monitor and decay constant are included in the final calculation of the error margins on the (pseudo-)plateau ages. Analytical data and parameters used for calculations (e.g.,isotopic ratios measured on K, Ca and Cl pure salts; mass discrimination; atmospheric argon ratios; J parameter; decay constants) and reference sources are available in appendix V. Meaningful ages are summarized in ►Table 7.7.

7.3.3 Results

The following lines aim to describe the styles, mineralogy and petrography of the host rocks and Mn ores in order to use their composition and textures to better constrain the formation of these minerals in the Tasdremt, Aoufour and Tiranimine deposits. These observations are supplemented by geochemical analyses on whole rock samples. Geochronological data are presented at the end of section and deeply discussed in a separate section as they question fundamentals of the $^{40}Ar/^{39}Ar$ method.

7.3.3.a Macroscopic features of the Mn ores

The Tasdremt manganese ores were mined between 1930 and 1960 (Bouladon and Meune, 1951; Lesavre, 1975) and are currently reinvestigated by the "Office National des Mines et des Hydrocarbures" (Office National des Mines et des Hydrocarbures, 2016). Bouladon and Meune (1951) identified three manganese levels in the Cretaceous succession (►Figs. 7.28 and 7.30). The first two (L1 and L2) are located at the base and top of the fossiliferous Cenomanian-Turonian dolostone (►Figs. 7.29b, c, e and f), while the third (L3) is located in the upper detritic Senonian series (►Fig. 7.29d). The manganese ore exhibits a composition of 14–78 wt.% MnO, and substantial enrichment in Pb (1.0-5.0 wt.% Pb) and Ba (1.5-8.2 wt.% Ba) with the presence of Pb-rich psilomelane and coronadite (►Tables 7.4 and 7.5).

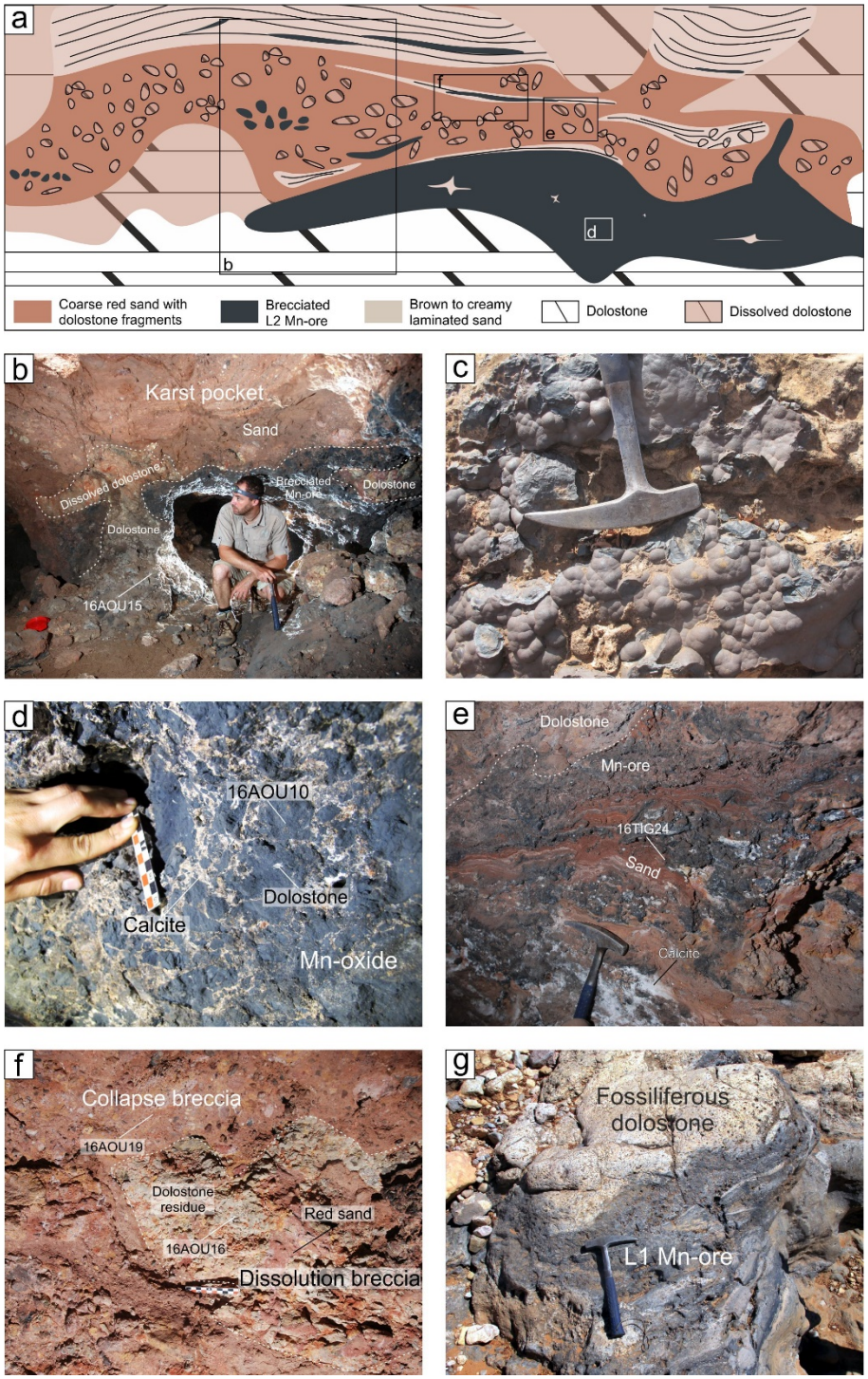

►**Fig. 7.31** Field observation of dissolution processes along the Tasdremt district. **a.** Sketch

illustrating the relationships between manganese ores, dolostones, sands and dissolution breccia. Other pictures are shown by white rectangles in ►Fig. 7.31a. **b.** Brecciated L2 orebody and its relation with the dissolved dolostone and karst cavities filled by sands in the Aoufour gallery. **c.** Botryoidal Mn oxides (hollandite) at the top of the Tasdremt mine. **d.** Brecciated L2 Mn ore filled by a late calcite cement in the Aoufour gallery. **e.** Karstic lenses in the Cenomanian dolostone (Tiranimine) filled with red sands interbedded with reworked Mn oxides blocks. Calcite is late and grows onto sands and Mn oxides. **f.** Relationship between a collapse and dissolution breccia at the top of the Cenomanian dolostone. The collapse breccia (with angular fragments of various origins) may be part of the upper detritic series (Senonian?), whereas the dissolution breccia preserves some residues of the Cenomanian dolostone. Both breccia are filled by a ferruginous matrix. **g.** Fossiliferous dolostone impregnated by Mn oxides (L1?) 2 m below the L2 level at Tiranimine.

The L1 layer is highly variable, from absent to only few cm thick depending on the location. This layer is located at the top of the infra-Cenomanian sands and clays at Tiranimine (►Fig. 7.29b). Bouladon and Jouravsky (1952) have considered this layer (L1) as the same as C1 and C2 orebodies observed in the Imini district (Gutzmer *et al.*, 2006 ; Dekoninck *et al.*, 2016a, 2016 b). The L3 orebody is rather a succession of different layers enclosed in dolostone levels of the siliciclastic Senonian series. According to Bouladon and Meune (1951), these layers are thin (5–10 cm) between Tiranimine and Tasdremt and located 20 meters above the L2 orebody. At Tasdremt, these levels are thicker (40 cm) and located 55 m beyond the Cenomanian-Turonian dolostone (►Figs. 7.29d and 7.30), but a level located 15 m up from the L2 orebody has been evidenced by Bouladon and Meune (1951). These levels are not observed in the Aoufour mine, because erosion has removed most of the upper Cretaceous series. Both the L1 and L3 orebodies disappear to the north and east (►Fig. 7.30).

The L2 orebody remains constant along the district and was considered as the main manganiferous ore mined for the production of metallurgic Mn (►Fig. 7.30). This layer is 80 cm thick at Tiranimine, 30–60 cm at Tasdremt (►Fig. 7.29c) and 20–50 cm at Aoufour (►Fig. 7.29e), while only traces are observed in the eastern part of the district and toward the north (Bouladon and Meune, 1951). The lower boundary of the layer is generally regular whereas the top is often brecciated (►Figs. 7.31a and b). The lower and middle parts of the L2 orebody are sometimes laminated showing yellow dolostone interbedded with Mn oxides. The upper part is progressively enriched in Mn oxides to form massive botryoidal concretions (►Fig. 7.31c) and blocks of psilomelane containing spots of partially dissolved dolostone nodules (►Fig. 7.31f; Bouladon and Meune, 1951). Stratiform layers of cryptocrystalline Mn oxides (wad) are located in small pockets made up of clays and sands (►Figs. 7.31b and e), resulting from dissolution and karstification of the host dolostone. Such dissolution process is clearly observed in the Aoufour mine, where white dolostone nodules are successively surrounded by a dolomitic red sand and sands with small blocks of dolostone, the latter being connected to clayey and sandy pockets

(►Fig. 7.31f). Taken together, these features characterize a dissolution breccia (►Fig. 7.31a). The main Mn ore is situated beneath or alongside these observations, indicating a close relationship between them (►Fig. 7.31a). In Tasdremt, the enclosing dolostone is porous and fractured (►Fig. 7.31c), along which clay levels (►Fig. 7.31e) and geodic cavities are filled by sands (►Fig. 7.31b), calcite or in rare cases by barite crystals (Bouladon and Meune, 1951). However, the most interesting feature of this layer is the presence of reworked fragments of the host dolostone, Cambrian dolostone and blocks of botryoidal Mn oxides in the top of the layer (►Fig. 7.29f), themselves cemented by either late carbonate (calcite; ►Fig. 7.31d), sand or a second generation of Mn oxides. The contact of these two generations of Mn oxides with the host dolostone is irregular showing dissolved patches of the host dolostone, which are connected to a network of veinlets (►Fig. 7.31b). Mn oxides also occur beneath the L2 layer as it is shown by small veinlets and fossil shells of the lowest fossiliferous dolostone, both filled by Mn oxides (►Fig. 7.31g). All these remobilization features at the top of the Cenomanian-Turonian dolostone indicate that the ore is reworked between the Cenomanian-Turonian dolostone and the Senonian detritic cover. One of the main consequences is the variation of the stratigraphic position of the L2 orebody, located beneath or above the Cenomanian-Turonian and Senonian boundary in the sandy dolostone or dolomitized sandstone and conglomerate (►Fig. 7.30). Bouladon and Meune (1951) described that the L2 layer could also lies unconformably onto the Cambrian dolostone heights. The same dolostone could also be brecciated at Tiranimine and filled by Mn oxides.

The lateral extension of the orebodies along the district is variable: the L2 orebody is observed at Aoufour, whereas L2-L3 levels are observed at Tasdremt, and L1-L2 are identified at Tiranimine (►Fig. 7.30). These variations can be significant even at local scale. For example, L2 and L3 are observed east of the Tasdremt mine, whereas L1 and L2 are observed few hundred m to the west. Such limited lateral extension of the orebodies is accompanied by changes in the stratigraphic position of the Mn ore. The L2 ore is located in the upper CT dolostone at Aoufour and Tiranimine (in contact with the Senonian sandstone), while the same ore is clearly situated in the Senonian conglomerates at Tasdremt. In the Tiranimine mine, the L1 (or L2?) level is divided into two orebodies located in the fossiliferous dolostone (►Fig. 7.31g). However, it seems that these levels often occur at the boundary between dolostone and conglomerates, as already suggested by Bouladon and Meune (1951). The lateral extension of these orebodies as well as their variations in the stratigraphic position indicate these layers to be rather lenses or pockets than continuous stratiform orebodies.

7.3.3.b Mineralogy and petrography of the host rocks

The host rock dolostone is composed of a micritic dolomite matrix in which sparitic dolomite crystals fill open voids. Both generations (see below) allow the dolostone to

be very porous as it is shown by numerous open voids, in which Mn oxides and calcite precipitate later (►Fig. 7.32a). Anhydrite ghosts were evidenced (►Fig. 7.32b) and support the hypothesis of a proximal deposition of the dolostone (Ambroggi, 1963; Rhalmi *et al.*, 2000). Quartz, feldspar and apatite are common remnants of detritic sedimentation, but their amount depends on the stratigraphic position (Bouladon and Meune, 1951). Fossil shells are also present and are replaced by either dolosparite, calcite or Mn oxides (►Fig. 7.31g). Calcite is observed as very late infill as it grows onto the dolomite rhombs and Mn oxides (►Fig. 7.32a). Such late calcite also cements fragments of the upper brecciated levels composed of Mn oxide, host dolostone (►Fig. 7.31d) and crisscross dolomite crystals and needles of hollandite group minerals. Dedolomitization texture is also observed (►Figs. 7.32a and c). Such replacement figure of dolomite by calcite strengthen the dissolution observed in the Cretaceous dolostones (►Fig. 7.31).

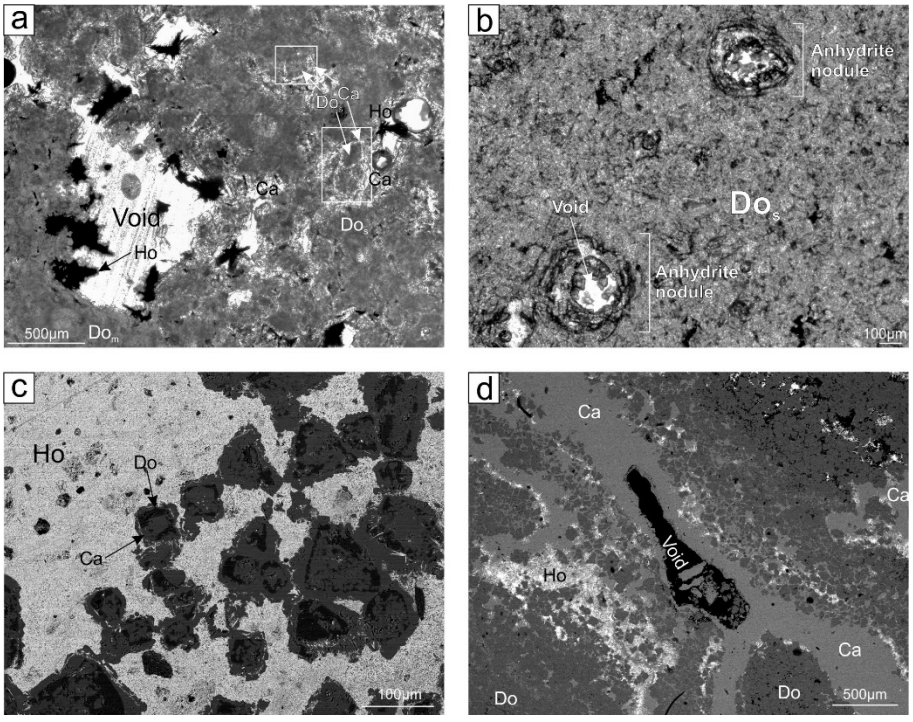

►**Fig. 7.32** Petrographic features of the host-rock. **a.** Micritic dolostone (Do_m) over which sparitic dolostone rhombs (Do_s), and hollandite group minerals (Ho) needles grow in open voids (Aoufour mine; Cenomanian-Turonian; 16AOU06). A late calcite (Ca) partly fills the porosity and replace some of the dolomite crystals (dedolomitization figures; white squares). **b.** Ghosts of anhydrite nodules in the coarse sparitic dolomite matrix (Aoufour mine; Cenomanian-Turonian; 16AOU08). **c.** Dedolomite crystal residues in the hollandite matrix (Tasdremt mine; Cenomanian-Turonian; 16TAS29). **d.** Mineralized levels in the dolostone levels of the upper detritic series (Senonian), showing Mn oxides and calcite filling voids of the host rock (Tasdremt).

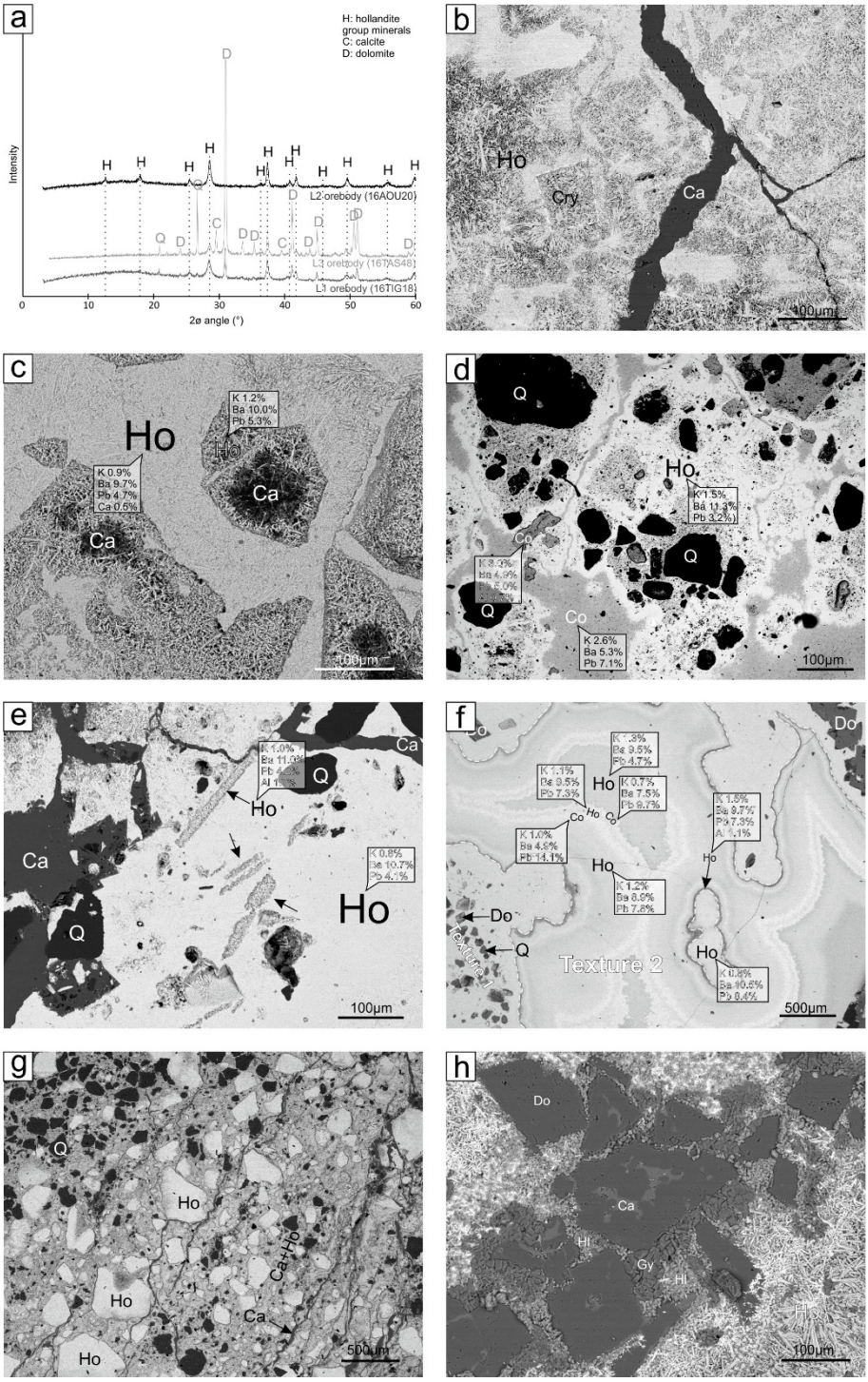

►**Fig. 7.33** Petrographic features of the Mn mineralization. **a.** XRD pattern of the three orebody

showing exclusively hollandite group minerals in a dolomite, calcite and quartz gangue. **b.** Epigenesis of dolomite crystals by cryptomelane in the L2 Tasdremt ore (16TAS22). **c.** Hollandite *s.s.* replacing partially dolomite crystals with calcite in the L2 Tirnaimine ore (16TIG08). **d.** Brecciated ore characterized by epigenetic figures and quartz remnants filled by coronadite in the L2 Aoufour ores (16AOU09). **e.** Epigenesis of lath-shaped crystals thought to be anhydrite and dolomite in the L1 Tiranimine ores (16TIG31). **f.** Growth bands of hollandite and coronadite (texture 2) onto epigenetic textures of the host rock dolostone (texture 1) in the L2 Tasdremt ores (16TAS10). Slight variations in the gray shades are the result of changes in the composition of hollandite and coronadite. **g.** Brecciated hollandite *s.s.* and quartz fragments filled by secondary Mn oxides and calcite in the Tiranimine ore (16TIG29). **h.** Gypsum and halite surrounding dolomite crystals within the hollandite *s.s.* matrix in the wad L1 Tasdremt ore (16TAS37).Ho=hollandite *s.s.*; Cry=cryptomelane; Co=coronadite; Ca=calcite; Q=quartz; Gy=gypsum; Hl=halite.

No specific features characterize the dolomitized sandstones and conglomerates of the upper detritic sequence (Senonian). They are composed of various fragments originating from the lower Cenomanian-Turonian dolostone, or bedrocks showing various mineralogical compositions (quartz, K-feldspar, biotite, ilmenite, kaolinite, dolomite, apatite, etc.). Sandy dolostone levels observed in the upper detritic Senonian sequence are heavily dissolved and brecciated showing dolomite crystals replaced by successively hollandite *s.s.* and calcite (►Fig. 7.32d).

7.3.3.c Mineralogy and petrography of the Mn ores

The mineralogy of the Mn ores displays hollandite group minerals as the only ore-forming minerals (►Figs. 7.31c and 7.33a), despite the fact that rare pyrolusite crystals have been described (Bouladon and Meune, 1951; Office National des Mines et des Hydrocarbures, 2016). Chemical analyses show an intermediate distribution of Ba^{2+}, K^{+} and Pb^{2+} between the end-members of the hollandite group minerals, respectively hollandite *s.s.*, coronadite and cryptomelane (►Tables 7.4 and 7.5). Most of the studied samples are hollandite end-member with subordinate amount of coronadite, their relative presence being determined by the dominant cation identified by EDS spectra. Cryptomelane end-member is poorly identified in the Tasdremt ores. Ba composition of these minerals ranges from 3.54 to 15.1%, K from 0 to 3.9% and Pb from 0 to 15.4%. Al and Ca could be present as well but the latter is more probably related to the presence of calcite disseminated between the hollandite group mineral crystals (►Fig. 7.32d). These minerals occur as small needles of 3–100 µm length and 1–10 µm width (►Figs. 7.33b and c), as usually observed in other supergene Mn deposits (Decrée *et al.*, 2010; Dekoninck *et al.*, 2016b, 2016a). All studied minerals are particularly enriched in Pb (►Fig. 7.33d; ►Table 7.5) compared to those of the Imini area (Dekoninck *et al.*, 2016a). There are no differences in the composition of hollandite group minerals following their position in the sandstones and dolostone, meaning they could originate from the same process. Hollandite group minerals are

also widely dispersed in the Cretaceous dolostones in the form of small needles forming star shapes between the dolomite crystals (►Fig. 7.32d).

The Tasdremt Mn ores display two different textures. Epigenetic textures are observed in the core of Mn orebodies: the whole dolostone seems to have been replaced by hollandite group minerals, as they preserve the rhombohedral habitus of the dolomite crystals when replacement is complete (►Fig. 7.33b) due to contrasted chemical composition of the hollandite group minerals. However, these minerals could also only partially replace the dolomite rhombs, showing only few hollandite needles growing into cavities (►Fig. 7.33c) within which calcite occupies central domains (►Fig. 7.33c). Such observation is also made in the upper Senonian dolostone levels. Another interesting feature of epigenetic processes of the host dolostone is the replacement of 0.2-0.3 mm long laths of a former mineral by hollandite *s.s.*, thought to be anhydrite laths (►Fig. 7.33e) as it has already been observed in the poorly mineralized fossiliferous dolostone (►Fig. 7.32b).

Colloform aggregates occur as a second textural feature of the Mn oxides (►Fig. 7.33f). They are often associated to brecciated zones where mineralizing fluids can readily pass through (►Fig. 7.33g). They grow onto the previous replacement textures (►Fig. 7.38f) or directly onto the host rock dolostone (►Fig. 7.31c), sandstones and conglomerates, but could also be brecciated themselves (►Fig. 7.33g). Most of the colloform Mn oxides are composed of hollandite end-member crystals (►Figs. 7.33d and f), but coronadite can be observed at the boundary between hollandite replacing the dolostone fabric and the subsequent colloform aggregates (►Fig. 7.33d). Some clay minerals (kaolinite) are associated within brecciated and dissolved carbonates.

Both manganese textures are brecciated and cemented later by calcite (►Figs. 7.33c and g). Barite is disseminated in the ore, probably because barium is not totally incorporated in the lattice of hollandite group mineral. Some clay minerals could be observed into the cavities between hollandite group minerals having replaced the dolomite rhombs. Gypsum and halite crystals are observed between dolomite crystals (►Fig. 7.33h). Their relative position with respect to the Mn oxides is quite interesting as they crystallize within small geodic cavities. Halite grows onto dolomite crystals and resulting cavities are subsequently filled by gypsum/anhydrite crystals. Hollandite group minerals seem to crystallize belatedly in the center of these cavities. Nevertheless, these observations are sometimes unclear and only restricted to specific samples in close relation with sand and wad accumulation.

►**Table 7.4** Major element composition (in wt. %).

Label	Rock type	Location	Rock	SiO_2	Al_2O_3	Fe_2O_3	FeO	MnO	MgO	CaO	Na_2O	K_2O	TiO_2	P_2O_5	LOI	Total	Mn/Fe
16TIG16	L1	Tiranimine	IC	4.76	0.86	0.58	0	14.23	11.27	28.35	0.05	0.41	0.05	0.10	35.52	96.20	52.5
16TIG24	L1 Wad		CT	6.04	0.43	0.19	0	22.80	12.90	18.81	0.11	0.46	0.02	0.03	31.60	93.41	252.5
16TIG31	L1 Breccia		CT	3.27	0.81	0.28	0	56.75	2.11	6.34	0.12	0.41	0.03	0.04	14.66	84.82	433.4
16TIG34	L1 Vein		CT	4.80	0.41	0.27	0	33.44	6.83	18.91	0.06	0.09	0.03	0.06	24.72	89.64	255.4
16AOU09	L2 Breccia	Aoufour	CT	8.40	1.64	0.80	0	41.25	0.47	15.16	0.14	1.95	0.09	0.06	18.90	88.88	108.8
16AOU10	L2		CT	1.99	0.65	0.20	0	61.18	0.49	3.56	0.19	2.49	0.02	0.08	11.81	82.75	467.2
16AOU21	L2 Wad		CT	3.69	0.80	0.65	0	72.16	0.19	0.51	0.22	1.16	0.03	0.13	11.09	90.64	242.1
16AOU19	L2 Sand		CT	40.20	4.12	1.92	0	1.59	9.91	14.39	0.07	1.59	0.28	0.04	24.12	98.25	1.8
16TAS26	L2	Tasdremt	CT	1.35	0.21	0.15	0	74.04	0.10	0.25	0.18	1.02	0.00	0.11	10.25	87.67	1024.8
16TAS29	L2		CT	1.34	0.27	0.16	0	78.24	0.08	0.45	0.19	1.21	0.01	0.08	10.23	92.27	962.6
16TAS37	L2 Wad		CT	4.57	0.62	0.64	0	18.20	14.11	21.95	0.20	0.83	0.05	0.23	34.06	95.47	62.0
16TAS10	L2		S	5.89	0.88	0.26	0	40.29	7.42	11.28	0.09	0.19	0.04	0.02	21.95	88.33	330.5
16TAS47	L3		S	1.02	0.27	0.15	0	15.89	13.99	27.08	0.04	0.45	0.01	0.04	36.48	95.43	219.9
16TAD05	Distal dolostone	Taddert	CT	4.80	1.27	0.20	0.2	0.07	18.74	29.19	0.02	0.28	0.06	0.02	44.15	99.02	0.4
16TAD08			CT	1.65	0.64	0.26	0	0.16	20.02	30.91	0.02	0.10	0.03	0.24	45.57	99.62	1.3
16TAD09			CT	0.54	0.21	0.00	0.1	0.17	20.05	30.41	0.04	0.04	0.01	0.02	46.98	98.57	3.8
16AOU07	Proximal dolostone	Aoufour	CT	3.10	0.98	0.29	0.1	0.16	19.51	29.01	0.02	0.22	0.04	0.10	44.83	98.37	0.9
16AOU15			CT	9.22	2.70	0.90	0.1	0.26	16.96	25.84	0.09	0.62	0.12	0.03	41.31	98.14	0.6
16AOU16			CT	0.95	0.36	0.23	0	0.33	17.94	33.12	0.04	0.08	0.01	0.07	46.51	99.67	3.0
16TIG26		Tiranimine	CT	29.81	2.27	0.19	0	0.38	13.63	20.59	0.03	0.74	0.16	0.04	31.30	99.14	4.2
16TIG32			CT	3.45	1.33	0.56	0	0.35	19.68	28.69	0.02	0.25	0.07	0.00	44.50	98.90	1.4
16TIG30			S	56.20	1.87	0.38	0.4	0.04	1.59	20.18	0.01	0.24	0.26	0.00	17.72	98.95	0.1
16TIG15	Dolostone		C	1.08	0.15	0.42	0	0.07	20.92	29.69	0.02	0.05	0.01	0.00	46.24	98.66	0.4

►**Table 7.5** Trace elements geochemistry (in ppm). Values with asterisk (*) are in weighted percent (wt. %). Values under the detection limit are indicated by "<" symbol.

Label	Sc	Be	Au	V	Cr	Co	Ni	Cu	Zn	Ga	Ge	As	Rb	Sr	Y	Zr	Nb	Mo	Ag	Sn	Sb	Cs	Ba	Hf	Ta	W	Tl	Pb	Bi	Th	U
16TIG16	<	<	<	115	<	61	<	140	<	16	<	17	5	571	8	36	<	28	<	<	0.7	0.5	15480	0.8	0.1	<	2.4	9930	<	0.6	0.9
16TIG24	<	<	7	151	30	103	<	250	<	24	<	21	2	1092	6	17	<	43	<	<	0.5	<	26770	0.4	0.1	<	3.7	1.78*	<	0.3	1.1
16TIG31	1	2	<	532	50	222	20	530	60	9	2	40	3	3181	2	9	<	250	<	<	1.2	<	81840	0.2	<	<	13.7	3.16*	0.5	0.4	5.3
16TIG34	<	1	<	192	30	137	<	280	30	5	1	25	<	1289	8	20	<	44	<	<	0.6	<	43220	0.5	<	<	2.8	2.91*	<	0.3	1.8
16AOU09	2	2	<	190	50	498	<	650	60	24	1	46	9	1605	4	32	<	78	<	<	0.8	0.6	36840	0.7	<	<	11.2	2.99*	<	1.1	2.6
16AOU10	1	3	12	285	40	685	30	1000	60	37	2	44	4	2370	<	14	3	250	<	<	1.1	<	52240	0.5	0.1	2	19.1	4.84*	<	0.5	4.3
16AOU21	1	2	31	114	40	578	30	780	80	11	2	43	11	1343	9	6	<	82	<	<	1	<	49420	0.2	0.1	<	17.3	4.88*	<	0.4	3.5
16AOU19	3	<	<	41	20	32	20	50	60	6	<	21	38	71	8	77	4	7	<	1	1.4	1.6	1662	1.9	0.3	<	0.9	919	<	3.2	1
16TAS26	<	3	25	245	130	653	30	2390	290	12	2	79	8	2005	3	<	<	250	<	<	0.7	<	58470	<	0.1	3	43.7	4.9*	<	<	8.8
16TAS29	<	3	15	248	100	669	30	2260	230	12	2	71	6	1766	5	<	<	250	<	<	0.7	<	51860	<	0.1	1	40.8	4.97*	<	<	8
16TAS37	2	<	6	167	30	142	<	330	30	16	<	22	5	417	7	28	<	62	<	<	0.6	<	15210	0.6	<	<	7.1	1.23*	<	0.6	1.6
16TAS10	1	2	<	389	110	182	20	700	60	7	1	32	2	2104	3	16	<	250	<	<	0.5	<	51610	0.4	0.1	<	11.7	3.71*	<	0.6	4.4
16TAS47	<	<	<	132	30	130	<	200	70	16	<	6	2	413	2	10	<	52	<	<	<	<	15770	0.2	<	<	4.7	1.21*	<	0.1	0.9
16TAD05	1	<	<	6	<	<	<	<	<	9	<	<	9	57	3	19	1	<	<	<	<	0.5	49	0.5	<	<	1	20	<	0.9	0.4
16TAD08	<	<	<	16	<	<	<	20	<	1	<	<	4	62	2	10	<	4	<	1	<	<	161	0.2	<	<	0	64	<	0.4	0.3
16TAD09	<	<	<	<	<	1	<	10	<	<	<	<	<	59	<	4	<	<	<	<	<	<	21	<	<	<	0.2	9	<	0.1	0.1
16AOU07	<	<	<	10	<	3	<	20	<	2	<	6	6	59	4	11	<	<	<	<	<	<	58	0.2	<	<	0	5	<	0.6	0.2
16AOU15	3	<	3	16	<	5	<	10	<	21	<	5	18	67	5	26	2	<	<	1	<	2	126	0.7	0.1	<	1.5	21	<	1.5	0.4
16AOU16	<	<	3	8	<	4	<	20	<	1	<	<	2	74	2	7	<	<	0.5	<	<	<	86	<	<	<	0.4	15	<	0.2	0.2
16TIG26	<	<	3	7	<	2	<	20	<	13	<	<	17	43	6	53	2	<	<	<	<	<	404	1.3	0.1	<	0.7	144	<	1.3	0.4
16TIG32	1	<	<	11	<	2	<	20	40	11	<	7	8	54	4	16	<	<	<	<	<	0.5	225	0.4	<	<	0.8	102	<	0.8	0.3
16TIG30	1	<	<	15	<	<	<	<	<	12	<	<	7	12	6	290	2	<	0.9	<	<	0.6	73	6.6	0.2	<	0.5	27	<	1.6	0.6
16TIG15	<	<	<	11	<	<	<	<	<	13	<	<	<	50	<	6	<	<	<	1	<	<	46	<	<	<	1	39	<	0.1	0.7

►**Table 7.6** Rare Earth Elements geochemistry (in ppm). Values under the detection limit are indicated by "<" symbol.

Label	La	Ce	Pr	Nd	Sm	Eu	Gd	Tb	Dy	Ho	Er	Tm	Yb	Lu	∑REE	La_N/Lu_N	Eu/Eu*	Ce/Ce*
16TIG16	13.4	12.8	2.32	8.5	1.6	0.52	1.5	0.2	1	0.2	0.5	0.07	0.4	0.06	43.07	2.38	1.58	0.52
16TIG24	14.2	34.7	2.37	7.8	1.6	0.3	1.3	0.2	0.9	0.1	0.4	0.05	0.3	0.05	64.27	3.03	0.98	1.36
16TIG31	23.4	61.9	2.62	8.1	1.4	0.67	1.2	0.1	0.5	0.1	0.3	<	0.2	0.03	100.52	8.32	2.43	1.80
16TIG34	19	47.6	3.09	11.1	1.9	0.69	1.5	0.2	0.9	0.2	0.4	0.06	0.3	0.05	86.99	4.05	1.92	1.42
16AOU09	19.3	15.3	2.14	7.3	1.4	0.49	1.2	0.2	1	0.2	0.5	0.06	0.3	0.04	49.43	5.15	1.78	0.54
16AOU10	23.1	19.2	2.52	7.1	1.3	0.06	1.1	0.2	1	0.2	0.5	0.07	0.5	0.08	56.93	3.08	0.24	0.57
16AOU21	27.2	7.7	3.46	12.4	2.2	0.49	2.2	0.3	1.5	0.3	0.7	0.08	0.4	0.06	58.99	4.84	1.05	0.18
16AOU19	12.7	25.2	2.56	9.7	1.8	0.43	1.6	0.3	1.7	0.3	1	0.16	1	0.16	58.61	0.85	1.19	1.01
16TAS26	19.6	6.2	4.79	17.8	3.2	0.66	2.3	0.3	1.5	0.2	0.6	0.07	0.4	0.05	57.67	4.18	1.14	0.15
16TAS29	19	7.8	4.63	16	2.8	0.78	2.1	0.3	1.3	0.2	0.6	0.07	0.4	0.05	56.03	4.05	1.51	0.19
16TAS37	10.5	6.8	2.25	9.2	1.8	0.46	1.7	0.2	0.9	0.2	0.4	0.06	0.3	0.04	34.81	2.80	1.24	0.32
16TAS10	14.3	21.5	1.95	6.7	1.3	0.47	1.1	0.2	0.7	0.1	0.4	<	0.3	0.05	49.07	3.05	1.85	0.93
16TAS47	6.2	9.6	1.19	4.1	0.8	0.08	0.8	0.1	0.6	0.1	0.3	<	0.2	0.03	24.1	2.20	0.47	0.81
16TAD05	2.9	5.5	0.66	2.8	0.5	0.13	0.4	<	0.5	<	0.3	<	0.2	0.03	13.92	1.03	1.37	0.91
16TAD08	2.7	3	0.42	1.9	0.3	0.07	0.4	<	0.3	<	0.2	<	0.1	0.02	9.41	1.44	0.95	0.64
16TAD09	1.6	1.3	0.21	0.9	0.2	0.06	0.2	<	0.2	<	<	<	<	0.01	4.68	1.71	1.41	0.51
16AOU07	2.9	4	0.54	2.1	0.3	0.09	0.3	<	0.4	<	0.2	<	0.1	<	10.93	-	1.41	0.73
16AOU15	6.2	8.3	0.87	3.5	0.7	0.14	0.7	0.1	0.8	0.2	0.5	0.06	0.4	0.05	22.52	1.32	0.94	0.81
16AOU16	2.3	2.5	0.35	1.1	0.1	<	0.3	<	0.3	0	0.2	<	0.2	0.02	7.37	1.23	-	0.64
16TIG26	8	10.3	2.01	8.5	1.5	0.32	1.3	0.2	1.1	0.2	0.5	0.08	0.5	0.08	34.59	1.07	1.08	0.59
16TIG32	5	6.1	1.09	4.3	0.7	0.21	0.7	0.1	0.6	0.1	0.3	<	0.3	0.04	19.54	1.33	1.41	0.60
16TIG30	5.4	11.1	1.2	4.5	0.9	0.2	0.9	0.2	1	0.2	0.8	0.12	0.8	0.13	27.45	0.44	1.04	0.99
16TIG15	0.7	1.1	0.17	0.6	0.1	0	0.1	<	<	<	<	<	<	<	2.77	-	0.00	0.73

7.3.3.d Geochemistry of the Tasdremt deposit

- *Host-rock dolostone, sandstone and conglomerate*

The chemical composition of dolostones includes variable content in SiO_2 (0.5-9.2 wt. % SiO_2) and Al_2O_3 (0.2-1.3 wt. % Al_2O_3), depending on the amount of reworked quartz, feldspar and kaolinite grains (►Table 7.4). Fe_2O_3 content varies between 0.1-1.0 wt.%, while FeO is between 0 and 0.4 wt. %, further indicating slightly reduced conditions during the deposition of carbonates. MnO is low (0.04-0.4) and might be attributed to disseminated Mn oxides, both in distal and proximal dolostones. This contamination of the host dolostone can also be depicted by anomalously high Ba and Pb (and Sr) contents of hollandite *s.s.* and coronadite (►Table 7.5). Note that Senonian dolostone exhibits a limestone composition, rather due to the presence of late meteoric calcite than truly sedimentary calcite (►Fig. 7.32d).

The total REE content is variable (∑REE=4.7-34.6 ppm), likely due to dispersed Mn oxides present in the dolostone (►Table 7.6). Compared to the UCC reference, all patterns are depleted, showing a negative Ce anomaly (Ce/Ce*=0.51-0.90), typically found in Phanerozoic marine dolostones (Piper, 1974; Palmer, 1985), exception made for Senonian samples where no anomaly is identified (Ce/Ce*=0.99; ►Fig. 7.34a). The absence of a Ce anomaly might be due to the high amount of late meteoric calcite in Senonian limestone (►Fig. 7.32d). This could also be the reason why Ce anomalies are not as sizeable as it should be in the other samples, within which calcite has been identified. Alternatively, these relatively slight Ce anomalies may result from a meteoric precipitation of some dolomite crystals as it has already been observed in the neighboring Imini district (Dekoninck *et al.*, 2016a, 2016b), or to the detrital component of the samples. Cambrian dolostone has a different geochemical content showing very low REE concentration (∑REE=2.8 ppm) due to the absence of HREE, and a slight Ce negative anomaly (Ce/Ce*=0.72; ►Table 7.6, ►Fig. 7.34a).

- *Manganese ores*

Mn ores contain up to 78 wt.% MnO, which corresponds to pure hollandite group minerals, but is often lower, ranging between 14.2-78.2 wt.% MnO, depending on the mineralogical percentage of these minerals (►Table 7.4). As Mn ores are often brecciated, they display several contaminant grains, such as dolomite, quartz and calcite, providing variable SiO_2 (1.3-6.0 wt. %), MgO (0.1-14.0 wt. %) and CaO (0.3-28.6 wt. %) concentrations. Other minerals, such as kaolinite, Fe oxides, feldspar and phosphates are poor or absent, providing low aluminum, iron and phosphorous content: 0.2-1.6 wt. % Al_2O_3, 0.15-0.84 wt. % Fe_2O_3 and 0.02-0.23 wt. % P_2O_5. Fe_2O_3 and P_2O_5 content is slightly higher where the detrital composition increases, showing a mixture of sand and cryptocrystalline Mn oxides, typically found in wad

(►Table 7.4). Absence of FeO corroborates the supergene nature of the manganiferous ore. Pb, Ba and K concentrations are high (1.0-4.88 wt.% Pb, 1.5-8.2 wt.% Ba and 0.1-2.5 wt.% K_2O; ►Tables 7.4 and 7.5) and related to the occurrence of massive hollandite group minerals, as it has already been shown in scanning electron microscopic views (►Fig. 7.33). Other metals could also be significantly trapped within tunnel-like structure of these Mn oxides. Sr concentration ranges between 0.04-0.32 wt.% due to its substitution with Ba in hollandite group minerals, but without forming the strontiomelane end-member ($SrMn_8O_{16}$; Meisser *et al.*, 1999). Cu and Co are also enriched with concentrations up to 2390 (140-2390 ppm Cu) and 685 ppm (61-685 ppm Co) positively correlated to the Mn content (►Fig. 7.34b). Maximum concentration of Cu and Co are found in pure hollandite. On the other hand, As, Ni and Zn are not particularly enriched (►Table 7.5). The use of Pb vs Zn concentration in Nicholson (1992) diagram allows discriminating "dubhite" type manganese ore (oxides formed by the weathering of a mineralized sequence) from other Mn accumulation types (►Fig. 7.34c). The Tasdremt ores plot in the "dubhite" field, close enough to the Imini ones to be equated. However, careful attention has to be paid in Nicholson plots, as they reflect only geochemical features and do not take into account petrographic nor field observations, the latter being discussed in the next section.

As well, the total REEs content is relatively low (∑REE=24.1-100.5 ppm with an average value of 56.8 ppm; ►Table 7.6), below the UCC reference (McLennan, 2001), which indicates that REEs are not significantly enriched in the Mn oxides. However, geochemical REE patterns are particularly interesting as the three orebodies display somewhat distinct shapes and anomalies (►Fig.7.34a). The main orebody (L2) shows a well-preserved negative Ce (Ce/Ce*=0.15-0.57) anomaly but a slight positive Eu anomaly (Eu/Eu*=1.04-1.77), whereas L1 Mn ores display slight positive Ce (Ce/Ce*=1.36-1.80) and Eu (Eu/Eu*=0.98-2.42) anomalies. Note that positive Eu anomalies could be induced by spectral interference with Ba (Cao *et al.*, 2001). Only two samples drift away from this rule. Sample 16AOU10, belonging to the L2 orebody, has a strong negative Eu anomaly, instead of having a positive one, whereas pattern of sample 16TAS10 (L2 orebody) can be likened to L1 one (►Fig. 7.34a). There is no straightforward evidence to differentiate the L3 ore level as only one sample has been investigated, but a clear negative Eu anomaly is seen (Eu/Eu*=0.50) with relatively lower normalized values compared to the L1 and L2 orebodies (►Fig. 7.34a). Such lower normalized REE content is due to the low Mn content (►Table 7.4), whereas calcite is widely present (►Fig. 7.31d). All normalized REEs measured on the Mn orebodies display asymmetric patterns with relatively higher enrichment in LREE-MREE than in HREE (La_N/Lu_N=2.2-8.32) compared to the UCC.

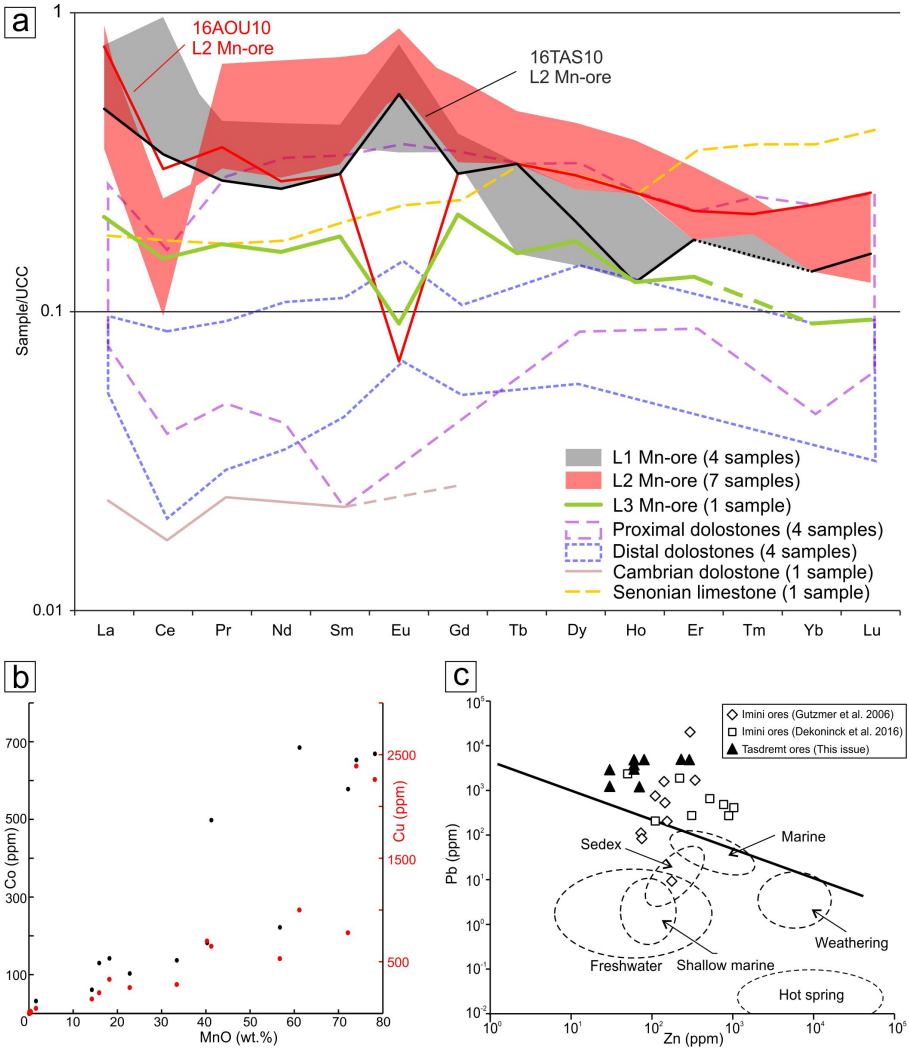

►**Fig. 7.34 a.** Rare Earth Elements (REE) patterns of the three Mn orebodies and host rocks. **b.** Plot showing the positive correlation between Co, Cu and Mn. **c.** Discrimination plot of Nicholson (1992) showing the location of the Tasdremt ores in the "dubhite" field, close to those of the Imini area (Gutzmer *et al.*, 2006; Dekoninck *et al.*, 2016b).

7.3.3.e $^{40}Ar/^{39}Ar$ spectra of the Tasdremt, Aoufour and Tiranimine deposits

Fourteen samples from three locations, Tiranimine (16TIG; ►Fig. 7.35a), Aoufour (16AOU; ►Fig. 7.35b) and Tasdremt (16TAS; ►Fig. 7.35c) were analyzed.

With the exception of four age spectra (16TAS02, 16AOU11, 13 and 17; ►Figs. 7.35b and c), which display a staircase shape, most of them show abnormally

high apparent ages in the low temperature steps, which rapidly decrease to stabilize in the mid-temperature domain. Nevertheless, it should be noted that samples 16TIG16, 16TAS49 and 16AOU10 (►Figs. 7.35a, b and c) are less affected by this disturbance in the low temperature steps. It is somewhat problematic as it hides information that could be recovered from the low temperature domain and in some ways penalizes interpretation of mid to high temperature steps. Several explanations could be invoked and maybe combined to interpret these low temperature high apparent ages. Excess of ^{40}Ar, frequently considered to explain such low temperature old apparent ages, is not a viable explanation in the supergene environment. The lack of a systematic correlation between $^{37}Ar_{Ca}/^{39}Ar_K$ (#Ca/K) ratios and apparent ages in the low temperature domain is not a compelling point and affect relationship with the degassing of more or less Ca-rich contaminant or inherited components even if in some cases it would be likely (e.g.,16TAS22, 16TIG28; ►Figs. 7.35a and c). It must be noted that small calcite and dolomite crystals were observed in some samples, and thus bring excess of Ca in the samples. $^{39}Ar_K$ loss through recoil during irradiation could also be considered and related to the degassing in the low temperature domain of poorly crystallized phases or very small crystals impacted by $^{39}Ar_K$ recoil during irradiation. This could explain some complex trajectories observed in correlation diagrams of some experiments (e.g.,16TAS10 or 16TIG35; ►Figs. 7.35a and c), suggesting some unconventional isotopic shifting.

Three $^{40}Ar^*/^{39}Ar_K$ analyses were excluded: 16TIG16, 16TIG29 and 16TAS49 (►Figs. 7.35a and c). Their $^{37}Ar_{Ca}/^{39}Ar_K$ spectra show that the whole degassing spectra is concomitant with the degassing of a substantial Ca-rich component. As hollandite group minerals are not expected to incorporate significant quantities of Ca in their crystalline structure and as neither Ca-bearing Mn oxides (i.e.,birnessite nor todorokite) were detected in samples from Tasdremt orebodies, analyzed K-Mn oxide samples cannot generate on its own such high $^{37}Ar_{Ca}/^{39}Ar_K$ values. Therefore, contamination of these samples by a Ca-rich phase(s) must be taken into consideration (i.e.,calcite or dolomite). This observation is corroborated by intermediate to high temperature degassing domain of sample 16TIG29, yielding the oldest apparent ages from this study, up to values (~92 Ma), which are not consistent with geological and petrographical observations (►Fig. 7.35a).

Age spectra obtained during this study allow calculation of a wide set of plateau and pseudo-plateau ages between ~65 Ma and ~84 Ma with substantial cluster of ages in the range 65.2-66.6 Ma and 80.8-82.0 Ma. Apart from the sole age at ~58 Ma detected through isochron analysis of low temperature degassing domain of sample 16TAS30, age cluster at ~65-67 Ma constitutes the youngest significant age component identified in this study (►Figs. 7.35a, b and c).

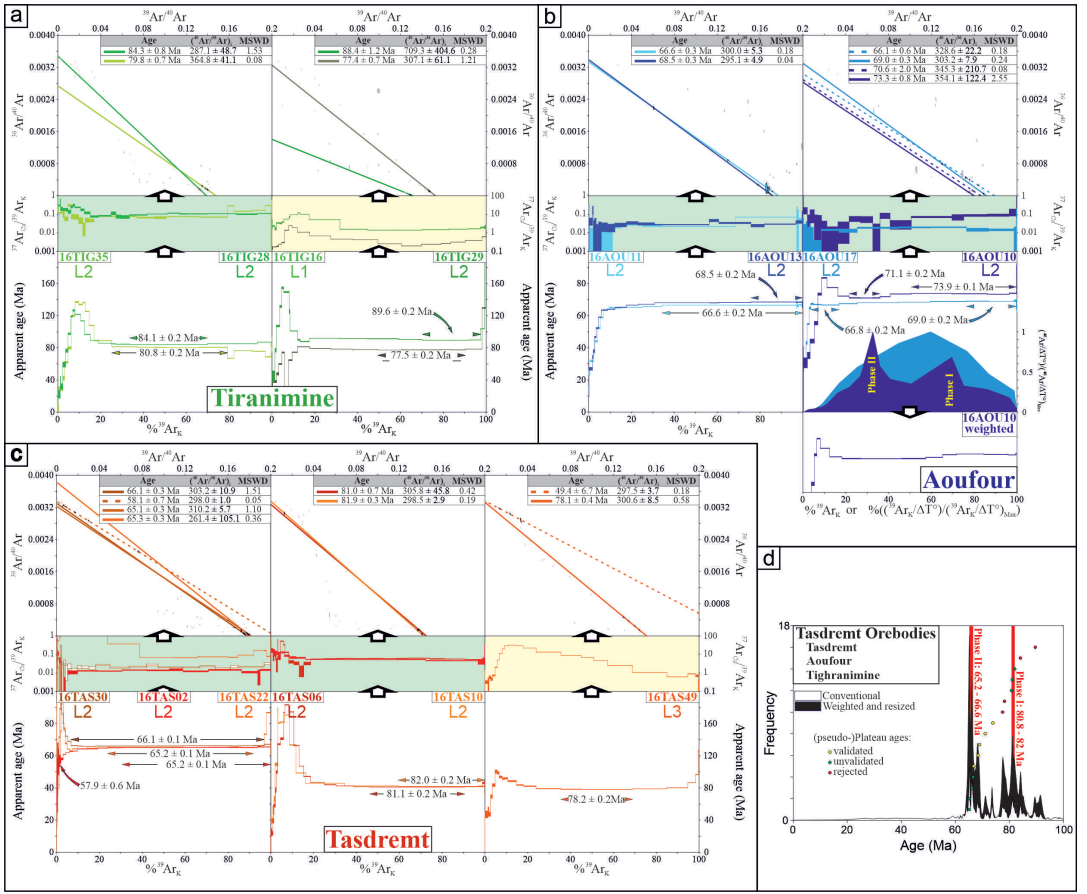
a
b
c
d
Tiranimine
Aoufour
Tasdremt
16TIG35
16TIG28
16TIG16
16TIG29
16AOU11
16AOU13
16AOU17
16AOU10
16AOU10 weighted
16TAS30
16TAS02
16TAS22
16TAS06
16TAS10
16TAS49
L1
L2
L3
Phase I
Phase II
Tasdremt Orebodies
Tasdremt
Aoufour
Tighranimine
Conventional
Weighted and resized
(pseudo-)Plateau ages:
validated
unvalidated
rejected
Frequency
Age (Ma)
Phase II: 65.2 - 66.6 Ma
Phase I: 80.8 - 82 Ma

►**Fig. 7.35** Incremental-heating spectra for the 14 Mn oxide grains from the Tiranimine (**a**), Aoufour (**b**) and Tasdremt (**c**) mines. **d**. Probability diagram of apparent ages. $^{40}Ar/^{39}Ar$ ages are summarized in ►Table 7.7. Apparent age error bars are at the 1σ level; errors in the J-parameter are not included. Plateau and pseudo-plateau ages (1σ uncertainties including errors in the J-parameter) are given when applicable.

7.3.4 Discussion

7.3.4.a Mineralization processes

The whole Cretaceous sequence (►Fig. 7.28) exhibits terrestrial (Senonian sandstone, conglomerate and red clays) and proximal facies (Cenomanian-Turonian carbonates), the latter being of shallow marine (supertidal) origin as attested by preserved fossils in the fossiliferous levels, anhydrite ghosts, quartz, feldspar and apatite grains (►Figs. 7.31g and 7.32b). However, most of these sedimentary features have been obliterated by further dolomitization, first by a micritic dolomite (►Fig. 7.32a), probably originating from early diagenesis close after the deposition of primary carbonates as suggested by Force *et al.* (1986) and Rhalmi *et al.* (2000) in adjacent areas. Secondly, the high porosity resulting from early dolomitization processes has led the pores to be partially filled by sparitic dolomite crystals (►Figs. 7.32a and b), occurring along with late meteoric diagenesis, as already shown in the nearby Imini area (Force *et al.*, 1986; Rhalmi *et al.*, 2000; Gutzmer *et al.*, 2006; Dekoninck *et al.*, 2016a).

Field and petrographic observations clearly show that most of the Mn orebodies of the Tasdremt area are related to the porous Cenomanian-Turonian dolostones (►Fig. 7.31), and to a lesser extent, to Senonian dolostone levels or dolomitized sandstones and conglomerates (►Figs. 7.28 and 7.30). A special attention was paid to analysis of the L2 Mn level, as this level additionally contains massive hollandite group minerals (hollandite *s.s.* and coronadite; ►Figs. 7.29c and e) and displays a relatively constant lateral extension (►Fig. 7.30) responsible for the past economic interest of the Tasdremt ores, although it is rather a succession of discontinuous lenses and pockets. The L1 and L3 orebodies have limited value as they are low-grade due to contamination by the host rock minerals (dolomite, calcite and quartz), and also to their sporadic occurrences along the district (►Fig. 7.30). However, ore-forming processes seem to be rather similar between these levels, showing post-sedimentation mineralization (►Figs. 7.33 and 7.36).

►**Table 7.7** Summary of $^{40}Ar/^{39}Ar$ ages of supergene Mn oxides in the Tasdremt district. [a]: pseudo-plateau age; * range of individual step-heating ages; [+]: integrated age determined by less than 20% of ^{39}Ar released; n.a. : not applicable.

Label	Outcrop	Mn level	Host-rock	Elevation (m)	Plateau age (Ma)	±2σ	Isochron age (Ma)	±2σ	Intercept $^{40}Ar/^{36}Ar$	±2σ	MSWD	Comments
16TAS02	Tasdremt mine	L2	/	/	57.9[+]	0.6	58.1	0.7	298.0	1.0	0.05	
					65.2	0.1	65.1	0.3	310.2	5.7	1.10	
16TAS06		L2	Senonian	775	81.1[a]	0.2	81.0	0.7	305.8	45.8	0.42	
16TAS10		L2	Senonian	775	82.0[a]	0.2	81.9	0.3	298.5	2.9	0.19	
16TAS22		L2	Cenomanian	780	65.2	0.1	65.3	0.3	261.4	105.1	0.36	
16TAS30		L2	Cenomanian	778	66.1	0.1	66.1	0.3	303.2	10.9	1.51	
16TAS49		L3	Senonian	783	78.2[a]	0.2	78.1	0.4	300.6	8.5	0.58	Excluded
16TIG16	Tiranimine mine	L1	infra-Cenomanian	749	77.5[a]	0.2	77.4	0.7	307.1	31.1	1.21	Excluded
16TIG28		L2	Cenomanian	757	84.1[a]	0.2	84.3	0.8	287.1	48.7	1.53	Excluded
16TIG29		L2	Cenomanian	758	89.6[a]	0.2	88.4	1.2	709.3	404.6	0.28	Excluded
16TIG35		L2	Cenomanian	760	80.8[a]	0.2	79.8	0.7	364.8	41.1	0.08	
16AOU10	Aoufour mine	L2	Cenomanian	812	71.1[+]	0.2	70.6	2.0	345.3	210.7	0.08	
					73.9[a]	0.1	73.3	0.8	354.1	122.4	2.55	
16AOU11		L2	Cenomanian	812	66.6	0.2	66.6	0.3	300.0	5.3	0.18	
16AOU13		L2	Cenomanian	812	68.5[a]	0.2	68.5	0.3	295.1	4.9	0.04	
16AOU17		L2	Cenomanian	812	66.8[+]	0.2	66.1	0.6	328.6	22.2	0.18	
					69.0[a]	0.2	69.0	0.3	303.2	7.9	0.24	

Bouladon and Meune (1951) already pointed out the progressive replacement of the host rock dolostone by Mn oxides. Such replacement is identical with the process evidenced by Dekoninck *et al.* (2016a) in the Imini district, especially in the upper C3 level. Needles of hollandite group minerals grow between dolomite crystals (►Figs. 7.32a and 7.33h), witness of the first ore-forming step, during which Mn oxides replace progressively the micritic matrix. Later on, rhombohedral crystals of dolomite were replaced by hollandite *s.s.*, given the preservation of the rhombohedral habitus in the heavily mineralized ore, further indicating replacement of dolomite crystals by Mn oxides (►Figs. 7.33b, c and e). However, this process is not an "atom per atom" replacement of the dolomite crystals, as commonly underlined by epigenetic process, but rather the filling of voids after the dissolution of dolomite rhombs. This stage is well demonstrated by partially filled rhombohedral cavities of hollandite group mineral needles (►Fig. 7.33c). It is important to highlight that only the L2 Mn level has clearly provided such epigenetic textures, likely because Mn enrichment was enhanced by partial dissolution of the dolostone at the boundary with the upper detritic series. This point is also evidenced by slightly different REE patterns between the three ore levels, suggesting that ore-forming processes or the composition of the mineralizing fluids have slightly differed (►Fig. 7.34a).

Following this first step deduced from observations only made in L2 ore level, the three orebodies have undergone a second enrichment process. Both processes could be synchronous. Secondary generations of Mn oxides precipitate after the breaking up of the ore (in the L2 level) or the host rock, in the form of hollandite *s.s.* and coronadite growth bands between reworked grains of the host rock (quartz and dolomite; ►Fig. 7.33e) or the first generation of Mn oxides (►Figs. 7.33d, f and g). The composition of these Mn oxides is mainly hollandite *s.s.* or Pb-rich hollandite with coronadite bands (►Fig. 7.33f), whereas cryptomelane end-member is almost never observed. The ore has probably undergone several brecciation events. Late meteoric calcite is the last mineral being precipitated (►Figs 7.31d, 7.33b and g). It clearly postdates the formation of Mn orebodies, but the precise timing is not known, as calcite could be recent (►Fig. 7.36). Dedolomitization textures (►Figs. 7.32a, c and d) corroborate the meteoric origin of calcite (Ayora *et al.*, 1998; Dewaide *et al.*, 2014).

As this two-step scenario clearly suggests a multistage formation of the Tasdremt manganiferous ores, ore-forming processes could have been reproduced during the formation of the Mn orebodies, for example by a long-lasting dissolution of the host dolostone (►Fig. 7.36) and reworking of Mn ores in karst sediments (►Fig. 7.31e).

7.3.4.b Timing of the hollandite group minerals

The unconventional age distribution of some $^{40}Ar/^{39}Ar$ degassing patterns needs a careful analysis using a range of tools, some of which are not widely used.

- *Elaborate tool to determine the age of supergene K-Mn oxides*

Results recovered from K-Mn oxide samples require the use of elaborate processing tools other than simple visual examination of conventional age spectra. A step-heating experiment aims at separating the various argon components present in a sample but the result is rarely perfect, because of both the degassing profile adopted, and the state of interpenetration of these components. These tools provide assistance in data interpretation. They are only different ways of visualizing the same data set in order to validate pseudo-plateau ages, which are sometimes the only information provided by age spectra in the supergene domain. De Putter *et al.* (2015) and (De Putter and Ruffet (submitted) presented in detail these tools. Three of them are quite classical: the inverse isochron diagram (correlation diagram; $^{36}Ar/^{40}Ar$ vs. $^{39}Ar_K/^{40}Ar^*$; Turner, 1971; Roddick *et al.*, 1980; Hanes *et al.*, 1985), the probability density diagrams first used for $^{40}Ar/^{39}Ar$ by Vasconcelos *et al.* (1992) and the pseudo-plateau age (PPA) concept (Cheilletz *et al.*, 1999). Others are more atypical and developed for the analysis of multiphase systems. Some of them take into account the degassing kinetics of argon during the step-heating procedure with the visualization of degassing peak(s) [degassing spectrum: $(^xAr/\Delta T°)/(^xAr/\Delta T°)_{Max}$ versus $\%^{39}Ar_K$, with x=36 to 40] and the use of weighted age spectra [apparent ages versus $\%(^{39}Ar_K/\Delta T°)/(^{39}Ar_K/\Delta T°)_{Max}$].

The examination of the degassing kinetics of argon (degassing spectrum: $(^xAr/\Delta T°)/(^xAr/\Delta T°)_{Max}$ versus $\%^{39}Ar_K$, with x=36 to 40) and the elaboration of wheighted age spectra are interesting tools as they integrate the modulation of degassing during the successive heating steps. A conventional age spectrum implicitly assumes that the degassing rate is constant when $^{39}Ar_K$ degassing weighting $[\%(^{39}Ar_K/\Delta T°)/(^{39}Ar_K/\Delta T°)_{Max}]$ allows the development of an age spectrum that integrates this degassing rate. (►Fig. 7.35d). The last used tool is the resizing of the age spectra. There are no identical experiments in their development because the degassing control is never the same. In order to have statistically comparable analyses, it may be worthwhile for each of them to have the same number of steps by resizing age spectra, each step representing the same amount of degassed $^{39}Ar_K$. Obviously, this resizing (slicing and/or recombination) of the steps (apparent ages) requires a reappraisal of their respective errors by respecting the principle of weighted averages. This tool is important when using probability density diagrams.

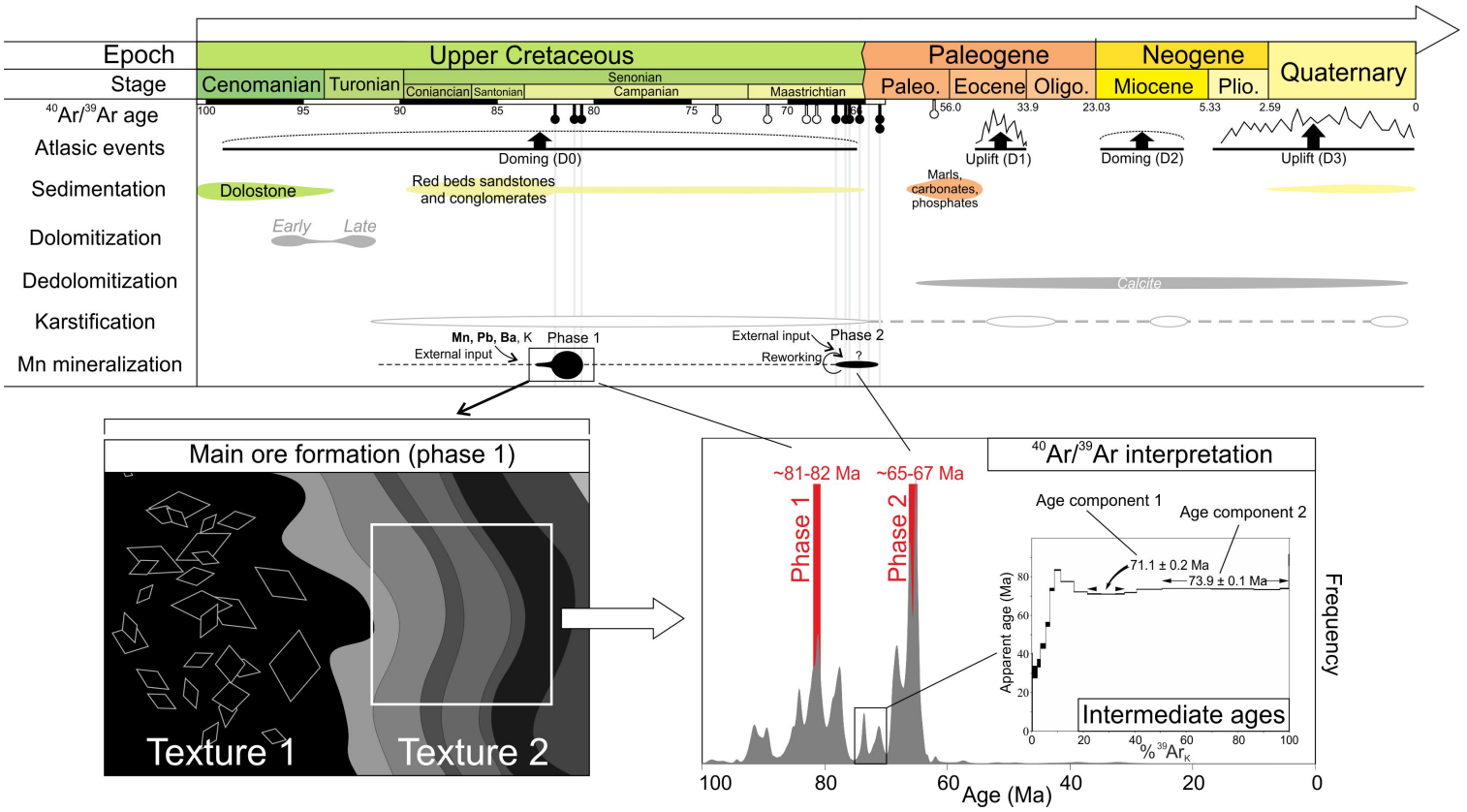
Epoch
Stage
Upper Cretaceous
Paleogene
Neogene
Quaternary
Cenomanian
Turonian
Senonian
Coniancian
Santonian
Campanian
Maastrichtian
Paleo.
Eocene
Oligo.
Miocene
Plio.
40Ar/39Ar age
100
95
90
85
80
75
70
56.0
33.9
23.03
5.33
2.59
0
Atlasic events
Doming (D0)
Uplift (D1)
Doming (D2)
Uplift (D3)
Sedimentation
Dolostone
Red beds sandstones and conglomerates
Marls, carbonates, phosphates
Dolomitization
Early
Late
Dedolomitization
Calcite
Karstification
Mn mineralization
Mn, Pb, Ba, K
External input
Phase 1
External input
Reworking
Phase 2
?
Main ore formation (phase 1)
Texture 1
Texture 2
40Ar/39Ar interpretation
~81-82 Ma
~65-67 Ma
Phase 1
Phase 2
Age component 1
Age component 2
71.1 ± 0.2 Ma
73.9 ± 0.1 Ma
Apparent age (Ma)
Intermediate ages
%39ArK
Frequency
100
80
60
40
20
0
Age (Ma)

►**Fig. 7.36** Time event chart of the Tasdremt manganese ores showing that Mn oxides have precipitated in two phases at ~81-82 Ma (phase 1) and likely at ~65-67 Ma (phase 2), according to dissolution processes. Full black cursors are certified $^{40}Ar/^{39}Ar$ plateaus ages. White cursors are uncertain ages and red cursors are invalid ages. Sedimentation periods in the Tasdremt area are based upon Ambroggi (1963) and Algouti *et al.* (1999). Karstification periods are suspected from emersive periods (Algouti *et al.*, 1999) according to the three main steps of the Atlas building (Leprêtre *et al.*, 2015b). Tectonic events are reported from Froitzheim (1984), Frizon de Lamotte *et al.* (2000), Leprêtre *et al.* (2015b, 2018). The main ore phase at ~81-82 Ma (phase 1) has led to the formation of two textures evidenced by petrographic observations. The second ore phase at ~65-67 Ma (phase 2) is evidenced by a reset of the $^{40}Ar/^{39}Ar$ dating system of the phase 1. New mineralization and/or remobilization of the former phase are likely due to brecciation and cementation by new generation of Mn oxides (►Fig. 7.33g).

The identification of characteristic disturbances of K-Mn oxide $^{40}Ar/^{39}Ar$ age spectra and their interpretation by e.g.,Vasconcelos *et al.* (1995), Ruffet *et al.* (1996), Hénocque *et al.* (1998), Hautmann and Lippolt (2000), Colin *et al.*(2005) and Beauvais *et al.*(2008) have provided a basis for the processing of data from this study. Nevertheless, the present Mn oxide formation context differs totally from previously investigated lateritic domains (see references above), which is reflected in originality of some of the obtained results (►Fig. 7.35) and difficulties encountered during data processing to identify some of the mineral growth phases.

- *The two late Cretaceous mineralization phases*

Plateau and pseudo-plateau age dispersion (~65-84 Ma) and observed age spectrum shapes suggest that, at least, two phases were registered within the Tasdremt ores. This is supported by age spectra yielded by samples 16AOU17 and 16AOU10 (►Fig. 7.35b). Apart from very low temperature steps (<4%), progressive increase of apparent ages shown by 16AOU17 age spectrum indicates that a component older than ~69 Ma was disturbed during an event at least as young as ~66.8 Ma. Its degassing spectrum does not evidence any specific degassing peak, which could suggest that this disturbing event could be linked to a crystalline support. The broadly similar shape of 16AOU10 age spectrum also expresses a disturbing of a component as old as ~74 Ma during an event younger than ~71 Ma. In this case, the degassing spectrum identifies two distinct phases, which suggest coexistence of two distinct crystalline components within a single analyzed grain (►Fig. 7.35b). The weighting of 16AOU10 age spectrum shows how substantial is this disturbing component. This suggests that both experiments relate, to varying degrees of disturbance and despite an imperfect dissociation of components, a similar history. The disturbing event evidenced by these two experiments is probably associated to the event identified by plateau and pseudo-plateau ages in the range 65.2-66.6 Ma yield by samples 16TAS02, 22 and 30 (►Fig. 7.35c) and 16AOU11 (►Fig. 7.35b). This event labelled "phase 2" is identified at the Cretaceous/Paleocene boundary and is associated with a

specific crystalline support, resulting from either neo-crystallization of a new mineral component, re-crystallization or resetting of a pre-existing mineral component.

Obviously, this phase 2 follows a phase 1, as old as ~74 Ma as suggested by pseudo-plateau in the high temperature steps of experiment 16AOU10 (►Fig. 7.35b). This phase 1 is probably characterized by plateau and pseudo-plateau ages in the range 80.8-82.0 Ma yielded by samples 16TAS06, 10 and by sample 16TIG35 (►Figs. 7.35a and c). Slightly older pseudo-plateau age at ~84 Ma calculated from saddle age spectrum displayed by sample 16TIG28 (►Fig. 7.35a) suggest a contamination as previously evoked for sample 16TIG29 (►Fig. 7.35a). Radiogenic components, which characterize the two evidenced phases, differ also with the measured and calculated $^{37}Ar_{Ca}/^{39}Ar_{K}$ ratios, the latter being slightly higher for phase 1 (≈ 0.05-0.06) than phase 2 (≈ 0.01-0.02). This difference is also observed for experiment 16AOU10 which registered the two phases, with a positive correlation between apparent ages and $^{37}Ar_{Ca}/^{39}Ar_{K}$ ratios, which both increase from low to high temperature steps (►Fig. 7.35b). This lowering of $^{37}Ar_{Ca}/^{39}Ar_{K}$ ratios from phase 1 to phase 2 must probably be related to an increase of K content of mineral component, which characterizes the youngest phase.

This set of analyses differs from observations carried out after analyses of K-Mn oxides, which crystallized in a strictly weathering domain as commonly highlighted in a lateritic profile (e.g.,Beauvais *et al.*, 2008; De Putter *et al.*, 2015 or De Putter *et al.*, in review; Dekoninck *et al.*, accepted with revision). In such supergene system, growth of several consecutive Mn oxide generations frequently proceeds through coalescence of successive set of crystals, with often a partial or total preservation of oldest phases. Such development results in intricate samples composed of mixed Mn oxide generations, within which oldest components often remain detectable. As part of this study, only two distinct events are detected. However, the impact of the Phase 2 on initial component related to phase 1 seems much more severe as evidenced by age spectrum yielded by sample 16AOU13 (►Fig. 7.35b). This age spectrum whose high temperature apparent ages culminate at ~68.5 Ma, approximately 2 Ma older than age assumed for phase 2 (65.2-66.6 Ma) suggests that component related to phase 1 (80.8-82.0 Ma) was almost totally erased. On closer observation, the shape of this age spectrum could evoke an $^{40}Ar^{*}$ loss by volumic diffusion as it was defined by Turner (1968), a notion quite different of mixing concept usually expected in supergene domain and for which questions processes involved in the development of such orebodies. All the results are summarized in the probability diagram of apparent ages (►Fig. 7.35d).

It must also be noticed that although particular attention was paid to carefully scrutinize the low to intermediate degassing domain of analyzed samples and may be because of the low temperature disturbance (high apparent ages) initially evoked,

none event younger than Campanian was detected, one sample excepted (16TAS02: 58.1 ± 0.7 Ma; ►Fig. 7.35c).

- *Timing of sedimentation, karstification and ore formation*

Even without geochronological data, reworked blocks of Mn oxides trapped between the Cenomanian-Turonian dolostone succession and the upper Senonian detritic series have suggested a Cretaceous age for the Mn mineralization (Bouladon and Meune, 1951), likely in several stages (►Figs. 7.29e, f and 7.36). Such observation also indicates emersive period after deposition of the Cenomanian-Turonian dolostones and Senonian series, the whole Senonian period being characterized by confined basins subjected to repeated exposure along the Atlas belt in the Aoulouz (Tasdremt) and Imini areas (Algouti *et al.*, 1999). Petrographic features have additionally demonstrated the late character of the ore, formed after sedimentation and diagenesis by progressive replacement of the dolostone fabric and filling porosity, giving a possible post-Cenomanian or post-Turonian age to the deposits.

It seems not easy to depict clearly how much time has been necessary to precipitate Mn oxides in the Tasdremt area, as they exhibit two major phases during early Campanian (~81-82 Ma) and at the Maastrichtian/Danian boundary (~65-67 Ma), which could characterize two main ore phases (►Fig. 7.35d) and suggest that a time lap of ~17 Ma has been necessary to precipitate the three Mn oxide levels, along with the development of a karst system (►Fig. 7.36). Hence, does the ore formation (1) occurred during a single Early Campanian event, (2) resulted of the remobilization of this primary deposition at ~81-82 Ma during the subsequent Maastrichtian/Danian event, or (3) rather related to cyclic inputs of Mn? The most consistent interpretation emerging from the processing of $^{40}Ar/^{39}Ar$ data is that the second phase at ~65-67 Ma expresses a perturbation or a reset of the K-Ar isotopic system of the former phase crystallized at ~81-82 Ma in connection with a (hydro?)thermal event. This total reset could have occurred by simple volume diffusion or results from a recrystallization/reworking of the former phase during the Maastrichtian/Danian one. It can sometimes be incomplete as suggested by some of the $^{40}Ar/^{39}Ar$ age spectra which evidence two age components within a single hollandite *s.l.* grain (i.e.,16AOU10 and 16AOU17; ►Fig. 7.35b) or staircase shaped age spectra such as 16AOU13. This implies that the 81-82 Ma phase would be the first and main (?) Mn ore phase. However, it cannot be excluded that the second phase at ~65-67 Ma is accompanied by new Mn mineralization, especially considering petrographic observations clearly indicating a multistage formation (►Fig. 7.33).

Dissolution processes have, therefore, affected the host dolostone after the deposition of the Cenomanian-Turonian carbonates, following the withdraw of the Cenomanian-Turonian sea. Such timing is supported by the observation that manganese ores were exposed and reworked along a pre-Senonian erosion surface

(Gutzmer *et al.*, 2006) and the occurrence of detrital manganese oxide grains within karst sediments, at least in the upper C3 level of Imini, and the L2 level of Tasdremt, both being located at the boundary with upper Senonian detritic series (Figs. 3c, e and f). $^{40}Ar/^{39}Ar$ ages obtained from K-Mn oxides in this level (►Fig. 7.35; ►Table 7.7) suggest the lowermost part of the so-called "Senonian upper detritic series" to be older than 65.2 $\pm$ 0.1 Ma and possibly 82 $\pm$ 0.2 Ma as they are replaced by Mn oxides. Alternatively, the upper part of these series could have been deposited concurrently with the ongoing development of karstification and formation of Mn oxides in the Cenomanian dolostone (►Fig. 7.36).

Karstification processes are known to be particularly active along the Senonian deposition in the High Atlas (Froitzheim *et al.*, 1988), but should also operate during Cenozoic times, as some K-Mn oxides are reworked within karstic-like sediments (►Fig. 7.36) and have provided Maastrichtian/Danian ages. Alternatively, one of these oxides dated at 80.8 $\pm$ 0.2 Ma is also reworked within a matrix made up of Mn oxides, dolomite, clays and quartz (►Fig. 7.35) and strengthen that Mn oxide precipitation has persisted during the second Mn event at ~65-67 Ma additionally to petrographic observation. Such karstification was probably accentuated through time, leading the karst cavities to be filled by various sands and blocks, as well as reworked fragments of the early Mn deposition stages (►Fig. 7.36). However, some brecciation (karstification?) events in the L2 ore level, postdate the latest phase of ore formation, and could be assigned to post-Cretaceous remobilization, without providing an accurate age, even if subtle young components are sometimes evidenced in the low temperature domain of some age spectra (►Fig. 7.35c). Such post-Cretaceous phases have not significantly changed the previous picture, ensuring only slight or negligible modifications of the previous phases likely by overprinting the former ore. Why this process has not persisted through Cenozoic times is a pending question to which a straight answer is not easy to build up. Several factors could be invoked, such as fluid composition, unable to transport manganese and associated metals efficiently, changes or depletion of the source rock, or more likely the absence of structures (i.e., tectonic, faults, folding) in which mineralizing fluids can circulate easily.

7.3.4.c Classification of the deposit

The close relation of Mn oxides to dissolution features (►Fig. 7.31) indicates that neutralization of the mineralizing fluids is related to the dissolution of carbonates, Mn oxides being located in dolostones. The mineralized Cenomanian-Turonian succession is only 10 to 20 m thick, or could be up to 55 m in thickness if the upper Senonian series are considered, suggesting that these sediments were not buried deeply and dissolution took place rapidly after sedimentation (►Fig. 7.36). Precipitation of Mn oxides in open voids, fractures and pores, related to dissolution (dissolution breccia) and karstification (collapse breccia, sand lenses, reworked

figures; ►Fig. 7.31f) processes define a karst-hosted type for the Tasdremt deposits, as it has already be concluded in the nearby Imini district (Gutzmer *et al.*, 2006; Dekoninck *et al.*, 2016b, 2016a). Geochemical investigations support a karst filling and the multistage formation of the Tasdremt Mn ores, either with high Pb content (Nicholson, 1992), by variations in the REE patterns of the three orebodies (►Fig. 7.34a), or consequently by the presence of tetravalent Mn oxides themselves. The negative Ce anomaly could be seen as an equivalent of the hydrogenous source for Mn in oceanic nodules (Fleet, 1983; Hein *et al.*, 1997, 2000), as they typically represent terrigeneous source of Mn, instead of the more widespread hydrothermal origin, providing positive anomalies (Fleet, 1983). A sedimentary Mn enrichment is unlikely considering the relatively poor thickness of Cretaceous carbonates and their poor enrichment in Mn (►Table 7.4), which were not able to supply sufficiently high amounts of Mn to form massive secondary Mn oxides. However, some questions arise from the geochemical footprint of the Tasdremt and Imini ores as they are strongly enriched in chemical elements usually attributed to hydrothermal manganese deposits, those being Pb, Cu, Mo, As, V and Zn (►Figs. 7.34b and c; ►Table 7.5) according to Nicholson (1992). Are the Imini and Tasdremt ores originating from hydrothermal solutions in an open karst system, or are they derived from a distant source, in which this atypical element association is enriched? Following the Nicholson (1992) classification, both deposits types could be involved. However, considering field and petrographic investigations, the source from which these ores are derived, may have a hydrothermal imprint, but rather by inheritance of older deposits reworked from the bedrock than truly hydrothermal system in an open karst system, because numerous Mn veins are described in the basement rocks (►Fig. 7.27b; Bouladon, 1948; Bouladon and Jouravsky, 1952, 1953; Bouladon *et al.*, 1955; Jouravsky, 1958; Pouit and Jouravsky, 1960a, 1961, 1962; Jouravsky, 1963; Jouravsky and Pouit, 1963; Gaudefroy *et al.*, 1965; Pouit, 1966; Sebbag, 1969; Choubert and Faure-Muret, 1973; Pouit, 1980; Lippolt and Hautmann, 1995). Nevertheless, it seems important to remind that the atypical behaviors observed during the processing of $^{40}Ar/^{39}Ar$ data suggested, for the Maastrichtian/Danian event (~65-67 Ma, phase 2), the possible occurrence of processes which could have been different of those encountered in a strictly weathering environment (i.e., 0-30°C in laterite *s.l.*), a thermally induced volume diffusion whose driving force could be hydrothermalism (>30°C).

7.3.4.d Source, transport and fluid composition

High oxidation potential probably not act as a single (main?) driver to the formation of massive Mn oxide layers, as the ore-forming processes are intimately related with carbonate dissolution. Dolomite break down, and related karstic features (i.e., dissolution and collapse breccia, karst cavities filled by sands and Mn oxides; ►Fig. 7.31) are also involved in the mineralization process, as acidic meteoric fluids could be buffered during carbonate dissolution, leading to rapid rise in pH values, and then precipitation of Mn oxides (►Fig. 7.37). The temperatures from which Mn

oxides have precipitated are probably close to weathering conditions observed in meteoric waters, but the disruption of most of the $^{40}Ar/^{39}Ar$ ages in phase 2 (►Fig. 7.35), showing different inherited or erased old age components, suggests a thermal effect to the (re)crystallization of Mn oxides, at least during the ~65-67 Ma event. This is the reason why we rather deal with supergene-hydrothermal fluids (>30°C) than truly weathering solutions (0-30°C) in the sense of those operating in a laterite *s.l.*, although further studies would adress this issue.

The association of Mn mineralization along with karstification of the host rock suggests that ore formation took place during terrestrial exposure periods, occurring after sedimentary and diagenetic settings. Two modes could be invoked to ensure effective transport of Mn, Ba and Pb: (1) the porosity of carbonates allows migration of O_2-poor shallow ground waters of meteoric origin slightly warmer than weathering conditions, and/or (2) the occurrence of salt in some samples (►Fig. 7.33h) with a high vegetation blanket in the Turonian-early Senonian hinterland (Rhalmi, 1992; Gutzmer *et al.*, 2006; Ali *et al.*, 2019), might support saline and acidic transport in the surface meteoric waters. The latter is, however, less predictable as the first main ore phase took place by the Campanian (~81-82 Ma), a period of burial conditions (Algouti *et al.*, 1999; Leprêtre *et al.*, 2015a). The joint effect of metal-bearing fluid neutralization by carbonate dissolution with O_2-rich conditions found in the open karst system have both favored precipitation of massive Mn oxides.

Source rock for karst-hosted deposits is usually not straightforward, as multiple parent material would generally supply metals to mineralizing fluids. Such interpretation needs careful attention and well constrained regional geological settings, as allochthon input of such atypical Mn, Ba and Pb association necessarily implies weathering/alteration of voluminous amount of rocks, probably originating from the hinterland during the Upper Cretaceous. The paleogeographic situation of the Upper Cretaceous Atlasic gulf indicates that the Imini and Tasdremt areas are located close enough to the Turonian paleoshoreline to undergo dissolution processes following the withdrawal of the Cenomanian-Turonian sea (Froitzheim, 1984; Froitzheim *et al.*, 1988; Thein, 1990; Rhalmi *et al.*, 1997, 2000; Frizon de Lamotte *et al.*, 2009) and emersion periods during the Senonian period (Algouti *et al.*, 1999). From the post-Cenomanian regression to the Eocene cover (Ambroggi, 1963), a period during which Mn mineralization proceeded as suggested by the two $^{40}Ar/^{39}Ar$ phases, the Tasdremt area is subjected to massive continental terrigeneous input accompanied by sporadic shallow marine incursions responsible for carbonate facies (Ambroggi, 1963; Algouti *et al.*, 1999). Interestingly, the western Anti Atlas was kept buried below a km thick sedimentary cover until middle/late Paleogene times (Ruiz *et al.*, 2011; Sebti, 2011; Leprêtre *et al.*, 2015a), indicating that source rocks for Mn mineralization are probably derived from the emerged High Atlas to the north

(►Fig. 7.37). Early Atlas tectonic activity has already been suggested by (1) an angular unconformity between Senonian and lower Tertiary sediments in the northern flank of the High Atlas axial zone (Froitzheim, 1984), (2) cooling in the thermal history of the western High Atlas (Leprêtre *et al.*, 2018), (3) changing in sedimentation style (Algouti *et al.*, 1999) and (4) a post-Cenomanian-Turonian erosion surface (Bouladon and Meune, 1951; Algouti *et al.*, 1999), which could account for late Cretaceous relief creation. Such interpretation implies that most of the karstification and dissolution processes in the Tasdremt area occurred after the deposition of the Cenomanian-Turonian dolostone, and additionally that mineralization processes and karstification persisted under a thick emerged sedimentary cover, as suspected by the second phase of $^{40}Ar/^{39}Ar$ data. This involves rather cryptokarstic formation of the Tasdremt ores than the more common karstification (without sedimentary cover) has already studied in other supergene deposits (Brouard, 1992; Nicaise, 1998; De Putter *et al.*, 2002; Bruyère, 2004). This further allows higher temperature mineralizing fluids (especially in the second $^{40}Ar/^{39}Ar$ phase) similarly to other Mn karst-type deposits (e.g., Varentsov, 1996). The presence of voluminous Precambrian volcanic (rhyolite and andesite), plutonic (granite and diamictite) and metamorphic rocks in the basement, and more interestingly of numerous Mn-Ba and base-metal deposits (Westerveld, 1951; Pouit and Jouravsky, 1960c; Pouit, 1964, 1976; Choubert and Faure-Muret, 1973), could have allowed the unusual metal association (Mn, Ba and Pb) to be extracted from their parental rocks, and finally to be precipitated in the Tasdremt dolomitized levels in one or two phases at ~81-82 Ma and ~65-67 Ma (►Figs. 7.36 and 7.37). Large stocks of Mesozoic Triassic-Jurassic basalts (CAMP; Verati *et al.*, 2007) in the High Atlas, now mostly eroded, could also be a reasonable source of metals, as they commonly contain up to 0.21 wt.% MnO (Bensalah *et al.*, 2013). Despite many sources could have contributed to the enrichment of the Tasdremt ores, there are no certainties about tracing them, but many possibilities for further investigations.

7.3.5 Metallogenic model

In the light of the previous discussion, the formation of the Tasdremt ores could be summarized in two phases (►Fig. 7.37):

(1) Phase 1 at ~81-82 Ma takes place after the deposition of carbonates in the Cenomanian-Turonian seashore and their early dolomitization. These rocks are exposed to meteoric agents after early Turonian period leading to the development of a karstic system by progressive dissolution of the host rock dolostone. Few inputs of Mn are expected before the first ore formation phase at ~81-82 Ma. However, the High Atlas bedrock further north could be weathered under the tropical Turonian climate (Rhalmi, 1992; Rhalmi *et al.*, 1997, 2000; Gutzmer *et al.*, 2006; Ali *et al.*,

2019). Some of the weathered material could then be eroded and facilitate the transport of Mn, Pb and Ba in acidic meteoric fluids due to the presence of organic acids originating from the dense vegetation blanket and precipitate Mn oxides within the Tasdremt deposits. Migration of surficial low pH or saline meteoric fluids toward the ongoing karst development brings supergene solutions to be buffered by the exposed Cenomanian-Turonian dolostones, and precipitate Mn oxides accordingly to increasing pH and highly oxidizing conditions. The presence of a Senonian cover at ~81-82 Ma is likely as these Mn oxides replace de lowermost part of the Senonian detritic series, although some of them are reworked within the lowermost part of these series. This further implies that acidic and O_2-poor ground water solutions are also consistent to be responsible of the Mn oxide deposition after oxidation and neutralization of the dissolved carbonates. Senonian sands can partially fill karstic voids with dolostone sands, originating from the in situ breaking up of the Cenomanian-Turonian dolostone.

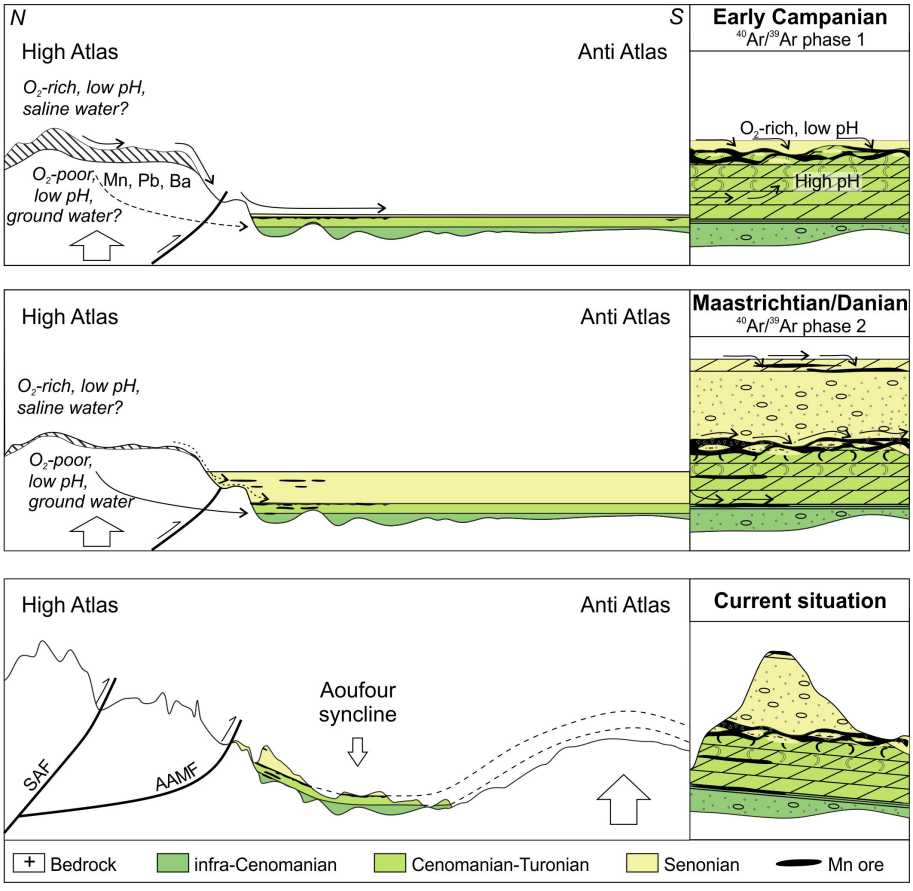

►**Fig. 7.37** Metallogenic model showing regional and local enrichment processes of the host

rocks by manganese oxides related to weathering/alteration and erosion of the late Cretaceous hinterland. SAF: South Atlasic Front; AAMF: Anti Atlas Major Fault.

(2) Phase 2 operates at the Maastrichtian/Danian boundary (~65-67 Ma), the latter being suitable either for new Mn mineralization or remobilization, although reset of the $^{40}Ar/^{39}Ar$ system is consistent with mixing component observed in some spectra (►Fig. 7.35; see discussion above). Transport of metals is probably more efficient in ground water solutions, in which depletion of oxygen is the main driver instead of a low pH in surficial fluids, the latter being inconsistent with the arid Senonian climate and the sedimentary cover. The early uplift of the Atlas during the late Cretaceous period could trigger fluid mobilization and therefore Mn transport and deposition in the dolostone and dolomitized sandstone after sedimentation or along with the deposition of the upper detritic sediments (Algouti *et al.*, 1999) favoring karstification and dissolution. Dolostone and lithological boundaries act as the main drain for carbonate dissolution and Mn precipitation under the Senonian cover.

A post Cretaceous period does not bring new Mn to the system but development of karst cavities could be enhanced through their progressive exposure coevally to the Atlas exhumation, without excluding further minor remobilization of the primary ore phases as suggested by geochronological data.

7.3.6 Tasdremt ores and their relation to Imini

Even though the Tasdremt Mn ores are clearly lower graded than the Imini mineralization, several parameters strengthen the genetic relation between them. (1) The occurrence of three *stratabound* orebodies (more discontinuous in the Tasdremt area), (2) the presence of massive hollandite group minerals in the C3 of Imini layer and (3) the development of karstic and dissolution figures in association with the formation of Mn oxides (karst-hosted deposit) are analogous features of the Imini ores (Gutzmer *et al.*, 2006 ; Dekoninck *et al.*, 2016b, 2016a). The C3 level observed in the Imini area displays similar textures with the Tasdremt ores, in which fragments of hollandite group minerals are cemented by a late calcite or late Mn oxides in the L2 level (Dekoninck *et al.*, 2016a). Another interesting point is the SW-NE direction of the orebodies suggesting that a common process is responsible for their orientation (►Fig. 7.27b), either by their rapid exposure to meteoric agents along the Cenomanian-Turonian shoreline (Thein, 1990; Lalaoui *et al.*, 1991) or alternatively to slight uplift of the area in relation to late Cretaceous Atlasic vertical movements (Froitzheim, 1984; Leprêtre *et al.*, 2018). In situ processes within the Imini and Tasdremt ores identify fracturation and dissolution as determinant factors to explain this position in a karstified dolostone, these rocks being more porous compared to other lithologies (►Figs. 7.27b, 7.28 and 7.30). The position of the L2 orebody at Tasdremt (and laterally equivalent C3 in the Imini area) is also conducted by

lithological discontinuities, along which meteoric fluids can circulate easily and finally accumulate large amounts of Mn (►Fig. 7.37).

However, based on mineralogical data, the absence of massive pyrolusite levels in the Tasdremt area, whereas Imini ores are strongly enriched, is a striking difference between these deposits. This together with higher Pb content and the relatively thin and discontinuous character of the orebodies penalize the economic interest of the Tasdremt ores, instead of the Imini ones, in which a clear benefit is due to large tonnage of the high quality pyrolusite-bearing ore. Tasdremt mineralization could have commercial value, at least, considering its similarity with the C3 orebody at Imini, used as metallurgical ore, or alternatively if Pb (and Ba) could be efficiently separated from Mn during metallurgical process. Such important difference between two deposits having much in common considering their ore-forming mechanism raises questions about the scarcity of the Tadremt ores in pyrolusite, and how these deposits could have evolved differently. The answer is not simple, but slight evidence in the geological background are worth being mentioned. Geochronological data of the hollandite group minerals in the Tasdremt ores produced early Campanian (~81-82 Ma) and Maastrichtian/Danian ages, which correspond to the setting up of a primary ore along with karstification and hydrothermal (?) remobilization after the deposition of Cretaceous sediments. Petrographic observations of the Imini ores show that most of the pyrolusite occurred after the formation of hollandite group minerals (Gutzmer *et al.*, 2006 ; Dekoninck *et al.*, 2016b, 2016a), suggesting that post-Cretaceous remobilization processes could have accounted for reworking and/or brought new Mn to the ore, those being enriched in pyrolusite (Dekoninck *et al.*, 2016b). Tectonic settings in the Imini area are likely stronger than in the Tasdremt area, resulting in folding and faulting of the Cenomanian-Turonian dolostones (Leprêtre *et al.*, 2015b), especially around the Imini inlier and Imini fault (►Fig. 7.27b), where most of the pyrolusite-rich ore occurs, pyrolusite grade decreasing westward (►Fig. 7.27b; Dekoninck *et al.*, 2016b). The Tasdremt and Aoufour synclines could have been isolated from further enrichment, as connection to major deformation zones were limited (►Figs. 7.27, c and 7.37). The absence of Triassic bedrock in the Tasdremt area (i.e., ~200 Ma basalts) could be an additional factor explaining such differences, as underlying Triassic-Jurassic basalts end in bevels upon the Paleozoic and Neoproterozoic bedrock in the Imini area (Leprêtre *et al.*, 2015b). In such a context, tectonic settings could have accounted for most of the Mn enrichment in the Imini area, mainly in the form of pyrolusite. The early signs of Atlasic deformation during late Cretaceous accounted for the primary formation of the Tasdremt and Imini ores.

All these features put together make the Tasdremt deposit a lateral equivalent of the Imini ores, although Mn is less enriched, leading us to consider a unique Imini-Tasdremt district of about 100 km-wide, following the south Atlasic front

(►Fig. 7.27b) and/or the Cenomanian paleoshoreline. The inner part of this mineralized belt has been nearly totally eroded by the Cenozoic uplift of the Siroua plateaus and related setting up of Miocene-Pliocene volcanism (►Fig. 7.27b), as only few spots of Mn enrichment in Cretaceous series are still identified between Imini and Tasdremt (Bouladon and Jouravsky, 1952).

7.3.7 Conclusion

X-ray diffraction and microscopical investigations point out that the Tasdremt ores are made up of hollandite group minerals [$(K,Ba,Pb)Mn_8O_{16}$], in which hollandite (Ba) and coronadite (Pb) are the dominant supergene minerals, providing the atypical Mn-Pb-Ba association. Petrographic observations further indicate that hollandite group minerals successively replace dolomite crystals and subsequently fill open cavities within the dissolved dolostone, whereas brecciated fragments of the Mn ore are cemented by other detrital materials and finally by a late meteoric calcite. This further suggests that mineralization postdates dolomitization of the host Cenomanian-Turonian dolostone, in relation to post-Turonian karstification periods. $^{40}Ar/^{39}Ar$ geochronological data on K-Mn oxides strengthen this interpretation as all obtained ages delimit at least one mineralizing phase at 81-82 Ma, despite a second phase at the Maastrichtian/Danian boundary (~65-67 Ma) is evidenced in relation to a reset of the $^{40}Ar/^{39}Ar$ system, remobilization and/or new inputs of Mn and associated metals forming the Mn oxides. In this scenario, the High Atlas hinterland has probably provided the Mn-Pb-Ba association via surficial acidic meteoric fluids or ground water depleted in oxygen, inherited from weathering/alteration of large volumes of basement rocks, their precise nature being unclear. The ongoing development of an open karst system brings higher Eh and pH to the Mn-bearing solutions, from which Mn oxides have precipitated. Remobilization processes have led the ore to be reworked during the late Cretaceous (~65-67 Ma) period and maybe more recently without significant changes in the ore mineralogy. The chemical composition of the ores, and their relation to dissolution of carbonates, are typical features of a karst-hosted deposit. The present study shows that the Tasdremt deposits are lateral equivalent of the world-class Mn Imini district, located 100 km toward the NE, and led us to consider a single Imini-Tasdremt district, most of the inner part having been removed during the Neogene Siroua exhumation. The absence of pyrolusite is a striking feature making the Tasdremt ores lower graded than the Imini ones, probably because Cenozoic faulting and folding may have induced several remobilizations and enrichment in the Imini area.

7.4 Polyphase Mn remobilizations in the high-grade Imini ores (High Atlas, Morocco) deciphered by K-Mn oxide dating: role of the Cenozoic Atlasic tectonics

Dating ore deposits remains challenging for mining research, as it constitutes one of the key factors in the ore system, including the source, the mobilization of fluids, the geometry of the metallogenic trap, and the precipitation of Mn-bearing minerals. The link with geodynamic episodes is clearly connected to the age determination (e.g., Lindgren, 1933; Blondel, 1937; Petrascheck, 1965; Laznicka, 1992, 2014). The duration of the ore deposition is also crucial as economic ore deposits are commonly formed in several mineralizing episodes (e.g., Vasconcelos et al., 1994; Ruffet et al., 1996; Hautmann and Lippolt, 2000; Li et al., 2007; Decrée et al., 2010a; De Putter et al., 2015; Dekoninck et al., 2018; Verhaert et al., 2018; see appendix III). The primary ore deposition and the subsequent supergene modifications need to be calibrated in the crystallizing sequence of the ore-forming minerals. The timing and the duration are important issues for economic mining as they strictly control the grade, the volume and the geometry of the ore.

Orebodies deposited alongside sedimentary planes (i.e., *stratabound*) are particularly debated given that geometrical criteria plead for a synsedimentary origin although other parameters, such as the mineralogical and geochemical composition of the ores envisage rather a post-sedimentary (diagenetic or supergene) origin. Direct dating of minerals forming the ores can bring robust constraints to feed this debate.

Most of the previous studies about the manganese deposits of Imini have considered that mineralization occurred early in the geological history of the deposits, simultaneously with the Cenomanian-Turonian dolostone deposition or just after, but before the deposition of the overlying Senonian conglomerates, sandstones and clays (Bouladon and Jouravsky, 1952; Force *et al.*, 1986; Thein, 1990; Lalaoui *et al.*, 1991; Rhalmi *et al.*, 1997). The latest model first developed by Gutzmer *et al.* (2006) identifies the main deposition phase to be associated with the development of an extensive karst system within the Cenomanian-Turonian dolostones, before Senonian times. These authors and more recently, Dekoninck *et al.* (2016a, 2016b, this chapter) also report that petrographical features, chemical and mineralogical composition of the manganese ores are not consistent with a synsedimentary origin. Alternative metallogenic models have also suggested an epigenetic (Pouit, 1964; Dekoninck *et al.*, 2016b, 2016a, this chapter) and diagenetic origin (Force *et al.*, 1986; Gutzmer *et al.*, 2006), but no direct dating has been carried out yet. Beaudoin *et al.* (1976) and Pouit (1976) stressed that no straightforward evidence allows to date the karstification precisely (i.e., associated with the mineralization), as it can occur from Cenomanian to Quaternary. However, the location of the mineralizing bodies on the border of the

High Atlas system and in front of a main Atlasic thrust questions this early formation (►Figs. 7.1a, 7.19b and c).

Following recent works aiming to define the structural context of the Imini area (Leprêtre *et al.*, 2015b, this chapter) and the petrographical and mineralogical investigations of the manganiferous orebodies (Dekoninck *et al.*, 2016a, this chapter), we present new data dealing with the age of the Imini deposits based upon K-Ar and $^{40}Ar/^{39}Ar$ dating of K-Mn oxides (hollandite group minerals). Our work stresses a protracted scenario of formation with an initial concentration remobilized by fluid circulation in agreement with the Cenozoic history of the Atlasic tectonics.

7.4.1 Sampling and analytical procedure

Sampling has been carried on adequate minerals for K-Ar and $^{40}Ar/^{39}Ar$ dating of the ore deposits of Imini. A similar approach has been conducted successfully to date supergene Mn ore deposits (e.g., Vasconcelos et al., 1994, 2008; Ruffet et al., 1996; Hénocque et al., 1998; Dammer et al., 1999; Li et al., 2007; Deng and Li, 2013; De Putter et al., 2015). The study of supergene K-bearing Mn oxides needs a careful attention as these oxides could be contaminated by older parental minerals originating from the host rock, making ages often difficult to interpret (Vasconcelos, 1999). However, such contamination is limited in the Imini district as the host rock dolostone contains little amount of K-bearing minerals (i.e., low amount of detrital K-feldspars and illite). Sampling of K-Mn oxides has been carried on four sites located along the mining district of Imini, from west to east: Far West, Lantenois, Timkit and Bou Aguioun (►Figs. 7.19b and 7.38).

Samples correspond to pure cryptomelane phases collected in *stratabound* orebodies or in veinlets filling fractures connected to the ore (►Fig. 7.38). All dated materials are therefore related to the second generation of Mn concentration associated to collomorphous cryptomelane (►Figs. 7.24 and 25; Dekoninck *et al.*, 2016b, 2016a, this chapter) indicating they are, at least, younger than a first (main?) mineralized event, as suggested by Gutzmer *et al.* (2006), and more recently confirmed by Dekoninck *et al.* (submitted, this chapter) in the genetically related Tasdremt deposit (►Fig. 7.27). Incidentally, such analyzed materials are similar to those dated by Dekoninck *et al.* (submitted, this chapter) in the Tasdremt area. These samples belong to the hollandite group minerals with the dominance of hollandite and cryptomelane, coronadite being subordinate mineral in some growth bands of the Imini deposits (Dekoninck *et al.*, 2016a, this thesis). One sample was taken from the Far West site (IM41a; ►Fig. 7.38a) in the C_3 ore level. Two samples (LAN18 and LAN59) come from the Lantenois gallery, both being situated in the C_3 Mn-level (►Fig. 7.38b). Three samples were collected at the Timkit operating site in the mixed

C_1-C_2 level, one sample (TIM) being a fracture-filling secant to the strata (►Fig. 7.38c). All remaining samples were collected at the eastern edge of the area in the Bou Aguioun mine (►Fig. 7.38d). Samples ECH102b and ECH98 were taken from the C_1 *stratabound* ore, while sample ECH101b was collected in stockwork veinlets connected to the *stratabound* ores (►Fig. 7.38d). ECH98 and ECH101b were separated in two samples, one being in the core of the cryptomelane vein at the contact with the mineralized dolostone, the other being located in the external rim of the growth bands, in contact with the late calcite (►Fig. 7.39a).

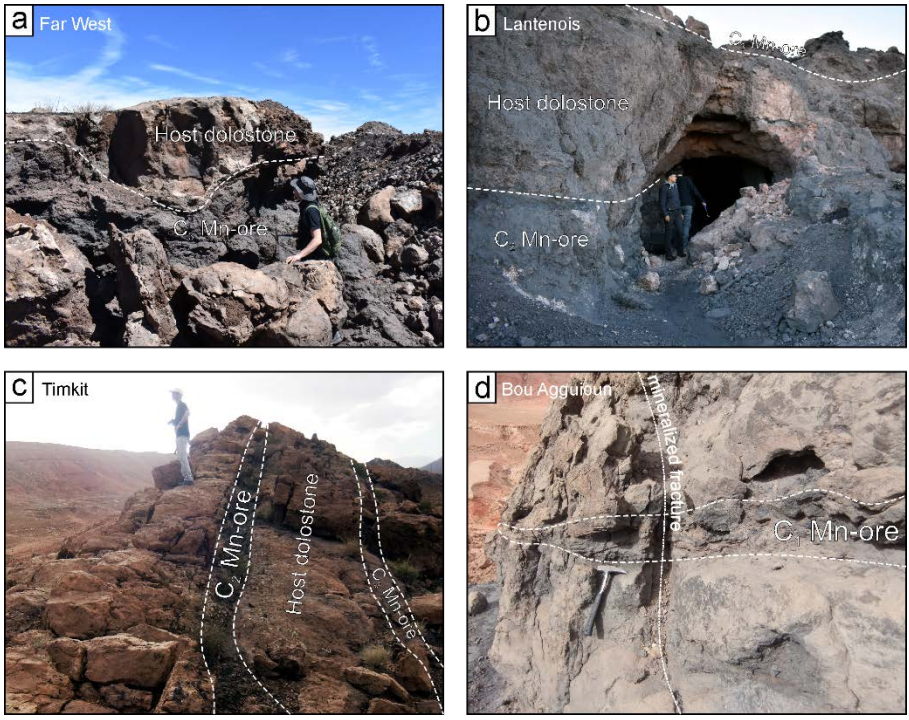

►**Fig. 7.38** Field observations of the four sampling sites (►Figs. 7.3a and 7.19b). **a.** C3 Mn ore composed mainly of hollandite group minerals in the Far West area (western edge of the district). **b.** C2 Mn ore composed of pyrolusite and C3 discontinuous orebody made up of hollandite group minerals in the Lantenois mining site. **c.** C2 and C3 orebodies at the Timkit site (east of the main mine). **d.** C1 Mn level with connected mineralized fractures at the eastern edge of the district (Bou Aguioun).

The mineralogical composition of the specimens was determined by X-ray diffraction analysis, with a BRUKER X-ray diffractometer, using a HI STAR GADDS CuKα detector to generate XRD patterns of powder samples.

K-Ar ages were determined in Activation Laboratories Ltd (Ontario, Canada; ►Table 7..8). The K concentration was performed by ICP. The argon analysis was performed using the isotope dilution procedure on noble gas mass spectrometer.

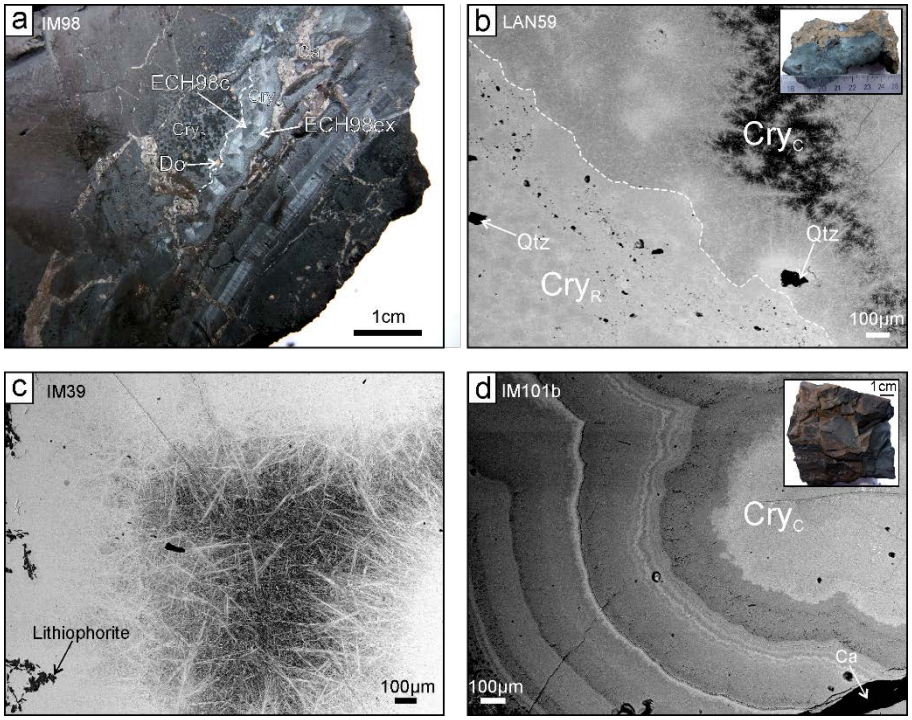

►**Fig. 7.44** Petrographic features of the studied cryptomelane. **a.** Botryoidal bands of cryptomelane (Cry_C) growing onto the mineralized dolostone (Cry_R) at Bou Aguioun sampling site. Individual late calcite veins (Ca) rework dolomite, quartz, feldspar and cryptomelane grains. **b.** Botryoidal bands of cryptomelane (Cry_C) growing onto the mineralized dolostone (Cry_R) at Lantenois sampling site showing some reworked quartz grains. **c.** Acicular needles of cryptomelane containing some lithiophorite crystal inclusions in the Timkit area. **d.** Growth bands of successive cryptomelane bands with variable compositions between K, Ba and Pb end-members in the Bou Aguioun deposit. Late calcite (Ca) cross collomorphous cryptomelane (Cry_C).

►**Table 7.8** K-Ar ages of hollandite group minerals in the Imini deposits

Label	Location	Ore type	Age (Ma)	+2σ (Ma)	$^{40}Ar_{rad}$, nl/g	%K
IM41a	Far West	C_3	73	2	6.565	2,31
TIM-2	Timkit	Fracture-filling	51.2	4.9	0.065	0,03
ECH102b	Bou Aguioun	C_1	47.5	1.3	4.092	2,23

►**Table 7.9** Summary of $^{40}Ar/^{39}Ar$ ages of supergene Mn-oxides in the Imini district. [a]: pseudo-plateau age; * range of ages which could be determined; [+]: spectra determined by less than 20% of ^{39}Ar released; n.a. : not applicable.

Label	Location	Ore type	Plateau age (Ma)	±2σ	Isochron age (Ma)	±2σ	Intercept $^{40}Ar/^{36}Ar$	±2σ	MSWD	Comments
LAN18	Lantenois	C_3	*							Discordant and staircase spectra
LAN59		C_3	*							
IM37	Timkit	C_1-C_2	45.2[a]	0.2	45.3	0.3	291.9	18.3	0.15	Saddle-shaped spectra, recoil effect
IM39		C_1-C_2	*							Discordant spectra, saddle spectra
ECH98c	Bou Aguioun	C_1	19.9	0.2	19.6	0.1	313.1	7.6	0.92	Recoil effect
ECH98ex		C_1	14.7	0.1	15.0	0.1	302.3	7.6	1.02	Hump-shaped spectra
ECH101bc		Stockwork	20	0.1	19.9	0.1	343.7	17.6	0.65	Recoil effect
			20.1 [a]	0.1						
ECH101bex		Stockwork	19.7 [a]	0.1						Recoil effect
			19.3 [a]	0.1						

Samples were analyzed with a $^{40}Ar/^{39}Ar$ laser probe and a Map 215mass spectrometer. Step-heating experimental procedure has already been described (Ruffet *et al.*, 1991, 1995, 1997). Analyses were performed on millimetric Mn oxide fragments, carefully handpicked under a binocular microscope. Blanks were performed routinely each first or third/fourth run, and are subtracted from the subsequent sample gas fractions. $^{40}Ar/^{39}Ar$ data are corrected for interfering isotopes and mass discrimination. Irradiation of samples was performed at Mac Master Nuclear Reactor (Hamilton, Ontario, Canada) in the 5C facility with Cd-shielding and lasted 115.8 h with a global efficiency (J/h) of 6.07 x 10-5 h-1. The irradiation standard was sanidine TCRs (28.608 ± 0.033 Ma according to Renne *et al.*, 1998, 2010, 2011). Apparent age errors are plotted at the 1σ level and do not include the errors on the $^{40}Ar^*/^{39}Ar_K$ ratio and age of the monitor and decay constant. Plateau ages were calculated if 70% or more of the $^{39}Ar_K$ was released in at least three or more contiguous steps, the apparent ages of which agreeing to within 1σ of the integrated age of the plateau segment. Pseudo-plateau ages can be defined with less than 70% of the $^{39}Ar_K$ released and possibly less than three contiguous steps. The errors on the $^{40}Ar^*/^{39}Ar_K$ ratio and age of the monitor and decay constant are included in the final calculation of the error margins on the (pseudo-)plateau ages or individually mentioned apparent ages. Significant ages are summarized in ►Table 7.9 and illustrated in ►Fig. 7.40. Analytical data and parameters used for calculations (e.g., isotopic ratios measured on K, Ca and Cl pure salts; mass discrimination; atmospheric argon ratios; J parameter; decay constants) and reference sources are available in supplementary data repository.

7.4.2 Results

7.4.2.a Mineralogy and petrography

Petrographic observations and XRD and SEM-EDS analyzes indicate convincingly that the studied samples are composed primarily of cryptomelane and hollandite *s.s.*, with minor amounts of lithiophorite and coronadite. Cryptomelane-hollandite typically displays the botryoidal texture formed by micrometric bands (►Figs. 4.39a and d), sometimes containing lithiophorite inclusions (►Fig. 7.39c). These collomorphous cryptomelane follow a first generation identified as the first mineralization event replacing the host dolostone (Cry_R; ►Figs. 7.25 and 7.39a and b; (Dekoninck *et al.*, 2016a, this chapter). Such microscopic bands result from incremental precipitation of cryptomelane needles, which are usually 1 µm in diameter and 3-500 µm long (►Figs. 7.39b and c), on the surface of a cavity or a previously precipitated Mn oxide layers (►Fig. 7.39d). Some quartz and dolomite grains could also be observed (►Figs. 7.39a and b) and result from the brecciation of the host rock dolostone along with the formation of the botryoidal generation of cryptomelane-hollandite (Dekoninck *et al.*, 2016a). Late calcite veins also cross the previous

generations of Mn oxyhydroxides (►Fig. 7.39d). The potassium composition of cryptomelane samples, based on EDS analyses and ICP (Dekoninck *et al.*, 2016b, this chapter; ►Table 7.4), range between 0.43 wt. % to 4.88 wt. % K_2O. These values are sufficiently high to yield reliable $^{40}Ar/^{39}Ar$ and K-Ar. Note that sample TIM-2 contains only 0.03 wt. % of K_2O (►Table 7.8), suggesting that this sample is rather hollandite *s.s.* or coronadite.

7.4.2.b Reliability of the K-Ar and $^{40}Ar/^{39}Ar$ dating

Eight samples were analyzed (►Tables 7.8 and 7.9). Samples 101-b-C and 101-b-EX were experimented in duplicate. This set of ten analyses yielded two irrefutable and concordant (2σ level) plateau ages at 19.7 ± 0.1 Ma (IM98-C) and 20.0 ± 0.1 Ma (101-b-C; ►Fig. 7.40). Consistently with its localization, in contact with the late calcite, sample IM98-EX displayed the youngest plateau age at 15.0 ± 0.1 Ma. These three plateau ages are supported by isochron calculations, respectively at 19.6 ± 0.1 Ma, 19.9 ± 0.1 Ma and 15.0 ± 0.1 Ma, although slightly high $(^{40}Ar/^{36}Ar)_i$ ratios for samples IM98-C and 101-b-C are identified (►Fig. 7.40; ►Table 7.9). These values are slightly higher than the atmospheric ratio (298.56) and probably arise from abnormally high apparent ages observed in the low temperature steps (see below) for both experiments.

The IM98-EX age spectrum expresses mixing of distinct radiogenic components with distinct ages. It suggests that the analyzed grain was composite with the occurrence of a secondary mineral component younger than ~15 Ma but whose age cannot be specified. With the exception of the previous sample IM98-EX, all obtained age spectra show abnormally high apparent ages in the low temperature steps, which rapidly decrease to reach significant orders of magnitude. Such behavior is seldom observed during the analyze of the K-Mn oxides, which more generally display staircase-shaped age spectra as with sample IM98-EX. In the context of a supergene environment, it is difficult to invoke excess of ^{40}Ar to explain such old apparent ages (►Fig. 7.40). The lack of obvious or systematic correlation between $^{37}Ar_{Ca}/^{39}Ar_K$ (# Ca/K) ratios and apparent ages in the low temperature domain does not establish a clear link with the degassing of more or less Ca-rich contaminant or inherited components.

There are some indications that part of these high apparent ages could relate to $^{39}Ar_K$ recoil. For example, a review of degassing kinetics of Ar isotopes $[(xAr/\Delta T°)/(xAr/\Delta T°)_{Max}$ versus $\%^{39}Ar_K$, with x=36 to 40] from one of the experiments performed on sample 101-b-EX evidences in the low temperature degassing domain individual peaks (increase and decrease of degassing rates; ►Fig. 7.40) for ^{40}Ar and ^{36}Ar but not for $^{39}Ar_K$. This suggests that some parts of the $^{39}Ar_K$ were moved and lost by recoil during irradiation (e.g., Ruffet *et al.*, 1995). Furthermore, such individualized degassing peaks could express distinct coexisting

physical/mineral supports. This would suggest mixing of contaminant/inherited phase (detrital material?) which otherwise are attested by older ages in the high temperature steps of experiments 101-b- EX but also 101-b-C, as it is the case in the Tasdremt ores (Dekoninck *et al.* submitted, this chapter). Similarly, the trajectory drawn by points in the isochron diagram of the experiments performed on sample IM37 also suggests a $^{39}Ar_K$ loss (►Fig. 7.40). However, in the present case, the high apparent ages in the low temperature domain are not correlated, unlike previously, with clearly individualized degassing peaks in the low temperature domain, when significant older apparent ages in the high temperature steps clearly suggest degassing of a contaminant or inherited component. Therefore, there might be several explanations to interpret these low temperature high apparent ages: $^{39}Ar_K$ loss, inheritance or contamination. They are problematic as they hide the low temperature degassing domain and penalize the interpretation of the intermediate to high temperature domains.

Even without a clear correlation between $^{37}Ar_{Ca}/^{39}Ar_K$ (# Ca/K) ratios and apparent ages, it is tempting to consider that saddle shaped age spectra, such as IM37, IM39 and maybe 101-b-EX, express a mixing of distinct radiogenic components with distinct ages and despite the fact that such combination usually yields more conventional staircase-shaped (LAN18 or 59, see below) or hump-shaped age spectra (e.g., IM98-EX; ►Fig. 7.40). This would proceed via a partial destabilization (dissolution, recrystallization, etc.) of an inherited (primary) component and the (neo-) crystallization of a secondary component, which led to various states of mixing or interpenetration. The saddle shaped age spectra would characterize relative contributions to degassing of these primary and secondary components, which inversely evolve during the heating procedure. In such context, the pseudo-plateau age at 45.2 ± 0.2 Ma calculated from IM37 experiment would be a maximum estimate of the age of the (neo-)crystallized component (►Fig. 7.40). On the other hand, this secondary component was incompletely resolved during IM39 degassing experiment probably as a result of a predominant degassing of the contaminant or inherited primary component whose age cannot be estimated, but could be supported by petrographic observations of Dekoninck *et al.* (2016a, this chapter; ►Fig. 7.25). Isochrone calculation performed on saddle basement of IM37 age spectrum yields coherent results with a perfectly concordant isochron age (45.3 ± 0.3 Ma) and a $(^{40}Ar/^{36}Ar)_I$ ratio close to the atmospheric one [298.56 ± 0.31 according to Lee *et al.* (2006)], suggesting that the secondary component was correctly separated from the primary one and that the age at ~45 Ma is valid (►Fig. 7.40).

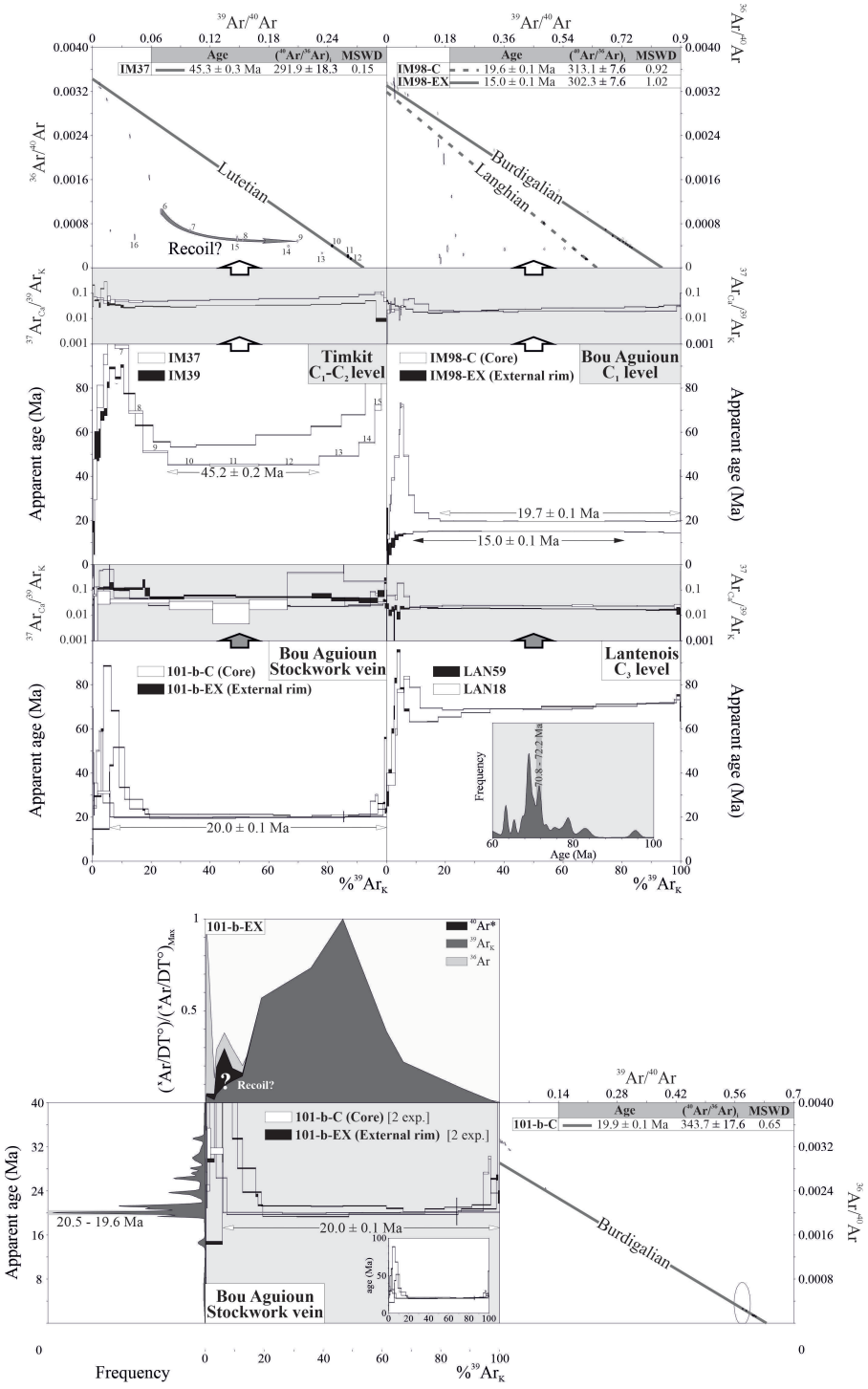

►**Fig. 7.40** Incremental-heating spectra for the eight Mn oxide grains from the Imini district.

$^{40}Ar/^{39}Ar$ ages are summarized in ►Table 7.8.

The subtle saddle shape of experiments 101-b-EX in their intermediate to high temperature domains could also characterize the coexistence of two distinct radiogenic components. Concordance of apparent ages of saddle basements with plateau age at 20.0 ± 0.1 Ma displayed by experiment 101-b-C suggests that the secondary component highlighted by 101-b-EX experiments would be Burdigalian in age (►Fig. 7.40). This convergence of apparent ages defines a huge peak at 19.6-20.5 Ma in the probability density diagram. The age of the primary component cannot be specified.

Low temperature apparent ages, excepted LAN18 and LAN59, yield much more familiar age spectra with an increase of apparent ages from low to high temperature steps (►Fig. 7.40). Age spectra have a very similar shape with concordant ages in the high temperature steps at ~71-72 Ma but distinct ones in the low to intermediate temperature steps probably impacted by high apparent ages segment. These staircase-shaped age spectra express mixing of two radiogenic components, after partial destabilization of a primary component during a subsequent disturbing event with (neo-)crystallization of a secondary component. Consequently, the low temperature apparent ages hide the low temperature domain of age spectra and in the present case precludes the characterization of the secondary component. On the other hand, these two age spectra suggest that the primary component of samples LAN18 and LAN59 would be at least as old as ~71-72 Ma. Such old components could also be a mixing of two older mineralization phases, as already evidenced in the genetically related Tasdremt deposits further west (Dekoninck *et al.* submitted, this chapter). The observations made in the K-Mn oxides of the Tasdremt deposit have shown that these complex $^{40}Ar/^{39}Ar$ spectra imply multi-components to be identified.

The complexity of the $^{40}Ar/^{39}Ar$ ages makes K-Ar geochronological data difficult to interpret accurately, as different age components could be present. Samples ECH102b and IM41a could be regarded as reliable ages at 47.5+1.3 Ma and 73+2.0 Ma, respectively, as these ages corroborate periods determined in $^{40}Ar/^{39}Ar$ spectra (►Fig. 7.40; ►Table 7.9). For example, discordant spectra of samples LAN18, LAN59 yield maximum ages between roughly 65 and 75 Ma (►Fig. 7.40) belonging to the range of values of sample ECH102b. These ages are also consistent with $^{40}Ar/^{39}Ar$ geochronological data of the primary ore stage in the laterally equivalent Tasdremt deposits further west (Dekoninck *et al.*, submitted, this chapter). Concordant spectra of sample IM37 (45.2 $\pm$ 0.2 Ma) could be considered as similar to the 47.5+1.3 Ma age of sample ECH102b (►Fig. 7.40; ►Table 7.8). Sample TIM-2 displays only 0.03 wt. % K_2O, which is very low for a cryptomelane composition, probably because coronadite and hollandite dominates the growth bands in this sample (►Table 7.8). However, the 51.2+4.9 Ma age could also be considered, as it is included in the same range than other K-Mn oxide ages (►Fig. 7.40; ►Table 7.9).

7.4.3 Discussion

7.4.3.a The Imini ore deposits: a long-lasting evolution

K-Ar and $^{40}Ar/^{39}Ar$ results obtained on 11 samples of the Imini ores (►Tables 7.8 and 7.9) define three groups: ~15-20, ~45-55, ~65-75 Ma. The ages have been produced on hollandite group minerals, which are the only phases that can be dated with K-derived techniques. Most of the Mn oxide volume observed in Imini is, however, formed by pyrolusite that cannot be dated (Vasconcelos 1999). Conclusions draws from the ore formation are therefore partial even if a definition of the mineral paragenesis is also indicative for a multistage formation, in which most of the pyrolusite is late, despite some early generation are proposed by Dekoninck *et al.* (2016a; ►Fig. 7.25). We also observe that hollandite group minerals are commonly associated to pyrolusite in open spaces and that they replace early and late dolomite crystals by epigenetic processes (►Fig. 7.24).

Some previous studies argue for an early formation of the Mn oxides during or after Cenomanian dolostone deposition and before the Senonian cover (Force *et al.*, 1986; Thein, 1990; Lalaoui *et al.*, 1991; Gutzmer *et al.*, 2006). The first ore stage(s) cannot be addressed by the geochronological data of the Imini ores and an early concentration cannot be ruled out, the ore evolving later during late Cretaceous and Tertiary. Such an early ore formation stage is evidenced in the genetically related Tasdremt deposits, in which Mn blocks are reworked within the upper Senonian series (Bouladon and Meune, 1951). $^{40}Ar/^{39}Ar$ dating of K-Mn oxides in this area clearly identify two mineralization phases at ~81-82 Ma and ~65-67 Ma (Dekoninck *et al.*, submitted, this chapter; ►Figs. 7.35 and 7.36). Therefore, imperfect ages obtained between 65 and 75 Ma in the Imini ores are probably mixing of radiogenic components of two late Cretaceous phases and supported by geochronological data in the Tasdremt area. Contamination cannot be ruled out.

The C3 level (composed exclusively of hollandite group minerals) forms the top level of the mineralization, from which the oldest ages were obtained between 65 and 75 Ma (►Fig. 7.40; ►Tables 7.8 and 7.9) on the western side of the Imini area (►Fig. 7.19b). These late Cretaceous ages are also observed in the laterally equivalent L2 level of Tasdremt, in which no Tertiary ages have been determined. Therefore, the petrographical and mineralogical homogeneity of the C3 level pleads for a massive Mn oxide precipitation at ~81-82 Ma and possibly at ~65-67 Ma. Ages are younger than sedimentation (Cenomanian-Turonian, 100.5-89.8 Ma) and strengthen the post-sedimentary model.

The three ages acquired around 45-52 Ma (respectively 45.2 ± 0.2, 47.5 ± 1.3 and 51.2 ± 4.9 Ma; the last age being poorly constrained due to a low K content) have been obtained on K-Mn oxides (cryptomelane and hollandite) crystals of the C1 and

C2 levels associated to fracture planes (►Fig. 7.38d). Volumetrically this phase is not dominant, as hollandite group minerals are dispersed within the massive pyrolusite ore. This actually shows up that Mn oxide precipitation occurred after the Cretaceous primary ore deposition detected at Tasdremt and in the western side of the Imini area (Far West).

Six ages have been obtained in the 15-20 Ma range, which belong to the Bou Aguioun deposit (east of the Imini district; ►Fig. 7.19b). This site allows the study of the C1-C2 pyrolusite-rich levels. Dated phases are deposited in open spaces in close contact with pyrolusite crystals, allowing us to consider these minerals in a single stage. Most of the ages define a narrow period between 19.3 to 20.1±0.1 Ma, which might characterize an overrepresentation of these samples. This might be linked to the easy access to the Bou Aguioun site and the quality of the recovered hollandite materials. It corresponds to relatively rare materials in comparison to the bulk of the dominant pyrolusite ore.

Following these ages, it clearly appears that the formation of the Mn oxides spanned over a large period ranging from late Cretaceous at ~81-82 Ma (Campanian-Maastrichtian) to Neogene (Burdigalian-Langhian; ►Fig. 7.41). This also shows that crystallization and recrystallization events are at the origin of the Imini deposit along a polyphase history. Events of *in situ* Mn remobilization of the primary late Cretaceous enrichment is most likely but potential allochthonous supply of Mn remains possible. Such interpretation could also explain the progressive enrichment of the ore through Cenozoic times as time is generally a good parameter leading to high-grade supergene deposits.

7.4.3.b Relationship of the ore formation with the tectonic history

The three age groups measured in the Imini and Tasdremt ore deposits on hollandite group crystals correspond to periods of geodynamic activity in the Atlas domain. Based upon surface and subsurface data in Algeria and Tunisia, two events are reported over the large scale of the Maghreb for the building of the Atlasic chain (Frizon de Lamotte *et al.*, 2000, 2009): Late Eocene (Atlasic phase) and Plio-Quaternary. In the Moroccan High Atlas, a third event is individualized during the Cenozoic by thermochronological data (Missenard *et al.*, 2008; Balestrieri *et al.*, 2009; Barbero *et al.*, 2011; Leprêtre *et al.*, 2018) and occurred during an Early to Middle Miocene phase. Following these guidelines, Leprêtre *et al.* (2015b, this chapter) concluded that the Imini area registered three events during the Cenozoic: (1) a Late Eocene event represented by large folds but minor structures aligned along the local N70° direction; (2) an Early and Middle Miocene event not related to an important shortening, setting gravity sheets and decollement nappes that provoke cover deformation; and (3) a Plio-Quaternary activity of basement faults, such as the deep thrust located below the Imini anticline (►Fig. 7.3). Leprêtre *et al.* (2015b, this

chapter) suggested that the ~N70° structures may be dated at the Miocene but they should be older (Eocene or Late Cretaceous).

An older event has also been evidenced and is associated to an early phase of the Atlas building during the Upper Cretaceous. Froitzheim (1984) and Froitzheim *et al.* (1988) described close to the Medinet fault, in the northern side of the High Atlas, an angular unconformity between Tertiary (probably Paleocene) limestones and Turonian and Senonian carbonate rocks. Similar conclusions have been drawn in the Middle Atlas (Martin, 1982; Herbig, 1988) or in the High Atlas (Cavallina *et al.*, 2018) with the identification of an early phase (pre-Maastrichtian) of local tectonic shortening. Role of salt has also been proposed to explain this deformation episode. This event is not associated to important relief building, even though the High Atlas realm was still submerged until the Middle Eocene (Leprêtre *et al.*, 2015a).

Three periods of relative tectonic instability and relief building are then in agreement with the measured ages at Imini: late Cretaceous (ages between 65-75 Ma belonging to a phase at ~81-82 Ma and a second at ~65-67 Ma), Late Eocene (ages between 45-52 Ma) and Early to Middle Miocene (ages between 15-20 Ma). The good match between radiometric ages and geodynamic phases suggests that the ore is partly controlled by surface deformation (►Fig. 7.41). For the last two events, cryptomelane ages record mainly the beginning of each phase. This may further indicate that Mn oxide precipitation occurred when fluids start to migrate and when undersaturated conditions existed within the porosity of the host rock dolostone.

Wavelength of deformation is different for these events and can generate various interactions between basement and cover rocks and circulating fluids. Eocene and Plio-quaternary phases are associated to faulting and folding development with a short to medium wavelength. The Imini Paleozoic anticline is the expression of the Plio-Quaternary deformation. The Miocene event corresponds to a doming, which might be controlled by a large lithospheric anomaly (Missenard *et al.*, 2008; Missenard and Cadoux, 2012). The approximately N70° structure of the ore belt (►Figs. 7.3a and 7.19b) are characterized by large wavelength and narrow opening. These events have probably generated different reliefs and consequently various gravity fluid flows.

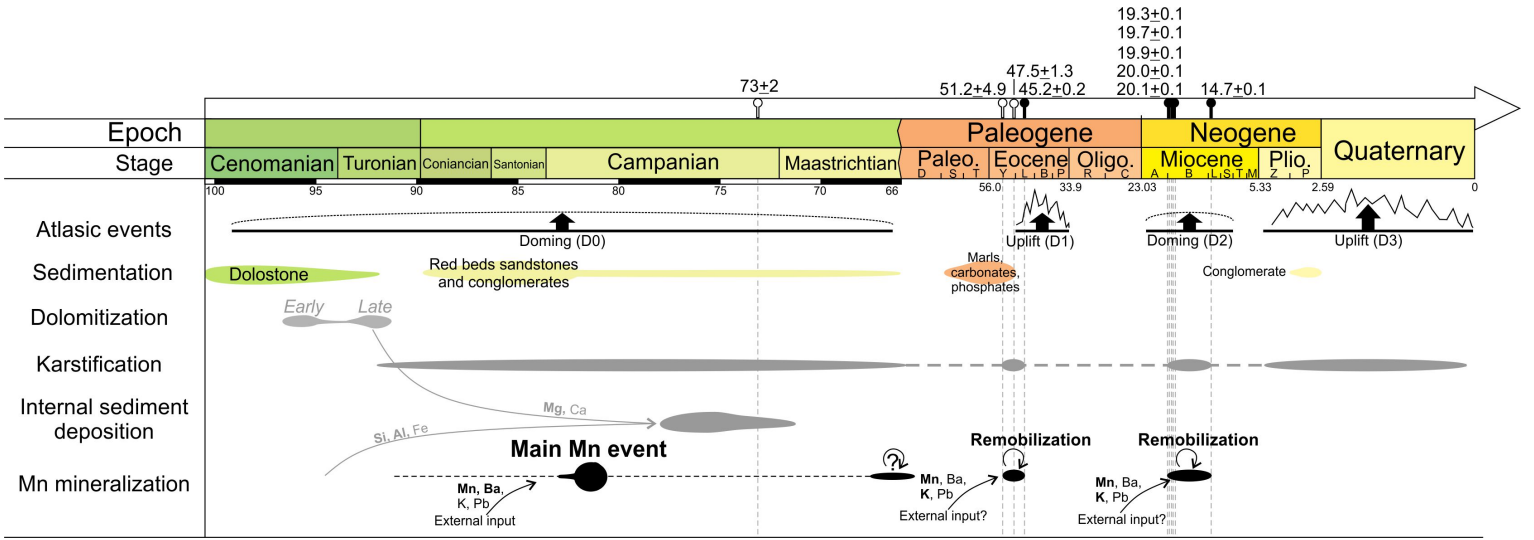

►**Fig. 7.41** Time-event chart of the Imini deposits illustrating the multistage character of the ore deposition based on petrographic observations and new geochronological data. $^{40}Ar/^{39}Ar$ (full black markers) and K-Ar (white markers) cryptomelane ages slightly predate the main tectonic events during the Cenozoic. See text for further discussion.

7.4.3.c Tectonic control on the Imini deposits

The present-day tectonic canvas of the Imini deposits shows that the ore is deformed and controlled by faults and flexures (geological map of the ore is available on the website of the Société Anonyme Chérifienne d'Etudes Minières – SACEM). The alignment of the ore (NNE-SSW) is oblique to the Imini anticline and fault (~N90°; ►Fig. 7.19b), showing that the main local structure does not controlled entirely the ore formation. The Imini anticline has however severely deformed the southern limb and verticalized the Cenomanian-Turonian dolostone (Timkit site; Leprêtre *et al.*, 2015b, this chapter). The structural canvas has not been really considered in previous studies on the Imini district. Gutzmer *et al.* (2006) mentioned that two episodes of normal faulting occurred in the area: post-Triassic and post-Senonian. The latter is marked by steep drag folding of the manganese-bearing carbonate unit and overlying Senonian red beds. On the contrary, the ore alignment is parallel to subtle ~N70° tectonic structures. These folds are associated to small-scale flexure with metric to decametric offset. One can see here that in the Lantenois mining site (►Fig. 7.19b), these flexures clearly control the mineralization, where mineralized dolostones are observed north of the flexure and barren dolostones occur south of the flexure (►Fig. 7.42). These structures have been interpreted by Leprêtre *et al.* (2015b, this chapter) to be gravity nappes formed during the Miocene doming.

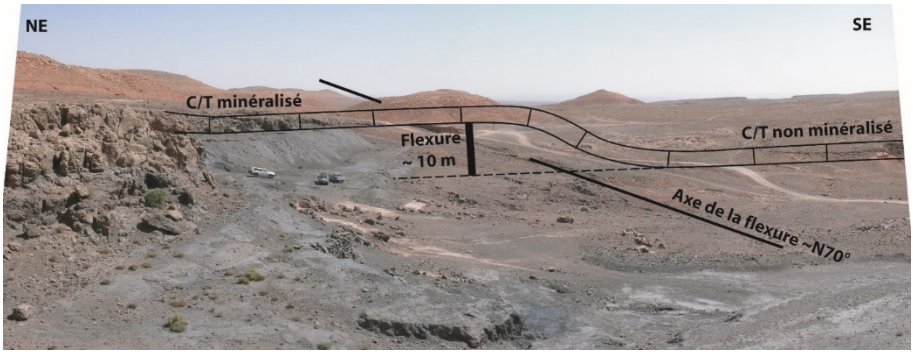

►**Fig. 7.42** Offset of the Cenomanian-Turonian level in the Lantenois site. A decametric flexure is observed corresponding to the limit of the mineralization: the southern bottom domain is barren whereas the three mineralized levels are observed in the northern domain. Orientation of the flexure is ~N70°.

Another important feature is evidenced by the geographical distribution of the geochronological data, displaying a gradation of the K-Mn oxide ages, from Cretaceous ages at the western edge of the Imini district (Far West mining site) to Miocene ages to the east in the Timkit and Bou Aguioun mines (►Fig. 7.19b). One can see here that such lateral evolution of geochronological data could be inferred by the presence of the Imini fault and fold, likely acting as an outset driver for fluid migration. Several key points could be proposed to support such approach: (1) The

Imini fault is directly in contact with the main manganese ores and could then be a drain for various mineralization; (2) The eastern zone is heavily enriched in massive pyrolusite, giving to the Imini ore its high grade and a good competitiveness in the world market (Dekoninck *et al.*, 2016b, this chapter; SACEM, 2016); (3) The Imini fault zone contains large quantities of barite (►Fig. 7.19b), a mineral also locally observed in the Imini ore itself (Dekoninck *et al.*, 2016a, this chapter); barium is also a dominant element accounting for the Imini ore grade, as it is accommodated within the widespread hollandite group minerals lattice; (4) Younger ages are concentrated around the Imini fault, whereas older ages are restricted to the western sector, in the C3 level and extent to the Tasdremt area to the west (►Fig. 7.27c). Observations made by Dekoninck *et al.* (submitted, this chapter) in the laterally equivalent Tasdremt deposit further west, show that pyrolusite is totally absent, probably because structural settings are different (i.e., absence of major tectonic structures). Furthermore, K-Mn oxide ages of theses deposits are restricted to late Cretaceous, corresponding to the early, thought to be primary, mineralization stage observed in the upper C3 level.

Consequently, this study shows that the Imini deposit is (partly?) controlled by local tectonic structures and that crystallization ages of the K-Mn oxides are consistent with main geodynamic Atlasic events. This further bring new perspectives to identify parameters that could control, at least, the age of K-Mn oxides, and additionally the ore formation/enrichment within the supergene zone. These features clearly indicate that the Imini ore formation is connected to the Atlas uplift. Sources of Mn and associated elements have to be identified locally in pre-enriched dolostones or in fertile rocks observed in the Atlas chain (Proterozoic basement, Triassic basalts, etc.).

7.4.4 Conclusion

The formation of the Imini Mn deposits has long been debated because its geometry does not fit with (1) the regional distribution of sedimentary rocks or erosion fronts, with (2) the main tectonic structure represented by the Imini anticline, or with (3) the nature of the basement rocks (Precambrian, Paleozoic or Triassic). This work proposes, besides K-Ar and $^{40}Ar/^{39}Ar$ dating on K-Mn oxides (cryptomelane and hollandite) of one part of the ore deposits combined with a reappraisal of the petrographical and mineralogical assemblage and the tectonic structure of the region, that the ore deposit is, at least, partly controlled by the movement of fluids generated by the building of the Atlasic relief.

For the first time, K-Ar and $^{40}Ar/^{39}Ar$ on K-Mn oxides from the Imini ore suggest at least three episodes of ore formation: a first around 65-75 Ma (probably a mixing of two phases at ~81-82 and ~65-67 Ma), a second at ~45-52 Ma and a third

at ~15-20 Ma. Earlier stages are not well recorded in the Imini ores, compared to the Tasdremt ones further west (Souss basin), but include late Cretaceous ages. Correspondence between these absolute radiometric ages and the periods of tectonic or surface activity in the High Atlas, and more generally in Morocco, pleads for a control of the geodynamic settings in the fluid circulation, precipitation and remobilization of the Imini Mn ores. These data confirm the polyphase origin of the Imini deposits, as suggested by petrological observations.

7.5 Thermal event(s) in the Imini and Tasdremt deposits

In addition to the formation model of the Imini-Tasdremt Mn ores, most of the ages obtained from the hollandite group minerals have shown some disruption in the low and high temperature domains displaying uncommon staircase spectra. As these results are somewhat difficult and unclear to interpret, it seems necessary to further discuss their origin as it could has an influence about the mechanism of formation of these Mn orebodies. Therefore, we have dated several growth bands of colloform samples of hollandite group minerals in the Tasdremt deposit (►Fig. 7.43), in addition to the 22 samples already described in the Imini (8 samples; ►Tables 7.8 and 9; Dekoninck *et al.*, 2016a, this chapter) and in the Tasdremt (14 samples; ►Table 7.7; Dekoninck *et al.*, submitted, this chapter) areas.

Colloform or botryoidal masses of Mn oxides and oxyhydroxides (formerly defined as psilomelane, see chapters 3 and 4) are commonly found in weathering and supergene Mn deposits, displaying well-identified growth bands as a witness of slight changes in the mineralizing fluid composition through their precipitation. Hollandite group minerals are particularly suitable to form such colloform textures as substitution are facilitated within the tunnel-like lattice with many cations occurring with different end-members (Post, 1999; Biagioni *et al.*, 2013). Their study find usefulness in the determination of accumulation rates as dating of the successive growth bands commonly provide a gradation of the ages from the core (young) to the outer shell (old) with a known thickness (Hénocque *et al.*, 1998; Dammer *et al.*, 1999; Li and Vasconcelos, 2002; Li *et al.*, 2007). In the following section, we attempt to figure out why such observation does not work in two concretions located in the Tasdremt deposit (►Figs. 7.27 and 7.28) and how important is the study of staircase shape spectra.

7.5.1 Material and methods

Two concretion samples of hollandite group minerals were examined in detail. Both concretions (16TAS26 and 16TAS29) were collected in the plateaus located on the

top of Tasdremt mine (►Fig. 7.28) and show the botryoidal habitus with concentric growth bands, which respectively constitute 13.9 and 13.7 millimeters thick sections (►Fig. 7.43). A 1 mm-thick slice of both polished samples (not embedded in resin) were previously sawed, in order to ensure their relative position when collecting grains. The crystallinity, purity and composition of the samples were determined XRD on aliquot samples. Finally, several grains were selected along both growth band sequences, initially in order to evaluate the growth rate of these Mn oxides. Ten grains were analyzed from concretion 16TAS26 (►Fig. 7.44a) and eleven from 16TAS29 (►Fig. 7.44b). The analytical procedure for $^{40}Ar/^{39}Ar$ measurements is the same than the one used in the Tasdremt, Tiranimine and Aoufour samples (see section 7.4.4.c).

These samples have been further analyzed with a field emission microprobe JEOL JXA-8530F in the department of Materiaalkunde (MTM) of the Katholiek Universiteit Leuven (KUL, Belgium) in order to quantify the chemical composition of major and minor elements of the hollandite group minerals (►Figs. 7.43a and b). Electron Probe Microanalysis (EPMA) measurements were performed every 200µm through the successive growth bands of each sample and collected with five spectrometers. The choice of the analyzed elements were based upon whole rock chemical analyses (►Tables 7.4, 7.5 and 7.6) and reported in ►Table 7.10.

7.5.2 Results

7.5.2.a Composition of Mn concretions

Whole rock analyses (►Tables 7.4, 7.5 and 7.6) have shown that major elements composing the 16TAS26 and 16TAS29 samples are Mn, Pb, Ba and K. As the sum of the chemical elements is not balanced to 100 wt. % of oxides (►Table 7.11), but in a range between 84-88 wt. %, we have evaluated that the remaining 12 to 16 wt. % could be attributed to the presence of other trace elements but mostly to water, as suggested in whole rock analyses with lost on ignition (LOI) of ~10 wt. % (►Table 7.4). The presence of water in the hollandite group minerals is a controversial issue as, formally, these minerals are anhydrous (Biagioni *et al.*, 2013). Only manjiroite ($NaMn_8O_{16}.nH_2O$) and mannardite ($Ba_xTi_{8-2x}V_{2x}O_{16}.2\text{-}xH_2O$) can include water molecules (Nambu and Tanida, 1967; Scott and Peatfield, 1986). However, some water has been detected in coronadite (Lindgren and Hillebrand, 1904; Post and Bish, 1989), cryptomelane (Richmond and Fleischer, 1942) and hollandite *s.s.* (Byström and Byström, 1950; Frondel *et al.*, 1960; Miura, 1986). As these oxides have a structure similar to zeolite, they should host minor amount of water in the tunnel, but this cannot discriminate between distinct species (Biagioni *et al.*, 2013).

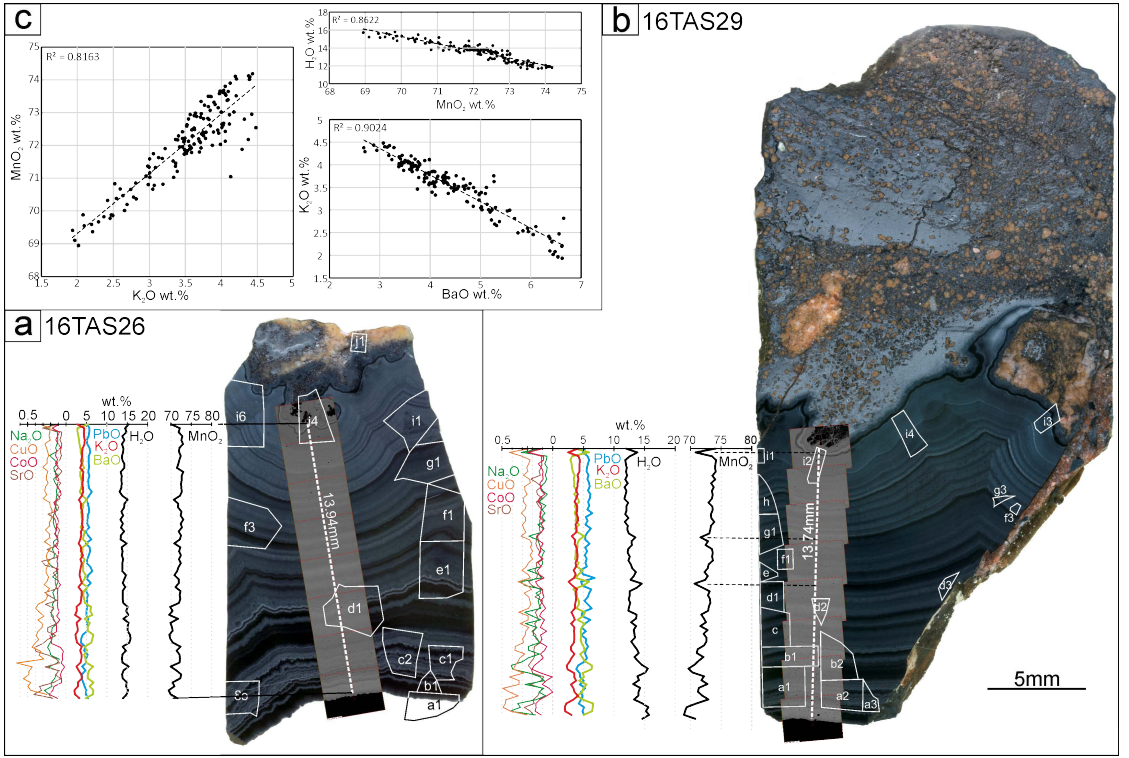

►**Fig. 7.43** Concretion samples of hollandite group minerals in the Tasdremt mine showing successive growth bands in hand specimen. Hollandite *s.s.* and coronadite growth bands of samples 16TAS26 (**a**) and 16TAS29 (**b**) and their chemical composition from the center to the outer rim by EPMA. White polyhedra are the location of samples analyzed for $^{40}Ar/^{39}Ar$ geochronology. White dotted lines are transect points, from which chemical measurements were taken every 200µm on a backscattered view background. The scale is given for both samples. **c.** Correlation diagrams of some elements showing positive or negative correlation trend lines.

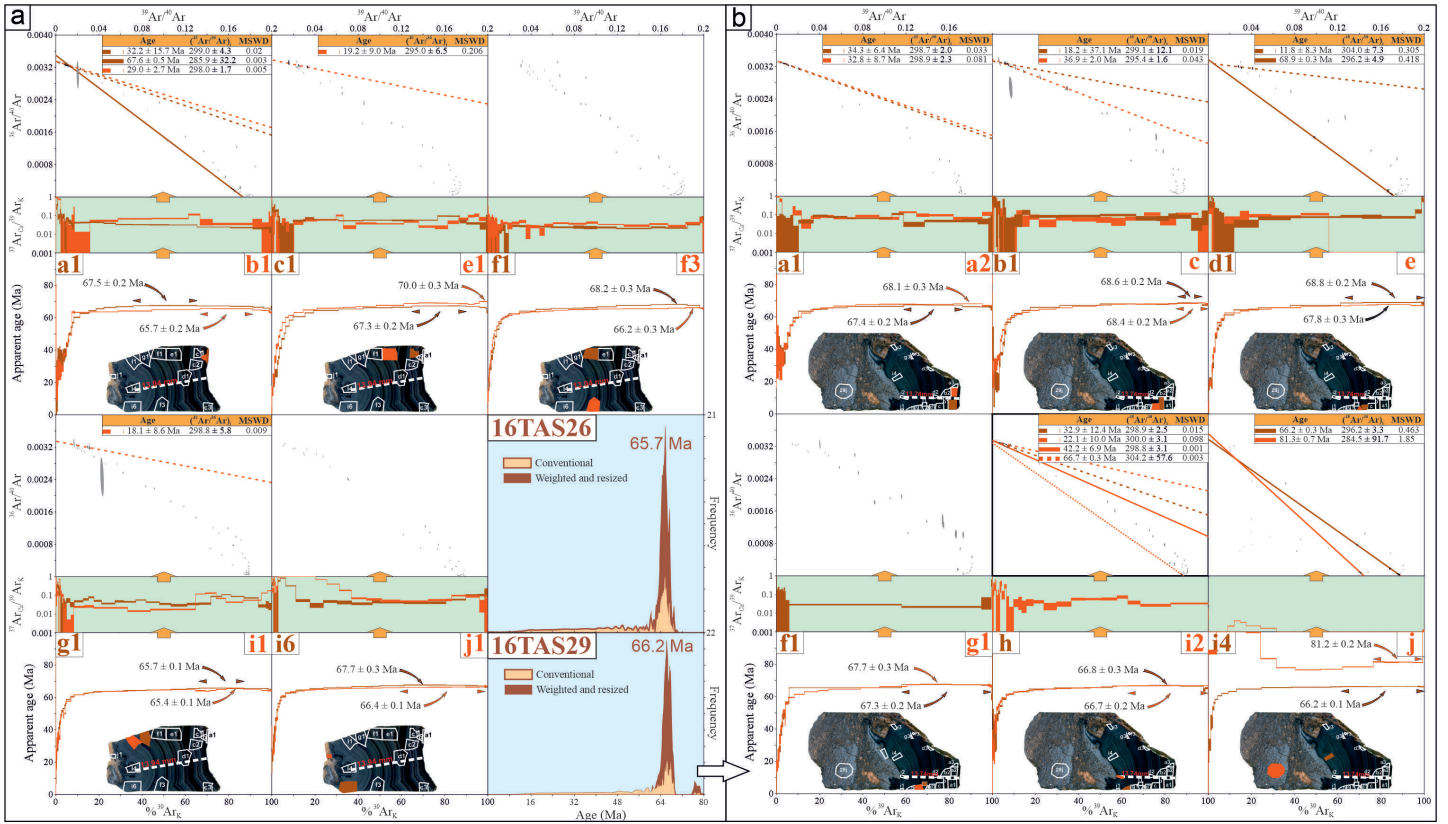

►**Fig. 7.44** Age distribution within the two concretions 16TAS26 (**a**) and 16TAS29 (**b**) in the Tasdremt deposit. Conventional and weighted ideograms are evidenced in blue for each sample.

The most striking evidence of EPMA analyses is that K_2O and BaO evolve reversely from the center to the outer rim of both concretions (►Figs. 7.43a and b). This chemical zonation is well-demonstrated by an anti-correlation between these elements (►Fig. 7.43c): BaO content increases progressively from the center to the border together with the amount of water (►Figs. 7.43a and b). On the other side, MnO_2 and K_2O are correlated (►Fig. 7.43c), showing increasing values toward the core of the growth bands. The behavior of PbO seems to follow K_2O content, without providing a clear correlation diagram of these elements. The composition of supergene solutions, in terms of minor elements (Cu, Co, Al, Si, Na, Sr, Mg and Ca), seems highly variable during the formation of Mn oxides (►Figs. 7.43a and b). Only CuO increases toward the center of the sample, reversely to BaO and water.

►**Table 7.10** Average composition of the hollandite group minerals concretions 16TAS26 and 16TAS29 (►Fig. 7.48) by EPMA analyses (n=143). All EPMA analyses are reported in supplementary material.

	Al_2O_3	SiO_2	BaO	Na_2O	MgO	CaO	K_2O	SrO	MnO_2	CoO	CuO	PbO	Total	H_2O
Minimum	0.04	0.00	2.68	0.07	0.00	0.04	1.93	0.05	68.94	0.00	0.18	3.58	84.20	11.68
Maximum	0.30	0.18	6.65	0.28	0.27	0.38	4.48	0.47	74.18	0.24	0.64	6.85	88.33	15.80
Average	0.08	0.08	4.45	0.15	0.06	0.15	3.51	0.17	72.06	0.11	0.29	5.26	86.37	13.63

7.5.2.b $^{40}Ar/^{39}Ar$ degassing patterns

All selected samples in both hand specimens display a similar pattern showing young ages in the low temperature steps, whereas mid to high temperature ranges display increasing ages without reaching a plateau or pseudo-plateau, forming the so-called staircase spectra (►Fig. 7.43). Sometimes, pseudo-plateau can be determined within the degassing pattern but they never represent more than 40% of the released $^{39}Ar_K$. This rather suggests mixing of age components centered on the second phase identified in the Tasdremt deposits at ~65-67 Ma, in which the initial stage at ~81-82 Ma has nearly totally been erased. Another method to visualize that $^{40}Ar/^{39}Ar$ data (as conventional plateau ages are lacking) is the use of weighted and resized ideograms, indicating clearly that, as a whole, samples 16TAS26 and 16TAS29 belong to the last phase of the primary ore formation and remobilization during late Cretaceous times at ~65.7 Ma and ~66.2, respectively (►Figs. 7.35 and 7.44).

Interestingly, inverse isochron diagrams ($^{36}Ar/^{40}Ar$ vs. $^{39}Ar_K/^{40}Ar^*$; Turner, 1971; Roddick *et al.*, 1980; Hanes *et al.*, 1985) could show younger ages, which are hidden in the low temperature steps of the degassing pattern. These ages belong to the Cenozoic period with $^{40}Ar/^{36}Ar$ intercept in good correlation with the atmospheric value (298.56 ± 0.104%) determined by Lee *et al.* (2006). These ages repeatedly cluster around 36.5 Ma and possibly to 10-20 Ma despite uncertainties are somewhat important enclosing several million years (2.0 to 15.7 Ma) and sometimes the age itself. True precipitation ages cannot be retrieved from such calculation but have interest showing that younger disruption of age spectra are likely in the Tasdremt

sector (►Fig. 7.35), whereas they are clearly identified as plateau ages in the Imini area (►Fig. 7.40). This strengthens the interpretation that Tasdremt ores have not well recorded such young ages and mineralization stage (Dekoninck *et al.*, submitted, this chapter). However, these young ages cannot explain the whole staircase shape of most of the samples by their own, supporting that older (Cretaceous) multicomponent ages are present in the whole concretion.

7.5.3 Can the destabilization of the K-Ar system infer a thermal origin of Mn oxides?

As no plateau and no gradation of the ages from the core to the outer rim of both concretions have been determined, no rate of Mn accumulation can be calculated. Such difficulties in interpreting these $^{40}Ar/^{39}Ar$ ages and additionally their distribution within a thin mineralizing sequence reproduced in two cogenetic samples question the process from which these minerals have precipitated (►Fig. 7.44). Zonation of ages within a colloform samples are commonly observed in **laterite profile** (e.g., Tambao; Hénocque *et al.*, 1998) and reveal that formation processes are radically different from those operating in the Tasdremt ores. For example, the Mn-rich weathering crust in the Tambao Mn deposit (Hénocque *et al.*, 1998) results from the *per descensum* weathering of a primary Mn-rich garnet protore owing to climatic conditions (Perseil and Grandin, 1978, 1985). The slow progression of meteoric fluids at ~20-25°C in a weathering profile usually accommodates successively the different growth bands with decreasing ages, these minerals remaining stable under these conditions without releasing their radiogenic argon through times. As such, observations cannot be implemented to the Tasdremt deposit, only pervasive water circulation at higher temperature than weathering conditions would be able to deeply destabilize or reset the K-Ar system by releasing some of the radiogenic argon (►Fig. 7.44). This finally provides younger apparent ages forming a diffusion curve (staircase spectra) generated by two (or more?) components, which have crystallized during, at least, two distinct periods. These observations strengthen the interpretation that Mn oxides in the Tasdremt (and Imini?) deposit(s) could have been modified or originated from slightly warmer conditions than those observed in laterite profile, their precise temperature being unclear but likely encompass supergene or low-temperature hydrothermal conditions as commonly reported in karst deposits (Varentsov, 1996).

The chemical composition of these growth bands also suggests that slightly higher temperatures could have operated after their precipitation, resulting in a reverse evolution of Ba and K, the Ba end-member of the hollandite group being more compatible with hydrothermal conditions (Post, 1999) than other end-members such as cryptomelane, commonly observed in weathering profiles (e.g., Ruffet *et al.*, 1996; Hénocque *et al.*, 1998; Li *et al.*, 2007; Gutzmer *et al.*, 2012; Bonnet *et al.*, 2014; De

Putter *et al.*, 2015; Vasconcelos and Carmo, 2018). Additionally, Pb-rich hollandite *s.l.* forming the coronadite end-member are also described in hydrothermal deposits (Hewett, 1971; Post, 1999; Glasby *et al.*, 2005). Another interesting point deals with the presence of barite, which is closely associated to the Imini deposit in the form of a thick vein (~5-10 meters) at the contact with Ordovician schists and the late Cretaceous succession (►Figs. 7.8 and 7.19b), as well as dispersed crystals within the Imini (►Figs. 7.21h and 7.25) and, to a lesser extent, the Tasdremt ores, barite being more compatible with hydrothermal settings, although it remains stable in the supergene environment (Hanor, 2000).

All this together allows low temperature solutions (hydrothermal?) to have reworked some of the Mn oxides. The main points are resumed by the following observations: (1) hollandite *s.l.* ages are disrupted by one or several thermal events; (2) barite is associated to the Imini deposit; (3) the presence of large amounts of hollandite *s.s.* and coronadite composing the ore instead of the more common cryptomelane in laterite *s.l.* could be of hydrothermal origin; and (4) the chemical composition of the ores contains chemical elements usually associated in hydrothermal Mn deposits (As, Cu, Mo, Pb, V and Zn). However, diffusion studies and modelling the degassing of the 40Ar/39Ar may address this issue. Further investigations on the stable isotope (i.e., strontium, oxygen and hydrogen) composition of barite and hollandite group minerals would also bring new elements to this topic. Such thermal effect is in good agreement with the geological settings because thermal doming has been suggested by low-temperature thermochronology with apatite fission track and (U-Th)/He dating during the late Cretaceous period (Leprêtre *et al.*, 2018). We could also infer that such conditions could have persisted during uplift and doming periods in the Atlas tectonic history, allowing shallow circulation of mineralizing fluids.

7.6 Synthetic metallogenic model of the Imini-Tasdremt Mn deposits

🔎The combination of a detailed structural background of the Imini and Tasdremt areas together with in-depth mineralogical, petrographical, geochemical and geochronological investigations of the Mn(-Pb-Ba) ores have allowed us to build up a well-constrained model in order to explain the formation and enrichment of the Imini-Tasdremt ores. The ores are composed of Mn oxides in the form of massive botryoidal hollandite group minerals (hollandite *s.s.* and coronadite) in the Tasdremt and Imini area, whereas pure pyrolusite extensively occurs in the Imini deposits only, forming the highest grade of Mn responsible for their high economic value. The metallogenic model highlights a multistage formation of the Mn oxides following the dissolution and the karstification of the host Cenomanian-Turonian dolostone, the

lower part of the Senonian series being epigenized in the Tasdremt area only. The formation of hollandite group minerals proceeds in two steps by (1) **the epigenesis of the host dolostone** and (2) **the formation of colloform Mn oxides in voids**. The geochemical composition of the ore and their close association to dissolution processes have defined a karst-hosted deposit.

The new set of K-Ar and ^{40}Ar-^{39}Ar dating on hollandite show that the first mineralization stage occurs in a narrow time window at the early Campanian (~81-82 Ma), clearly after the dolomitization and the karstification of the host carbonates. The Mn deposition is consistent with O_2-poor ground-water circulation originating from the exhumed Atlas bedrock to the north, altering basement rocks, feeding temporary aquifers and finally precipitating hollandite group minerals following the rapid rise in pH and Eh in the karstified dolostone. A second thermal (?) event at the Maastrichtian/Danian boundary (~65-67 Ma) has partially or totally reset the K-Ar system, remobilized the first ore stage and/or brought new mineralization. Such event explains scattered ages and staircase $^{40}Ar/^{39}Ar$ spectra between these two phases. Late Cretaceous ages are clearly evidenced in the Tasdremt area, whereas some discordant $^{40}Ar/^{39}Ar$ spectra cannot allow a clear identification of these early mineralization stages in the Imini area.

The different structural settings in the western part of the district (Tasdremt area), where only poor deformation and faulting are observed, limits the Mn remobilization and the subsequent mineralization during the Cenozoic era, whereas the Imini sector records the precipitation and/or remobilization of hollandite group minerals in two episodes dated at ~45-52 Ma and ~14-20 Ma. These events are particularly interesting as they corroborate the first and second pulses of the Atlas exhumation identified in the area (Leprêtre *et al.*, 2015b), those being connected to a Late Eocene tectonic uplift and the Early(?)-Middle Miocene doming, respectively. Another remarkable observation is that the young ages belong to the C1 and C2 levels (nearly absent in the Tasdremt area), whereas the late Cretaceous ages are reported within the C3 (Imini) and the laterally equivalent L2 (Tasdremt) orebodies. This together with the massive occurrence of pyrolusite in the C1 and C2 orebodies at Imini and given their absence in the Tasdremt area makes consistent that young ages are correlated to the formation of pyrolusite. In other words, the precipitation of hollandite group minerals and pyrolusite within the C1 and C2 levels is driven by the first and second steps of the Atlas building, probably because a gradient is created by the uplift/doming of the High Atlas, leaching the bedrock further north and precipitating Mn(-Pb-Ba) in the form of Mn oxides within the Cenomanian-Turonian carbonates. This process is similar to the mechanisms which have operated in the early mineralization stages, namely by increasing pH and Eh conditions given by the dissolved host dolostone. Structural settings such as the Imini fault, flexures of the host rock dolostone or the bevel end of Triassic basalts and terrigeneous sediments

above the Imini inlier are suitable traps for Mn mineralization delimiting a SW-NE orientation of the mineralization, which is, moreover, roughly parallel to the N70°E Atlasic direction.

The denudation of the Cenomanian-Turonian dolostone has probably been limited since their formation, at least until the main Pliocene-Quaternary tectonic uplift of the High Atlas, supporting that Mn oxide formation took place under a Cenozoic and late Cretaceous cover. This also questions the conditions under which these minerals have precipitated as some staircase spectra and multicomponent phases support temperatures slightly (?) higher than those commonly reported in laterite profiles, owing to a supergene formation of the Mn oxides although this issue still needs other critical data.

Prospects for future studies would also insist on the dolomitization processes operating before (and after ?) the main ore formation. Investigating the various generations of carbonates and the creation of a porosity will address some questions dealing with the position of the Mn orebodies within the Cenomanian-Turonian dolostones (and not in Cambrian dolostone levels for example), as well as their close relation with the mineralization processes. New techniques of dating carbonates would be helpful to constrain the timing of the different carbonates with the U-Pb methodology (see chapter 4). Tracing sources of the Mn and associated metals in the bedrock of foreign areas is an additional point that would bring insights to the formation process of the Imini-Tasdremt ores. Potential sources implies the Neoproterozoic volcanic rocks, the Triassic basalts, or older Precambrian Mn ores, among other various possibilities. Finaly, a special care should be taken into the dating of Fe oxides (i.e., goethite) by the (U-Th)/He method (see chapter 4), if so (see Michèle Verhaert thesis), to nuance or strengthen the interpretation based upon the K-Ar system.

7.7 References

Algouti, Ah, Algouti, Ab, Taj-Eddine, K., 1999. Le Sénonien du Haut Atlas occidental, Maroc: sédimentologie, analyse séquentielle et paléogéographie. J. Afr. Earth Sci. 29, 643–658. https://doi.org/10.1016/S0899-5362(99)00121-9

Ali, S., Stattegger, K., Liu, Z., Khélifi, N., Kuhnt, W., 2019. Paleoclimatic and paleoenvironmental reconstruction at Tarfaya Atlantic coastal basin (Morocco) based on clay mineral records from Upper Cretaceous to Quaternary. Arab. J. Geosci. 12. https://doi.org/10.1007/s12517-018-4156-4

Ambroggi, R., 1963. Etude géologique du versant méridional du haut atlas occidental et de la plaine du Souss. Notes Mém. Serv. Géologique Maroc 209–213.

Ayora, C., Taberner, C., Saaltink, M.W., Carrera, J., 1998. The genesis of dedolomites: a discusion based on reactive transport modeling. J. Hydrol. 209, 346–365. https://doi.org/10.1016/S0022-1694(98)00095-X

Babault, J., Teixell, A., Arboleya, M.L., Charroud, M., 2008. A Late Cenozoic age for long-wavelength surface uplift of the Atlas Mountains of Morocco. Terra Nova 20, 102–107. https://doi.org/10.1111/j.1365-3121.2008.00794.x

Balestrieri, M.L., Moratti, G., Bigazzi, G., Algouti, A., 2009. Neogene exhumation of the Marrakech High Atlas (Morocco) recorded by apatite fission-track analysis. Terra Nova 21, 75–82. https://doi.org/10.1111/j.1365-3121.2008.00857.x

Barbero, L., Jabaloy, A., Gómez-Ortiz, D., Pérez-Peña, J.V., Rodríguez-Peces, M.J., Tejero, R., Estupiñán, J., Azdimousa, A., Vázquez, M., Asebriy, L., 2011. Evidence for surface uplift of the Atlas Mountains and the surrounding peripheral plateaux: Combining apatite fission-track results and geomorphic indicators in the Western Moroccan Meseta (coastal Variscan Paleozoic basement). Tectonophysics, TOPO-EUROPE II - From Iberia to the Carpathians and analogues 502, 90–104. https://doi.org/10.1016/j.tecto.2010.01.005

Beauchamp, W., Allmendinger, R.W., Barazangi, M., Demnati, A., Alji, M.E., Dahmani, M., 1999. Inversion tectonics and the evolution of the High Atlas Mountains, Morocco, based on a geological-geophysical transect. Tectonics 18, 163–184. https://doi.org/10.1029/1998TC900015

Beaudoin, B., Lesavre, A., Pelissonnier, H., 1976. Action des eaux superficielles dans le gisement de manganese d'Imini (Maroc). Bull. Société Géologique Fr. 18, 95–100. https://doi.org/10.2113/gssgfbull.S7-XVIII.1.95

Beauvais, A., Ruffet, G., Hénocque, O., Colin, F., 2008. Chemical and physical erosion rhythms of the West African Cenozoic morphogenesis: The ^{39}Ar-^{40}Ar dating of supergene K-Mn oxides. J. Geophys. Res. 113. https://doi.org/10.1029/2008JF000996

Benammi, M., Arbi Toto, E., Chakiri, S., 2001. Les chevauchements frontaux du Haut Atlas central marocain : styles structuraux et taux de raccourcissement différentiel entre les versants nord et sud. Comptes Rendus Académie Sci. - Ser. IIA - Earth Planet. Sci. 333, 241–247. https://doi.org/10.1016/S1251-8050(01)01628-7

Bensalah, M.K., Youbi, N., Mata, J., Madeira, J., Martins, L., El Hachimi, H., Bertrand, H., Marzoli, A., Bellieni, G., Doblas, M., Font, E., Medina, F., Mahmoudi, A., Beraâouz, E.H., Miranda, R., Verati, C., De Min, A., Ben Abbou, M., Zayane, R., 2013. The Jurassic–Cretaceous basaltic magmatism of the Oued El-Abid syncline (High Atlas, Morocco): Physical volcanology, geochemistry and geodynamic implications. J. Afr. Earth Sci. 81, 60–81. https://doi.org/10.1016/j.jafrearsci.2013.01.004

Biagioni, C., Capalbo, C., Pasero, M., 2013. Nomenclature tunings in the hollandite supergroup. Eur. J. Mineral. 25, 85–90. https://doi.org/10.1127/0935-1221/2013/0025-2255

Blondel, F., 1937. La géologie et les mines des vieilles plateformes. Bull. Minéralogie 60, 147–148.

Bonnet, N.J., Beauvais, A., Arnaud, N., Chardon, D., Jayananda, M., 2014. First ^{40}Ar/^{39}Ar dating of intense Late Palaeogene lateritic weathering in Peninsular India. Earth Planet. Sci. Lett. 386, 126–137. https://doi.org/10.1016/j.epsl.2013.11.002

Bouabdellah, M., Slack, J.F. (Eds.), 2016. Mineral deposits of North Africa, Mineral Resource Reviews. Springer International Publishing, Cham. https://doi.org/10.1007/978-3-319-31733-5

Bouillin, J.P., 1986. Le bassin maghrebin; une ancienne limite entre l'Europe et l'Afrique a l'ouest des Alpes. Bull. Société Géologique Fr. II, 547–558. https://doi.org/10.2113/gssgfbull.II.4.547

Bouladon, J., 1948. Note sommaire sur Tiouine, Imini, Tasdremt (Microfiche No. 90). Centre National de Documentation, Rabat.

Bouladon, J., Jouravsky, G., 1953. Hollandite dans les gisements de manganèse du Maroc du Sud. Notes Mém. Serv. Géologique Maroc 7, 253–255.

Bouladon, J., Jouravsky, G., 1952. Géologie des gites minéraux marocains: Manganèse. Presented at the Congrès Géologique International, Alger, pp. 44–80.

Bouladon, J., Jouravsky, G., Colson, C., 1955. Les gisements de manganèse volcanogènes de Tiouine (Infracambrien du sud marocain) : étude pétrographique et métallogénique. Notes Mém. Serv. Géologique Maroc 8, 112.

Bouladon, J., Meune, M., 1951. le gisement de Tasdremt (Haut Sous) : Un gîte sédimentaire de manganèse plombifère dans le mésocrétacé. Notes Mém. Serv. Géologique Maroc 4, 221–250.

Bracène, R., Frizon de Lamotte, D., 2002. The origin of intraplate deformation in the Atlas system of western and central Algeria: from Jurassic rifting to Cenozoic–Quaternary inversion. Tectonophysics,

Paleostresses and Tectonics in the Peri-Tethyan Margins 357, 207–226. https://doi.org/10.1016/S0040-1951(02)00369-4

Brede, R., Hauptmann, M., Herbig, H.-G., 1992. Plate tectonics and intracratonic mountain ranges in Morocco - The mesozoic-cenozoic development of the Central High Atlas and the Middle Atlas. Geol. Rundsch. 81, 127–141. https://doi.org/10.1007/BF01764544

Brouard, E., 1992. Étude des cryptokarsts tertiaires de la Forêt de Bessède (Périgord, France) et de l'Entre Sambre et Meuse (Belgique) : lithologie, géochimie, néogenèse et évolution des systèmes karstiques (Unpublished Ph.D. thesis). Université Paris Sud, Orsay.

Brun, J.-P., Fort, X., 2011. Salt tectonics at passive margins: Geology versus models. Mar. Pet. Geol. 28, 1123–1145. https://doi.org/10.1016/j.marpetgeo.2011.03.004

Bruyère, D., 2004. Néogenèses silico-alumineuses en contexte cryptokarstique : l'halloysite de Beez (Namur, Belgique) et de Aïn Khamouda (Kasserine, Tunisie) (Unpublished Ph.D. thesis). Université Paris Sud, Orsay.

Byström, A., Byström, A.M., 1950. The crystal structure of hollandite, the related manganese oxide minerals, and α-MnO2. Acta Crystallogr. 3, 146–154. https://doi.org/10.1107/S0365110X5000032X

Cao, X., Yin, M., Wang, X., 2001. Elimination of the spectral interference from polyatomic ions with rare earth elements in inductively coupled plasma mass spectrometry by combining algebraic correction with chromatographic separation. Spectrochim. Acta Part B At. Spectrosc. 56, 431–441. https://doi.org/10.1016/S0584-8547(01)00170-7

Cavallina, C., Papini, M., Moratti, G., Benvenuti, M., 2018. The late Mesozoic evolution of the Central High Atlas domain (Morocco): Evidence from the paleo-drainage record of the Adrar Aglagal syncline. Sediment. Geol. 376, 1–17. https://doi.org/10.1016/j.sedgeo.2018.08.003

Charrière, A., 1996. Palaeogeographic and palaeotectonic framework of the Middle Atlasic Cretaceous basins (Morocco) according to recent stratigraphic data. Bull. Soc. Geol. Fr. 167, 617–626.

Charrière, A., Andreu, B., Ciszak, R., Kennedy, W.J., Rossi, A., Vila, J.-M., 1998. La transgression du Cénomanien supérieur dans la Haute Moulouya et le Moyen Atlas méridional, Maroc. Geobios 31, 551–569. https://doi.org/10.1016/S0016-6995(98)80043-0

Charrière, A., Dépêche, F., Feist, M., Grambast-Fessard, N., Jaffrezo, M., Peybernès, B., Ramalho, M., 1994. Microfaunes, microflores etpaléoenvironnements successifs dans la formation d'El Mers (Bathonien-?Callovien) du synclinal de Skoura (Moyen-Atlas, Maroc). Geobios 27, 157–174. https://doi.org/10.1016/S0016-6995(94)80002-2

Charrière, A., Haddoumi, H., Mojon, P.-O., 2005. Découverte de Jurassique supérieur et d'un niveau marin du Barrémien dans les « couches rouges » continentales du Haut Atlas central marocain : implications paléogéographiques et structurales. Comptes Rendus Palevol 4, 385–394. https://doi.org/10.1016/j.crpv.2005.04.009

Cheilletz, A., Ruffet, G., Marignac, C., Kolli, O., Gasquet, D., Féraud, G., Bouillin, J.P., 1999. $^{40}Ar/^{39}Ar$ dating of shear zones in the Variscan basement of Greater Kabylia (Algeria). Evidence of an Eo-Alpine event at 128 Ma (Hauterivian-Barremian boundary): Geodynamic consequences. Tectonophysics 306, 97–116. https://doi.org/10.1016/S0040-1951(99)00047-5

Choubert, G., 1970. Carte géologique de l'Anti-Atlas central et de la zone synclinale de Ouarzazate (1:200000). Notes et mémoires du Service géologique du Maroc.

Choubert, G., 1963. Histoire géologique du domaine de l'Anti-Atlas, in: Géologie Du Maroc. Rabat, pp. 75–194.

Choubert, G., 1957. Carte géologique du Maroc, 70, feuille de Marrakech. Notes et mémoires du Service géologique du Maroc.

Choubert, G., 1945. Note preliminaire sur le Pontien au Maroc; essai de synthese orogenique du Maroc atlasique. Notes Mém. Serv. Géologique Maroc 65.

Choubert, G., Faure-Muret, A., 1973. The Precambrian iron and manganese deposits of the Anti-Atlas, in: Genesis of Precambrian Iron and Manganese Deposits. Presented at the Unesco Earth Sciences Symposium, Kiev, pp. 115–124.

Choubert, G., Faure-Muret, A., 1962. Evolution du domaine atlasique marocain depuis les temps paléozoïques, in: Livre à la Mémoire du Professeur Paul Fallot, Mémoire Hors Série. Société Géologique de France, Paris, pp. 447–527.

Colin, F., Beauvais, A., Ruffet, G., Henocque, O., 2005. First $^{40}Ar/^{39}Ar$ geochronology of lateritic manganiferous pisolites: Implications for the Palaeogene history of a West African landscape. Earth Planet. Sci. Lett. 238, 172–188. https://doi.org/10.1016/j.epsl.2005.06.052

Dammer, D., McDougall, I., Chivas, A.R., 1999. Timing of weathering-induced alteration of manganese deposits in Western Australia; evidence from K/Ar and $^{40}Ar/^{39}Ar$ dating. Econ. Geol. 94, 87–108. https://doi.org/10.2113/gsecongeo.94.1.87

De Putter, T., André, L., Bernard, A., Dupuis, C., Jedwab, J., Nicaise, D., Perruchot, A., 2002. Trace element (Th, U, Pb, REE) behaviour in a cryptokarstic halloysite and kaolinite deposit from Southern Belgium: importance of "accessory" mineral formation for radioactive pollutant trapping. Appl. Geochem. 17, 1313–1328. https://doi.org/10.1016/S0883-2927(02)00022-7

De Putter, T., Ruffet, G., Submitted. Supergene manganese ore records 75 Myr-long Campanian to Pleistocene geodynamic evolution and weathering history of the Central African Great Lakes Region - tectonics drives, climate helps. Gondwana Res.

De Putter, T., Ruffet, G., Yans, J., Mees, F., 2015. The age of supergene manganese deposits in Katanga and its implications for the Neogene evolution of the African Great Lakes Region. Ore Geol. Rev. 71, 350–362. https://doi.org/10.1016/j.oregeorev.2015.06.015

de Villiers, J.E., 1983. The manganese deposits of Griqualand West, South Africa; some mineralogic aspects. Econ. Geol. 78, 1108–1118. https://doi.org/10.2113/gsecongeo.78.6.1108

Decrée, S., Deloule, É., Ruffet, G., Dewaele, S., Mees, F., Marignac, C., Yans, J., De Putter, T., 2010a. Geodynamic and climate controls in the formation of Mio–Pliocene world-class oxidized cobalt and manganese ores in the Katanga province, DR Congo. Miner. Deposita 45, 621–629. https://doi.org/10.1007/s00126-010-0305-8

Decrée, S., Ruffet, G., Putter, T.D., Baele, J.-M., Recourt, P., Jamoussi, F., Yans, J., 2010b. Mn oxides as efficient traps for metal pollutants in a polyphase low-temperature Pliocene environment: A case study in the Tamra iron mine, Nefza mining district, Tunisia. J. Afr. Earth Sci. 57, 249–261. https://doi.org/10.1016/j.jafrearsci.2009.08.005

Dekoninck, A., Bernard, A., Barbarand, J., Saint-Bezar, B., Missenard, Y., Lepretre, R., Saddiqi, O., Yans, J., 2016a. Detailed mineralogy and petrology of manganese oxyhydroxide deposits of the Imini district (Morocco). Miner. Deposita 51, 13–23. https://doi.org/10.1007/s00126-015-0590-3

Dekoninck, A., Leprêtre, R., Saddiqi, O., Barbarand, J., Yans, J., 2016b. The high-grade Imini manganese district—karst-hosted deposits of mn oxides and oxyhydroxides, in: Bouabdellah, M., Slack, J.F. (Eds.), Mineral Deposits of North Africa. Springer International Publishing, Cham, pp. 575–594.

Dekoninck, A., Moussi, B., Vennemann, T., Jamoussi, F., Mattielli, N., Decrée, S., Chaftar, H.-R., Hatira, N., Yans, J., 2018. Mixed hydrothermal and meteoric fluids evidenced by unusual H- and O-isotope compositions of kaolinite-halloysite in the Fe(-Mn) Tamra deposit (Nefza district, NW Tunisia). Appl. Clay Sci. 163, 33–45. https://doi.org/10.1016/j.clay.2018.07.007

Delvaux, D., Sperner, B., 2003. New aspects of tectonic stress inversion with reference to the TENSOR program. Geol. Soc. Lond. Spec. Publ. 212, 75–100. https://doi.org/10.1144/GSL.SP.2003.212.01.06

Deng, X., Li, J., 2013. 40Ar/39Ar dating of cryptomelane from the Baye manganese deposit, SW Yunnan, China: Implications for growth rate of supergene Mn-oxide veins. Sci. China Earth Sci. 56, 1654–1663. https://doi.org/10.1007/s11430-013-4591-8

Dewaide, L., Baele, J.-M., Collon-Drouaillet, P., Quinif, Y., Rochez, G., Vandycke, S., Hallet, V., 2014. Karstification in dolomitized Waulsortian mudmounds (Belgium). Geol. Belg. 17, 43–51.

Dewey, J.F., Helman, M.L., Knott, S.D., Turco, E., Hutton, D.H.W., 1989. Kinematics of the western Mediterranean. Geol. Soc. Lond. Spec. Publ. 45, 265–283. https://doi.org/10.1144/GSL.SP.1989.045.01.15

Dresch, J., 1941. Recherches sur l'évolution du relief dans le Massif central du Grand Atlas, le Haouz et le Sous (Unpublished Ph.D. thesis). Tours.

El Arabi, E.H., 2007. La série permienne et triasique du rift haut-atlasique: nouvelles datations; évolution tectono-sédimentaire (Unpublished Ph.D. thesis). Université Hassan II, Casablanca.

El Arabi, E.H., 1988. Le '"Permo-Trias"' du flanc sud du Haut Atlas de Marrakech. Sédimentologie, cartographie et paléogéographie (Unpublished Ph.D. thesis). Université Joseph Fourrier, Grenoble.

El Arabi, E.H., Ferrandini, J., Essamoud, R., 2003. Triassic stratigraphy and structural evolution of a rift basin: the Eç Çour basin, High atlas of Marrakech, Morocco. J. Afr. Earth Sci. 36, 29–39. https://doi.org/10.1016/S0899-5362(03)00020-4

El Arabi, E.H., Hafid, M., Ferrandini, J., Essamoud, R., 2006. Interprétation de la série syn-rift haut-atlasique en termes de séquences tectonostratigraphiques, transversale de Telouet, Haut Atlas (Maroc). Notes Mém Serv Géol Maroc 541, 93–101.

El Euchi, H., 1993. La Tunisie du Centre-Ouest de l'Aptien à l'actuel : Tectonique coulissante, dynamique sédimentaire associée et évolution du champ de contraintes Moi-Plio-Quaternaire (Unpublished Ph.D. thesis). University of Tunis, Tunis.

El Harfi, A., Lang, J., Salomon, J., Chellai, E., 2001. Cenozoic sedimentary dynamics of the Ouarzazate foreland basin (Central High Atlas Mountains, Morocco). Int. J. Earth Sci. 90, 393–411. https://doi.org/10.1007/s005310000115

Ennih, N., Laduron, D., Greiling, R.O., Errami, E., de Wall, H., Boutaleb, M., 2001. Superposition de la tectonique éburnéenne et panafricaine dans les granitoïdes de la bordure nord du craton ouest africain, boutonniére de Zenaga, Anti-Atlas central, Maroc. J. Afr. Earth Sci. 32, 677–693. https://doi.org/10.1016/S0899-5362(02)00048-9

Ennih, N., Liégeois, J.-P., 2001. The Moroccan Anti-Atlas: the West African craton passive margin with limited Pan-African activity. Implications for the northern limit of the craton. Precambrian Res. 112, 289–302. https://doi.org/10.1016/S0301-9268(01)00195-4

Ensslin, R., 1992. Cretaceous synsedimentary tectonics in the Atlas system of Central Morocco. Geol. Rundsch. 81, 91–104. https://doi.org/10.1007/BF01764542

Errarhaoui, K., 1998. Structure du Haut Atlas: plis et chevauchements du socle et de couverture (interprétations des données géophysiques et géologiques) (Unpublished Ph.D. thesis). Université Paris Sud, Orsay.

Ettachfini, E.M., Souhel, A., Andreu, B., Caron, M., 2005. The Cenomanian-Turonian boundary in the Central High Atlas, Morocco. Geobios 38, 57–68. https://doi.org/10.1016/j.geobios.2003.07.003

Faure-Muret, A., Choubert, G., 1971. Le Maroc. Domaine rifain et atlasique. Tecton. Afr. 17–46.

Fleet, A.J., 1983. Hydrothermal and Hydrogenous Ferro-Manganese Deposits: Do They form a Continuum? The Rare Earth Element Evidence, in: Rona, P.A., Boström, K., Laubier, L., Smith, K.L. (Eds.), Hydrothermal Processes at Seafloor Spreading Centers. Springer US, Boston, MA, pp. 535–555. https://doi.org/10.1007/978-1-4899-0402-7_23

Force, E.R., Back, W., Spiker, E.C., Knauth, L.P., 1986. A ground-water mixing model for the origin of the Imini manganese deposit (Cretaceous) of Morocco. Econ. Geol. 81, 65–79. https://doi.org/10.2113/gsecongeo.81.1.65

Frizon de Lamotte, D., Leturmy, P., Missenard, Y., Khomsi, S., Ruiz, G., Saddiqi, O., Guillocheau, F., Michard, A., 2009. Mesozoic and Cenozoic vertical movements in the Atlas system (Algeria, Morocco, Tunisia): An overview. Tectonophysics 475, 9–28. https://doi.org/10.1016/j.tecto.2008.10.024

Frizon de Lamotte, D., Saint Bezar, B., Bracène, R., Mercier, E., 2000a. The two main steps of the Atlas building and geodynamics of the western Mediterranean. Tectonics 19, 740–761. https://doi.org/10.1029/2000TC900003

Frizon de Lamotte, D., Saint Bezar, B., Bracène, R., Mercier, E., 2000b. The two main steps of the Atlas building and geodynamics of the western Mediterranean. Tectonics 19, 740–761. https://doi.org/10.1029/2000TC900003

Frizon de Lamotte, D., Zizi, M., Missenard, Y., Hafid, M., Azzouzi, M.E., Maury, R.C., Charrière, A., Taki, Z., Benammi, M., Michard, A., 2008. The Atlas System, in: Michard, André, Saddiqi, O., Chalouan, A., Lamotte, D.F. de (Eds.), Continental Evolution: The Geology of Morocco. Springer Berlin Heidelberg, Berlin, Heidelberg, pp. 133–202. https://doi.org/10.1007/978-3-540-77076-3_4

Froitzheim, N., 1984. Late Cretaceous vertical tectonics in the High Atlas SW of Marrakech/Morocco - Reconstruction of tectonic movements in an early stage of the High Atlas orogenesis. Neues Jahrb. Für Geol. Paläontol.-Monatshefte 463–471.

Froitzheim, N., Stets, J., Wurster, P., 1988. Aspects of Western High Atlas tectonics, in: Jacobshagen, V.H. (Ed.), The Atlas System of Morocco. Springer-Verlag, Berlin/Heidelberg, pp. 219–244. https://doi.org/10.1007/BFb0011595

Frondel, C., Marvin, U.B., Ito, J., 1960. New data on birnessite and hollandite. Am. Mineral. 45, 871–875.

Fullea, J., Fernàndez, M., Afonso, J.C., Vergés, J., Zeyen, H., 2010. The structure and evolution of the lithosphere–asthenosphere boundary beneath the Atlantic–Mediterranean Transition Region. Lithos 120, 74–95. https://doi.org/10.1016/j.lithos.2010.03.003

Fullea, J., Fernàndez, M., Zeyen, H., Vergés, J., 2007. A rapid method to map the crustal and lithospheric thickness using elevation, geoid anomaly and thermal analysis. Application to the Gibraltar Arc System, Atlas Mountains and adjacent zones. Tectonophysics 430, 97–117. https://doi.org/10.1016/j.tecto.2006.11.003

Gasquet, D., Ennih, N., Liégeois, J.-P., Soulaimani, A., Michard, A., 2008. The Pan-African Belt, in: Michard, André, Saddiqi, O., Chalouan, A., Lamotte, D.F. de (Eds.), Continental Evolution: The Geology of Morocco. Springer Berlin Heidelberg, Berlin, Heidelberg, pp. 33–64.

Gasquet, D., Levresse, G., Cheilletz, A., Azizi-Samir, M.R., Mouttaqi, A., 2005. Contribution to a geodynamic reconstruction of the Anti-Atlas (Morocco) during Pan-African times with the emphasis on inversion tectonics and metallogenic activity at the Precambrian–Cambrian transition. Precambrian Res. 140, 157–182. https://doi.org/10.1016/j.precamres.2005.06.009

Gaudefroy, C., Bouladon, J., Permingeat, F., 1965. Une chlorite magnésienne (corundophyllite) du gîte de manganèse de Tachgagalt (Anti-Atlas) et sa signification génétique. Notes Mém. Serv. Géologique Maroc 24, 95–98.

Gaudefroy, G., 1960. Caractères distinctifs de la pyrolusite - ex manganite (application au minerai de l'Imini). Notes Serv. Géologique Maroc. 19, 77–86.

Gauthier, H., 1957. Contribution A l'étude géologique des formations post-liasiques des bassin du Dadès et du Haut-Todra (Maroc méridional). Notes Mém. Serv. Géologique Maroc 119, 1–212.

Gebert, H., 1989. Schichtgebundene Manganlagerstätten. F. Enke, Stuttgart.

Ghandriche, H., 1991. Modalités de la superposition de structures de plissementchevauchement d'âge alpin dans les Aurès (Algérie) (Unpublished Ph.D. thesis). Université Paris Sud, Orsay.

Glasby, G.P., Papavassiliou, C.T., Mitsis, J., Valsami-Jones, E., Liakopoulos, A., Renner, R.M., 2005. The Vani manganese deposit, Milos island, Greece: A fossil stratabound Mn−Ba−Pb−Zn−As−Sb−W-rich hydrothermal deposit, in: Developments in Volcanology. Elsevier, pp. 255–291. https://doi.org/10.1016/S1871-644X(05)80045-2

Görler, K., Helmdach, F.-F., Gaemers, P., Heissig, K., Hinsch, W., Mädler, K., Schwarzhans, W., Zucht, M., 1988. The uplift of the central High Atlas as deduced from Neogene continental sediments of the Ouarzazate province, Morocco. Atlas Syst. Moroc. 15, 361–404.

Gouiza, M., Charton, R., Bertotti, G., Andriessen, P., Storms, J.E.A., 2017. Post-Variscan evolution of the Anti-Atlas belt of Morocco constrained from low-temperature geochronology. Int. J. Earth Sci. 106, 593–616. https://doi.org/10.1007/s00531-016-1325-0

Guibas, L., Stolfi, J., 1985. Primitives for the manipulation of general subdivisions and the computation of Voronoi. ACM Trans Graph 4, 74–123. https://doi.org/10.1145/282918.282923

Gutzmer, J., Beukes, N.J., 1997. Mineralogy and mineral chemistry of oxide-facies manganese ores of the Postmasburg Manganese Field, South Africa. Mineral. Mag. 61, 213–231. https://doi.org/10.1180/minmag.1997.061.405.05

Gutzmer, J., Beukes, N.J., Rhalmi, M., Mukhopadhyay, J., 2006. Cretaceous karstic cave-fill manganese-lead-barium deposits of Imini, Morocco. Econ. Geol. 101, 385–405. https://doi.org/10.2113/gsecongeo.101.2.385

Gutzmer, J., Du Plooy, A.P., Beukes, N.J., 2012. Timing of supergene enrichment of low-grade sedimentary manganese ores in the Kalahari Manganese Field, South Africa. Ore Geol. Rev. 47, 136–153. https://doi.org/10.1016/j.oregeorev.2012.04.003

Haddoumi, H., Charrière, A., Andreu, B., Mojon, P.-O., 2008. Les dépôts continentaux du Jurassique moyen au Crétacé inférieur dans le Haut-Atlas oriental (Maroc): Paléoenvironnements successifs et signification paléogéographique, Notebooks on geology. ed, Carnets de géologie. Brest.

Haddoumi, H., Charrière, A., Mojon, P.-O., 2010. Stratigraphie et sédimentologie des "Couches rouges" continentales du Jurassique-Crétacé du Haut Atlas central (Maroc) : implications paléogéographiques et géodynamiques. Geobios 43, 433–451. https://doi.org/10.1016/j.geobios.2010.01.001

Hafid, M., Zizi, M., Bally, A.W., Ait Salem, A., 2006. Structural styles of the western onshore and offshore termination of the High Atlas, Morocco. Comptes Rendus Geosci., Quelques développements récents sur la géodynamique du Maghreb 338, 50–64. https://doi.org/10.1016/j.crte.2005.10.007

Hanes, J.A., York, D., Hall, C.M., 1985. An $^{40}Ar/^{39}Ar$ geochronological and electron microprobe investigation of an Archaean pyroxenite and its bearing on ancient atmospheric compositions. Can. J. Earth Sci. 22, 947–958. https://doi.org/10.1139/e85-100

Hanor, J.S., 2000. Barite-celestine geochemistry and environments of formation. Rev. Mineral. Geochem. 40, 193–275. https://doi.org/10.2138/rmg.2000.40.4

Hautmann, S., Lippolt, H.J., 2000. $^{40}Ar/^{39}Ar$ dating of central European K–Mn oxides — a chronological framework of supergene alteration processes during the Neogene. Chem. Geol. 170, 37–80. https://doi.org/10.1016/S0009-2541(99)00241-7

Hein, J.R., Koschinsky, A., Bau, M., Manheim, F.T., Kang, J.-K., Roberts, L., 2000. Cobalt-rich ferromanganese crusts in the Pacific, in: Handbook of Marine Minerals Deposits. CRC Press LLC, Boca Raton, pp. 239–279.

Hein, J.R., Koschinsky, A., Halbach, P., Manheim, F.T., Bau, M., Kang, J.-K., Lubick, N., 1997. Iron and manganese oxide mineralization in the Pacific. Geol. Soc. Lond. Spec. Publ. 119, 123–138. https://doi.org/10.1144/GSL.SP.1997.119.01.09

Helmdach, F.-F., 1988. The ostracode fauna of the Ait Kandoula region, systematic description, in: Jacobshagen, V.H. (Ed.), The Atlas System of Morocco: studies on its geodynamic evolution, Lecture Notes in Earth Sciences. Springer Berlin Heidelberg, Berlin, Heidelberg, pp. 405–432. https://doi.org/10.1007/BFb0011602

Hem, J.D., 1963. Chemical equilibria and rates of manganese oxidation, United States Government Printing Office. ed, Geological Survey Water-Supply Paper. Washigton DC.

Hénocque, O., Ruffet, G., Colin, F., Féraud, G., 1998. $^{40}Ar/^{39}Ar$ dating of West African lateritic cryptomelanes. Geochim. Cosmochim. Acta 62, 2739–2756. https://doi.org/10.1016/S0016-7037(98)00185-9

Herbig, H.-G., 1988. Synsedimentary tectonics in the Northern Middle Atlas (Morocco) during the late Cretaceous and Tertiary, in: Jacobshagen, V.H. (Ed.), The Atlas System of Morocco: Studies on Its Geodynamic Evolution, Lecture Notes in Earth Sciences. Springer Berlin Heidelberg, Berlin, Heidelberg, pp. 321–337. https://doi.org/10.1007/BFb0011599

Hewett, D.F., 1971. Coronadite; modes of occurrence and origin. Econ. Geol. 66, 164–177. https://doi.org/10.2113/gsecongeo.66.1.164

Hill, T.P., Werner, M.A., Horton, M.J., 1967. Chemical composition of sedimentary rocks in Colorado, Kansas, Montana, Nebraska, North Dakota, South Dakota, and Wyoming, United States Géological Survey.

Hollard, H., 1985. Carte géologique du Maroc, 260. Notes et mémoires du Service géologique du Maroc.

Jabour, H., Dakki, M., Nahim, M., Charrat, F., El Alji, M., Hssain, M., Oumalch, F., El Abibi, R., 2004. The Jurassic depositional system of Morocco, geology and play concepts. MAPG Mém. 1, 5–39.

Jacobshagen, V., Brede, R., Hauptmann, M., Heinitz, W., Zylka, R., 1988. Structure and post-Palaeozoic evolution of the central High Atlas, in: Jacobshagen, V.H. (Ed.), The Atlas system of Morocco: studies on its geodynamic evolution, Lecture Notes in Earth Sciences. Springer Berlin Heidelberg, Berlin, Heidelberg, pp. 245–271. https://doi.org/10.1007/BFb0011596

Jiménez-Munt, I., Fernàndez, M., Vergés, J., Garcia-Castellanos, D., Fullea, J., Pérez-Gussinyé, M., Afonso, J.C., 2011. Decoupled crust-mantle accommodation of Africa-Eurasia convergence in the NW Moroccan margin. J. Geophys. Res. 116. https://doi.org/10.1029/2010JB008105

Jouravsky, G., 1963. Filons de manganèse dans les formations volcaniques du Précambrien III de l'Anti-Atlas. Etude métallogénique. Notes Mém. Serv. Géologique Maroc 22, 81–92.

Jouravsky, G., 1958. Quelques observations nouvelles sur des gîtes de manganèse du Maroc. Mines Géologie Energ. 48.

Jouravsky, G., Pouit, G., 1963. Filons et couches de manganèse dans la région d'El-Borj (Anti-Atlas). Notes Mém. Serv. Géologique Maroc 22, 93–98.

Kaislaniemi, L., Hunen, J. van, 2014. Dynamics of lithospheric thinning and mantle melting by edge-driven convection: Application to Moroccan Atlas mountains. Geochem. Geophys. Geosystems 15, 3175–3189. https://doi.org/10.1002/2014GC005414

Khomsi, S., Bédir, M., Soussi, M., Ben Jemia, M.G., Ben Ismail-Lattrache, K., 2006. Mise en évidence en subsurface d'événements compressifs Éocène moyen–supérieur en Tunisie orientale (Sahel) : généralité de la phase atlasique en Afrique du Nord. Comptes Rendus Geosci., Quelques développements récents sur la géodynamique du Maghreb 338, 41–49. https://doi.org/10.1016/j.crte.2005.11.001

Kuleshov, V., 2016. Isotope geochemistry: the origin and formation of manganese rocks and ores. Elsevier, Amsterdam Boston Heidelberg London New York Oxford Paris San Diego San Francisco Singapore Sydney Tokyo.

Laffitte, R., 1939. Etudes géologique de l'Aurès. Bull. Serv. Carte Géologique Algér. 15.

Lafforgue, L., 2016. Place de la minéralisation de manganèse de Bouarfa dans l'évolution méso-cénozoique de l'oriental marocain (PhD). Université Paris Sud, Paris.

Lafforgue, L., Barbarand, J., Missenard, Y., Brigaud, B., Saint-Bezar, B., Dekoninck, A., Yans, J., 2015. Origin of the Bouarfa Manganese ore deposit (Eastern High Atlas, Morocco): insights from petrography and geochemistry of the mineralization. Presented at the 13th SGA Biennial Meeting, Nancy.

Lalaoui, M.D., 1987. Étude sédimentologique et métallogénique du gisement manganésifère de l'Imini (PhD). Marrakech, Marrakech.

Lalaoui, M.D., Beauchamp, J., Sagon, J.-P., 1991. Le gisement de manganèse de l'Imini (Maroc) : un dépôt sur la ligne de rivage. Chron. Rech. Minière 23–36.

Laville, E., 1975. Tectonique et microtectonique d'une partie du versant sud du Haut-Atlas marocain (Boutonnière de Skoura, Nappe de Toundout) (Unpublished Ph.D. thesis). Université de Montpellier, Montpellier.

Laville, E., Lesage, J.-L., Seguret, M., 1977. Geometrie, cinematique (dynamique) de la tectonique atlasique sur le versant sud du Haut Atlas marocain; apercu sur les tectoniques hercyniennes et tardi-hercyniennes. Bull. Société Géologique Fr. S7-XIX, 527–539. https://doi.org/10.2113/gssgfbull.S7-XIX.3.527

Laville, E., Piqué, A., 1992. Jurassic penetrative deformation and Cenozoic uplift in the Central High Atlas (Morocco): A tectonic model. structural and orogenic inversions. Geol. Rundsch. 81, 157–170. https://doi.org/10.1007/BF01764546

Laville, E., Pique, A., Amrhar, M., Charroud, M., 2004. A restatement of the Mesozoic Atlasic Rifting (Morocco). J. Afr. Earth Sci. 38, 145–153. https://doi.org/10.1016/j.jafrearsci.2003.12.003

Lawson, C.L., 1977. Software for C1 Surface Interpolation, in: Rice, J.R. (Ed.), Mathematical Software. Academic Press, pp. 161–194. https://doi.org/10.1016/B978-0-12-587260-7.50011-X

Laznicka, P., 2014. Giant metallic deposits—A century of progress. Ore Geol. Rev. 62, 259–314. https://doi.org/10.1016/j.oregeorev.2014.03.002

Laznicka, P., 1992. Manganese deposits in the global lithogenetic system: Quantitative approach. Ore Geol. Rev. 7, 279–356. https://doi.org/10.1016/0169-1368(92)90013-B

Le Roy, P., Piqué, A., Le Gall, B., Aït Brahim, L., Morabet, A.M., Demnati, A., 1997. The Triassic-Liassic basins of western Morocco and the diachronous intracontinental Central Atlantic rifting. Bull. Soc. Geol. Fr. 168, 637–648.

Lee, D.T., Schachter, B.J., 1980. Two algorithms for constructing a Delaunay triangulation. Int. J. Comput. Inf. Sci. 9, 219–242. https://doi.org/10.1007/BF00977785

Lee, J.-Y., Marti, K., Severinghaus, J.P., Kawamura, K., Yoo, H.-S., Lee, J.B., Kim, J.S., 2006. A redetermination of the isotopic abundances of atmospheric Ar. Geochim. Cosmochim. Acta 70, 4507–4512. https://doi.org/10.1016/j.gca.2006.06.1563

Leprêtre, R., Missenard, Y., Barbarand, J., Gautheron, C., Jouvie, I., Saddiqi, O., 2018. Polyphased inversions of an intracontinental rift: case study of the Marrakech High Atlas, Morocco. Tectonics 37, 818–841. https://doi.org/10.1002/2017TC004693

Leprêtre, R., Missenard, Y., Barbarand, J., Gautheron, C., Saddiqi, O., Pinna-Jamme, R., 2015a. Postrift history of the eastern central Atlantic passive margin: Insights from the Saharan region of South Morocco: Postrift Evolution Moroccan Margin. J. Geophys. Res. Solid Earth 120, 4645–4666. https://doi.org/10.1002/2014JB011549

Leprêtre, R., Missenard, Y., Saint-Bezar, B., Barbarand, J., Delpech, G., Yans, J., Dekoninck, A., Saddiqi, O., 2015b. The three main steps of the Marrakech High Atlas building in Morocco: Structural evidences from the southern foreland, Imini area. J. Afr. Earth Sci. 109, 177–194. https://doi.org/10.1016/j.jafrearsci.2015.05.013

Lesavre, A., 1975. Le gisement de manganèse d'Imini (Maroc) (PhD). Pierre-et-Marie-Curie, Paris.

Li, J.-W., Vasconcelos, P., 2002. Cenozoic continental weathering and its implications for the palaeoclimate: evidence from $^{40}Ar/^{39}Ar$ geochronology of supergene K–Mn oxides in Mt Tabor, central Queensland, Australia. Earth Planet. Sci. Lett. 200, 223–239. https://doi.org/10.1016/S0012-821X(02)00594-0

Li, J.-W., Vasconcelos, P., Zhang, W., Deng, X.-D., Duzgoren-Aydin, N., Yan, D.-R., Zhang, J.-Q., Hu, M.-A., 2007. Timing and duration of supergene mineralization at the Xinrong manganese deposit, western Guangdong Province, South China: cryptomelane $^{40}Ar/^{39}Ar$ dating. Miner. Deposita 42, 361–383. https://doi.org/10.1007/s00126-006-0118-y

Lindgren, W., 1933. Mineral deposits, 4th ed. McGraw-Hill Book Company, Incorporated, York.

Lindgren, W., Hillebrand, W.F., 1904. Minerals from the Clifton-Morenci District, Arizona. Am. J. Sci. s4-18, 448–460. https://doi.org/10.2475/ajs.s4-18.108.448

Lippolt, H.J., Hautmann, S., 1995. $^{40}Ar/^{39}Ar$ ages of Precambrian manganese ore minerals from Sweden, India and Morocco. Miner. Deposita 30, 246–256. https://doi.org/10.1007/BF00196360

Martin, J., 1982. Le Moyen Atlas Central, étude géomorphologique. Notes Mém. Serv. Géologique Maroc 258, 445.

Marzoli, A., Bertrand, H., Knight, K.B., Cirilli, S., Buratti, N., Vérati, C., Nomade, S., Renne, P.R., Youbi, N., Martini, R., Allenbach, K., Neuwerth, R., Rapaille, C., Zaninetti, L., Bellieni, G., 2004. Synchrony of the Central Atlantic magmatic province and the Triassic-Jurassic boundary climatic and biotic crisis. Geology 32, 973–976. https://doi.org/10.1130/G20652.1

Mattauer, M., Tapponnier, P., Proust, F., 1977. Sur les mecanismes de formation des chaines intracontinentales; l'exemple des chaines atlasiques du Maroc. Bull. Société Géologique Fr. S7-XIX, 521–526. https://doi.org/10.2113/gssgfbull.S7-XIX.3.521

Maynard, J.B., 2014. Manganiferous sediments, rocks, and ores, in: Treatise on Geochemistry. Elsevier, pp. 327–349.

Maynard, J.B., 2010. The chemistry of manganese ores through time: a signal of increasing diversity of earth-surface environments. Econ. Geol. 105, 535–552. https://doi.org/10.2113/gsecongeo.105.3.535

McLennan, S.M., 2001. Relationships between the trace element composition of sedimentary rocks and upper continental crust. Geochem. Geophys. Geosystems 2, 24. https://doi.org/10.1029/2000GC000109

Medina, F., 1991. Superimposed extensional tectonics in the Argana Triassic formations (Morocco), related to the early rifting of the Central Atlantic. Geol. Mag. 128, 525–536. https://doi.org/10.1017/S0016756800018665

Meisser, N., Perseil, E.-A., Brugger, J., Chiappero, P.-J., 1999. Strontiomelane, $SrMn^{4+}{}_6Mn^{3+}$, a new mineral of the cryptomelane group from St. Marcel-Praborna, Aosta Valley, Italy. Can. Mineral. 37, 673–678.

Mekireche, K., Sabaou, N., Zazoun, R.-S., 1998. Critical factors in the exploration of an Atlas intramontane basin; the Western Hodna Basin of northern Algeria. Geol. Soc. Lond. Spec. Publ. 132, 423–432. https://doi.org/10.1144/GSL.SP.1998.132.01.24

Mercier, E., Outtani, F., De Lamotte, D.F., 1997. Late-stage evolution of fault-propagation folds: principles and example. J. Struct. Geol. 19, 185–193. https://doi.org/10.1016/S0191-8141(96)00081-8

Michard, A., Saddiqi, O., Chalouan, A., Lamotte de Lamotte, F. (Eds.), 2008. Continental evolution: The geology of Morocco: structure, stratigraphy, and tectonics of the Africa-Atlantic-Mediterranean triple junction, Lecture Notes in Earth Sciences. Springer-Verlag, Berlin Heidelberg.

Michard, A., Saddiqi, O., Missenard, Y., Oukassou, M., Barbarand, J., 2017. Les grandes régions géologiques du Maroc ; diversité et soulèvement d'ensemble. Géologues Rev. Off. Société Géologique Fr. 4–12.

Miller, K.G., Kominz, M.A., Browning, J.V., Wright, J.D., Mountain, G.S., Katz, M.E., Sugarman, P.J., Cramer, B.S., Christie-Blick, N., Pekar, S.F., 2005. The Phanerozoic record of global sea-level change. Science 310, 1293–1298. https://doi.org/10.1126/science.1116412

Missenard, Y., 2006. Le relief des Atlas Marocains: Contribution des processus asthénosphériques et du raccourcissement crustal, aspects chronologiques (Unpublished Ph.D. thesis). Université Paris Sud, Orsay.

Missenard, Y., Cadoux, A., 2012. Can Moroccan Atlas lithospheric thinning and volcanism be induced by Edge-Driven Convection? Terra Nova 24, 27–33. https://doi.org/10.1111/j.1365-3121.2011.01033.x

Missenard, Y., Saddiqi, O., Barbarand, J., Leturmy, P., Ruiz, G., El Haimer, F.-Z., Frizon de Lamotte, D., 2008. Cenozoic denudation in the Marrakech High Atlas, Morocco: insight from apatite fission-track thermochronology. Terra Nova 20, 221–228. https://doi.org/10.1111/j.1365-3121.2008.00810.x

Missenard, Y., Taki, Z., Frizon de Lamotte, D., Benammi, M., Hafid, M., Leturmy, P., Sébrier, M., 2007. Tectonic styles in the Marrakesh High Atlas (Morocco): The role of heritage and mechanical stratigraphy. J. Afr. Earth Sci. 48, 247–266. https://doi.org/10.1016/j.jafrearsci.2007.03.007

Missenard, Y., Zeyen, H., Frizon de Lamotte, D., Leturmy, P., Petit, C., Sébrier, M., Saddiqi, O., 2006. Crustal versus asthenospheric origin of relief of the Atlas Mountains of Morocco. J. Geophys. Res. Solid Earth 111, n/a-n/a. https://doi.org/10.1029/2005JB003708

Miura, H., 1986. The crystal structure of hollandite. Mineral. J. 13, 119–129. https://doi.org/10.2465/minerj.13.119

Moret, L., 1931. Les ressources minérales et les mines du Maroc français. Rev. Géographie Alp. 18, 261–302.

Nambu, M., Tanida, K., 1967. Manjiroite, a new manganese dioxide mineral, from Kohare Mine, Iwate Prefecture, Japan. J. Jpn. Assoc. Mineral. Petrol. Econ. Geol. 58, 39–54. https://doi.org/10.2465/ganko1941.58.39

Neltner, L., 1938. Etudes géologique dans le Sud Marocain (Haut-Atlas et Anti-Atlas). Notes Mém. Serv. Géologique Maroc.

Neltner, L., 1933. Le manganèse dans les possessions françaises. Ressour. Minérales Fr. Outremer Paris Publ. Bur. Etudes Géologiques Minières Colon. 2, 81–144.

Nicaise, D., 1998. L'halloysite des cryptokarsts de l'Entre-Sambre-et-Meuse (Belgique) : synthèse géologique, minéralogique et géochimique (Unpublished Ph.D. thesis). Université Paris Sud, Orsay.

Nicholson, K., 1992. Genetic types of manganese oxide deposits in Scotland; indicators of paleo-ocean-spreading rate and a Devonian geochemical mobility boundary. Econ. Geol. 87, 1301–1309. https://doi.org/10.2113/gsecongeo.87.5.1301

Nomade, S., Knight, K.B., Beutel, E., Renne, P.R., Verati, C., Féraud, G., Marzoli, A., Youbi, N., Bertrand, H., 2007. Chronology of the Central Atlantic Magmatic Province: Implications for the Central Atlantic rifting processes and the Triassic? Jurassic biotic crisis. Palaeogeogr. Palaeoclimatol. Palaeoecol. 244, 326–344. https://doi.org/10.1016/j.palaeo.2006.06.034

Office National des Mines et des Hydrocarbures, 2016. District de manganèse de Tasdremt-Aoufour (province de Taroudant, Maroc). Rabat.

Orcel, J., 1942. La Coronadite et le minerai qui la renferme dans les gîtes de manganèse de l'Imini. Sud Maroc. Bull. Société Fr. Minéralogie 65, 73–111.

Ouanaimi, H., Petit, J.P., 1992. La Limite sud de la chaine hercynienne dans le Haut Atlas marocain; reconstitution d'un saillant non deforme. Bull. Société Géologique Fr. 163, 63–72.

Oukassou, M., Saddiqi, O., Barbarand, J., Sebti, S., Baidder, L., Michard, A., 2013. Post-Variscan exhumation of the Central Anti-Atlas (Morocco) constrained by zircon and apatite fission-track thermochronology. Terra Nova 25, 151–159. https://doi.org/10.1111/ter.12019

Palmer, M.R., 1985. Rare earth elements in foraminifera tests. Earth Planet. Sci. Lett. 73, 285–298. https://doi.org/10.1016/0012-821X(85)90077-9

Parizot, O., 2017. Contexte structural du gisement manganésifère de Tasdremt, Bassin du Souss, Maroc (Mémoire). Université Paris Sud, Orsay.

Pastor, A., Teixell, A., Arboleya, M.L., 2012. Rates of quaternary deformation in the ouarzazate basin (southern atlas front, Morocco). Ann. Geophys. 55, 1003–1016. https://doi.org/10.4401/ag-4940

Perseil, E.-A., Grandin, G., 1985. Altération supergène des protores à grenats manganésifères dans quelques gisements d'Afrique de l'Ouest. Miner. Deposita 20, 211–219.

Perseil, E.-A., Grandin, G., 1978. Evolution minéralogique du manganèse dans trois gisements d'Afrique de l'Ouest: Mokta, Tambao, Nsuta. Miner. Deposita 13, 295–311.

Petrascheck, W.E., 1965. Typical features of metallogenic provinces. Econ. Geol. 60, 1620–1634. https://doi.org/10.2113/gsecongeo.60.8.1620

Piper, D.Z., 1974. Rare earth elements in the sedimentary cycle: A summary. Chem. Geol. 14, 285–304. https://doi.org/10.1016/0009-2541(74)90066-7

Piqué, A., Tricart, P., Guiraud, R., Laville, E., Bouaziz, S., Amrhar, M., Ait Ouali, R., 2002. The Mesozoic–Cenozoic Atlas belt (North Africa): an overview. Geodin. Acta 15, 185–208. https://doi.org/10.1016/S0985-3111(02)01088-4

Post, J.E., 1999. Manganese oxide minerals: crystal structures and economic and environmental significance. Proc. Natl. Acad. Sci. 96, 3447–3454. https://doi.org/10.1073/pnas.96.7.3447

Post, J.E., Bish, D.L., 1989. Rietveld refinement of the coronadite structure. Am. Mineral. 74, 913–917.

Pouit, G., 1980. Manganèse. Notes Mém. Serv. Géologique Maroc Rabat 13, 61–67.

Pouit, G., 1976. La concentration de manganèse de l'Imini (Maroc) peut-elle être d'origine karstique ? Comptes Rendus Somm. Société Géologique Fr. 5, 227–229.

Pouit, G., 1966. Le manganèse dans le Permo-Trias au Maroc : étude métallogénique et comparaison avec les minéralisations dans le Précambrien III. Notes Mém. Serv. Géologique Maroc 27, 117–122.

Pouit, G., 1964. Les gîtes de manganèse marocains encaissés dans les Formations carbonatées : éléments pour une synthèse. Chron. Mines Rech. Minière 371–380.

Pouit, G., Jouravsky, G., 1962. Le gîte de manganèse d'Aït-Iggelt (Anti-Atlas) : un exemple de minéralisation pénécontemporaine de la série encaissante. Mines Géologie Energ. 41–47.

Pouit, G., Jouravsky, G., 1961. Les indices de manganèse du Jbel Sour (Haut Atlas de Marrakech) : Relation entre minéralisation et structure paléinsulaire. Mines Géologie Energ. 36–37.

Pouit, G., Jouravsky, G., 1960a. Présence de filons de manganèse d'âge post-Triasique ou post-Cénomanien dans la région de l'Imini (province de Ouarzazate, Sud marocain). Notes Mém. Serv. Géologique Maroc 19, 61–67.

Pouit, G., Jouravsky, G., 1960b. Le gisement de manganèse de Tizi-n-Isdid (région de l'Ounein, Haut Atlas). Mines Géologie Energ. 21–29.

Pouit, G., Jouravsky, G., 1960c. Présence de filons de manganèse d'âge post-triasique ou post-Cénomanien dans la région de l'Imini. Notes Mém. Serv. Géologique Maroc 19, 61–67.

Proust, F., Petit, J.-P., Tapponnier, P., 1977. L'accident du Tizi n'Test et le role des decrochements dans la tectonique du Haut Atlas occidental (Maroc). Bull. Société Géologique Fr. S7-XIX, 541–551. https://doi.org/10.2113/gssgfbull.S7-XIX.3.541

Qarbous, A., Medina, F., Hoepffner, C., 2008. Brittle tectonics and state of stress in the basin of Titzi n'Test (High Atlas, Morocco) during the Tertiary inversion. Estud. Geol. 64, 17–30.

Qarbous, A., Medina, F., Hoepffner, C., Ahmamou, M., Errami, A., Bensahal, A., 2003. La chronologie du fonctionnement de la zone de failles de Tizi n'Test: apport de l'étude des bassins stéphano-autuniens et permo-triasiques du Haut Atlas occidental (Maroc). Bull Inst Sci Rabat 25, 43–53.

Renne, P.R., Balco, G., Ludwig, K.R., Mundil, R., Min, K., 2011. Response to the comment by W.H. Schwarz et al. on "Joint determination of 40K decay constants and $^{40}Ar^{*}/^{40}K$ for the Fish Canyon sanidine standard, and improved accuracy for $^{40}Ar/^{39}Ar$ geochronology" by P.R. Renne et al. (2010). Geochim. Cosmochim. Acta 75, 5097–5100. https://doi.org/10.1016/j.gca.2011.06.021

Renne, P.R., Mundil, R., Balco, G., Min, K., Ludwig, K.R., 2010. Joint determination of ^{40}K decay constants and $^{40}Ar^{*}/^{40}K$ for the Fish Canyon sanidine standard, and improved accuracy for $^{40}Ar/^{39}Ar$ geochronology. Geochim. Cosmochim. Acta 74, 5349–5367. https://doi.org/10.1016/j.gca.2010.06.017

Renne, P.R., Swisher, C.C., Deino, A.L., Karner, D.B., Owens, T.L., De Paolo, D.J., 1998. Intercalibration of standards, absolute ages and uncertainties in $^{40}Ar/^{39}Ar$ dating. Chem. Geol. 145, 117–152. https://doi.org/10.1016/S0009-2541(97)00159-9

Rhalmi, M., 1992. Les systèmes sédimentaires cénomano-turoniens et sénoniens de la région manganésifère d'Imini (Haut-Atlas Central, Maroc) et leur évolution diagénétique (PhD). Bourgogne, Dijon.

Rhalmi, M., Pascal, A., Chellai, E., 2000. Lithobiostratigraphie, diagenèse et paléogéographie au Cénomanien supérieur-Turonien inférieur des bassins sud-atlasiques marocains. Géologie Alp. 76, 135–149.

Rhalmi, M., Pascal, A., Lang, J., 1997. Contrôle sédimentaire et diagénétique de la minéralisation manganésifère au cours du Crétacé Supérieur dans la région d'Imini (Haut-Atlas central, Maroc). Comptes Rendus L'Académie Sci. Sér. 2 Sci. Terre Planètes 323, 213–220.

Richmond, W.E., Fleischer, M., 1942. Cryptomelane, a new name for the commonest of the '"psilomelane"' minerals. Am. Mineral. 27, 607–610.

Roddick, J.C., Cliff, R.A., Rex, D.C., 1980. The evolution of excess argon in alpine biotites - a ^{40}Ar-^{39}Ar analysis. Earth Planet. Sci. Lett. 48, 185–208. https://doi.org/10.1016/0012-821X(80)90181-8

Rosenbaum, G., Lister, G.S., Duboz, C., 2002. Relative motions of Africa, Iberia and Europe during Alpine orogeny. Tectonophysics 359, 117–129. https://doi.org/10.1016/S0040-1951(02)00442-0

Ruffet, G., Féraud, G., Amouric, M., 1991. Comparison of ^{40}Ar-^{39}Ar conventional and laser dating of biotites from the North Trégor Batholith. Geochim. Cosmochim. Acta 55, 1675–1688. https://doi.org/10.1016/0016-7037(91)90138-U

Ruffet, G., Féraud, G., Balèvre, M., Kiénast, J.-R., 1995. Plateau ages and excess argon in phengites: an ^{40}Ar/^{39}Ar laser probe study of Alpine micas (Sesia Zone, Western Alps, northern Italy). Chem. Geol. 121, 327–343. https://doi.org/10.1016/0009-2541(94)00132-R

Ruffet, G., Gruau, G., Ballèvre, M., Féraud, G., Philippot, P., 1997. Rb/Sr and ^{40}Ar/^{39}Ar laser probe dating of high-pressure phengites from the Sesia zone (Western Alps): underscoring of excess argon and new age constraints on the high-pressure metamorphism. Chem. Geol. 141, 1–18. https://doi.org/10.1016/S0009-2541(97)00052-1

Ruffet, G., Innocent, C., Michard, A., Féraud, G., Beauvais, A., Nahon, D., Hamelin, B., 1996. A geochronological and study of K-Mn oxides from the weathering sequence of Azul, Brazil. Geochim. Cosmochim. Acta 60, 2219–2232. https://doi.org/10.1016/0016-7037(96)00080-4

Ruiz, G.M.H., Sebti, S., Negro, F., Saddiqi, O., Frizon de Lamotte, D., Stockli, D., Foeken, J., Stuart, F., Barbarand, J., Schaer, J.-P., 2011. From central Atlantic continental rift to Neogene uplift - western Anti-Atlas (Morocco): From central Atlantic continental rift to Neogene uplift. Terra Nova 23, 35–41. https://doi.org/10.1111/j.1365-3121.2010.00980.x

SACEM, 2016. Les mines de l'Imini (Rapport d'activité). Société Anonyme Chérifienne d'Etudes Minières, Casablanca.

Saddiqi, O., Baidder, L., Michard, A., 2011. Haut Atlas et Anti-Atlas, Circuit Oriental, in: Mouttaqi, A., Rjimati, E.C., Maacha, L., Michard, A., Soulaimani, A., Ibouh, H. (Eds.), Nouveaux Guides Géologiques et Miniers Du Maroc. Rabat, pp. 11–75.

Saint-Bézar, B., Frizon de Lamotte, D., Morel, J.L., Mercier, E., 1998. Kinematics of large scale tip line folds from the High Atlas thrust belt, Morocco. J. Struct. Geol. 20, 999–1011. https://doi.org/10.1016/S0191-8141(98)00031-5

Scott, J.D., Peatfield, G.R., 1986. Mannardite $[Ba.H_2O](Ti_6V^{3+}{}_2)O_{16}$, a new mineral species, and new data on redledgeite. Can. Mineral. 24, 55–66.

Sebbag, I., 1969. Inventaire général des gîtes et indices de cuivre, manganèse, plomb, fer, or et argent du Jbel Sarhro oriental. Mines Géologie Energ. 35–48.

Seber, D., Barazangi, M., Tadili, B.A., Ramdani, M., Ibenbrahim, A., Ben Sari, D., 1996. Three-dimensional upper mantle structure beneath the intraplate Atlas and interplate Rif mountains of Morocco. J. Geophys. Res. Solid Earth 101, 3125–3138. https://doi.org/10.1029/95JB03112

Sébrier, M., Siame, L., Zouine, E.M., Winter, T., Missenard, Y., Leturmy, P., 2006. Active tectonics in the Moroccan High Atlas. Comptes Rendus Geosci., Quelques développements récents sur la géodynamique du Maghreb 338, 65–79. https://doi.org/10.1016/j.crte.2005.12.001

Sebti, S., 2011. Mouvements Verticaux de l'Anti-Atlas Occidental marocain (Kerdous & Ifni): Thermochronologie par traces de fission (Unpublished Ph.D. thesis). Hassan II-Aïn Chock, Casablanca.

Seward, T.M., Barnes, H.L., 1997. Metal transport by hydrothermal ore fluids, in: Geochemistry of Hydrothermal Ore Deposits. Wiley, New York, pp. 435–486.

Snoke, A.W., Schamel, S., Karasek, R.M., 1988. Structural evolution of Djebel Debadib Anticline: A clue to the regional tectonic style of the Tunisian Atlas. Tectonics 7, 497–516. https://doi.org/10.1029/TC007i003p00497

Tabuce, R., Adnet, S., Cappetta, H., Noubhani, A., Quillevere, F., 2005. Aznag (Ouarzazate basin, Morocco), a new African middle Eocene (Lutetian) vertebrate-bearing locality with selachians and mammals. Bull. Société Géologique Fr. 176, 381–400. https://doi.org/10.2113/176.4.381

Taylor, S.R., McLennan, S.M., 1985. The continental crust: its composition and evolution: an examination of the geochem. record preserved in sedimentary rocks, Geoscience texts. Blackwell, Oxford.

Teixell, A., Arboleya, M.-L., Julivert, M., Charroud, M., 2003. Tectonic shortening and topography in the central High Atlas (Morocco). Tectonics 22. https://doi.org/10.1029/2002TC001460

Teixell, A., Ayarza, P., Zeyen, H., Fernandez, M., Arboleya, M.-L., 2005. Effects of mantle upwelling in a compressional setting: the Atlas Mountains of Morocco. Terra Nova 17, 456–461. https://doi.org/10.1111/j.1365-3121.2005.00633.x

Tesón, E., 2005. Estudio estructural del margen sur del Alto Atlas entre los valles del Dades y el Mgoun. Trabajo de investigación (Master Thesis). Universita Autonoma Barcelona, Bellaterra.

Tesón, E., Pueyo, E.L., Teixell, A., Barnolas, A., Agustí, J., Furió, M., 2010. Magnetostratigraphy of the Ouarzazate Basin: Implications for the timing of deformation and mountain building in the High Atlas Mountains of Morocco. Geodin. Acta 23, 151–165. https://doi.org/10.3166/ga.23.151-165

Tesón, E., Teixell, A., 2008. Sequence of thrusting and syntectonic sedimentation in the eastern Sub-Atlas thrust belt (Dadès and Mgoun valleys, Morocco). Int. J. Earth Sci. 97, 103–113. https://doi.org/10.1007/s00531-006-0151-1

Thein, J., 1990. Paleogeography and geochemistry of the "Cenomano-Turonian" formations in the manganese district of Imini (Morocco) and their relation to ore deposition. Ore Geol. Rev. 5, 257–291. https://doi.org/10.1016/0169-1368(90)90034-K

Turner, G., 1971. 40Ar/39Ar ages from the lunar maria. Earth Planet. Sci. Lett. 11, 169–191. https://doi.org/10.1016/0012-821X(71)90161-0

Turner, G., 1968. The distribution of potassium and argon in chondrites, in: Ahrens, L.H. (Ed.), Origin and Distribution of the Elements, International Series of Monographs in Earth Sciences. Pergamon, pp. 387–398. https://doi.org/10.1016/B978-0-08-012835-1.50039-8

Turner, S., Buseck, P.R., 1979. Manganese oxide tunnel structures and their intergrowths. Science 203, 456–458. https://doi.org/10.1126/science.203.4379.456

Varentsov, I.M., 1996. Manganese ores of supergene zone: Geochemistry of formation, Solid Earth Sciences Library. Springer Netherlands, Dordrecht.

Vasconcelos, P.M., 1999. K-Ar and $^{40}Ar/^{39}Ar$ geochronology of weathering processes. Annu. Rev. Earth Planet. Sci. 27, 183–229. https://doi.org/10.1146/annurev.earth.27.1.183

Vasconcelos, P.M., Becker, T.A., Renne, P.R., Brimhall, G.H., 1992. Age and duration of weathering by 40K-40Ar and $^{40}Ar/^{39}Ar$ analysis of potassium-manganese oxides. Science 258, 451–455. https://doi.org/10.1126/science.258.5081.451

Vasconcelos, P.M., Carmo, I. de O., 2018. Calibrating denudation chronology through $^{40}Ar/^{39}Ar$ weathering geochronology. Earth-Sci. Rev. 179, 411–435. https://doi.org/10.1016/j.earscirev.2018.01.003

Vasconcelos, P.M., Knesel, K.M., Cohen, B.E., Heim, J.A., 2008. Geochronology of the Australian Cenozoic: a history of tectonic and igneous activity, weathering, erosion, and sedimentation. Aust. J. Earth Sci. 55, 865–914. https://doi.org/10.1080/08120090802120120

Vasconcelos, P.M., Renne, P.R., Becker, T.A., Wenk, H.-R., 1995. Mechanisms and kinetics of atmospheric, radiogenic, and nucleogenic argon release from cryptomelane during analysis. Geochim. Cosmochim. Acta 59, 2057–2070. https://doi.org/10.1016/0016-7037(95)00126-3

Vasconcelos, P.M., Renne, P.R., Brimhall, G.H., Becker, T.A., 1994. Direct dating of weathering phenomena by and K-Ar analysis of supergene K-Mn oxides. Geochim. Cosmochim. Acta 58, 1635–1665. https://doi.org/10.1016/0016-7037(94)90565-7

Verati, C., Rapaille, C., Féraud, G., Marzoli, A., Bertrand, H., Youbi, N., 2007. $^{40}Ar/^{39}Ar$ ages and duration of the Central Atlantic Magmatic Province volcanism in Morocco and Portugal and its relation to the Triassic–Jurassic boundary. Palaeogeogr. Palaeoclimatol. Palaeoecol. 244, 308–325. https://doi.org/10.1016/j.palaeo.2006.06.033

Verhaert, M., Bernard, A., Saddiqi, O., Dekoninck, A., Essalhi, M., Yans, J., 2018. Mineralogy and Genesis of the Polymetallic and Polyphased Low Grade Fe-Mn-Cu Ore of Jbel Rhals Deposit (Eastern High Atlas, Morocco). Minerals 8, 39. https://doi.org/10.3390/min8020039

Vially, R., Letouzey, J., Benard, F., Haddadi, N., Desforges, G., Askri, H., Boudjema, A., 1994. A basin inversion along the North African margin: the Saharan Atlas (Algeria), in: Roure, F. (Ed.), Peri-Tethyan Platforms. Paris, pp. 79–118.

Westerveld, J., 1951. Les gîtes de manganèse du domaine atlasique au Maroc français et leur classification géologique. Geol. En Mijnb. 2, 25–52.

Wurster, P., Stets, J., 1992. Sedimentation in the Atlas Gulf II: mid-Cretaceous events, in: von Rad, U. (Ed.), Geology of the Northwest African Continental Margin. Berling, pp. 439–458.

Youbi, N., Kouyaté, D., Söderlund, U., Ernst, R.E., Soulaimani, A., Hafid, A., Ikenne, M., El Bahat, A., Bertrand, H., Rkha Chaham, K., Ben Abbou, M., Mortaji, A., El Ghorfi, M., Zouhair, M., El Janati, M., 2013. The 1750 Ma Magmatic Event of the West African Craton (Anti-Atlas, Morocco). Precambrian Res. 236, 106–123. https://doi.org/10.1016/j.precamres.2013.07.003

Zeyen, H., Ayarza, P., Fernàndez, M., Rimi, A., 2005. Lithospheric structure under the western African-European plate boundary: A transect across the Atlas Mountains and the Gulf of Cadiz: Atlas-Gulf of Cadiz Lithosphere. Tectonics 24, 1-16. https://doi.org/10.1029/2004TC001639

Zouhri, S., Kchikach, A., Saddiqi, O., Haïmer, F.Z.E., Baidder, L., Michard, A., 2008. The Cretaceous-Tertiary Plateaus, in: Michard, André, Saddiqi, Omar, Chalouan, A., Lamotte, D.F. de (Eds.), Continental Evolution: The Geology of Morocco. Springer Berlin Heidelberg, Berlin, Heidelberg, pp. 331–358.

Chapter 8

The mixed hydrothermal-supergene Fe(-Mn) deposit of Tamra (North Tunisia)

Chapter 8

The mixed hydrothermal-supergene Fe(-Mn) Tamra deposit (North Tunisia)

Northern Tunisia belongs to the Alpine Maghrebide belt, extending over more than 2000 km from Morocco to eastern Algeria, and finally stretched to the northeast in Tunisia and Sicily (►Fig. 4.1). This belt results from the Tertiary collision between northern Africa and a small Meso-Mediterranean plates, as part of the development of the Alpine chain (Piqué, 2002; Guerrera *et al.*, 2005; Michard *et al.*, 2006). The whole Maghrebide belt is divided into (1) an Internal Zone, with basement nappes (internal massifs) derived from the Meso-MMediterranean plate, and a complex series of flysch slices (or Flysch Zone) at their front, both of them being thrust over (2) the Tellian nappes (or Tellian Zone), which are, in turn, thrust onto (3) the folded autochthonous units of the foreland (Tellian Atlas and Saharan Platform; ►Figs. 4.1 and 8.1). The Tellian nappes (the so-called Nappe Zone on land) are actually the former passive margin of northern Africa, whereas the Tellian Atlas resulted from the Eocene tectonic inversion of the Mesozoic rift system (Masrouhi *et al.*, 2008; Decrée *et al.*, 2016). The Tellian Atlas contains (1) an internal diapiric part with Triassic cores known as the Dome Zone; and (2) an external domain, which was reworked by extension during the late Tertiary, corresponding to the Graben Zone (►Fig. 8.1).

The Nefza mining district in Northern Tunisia displays a wide variety of base and precious metal deposits (►Fig. 8.1) in a relatively short time window (►Fig. 8.2) and a narrow area of approximately 20 km in the east-west axis and 7 kilometers in the north-south axis (►Fig. 8.3). These mineral deposits are in close association to Serravalian to Messinian magmatic and volcanic rocks, which have enhanced polymetallic mineralization and a hydrothermal activity (►Fig. 8.3; Decrée *et al.*, 2016). These high concentrations of metals belong to a larger zone crossing over northern Tunisia, and follow the Ghardimaou-Cap Serrat shear zone (►Fig. 8.2; Decrée *et al.*, 2013, 2014). Such mineralization in the Nefza area includes the Messinian Sedex Pb-Zn deposits of Sidi Driss and Douahria (Decrée *et al.*, 2008b), the Tortonian IOCG (Fe-Cu-Au-REE-U) Oued Belif breccia (Decrée *et al.*, 2013) and the late Miocene to Pliocene weathering-hydrothermal Tamra Fe-Mn sediments (Decrée *et al.*, 2008a, 2010), all being formed since late Miocene times (►Fig. 8.2), among other mineralization events in the vicinity of the Nefza polymetallic district (Decrée *et al.*, 2016).

A particular interest has been taken from the Fe-Mn Tamra deposit in the northern part of the district (►Fig. 8.3), as some part of the Fe-rich weathering sequence is enriched in Mn oxides, both being associated with kaolinite-halloysite clays (Decrée *et al.*, 2008a, 2010; Moussi *et al.*, 2011; Moussi, 2012). Kaolinite(-halloysite) and goethite(-hematite) are well-known materials to assess the temperature of formation of supergene deposits, thanks to their light oxygen and hydrogen isotope composition (Yapp, 1990, 2000; Gilg and Sheppard, 1996; Sheppard and Gilg, 1996). Such approach is interesting to settle the weathering and/or hydrothermal alteration origin of this deposit, as hydrothermal activity has persisted since the setting up of

volcanism in the area (►Fig. 8.2), and led some metals to be enriched in the Mn-rich part of the Tamra deposit (►Fig. 8.3). The presence of kaolinite-halloysite spots and goethite-hematite within the Tamra sequence is a remarkable opportunity to evaluate the temperature of mineralizing fluids in the supergene (?) environment and therefore the conditions under which Mn oxides have precipitated, as hollandite *s.s.* and coronadite have provided relevant ages (3.35 ± 0.07 and 4.7 ± 0.1 Ma; Decrée *et al.*, 2010), accordingly to the deposition phases and enrichment of these Fe-Mn ores.

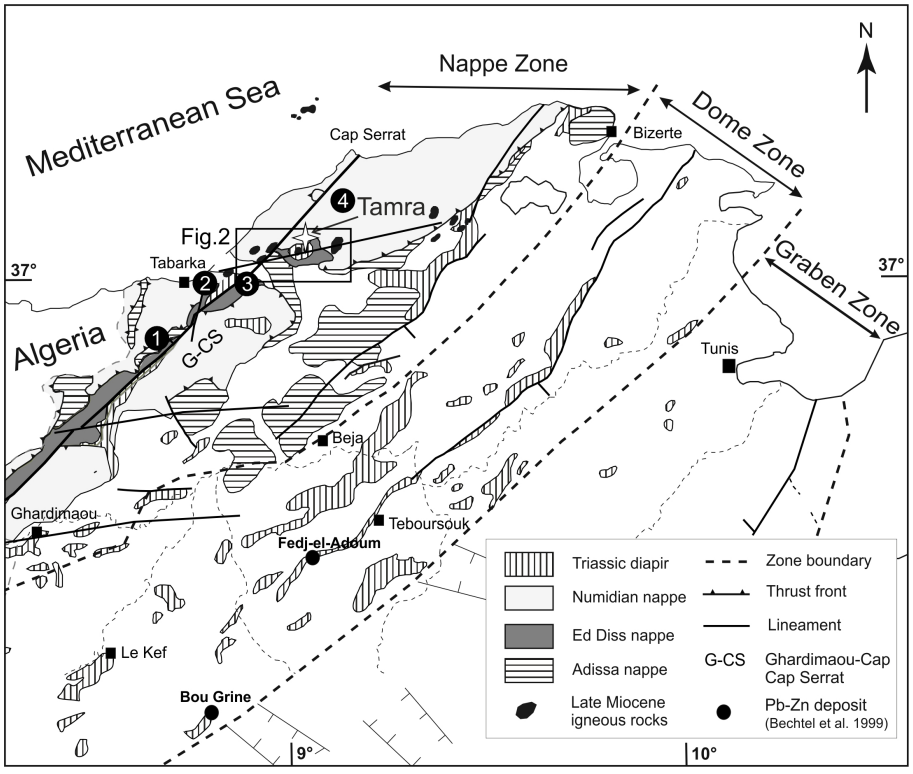

►**Fig.8.1** Tectonic map of central and northern Tunisia showing the location of the Nefza area (►Fig. 8.3) and the Bou Grine and Fedj-el-Adoun Pb-Zn deposits. Numbers refer to sampling site: 1-Ain Drahan (14AD01), 2-Sidi Bader (14SB01, 14SB02), 3-Ain Sebaa (14ME02), 4-Om-Tébal (OMS2; modified after Rouvier *et al.*, 1985; Bouaziz *et al.*, 2002; Bouhlel *et al.*, 2013; Decrée *et al.*, 2016).

This chapter is based on the published paper "*Mixed hydrothermal and meteoric fluids evidenced by unusual H- and O-isotope compositions of kaolinite-halloysite in the Fe(-Mn) Tamra deposit (Nefza district, NW Tunisia)*" authored by Dekoninck Augustin, Moussi Béchir, Vennemann Torsten, Jamoussi Fakher, Mattielli Nadine, Decrée Sophie, Chaftar Hédi-Ridha, Hatira Nouri and Yans Johan in Applied Clay Science in 2018 (Dekoninck *et al.*, 2018).

8.1 Introduction

In the weathering environment, the isotopic composition of hydrogen and oxygen in water is related to the climatic conditions (Savin and Epstein, 1970). Some authigenic clay minerals and goethite are known to crystallize in isotopic equilibrium with meteoric water and, once crystallized, are resistant to isotopic exchange under the near surface conditions thanks to the slow isotopic exchange at low temperature (Yapp, 1990; Sheppard and Gilg, 1996; Savin and Hsieh, 1998). Sheppard and Gilg (1996) showed that oxygen and hydrogen composition of present-day kaolinite formed from meteoric water is largely temperature dependent and aligned along the "kaolinite line", which is parallel to the meteoric water line. Yapp (1990) drew the same conclusion for supergene goethite. Therefore, any process (diagenesis, evaporation, hydrothermalism…) which do not equilibrate goethite and kaolinite with meteoric waters would record a shift in the oxygen and hydrogen isotope composition. In natural systems, processes of fluid/rock interactions could lead to isotopic exchange between a mineralizing fluid and bedrocks for example, but also between a matrix progressively infiltrated by external fluids in an open system (Savin and Lee, 1988). Dissolution-precipitation of minerals could change the isotopic composition of the fluid (weathering, hydrothermal, diagenetic). This is especially the case for oxygen, given its availability in most of the common minerals (i.e. silicates, oxides, and carbonates) compared to hydrogen (hydroxides, hydrous silicates). For example, carbonates concentrate ^{18}O in their structure in contrast to other minerals (Garlick, 1966; Taylor, 1968; Kohn and Valley, 1998a, 1998b, 1998c; Hoefs, 2009), and when dissolved, release heavy oxygen to the fluids, which are depleted in ^{18}O (meteoric fluids). However, the range of these modifications depends on the isotopic fractionation, on the initial difference in isotopic composition between the fluid and the mineral, and on the temperature between the mineralizing fluid and minerals (Girard and Fouillac, 1995).

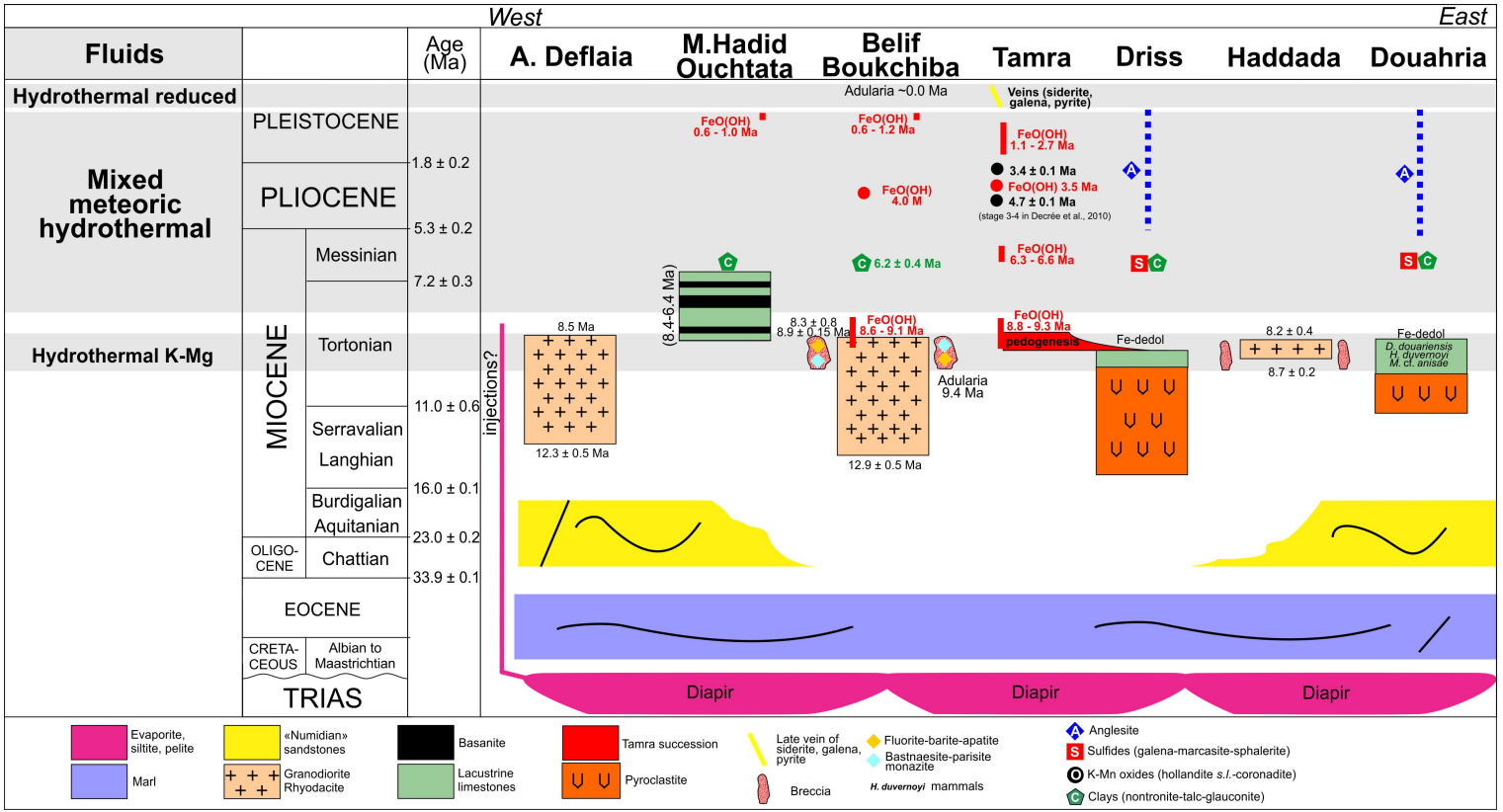

►**Fig.8.2** Timing of the main sedimentary, magmatic and mineralization events recorded in the Nefza area (Yans, pers. com.) in a west to east transect (see location of these sites in ►Fig.8.3). (U–Th)/He dating on goethite (FeOOH) have been performed by M. Verhaert (PhD in progress).

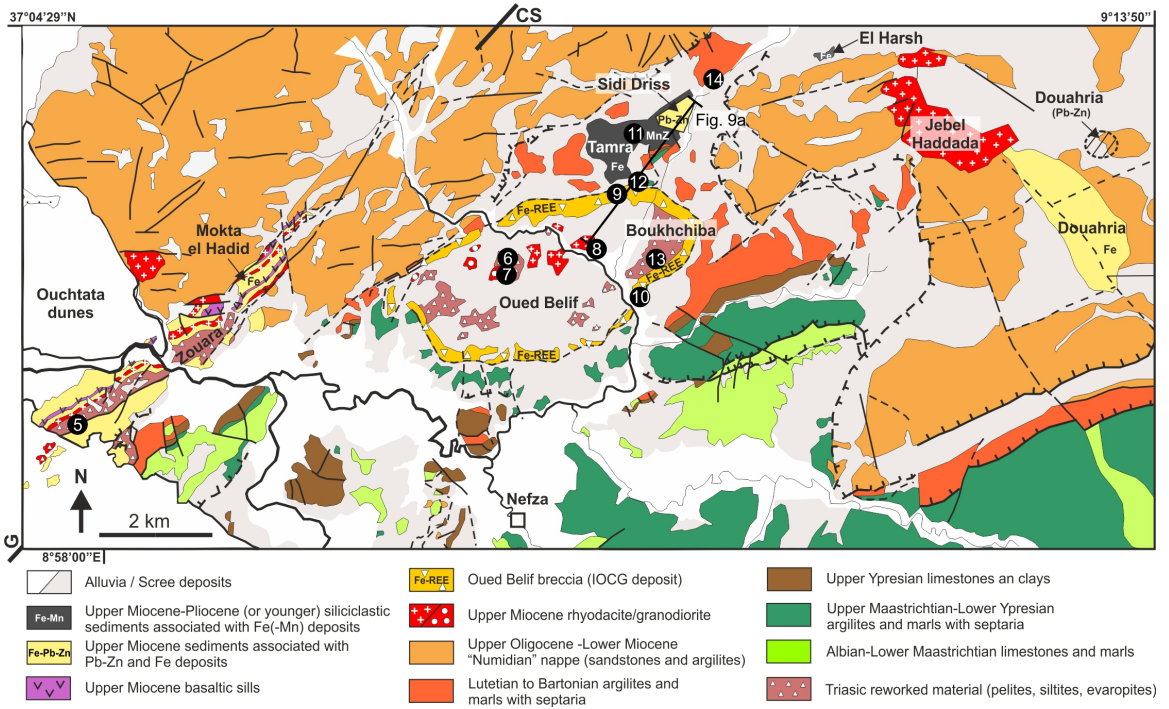

►**Fig.8.3** Simplified geologic map of the Nefza district showing the location of the Tamra deposit in the northern part of the district and the location of the cross section (►Fig.8.9; modified after Gottis and Sainfeld, 1952; Batik, 1980; Rouvier, 1987). Numbers refer to sampling sites: 5-Ouchtata Triassic sediments (14OU03, OUCHTATA), 6-Chabet El Ain skarn (14CEA02), 7-Ragoubet El Alia granodiorite (OB48-79), 8-Ragoubet Sidi Ahmed rhyodacite (14AA02, OB45-42, OB45-78), 9-Tamra Oued Belif breccia (BR01), 10-Boukhchiba Oued Belif breccia (14OB02), 11-Tamra deposit (ABT1, CAT7, CAT7.5, ZMNWL8, 14TAM09, 14MnTAM, 14TAM07, CP04-3, CP04-35), 12-Tamra mine (south) marls (14TAM16), 13-Boukhchiba Fe-deposit (14BK01, 14BK11), 14-Tamra village marls (14ET02, 14ET03, EM04/11).

The Nefza mining district (NW Tunisia) illustrates the complexity of mixing fluids well and their interaction with volcanic and sedimentary rocks during the genesis of various types of deposits (►Fig. 8.1 and 8.3; Decrée *et al.*, 2008b, 2013, 2014, 2016; Moussi *et al.*, 2011). The area has successively been affected by Serravalian to Tortonian felsic magmatism, which is responsible for contact metamorphism of Late Cretaceous to Eocene marls into skarn (Decrée *et al.*, 2014), and also for the setting up of a Miocene Fe-Cu-Au-(U-REE) volcanic breccia around a Triassic diapiric dome (►Fig. 8.2; Decrée *et al.*, 2013). The extensional conditions allowed the generation of Tortonian to Messinian basaltic flows and the deposition of two Late Miocene to Pliocene continental (siliciclastic and carbonate) deposits containing the Sidi Driss SEDEX Pb-Zn (Sidi Driss) and the Tamra Fe(-Mn) deposits (Decrée *et al.*, 2008b, 2008a, 2010). The synsedimentary pedogenesis through the 50 m thick Tamra sediments and the later weathering/hydrothermal circulation have led to the enrichment in Fe and other elements in the sediments (Decrée *et al.*, 2008a, 2010). Local concentration of "white clays" composed of kaolinite and halloysite is associated with the Fe oxide ore (Moussi *et al.*, 2011), and is considered to determine both meteoric and hydrothermal contributions. Therefore, hydrogen and oxygen isotope analyzes of the white clays, associated with iron oxides and hydroxides, may help to redefine the process, which took place during mineralization in the Nefza mining district, taking into account the complexity and relationships of the rock varieties.

8.2 Geological setting

8.2.1 Geological framework

The Tamra Fe-Mn deposit is located in the Nefza mining district (NW of Tunisia, ►Fig. 8.1), which has been well-known for its base-metal deposits since the first half of the 20th century (Gottis and Sainfeld, 1952). The Nefza district is located in the Tellian "Nappe Zone" of Northern Tunisia, which is characterized by the Ed Diss Upper Cretaceous to Eocene thrust sheets (Burollet, 1991; Rouvier, 1994; Ould Bagga *et al.*, 2006), and the overlying Oligocene "Numidian Nappe" (►Figs. 8.1 and 8.2; Rouvier, 1977). Carbonates and marls from the Ed Diss sheet (Negra, 1987) are overlain by the "Numidian Nappe", which is composed of claystone and sandstone Oligocene to Burdigalian in age. Serravalian to Late Tortonian felsic magmatism (12.9 $\pm$ 0.5 Ma to 8.2 $\pm$ 0.4 Ma; (Badgasarian, 1972; Bellon, 1976; Rouvier, 1977; Faul and Foland, 1980; Decrée *et al.*, 2013) resulted in the emplacement of granodiorite and volcanic rhyodacite (Mauduit, 1978; Rouvier, 1994; Savelli, 2002; Decrée *et al.*, 2014). Skarn deposits were formed in contact with late Cretaceous-Eocene marls (►Fig. 8.3; Decrée *et al.*, 2013). The most prominent feature of the area

is the 7 km long and 3 km wide Oued Belif ring-shaped structure (Rouvier, 1987), characterized by a Fe-rich breccia containing reworked fragments of the regional substrates, and a small amount of volcanic-related material (Decrée *et al.*, 2013). This breccia encloses Triassic salt-related rocks linked to the top of a diapiric dome, and Serravalian-Late Tortonian magmatic bodies (►Figs. 8.2 and 8.3). A regional shallow magmatic sill (20 km in diameter and up to 0.7-0.9 km in thickness) located 500 m below the Oued Belif structure is considered to be the root of magmatic activity in the Nefza area (Jallouli *et al.*, 2003), and could be responsible for the high thermal gradient (> 100°C/ km) in the area (Jallouli *et al.*, 1996). The origin of the IOCG Oued Belif breccia is likely to originate from mixing fluids between magmatic-hydrothermal, and basinal (evaporite) brines. K-Fe alteration event slightly predating the main mineralization is dated at 9.2 $\pm$ 0.25 Ma on adularia (Decrée *et al.*, 2013). Subsequent magmatic activity during the Tortonian to Messinian (~8.4 and 6.9-6.4 Ma) erupted basaltic flows in the western part of the Nefza area (►Fig. 8.3; Bellon, 1976; Rouvier, 1977, 1994) under extensional conditions (Mauduit, 1978; Maury *et al.*, 2000; Jallouli *et al.*, 2003).

Two generations of post-nappe continental to open-marine extensional basins overly the nappe pile and the magmatic rocks. They are both controlled by reactivation of NE-SW normal faults. The Sidi Driss and Douahria Messinian basins were inverted at the end of the Messinian period to form synclines (►Fig. 8.3). They were composed of Late Miocene algal carbonates and/or evaporites (Decrée *et al.*, 2008b), subsequently replaced by Pb-Zn sulfides, consisting of Messinian (or younger) SEDEX Pb-Zn deposit. The ore is characterized by galena and sphalerite, which is associated with As-bearing marcasite and pyrite, celestite, and barite. Mineralizing fluids have a maximum estimated temperature of 150°C and are most likely influenced by Late Miocene magmatic activity (e.g., Messinian basalts, Decrée *et al.*, 2008b). The Mio-Pliocene (or younger) Tamra basin unconformably overlies Eocene folded marls, the Oued Belif breccia (south) and the Sidi Driss basin (east), (►Fig. 8.3; Berthon, 1922; Dermech, 1990; Decrée *et al.*, 2008a, 2010). The Tamra Formation is a siliciclastic sequence (►Fig. 8.4) enriched in iron (►Fig. 8.5a), which is interbedded with white clay lenses, the abundance of some of them having defined a specific “White Clay Zone” (►Figs. 8.4 and 8.5b, c). In the area, two other ferruginous post-nappe basins are: (1) the Late Miocene Moktha el Hadid Formation, where hematite-rich halos surround basaltic flows, and (2) the Pliocene El Harch basin containing Tamra-like deposits (►Figs. 8.2 and 8.3; Decrée *et al.*, 2008a).

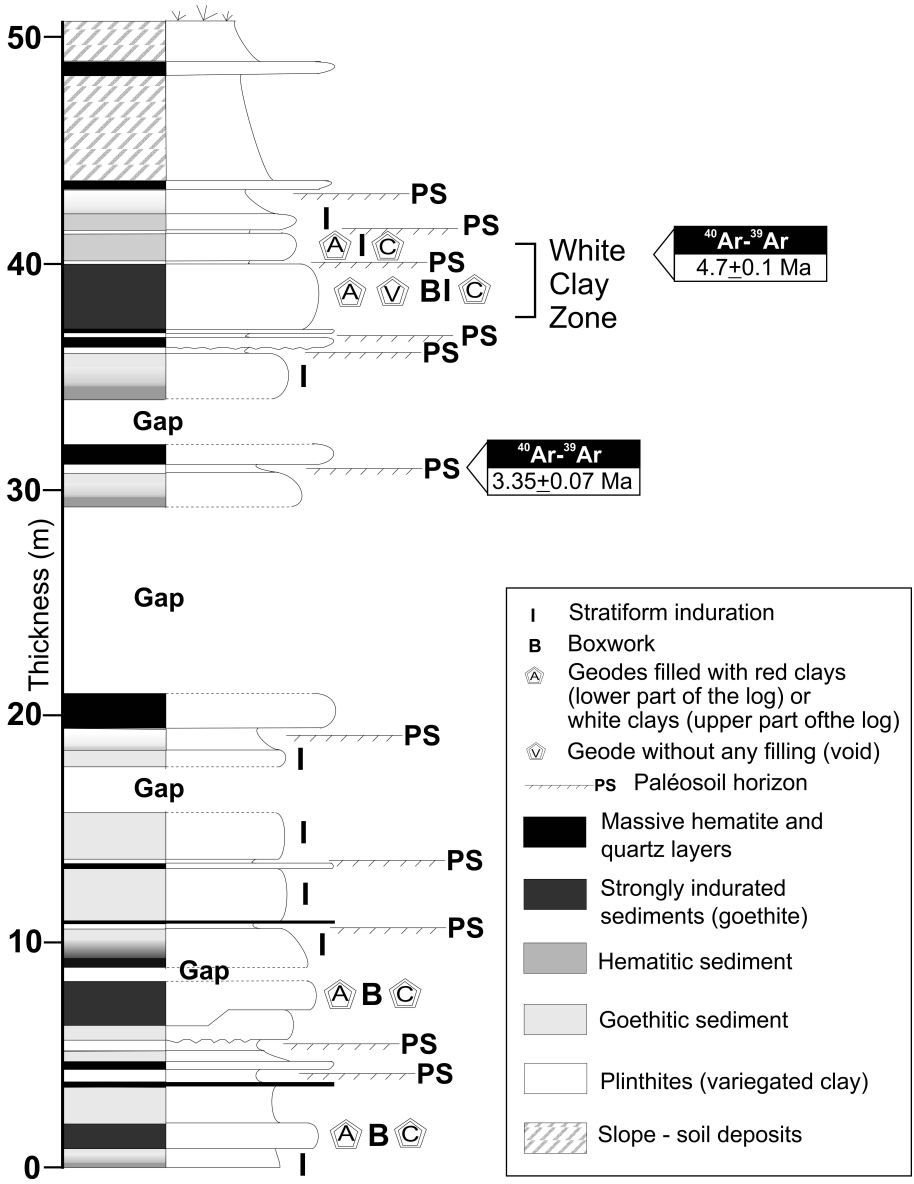

►**Fig.8.4** Synthetic log of the Tamra Formation and location of the "White Clay Zone" (Decrée *et al.*, 2008a). $^{40}Ar/^{39}Ar$ ages of hollandite group minerals are also indicated (Decrée *et al.*, 2010).

Middle to Late Miocene magmatic intrusions have enhanced hydrothermal fluid circulation that may be (at least partly) responsible for the numerous mineralizing events observed in the area (Decrée *et al.*, 2013, 2014). Both magmatism and hydrothermal mineralization are related to a set of fractures inherited from the Variscan basement (Piqué *et al.*, 2002). Miocene diapiric extrusions and late basaltic

sills and dikes follow a NE-SW direction corresponding to the Ghardimaou-Cap Serrat sinistral shear zone (G-CS in ►Figs. 8.1 and 8.3). This major shear zone, thought to be of lithospheric scale (Decrée *et al.*, 2016), directly or indirectly controlled several series of local mineral occurrences and deposits, such as the Oued Belif breccia and the Late Miocene Pb-Zn sedimentary exhalative (SEDEX) deposits of Sidi Driss and Douahria (Decrée *et al.*, 2008b, 2013, 2014, 2016). In that context, the structural discontinuities (normal faults, thrust sheet boundaries, magmatic contacts and deformed plutons) are likely to have served as major fluid conduits (►Fig. 8.5a; Decrée *et al.*, 2008b). Other Cu-Ag-Au deposits are located along minor WSW-ENE fault zones in the area (Decrée *et al.*, 2013, 2016). The Nefza area is still hydrothermally active, with numerous hot springs from 35 up to 70°C (Gharbi, 1977; Zouiten, 1999) and regional thermal gradients up to 100°C/km (Jallouli *et al.*, 1996). Low discharge springs from 26 to 27°C are present in the Sidi Driss (Stefanov and Ouchev, 1972; Dermech, 1990) and Tamra deposits (Decrée *et al.*, 2010).

8.2.2 Tamra Fe-Mn deposit

The Fe-Mn Tamra mine is known since Roman times (Berthon, 1922) for its high content in iron (avg. 50 wt.% Fe, Gottis and Sainfeld, 1952). Since 1884, it has been intensively mined as some other parts of the Nefza mining district. Today, the low quality of the iron ore (~1% wt. As) allows Tamra sediments to be used in the local cement industry. The eastern part of the deposit, which is overlying the Sidi Driss deposit, shows higher content of manganese oxides. It has been described as a distinct zone of the deposit (►Fig. 8.3; Manganese Zone, MnZ; Decrée *et al.*, 2008a).

The Tamra Formation is a 50-m thick siliciclastic and/or volcanoclastic series of ferruginous sediments, where almost all sedimentary textures have been overprinted by Fe(-Mn) oxide assemblages (►Fig. 8.5a, Decrée *et al.*, 2008a). Despite the lack of sedimentary structures, the whole Formation comprises an irregular succession of few centimeters to few meters thick shallowing-upward sequences, finishing by a subaerial/pedogenesis episode at the top of each sequence (►Fig. 8.4 and 8.5a). Each sequence comprises: (1) a basal 1-m thick highly indurated siliciclastic sedimentary unit composed of hematite and quartz, with an erosional base (*lower horizon*); (2) an intermediate fining-upward sequence of a few meters thick made up of reddish hematite-bearing sediments at the base, and yellowish goethite-bearing sediments at the top (*intermediate horizon*); and (3) an upper variegated mottled clay horizon, a few decimeters thick (*upper horizon*). Synsedimentary weathering/pedogenesis is thus well attested in the Tamra Formation.

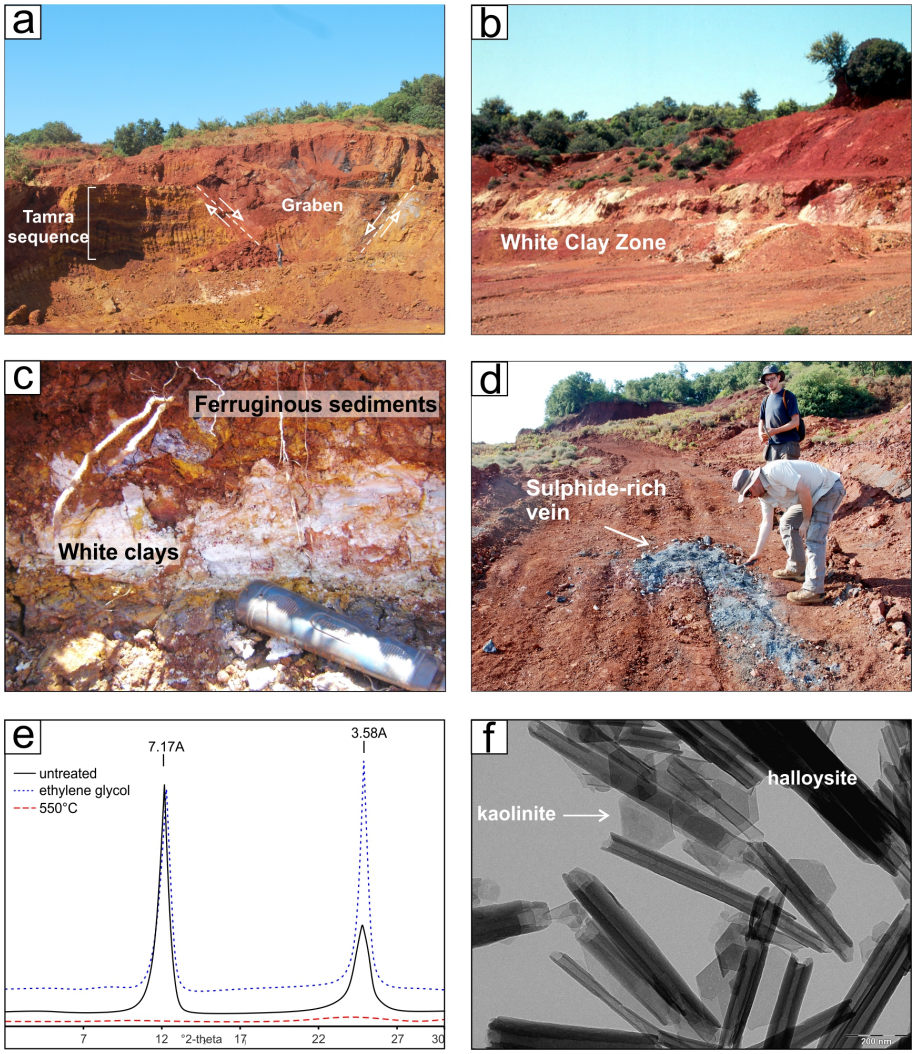

►**Fig.8.5 a.** Overview of the ferruginous Tamra sequence affected by normal faults. **b.** Iron mine of Tamra showing the "White Clay Zone" in the ferruginous sediments. **c.** Focus on a white clay level embedded in the ferruginous matrix. **d.** Late sulphide-rich vein (pyrite, galena and siderite) crosscutting the whole Tamra Formation. **e.** XRD pattern of Tamra white clays (sample 14TAM09) showing the typical 7.17A reflection and 3.59A harmonic. **f.** TEM view of typical halloysite nanotubes and hexagonal flakes of kaolinite in sample HT1 (Decrée *et al.*, 2008a; Moussi *et al.*, 2011).

The age of the Tamra Formation is not precisely known, but is supposedly Mio-Pliocene or younger according to the 1:50000 geological map of Nefza (Rouvier, 1977, 1994) and the ^{40}Ar-^{39}Ar ages of 4.7 $\pm$0.1 Ma and 3.35 $\pm$0.07 Ma obtained on late Mn oxides (►Fig. 8.4, Decrée *et al.*, 2010). These latter ages indicate a *per descensum* evolution of a weathering front from the upper part (older age) to the lower

part (younger age), as well as a rapid deposition of the Tamra Formation during a regional extensional tectonic regime (►Fig. 8.5a, Bouaziz *et al.*, 2002). Bouzouada (1992) describes this basin as a synclinal structure with E-W to ENE-WSW axis to the west, and NNE-SSW to the east. A fault network of directions N-S to N140, N10 to N40 and E-W has affected this basin and has played an important role in the variation of facies both vertically and laterally. The normal faults N-S, N140 and E-W are indeed synsedimentary faults (►Fig. 8.5a).

The primary early diagenetic and/or pedogenic pre-concentration of iron is linked to meteoric fluids feeding temporary aquifers, which were involved in seasonal Fe concentration processes (►Fig. 8.6; *Stage 1*; Decrée *et al.*, 2008a). Primary pedogenesis was reinforced by a recurrent progressive and pervasive polycyclic pedogenesis of each sedimentary sequence (Decrée *et al.*, 2008a). It corresponds to the main pedogenic Fe event that has provided the current iron ore in the Tamra deposit (►Fig. 8.6; *Stage 2*). A primary Fe-rich sedimentary deposition could also be considered given the nearby Oued Belif breccia (Decrée *et al.*, 2008a). Decrée *et al.* (2010) have proposed a refined analyzes of the Mn mineralization and the effect of hydrothermal fluids on the chemistry of the ore after the primary pedogenic/diagenetic enrichment. According to them, this hydrothermal enrichment was superimposed on the weathering conditions found in the Tamra sequence at the same time, and has led to the formation of Mn oxides, first with hollandite, romanechite and Sr-cryptomelane at 4.7$\pm$0.1 Ma (►Fig. 8.6; *Stage 3*), and then coronadite, chalcophanite, amorphous Mn oxides and kaolinite at 3.35$\pm$0.07 Ma (►Fig. 8.6; *Stage 4*). Mn oxides extensively occur as coatings filling fractures, creating *per descensum* structures commonly found in other supergene manganese deposits of North Africa (Dekoninck *et al.*, 2016b, 2016a, see chapter 7; Verhaert *et al.*, 2018, see annex 3, this thesis). The hydrothermal contribution is supported by enrichment in Fe, Mn, Pb, Zn and As in the later stages (►Fig. 8.6; *Stages 3 and 4*), and is considered to be the result of fluid-driven hydrothermal circulation in the underlying Sidi Driss Pb-Zn deposit, which is enriched in those elements (Decrée *et al.*, 2008a, 2008b, 2010). Such hydrothermal activity is also supported by (1) the high regional thermal activity, (2) the high geothermal gradient (Jallouli *et al.*, 2003), (3) the emplacement of late sulphide deposits (►Fig. 8.5d; Decrée *et al.*, 2008b, 2016), and (4) the occurrence of thermal springs throughout the district (e.g., Decrée *et al.*, 2010). Intense local fracturing has allowed for the circulation of hydrothermal and meteoric fluids, which have promoted the alteration of sand and the formation of clays (►Fig. 8.5a). Messinian magmatism could have influenced the circulation of mineralizing fluids at least during the earlier stages of the ore formation. The occurrence of late and reduced mineral veins (galena, pyrite and siderite) crosscutting the whole Tamra Formation contrasts with the highly oxidized minerals of the Tamra deposit (►Fig. 8.5d). These veins probably reached temperatures close to 80°C in the Sidi Driss sulphide deposit, as noted by Decrée *et al.* (2008b), and 30°C in several recent springs of the Nefza district (Stefanov and

Ouchev, 1972; Gharbi, 1977; Dermech, 1990; Zouiten, 1999). Three acidic springs occur in the Tamra mine (5–6 pH units, Decrée *et al.*, 2010).

8.2.3 Kaolinite-halloysite formation

White clay assemblages composed of kaolinite and halloysite have been observed in several spots in the Tamra deposit, but mainly in the "White Clay Zone" with relatively low lateral extension (►Figs. 8.4 and 5b, c). Kaolinite-halloysite usually fills open cavities or porosity, and replaces primary 2:1 smectites (Decrée *et al.*, 2008a). Their formation is considered to be the result of early pedogenic/weathering processes affecting each sequence, as well as the downward percolation of meteoric fluids during late weathering/diagenetic stages, the latter being observed only in the upper part of the Tamra sequence (Decrée *et al.*, 2008a). Most of the kaolinite-halloysite levels are associated with early mineralization stages (►Fig. 8.6; *Stages 1 and 2*). However, minor amounts of these minerals could be intimately mixed with late stage Mn oxides (►Fig. 8.6; *Stage 4*) suggesting that they are connected to hydrothermal inputs (Decrée *et al.*, 2010).

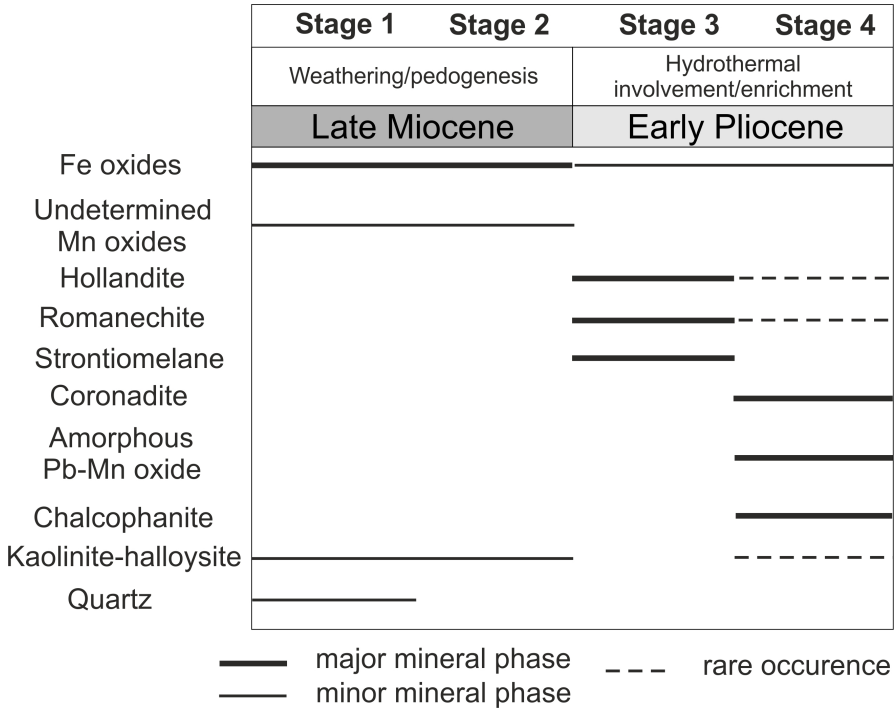

►**Fig.8.6** Paragenetic sequence of the mineral phases showing the 4 stages observed in the Tamra Fe-Mn deposit (modified after Decrée *et al.*, 2010).

White clays are present in the *intermediate horizon* defined by Decrée *et al.* (2008a), where they form micro-aggregates in association with Fe(III) minerals. The horizon is indurated by hematitic sediments at the base and goethitic sediments at the top, which are responsible for geodic cavities filled by kaolinite and halloysite. This *intermediate horizon* undergoes a nearly complete weathering/alteration, which has led to a heavy remobilization of iron and the formation of goethite and hematite, as well as the neoformation of 1:1 white clays by recombination of released Si and Al. The occurrence of white clay spots in the mottled gray clay *upper horizon* (only a few centimeters thick) would be linked to the transformation of primary 2:1 smectites in cation-free 1:1 clays than to their neoformation in cavities as it was observed in the *intermediate horizon* (Decrée *et al.*, 2008a). A late diagenetic evolution phase has turned the upper 20 m of the Tamra Formation into pure Fe-free white 1:1 clays, coevally to the neoformation of Mn oxides. The reconcentration and/or precipitation of pure Fe-free white clays at the interface between lithologies with contrasting permeability is linked to the destabilization of clay aggregates in the upper part of the profile, to their migration, and finally to their precipitation in cavities at the interface with impervious layers. According to this process, halloysite could be locally dominant (►Fig. 8.5b, c; Decrée *et al.*, 2008a). Some similarities with the Boukhchiba and Douahria mines (location in ►Fig. 8.3) can be found taking into account the occurrence in both deposits of white clay levels and nodules.

8.3 Materials and methods

8.3.1 Mineralogical analyses

Mineralogical analyzes of bulk rock samples (14MnTAM, 14TAM07, 14OU03, OUCHTATA, 14SB01, 14ET02, 14ET03, EM04/11, OB48-79, 14CEA02, 14OB02, 14BK11, BR01, 14AA02, 14BK01, OB45-78, OB45-42) and oriented aggregates (14TAM09, 14SB02, 14AD01, 14TAM16, 14ME02, 14AA02, 14BK01) have included X-ray diffraction (XRD) at the PC2 platform (UNamur) using an X-ray Panalytical X'Pert Pro and a PHILLIPS diffractometers (CuKα radiation; ►Table 8.1). Oriented aggregates were treated with ethylene glycol and heated at 550 ºC, following the methodology of Holtzapffel (1985; ►Fig. 8.5e). Other mineralogical analyzes from Moussi (2012; ABT1, CAT7.5, CAT7, ZMNWL8, OMS2) and Decrée *et al.* (2008a; CP04-3, CP04-35) have been taken into account. Clay samples were further investigated at the University of Namur (Belgium), using a transmission electron microscope Jeol JEM 100 CX II, with an emission source of 100 kV. Samples must be transparent to electrons. Hence, depending on their nature, their thickness had to be less than 30–100 nm, a condition which was generally met

with diluted suspensions of natural clays. A drop of the suspension is air dried on a Cu grid, coated with a thin carbon film in which microscopic holes were drilled.

8.3.2 Stable isotope geochemistry

A total of twenty-nine samples were analyzed: eighteen were samples collected in the field (14TAM07, 14TAM09, 14MnTAM, 14TAM16, 14OU03, OUCHTATA, 14SB01, 14SB02, 14AD01, 14ET02, 14ET03, 14ME02, 14CEA02, 14OB02, 14BK01, 14BK11, BR01, 14AA02), and eleven were previously collected by Decrée *et al.* (2008b; CP04-3, CP04-35), Moussi (2012; ABT1, CAT7.5, CAT7, ZMNWL8, OMS2), Ben Abdallah (2013; OB45-78, OB45-42, OB45-79) and the "Office National des Mines de Tunisie" (ONM; EM04/11; ►Table 8.1; ►Figs. 8.1 and 8.3). The twenty-nine samples were analyzed at the Institute of Earth Surface Dynamics of the University of Lausanne (Switzerland) for their oxygen and hydrogen isotope compositions. Silicates (quartz, feldspars, clays; ►Table 8.1) and oxides (goethite-hematite) were analyzed for their $\delta^{18}O$ values in all rock types (rhyodacites, claystone, sandstone, marls, skarns). Hydrogen isotope compositions were measured on hydrous silicates (kaolinite-halloysite), and hydroxides (goethite-hematite; ►Table 8.1). Five samples of the white clay levels (outcrop 11 in ►Fig. 8.3; ABT1, 14TAM09, CAT7.5, CAT7, ZMNWL8) and four of Fe(III) minerals (outcrop 11 in ►Fig. 8.3; 14MNTAM, CP04-3, CP04-35, 14TAM07) were collected respectively in the kaolinite-halloysite levels and goethite-hematite concretions in the Tamra deposit. In order to compare the conditions of the Tamra ores with other places in the Nefza district, two samples with high goethite-hematite content from Triassic weathered pyrites (outcrop 5 in ►Fig. 8.3; 14OU03, OUCHTATA), which were contained in carbonates, were added to the Fe oxide set, as well as three samples of the ferruginous deposits from Oued Belif (outcrops 9, 10 and 13 in ►Fig. 8.3; 14OB02, 14BK11, BR01) In addition, other samples were collected from the bedrock of the Nefza area to analyze the stable isotopic composition of oxygen and hydrogen. Finally, other samples were analyzed for their H and O stable isotope compositions (►Table 8.2): samples of two granodiorites in borehole OB45 at Ragoubet Sidi Ahmed (outcrop 8 in ►Fig. 8.3; OB45-78, OB45-42), two rhyodacites at Boukhchiba (outcrop 13 in ►Fig. 8.3; 14BK01) and Ragoubet Sidi Ahmed (outcrop 8 in ►Fig. 8.3; 14AA02), two skarns at Chabet El Ain (outcrop 6 in Fig. 2) and Ragoubet El Alia (outcrop 7 in ►Fig. 8.3, 14CEA02), 5 marls at Tamra mine (outcrop 12 in ►Fig. 8.3; 14TAM16), Tamra village (outcrop 14 in ►Fig. 8.3; 14ET02, 14ET03, EM04/11) and Ain Sebaa (outcrop 3 in ►Fig. 8.1; 14ME02), two clayey levels at Om-Tebal (outcrop 4 in ►Fig. 8.1; OMS2) and Sidi Bader (outcrop 2 in ►Fig. 8.1; 14SB02) and two sandstones of the Oligocene Numidian sandstone at Ain Drahan (outcrop 1 in ►Fig. 8.1; 14AD01) and Sidi Bader (outcrop 2 in ►Fig. 8.1; 14SB01).

All silicates and Fe-hydroxides of the Nefza area were analyzed for their oxygen isotope compositions. These analyzes were obtained using a CO_2-laser fluorination line coupled to a Finnigan MAT 253 gas source mass spectrometer according to a method, which was adapted after Vennemann *et al.* (2001). Between 2 and 3 mg of non-carbonated powder were loaded onto a small Pt-sample holder and pumped out to a vacuum of about 10^{-6} mbar. After prefluorination of the sample chamber, the samples were heated with a CO_2-laser in the presence of pure F_2. Excess F_2 was separated from the O_2 produced by conversion to Cl_2 by KCl held at 150°C. The extracted O_2 was then introduced into the inlet of the mass spectrometer. Oxygen isotope compositions are given in the standard δ-notation and are expressed relative to the Vienna Standard Mean Ocean Water (VSMOW) in permil (‰). Replicate oxygen isotope analyses of the LS-1 in-house quartz standard gave an average value of 18.10 ± 0.06‰ (2SD, n = 4) for $\delta^{18}O$. The oxygen and carbon isotope compositions of carbonates (marls, skarns) were determined on 100 to 1200 µg whole rock or carbonate powders using 100% H_3PO_4 dissolution at 70°C with an automated GasBench II preparation unit attached to a Thermo Finnigan DeltaPlus XL mass spectrometer and a He-carrier gas system (Spötl and Vennemann, 2003). The results are given in the standard δ-notation, which is expressed relative to VSMOW in permil (‰) for oxygen and relative to VPDB for carbon. Reproducibility for the analyses estimated based on repeated analyses of the in-house Carrara Marble standard (CM; n = 9), gave an external precision (1SD) of ±0.11 ‰ for $\delta^{18}O$ and 0.08 ‰ for $\delta^{13}C$.

The hydrogen isotope composition of clay, Fe oxides and bulk samples together with their water content were determined with a zero-blank auto-sampler and a High-Temperature Conversion Elemental Analyzer (TC-EA; Bauer and Vennemann, 2014) after drying in a vacuum desiccator overnight. The amount of powder needed for Fe oxides is between 2 and 3 mg, 0.5-1.0 mg for kaolinite samples, 3.0-4.0 mg for clayey samples and 4.0-5.0 mg for whole rock materials. Marls were decarbonated before the measurements. In-house reference materials of biotite (G1; δD = -64 ±1.6 ‰) and kaolinite (K-17; δD = -125 ±1.3 ‰) were used to calibrate the measured isotopic compositions (Bauer and Vennemann, 2014). The isotopic composition of hydrogen is expressed in the "δ-notation", relative to VSMOW in permil (‰). All the measurements of samples and standards were replicated but only their average value are presented in ►Table 8.1.

►**Table 8.1** Stable isotope composition of the Nefza area rocks. *: replicate analyses, +: decarbonated sample, WR: whole rock sample, <2 µm: oriented aggregates with <2 µm fraction preparation, Q: quartz, Kaol: kaolinite, I: illite, Gt: goethite, Hem: hematite, Py: pyrite, H: halloysite, Cal: calcite, Fsp: feldspars, Sm: smectite, Chl: chlorite, I-Sm: intermixed layers of illite-smectite, Pl: plagioclase, Kfs: K-feldspar, Mcs: micas, Gs: gypsum, Am: amphibole. ONM sample comes from drill cores of the "Office National des Mines". See ►Figs. 8.1 and 8.3 for the location of the sample (column 3).

Label	Material type	Outcrop	Age	Mineralogy	$\delta^{18}O_{VSMOW}$ (‰)	δD_{VSMOW} (‰)	H_2O wt. %	$\delta^{18}O_{carb\ VSMOW}$ (‰)	$\Delta^{13}C_{car\ b\ VPDB}$ (‰)	Material origin
ABT1 (<2 µm)	White clay	(11)	Late Miocene - Pliocene	Kaol, H	19.2	-91	9.8			Moussi (2012)
14TAM09 (<2 µm)					21.9	-72	14.9			This issue
CAT7,5 (<2 µm)					21.3	-93	9.7			
CAT7 (<2 µm)					23.8	-123	16.4			Moussi (2012)
ZMNWL8 (<2µm)*					24.3	-95	10.3			
					25.4	-70	17.2			
14MnTAM (WR)	Fe ore	(5)	Trias	Gt	-2.0	-127	12.7			This issue
CP04-3 (WR)				Hem, I, I-Sm, Q	-1.0	-156	7.4			Decrée *et al.* (2008b)
CP04-35 (WR)				Gt, Hem, I, I-Sm, Q	5.1	-142	3.2			
14TAM07 (WR)				Gt, Hem	-1.3	-132	6.0			
14OU03 (WR)				Gt, Py, Q	N.A.	-132	5.4			This issue
OUCHTATA (WR)				Gt, Hem	0.2	-125	8.5			
OMS2 (WR)	Claystone	(4)		Q, Kaol, I	18.8	-72	8.4			Moussi (2012)
14SB02 (<2 µm)		(2)		Q, Kaol, I	16.1	-63	8.9			
14AD01 (<2 µm)*	Sandstone	(1)	Oligocene (Numidian)	Q, Sm, Kaol	18.0 18.4	-59	11.0			This issue
14SB01 (WR)*		(2)		Q, Kaol	14.5 14.6	-75	1.4			
14TAM16 (<2 µm)	Marl	(12)	Lutetian-Bartonian		23.5	-61	14.8	26.6	1.10	
14ET03 (WR)	Marl (septaria)	(14)		Cal, Q, Fsp	-	-96	-	28.8	-0.12	

►**Table 8.1** suite.

Label	Material type	Outcrop	Age	Mineralogy	$\delta^{18}O_{VSMOW}$ (‰)	δD_{VSMOW} (‰)	H_2O wt. %	$\delta^{18}O_{carb\ VSMOW}$ (‰)	$\Delta^{13}C_{carb\ VPDB}$ (‰)	Material origin
14ET02 (WR)	Marl (weathered)	(14)	Lutetian-Bartonian	Cal, Q, Kaol	-	-96	11.9	27.4	-1.30	This issue
14ET02+				Q, Kaol	-	-72	-	-	-	
EM04/11 (WR)				Q, Cal, Kaol, Sm	-	-64	7.7	23.8	-0.21	ONM
14ME02 (< 2µm)		(3)	Albian-Maastrichtian	Q, I	25.8	-65	4.5	25.6	-0.78	This issue
OB48-79 (WR)	Skarn	(7)	Serravalian-Tortonian	Cal, Gp, Am, Q	27.4	-67	3.2	28.2	1.23	Ben Abdallah (2013)
14CEA02 (WR)	Skarn (weathered)	(6)		Cal, Q, Fsp	-	-92	0.5	27.6	1.05	
14OB02 (WR)	Oued Belif breccia	(10)		Gt, Kfs, Q	3.9	-132	9.4			
14BK11 (WR)		(13)		Gt, Kfs	-1.6	-132	12.4			
BR01 (WR)		(9)		Gt, Kfs, Q	5.9	-113	8.3			This issue
14AA02 (<2 µm)	Rhyodacite (weathered)	(8)	<Tortonian	Sm, Kaol	20.7	-68	9.1			
14BK01 (WR)	Rhyodacite	(13)		Q, I, Kaol, Sm, Chl	15.9	-72	5.6			
14BK01 (<2 µm)*					18.8 19.3	-48 -48	13.3			
OB45-78 (WR)	Granodiorite	(8)	Serravalian-Tortonian	Pl, Kfs, Q, Mcs	15.1	-84	0.4			Ben Abdallah (2013)
OB45-42 (WR)	Granodiorite (weathered)		<Tortonian	Kfs, Pl, Q, Mcs	16.0	-80	0.7			

►**Table 8.2** Chemical composition of the white clays CAT7, CAT7.5, ABT1 and ZMNWL8 determined by X-ray fluorescence, using a Panalytical Axios Dispersive XRF Spectrometer. The loss-on-ignition was evaluated from the weight difference between samples heated at 100ºC and 1000ºC. - = not analyzed. The results are expressed in weight concentration percent of oxides (Moussi *et al.*, 2011; Moussi, 2012).

	CAT7	CAT7,5	ZMNWL8	ABT1
SiO_2	41.37	43.53	43.64	39.38
Al_2O_3	36.14	39.15	39.16	36.55
Fe_2O_3	4.56	0.24	0.53	0.52
MgO	0.08	0.04	-	-
MnO	<0.01	0.01	-	-
CaO	0.04	0.05	0.1	0.1
Na_2O	0.07	0.03	-	-
K_2O	0.07	<0.02	0.42	0.03
P_2O_5	<0.01	0.03	0.04	0.03
TiO_2	0.06	0.01	0.03	0.02
H_2O	17.6	16.9	14.2	22.9
Total	100	100	98.12	99.53

8.3.3 Pb-Pb isotope measurements

Pb isotopic analyses were performed on five kaolinite-halloysite samples (►Table 8.3) at the Laboratoire G-Time (Université Libre de Bruxelles, ULB, Belgium). The total acid dissolution and lead purification were realized according to the procedure described in Weis *et al.* (2006) and Renson *et al.* (2011). The Pb isotopes were measured on a Nu Plasma Multi-Collector Inductively Coupled Plasma Mass Spectrometer (MC-ICP-MS from Nu Instruments) by applying a static multicollection in dry mode. Tl standard solution was added as dopant to all samples and Pb standards (Pb-Tl ratio of 4 or 5) in order to automatically correct the Pb isotopic ratios for mass fractionation bias. Also, the sample standard bracketing method was applied to correct instrumental drift. During the period of analyses, repeated measurements of the Pb NBS981 standard (n = 22) gave average values of $^{208}Pb/^{204}Pb$ ($\pm 2\sigma_n$; 36.7134 $\pm$ 0.0008), $^{207}Pb/^{204}Pb$ (15.4968$\pm$ 0.0003) and $^{206}Pb/^{204}Pb$ (16.9406 $\pm$ 0.0004). All the reported values were normalized using the recommended values from Galer and Abouchami (1998): $^{208}Pb/^{204}Pb$ (36.7219 $\pm$ 0.0044), $^{207}Pb/^{204}Pb$ (15.4963$\pm$ 0.0016) and $^{206}Pb/^{204}Pb$ (16.9405 $\pm$ 0.0051).

►**Table 8.3** Lead isotope ratio of kaolinite-halloysite samples of the Tamra deposit. 2se refers to 2 standard errors, *: replicate analyzes.

Sample	Age	$^{208}Pb/^{204}Pb$	2se	$^{207}Pb/^{204}Pb$	2se	$^{206}Pb/^{204}Pb$	2se
14TAM09 (<2 µm)	<Zanclean	38.8671	0.0026	15.6681	0.0009	18.7720	0.0010
ABT1		38.8403	0.0022	15.6629	0.0009	18.7716	0.0010
CAT7		38.8446	0.0015	15.6699	0.0006	18.7611	0.0006
CAT7,5*		38.8654	0.0016	15.6687	0.0006	18.7786	0.0007
		38.8592	0.0014	15.6679	0.0006	18.7785	0.0006
ZMNWL8		38.8623	0.0015	15.6670	0.0006	18.7763	0.0007

8.4 Mineralogy

Whole rock samples of ABT1, CAT7, CAT7.5, ZMNWL8 (Moussi, 2012) and 14TAM09 had a composition of 100% of phyllosilicates. However, some variations in the SiO_2 content of the chemical composition of ABT1, CAT7, ZMNWL8 and CAT7.5 might indicate the presence of quartz (►Table 8.2; Moussi *et al.*, 2011; Moussi, 2012). When heated by laser ablation in the oxygen isotope protocol, these samples show a small amount of quartz grains. The increase in the Fe_2O_3 content, especially in sample CAT7, and the occurrence of pinkish/reddish tints in the white clays might be due to disseminated co-genetic Fe oxides (►Fig. 8.5c; ►Table 8.3). The fraction <2 µm (Brindley and Brown, 1980) consists of kaolinite (►Fig. 8.5e, ►Table 8.1), while halloysite is evidenced by TEM images, which shows the typical tube structure in association with hexagonal flakes of kaolinite (►Fig. 8.5f, Caillère *et al.*, 1982).

8.5 Stable isotope results

All new following results focus on the Tamra ores, first presenting the kaolinite-halloysite white clays (►Fig. 8.7a), and then the associated Fe oxides $\delta^{18}O$ and δD values (►Fig. 8.7b). These items are finally integrated in the large set of $\delta^{18}O$ and δD values of the country rock types (►Fig. 8.7c; magmatic, metamorphic and sedimentary), in order to have a better view of these stable isotopes in the Nefza area. In addition, new Pb-Pb isotopes of the kaolinite-halloysite are considered in the set of data already studied by Decrée *et al.* (2013, 2014; ►Fig. 8.8).

8.5.1 $\delta^{18}O$—δD values

The kaolinite-halloysite samples are strongly enriched in ^{18}O, with $\delta^{18}O$ values from 19.2 to 25.4 ‰, while δD values are between -70 and -123 ‰ (►Fig. 8.7a; ►Table 8.1). The effect of detrital quartz on the isotopic composition would be a decrease in the $\delta^{18}O$ values, considering that quartz from high temperature rocks (magmatic and metamorphic rocks) and of non-diagenetic origin would generally have lower $^{18}O/^{16}O$ ratios compared to clay minerals formed at low temperatures (e.g., (Savin and Epstein, 1970). In the diagram (►Fig. 8.7a), all kaolinite-halloysite samples plot on the right side of the “kaolinite line” defined by Savin and Epstein (1970), which is considered to be the normal trend for kaolinite in equilibrium with meteoric waters at 25°C.

In the Tamra deposit, goethite and hematite are often associated with small amounts of quartz and clays (Decrée *et al.*, 2008a). Despite that the absolute $\delta^{18}O$ and

δD values differ from those of the kaolinite-halloysite, they both have similar trends. Two samples plot along the 25°C line of Yapp (1990), which is considered as an equivalent of the kaolinite line for goethite ($\delta^{18}O$ = -1.3 and -2.0 ‰, δD = -127 and -132 ‰), while two other samples are close to the temperature lines that would correspond to fractionations established at 0°C ($\delta^{18}O$ = -1.0 and 5.1, and δD = -142 and -156 ‰; ►Fig. 8.7b). Some of the goethite-hematite were clearly in equilibrium with meteoric waters, as they plot on the 25°C line. However, some of them could be in disequilibrium with temperatures below 25°C (►Fig. 8.7b), as already shown in kaolinite-halloysite samples. These goethite and hematite could also have been contaminated by small amounts of quartz and clay impurities (►Table 8.1). The comparison of Tamra iron ores with other Fe oxides in the district shows that Ouchtata goethite, which are hosted in Triassic carbonates, plots along the 25°C line (►Fig. 8.7b) and obviously results from the weathering of Triassic pyrite. However, some Fe oxides of the Oued Belif breccia have higher $\delta^{18}O$ values compared to the Ouchtata weathering Fe oxides, which may be explained by a small quantity of quartz and K-feldspars in the ferruginous matrix (Decrée *et al.*, 2013), or even by the influence of hydrothermal fluids that could have precipitated the Fe oxides (►Fig. 8.7b and c; ►Table 8.1).

Plutonic and volcanic rocks in the Nefza area have high $\delta^{18}O$ values for igneous rocks of granitic composition (15.1 to 16.0 ‰) and δD (-72 to -84 ‰), when compared to values compiled by Hoefs (2009). This might suggest some late low-temperature alterations of these rocks. Alternatively, they might include a higher contribution of the S-type granites (e.g., Hoefs, 2009), as suggested by the peraluminous trend of some rhyodacites (Decrée *et al.*, 2014). The clay fraction of their weathering products has higher $\delta^{18}O$ and δD values, with a range between 19.0 and 20.7 ‰, and -48 and -68 ‰ respectively (►Fig. 8.7c). These values differ from the Tamra white clays $\delta^{18}O$ and δD, probably because the mineral assemblage is composed of smectite, kaolinite, illite and chlorite (►Table 8.1).

The metamorphic rocks in the close vicinity of the Tamra deposit are represented by scarce skarns, when in contact with plutonic rocks and Cretaceous to Eocene marls (►Fig. 8.3, Decrée *et al.*, 2013). The $\delta^{18}O$ values of these skarns are the highest of the area, probably because the primary carbonates were deposited in a marine environment. From bulk rocks, the separated carbonate fractions have $\delta^{18}O$ values between 27.6 to 28.2 ‰, while the δD values of the hydrous silicate fraction vary from -67 to -92 ‰ (►Fig. 8.7c; ►Table 8.1). Therefore, only clay minerals contain hydrogen in their structure and provide enough hydrogen to be properly analyzed for their δD values.

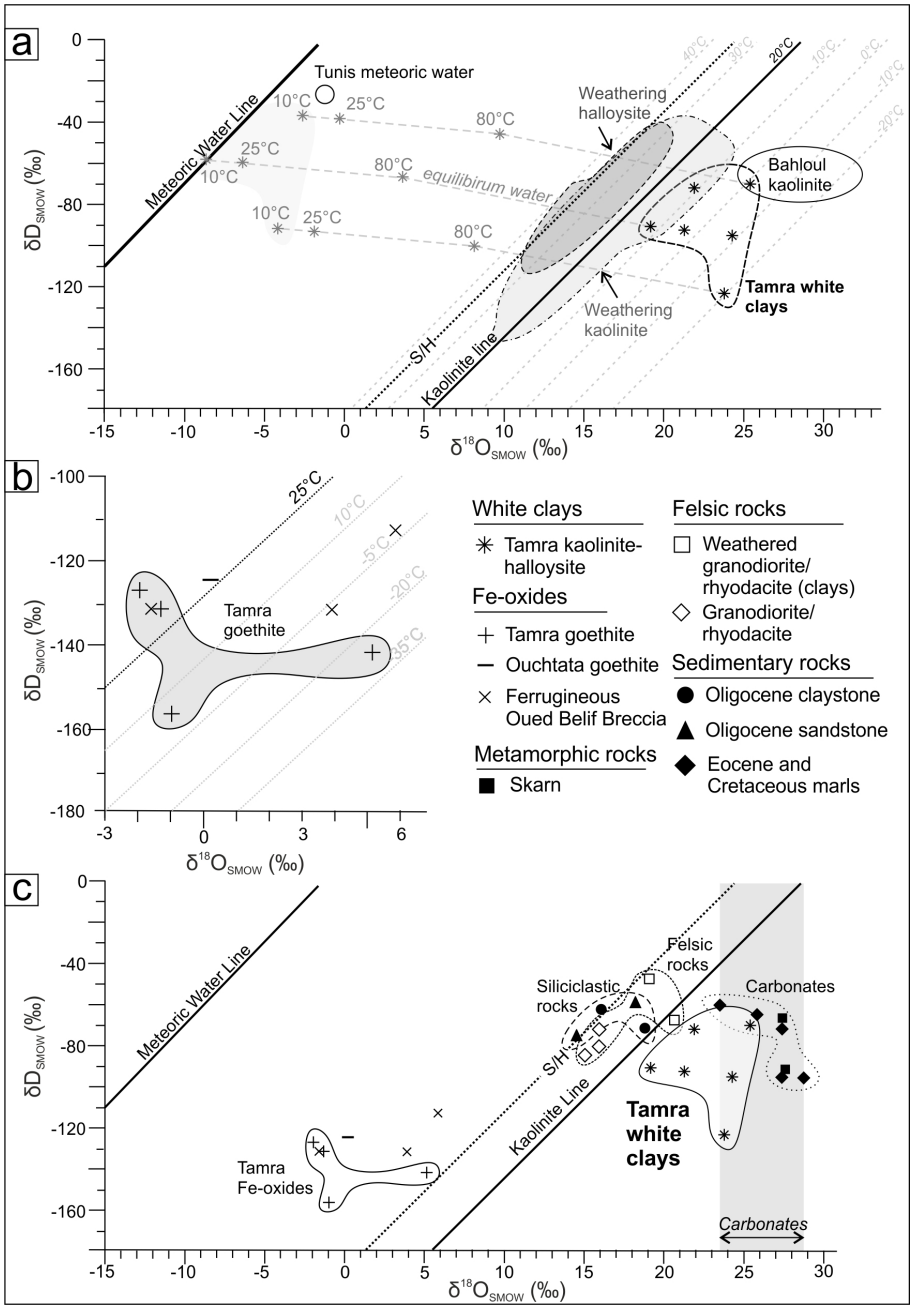

►**Fig.8.7 a.** δD and $\delta^{18}O$ plot of kaolinite-halloysite samples of the Tamra Formation, with known data of weathering kaolinite (gray area) and halloysite (dark gray area, Sheppard and Gilg, 1996) as well as kaolinite of the Bahloul Formation hosting the Bou Grine Pb-Zn deposit (Bechtel *et al.*, 1999). Calculated equilibrium waters at 10°C, 25°C and 80°C are represented by light gray stars connected by dashed lines. The meteoric water, kaolinite weathering (Savin and Epstein, 1970) and supergene/hypogene lines (S/H, Sheppard and Gilg, 1996) are given for

reference. Intermediate temperature lines are calculated from equations in Sheppard and Gilg (1996). **b.** Goethite and hematite samples of the Nefza area in a δD and $\delta^{18}O$ plot. Temperature lines are calculated from Yapp (1990). **c.** δD and $\delta^{18}O$ plot showing the stable isotope compositions of felsic, siliciclastic and carbonate rocks with Fe oxides and white clays of the Tamra mine (►Table 8.1). Carbonate values are indicated in gray shades on the right of the diagram. Carbonate range of values are given by gray shades.

The Cretaceous to Eocene marls show values enriched in ^{18}O, reaching 28.8 ‰, which are similar to the $\delta^{18}O$ values of the skarn (►Fig. 8.7c, ►Table 8.1). In detail, the O isotope compositions in calcite from marls (23.8 to 28.8 ‰; gray shade area in ►Fig. 8.7c) are enriched in ^{18}O in contrast to the clay (and quartz) fraction within these same host rocks (kaolinite, illite, and quartz; 22.3 to 25.8 ‰). The δD is only analyzed in the clay fraction within these rocks, ranging from -64 to -96 ‰, due to only clay minerals that could contain hydrogen in their structure.

The $\delta^{18}O$ of the Oligocene sandstones range from +14.5 to +18.4 ‰, and their δD from -59 to -75 ‰ (►Fig. 8.7c). These isotopic compositions reflect the abundance of quartz and subordinate amounts of kaolinite and smectite. The $\delta^{18}O$ and δD values from the Numidian claystone lenses interlayered with the sandstones are similar ($\delta^{18}O$ = 16.1 and 18.8 ‰, δD = -63 and -72 ‰). All data obtained from the Oligocene whole rocks plot on the left side of the kaolinite line (►Fig. 8.7c).

8.5.2 Pb-Pb isotope composition

The Pb isotopic ratios of the white clay samples from the Tamra formation have been integrated in the large set of Pb isotope data available for the Nefza district (►Fig. 8.8; Decrée *et al.*, 2014). No age correction on the Pb isotopic ratios were needed, given their relatively recent age of formation (Late Miocene). Kaolinite-halloysite samples show similar $^{206}Pb/^{204}Pb$ (18.761–18.779) and $^{208}Pb/^{204}Pb$ (38.840–38.867) ratios, falling in a narrow window (►Fig. 8.8, ►Table 8.3). As a whole, the Pb isotopic data of the white clays belong to a trend defined by the Pb-Pb values from various mineral occurrences of the district, including the Oued Belif breccia ferruginous matrix (Decrée *et al.*, 2013), the Tamra, Douahria, El Harsh, Mokta el-Hadid Fe oxides, and the Sidi Driss and Douahria galena (►Fig. 8.8; Decrée *et al.*, 2014).

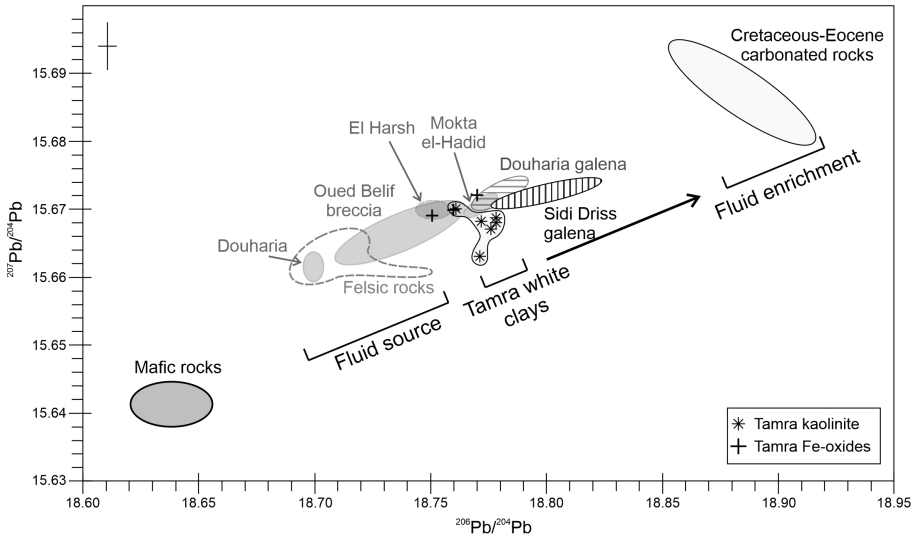

►**Fig. 8.8** Fe oxides of Douahria, Oued Belif breccia, El Harsh, Mokta el-Hadid, and galena of the Douahria and Sidi Driss deposits (modified after Decrée *et al.*, 2014) together with the Tamra white clay levels plotted on a $^{207}Pb/^{204}Pb$ vs. $^{206}Pb/^{204}Pb$ diagram (►Table 8.3). Felsic rocks and Cretaceous-Eocene carbonated substratum rocks are also reported on this graph (Decrée *et al.*, 2008a, 2008b). Pb isotopic ratios are not recalculated for the white clays of Tamra considering recent age of the samples. The error bar represents the mean for the standard deviations.

8.6 Origin of the white clays in the Tamra ores

The unusual stable isotope compositions recorded in the halloysite-kaolinite of the Tamra deposit are not in equilibrium with pure meteoric waters: the combined $\delta^{18}O$ and δD values of pure kaolinite-halloysite plot on the right side of the kaolinite reference line. The $\delta^{18}O$ values are higher than those of detrital kaolinites (►Fig. 8.7a; Sheppard and Gilg, 1996) and also higher temperature kaolinite (hydrothermal). The measured stable isotope compositions correspond to unrealistic temperature conditions below 0°C (►Fig. 8.7a). For instance, the calculated isotopic compositions of the coexisting water, which are in equilibrium with the kaolinite and halloysite at 10 to 25°C, show higher $\delta^{18}O$ values compared to the meteoric water line that represents the present day meteoric water for kaolinite formed at 25°C. The isotope composition of weathering halloysite as compiled by Sheppard and Gilg (1996), plots on the left side of the kaolinite line (light gray area in ►Fig. 8.7a). Mixing those regular halloysite crystals with kaolinite would produce a decrease in $\delta^{18}O$, which is not recorded in the Tamra white clays. Furthermore, co-genetic Fe oxides show the same trend compared to white clays, i.e. high $\delta^{18}O$ values for some goethite are reported on the right side of the 25°C line (for goethite after Yapp, 1990), which strengthens the interpretation based on the values of $\delta^{18}O$ and δD (►Fig. 8.7b).

Nevertheless, some of these goethite and hematite crystals plot on the equilibrium lines with meteoric waters, which means that they were also formed under supergene conditions as suggested by Decrée *et al.* (2008a). Such high $\delta^{18}O$ values are unusual and might indicate that the Tamra white clays (and some goethite) are not exclusively formed by weathering processes in the presence of pure meteoric water. They could have crystallized either (1) in the presence of highly evaporated meteoric waters, and/or (2) from waters that have previously intensive interactions with the country rocks at higher temperatures or even with magmatic fluids.

The first hypothesis (1) is deduced by the large variation recorded in the kaolinite and halloysite δD values (►Fig. 8.7a) that could be attributed to meteoric waters that have experienced evaporation before their circulation within the bedrock. Evaporation processes affecting superficial waters would also have an effect on the isotopic composition: the heavier isotopes of oxygen and hydrogen are both favored in the residual meteoric fluid, leading to increasing and variable $\delta^{18}O$ and δD values (e.g., Bechtel *et al.*, 1999). Such evaporation effect on the stable isotopes needs to be moderate with the paleoclimatic conditions that occurred during the deposition and the ore formation/enrichment of the Tamra succession. Late Miocene sediments recorded a change from a dry to a wet climate in North Africa, even more humid than today. The dry Tortonian climate changed to humid conditions (known as the "Zeit Wet Phase") extending into the uppermost Tortonian and the lowermost Pliocene. Afterward, North Africa experienced a prolonged wet period during the Messinian, which is related to the interaction of Asian monsoon and the low stand of the Mediterranean Sea. The association of deserts and monsoons explains why the Mediterranean basin could be subject to desiccation (e.g. Messinian Salinity Crisis) while the areas in the south were receiving abundant rainfall (deMenocal and Bloemendal, 1995; Griffin, 2002; Gladstone *et al.*, 2007). The Pliocene and Pleistocene were subject to alternating dry and wet episodes that did not match the "Zeit Wet Phase" intensity and length (e.g., Griffin, 1999, 2002; Köhler *et al.*, 2010). While the following evaporation effect is consistent with the arid or subdesertic climate (Suc *et al.*, 1995), particularly considering the hydromorphic pedogenesis, which have occurred during the ferralitisation of the Tamra sediments (Decrée *et al.*, 2008a), the δD values of kaolinite-halloysite and goethite-hematite are probably too low to consider this process alone. The ^{2}H isotope would indeed be favored, and provide higher δD values as it has been observed in the Bahloul Formation (►Fig. 8.7a; Bechtel *et al.*, 1999). As this is not the case, the following O-isotope exchange model between hydrothermal/magmatic fluids with the basement rocks (2) could be a better interpretation.

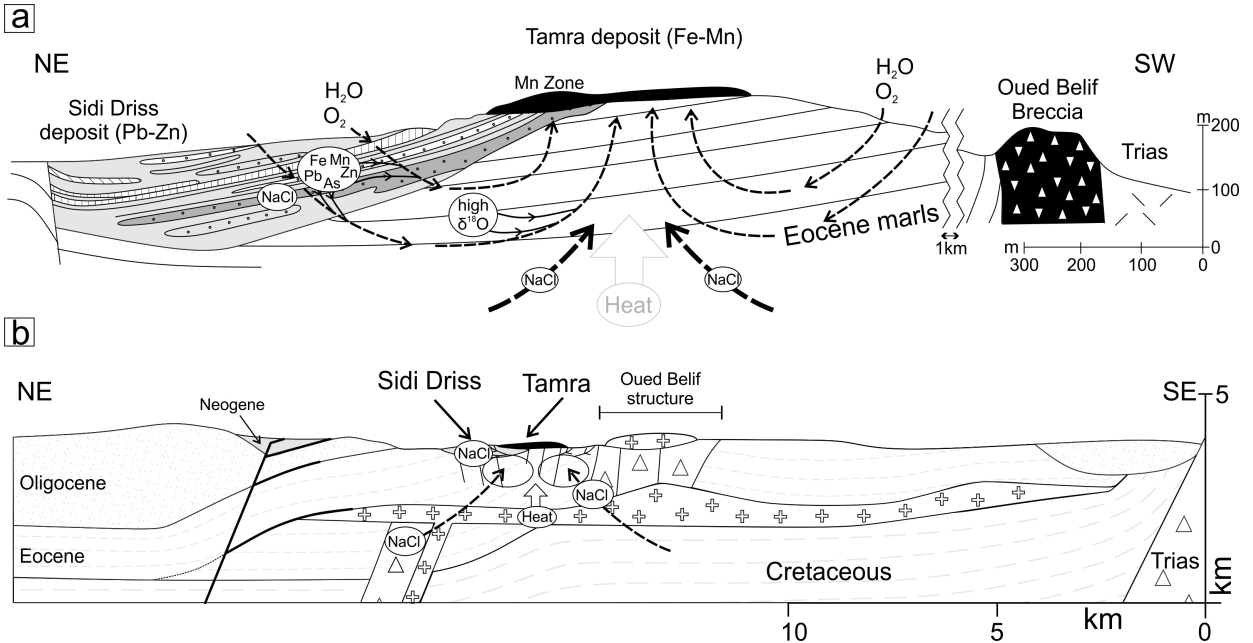

►**Fig. 8.9** Schematic cross section showing the Nefza area. **a.** Genetic model for the Tamra deposit hydrothermal enrichment and formation of the white clay levels. Mixing of meteoric fluids with saline hydrothermal solutions have led to alteration and transport of metals in the Tamra deposit. Leaching of the Pb-Zn Sidi Driss deposit has enriched mineralizing fluids in Fe, Mn, Pb, Zn, and As and subsequently crystallized late Mn oxides in the Tamra section (Decrée *et al.*, 2010). Fluid-rock interaction with underlying marls was responsible for heavy $\delta^{18}O$ related to carbonate phases, resulting in white clay formation in the Tamra deposit (adapted from Decrée *et al.*, 2008a). **b.** Large scale model (adapted from Decrée *et al.*, 2008b) and references therein) showing the thermally driven circulation involved in the formation of SEDEX type Pb-Zn Sidi Driss ores. Such thermal activity probably persisted until current times as many thermal springs are still observed (Decrée *et al.*, 2010). Note the contribution of deeper fluids originated from Triassic salt diapir, the heat flow related to the shallow magmatic sill underlying the Nefza area and normal faults acting as main drains for mineralization (Jallouli *et al.*, 2003).

$\delta^{18}O$ and δD values of the kaolinite-halloysite samples also have a large range of values consistent with an input of heavy oxygen during their formation or during subsequent alteration. In this second hypothesis (2), fluids with higher ^{18}O content compared to pure meteoric waters have contributed to the high $\delta^{18}O$ values measured for some samples relative to values recorded in kaolinites worldwide (Sheppard and Gilg, 1996; gray areas in ►Fig. 8.7a). The high $\delta^{18}O$ values may be the result of fluid-rock interaction with the basement rocks and supported by a high heat gradient related to magmatic intrusions. The presence of high $\delta^{18}O$ carbonates in the underlying Cretaceous to Eocene marls and/or skarns facilitates a fluid buffering towards higher ^{18}O contents (►Fig. 8.7c). This hypothesis suggests that these kaolinite-halloysite were formed after synsedimentary weathering/pedogenesis and/or were altered in the presence of deeper hydrothermal fluids derived a few hundred meters beneath the Tamra deposit (►Figs. 8.9a and b). The latter has been enhanced by alteration of the carbonated substratum, which may also have led to the enrichment of the mineralizing fluid in ^{18}O, and to the crystallization of kaolinite-halloysite and/or destabilization of the previously formed clay assemblages in the Tamra section (►Fig. 8.9a). The occurrence of hydrothermal halloysite has already been mentioned in previous works (Hilali *et al.*, 1968; Minato *et al.*, 1981; Spencer, 1991; Lorenzoni *et al.*, 1995; Nicaise, 1998; Joussein *et al.*, 2005). The origin of this hydrothermal fluid could be meteoric, but a contribution of saline fluids is also consistent with the presence of a Triassic diapir beneath the surface of the Oued Belif structure a few hundred meters to the south of the Tamra deposit, and evaporite sediments in the underlying Sidi Driss basin (►Figs. 8.3, 8.9a and b). The temperatures of the fluid responsible for the Pb-Zn ore in the underlying Sidi Driss deposit range from 80°C (early mineral assemblage) to 150°C (late mineral assemblage, Decrée *et al.*, 2008b). However, these temperatures are probably not reached in the Tamra deposit because hydrothermal halloysite and kaolinite generally precipitate at low temperature (<80°C or <61–110°C, e.g.; Joussein *et al.*, 2005). On the basis of the considered white clay samples and an estimated temperature of 80°C, the modeling suggests a calculated isotope composition for a hot meteoric/magmatic fluid at 80°C of -46 to -101 ‰ for δD, and 3.6 to 9.8 ‰ for $\delta^{18}O$ (►Fig. 8.7a). Mixing the superficial O_2-rich meteoric waters with deeper saline hot brines could have triggered the formation of halloysite (and associated alteration minerals) in the Tamra deposit (►Figs. 8.9a and b). The contribution of hydrothermal and meteoric fluids induced the crystallization of the typical supergene phases composed of hollandite, coronadite and chalcophanite, coexisting with kaolinite lenses at temperature less than those recorded in the Sidi Driss deposit. The timing of such process is poorly constrained but probably occurred during late diagenesis, coevally to hydrothermal enrichment described by Decrée *et al.* (2010; ►Fig. 8.6).

Considering the similarity between stable isotope compositions of the Tamra clays with those obtained by Bechtel *et al.* (1999) in the Bahloul Formation

(►Fig. 8.7a), and the presence of diapirism in the vicinity of both formations, saline fluids could have contributed to the transportation of base metals. Fluid inclusions of late calcite in the underlying Sidi Driss deposit corroborate this statement with 11.7 to 18.3 wt.% NaCl (Decrée *et al.*, 2008b). This high salinity, together with relatively low temperatures (<150°C), could have influenced the hydrogen and oxygen isotope composition of the fluid, as shown by experimental studies made by Truesdell (1974) and Horita *et al.* (1993). These authors showed that water composition can be more or less saline and does not directly influence the isotopic composition unless salinities are very high at such low temperatures of exchange. These features are in agreement with the conclusion learned from the Pb-Zn Bou Grine mine, where the origin of kaolinite is explained by the interaction of sedimentary pristine kaolinite with ^{18}O-rich hot saline brines (170 -250°C, 16-33 eq wt.% NaCl; Charef and Sheppard, 1987; Bechtel *et al.*, 1999).

Pb-Pb isotope results of the Fe and Pb ores define a clear trend ranging between the Nefza felsic magmatic rocks, and the carbonate substratum (►Fig. 8.8). This suggests that the origin of Pb is not only related to felsic rocks but also to the substratum (Decrée *et al.*, 2014). As a whole, the white clays plot on this trend, suggesting the same origin as the one for other Fe and Pb-Zn ores in the Nefza area (Decrée *et al.*, 2008a, 2008b). It would imply that (1) mineralizing processes are quite similar to Sidi Driss and Tamra sequences and (2) mineralizing fluids from hydrothermal activity were related to magmatic bodies (►Fig. 8.9b), passing through the carbonated substratum and forming Fe oxides (hematite, goethite), Mn oxides (hollandite, romanechite, strontiomelane, coronadite, Pb-Mn oxides, chalcophanite), quartz and kaolinite-halloysite (►Fig. 8.9a), and finally imposing their $\delta^{18}O$ and δD isotopic signatures. Such specific O and H isotopic compositions of the white clays can suggest the intervention of the same fluid, which was responsible for the white clay genesis and the late enrichment in Fe, Mn, Pb, Zn, and As (►Fig. 8.6; *Stages 3 and 4*). Decrée *et al.* (2008a, b) pointed out the relation between the Tamra deposit and the underlying Sidi Driss deposit: the enrichment of Mn, Pb, Zn, Fe, and As in both deposits suggests that Fe-bearing fluids percolated through the Sidi Driss sulfide deposit before the enrichment of the Tamra ores. This late event indicates that hydrothermal activity has persisted in the Nefza mining district (Decrée *et al.*, 2014) after the deposition and Fe-enrichment of the Tamra sediments. The enrichment in Pb-Zn of the co-genetic Mn oxyhydroxide (chalcophanite, hollandite group minerals, romanechite) from the Tamra deposit is the result of reactivation of convection cells and leaching of hydrothermal fluid through the Sidi Driss deposit (Decrée *et al.*, 2008a, 2008b, 2010). Thermal anomalies have occurred since Late Serravallian-Tortonian times (Jallouli *et al.*, 1996), the most striking example being the Messinian mafic magmatism (Decrée *et al.*, 2013) and the current thermal springs (Zouiten, 1999).

The tectonic event favoring hydrothermal circulation at that time might be associated with the extensional opening of the late Miocene basins (Bouaziz *et al.*, 2002) allowing the formation of the Tamra and Sidi Driss basins that are delineated by normal faults beneath and inside the Tamra deposit (►Fig. 8.9b). Fluid flow was facilitated by the enhanced geothermal gradient, thanks to the intrusion of the shallow sill (Jallouli *et al.*, 1996, 2003; ►Fig. 8.9b). In that context, structural discontinuities (thrust sheet boundaries, magmatic contacts and deformed plutons) could have served as main drains (Fig. 8.9b; Decrée *et al.*, 2008b). This alteration process is not so clear as petrogenetic process related to hematite and goethite: the stable isotopes indicate that some of the goethite crystals/mineralization were equilibrated with meteoric waters and plot along the 25°C line, while others must have formed in the presence of the above-mentioned higher ^{18}O fluids (►Fig. 8.7b). Therefore, the formation of Fe oxides can be generated through synsedimentary weathering/pedogenesis, but also through hydrothermal fluid activities.

8.7 Conclusion

The high $\delta^{18}O$ values of the kaolinite-halloysite and goethite-hematite of the Fe(-Mn) Tamra deposit show that these latter minerals did not originate solely from an equilibrium state with pure meteoric waters. The most appropriate explanation for their relatively heavy isotopic values is a hydrothermal fluid-rock interaction of the meteoric fluid with the underlying carbonate rocks (marls and skarns), after deposition added to the synsedimentary weathering/pedogenesis of the Tamra succession. Such enrichment in the ^{18}O content of the fluid and clay minerals precipitating from the fluids is unusual and only observed in the adjacent Bahloul Formation hosting the Pb-Zn Bou Grine deposit. The occurrence of halloysite and kaolinite lenses in the Tamra deposit is assumed to be formed by a direct precipitation from hydrothermal fluids, or by a secondary fluid-mineral exchange during a post-depositional hydrothermal alteration of primary clays first formed during weathering. The structural discontinuities (mainly normal faults) may have supported the fluid migration. Pb isotopes of the white clays indicate that the source fluid could be influenced by felsic magmatism, when the carbonate bedrock is responsible for the enrichment of the fluid in $^{206}Pb/^{204}Pb$ and $^{207}Pb/^{204}Pb$ as it has been recorded in the halloysite-kaolinite and other mineralization of the Nefza district. The close relation between Tamra ore deposition and the intrusion of a Triassic diapir into evaporites (also attributed to the Pb-Zn enrichment in the Bou Grine deposit) stimulates the occurrence of saline fluids that have facilitated the transportation of metals.

🔎 The mineralizing fluid could be responsible for the ore enrichment in Mn, Fe, As, Pb, and Zn, and thus the formation of late Mn oxides in the Tamra deposit. As the Mn-rich zone of the Tamra deposit rest upon the Sedex Pb-Zn Sidi Driss deposit, we

could infer that these Mn oxides minerals have probably a hydrothermal signature, as it is the case for other cogenetic ore forming minerals of the Tamra deposit (i.e., kaolinite, halloysite, goethite and hematite). This further indicates that Mn oxides are not only associated to a strictly weathering environment, but could also be formed under warmer conditions, owing to hydrothermal circulation in the near surface environment as it was already suggested in the Imini-Tasdremt district (chapter 7).

8.8 References

Badgasarian, G.P., 1972. Age radiométrique du volcanisme néogène du Nord de la Tunisie. Notes Serv. Géologique Tunis. 40, 79–85.

Batik, P., 1980. Carte Géologique de la Tunisie au 1:50000 - Hédil, feuille n°11.

Bauer, K.K., Vennemann, T.W., 2014. Analytical methods for the measurement of hydrogen isotope composition and water content in clay minerals by TC/EA. Chem. Geol. 363, 229–240. https://doi.org/10.1016/j.chemgeo.2013.10.039

Bechtel, A., Savin, S.M., Hoernes, S., 1999. Oxygen and hydrogen isotopic composition of clay minerals of the Bahloul Formation in the region of the Bou Grine zinc–lead ore deposit (Tunisia): evidence for fluid–rock interaction in the vicinity of salt dome cap rock. Chem. Geol. 156, 191–207.

Bellon, N., 1976. Séries magmatiques néogènes et quaternaires du pourtour de la Méditerranée occidentale comparées dans leur cadre géodynamique. Implications géodynamiques (Unpublished Ph.D. thesis). Université Paris Sud, Orsay.

Ben Abdallah, R., 2013. Les phyllosilicates de la structure de l'Oued Bélif (Nefza, Tunisie septentrionale): minéralogie, géochimie et signification thermique (Unpublished Ph.D. thesis). Université de Carthage, Tunis.

Berthon, L., 1922. L'industrie minérale en Tunisie. Service des Mines de Tunisie.

Bouaziz, S., Barrier, E., Soussi, M., Turki, M.M., Zouari, H., 2002. Tectonic evolution of the northern African margin in Tunisia from paleostress data and sedimentary record. Tectonophysics 357, 227–253. https://doi.org/10.1016/S0040-1951(02)00370-0

Bouhlel, S., Garnit, H., Bejaoui, J., Skaggs, S.A., 2013. Lead isotopes signatures of the MVT lead-zinc (±F) deposits across Central-North Tunisia: Evidence for the heterogeneity in uranium component of the underlying source rocks, in: Mineral Deposit Research for a High-Tech World. Presented at the 12th Biennial SGA Meeting, Uppsala, pp. 612–615.

Bouzouada, R., 1992. Géologie, minéralogie et paragenèses des gites de fer du District des Nefza. Répartition des sulfures et des impuretés. (Unpublished DEA). Université de Tunis, Tunis.

Brindley, G.W., Brown, G. (Eds.), 1980. Crystal structures of clay minerals and their X-Ray identification. Mineralogical Society of Great Britain and Ireland, Colchester and London. https://doi.org/10.1180/mono-5

Burollet, P.F., 1991. Structures and tectonics of Tunisia. Tectonophysics 195, 359–369.

Caillère, S., Hénin, S., Rautureau, M., 1982. Minéralogie des argiles, 2nd, Actualités scientifiques et agronomiques de l'I.N.R.A. Masson, Paris ; New York.

Charef, A., Sheppard, S.M.F., 1987. Pb-Zn mineralization associated with diapirism: Fluid inclusion and stable isotope (H, C, O) evidence for the origin and evolution of the fluids at Fedj-el-Adoum, Tunisia. Chem. Geol. 61, 113–134.

Decrée, S., De Putter, T., Yans, J., Moussi, B., Recourt, P., Jamoussi, F., Bruyère, D., Dupuis, C., 2008a. Iron mineralisation in Mio-Pliocene sediments of the Tamra iron mine (Nefza mining district, Tunisia): Mixed influence of pedogenesis and hydrothermal alteration. Ore Geol. Rev. 33, 397–410.

Decrée, S., Marignac, C., Abidi, R., Jemmali, N., Deloule, E., Souissi, F., 2016. Tectonomagmatic Context of Sedex Pb–Zn and Polymetallic Ore Deposits of the Nappe Zone Northern Tunisia, and Comparisons with MVT Deposits in the Region, in: Bouabdellah, M., Slack, J.F. (Eds.), Mineral Deposits of North Africa. Springer International Publishing, Cham, pp. 497–525. https://doi.org/10.1007/978-3-319-31733-5_20

Decrée, S., Marignac, C., De Putter, T., Deloule, E., Liégeois, J.-P., Demaiffe, D., 2008b. Pb–Zn mineralization in a Miocene regional extensional context: The case of the Sidi Driss and the Douahria ore deposits (Nefza mining district, northern Tunisia). Ore Geol. Rev. 34, 285–303.

Decrée, S., Marignac, C., De Putter, T., Yans, J., Clauer, N., Dermech, M., Aloui, K., Baele, J.-M., 2013. The Oued Belif Hematite-Rich Breccia: A Miocene Iron Oxide Cu-Au-(U-REE) Deposit in the Nefza Mining District, Tunisia. Econ. Geol. 108, 1425–1457. https://doi.org/10.2113/econgeo.108.6.1425

Decrée, S., Marignac, C., Liégeois, J.-P., Yans, J., Ben Abdallah, R., Demaiffe, D., 2014. Miocene magmatic evolution in the Nefza district (Northern Tunisia) and its relationship with the genesis of polymetallic mineralizations. Lithos 192–195, 240–258. https://doi.org/10.1016/j.lithos.2014.02.001

Decrée, S., Ruffet, G., Putter, T.D., Baele, J.-M., Recourt, P., Jamoussi, F., Yans, J., 2010. Mn oxides as efficient traps for metal pollutants in a polyphase low-temperature Pliocene environment: A case study in the Tamra iron mine, Nefza mining district, Tunisia. J. Afr. Earth Sci. 57, 249–261.

Dekoninck, A., Bernard, A., Barbarand, J., Saint-Bezar, B., Missenard, Y., Lepretre, R., Saddiqi, O., Yans, J., 2016a. Detailed mineralogy and petrology of manganese oxyhydroxide deposits of the Imini district (Morocco). Miner. Deposita 51, 13–23. https://doi.org/10.1007/s00126-015-0590-3

Dekoninck, A., Leprêtre, R., Saddiqi, O., Barbarand, J., Yans, J., 2016b. The high-grade Imini manganese district—karst-hosted deposits of mn oxides and oxyhydroxides, in: Bouabdellah, M., Slack, J.F. (Eds.), Mineral Deposits of North Africa. Springer International Publishing, Cham, pp. 575–594.

Dekoninck, A., Moussi, B., Vennemann, T., Jamoussi, F., Mattielli, N., Decrée, S., Chaftar, H.-R., Hatira, N., Yans, J., 2018. Mixed hydrothermal and meteoric fluids evidenced by unusual H- and O-isotope compositions of kaolinite-halloysite in the Fe(-Mn) Tamra deposit (Nefza district, NW Tunisia). Appl. Clay Sci. 163, 33–45.

de Menocal, P.B., Bloemendal, J., 1995. Plio-Pleistocene climatic variability in subtropical Africa and the paleoenvironment of Hominid evolution: A combined data-model approach, in: Vrba, E.S., Denton, G.H., Partridge, T.C., Burckle, L.H., Paleoclimate and evolution, with emphasis on Human origins. Yale University Press, New Haven, pp. 262–288.

Dermech, M.-N., 1990. Le complexe de l'Oued Bélif - Sidi Driss (Tunisie septentrionale). Hydrothermalisme et métallogénie (Unpublished Ph.D. thesis). Université Pierre et Marie Curie - Paris VI, paris.

Faul, H., Foland, K., 1980. L'âge des rhyodacites de Nefza-Sedjenane. Notes Service Géologique Tunisie, Travaux de Géologie Tunisienne 14, 47–49.

Galer, S.J.G., Abouchami, W., 1998. Practical application of lead triple spiking for correction of instrumental mass discrimination. Mineral. Mag. 62A, 491–492.

Garlick, G.D., 1966. Oxygen isotope fractionation in igneous rocks. Earth Planet. Sci. Lett. 1, 361–368.

Gharbi, M., 1977. Etude des minéralisations mercurifères de l'accident Ghardimaou-Cap Serrat (Tunisie du Nord-Ouest) (Unpublished Master thesis). Ecole Nationale Supérieure de Géologie Appliquée et de Prospection Minière de Nancy, Nancy.

Gilg, H.A., Sheppard, S.M.F., 1996. Hydrogen isotope fractionation between kaolinite and water revisited. Geochim. Cosmochim. Acta 60, 529–533. https://doi.org/10.1016/0016-7037(95)00417-3

Girard, J.-P., Fouillac, A.-M., 1995. Oxygen and hydrogen isotope geochemistry of clays: examples of application to diagenetic and geothermal environments. Bull. - Cent. Rech. Explor.-Prod. Elf Aquitaine 19, 167–195.

Gladstone, R., Flecker, R., Valdes, P., Lunt, D., Markwick, P., 2007. The Mediterranean hydrologic budget from a Late Miocene global climate simulation. Palaeogeogr. Palaeoclimatol. Palaeoecol. 251, 254–267.

Gottis, C., Sainfeld, P., 1952. Les gîtes métallifères tunisiens, in: Monographie Régionales, 2. Presented at the 19ème Congrès Géologique International, Tunisie, p. 104.

Griffin, D.L., 2002. Aridity and humidity: two aspects of the late Miocene climate of North Africa and the Mediterranean. Palaeogeogr. Palaeoclimatol. Palaeoecol. 182, 65–91.

Griffin, D.L., 1999. The late Miocene climate of northeastern Africa: unravelling the signals in the sedimentary succession. J. Geol. Soc. 156, 817–826.

Guerrera, F., Martín-Martín, M., Perrone, V., Tramontana, M., 2005. Tectono-sedimentary evolution of the southern branch of the Western Tethys (Maghrebian Flysch Basin and Lucanian Ocean): consequences for Western Mediterranean geodynamics. Terra Nova 17, 358–367.

Hilali, E.A., Nataf, M., Ortelli, L., 1968. Les gites de kaolin du Maroc, in: Proceedings of Symposium I, Kaolin deposits in the world, B overseas Countries. Presented at the 23rd International Geological Congress, Prague, pp. 55–59.

Hoefs, J., 2009. Stable isotope geochemistry, Sixth edition. ed. Springer, Berlin.

Horita, J., Wesolowski, D.J., Cole, D.R., 1993. The activity-composition relationship of oxygen and hydrogen isotopes in aqueous salt solutions: I. Vapor-liquid water equilibration of single salt solutions from 50 to 100°C. Geochim. Cosmochim. Acta 57, 2797–2817.

Jallouli, C., Inoubli, M.H., Albouy, Y.Y., 1996. Le corps igné de Nefza (Tunisie septentrionale): caractéristiques géophysiques et discussion du mécanisme de sa mise en place. Notes Serv. Géologique Tunis. 109–1023.

Jallouli, C., Mickus, K., Turki, M.M., Rihane, C., 2003. Gravity and aeromagnetic constraints on the extent of Cenozoic volcanic rocks within the Nefza–Tabarka region, northwestern Tunisia. J. Volcanol. Geotherm. Res. 122, 51–68.

Joussein, E., Petit, S., Churchman, J., Theng, B., Righi, D., Delvaux, B., 2005. Halloysite clay minerals – a review. Clay Miner. 40, 383–426.

Köhler, C.M., Heslop, D., Krijgsman, W., Dekkers, M.J., 2010. Late Miocene paleoenvironmental changes in North Africa and the Mediterranean recorded by geochemical proxies (Monte Gibliscemi section, Sicily). Palaeogeogr. Palaeoclimatol. Palaeoecol. 285, 66–73.

Kohn, M.J., Valley, J.W., 1998a. Oxygen isotope geochemistry of the amphiboles: isotope effects of cation substitutions in minerals. Geochim. Cosmochim. Acta 62, 1947–1958.

Kohn, M.J., Valley, J.W., 1998b. Effects of cation substitutions in garnet and pyroxene on equilibrium oxygen isotope fractionations. J. Metamorph. Geol. 16, 625–639.

Kohn, M.J., Valley, J.W., 1998c. Obtaining equilibrium oxygen isotope fractionations from rocks: theory and examples. Contrib. Mineral. Petrol. 132, 209–224.

Lorenzoni, P., Mirabella, A., Bidini, D., Lulli, L., 1995. Soil genesis on trachytic and leucititic lavas of Cimini volcanic complex (Latium, Italy). Geoderma 68, 79–99.

Masrouhi, A., Ghanmi, M., Slama, M.-M.B., Youssef, M.B., Vila, J.-M., Zargouni, F., 2008. New tectono-sedimentary evidence constraining the timing of the positive tectonic inversion and the Eocene Atlasic phase in northern Tunisia: Implication for the North African paleo-margin evolution. Comptes Rendus Geosci. 340, 771–778.

Mauduit, F., 1978. Le volcanisme néogène de la Tunisie continentale (Unpublished Ph.D. thesis). Université Paris Sud, Orsay.

Maury, R.C., Fourcade, S., Coulon, C., El Azzouzi, M., Bellon, H., Coutelle, A., Ouabadi, A., Semroud, B., Megartsi, M., Cotten, J., Belanteur, O., Louni-Hacini, A., Piqué, A., Capdevila, R., Hernandez, J., Réhault, J.-P., 2000. Post-collisional Neogene magmatism of the Mediterranean Maghreb margin: a consequence of slab breakoff. Comptes Rendus Académie Sci. - Ser. IIA - Earth Planet. Sci. 331, 159–173.

Michard, A., Negro, F., Saddiqi, O., Bouybaouene, M.L., Chalouan, A., Montigny, R., Goffé, B., 2006. Pressure–temperature–time constraints on the Maghrebide mountain building: evidence from the Rif–Betic transect (Morocco, Spain), Algerian correlations, and geodynamic implications. Comptes Rendus Geosci., Quelques développements récents sur la géodynamique du Maghreb 338, 92–114.

Minato, H., Kusukabe, H., Inoue, A., 1981. Alteration reactions of halloysite under hydrothermal conditions with acidic solutions, in: Proceedings of the 7th International Clay Conference. Presented at the International Clay Conference Development in Sedimentology, Bologna and Pavia, pp. 565–572.

Moussi, B., 2012. Mode de genèse et valorisation de quelques argiles de la région de Nefza-Sejnane (Tunisie septentrionale) (Unpublished Ph.D. thesis). Université de Carthage, Tunis.

Moussi, B., Medhioub, M., Hatira, N., Yans, J., Hajjaji, W., Rocha, F., Labrincha, J.A., Jamoussi, F., 2011. Identification and use of white clayey deposits from the area of Tamra (northern Tunisia) as ceramic raw materials. Clay Miner. 46, 165–175. https://doi.org/10.1180/claymin.2011.046.1.165

Negra, L., 1987. Pétrologie, minéralogie et géochimie des minéralisations et des roches encaissantes des basins associés aux structures tectoniques et magmatiques de l'Oued Bélif et du Jebel Haddada (Nord des Nefza, Tunisie septentrionale) (Unpublished Ph.D. thesis). Université Paris Sud, Orsay.

Nicaise, D., 1998. L'halloysite des cryptokarsts de l'Entre-Sambre-et-Meuse (Belgique) : synthèse géologique, minéralogique et géochimique (Unpublished Ph.D. thesis). Université Paris Sud, Orsay.

Ould Bagga, M.A., Abdeljaouad, S., Mercier, E., 2006. The Tunissian "zone des nappes": a slightly inverted mesocenozoic continental margin (Taberka/Jendouba; northwestern Tunisia). Bull. Soc. Geol. Fr. 177, 145–154. https://doi.org/10.2113/gssgfbull.177.3.145

Piqué, A., 2002. The Mesozoic–Cenozoic Atlas belt (North Africa): an overview. Geodin. Acta 15, 185–208.

Piqué, A., Tricart, P., Guiraud, R., Laville, E., Bouaziz, S., Amrhar, M., Ait Ouali, R., 2002. The Mesozoic–Cenozoic Atlas belt (North Africa): an overview. Geodin. Acta 15, 185–208.

Renson, V., Coenaerts, J., Nys, K., Mattielli, N., Vanhaecke, F., Fagel, N., Claeys, P., 2011. Lead isotopic analysis for the identification of late bronze age pottery from Hala Sultan Tekke (Cyprus). Archaeometry 53, 37–57.

Rouvier, H., 1994. Notice explicative de la carte géologique de la Tunisie au 1:50000 - Nefza, feuille n°10 (Notice). Office National des Mines, Direction de la Géologie, Tunis.

Rouvier, H., 1987. Carte Géologique de la Tunisie au 1:50000 - Nefza, feuille n°10.

Rouvier, H., 1977. Géologie de l'extrême Nord-Tunisien: tectoniques et paléogéographie superposées à l'extrémité orientale de la chaîne Nord-Maghrebine (Unpublished Ph.D. thesis). Université Pierre et Marie Curie - Paris VI, Paris.

Rouvier, H., Perthuisot, V., Mansouri, A., 1985. Pb-Zn deposits and salt-bearing diapirs in Southern Europe and North Africa. Econ. Geol. 80, 666–687. https://doi.org/10.2113/gsecongeo.80.3.666

Savelli, C., 2002. Time–space distribution of magmatic activity in the western Mediterranean and peripheral orogens during the past 30 Ma (a stimulus to geodynamic considerations). J. Geodyn. 34, 99–126. https://doi.org/10.1016/S0264-3707(02)00026-1

Savin, S.M., Epstein, S., 1970. The oxygen and hydrogen isotope geochemistry of clay minerals. Geochim. Cosmochim. Acta 34, 25–42. https://doi.org/10.1016/0016-7037(70)90149-3

Savin, S.M., Hsieh, J.C.., 1998. The hydrogen and oxygen isotope geochemistry of pedogenic clay minerals: principles and theoretical background. Geoderma 82, 227–253. https://doi.org/10.1016/S0016-7061(97)00103-1

Savin, S.M., Lee, M., 1988. Isotopic studies of phyllosilicates, in: Hydrous Phyllosilicates (Exclusive of Micas), Reviews in Mineralogy. Mineralogical Society of America, pp. 189–223.

Sheppard, S.M.F., Gilg, H.A., 1996. Stable isotope geochemistry of clay minerals. Clay Miner. 31, 1–24. https://doi.org/10.1180/claymin.1996.031.1.01

Spencer, C., 1991. Mémento des roches et minéraux industriels: halloysite (No. R33266). BRGM, Orléans.

Spötl, C., Vennemann, T.W., 2003. Continuous-flow isotope ratio mass spectrometric analysis of carbonate minerals. Rapid Commun. Mass Spectrom. 17, 1004–1006. https://doi.org/10.1002/rcm.1010

Stefanov, S.H., Ouchev, A., 1972. Gisement plombo-zincifère de Sidi Driss (Rapport géologique avec estimation des réserves, Unpublished Internal Report). Office National des Mines, Tunis.

Suc, J.-P., Diniz, F., Leroy, S., Poumot, C., Bertini, A., Clet-Pellerin, M., Bessais, E., Zheng, Z., Dupont, L., Ferrier, J., 1995. Zanclean (~ Brunssumian) to early Piacenzian (~ early-middle Reuverian) climate from 4° to 54° north latitude (West Africa, West Europe and West Mediterranean areas). Meded. Rijks Geol. Dienst 43–56.

Taylor, H.P., 1968. The oxygen isotope geochemistry of igneous rocks. Contrib. Mineral. Petrol. 19, 1–71. https://doi.org/10.1007/BF00371729

Truesdell, A.H., 1974. Oxygen isotope activities and concentrations in aqueous salt solutions at elevated temperatures: Consequences for isotope geochemistry. Earth Planet. Sci. Lett. 23, 387–396. https://doi.org/10.1016/0012-821X(74)90128-9

Vennemann, T.W., Morlok, A., von Engelhardt, W., Kyser, K., 2001. Stable isotope composition of impact glasses from the Nördlinger Ries impact crater, Germany. Geochim. Cosmochim. Acta 65, 1325–1336. https://doi.org/10.1016/S0016-7037(00)00600-1

Verhaert, M., Bernard, A., Saddiqi, O., Dekoninck, A., Essalhi, M., Yans, J., 2018. Mineralogy and genesis of the polymetallic and polyphased low grade Fe-Mn-Cu Ore of Jbel Rhals deposit (Eastern High Atlas, Morocco). Minerals 8, 39. https://doi.org/10.3390/min8020039

Weis, D., Kieffer, B., Maerschalk, C., Barling, J., de Jong, J., Williams, G.A., Hanano, D., Pretorius, W., Mattielli, N., Scoates, J.S., Goolaerts, A., Friedman, R.M., Mahoney, J.B., 2006. High-precision isotopic characterization of USGS reference materials by TIMS and MC-ICP-MS: isotopic study of USGS reference materials. Geochem. Geophys. Geosystems 7, n/a-n/a. https://doi.org/10.1029/2006GC001283

Yapp, C.J., 2000. Climatic implications of surface domains in arrays of dD and d^{18}O from hydroxyl minerals: Goethite as an example. Geochim. Cosmochim. Acta 64, 2009–2025.

Yapp, C.J., 1990. Oxygen isotopes in iron (III) oxides: 1. Mineral-water fractionation factors. Chem. Geol. 85, 329–335. https://doi.org/10.1016/0009-2541(90)90010-5

Zouiten, S., 1999. Application de la géothermométrie chimique aux eaux des sources thermales du Nord de la Tunisie (Unpublished Ph.D. thesis). Univeristé de Tunis II, Tunis.

Chapter 9

General discussion and conclusion

Chapter 9

General discussion and conclusion

In this last chapter, general concepts of supergene and weathering processes are examined based upon the observations and the preliminary conclusions drawn in the previous chapters. This discussion includes elements that have been observed in the Mn veins of the Vosges massif (chapter 5), the Mn-rich sediments of the Stavelot massif (chapter 6), the karst-hosted Mn deposits of the Imini-Tasdremt district (chapter 7), and the mixed hydrothermal Fe-Mn Tamra deposit of the polymetallic Nefza district (chapter 8). All these Mn deposits have recorded weathering and supergene processes with various intensities and in different geodynamic settings. In this chapter, I bring new crucial insights related to the precipitation and the composition of the K-bearing Mn oxides, and I then propose new interpretations about the connection between the age(s) of supergene/weathering deposits, geodynamics and climate.

9.1 Characterization of Mn oxides in the supergene zone of Mn protores

Within the supergene zone of primary deposits or rocks (protores), the suitability of a mineral to release its metal content to further precipitate more oxidized secondary phases depends on its reactivity to surficial meteoric or ground waters, which are mainly guided by the Eh, the pH and the temperature (see chapters 2 and 3). In Mn deposits, this generally results in the oxidation of either Mn^{2+} hosted in carbonates (i.e., rhodochrosite, kutnohorite…, see chapters 5 and 6), or Mn^{2+} and Mn^{3+} accommodated in silicates (i.e., braunite; see chapter 5) and in primary Mn oxides (i.e., hausmannite, manganite; see chapter 5), to form various Mn oxides (see chapter 3).

As the protore type determines the primary Mn-bearing minerals, I have tentatively positioned the hollandite group minerals within parageneses, the latter being only possible when an accurate and deep characterization of both the primary and secondary ores is carried out (see chapters 5 to 8). Therefore, the supergene mineral assemblage occurring within the different types of supergene deposits most often displays various secondary Mn oxides, which result from the destabilization of primary minerals (►Figs. 9.1 and 9.2). Such interpretation has been demonstrated for Mn oxides that have precipitated in gossans in the Vosges (chapter 5) and in the laterite profile in the Stavelot massif (chapter 6), and in the larger supergene zone in the Imini-Tasdremt and Tamra districts (chapters 7 and 8). Weathering/supergene conditions operating within these deposits are further discussed in the following section.

9.1.1 Weathering crust of vein-ore type

Weathering capping the upper part of hypogene ores are generally small-scale Mn concentrations in which plethora of Mn oxides are reported (see chapter 3; ►Figs. 9.1a). For example, this zone is well known in sulfide deposits clearly delimiting several horizons, which are guided by the evolution of the ore-forming minerals from sulfides in deepest zones, to carbonate at intermediate levels, and finally to oxides in shallower levels (see chapter 2; i.e., Reich and Vasconcelos, 2015). This sequence could also be depicted in the highly weathered zones of primary Mn-rich rocks (see chapter 3).

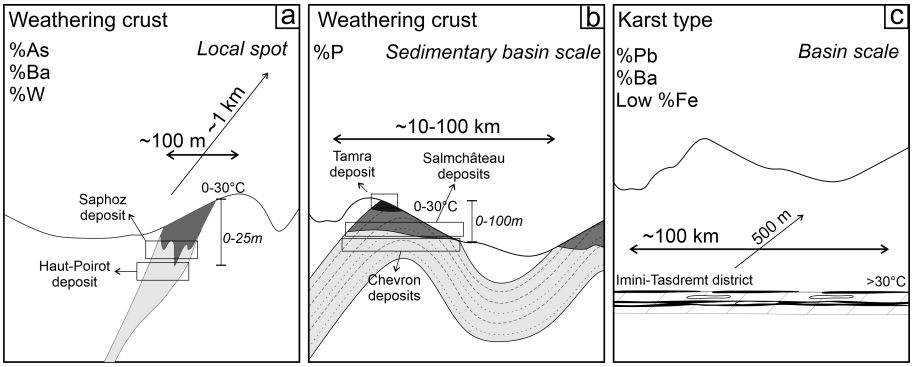

►**Fig. 9.1** Sketches of the supergene Mn deposits studied in this thesis and their main features (trace element enrichment, size, etc.). **a.** Mn weathering crust developed upon a hypogene Mn vein of small extension (Vosges; chapter 5). **b.** Weathering crust deposit forming over Mn-rich sediments depending on the protore extension (Stavelot; chapter 6). Note that the Tamra ore does not strictly fit with laterization but also with the setting up of hydrothermal activity (see chapter 8). **c.** Karst type deposits formed under a sedimentary cover probably resulting in a higher temperature of formation (i.e., Imini-Tasdremt; chapter 7). The geometry depends on the size of the trap.

Chapter 5 presents two Mn-vein type deposits related to magmatic (Haut Poirot) and volcanic (Saphoz) bodies in the Vosges massif. Both deposits record weak weathering zones forming a thin profile (nearly absent in the Haut-Poirot deposit), in which the hypogene ore has been upgraded due to the presence of Mn oxides (►Fig. 9.1a). Although primary minerals are different between the Haut-Poirot (braunite-pyrolusite) and the Saphoz (rhodochrosite-braunite-hausmannite) deposits (see chapter 5), both identify the hollandite end-member as an early weathering mineral depleted in K and Pb below the weathering cap (►Figs. 9.1a and 9.2a). The reason why the cryptomelane end-member is rarely observed is a pending question, considering that host rocks (granite or trachyte) enclosing the Mn-bearing veins contain significant amounts of K-bearing minerals (i.e., K-feldspars or micas). The interaction of these minerals with meteoric agents commonly results in the release of K^+ in weathering solution (see chapter 2). Potassium then recombines with Mn^{2+}

originating from the primary assemblage (i.e., rhodochrosite, braunite, hausmannite), and precipitates the K-rich end-member of the hollandite supergroup (►Fig. 9.2a; see chapters 3 and 6; Nahon and Parc, 1990). Therefore, the preservation of nearly pure hollandite *s.s.* instead of cryptomelane is probably related to the occurrence of barite as a gangue mineral, which means that Ba is able to limit the transport of Mn and inhibit its combination with K^+ released from the host rock. This strengthens the fact that the precipitation of hollandite *s.s.* is local and favored in the weathering zone of Mn veins. For example, the Haut-Poirot deposit showed that hollandite *s.s.* is clearly connected to barite crystals, replacing well-crystallized pyrolusite over short distances (►Fig. 9.2b). However, some doubts persist on the real nature of these hollandite *s.s.*, as they could originate from either hydrothermal or supergene fluids (see discussion below).

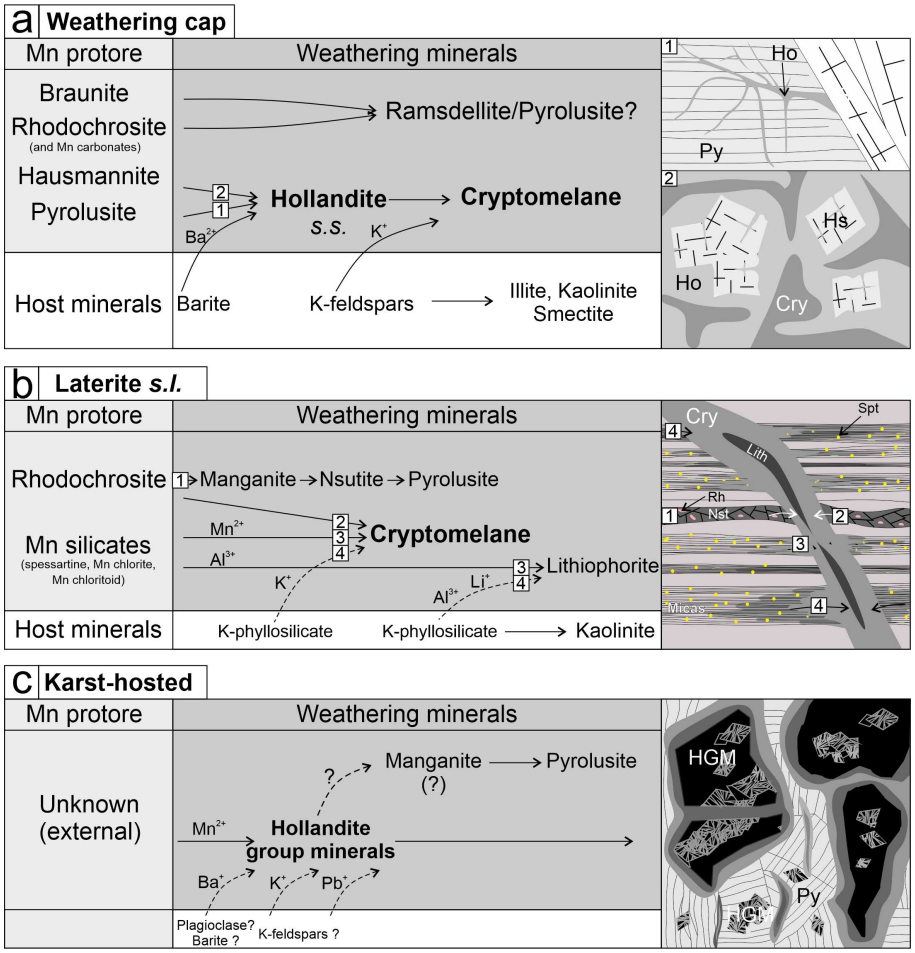

►**Fig. 9.2** Position of the hollandite group minerals (hollandite, cryptomelane and coronadite) and mineralogical relations between minerals in the different supergene Mn deposits studied in this thesis. **a.** Weathering crust in the Vosges massif. **b.** Laterite *s.l.* in the Stavelot massif.

c. Karst-hosted mineralization in the Imini-Tasdremt district. Ba=barite; Py=pyrolusite; Hs=hausmannite; Ho=hollandite s.s.; Cry=cryptomelane; Spt=spessartine; Rh=rhodochrosite; Nst=nsutite; Lith=lithiophorite; HGM=hollandite group minerals.

It is also difficult to determine whether vein deposits are more or less able to provide thick gossan because other parameters inherent in the geodynamic setting of the Vosges massif allow erosion to be favored instead of weathering (►Fig. 9.1a). Therefore, a clear mineralizing sequence within Mn gossan is not highlighted, given that most observations are not possible due to their poor vertical extension. However, hollandite *s.s.* seems to be one of the first minerals to precipitate within this sequence. Other intermixed minerals (i.e., cation-free Mn oxides) crystallize later following increasing O_2 conditions of the weathering solutions (►Fig. 9.2a). This makes the observation of supergene cryptomelane or hollandite difficult because strong weathering conditions are able to transform the primary silicate ore into Mn oxides. Another role limiting the extent of weathering in these settings could be played by primary minerals, such as braunite, given that the latter might remain stable under supergene conditions (Gutzmer and Beukes, 1996a; Johnson *et al.*, 2016).

Some metals are significantly enriched in Mn gossan of these hydrothermal veins including As, Ba and W, and directly relate to the composition of the protores, in which arsenates (i.e., pyrobelonite, As-florencite), barite and tungstate (i.e., scheelite) occur. Tungsten could be incorporated in small quantities within the hollandite *s.s.* lattice, sometimes called "tungomelane" (see chapter 5; Picot and Johan, 1982).

9.1.2 Weathering crust deposits in laterite s.l.

Mn laterization (see chapter 2) is a well-known (documented in the literature) process because it mostly develops over Mn-rich sedimentary (and metamorphic) protores, which constitutes an important source of Mn ores around the world (Laznicka, 1992; Varentsov, 1996; Roy, 2006; Maynard, 2014; Kuleshov, 2016). Sediments display very large deposits in a given area, depending on (1) the size of the sedimentary basin, and (2) their subsequent exposure to weathering agents (►Fig. 9.1b).

Mineralizing sequences within these rocks are also identified (Nahon and Parc, 1990; see chapter 3) and the K-bearing end-member of the hollandite supergroup (cryptomelane) is systematically observed as a result of the recombination of the Mn released from primary minerals (i.e., rhodochrosite, spessartine; see chapter 6) with the enclosing K-phyllosilicates (illite, muscovite, etc.; ►Fig. 9.2b). This means that cryptomelane is likely to be observed in any sedimentary deposits having a siliciclastic origin. The only restriction is that the Mn-bearing primary minerals are dissolved to release the Mn metal. Following the observations made in the Stavelot massif

(chapter 6), rhodochrosite is particularly able to release its Mn content, far more than spessartine or thermodynamically stable Mn-rich silicates (i.e., Mn-rich chloritoid and chlorite), as suggested by Parc *et al.*(1989). Therefore, rhodochrosite protores associated with K-bearing silicates are particularly likely to precipitate K-Mn oxides, whether or not the Mn-rich sedimentary rock has been metamorphosed, rhodochrosite being stable under diagenetic to metamorphic conditions (Johnson *et al.*, 2016). Nevertheless, many world-class supergene Mn deposits also formed by weathering of Mn silicates (i.e., Nahon and Parc, 1990; Varentsov, 1996; Kuleshov, 2016). The observations of cryptomelane show that it occurs in the whole laterite *s.l.*, from laterite *s.s.* to the top (Parc *et al.*, 1989) down to the fissured zone, given the observations made in the Ardenne massif (►Fig. 9.1b). Within the mineralizing sequence, cryptomelane occurs after the replacement of former carbonates by cation-free Mn oxides (i.e., nsutite, manganite, ramsdellite, pyrolusite), where K-Mn oxides precipitate in veins crossing over the host rocks (see chapter 6). Other Mn oxides are also associated to sedimentary protores allowing, for example, the formation of lithiophorite in close association with cryptomelane, the former being able to accommodate some strategic metals, such as Li from micas destabilization, Co or Ni which are dispersed within the primary Mn ore (formerly oxides according to Johnson *et al.*, 2016; see chapter 6). Mn is obviously the best concentrated element within such laterite *s.l.*, forming numerous cation-free Mn oxides and therefore containing less contaminants.

The main driver for Mn precipitation is the oxidation of primary diagenetic and/or metamorphic Mn-bearing carbonates. The Mn released from these minerals migrate locally for only several meters to be concentrated within the Mn-rich sediments and not in surrounding rocks. Fe is not well separated as it is primarily enriched in the sediments, and it remains stable within the oxidation zone in the form of hematite. Metals such as Co, Ni, Cu and Zn are enriched as in other types of Mn weathering products.

9.1.3 Karst-hosted deposits

Trapping Mn fluids to further precipitate Mn oxides in karst-hosted deposits implies the transport of Mn and associated metals over significant distances with O_2-depleted and/or acidic fluids, likely moving in ground waters. The protore(s) is(are) not identified. Their precipitation in carbonated rocks (dolostones) is due to the joint increase of pH and Eh, respectively buffering acidic Mn-bearing fluids and oxidizing in a O_2-rich karst environment (see chapter 7). The mineralogy is simpler, showing the precipitation of hollandite group minerals and pyrolusite (►Fig. 9.2c), thus avoiding the contamination of detritic components in the Imini-Tasdremt district. The latter is quite unusual because karst-hosted deposits usually concentrate Fe, Si and Al

to a higher level than other Mn accumulations (Maynard, 2010). This is however not the case in the Imini-Tasdremt ores, which means that karst-hosted deposits are able to efficiently separate detrital components and iron from manganese, probably because of a higher oxidation state and their location alongside pockets of karst-filling sands.

According to Varentsov (1996), such karst-hosted Mn deposits are often characterized by a dualistic nature of superficial meteoric waters and of relatively deep supergene-epigenetic fluids. These processes are caused by the high dissolution and migration of the solutions in subsurface waters, which usually arise from hydrothermal fluids (100–200°C), formerly supplied by endogenic sources (e.g., Gutzmer and Beukes, 1996b; Varentsov, 1996). Mn and other metals (Ba, Pb, K, etc.) enrichment in the mineralizing fluids proceeds by leaching unstable carbonates and silicate minerals in the zone of tectonic deformation (Varentsov, 1996). Their migration is enhanced by the carbonate porosity and fractures. This definition could be applied to the Imini-Tasdremt deposits, but epigenetic conditions are difficult to interpret as a deep burial, owing to low metamorphism, does not fit with the geological background of the area and the periods of uplift post-dating the late Cretaceous ore formation. It is likely that Mn behaves differently in this system than in laterite *s.l.*, because with higher temperatures and enrichment may be responsible for the ore formation (►Fig. 9.1c; see chapter 7 and discussion below).

The size of karst deposits is difficult to estimate, but the Imini-Tasdremt district has proven that such Mn mineralization could spread over several dozens of kilometers with variable dimensions of the orebodies (discontinuous) along the district. Porous dolostone is particularly suitable to accommodate Mn oxides (rather than limestone), and delimits the size of the trap and therefore the geometry of the deposit. Tectonic settings are as crucial as the nature of the host rock in order to provide sufficiently high fluid gradients to leach the bedrock. This further points out that the presence of karst-hosted Mn mineralization in the close vicinity of a tectonically active area (High Atlas Mountain in Morocco; see chapter 7) has led to one of the purest pyrolusite-bearing Mn deposit described in the world (Varentsov, 1996).

9.1.4 Textures of the Mn oxides

Supergene Mn ores from the different deposit types display common textural features, particularly well evidenced by the hollandite group minerals. The study of these textures has a real added value because it helps ore geologists to identify the processes of formation and the presence (or not) of different generations of ore forming minerals. Such characterization is also important to determine the nature of K-Mn

oxides from which K-Ar and $^{40}Ar/^{39}Ar$ dating can be retrieved (►Fig. 9.2). Hollandite group minerals are particularly interesting as they enhance contrasts in backscattered electron views (SEM) thanks to the presence of chemical elements with variable atomic weight, namely, K, Pb, Ba, Na, Sr. Following the microscopic investigations made about the different supergene ore types, two main textures are evidenced: (1) a replacement of host minerals, and (2) a filling of open spaces and cavities.

(1) The **replacement** of host minerals is the first texture observed, whether or not the replaced mineral is rich in Mn. This texture is particularly observed in the Imini-Tasdremt ores, where hollandite group minerals preserve the rhombohedral shape of Mn-free dolomite crystals in most parts of the deposit (see chapter 7; ►Fig. 9.2c). This makes carbonates suitable hosts for Mn oxide precipitation after their dissolution. In the Saphoz deposit, hausmannite is partly replaced by hollandite *s.s.* (see chapter 5), whereas in the Stavelot massif some rhodochrosite and spessartine crystals are replaced by nsutite, cryptomelane and/or lithiophorite (see chapter 6). The replacement of primary Mn-bearing minerals by secondary Mn oxides is likely to be an "atom by atom" replacement, limiting the motion of Mn into the weathering solutions, whereas Mn-free minerals (e.g., dolomite) are dissolved and then filled by secondary Mn oxides, as shown by the observations made in the Imini-Tasdremt district (see chapter 7).

(2) The **opening of cavities** and spaces by dissolution or fracturing processes in the supergene zone offers a free access to mineralizing fluids, which generally result in the formation of botryoidal Mn oxides, showing the typical growth bands. These bands are highly visible in the hollandite group minerals, as they show contrasted compositions resulting from the evolution of the mineralizing fluid (see chapter 7). Because some chemical elements are selectively removed from the mineralizing fluid to precipitate various Mn oxides, the fluid becomes temporarily depleted in the precipitated elements, unless this solution is continuously fed by new inputs of elements. This allows, for example, some trace metals (Cu, Co, Zn, etc.) to be accommodated within some of these bands to a higher level. This could also lead to the precipitation of other minerals at the end of the sequence (i.e., lithiophorite in the Stavelot massif; see chapter 6). Such texture is often targeted for geochronological studies, given that contaminants (especially carbonates) are poor and generally provide more stable $^{40}Ar/^{39}Ar$ spectra, which can be fully interpreted.

As both textures are close in space and likely in time, they might have an impact on the quality of the ores, as contaminations could be different. A texturally replacement of the host rock leaves some chemically resistant minerals (i.e., quartz, apatite, etc.; see chapter 2) to be preserved within the ores, whereas Mn oxides formed in open spaces, generally contain few impurities and higher grade ores, which are

sometimes enriched in other metals, such as Co or Cu, depending on the availability of these metals within the protore.

9.1.5 Environment of formation in the supergene zone

In a broad sense it should be considered that weathering and supergene processes rely upon the definition of processes operating when fluids progress downward (laterite *sensu lato*) under surface temperatures in a range of ~0–30°C at atmospheric pressure (see chapter 2). In opposition, hydrothermal and hypogene processes imply the upward migration of mineralizing fluids, most often at high temperatures in various geological settings (70-400°C; see chapter 2 for the definition; Bustillo Revuelta, 2018). Some evidences drawn from the study of Mn oxides and associated minerals, show that they can precipitate under higher temperatures than those allowed by the weathering processes (hydrothermal fluids?). For example, the identification of mixed component $^{40}Ar/^{39}Ar$ spectra (see chapter 7) and the disruption of stable isotopes in co-genetic minerals (i.e., kaolinite and goethite; see chapter 8) are witness of this statement.

9.1.5.a Signs of a hydrothermal input in the formation of Mn oxides

The formation (or remobilization) of Mn oxides in the Imini-Tasdremt district is probably not correlated to classical weathering conditions, such as those commonly registered in a laterite *s.l.*, at least at some stages of the ore formation process. This further supports the assumption that Mn oxides could be stable under slightly hydrothermal conditions (see chapter 7). Several tiny elements suggest that Mn mineralization in this karst-hosted deposits could have recorded **higher temperatures** after or during their formation: (1) the mixed component $^{40}Ar/^{39}Ar$ spectra delimiting a 65–67 Ma (re)crystallization peak; (2) the enrichment in Pb and Ba of these ores; (3) the association of massive barite veins (hydrothermal origin?) in the Imini district; and (4) the dissolution and formation of Mn oxides under a cover of late Cretaceous to Oligocene sediments (see chapter 7). Further investigations, for example, in the diffusion and modelling of the Ar-Ar data or in the stable isotope study of co-genetic minerals (i.e., goethite or kaolinite; see Michèle Verhaert thesis) would address this issue. Without being strictly hydrothermal conditions, temperatures may be higher than the common 0–30°C observed within a laterite *s.l.*, which is typical of some economic Mn karst-hosted deposits (Varentsov, 1996). Therefore, *karst-hosted* Mn accumulations cannot always be classified in the same way than the *weathering crust* deposits (see chapter 3). Consequently, the Imini-Tasdremt deposit is probably related to a deeper ore deposition in karst, whereas the Mn deposit in the Vosges and the Stavelot massifs are of a “laterite type” ore resulting from the *in situ* enrichment of Mn protore.

Furthermore, the Tamra deposit (chapter 8) has proven that laterite-like sediments (►Fig. 2.3) are able to partially preserve their primary features, whereas the geochemistry of the ore-forming minerals (i.e., goethite-hematite and kaolinite-halloysite; see chapter 8) associated with co-genetic Mn oxides has been subsequently modified, or these minerals have precipitated from hydrothermal solutions related to volcanic activity in the area. The feasibility of Pb- and Ba-rich hollandite group minerals to decipher the hydrothermal nature of Mn ores is not straightforward, but there are evidence showing that these minerals can be observed in the upper part of hydrothermal systems (see chapter 3). The formation of hollandite group minerals, especially those containing significant amounts of Pb and Ba, could therefore have a hydrothermal origin as already pointed out in the Milos Island (Greece; Glasby *et al.*, 2005), Ba and Pb being able to be concentrated through hydrothermal processes (i.e., Decrée *et al.*, 2008). Following the observation in the Imini-Tasdremt district, the perturbation of hollandite ages in a single mm-size concretion suggests a thermal modification or a remobilization after their formation. These observations combined with those related to co-genetic kaolinite-halloysite and goethite and of dated coronadite, and hollandite of the Tamra deposit (Decrée *et al.*, 2010), show that these minerals could record the age of low-temperature hydrothermal fluid interactions.

9.1.5.b Method(s) to assess the temperature and the timing of Mn oxides

Coupling the oxygen and hydrogen stable isotopes of co-genetic minerals (see chapter 8) is useful to determine the conditions under which these minerals have precipitated or have been reset. The Tamra deposit case has shown that weathering conditions were obliterated by a hydrothermal imprint. Too many issues unravel the Nefza area, given that the hydrothermal signature has belatedly enriched some metals. Therefore, the meteoric signal of kaolinite and goethite of the former pedogenesis has been obliterated (see chapter 8).

Additionally, the careful study of $^{40}Ar/^{39}Ar$ age spectra on K-bearing Mn oxides is also useful to depict the process by which these minerals have precipitated, besides the more conventional age determination by the K-Ar system (K-Ar and $^{40}Ar/^{39}Ar$ methods). Evaluating the degassing pattern of these minerals is of paramount importance because they often display multi component spectra, for example, with different values between total fusion, isochrones and plateau ages. This therefore results in misleading age interpretations, i.e., a shifting of several millions to dozens of millions of years or meaningless ages (see chapter 7). Because the thermal processes render the interpretation of K-Mn oxide ages more complex, the K-Ar dating of hollandite group minerals should be avoided in geological studies when treated alone without any $^{40}Ar/^{39}Ar$ counterpart. We can enlarge this recommendation to every sample studied by the K-Ar geochronology, given the complexity of some

$^{40}Ar/^{39}Ar$ spectra in the supergene environment to determine the age of K-Mn oxides. For example, we can question why K-Ar dating on K-Mn oxides are systematically older than their $^{40}Ar/^{39}Ar$ counterpart (see chapter 6).

Combining both the temperature of formation and the timing within a single mineral or sample should also be considered. For example, the joint study of the stable isotopes and the U-Th(He) dating method (see chapters 2 and 4) is possible on aliquot samples of supergene goethite (see chapter 8), which could therefore accurately assess the absolute timing and the temperature of weathering solutions. Geochemical and EPMA analyzes (see chapter 4) of two Mn concretions in the Tasdremt deposits have shown that hollandite group minerals can host 10 to 16 wt.% of water in their structure (see chapter 7). Therefore, the δD-$\delta^{18}O$ system should also be directly tested in hollandite group minerals and in other Mn oxides in order to estimate the formation temperature and especially to evaluate the past climates recorded within the weathering crust. As K-Mn oxide could be dated by the K-Ar system (see chapter 4) and would correctly respond to slight uplift periods in specific conditions (see discussion below), they would additionally record the composition of the fluids from which they have precipitated. One can see here the importance of such a tool (see chapter 4) in constraining with accuracy paleotemperatures over an order of magnitude of a million year. Therefore, the suitability of hollandite group minerals to support both oxygen and hydrogen isotope investigations, as it is the case in goethite and clay minerals (see chapters 4 and 8), is a new track that geologists and geochemists should follow to clearly identify the temperature and the absolute timing of the formation of these minerals together.

9.2 K-Mn oxides as a tool for dating geodynamic events

In this manuscript, special care has been taken for the significance of ages registered by the precipitation of K-bearing Mn oxides belonging to the hollandite supergroup. A link between these ages and their feasibility to date uplift periods is suggested and supported by several observations in different geodynamic settings in the Vosges and Black Forest massifs (France, chapter 5), in the Stavelot massif (Belgium, chapter 6), and in the Imini-Tasdremt district (Morocco, chapter 7). It is worth mentioning that climate remains a determinant factor in the development of weathering, as much as geodynamics, although they definitely both act in different ways. The **climate** and the environment determine the **kinetics** of weathering processes, depending on the environmental conditions of a given area, whereas **geodynamics** plays a role in **creating the "relief", including the gradient for the migration of meteoric fluids, and determining the time** during which a rock is exposed to weathering agents.

In this section, I question the reliability of $^{40}Ar/^{39}Ar$ and K-Ar ages of K-Mn oxides to estimate periods of uplift and their importance in the dating of weathering/supergene processes. I also present the most suitable sampling sites (including geological and metallogenetical settings) that can help to decipher periods of uplift (►Fig. 9.3), which are mostly interpreted from the set of $^{40}Ar/^{39}Ar$ ages obtained in the Imini-Tasdremt district.

9.2.1 Relation between geodynamic and supergene processes

Chapter 2 has presented most of the scientific knowledge about the parameters responsible for the development of thick weathering, including the climate and geodynamics as the majors. The latter has probably been underestimated in the representation of ages recovered from some K-Mn oxides, given that a good correlation of these ages with uplift periods is evidenced in the Imini-Tasdremt district (chapter 7). Two other independent areas also suggest such connection in the Vosges (and Black Forest) massif(s) (chapter 5) and the Stavelot massif (chapter 6).

The most striking evidence comes from the Imini-Tasdremt area (chapter 7), according to which the primary late Cretaceous Mn oxide ore dated at 81–82 Ma and 65–67 Ma in Tasdremt has been upgraded by new mineralization or/and by reworking some of the older ones (i.e., at Imini) during an Early Eocene and a Miocene period. These ages fit well with the first two steps of the Atlas building further north (see chapter 7). The Cenozoic age distribution mostly belongs to the Miocene period (Burdigalian-Langhian) coevally with a **doming period,** rather than truly a tectonic uplift and the creation of high reliefs, such as those reported during the late Eocene and Quaternary events (see chapter 7). Regardless of the tectonic regime considered during the three steps of the Atlas building (Frizon de Lamotte *et al.*, 2000; Leprêtre *et al.*, 2015), the position of the Imini ores in a foreland basin suggests a **slight uplift** compared to the core of the belt.

A similar interpretation is suggested in the southern part of the Stavelot massif, where intensification of **doming uplift** by the late Oligocene until today in the Ardenne massif (Belgium) is correlated to ages obtained at the base of the saprolite (see chapter 6). Older periods cannot be observed as the upper part of the laterite *s.l.* has been removed by successive phases of erosion since the development of Mesozoic and Cenozoic weathering periods. For example, other places in the Ardenne (Belgium) still record Eocene and Early Cretaceous weathering periods.

The Vosges Mountain has not recorded such detailed events because erosion has persisted in a stronger way, but also because the studied Mn vein deposits have a very local extension not exceeding one kilometer, therefore not allowing complete observations of the gossan zone (see chapter 5; ►Fig. 9.1). However, the neighboring

Black Forest has preserved the most recent Miocene-Quaternary episode, which could be correlated to the uplift of the Vosges and the Black Forest on the shoulders of the Rhine Graben rifting. Other ages across western Europe massifs (Hautmann and Lippolt, 2000) also suggest that a large scale weathering of Mn-vein type deposits has occurred since Miocene periods until today (►Fig. 9.4).

Even if the connection between weathering/supergene processes and geodynamics is not perfect in the Vosges (France; chapter 5) and in the Ardenne (Belgium; chapter 6), due to incomplete observations of the laterite profile (►Figs. 9.1 and 9.3), such connection is clearly supported by different evidence in the foreland basin of the High Atlas Mountain (chapter 7). The ages recovered from K-Mn oxides in the Imini-Tasdremt area are correlated to the Atlas formation, where erosion is not as strong as in the core of the belt, allowing the preservation of the deformation in the sedimentary series (and not their erosion). The Mn ores in the Imini area are located in a tectonically structured zone of this foreland (unlike Tasdremt), especially in close association with the bevel termination of Triassic and Jurassic rocks, and the Ordovician Imini inlier (►Figs. 7.2). The correlation of Cenozoic ages with the first two steps of the Atlas building allows connecting the ages obtained in the karst-hosted Imini deposit with the uplift and the deformation of the area, the third step being still active. Such interpretation is also supported by the absence of Cenozoic mineralization in the western part of the district (Tasdremt), where only the first late Cretaceous deposition at 81–82 Ma (and possibly 65–67 Ma) is reported. It is worth noting that the ore-forming process in the Imini-Tasdremt ores do probably not belong to strictly weathering conditions, but rather to higher temperatures during some stages of the ore formation (see discussion above and chapter 7).

9.2.2 Effect of tectonic regime in age preservation

Tectonic uplift regime favors erosion rather than preservation of the weathering profiles (►Fig. 9.3). Such tectonic activity results in a relatively high rate of denudation and the creation of important reliefs, and does not allow old ages to be conserved. Therefore, **foreland basins** of recently exhumed massifs or weaker deformation zones (doming, etc.), which do not record fast uplift but rather **slow vertical motion,** are probably the best targets for collecting samples of K-Mn oxides. Hence, they can provide accurate and well-constrained ages representing the whole history of a depositional site, regardless of the climatic or the geodynamics interpretation. Paradoxically, most of the protores of vein-type deposits are situated in the core of ancient massifs or orogenic zones (e.g., Pyrenees, Vosges), from which a weathering crust could efficiently develop, but would rapidly be eroded (if structural domains are reactivated), providing recent ages of weathering-forming minerals (see chapter 5).

Areas where **doming uplift** prevailed are probably the best targets to investigate the whole history of weathering, as denudation rates are slow and favor deep weathering instead of erosion dynamic. Such tectonic settings are well-known in shield and cratonic areas (e.g., Australia, West Africa, Brazil, India, etc.; Ruffet *et al.*, 1996; Li *et al.*, 2007; Bonnet *et al.*, 2014; De Putter *et al.*, 2015; Guillocheau *et al.*, 2018; Vasconcelos and Carmo, 2018) following which Cenozoic ages, most often enclosed within the Miocene range, are preserved (Vasconcelos, 1999). The Ardenne massif is probably located in such setting, because some weathering deposits record periods as old as Early Cretaceous (►Figs. 9.1b and 9.3, see chapter 6). However, the acceleration uplift in the Quaternary is responsible for the denudation of the laterite *s.s.* zone, at least in elevated topographic areas, such as those studied in the Stavelot massif. This has led Eocene or Cretaceous periods, possibly registered in the upper part of the saprolite, to be removed.

9.2.3 Which supergene Mn deposit(s) to investigate the geodynamic effect?

The interpretation of K-bearing Mn oxide ages coming from different supergene deposits brings interesting and crucial elements to identify appropriate sites that aim to evidence the geodynamic-supergene connection (►Fig. 9.3).

Mn-rich weathering crust developing above hypogene veins are generally of small scale and most often located in tectonically active areas (or ancient massifs often reactivated), thereby limiting the development of thick weathering profiles, such as those observed within laterites *s.l.* This favorrs rapid erosion (►Fig. 9.3). Consequently, this limits the preservation of ages older than the Miocene period (i.e., the Vosges and the Black Forest massifs; chapter 5; ►Fig. 9.4). Similarly, the weathering of sedimentary rocks in slightly uplifted areas (i.e., Ardenne massif; chapter 6) mostly preserves young ages depending on their exposure and altitude. However, weathering crust deposits of sedimentary Mn protores are somewhat less reactive to erosion due to their larger scale (►Fig. 9.1). For example, the Salmchâteau deposits have preserved ages as old as late Oligocene, whereas other exposed (lower elevated) areas of the Ardenne still record periods as old as Cretaceous (see chapter 6).

As both gossans and laterite *s.l.* of Mn-rich protores are located at the interface between the atmosphere and the lithosphere, we cannot convincingly separate the geodynamic from the climate effect and their input on the age record. Although both climate and geodynamics act together (see chapter 2), these weathering deposits may record climatic conditions obscuring the hidden geodynamic effect that could be recovered from K-Mn oxides. The karst-hosted Mn Imini-Tasdremt deposits (see chapter 7) allow the observation of ages, which are likely to be exclusively related

to geodynamics because climate could not be involved directly in the formation of K-bearing Mn oxides, given that they occur under a sedimentary cover. Although the mineralizing fluids might have a meteoric origin (ground waters), their circulation in basement rocks has modified their physical parameters (temperature and pressure) and composition. These modifications have already been discussed in the previous section, as supergene conditions of karst deposits could differ from those operating in laterite *s.l*. Therefore, karst-hosted Mn deposits (and in a wider view allochthon deposits of Mn) are probably the best targets to investigate the timing of vertical movements in a given area, as they are less influenced (protected ?) by direct climatic conditions.

In such a context, the Imini-Tasdremt ores perfectly combine different settings previously mentioned, i.e., (1) karstification occurs under a cover of sediments, the latter acting as a protection blanket for erosion and the direct climatic effect, (2) the formation of the ore develops deeper without reaching high temperature conditions (see discussion on the hydrothermal origin of these deposits in this chapter) and (3) the deposit is located in the foreland zone of the Atlas orogenic belt where deformations are weak, but still records vertical movements (►Fig. 9.2). Although such a tool seems to be site-specific, it remains interesting to further investigate its usefulness and systematic application in other geological and geodynamic settings.

9.2.4 Geodynamics versus climate

Obviously, there is still a predominant effect of **climate and environment** (see chapter 2) on the development of weathering profiles upon Mn-rich protores and rocks. The availability of water ("fluids") is undoubtedly the most essential parameter that triggers chemical reactions to transform primary minerals into secondary ones. This delimits the total water/rock ratio. These fluids also facilitate the leaching of mobile elements and their transport away from the laterite *s.l*. The temperature of the fluids is controlled by the climatic conditions, which intensifies the chemical reactions. Vegetation also multiplies in humid and/or warm climatic conditions (i.e., tropical) and modifies the physical parameter and the chemical composition of the weathering waters (see chapter 2). Therefore, climate and environment mainly act in the kinetics of weathering processes and in the development of laterite profiles that form secondary minerals, including Mn oxides. However, without being exposed to favorable geodynamic settings, basement rocks cannot weather nor erode (see chapter 2). **Geodynamic regimes determine the timing** of exposure and, more importantly, the denudation of the weathered rocks (see discussion above), thereby delimiting their preservation through times. Consequently, the significance of the $^{40}Ar/^{39}Ar$ ages recovered from K-Mn oxides should reflect, in some cases (e.g., the Imini-Tasdremt Mn ores fit well with geodynamic events), a geodynamic component,

given that this component determines the timing of exposure to weathering agents and erosion, climate being a kinetic driver following the exposure of rocks.

The Salmchâteau and to a lesser extent the Chevron Mn deposits (Stavelot massif; chapter 6), belong to the lower part of the weathering profile, respectively occurring at the base of the saprolite or within the fissured horizon. The climate in western Europe during the Cenozoic does not record tropical conditions, but rather temperate conditions, which questions, within a saprolite, the climatic (i.e., tropical conditions) factor alone because ages (~26 to 5 Ma; ►Fig. 9.4) at the base of the saprolite are contemporaneous with the onset of the Ardenne uplift. Tropical climatic conditions are evidenced at least during earlier periods reported in other weathering mantles in the Ardenne, during a Paleogene (Morialmé) and an Early Cretaceous phase (Transinne). The upper part of this saprolite (and laterite *s.s.*) is no more observed in the Stavelot massif because it has been recently eroded. Similarly, the uplift history of the Vosges and the Black Forest massifs only allows more recent phases to be preserved because the uplift is strong, culminating at more than 1000 meters, compared to the uppermost part of the Ardenne (~700 m). The weathering zone (i.e., laterite *s.s.* and saprolite) has not been observed in the studied sampling sites of the inner Vosges, but we suspect recent traces to be related to their current exposure (see chapter 5).

Therefore, these issues about the prevailing effect of geodynamics on the K-Mn oxide age record, which have been raised for example by Migoń and Lidmar-Bergström (2002), are explored in the context of this work and show that geodynamics probably prevails over tropical climate in the age record (not in the kinetic of weathering profile development). However, an important point to take into account is the precipitation (quite constant in western Europe during the Cenozoic; Mosbrugger *et al.*, 2005), which determines the availability of water. This results in a high water-rock ratio, favoring probably slower reaction than in tropical conditions with high temperatures, but sufficiently enough to maintain the weathering reactions. Therefore, it is difficult to separate which effect prevails in laterite profiles. Hence, both parameters are important, which is probably not the case for karst-hosted deposits. There are many possibilities to explain the concentration of Neogene (mostly Miocene) ages in the K-Mn oxide record of Western Europe and North Africa (►Fig. 9.4), including that these products may reflect probably their last exposure phase to weathering agents and/or the denudation of the upper part of the laterite *s.l.* and associated older ages. Such Neogene event has been identified by Vasconcelos (1999) at a global scale, who suggested that climate seems to be an important parameter in other places of the world, and that Neogene would be the last weathering phase that is preferentially preserved in the global age record.

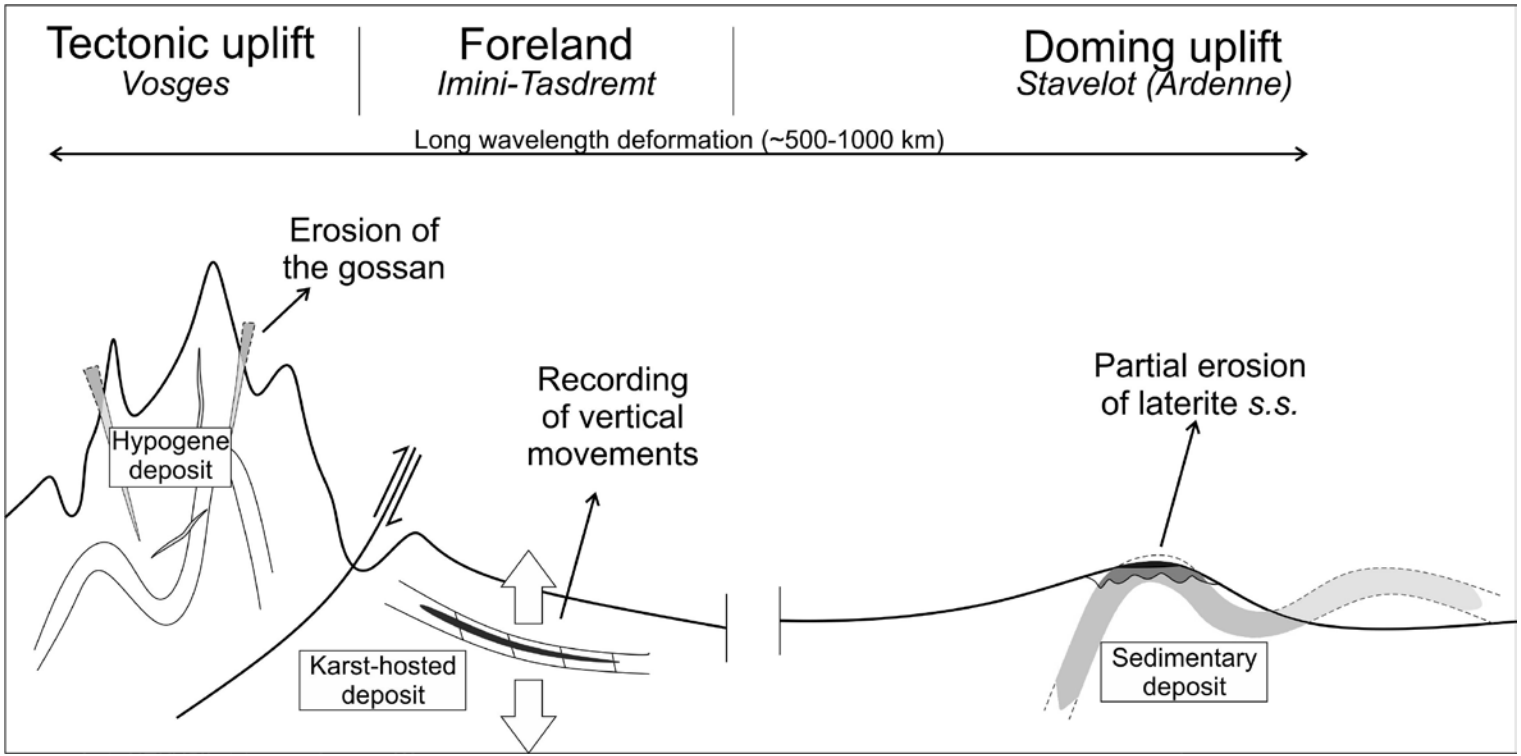

►**Fig. 9.3** Position of the studied areas in an idealized view of an orogenic belt showing that gossan and laterite profiles are not able to completely preserve the geological record of supergene processes in K-Mn oxides, as the upper part is often eroded either at short (gossan) or long term (weathering crust). The most suitable phases to decipher the entire supergene history and the effect of geodynamic in the $^{40}Ar/^{39}Ar$ records are karst-hosted deposits located in foreland basins.

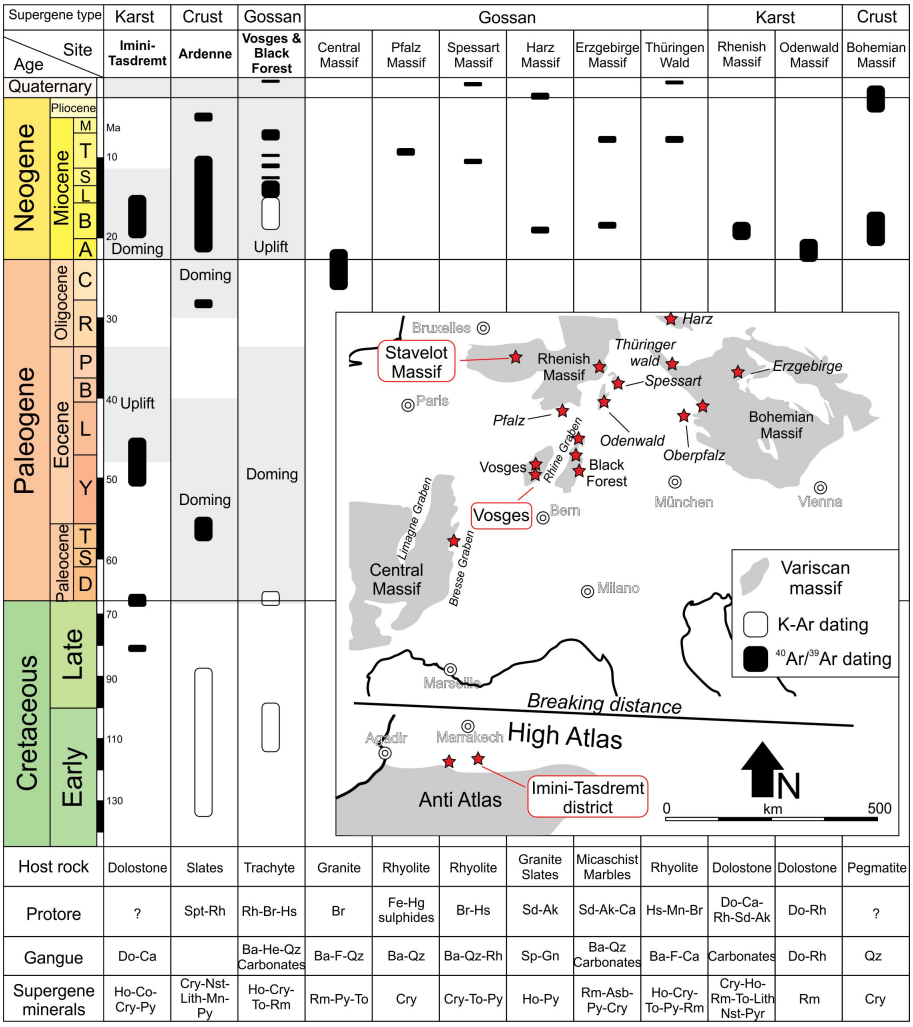

►**Fig. 9.4** Summary of age distribution which has been obtained from K-bearing Mn oxides and romanechite in the framework of this thesis and from data of other Variscan massifs in Central and Western Europe (Hautmann and Lippolt, 2000; Yans, 2003; Thiry *et al.*, 2006; Dill *et al.*, 2010; Dill and Wemmer, 2012; Demoulin *et al.*, 2018), showing that Mn oxides mostly occur within the Neogene system. Gray shades delimit periods of uplift in the three sampling areas. Abbreviations: Spt=spessartine; Rh=rhodochrosite; Br=braunite; Hs=hausmannite; Sd=siderite; Ak=ankerite; Ca=calcite; Mn=manganite; Do=dolomite; Ba=barite; He=hematite; Qz=quartz; F=fluorite; Sp=sphalerite; Gn=galena; Ho=hollandite; Co=coronadite; Cry=cryptomelane; Py=pyrolusite; Nst=nsutite; Lith=lithiophorite; Rm=romanechite; To=todorokite; Asb=asbolane.

9.3 Metallogeny of supergene Mn deposits

A lot of work has been done in the past to show that weathering processes significantly enrich less mobile elements (i.e., Al, Fe, Mn, Si) and associated (strategic) metals (Co, Ni, etc.; see chapters 2 and 3). These models perfectly corroborate the observations made in the Vosges (chapter 5) and the Stavelot (chapter 6) massifs and their applications to Mn deposits. The occurrence of high grade Mn ores in the ~100 km Imini-Tasdremt district is the most obvious indicator that supergene processes are significant factors in the creation of unconventional karst deposits. Dolostone levels in the foreland basin of a tectonically active area are probably targets for such type of deposit that can, furthermore, unravel the geodynamic history.

9.4 General conclusion

Besides the fundamental aspects of this thesis, the in-depth mineralogical, petrological and geochemical characterization of the supergene zone of Mn deposits (Vosges, Stavelot, Imini-Tasdremt and Tamra areas) has allowed to build up consistent parageneses and metallogenic models for each sampling site. These models have been improved thanks to the dating of K-bearing Mn oxides by the K-Ar system, which has, in absolute terms, positioned these oxides in the geological agenda of each area.

K-bearing Mn oxides precipitate in the earliest stage of weathering in each of the supergene deposits that have been investigated in this thesis. Their formation is limited within the weathering crust of Mn-rich veins in the Vosges massif (France), because erosion has removed most of the oxidation zone. Additionally, K-free hollandite *s.s.* is favored through the recombination of the released Mn with the Ba of the gangue minerals (barite), which limits the age measurements. The weathering of sedimentary protores in the Stavelot massif (Belgium) seems to systematically precipitate cryptomelane, given that the sediments contain substantial amounts of K, which is released from micas epigenesis. Rhodochrosite seems to be the most suitable phase to release its Mn content. As opposed to weathering crust types, karst hosted deposits of the Imini-Tasdremt district (Morocco) are able to trap a variety of K-Mn oxides belonging to the hollandite supergroup. The precipitation mechanism involves a joint increase of pH and Eh, which are triggered by the dissolution of carbonates. A new data interpretation of $^{40}Ar/^{39}Ar$ spectra indicates that the temperatures of formation could be higher than those operating in laterites *s.l.*, owing to hydrothermal conditions. However, this interpretation needs further studies about the thermal diffusion modelling of the samples. Stable hydrogen and oxygen isotope data of co-genetic kaolinite-halloysite and goethite-hematite of Fe-Mn ores in the Tamra deposit (Tunisia) also evidences such hydrothermal origin of Mn oxides.

The Mn Imini-Tasdremt district demonstrates, for the first time, that the ages recorded by the K-bearing Mn oxides (hollandite *s.s.*, coronadite and cryptomelane) are correlated to the uplift phases of the Atlas during late Cretaceous and Cenozoic times. The geodynamic interpretation of these ages is strengthened by the fact that karst deposits are less influenced by the direct climatic conditions, although mineralizing fluids may have a meteoric origin. Therefore, the most suitable sampling sites to evidence the geodynamic contribution on the age of supergene minerals belong to the karstic type.

The creation of "relief" is actually considered as the secondary main driver for the development of weathering profiles, behind climate that controls the physical and chemical parameters of the formation of such profile. As water is needed to weather primary Mn-rich minerals into secondary one, environment and climate are essential parameters determining the kinetics of the chemical reactions. Consequently, it remains difficult to separate the climatic from the geodynamic component in the weathering crust of Mn-rich rocks, as interactions with the environment are pervasive. However, the age of some of the secondary Mn oxides hosting structural K (hollandite supergroup) may reflect geodynamics rather than climate, as it delimits the timing of exposure to weathering agents. Stable tectonic areas usually allow weathering processes to persist over long periods from millions to dozens of millions of years. However, the age distribution delimiting a time window of several millions years in weathering profiles would generally reflect the periods of exposure (and thus probably the geodynamic component), whereas each age taken independently might be interpreted as favorable climates, as suggested by the data obtained in the Stavelot massif. When uplift is slow, thereby limiting denudation, the whole history of a weathering profile may be preserved and the different weathering periods may still be present. Doming regime is preferred and positions suitable sampling sites at some distance from an orogenic belt (i.e., long wavelength deformation), in foreland basins or cratonic areas.

The effect of geodynamics in the metallogenesis of manganese in the supergene zone of Mn-rich deposits is derived from the characterization of these Mn mineralization. For example, geodynamics plays a key role in the enrichment of pyrolusite in the western part of the ~100 km Imini-Tasdremt district (Imini deposits), as a correlation exists with the K-Mn oxide ages and the building steps of the Atlas belt. This is one of the most prominent results, showing that metallogenic models are essential tools that allow a good visualization of the ore forming processes for their sustainable exploration and exploitation. The importance of these metallogenic models relies upon their usefulness to mining and prospecting companies, as they better constrain the origin, the geometry and the composition of the primary and secondary ores. These principles should be further applied to other deposits in the world.

Additional research should be performed to confirm such data in other geological settings, for example identifying other bias that would improve our understanding of these objects and the connection between ages and geodynamics that can be recovered from K-Mn oxides. It is also necessary to better constrain the nature of hollandite group minerals, as they are suspected to be formed under slightly hydrothermal conditions. Evaluating their potential for hydrogen and oxygen isotopic studies, similarly to the kaolinite and goethite systems, would be useful to constrain their formation, timing and temperature. The careful study of $^{40}Ar/^{39}Ar$ spectra of K-bearing Mn oxides would also complement this approach, besides the more conventional age determination. In such that way thermal diffusion modelling should be investigated. The economic potential of supergene Mn deposits has to be deeply considered, given that some elements could be used as by-products. For example, the potential of micaceous protores to stimulate Li concentration in lithiophorite in the oxidation zone of Mn-rich deposits, or the concentration of other metals (i.e., Co), are interesting features to improve the value of supergene and weathering deposits.

9.5 References

Bonnet, N.J., Beauvais, A., Arnaud, N., Chardon, D., Jayananda, M., 2014. First $^{40}Ar/^{39}Ar$ dating of intense Late Palaeogene lateritic weathering in Peninsular India. Earth Planet. Sci. Lett. 386, 126–137. https://doi.org/10.1016/j.epsl.2013.11.002

Bustillo Revuelta, M., 2018. Mineral Resources, Springer Textbooks in Earth Sciences, Geography and Environment. Springer International Publishing, Cham. https://doi.org/10.1007/978-3-319-58760-8

De Putter, T., Ruffet, G., Yans, J., Mees, F., 2015. The age of supergene manganese deposits in Katanga and its implications for the Neogene evolution of the African Great Lakes Region. Ore Geol. Rev. 71, 350–362. https://doi.org/10.1016/j.oregeorev.2015.06.015

Decrée, S., Marignac, C., De Putter, T., Deloule, E., Liégeois, J.-P., Demaiffe, D., 2008. Pb–Zn mineralization in a Miocene regional extensional context: The case of the Sidi Driss and the Douahria ore deposits (Nefza mining district, northern Tunisia). Ore Geol. Rev. 34, 285–303. https://doi.org/10.1016/j.oregeorev.2008.01.002

Decrée, S., Ruffet, G., Putter, T.D., Baele, J.-M., Recourt, P., Jamoussi, F., Yans, J., 2010. Mn oxides as efficient traps for metal pollutants in a polyphase low-temperature Pliocene environment: A case study in the Tamra iron mine, Nefza mining district, Tunisia. J. Afr. Earth Sci. 57, 249–261. https://doi.org/10.1016/j.jafrearsci.2009.08.005

Demoulin, A., Barbier, F., Dekoninck, A., Verhaert, M., Ruffet, G., Dupuis, C., Yans, J., 2018. Erosion Surfaces in the Ardenne–Oesling and Their Associated Kaolinic Weathering Mantle, in: Demoulin, A. (Ed.), Landscapes and Landforms of Belgium and Luxembourg. Springer International Publishing, Cham, pp. 63–84. https://doi.org/10.1007/978-3-319-58239-9_5

Dill, H.G., Hansen, B., Keck, E., Weber, B., 2010. Cryptomelane: A tool to determine the age and the physical–chemical regime of a Plio-Pleistocene weathering zone in a granitic terrain (Hagendorf, SE Germany). Geomorphology 121, 370–377. https://doi.org/10.1016/j.geomorph.2010.05.004

Dill, H.G., Wemmer, K., 2012. Origin and K/Ar age of cryptomelane-bearing Sn placers on silcretes, SE Germany. Sediment. Geol. 275–276, 70–78. https://doi.org/10.1016/j.sedgeo.2012.07.016

Frizon de Lamotte, D., Saint Bezar, B., Bracène, R., Mercier, E., 2000. The two main steps of the Atlas building and geodynamics of the western Mediterranean. Tectonics 19, 740–761. https://doi.org/10.1029/2000TC900003

Glasby, G.P., Papavassiliou, C.T., Mitsis, J., Valsami-Jones, E., Liakopoulos, A., Renner, R.M., 2005. The Vani manganese deposit, Milos island, Greece: A fossil stratabound Mn−Ba−Pb−Zn−As−Sb−W-rich hydrothermal deposit, in: Developments in Volcanology. Elsevier, pp. 255–291. https://doi.org/10.1016/S1871-644X(05)80045-2

Guillocheau, F., Simon, B., Baby, G., Bessin, P., Robin, C., Dauteuil, O., 2018. Planation surfaces as a record of mantle dynamics: The case example of Africa. Gondwana Res., Rifting to Passive Margins 53, 82–98. https://doi.org/10.1016/j.gr.2017.05.015

Gutzmer, J., Beukes, N.J., 1996a. Mineral paragenesis of the Kalahari managanese field, South Africa. Ore Geol. Rev. 11, 405–428. https://doi.org/10.1016/S0169-1368(96)00011-X

Gutzmer, J., Beukes, N.J., 1996b. Karst-hosted fresh-water Paleoproterozoic manganese deposits, Postmasburg, South Africa. Econ. Geol. 91, 1435–1454. https://doi.org/10.2113/gsecongeo.91.8.1435

Hautmann, S., Lippolt, H.J., 2000. $^{40}Ar/^{39}Ar$ dating of central European K–Mn oxides — a chronological framework of supergene alteration processes during the Neogene. Chem. Geol. 170, 37–80. https://doi.org/10.1016/S0009-2541(99)00241-7

Johnson, J.E., Webb, S.M., Ma, C., Fischer, W.W., 2016. Manganese mineralogy and diagenesis in the sedimentary rock record. Geochim. Cosmochim. Acta 173, 210–231. https://doi.org/10.1016/j.gca.2015.10.027

Kuleshov, V., 2016. Isotope geochemistry: the origin and formation of manganese rocks and ores. Elsevier, Amsterdam Boston Heidelberg London New York Oxford Paris San Diego San Francisco Singapore Sydney Tokyo.

Laznicka, P., 1992. Manganese deposits in the global lithogenetic system: Quantitative approach. Ore Geol. Rev. 7, 279–356. https://doi.org/10.1016/0169-1368(92)90013-B

Leprêtre, R., Missenard, Y., Saint-Bezar, B., Barbarand, J., Delpech, G., Yans, J., Dekoninck, A., Saddiqi, O., 2015. The three main steps of the Marrakech High Atlas building in Morocco: Structural evidences from the southern foreland, Imini area. J. Afr. Earth Sci. 109, 177–194. https://doi.org/10.1016/j.jafrearsci.2015.05.013

Li, J.-W., Vasconcelos, P., Duzgoren-Aydin, N., Yan, D.-R., Zhang, W., Deng, X.-D., Zhao, X.-F., Zeng, Z.-P., Hu, M.-A., 2007. Neogene weathering and supergene manganese enrichment in subtropical South China: An $^{40}Ar/^{39}Ar$ approach and paleoclimatic significance. Earth Planet. Sci. Lett. 256, 389–402. https://doi.org/10.1016/j.epsl.2007.01.021

Maynard, J.B., 2014. Manganiferous sediments, rocks, and ores, in: Treatise on Geochemistry. Elsevier, pp. 327–349.

Maynard, J.B., 2010. The chemistry of manganese ores through time: a signal of increasing diversity of earth-surface environments. Econ. Geol. 105, 535–552. https://doi.org/10.2113/gsecongeo.105.3.535

Migoń, P., Lidmar-Bergström, K., 2002. Deep weathering through time in central and northwestern Europe: problems of dating and interpretation of geological record. CATENA 49, 25–40. https://doi.org/10.1016/S0341-8162(02)00015-2

Mosbrugger, V., Utescher, T., Dilcher, D.L., 2005. Cenozoic continental climatic evolution of Central Europe. Proc. Natl. Acad. Sci. 102, 14964–14969. https://doi.org/10.1073/pnas.0505267102

Nahon, D., Parc, S., 1990. Lateritic concentrations of manganese oxyhydroxides and oxides. Geol. Rundsch. 79, 319–326. https://doi.org/10.1007/BF01830628

Parc, S., Nahon, D., Tardy, Y., Vieillard, P., 1989. Estimated solubility products and fields of stability for cryptomelane, nsutite, birnessite, and lithiophorite based on natural lateritic weathering sequences. Am. Mineral. 74, 466–475.

Picot, P., Johan, Z., 1982. Atlas of ore minerals. BRGM ; Elsevier, Orléans, Cedex, France : Amsterdam, Netherlands.

Reich, M., Vasconcelos, P.M., 2015. Geological and Economic Significance of Supergene Metal Deposits. Elements 11, 305–310. https://doi.org/10.2113/gselements.11.5.305

Roy, S., 2006. Sedimentary manganese metallogenesis in response to the evolution of the Earth system. Earth-Sci. Rev. 77, 273–305. https://doi.org/10.1016/j.earscirev.2006.03.004

Ruffet, G., Innocent, C., Michard, A., Féraud, G., Beauvais, A., Nahon, D., Hamelin, B., 1996. A geochronological and study of K-Mn oxides from the weathering sequence of Azul, Brazil. Geochim. Cosmochim. Acta 60, 2219–2232. https://doi.org/10.1016/0016-7037(96)00080-4

Thiry, M., Quesnel, F., Yans, J., Wyns, R., Vergari, A., Theveniaut, H., Simon-Coiçon, R., Ricordel, C., Moreau, M.-G., Giot, D., Dupuis, C., Bruxelles, L., Barbarand, J., Baele, J.-M., 2006. Continental France and Belgium during the early Cretaceous: paleoweatherings and paleolandforms. Bull. Société Géologique Fr. 177, 155–175. https://doi.org/10.2113/gssgfbull.177.3.155

Varentsov, I.M., 1996. Manganese ores of supergene zone: Geochemistry of formation, Solid Earth Sciences Library. Springer Netherlands, Dordrecht.

Vasconcelos, P.M., 1999. $^{40}Ar/^{39}Ar$ Geochronology of supergene processes in ore deposits, in: Lambert, D.D., Ruiz, J. (Eds.), Application of Radiogenic Isotopes to Ore Deposit Research and Exploration, Reviews in Economic Geologists. Society of Economic Geologists, pp. 73–112.

Vasconcelos, P.M., Carmo, I. de O., 2018. Calibrating denudation chronology through 40Ar/39Ar weathering geochronology. Earth-Sci. Rev. 179, 411–435. https://doi.org/10.1016/j.earscirev.2018.01.003

Yans, J., 2003. Chronologie des sédiments kaoliniques à faciès wealdien (Barrémien moyen à Albien supérieur ; Bassin de Mons) et de la saprolite polyphasée (Crétacé inférieur et Miocène inférieur) de la Haute-Lesse (Belgique) : implications géodynamiques et paléoclimatiques (Unpublished Ph.D. thesis). Faculté Polytechnique de Mons, Université de Paris XI Orsay, Mons.

Appendices

Appendix I - Ressources du sous-sol wallon : historique, état des lieux et perspectives

Yans, J., Dekoninck, A., 2016. Ressources du sous-sol wallon : historique, état des lieux et perspectives. Mines et Carrières Hors Série 18, 5–12.

Dans un pays où les ressources du sous-sol sont une compétence régionale, la Wallonie recense une assez forte densité de carrières naturellement intégrées dans leur environnement. Le présent article dresse un instantané de l'activité extractive en Wallonie, où siègent plusieurs leaders mondiaux dans le domaine de la valorisation des ressources minérales. A l'heure où l'Europe (re)met l'accent sur la nécessité d'une saine gestion des ressources géologiques indispensables à de nombreux secteurs économiques locaux, régionaux, nationaux, européens et mondiaux, nous esquissons les conditions des futures exploitations wallonnes, dans une perspective résolument prospective.

Appendix II - Mineralogical and geochemical characterization of supergene Cu–Pb–Zn–V ores in the Oriental High Atlas, Morocco

Verhaert, M., Bernard, A., Dekoninck, A., Lafforgue, L., Saddiqi, O., Yans, J., 2017. Mineralogical and geochemical characterization of supergene Cu–Pb–Zn–V ores in the Oriental High Atlas, Morocco. Mineralium Deposita. https://doi.org/10.1007/s00126-017-0753-5

In the Moroccan High Atlas, two sulfide deposits hosted by Jurassic dolostones underwent significant weathering. In the Cu deposit of Jbel Klakh, several stages of supergene mineralization are distinguished: (1) the replacement of hypogene sulfides in the protolith (chalcopyrite) by secondary sulfides in the cementation zone (bornite, digenite, chalcocite, covellite), (2) the formation of oxidized minerals in the saprolite (malachite, azurite, brochantite) where the environment becomes more oxidizing and neutral, and (3) the precipitation of late carbonates (calcite) and iron (hydr-)oxides in the laterite. The precipitation of carbonates is related to the dissolution of dolomitic host rocks, which buffers the fluid acidity due to the oxidation of sulfides. In the Jbel Haouanit Pb–Zn deposit, the mineral assemblage is dominated by typical calamine minerals, Cu minerals (chalcocite, covellite, malachite), and a Cu–Pb–Zn vanadate (mottramite). Galena is successively weathered in anglesite and cerussite. Sphalerite is weathered in smithsonite, which is rapidly replaced by hydrozincite. Late iron (hydr-)oxides are mainly found at the top of both deposits (laterite). Both deposits are thus characterized by specific mineral zoning, from laterite to protolith, related to variations in the mineralogy and ore grades and probably caused by varying Eh-pH conditions.

For the complete paper, see http://link.springer.com/10.1007/s00126-017-0753-5.

Appendix III - Mineralogy and Genesis of the Polymetallic and Polyphased Low Grade Fe-Mn-Cu Ore of Jbel Rhals Deposit (Eastern High Atlas, Morocco)

Verhaert, M., Bernard, A., Saddiqi, O., Dekoninck, A., Essalhi, M., Yans, J., 2018. Mineralogy and Genesis of the Polymetallic and Polyphased Low Grade Fe-Mn-Cu Ore of Jbel Rhals Deposit (Eastern High Atlas, Morocco). Minerals 8, 39. https://doi.org/10.3390/min8020039

The Jbel Rhals deposit, located in the Oriental High Atlas of Morocco, hosts a polymetallic Fe-Mn-Cu ore. Large metric veins of goethite and pyrolusite cut through Paleozoic schists that are overlaid by Permian-Triassic basalts and Triassic conglomerates. The genesis of this deposit is clearly polyphased, resulting from supergene processes superimposed over hydrothermal phases. The flow of Permian-Triassic basalts probably generated the circulation of hydrothermal fluids through the sedimentary series, the alteration of basalts and schists, and the formation of hydrothermal primary ore composed of carbonates (siderite) and Cu-Fe sulfides. Several episodes of uplift triggered the exhumation of ores and host rocks, generating their weathering and the precipitation of a supergene ore assemblage (goethite, pyrolusite, malachite and calcite). In the Paleozoic basement, Fe-Mn oxihydroxides are mostly observed as rhombohedral crystals that correspond to the pseudomorphose of a primary mineral thought to be siderite; goethite precipitated first, rapidly followed by pyrolusite and other Mn oxides. Malachite formed later, with calcite, in fine millimetric veins cutting through host-rock schists, conglomerates and Fe-Mn ores.

For the complete paper, see http://www.mdpi.com/2075-163X/8/2/39.

Appendix IV – Raw $^{40}Ar/^{39}Ar$ data of the Stavelot deposits (Ardenne, Belgium; chapter 6)

Incremental Heating		$^{36}Ar_{Atm}$ [V]	$^{37}Ar_{Ca}$ [V]	$^{38}Ar_{Cl}$ [V]	$^{39}Ar_{K}$ [V]	$^{40}Ar_{R}$ [V]	Age (Ma)	± 2σ	$^{40}Ar_{R}$ (%)	$^{39}Ar_{K}$ (%)	K/Ca	± 2σ
15HEB01												
15HEB01-1		0.2910188	0.841254	0.2499464	22.3076	43.9076	15.25	± 0.70	33.74	1.14	11.4	± 2.7
15HEB01-2		0.2670785	0.990838	0.2171395	26.0899	52.3405	15.54	± 0.60	39.80	1.34	11.3	± 2.7
15HEB01-3		0.2186269	0.978379	0.2271210	28.1020	59.2319	16.32	± 0.69	47.73	1.44	12.4	± 2.3
15HEB01-4		0.1614849	0.785052	0.1513376	29.1462	60.4044	16.05	± 0.43	55.72	1.49	16.0	± 5.7
15HEB01-5		0.1339893	1.188340	0.1076089	35.2324	76.1233	16.73	± 0.26	65.59	1.81	12.7	± 2.2
15HEB01-6		0.1212747	1.180469	0.1264744	34.2868	77.4588	17.49	± 0.28	68.17	1.76	12.5	± 2.2
15HEB01-7		0.1342146	1.743142	0.1522588	50.2577	119.9488	18.47	± 0.20	74.92	2.58	12.4	± 2.5
15HEB01-8		0.1456532	2.795495	0.1452036	75.5902	174.3241	17.85	± 0.12	79.93	3.88	11.6	± 0.9
15HEB01-9		0.2043368	4.750342	0.1585499	138.3562	292.0648	16.35	± 0.09	82.55	7.09	12.5	± 0.6
15HEB01-10	p	0.2162737	6.076899	0.1507601	168.1578	343.0480	15.80	± 0.09	83.96	8.62	11.9	± 0.6
15HEB01-11	p	0.2564614	8.871770	0.1220167	248.7741	499.2491	15.54	± 0.07	86.46	12.76	12.1	± 0.3
15HEB01-12	p	0.2462136	9.937057	0.0732660	282.2743	565.8812	15.53	± 0.07	88.23	14.47	12.2	± 0.3
15HEB01-13	p	0.1313795	5.021592	0.0572989	136.0088	271.0517	15.44	± 0.10	87.10	6.97	11.6	± 0.5
15HEB01-14	p	0.1712365	9.252776	0.0514706	259.9097	528.9204	15.76	± 0.07	90.87	13.33	12.1	± 0.3
15HEB01-15		0.1146689	7.011806	0.0000000	208.1428	441.1129	16.41	± 0.20	92.47	10.67	12.8	± 0.4
15HEB01-16		0.0423089	3.693297	0.0000000	104.0852	247.5606	18.41	± 0.39	94.82	5.34	12.1	± 0.7
15HEB01-17		0.0093223	2.673905	0.0000000	74.6644	216.6196	22.43	± 0.54	98.42	3.83	12.0	± 1.1
15HEB01-18		0.0000000	0.789686	0.0000000	22.7068	107.6351	36.51	± 0.40	99.80	1.16	12.4	± 4.8
15HEB01-19		0.0000000	0.111797	0.0000000	6.2121	63.0733	77.31	± 1.88	99.90	0.32	23.9	± 120.2
15HEB03												
15HEB03-1		0.2595100	1.318711	0.0648301	28.6286	62.3915	16.87	± 0.30	44.77	2.16	9.3	± 2.4
15HEB03-2		0.2120658	1.836305	0.1164779	29.1703	85.6679	22.70	± 1.65	57.64	2.20	6.8	± 0.8
15HEB03-3		0.1389869	1.036123	0.1306369	21.8970	85.8102	30.23	± 2.15	67.52	1.65	9.1	± 2.3
15HEB03-4		0.1393272	1.446567	0.0844815	21.2752	116.0342	41.94	± 2.21	73.71	1.61	6.3	± 1.0
15HEB03-5		0.1318839	1.160494	0.0904131	17.6119	129.7615	56.43	± 2.65	76.83	1.33	6.5	± 1.7
15HEB03-6		0.1847085	1.570226	0.0978761	27.4481	129.7615	50.49	± 1.71	76.71	2.07	7.5	± 1.4
15HEB03-7		0.2603712	2.603361	0.1210859	50.5562	129.7615	47.75	± 0.97	80.24	3.81	8.4	± 0.8
15HEB03-8		0.2847293	3.851960	0.1148389	86.6893	129.7615	34.01	± 0.57	81.82	6.54	9.7	± 0.5
15HEB03-9		0.3017133	5.725379	0.0693824	143.5291	129.7615	23.39	± 0.35	82.75	10.83	10.8	± 0.5

15HEB03-10		0.2943545	7.420735	0.0000000	208.4750	129.7615	21.70	± 0.25	86.79	15.73	12.1	± 0.5
15HEB03-11	p	0.2593345	7.832686	0.0000000	214.2924	129.7615	19.87	± 0.23	87.49	16.17	11.8	± 0.4
15HEB03-12	p	0.2025012	6.924728	0.0000000	189.1024	129.7615	20.19	± 0.26	88.89	14.27	11.7	± 0.5
15HEB03-13		0.1344256	4.861555	0.0000000	134.5799	129.7615	32.93	± 0.37	93.34	10.15	11.9	± 0.6
15HEB03-14		0.0688797	2.039521	0.0000000	59.0956	129.7615	69.62	± 0.83	96.26	4.46	12.5	± 1.8
15HEB03-15		0.0284066	0.829640	0.0000000	28.0362	129.7615	64.65	± 1.70	96.48	2.12	14.5	± 4.9
15HEB03-16		0.0301737	0.836635	0.0000000	17.0839	129.7615	71.41	± 2.77	94.63	1.29	8.8	± 2.9
15HEB03-17		0.0410908	0.959465	0.0000000	21.1805	129.7615	105.74	± 2.22	96.00	1.60	9.5	± 2.7
15HEB03-18		0.0928263	2.111275	0.0006581	26.6861	129.7615	139.52	± 1.76	94.73	2.01	5.4	± 0.6
15TDP25a												
15TDP25a-1		0.0648591	0.033342	0.0457880	11.7083	21.3809	14.14	± 2.71	52.58	0.65	151.0	± 2146.3
15TDP25a-2		0.0740860	0.407469	0.0499729	10.8921	14.0385	9.99	± 3.37	38.96	0.61	11.5	± 13.3
15TDP25a-3		0.0611179	0.404316	0.0691810	15.3386	28.6556	14.46	± 1.84	61.15	0.86	16.3	± 19.4
15TDP25a-4		0.0410161	0.806489	0.0677202	14.9981	28.6297	14.78	± 1.87	70.01	0.84	8.0	± 4.1
15TDP25a-5		0.0645423	0.654733	0.0785613	22.3674	35.1920	12.19	± 1.32	64.60	1.25	14.7	± 9.0
15TDP25a-6		0.0568788	0.999148	0.1132613	26.4035	40.0667	11.76	± 1.18	70.13	1.48	11.4	± 4.4
15TDP25a-7		0.0466851	1.204731	0.0000000	32.2255	51.3540	12.34	± 0.92	78.45	1.80	11.5	± 4.4
15TDP25a-8		0.0372807	1.136067	0.0000000	33.2429	50.2378	11.71	± 0.91	81.59	1.86	12.6	± 4.5
15TDP25a-9		0.0237214	1.344980	0.0859306	30.1418	43.3835	11.15	± 0.47	85.59	1.68	9.6	± 1.4
15TDP25a-10		0.0370758	1.656931	0.1525987	40.4018	56.8720	10.91	± 0.36	83.37	2.26	10.5	± 1.2
15TDP25a-11		0.0414590	2.291658	0.1796605	54.7640	77.2644	10.93	± 0.29	85.81	3.06	10.3	± 1.3
15TDP25a-12	p	0.0935916	5.378869	0.1415727	140.6328	192.1549	10.59	± 0.45	86.88	7.86	11.2	± 0.8
15TDP25a-13	p	0.0890764	6.290745	0.1165261	171.4435	243.1699	10.99	± 0.35	89.68	9.58	11.7	± 0.8
15TDP25a-14	p	0.1338742	9.989258	0.0624794	272.0721	392.9850	11.19	± 0.23	90.30	15.21	11.7	± 0.5
15TDP25a-15	p	0.1082510	10.343721	0.0028896	274.7997	407.1196	11.48	± 0.22	92.16	15.36	11.4	± 0.4
15TDP25a-16	p	0.0675248	7.660142	0.0263146	200.6716	307.9413	11.89	± 0.30	93.36	11.22	11.3	± 0.6
15TDP25a-17	p	0.0586474	7.393822	0.0000000	194.1268	295.2619	11.78	± 0.31	93.89	10.85	11.3	± 0.6
15TDP25a-18		0.0171371	2.699876	0.0000000	66.8662	109.4213	12.67	± 0.90	95.04	3.74	10.6	± 1.5
15TDP25a-19		0.0175893	3.118698	0.0233851	84.3447	138.1107	12.68	± 0.72	95.83	4.71	11.6	± 1.4
15TDP25a-20		0.0094561	1.657680	0.0000000	44.8509	72.1261	12.46	± 1.34	95.72	2.51	11.6	± 3.0
15TDP25a-21		0.0170819	1.923008	0.0078347	46.9690	74.1863	12.23	± 1.29	93.09	2.63	10.5	± 2.3
15TDP25b												
15TDP25b-1		0.0311313	0.525561	0.1297971	10.9562	15.1993	10.75	± 3.17	62.03	0.88	9.0	± 5.8
15TDP25b-2		0.0376468	0.446106	0.0980308	16.2302	22.1111	10.56	± 2.14	66.21	1.30	15.6	± 11.6

15TDP25b-3		0.0368879	1.226248	0.1587598	25.1286	35.8905	11.07	± 1.38	76.31	2.02	8.8	± 2.8
15TDP25b-4		0.0453852	1.250923	0.1571414	31.6984	44.8256	10.96	± 1.09	76.57	2.55	10.9	± 3.0
15TDP25b-5		0.0593494	1.906711	0.1519797	44.9803	66.5212	11.46	± 0.77	78.73	3.61	10.1	± 1.9
15TDP25b-6		0.0415403	1.911087	0.1223077	48.0273	78.0334	12.58	± 0.73	85.96	3.86	10.8	± 2.2
15TDP25b-7	p	0.0890202	6.172750	0.2984268	130.0764	190.6720	11.36	± 0.28	87.37	10.45	9.1	± 0.4
15TDP25b-8	p	0.1333429	11.789726	0.1849090	264.8719	371.1127	10.86	± 0.14	89.84	21.28	9.7	± 0.2
15TDP25b-9	p	0.1434462	13.060756	0.0575311	303.0266	437.2948	11.18	± 0.12	90.61	24.34	10.0	± 0.2
15TDP25b-10		0.1075951	11.011778	0.0000000	255.6693	395.7939	11.99	± 0.15	92.03	20.54	10.0	± 0.2
15TDP25b-11		0.0279433	3.523204	0.0000000	85.5496	158.6052	14.35	± 0.42	94.58	6.87	10.4	± 0.7
15TDP25b-12		0.0038156	1.361489	0.0000000	28.7729	64.4570	17.33	± 1.26	97.86	2.31	9.1	± 1.1
BH311												
BH311-1		0.4102893	1.764547	0.1035687	26.7547	31.4920	9.13	± 0.59	20.58	1.21	6.5	± 1.0
BH311-2		0.1567986	1.560130	0.1218546	12.7811	13.8050	8.38	± 0.87	22.91	0.58	3.5	± 0.8
BH311-3		0.2027568	1.345232	0.1145077	21.2968	27.1789	9.90	± 0.55	31.13	0.97	6.8	± 1.0
BH311-4		0.0670349	0.000000	0.0629688	8.8891	12.5910	10.99	± 1.13	38.76	0.40	31.5	± 85.7
BH311-5		0.0847985	0.603143	0.0510280	12.9076	18.7668	11.28	± 0.82	42.70	0.59	9.2	± 3.6
BH311-6		0.1311886	0.678437	0.0967096	24.4081	33.4379	10.63	± 0.48	46.16	1.11	15.5	± 4.2
BH311-7		0.0739853	0.184799	0.0430855	20.1818	29.2106	11.22	± 0.46	56.98	0.92	47.0	± 67.7
BH311-8		0.0618187	0.280926	0.0623561	18.7893	27.0238	11.15	± 0.50	59.43	0.85	28.8	± 18.4
BH311-9		0.0923807	0.852706	0.1449386	34.5410	52.5048	11.79	± 0.32	65.52	1.57	17.4	± 4.7
BH311-10		0.1069536	1.363434	0.0339812	44.4755	67.5174	11.77	± 0.22	67.82	2.02	14.0	± 3.4
BH311-11		0.1462769	2.047579	0.1090429	71.9364	109.0522	11.75	± 0.15	71.29	3.27	15.1	± 1.2
BH311-12	p	0.0968534	2.090421	0.1146301	52.7837	78.3219	11.51	± 0.20	72.89	2.40	10.9	± 1.1
BH311-13	p	0.1596640	4.009839	0.0664931	112.0982	163.4856	11.31	± 0.26	77.21	5.09	12.0	± 1.2
BH311-14	p	0.1225256	3.237790	0.0752478	98.1555	144.4238	11.41	± 0.30	79.54	4.46	13.0	± 1.5
BH311-15	p	0.1233478	4.095400	0.0262057	122.6850	182.2036	11.52	± 0.24	82.88	5.57	12.9	± 1.3
BH311-16	p	0.1921031	6.855309	0.0431585	209.6741	308.5026	11.41	± 0.14	83.99	9.52	13.2	± 0.8
BH311-17	p	0.1715236	6.336552	0.0358889	203.0142	298.6922	11.41	± 0.15	85.01	9.22	13.8	± 0.9
BH311-18	p	0.1637620	6.985261	0.0373992	215.3627	318.6497	11.47	± 0.04	86.32	9.78	13.3	± 0.4
BH311-19	p	0.0536342	2.379546	0.0491217	85.2995	127.9129	11.63	± 0.05	88.47	3.87	15.4	± 1.4
BH311-20	p	0.1123795	6.082292	0.0063823	190.4496	282.7698	11.51	± 0.04	88.97	8.65	13.5	± 0.6
BH311-21	p	0.0720009	3.694099	0.0000000	132.6760	195.8273	11.45	± 0.05	89.67	6.02	15.4	± 1.1
BH311-22	p	0.0241794	1.964363	0.0562503	45.9871	67.7830	11.43	± 0.07	89.93	2.09	10.1	± 2.0
BH311-23	p	0.0386702	2.373712	0.0000000	72.2644	105.6272	11.34	± 0.04	89.70	3.28	13.1	± 0.9
BH311-24	p	0.0217841	1.156702	0.0000000	44.1390	64.6811	11.36	± 0.09	90.40	2.00	16.4	± 2.5
BH311-25	p	0.0382135	2.841729	0.0013941	71.0424	102.9190	11.24	± 0.05	89.57	3.23	10.7	± 1.0

BH311-26	p	0.0202999	2.154411	0.0000000	43.1907	63.4200	11.39	± 0.12	90.81	1.96	8.6	± 2.0
BH311-27	p	0.0142944	0.510541	0.0000000	30.7414	45.0994	11.38	± 0.08	90.89	1.40	25.9	± 16.0
BH311-28	p	0.0253697	1.564327	0.0000000	53.6420	78.7179	11.38	± 0.07	90.76	2.44	14.7	± 2.0
BH311-29	p	0.0193304	1.671371	0.0000000	35.3293	51.3059	11.26	± 0.12	89.44	1.60	9.1	± 6.0
BH311-30	p	0.0197687	1.506443	0.0200841	34.6269	50.2442	11.25	± 0.11	89.05	1.57	9.9	± 6.9
BH311-31	p	0.0110526	0.662072	0.0000000	15.7200	23.2132	11.45	± 0.27	87.16	0.71	10.2	± 16.1
BH311-32		0.0065313	0.956908	0.0000000	14.3337	22.3342	12.08	± 0.30	91.52	0.65	6.4	± 7.2
BH311-33		0.0042734	1.021314	0.0000000	10.8321	17.0713	12.22	± 0.43	92.58	0.49	4.6	± 4.7
BH311-34		0.0081165	0.096196	0.0000000	11.6818	17.3964	11.55	± 0.32	87.38	0.53	52.2	± 572.7
BH311-b												
BH311-b-1		0.0233117	0.626845	0.0944429	12.6515	17.5713	10.77	± 4.69	71.48	0.82	8.7	± 3.8
BH311-b-2		0.0341008	1.047011	0.1039238	17.0327	22.7958	10.38	± 3.48	69.00	1.11	7.0	± 1.1
BH311-b-3		0.0411537	1.206365	0.1587720	18.8959	23.4334	9.62	± 3.14	65.50	1.23	6.7	± 2.3
BH311-b-4		0.0362623	1.184020	0.1160727	23.3123	31.8506	10.60	± 2.54	74.43	1.52	8.5	± 1.4
BH311-b-5	p	0.0181709	0.625158	0.0838341	25.0074	37.3054	11.57	± 0.47	86.92	1.63	17.2	± 31.2
BH311-b-6	p	0.0360467	1.431378	0.1435542	56.0320	83.0965	11.50	± 0.22	88.13	3.64	16.8	± 13.4
BH311-b-7	p	0.0364671	2.097083	0.1140427	80.4817	121.3933	11.70	± 0.15	91.31	5.23	16.5	± 9.1
BH311-b-8	p	0.0358308	1.681019	0.1024858	90.9145	138.2886	11.79	± 0.13	92.34	5.91	23.3	± 16.0
BH311-b-9	p	0.0192938	1.383629	0.0516756	44.3333	67.7400	11.85	± 0.27	91.70	2.88	13.8	± 11.6
BH311-b-10	p	0.0139303	0.948354	0.0000000	34.5452	51.8648	11.64	± 0.34	92.10	2.25	15.7	± 18.8
BH311-b-11	p	0.0126219	0.863256	0.1320598	36.8873	56.4484	11.87	± 0.33	93.25	2.40	18.4	± 24.1
BH311-b-12	p	0.0217200	1.677603	0.1151432	63.3157	96.0684	11.77	± 0.19	93.18	4.12	16.2	± 11.1
BH311-b-13	p	0.0196752	1.580617	0.0974732	52.1461	78.9550	11.74	± 0.23	92.59	3.39	14.2	± 10.2
BH311-b-14	p	0.0328304	1.943362	0.1323357	72.5891	107.5116	11.49	± 0.17	91.18	4.72	16.1	± 9.4
BH311-b-15	p	0.0259626	1.386923	0.1317778	68.2891	101.9189	11.57	± 0.18	92.44	4.44	21.2	± 17.8
BH311-b-16	p	0.0386384	2.435365	0.1260278	107.4912	161.3949	11.64	± 0.11	92.83	6.99	19.0	± 8.9
BH311-b-17	p	0.0378251	3.106069	0.0000000	104.7546	157.3061	11.64	± 0.05	92.81	6.81	14.5	± 1.5
BH311-b-18	p	0.0685186	5.574728	0.0375002	218.1857	330.0033	11.73	± 0.04	93.65	14.19	16.8	± 1.0
BH311-b-19	p	0.0586978	4.365788	0.0145819	181.2652	276.5795	11.83	± 0.04	93.54	11.79	17.9	± 1.5
BH311-b-20	p	0.0337694	3.084685	0.0470512	113.2227	174.9167	11.98	± 0.05	94.04	7.36	15.8	± 2.5
BH311-b-21	p	0.0171593	1.732401	0.0000000	59.4754	92.3510	12.04	± 0.07	94.24	3.87	14.8	± 3.5
BH311-b-22		0.0017878	0.468320	0.0000000	22.1029	35.1392	12.33	± 0.15	97.93	1.44	20.3	± 14.7
BH311-b-23		0.0042561	0.951504	0.0000000	14.6065	22.2567	11.82	± 0.22	94.09	0.95	6.6	± 2.8
BH311-b-24		0.0008894	0.000000	0.0000000	6.4914	10.2071	12.19	± 0.60	96.91	0.42	33.4	± 129.2

BH311-b-25		0.0011486	0.387011	0.0295918	7.3862	11.5857	12.16	± 0.56	96.57	0.48	8.2	± 7.7
BH311-b-26		0.0007607	0.337343	0.0000000	6.1934	9.9352	12.44	± 0.96	97.21	0.40	7.9	± 10.9
BIHD-009												
BIHD-009-1		0.0749384	0.362000	0.1144061	18.66562	46.5806	19.31	± 0.74	67.60	2.76	22.2	± 19.6
BIHD-009-2		0.0300703	0.266524	0.0448318	7.77368	19.4549	19.37	± 1.70	68.46	1.15	12.5	± 15.4
BIHD-009-3		0.0222443	0.293660	0.0000000	8.50950	23.6635	21.50	± 1.62	78.05	1.26	12.5	± 13.2
BIHD-009-4		0.0115250	0.456864	0.0000000	4.66932	13.0854	21.67	± 2.82	79.13	0.69	4.4	± 3.2
BIHD-009-5		0.0203133	0.413104	0.0018766	10.52945	30.5545	22.43	± 1.26	83.35	1.56	11.0	± 8.5
BIHD-009-6		0.0542213	0.531801	0.0130768	31.89265	99.5251	24.12	± 0.45	85.90	4.72	25.8	± 14.1
BIHD-009-7		0.0441520	0.807094	0.0393803	34.33431	115.5331	25.99	± 0.40	89.62	5.08	18.3	± 6.6
BIHD-009-8	p	0.0709623	0.904548	0.1022080	64.40906	224.0698	26.86	± 0.23	91.21	9.54	30.6	± 11.1
BIHD-009-9	p	0.0618715	0.975744	0.0773238	63.95533	222.5300	26.87	± 0.23	92.17	9.47	28.2	± 9.3
BIHD-009-10	p	0.1028773	2.261744	0.1960734	121.60910	420.5911	26.71	± 0.17	93.02	18.01	23.1	± 13.4
BIHD-009-11	p	0.0897656	2.006584	0.0852690	95.81009	331.2051	26.69	± 0.19	92.35	14.19	20.5	± 9.5
BIHD-009-12	p	0.1023482	2.129375	0.0670562	111.77742	391.4232	27.04	± 0.17	92.59	16.55	22.6	± 10.0
BIHD-009-13		0.0406318	1.140966	0.0197067	54.03348	193.4667	27.64	± 0.32	93.92	8.00	20.4	± 16.7
BIHD-009-14		0.0218276	0.642175	0.0153768	29.79300	108.5203	28.12	± 0.53	94.15	4.41	19.9	± 29.1
BIHD-009-15		0.0079818	0.337415	0.0000000	12.52424	45.9380	28.31	± 1.24	94.88	1.85	16.0	± 45.3
BIHD-009-16		0.0062685	0.484616	0.0000000	4.95427	16.1047	25.11	± 3.16	89.45	0.73	4.4	± 8.6
RA8433a												
RA8433a-1		0.4458296	0.520067	0.0246987	1.54055	4.559993	22.88	± 9.89	3.35	1.12	1.27	± 0.71
RA8433a-2	p	0.3499717	0.822171	0.0504162	2.40780	2.504948	8.08	± 5.68	2.36	1.76	1.26	± 0.37
RA8433a-3	p	0.2374760	1.067847	0.0490442	3.58196	2.658802	5.77	± 3.60	3.65	2.62	1.44	± 0.28
RA8433a-4	p	0.3168690	1.879491	0.1145169	5.88930	2.577006	3.40	± 4.06	2.68	4.30	1.35	± 0.23
RA8433a-5	p	0.2898913	1.821619	0.1421661	5.55190	2.109879	2.95	± 4.30	2.40	4.05	1.31	± 0.23
RA8433a-6	p	0.2663085	1.638672	0.0463633	5.10989	4.911362	7.46	± 4.45	5.87	3.73	1.34	± 0.16
RA8433a-7	p	0.3821681	1.876265	0.0065871	6.84658	3.360687	3.81	± 3.54	2.89	5.00	1.57	± 0.24
RA8433a-8	p	0.5249256	2.488922	0.0511612	9.45155	4.738131	3.90	± 2.87	2.96	6.90	1.63	± 0.16
RA8433a-9	p	0.8704577	4.061740	0.0558111	16.48129	11.903455	5.61	± 2.12	4.42	12.03	1.74	± 0.12
RA8433a-10	p	0.9908796	9.062190	0.1545345	36.51812	28.485646	6.06	± 1.05	8.86	26.66	1.73	± 0.05
RA8433a-11	p	0.3253796	4.484043	0.0564843	15.71343	8.128821	4.02	± 1.65	7.78	11.47	1.51	± 0.15
RA8433a-12		0.3171644	4.842079	0.0358763	15.08122	6.862241	3.54	± 0.76	6.81	11.01	1.34	± 0.06
RA8433a-13		0.1476196	2.120423	0.0000000	6.03636	1.765559	2.27	± 3.55	3.88	4.41	1.22	± 0.17
RA8433a-14		0.1878508	2.105054	0.0000000	6.76429	2.123875	2.44	± 3.36	3.68	4.94	1.38	± 0.18
RA8433b												
RA8433b-1	p	0.1002340	1.314142	0.0840657	6.24363	1.04321	1.30	± 4.07	3.40	1.94	2.04	± 1.18

RA8433b-2	p	0.1067656	1.663421	0.0832572	6.68639	1.92181	2.23	± 3.87	5.73	2.08	1.73	± 0.79
RA8433b-3	p	0.2248103	2.999889	0.1504160	14.09410	7.84642	4.33	± 2.02	10.54	4.39	2.02	± 0.51
RA8433b-4	p	0.2349614	2.830016	0.1230097	12.46721	6.29159	3.92	± 2.12	8.30	3.88	1.89	± 0.51
RA8433b-4bis	p	0.3653750	3.556917	0.1241943	17.26151	11.55236	5.20	± 1.65	9.65	5.38	2.09	± 0.43
RA8433b-5	p	0.6522682	4.956018	0.1919999	23.34139	11.76066	3.92	± 1.42	5.74	7.27	2.03	± 0.34
RA8433b-6	p	0.9982098	9.560729	0.2265944	49.80972	32.16613	5.02	± 1.05	9.82	15.51	2.24	± 0.05
RA8433b-7	p	0.6327570	9.941560	0.1635837	47.78020	22.26893	3.62	± 0.98	10.62	14.88	2.07	± 0.06
RA8433b-8	p	0.3266891	5.966914	0.0823558	27.61976	11.65620	3.28	± 1.61	10.75	8.60	1.99	± 0.10
RA8433b-9		0.2350862	6.130812	0.0309374	20.36219	3.85851	1.47	± 0.80	5.25	6.34	1.43	± 0.04
RA8433b-10		0.2924348	7.399526	0.1100743	26.29637	3.62237	1.07	± 0.65	4.01	8.19	1.53	± 0.05
RA8433b-11		0.3263357	8.524292	0.1157534	28.43919	2.98754	0.82	± 0.64	3.00	8.86	1.43	± 0.05
RA8433b-12		0.2802655	7.439188	0.1254995	23.87117	3.49610	1.14	± 0.71	4.04	7.43	1.38	± 0.05
RA8433b-13		0.1607263	4.040571	0.0562189	13.53953	3.62952	2.08	± 1.21	7.08	4.22	1.44	± 0.09
RA8433b-14		0.0273361	0.825342	0.0494948	3.26726	0.47453	1.13	± 4.35	5.53	1.02	1.70	± 0.46
RA8432												
RA8432-1		0.0712724	0.752185	0.2060218	18.5946	20.1076	8.39	± 0.28	48.63	0.65	10.6	± 2.8
RA8432-2	p	0.0357178	0.278660	0.2187887	17.4821	26.7116	11.85	± 0.85	71.35	0.61	27.0	± 91.6
RA8432-3	p	0.0380114	0.148564	0.1677880	19.6893	29.0941	11.46	± 0.73	71.81	0.69	57.0	± 361.5
RA8432-4	p	0.0334445	0.124092	0.1864728	18.6912	27.5002	11.41	± 0.78	73.21	0.65	64.8	± 489.8
RA8432-5	p	0.0296063	0.514371	0.1647303	19.9620	28.8642	11.21	± 0.73	76.35	0.70	16.7	± 30.6
RA8432-6	p	0.0334974	0.365309	0.2131085	24.8482	36.7923	11.48	± 0.59	78.40	0.87	29.2	± 75.7
RA8432-7	p	0.0330725	0.463098	0.1956423	24.9738	36.0783	11.20	± 0.59	78.27	0.87	23.2	± 47.7
RA8432-8	p	0.0371220	0.370302	0.1291626	30.5898	44.5814	11.30	± 0.48	79.83	1.07	35.5	± 91.4
RA8432-9		0.0362013	0.728353	0.1656326	34.3561	52.6957	11.89	± 0.42	82.69	1.20	20.3	± 26.6
RA8432-10		0.0347859	0.375225	0.1758899	36.7861	58.7172	12.37	± 0.40	84.66	1.28	42.2	± 105.7
RA8432-11		0.0278175	0.369987	0.1617023	38.0900	62.9503	12.81	± 0.39	87.99	1.33	44.3	± 115.8
RA8432-12		0.0223574	1.233124	0.0924529	48.4306	83.1386	13.31	± 0.31	92.16	1.69	16.9	± 13.3
RA8432-13		0.0447357	1.267489	0.0874545	76.3799	131.6210	13.36	± 0.20	90.41	2.67	25.9	± 19.2
RA8432-14		0.0807669	2.388994	0.3806716	137.9262	245.1280	13.77	± 0.07	90.68	4.82	24.8	± 5.9
RA8432-15		0.1002561	2.838343	0.3950314	176.4610	324.3008	14.24	± 0.06	91.19	6.16	26.7	± 5.5
RA8432-16		0.1644023	3.934594	0.5754463	225.9031	393.6700	13.51	± 0.07	88.58	7.89	24.7	± 3.6
RA8432-17		0.1578156	4.174949	0.5004244	270.9722	490.4028	14.02	± 0.05	90.87	9.46	27.9	± 3.8

RA8432-18		0.1860189	5.247713	0.4634604	310.5312	575.2339	14.35	± 0.06	90.84	10.84	25.4	± 2.7
RA8432-19		0.1686726	4.836652	0.3758555	313.9002	594.0682	14.66	± 0.06	91.83	10.96	27.9	± 3.8
RA8432-20		0.1424774	4.662641	0.2531630	264.0558	502.0530	14.73	± 0.06	91.83	9.22	24.4	± 3.2
RA8432-21		0.1541625	5.538023	0.1973000	319.2633	623.0754	15.12	± 0.06	92.76	11.15	24.8	± 2.6
RA8432-22		0.0759625	3.673991	0.0828069	220.3222	441.0394	15.51	± 0.06	94.72	7.69	25.8	± 3.9
RA8432-23		0.0224115	1.037099	0.0063959	69.5018	140.8331	15.70	± 0.11	95.07	2.43	28.8	± 16.1
RA8432-24		0.0335173	2.581532	0.0000000	146.2864	300.1096	15.89	± 0.07	96.36	5.11	24.4	± 5.4
RN859												
RN859-1	p	2.0120367	2.015809	0.8635169	39.3435	50.1461	9.89	± 1.71	7.77	1.96	8.4	± 3.4
RN859-2	p	0.8243628	1.087757	0.5133297	29.5120	44.9777	11.82	± 1.09	15.57	1.47	11.7	± 8.9
RN859-3	p	0.4085199	0.815395	0.3422356	24.8499	36.5834	11.42	± 0.83	23.22	1.24	13.1	± 13.0
RN859-4	p	0.3267740	1.174790	0.4235287	35.2642	52.7322	11.60	± 0.44	35.24	1.76	12.9	± 8.9
RN859-5	p	0.2140956	0.991333	0.2975636	37.4494	55.6556	11.52	± 0.36	46.66	1.87	16.2	± 12.8
RN859-6	p	0.1557834	1.125386	0.2393757	38.3238	57.5334	11.64	± 0.37	55.35	1.91	14.6	± 10.0
RN859-7	p	0.1235356	1.183770	0.2383765	43.1421	65.5250	11.78	± 0.28	63.96	2.15	15.7	± 10.4
RN859-8	p	0.1023027	1.406649	0.2141505	45.1248	69.8192	12.00	± 0.27	69.48	2.25	13.8	± 7.6
RN859-9		0.0716359	0.997746	0.2388042	41.9412	67.9530	12.56	± 0.28	75.90	2.09	18.1	± 14.0
RN859-10		0.0696027	1.827145	0.3349328	58.6561	98.8024	13.06	± 0.20	82.38	2.92	13.8	± 6.1
RN859-11		0.0892497	3.758707	0.1779687	164.4479	297.5575	14.02	± 0.09	91.41	8.19	18.8	± 4.0
RN859-12		0.0943695	3.763524	0.1022544	161.5987	290.0349	13.91	± 0.11	90.78	8.05	18.5	± 1.0
RN859-13		0.1457489	6.791052	0.1294786	295.2952	543.9129	14.27	± 0.07	92.21	14.71	18.7	± 0.7
RN859-14		0.0747547	3.538953	0.0651696	156.2576	291.6590	14.46	± 0.11	92.51	7.78	19.0	± 1.2
RN859-15		0.0963043	6.020120	0.0000000	283.7768	541.6888	14.79	± 0.07	94.55	14.13	20.3	± 0.9
RN859-16		0.0518710	4.212021	0.0000000	222.5443	435.2626	15.15	± 0.09	96.14	11.08	22.7	± 1.0
RN859-17		0.0258502	3.221863	0.0000000	128.2917	260.0197	15.70	± 0.13	96.70	6.39	17.1	± 1.0
RN859-18		0.0298288	3.104383	0.0000000	146.9441	300.2437	15.83	± 0.12	96.70	7.32	20.4	± 1.9
RN859-19		0.0142516	1.107658	0.0000000	54.8581	112.1830	15.84	± 0.29	95.94	2.73	21.3	± 4.9
TDPR-003												
TDPR-003-1		0.5463296	2.154838	0.4746321	54.3721	62.6324	8.94	± 0.55	27.89	1.70	10.9	± 2.4
TDPR-003-2		0.2715509	1.213279	0.2077658	29.7483	40.3880	10.53	± 0.85	33.40	0.93	10.5	± 4.1
TDPR-003-3		0.4028831	1.412223	0.1883138	30.5819	45.5237	11.54	± 0.88	27.61	0.96	9.3	± 3.6
TDPR-003-4		0.1529681	0.014071	0.0737546	10.4087	14.4750	10.79	± 2.41	24.21	0.33	318.1	± 11406.3
TDPR-003-5		0.1950302	0.286942	0.1056623	12.7923	21.9343	13.29	± 1.93	27.52	0.40	19.2	± 31.9
TDPR-003-6		0.7269730	1.903307	0.2984099	44.0872	71.9966	12.66	± 0.76	25.06	1.38	10.0	± 2.7

TDPR-003-7		0.6034725	1.268934	0.2411476	43.9480	61.4932	10.85	± 0.70	25.60	1.37	14.9	± 5.6
TDPR-003-8		0.2743091	1.308648	0.1664594	34.1039	37.3922	8.51	± 0.77	31.48	1.07	11.2	± 4.4
TDPR-003-9		0.2387268	2.061971	0.1921339	48.3723	52.3829	8.40	± 0.53	42.45	1.51	10.1	± 2.4
TDPR-003-10		0.1775705	1.680489	0.2296643	47.4107	69.6800	11.40	± 0.52	56.83	1.48	12.1	± 3.8
TDPR-003-11		0.1401156	1.525537	0.1463850	42.9904	89.4233	16.11	± 0.59	68.14	1.34	12.1	± 4.1
TDPR-003-12		0.1137020	1.842698	0.1531700	39.7790	85.1294	16.57	± 0.61	71.47	1.24	9.3	± 2.5
TDPR-003-13		0.0611224	1.095025	0.1242566	26.2050	60.5022	17.87	± 0.91	76.76	0.82	10.3	± 4.7
TDPR-003-14		0.0661505	1.061209	0.1432721	35.2295	86.5822	19.02	± 0.68	81.32	1.10	14.3	± 6.7
TDPR-003-15		0.0512555	1.278559	0.1457097	35.6704	103.1675	22.36	± 0.68	86.94	1.12	12.0	± 4.8
TDPR-003-16		0.0418801	0.690091	0.0950498	30.8107	87.7362	22.02	± 0.77	87.38	0.96	19.2	± 13.8
TDPR-003-17		0.0470990	1.054845	0.0759819	39.3329	110.5534	21.73	± 0.62	88.55	1.23	16.0	± 7.5
TDPR-003-18		0.0490468	1.626513	0.1720285	56.0956	146.9697	20.27	± 0.26	90.72	1.75	14.8	± 11.1
TDPR-003-19		0.0458602	1.118298	0.1012200	60.1873	158.3592	20.35	± 0.25	91.81	1.88	23.1	± 25.3
TDPR-003-20		0.0488070	1.451596	0.1181256	72.1521	176.1306	18.89	± 0.21	92.09	2.26	21.4	± 17.9
TDPR-003-21		0.0472154	1.572526	0.0777710	79.3597	200.7262	19.57	± 0.20	93.17	2.48	21.7	± 17.0
TDPR-003-22		0.0789183	2.691177	0.0706199	146.9016	352.8241	18.59	± 0.12	93.45	4.59	23.5	± 10.6
TDPR-003-23		0.0883307	3.317781	0.0629495	157.9152	367.5595	18.02	± 0.11	93.01	4.94	20.5	± 7.5
TDPR-003-24	p	0.0580784	2.248802	0.0128556	109.3945	250.6785	17.74	± 0.14	93.22	3.42	20.9	± 11.3
TDPR-003-25	p	0.1005061	3.414375	0.0020731	179.2458	402.3910	17.38	± 0.10	92.75	5.61	22.6	± 8.1
TDPR-003-26	p	0.1057093	4.534952	0.0000000	213.1093	481.2423	17.48	± 0.09	93.53	6.67	20.2	± 5.4
TDPR-003-27	p	0.0911768	4.348679	0.0000000	180.7311	411.4666	17.62	± 0.10	93.48	5.65	17.9	± 5.0
TDPR-003-28	p	0.1124473	5.504724	0.0000000	231.0084	521.9494	17.49	± 0.09	93.64	7.22	18.0	± 4.0
TDPR-003-29	p	0.1098404	4.982758	0.0000000	240.8445	549.8607	17.67	± 0.08	94.05	7.53	20.8	± 1.7
TDPR-003-30	p	0.0932354	4.392947	0.0000000	228.4425	530.4977	17.98	± 0.07	94.69	7.14	22.4	± 2.1
TDPR-003-31		0.0573732	4.028751	0.0054155	175.7210	430.2091	18.95	± 0.07	95.84	5.50	18.8	± 2.0
TDPR-003-32		0.0320255	1.511636	0.0150815	105.6421	267.7159	19.61	± 0.09	96.23	3.30	30.1	± 8.2
TDPR-003-33		0.0292582	1.982232	0.0329758	110.3145	298.4665	20.93	± 0.09	96.85	3.45	23.9	± 4.5
TDPR-003-34		0.0288907	2.090951	0.0445102	103.8026	319.5497	23.79	± 0.09	97.10	3.25	21.3	± 4.7
TDPR-003-35		0.0100052	0.187280	0.0657644	40.5535	148.9403	28.35	± 0.15	97.80	1.27	93.1	± 202.0
TDPR-003-36		0.0133203	0.484186	0.0546833	43.5613	184.8550	32.71	± 0.16	97.70	1.36	38.7	± 29.8
TDPR-003-37		0.0179902	1.006152	0.0120252	39.0050	197.2704	38.92	± 0.20	97.19	1.22	16.7	± 7.5
TDPR-003-38		0.0092079	0.440809	0.0558463	17.5650	129.4708	56.45	± 0.50	97.82	0.55	17.1	± 15.0
VERLEU 1399												
VERLEU 1399-1	p	0.8079923	0.460214	0.0771746	13.2834	14.9705	8.75	± 2.88	5.90	0.35	12.4	± 10.0
VERLEU 1399-2	p	1.3475224	0.627599	0.2548846	24.3449	23.8979	7.62	± 2.11	5.66	0.64	16.7	± 9.5

VERLEU 1399-3	p	1.2465527	1.259702	0.2960201	31.8846	40.6556	9.89	± 1.52	9.93	0.83	10.9	± 3.2
VERLEU 1399-4	p	0.3804901	0.153327	0.1015782	19.5848	26.2917	10.41	± 0.75	18.93	0.51	54.9	± 109.4
VERLEU 1399-5	p	0.3339335	0.213365	0.1215415	22.1089	31.6063	11.09	± 0.61	24.22	0.58	44.6	± 52.7
VERLEU 1399-6	p	0.3782233	0.558341	0.1407285	26.5995	36.0171	10.50	± 0.58	24.33	0.70	20.5	± 7.7
VERLEU 1399-7	p	0.2815964	0.407576	0.0703262	29.1344	37.8023	10.07	± 0.43	31.17	0.76	30.7	± 20.2
VERLEU 1399-8	p	0.1940933	0.655541	0.0866062	25.1557	32.6873	10.08	± 0.41	36.20	0.66	16.5	± 6.4
VERLEU 1399-9	p	0.2042433	0.950302	0.1203689	33.9086	43.0925	9.86	± 0.30	41.52	0.89	15.3	± 3.9
VERLEU 1399-10	p	0.1645965	1.109810	0.1225541	35.6051	44.8734	9.78	± 0.29	47.81	0.93	13.8	± 3.3
VERLEU 1399-11	p	0.1574717	1.424990	0.1818067	46.6617	62.0755	10.32	± 0.23	56.92	1.22	14.1	± 2.9
VERLEU 1399-12	p	0.2451756	1.718442	0.2407841	68.8596	89.9779	10.14	± 0.17	55.17	1.80	17.2	± 2.1
VERLEU 1399-13		0.2925831	2.487854	0.2957255	98.8658	134.3790	10.54	± 0.13	60.59	2.59	17.1	± 1.5
VERLEU 1399-14		0.3146578	2.537080	0.3217904	126.8864	176.6675	10.80	± 0.12	65.22	3.32	21.5	± 2.1
VERLEU 1399-15		0.3247056	3.324424	0.3364360	159.2500	226.0671	11.01	± 0.09	69.87	4.16	20.6	± 1.6
VERLEU 1399-16		0.3607656	4.132811	0.2764382	214.3449	311.0153	11.25	± 0.07	74.10	5.60	22.3	± 1.3
VERLEU 1399-17		0.3337898	4.300983	0.1828171	222.3709	327.9165	11.44	± 0.07	76.49	5.81	22.2	± 2.1
VERLEU 1399-18		0.3772500	5.445074	0.1724335	279.7911	422.0581	11.70	± 0.06	78.71	7.32	22.1	± 1.0
VERLEU 1399-19		0.5565872	7.338851	0.2170479	425.5831	652.0573	11.88	± 0.06	79.46	11.13	24.9	± 0.8
VERLEU 1399-20		0.5695532	7.935624	0.1319856	454.5857	702.4179	11.98	± 0.06	80.26	11.89	24.6	± 0.8
VERLEU 1399-21		0.2909367	5.744153	0.0000000	290.9430	454.6287	12.12	± 0.06	83.66	7.61	21.8	± 1.2
VERLEU 1399-22		0.2563960	6.489449	0.0000000	348.8366	550.2984	12.23	± 0.05	87.43	9.12	23.1	± 0.9
VERLEU 1399-23		0.0826895	4.459728	0.0000000	241.1278	389.9923	12.54	± 0.05	93.58	6.31	23.2	± 1.3
VERLEU 1399-24		0.0378662	2.669983	0.0000000	156.3198	254.5467	12.62	± 0.06	95.25	4.09	25.2	± 2.8
VERLEU 1399-25		0.0089458	0.652987	0.0003543	45.6171	74.9024	12.73	± 0.17	96.04	1.19	30.0	± 12.4
VERLEU 1399-26		0.0461407	3.250072	0.0000000	177.5242	287.5824	12.56	± 0.06	94.93	4.64	23.5	± 2.6
VERLEU 1399-27		0.0188719	1.070322	0.0146618	70.9129	114.0513	12.47	± 0.12	94.79	1.85	28.5	± 7.0
VERLEU 1399-28		0.0151322	0.473241	0.0000000	53.5644	85.7377	12.41	± 0.15	94.50	1.40	48.7	± 27.6
VERLEU 1399-29		0.0152758	0.198615	0.0160584	45.5337	71.6055	12.19	± 0.17	93.53	1.19	98.6	± 121.0
VERLEU 1399-30		0.0034559	0.437450	0.0239970	19.7684	32.2264	12.64	± 0.38	96.37	0.52	19.4	± 15.9
VERLEU 1399-31		0.0016237	0.242739	0.0820252	15.2464	25.2311	12.83	± 0.50	97.57	0.40	27.0	± 29.1

Appendix V – Raw $^{40}Ar/^{39}Ar$ data of the Tasdremt deposits (Souss basin, Morocco; chapter 7)

step	^{40}Ar	Error ^{40}Ar	^{39}Ar	Error ^{39}Ar	^{38}Ar	Error ^{38}Ar	^{37}Ar	Error ^{37}Ar	^{36}Ar	Error ^{36}Ar	$^{40}Ar^*/^{39}Ar_K$	Error $^{40}Ar^*/^{39}Ar_K$	Apparent age (My)	Error Age (My)	Delay to irradiation (day)
16TAS10															
1	2442.391	0.884	46.823	0.048	0.000	0.015	0.105	0.019	7.903	0.023	3.336	0.299	39.558	3.511	214.964
2	744.029	0.544	19.238	0.062	0.000	0.018	0.033	0.020	2.278	0.028	4.432	0.458	52.370	5.343	214.984
3	775.741	0.778	22.815	0.069	0.002	0.015	0.046	0.016	2.241	0.022	5.619	0.319	66.146	3.698	214.994
4	1276.847	0.440	54.831	0.165	0.002	0.012	0.098	0.022	2.641	0.029	9.414	0.177	109.488	2.050	215.014
5	105.393	0.097	5.809	0.020	0.000	0.009	0.042	0.013	0.058	0.007	15.420	0.361	176.037	3.993	215.064
6	872.780	0.466	53.262	0.117	0.002	0.010	0.082	0.020	0.449	0.009	14.044	0.066	160.997	0.978	215.084
7	1312.604	1.395	83.122	0.088	0.000	0.009	0.155	0.015	0.510	0.008	14.113	0.045	161.762	0.823	215.124
8	1606.504	1.001	100.773	0.093	0.002	0.013	0.125	0.015	0.390	0.007	14.922	0.036	170.610	0.796	215.144
9	1633.882	0.516	134.619	0.179	0.000	0.015	0.135	0.018	0.305	0.016	11.558	0.042	133.526	0.721	215.174
10	1815.849	0.549	204.401	0.171	0.000	0.014	0.194	0.016	0.338	0.017	8.463	0.029	98.726	0.524	215.194
11	6097.762	2.971	810.662	0.726	0.012	0.012	0.627	0.024	0.709	0.015	7.318	0.014	85.677	0.389	215.794
12	7958.086	1.680	1112.075	0.591	0.000	0.014	0.837	0.021	0.612	0.018	7.044	0.012	82.544	0.366	215.814
13	4011.518	1.117	568.499	0.523	0.000	0.013	0.437	0.024	0.229	0.018	6.986	0.015	81.886	0.378	215.834
14	3739.751	1.615	531.124	0.406	0.000	0.011	0.350	0.018	0.181	0.015	6.989	0.014	81.910	0.374	215.854
15	3938.100	1.999	559.484	0.376	0.003	0.011	0.370	0.016	0.180	0.015	6.992	0.014	81.945	0.372	215.874
16	996.585	0.862	137.438	0.197	0.003	0.020	0.081	0.025	0.136	0.013	7.010	0.032	82.161	0.497	215.914
Fusion	344.229	0.486	4.404	0.029	0.005	0.010	0.012	0.010	1.085	0.009	6.933	0.722	81.274	8.281	215.934
16TAS22															
1	11622.166	4.510	24.077	0.080	0.014	0.013	0.374	0.015	39.614	0.114	6.559	2.873	77.126	33.078	215.984
2	7452.401	3.486	141.928	0.177	0.000	0.013	1.314	0.032	24.257	0.044	3.112	0.280	37.012	3.304	216.004
3	1490.400	0.697	64.220	0.082	0.003	0.011	0.475	0.024	4.455	0.028	3.194	0.168	37.975	1.988	216.024
4	3613.432	1.886	241.848	0.243	0.007	0.014	1.994	0.033	9.092	0.039	4.140	0.079	49.062	0.945	216.054
5	2031.417	0.715	227.913	0.228	0.000	0.012	2.693	0.039	3.101	0.029	5.087	0.046	60.111	0.592	216.074
6	849.257	0.750	96.780	0.123	0.000	0.010	1.740	0.034	0.851	0.018	6.394	0.059	75.231	0.749	216.114
7	1214.444	0.397	126.011	0.150	0.000	0.021	3.767	0.057	0.881	0.017	7.876	0.045	92.226	0.636	216.134
8	2586.150	1.235	262.294	0.158	0.000	0.011	17.017	0.069	1.851	0.021	8.335	0.032	97.458	0.538	216.154
9	2210.230	1.191	293.168	0.248	0.009	0.015	27.893	0.086	1.726	0.033	6.551	0.037	77.042	0.535	216.174
10	2116.538	0.872	323.747	0.251	0.000	0.014	38.138	0.150	1.856	0.032	5.746	0.032	67.743	0.469	216.194
11	2985.426	0.888	500.399	0.241	0.000	0.014	55.088	0.159	2.308	0.013	5.441	0.014	64.211	0.313	216.214

12	2627.808	1.357	469.115	0.410	0.006	0.009	28.596	0.114	1.267	0.040	5.322	0.027	62.838	0.410	220.814
13	13862.844	24.791	2473.917	1.334	0.000	0.008	79.748	0.136	3.752	0.039	5.446	0.014	64.271	0.313	220.834
14	19770.585	8.904	3553.412	1.697	0.000	0.012	47.402	0.119	2.584	0.040	5.489	0.009	64.767	0.289	220.864
15	30779.748	16.935	5535.019	1.748	0.000	0.019	26.432	0.114	2.005	0.039	5.525	0.009	65.191	0.288	220.884
16	32350.380	16.313	5833.760	1.736	0.000	0.009	5.143	0.058	1.059	0.018	5.532	0.008	65.267	0.286	220.924
17	23249.340	12.290	4192.566	1.954	0.000	0.030	3.635	0.055	0.789	0.024	5.530	0.009	65.244	0.288	220.944
18	30075.354	9.055	5427.685	1.754	0.034	0.028	5.206	0.075	0.974	0.038	5.529	0.008	65.232	0.286	220.964
19	8997.456	2.987	1626.179	0.693	0.000	0.014	1.469	0.039	0.266	0.023	5.525	0.009	65.185	0.289	220.984
20	14812.015	4.295	2674.911	0.865	0.000	0.012	3.179	0.035	0.551	0.026	5.519	0.008	65.120	0.286	221.014
21	10207.223	2.177	1790.840	0.748	0.000	0.011	3.792	0.030	0.732	0.011	5.631	0.009	66.412	0.292	221.044
22	2906.860	1.638	454.636	0.258	0.000	0.014	0.941	0.034	0.330	0.017	6.236	0.015	73.413	0.349	221.054
Fusion	5692.434	2.426	718.922	0.408	0.000	0.007	0.731	0.029	1.386	0.020	7.412	0.016	86.921	0.402	221.084
16TIG16															
1	1616.957	1.179	44.395	0.072	0.000	0.010	0.088	0.017	5.262	0.036	2.134	0.303	25.564	3.601	221.134
2	5593.521	1.517	221.826	0.197	0.001	0.006	0.503	0.016	16.901	0.048	3.194	0.136	38.127	1.609	221.154
3	2817.011	1.252	125.091	0.074	0.012	0.007	0.306	0.022	8.022	0.038	3.996	0.137	47.570	1.617	221.174
4	3085.293	1.096	198.687	0.226	0.006	0.006	0.628	0.009	7.236	0.017	5.039	0.067	59.786	0.822	221.194
5	1843.476	0.652	159.698	0.164	0.005	0.011	0.613	0.031	2.938	0.032	6.285	0.070	74.262	0.865	221.804
6	2380.418	23.378	238.806	2.026	0.023	0.011	4.186	0.128	6.527	0.124	2.203	0.187	26.376	2.226	221.824
7	2040.716	2.336	203.755	0.292	0.004	0.011	6.497	0.035	3.393	0.042	5.479	0.069	64.907	0.848	221.844
8	2717.977	1.244	318.661	0.276	0.000	0.014	7.727	0.054	2.712	0.037	6.295	0.040	74.387	0.554	221.864
9	5689.561	3.237	737.397	0.607	0.008	0.011	10.155	0.083	2.470	0.041	6.897	0.022	81.336	0.423	221.904
10	8956.959	3.884	1242.188	0.739	0.000	0.010	10.746	0.075	2.626	0.032	6.707	0.015	79.148	0.368	221.924
11	8894.549	3.129	1286.258	0.906	0.000	0.013	7.497	0.033	1.510	0.037	6.661	0.014	78.615	0.364	221.954
12	10370.795	2.549	1529.084	0.475	0.026	0.010	8.178	0.085	1.407	0.043	6.597	0.013	77.881	0.355	221.974
13	9540.649	2.104	1408.768	0.603	0.000	0.011	4.602	0.035	1.403	0.036	6.549	0.013	77.317	0.352	222.014
14	7975.640	3.278	1184.040	0.763	0.009	0.010	2.948	0.042	0.958	0.039	6.560	0.015	77.450	0.361	222.054
15	7835.373	3.142	1165.058	0.862	0.002	0.014	3.561	0.030	0.933	0.024	6.556	0.013	77.408	0.351	222.074
16	3827.808	1.763	564.566	0.208	0.000	0.014	1.901	0.029	0.496	0.033	6.591	0.020	77.809	0.395	222.094
17	5942.836	2.462	873.331	0.582	0.000	0.009	3.510	0.042	0.951	0.022	6.560	0.014	77.451	0.355	222.134
18	7072.596	1.907	1013.823	0.457	0.000	0.013	5.052	0.054	1.462	0.027	6.638	0.014	78.346	0.360	222.154
19	2976.319	1.255	217.563	0.221	0.009	0.011	1.695	0.046	2.001	0.029	11.149	0.050	129.722	0.772	222.184
Fusion	1550.299	0.734	15.131	0.060	0.013	0.018	0.270	0.021	3.607	0.032	33.823	0.758	367.890	7.601	222.204
16TIG35															
1	1842.721	0.756	30.514	0.056	0.005	0.013	0.075	0.025	6.332	0.023	0.333	0.385	4.013	4.642	222.804
2	4438.606	1.267	142.739	0.118	0.017	0.015	0.215	0.017	14.140	0.067	2.444	0.206	29.276	2.448	222.824

3	1656.562	0.651	57.291	0.146	0.012	0.017	0.082	0.034	5.024	0.035	3.558	0.224	42.453	2.648	222.844
4	2690.034	1.010	115.166	0.138	0.000	0.014	0.084	0.021	7.228	0.025	5.226	0.121	62.021	1.436	222.864
5	1851.216	0.615	110.416	0.201	0.000	0.021	0.434	0.051	3.837	0.048	6.777	0.141	80.031	1.667	222.904
6	1929.133	0.784	131.287	0.128	0.000	0.021	0.129	0.037	2.041	0.027	10.262	0.071	119.847	0.942	222.924
7	1760.632	0.717	125.210	0.193	0.005	0.020	0.117	0.033	1.007	0.028	11.812	0.072	137.273	0.985	222.944
8	1770.862	0.351	135.565	0.135	0.008	0.022	0.082	0.029	0.759	0.026	11.516	0.062	133.952	0.886	222.964
9	1058.071	0.803	81.479	0.109	0.000	0.007	0.021	0.014	0.376	0.017	11.722	0.068	136.264	0.943	223.004
10	1730.536	0.446	145.152	0.123	0.003	0.009	0.090	0.022	0.620	0.018	10.755	0.043	125.405	0.702	223.014
11	1635.741	0.587	161.905	0.201	0.000	0.008	0.094	0.017	0.544	0.022	9.190	0.045	107.687	0.676	223.044
12	5007.185	2.011	610.410	0.422	0.011	0.016	0.580	0.018	1.473	0.022	7.557	0.018	89.014	0.422	223.064
13	6307.838	2.170	855.349	0.411	0.000	0.033	0.832	0.053	1.609	0.073	6.879	0.028	81.200	0.464	223.104
14	4450.546	1.365	616.860	0.182	0.000	0.028	0.515	0.043	0.866	0.032	6.856	0.019	80.937	0.399	223.124
15	2761.299	1.343	386.755	0.305	0.000	0.028	0.320	0.044	0.478	0.033	6.828	0.028	80.621	0.465	223.144
16	8068.173	1.887	1134.677	0.331	0.008	0.028	1.056	0.044	1.283	0.035	6.831	0.014	80.652	0.371	223.164
17	6881.198	1.999	969.005	0.530	0.000	0.031	0.850	0.043	1.061	0.036	6.832	0.016	80.660	0.379	223.184
18	1533.212	0.849	219.205	0.171	0.000	0.008	0.706	0.029	1.067	0.023	5.646	0.034	66.916	0.487	228.064
19	4337.128	2.386	615.003	0.231	0.000	0.007	1.009	0.036	1.328	0.028	6.480	0.018	76.591	0.380	228.084
20	3197.099	1.892	448.382	0.423	0.000	0.008	0.827	0.028	1.218	0.032	6.397	0.025	75.638	0.428	228.114
21	1442.963	0.668	194.340	0.286	0.000	0.007	0.641	0.025	1.133	0.024	5.801	0.040	68.715	0.549	228.134
22	295.316	0.161	31.066	0.070	0.000	0.009	0.010	0.027	0.257	0.017	7.154	0.165	84.383	1.930	228.174
Fusion	498.660	0.243	7.999	0.034	0.000	0.008	0.029	0.023	1.526	0.024	7.183	0.912	84.710	10.518	228.764
16AOU17															
1	394.151	0.296	49.282	0.081	0.000	0.006	0.006	0.027	0.979	0.022	2.262	0.136	27.081	1.618	228.804
2	994.198	0.458	123.857	0.159	0.000	0.008	0.017	0.023	2.307	0.026	2.650	0.069	31.686	0.826	228.824
3	366.980	0.369	59.966	0.077	0.008	0.008	0.000	0.027	0.523	0.015	3.617	0.078	43.105	0.934	228.844
4	731.473	0.283	123.604	0.219	0.001	0.009	0.000	0.027	0.570	0.014	4.609	0.038	54.749	0.495	228.864
5	529.617	0.307	84.117	0.129	0.009	0.008	0.000	0.024	0.253	0.015	5.456	0.054	64.639	0.681	228.914
6	926.350	0.560	141.615	0.124	0.003	0.007	0.004	0.027	0.439	0.022	5.677	0.047	67.206	0.612	228.934
7	2744.113	1.514	430.124	0.342	0.000	0.009	0.000	0.018	1.136	0.027	5.648	0.023	66.868	0.381	228.964
8	5853.191	1.724	966.387	0.602	0.000	0.007	0.153	0.017	1.552	0.032	5.626	0.014	66.606	0.322	228.984
9	5892.008	2.026	990.327	0.413	0.000	0.009	0.145	0.032	0.953	0.028	5.705	0.013	67.531	0.315	229.014
10	13281.803	5.855	2251.451	1.575	0.000	0.009	0.467	0.041	1.421	0.025	5.752	0.010	68.071	0.306	229.034
11	10180.537	6.548	1740.490	1.629	0.000	0.009	0.379	0.033	0.619	0.027	5.782	0.011	68.419	0.312	229.054
12	11582.463	5.551	1971.315	1.311	0.000	0.013	0.435	0.034	0.629	0.032	5.819	0.011	68.851	0.310	229.084
13	7147.332	2.649	1213.733	0.720	0.000	0.018	0.201	0.040	0.371	0.031	5.835	0.012	69.044	0.316	229.114
14	8127.176	2.178	1377.623	0.806	0.000	0.009	0.221	0.030	0.505	0.025	5.828	0.011	68.963	0.310	229.134

15	984.336	0.561	128.645	0.109	0.000	0.006	0.000	0.029	0.812	0.019	5.859	0.046	69.319	0.605	229.154
16	157.092	0.262	23.551	0.096	0.013	0.010	0.030	0.014	0.085	0.020	5.671	0.251	67.137	2.931	233.784
Fusion	223.635	0.236	14.889	0.040	0.000	0.018	0.000	0.029	0.486	0.017	5.610	0.337	66.430	3.932	233.794
16TAS02															
1	67569.670	10.415	17.043	0.089	0.042	0.024	0.280	0.019	235.425	0.274	-34.311	21.529	-469.333	336.259	233.844
2	9746.693	3.601	39.951	0.057	0.005	0.010	0.111	0.013	33.311	0.051	2.631	1.329	31.419	15.738	233.864
3	3595.444	1.276	17.257	0.023	0.000	0.014	0.108	0.023	12.216	0.055	3.495	1.430	41.623	16.837	233.884
4	4326.945	2.030	31.207	0.055	0.003	0.016	0.039	0.021	14.597	0.049	3.275	0.850	39.027	10.023	233.924
5	22880.106	4.291	140.979	0.097	0.000	0.014	0.148	0.027	76.668	0.105	4.901	0.863	58.107	10.065	233.944
6	8629.930	2.318	77.881	0.124	0.000	0.012	0.096	0.017	28.548	0.110	4.732	0.698	56.132	8.156	233.964
7	9982.086	3.586	171.011	0.178	0.000	0.011	0.088	0.029	31.682	0.047	4.772	0.300	56.595	3.510	233.984
8	4827.845	1.937	145.304	0.167	0.000	0.010	0.036	0.025	14.268	0.029	4.830	0.167	57.277	1.962	234.014
9	4178.295	2.374	320.994	0.338	0.000	0.010	0.017	0.015	9.040	0.014	4.892	0.052	58.002	0.648	234.034
10	2102.101	0.779	344.308	0.210	0.000	0.012	0.005	0.015	1.187	0.015	5.137	0.018	60.853	0.328	234.064
11	3473.719	1.018	610.779	0.326	0.002	0.011	0.068	0.016	1.038	0.012	5.226	0.012	61.892	0.290	234.084
12	6530.254	1.959	1163.949	0.444	0.001	0.012	0.125	0.025	1.302	0.021	5.318	0.011	62.959	0.288	234.124
13	16670.581	5.190	2956.261	1.286	0.000	0.021	0.383	0.026	2.515	0.029	5.425	0.009	64.205	0.287	234.144
14	20222.642	3.910	3605.908	1.260	0.019	0.026	0.452	0.021	1.965	0.020	5.483	0.009	64.879	0.286	234.174
15	20467.758	7.254	3663.835	1.533	0.018	0.021	0.523	0.023	1.471	0.037	5.503	0.009	65.111	0.288	234.194
16	18546.369	1.466	3346.912	0.943	0.000	0.013	0.457	0.033	0.855	0.022	5.500	0.008	65.078	0.285	234.784
17	11316.230	4.925	2038.742	1.669	0.000	0.013	0.302	0.040	0.571	0.022	5.502	0.010	65.105	0.292	234.804
18	20820.635	3.220	3736.322	1.059	0.000	0.017	0.451	0.037	1.198	0.020	5.512	0.008	65.220	0.286	234.824
19	16488.263	3.237	2946.246	1.173	0.000	0.017	0.424	0.033	1.092	0.035	5.522	0.009	65.333	0.289	234.854
20	11018.078	3.196	1968.766	0.760	0.003	0.016	0.282	0.021	0.734	0.037	5.521	0.010	65.326	0.294	234.884
21	13316.119	5.765	2375.173	1.614	0.054	0.017	0.257	0.031	1.096	0.030	5.505	0.010	65.138	0.293	234.904
22	1926.482	1.885	334.184	0.268	0.000	0.011	0.027	0.020	0.288	0.034	5.547	0.032	65.628	0.459	234.924
Fusion	9950.907	3.652	1600.698	1.206	0.000	0.016	0.228	0.021	3.974	0.039	5.531	0.014	65.436	0.315	234.944
16TAS06															
1	1315.150	1.012	6.116	0.048	0.000	0.009	0.065	0.025	4.526	0.026	0.623	1.689	7.480	20.238	234.984
2	5262.133	2.627	76.590	0.057	0.009	0.011	0.137	0.023	17.614	0.031	2.073	0.374	24.778	4.442	235.004
3	2001.006	0.863	71.804	0.061	0.000	0.006	0.126	0.023	6.425	0.040	1.957	0.213	23.404	2.526	235.014
4	2181.989	0.738	67.301	0.133	0.000	0.008	0.065	0.018	6.771	0.038	3.286	0.230	39.125	2.710	235.044
5	3891.749	0.970	117.042	0.117	0.000	0.013	0.116	0.026	11.468	0.028	4.885	0.171	57.852	2.008	235.074
6	1403.987	0.749	49.415	0.079	0.002	0.013	0.049	0.024	3.729	0.042	6.585	0.279	77.562	3.227	235.094
7	2566.256	1.164	108.903	0.121	0.000	0.016	0.037	0.025	5.665	0.051	8.538	0.165	99.931	1.919	235.114

8	3889.641	1.092	202.060	0.148	0.006	0.004	0.126	0.026	5.385	0.030	11.596	0.071	134.430	0.965	235.774
9	4156.186	3.393	230.753	0.321	0.003	0.004	1.145	0.058	4.715	0.094	12.212	0.129	141.297	1.551	235.784
10	2090.179	0.696	111.473	0.096	0.011	0.004	0.354	0.023	1.438	0.014	15.133	0.056	173.521	0.932	235.804
11	4728.041	2.174	261.841	0.250	0.000	0.016	0.327	0.020	1.906	0.037	16.051	0.055	183.532	0.954	235.834
12	6225.738	2.049	381.067	0.239	0.006	0.005	0.148	0.027	1.573	0.021	15.231	0.033	174.592	0.793	235.864
13	4794.069	1.758	384.238	0.300	0.020	0.007	0.125	0.024	1.474	0.022	11.433	0.028	132.602	0.627	235.894
14	3245.044	1.904	327.801	0.319	0.002	0.010	0.048	0.028	0.887	0.012	9.167	0.022	107.091	0.507	235.914
15	4438.309	3.092	513.992	0.333	0.009	0.009	0.162	0.030	1.126	0.013	8.048	0.018	94.343	0.437	235.934
16	7806.865	3.932	988.594	0.586	0.004	0.009	0.528	0.027	1.867	0.019	7.396	0.015	86.882	0.397	235.974
17	6598.470	2.383	869.449	0.576	0.007	0.012	0.471	0.037	1.466	0.027	7.145	0.016	84.009	0.391	235.994
18	9575.886	2.381	1288.838	0.437	0.000	0.011	0.747	0.031	2.024	0.015	7.019	0.012	82.559	0.369	236.014
19	8364.349	2.085	1138.083	0.696	0.000	0.017	0.643	0.023	1.790	0.021	6.938	0.014	81.620	0.371	236.044
20	6854.208	3.782	948.769	0.966	0.000	0.014	0.540	0.028	1.245	0.019	6.888	0.015	81.045	0.375	236.064
21	7442.923	2.583	1035.144	0.460	0.007	0.011	0.579	0.018	1.190	0.020	6.901	0.013	81.195	0.366	236.114
22	5547.265	1.963	772.858	0.240	0.000	0.008	0.435	0.029	0.893	0.020	6.886	0.014	81.028	0.368	236.134
23	11781.400	3.148	1639.813	1.005	0.000	0.009	0.981	0.032	1.888	0.016	6.895	0.012	81.128	0.362	236.144
24	7640.138	5.325	1056.440	0.967	0.003	0.009	0.583	0.026	1.345	0.017	6.907	0.014	81.263	0.374	236.164
25	10693.977	0.899	1498.800	0.482	0.000	0.006	0.800	0.017	1.468	0.024	6.894	0.012	81.124	0.360	236.794
26	9632.074	4.295	1295.515	0.898	0.000	0.014	0.655	0.016	2.455	0.028	6.929	0.015	81.520	0.376	236.814
Fusion	2370.241	1.340	168.257	0.152	0.000	0.008	0.085	0.018	3.941	0.047	7.344	0.094	86.291	1.130	236.834
16AOU11															
1	325.999	0.221	48.783	0.071	0.000	0.011	0.000	0.026	0.784	0.020	2.032	0.122	24.258	1.453	236.874
2	1107.258	0.620	167.963	0.205	0.000	0.013	0.000	0.029	2.282	0.030	2.668	0.058	31.789	0.696	236.894
3	257.333	0.319	51.471	0.041	0.000	0.012	0.000	0.026	0.327	0.021	3.177	0.122	37.791	1.441	236.914
4	572.978	0.306	118.077	0.165	0.000	0.011	0.000	0.019	0.468	0.023	3.723	0.058	44.209	0.710	236.934
5	628.511	0.539	116.993	0.085	0.020	0.016	0.000	0.034	0.395	0.023	4.418	0.058	52.342	0.716	236.974
6	834.087	0.418	142.113	0.140	0.000	0.013	0.006	0.022	0.450	0.016	4.978	0.035	58.871	0.477	236.994
7	1483.626	0.568	245.119	0.188	0.002	0.009	0.013	0.023	0.564	0.008	5.415	0.015	63.950	0.319	237.014
8	902.637	0.451	150.093	0.154	0.007	0.009	0.000	0.026	0.277	0.018	5.509	0.037	65.039	0.506	237.034
9	2314.750	1.050	391.548	0.323	0.005	0.004	0.093	0.027	0.612	0.031	5.491	0.026	64.828	0.399	237.064
10	5424.119	2.401	925.744	0.510	0.014	0.007	0.241	0.025	1.195	0.017	5.518	0.011	65.141	0.300	237.094
11	5019.639	1.853	863.610	0.681	0.000	0.009	0.209	0.033	0.822	0.029	5.569	0.014	65.737	0.316	237.114
12	18649.145	4.003	3214.076	0.592	0.000	0.008	0.651	0.023	2.130	0.061	5.643	0.010	66.592	0.300	237.134
13	15764.008	20.885	2681.862	2.912	0.016	0.014	1.779	0.043	2.539	0.015	5.641	0.013	66.572	0.316	237.164
14	92.961	0.073	15.520	0.033	0.000	0.008	0.000	0.023	0.018	0.013	5.692	0.246	67.167	2.859	255.004
15	131.579	0.165	22.169	0.055	0.003	0.008	0.021	0.017	0.020	0.011	5.715	0.142	67.423	1.672	255.024

16	324.195	0.240	54.955	0.132	0.000	0.009	0.029	0.034	0.064	0.012	5.599	0.065	66.085	0.804	255.044
Fusion	1396.878	0.780	182.687	0.186	0.000	0.009	0.057	0.018	1.279	0.017	5.651	0.033	66.686	0.473	255.064
16AOU13															
1	896.090	0.679	24.378	0.049	0.000	0.011	0.027	0.030	3.002	0.021	1.083	0.315	12.957	3.755	255.124
2	2314.457	0.851	215.154	0.160	0.000	0.009	0.063	0.027	6.323	0.045	2.253	0.078	26.858	0.927	255.144
3	373.905	0.309	47.626	0.040	0.001	0.008	0.058	0.027	0.820	0.013	2.891	0.085	34.386	1.006	255.164
4	588.224	0.329	96.911	0.081	0.000	0.010	0.000	0.028	0.968	0.020	3.190	0.062	37.906	0.748	255.184
5	490.147	0.359	95.722	0.265	0.000	0.014	0.000	0.038	0.397	0.014	3.938	0.046	46.686	0.572	255.204
6	832.090	1.022	156.898	0.214	0.009	0.008	0.000	0.025	0.491	0.017	4.419	0.034	52.306	0.455	255.794
7	1075.427	0.470	186.553	0.120	0.000	0.005	0.000	0.025	0.507	0.014	5.003	0.025	59.105	0.379	255.814
8	2364.876	1.696	396.667	0.382	0.000	0.007	0.024	0.026	0.831	0.015	5.384	0.017	63.521	0.326	255.834
9	2842.716	1.052	478.857	0.341	0.003	0.005	0.027	0.025	0.857	0.023	5.447	0.018	64.257	0.337	255.854
10	4400.205	1.757	749.031	0.615	0.000	0.006	0.096	0.028	0.982	0.014	5.525	0.012	65.161	0.302	255.874
11	4530.411	2.845	771.575	0.662	0.000	0.010	0.173	0.031	0.679	0.017	5.649	0.013	66.599	0.311	255.914
12	6171.721	3.870	1049.758	0.830	0.000	0.012	0.208	0.030	0.799	0.020	5.691	0.012	67.084	0.309	255.934
13	20916.131	7.527	3556.878	2.023	0.000	0.008	0.640	0.029	1.657	0.026	5.779	0.009	68.092	0.302	255.964
14	3658.319	2.635	624.328	0.390	0.000	0.012	0.188	0.029	0.265	0.011	5.771	0.011	68.009	0.309	255.984
15	12229.269	12.386	2084.771	0.961	0.012	0.011	0.459	0.041	0.778	0.016	5.792	0.011	68.244	0.308	256.004
16	5089.109	1.617	867.757	0.391	0.000	0.006	0.139	0.023	0.260	0.017	5.811	0.010	68.465	0.307	256.044
17	12157.271	7.720	2053.553	1.801	0.002	0.011	0.392	0.019	0.990	0.016	5.814	0.011	68.499	0.309	256.064
18	2553.065	1.462	406.163	0.163	0.000	0.007	0.102	0.018	0.721	0.030	5.805	0.025	68.402	0.400	256.084
Fusion	741.820	0.574	45.372	0.058	0.000	0.009	0.023	0.022	1.674	0.027	5.692	0.184	67.087	2.146	256.114
16TAS30															
1	2335.707	1.418	11.902	0.040	0.000	0.010	0.000	0.034	8.055	0.036	0.074	1.360	0.885	16.305	256.154
2	4530.413	1.668	104.070	0.215	0.000	0.009	0.000	0.028	14.978	0.028	1.824	0.236	21.745	2.798	256.174
3	1833.026	0.971	81.014	0.122	0.000	0.006	0.052	0.021	5.697	0.038	2.263	0.175	26.948	2.072	256.794
4	4674.429	2.237	245.877	0.389	0.000	0.007	0.053	0.024	13.208	0.045	3.461	0.102	41.046	1.207	256.814
5	1356.850	0.795	158.520	0.150	0.000	0.009	0.000	0.024	1.371	0.011	6.085	0.030	71.556	0.453	256.834
6	1587.094	1.071	173.977	0.277	0.000	0.008	0.005	0.033	0.924	0.018	7.624	0.038	89.215	0.566	256.864
7	1845.321	1.276	176.042	0.206	0.009	0.009	0.328	0.033	1.184	0.026	8.610	0.050	100.435	0.705	256.884
8	469.376	0.417	57.534	0.052	0.005	0.010	0.000	0.024	0.111	0.014	7.638	0.074	89.379	0.919	257.064
9	1872.123	1.206	240.100	0.296	0.000	0.012	0.020	0.022	0.394	0.027	7.362	0.037	86.216	0.550	257.084
10	1238.598	0.685	166.679	0.090	0.000	0.008	0.009	0.031	0.358	0.015	6.846	0.030	80.310	0.474	257.104
11	2249.019	1.030	304.463	0.279	0.000	0.007	0.079	0.019	1.018	0.015	6.456	0.021	75.824	0.397	257.124
12	2729.872	1.805	414.073	0.208	0.000	0.010	0.038	0.028	0.708	0.024	6.131	0.021	72.086	0.382	257.144
13	4288.951	1.864	688.423	0.479	0.013	0.013	0.105	0.028	0.957	0.013	5.860	0.012	68.964	0.318	257.174

14	7205.848	5.616	1205.173	1.136	0.009	0.014	0.119	0.016	1.548	0.018	5.638	0.013	66.392	0.310	257.194
15	5034.386	3.454	873.462	0.698	0.007	0.011	0.117	0.017	0.559	0.020	5.610	0.012	66.068	0.307	257.804
16	7926.981	6.003	1375.211	0.987	0.001	0.012	0.177	0.025	0.928	0.017	5.600	0.011	65.953	0.300	257.824
17	7582.518	4.797	1333.875	0.660	0.000	0.014	0.150	0.024	0.549	0.022	5.596	0.010	65.912	0.298	259.024
18	15551.938	11.669	2725.543	2.728	0.000	0.012	0.443	0.029	1.289	0.021	5.601	0.011	65.964	0.301	259.044
19	21790.861	14.830	3831.006	2.055	0.000	0.022	0.453	0.028	1.431	0.038	5.611	0.010	66.081	0.296	259.074
20	18834.189	6.788	3317.254	1.306	0.000	0.016	0.441	0.028	1.171	0.028	5.607	0.009	66.033	0.292	259.094
21	12615.799	9.570	2225.060	1.274	0.000	0.018	0.364	0.037	0.691	0.025	5.612	0.010	66.092	0.297	259.114
22	27522.341	33.013	4860.525	5.837	0.015	0.028	0.592	0.029	1.289	0.014	5.617	0.012	66.150	0.309	259.154
23	18475.404	6.981	3251.394	1.114	0.000	0.015	0.393	0.016	1.041	0.008	5.621	0.009	66.196	0.291	259.174
24	16988.929	11.350	2988.447	1.825	0.000	0.020	0.421	0.024	0.949	0.019	5.624	0.010	66.239	0.296	259.204
25	17031.724	10.258	3015.585	1.588	0.000	0.020	0.314	0.027	0.538	0.014	5.627	0.009	66.270	0.293	261.824
26	8038.493	5.493	1424.111	0.964	0.011	0.012	0.183	0.024	0.297	0.017	5.615	0.010	66.135	0.297	261.844
27	28773.560	19.717	5058.539	4.034	0.057	0.031	0.627	0.025	1.580	0.022	5.629	0.010	66.290	0.297	261.864
28	7609.878	5.556	1255.457	1.133	0.037	0.009	0.232	0.027	1.669	0.032	5.709	0.014	67.216	0.321	261.884
Fusion	2540.387	0.945	59.113	0.114	0.000	0.011	0.134	0.028	7.658	0.068	5.490	0.395	64.680	4.581	261.904
16TIG28															
1	3241.825	0.913	8.664	0.038	0.007	0.009	0.058	0.036	11.385	0.055	-6.662	2.714	-81.643	34.024	262.054
2	11219.275	9.640	141.779	0.085	0.015	0.011	0.244	0.024	37.813	0.035	1.862	0.420	22.171	4.974	262.074
3	1356.687	0.792	26.808	0.049	0.007	0.010	0.081	0.023	4.368	0.020	3.445	0.335	40.811	3.924	262.094
4	7885.105	5.165	140.813	0.218	0.019	0.010	0.163	0.039	25.908	0.047	2.698	0.302	32.047	3.557	262.124
5	9313.980	4.698	191.031	0.215	0.000	0.008	0.202	0.026	28.857	0.079	5.014	0.266	59.101	3.098	262.154
6	5048.360	5.182	151.892	0.219	0.013	0.007	0.155	0.029	14.019	0.066	6.535	0.199	76.661	2.302	262.174
7	3674.933	2.268	162.391	0.146	0.000	0.007	0.131	0.026	8.033	0.033	8.351	0.106	97.398	1.267	262.194
8	2567.870	1.853	146.221	0.146	0.009	0.007	0.215	0.031	3.722	0.015	10.266	0.062	119.001	0.852	262.794
9	1851.150	2.301	115.097	0.200	0.002	0.006	0.206	0.032	2.080	0.034	10.938	0.099	126.526	1.219	262.814
10	5308.464	2.347	382.479	0.153	0.000	0.006	0.515	0.035	4.557	0.012	10.507	0.034	121.705	0.627	262.834
11	2802.156	0.897	241.414	0.193	0.012	0.006	0.242	0.035	1.569	0.016	9.795	0.031	113.710	0.580	262.854
12	3727.547	3.528	392.836	0.439	0.005	0.006	0.270	0.038	1.715	0.036	8.280	0.034	96.584	0.556	262.874
13	4455.401	2.776	526.580	0.502	0.000	0.007	0.231	0.027	1.607	0.013	7.625	0.019	89.128	0.424	262.914
14	6526.146	5.194	813.966	0.705	0.000	0.013	0.385	0.027	2.056	0.018	7.333	0.017	85.797	0.405	262.934
15	2484.444	2.177	315.865	0.355	0.000	0.008	0.206	0.037	0.710	0.023	7.264	0.027	85.009	0.465	262.964
16	2584.655	0.832	332.838	0.266	0.000	0.007	0.144	0.031	0.684	0.014	7.215	0.019	84.451	0.410	262.984
17	4063.052	2.677	529.115	0.380	0.000	0.011	0.218	0.042	0.899	0.017	7.232	0.017	84.645	0.398	263.004
18	8783.274	4.595	1161.789	0.797	0.019	0.011	0.606	0.036	1.660	0.015	7.193	0.014	84.200	0.381	263.064
19	10063.907	5.897	1338.199	0.918	0.016	0.011	0.789	0.024	1.758	0.021	7.188	0.014	84.143	0.382	263.084

20	5697.602	1.837	758.456	0.362	0.016	0.011	0.496	0.019	0.995	0.021	7.182	0.015	84.066	0.385	263.104
21	4064.536	1.670	543.228	0.284	0.012	0.011	0.322	0.018	0.688	0.018	7.164	0.016	83.860	0.389	263.124
22	9380.057	3.012	1255.997	0.332	0.007	0.011	0.749	0.029	1.383	0.015	7.198	0.012	84.253	0.373	263.144
23	14083.549	7.225	1872.264	1.461	0.005	0.005	1.152	0.033	1.881	0.023	7.281	0.014	85.198	0.383	263.184
24	10248.884	7.230	1357.179	0.891	0.000	0.008	0.776	0.056	1.515	0.018	7.277	0.014	85.156	0.385	263.204
Fusion	8766.674	4.673	951.042	0.710	0.010	0.008	0.587	0.021	5.952	0.048	7.455	0.025	87.186	0.462	263.794
16TAS49															
1	2986.682	2.585	5.396	0.035	0.000	0.012	0.000	0.033	10.296	0.027	0.431	3.294	5.184	39.544	277.864
2	9472.434	3.474	128.503	0.114	0.006	0.010	0.175	0.032	30.948	0.034	3.956	0.381	47.005	4.469	277.894
3	1179.248	0.946	39.604	0.067	0.000	0.009	0.048	0.038	3.495	0.066	4.246	0.504	50.407	5.899	277.904
4	3091.916	4.102	73.025	0.099	0.000	0.010	0.183	0.031	9.684	0.021	3.982	0.231	47.312	2.717	277.924
5	2693.820	1.082	90.847	0.139	0.000	0.007	0.183	0.035	7.477	0.047	5.874	0.203	69.368	2.366	277.944
6	2690.638	1.598	114.897	0.172	0.000	0.010	0.350	0.027	6.512	0.047	7.100	0.153	83.515	1.792	277.984
7	2690.785	2.609	101.462	0.166	0.000	0.009	0.849	0.031	6.372	0.055	8.568	0.192	100.312	2.229	278.004
8	1458.593	0.909	77.114	0.110	0.000	0.009	1.587	0.030	2.935	0.035	8.432	0.151	98.766	1.766	278.024
9	2583.426	0.914	142.454	0.139	0.000	0.009	6.592	0.046	5.566	0.048	7.985	0.120	93.658	1.430	278.044
10	1849.053	1.475	104.618	0.102	0.000	0.016	8.578	0.045	4.303	0.024	7.802	0.097	91.562	1.170	278.064
11	2614.852	1.617	148.199	0.143	0.006	0.007	17.381	0.078	6.505	0.026	7.838	0.088	91.973	1.081	278.094
12	6038.222	4.581	397.838	0.355	0.000	0.010	51.052	0.090	14.853	0.071	7.535	0.080	88.504	0.982	278.114
13	3975.925	4.989	323.138	0.561	0.000	0.008	38.725	0.110	9.087	0.031	7.113	0.056	83.662	0.733	278.134
14	5661.813	2.458	573.376	0.297	0.003	0.007	52.129	0.168	10.165	0.039	6.989	0.037	82.237	0.540	278.164
15	9331.400	3.546	1112.808	1.111	0.025	0.013	61.262	0.161	11.732	0.026	6.704	0.023	78.952	0.420	278.174
16	6996.634	2.279	916.998	0.614	0.000	0.005	25.500	0.146	5.995	0.050	6.656	0.023	78.406	0.422	291.924
17	4225.901	1.171	572.800	0.308	0.004	0.004	12.291	0.081	2.900	0.021	6.629	0.019	78.086	0.387	291.944
18	4339.141	1.987	612.438	0.503	0.001	0.007	9.043	0.049	2.034	0.021	6.628	0.017	78.074	0.379	291.964
19	7613.592	2.474	1106.147	0.614	0.000	0.006	8.759	0.065	2.033	0.031	6.637	0.014	78.179	0.362	291.984
20	10589.515	3.417	1548.139	0.944	0.000	0.006	5.170	0.029	1.485	0.014	6.703	0.011	78.941	0.351	292.024
21	6412.956	3.255	925.501	0.796	0.005	0.007	1.807	0.034	0.727	0.015	6.798	0.013	80.040	0.362	292.044
22	2641.784	1.788	346.946	0.281	0.000	0.005	0.980	0.029	0.457	0.011	7.361	0.017	86.509	0.406	292.064
23	1058.095	1.006	122.251	0.144	0.000	0.005	0.273	0.036	0.218	0.013	8.252	0.037	96.709	0.576	292.084
Fusion	417.894	0.265	35.155	0.074	0.000	0.006	0.020	0.024	0.138	0.008	10.821	0.078	125.793	1.016	292.104
16AOU10															
1	7045.205	3.407	14.238	0.055	0.029	0.007	0.051	0.032	24.283	0.052	0.574	2.820	6.852	33.622	292.144
2	4666.797	2.148	113.242	0.116	0.009	0.007	0.061	0.024	15.100	0.066	2.588	0.269	30.717	3.163	292.154
3	2330.833	1.644	75.546	0.094	0.000	0.006	0.000	0.022	7.269	0.022	2.977	0.173	35.283	2.042	292.794
4	2693.212	1.801	118.935	0.167	0.007	0.006	0.039	0.026	7.770	0.019	3.737	0.116	44.182	1.362	292.824

5	1403.250	0.791	99.938	0.133	0.004	0.006	0.000	0.029	3.230	0.027	4.694	0.097	55.334	1.153	292.844
6	1056.537	0.713	106.546	0.120	0.000	0.007	0.000	0.029	1.356	0.020	6.259	0.062	73.405	0.771	292.864
7	1245.454	0.635	149.956	0.226	0.006	0.007	0.000	0.020	0.623	0.011	7.137	0.029	83.465	0.478	292.904
8	2185.747	1.574	312.696	0.202	0.000	0.009	0.000	0.021	0.435	0.009	6.620	0.016	77.546	0.366	292.924
9	2027.862	0.947	318.291	0.281	0.009	0.011	0.021	0.018	0.276	0.008	6.152	0.013	72.177	0.335	292.944
10	1972.298	0.802	315.486	0.427	0.001	0.008	0.058	0.018	0.251	0.010	6.057	0.016	71.078	0.344	293.024
11	2194.912	1.288	351.200	0.430	0.009	0.010	0.061	0.023	0.285	0.011	6.050	0.016	71.001	0.343	293.034
12	1264.297	0.936	201.010	0.242	0.000	0.008	0.000	0.019	0.181	0.010	6.059	0.020	71.111	0.373	293.054
13	1801.153	0.607	285.516	0.235	0.007	0.008	0.077	0.026	0.221	0.013	6.123	0.017	71.844	0.356	293.074
14	3831.726	1.485	597.887	0.568	0.000	0.005	0.058	0.029	0.355	0.012	6.271	0.013	73.545	0.338	293.114
15	7406.434	2.388	1152.317	0.887	0.028	0.003	0.256	0.025	0.638	0.016	6.306	0.011	73.943	0.332	293.134
16	2132.421	1.215	332.152	0.201	0.004	0.003	0.075	0.026	0.202	0.010	6.282	0.014	73.675	0.344	293.154
17	4296.902	2.123	671.334	0.350	0.016	0.006	0.183	0.024	0.374	0.015	6.279	0.012	73.637	0.335	293.174
18	3942.648	1.651	616.489	0.604	0.015	0.007	0.174	0.026	0.379	0.014	6.257	0.013	73.386	0.339	293.194
19	1342.465	0.970	207.520	0.239	0.004	0.008	0.087	0.035	0.153	0.008	6.300	0.018	73.877	0.371	293.794
Fusion	110.586	0.245	11.800	0.077	0.009	0.008	0.077	0.035	0.083	0.010	7.594	0.265	88.683	3.041	293.814
16TIG29															
1	925.926	0.922	5.917	0.023	0.011	0.006	0.059	0.030	3.191	0.016	0.475	1.148	5.674	13.680	293.844
2	3303.689	1.231	42.565	0.054	0.002	0.006	0.307	0.021	10.876	0.057	3.801	0.554	44.887	6.469	293.864
3	840.841	0.767	21.911	0.038	0.000	0.006	0.114	0.020	2.417	0.009	6.604	0.221	77.282	2.555	293.894
4	1343.240	0.726	53.602	0.062	0.000	0.009	0.557	0.024	3.002	0.008	9.227	0.109	107.084	1.303	293.914
5	596.493	0.528	32.361	0.100	0.000	0.008	0.322	0.026	0.829	0.012	11.407	0.126	131.491	1.503	293.944
6	625.813	0.435	34.573	0.128	0.007	0.008	0.396	0.022	0.606	0.011	13.496	0.118	154.565	1.439	293.964
7	1359.090	0.437	83.993	0.068	0.001	0.007	1.402	0.031	1.099	0.016	13.039	0.069	149.538	0.974	293.984
8	209.807	0.206	15.335	0.041	0.006	0.007	0.330	0.027	0.192	0.011	10.850	0.220	125.278	2.511	294.004
9	1343.268	0.878	121.866	0.157	0.004	0.004	3.513	0.041	1.409	0.011	8.691	0.040	101.032	0.618	294.034
10	401.133	0.452	40.594	0.063	0.000	0.008	1.453	0.035	0.477	0.012	7.715	0.098	89.970	1.180	294.054
11	1344.318	0.820	148.677	0.229	0.006	0.007	4.501	0.058	1.300	0.009	7.562	0.032	88.223	0.515	294.074
12	4177.965	1.935	493.097	0.262	0.003	0.007	7.722	0.063	1.967	0.016	7.883	0.019	91.883	0.434	294.094
13	3569.991	2.030	445.449	0.303	0.000	0.006	2.114	0.049	0.549	0.012	7.857	0.016	91.581	0.419	294.134
14	3984.400	1.850	500.710	0.202	0.009	0.005	2.131	0.040	0.525	0.021	7.837	0.017	91.350	0.425	294.154
15	2957.629	1.709	378.679	0.200	0.003	0.009	1.607	0.030	0.295	0.013	7.767	0.016	90.555	0.415	294.174
16	3224.735	1.421	418.333	0.221	0.000	0.004	1.778	0.031	0.304	0.007	7.687	0.013	89.648	0.398	296.794
17	2507.469	1.292	326.713	0.223	0.006	0.004	1.499	0.031	0.239	0.008	7.664	0.015	89.383	0.405	296.814
18	1458.363	0.672	188.162	0.228	0.007	0.005	0.894	0.022	0.164	0.010	7.705	0.022	89.853	0.445	296.834
19	628.475	0.585	67.688	0.106	0.000	0.004	0.380	0.023	0.151	0.006	8.882	0.037	103.197	0.598	296.854

Fusion	552.268	0.480	23.963	0.096	0.000	0.005	0.145	0.028	0.378	0.006	18.807	0.127	211.938	1.596	296.874